David M. Parham
Joseph D. Khoury
M. Beth McCarville
Editors

Pediatric Malignancies: Pathology and Imaging

Springer

David M. Parham • Joseph D. Khoury
M. Beth McCarville
Editors

Pediatric Malignancies: Pathology and Imaging

Springer

Editors
David M. Parham
Department of Pathology and Laboratory Medicine
Children's Hospital Los Angeles
University of Southern California
Los Angeles, CA, USA

M. Beth McCarville
Department of Radiological Sciences
St. Jude Children's Research Hospital
Memphis, TN, USA

Joseph D. Khoury
Associate Professor of Pathology and Laboratory Medicine
The University of Texas M.D. Anderson Cancer Center
Houston, TX, USA

ISBN 978-1-4939-1728-0 ISBN 978-1-4939-1729-7 (eBook)
DOI 10.1007/978-1-4939-1729-7
Springer New York Heidelberg Dordrecht London

Library of Congress Control Number: 2014953849

Preface

The past 30 years bear witness to a profound evolution in our ability to diagnose pediatric cancers. What were once common diagnostic dilemmas are now routinely categorized with the help of ancillary tests such as immunohistochemistry, fluorescence in situ hybridization, and a myriad of molecular diagnostics tools. We are now moving into an unprecedented new realm wherein personalized medicine will require panels of tests not only for diagnosis but also for customizable therapy guided by somatic mutation analysis. As our ability to diagnose pediatric cancer has steadily grown, our diagnostic specimens have shrunk. Previous surgical approaches often required complete and sometimes radical tumor excision prior to embarking on therapy. Now, however, we initially obtain small biopsies for tumors that are treated with neoadjuvant therapy and subsequently excised. These biopsies may include fine-needle specimens that minimize the cost and morbidity of biopsy. Unlike the images of classical pathology texts, our gross excisions are now often distorted by the results of chemoreductive therapy. This makes gross pathology less useful for diagnosis, while increasing our reliance on imaging studies for evaluation of patient material. Despite the sophistication of genetic advances, the importance of a solid diagnostic foundation based on routine microscopy and diagnostic imaging studies continues to have a prominent place in daily clinical practice.

Many common denominators are shared between diagnostic pathology and diagnostic imaging, despite differences in the tools of each of the trades. Both necessitate a broad fund of knowledge of human diseases, a reliance on morphological skills, attention to intricate details, and a mastery of judicious use of complex techniques to examine tissues and organs. In spite of such interdependence, few textbooks address the important interplay between pathology and diagnostic radiology. It is our hope and intention that this textbook will offer pathologists a basic knowledge of diagnostic imaging and will give diagnostic radiologists a fundamental understanding of the pathology of pediatric cancers. We strongly believe that such knowledge inevitably leads to better patient care, our ultimate common denominator. This book is recommended for pathologists, radiologists, and oncologists who diagnose and treat childhood cancers. It is also intended to serve as a reference for those who wish a more in-depth knowledge of diagnostic imaging, pathology, and genetic approaches to childhood cancers. Because of page limitations, we have purposely avoided reference to benign entities, except within the context of a differential diagnosis. However, some entities that are included may have a "benign" behavior in the majority of patients, but possess the potential for metastasis in some. Our ability to predict metastasis is evolving, and we expect that future studies will yield more reliable ways to determine metastatic potential.

We wish to thank our publisher, Springer, for their patience in allowing us to assemble this multidisciplinary text, and our editors, Richard Hruska and Elizabeth Orthmann, for their help in facilitating it. We would also like to thank our chapter authors for their generous assistance, cooperation, and expertise in putting this book together. We thank Teresa Hensen,

Rosanna Desrochers, Leiloni Gilbert, and Erika Thompson for secretarial help in writing and editing chapters. We thank our supporting institutions and their staff, The University of Texas M.D. Anderson Cancer Center, the University of Oklahoma, Children's Hospital of Los Angeles, and St. Jude Children's Research Hospital, for their support and forbearance in allowing us the time to write and edit the text. Finally, we wish to thank our spouses and family, Jean, Leah, Sophie, Gabriel, Matty, Sean, and Keegan for their love and forgiveness for the missed time at home.

Los Angeles, CA, USA — David M. Parham
Houston, TX, USA — Joseph D. Khoury
Memphis, TN, USA — M. Beth McCarville

Contents

Contributors

Isabel Colmenero, M.D. Birmingham Children's Hospital, Birmingham, West Midlands, UK

Christine Fuller, M.D. Department of Pathology, Virginia Commonwealth University Health System, Richmond, VA, USA

Kar-Ming Fung, M.D., Ph.D. Department of Pathology, University of Oklahoma Health Sciences Center, Oklahoma City, OK, USA

R. Paul Guillerman, M.D. Department of Pediatric Radiology, Baylor College of Medicine, Texas Children's Hospital, Houston, TX, USA

Daniela Hoehn, M.D., Ph.D. Columbia University Medical Center, New York, NY, USA

New York Presbyterian Hospital, New York, NY, USA

Simon Ching-Shun Kao, M.B.B.S., D.M.R.D., D.A.B.R. Department of Radiology, University of Iowa Healthcare, Iowa City, IA, USA

Sue C. Kaste, D.O. St. Jude Children's Research Hospital, Memphis, TN, USA

Geetika Khanna, M.D., M.S. St Louis Children's Hospital, Washington University School of Medicine – MIR, St Louis, MO, USA

Joseph D. Khoury, M.D. The University of Texas M.D. Anderson Cancer Center, Houston, TX, USA

Marcia Komlos Kukreja, M.D. Department of Radiology, Baylor College of Medicine, Texas Children's Hospital, Houston, TX, USA

Vasiliki Leventaki, M.D. St. Jude Children's Research Hospital, Memphis, TN, USA

Jenny Lin, M.D. Department of Pathology and Pediatrics, Emory University School of Medicine, Children's Healthcare of Atlanta, Atlanta, GA, USA

Sanam Loghavi, M.D. The University of Texas M.D. Anderson Cancer Center, Houston, TX, USA

Philip Luthert, B.Sc., M.B.B.S. Department of Eye Pathology, UCL Institute of Ophthalmology and Moorfields Eye Hospital, London, UK

M. Beth McCarville, M.D. St. Jude Children's Research Hospital, Memphis, TN, USA

Kieran McHugh, F.R.C.R., F.R.C.P.I., D.C.H. Great Ormond Street Hospital for Children, London, UK

Mina M. Naguib, M.D. Department of Pathology and Pediatrics, Emory University School of Medicine, Healthcare of Atlanta, Atlanta, GA, USA

David M. Parham, M.D. Department of Pathology and Laboratory Medicine, Children's Hospital Los Angeles, Los Angeles, CA, USA

University of Southern California, Los Angeles, CA, USA

Bruce R. Pawel, M.D. Perelman School of Medicine at the University of Pennsylvania, Philadelphia, PA, USA

The Children's Hospital of Philadelphia, Philadelphia, PA, USA

Kalliopi Petropoulou, M.D. Department of Radiology, State University of New York (SUNY) Upstate, Syracuse, NY, USA

Alfredo Pinto-Rojas, M.D. University of Calgary, Calgary, AB, Canada

Anand Raju, M.D. St. Jude Children's Research Hospital, Memphis, TN, USA

Miguel Reyes-Múgica, M.D. University of Pittsburgh School of Medicine, Pittsburgh, PA, USA

Children's Hospital of Pittsburgh, UPMC, Pittsburgh, PA, USA

Jon M. Rowland, M.D., Ph.D. UCSF Benioff Children's Hospital Oakland, Oakland, CA, USA

Rakhee Kisan Sansgiri, M.D. St. Jude Children's Research Hospital, Memphis, TN, USA

Irene Scheimberg, M.D., F.R.C.Path. The Royal London Hospital, London, UK

Neil J. Sebire, M.D., F.R.C.Path. Great Ormond Street Hospital for Children, London, UK

Bahig M. Shehata, M.D. Department of Pathology and Pediatrics, Emory University School of Medicine, Children's Healthcare of Atlanta, Atlanta, GA, USA

Alexander J. Towbin, M.D. Department of Radiology, Neil D. Johnson Chair of Radiology Informatics, Cincinnati Children's Hospital Medical Center, Cincinnati, OH, USA

Esben Vogelius, M.D. Cleveland Clinic, Cleveland, OH, USA

Stephan D. Voss, M.D., Ph.D. Department of Radiology, Boston Children's Hospital, Boston, MA, USA

Zhongxin Yu, M.D. Department of Pathology, University of Oklahoma Health Sciences Center, Oklahoma City, OK, USA

Laboratory Techniques Used in the Diagnosis of Pediatric Tumors

1

Daniela Hoehn and Sanam Loghavi

Introduction

Appropriate diagnosis of pediatric tumors requires an integrative approach utilizing several clinical and diagnostic resources, including a comprehensive clinical exam, diagnostic imaging studies, and a variety of laboratory techniques. The role of the latter cannot be emphasized enough. Routine laboratory techniques include microscopic evaluation, immunohistochemistry, flow cytometry, conventional cytogenetics, and molecular diagnostic studies.

Fine-Needle Aspiration and Core Biopsy

In clinical practice, the initial approach to the diagnosis of a newly discovered tumor often involves fine-needle aspiration (FNA) and a concurrent core needle biopsy. While the use of FNA in the pediatric population is less widespread than core needle biopsy sampling, cytologic evaluation may be helpful in particular situations as long as diagnostic pitfalls that are specific to the pediatric population are recognized [1]. Usually, these samples are obtained under imaging guidance, including ultrasound for more superficial and accessible lesions and computed tomography (CT) and magnetic resonance imaging (MRI) for lesions involving visceral organs or those that are deeply situated and less accessible percutaneously. The advantage of FNA and core needle biopsy samples is that they are of limited invasiveness and offer a balance between adequate sampling and potential morbidities associated with surgical sampling [2]. It should be noted that minimally invasive sampling approaches of pediatric tumors may occasionally present specific issues that should be kept in mind when sampling options are considered. For example, percutaneous sampling approaches for bone tumors should avoid contamination of fascial compartments through tumor seeding. Additionally, sampling of localized renal tumors in young children who are ultimately diagnosed when Wilms tumor might result in the patient being upstaged due to iatrogenic breach of the tumor capsule.

Intraoperative Evaluation

The main indications for frozen section evaluation in pediatric tumors include assessment for malignancy, evaluation of tissue adequacy, margin assessment, and allocation of tissue to appropriate ancillary studies on the basis of the preliminary working diagnosis [3]. Intraoperative consultations also offer an opportunity to perform touch imprints and scrape preparations, both of which help in assessing sampling adequacy and offer superior cytologic details compared to frozen section tissue samples while largely preserving the specimen for permanent histologic processing. In addition both methods are rapid and simple, and can be performed on site. In addition air-dried touch preparations without subsequent processing can be archived at 4 °C for days or weeks, or they can be frozen at −70 °C and utilized much later for additional ancillary studies such as fluorescence in situ hybridization (FISH) and molecular diagnostics.

From the standpoint of triaging freshly acquired tissue samples, it is important to note that the only techniques with an absolute requirement for viable tissue include flow cytometry and conventional cytogenetics. Most other techniques, including FISH and molecular diagnostics, can currently be performed reliably on formalin-fixed paraffin-embedded (FFPE) material. Accordingly, fresh tissue should be procured in cases where such techniques are needed. In cases

D. Hoehn, M.D., Ph.D. (✉)
Pathology and Cell Biology, Columbia University Medical Center, 630 West 168 Street, Vanderbilt Clinic – VC 14-239, New York, NY 10032, USA

New York Presbyterian Hospital, New York, NY, USA
e-mail: Dh2315@cumc.columbia.edu

S. Loghavi, M.D.
The University of Texas M.D. Anderson Cancer Center, Houston, TX, USA

D.M. Parham et al. (eds.), *Pediatric Malignancies: Pathology and Imaging*,
DOI 10.1007/978-1-4939-1729-7_1,

where tissue is limited, prioritization should be based on differential diagnostic considerations and should be communicated between the pathologist and surgeon or interventional radiologist. For example, flow cytometric evaluation is of less significance in a patient with suspected sarcoma or Hodgkin lymphoma.

Immunohistochemistry

Immunohistochemistry (IHC) is an integral part of diagnostic pathology. Immunohistochemistry combines histological, immunological, and biochemical techniques for the identification of specific antigens by means of antigen-antibody complex formation tagged with a chromogen (Fig. 1.1). Among the many advantages of IHC is its ability to permit visualization of antigen distribution within tissues. In addition to providing a qualitative assessment of tissue composition, IHC is amenable for semiquantitative and fully quantitative approaches for cell enumeration.

Techniques to produce quality antibodies for clinical immunohistochemistry have improved dramatically over the past few decades. Antibodies against a specific antigen can be monoclonal or polyclonal, and they may be produced in a variety of hosts (commonly mouse or rabbit) against a wide array of epitopes. In comparison with the nascent years of IHC technology a few decades ago when frozen tissue was required and manual staining methods were predominant, immunostaining techniques are currently much more robust, automated, and amenable to being performed on a variety of tissue fixatives and tissue processing techniques. Nonetheless, IHC quality remains a function of a broad range of factors that include antibody specificity, antibody dilution and incubation conditions, antigen retrieval, tissue fixation, decalcification methods, and histologic processing [4]. For example, the length of tissue fixation and type of fixative might significantly alter a target epitope and thus impact IHC quality [5, 6]. Tissue processing techniques may similarly impact IHC particularly when novel techniques such as microwave are introduced.

More recently, colorimetric in situ hybridization (ISH) stains have become widely available. These stains are typically performed on the same automated platforms on which IHC is done. Instead of an antigen-antibody design, ISH entails the use of chromogen-tagged nucleic acids complementary to target DNA or RNA sequences [7]. Like IHC, ISH permits the identification of target sequences in a tissue-specific context. Commonly used ISH stains include those for the detection of human papillomavirus DNA, Epstein-Barr virus RNA, and immunoglobulin light-chain mRNA transcripts.

Interpretation of IHC requires a thorough knowledge of histology, antigen distribution in tissue, and antigen distribution in cells (membranous, cytoplasmic, and/or nuclear), and knowledge of potential artifacts that may impact staining quality. Accordingly, it is necessary to distinguish true staining from nonspecific cross-reactivity or background "noise." Required elements to ensure adequate IHC quality include the use of positive and negative controls as well as systematic validation processes to ensure that critical components of IHC staining (e.g., buffers, color development kits) are performing optimally.

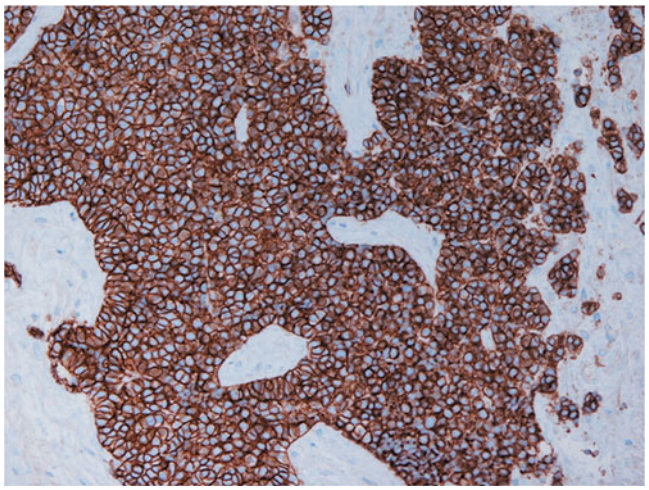

Fig. 1.1 CD99 immunohistochemistry in a case of Ewing sarcoma family tumor demonstrates diffuse strong expression of the CD99 antigen by tumor cells

Flow Cytometry Analysis

Multicolor flow cytometry analysis (FCA) is an invaluable laboratory tool for the characterization of hematolymphoid malignancies. It permits multiparametric measurement of cellular properties that include size, cytoplasmic complexity, and antigen expression. A typical flow cytometer is composed of a laminar flow cell transport system, one to several laser lights, photodetectors, and a computer-based data management system. The intricate design of flow cytometers ensures that cells flowing in a fluid sheath are hydrodynamically focused to intercept laser light at a specific frequency. The interaction of the laser light with the cell results in light scatter and, in the presence of bound fluorochrome-tagged antibodies, excitation and resultant emission of light at a different wavelength. These events are captured by sensitive photodetectors and converted to measurable parameters. Scattered light captured by a detector positioned at a right angle (90°) from the laser source measures cytoplasmic complexity whereas scattered light captured by detectors along the original trajectory of the laser beam (180°) measures cell size.

Flow cytometry analysis is a robust tool to simultaneously assess coexpression of multiple antigens expressed by cells

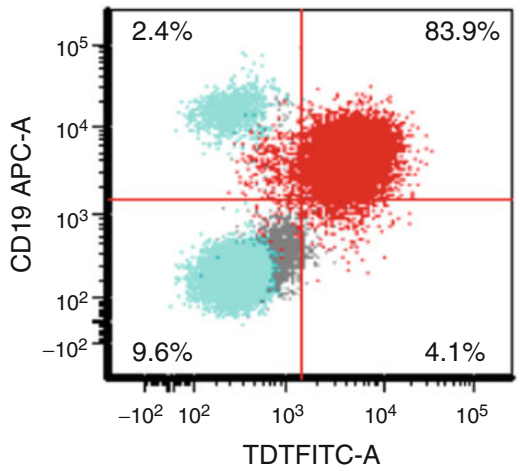

Fig. 1.2 Flow cytometry analysis of a case of B lymphoblastic leukemia/lymphoma demonstrating TdT expression by CD19-positive blasts (*red*). In this plot, the lymphocyte gate is highlighted in *turquoise*. Note the presence of a small population of normal CD19-positive B cells (*upper left-hand quadrant*) as well as a population of normal T cells (CD19 negative) (*lower left-hand quadrant*)

(Fig. 1.2). This is useful to many clinical assays including cell lineage determination, biomarker detection, minimal residual disease assessment, enumeration of cell subsets (e.g., stem cells, T-cell subsets), and measurement of proliferation and apoptosis.

For such applications, antibodies with covalently linked fluorescent molecules (fluorochromes) are used to identify target antigens and provide a means for qualitative and quantitative assessment of antigen expression. This ability to perform multiparametric analysis on an individual cell offers FCA a distinct advantage over immunohistochemistry particularly in hematolymphoid disorders [8]. On the other hand, the use of FCA to evaluate solid tumors remains technically limited.

Cytogenetics

Conventional cytogenetic analysis (cytogenetics) is a laboratory discipline that involves the study of chromosomes, also known as karyotyping. Chromosomal alterations are common in cancer and are broadly categorized into recurrent and nonrecurrent abnormalities. Tumors arising in the pediatric age group are more likely than those arising in adults to harbor recurrent cytogenetic abnormalities. Frequently, such recurrent cytogenetic abnormalities are integral elements of pediatric cancer pathogenesis and their detection has emerged as an important adjunct for diagnostic evaluation.

For conventional cytogenetic analysis of tissue samples viable fresh cells are required for analysis. The average viable human cell divides once every 24 h and certain cell types, such as lymphocytes, do not divide at all, which mandates special culture techniques and growth stimulation of the cell of interest to increase the yield of analyzable material. Bone marrow is typically cultured for 24–48 h whereas lymphocytes from tissue may require 3–4 days in culture medium containing proliferation inducers for maximum yield. Cultured cells are then subjected to metaphase arrest before being processed to prepare chromosome spreads. Chromosomes are then stained, most commonly with Giemsa or Wright stains, for visualization of the characteristic banding patterns. Positively charged dyes in stains bind to the negatively charged DNA in chromosomes.

Conventional cytogenetic analysis begins with the identification of chromosomes typically by analyzing 20 metaphases. Chromosomes are aligned in pairs sequentially from chromosome 1 to 22 followed by the pair of sex chromosomes. Chromosomal abnormalities are broadly divided into numerical and structural. Numerical abnormalities (aneuploidy) result in deviation from the usual diploid complement of 46 chromosomes and result either in hyperploidy or hypoploidy. The spectrum of structural chromosomal abnormalities is broad. Most common alterations in pediatric cancers are balanced translocations resulting in pathologic juxtaposition of genes that normally belong on different chromosomes. The first step is to assess the number of chromosomes, a total of 46 in a normal diploid human cell.

While providing important information in the laboratory work-up of pediatric tumors, conventional cytogenetics in tumors has some disadvantages. Among the salient disadvantages is the absolute requirement for viable tumor tissue and the intensive time and labor requirements that are inherent in cytogenetic techniques. Furthermore, subtle cytogenetic alterations such as cryptic translocations or inversions are often impossible to recognize due to the typically low resolution of routine cancer cytogenetics methods. These limitations have led laboratories to rely on FISH, which generally bypasses most of the limitations of conventional cytogenetics. Other cytogenetic techniques such as array comparative genomic hybridization (CGH) have also made their way into diagnostic laboratories, but their clinical use remains limited particularly for pediatric tumors.

Fluorescence In Situ Hybridization

The use of FISH has grown exponentially over the past decade and plays a critical role in the laboratory work-up of many pediatric cancers [9]. In FISH, fluorochrome-tagged DNA probes designed to be complementary to a specific area of a chromosome (locus) are used to make qualitative and quantitative assessments regarding the targeted locus. Staining can be performed on a broad range of sample types, including touch preparations, smears, and FFPE tissue

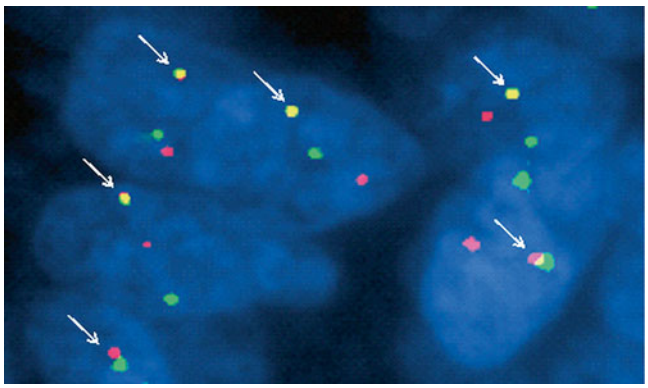

Fig. 1.3 Fluorescence in situ hybridization signals may be juxtaposed signals (*arrows*) or separate. Depending on the design of the assay probes, these patters might represent fusion or rearrangement at a particular locus. In this example of an *EWSR1* breakapart probe demonstrating gene rearrangement (separate signals) in a case of Ewing sarcoma family tumor. Fused signals (*arrows*) represent the intact *EWSR1* allele

sections. Probes are incubated and allowed to hybridize to target DNA and then, after applying a background nuclear stain, signals are visualized on a fluorescent microscope. The availability of fluorochromes with different light emission characteristics allows simultaneous application of probes of different colors and thereby permits a wider range of data to be obtained.

Probes used in FISH provide important cytogenetic data and this depends to a large extent on the design of the probe and, as applicable, the composition of probes that occasionally comprise a FISH assay. Information about a specific locus obtained from FISH may be quantitative or qualitative. For instance, while a probe might indicate rearrangement involving a specific locus (e.g., *MYC* gene), it could also demonstrate copy number changes (gains/losses) at that particular locus. Probes can be designed to provide information if detected signals are juxtaposed (fusion probes) or located farther apart than they should (breakapart probes) (Fig. 1.3). In addition, by combining FISH probes designed to be complementary to a particular gene with other probes targeting the centromeric portion of a chromosome, a FISH assay can distinguish between copy number alterations resulting from focal chromosomal deletions and those that are secondary to the loss of an entire chromosome.

The many advantages of FISH have positioned it as an indispensable laboratory technique particularly in cancer. Advancements in FISH techniques now allow testing to be reliably performed on FFPE and have largely mitigated many of the limitations of conventional cytogenetics. In addition, FISH assays can be performed rapidly and their interpretation is less intricate than that involved in conventional cytogenetic analysis.

Molecular Diagnostics

Mutations are an integral component of cancer at the molecular level. Common molecular aberrations include point mutations, insertions/deletions (indels), amplifications, translocations, and DNA methylation variations. Characterization of these aberrancies is a critical component of the pathologic evaluation of tumors at diagnosis and during follow-up particularly for pediatric tumors since many harbor characteristic nonrandom molecular alterations [10–12]. Some of the more commonly used assays in the practice of diagnostic molecular pathology include polymerase chain reaction (PCR), DNA sequencing methods, array CGH, gene expression profiling, and microRNA profiling. PCR and DNA sequencing are the most widely used methods in routine laboratory practice.

All molecular techniques start with DNA or RNA extraction from a sample that could be fresh and unfixed or from FFPE material. In PCR-based methods, a limited segment of DNA or RNA (cDNA) is amplified and usually subsequently sequenced to identify a mutation or detect a pathogenic fusion resulting from a chromosomal translocation/inversion. Such methods are generally sensitive and specific, especially when amplification products are subsequently sequenced or otherwise confirmed, with a reasonably quick turnaround time frame. Automation of a sizeable component of the technical aspect of molecular testing has become widely adopted particularly in laboratories with high volumes. Interpretation of results is generally straightforward and is less time consuming than cytogenetic analysis. High-throughput, or next-generation, sequencing technologies parallelize DNA sequencing producing thousands or millions of sequences concurrently. Although these nascent methods are gradually being adopted in clinical molecular diagnostics their clinical role in pediatric oncology has not been established yet [13].

References

1. Monaco SE, Teot LA. Cytopathology of pediatric malignancies: where are we today with fine-needle aspiration biopsies in pediatric oncology? Cancer Cytopathol. 2014;122(5):322–36.
2. Garrett KM, Fuller CE, Santana VM, Shochat SJ, Hoffer FA. Percutaneous biopsy of pediatric solid tumors. Cancer. 2005; 104(3):644–52.
3. Coffin CM, Spilker K, Zhou H, Lowichik A, Pysher TJ. Frozen section diagnosis in pediatric surgical pathology: a decade's experience in a children's hospital. Arch Pathol Lab Med. 2005;129(12):1619–25.
4. O'Hurley G, Sjostedt E, Rahman A, Li B, Kampf C, Ponten F, et al. Garbage in, garbage out: a critical evaluation of strategies used for validation of immunohistochemical biomarkers. Mol Oncol. 2014;21.
5. D'Amico F, Skarmoutsou E, Stivala F. State of the art in antigen retrieval for immunohistochemistry. J Immunol Methods. 2009; 341(1–2):1–18.

6. Hewitson TD, Wigg B, Becker GJ. Tissue preparation for histochemistry: fixation, embedding, and antigen retrieval for light microscopy. Methods Mol Biol. 2010;611:3–18.
7. Cassidy A, Jones J. Developments in in situ hybridisation. Methods. 2014.
8. Heel K, Tabone T, Rohrig KJ, Maslen PG, Meehan K, Grimwade LF, et al. Developments in the immunophenotypic analysis of haematological malignancies. Blood Rev. 2013;27(4):193–207.
9. Das K, Tan P. Molecular cytogenetics: recent developments and applications in cancer. Clin Genet. 2013;84(4):315–25.
10. Cerrone M, Cantile M, Collina F, Marra L, Liguori G, Franco R, et al. Molecular strategies for detecting chromosomal translocations in soft tissue tumors (review). Int J Mol Med. 2014;33(6):1379–91.
11. Khoury JD. Ewing sarcoma family of tumors. Adv Anat Pathol. 2005;12(4):212–20.
12. Romeo S, Dei Tos AP. Clinical application of molecular pathology in sarcomas. Curr Opin Oncol. 2011;23(4):379–84.
13. Xuan J, Yu Y, Qing T, Guo L, Shi L. Next-generation sequencing in the clinic: promises and challenges. Cancer Lett. 2013;340(2):284–95.

Imaging Techniques Used in the Diagnosis of Pediatric Tumors

2

M. Beth McCarville

Radiologic imaging plays a pivotal role in the diagnosis of pediatric malignancies. In many cases the radiologist is the first to suggest the possibility of a malignancy based on imaging findings. Imaging features of primary malignancies are invaluable in providing a differential diagnosis and often direct the subsequent clinical and imaging work-up of the patient. Diagnostic imaging is also crucial in detecting metastatic disease in both solid and hematologic malignancies and, therefore, impacts therapeutic decision making. The currently available imaging modalities include plain-film radiography, ultrasonography (US), computed tomography (CT), magnetic resonance imaging (MRI), and nuclear medicine. Each of these modalities has a unique and important role in the assessment of children with cancer. Because the potential detrimental effects of ionizing radiation are compounded in children relative to adults, when choosing an imaging modality it is essential to minimize radiation exposure as much as possible and to adhere to the "as low as reasonably achievable" or ALARA principle [1–3]. In this chapter I will review the advantages and limitations of each imaging modality relative to the initial assessment of children with cancer. Tumor-specific imaging findings are presented in detail within the chapter devoted to each malignancy.

Plain-Film Radiography

Plain-film radiography is usually the first imaging procedure performed when a child is diagnosed with cancer. Plain radiographs have the advantage of being relatively quick to obtain, easy to perform, generally available at all hours, usually well tolerated, and relatively low cost and producing only low radiation exposure. However, relative to cross-sectional imaging modalities, the spatial resolution of plain radiographs is limited and additional imaging is required. Despite this limitation, X-ray examinations can provide invaluable information regarding an area of clinical concern. For example, when the evaluation of a child with bone pain includes plain-film radiography the aggressiveness of a bony process is reflected by specific radiographic findings. Signs of malignancy include sunburst or lamellar periosteal reaction, cortical destruction, a Codman triangle, and evidence of a soft tissue mass (Fig. 2.1) [4]. Although MRI provides superior soft-tissue detail of bone and soft-tissue tumor correlation with the plain radiograph remains essential to the diagnosis of these malignancies. Abdominal radiographs of a child with abdominal pain might reveal organomegaly, abdominal mass effect, or abnormal abdominal calcifications due to intraperitoneal or retroperitoneal malignancies (Fig. 2.2). Plain radiographs of the chest can reveal mediastinal or hilar adenopathy, splaying of the ribs, or rib destruction due to malignancies such as lymphoma, neuroblastoma, or Askin tumor. Such information guides the subsequent imaging and laboratory work-up and can be useful to the pathologist when arriving at a final diagnosis.

Ultrasonography

Medical ultrasonography (US) utilizes handheld transducers that are placed on the body surface and emit and receive sound waves ranging from 2 to 20 MHz. Higher frequencies provide higher resolution images but have only limited tissue penetration while lower frequency waves penetrate deeper but provide less image resolution. Modern broadband ultrasound transducers are designed to allow the operator to adjust the emitted sound wave frequency for visualization of a structure of interest. In general, frequencies in the range of 8–20 MHz image structures near the transducer and frequencies in the 2–6 MHz range image deeper structures [5, 6]. Tissue harmonic imaging and pulse inversion harmonic imaging allow the transducer to

M.B. McCarville, M.D. (✉)
Radiological Sciences, St. Jude Children's Research Hospital,
262 Danny Thomas Place, Memphis, TN 38105, USA
e-mail: beth.mccarville@stjude.org

D.M. Parham et al. (eds.), *Pediatric Malignancies: Pathology and Imaging*,
DOI 10.1007/978-1-4939-1729-7_2, © Springer Science+Business Media New York 2015

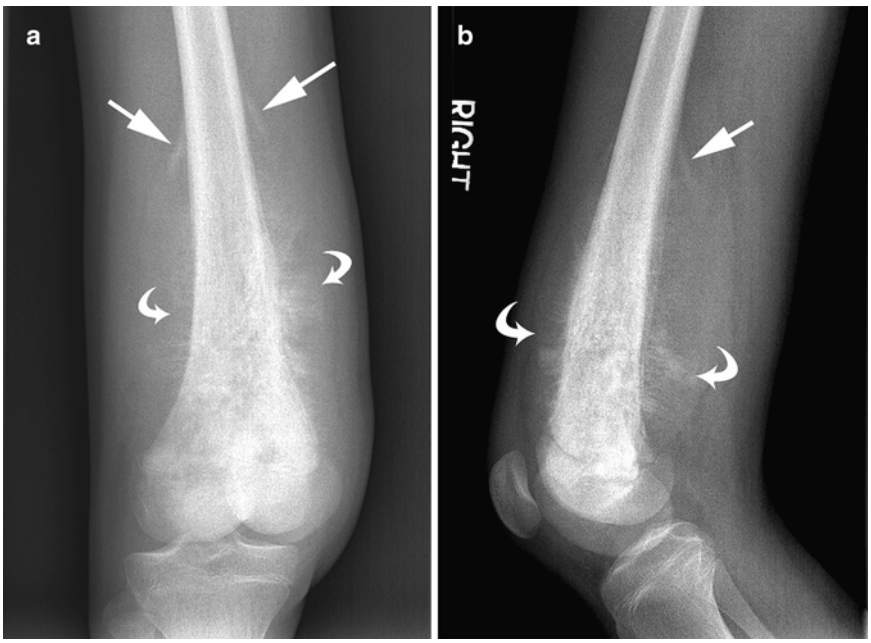

Fig. 2.1 These (**a**) anterior-posterior (AP) and (**b**) lateral femur radiographs of a patient with osteosarcoma reveal features typical of a malignant bone tumor including Codman triangles (*arrows*) and sunburst periosteal reaction (*curved arrows*)

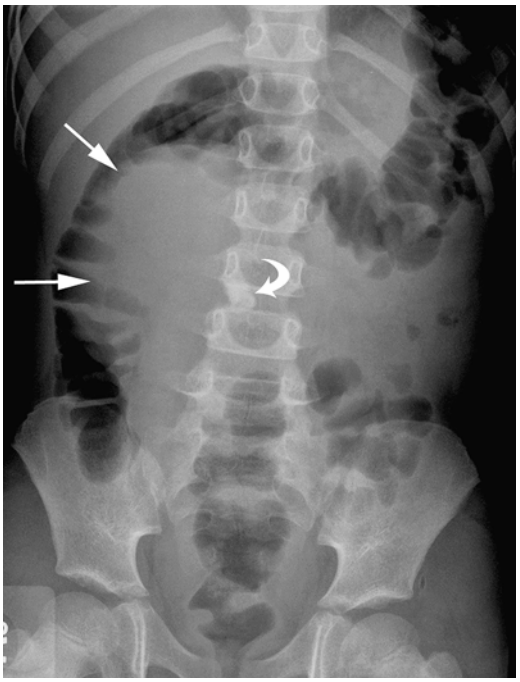

Fig. 2.2 This AP abdominal radiograph of a girl with *right* ovarian teratoma reveals mass effect on the *right* colon (*arrows*) and a toothlike abdominal calcification (*curved arrow*), features suggestive of this diagnosis

receive both the fundamental transmitted frequency and its harmonic frequencies and have become standard in many applications. These techniques increase the contrast of lesions while reducing the effect of some artifacts, but are limited to shallower depths [6].

Children are ideal candidates for US because their small body habitus, relative to adults, allows placement of the US transducer near the structure of interest, thus reducing signal attenuation. Ultrasound has numerous other advantages that make it particularly useful in the pediatric population. Perhaps most importantly it does not expose the patient to the potential harmful effects of radiation, a topic of considerable concern in this age group. It has the added benefits of being portable, does not require sedation, has Doppler capabilities to dynamically assess vascularity, allows real-time visualization of the movement of abdominal structures relative to each other and is less costly than CT and MRI. Additionally, US is usually readily available and does not require pre-procedure preparation. Drawbacks of US are that it is operator dependant, lacks image resolution compared to CT and MRI, is limited by artifact caused by bowel gas, and it can be difficult to visualize deep-seated structures in obese or adult-size patients.

Despite these potential limitations US remains the modality of choice for the initial assessment of a suspected abdominal mass in children and can provide important clues to the diagnosis. For example, real-time assessment of a right upper quadrant mass allows visualization of the mass relative to the liver and kidney during respiration. During continuous dynamic US imaging, masses separate from these solid organs move independently during breathing whereas masses arising within them move in union with their organ of origin. Ultrasound can reveal the solid or cystic nature of a mass, information that can be extremely useful. Cystic structures appear anechoic or sonolucent on US while solid tissue appears echogenic (Fig. 2.3). Regarding liver masses, US

can reveal whether the tumor is solitary or multifocal as is seen with multifocal or diffuse hepatic hemangiomas of infancy, metastatic neuroblastoma, and multifocal hepatoblastoma [7]. Ultrasound can detect calcifications within tumor which appear as bright echogenic foci with posterior shadowing. This finding might suggest an ovarian teratoma when seen in association with an abdominal or pelvic mass in an adolescent girl or neuroblastoma when associated with a retroperitoneal mass in a young child [8]. With the use of high-resolution transducers, US is ideal for assessment of superficial structures such as the thyroid, the scrotum, the eyes, and soft-tissue masses in the head, neck, or extremities (Fig. 2.4). Taken together with the clinical presentation and age of the patient, US imaging features of abnormalities of these structures can often provide a specific diagnosis or greatly narrow the differential diagnosis [9–12].

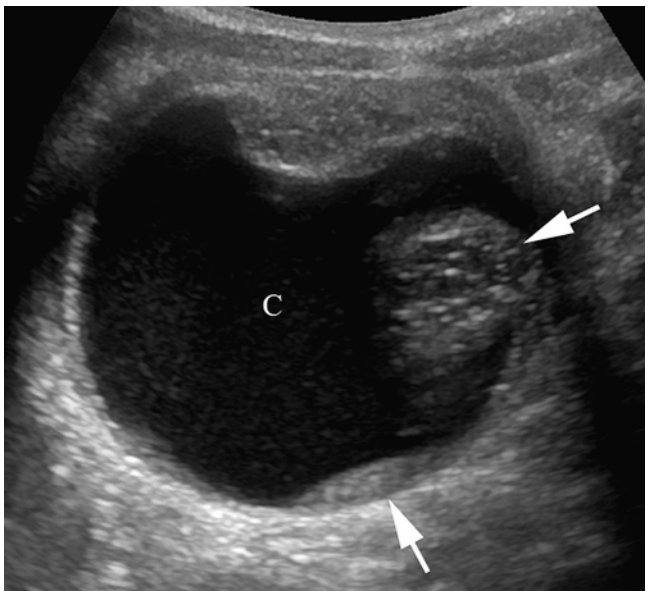

Fig. 2.3 This transverse ultrasound (US) image of an ovarian teratoma reveals the cystic (C) and solid (*arrows*) components that are typical of this tumor

Doppler evaluation has numerous applications in the assessment of pediatric tumors. It can show increased blood flow and disorganized vasculature in tumors such as in testicular lymphoma or primary gonadal germ cell tumors [12]. Doppler of hepatic hemangiomas typically shows both arterial and venous waveforms with minimal systolic-diastolic variation in contrast to primary liver malignancies that show high-velocity blood flow [7]. Doppler is also useful in detecting vascular invasion, such as invasion of the renal vein and inferior vena cava by Wilms tumor or the hepatic or portal veins by hepatoblastoma [7, 13].

Because it does not involve ionizing radiation and does not require sedation, ultrasound is particularly appealing for screening patients with syndromes that predispose them to developing abdominal tumors. For example, patients with Beckwith-Wiedemann, Denys-Drash, WAGR (Wilms tumor, aniridia, genitourinary anomalies, mental retardation), Fanconi anemia, and several other syndromes have a risk of developing Wilms tumor (WT). However, the utility of US screening in these patients remains controversial [14]. Due to the rarity of these syndromes no randomized trials have been performed to compare the outcome of screened versus unscreened patients. Furthermore, because survival of patients with WT is greater than 90 % for those with localized disease and over 70 % for those with metastatic disease the benefit of early detection is debatable. Regardless, current efforts are aimed at identifying patients at the earlier and more treatable stages of disease [15, 16]. While there is no physical harm from sonography the emotional stress caused by vigilant screening should not be ignored. Current recommendations for screening children with

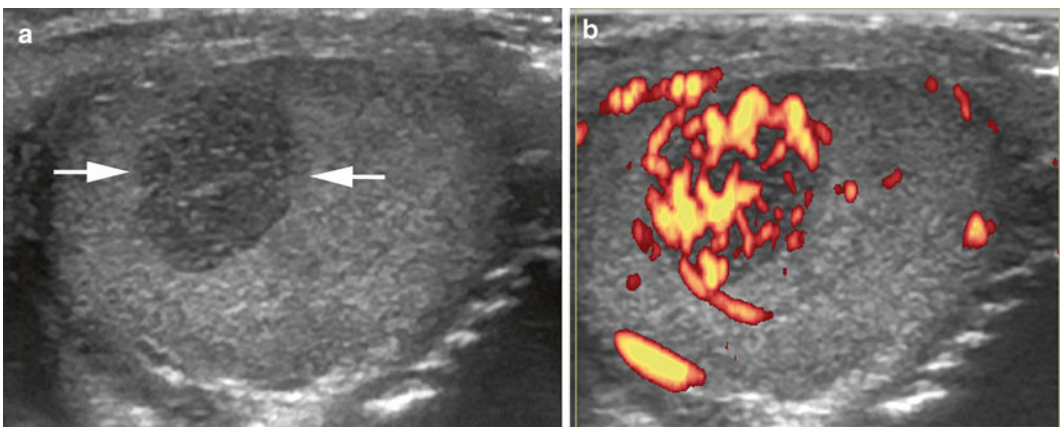

Fig. 2.4 This (**a**) transverse US image of the testicle reveals a well-defined, small, solid, hypoechoic mass (*arrows*) that on (**b**) power Doppler imaging appears hypervascular (*orange structures*) in this boy with a testicular Sertoli-Leydig cell tumor

various syndromes that predispose them to Wilms tumor have recently been published. The kidneys should be imaged with a high-resolution transducer; generally a 7–10 MHz transducer for infants and 6–8 MHz transducer for toddlers. When suspicious lesions are identified the imaging should be repeated within 1 week at a specialist center [14]. Children with other cancer predisposition syndromes also benefit from abdominal screening US to detect associated tumors in other organs. This subject is beyond the scope of this chapter but has been recently reviewed [17].

In the pediatric oncology setting US is valuable for guiding biopsy of newly diagnosed masses. In experienced hands US can safely be used to guide biopsy of a wide variety of tumors including rhabdomyosarcoma, non-rhabdomyosarcoma, soft-tissue sarcomas, neuroblastoma, hepatoblastoma, peripheral pulmonary lesions, and even anterior mediastinal masses requiring core biopsy [18–23]. Ultrasound guidance has the advantage of allowing real-time assessment of tumor vascularity and the relationship of the tumor to major vessels. This information can alert the interventional radiologist to the potential for post-procedural hemorrhage and help direct biopsy away from vascular structures. Additionally, because US machines are portable they can be used as a secondary guidance device in conjunction with CT or fluoroscopically directed biopsies [18, 23].

Computed Tomography

In pediatric oncology, cross-sectional imaging modalities (CT and MRI) are essential tools in patient management. These modalities provide valuable information for formulating a differential diagnosis, staging the tumor, monitoring treatment response, and detecting recurrences. However, with regard to CT, it is important to consider that the developing tissues of pediatric patients are more sensitive to the harmful effects of ionizing radiation than those of adults. Additionally, relative to adults, children have a longer lifespan in which to develop adverse sequelae of radiation exposure, which can occur decades later [24]. The pediatric radiologist must have knowledge of the proper use of these imaging modalities so that they can assist oncologists, surgeons, and radiation oncologists in developing rational and appropriate imaging guidelines for therapeutic protocols.

Since the sentinel article by Pierce and Preston in 2000 describing the effects of low-dose radiation exposure [25], there has been an increasing awareness of the detrimental effects of ionizing radiation in children, especially from CT scans. Since then significant progress has been made in reducing the number of CT scans performed, particularly in the pediatric emergency setting. Advances have also been made in optimizing the scanning technique to reduce radiation dose while maintaining image quality [26–28]. However, children with cancer are particularly at risk because they undergo repeated exposure to radiation and the effects are cumulative over time. Modern cancer therapies have resulted in an overall survival rate of 83 % in children [29] and, therefore, the long-term effects of cancer therapy, including radiation exposure, are now being fully realized. Late effects from cancer therapy are becoming the driving force in tailoring pediatric cancer therapies and challenge the radiologist to apply the ALARA principle whenever possible.

The primary ways to minimize radiation exposure from CT are to require justification for the scan being done and optimization of the technique. In general, a CT is not indicated if the same information can be obtained from a modality that does not involve radiation. Many pediatric cancer therapy protocols consider CT and MRI to be equivalent in terms of assessing local disease. However, there is little scientific data on which to base a decision regarding the use of CT versus MRI in pediatric abdominal imaging [30]. Although it exposes the patient to radiation, CT offers the ability to cover a large anatomic area, provides excellent spatial resolution with minimal motion artifact and high-quality reconstructed multiplanar images, and is not operator dependant. In contrast, MRI requires substantial technical expertise and long scan times that often necessitate sedation. However, MRI has the important benefit of not utilizing radiation while offering multiplanar imaging with inherent tissue contrast, the ability to characterize tissue with various pulse sequences, and the added potential of providing functional information. The decision to use CT or MRI will depend on the local institution's standard of practice, the availability of pediatric sedation, and the radiologist's confidence in performing and interpreting the imaging examination.

Current-day multidetector helical CT (MDCT) scanners allow very rapid image acquisition while maintaining image resolution. These scanners comprise a gantry containing multiple detectors arranged in rows opposite the X-ray tube. The gantry rotates continuously around the patient acquiring data from multiple slices simultaneously as the patient moves through the scanner. Because data are acquired volumetrically, the scan time is shortened while ensuring that small lesions are not missed between slices. Additionally, the quality of multiplanar reconstructed images is greatly improved (Fig. 2.5). Relative to single-slice scanners, MDCT images provide a more accurate assessment of tumor size and a better depiction of the relationship between the tumor and vital structures [5, 31]. Recent advances in MDCT technology include faster gantry rotation times, increased number of detector rows, and dual X-ray tube sources. It is now possible to scan entire body sections in a few seconds or even less than a second. This technology has resulted in a dramatic decrease in the need for sedation while diminishing problems with motion artifact.

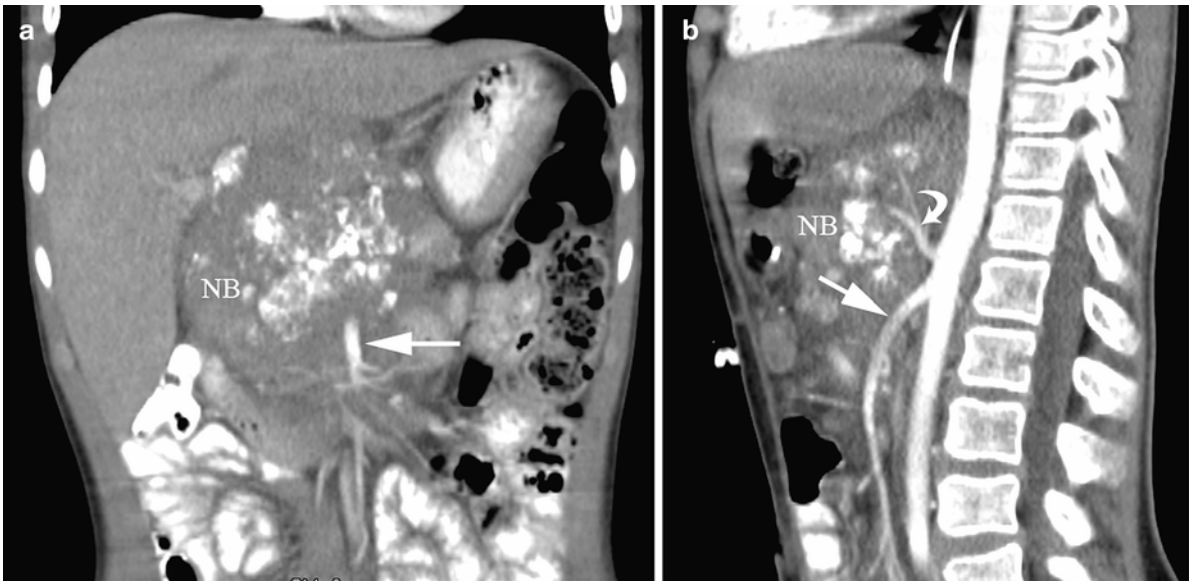

Fig. 2.5 These (**a**) coronal and (**b**) sagittal reconstructed computed tomography images provide valuable information regarding the relationship of this neuroblastoma (NB) to the superior mesenteric (*straight arrows*) and celiac axis (*curved arrow*) arteries which it encases. Such information is crucial for surgical planning

In the past CT scanning protocols designed for adults were not modified for use in children. With increased awareness and education regarding the harmful effects of radiation from CT scanning in children, significant efforts to minimize radiation dose have been undertaken by industry and the radiology community. Parameters that should be modified for pediatric CT scanning include the tube current (milliampere, mA), tube voltage (kilovoltage peak, kVp), gantry rotation time (second), and pitch.

Tube current has a significant impact on radiation dose and image noise; increases in tube current result in a proportional increase in dose while decreasing current results in increasing image noise. Modern MDCT scanners are equipped with automatic tube current modulation (ATCM) devices that dynamically adjust tube current during scanning in response to the geometry and density of the body part being scanned. The goal of ATCM is to maintain an acceptable image noise level while minimizing radiation dose from tube current [32]. It should be noted that specific pediatric ATCM settings are not universally available on modern scanners and scientific literature regarding appropriate weight, age, body region, and indication-based reference settings is lacking. Therefore, ATCM should be used with care in children [33].

The kVp has an exponential relationship with radiation dose and can substantially reduce radiation dose if optimized. Lowering the tube voltage also lowers the production of scattered radiation. In children weighing ≤45 kg, a tube voltage of 80–100 kVp is usually adequate. For adolescents, a kVp of 100 for the chest and 120 for the abdomen is recommended. Areas with high intrinsic contrast, such as the chest and bones, can be scanned at 80–100 kVp. Recent studies in pediatric phantoms have shown that even lower kVp (approximately 60) may be sufficient for some indications. However, scanner-related parameters, such as tube filtration and scanner geometry, can sometimes negatively impact image quality with lower kVp [33].

Most modern MDCT scanners use rotation times of 0.3–0.5 s resulting in a reduction in radiation exposure, the need for sedation, and motion artifact. Shorter scan times, however, can result in a decrease in the number of profiles that can be used for image reconstruction and, subsequently, an increase in image noise. For optimal image resolution a rotation time of 0.5 s is recommended [32, 33].

The pitch is the ratio between table movement and number of detectors multiplied for section width (collimation). An increase in pitch can result in a reduction in scan time and, in some scanners, a reduction in dose. However, in modern MDCT scanners increasing the pitch can cause a dose increase due to overranging and can also reduce spatial resolution. In general, a pitch of 1–1.5 is currently recommended [32].

Oral contrast material is usually indicated for CT imaging of the abdomen or pelvis and the use of oral contrast material for MDCT is not different than for single-slice CT. Iodinated intravenous (IV) contrast agents should always be used for imaging the neck, abdomen, and pelvis. The use of IV contrast in the chest will depend on the indication for the examination. In our practice, if there is a concern for adenop-

athy or when there is a primary solid tumor arising in the chest, IV contrast material is used. When chest CT is performed solely to evaluate for pulmonary metastatic disease we do not administer IV contrast material. Due to the very rapid scan times attainable with MDCT scanners it is essential to adjust scanning to allow the IV contrast agent adequate time to reach the area of interest as the area is being scanned. In general, scanning should begin later with MDCT scanners compared to single-slice scanners. Pre-contrast imaging has no role in pediatric oncologic imaging and should not be performed [34]. Post-contrast, multiphase imaging in children is rarely indicated and is also strongly discouraged. An exception is in the evaluation of newly diagnosed liver tumors. The pattern of tumor enhancement on immediate- and delayed-phase post-contrast images can help distinguish hemangiomas from hepatoblastoma. At our institution, we have found that the relationship between a liver tumor and the hepatic and portal veins is best defined when imaging is performed during the arterial and portal venous phases of enhancement. Such information is crucial in determining which Couinaud's segments are involved and helps guide surgical planning. Specific guidelines for the administration of IV contrast agents and injection techniques (including volume, injection rate, hand injection versus power injector) in children, using MDCT technology, are available in the literature [31].

Magnetic Resonance Imaging

Magnetic resonance imaging plays a pivotal role in the evaluation of newly diagnosed cancer in children. This modality incorporates a strong magnetic field to align hydrogen nuclei within the body. Once aligned the nuclei precess or "wobble" at a frequency proportional to the magnetic field strength. Pulsed radiofrequency (RF) waves are then applied which alter the spin of hydrogen nuclei. When the RF pulse is turned off the nuclei return to their original alignment and energy is released. The released energy is converted to an electrical impulse in a wire within a receiver coil. Spatial encoding is used to localize the site within the body from which the signal originated and, using Fourier transformation (the same mathematical model used to produce a CT image), an MR image is created. Each sampled voxel is assigned a shade of gray that depends on the amount of hydrogen nuclei within it and the rate of equilibrium of hydrogen nuclei back to the original, pre-RF pulse, alignment [5].

Conventional MR imaging relies on several scanning parameters. The RF pulse repetition time (TR) occurs with a time constant, T1. The signal produced in the receiver coil decays exponentially at time constant T2. The time between the initial RF pulse and data collection is the echo time, TE. These parameters can be manipulated so that a T1-weighted (T1W) or T2-weighted (T2W) image is produced. Images acquired with a short TR (300–600 ms) and short TE (10–20 ms) are T1 weighted. On T1W images tissue with short T1 relaxation times (e.g., fat, melanin, gadolinium contrast agent) have high signal intensity and those with longer T1 relaxation times (e.g., water, hemosiderin) have intermediate or low signal intensity. T2W images are produced by using longer TR (>2,000 ms) and a longer TE (>80 ms). On T2W images substances with short T2 relaxation times (e.g., white matter, fibrosis) have low-to-intermediate signal intensity and tissues with longer T2 relaxation times (e.g., edema, tumor, fluid) have higher signal intensity (Fig. 2.6a, b). Additional pulse sequences, beyond these conventional spin-echo sequences, are continually being developed. The inversion recovery sequence (IR)

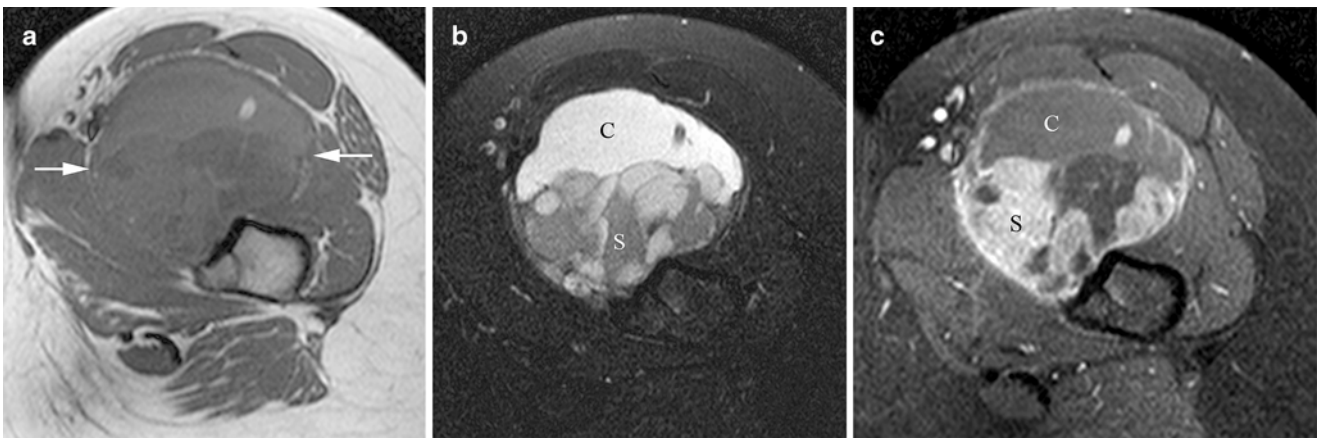

Fig. 2.6 In this patient with a synovial sarcoma the (**a**) non-contrast-enhanced T1W axial magnetic resonance image shows mixed signal intensity of the tumor (*arrows*) while the (**b**) T2W fat-saturated image reveals its partially cystic (C) and solid (S) nature. (**c**) Post-contrast imaging further delineates the enhancing solid (S) and non-enhancing cystic (C) components

selectively nullifies signal from tissue based on its T1 relaxation time and a selected inversion time (TI). A variant of the IR sequence, the short tau inversion recovery (STIR) sequence, selectively suppresses fat and enhances fluid signal. This sequence has proven valuable in oncologic imaging because tumors, which have high water content, are generally readily visible [5].

Using various pulse sequences MRI can delineate between normal and abnormal soft tissues better than CT and with the advantage of not exposing the patient to ionizing radiation. In addition to improved soft tissue characterization, with MRI the beam hardening artifact caused by bone on CT imaging is eliminated [5]. These features make MRI the ideal modality for imaging the brain, spine, neck, and extremities. In the past, the multiplanar capabilities of MR, which allow assessment of structures in the axial, coronal, and sagittal planes, were an additional advantage over CT. However, with the advent of MDCT and improved image resolution of coronal and sagittal reconstructed CT images, this advantage no longer holds. A limitation of MR is the long scan times which often require sedation of young patients. Distraction techniques, such as video goggles and audio systems, can help minimize patient motion and avoid the use of sedation in some patients [35]. Long image acquisition times make MRI of lesions in the trunk very susceptible to degradation from respiratory movement, cardiac and vascular pulsations, and bowel peristalsis. Techniques to reduce artifact from bowel peristalsis include keeping the patient from ingesting food or fluid for 4 h before the study and administration of glucagon [35, 36]. Rapid scanning techniques can also help minimize motion artifact. These include low flip angle gradient echo sequences, turbo spin-echo sequences, single-shot sequences, echo planar imaging, and periodically rotated overlapping parallel lines with enhanced reconstruction (PROPELLER) [5, 35]. These faster sequences allow image acquisition during breathholding and coverage of a larger body area in a shorter time period and reduce the potential for motion artifact. Besides the long scan times, other disadvantages of MRI include its high cost, limited availability, relative insensitivity to calcification, and limited ability to assess lung parenchyma [5].

Intravenous gadolinium-based contrast agents are often used in MRI, similar to iodinated contrast agents for CT imaging. These agents are paramagnetic and cause shortening of the T1 and T2 relaxation times. Most gadolinium agents diffuse freely across the vascular membrane and, therefore, reflect both perfusion and diffusion [5]. These agents tend to make tumors more conspicuous and are useful for identifying intra-tumoral necrosis or confirming solid components of partially cystic tumors (Fig. 2.6c). The combination of various pre-contrast-enhanced MR sequences and post-contrast T1W, fat-suppressed imaging allows assessment of tumor margins, determination of extension across fascial planes, invasion of bone and joints, and involvement of the neurovascular bundle [5, 37]. Gadolinium contrast agents are well tolerated and allergic reactions in children are very rare. However, these agents have been associated with development of nephrogenic systemic fibrosis (NSF) in patients with acute or chronic renal insufficiency. NSF is characterized by progressive tissue fibrosis, usually beginning in the skin of extremities, progressing over weeks to months to involve extra-cutaneous structures including bone, muscle, heart, lungs, and esophagus. This process can be transient, with clinical improvement, or progressive causing severe joint contractures, loss of ambulation, and even death. Therefore, patients should be screened for evidence of renal disease prior to administration of gadolinium-based contrast agents. Patients with an estimated glomerular filtration rate below 30 mL/min/1.73 m^2 are at high risk of developing NSF. A detailed discussion of the association between gadolinium contrast agents and NSF, and recommendations for gadolinium use in patients with renal disease, has recently been published [38].

An emerging technology for staging solid tumors and lymphoma is whole-body MRI (WBMRI). The development of multichannel coils, fast turbo sequences, the parallel acquisition technique (PAT), and moveable tables are enabling this technology to become more feasible in clinical practice. The goal of WBMRI is to image the entire body in the shortest possible time using the minimum number of sequences, preferably only one. This technique was initially developed as a method of assessing for skeletal metastases but has proven to be valuable in detecting extraskeletal sites of disease [39]. Most recently, the IR sequences, either STIR or turbo inversion recovery magnitude (TIRM), have been recommended [40, 41]. These sequences employ a combination of proton density, T1 and T2 contrast with inherent fat suppression [40]. STIR has been reported to be more sensitive than T1-weighted sequences for the detection of metastases because metastases appear bright on STIR sequences [39].

When using WBMRI in children, knowledge of the MR appearance of normal bone marrow is crucial to interpreting the images. Throughout childhood bone marrow converts from hematopoietic to fatty marrow in a peripheral to central fashion (feet to hips and hands to shoulders) and from the central diaphysis to the metaphysis within each bone [42]. Some investigators caution that STIR may mask lesions in very young children with hematopoietic marrow because it is very cellular and normally appears bright on this sequence. Those investigators suggest in-phase and out-of-phase pulse sequences and the use of reticuloendothelial system-specific contrast agents which suppress the signal intensity of normal marrow but not of neoplastic marrow [43]. Depending on the method employed, whole-body MRI can be accomplished in 15–50 min [41]. In a recent study, using STIR sequences and

PAT technology, WBMRI in children with small-cell tumors had a sensitivity for skeletal metastases of 97.5 % and specificity of 99.4 % compared to skeletal scintigraphy with a sensitivity of 30 % and specificity of 99.4 % and PET-CT with a sensitivity of 90.0 % and specificity of 100 % [44]. The obvious benefit of WBMRI in this setting is the lack of ionizing radiation.

Conventional WBMRI incorporates a large amount of data including that of normal structures such as fat and muscles. As a result image interpretation can be time consuming and subtle lesions can be overlooked. Recently diffusion-weighted (DWI) whole-body MRI has been introduced as an alternative to conventional WBMRI. This technique utilizes a spin-echo sequence and two strong gradients (motion-probing gradients) on either side of the 180° refocusing pulse. This is basically a T2W sequence with the application of two strong MPGs resulting in a decrease in signal intensity of all structures. The amount of signal decrease is not the same for all structures and depends on the degree of apparent diffusion that occurs between the MPGs. Structures with low diffusivity are less suppressed than those with a high degree of diffusion or perfusion (e.g., vascular structures, cerebrospinal fluid, urine). Because most lesions, both benign and malignant, have relatively impeded diffusivity, they lose less signal than adjacent normal background tissue resulting in a high lesion-to-background contrast. This approach to WBMRI has the potential to improve lesion detection while decreasing interpretation time [45]. A DWI whole-body examination can be performed in about 20–30 min. A comprehensive review of DWI in pediatric malignant lymphoma was recently published [45].

Nuclear Medicine

Nuclear medicine employs radiolabeled isotopes that are designed to interact with specific organs or cellular processes. Studies are performed by intravenously injecting the radiotracer and then waiting for an appropriate period of time to allow the desired distribution of the radiotracer within the body. As the radioisotope decays the emitted radiation can be detected by cameras designed to detect a specific level of energy. In general, there are two types of radioisotopes in clinical use, single-photon emitters, detected with a gamma camera, and positron emitters, detected with positron emission tomography (PET) cameras. Because the detection sensitivity of the cameras is very high, radiopharmaceuticals can be administered in very small doses that do not perturb normal physiologic processes. Nuclear imaging is quantitative, or at least semiquantitative; therefore, image intensity (or counts) corresponds to the concentration of the radiopharmaceutical. While nuclear medicine studies provide valuable functional and metabolic information, the resulting images have coarse spatial resolution, expressed as the full-width half-maximum of the system point or line-spread function. Resolution ranges from about 5 mm for PET imaging to 10 mm for single-photon emission computed tomography (SPECT) cameras. Therefore, relative to CT and MRI, anatomic definition on nuclear medicine images is poor. The ability to co-register and fuse nuclear medicine images with conventional imaging studies helps to overcome this limitation. An additional drawback of nuclear medicine imaging is the inherent radiation exposure. Although radiation doses from nuclear medicine imaging procedures are low, they are not negligible [46]. Also, because nuclear medicine imaging studies can be lengthy, sedation is often required for young patients.

In pediatric oncology, nuclear medicine imaging is essential in the evaluation of patients with neuroblastoma, bone and soft-tissue sarcomas, and lymphoma. The most commonly used radioisotopes are the single-photon emitters, iodine^{123}-labeled metaiodobenzylguanidine (I^{123} MIBG) and technetium^{99m}-labeled methylene diphosphonate (Tc^{99m} MDP), and the positron emitter, F^{18}-labeled fluorodeoxyglucose (F^{18}-FDG). I^{123} MIBG is a norepinephrine analog that concentrates in adrenergic storage vesicles of neural crest tissues and is used to assess patients with neuroblastoma. Tc^{99m} MDP is taken up in sites of osteoblastic activity and is useful in identifying sites of bony metastatic disease in patients with bone and soft-tissue sarcomas. F^{18}-FDG is a nonspecific glucose analog that is taken up in all sites of metabolic activity and is used to assess patients with a variety of malignancies including lymphomas and solid tumors.

Gamma cameras (also known as scintillation or Anger cameras) have been the predominant imaging device in nuclear medicine for many years. These cameras have large detector areas (usually rectangular in shape) that allow fairly rapid data acquisition from a large area of the body. Gamma camera crystals are made of NaI(Tl) that vary in thickness from one-quarter of an inch (with the best spatial resolution but lowest sensitivity) to 1 in. (with the highest sensitivity but coarsest resolution). Most cameras comprise three-eighths inch thick crystals, which provide the optimum balance between sensitivity and resolution. The energy arising from decay of single-photon emitters strikes and may produce a scintillation within the crystal. The scintillation results in the production of light that is detected in a photomultiplier tube backing the crystal and is used to generate an image [46]. During static imaging, the injected patient lies on a table over the gamma camera until a sufficient number of counts (signals) are collected from that body area to gen-

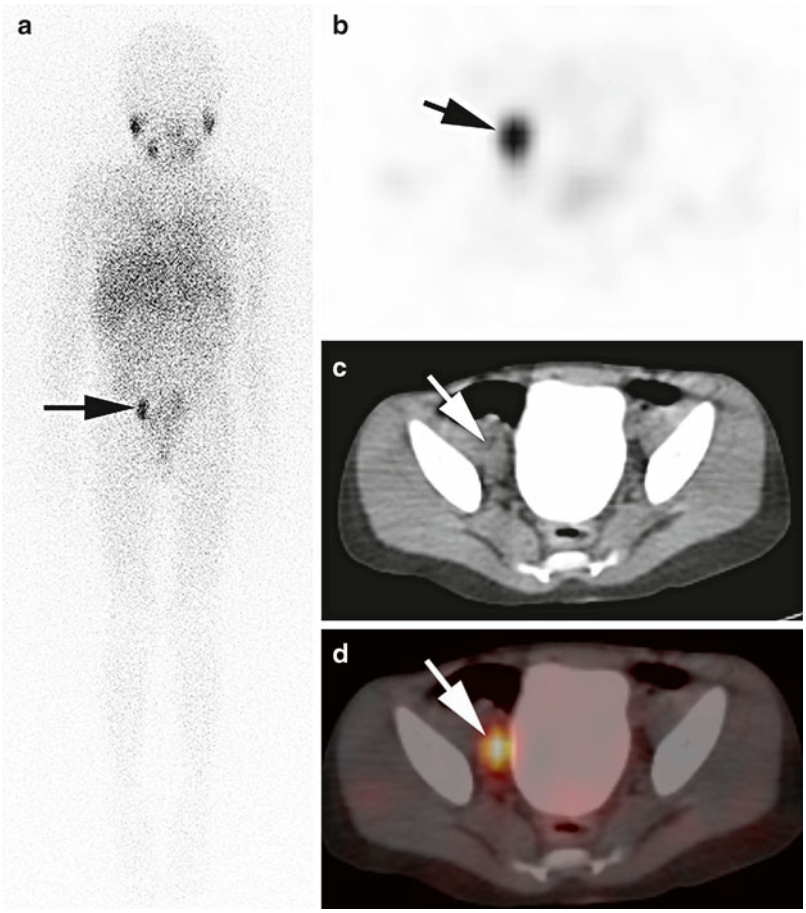

Fig. 2.7 On this (**a**) whole-body planar I^{123}-metaiodobenzylguanidine image the focus of activity in the *right* pelvis (*arrow*) is difficult to localize to bone, lymph node, or other soft tissues. These transverse (**b**) SPECT, (**c**) CT, and (**d**) fused SPECT-CT images accurately localize the activity to an iliac lymph node (*arrow*)

erate a planar image. Typically, the patient is sequentially moved over the camera in contiguous increments until the entire body is imaged.

Single-photon emission computed tomography (SPECT) imaging utilizes a gamma camera to acquire projection images from multiple angles as the camera rotates around the body. These tomographic images allow more accurate localization of sites of radioactivity within the body, compared to planar images [47]. The acquired data is corrected for non-uniform scanner response and other signal-degrading effects and then reconstructed into 5–10 mm thick transverse tissue-section images. In general SPECT imaging requires 20–30 min of acquisition time to obtain 60–120 projection images at 6° to 3° angular increments, respectively. Because of the lengthy acquisition time, whole-body SPECT imaging (from skull vertex to toes) remains impractical at the present time [46]. More recently, SPECT imaging systems have been combined with conventional computed tomography to produce hybrid SPECT-CT scanners, similar in concept to PET-CT scanners. The co-registered SPECT and CT images provide both functional and anatomic information and allow more accurate localization of sites of radioactivity (Fig. 2.7). These hybrid images have been shown to improve the sensitivity and specificity of SPECT imaging by improving lesion conspicuity, reducing false negatives and clarifying indeterminate findings [47]. In pediatric oncology SPECT-CT imaging has proven valuable for I^{123} MIBG imaging of patients with neuroblastoma, for I^{123} and I^{131} imaging to localize neck activity in children with papillary thyroid cancer, and for Tc^{99m} sulfur colloid sentinel node lymphoscintigraphy of patients with melanoma [48–50].

PET imaging is based on the annihilation coincidence detection of two collinear (180° apart) 511 keV gamma rays resulting from the mutual annihilation of a positron and electron. PET cameras comprise a series of rings containing individual, small-area detectors that completely encircle the patient and typically span a longitudinal distance of 10–20 cm. When the PET camera detects two 511 keV photons of energy coming from opposite directions, at the same time, a signal is produced. The most recent development in PET imaging is time-of-flight (TOF) scanning which utilizes the measured difference between detection times of the two

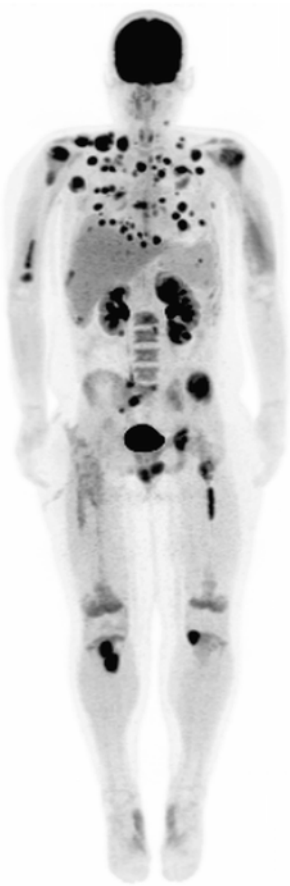

Fig. 2.8 This whole-body maximum intensity projection F^{18}-fluorodeoxyglucose (FDG) positron emission tomography image reveals extensive metastatic disease from adrenocortical carcinoma evidenced as innumerable foci of FDG avidity, throughout the lungs and bones and in lymph nodes

annihilation photons arising from a specific positron decay. TOF imaging allows approximate spatial localization of the event along the line of response with approximately 5–10 ns of coincidence time resolution. This approach reduces the random coincidence rate and improves the signal-to-noise ratio [46]. The most common clinically used positron-emitting radioisotope is fluorine-18-fluorodeoxyglucose (FDG) which is a radiolabeled glucose analog that is transported across cell membranes and phosphorylated but cannot be dephosphorylated. The trapped FDG appears as a focus of activity on the PET image and the intensity of the activity reflects the amount of trapped FDG. In oncology, FDG-PET imaging capitalizes on the fact that tumors are highly metabolically active and accumulate more glucose (and FDG) than normal tissue (Fig. 2.8) [51].

PET imaging requires a technique for soft-tissue attenuation correction. Hounsfield unit intensity measurements, obtained with CT, directly correlate with soft-tissue attenuation of the X-ray beam. Hounsfield unit measurements can also be used to correct the soft-tissue attenuation effects of the 511 keV photons emitted by radioisotopes used for PET scanning. Therefore, modern PET scanners almost universally integrate CT scanners that serve two purposes. First, the low-dose CT imaging provides the attenuation correction factors for PET imaging. Secondly, and equally important, these hybrid systems allow co-registration of PET and CT images, thus allowing accurate localization of sites of radioactivity within the body. The ability to co-register the anatomic and functional imaging also allows for more accurate distinction between sites of normal metabolic activity, such as brown fat, and pathologic processes.

Although low-dose CT scans are generally performed for PET-CT scanning, there continues to be growing concern regarding radiation exposure in children, especially those requiring repeated radiologic examination during cancer therapy. This has spurred the development of PET-MRI scanners which have recently reached the clinical arena. MRI has the ability to provide superior characterization of soft-tissue structures, particularly in the head and extremities, compared to CT. Furthermore, MRI can provide metabolic and functional information with the use of diffusion-weighted and dynamic contrast-enhanced imaging. The challenge with the development of PET-MRI has been in translating MRI signal intensities into attenuation correction factors for the PET images. This is a major challenge since signal intensities from anatomic structures vary depending on inherent T1 and T2 properties, magnetic field strength, choice of pulse sequence, use of gradients, and choice of radiofrequency coil. An additional challenge is the incorporation of PET scanners into high-strength magnetic fields. Despite these limitations, the development of PET-MRI scanners could revolutionize our approach to clinical molecular imaging since the functional and anatomic information that can be derived from both modalities should be synergistic. Another benefit of PET-MRI in the pediatric setting is that it could allow for acquisition of diagnostic MR images and PET images in one imaging session, thus reducing the number of sedations needed for very young patients. This hybrid modality holds great potential but requires validation in clinical trials and an assessment of its impact on diagnostic accuracy, patient management, and cost efficiency [52].

Conclusion

Diagnostic imaging plays a vital role in assessing children with cancer. Imaging generally begins with planar studies but ultimately cross-sectional imaging is required to fully evaluate both the primary tumor and potential metastatic sites. The radiologist should be aware of the strengths and limitations of each modality with respect to the clinical scenario, tumor location, and suspected histology. Attempts

should always be made to minimize radiation exposure as much as possible without compromising the care of the patient. In the future, molecular and functional imaging modalities will further complement anatomic imaging and likely play a larger and more important role in assessing the biological behavior of tumors.

References

1. Brenner DJ, Hall EJ. Computed tomography–an increasing source of radiation exposure. N Engl J Med. 2007;357:2277–84.
2. Donaldson SS. Lessons from our children. Int J Radiat Oncol Biol Phys. 1993;26:739–49.
3. Brody AS, Frush DP, Huda W, et al. Radiation risk to children from computed tomography. Pediatrics. 2007;120:677–82.
4. McCarville MB. The child with bone pain: malignancies and mimickers. Cancer Imaging. 2009;9(Spec No A):S115–21.
5. Guillerman RP, McCarville MB, Kaste SC, et al. Imaging studies in the diagnosis and management of pediatric malignancies. In: Pizzo PA, Poplack's DG, editors. Principles and practice of pediatric oncology. Philadelphia, PA: Lippincott Williams & Wilkins; 2011. p. 216–77.
6. Gritzmann N, Evans DH. Recent progress in diagnostic ultrasound techniques. Ultraschall Med. 2008;29:320–2.
7. McCarville MB, Roebuck DJ. Diagnosis and staging of hepatoblastoma: imaging aspects. Pediatr Blood Cancer. 2012;59(5):793–9.
8. Epelman M, Chikwava KR, Chauvin N, et al. Imaging of pediatric ovarian neoplasms. Pediatr Radiol. 2011;41:1085–99.
9. Brennan RC, Wilson MW, Kaste SC, et al. US and MRI of pediatric ocular masses with histopathological correlation. Pediatr Radiol. 2012;42:738–49.
10. Martinoli C, Valle M, Malattia C, et al. Paediatric musculoskeletal US beyond the hip joint. Pediatr Radiol. 2011;41 Suppl 1:S113–24.
11. Rosenberg HK. Sonography of pediatric neck masses. Ultrasound Q. 2009;25:111–27.
12. Sung EK, Setty BN, Castro-Aragon I. Sonography of the pediatric scrotum: emphasis on the Ts-torsion, trauma, and tumors. Am J Roentgenol. 2012;198:996–1003.
13. Riccabona M. Imaging of renal tumours in infancy and childhood. Eur Radiol. 2003;13 Suppl 4:L116–29.
14. Owens CM, Brisse HJ, Olsen OE, et al. Bilateral disease and new trends in Wilms tumour. Pediatr Radiol. 2008;38:30–9.
15. Craft AW, Parker L, Stiller C, et al. Screening for Wilms' tumour in patients with aniridia, Beckwith syndrome, or hemihypertrophy. Med Pediatr Oncol. 1995;24:231–4.
16. Choyke PL, Siegel MJ, Craft AW, et al. Screening for Wilms tumor in children with Beckwith-Wiedemann syndrome or idiopathic hemihypertrophy. Med Pediatr Oncol. 1999;32:196–200.
17. Monsalve J, Kapur J, Malkin D, et al. Imaging of cancer predisposition syndromes in children. Radiographics. 2011;31:263–80.
18. Garrett KM, Fuller CE, Santana VM, Shochat SJ, Hoffer FA. Percutaneous biopsy of pediatric solid tumors. Cancer. 2005; 104(3):644–52.
19. Fontalvo LF, Amaral JG, Temple M, et al. Percutaneous US-guided biopsies of peripheral pulmonary lesions in children. Pediatr Radiol. 2006;36:491–7.
20. Amaral JG, Schwartz J, Chait P, et al. Sonographically guided percutaneous liver biopsy in infants: a retrospective review. Am J Roentgenol. 2006;187:W644–9.
21. Chowdhury T, Barnacle A, Haque S, et al. Ultrasound-guided core needle biopsy for the diagnosis of rhabdomyosarcoma in childhood. Pediatr Blood Cancer. 2009;53:356–60.
22. McCrone L, Alexander S, Karsli C, et al. US-guided percutaneous needle biopsy of anterior mediastinal masses in children. Pediatr Radiol. 2012;42:40–9.
23. Shin HJ, Amaral JG, Armstrong D, et al. Image-guided percutaneous biopsy of musculoskeletal lesions in children. Pediatr Radiol. 2007;37:362–9.
24. Hall EJ. Lessons we have learned from our children: cancer risks from diagnostic radiology. Pediatr Radiol. 2002;32:700–6.
25. Pierce DA, Preston DL. Radiation-related cancer risks at low doses among atomic bomb survivors. Radiat Res. 2000;154:178–86.
26. Goske MJ, Applegate KE, Bulas D, et al. Image gently: progress and challenges in CT education and advocacy. Pediatr Radiol. 2011;41 Suppl 2:461–6.
27. Slovis TL. Where we were, what has changed, what needs doing: a decade of progress. Pediatr Radiol. 2011;41 Suppl 2:456–60.
28. Townsend BA, Callahan MJ, Zurakowski D, et al. Has pediatric CT at children's hospitals reached its peak? Am J Roentgenol. 2010; 194:1194–6.
29. Section 28 Childhood Cancer by Site. Incidence, survival and mortality. http://seer.cancer.gov/csr/1975_2009_pops09/results_merged/sect_28_childhood_cancer.pdf.
30. Olsen OE. Imaging of abdominal tumours: CT or MRI? Pediatr Radiol. 2008;38 Suppl 3:S452–8.
31. Donnelly LF, Frush DP. Pediatric multidetector body CT. Radiol Clin North Am. 2003;41:637–55.
32. Granata C, Magnano G. Computerized tomography in pediatric oncology. Eur J Radiol. 2013;82(7):1098–107.
33. Nievelstein RA, van Dam IM, van der Molen AJ. Multidetector CT in children: current concepts and dose reduction strategies. Pediatr Radiol. 2010;40:1324–44.
34. McHugh K, Disini L. Commentary: for the children's sake, avoid non-contrast CT. Cancer Imaging. 2011;11:16–8.
35. States LJ, Meyer JS. Imaging modalities in pediatric oncology. Radiol Clin North Am. 2011;49:579–88. v.
36. Gutzeit A, Binkert CA, Koh DM, et al. Evaluation of the antiperistaltic effect of glucagon and hyoscine on the small bowel: comparison of intravenous and intramuscular drug administration. Eur Radiol. 2012;22:1186–94.
37. Stein-Wexler R. MR imaging of soft tissue masses in children. Magn Reson Imaging Clin N Am. 2009;17:489–507. vi.
38. Kaewlai R, Abujudeh H. Nephrogenic systemic fibrosis. Am J Roentgenol. 2012;199:W17–23.
39. Mazumdar A, Siegel MJ, Narra V, et al. Whole-body fast inversion recovery MR imaging of small cell neoplasms in pediatric patients: a pilot study. Am J Roentgenol. 2002;179:1261–6.
40. Darge K, Jaramillo D, Siegel M. Whole-body MRI in children: current status and future applications. Eur J Radiol. 2008;68:289–98.
41. Goo HW. Regional and whole-body imaging in pediatric oncology. Pediatr Radiol. 2011;41 Suppl 1:S186–94.
42. Babyn PS, Ranson M, McCarville MB. Normal bone marrow: signal characteristics and fatty conversion. Magn Reson Imaging Clin N Am. 1998;6:473–95.
43. Daldrup-Link HE, Franzius C, Link TM, et al. Whole-body MR imaging for detection of bone metastases in children and young adults: comparison with skeletal scintigraphy and FDG PET. Am J Roentgenol. 2001;177:229–36.
44. Kumar J, Seith A, Kumar A, et al. Whole-body MR imaging with the use of parallel imaging for detection of skeletal metastases in pediatric patients with small-cell neoplasms: comparison with skeletal scintigraphy and FDG PET/CT. Pediatr Radiol. 2008;38:953–62.
45. Kwee TC, Takahara T, Vermoolen MA, et al. Whole-body diffusion-weighted imaging for staging malignant lymphoma in children. Pediatr Radiol. 2010;40:1592–602. quiz 1720–1.
46. Zanzonico P. Principles of nuclear medicine imaging: planar, SPECT, PET, multi-modality, and autoradiography systems. Radiat Res. 2012;177:349–64.

47. Brandon D, Alazraki A, Halkar RK, et al. The role of single-photon emission computed tomography and SPECT/computed tomography in oncologic imaging. Semin Oncol. 2011;38:87–108.
48. Kim HY, Gelfand MJ, Sharp SE. SPECT/CT imaging in children with papillary thyroid carcinoma. Pediatr Radiol. 2011;41:1008–12.
49. Klode J, Poeppel T, Boy C, et al. Advantages of preoperative hybrid SPECT/CT in detection of sentinel lymph nodes in cutaneous head and neck malignancies. J Eur Acad Dermatol Venereol. 2011;25:1213–21.
50. Soderberg M, Mattsson S, Oddstig J, et al. Evaluation of image reconstruction methods for 123I-MIBG-SPECT: a rank-order study. Acta Radiol. 2012;53(7):778–84.
51. Rohren EM, Turkington TG, Coleman RE. Clinical applications of PET in oncology. Radiology. 2004;231:305–32.
52. Voss SD. Pediatric oncology and the future of oncological imaging. Pediatr Radiol. 2011;41 Suppl 1:S172–85.

Soft Tissue Sarcomas

3

David M. Parham, Sue C. Kaste, Anand Raju, and M. Beth McCarville

Overview and Classification

Soft tissue tumors can be broadly defined as neoplasms that arise within connective tissue and supporting structures such as blood vessels, nerves, muscle, and adipose tissue. However, this fails to convey the principle that these lesions may arise within viscera as well as soft tissue, and that most of the tumefactions of connective tissue represent reactive or inflamed tissue rather than autonomous growths.

WHO Classification

In 2005, 2013 [1], the World Health Organization (WHO) included cell types updated a classification system of soft tissue neoplasms that was based on two factors: supposed cell of origin (or phenotype), and behavior, the latter separated into benign, borderline, and malignant lesions. Table 3.1 lists the WHO classification as published at that time, although a few modifications have since been suggested [1]. Most of these lesions affect children and adolescents of various ages, and even the ones that primarily occur in adults will occasionally arise in pediatric patients. This classification has great value in systematizing diagnosis and predicting behavior, but it suffers from the fact that there are a great number of heterogeneous entities, few of which occur with sufficient regularity to perform prospective therapeutic trials in a timely fashion, even in large multi-institutional trials such as run by the Children's Oncology Group (COG).

Grading

The problem of treating a large, heterogeneous group of diagnoses, most being rare entities, has been partially solved by the COG with the use of sarcoma grading. In 1987, the Pediatric Oncology Group (POG) began a prospective trial testing the value of grading in prognosis and stratification of childhood soft tissue sarcomas other than rhabdomyosarcoma or Ewing tumors. A system based on both histological diagnosis and more traditional factors such as mitotic count and necrosis was devised [2] (Table 3.2) and effectively separated patients with good and bad outcomes [3].

A sarcoma grading system was also devised by Coindre et al. for the Fédération Nationale des Centres de Lutte Contre le Cancer (FNLCC) [4] and is based on scoring of three parameters: mitoses, necrosis, and differentiation (Table 3.3). In a retrospective study of POG patients, this system also predicted tumor behavior of pediatric sarcomas [5].

Morphologic Classification

Pediatric soft tissue tumors can be separated into broad morphological categories, as an aid for differential diagnosis and ancillary testing. However, tumors overlap considerably among categories; for example rhabdomyosarcoma may be a round cell, spindle cell, epithelioid, or myxoid neoplasm, and there are fibroma-like variants of epithelioid sarcoma.

A list of round cell soft tissue neoplasms appears in Table 3.4. These lesions comprise blastemal neoplasms with little or no differentiation, so that a large panel of ancillary tests may be necessary for diagnosis. The initial approach with these lesions is to consider the most commonly occurring ones—rhabdomyosarcoma, Ewing sarcoma, lymphoma, and

D.M. Parham, M.D. (✉)
Department of Pathology and Laboratory Medicine, Children's Hospital Los Angeles/University of Southern California, 4650 Sunset Blvd., #43, Los Angeles, CA 90027, USA
e-mail: daparham@chla.usc.edu

S.C. Kaste, D.O.
Radiological Sciences, St. Jude Children's Research Hospital, 262 Danny Thomas Place, Memphis, TN 38105-3678, USA
e-mail: sue.kaste@sdude.org

A. Raju, M.D. • M.B. McCarville, M.D.
St. Jude Children's Research Hospital, Memphis, TN, USA
e-mail: beth.mccarville@stjude.org

D.M. Parham et al. (eds.), *Pediatric Malignancies: Pathology and Imaging*,
DOI 10.1007/978-1-4939-1729-7_3, © Springer Science+Business Media New York 2015

Table 3.1 WHO classification of soft tissue neoplasms

Adipocytic neoplasms
Fibroblastic/myofibroblastic neoplasms
Fibrohistiocytic neoplasms
Smooth muscle tumors
Pericytic tumors
Skeletal muscle neoplasms
Vascular neoplasms
Chondro-osseous neoplasms
Neoplasms of indeterminate histogenesis

Table 3.2 Pediatric oncology group grading system for childhood sarcomas

Grade 1
Myxoid and well-differentiated liposarcoma
Well-differentiated or infantile (<4 years old) fibrosarcoma
Well-differentiated or infantile (<4 years old) hemangiopericytoma
Well-differentiated malignant peripheral nerve sheath tumor
Angiomatoid malignant fibrous histiocytoma
Deep-seated dermatofibrosarcoma protuberans
Extraosseous myxoid chondrosarcoma
Grade 2
<15 % of the surface area shows necrosis
Mitotic count <5 mitotic figures/10 hpf with 40× objective
Nuclear atypia is not marked
The tumor is not markedly cellular
Grade 3
Pleomorphic or round-cell liposarcoma
Mesenchymal chondrosarcoma
Extraskeletal osteogenic sarcoma
Malignant triton tumor
Alveolar soft part sarcoma
Any other sarcoma not included in grade 1 and showing >15 % necrosis and/or >4 mitotic figures/10 hpf with 40× objective

Table 3.3 FNLCC system for grading sarcomas

Differentiation score
1: Closely resembles normal adult mesenchymal tissues
2: Resembles normal mesenchymal tissues but not closely
3: Embryonal, undifferentiated, or indeterminate histogenesis
Mitotic count (hpf, a hpf measures 0.1734 mm^3)
1: 0–9/10
2: 10–19/10
3: >19/10
Geographic necrosis
0: None
1: <50 % of tumor
2: >49 % of tumor
Grade
1: Total score of 1–3
2: Total score of 4–5
3: Total score of 6–8

Table 3.4 Round cell neoplasms

Rhabdomyosarcoma
Lymphoma/leukemia
Neuroblastoma
Ewing sarcoma
Desmoplastic small round cell tumor
Synovial sarcoma
MPNST
Germinoma
Round cell liposarcoma
Small cell osteosarcoma
Mesenchymal chondrosarcoma
Undifferentiated sarcoma
Histiocytic lesions such as giant cell tumor of tendon sheath
Organ-based embryonal tumors such as Wilms tumor and hepatoblastoma

Table 3.5 Spindle cell soft tissue tumors

Nodular fasciitis
Proliferative fasciitis/myositis
Fibromatosis of various types
Myofibrosarcoma
Inflammatory myofibroblastic tumor
Dermatofibrosarcoma protuberans
Juvenile xanthogranuloma/benign fibrous histiocytoma
Infantile fibrosarcoma
Adult-type fibrosarcoma
Monophasic spindle cell synovial sarcoma
Solitary fibrous tumor
Myxoinflammatory fibroblastic sarcoma
Spindle cell rhabdomyosarcoma
Undifferentiated sarcoma, particularly pleomorphic sarcoma (“MFH”)
Gastrointestinal stromal tumor (GIST)
Leiomyosarcoma
Schwannoma
Neurofibroma
MPNST
Angiomatoid fibrous histiocytoma
Plexiform fibrohistiocytic tumor
Dedifferentiated liposarcoma

neuroblastoma—and then to tailor the immunostain panel to exclude these lesions. Positively staining lesions may be confirmed by genetic tests, and if discrepancies or unresolved results occur, a wider test panel can be used for less common tumors.

Spindle cell neoplasms are listed in Table 3.5. Unlike round cell neoplasms, many in this group are benign, but they may be locally aggressive and frequently recurrent. Many of the malignant lesions are relatively common in adults but rare in children. Often, they comprise fibroblastic tumors, for which immunostains may have limited utility after myogenic and neural neoplasms have been excluded.

Table 3.6 Epithelioid soft tissue neoplasms

Epithelioid sarcoma
Vascular tumors
Epithelioid rhabdomyosarcoma
Epithelioid GIST
Rhabdoid tumor of soft tissue
Epithelioid MPNST
Myomelanocytic tumors of soft tissue (PEComas)
Monophasic epithelial cell synovial sarcoma
Alveolar soft part sarcoma
Clear cell sarcoma of soft tissue
Myoepithelial tumor of soft tissue (parachordoma)
Perineurioma
Sclerosing epithelioid fibrosarcoma

Table 3.7 Myxoid soft tissue neoplasms

Intramuscular myxoma
Lipoblastoma
Myxoid liposarcoma
Well-differentiated liposarcoma/atypical lipomatous tumor
Pleomorphic liposarcoma
Myxoinflammatory fibroblastic sarcoma
Myxofibrosarcoma
Myxoid DFSP
Giant cell fibroblastoma
Schwannoma
Neurofibroma
Extraskeletal myxoid chondrosarcoma
Embryonal rhabdomyosarcoma
Myxoid leiomyosarcoma
Myxoid solitary fibrous tumor
Low-grade fibromyxoid sarcoma

Epithelioid neoplasms, are listed in Table 3.6, but with the exception of hemangiomas comprise an uncommon group of entities. Some, like perivascular epithelioid cell tumors (PEComas) and alveolar soft part sarcoma, have no non-neoplastic cellular counterpart. Others, like epithelioid sarcomas, myoepithelial tumors, or clear cell sarcomas of soft tissue, represent mesenchymal counterparts of carcinomas, pleomorphic adenomas, or melanomas respectively. Still others represent rare variants of other soft tissue sarcomas such as malignant peripheral nerve sheath tumor, rhabdomyosarcoma, or synovial sarcoma. All are characterized by cells with abundant, variably eosinophilic cytoplasm, cell junctions, and variable staining for epithelial markers like cytokeratin and epithelial membrane antigen.

Myxoid neoplasms are listed in Table 3.7. These all contain variable, often predominant, amounts of loose, mucoid stroma rich in proteoglycans. This category contains lesions that have traditionally been difficult to diagnose and hard to predict, but current genetic testing has eased much of this burden, and new tests are described on a regular basis. Most of these are benign neoplasms, intermediate tumors, or low-grade sarcomas, but they may progress to high-grade lesions. For example, myxoid liposarcoma is a low-grade sarcoma that has a high-grade counterpart, round cell liposarcoma. Similarly, low-grade fibromyxoid sarcomas may progress into cellular, aggressive lesions upon recurrence.

Approach to Imaging of Soft Tissue Tumors

Evaluation of soft tissue tumors often begins with obtaining a clinical history and performing a physical evaluation, with the patient's age being critical in narrowing the differential diagnosis. The presenting concern is often a palpable mass, with larger lesions frequently presenting with pain. Important clinical information includes the presence of any pre-existing conditions, location, duration, growth pattern of the lesion, overlying skin abnormalities, changes in appearance of the mass, and any associated systemic symptoms [6].

Imaging studies are usually required when the clinical and physical examination findings do not completely define the diagnosis. Imaging is used to determine tumor extent and relation of the mass to surrounding anatomic structures. Imaging can also differentiate the origin of the mass from bone or soft tissues when this cannot be delineated on physical examination.

When soft tissue lesions are small and superficial, ultrasound is usually the investigation of choice because it is readily available, relatively easy to perform, lacks ionizing radiation, has no contraindications, is low cost, and does not require sedation or general anesthesia. High-frequency linear array transducers should be used to evaluate soft tissue masses, with the complimentary use of convex array transducers for larger and deeper lesions. Ultrasonography is particularly helpful in distinguishing solid from cystic lesions. Routine use of spectral and color Doppler is necessary to determine whether intra-lesional blood flow exists and to assess the amount of flow within the lesion [6]. The ability to show blood flow by color Doppler increases the specificity of the diagnoses of vascular and inflammatory lesions. The specificity of gray-scale ultrasonography in the diagnosis of soft tissue tumors is only about 40 %; however, ultrasound is useful in planning further imaging [6, 7].

Despite being expensive and sometimes requiring sedation or general anesthesia, magnetic resonance imaging (MRI) is the imaging modality of choice for evaluating pediatric soft tissue masses because of its high tissue contrast and multiplanar capabilities, and it is an excellent modality for most large and deep lesions. MRI is particularly important in presurgical management of soft tissue tumors to determine the soft tissue extension and the relationship of the tumor to the bone, neurovascular structures, and the joint. This modal-

ity is also used to monitor the response of soft tissue tumors to therapy. Combining T1- and T2-weighted imaging forms the basis of MRI. Fat-suppressed images are helpful in evaluating lesions in subcutaneous tissues. Most soft tissue masses have similar features on MR images: hypointense on T1-weighted (T1W) images, hyperintense on T2-weighted images, and a pseudocapsule.

Gadolinium-enhanced MR imaging is important in evaluating tumor viability and perilesional soft tissue edema. While MRI may be of limited utility in determining a particular diagnosis it can help in differentiating benign from malignant processes. Malignant MRI characteristics include heterogeneous signal, neurovascular encasement, invasion of bone, and asymmetric margins. MRI is crucial for verifying the extent of the lesion, which helps in determining resectability [7]. Multiplanar capabilities allow delineation of the 3-dimensional relationship of a soft tissue mass to adjacent structures.

The role of other modalities, including plain radiography and computed tomography (CT), is very limited. Plain radiography may be used to evaluate and assess the bony involvement of a soft tissue mass or the osseous origin of a presumed soft tissue lesion. The role of CT in evaluating soft tissue tumors is limited because tissue characterization is not well defined by CT. However, CT is helpful in detecting calcification or ossification within a lesion but is usually used with MRI when this is in question. CT should rarely be used as the primary imaging modality because it requires radiation exposure to the patient and yields less tissue contrast than does MRI [6–8].

Positron emission tomography (PET) has a growing role as an imaging modality that is used with MR and CT imaging to detect the primary site, assign stage, and direct management of sarcomas. PET imaging with F^{18}-fluorodeoxyglucose (FDG-PET) and FDG-PET/computed tomography (PET-CT) are increasingly important imaging techniques in the noninvasive evaluation and monitoring of known or suspected malignant disease in children. The advent of dual-modality PET/CT imaging systems has added unprecedented diagnostic capability by revealing the precise anatomic location of metabolic information, thus allowing metabolic characterization of normal and abnormal structures [9].

Fibroblastic Tumors

Pediatric fibroblastic tumors comprise a heterogeneous array of diverse lesions that must be discriminated from reactive processes. Pediatric reparative tissues often contain exuberant proliferations of fibroblasts and myofibroblasts, necessitating careful observation and clinical correlation. Quasineoplastic lesions may show abnormal fibroblastic growth, such as IgG4 plasma cell proliferations, soft tissue HHV8, mycobacterial, or Histoplasma infections, or poorly understood lesions such as sclerosing mediastinitis. However, some lesions formerly considered reactive "inflammatory pseudotumors" have now been shown to be clonal proliferations derived from specific genetic mutations or translocations.

Fibroblastic Tumors of Intermediate Malignancy

Infantile Fibrosarcoma

Definition: Infantile fibrosarcoma is a low-grade but locally invasive fibroblastic neoplasm that typically arises in the extremities of newborns. It contains a characteristic chromosomal translocation shared by morphologically and clinically diverse infantile neoplasms.

Clinical Features and Epidemiology

Infantile fibrosarcomas are relatively uncommon lesions, comprising about 10 % of pediatric sarcomas in many series [2, 10]. However, they comprise a substantial component of congenital and infantile soft tissue sarcomas [11]. As such they generally arise in very young infants and are one of the most common forms of soft tissue sarcoma in this age group. These lesions usually form large, bulky, expansile tumors that extensively invade adjacent tissues, including bone. They most commonly arise from the distal portions of the extremities, particularly the forearm and lower leg, but unexpected origins such as heart and lung have been reported [12].

Imaging Features

Infantile fibrosarcoma (IFS) often presents as a rapidly enlarging soft tissue mass in an extremity at or shortly after birth. These tumors may cause a violaceous skin discoloration similar to hemangiomas. Superficial skin ulcerations communicating with large draining veins can result in life-threatening bleeding. The most common plain radiographic finding of IFS is a soft tissue mass that grows rapidly on follow-up imaging. There have been no reports of tumor ossification or matrix calcification (Fig. 3.1a) [13, 14]. The adjacent bone may show deformity and cortical thickening with failure of normal tubulation. Destruction of bone is rare and associated with extensive soft tissue tumors that may cause widespread bony erosion. Bone destruction, when present, is usually well defined and associated with periosteal reaction only very late in the process [13, 15]. There are only a few reports of the sonographic appearance of IFS [15–17]. In one report this tumor appeared as a homogenous hyperechoic mass, while others report a mass with solid and

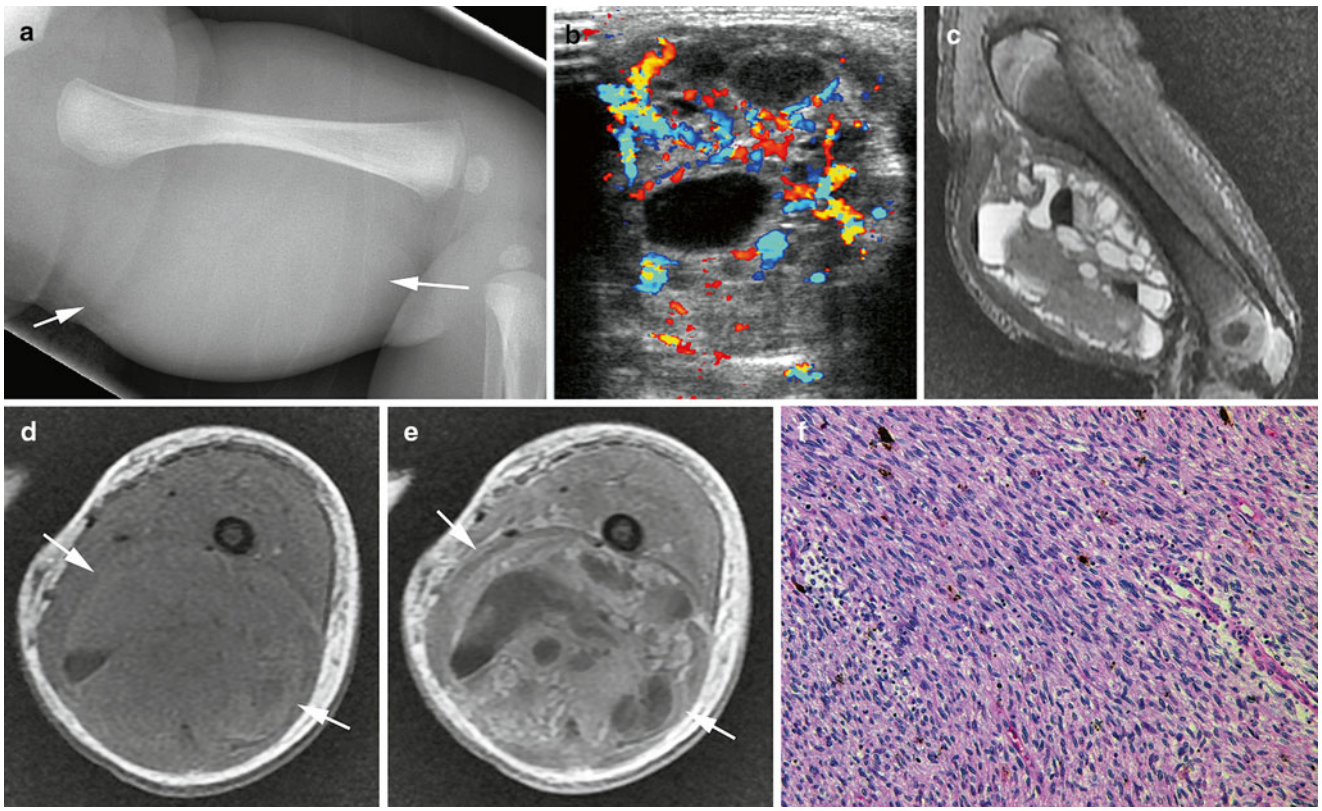

Fig. 3.1 Infantile fibrosarcoma. A 2-month-old boy presented with right thigh swelling subsequently diagnosed with infantile fibrosarcoma. (**a**) Lateral radiograph shows large soft tissue mass (*arrows*) without matrix calcification or bone involvement. (**b**) Transverse Doppler ultrasound image shows a hypervascular mass with cystic and solid components. (**c**) Sagittal T2W MR image shows a large, well-circumscribed, solid and cystic soft tissue mass without bone involvement. Note fluid-fluid levels and variability of signal within cysts due to blood products. (**d**) Axial T1W MR image shows a heterogeneous mass (*arrows*) that (**e**) enhances heterogeneously after contrast administration. (**f**) Histologically, infantile fibrosarcoma comprises streaming dense fascicles of spindle cells resembling the "herring bone" pattern of adult fibrosarcoma

cystic components and mixed echogenicity or a mass that was isoechoic with muscle. Doppler ultrasound may demonstrate the hypervascular nature of these tumors (Fig. 3.1b). CT has the advantage of demonstrating bony involvement; however, it exposes the patient to the potentially harmful effects of radiation.

MRI is the preferred cross-sectional imaging modality because it avoids radiation and provides superior soft tissue characterization and delineation of tumor margins, features important in surgical planning. When tissue planes are violated, or neurovascular involvement is present, surgical resection alone is unlikely to provide local control [13, 14]. On MRI these tumors appear as mixed solid and cystic masses due to internal necrosis and hemorrhage (Fig. 3.1c, d). Initially the solid components appear intermediate or hypointense on T1W images and hyperintense on T2W images due to a high cellular content. As tumors mature they may appear more hypointense on T2W images due to increasing collagen accumulation within areas of fibrosis. Tumors typically demonstrate a heterogeneous pattern of contrast enhancement (Fig. 3.1e) [13, 14, 17]. Conventional or MR angiography will show tumor hypervascularity with disorganized vessels and large draining veins [13, 15, 18, 19].

Molecular Genetics

Infantile fibrosarcomas contain a reciprocal translocation, the t(12;15)(p16;q25) [20], which fuses the *TEL* (or *ETV6*) proto-oncogene on chromosome 12 with the *NTRK3* on chromosome 15. These genes are located on the distal long arms of the two chromosomes and were not discovered until relatively recently compared with other established translocations [20]. Also known as *ETV6*, *TEL* encodes a helix-loop-helix DNA transcription factor that is often dysregulated in childhood acute lymphoblastic leukemia [21]. *NTRK3*, alias *TRKC*, encodes neurotrophin 3, a signal transduction molecule activated by nerve growth factor and expressed by some neuroblastomas [22]. The fusion transcript produced by this translocation acts as an aberrant tyrosine kinase capable of transformation of multiple cell lineages [23]. Neoplasms associated with the *TEL-NTRK3* fusion include infantile fibrosarcoma, cellular mesoblastic nephroma, congenital bronchopulmonary myofibroblastic tumor, and secretory carcinoma of the breast [24].

Gross and Microscopic Features

Infantile fibrosarcomas produce bulky, invasive, fibrous masses that have a whorled, pale grey, nonencapsulated appearance like that of other fibrous lesions. Microscopically, the tumor extensively infiltrates and destroys adjacent fat, connective tissue, muscle, underlying bone, and overlying skin. Lesional cells display plump to elongated spindly profiles with a high degree of cellularity and mitotic activity (Fig. 3.1f). In spite of these factors and the presence of geographic necrosis, these lesions should be considered grade 1 sarcomas [2]. The tumor cells form whorled arrays, often with the classic herringbone pattern, or they may display a hemangiopericytomatous appearance reminiscent of infantile myofibroma [25].

Immunohistochemistry and Other Special Stains

Ancillary stains have limited value in the diagnosis of infantile fibrosarcoma. As expected, vimentin, smooth muscle actin, and occasionally desmin are positive, reflecting their myofibroblastic content. Trichrome stains highlight intercellular collagen, and reticulin stains reveal investment of the tumor cells by a fine lacework of reticulin fibers, characteristic of fibrosarcoma and hemangiopericytoma.

Molecular Diagnostic Features and Cytogenetics

Besides the t(12;15) described above, infantile fibrosarcomas often contain extra copies of chromosome 8, 11, 17, and 20 [26], particularly chromosome 8, but these are common in other sarcomas. Both Fluorescence In-situ Hybridization (FISH) and Reverse Transcriptase-Polymerase Chain Reaction (RT-PCR) can be profitably used to diagnose lesions with *TEL-NTRK3* fusions [27, 28]. This testing has recently been utilized to define new categories of non-fibrosarcomatous infantile sarcoma [29] and to diagnosis infantile fibrosarcoma in unexpected locations [12].

Prognostic Features

In spite of its ominous appearance, infantile fibrosarcoma generally shows only local aggressiveness and infrequently metastasizes [30]. However, its destructive nature frequently leads to radical local surgery, such as amputation, but preoperative chemotherapy may decrease its size and allow a more conservative approach [31].

Sclerosing Epithelioid Fibrosarcoma

Definition: Sclerosing epithelioid fibrosarcoma is a low-grade fibrosarcoma containing fibroblastic cells embedded in a dense collagenous stroma.

Clinical Features and Epidemiology

Sclerosing epithelioid fibrosarcoma is a rare neoplasm recognized only recently and primarily occurring in young adults, but with an age range that includes adolescents [32]. The lesions most commonly occur in the lower extremities, but diverse sites have been reported [33]. Approximately one-third have metastasized at presentation, and about 85 % eventually metastasize, belying the low-grade histological appearance. Only 89 patients had been reported by 2008 [33]. Lesions may arise in bone as well as soft tissue [34].

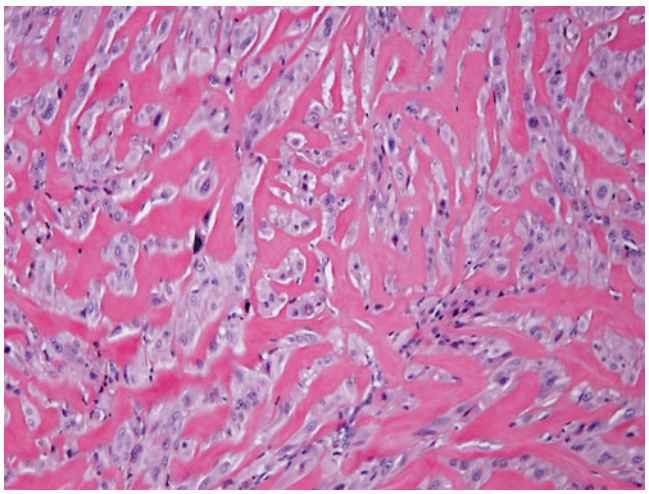

Fig. 3.2 Sclerosing epithelioid fibrosarcoma. Dense strands of thick, osteoid-like collagen intersect cords of epithelioid fibroblasts

Imaging Features

The imaging features of sclerosing epithelioid fibrosarcoma have not been well described.

Molecular Genetics

Sclerosing epithelioid fibrosarcomas contain rearrangements of the *FUS* gene similar to those occurring in low-grade fibromyxoid sarcoma (see below) [35, 36]. This suggests that it represents a variant of that tumor and not a separate, distinct entity.

Gross and Microscopic Features

Sclerosing epithelioid fibrosarcomas are densely fibrous, invasive lesions with destruction of adjacent tissues, including bone. This latter feature may lead to confusion as to whether it has a bony or soft tissue primary site [34]. Microscopically this leads to difficulty in diagnosis, as the tumor contains a densely sclerotic collagenous stroma resembling osteoid (Fig. 3.2). The stroma invests bland appearing, monomorphic, epithelioid cells [32] that form nests and cords resembling carcinoma.

Immunohistochemistry and Other Special Stains

Immunohistochemistry has limited value in the diagnosis of sclerosing epithelioid fibrosarcoma. EMA, S100, and cytokeratin positivity may be seen [32].

Molecular Diagnostic Features and Cytogenetics

Cytogenetic analysis of sclerosing epithelioid fibrosarcoma may reveal multiple chromosomal rearrangements [37]. *FUS* rearrangement may be detected by FISH [35].

Prognostic Features

Unfortunately, in spite of its low-grade appearance, sclerosing epithelioid fibrosarcoma is an aggressive lesion that shows chemoresistance [34]. Therefore, survival is linked to the adequacy of excision. Head and neck lesions appear to fare worse than those in other sites, and overall survival is about one-third at 3.5 years, with approximately the same number surviving with disease [33].

Myofibrosarcoma

Definition: Myofibrosarcoma, also known as low-grade myofibroblastic sarcoma [38], is a neoplastic with features intermediate between fibrosarcoma and leiomyosarcoma. It is generally a low- to intermediate-grade sarcoma that is locally aggressive but showing limited capacity for distant spread [39].

Clinical Features and Epidemiology

Myofibrosarcoma is an uncommon lesion that occurs in both children and adults, primarily the latter. In children, it has a predilection for the head and neck region [40]. It is a locally invasive lesion that may involve the bone of the maxilla or mandible.

Imaging Features

There is limited literature regarding the imaging features of myofibrosarcoma. In one case report the tumor arose from the nasal bone in a 4-year-old girl and was a small, solid, well-defined mass causing bone thinning on CT imaging. On MRI it appeared as a homogenous solid mass, isointense to muscle on T1W images and hyperintense on T2W images. After administration of gadolinium contrast the tumor demonstrated homogenous enhancement [41].

Molecular Genetics

At present, there are no genetic features that distinguish myofibrosarcoma.

Gross and Microscopic Features

Grossly, myofibrosarcomas form infiltrative, pale grey lesions with invasion and destruction of adjacent tissues. Microscopically, they contain whorls and bundles of cells with fusiform nuclei and moderate amounts of pink to purple cytoplasm (Fig. 3.3). The tumor cells may form storiform arrays. These lesions are composed of myofibroblasts, which are ultrastructurally defined by the presence of ergastoplasm, peripheral microfilaments, and anchoring filaments (fibronexus junctions) [42].

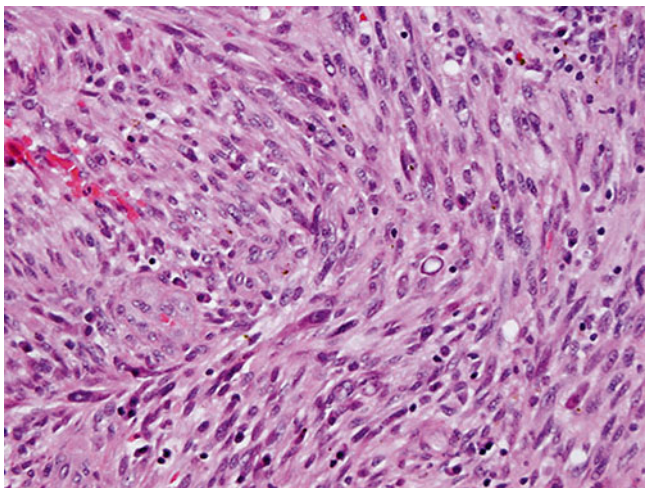

Fig. 3.3 Myofibrosarcoma. Dense, whorled bundles of plump spindle cells contain mildly enlarged fusiform nuclei and tapering purplish cytoplasm

By convention, low-grade myofibrosarcomas show moderate atypia and mitotic activity [38]. With higher grade features, one should consider the diagnosis of pleomorphic undifferentiated sarcoma ("malignant fibrous histiocytoma") [43, 44]. Myofibroblastic sarcomas thus exhibit a range of histological appearances.

Immunohistochemistry and Other Special Stains

As with ultrastructure, the combination of a smooth muscle and fibroblastic phenotype defines myofibrosarcoma. Thus, all lesions are vimentin-positive, most are smooth muscle actin- or muscle-specific actin-positive, and some are desmin-positive [39]. However, they are negative for calponin, separating them from leiomyosarcoma [45], and for myogenin or MyoD, separating them from rhabdomyosarcoma [46].

Molecular Studies

Molecular testing in myofibrosarcoma is primarily an exercise in exclusion, as they have no distinguishing features. However, their lack of ALK or TEL rearrangements separates them from inflammatory myofibroblastic tumor or infantile fibrosarcoma, respectively [43, 47], and they do not show the beta catenin pathway alterations typical of desmoid fibromatosis [48].

Prognostic Features

Myofibrosarcomas are relatively low-grade, indolent sarcomas that infrequently metastasize, so the major feature that predicts behavior is the adequacy of excision. They frequently recur, with untoward consequences in head and neck locations [40].

Low-Grade Fibromyxoid Sarcoma

Definition: Low-grade fibromyxoid sarcoma, a very descriptive term, is a connective tissue neoplasm of intermediate malignancy and mixed fibrocollagenous and mucinous stromal content.

Clinical Features and Epidemiology

In the pediatric age spectrum, low-grade fibromyxoid sarcoma mostly arises in adolescents, and it also occurs in young adults [49]. It usually arises in the lower extremity and groin but may affect unusual sites such as the big toe [50]. It is a rare lesion, but it is consistently included in large retrospective reviews of fibrosarcomatous lesions [51].

Imaging Features

A recent review of the imaging of 22 patients with low-grade fibromyxoid sarcoma found that most tumors arose in the deep soft tissues of the lower extremity and had an average size of about 6 cm. Tumors were solitary at diagnosis but multiple at local recurrence. On plain radiography tumors were visible as soft tissue masses without calcification or bone involvement. On sonography tumors were solid with intralesional nodules and predominantly hypoechoic at the periphery and hyperechoic centrally. Arterial flow was evident by Doppler evaluation. On non-contrast enhanced CT the tumors were heterogeneous but predominantly hypodense to muscle with internal isointense areas. After contrast administration most tumors contained peripheral or internal enhancing areas. On CT several tumors had internal calcifications that were puntate or linear and several showed bone erosion. On MRI most tumors were hypo- or isointense to muscle on T1W images and were hyperintense on T2W sequences. Many displayed a unique brain gyriform pattern of alternating folds of hypo- and hyperintense signal intensity or had intralesional nodules evident on T2W sequences. Contrast enhancement was variable and felt to reflect high cellularity of fibrous tissue, which appeared hypointense on T2W sequences and enhanced intensely, and non-enhancing myxoid tissue that appeared hyperintense on T2W imaging [52].

Molecular Genetics

A reciprocal translocation affecting chromosome 16, the t(7;16)(q33;p11) or the t(11;16)(p11;p11), characterizes low-grade fibromyxoid sarcoma [36] and respectively fuses *CREB3L1* or *CREB3L2* with *FUS*. *FUS* encodes a protein involved in transcriptional activation and protein/RNA binding. Both CREB3L1 and CREB3L2 belong to the leucine zipper family of transcription factors and normally activate stress proteins in the endoplasmic reticulum.

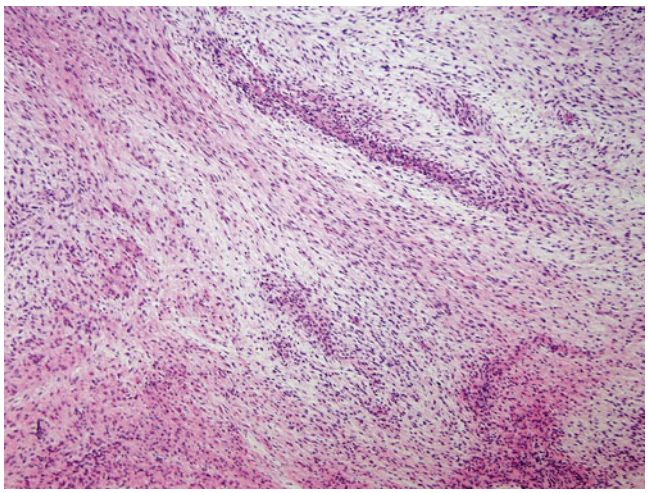

Fig. 3.4 Low-grade fibromyxoid sarcoma. Bundles of fibroblastic cells enmeshed in collagen alternate with relatively hypocellular strands of myxoid stroma

Gross and Microscopic Features

Low-grade fibromyxoid sarcoma forms deceptively well-circumscribed but nonencapsulated masses, with well-contoured, fibrous to myxoid cut surfaces [49]. Low power magnification reveals contrasting areas of myxoid and fibrous stroma, containing cells arrayed in a swirling growth pattern (Fig. 3.4) [53]. The tumor cells have a deceptively bland appearance and consist of fibroblasts and occasional myofibroblasts [49]. However, with progression and recurrence the lesions can become increasingly cellular with moderate pleomorphism [53].

Some low-grade fibromyxoid tumors contain foci of giant rosettes with collagenous cores rimmed by round to oblong nuclei. This lesion was originally described as a separate neoplasm, "hyalinizing spindle cell tumor with giant rosettes" [54]. However, it is now considered a variant and not a distinct entity, as it bears the molecular abnormalities of low-grade fibromyxoid tumor.

Immunohistochemistry and Other Special Stains

As with most fibroblastic neoplasms, immunohistochemistry has limited value in diagnosis of low-grade fibromyxoid sarcoma, which mostly stains with nonspecific markers such as vimentin but with occasional positivity for cytokeratin and actin [49]. Of note, the cells surrounding rosettes stain for neural markers such as S100, neuron-specific enolase, and Leu 22 [54]. Because of the characteristic gene fusions, there is overexpression of MUC4, which can be used for ancillary diagnosis [55, 56].

Molecular Diagnostic Features and Cytogenetics

Molecular studies offer confirmation of the diagnosis of low-grade fibromyxoid tumor and separate it from other fibrocollagenous and myxoid neoplasms [57, 58]. FISH is a suitable means for detecting FUS rearrangement [59], and RT-PCR detects most tumors [60], with the caveat that fusion variants may not be detected in a single probe study.

Array studies of low-grade fibromyxoid sarcoma show a characteristic gene expression pattern, with upregulation of *FOXL1* and *CD24* [56].

Prognostic Features

Accurate prediction of low-grade fibromyxoid sarcoma behavior requires years of follow-up, as recognized in the initial reports of this lesion [53]. Most deaths do not occur until after 5 years, as the tumor appears to pursue a slow, relentless course if not completely excised at initial surgery. On the other hand, long-term survival is possible even with metastasis [49].

Malignant Fibroblastic Neoplasms

"Adult-Type" Fibrosarcoma

Adult-type fibrosarcomas are distinguished from infantile fibrosarcomas not only by the obvious age difference but also by molecular features and clinical behavior. As fibroblastic neoplasms have become increasingly subcategorized, the entity of adult-type fibrosarcomas has become vanishingly rare, particularly in the pediatric age group [51], so they will not be further discussed. Rare childhood cases may occur as second malignant neoplasms or post-irradiation sarcomas [61].

So-Called Fibrohistiocytic Tumors

The term "fibrous histiocytoma" has been the source of considerable debate in recent years, as many of these tumors are derived from neither fibroblasts nor histiocytes. Benign and intermediate lesions in this category often have features of dermal dendrocytes [62, 63], whereas malignant lesions have been a "wastebasket" category for a wide variety of pleomorphic, undifferentiated sarcomas [64, 65]. However, this category of lesions persists because of its historical stature and its familiarity among pathologists and clinicians, largely because of its characteristic storiform histology.

Intermediate Fibrohistiocytic Neoplasms

Dermatofibrosarcoma Protuberans (DFSP)/ Giant Cell Fibroblastoma

Definition: Dermatofibrosarcoma protuberans (DFSP) and giant cell fibroblastoma comprise a spectrum of low-grade malignancies characterized by a *COL1A1/PDGFB* fusion and typically occurring in superficial soft tissues.

Clinical Features and Epidemiology

Both DFSP and fibrosarcoma most commonly occur in dermal and subcutaneous tissues, which they expand in a plaque-like fashion. Although they are locally invasive, they rarely metastasize. DFSP more commonly occurs in young adults, whereas giant cell fibroblastoma more commonly occurs in young children. Some tumors show both histologies or convert subtypes with recurrence. Occasionally, lesions occur in deep soft tissues.

Imaging Features

Gross imaging characteristics of DSFP demonstrate involvement and location in the skin and subcutaneous adipose tissue with rare involvement of the underlying muscle. Radiographically, a nodular or multinodular soft tissue mass lacking calcifications is seen [66–69]. Typically, bony infiltration and periosteal reaction are absent [66]. Rarely, these tumors demonstrate more aggressive behavior with violation of dermal planes, bony infiltration [66], and intracranial extension [70, 71].

Because of the typically superficial location of these nodular/multinodular lesions, ultrasound can provide important information regarding the size, dermal and fascial plane involvement, and, in cases of involvement into the deep soft tissue layers, tumor effect on adjacent tissues and structures (Fig. 3.5a). Ultrasound characteristics vary from decreased echogenicity through iso-echogenicity and hyperechogenicity relative to adjacent soft tissues [72, 73]; lesions may demonstrate heterogeneous echotexture [74]. Moderate to increased vascularity may be demonstrated [72, 75]. Histopathologic correlation revealed hypoechoic areas to be composed of tumor cells and those of heterogeneous echogenicity to be composed of fibrous tissues intermixed with tumor cells [76].

DFSP lesions may be multiple small nodules or coalesce into a plaque. Linear extensions along the skin and satellite lesions may be demonstrated. Tumor attenuation is similar to or greater than that of muscle [67]. These lesions lack calcifications by CT, may be lobulated [72], and demonstrate enhancement with intravenous contrast administration [72].

MR signal characteristics are nonspecific and on T1- and T2-weighted sequences are similar to or slightly less intense than muscle and similar to or more intense than fat on T1- and T2-weighted sequences, respectively (Fig. 3.5b–d). On short tau inversion recovery (STIR) or fat suppressed T2-weighted sequences (Fig. 3.5b–d), signal is typically increased but may be heterogeneous in the presence of necrosis or hemorrhage; cystic areas and fluid-fluid levels may result [74, 77, 78]. DSFP lesions enhance moderately with gadolinium contrast administration [68, 69, 77]. MR is particularly useful for preoperative planning [69, 78–80]. One case report suggests that a negative choline peak on (1H) MR spectro sccopy (MRS) may be useful in suggesting the diagnosis of DFSP in a highly vascular subcutaneous mass [81].

DFSP are known to recur and are typically readily identifiable clinically. Limited experience suggests that 18F FDG PET imaging is useful in detecting small sites of disease recurrence [82].

Molecular Genetics

COL1A1 PDGFB fusions characterize both DFSP and giant cell fibroblastoma [83]. DFSPs typically contain ring chromosomes with multiple copies *COL1A1/PDGFB* [84], whereas giant cell fibroblastomas more often contain a reciprocal t(17;22)(q22;q13) [85]; some contain an unbalanced translocation [86]. Pigmented DFSP (Bednar tumor) and myxoid DFSP also contain the *COL1A1/PDGFB* fusion [83].

Gross and Microscopic Features

Grossly, both DFSP and giant cell fibroblastoma form grey-tan fibrous lesions with nonencapsulated, infiltrative borders, with the latter having a looser appearance. Myxoid variants of DFSP have a somewhat gelatinous appearance, whereas the pigmented variant may be brown or brownish-yellow.

Microscopically, DFSP contains distinctive pinwheel-shaped bundles of spindle cells arranged in a storiform pattern, resembling the weave in a wicker-bottom chair (Fig. 3.5e). A rich microvasculature usually nourishes these lesions. Modest mitotic activity, up to 5 mitoses per 10 high power fields, is typically present. The borders of DFSP characteristically infiltrate adjacent soft tissues, entrapping collagen bundles, nerves, and vessels and showing no hint of encapsulation. Sometimes this phenomenon imparts a somewhat neural appearance, with a suggestion of waviness and streaming.

Some lesions contain similar plump spindle cells, but with a marked reduction in cellularity and increase in myxoid stroma. These myxoid variants may contain larger, pleomorphic giant cells that segue into giant cell fibroblastoma. Pigmented lesions, known as Bednar tumors, contain melanin. Some DFSPs have a fibrosarcomatous component with greater cellularity, larger, more pleomorphic cells arranged in a herringbone pattern, and more mitoses [51].

Giant cell fibroblastomas have much less cellularity and contain loose bundles of collagen separated by ectatic blood vessels and slender, wavy tumor cells. Sprinkled within this matrix are scattered multinucleated cells with large round nuclei and inconspicuous nucleoli, arrayed around the ectatic vessels or distributed haphazardly (Fig. 3.5f). Giant cell fibroblastoma may also contain zones of higher cellularity that resemble DFSP, and vice versa [87].

Immunohistochemistry and Other Special Stains

Of all stains for confirmation of DFSP/giant cell fibroblastoma, the most useful is CD34, whose positivity in these tumors usually separates them from similar tumors like deep fibrous histiocytoma or juvenile xanthogranuloma [88, 89]. CD34 staining may be lost in foci of secondary fibrosarcoma [90]. Histiocytic markers like CD163, CD68, or Factor XIIIa are expressed by a minority of DFSPs [91].

Molecular Diagnostic Features and Cytogenetics

With DFSP/giant cell fibroblastoma, cytogenetics may demonstrate a ring chromosome or the t(17;22), and RT-PCRT or FISH can show *COL1A1/PDGFRB* fusion [86, 92].

Prognostic Features

DFSP and giant cell fibroblastoma are low-grade sarcomas with a metastasis rate of less than 10 % [93]. Local recurrence is common after incomplete resection [94]. Lesions with fibrosarcomatous change do not necessarily indicate a worse prognosis, particularly with complete excision [90, 93]. Because of involvement of the PDGF axis, aggressive tumors may be susceptible to therapy with imatinib [95].

Angiomatoid Fibrous Histiocytoma

Definition: Angiomatoid fibrous histiocytoma is a low-grade, cystic neoplasm occurring in subcutaneous tissues and containing blood-filled spaces surrounded by cells resembling histiocytes.

Clinical Features and Epidemiology

Angiomatoid fibrous histiocytomas usually occur in older children and adolescents. In the original series [96], the median age was 13 years. Originally, these lesions were considered adolescent variants of "malignant fibrous histiocytoma," but because of their indolent behavior the term "malignant" was later dropped [97]. They occur only rarely and comprise 0.3 % of all soft tissue neoplasms [98]. Occasionally patients present with constitutional symptoms, such as fever, anemia, elevated erythrocyte sedimentation rate, and even polyarteritis nodosa [99]. Lesions mostly occur in extremities but may include areas bearing lymphoid tissue, such as the antecubitus, axilla, inguinum, and supraclavicular region [100].

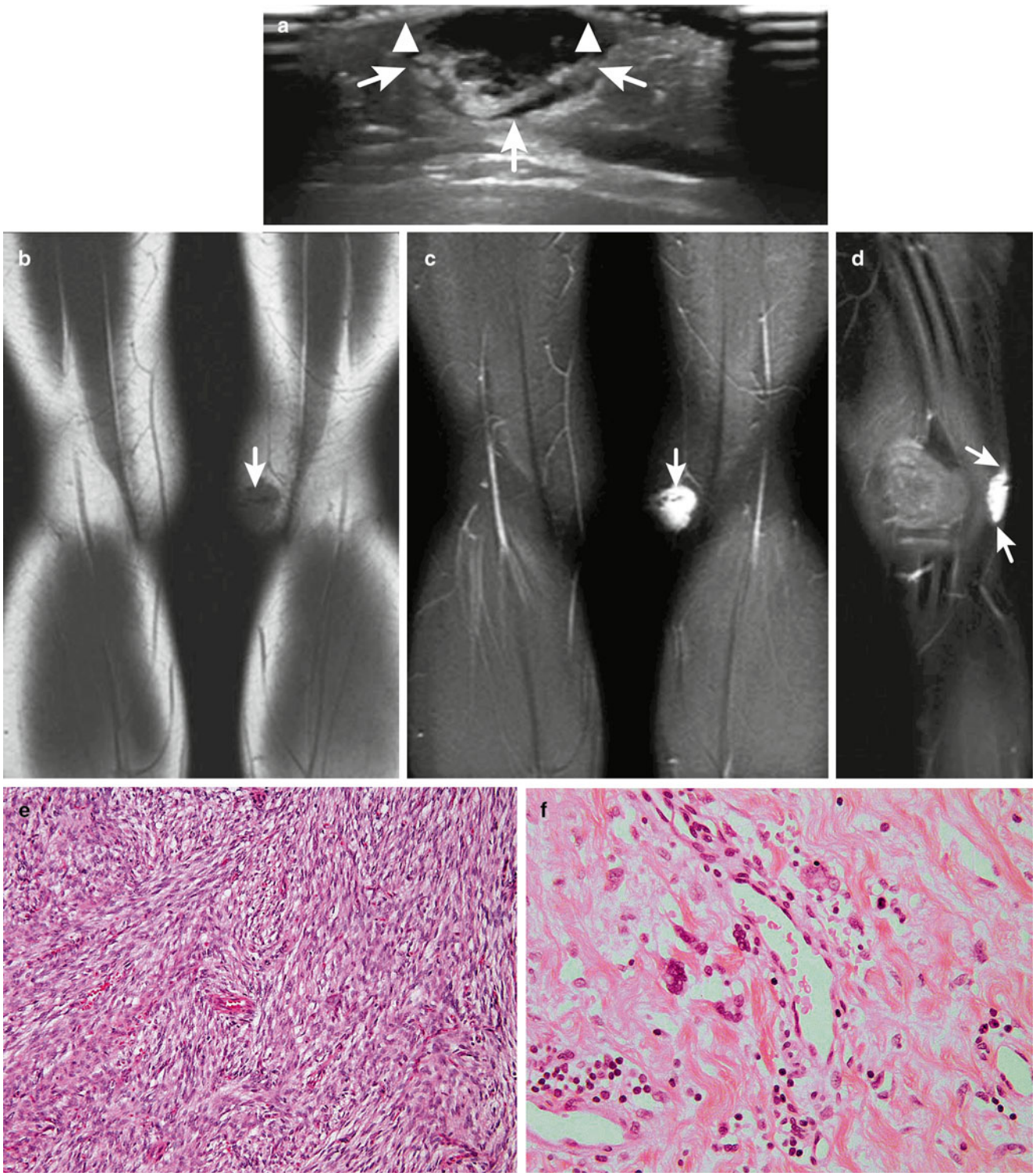

Fig. 3.5 Dermatofibrosarcoma protuberans. (**a**) A 4-year-old boy with a 2×1.8×7 cm mass in the left popliteal fossa, post-incisional biopsy. Longitudinal ultrasound image demonstrates an irregular, heterogeneous nodular soft tissue mass (*arrows*), just deep to the skin (*arrowheads*). (**b**) Coronal non-contrast T1-weighted MR shows the irregular margins of the mass within the subcutaneous fat; the mass is isointense with muscle. (**c**) Short tau inversion recovery (STIR) image shows increased signal emanating from the mass. The horizontally oriented *dark line* (*arrow*) through the mass is the healed surgical scar from prior incisional biopsy. (**d**) The mass enhances briskly with administration of intravenous contrast material on this sagittal contrast-enhanced T1-weighted image with fat suppression. Also note, the tiny strands of enhancing soft tissue extending superiorly and inferiorly (*arrows*) into the adjacent subcutaneous fat. (**e**) Classical dermatofibrosarcoma protuberans containing swirling, tightly interlaced, storiform bundles of spindle cells. (**f**) Giant cell fibrosarcoma with loose collagenous stroma, ecstatic vessels, and multinucleated fibroblasts

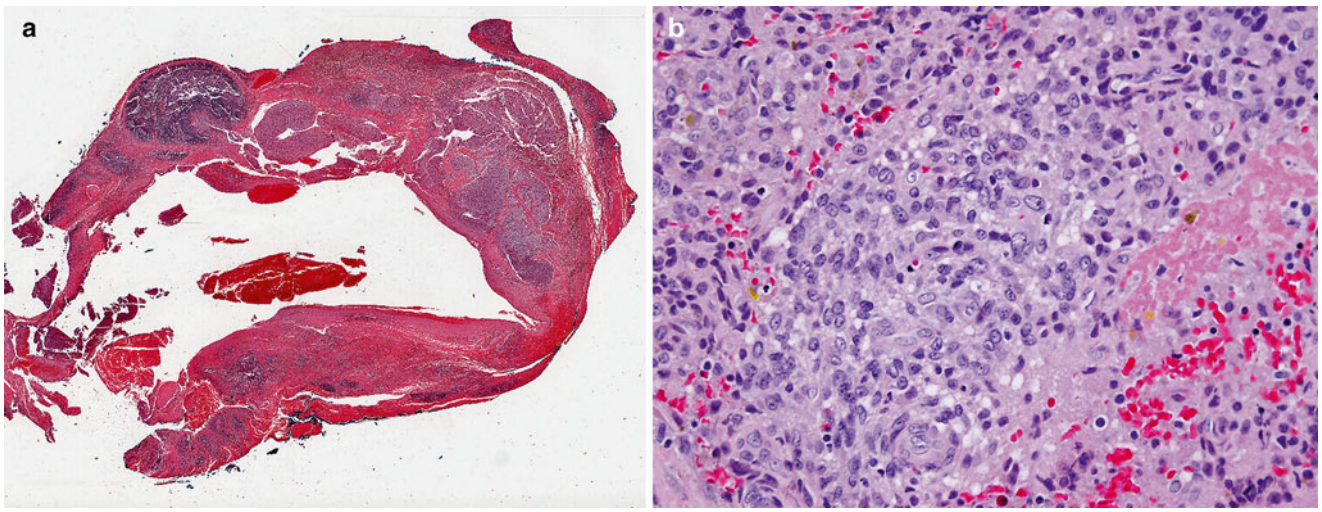

Fig. 3.6 Angiomatoid fibrous histiocytoma. (**a**) Blood-filled cystic spaces and a peripheral shell of lymphocytes characterize the low power appearance of this lesion. (**b**) High power view illustrating plump, histiocytoid tumor cells, moderately pleomorphic nuclei, and scattered erythrocytes and siderophages

Imaging Features

The imaging appearances of angiomatoid fibrous histiocytoma have not been well defined. Several reports, however, describe a striking MRI feature of multiple cystic areas with fluid-fluid levels within a soft tissue mass. These cystic areas and fluid levels correspond to the blood-filled spaces seen histopathologically. While this MR feature may be characteristic of angiomatoid fibrous histiocytoma it is not specific to it. On MR these tumors tended to be well defined by a fibrous pseudocapsule that appeared dark on both T1 and T2W sequences and demonstrated prominent contrast enhancement [101]. A single case of angiomatoid fibrous histiocytoma of bone has been reported. This tumor markedly expanded the bone but did not disrupt the cortex. It contained very large cystic areas with fluid-fluid levels, an appearance similar to aneurysmal bone cyst. However, the cystic areas of angiomatoid fibrous histiocytoma were larger than those typically seen in aneurysmal bone cyst and the septal enhancement was less pronounced. The bone tumor also had a fibrous pseudocapsule similar to that described above for soft tissue angiomatoid fibrous histiocytoma [102].

Molecular Genetics

Angiomatoid fibrous histiocytoma either contains a fusion of *EWSR1* with *ATF1* on chromosome 12, analogous to clear cell sarcoma [103, 104], or more frequently, *EWSR1* with *CREB1*. The latter occurs more frequently, and alternate *FUS-ATF1* fusions may be seen [105].

Gross and Microscopic Features

Angiomatoid fibrous histiocytomas usually occur in superficial soft tissues but occasionally arise in deep locations [103]. They typically form relatively small masses, 2–4 cm in diameter [98]. These form well-circumscribed firm nodules containing blood-filled, cystic spaces (Fig. 3.6a). Microscopically, the nodules contain a peripheral fibrous pseudocapsule with abundant lymphocytes, often bearing germinal centers and creating a strong resemblance to nodal metastases. Central spaces contain blood but do not have a true endothelial lining. Occasional lesions lack cystic spaces but still exhibit the reactive lymphoid shell [100]. Chronic hemorrhage with hemosiderin-laden macrophages is frequent. Single or multiple aggregates of ovoid to plump spindle cells with bland nuclei and amphophilic to lightly eosinophilic cytoplasm comprise the neoplastic component of the tumor (Fig. 3.6b). Occasional lesions show prominent nuclear pleomorphism and mitotic activity [106].

Immunohistochemistry and Other Special Stains

Angiomatoid fibrous histiocytomas often express myoid markers such as desmin and calponin, and occasionally actin and caldesmin, but not MyoD or myogenin [100, 107]. CD99 and CD68 are positive in many cases, but of note, histiocytic/dendritic cell markers like lysozyme, CD21, S100, and CD35 are negative [100].

Molecular Diagnostic Features and Cytogenetics

Break-apart FISH for *EWSR1* may be used for diagnosis of angiomatoid fibrous histiocytoma [108], particularly in cases with atypical histology [106]. Rare lesions lack *EWR1* fusions but show *FUS* rearrangement [108]. Neither FISH nor RT-PCR distinguishes angiomatoid fibrous histiocytoma from clear cell sarcoma, but S100 immunostains may be of value [100].

Prognostic Features

Angiomatoid fibrous histiocytoma is generally an indolent lesion. Metastases occur in less than 5 % of tumors [98]; recurrence is rare in lesions <5 cm [109]. Aggressive behavior

has been associated with adult onset, larger size (>5 cm), deep location, recurrence, and atypical mitoses [109, 110]. Metastases may grow rapidly and show chemoresistance [111]. Predictors of bad outcome include head and neck location and deep invasion, but not histologic parameters like mitotic rate and pleomorphism [97].

Plexiform Fibrohistiocytic Tumor

Definition: Plexiform fibrohistiocytic tumor (PFT) is a borderline neoplasm composed of small nodules of fibrohistiocytic cells and arising in the deep dermis and soft cutis.

Clinical Features and Epidemiology

PFT primarily affects children and young adults, with a median age of 14 years reported in the first large series [112]. However, a wide age range exists within children, and the lesion occasionally arises in infants [112–114]. It preferentially involves the upper extremities, particularly the hand and wrist, but it may also arise in the trunk, lower extremities, and head [115, 116]. Typically PFT arises in the subcutaneous tissues, but sometimes it occurs only in the dermis [117].

PFTs occur relatively rarely, with only occasional examples reported in COG studies. Only 123 cases were reported in the 2007 review by Taher and Pushpanathan [116]. It preferentially affects females, with a female:male ratio of 6:1 [118], but no racial or geographic predilection has been reported [116].

Generally, PFTs present as deep-seated solitary rubbery nodules that raise the overlying skin. They grow slowly and insidiously, often with a long delay in diagnosis of months to years [112].

Imaging Features

The imaging features of this tumor have not been well described.

Molecular Genetics

There have been few genetic or cytogenetic analyses of PFT, probably because of their relative circumscription and presentation. One study reported a 46,X,del(X)(q13), in a single case, but no molecular or cytogenetic features have been described as typical of this lesion [114].

Gross and Microscopic Features

Grossly, PFTs typically form a nonencapsulated, firm, pale grey mass in the deep dermis or subcutis, with an average size of 2.5 cm (range 0.5–8.0 in one series [118]. They may invade underlying skeletal muscle [118].

Microscopically, sections of PFTs exhibit a characteristic multinodular, infiltrative appearance, with small nodules of tumor separated by intervening fibroconnective tissue (Fig. 3.7). The nodules comprise small collections of epithelioid macrophage-like cells or plump spindle cells, in variable proportions. Variable numbers of multinuclear cells infiltrate these foci. Mitotic activity is generally low, <3 per 10 high power fields, and atypical mitoses or significant atypia are unusual features [118].

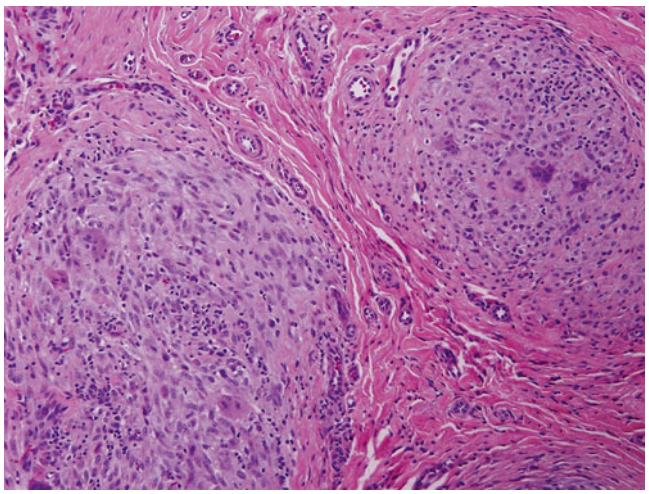

Fig. 3.7 Plexiform fibrohistiocytic tumor. The lesion comprises nodules of spindle cells, monocytoid cells, and giant cells, separated by deep dermal collagen

Immunohistochemistry and Other Special Stains

PFTs express a limited palette of antigens, typically vimentin and smooth muscle actin, with CD68 in epithelioid giant cells. Important negative stains include Factor XIIIa, CD34, NK1C3, and beta-catenin [119].

Molecular Diagnostic Features and Cytogenetics

Genetic studies of PFT have been limited, and no recurring abnormalities are reported [114].

Prognostic Features

Initial studies of PFT suggested that it only rarely metastasized to lymph nodes and never to distant sites [120]. However, newer reports of pulmonary metastasis have appeared. Because of a tendency to recur locally, complete marginal excision of PFT is recommended [116].

Malignant Fibrohistiocytic Neoplasms

Undifferentiated Pleomorphic Sarcoma

Definition: Undifferentiated pleomorphic sarcoma (UPS; formerly called malignant fibrous histiocytoma) is a high-grade, spindle cell sarcoma containing pleomorphic cells that resemble macrophages and showing no more than fibroblastic or myofibroblastic differentiation.

Clinical Features and Epidemiology

Although once the most common adult sarcoma, the incidence of UPS has waned with the advent of molecular and immunological techniques. It is even rarer in children and generally occurs in adolescents [109]. Most commonly, the lesion arises in the extremities, but the head, neck, or trunk may also be primary sites [109]. There appears to be a particular predilection to the head in children [121], who may have a history of prior irradiation [109].

UPS in children differs from that in adults in that most pediatric cases are in the dermis and soft tissues of the head and neck region rather than in the extremities.

Imaging Features

UPS are usually multinodular, well circumscribed, and lobulated. Calcification or ossification may be seen in some tumors. The role of plain radiography is very limited and nonspecific in evaluating these tumors and may show deep, soft tissue swelling, calcification, or underlying osseous involvement (Fig. 3.8a) [122, 123].

On gray-scale ultrasound images, a hypoechoic lesion that is well encapsulated can be seen in the deep soft tissues. Discrete intratumoral echogenic areas with acoustic shadowing may be seen if calcification is present. Intratumoral hemorrhage may be present and usually appears as an echogenic area without acoustic shadowing.

MRI is the modality of choice for evaluating these tumors, which may have varying signal characteristics due to variations in myxoid contents and cellularity. UPS is usually isointense to slightly hyperintense to muscle on T1-weighted images and has heterogeneous signal intensity on T2-weighted images (Fig. 3.8b–d). T1- and T2-weighted images of these tumors may have low-signal internal septations because of fibrous bands or acellular streaks [122, 123].

Molecular Genetics

The molecular features of pediatric UPS mirror those of adult tumors [124]. Particularly noteworthy is amplification of chromosome 12q13-14, containing protooncogenes such as *CHOP, SAS, MDM2,* and *CDK4* [124]. However, this finding suggests that these lesions are dedifferentiated liposarcomas [125, 126].

Gross and Microscopic Features

UPS typically forms bulky, infiltrative masses that may have a fibrous, grey-tan cut surface or contain areas of hemorrhage and necrosis. They often arise within musculature, but subcutaneous and fascial tissues may be involved.

UPS by definition is a pleomorphic spindle cell sarcoma, usually containing variably plump spindle cells arrayed in a storiform pattern (Fig. 3.8e). The tumor cells range from plump spindle cells to epithelioid cells with variable, often striking, degrees of nuclear pleomorphism, atypia, and hyperchromasia. Also by definition, there should be no identifiable line of differentiation other than fibroblasts or myofibroblasts; otherwise, the lesion is best considered a dedifferentiated form of another tumor type. Mitoses are generally frequent, with atypical forms (Fig. 3.8e), and geographic necrosis is often present.

Immunohistochemistry and Other Special Stains

This diagnosis requires a panel of stains to rule out dedifferentiated tumors of other types. One should exclude pleomorphic or dedifferentiated variants of rhabdomyosarcoma, leiomyosarcoma, liposarcoma, and nerve sheath tumors, as well as lymphoma, carcinoma, and melanoma [64]. Otherwise there are nonspecific positive reactions to vimentin and CD68, with weak and variable smooth muscle actin positivity.

Vascular Tumors

Intermediate Vascular Tumors

Kaposiform Hemangioendothelioma

Definition: Kaposiform hemangioendothelioma (KH) is a locally aggressive vascular lesion containing immature endothelial cells arranged in bundles and fascicles, often with platelet trapping.

Clinical Features and Epidemiology

KH typically occurs in young children, often infants, although cases in older children and adults have been recognized. It arises in superficial soft tissue but often involves deep soft tissues, bone, or viscera. Often, patients show signs of consumptive coagulopathy as a result of platelet trapping within the lesion (Kasabach–Merritt syndrome), and lesions may bleed profusely following initial biopsy or incomplete attempts at excision.

Imaging Features

There are few articles describing the imaging features of KH. In one review of 21 children, the main MRI findings were diffuse enhancement after contrast administration, poorly defined tumor margins, skin thickening, stranding of subcutaneous fat, blood product deposits within the tumor and small feeding and draining vessels (Fig. 3.9a, b) [127]. The tumor is locally invasive and there are reports of secondary bone erosion and cortical destruction [128–130]. Tumors grow rapidly and are often associated with skin discoloration [131]. There may be local-regional nodal spread but distant metastasis has not been reported. Common primary sites include the cervicofacial area, extremities, peritoneum, and retroperitoneum [131, 132]. These clinical and imaging features in a patient with Kasabach–Merritt phenomenon should suggest a diagnosis of KH.

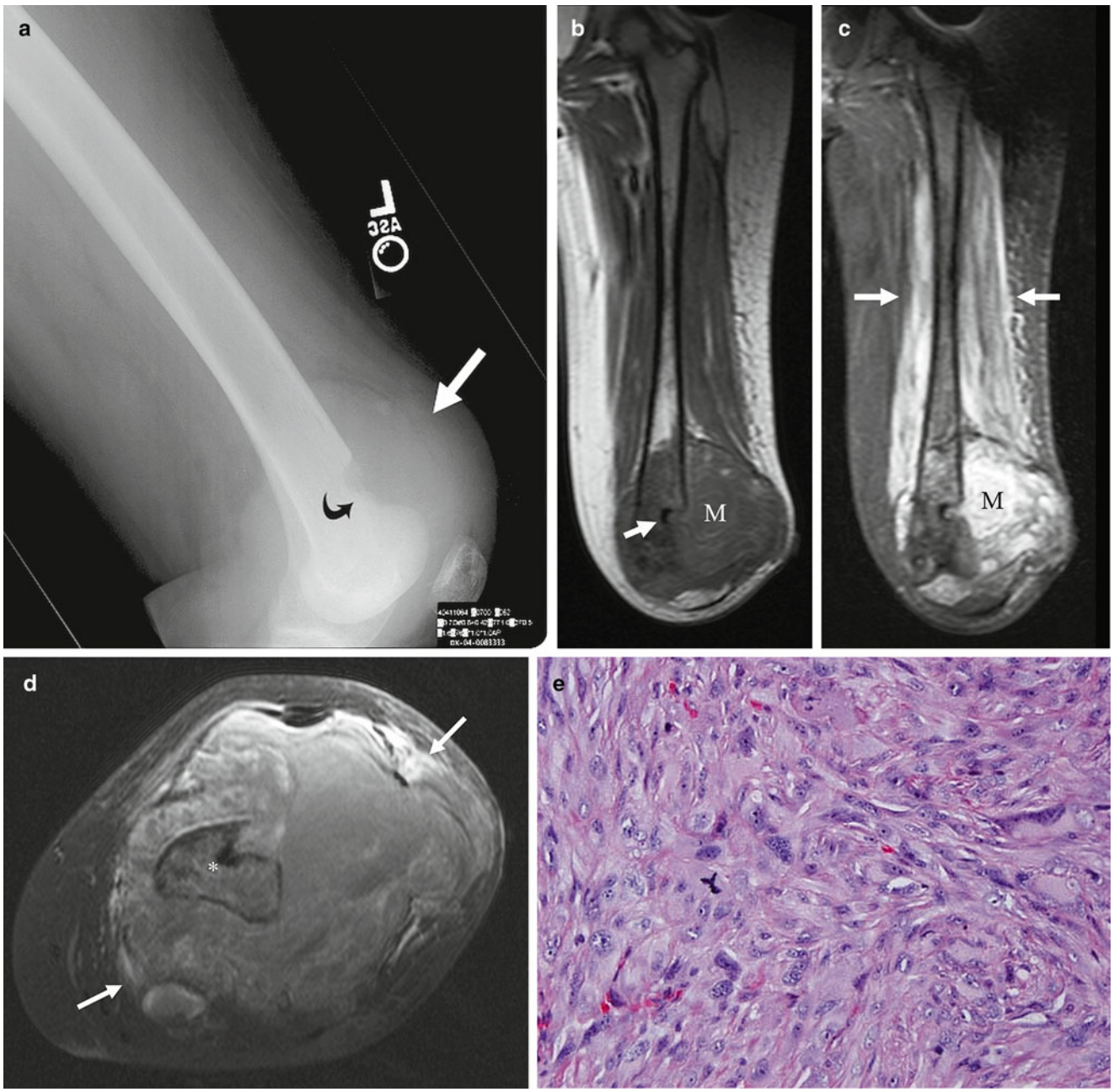

Fig. 3.8 Undifferentiated pleomorphic sarcoma (malignant fibrous histiocytoma) in an 18-year-old boy with primary site in the left thigh. (**a**) This lateral radiograph demonstrates a non-calcified, soft tissue mass (*straight arrows*) that destroys the distal femoral cortex (*curved arrow*). (**b**) On this coronal T1W, non-contrast-enhanced image the mass (*M*) is heterogeneous but predominantly isointense to muscle. Direct invasion of the distal femur is evident (*arrow*). (**c**) The tumor (*M*) is heterogeneous on this T2W coronal image. Involvement of the distal femur is again evident. Extensive surrounding soft tissue edema appears as bright signal throughout the thigh muscles (*arrows*). (**d**) This post-contrast T1W axial image shows heterogeneous but fairly minimal enhancement of tumor (*arrows*) perhaps due to ischemia. Adjacent bone invasion (*asterisk*) is again noted. (**e**) The lesion contains dense, storiform fascicles of pleomorphic cells with large, pleomorphic nuclei and atypical mitosis

Gross and Microscopic Features

Kaposiform hemangioendothelioma forms a hemorrhagic, fibrous mass with poorly circumscribed borders. It comprises small slit-like vascular channels surrounded by spindle to epithelioid cells and arranged in lobules or discrete nodules (Fig. 3.9c). Some lesions contain more discrete, rounded open channels, resembling a hemangioma or bloody lymphangioma, particularly at the periphery. Platelet rich microthrombi, highlighted by CD31, may be seen within nests of pericytes and epithelioid tumor cells. Erythrocyte fragments and hemosiderin may also be conspicuous.

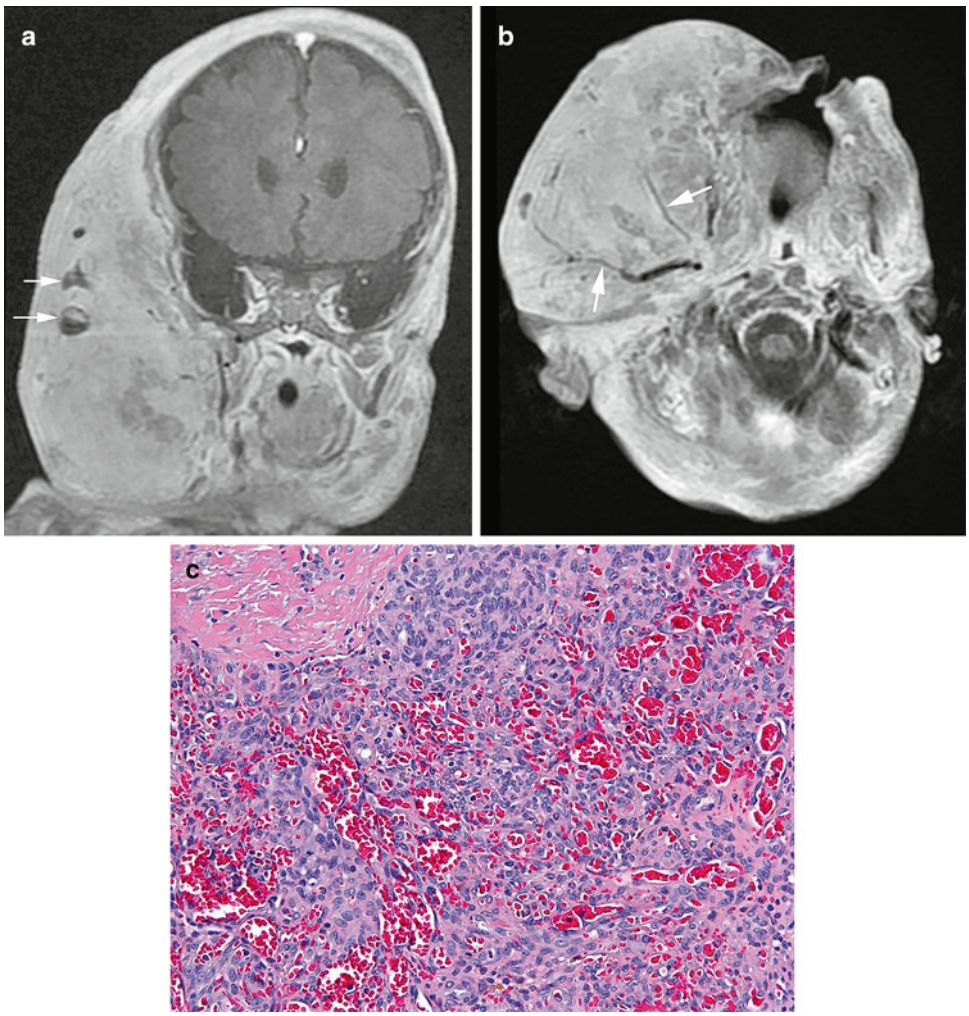

Fig. 3.9 Kaposiform hemangioepithelioma. A 3-week-old with Kasabach– Merritt syndrome and large cervico-facial lesion. (**a**) Coronal T1W contrast-enhanced magnetic resonance image shows an extensive, diffusely enhancing mass involving the right face and neck. Several cystic foci with fluid-fluid levels are due to blood products (*arrows*). (**b**) T1W axial post-contrast image shows diffuse enhancement and numerous small vessels (*arrows*) coursing throughout the tumor. (**c**) Histologically, Kaposiform hemangioendothelioma comprises irregular vascular channels lined by clusters of epithelioid and spindle cells

Immunohistochemistry and Other Special Stains

KH generally shows expression of both lymphatic and blood vascular endothelial markers. These factors appear to be upregulated by Prox-1, a transcription factor that induces programming of blood vessels into lymphatics as well as promoting invasiveness and aggressive behavior [133]. Prox-1 appears to be a good immunomarker of KH and tufted angioma, a rare related tumor [134]. In addition, KH shows biphenotypic expression of CD31, CD34, podoplanin (D2-40), and (variably) factor VIIIa related antigen (von Willebrand factor) [134, 135].

Prognostic Features

KH can be cured with complete excision, but incompletely excised lesions may cause significant bleeding and result in the patients' demise. A variety of medical options are available, including chemotherapy, immune modulators, and radiation [135].

Malignant Vascular Tumors

Angiosarcoma

Definition: Angiosarcoma is an invasive, malignant neoplasm composed of neoplastic endothelial cells forming irregular vascular channels.

Clinical Features and Epidemiology

Angiosarcomas are quite rare in children, but a few published series exist [136–138]. These relatively small series show a wide age range, from infancy through adolescence, with a median of 11 years. The viscera, particularly the heart, are affected among deep lesions [137], and superficial lesions tend to involve the extremities of girls [138]. Lesions may present as cutaneous ecchymoses that are confused with hematoma [138]. A significant proportion have an underlying

genetic defect, such as neurofibromatosis 1 (NF1), hemihypertrophy, or Aicardi syndrome, and there may be a history of prior irradiation [137, 138]. Kasabach–Merritt syndrome is not typically present.

Imaging Features

Imaging characteristics of angiosarcomas, regardless of their location, readily reflect the vascular aggressive nature of this tumor (Fig. 3.10a–e). Most imaging publications describe these tumors in liver and spleen but they may occur elsewhere. Organomegaly [139, 140] and metastatic disease [139, 141] are common findings at the time of diagnosis.

By ultrasound, angiosarcoma and its metastases appear as heterogeneous solid masses with varying degrees of cystic areas that likely represent hemorrhage or necrosis [139, 141].

By CT, angiosarcoma may be nodular or diffuse and it may reveal satellite nodules or punctate calcifications [139–141] (Fig. 3.10a, d, e). It may be mass-like or an en plaque subcutaneous lesion within a lymphedematous extremity. By MR, it has a nonspecific appearance with increased T2 and intermediate T1 signal intensity. Non-enhancing areas of hemorrhage may be seen in areas with increased T1 signal [77, 142] (Fig. 3.10b, c). MR signal characteristics reflect the vascularity and hemorrhage of the lesions. Heterogeneous enhancement that progresses and persists on delayed images can be shown using dynamic contrast-enhanced techniques [143]. Hemosiderin-laden nodules may appear as low-signal intensity foci on all sequences [141, 144].

When angiosarcoma occurs in the extremities, MR can delineate tumor nodules from surrounding lymphedematous soft tissues. It comprises a lobulated mass of low to intermediate signal by T1-weighted imaging. Because of fibrous stroma, these tumors also have decreased signal on T2-weighted sequences. The administration of intravenous contrast results in diffuse or heterogeneous tumor enhancement [72, 142]. Fluid-fluid levels may be present [145].

Though experience is limited, 18F FDG PET appears to have a developing role in grading [146] and staging [147, 148] angiosarcoma. 18F FDG may potentially be useful for distinguishing angiosarcoma from cavernous hemangiomas, as the latter has been reported to have low FDG avidity [149].

Gross and Microscopic Features

Angiosarcomas form hemorrhagic, nodular masses with varying size, often with ill-defined borders resembling hematoma. Histologically, they contain aggregates of irregular vascular channels lined by atypical cells with large, irregular, nuclei (Fig. 3.10f). Both epithelioid and spindle cells form cords, strands, and nests that slice into adjacent fibrofatty or muscular tissue. The vascular channels exhibit irregular, anastomosing profiles with sinusoidal features. Necrosis and mitotic activity are frequent.

Immunohistochemistry and Other Special Stains

Due to the rarity of pediatric angiosarcomas, immunohistological data is sparse, but the tumors express vascular markers such as CD31, CD34, and factor VIII-related antigen (von Willebrand factor). Podoplanin expression is generally absent [137], but cytokeratin expression is not unusual.

Prognostic Features

Pediatric angiosarcomas are usually high-grade sarcomas that exhibit aggressive local invasion and metastasis. Local control is difficult, and the lesions do not respond to traditional chemotherapy [136]. However, there are some survivors [137] particularly among superficial, easily accessed lesions [138].

Malignant Adipose Tumors

Myxoid/round Cell Liposarcoma

Definition: A malignant tumor composed of malignant lipoblasts embedded in an abundant myxoid stroma (myxoid liposarcoma) or forming dense cellular aggregates (round cell liposarcoma).

Clinical Features and Epidemiology

Although liposarcomas now comprise the most common adult sarcoma group, they occur relatively infrequently in children. Nevertheless, they rank first among adult-type sarcomas occurring in the pediatric age group. In one relatively large series of 82 cases [125], there was a roughly 1:2 male:female ratio, and ages ranged from 5 to 22 years, with a median of 15.5 years. The tumors occurred in a wide array of locations, mostly in the soft tissue of extremities. Conventional myxoid and round cell liposarcomas constituted 71 % of cases.

Imaging Features

Myxoid liposarcoma contains prominent myxoid tissue, branching capillaries, and less than 10 % fat, but usually lacks necrosis [72, 150]. Extremity lesions are typically intermuscular [151, 152].

Ultrasound interrogation is useful to characterize the lesion and readily demonstrates its complex, solid nature [77, 152] and hypervascular areas [72]. Decreased attenuation of the lesion as seen on CT may mimic a cyst but can usually be differentiated using ultrasound [152].

CT and MR of myxoid liposarcoma are very similar. It forms a large, usually well-defined lobulated mass when located in soft tissues and has mixed lytic and blastic characteristics when located within the skeleton [151]. Lesions often lack fat signal and demonstrate findings of increased water content [142, 151]. MR typically demonstrates the

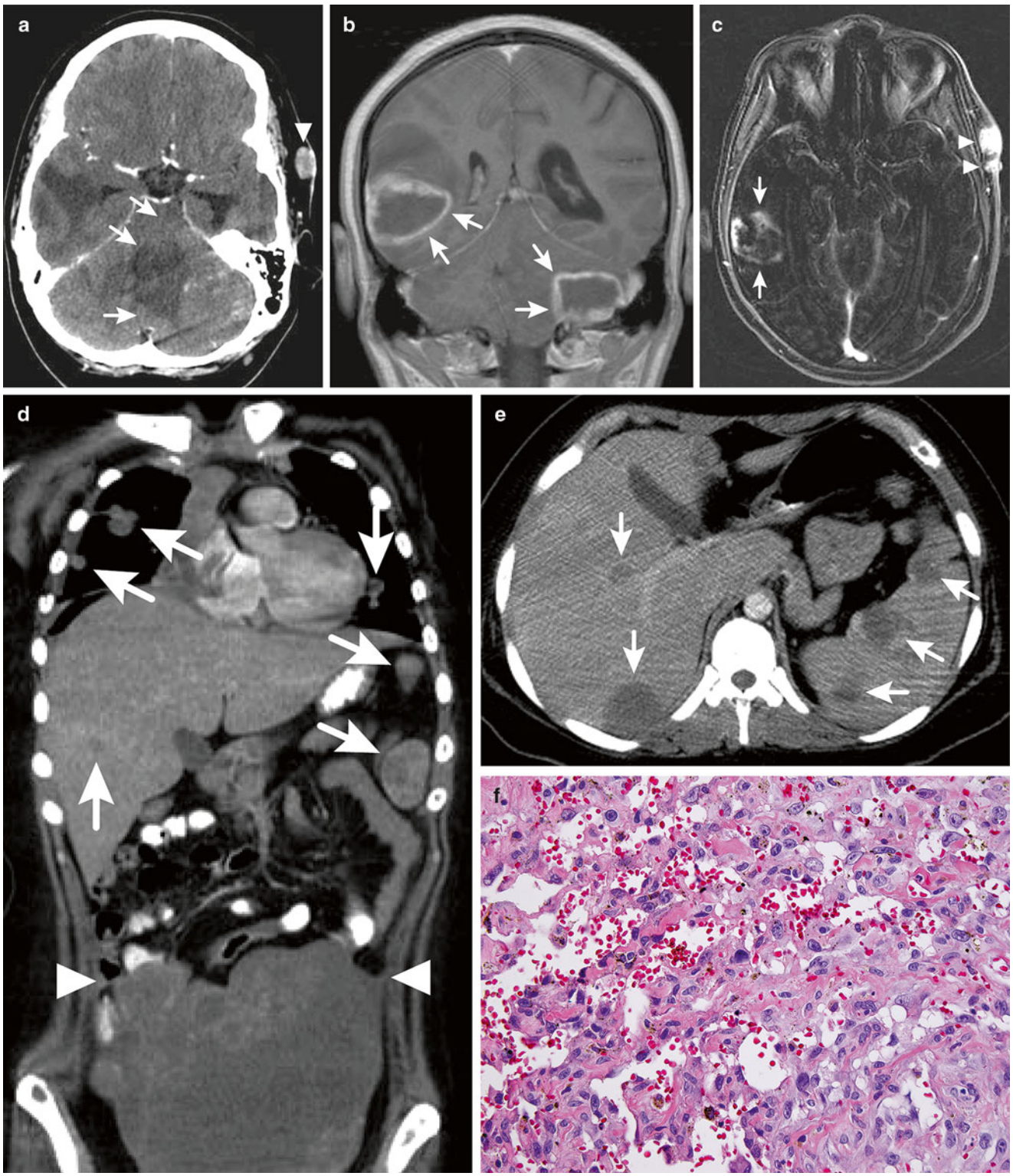

Fig. 3.10 Angiosarcoma. (**a**–**c**). A 19-year-old girl presented with headaches, exacerbated by turning her head, nausea and vomiting. She was subsequently diagnosed with metastatic angiosarcoma. (**a**) Axial contrast-enhanced CT through the temporal lobes. (**b**) Coronal contrast-enhanced T1-weighed MR through the midline brain. (**c**) Axial contrast-enhanced subtracted MR through the temporal lobes images shows multiple heterogeneously enhancing intracranial metastases (*arrows*) associated with vasogenic and effacing the CSF spaces. Note the briskly enhancing subcutaneous nodules in the left temporal region (*arrowheads*). (**d**) Coronal reformatted contrast-enhanced CT showing multiple metastases (*arrows*) involving the lungs, pleura, liver, and spleen. The large heterogeneously pelvic mass enhances heterogeneously and has extension to the adjacent peritoneal surface (*arrowheads*). (**e**) Axial contrast-enhanced CT image through the upper abdomen demonstrates multiple low-density metastases throughout the liver and spleen (arrows). (**f**) A histological section of pediatric angiosarcoma contains irregular vascular channels lined by epithelioid endothelial cells with enlarged, hyperchromatic nuclei

large size and well-defined multilobulated contours [72, 150, 151, 153] (Figs. 3.11a–d). MR characteristics may vary according to the histologic makeup of the lesions [153]. Lesions may mimic a cyst due to the high water content, evidenced on MR by decreased T1- and markedly increased T2-signal intensity [150]. Adipose tissue may be seen as small nodules or located within septations. Intravenous contrast administration may aid by demonstrating enhancing septations in cysts and solid components within sarcomas [72, 150, 153–155]. The extent and distribution of enhancement varies with the distribution of nodularity (peripheral, central, or diffuse) [77] and location (soft tissues or skeleton) [151]. Mucinous areas lack enhancement, leading to a heterogeneous pattern [150]. Areas of round cell proliferation may demonstrate more diffuse enhancement [77]. Areas of hemorrhage may also occur [72].

Molecular Genetics

Myxoid and round cell liposarcoma contain a characteristic t(12;16)(q13;p11) [156] that fuses the *CHOP* and *FUS* genes and creates a chimeric gene product showing transformative properties and affecting transcription of adipogenic genes [157, 158].

Gross and Microscopic Features

Liposarcomas form bulky masses that have lobular contours and yellow to white cut surfaces that resemble fat.

Myxoid liposarcomas contain relatively bland appearing lipoblasts with cytoplasm vacuoles, enmeshed in an abundant myxoid stroma (Fig. 3.11e). Thin arcuate capillaries course through this mileau and recreate an appearance akin to pulmonary edema. Round cell liposarcomas, in contrast, form aggregates and sheets of primitive lipoblasts that resemble other round cell sarcomas (Fig. 3.11f). A mixture of round cell and myxoid foci often occurs. In addition to these classic histologies, Alaggio et al. [125] describe variant forms with large pleomorphic nuclei, giant cells, and atypical mitoses resembling pleomorphic liposarcoma.

Immunohistochemistry and Other Special Stains

Immunohistochemistry has limited value in diagnosis of liposarcoma, but like normal adipocytes these tumors generally express S100.

Molecular Diagnostic Features and Cytogenetics

The *FUS-CHOP* fusion may be detected by RT-PCR, and a *FUS* or *CHOP* rearrangement may be demonstrated by break-apart FISH [159]. *EWS* replaces FUS as the fusion partner of *CHOP* in about 10 % of cases [160] and should be tested by FISH in cases with typical histology and no *FUS* rearrangement.

Prognostic Features

Myxoid liposarcoma is a low-grade malignancy (Grade 1 in the POG grading schema), whereas round cell liposarcoma is a high-grade malignancy (Grade 3 in the POG schema). In Alaggio's series [125], adverse features such as metastases or local recurrence occurred in only 1 of 41 grade 1 liposarcomas but affected 7 of 9 patients with high-grade tumors. Seven of 10 patients with pleomorphic myxoid liposarcoma died of disease.

Well-Differentiated/Dedifferentiated Liposarcoma

Definition: Well-differentiated and dedifferentiated liposarcoma are morphologically divergent tumors of malignant lipoblasts, both characterized by amplification of chromosome 12q13-14.

Clinical Features and Epidemiology

In contrast to myxoid/round cell liposarcomas, well differentiated and dedifferentiated liposarcomas (WD/DDL) are rare in children. Of four adolescent patients described by Alaggio et al. [125], two were male and two were female, with ages ranging from 12 to 19 years. The lesions all involved deep soft tissues. An intriguing report suggests a relationship between constitutional *TP53* mutation and pediatric well-differentiated liposarcoma [161].

In adults, common locations of well-differentiated liposarcoma include the lower extremities (50 %), retroperitoneum (20–33 %), upper extremity (14 %), and trunk (12 %). Extremity lesions are commonly intramuscular but may be intermuscular and subcutaneous. The most common clinical presentation is a patient with a painless, soft tissue mass that has grown slowly over months to years. Retroperitoneal lesions are typically large at diagnosis and have a high local recurrence rate after surgical resection [152].

Imaging Features

WD/DDL may be apparent as a soft tissue mass on plain film radiography. Fat is often seen on plain films of large extremity lesions but is rarely seen in retroperitoneal masses. Calcification is present on radiography or CT in 10–30 % of tumors. Bony involvement is very rare [152].

Sonography typically demonstrates a heterogeneous, multilobulated, well-defined mass. The identification of hyperechoic fat within WD/DDL on ultrasound is not sensitive or specific, as other pediatric tumors, such as germ cell tumor and lipoblastoma, contain fat [152].

On CT and MRI, well-differentiated liposarcoma usually appears as a predominantly (about 75 %) lipomatous mass containing non-fat components. such as thick septa

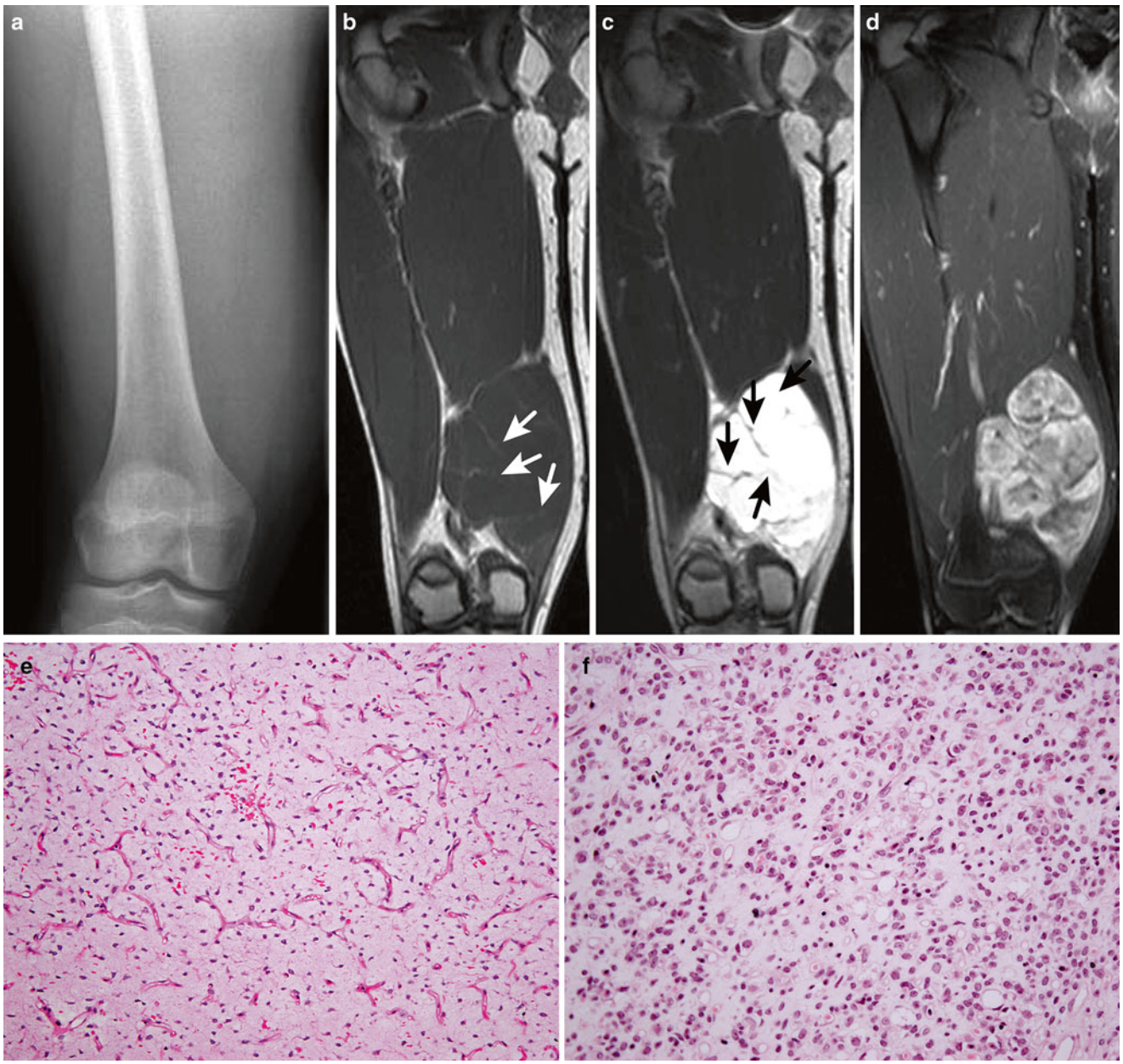

Fig. 3.11 Myxoid liposarcoma. (**a**–**d**) A 14-year-old boy presented with a firm thigh mass, noted 1 year prior, with recent increase in size. (**a**) Anteroposterior radiograph shows fullness in the distal medial thigh soft tissues without bony abnormality or soft tissue calcifications. The density of the soft tissues is the same as muscle. (**b**, **c**) Coronal non-contrast MR through the same region shows a multilobulated soft tissue mass whose signal intensity is the same as muscle on T1-weighted sequence (**b**) but intensely bright signal on STIR sequence (**c**). The mass lacks a significant fat component which would manifest as bright signal on T1-weighted imaging (similar to the white subcutaneous fat) and dark on STIR and fat saturated contrast-enhanced T1. Note multiple septae within the mass (*arrows*). (**d**) With administration of intravenous contrast, heterogeneous enhancement within the nodules is noted. (**e**) Myxoid liposarcoma containing a bland, mucinous stroma with scattered lipoblasts, intersected by a rich plexus of arcuate capillaries. (**f**) Round cell liposarcoma with increased cellular density and less stroma. The cells appear undifferentiated, but lipoblastic differentiation with cytoplasmic lipid vacuoles can be noted on close inspection

that may be nodular. Focal nodular or globular non-fat components, usually measuring less than 2 cm in size, suggest well-differentiated liposarcoma. After administration of gadolinium contrast agent, the septa demonstrate moderate to marked enhancement [152]. On PET-CT, well-differentiated liposarcoma demonstrates minimal FDG avidity, reflecting the low-grade nature of this malignancy [152, 162].

Molecular Genetics

Both well-differentiated and dedifferentiated liposarcoma exhibit genetic amplification affecting the chromosome 12q13-14 region. This leads to overexpression of protooncogenes such as *MDM2, CDK4, GLI, CHOP,* and *SAS* [126, 163]. The resultant genomic instability is potentiated by mutations of *TP53* [164].

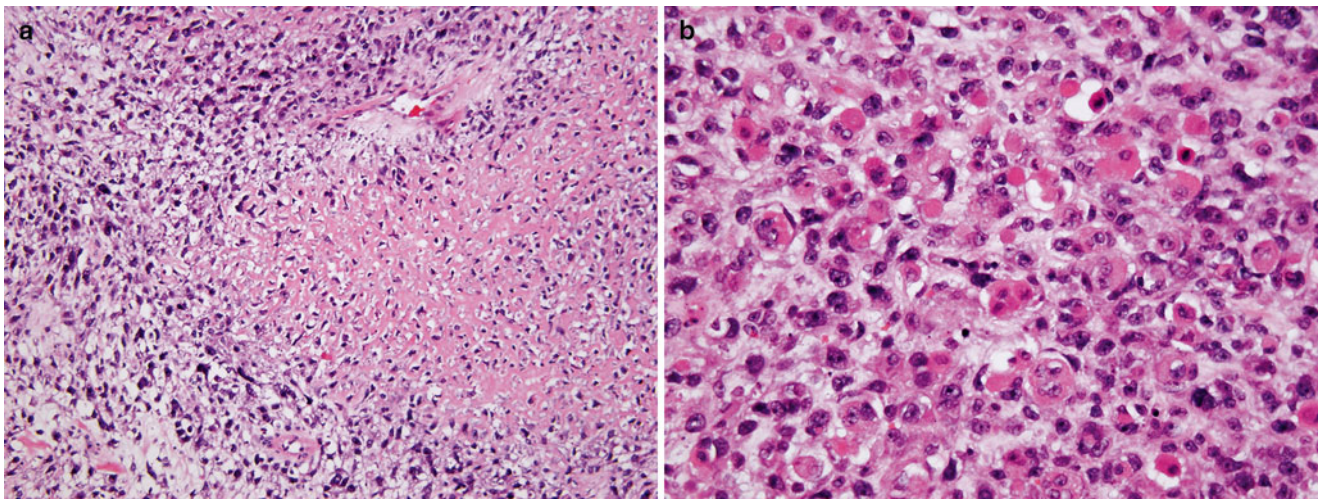

Fig. 3.12 Dedifferentiated liposarcoma. (**a**) This lesion contains large cells with angulated, hyperchromatic nuclei. Tumor cells show lipoblastic differentiation with lipid vacuoles. Prominent in the *right central portion* of the figure is a wedge-shaped area of osteoid production. (**b**) In another portion of the lesion, there is prominent rhabdomyoblastic differentiation. Cells contain abundant, brightly eosinophilic cytoplasm

Microscopic Features

Well-differentiated liposarcomas and atypical lipomatous tumors histologically and genetically comprise the same lesion, distinguished by the deep location of the former lesion and the superficiality of the latter [165]. These lesions largely consist of mature fat containing interspersed cells with enlarged, hyperchromatic, atypical nuclei. Conversely, dedifferentiated liposarcomas typically contain little fat and primarily comprise a high-grade storiform lesion resembling UPS. Low-grade spindle cell forms should not be confused with spindle cell lipoma [166]. Dedifferentiated liposarcomas often contain foci of heterologous differentiation into chondrosarcoma, osteosarcoma (Fig. 3.12a), and/or rhabdomyosarcoma (Fig. 3.12b). Often, tumors are mixed, with dedifferentiated liposarcoma foci abruptly merging with well-differentiated liposarcoma.

Immunohistochemistry and Other Special Stains

Immunostains for MDM2 and CDK4 may be used to confirm the overexpression of these proteins resulting from genetic amplication [167].

Molecular Diagnostic Features and Cytogenetics

Cytogenetically, the genetic amplication of well-differentiated/ dedifferentiated liposarcoma is characterized by ring or marker chromosomes. *MDM2* amplification may be detected by FISH [163], and overexpression is seen with immunohistochemistry. However, immunostains of pediatric lesions may demonstrate MDM2-negativity and p53-positivity [161].

Prognostic Features

The rare reports of well-differentiated/dedifferentiated liposarcoma in children suggest that they have a good outcome if completely excised [125].

Malignant Myogenous Tumors

Two myogenous sarcomas occur in children: rhabdomyosarcoma and leiomyosarcoma. Rhabdomyosarcoma is the most common pediatric soft tissue sarcoma and comprises more than one-half of all soft tissue malignancies. Leiomyosarcomas conversely are unusual in children. Pediatric rhabdomyosarcomas are classified by histology into two main types: embryonal and alveolar. Adult pleomorphic rhabdomyosarcomas are practically nonexistent in children [168].

Embryonal Rhabdomyosarcoma

Definition: Embryonal rhabdomyosarcomas (ERMS) are malignant soft tissue neoplasms arising from primitive mesenchymal cells and showing a variable capacity for neoplastic myogenesis. They form a morphologically diverse group of neoplasms that encompasses several subtypes.

Clinical Features and Epidemiology

ERMS occur most frequently among rhabdomyosarcomas and indeed among pediatric sarcomas in general. They show a pronounced proclivity to occur in younger children and are

infrequent in patients over the age of 5 years. They occur at every body site and are somewhat more common in males. Typical sites of origin are the genitourinary tract (including the scrotal sac), head, and neck. Other sites include the abdomen, the biliary tree, and the extremities, the latter site being relatively uncommon.

The anatomic diversity of ERMS is matched by a corresponding plethora of presenting signs and symptoms, related to space-occupying masses occurring in hollow viscera and body cavities. Common presentations include exophthalmos in orbital tumors, nasal obstruction in sinonasal tumors, jaundice in biliary tumors, and urinary obstruction in bladder and prostate lesions.

Imaging Features

Imaging ERMS by plain radiograph is of limited use; it may appear as a soft tissue mass similar to muscle. If diagnosed early, then no osseous abnormality is seen, however, if diagnosed later, these tumors may have adjacent extensive osseous destruction that may be seen on radiography. Gray-scale ultrasound images show a slightly hypoechoic or hyperechoic, often inhomogeneous, soft tissue mass, sometimes with markedly increased blood flow on color Doppler, although cases with low vascular density have been documented. When ERMS occurs at the bladder base (from the bladder or prostate), it usually appears as an intraluminal hyper- or hypoechoic mass protruding into the bladder lumen resembling a cluster of grapes (Fig. 3.13a). Tumors at the bladder base may cause bladder outlet obstruction and be associated with nonspecific bladder-wall thickening and hydronephrosis [6, 122, 123].

CT evaluation of ERMS usually shows a heterogeneous soft tissue lesion that is nonspecific and vigorously enhances after the administration of contrast (Fig. 3.13b). ERMS in the orbital region usually appears homogeneous and isodense to muscle. Intratumoral hemorrhage has a heterogeneous appearance on CT images. Destruction of underlying bone is seen in one-fourth of tumors, with periostitis, bone destruction, sclerosis, and bony remodeling visible on CT and plain radiographic images. ERMS have nonspecific features on MR images. These tumors are usually isointense or hyperintense to muscle on T1-weighted images. On T2-weighted images, they have high signal that heterogeneously enhances after gadolinium administration (Fig. 3.13c). Tumor necrosis and cystic areas, if present, appear as low signal on T1-weighted images and high signal on T2-weighted images. Orbital ERMS may extend intracranially or to the adjacent paranasal sinuses [122]. These lesions usually appear to be heterogeneous, with signal that is low or isointense to surrounding brain on T1-weighted images. Surrounding bony destruction, if present, is poorly delineated by MRI, and CT may be required to assess any osseous involvement. Extraorbital head and neck ERMS have similar imaging features; however, it is important to assess parameningeal extension, which affects the surgical approach and resectability. Post-contrast T1-weighted imaging with fat suppression is useful to assess cranial nerve involvement.

Molecular Genetics

On gene expression array studies, ERMS shows a diversity of molecular perturbations that significantly vary among tumors [169]. However, epigenetic studies reveal a striking loss of heterozygosity for portions of chromosome 11p, particularly evident at 11p15.5 [170, 171]. This appears to result primarily from uniparental disomy, resulting in altered expressed of imprinted genes ones [172].

Gross and Microscopic Features

Grossly, ERMS forms a fleshy, lobulated, grey-tan mass that may show areas of necrosis and hemorrhage. The botryoid variant of ERMS exhibits characteristic grape-like polyps that protrude from the epithelial surface of a hollow viscus (Fig. 3.13d). The spindle cell variant on section displays the whorled, firm, scar-like features of a fibromatous lesion.

Embryonal rhabdomyosarcoma, as the name implies, recapitulates the stages of embryonal myogenesis. The stage of myogenesis varies among tumors and even among microscopic fields. Some lesions contain the primitive mesenchymal stem cell features of post-somitic cells with slightly oblong, small, hyperchromatic nuclei and variable amounts of amphophilic cytoplasm bounded by stellate to elongate contours. These may produce a mucoid intercellular stroma or cluster together in dense packets. Tumors, especially on limited biopsies, thus may appear loosely cellular, dense, or loose and dense, the latter pattern resembling early limb musculature formation (Fig. 3.13e).

As embryonal musculature ages, cells acquire progressively more eosinophilic cytoplasm and assume a pinker hue to form rhabdomyoblasts. Rhabdomyoblasts are also a feature of RMS, and they become more prominent and numerous with successful therapy as tumor cells are forced either to die or to differentiate. Like density, this quality is highly variable in ERMS, and one observes either few or no rhabdomyoblasts in some tumors or a rhabdomyoma-like plethora in others. In rare tumors, particularly in the uterocervical region, cartilage may also be observed. With terminal differentiation, rhabdomyoblasts become multinucleated, nuclei sometimes arranged in tandem. As a result of this differentiation process, the cytological content of ERMS varies, and odd cellular contours give rise to names such as "strap cell," "tadpole cell," "racquet cell," "spider cell," and "broken straw sign" (Fig. 3.13f).

Subtypes of ERMS include botryoid, spindle cell, and anaplastic variants. Botryoid rhabdomyosarcoma (BRMS)

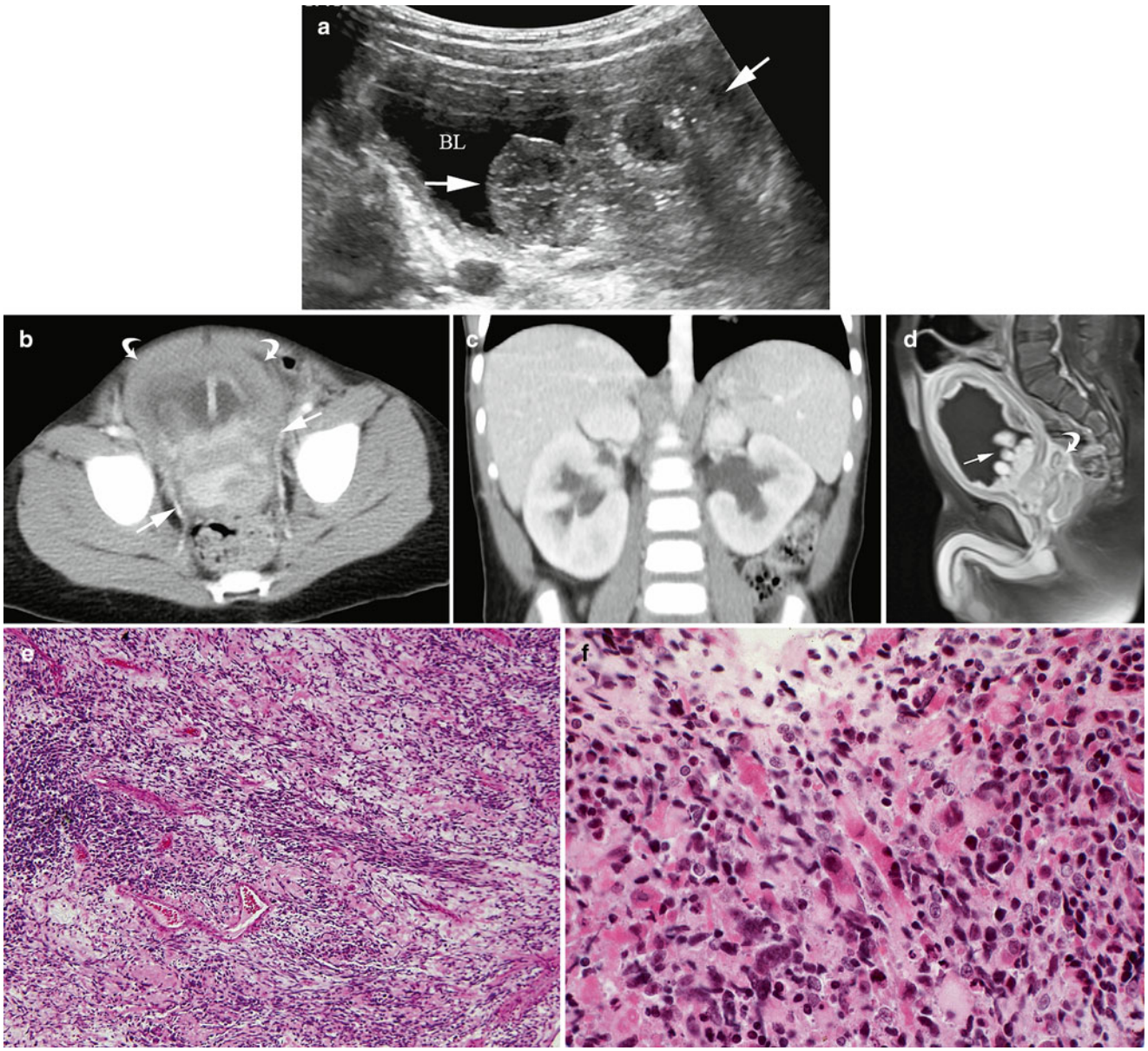

Fig. 3.13 Embryonal rhabdomyosarcoma. (**a**–**d**) This 2-year-old boy with embryonal rhabdomyosarcoma of the bladder base and prostate presented with abdominal pain and urinary dribbling. (**a**) Sagittal ultrasound image shows a lobulated, solid mass (*arrows*) in the bladder lumen (BL). (**b**) Post-contrast axial CT shows a heterogeneously enhancing mass at the bladder base and in the prostate (*straight arrows*) and diffuse bladder wall thickening (*curved arrows*) likely due to chronic bladder outlet obstruction. (**c**) Coronal CT image shows bilateral hydronephrosis secondary to bladder outlet obstruction. (**d**) Post-contrast T1W sagittal MR image shows the classic "cluster of grapes" appearance of the bladder tumor (*straight arrow*) as well as the prostate mass (*curved arrow*) and diffuse bladder wall thickening. (**e**) A low power photomicrograph of embryonal rhabdomyosarcoma shows a mixture of densely compacted cells and loose, myxoid zones. (**f**) At higher power, tumor cells show rhabdomyoblastic differentiation, with peripheralized nuclei, elongate, strap-shaped profiles, and brightly eosinophilic cytoplasm.

forms grape-like polyps by extrusion from a mucosal surface (Fig. 3.13d), whose epithelium abuts a dense cellular lamina known as the "cambium layer." Spindle cell rhabdomyosarcoma (SCRMS), considered a separate subtype by some, comprises dense fascicles of smooth muscle-like cells arranged in whorls or herring bones. SCRMS should contain rhabdomyoblasts on close inspection, separating them from leiomyosarcoma, and they usually occur in the paratesticular region or head and neck. Pediatric SCRMS often co-exist with ERMS foci.

Anaplasia, defined by enlarged, hyperchromatic nuclei and multipolar mitoses, occurs as single isolated cells in some ERMS and as prominent clonal populations in others. These are thus divided into "focal" and "diffuse" types,

Table 3.8 IRSG staging of rhabdomyosarcoma

Stage	Site	Size	Node status (N)	Metastasis (M)
1	Orbit	Any	N0, N1, or NX	M0
	Non-parameningeal head and neck			
	GU non-bladder, non-prostate			
	Biliary tract/liver			
2	Bladder/prostate	<5 cm	N0 or NX	M0
	Extremity			
	Cranial parameningeal			
	Other sites			
3	Extremity	<5 cm	N1	M0
	Cranial parameningeal			
	Other sites	>5 cm	N0, N1 or NX	
4	Any	Any	Any	M1

N0 negative lymph nodes by clinical or radiological examination, *N1* enlarged lymph nodes by clinical or radiological examination, *NX* indeterminate lymph nodes, *M0* no distant metastasis, *M1* distant metastasis

respectively. The latter may resemble adult pleomorphic rhabdomyosarcoma, particularly when occurring in SCRMS, but pleomorphic rhabdomyosarcomas occur rarely in children, if at all.

Immunohistochemistry and Other Special Stains

All variants of RMS, including ERMS, express muscle proteins analogous to their normal cellular counterparts. The most commonly used include desmin, muscle-specific actin (the epitope recognized by clone HHF-35), myogenin (myf4), and MyoD (myf3) [173]. Myoglobin can be used to highlight differentiated cells, which may be useful following chemotherapy. For nuclear transcription factors such as MyoD and myogenin, the staining should be nuclear and not cytoplasmic, which is nonspecific.

Immunohistochemistry also aids in RMS classification, as ERMS shows a relatively heterogeneous myogenin expression, instead of the strong diffuse myogenin expression typical of alveolar rhabdomyosarcoma (ARMS) [174]. Newer markers include HMGA2 [169], which typically stains ERMS and fails to stain fusion-positive ARMS, and AP2β [175], which shows diffuse positivity in ARMS and negative staining in ERMS.

Molecular Diagnostic Features and Cytogenetics

Standard karyotyping studies of ERMS have generally been non-revealing, but comparative genomic hybridization shows a recurring pattern of chromosomal loss and gain [176].

Microarray-based studies show a rather heterogeneous pattern of gene expression, likely related to the diversity of morphology and differences in myodifferentiation among tumors, as well as variable chromosomal loss and gain [169].

Table 3.9 IRSG grouping of rhabdomyosarcoma

Group 1: Completely resected
(A) Confined to organ of origin
(B) Spread to contiguous structures
Group 2: Grossly resected with
(A) Microscopic residual disease
(B) Involved nodes completely resected
(C) Involved node with evidence of microscopic residua or involvement of most distant node
Group 3: Gross residual disease
(A) Biopsy only
(B) Gross major resection of >50 % of tumor volume
Group 4: Distant metastasis (fluid cytologic involvement may be used as evidence)

Prognostic Features

Prognostication of ERMS is a somewhat confusing affair based on stage, group, and age. Intergroup Rhabdomyosarcoma Study Group (IRSG) staging depends on clinical and radiological factors that include site and clinical evidence of lymph node or distant metastasis (Table 3.8) [177]. Grouping depends on pathological evaluation of adequacy of excision and lymph node metastasis (Table 3.9). Age is an independent predictor of ERMS outcome [178], which is worse in adolescents and infants. All of these factors have been used with histological classification to separate patients treated by COG protocols into three subgroups: low risk, intermediate risk, and high risk. Among current published protocols, low-risk patients have overall survival of 80–90 % at 5 years [177], whereas intermediate risk patients have 4-year failure-free survivals of approximately 70 % [179]. High-risk patients, who primarily have ARMS, fare much worse, with an overall 4-year survival of 23 % [180].

Alveolar Rhabdomyosarcoma

Definition: Alveolar rhabdomyosarcoma (ARMS) is an aggressive, high-grade malignancy composed of uniform round cells with arrested early myogenic differentiation. Some feel that ARMS is best defined by genetic features rather than histology [181].

Clinical Features and Epidemiology

In contrast to ERMS, ARMS cases predominate in the extremities and parameningeal regions. Other favored sites include the sinonasal regions and perineum. Outside of the sinonasal tract, relatively few ARMS occur in sites favored by ERMS, such as genitourinary tract, biliary tree, orbit, and middle ear. Unusual presentations include breast metastases and leukemic disease with no apparent primary tumor.

In contradistinction to ERMS, ARMS occurs within a wide age range, making it more common in older children and adolescents. It occurs less frequently than ERMS and comprises about 20–30 % of RMS cases in most series. The frequency decreases further if only fusion-positive cases are considered.

Typically, ARMS presents as a growing, expansive mass that may invade adjacent structures such as bone. The patients may suffer from progressive loss of weight and energy prior to diagnosis, and extensive metastases may be found at diagnosis. Metastatic sites include bone marrow, lymph nodes, and lungs.

Imaging Features

Alveolar rhabdomyosarcoma (ARMS) is most commonly seen in the extremities, presenting as a painless soft tissue mass. Plain radiographic images are nonspecific and may show soft tissue swelling. Ultrasound images may show a hypoechoic or hyperechoic, often inhomogeneous, soft tissue mass. Color Doppler images show multiple vessels within the lesion. These tumors are very aggressive, and extensive involvement of adjacent structures is often seen at the time of diagnosis. CT usually shows a nonspecific enhancing lesion and is helpful in assessing for underlying osseous involvement and lymphadenopathy at the time of diagnosis [6, 122]. CT is important for assessing the extent of parameningeal involvement and invasion into surrounding structures, especially in orbital and extraorbital parameningeal ARMS. On MR images, the characteristics of ARMS are nonspecific, appearing as intermediate signal on T1-weighted images and intermediate to high signal on T2-weighted images. Enhancement is vigorous, and prominent high-flow vessels might be observed (Fig. 3.14a–c). MRI is useful to determine if there is vascular encasement [7, 69, 122]. CT and MRI are helpful in detecting nodal disease [122] (Fig. 3.14a–c).

Molecular Genetics

ARMS are characterized by the translocations t(2;13)(q35;q14) and t(1;13)(p36;q14). These fuse *FOXO1* (formerly *FKHR*) with the homeobox genes *PAX3* and *PAX7*, respectively. The highly expressed *PAX3*-FOXO1 fusion affects numerous downstream targets, whereas the *PAX7-FOXO1* usually becomes overexpressed because of gene amplification. *PAX3-FOXO1*-positive tumors also show gene amplification affecting other regions, including the 12p12-14 region that includes the *CDK4*, *MDM2*, and *GLI* protooncogenes and the 2p region that includes *N-MYC* [182].

A variable subset of tumors with ARMS histology show no evidence of PAX fusions. A few of these are "low expressors" that have evidence of DNA fusion but lack detectable fusion gene product for RNA-based assays. Rarely, they contain alternate fusions that substitute *NCOA1*, *NCOA2*, or *AFX* for *FOXO1* or *FGFR* for a *PAX* gene. However, the majority show a gene expression pattern more characteristic of ERMS than ARMS [182].

Gross and Microscopic Features

ARMS forms an infiltrative, soft tissue mass, frequently intramuscular, with nonencapsulated boundaries and a fleshy, grey-tan cut surface. On a low power objective, one is struck by the monotony of ARMS cells, which present the typical pattern of the "undifferentiated small round blue cell tumor." There are two basic histological patterns: the classic alveolar pattern, as originally described by Riopelle and Thériault [183], and the solid pattern [184]. In tumors with classical ARMS histology (Fig. 3.14d), delicate fibrovascular septa subtend the primitive cells into a pseudo-alveolar arrangement, heightened by the tendency of the cells to dissociate with the septa and form "floating clusters." However, a row of single cells maintains a septal attachment in a picket row fashion. Usually, histologically obvious myogenesis is scant, but some tumors form multinucleate giant cells analogous to the fused myoblasts seen in embryos.

Solid variant ARMS lacks septa but instead forms solid, patternless sheets of primitive round cells that usually lack obvious differentiation (Fig. 3.14e). Both forms of ARMS contain monomorphous nuclei with smooth nuclear contours, variably clumped chromatin, and mildly conspicuous nucleoli. Cytoplasm is scant, and cytoplasmic boundaries may be indistinct. On cytological preparations, there may be cytoplasmic vacuoles, and ARMS cells may mimic neoplastic B cells [185]. A rim of eosinophilic cytoplasm, a sign of early myogenesis, may be present in some cells.

Some RMS contain histologic foci resembling both ARMS and ERMS [186]. These "mixed RMS" have been considered ARMS cases in recent years [168, 187], but it has become apparent that most do not have the biological features of ARMS.

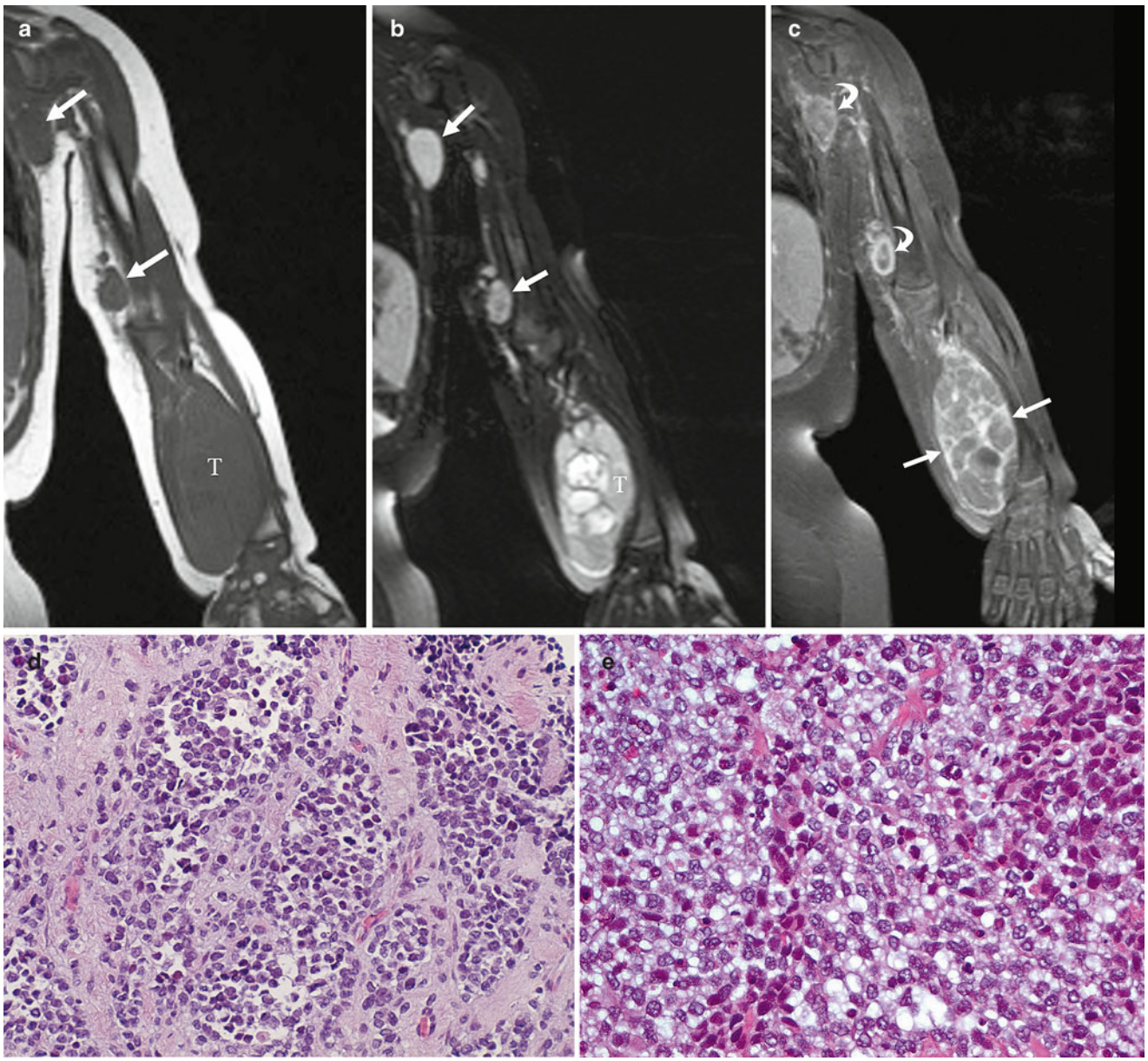

Fig. 3.14 Alveolar rhabdomyosarcoma. (**a**–**c**) A 2-year-old boy with forearm alveolar rhabdomyosarcoma. (**a**) Coronal non-contrast-enhanced T1W MR image shows the primary tumor (T) to be isointense to muscle. Epitrochlear and axillary lymphadenopathy is evident (*arrows*). (**b**) Coronal short tau inversion recovery MRI shows the tumor (T) to be heterogeneous. Nodal spread is again noted (*arrows*). (**c**) On this post-contrast T1W MR image the tumor (*straight arrows*) shows inhomogeneous enhancement with non-enhancing areas consistent with necrosis. The involved nodes also enhance (*curved arrows*). (**d**) Classical alveolar rhabdomyosarcoma histology, with fibrous septa dividing discohesive nests of primitive cells. (**e**) Solid variant alveolar rhabdomyosarcoma showing no fibrous septa but compromising patternless sheets of undifferential small round cells. In spite of the seeming lack of differentiation, there was strong, diffuse myogenin expression (not shown)

Immunohistochemistry and Other Special Stains

Like ERMS, ARMS typically expresses markers of primitive myogenesis, particularly desmin, myogenin, and MyoD. The latter two immunostains show strong, diffuse, nuclear positivity, not the heterogeneous, speckled positivity of ERMS. Cytoplasmic staining should not be considered positive for MyoD or myogenin [188]. A variant of SCRMS, the sclerosing RMS, has ARMS-like features such as thick fibrous septa and strong MyoD positivity, but myogenin positivity is typically weak or even absent.

Newer immunohistochemical markers of ARMS have been developed as a result of expression array analysis. AP2β and beta-cadherin appear to be particularly potent markers of fusion-positive ARMS [189].

Molecular Diagnostic Features and Cytogenetics

PAX3-FOXO1 and *PAX7-FOXO1* fusions can be successfully detected using either RT-PCR [190, 191] or FISH [192]. FISH of *PAX7-FOXO1* often shows amplification with a multitude of nuclear signals. Either of these methods yields sensitive, specific results, but one should carefully mark definite ARMS foci prior to FISH in order to prevent false negative testing. ARMS often shows tetraploidy on routine karyotypes, flow cytometry [193], and FISH studies.

Prognostic Features

ARMS acts in aggressive fashion, with worse outcomes than ERMS [194]. As a result, COG studies have not included ARMS cases in low-risk protocols [177]. In intermediate risk trials [179], ARMS patients showed a 4-year survival of 52–68 % for Stage 2/3 or Group II/III and 77–88 % for l Stage 1 or Group 1. ARMS patients comprise the majority of high-risk patients, who suffered an overall survival rate of 23 % at 5 years.

For PAX fusion-positive patients, survival is even worse [195]. Fusion positivity imparts a distinctive biological signature that associates with aggressive tumor behavior and poor survival [189, 196, 197]. However, in one series, ARMS patients with *PAX7-FOXO1* fusions showed better survival than those with *PAX3-FOXO1* fusions or fusion negativity [198].

Leiomyosarcoma

Definition: Leiomyosarcomas are malignant spindle cell neoplasms comprised of neoplastic smooth muscle. There is diagnostic overlap with myofibrosarcoma, but leiomyosarcomas should show more advanced differentiation.

Clinical Features and Epidemiology

Leiomyosarcomas predominately occur in adults and are relatively rare in children. In the POG series, they comprised only 7 % of 133 non-rhabdomyosarcomatous soft tissue sarcomas [5]. Well-defined series of pediatric leiomyosarcomas [199–201] report a wide age range including both infants and late adolescents [201]. Surprisingly, there is no gender predominance as observed in adults [199].

Leiomyosarcomas have interesting clinical associations, such as their predilection for occurring in unusual sites in pediatric AIDS patients [202]. AIDS-associated leiomyosarcomas appear to be EBV-driven and can occur in other forms of immunodeficiency, such as organ transplantation or primary genetic diseases. Secondary leiomyosarcomas occur in patients with other childhood malignancies.

Childhood leiomyosarcomas occur in a variety of sites [202]. As with adults, primary sites include skin, soft tissue, and gastrointestinal tract. It is critical to separate the latter lesions from gastrointestinal stromal tumors (GIST), as treatment is dramatically different.

Imaging Features

Leiomyosarcoma may arise in the deep soft tissues (within muscle or between muscles), superficial soft tissues, in the retroperitoneum, the genitourinary tract, or gastrointestinal (GI) tract. It is the most common sarcoma to arise from large vessels. Extremity tumors often present as a painless, slowly enlarging mass, most commonly involving the thigh. Tumors in the peritoneum and retroperitoneum can progress silently and often are very large at the time of diagnosis. Gastrointestinal tumors typically exhibit an extraluminal growth pattern resulting in large masses that cause only late obstruction and, therefore, are large at the time of diagnosis [203]. Metastasis occurs most frequently in the lung followed by the liver and peritoneal surfaces [77, 204].

About 17 % of extremity leiomyosarcomas show mineralization that is evident on plain film radiography and CT [205]. On sonography, retroperitoneal tumors appear solid with cystic spaces that have irregular walls. The solid component may appear isoechoic to liver or hyperechoic. The cystic components may contain internal low-level echoes or may be anechoic. The true extent of tumor is difficult to assess by ultrasound and additional cross-sectional imaging is required.

On CT retroperitoneal leiomyosarcomas form large, solid masses with cystic areas due to necrosis. Hyperdense foci, due to hemorrhage, may be present. There may be discordance between the sonographic and CT appearance of retroperitoneal tumors. Computed tomography may suggest large necrotic areas that appear solid on ultrasound. These areas are felt to represent nonliquified necrotic or avascular areas of tumor [206]. Smaller masses may be entirely solid on CT imaging [206]. Leiomyosarcomas arising from the GI tract are also generally large masses that are inhomogeneous on CT. Air or air-fluid levels may be present in GI tumors, reflecting communication with the bowel lumen [207].

On MRI the solid component of leiomyosarcoma is typically isointense to muscle on T1-weighted sequences, variably hyperintense on T2W images, and demonstrates prominent contrast enhancement (Fig. 3.15a–c) [77]. Areas of necrosis appear hypointense on T1W images. On T2W images necrotic areas show intermediate to high signal intensity due to water content. Hemorrhage, when present, may produce fluid-fluid levels [206]. The imaging features of leiomyosarcoma overlap those of GIST, and these tumors cannot be distinguished based on imaging. GISTs are far more common in the GI tract than leiomyosarcomas [208].

Molecular Genetics

Leiomyosarcomas typically contain a range of cytogenetic aberrations, with imbalance of chromosome 9 [209], overrepresentation of genes on 12q13-15 [210], and hypermethylation of *RASSF1A* [211]. EBV-associated leiomyosarcomas

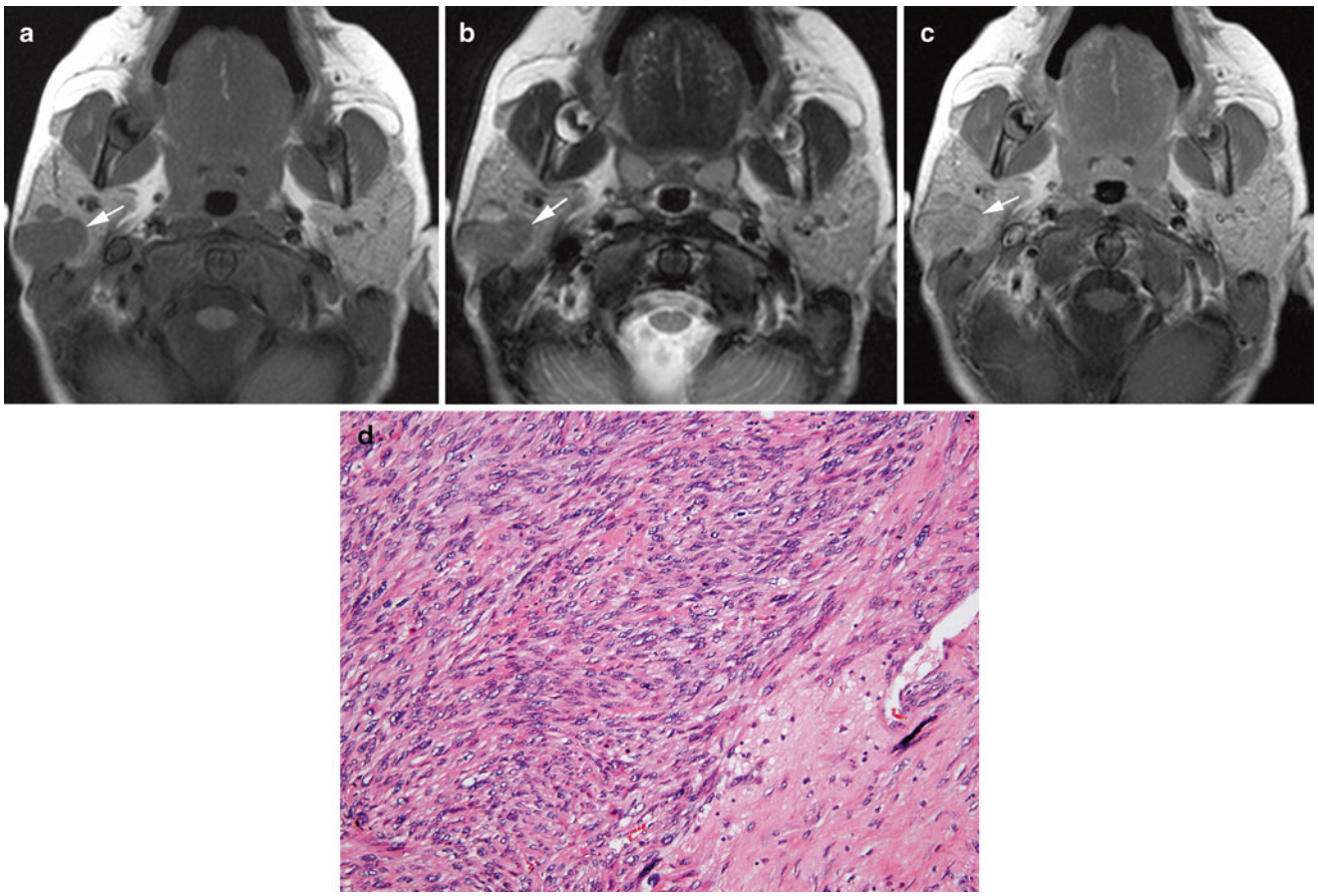

Fig. 3.15 Leiomyosarcoma. A 6-year-old HIV+boy with painful lump in area of right parotid. (**a**) T1W axial MR image shows a well-circumscribed right parotid mass (*arrow*) that is isointense to muscle. (**b**) T2W axial MR shows the mass (*arrow*) to be slightly hyperintense to muscle. (**c**) Post-contrast T1W MR image shows prominent enhancement of the tumor (*arrow*). (**d**) A photomicrograph of pediatric leiomyosarcoma illustrates tight fascicles of fusiform cells containing blunt-ended nuclei, moderately eosinophilic cytoplasm, and occasional vacuoles

show multiclonality that suggests multiple infection events rather than metastasis [212].

Gross and Microscopic Features

Leiomyosarcomas are malignant lesions that show the hypercellularity, interwoven and streaming arrangement, and mitotic activity characteristic of spindle cell sarcomas. Grossly, they are infiltrative, nonencapsulated tumors with bulging, firm, pale tan surfaces, often with zones of necrosis and hemorrhage. Cytologically, they characteristically contain blunted, cigarlike nuclei with perinuclear vacuoles (Fig. 3.15d). Their cytoplasm usually stains variably eosinophilic, but bright eosinophilia may indicate rhabdomyosarcoma (which should always be excluded).

Smooth muscle tumors associated with EBV infection may contain primitive small cell foci and T-lymphocyte infiltrates. They may lack pleomorphism, and histology does not appear to correlate with outcome [212].

Immunohistochemistry and Other Special Stains

Typically, leiomyosarcomas contain abundant microfilaments, giving them strong positivity with smooth muscle actin and muscle specific actin. However, a small percentage of embryonal rhabdomyosarcomas are also smooth muscle actin-positive [213]. To exclude spindle cell rhabdomyosarcoma, myogenin, myoglobin, and MyoD are thus useful. Smooth muscle actin positivity is also shared by a variety of myofibroblastic and myoepithelial tumors, so it should not be used as a sole diagnostic marker. To this end, additional markers of smooth muscle such as desmin and caldesmon are useful to support the diagnosis [45]. Stains for c-kit should be negative, which is important to exclude GIST.

Molecular Diagnostic Features and Cytogenetics

EBV testing should be performed on patients with various forms of immunodeficiency. This can be accomplished by in situ hybridization for EBV early RNAs (EBER) [212].

Prognostic Features

Although a tumor grade based on mitoses, pleomorphism, and necrosis may be assigned to leiomyosarcomas, their behavior does not always correlate with these parameters. As a result, factors such as tumor size, depth, resectability, and site must be considered [200].

Extraosseous Lesions Usually Occurring in Bone

A variety of bone neoplasms, including Ewing sarcoma, chondrosarcoma, giant cell tumor, aneurysmal bone cyst, and osteosarcoma, on occasion occur within extraosseous sites as primary lesions. Of these, the most frequently recurring childhood soft tissue sarcomas include Ewing sarcoma and mesenchymal chondrosarcoma. These are more fully covered in the chapter on bone sarcomas. Suffice it to say that soft tissue sarcomas that invade bone, and vice versa, can be a source of diagnostic and therapeutic uncertainty, and careful radiographic studies are of utmost importance in these situations.

Malignant Tumors of Indeterminate Histogenesis

Synovial Sarcoma

Definition: Synovial sarcomas are tumors of uncertain cell lineage, showing variable epithelial differentiation and cytogenetically characterized by the t(X;18) translocation.

Clinical Features and Epidemiology

Synovial sarcoma are relatively common in pediatrics and are the third most frequent soft tissue sarcoma, following rhabdomyosarcoma and soft tissue Ewing sarcoma [214]. In the Kiel Pediatric Tumor Registry, it accounted for 6 % of all soft tissue sarcomas [214], and in the POG and COG studies, it has been the most common "non-rhabdomyosarcoma soft tissue sarcoma" NRSTS [5].

Among children, synovial sarcoma primarily occurs in adolescents, with a median age of 13–14 years. However, the age range is wide, and lesions may occur in children as young as 14 months [214]. The primary site widely varies, although lower extremity lesions predominate. Other soft tissue sites include upper extremities, head and neck, and intra-abdominal and intrathoracic locations. Visceral tumors occasionally arise in organs such as the kidney and heart [215]. Rare intraneural lesions invite confusion with malignant peripheral nerve sheath tumors [216, 217].

Imaging Features

Although synovial sarcoma can occur in the head, neck, and trunk; approximately 85 % are extremity tumors that are para-articular in location. This tumor may arise from tendon sheaths, bursae, or joint capsules, but is seldom intra-articular and typically does not arise from synovium [218–220]. Patients most commonly present with a painless mass that has been present for weeks to years in the soft tissues of the lower extremity [219]. Other patterns of presentation include a pretumor phase of pain and tenderness without a mass, acute arthritis or bursitis, a chronic joint contracture, or a mass noted after trauma [219].

About one-third of synovial sarcomas contain calcification that may be apparent on radiographs or CT but can be overlooked on MRI [218, 221, 222]. Plain film radiography, CT, or MRI may also demonstrate cortical thinning, erosion, or invasion of adjacent bone, which occurs in 10–20 % of cases [221]. On MR images, synovial sarcomas tend to be large, rounded, or lobulated lesions (Fig. 3.16a); in one study the mean diameter was 9 cm [220]. Tumors often have fairly sharply defined margins and may be largely cystic. Subsequently, synovial sarcoma has been reported to be the most common malignant tumor to be misdiagnosed as a benign lesion (such as ganglion cyst or hematoma) based on MRI [223]. On imaging, synovial sarcomas tend to displace adjacent structures, such as muscle, fat, and tendons, but may encase the neurovascular bundle [220, 222]. In a review of MR imaging features of 34 synovial sarcomas, a triple-signal intensity on T2-weighted images was seen in 35 % of cases. This pattern consisted of mixtures of high signal intensity similar to fluid; intermediate signal intensity that was iso- or slightly hyperintense to fat; and slightly lower signal intensity, resembling fibrous tissue (Fig. 3.16b). In the same study, tumors less than 5 cm in diameter had homogeneously low-signal intensity on T1-weighted images and marked heterogeneity on T2-weighted images [220] (Fig. 3.16a, b). Others have described a heterogeneous, multiloculated appearance with various degrees of internal septations, with or without fluid-fluid levels probably due to internal hemorrhage [222]. After administration of contrast material there is usually prompt and heterogeneous enhancement, which may demonstrate nodularity within a cystic lesion (Fig. 3.16c). The presence of nodularity should raise suspicion of synovial sarcoma, and biopsy should be directed toward the solid nodule [77].

Molecular Genetics

Synovial sarcomas contain a reciprocal translocation, the t(X;18)(p11;q11), which fuses the *SS18* (alias *SYT*) gene on chromosome 18q11 with one of several *SSX* genes on chromosome Xp11. The *SSX* genes comprise contiguous loci that include *SSX1*, *SSX2*, and *SSX4*.

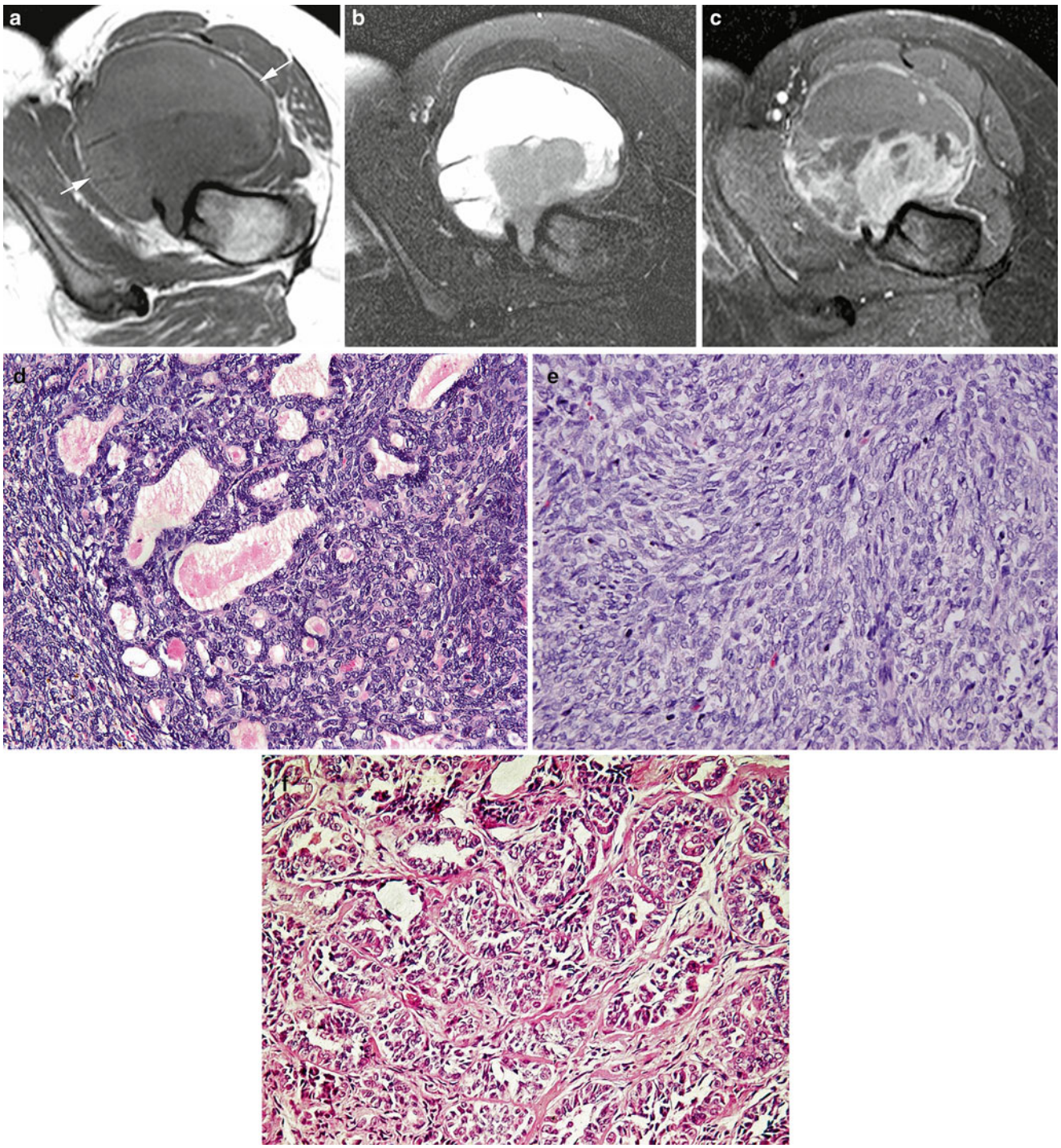

Fig. 3.16 Synovial sarcoma. A 14-year-old girl with intermittent left hip pain for 1 year. (**a**) T1W axial MR image shows a large, sharply defined, complex cystic mass (*arrows*) near the left hip joint. (**b**) T2W axial image shows the triple-signal intensity often seen with synovial sarcoma on T2W images; high signal consistent with fluid, intermediate signal that is iso- or slightly hyperintense to fat and slightly lower signal resembling fibrous tissue. (**c**) T1W post-contrast-enhanced image shows enhancement of a nodular component of this largely cystic tumor. (**d**) The typical biphasic histologic appearance of synovial sarcoma comprises well-formed glands embedded within dense fascicles of slender spindle cells. (**e**) Monophasic spindle cell synovial sarcoma contains only spindle cells, with vague epithelioid features such as loose clusters of cells with increased amounts of cytoplasm and large nuclei. (**f**) Monophasic epithelioid synovial sarcoma comprises mainly well-formed epithelial cells, with little intervening spindle cell component

Gross and Microscopic Features

Synovial sarcomas form infiltrative, nonencapsulated masses that permeate adjacent tissues and have a tendency to spread along fascial planes. Bony invasion may invite confusion with osseous neoplasms. Low-grade tumors may undergo cystic degeneration. The tumors have a pale grey-tan, fibrous surface and may be gritty if microcalcification is present.

A biphasic pattern with well-formed glands embedded within a dense spindle cell stroma comprises the prototypic form of synovial sarcoma (Fig. 3.16d). The epithelial component typically shows only mild to moderate nuclear atypia, whereas the spindle cells form elongated, intertwining cellular bundles akin to fibrosarcoma, with significant hypercellularity and nuclear hyperchromasia. Mitotic count varies, depending on nuclear grade, and grade 2 lesions may contain surprisingly few. This parameter seems to vary inversely with mast cell content, which may be prominent in low-grade tumors. Microcalcifications may be noted.

Synovial sarcomas show a variety of histological appearances. Monophasic spindle cell synovial sarcomas contain no glands or well-formed epithelial cells (Fig. 3.16e). However, vague epithelioid aggregates with rounded cellular contours and slightly more cytoplasm comprise common but often subtle features. Poorly differentiated monophasic synovial sarcomas primarily contain sheets of undifferentiated round cells that invite confusion with Ewing sarcoma and other round cell neoplasms. They typically show a brisk mitotic rate and are high-grade neoplasms.

Rarely, the epithelial component of synovial sarcoma predominates, forming anastomosing glands, canals, and cellular aggregates (Fig. 3.16f). An inconspicuous interglandular spindle cell component may be found with careful examination.

Immunohistochemistry and Other Special Stains

Positivity for cytokeratin and/or EMA typifies the majority of synovial sarcomas [214, 224]. EMA is a more sensitive marker than cytokeratin. BCL2 is usually positive but relatively nonspecific. A new marker of synovial sarcoma, TLE1, was discovered via gene array studies, but its specificity has been questioned [225]. S100 is often positive, negating its utility in distinction of S100 from nerve sheath tumors [224]. Similarly, frequent CD99 positivity renders it useless in separating synovial sarcomas from Ewing sarcomas [224].

Molecular Diagnostic Features and Cytogenetics

Routine karyotyping detects the t(X;18) of synovial sarcomas, but ancillary genetic testing is more commonly used today. Testing for *SSX-SS18* fusions can be performed using PCR-based methods [226] or FISH, the latter typically with a break-apart *SS18* (*SYT*) approach [227].

Prognostic Features

Grading is an important part of evaluating synovial sarcomas and is used for separation of treatment groups with COG protocols. Mitosis counting is the most commonly used parameter [5]. A variety of other parameters, including mast cell content, rhabdoid cells, and calcification, have also been used [228].

Alveolar Soft Part Sarcoma

Definition: Alveolar soft part sarcoma (ASPS) is a rare malignant soft tissue neoplasm of unknown histogenesis, containing cells with distinctive organoid histology, characteristic cytoplasmic crystals, and an *ASPL-TFE3* genetic fusion.

Clinical Features and Epidemiology

ASPS primarily occurs in the extremities of young adults, but the age range includes young children and older adults. In pediatrics, mostly adolescents are affected. The age range spanned from 2 to 71 years in one large study, with medians of 22 for females and 27 for males [229]. In patients less than 20 years, there appears to be a female predominance, but not in older patients [229].

ASPS typically occurs within skeletal muscle or fascia. Areas affected include the extremities, buttocks, and abdominal and chest wall; mostly frequently tumors arise from the thigh and buttocks [229]. Head and neck tumors also occur, particularly in children and in the tongue [230]. Tumors may arise in unexpected [231] locations. The presenting symptoms are generally those of a growing mass, and ASPS may grow very slowly.

Imaging Features

Alveolar soft part sarcoma typically presents as a painless, soft, slow-growing soft tissue mass and is commonly seen in girls, usually arising in the head and neck, trunk, and extremities in children and adolescents. Smaller tumor size is typically associated with a better outcome, although this association is controversial and indolent progression is the rule. Unenhanced CT images show that alveolar soft part sarcoma is less attenuated than muscle. On post-contrast CT there is significant peripheral enhancement, with central low-density necrosis or uniform isodensity or hyperdensity [7, 122]. These tumors appear to be well-circumscribed on MR images (Fig. 3.17a–c) and, unlike many soft tissue sarcomas, are of moderate- to high-signal intensity on T1-weighted images, perhaps because of abundant but slow blood flow through tumor vessels (Fig. 3.17a). This sarcoma is heterogeneously hyperintense on T2-weighted images (Fig. 3.17b) [69]. Dilated vessels in and around the lesion account for serpiginous areas of signal void. Enhancement is vigorous (Fig. 3.17c).

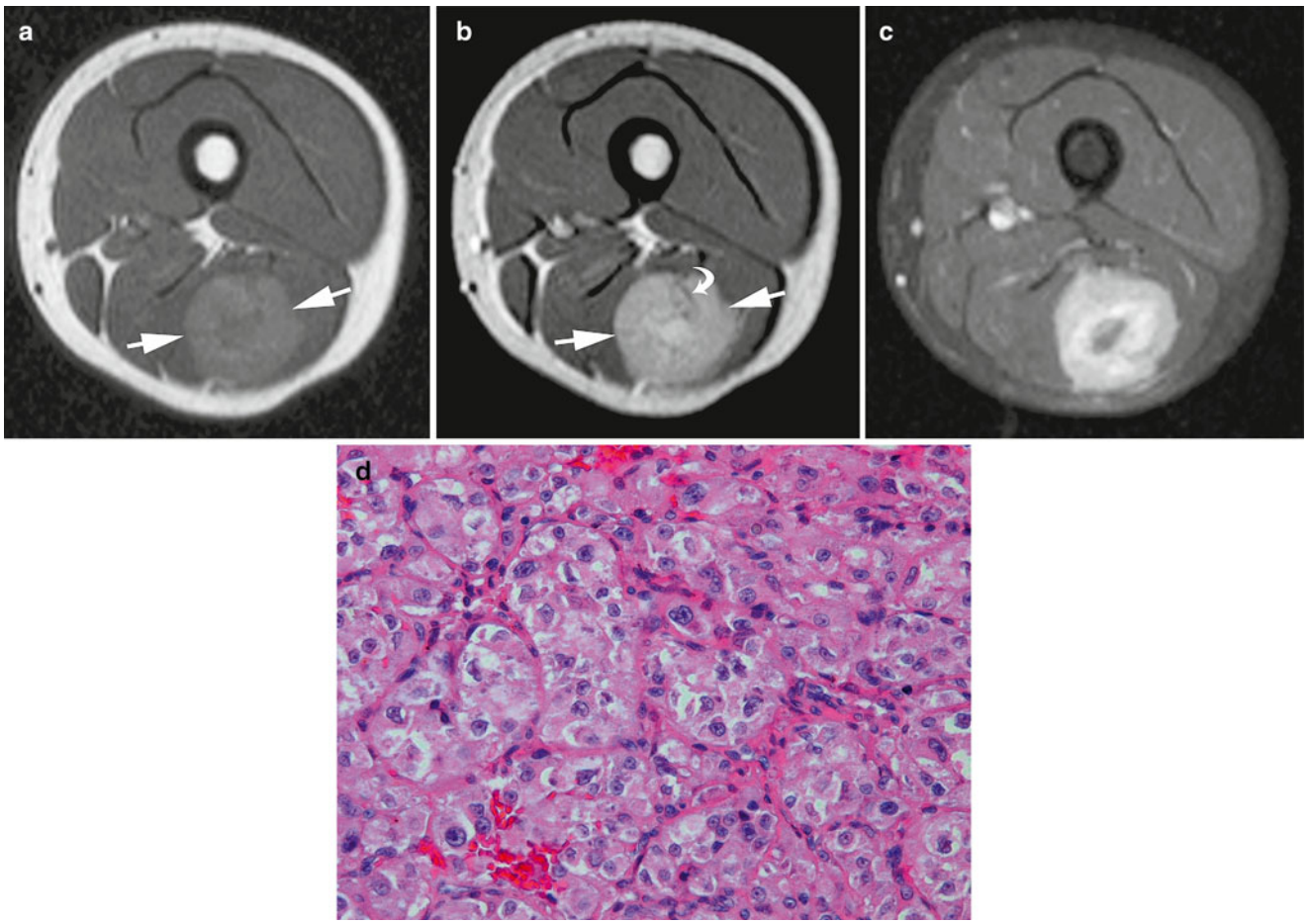

Fig. 3.17 Alveolar soft part sarcoma. A 9-year-old girl with alveolar soft part sarcoma of the left thigh. (**a**) Axial non-contrast-enhanced T1W MR image shows the well-defined, deeply seated mass (*arrows*) to be slightly hyperintense to muscle with a hypointense center. (**b**) Axial T2W MR shows the mass to be hyperintense to muscle with a more hyperintense central focus suggesting necrosis. Several small vessels within the mass are evident as flow voids (*curved arrow*). (**c**) Axial contrast-enhanced T1W MR shows fairly intense diffuse enhancement except centrally, consistent with central necrosis. High T1W signal intensity, well-defined margins, central necrosis, and intratumoral vessels are imaging features known to be associated with ASPS. (**d**) Photomicrograph of alveolar soft part sarcoma, illustrating clusters of polygonal cells with eosinophilic cytoplasm and uniform round nuclei, transected by a fine capillary network

Molecular Genetics

ASPS characteristically contains an unbalanced translocation, the der(17)t(X;17)(p11.2;q25), which fuses the *TFE3* gene on chromosome 17 with the *ASPL* gene on chromosome X [232]. The resultant *ASPL-TFE3* fusion gene acts as an aberrant transcription factor that promotes neoplastic transformation and proliferation. *TFE3* encodes a basic helix-loop-helix leucine zipper protein, and *ASPL-TFE3* fusion leaves the coding region intact, indicating upstream promoter dysregulation [232].

Gross and Microscopic Features

On cut section ASPS forms firm, bulging masses, with a variegated yellow-tan color alternating with frequent necrosis and hemorrhage. It may appear to be encapsulated, but this observation is usually false on microscopic examination. Tumor sizes show a wide range.

The histological features of ASPS show constant repetition, an observation unique in soft tissue pathology [232]. These include uniform, organoid clusters of cells separated by a rich fibrovascular framework and forming the characteristic alveolar histology (Fig. 3.17d). The polygonal tumor cells within these clusters contain eccentric round nuclei and granular, moderately eosinophilic cytoplasm, somewhat reminiscent of weakly staining rhabdomyoblasts but lacking fibrils or striations. The resultant epithelioid appearance may also resemble carcinoma, particularly when the cells contain clear cytoplasm. Pediatric tumors may lack the characteristic organoid appearance and instead display patternless sheets of cells lacking fibrovascular septa but showing similar cytological features [232].

ASPS characteristically contains cytoplasmic needle shaped crystals that are accentuated by diastase-resistant PAS staining. By electron microscopy, the crystals comprise

large rhomboidal structures with a periodic substructure. Some ASPS however lack crystals, so these structures cannot be relied upon for diagnosis in all cases, and careful prolonged search may be necessary in other cases [233]. Similar structures may be observed in intrafusal muscle spindle cells and in other tumors [234].

Immunohistochemistry and Other Special Stains

Staining for muscle markers [235] and neural markers [236] has led to competing hypotheses on the histogenesis of ASPS [237]. However, desmin, actin, and synaptophysin positivity are inconstant features and cannot be used for diagnosis. In particular, globular appearing cytoplasmic MyoD positivity is common [238]. However, cytoplasmic MyoD expression is a nonspecific common finding in a variety of sarcomas [174].

Of more practical use are antibodies against TFE protein, which uniformly decorate ASPS nuclei in a sensitive and specific manner [232]. A similar phenomenon occurs in translocation carcinoma of the kidney, which also contains an *ASPL-TFE3* fusion. TFE3 expression also occurs in a distinctive subset of PEComas and limits its use in differentiating these two neoplasms [239].

Molecular Diagnostic Features and Cytogenetics

ASPL-TFE3 fusion may be detected by both RT-PCR and FISH [240].

Prognostic Features

ASPS acts in a relatively indolent but inexorable manner, leading to long-term survival but eventual demise [229]. In the Memorial Sloan Kettering series [229], patients with localized tumors had survival rates of 77 % at 2 years, 60 % at 5 years, 38 % at 10 years, and 15 % at 20 years (median 6 years). Children appear to show better survival than adults [230], but this phenomenon may be deceptive in light of the slow growth of these lesions. Complete surgical resection holds the best chance for cure, as ASPS shows chemoresistance to current therapy. In the POG grading schema, all pediatric ASPS are high grade (grade 3), regardless of histological features [5].

Perivascular Epithelioid Cell Tumor (PEComa)/Myomelanocytic Tumor

Definition: PEComas comprise a group of clinically divergent neoplasms characterized by their content of a unique cell type, the perivascular epithelioid cell, which coexpresses a myogenic and melanocytic phenotype but does not exist as a non-neoplastic entity. One type of PEComa, the clear cell myomelanocytic tumor, shows a propensity to occur in soft tissue and bone.

Clinical Features and Epidemiology

Included in the PEComa category are renal angiomyolipoma, epithelioid angiomyolipoma of liver and kidney, lymphangioleiomyomatosis, clear cell tumor ("sugar tumor") of the lung, and clear cell myomelanocytic tumors of soft tissue, bone, and a variety of viscera. The last category most commonly occurs in soft tissue, but it is the rarest subtype of PEComa and lacks the association with tuberous sclerosis seen with the other forms. As such, it is an exceedingly rare neoplasm.

For some undefined reason, clear cell myomelanocytic tumor shows a strong propensity to occur in the ligamentum teres or falciform ligament of children [241]. In a series of six patients reported by Folpe et al. [241], ages ranged from 3 to 21 years, with a median of 11 years. Patients presented with abdominal pain, an abdominal mass, or both. Similar lesions are reported in bone [242, 243] and other soft tissue sites, particularly in the retroperitoneum, viscera, abdomen, and pelvis [244]. Outside of tumors arising in the ligamentum teres and falciform ligament or in occasional adolescents, soft tissue PEComas rarely affect children.

Imaging Features

The imaging features of soft tissue PEComas have not been well described.

Molecular Genetics

PEComas of bone and soft tissue described to date have not been found to contain a recurring genetic alteration, outside of a small subset that harbors *TFE3* fusions [245]. Sporadic single reports of translocations have appeared [242].

Gross and Microscopic Features

PEComas of the ligamentum teres or falciform ligament measured 5–20 cm [241]. They have firm, grey-tan cut surfaces with focal hemorrhage and cystic degeneration.

PEComas of bone and soft tissue contain a rich, arborizing vasculature that should be apparent under a low power objective. This vasculature is analogous to that seen in angiomyolipomas, but a fatty component is lacking. The vessels subtend PEComa cells into a fascicular or nested pattern resembling renal cell carcinoma and clear cell sarcoma (Fig. 3.18). These cells contain a clear to lightly eosinophilic cytoplasm with epithelioid or spindled contours and distinct boundaries. Nuclei are generally round with even membranes and chromatin, but pleomorphism and occasional giant cells may be apparent, the latter sometimes resembling the "spider cells" of rhabdomyoma. Some tumors show perivascular hyalinization that accentuates the nested pattern [244]. Rare examples contain a sparse amount of melanin pigment. Tumor cellularity is variable but generally low to moderate.

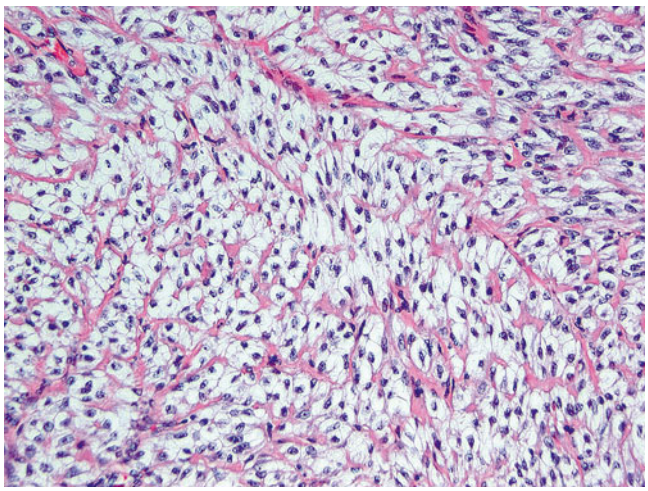

Fig. 3.18 Clear cell myomelanocytic tumor (PEComa), containing uniform epithelioid cells with clear cytoplasm, clustered by a richly arborizing microvasculature

Immunohistochemistry and Other Special Stains

Coexpression of melanocytic markers, particularly HMB45, and muscle markers, particularly smooth muscle actin and myosin, characterizes PEComas. Other melanoma markers such as melan A and MiTF may be positive, but S100 and desmin are typically negative. TFE3 positivity, perhaps related to genetic fusion [245], is seen in a small subset. CD34 should be negative.

Prognostic Features

A variably benign behavior characterizes PEComas as a group, but malignancy is exhibited by a subset of non-renal, non-pulmonary cases [246]. Folpe et al. have published a set of criteria for predicting PEComa clinical behavior [247]. They separate lesions into "benign," "uncertain," and "malignant" categories. Benign PEComas are smaller than 5 cm, contain non-infiltrative borders, have a low to intermediate nuclear grade and cellularity, show a mitotic rate of ≤1/50 hpf, and lack either necrosis or vascular invasion. PEComas of uncertain malignant features may show nuclear pleomorphism, contain giant cells, or measure >5 cm, but otherwise should have similar findings. Malignant PEComas exhibit two or more worrisome features, i.e., size >5 cm, mitotic rate >1/50 hpf, infiltrative borders, high nuclear grade or cellularity, necrosis, or vascular invasion.

Rhabdoid Tumor of Soft Tissue

Definition: Rhabdoid tumor is a high-grade, aggressive infantile sarcoma that occurs in viscera and soft tissue. A related tumor, the atypical teratoid-rhabdoid tumor, occurs in the CNS. It contain is characteristic cytoplasmic inclusions and genetic deletions affecting chromosome 22q11.

Clinical Features and Epidemiology

Rhabdoid tumors primarily occur in infants, and the diagnosis should be suspect in older patients. That said, their morphological and genetic features overlap with a variety of other neoplasms that usually occur in older patients; particularly noteworthy in this latter group is proximal epithelioid sarcomas. This has led to confusion in the literature, and it is well accepted that a variety of carcinomas and sarcoma may show rhabdoid features [248].

Fortunately, rhabdoid tumors are relatively rare entities, considering their aggressive behavior and dismal prognosis. Most commonly, they occur in the kidney, but they also occur in various visceral organs and soft tissue. Axially based neoplasms form a prominent component of soft tissue tumors [249], suggesting an association with axial embryogenesis. Extremity-based rhabdoid tumors are usually proximal. The lesions often grow rapidly and may reach an alarming size, but superficial cutaneous rhabdoid tumors may be discovered in sufficient time to allow complete excision, the best chance for cure [250].

Imaging Features

Most common in the kidney, rhabdoid tumors also have been described in the liver, brain, tongue, neck, chest, heart, pelvis, extremities, and other sites [251, 252].

The imaging characteristics of soft tissue rhabdoid tumors are not well known, largely because of the rarity of these tumors [251]. In the largest reported case series, no specific imaging features were observed that could prove diagnostic for these tumors; however, soft tissue rhabdoid tumors have a tendency to be large and hypodense on CT images and show heterogeneous hyperintensity on T2-weighted MR images (Fig. 3.19a–c) [251].

Molecular Genetics

Rhabdoid tumors characteristically contain variable deletions of chromosome 22q11 that affect a common region, *INI1* (also known as *SMARCB1*, *hSNF5*, or *BAF47*). This gene encodes a protein that forms part of a histone-binding SWI-SNF complex which is important in chromosomal maintenance [253]. Normal cells ubiquitously express INI1, as do most neoplasms [254]. A subset of patients with rhabdoid tumors show constitutional deletions and are at risk for multiple tumors [255].

Gross and Microscopic Features

Beckwith and Palmer [256] initially termed rhabdoid tumors "rhabdomyosarcomatoid forms of Wilms tumor" because of their classic rhabdomyosarcoma-like appearance, which comprises patternless sheets of cells with moderately abundant eosinophilic cytoplasm and eccentric nuclei. The nuclei often contain a large, prominent nucleolus, and the cytoplasm typically contains a hyaline inclusion made of whorled

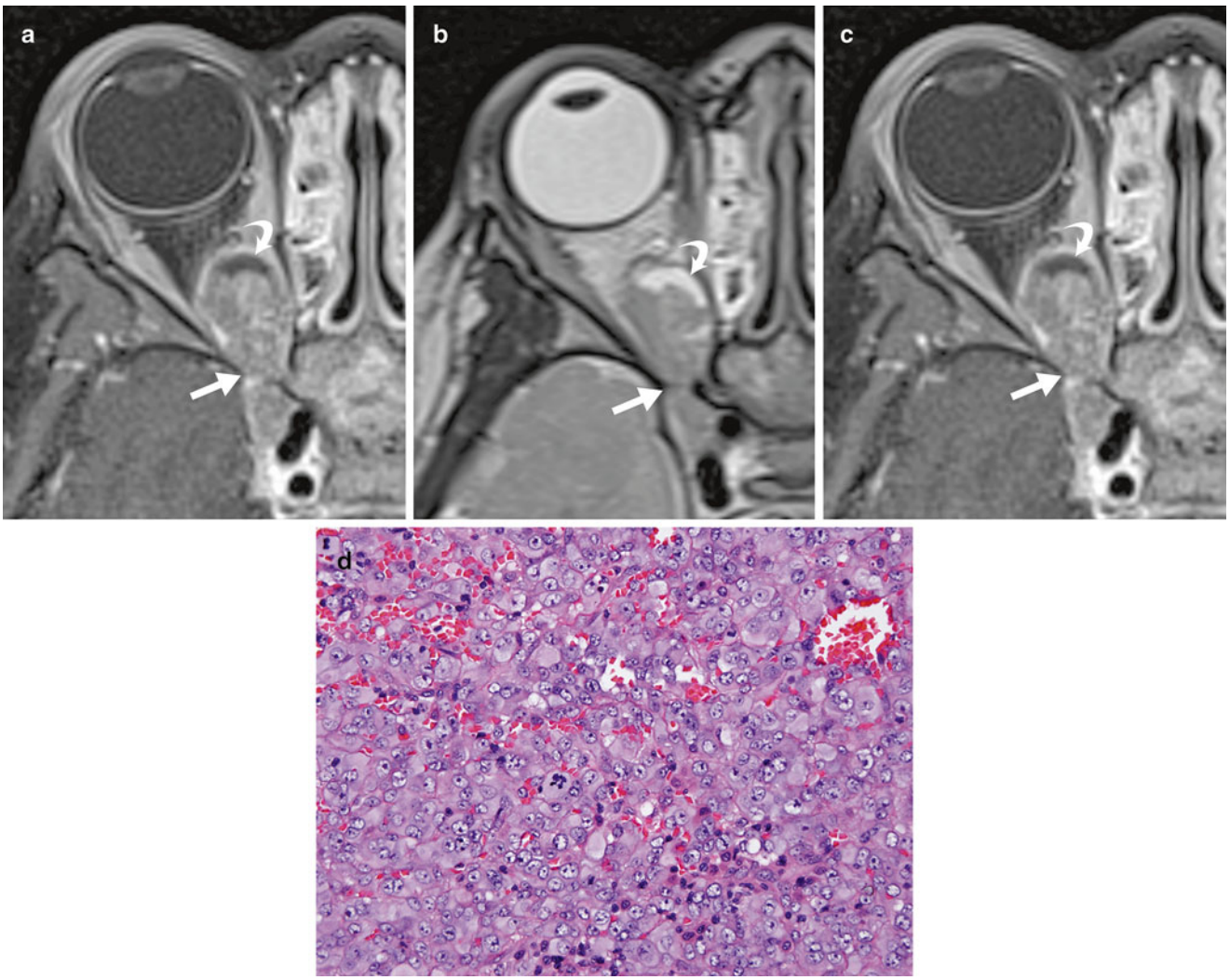

Fig. 3.19 Rhabdoid tumor. A 2-year-old girl with right orbital rhabdoid tumor. (**a**) Non-contrast-enhanced T1W image shows the tumor to be predominantly solid and isointense to muscle. The anterior aspect is hypointense on this sequence, is bright on (**b**) T2W images, and (**c**) non-enhancing on post-contrast T1W imaging, consistent with a cystic or necrotic component (*curved arrows*). Note heterogeneous contrast enhancement of solid component. The tumor extends through the optic canal (*straight arrows*). (**d**) Patternless sheets of epithelioid cells usually characterize this lesion. The tumor cells contain eccentric nuclei and variable eosinophilic cytoplasm, usually with ovoid paranuclear inclusions. Although they show no obvious differentiation, polyphenotypia is usually noted with immunochemistry (not shown)

masses of intermediate filaments (Fig. 3.19d) [257]. There is considerable histological variation [258], including small round blue cell forms that resemble lymphoma or histocytic sarcoma. Lesions with characteristic clinical, immunohistochemical, and/or genetic findings may lack the classical histology of this tumor [254].

Immunohistochemistry and Other Special Stains

Characteristically, rhabdoid tumors co-express a variety of intermediate filaments, particularly vimentin and cytokeratin [249]. Their epithelial nature is confirmed by EMA staining, but a confusing array of polyphenotypia may occur, with positive neural markers and CD99 [249]. Recently, INI1 has emerged as a major diagnostic marker, in that rhabdoid tumors generally show negative staining that contrasts with normal cells and the majority of other tumors [254, 259]. However, a growing list of other INI1-negative tumors is emerging [253].

Molecular Diagnostic Features and Cytogenetics

Early cytogenetic studies seemed to indicate that rhabdoid tumors show minimal karyotypic alterations [260], but monosomy 22 appeared frequent in atypical teratoid rhabdoid tumors. Additional work indicated that lesions lacking karyotypic abnormalities probably contained submicroscopic deletions of chromosome 22q11 and many showed loss of expression without apparent gene deletion [261]. Translocations may involve this region [262]. *BCR*, the gene

translocated in chronic myelogenous leukemia, abuts the *INI1* locus and may be useful as a surrogate deletion marker in FISH studies [263].

Prognostic Features

Malignant rhabdoid tumors have a well-deserved reputation for clinical aggressiveness and dismal outcome [264]. Although occasional case reports document cures with combination chemotherapy [265], the best chance for survival remains complete excision [249].

Epithelioid Sarcoma

Definition: Epithelioid sarcoma is a malignant soft tissue lesion showing squamous epithelial cell differentiation and immunophenotypic characteristics.

Clinical Features and Epidemiology

Epithelioid sarcoma is primarily a lesion of older children and adolescents, although some are described in young children [266]. There may be some overlap in the latter cases with rhabdoid tumor of soft tissue [253]. Most epithelioid sarcomas occur in distal soft tissues, particularly that of the upper extremity and hand [267]. The proximal variant of epithelioid sarcoma shows a tendency to occur in more axial locations [268]. Epithelioid sarcomas form infiltrative lesions that spread along tendons and aponeuroses. The primary lesion may be inconspicuous, leading to diagnosis only with the appearance of lymph nodal metastasis [267]. Nodal metastasis occurs in about 40 % of patients [266]. Some lesions are relatively indolent, but others grow quickly. There may be a clinical resemblance to ganglion cyst. Most patients are male. Symptoms include pain and nerve compression.

Imaging Features

Epithelioid sarcoma may present as single or multiple nodules, sometimes elevated on the skin or as deep infiltrative lesions. Necrosis or hemorrhage may develop. On radiographs, calcifications are seen in about 20 % of cases [72, 269]. Deep, longer-standing lesions may cause secondary changes in adjacent bone such as cortical thickening [269, 270].

MR characteristics are nonspecific and widely variable but reflect areas of hemorrhage, fibrosis, and varying degrees of cellularity (Fig. 3.20a–c). Peritumoral edema is common [269]. The infiltrative growth pattern of epithelioid sarcoma can be readily defined by MR. These tumors are characterized by T1-weighted signal that is isointense with muscle, heterogeneous T2-weighted signal, and enhancement with intravenous gadolinium contrast administration [269, 270].

The limited experience available to date with 18F FDG in imaging epithelioid sarcoma suggests a role in the staging of primary disease and detection of distant metastases [270].

Molecular Genetics

Deletions of the *INI1* gene characterize both conventional and proximal subtypes of epithelioid sarcoma [268]. Some tumors lack *INI1* deletions, suggesting alternate methods of gene inactivation [261].

Gross and Microscopic Features

Gross features of epithelioid sarcoma include one or more firm, unencapsulated nodules, poorly circumscribed margins, and sometimes foci of caseous necrosis. The overlying skin may be ulcerated, with draining sinus tracts. Low power examination of epithelioid sarcomas, particularly the conventional type, often reveals central foci of necrosis surrounded by cuffs of epithelioid cells, resembling tubercles. The tumor cells can show prominent squamous differentiation, replete with polygonal outlines, eosinophilic cytoplasm, and desmosomal junctions (Fig. 3.20d). Occasional giant cells may be seen, and calcification may be present. Recruitment of myofibroblasts within the tumor leads to intercellular collagen deposition. At times the lesion looks deceptively bland, very much like deep granuloma annulare. Occasional lesions may resemble epithelioid angiosarcoma. Rare examples have a fibroma-like appearance that can be confused with spindle cell tumors [271].

The proximal variant of epithelioid sarcoma typically shows features of a higher grade tumor (Fig. 3.20e) and contains many rhabdoid cells [253]. This latter feature has led to confusion in the literature between epithelioid sarcoma and rhabdoid tumor [272], but the two neoplasms comprise distinct clinicopathologic entities [253].

Immunohistochemistry and Other Special Stains

Co-expression of vimentin, cytokeratin, and EMA characterizes epithelioid sarcomas. About one-half express CD34, which can help diagnose tumors with aberrant staining [273]. Like rhabdoid tumor, some cases show polyphenotypia and expression of unexpected cell markers [274]. INI1 negativity is seen in both proximal and classical forms [268].

Molecular Diagnostic Features and Cytogenetics

With cytogenetic study, epithelioid sarcomas may show deletions or translocations involving chromosome 22q11 [253, 275]. *INI1* loss may be demonstrated with FISH probes [276].

Prognostic Features

In general, proximal epithelioid sarcomas show an aggressive behavior, with worse outcomes than distal ones [277]. Other indicators of poor prognosis include lymph node metastasis and vascular invasion [277–279]. Factors associated with better outcome include lower grade, female sex, younger age, size <2 cm, and presence of lymphocytic infiltration [280].

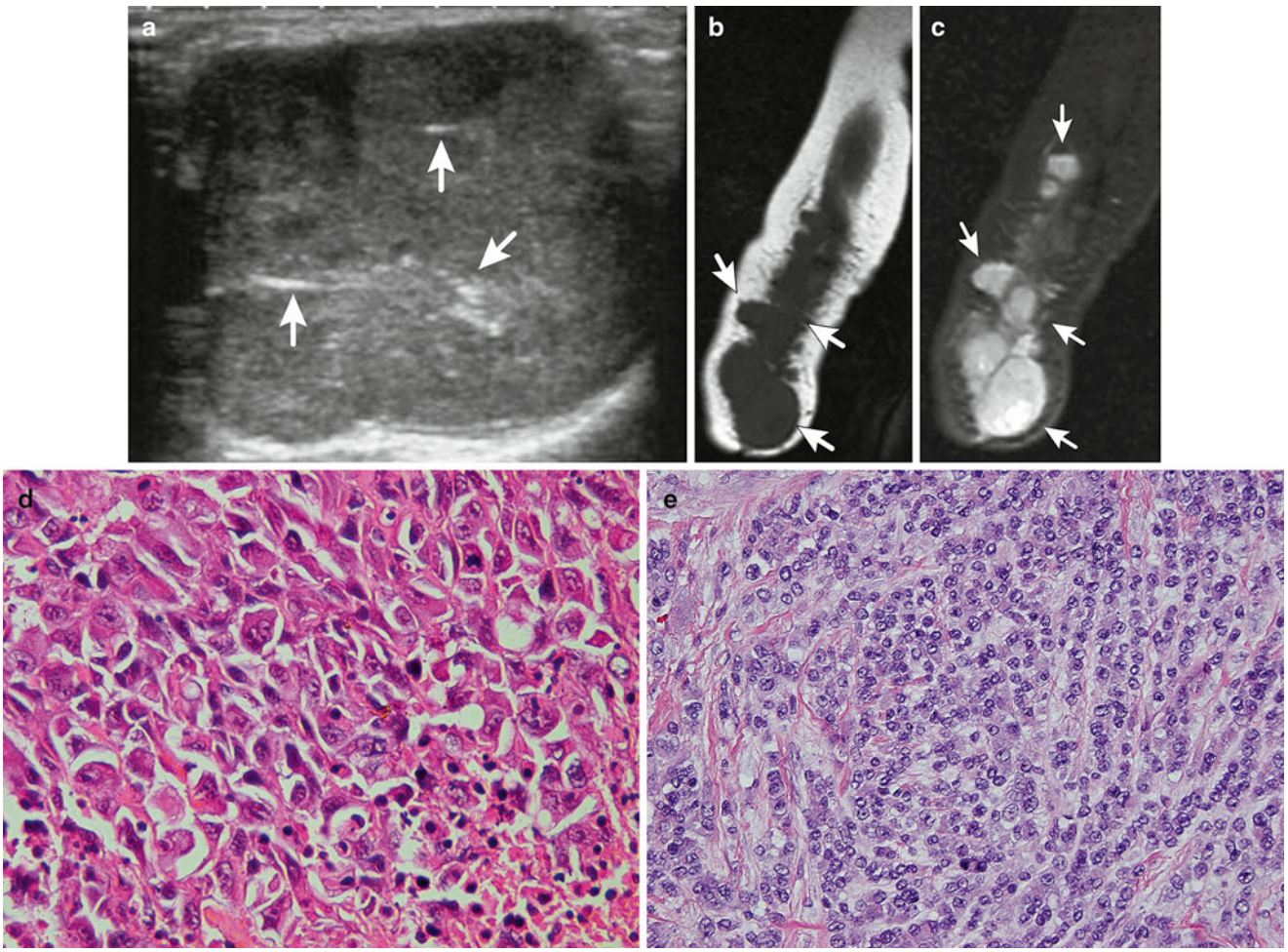

Fig. 3.20 Epithelioid sarcoma. (**a**–**c**) Recurrent epithelioid sarcoma in a 5-month-old boy born with a golf ball-sized mass right forearm. At diagnosis, ultrasound image (**a**) shows a well-circumscribed solid subcutaneous mass with scattered central strands of fibrosis (*arrows*). The surgical margins were positive for residual tumor. At presentation of disease recurrence, sagittal T1-weighted (**b**) and short tau inversion recovery (STIR; **c**) show multiple subcutaneous nodules tracking from the primary site of disease proximally to the elbow, sparing involvement of bone. On T1-weighted sequence (**b**), the nodules are isointense with muscle. On STIR (**c**), they demonstrate increased signal (*arrows*). (**d**) On histological examination, classical epithelioid sarcomas show squamous differentiation and resemble carcinoma. Note the zonal necrosis in the lower figure. (**e**) Proximal variant of epithelioid sarcoma comprises sheets of rhabdoid cells with eosinophilic cytoplasm and paranuclear inclusions. This example has a primitive, small cell appearance and forms epithelioid strands of tumor cells

Clear Cell Sarcoma of Soft Tissue (Melanoma of Soft Parts)

Definition: Clear cell sarcoma of soft parts is a fully malignant soft tissue sarcoma showing melanocytic features and containing a characteristic *EWS* translocation. It should not be confused with the unrelated clear cell sarcoma of the kidney.

Clinical Features and Epidemiology

Clear cell sarcoma occurs only rarely, and is even rarer in the pediatric population. Among 185 patients entered on POG soft tissue sarcoma trials, only 5 (3.8 %) had a clear cell sarcoma [5]. There is a slight male predominance (1.5:1), and the median age was 30 in one large series, with the youngest patient being 13 years old [281]. Lesions typically appear in the foot, ankle, leg, and knee [282], although some arise in the trunk. Patients often complain of pain of long duration [283].

Imaging Features

Up to 40 % of clear cell sarcomas occur near the Achilles tendon or plantar aponeurosis. Radiographs may reveal a soft tissue mass. Although involvement of adjacent bone is occasionally encountered, calcification is rare. On MR images, clear-cell sarcomas are typically sharply demarcated and homogeneous and are not often associated with intratumoral necrosis or osseous destruction. These tumors are slightly

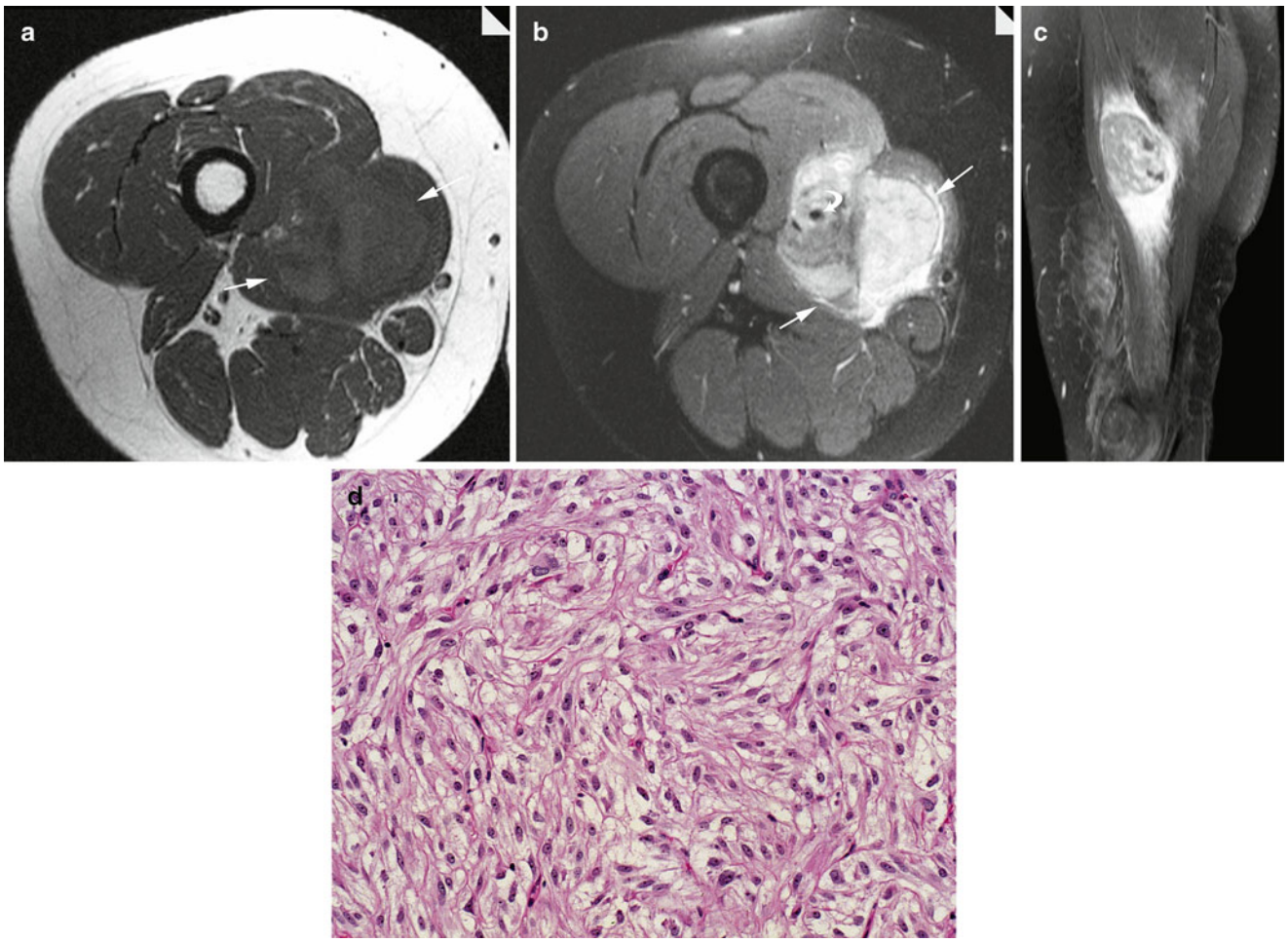

Fig. 3.21 Clear cell sarcoma of soft parts. (**a**–**c**) An 11-year-old girl with clear cell sarcoma of the right thigh. (**a**) Axial non-contrast-enhanced T1W MR image shows the tumor (*arrows*) to be slightly hyperintense to muscle but difficult to visualize. (**b**) Axial T2W MR image shows the tumor (*straight arrows*) to be sharply marginated and very heterogeneous. Low-signal areas within the tumor partially correspond to hyperintense areas seen in 1a and are probably due to melanin. The tumor encases the neurovascular bundle (*curve arrow*) making surgical resection difficult. (**c**) Sagittal contrast-enhanced T1W image shows minimal tumor enhancement with extensive surrounding edema. Non-enhancing foci within the tumor likely represent areas of necrosis. (**d**) Microscopic image of clear cell sarcoma, containing epithelioid cells in whorled clusters. The cells contain clear cytoplasm. They co-expressed smooth muscle actin and HMB-45 (not shown)

hyperintense to skeletal muscle on T1-weighted MR images [284], perhaps because of the presence of melanin (Fig. 3.21a). Areas of low-signal intensity relative to muscle on T2-weighted images, are also presumably due to melanin content (Fig. 3.21b); however, most lesions are of intermediate to high signal intensity on this sequence. The tumors demonstrate enhancement after administration of gadolinium (Fig. 3.21c).

Molecular Genetics

Characteristically, clear cell sarcoma of soft tissue contains a reciprocal translocation, the t(12;22)(q13;q12) [283]. The resultant *EWS-ATF1* gene produces a chimeric protein containing the transactivation locus of *EWS* and the basic leucine zipper region of *ATF1*. This fusion frees ATF1 protein from the control of cAMP and produces aberrant DNA transcription, with upregulation of MiTF and other melanocytic proteins [285]. The genetic features of clear cell sarcoma distinctly differ from those of melanoma [283].

Gross and Microscopic Features

Grossly, clear cell sarcomas form deep-seated, infiltrative masses, intimately bound to adjacent tendons and aponeuroses. Lesions may infiltrate into overlying dermis but do not ulcerate the skin. They display a firm, fleshy, grey cut surface, sometimes with necrosis, hemorrhage, cystic change, and/or brown to black pigment.

The tumor cells form a nested to fascicular packet-forming growth pattern, outlined by fibrovascular septa (Fig. 3.21d), at times reminiscent of alveolar rhabdomyosarcoma [282, 283].

Others show a more diffuse epithelioid appearance, contain lymphocytic infiltrates, and resemble seminoma. The lesions typically contain uniform cells with round to oval nuclei, vesicular chromatin, and prominent red nucleoli. The cytoplasm is moderately abundant and usually clear, although slight eosinophilia and even rhabdoid cells may be seen. Occasional giant cell formation and pleomorphism are not unusual features. Some clear cell sarcomas contain melanin pigment, which can be accentuated by the Fontana melanin stain [283].

Immunohistochemistry and Other Special Stains

Melanocytic marker expression characterizes clear cell sarcoma and reflects its content of premelanomes and melanosomes on ultrastructural examination. Melanocytic proteins expressed by clear cell sarcoma include S100 (the most sensitive marker), HMB45, MiTF, and melan A. The latter proteins may be found focally in some cases and not at all in a few others [281, 282]. Positive staining may also be present for bcl2 (most tumors), synaptophysin and CD57 (about one-half of cases), and CD56, CD117, EMA, cytokeratin, and CD34 (occasional). Muscle markers such as desmin and actin are negative [281].

Molecular Diagnostic Features and Cytogenetics

The characteristic *EWS-ATF1* of clear cell sarcoma may be detected by RT-PCR [281], and *EWS* rearrangement may be demonstrated by FISH [160]. The latter test is potentially useful in separating clear cell sarcoma from melanoma. However, one should keep alternate translocations such as the t(2;22) in mind when interpreting these results.

Prognostic Features

Regional lymph node and/or distant metastases are feared consequences of clear cell sarcoma and occur in over one-half of patients [283]. Prognostic factors predictive of metastases have been controversial; some authors find no value in pathological findings, whereas others have found tumor size and necrosis to be prognostic [283]. Nevertheless, a slow progression characterizes clear cell sarcoma, and in one recent study the survival rate drops from 63 % at 5 years to 25 % at 10 years [281, 286]. Radical excision is the treatment of choice, as chemotherapy offers little benefit [286].

Myoepithelial Tumor of Soft Tissues (Parachordoma)

Definition: Myoepithelial tumors of soft tissue (also known as mixed tumor; formerly known as parachordoma or chordoid sarcoma [287]) comprise a group of benign and malignant lesions that show a myoepithelial phenotype and occur in deep and superficial soft tissues.

Clinical Features and Epidemiology

The recent description of myoepithelial tumor as a soft tissue lesion precludes adequate epidemiology, but its predecessor parachordoma was a distinctly rare and unusual neoplasm—only three cases had been reported as late as 1995 [287]! These are mainly adult tumors, but about one quarter of them arise in children [288]. Patient ages have ranged from newborn to 17 years, with a median of 9 years. No gender predilection is apparent. Reported Lesions arose in a variety of locations, including extremities (14 cases), trunk (6 cases), head and neck (4 cases), mediastinum (3 cases), retroperitoneum (1 case), and heart (1 case). Symptoms arose from a growing mass, with or without pain.

Imaging Features

There are few articles describing the imaging features of myoepithelial tumor of soft tissue. On CT imaging this tumor has been described as a well-defined, diffusely enhancing homogenous or slightly heterogeneous tumor that generally lacks calcification, fat, or bony involvement. On MRI myoepithelial tumors of soft tissue may appear hypo- to isointense on T1W images, hyperintense on T2W images, and diffusely enhancing after contrast administration [289].

Molecular Genetics

No single molecular alteration characterizes myoepithelial tumors of soft tissue. Deletion of *INI1* is a recurring but not universal theme [253], and *EWS* rearrangement occurs in almost one-half of cases [290].

Gross and Microscopic Features

A thin pseudocapsule often circumscribes myoepithelial tumors of soft tissue. In one series, sizes of pediatric myoepithelial carcinomas ranged from 1.3 to 12 cm (median 4.7 cm) [288], whereas in a larger series that included adults, tumors ranged from 1.7 to 20 cm (median 4.7 cm) [291]. Cut surfaces showed a considerable heterogeneity that included fleshy, gelatinous, and gritty features, with variable degrees of necrosis.

Low power microscopic examination of soft tissue myoepithelial tumors reveals a distinctly lobular or multinodular appearance. Lobules show peripheral cellular condensation and contain myxoid to hyaline stroma enmeshing cells in a variety of histological patterns, including reticular, trabecular, nested, and solid features (Fig. 3.22a). Variable proportions of epithelioid, clear, spindle, and plasmacytoid cells constitute these tumors. Some have a small blue round cell appearance, and occasional examples contain ducts, cartilage, bone, or calcification [288]. Like the physaliferous cells of chordoma, cells may contain numerous vacuoles (Fig. 3.22b), hence the older term "parachordoma" [287].

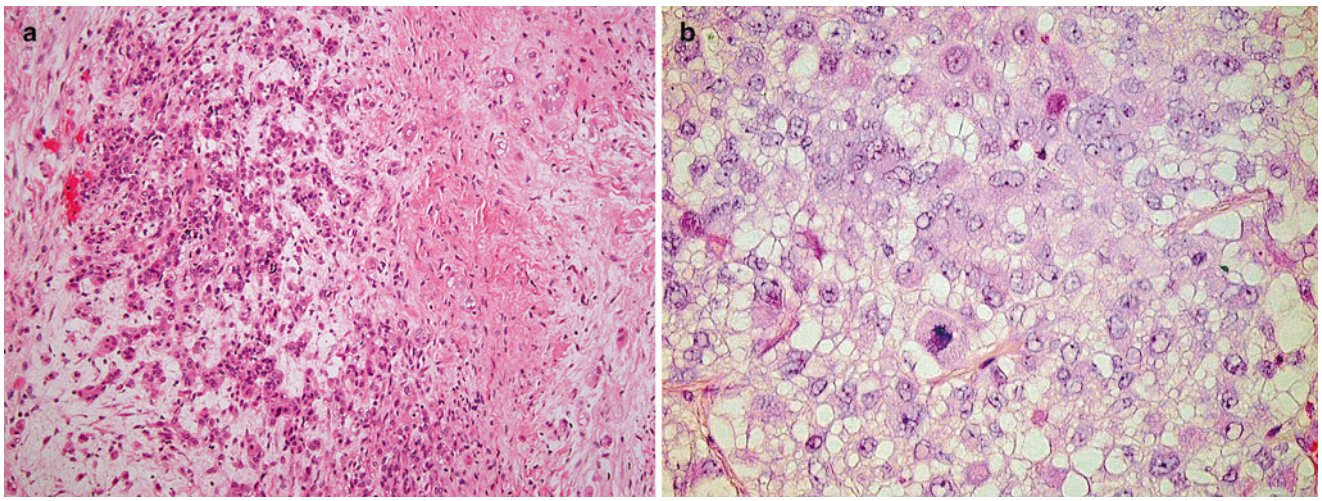

Fig. 3.22 Myoepithelial tumor of soft tissues (parachordoma). (**a**) Poorly defined aggregates of epithelioid cells are separated by myxoid stroma on the *left*. Dense collagen is noted on the *right*. (**b**) Higher power photograph highlights cytoplasmic vacuoles resembling those of physaliferous cells seen in chordoma

Immunohistochemistry and Other Special Stains

Like mixed tumors of salivary glands, myoepithelial tumors of soft tissue co-express cytokeratin, actin, and S100. Cytokeratin expression is a ubiquitous finding, but different antibodies give differing results [291]. Most cases also show positivity for EMA, S100, or GFAP. Smooth muscle markers actin and calponin are positive in most tumors, whereas desmin is usually negative [291]. CD34 is also typically negative, but CD99 is often positive. INI1 expression is lost in about one-half of tumors [291]. Brachyury expression is absent [292].

Molecular Diagnostic Features and Cytogenetics

A variety of cytogenetic abnormalities have been recorded with pediatric myoepithelial carcinoma of soft tissue. A recent study found *EWS* rearrangement in about one-half by FISH [290]. *EWS* fuses with *POU5F1*, *PBX1*, or *ZNF444*. Cases with *EWS-POU5F1* contain cells with clear cytoplasm.

Prognostic Features

About one-half of pediatric myoepitheliomas recur, in spite of clean surgical margins [288]. Almost all with marginal involvement recur, whereas wide margins predict good outcome. In one series of 23 patients, 12 developed metastases to a variety of locations, mostly lung and lymph node, and 10 had died after 10 days to 39 months (median 9 months) [288]. There was no correlation of survival with age, site, or mitotic rate. In a larger series of 101 patients from all ages and histologies, no clinical or histological parameters correlated with outcome [291].

Desmoplastic Small Round Cell Tumor

Definition: Desmoplastic small round cell tumor (DSRCT) is a highly malignant primitive sarcoma that shows a profound tendency for intra-abdominal origin, polyphenotypic expression of cell markers, and fusion of *EWS* and *WT1* genes.

Clinical Features and Epidemiology

In pediatrics, DSRCT primary arises in adolescents. Among 51 patients from Mayo Clinic [293] and Memorial Sloan Kettering Cancer Center [294], patient ages ranged from 6 to 54 years. DSRCT shows a marked predilection for males, with M:F ratios of 29:3 and 16:3 in the aforementioned series. Almost all DSRCTs arise in the abdomen, usually within the abdominal cavity. However, rare lesions arise in intrascrotal, pleural, and even CNS and extremity locations.

Symptoms and signs of DSRCTs usually relate to their predominately abdominal location and include abdominal pain, weight loss, hernia, ascites, increased girth, constipation, and hepatosplenomegaly [293]. Laparotomy typically reveals peritoneal implants, often with hepatic involvement.

Fortunately, DSRCTs are rare neoplasms; only 32 were seen at Mayo Clinic over an 8-year period [293].

Imaging Features

Because most DSRCTs arise in the abdomen or pelvis and spread diffusely throughout the peritoneum, the most common imaging finding is peritoneal thickening, nodules and bulky masses arising from the omentum or mesentery. Solitary, primary peritoneal masses, however, can occur without peritoneal spread. Peritoneal primary tumors tend to

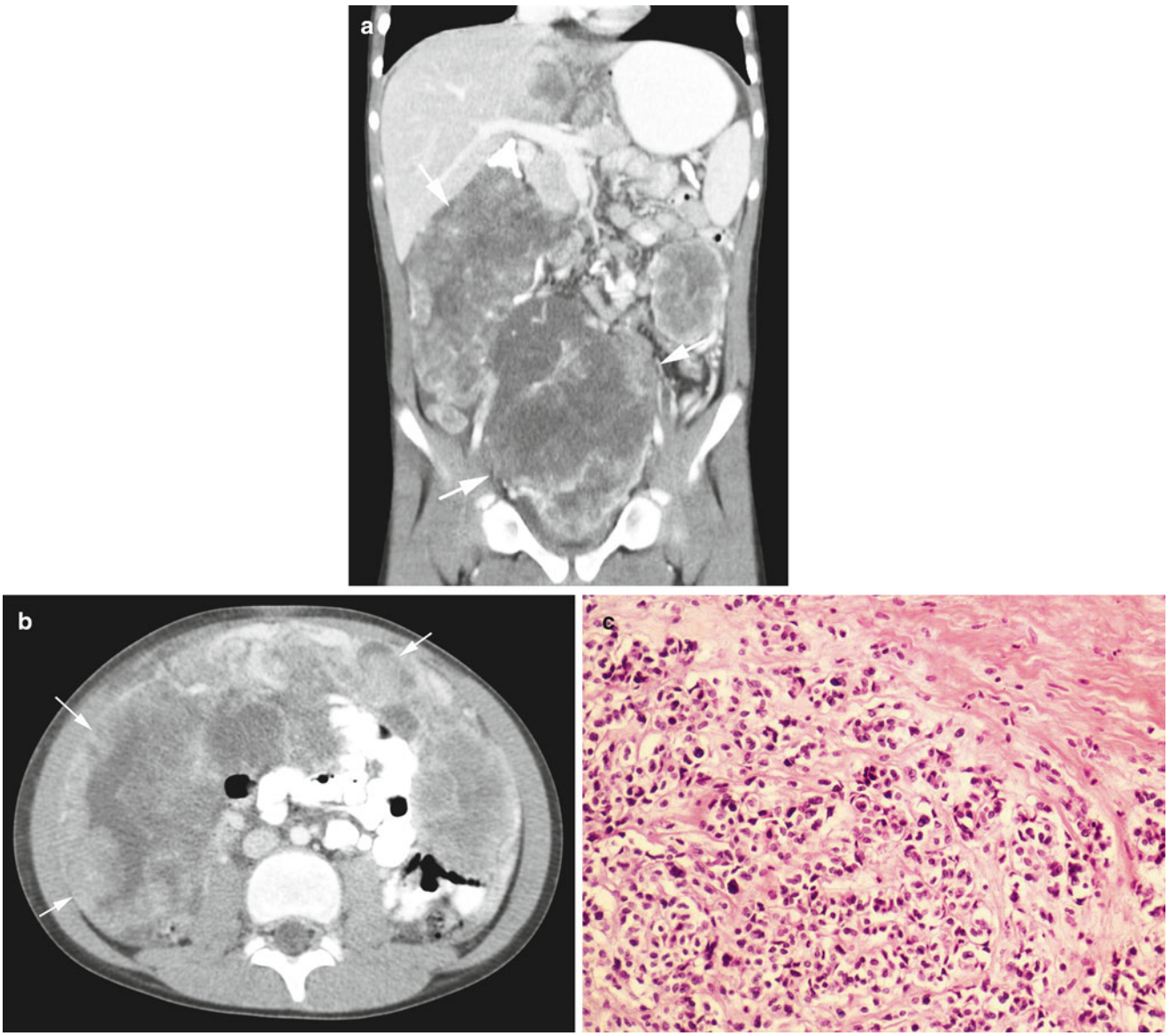

Fig. 3.23 Desmoplastic small round cell tumor. An 11-year-old boy presented with abdominal pain and mass. (**a**) Reconstructed coronal post-contrast CT image shows large, lobulated and partially necrotic peritoneal and pelvic masses (*arrows*). (**b**) Axial post-contrast CT image shows omental caking (*arrows*) typical of this tumor. (**c**) Variably sized nests of primitive round cells are embedded within a collagenous stroma in this intra-abdominal neoplasm. The lesion was positive for EMA, cytokeratin, S100, NSE, vimentin, and desmin (not shown)

be large, often 10 cm or larger at the time of diagnosis (Fig. 3.23a, b). Tumor masses displace adjacent structures but may cause bowel and ureteral obstruction. Masses are usually heterogeneous on CT and often contain central hypodense areas reflecting hemorrhage or necrosis. Tumors may contain punctuate calcification. Associated malignant ascites is a common finding [295, 296].

On MRI, DSRCTs demonstrate a heterogeneous signal, predominantly hypointense on T1W images and hyperintense on T2W sequences, with inhomogeneous enhancement after administration of contrast material. In one report, tumors contained areas that were hypointense on T2W images and enhanced mildly after contrast administration. These areas were felt to represent densely desmoplastic tissue. Also noted was the presence of fluid-fluid levels on T2W images and hyperintense foci on T1W images due to intratumoral hemorrhage [296]. Lymphatic and hematogenous (lung, liver, bone) metastasis occurs in about 50 % of patients at presentation, and careful attention should be paid to the bones, solid organs, and nodal basins for evidence of metastatic disease [295, 296]. A preliminary report of the value of FDG PET-CT found that DSRCTs are FDG avid, and this modality can reveal occult sites of disease not detected by conventional imaging [296].

Molecular Genetics

DSRCT contains a reciprocal translocation, the t(11;22)(p13;q12), which produces an *EWS-WT1* fusion [297]. The resultant protein transactivates the zinc finger region of WT1 and thus dysregulates DNA transcription.

Gross and Microscopic Features

DSRCT produces firm, multinodular masses with a grey-tan, solid cut surface, usually with attached mesentery or omentum.

Histologically, a dense collagenous stroma contains variably sized and contoured nests of cohesive small round cells (Fig. 3.23c), which sometimes occur in nests or sheets. The tumor cells generally contain round hyperchromatic nuclei, inconspicuous nucleoli, and modest amounts of ill-defined cytoplasm. Some cells contain more abundant, epithelioid cytoplasm, sometime producing rhabdoid cells. Occasional tubules, glands, and rosettes may be found [298]. Central geographic necrosis commonly occurs.

If one uses the *WT1-EWS* as a diagnostic standard, then a wider range of unexpected findings emerge including variations in cellularity, architecture, and immunoreactivity. About one-third of cases show unexpected findings, such as spindle cells, a lack of significant desmoplasia, or a zellballen or carcinoid-like appearance [299, 300].

Immunohistochemistry and Other Special Stains

Polyphenotypia, with expression of epithelial, neural, and mesenchymal markers, characterizes DSRCT [294]. These markers include cytokeratin and EMA (epithelium), neuron-specific enolase and CD57 (nerve), and desmin and vimentin (mesenchyme). Although negative in some cases, desmin stains characteristically produce a globoid or dot-like pattern of staining. Other variably positive markers include CD99, NB84, synaptophysin, CD15, actin, myoglobin, and chromogranin [293, 300]. WT1 stains are positive, if the antibody is directed against the carboxyl portion of the fusion protein [293]. INI1 stains show nuclear staining, differentiating DSRCT from rhabdoid tumor and epithelioid sarcoma.

Molecular Diagnostic Features and Cytogenetics

The t(11;22)(p13;q12) may be demonstrated by routine karyotype [301], and the *EWS-WT1* fusion can be shown by RT-PCR or FISH [293].

Prognostic Features

DSRCT carries a dismal prognosis, with survival rates of 30 % at 5 years, persistent disease after therapy, and widespread abdominal seeding similar to ovarian carcinoma [294]. However, recent reports suggest a better outcome with multimodality therapy, dependent upon neoadjuvant chemotherapy, complete surgical resection (including implants), and judicious adjuvant radiation [302].

Undifferentiated Sarcomas

Definition: The term "undifferentiated sarcoma" currently encompasses a wide array of neoplasms with considerable histological and molecular heterogeneity. It is primarily based on absence of cytological differentiation, indefinite nature of immunophenotypic features, and lack of a defining genetic aberration such as a well-characterized gene fusion or deletion. The lesion should have definite features of malignancy, such as hypercellularity, mitotic activity (with atypical figures), nuclear pleomorphism, and geographic necrosis.

Clinical Features and Epidemiology

Because of the lack of clear cut clinicopathological definition of undifferentiated sarcoma, characterization of clinical features becomes difficult. In a review of 34 undifferentiated sarcomas that were treated on IRSG protocols [303], ages ranged from 0 to 20 years, with a mean of 9 years. There was a slight male predominance, and most occurred in the extremities. The remainder arose in a variety of axial soft tissue and visceral locations. Most measured more than 5 cm and were either Group 3 or Group 4 (see Table 3.9). Undifferentiated sarcomas comprised less than 10 % of all IRSG cases.

Imaging Features

The imaging features of undifferentiated sarcomas have not been described.

Molecular Genetics

By definition, undifferentiated sarcomas should have no defining genetic features. However, *CIC-DUX4* fusions have been described in some [304].

Gross and Microscopic Features

For lack of a better method of delineation, undifferentiated sarcomas may be separated into spindle cell lesions, which coincide with pleomorphic sarcoma (formerly MFH; see above) and small cell lesions resembling Ewing sarcoma. Undifferentiated infantile sarcomas with myxoid features have been described as an entity by Alaggio et al. [29]. Unclassified sarcomas comprise a large portion of tumors in the current COG study of non-rhabdomyosarcomatous soft tissue sarcomas (NRSTS) [unpublished data]. Of these, many lack sufficient immunohistochemical and genetic data to exclude defined lesions, whereas others appear to be bona fide "undifferentiated sarcomas." Additional studies will soon be forthcoming on these enigmatic neoplasms. Recent publications suggest that *CIC-DUX4* fusion sarcomas have characteristic morphological features such as extensive necrosis, mild nuclear pleomorphism, coarse chromatin, prominent nucleoli, and foci of clear cells and myxoid matrix [305]. Lymph node metastasis, an unusual feature with Ewing sarcoma, also appears to be a distinctive feature of *CIC-DUX4* sarcomas [306].

Immunohistochemistry and Other Special Stains

By definition, lesions should not show features of a differentiating phenotype, i.e., myogenic, epithelial, or neural features. However, it is well accepted that certain markers are non specific, so they do not necessarily exclude this diagnosis. Examples include CD99, vimentin, neuron-specific enolase, CD56, CD68, and alpha-1-antitrysin. In particular, variable CD99 expression may occur with *CIC-DUX4* fusion tumors [307, 308], as well as occasional expression of cytokeratin and S100 [305, 306].

Molecular Diagnostic Features and Cytogenetics

By definition, no specific genetic features may be present, although undifferentiated sarcomas may show chromosomal deletions and additions. *CIC-DUX6* fusion has been reported in some [304] and may be detected by RT-PCR [306, 307].

Prognostic Features

In older IRSG studies that preceded the COG, undifferentiated sarcoma was an aggressive tumor that behaved more aggressively than ERMS and more like ARMS. Unfortunately, because they preceded modern genetic lesions, this group of neoplasms suffers from probable heterogeneity and likely includes lesions such as poorly differentiated synovial sarcoma. Prognosis was improved in a later review that included modern diagnostic techniques [303]. Current COG studies place undifferentiated sarcomas into a treatment category separate from rhabdomyosarcoma. Some data indicate that *CIC-DUX4* fusions impart a poor prognosis [307], but this has not been tested with COG data.

Acknowledgment The authors thank Ali Nael, M.D. for editorial review of this chapter.

References

1. Fletcher CD. The evolving classification of soft tissue tumours: an update based on the new WHO classification. Histopathology. 2006;48:3–12.
2. Parham D, Pao W, Pratt C, et al. A histological grading system of prognostic significance for childhood – adolescent soft tissue sarcomas other than rhabdomyosarcoma. Mod Pathol. 1990;3:78A.
3. Pratt CB, Maurer HM, Gieser P, et al. Treatment of unresectable or metastatic pediatric soft tissue sarcomas with surgery, irradiation, and chemotherapy: a Pediatric Oncology Group study. Med Pediatr Oncol. 1998;30:201–9.
4. Coindre JM, Trojani M, Contesso G, et al. Reproducibility of a histopathologic grading system for adult soft tissue sarcoma. Cancer. 1986;58:306–9.
5. Khoury JD, Coffin CM, Spunt SL, et al. Grading of nonrhabdomyosarcoma soft tissue sarcoma in children and adolescents: a comparison of parameters used for the Federation Nationale des Centers de Lutte Contre le Cancer and Pediatric Oncology Group Systems. Cancer. 2010;116:2266–74.
6. Navarro OM. Soft tissue masses in children. Radiol Clin North Am. 2011;49:1235–59, vi–vii.
7. Siegel MJ. Magnetic resonance imaging of musculoskeletal soft tissue masses. Radiol Clin North Am. 2001;39:701–20.
8. Stein-Wexler R. MR imaging of soft tissue masses in children. Magn Reson Imaging Clin N Am. 2009;17:489–507. vi.
9. Jadvar H, Connolly LP, Fahey FH, et al. PET and PET/CT in pediatric oncology. Semin Nucl Med. 2007;37:316–31.
10. Harms D. Soft tissue sarcomas in the Kiel Pediatric Tumor Registry. Curr Top Pathol. 1995;89:31–45.
11. Isaacs Jr H. Congenital and neonatal malignant tumors. A 28-year experience at Children's Hospital of Los Angeles. Am J Pediatr Hematol Oncol. 1987;9:121–9.
12. Kogon B, Shehata B, Katzenstein H, et al. Primary congenital infantile fibrosarcoma of the heart: the first confirmed case. Ann Thorac Surg. 2011;91:1276–80.
13. Vinnicombe SJ, Hall CM. Infantile fibrosarcoma: radiological and clinical features. Skeletal Radiol. 1994;23:337–41.
14. Canale S, Vanel D, Couanet D, et al. Infantile fibrosarcoma: magnetic resonance imaging findings in six cases. Eur J Radiol. 2009;72:30–7.
15. Fink AM, Stringer DA, Cairns RA, et al. Pediatric case of the day. Congenital fibrosarcoma (CFS). Radiographics. 1995;15:243–6.
16. Durin L, Jeanne-Pasquier C, Bailleul P, et al. Prenatal diagnosis of a fibrosarcoma of the thigh: a case report. Fetal Diagn Ther. 2006;21:481–4.
17. Eich GF, Hoeffel JC, Tschappeler H, et al. Fibrous tumours in children: imaging features of a heterogeneous group of disorders. Pediatr Radiol. 1998;28:500–9.
18. McCarville MB, Kaste SC, Pappo AS. Soft-tissue malignancies in infancy. AJR Am J Roentgenol. 1999;173:973–7.
19. Pousti TJ, Upton J, Loh M, et al. Congenital fibrosarcoma of the upper extremity. Plast Reconstr Surg. 1998;102:1158–62.
20. Knezevich SR, McFadden DE, Tao W, et al. A novel ETV6-NTRK3 gene fusion in congenital fibrosarcoma. Nat Genet. 1998;18:184–7.
21. Rubnitz JE, Downing JR, Pui CH, et al. TEL gene rearrangement in acute lymphoblastic leukemia: a new genetic marker with prognostic significance. J Clin Oncol. 1997;15:1150–7.
22. Yamashiro DJ, Nakagawara A, Ikegaki N, et al. Expression of TrkC in favorable human neuroblastomas. Oncogene. 1996;12:37–41.
23. Lannon CL, Sorensen PH. ETV6-NTRK3: a chimeric protein tyrosine kinase with transformation activity in multiple cell lineages. Semin Cancer Biol. 2005;15:215–23.
24. Lae M, Freneaux P, Sastre-Garau X, et al. Secretory breast carcinomas with ETV6-NTRK3 fusion gene belong to the basal-like carcinoma spectrum. Mod Pathol. 2009;22:291–8.
25. Alaggio R, Barisani D, Ninfo V, et al. Morphologic overlap between infantile myofibromatosis and infantile fibrosarcoma: a pitfall in diagnosis. Pediatr Dev Pathol. 2008;11:355–62.
26. Mandahl N, Heim S, Rydholm A, et al. Nonrandom numerical chromosome aberrations (+8, +11, +17, +20) in infantile fibrosarcoma. Cancer Genet Cytogenet. 1989;40:137–9.
27. Bourgeois JM, Knezevich SR, Mathers JA, et al. Molecular detection of the ETV6-NTRK3 gene fusion differentiates congenital fibrosarcoma from other childhood spindle cell tumors. Am J Surg Pathol. 2000;24:937–46.
28. Makretsov N, He M, Hayes M, et al. A fluorescence in situ hybridization study of ETV6-NTRK3 fusion gene in secretory breast carcinoma. Genes Chromosomes Cancer. 2004;40:152–7.
29. Alaggio R, Ninfo V, Rosolen A, et al. Primitive myxoid mesenchymal tumor of infancy: a clinicopathologic report of 6 cases. Am J Surg Pathol. 2006;30:388–94.
30. Nonaka D, Sun CC, Nonaka D, et al. Congenital fibrosarcoma with metastasis in a fetus. Pediatr Dev Pathol. 2004;7:187–91.

31. Russell H, Hicks MJ, Bertuch AA, et al. Infantile fibrosarcoma: clinical and histologic responses to cytotoxic chemotherapy. Pediatr Blood Cancer. 2009;53:23–7.
32. Meis-Kindblom JM, Kindblom LG, Enzinger FM. Sclerosing epithelioid fibrosarcoma. A variant of fibrosarcoma simulating carcinoma. Am J Surg Pathol. 1995;19:979–93.
33. Ossendorf C, Studer GM, Bode B, et al. Sclerosing epithelioid fibrosarcoma: case presentation and a systematic review. Clin Orthop Relat Res. 2008;466:1485–91.
34. Grunewald TG, Von LI, Weirich G, et al. Sclerosing epithelioid fibrosarcoma of the bone: a case report of high resistance to chemotherapy and a survey of the literature. Sarcoma. 2010;2010: 431627.
35. Rekhi B, Folpe AL, Deshmukh M, et al. Sclerosing epithelioid fibrosarcoma-a report of two cases with cytogenetic analysis of fus gene rearrangement by FISH technique. Pathol Oncol Res. 2011;17:145–8.
36. Guillou L, Benhattar J, Gengler C, et al. Translocation-positive low-grade fibromyxoid sarcoma: clinicopathologic and molecular analysis of a series expanding the morphologic spectrum and suggesting potential relationship to sclerosing epithelioid fibrosarcoma: a study from the French Sarcoma Group. Am J Surg Pathol. 2007;31:1387–402.
37. Donner LR, Clawson K, Dobin SM. Sclerosing epithelioid fibrosarcoma: a cytogenetic, immunohistochemical, and ultrastructural study of an unusual histological variant. Cancer Genet Cytogenet. 2000;119:127–31.
38. Mentzel T, Dry S, Katenkamp D, et al. Low-grade myofibroblastic sarcoma: analysis of 18 cases in the spectrum of myofibroblastic tumors. Am J Surg Pathol. 1998;22:1228–38.
39. Montgomery E, Goldblum JR, Fisher C. Myofibrosarcoma: a clinicopathologic study. Am J Surg Pathol. 2001;25:219–28.
40. Smith DM, Mahmoud HH, Jenkins JJ, et al. Myofibrosarcoma of the head and neck in children. Pediatr Pathol Lab Med. 1995; 112:275–81.
41. Fujiwara M, Yuba Y, Wada A, et al. Myofibrosarcoma of the nasal bone. Am J Otolaryngol. 2005;26:265–7.
42. Eyden B. The myofibroblast: an assessment of controversial issues and a definition useful in diagnosis and research. [Review] [97 refs]. Ultrastruct Pathol. 2001;25:39–50.
43. Fisher C. Myofibroblastic malignancies. [Review] [92 refs]. Adv Anat Pathol. 2004;11:190–201.
44. Montgomery E, Fisher C. Myofibroblastic differentiation in malignant fibrous histiocytoma (pleomorphic myofibrosarcoma): a clinicopathological study. Histopathology. 2001;38:499–509.
45. Hisaoka M, Wei-Qi S, Jian W, et al. Specific but variable expression of h-caldesmon in leiomyosarcomas: an immunohistochemical reassessment of a novel myogenic marker. Appl Immunohistochem Mol Morphol. 2001;9:302–8.
46. Cessna MH, Zhou H, Perkins SL, et al. Are myogenin and myoD1 expression specific for rhabdomyosarcoma? A study of 150 cases, with emphasis on spindle cell mimics. Am J Surg Pathol. 2001; 25:1150–7.
47. Cessna MH, Zhou H, Sanger WG, et al. Expression of ALK1 and p80 in inflammatory myofibroblastic tumor and its mesenchymal mimics: a study of 135 cases. Mod Pathol. 2002;15:931–8.
48. Bhattacharya B, Dilworth HP, Iacobuzio-Donahue C, et al. Nuclear beta-catenin expression distinguishes deep fibromatosis from other benign and malignant fibroblastic and myofibroblastic lesions. Am J Surg Pathol. 2005;29:653–9.
49. Vernon SE, Bejarano PA. Low-grade fibromyxoid sarcoma: a brief review. Arch Pathol Lab Med. 2006;130:1358–60.
50. Kaoutar Z, Benlemlih A, Taoufiq H, et al. Low-grade fibromyxoid sarcoma arising in the big toe. South Med J. 2011;104:241–3.
51. Bahrami A, Folpe AL. Adult-type fibrosarcoma: a reevaluation of 163 putative cases diagnosed at a single institution over a 48-year period. Am J Surg Pathol. 2010;34:1504–13.
52. Hwang S, Kelliher E, Hameed M. Imaging features of low-grade fibromyxoid sarcoma (Evans tumor). Skeletal Radiol. 2012;41: 1263–72.
53. Evans HL. Low-grade fibromyxoid sarcoma: a report of 12 cases. Am J Surg Pathol. 1993;17:595–600.
54. Lane KL, Shannon RJ, Weiss SW. Hyalinizing spindle cell tumor with giant rosettes: a distinctive tumor closely resembling low-grade fibromyxoid sarcoma. Am J Surg Pathol. 1997;21: 1481–8.
55. Doyle LA, Moller E, Dal Cin P, et al. MUC4 is a highly sensitive and specific marker for low-grade fibromyxoid sarcoma. Am J Surg Pathol. 2011;35:733–41.
56. Moller E, Hornick JL, Magnusson L, et al. FUS-CREB3L2/L1-positive sarcomas show a specific gene expression profile with upregulation of CD24 and FOXL1. Clin Cancer Res. 2011;17: 2646–56.
57. Matsuyama A, Hisaoka M, Shimajiri S, et al. Molecular detection of FUS-CREB3L2 fusion transcripts in low-grade fibromyxoid sarcoma using formalin-fixed, paraffin-embedded tissue specimens. Am J Surg Pathol. 2006;30:1077–84.
58. Downs-Kelly E, Goldblum JR, Patel RM, et al. The utility of fluorescence in situ hybridization (FISH) in the diagnosis of myxoid soft tissue neoplasms. Am J Surg Pathol. 2008;32:8–13.
59. Patel RM, Downs-Kelly E, Dandekar MN, et al. FUS (16p11) gene rearrangement as detected by fluorescence in-situ hybridization in cutaneous low-grade fibromyxoid sarcoma: a potential diagnostic tool. Am J Dermatopathol. 2011;33:140–3.
60. Mertens F, Fletcher CD, Antonescu CR, et al. Clinicopathologic and molecular genetic characterization of low-grade fibromyxoid sarcoma, and cloning of a novel FUS/CREB3L1 fusion gene. Lab Invest. 2005;85:408–15.
61. Bisogno G, Sotti G, Nowicki Y, et al. Soft tissue sarcoma as a second malignant neoplasm in the pediatric age group. Cancer. 2004;100:1758–65.
62. Horenstein MG, Prieto VG, Nuckols JD, et al. Indeterminate fibrohistiocytic lesions of the skin: is there a spectrum between dermatofibroma and dermatofibrosarcoma protuberans? Am J Surg Pathol. 2000;24:996–1003.
63. Rudolph P, Schubert B, Wacker HH, et al. Immunophenotyping of dermal spindle cell tumors: diagnostic value of monocyte marker Ki-M1p and histogenetic considerations. Am J Surg Pathol. 1997; 21:791–800.
64. Fletcher CDM. Pleomorphic malignant fibrous histiocytoma: fact or fiction? A critical reappraisal based on 159 tumors diagnosed as pleomorphic sarcoma. Am J Surg Pathol. 1992;16:213–28.
65. Brooks JJ. The significance of double phenotypic patterns and markers in human sarcomas: a new model of mesenchymal differentiation. Am J Pathol. 1986;125:113–23.
66. Garg MK, Yadav MK, Gupta S, et al. Dermatofibrosarcoma protuberans with contiguous infiltration of the underlying bone. Cancer Imaging. 2009;9:63–6.
67. Kransdorf MJ, Meis-Kindblom JM. Dermatofibrosarcoma protuberans: radiologic appearance. AJR Am J Roentgenol. 1994; 163:391–4.
68. Torreggiani WC, Al-Ismail K, Munk PL, et al. Dermatofibrosarcoma protuberans: MR imaging features. AJR Am J Roentgenol. 2002; 178:989–93.
69. Laffan EE, Ngan BY, Navarro OM. Pediatric soft-tissue tumors and pseudotumors: MR imaging features with pathologic correlation: part 2. Tumors of fibroblastic/myofibroblastic, so-called fibrohistiocytic, muscular, lymphomatous, neurogenic, hair matrix, and uncertain origin. Radiographics. 2009;29:e36.
70. Kim SD, Park JY, Choi WS, et al. Intracranial recurrence of the scalp dermatofibrosarcoma. Clin Neurol Neurosurg. 2007;109:172–5.
71. Abe T, Kamida T, Goda M, et al. Intracranial infiltration by recurrent scalp dermatofibrosarcoma protuberans. J Clin Neurosci. 2009;16:1358–60.

72. Morel M, Taieb S, Penel N, et al. Imaging of the most frequent superficial soft-tissue sarcomas. Skeletal Radiol. 2011;40:271–84.
73. Parajuly SS, Peng YL. Sonography of dermatofibrosarcoma protuberans in the skin over breast. J Med Ultrasound. 2010;18:130–5.
74. Liu SZ, Ho TL, Hsu SM, et al. Imaging of dermatofibrosarcoma protuberans of breast. Breast J. 2010;16:541–3.
75. Widmann G, Riedl A, Schoepf D, et al. State-of-the-art HR-US imaging findings of the most frequent musculoskeletal soft-tissue tumors. Skeletal Radiol. 2009;38:637–49.
76. Shin YR, Kim JY, Sung MS, et al. Sonographic findings of dermatofibrosarcoma protuberans with pathologic correlation. J Ultrasound Med. 2008;27:269–74.
77. Walker EA, Salesky JS, Fenton ME, et al. Magnetic resonance imaging of malignant soft tissue neoplasms in the adult. Radiol Clin North Am. 2011;49:1219–34, vi.
78. Riggs K, McGuigan KL, Morrison WB, et al. Role of magnetic resonance imaging in perioperative assessment of dermatofibrosarcoma protuberans. Dermatol Surg. 2009;35:2036–41.
79. Thornton SL, Reid J, Papay FA, et al. Childhood dermatofibrosarcoma protuberans: role of preoperative imaging. J Am Acad Dermatol. 2005;53:76–83.
80. Serra-Guillen C, Sanmartin O, Llombart B, et al. Correlation between preoperative magnetic resonance imaging and surgical margins with modified Mohs for dermatofibrosarcoma protuberans. Dermatol Surg. 2011;37:1638–45.
81. Djilas-Ivanovic D, Prvulovic N, Bogdanovic-Stojanovic D, et al. Dermatofibrosarcoma protuberans of the breast: mammographic, ultrasound, MRI and MRS features. Arch Gynecol Obstet. 2009; 280:827–30.
82. Basu S, Baghel NS. Recurrence of dermatofibrosarcoma protuberans in post-surgical scar detected by 18F-FDG-PET imaging. Hell J Nucl Med. 2009;12:68.
83. Maire G, Martin L, Michalak-Provost S, et al. Fusion of COL1A1 exon 29 with PDGFB exon 2 in a der(22)t(17;22) in a pediatric giant cell fibroblastoma with a pigmented Bednar tumor component. Evidence for age-related chromosomal pattern in dermatofibrosarcoma protuberans and related tumors. Cancer Genet Cytogenet. 2002;134:156–61.
84. Orndal C, Mandahl N, Rydholm A, et al. Supernumerary ring chromosomes in five bone and soft tissue tumors of low or borderline malignancy. Cancer Genet Cytogenet. 1992;60:170–5.
85. Pedeutour F, Simon MP, Minoletti F, et al. Translocation, t(17;22)(q22;q13), in dermatofibrosarcoma protuberans: a new tumor-associated chromosome rearrangement. Cytogenet Cell Genet. 1996;72:171–4.
86. Terrier-Lacombe MJ, Guillou L, Maire G, et al. Dermatofibrosarcoma protuberans, giant cell fibroblastoma, and hybrid lesions in children: clinicopathologic comparative analysis of 28 cases with molecular data – a study from the French Federation of Cancer Centers Sarcoma Group. Am J Surg Pathol. 2003;27:27–39.
87. Sigel JE, Bergfeld WF, Goldblum JR. A morphologic study of dermatofibrosarcoma protuberans: expansion of a histologic profile. J Cutan Pathol. 2000;27:159–63.
88. Tardio JC, Tardio JC. CD34-reactive tumors of the skin. An updated review of an ever-growing list of lesions. [Review] [171 refs]. J Cutan Pathol. 2009;36:89–102.
89. Haycox CL, Odland PB, Olbricht SM, et al. Immunohistochemical characterization of dermatofibrosarcoma protuberans with practical applications for diagnosis and treatment. [see comments.]. [Review] [38 refs]. J Am Acad Dermatol. 1997;37:438–44.
90. Goldblum JR, Reith JD, Weiss SW. Sarcomas arising in dermatofibrosarcoma protuberans: a reappraisal of biologic behavior in eighteen cases treated by wide local excision with extended clinical follow up. Am J Surg Pathol. 2000;24:1125–30.
91. Sachdev R, Sundram U. Expression of CD163 in dermatofibroma, cellular fibrous histiocytoma, and dermatofibrosarcoma protuberans: comparison with CD68, CD34, and Factor XIIIa. J Cutan Pathol. 2006;33:353–60.
92. Sozzi G, Minoletti F, Miozzo M, et al. Relevance of cytogenetic and fluorescent in situ hybridization analyses in the clinical assessment of soft tissue sarcoma. Hum Pathol. 1997;28:134–42.
93. Connelly JH, Evans HL. Dermatofibrosarcoma protuberans: a clinicopathologic review with emphasis on fibrosarcomatous areas. Am J Surg Pathol. 1992;16:921–5.
94. Marks LB, Suit HD, Rosenberg AE, et al. Dermatofibrosarcoma protuberans treated with radiation therapy. Int J Radiat Oncol Biol Phys. 1989;17:379–84.
95. Abrams TA, Schuetze SM, Abrams TA, et al. Targeted therapy for dermatofibrosarcoma protuberans. [Review] [39 refs]. Curr Oncol Rep. 2006;8:291–6.
96. Enzinger FM. Angiomatoid malignant fibrous histiocytoma: a distinct fibrohistiocytic tumor of children and young adults simulating a vascular neoplasm. Cancer. 1979;44:2147–57.
97. Costa MJ, Weiss SW. Angiomatoid malignant fibrous histiocytoma. A follow-up study of 108 cases with evaluation of possible histologic predictors of outcome. Am J Surg Pathol. 1990;14: 1126–32.
98. Thway K. Angiomatoid fibrous histiocytoma: a review with recent genetic findings. Arch Pathol Lab Med. 2008;132:273–7.
99. Hothi D, Brogan PA, Davis E, et al. Polyarteritis nodosa as a presenting feature of angiomatoid fibrous histiocytoma. Rheumatology (Oxford). 2004;43:245–6.
100. Fanburg-Smith JC, Miettinen M. Angiomatoid "malignant" fibrous histiocytoma: a clinicopathologic study of 158 cases and further exploration of the myoid phenotype. Hum Pathol. 1999;30: 1336–43.
101. Ajlan AM, Sayegh K, Powell T, et al. Angiomatoid fibrous histiocytoma: magnetic resonance imaging appearance in 2 cases. J Comput Assist Tomogr. 2010;34:791–4.
102. Petrey WB, LeGallo RD, Fox MG, et al. Imaging characteristics of angiomatoid fibrous histiocytoma of bone. Skeletal Radiol. 2011;40:233–7.
103. Raddaoui E, Donner LR, Panagopoulos I. Fusion of the FUS and ATF1 genes in a large, deep-seated angiomatoid fibrous histiocytoma. Diagn Mol Pathol. 2002;11:157–62.
104. Hallor KH, Mertens F, Jin Y, et al. Fusion of the EWSR1 and ATF1 genes without expression of the MITF-M transcript in angiomatoid fibrous histiocytoma. Genes Chromosomes Cancer. 2005;44:97–102.
105. Rossi S, Szuhai K, Ijszenga M, et al. EWSR1-CREB1 and EWSR1-ATF1 fusion genes in angiomatoid fibrous histiocytoma. Clin Cancer Res. 2007;13:7322–8.
106. Weinreb I, Rubin BP, Goldblum JR. Pleomorphic angiomatoid fibrous histiocytoma: a case confirmed by fluorescence in situ hybridization analysis for EWSR1 rearrangement. J Cutan Pathol. 2008;35:855–60.
107. Fletcher CDM. Angiomatoid "malignant fibrous histiocytoma": an immunohistochemical study indicative of myoid differentiation. Hum Pathol. 1991;22:563–8.
108. Tanas MR, Rubin BP, Montgomery EA, et al. Utility of FISH in the diagnosis of angiomatoid fibrous histiocytoma: a series of 18 cases. Mod Pathol. 2010;23:93–7.
109. Corpron CA, Black CT, Raney RB, et al. Malignant fibrous histiocytoma in children. J Pediatr Surg. 1996;31:1080–3.
110. Cole CH, Magee JF, Gianoulis M, et al. Malignant fibrous histiocytoma in childhood. Cancer. 1993;71:4077–83.
111. Chow LT, Allen PW, Kumta SM, et al. Angiomatoid malignant fibrous histiocytoma: report of an unusual case with highly aggressive clinical course. J Foot Ankle Surg. 1998;37:235–8.

112. Enzinger FM, Zhang RY. Plexiform fibrohistiocytic tumor presenting in children and young adults. An analysis of 65 cases. Am J Surg Pathol. 1988;12:818–26.
113. Jafarian F, McCuaig C, Kokta V, et al. Plexiform fibrohistiocytic tumor in three children. Pediatr Dermatol. 2006;23:7–12.
114. Leclerc-Mercier S, Pedeutour F, Fabas T, et al. Plexiform fibrohistiocytic tumor with molecular and cytogenetic analysis. Pediatr Dermatol. 2011;28:26–9.
115. Segura LG, Harris J, Wang B, et al. Plexiform fibrohistiocytic tumor: a rare low-grade malignancy of children and young adults. Arch Otolaryngol Head Neck Surg. 2002;128:966–70.
116. Taher A, Pushpanathan C. Plexiform fibrohistiocytic tumor: a brief review. Arch Pathol Lab Med. 2007;131:1135–8.
117. Zelger B, Weinlich G, Steiner H, et al. Dermal and subcutaneous variants of plexiform fibrohistiocytic tumor. Am J Surg Pathol. 1997;21:235–41.
118. Remstein ED, Arndt CA, Nascimento AG. Plexiform fibrohistiocytic tumor: clinicopathologic analysis of 22 cases. Am J Surg Pathol. 1999;23:662–70.
119. Jacobson-Dunlop E, White Jr CR, Mansoor A. Features of plexiform fibrohistiocytic tumor in skin punch biopsies: a retrospective study of 6 cases. Am J Dermatopathol. 2011;33:551–6.
120. Angervall L, Kindblom LG, Lindholm K, et al. Plexiform fibrohistiocytic tumor. Report of a case involving preoperative aspiration cytology and immunohistochemical and ultrastructural analysis of surgical specimens. Pathol Res Pract. 1992;188:350–6. discussion 356-359.
121. Alaggio R, Collini P, Randall RL, et al. Undifferentiated high-grade pleomorphic sarcomas in children: a clinicopathologic study of 10 cases and review of literature. Pediatr Dev Pathol. 2010;13:209–17.
122. Stein-Wexler R. Pediatric soft tissue sarcomas. Semin Ultrasound CT MR. 2011;32:470–88.
123. Colleran G, Madewell J, Foran P, et al. Imaging of soft tissue and osseous sarcomas of the extremities. Semin Ultrasound CT MR. 2011;32:442–55.
124. Palmer JL, Masui S, Pritchard S, et al. Cytogenetic and molecular genetic analysis of a pediatric pleomorphic sarcoma reveals similarities to adult malignant fibrous histiocytoma. Cancer Genet Cytogenet. 1997;95:141–7.
125. Alaggio R, Coffin CM, Weiss SW, et al. Liposarcomas in young patients: a study of 82 cases occurring in patients younger than 22 years of age. Am J Surg Pathol. 2009;33:645–58.
126. Coindre JM, Hostein I, Maire G, et al. Inflammatory malignant fibrous histiocytomas and dedifferentiated liposarcomas: histological review, genomic profile, and MDM2 and CDK4 status favour a single entity. J Pathol. 2004;203:822–30.
127. Sarkar M, Mulliken JB, Kozakewich HP, et al. Thrombocytopenic coagulopathy (Kasabach-Merritt phenomenon) is associated with Kaposiform hemangioendothelioma and not with common infantile hemangioma. Plast Reconstr Surg. 1997;100:1377–86.
128. Hsiao CC, Chen CC, Ko SF, et al. A case of axillary kaposiform hemangioendothelioma resembles a soft tissue sarcoma. J Pediatr Hematol Oncol. 2005;27:596–8.
129. Lalaji TA, Haller JO, Burgess RJ. A case of head and neck kaposiform hemangioendothelioma simulating a malignancy on imaging. Pediatr Radiol. 2001;31:876–8.
130. Zhu Y, Qiu G, Zhao H, et al. Kaposiform hemangioendothelioma with adolescent thoracic scoliosis: a case report and review of literature. Eur Spine J. 2011;20 Suppl 2:S309–13.
131. DeFatta RJ, Verret DJ, Adelson RT, et al. Kaposiform hemangioendothelioma: case report and literature review. Laryngoscope. 2005;115:1789–92.
132. Mukerji SS, Osborn AJ, Roberts J, et al. Kaposiform hemangioendothelioma (with Kasabach Merritt syndrome) of the head and neck: case report and review of the literature. Int J Pediatr Otorhinolaryngol. 2009;73:1474–6.
133. Dadras SS, Skrzypek A, Nguyen L, et al. Prox-1 promotes invasion of kaposiform hemangioendotheliomas. J Invest Dermatol. 2008;128:2798–806.
134. Le Huu AR, Jokinen CH, Rubin BP, et al. Expression of prox1, lymphatic endothelial nuclear transcription factor, in Kaposiform hemangioendothelioma and tufted angioma. Am J Surg Pathol. 2010;34:1563–73.
135. North PE. Pediatric vascular tumors and malformations. Surg Pathol Clin. 2010;2010:455–95.
136. Bien E, Stachowicz-Stencel T, Balcerska A, et al. Angiosarcoma in children – still uncontrollable oncological problem. The report of the Polish Paediatric Rare Tumours Study. Eur J Cancer Care (Engl). 2009;18:411–20.
137. Deyrup AT, Miettinen M, North PE, et al. Angiosarcomas arising in the viscera and soft tissue of children and young adults: a clinicopathologic study of 15 cases. Am J Surg Pathol. 2009;33:264–9.
138. Deyrup AT, Miettinen M, North PE, et al. Pediatric cutaneous angiosarcomas: a clinicopathologic study of 10 cases. Am J Surg Pathol. 2011;35:70–5.
139. Thompson WM, Levy AD, Aguilera NS, et al. Angiosarcoma of the spleen: imaging characteristics in 12 patients. Radiology. 2005;235:106–15.
140. Qiu LL, Yu RS, Chen Y, et al. Sarcomas of abdominal organs: computed tomography and magnetic resonance imaging findings. Semin Ultrasound CT MR. 2011;32:405–21.
141. Abbott RM, Levy AD, Aguilera NS, et al. From the archives of the AFIP: primary vascular neoplasms of the spleen: radiologic-pathologic correlation. Radiographics. 2004;24:1137–63.
142. Lalwani N, Prasad SR, Vikram R, et al. Pediatric and adult primary sarcomas of the kidney: a cross-sectional imaging review. Acta Radiol. 2011;52:448–57.
143. Chung EM, Lattin Jr GE, Cube R, et al. From the archives of the AFIP: pediatric liver masses: radiologic-pathologic correlation. Part 2. Malignant tumors. Radiographics. 2011;31:483–507.
144. Kaneko K, Onitsuka H, Murakami J, et al. MRI of primary spleen angiosarcoma with iron accumulation. J Comput Assist Tomogr. 1992;16:298–300.
145. Van Dyck P, Vanhoenacker FM, Vogel J, et al. Prevalence, extension and characteristics of fluid-fluid levels in bone and soft tissue tumors. Eur Radiol. 2006;16:2644–51.
146. Benz MR, Dry SM, Eilber FC, et al. Correlation between glycolytic phenotype and tumor grade in soft-tissue sarcomas by 18F-FDG PET. J Nucl Med. 2010;51:1174–81.
147. Vasanawala MS, Wang Y, Quon A, et al. F-18 fluorodeoxyglucose PET/CT as an imaging tool for staging and restaging cutaneous angiosarcoma of the scalp. Clin Nucl Med. 2006;31:534–7.
148. Freudenberg LS, Rosenbaum SJ, Schulte-Herbruggen J, et al. Diagnosis of a cardiac angiosarcoma by fluorine-18 fluordeoxyglucose positron emission tomography. Eur Radiol. 2002;12 Suppl 3:S158–61.
149. Shimada K, Nakamoto Y, Isoda H, et al. FDG PET for giant cavernous hemangioma: important clue to differentiate from a malignant vascular tumor in the liver. Clin Nucl Med. 2010;35:924–6.
150. Drevelegas A, Pilavaki M, Chourmouzi D. Lipomatous tumors of soft tissue: MR appearance with histological correlation. Eur J Radiol. 2004;50:257–67.
151. Sheah K, Ouellette HA, Torriani M, et al. Metastatic myxoid liposarcomas: imaging and histopathologic findings. Skeletal Radiol. 2008;37:251–8.
152. Murphey MD, Arcara LK, Fanburg-Smith J. From the archives of the AFIP: imaging of musculoskeletal liposarcoma with radiologic-pathologic correlation. Radiographics. 2005;25:1371–95.

153. Song T, Shen J, Liang BL, et al. Retroperitoneal liposarcoma: MR characteristics and pathological correlative analysis. Abdom Imaging. 2007;32:668–74.
154. van Vliet M, Kliffen M, Krestin GP, et al. Soft tissue sarcomas at a glance: clinical, histological, and MR imaging features of malignant extremity soft tissue tumors. Eur Radiol. 2009;19:1499–511.
155. Jelinek JS, Kransdorf MJ, Shmookler BM, et al. Liposarcoma of the extremities: MR and CT findings in the histologic subtypes. Radiology. 1993;186:455–9.
156. Sreekantaiah C, Karakousis CP, Leong SP, et al. Cytogenetic findings in liposarcoma correlate with histopathologic subtypes. Cancer. 1992;69:2484–95.
157. Kuroda M, Ishida T, Takanashi M, et al. Oncogenic transformation and inhibition of adipocytic conversion of preadipocytes by TLS/FUS-CHOP type II chimeric protein. Am J Pathol. 1997;151:735–44.
158. Panagopoulos I, Hoglund M, Mertens F, et al. Fusion of the EWS and CHOP genes in myxoid liposarcoma. Oncogene. 1996;12:489–94.
159. Bode-Lesniewska B, Frigerio S, Exner U, et al. Relevance of translocation type in myxoid liposarcoma and identification of a novel EWSR1-DDIT3 fusion. Genes Chromosomes Cancer. 2007;46:961–71.
160. Romeo S, Dei Tos AP. Soft tissue tumors associated with EWSR1 translocation. Virchows Arch. 2010;456:219–34.
161. Debelenko LV, Perez-Atayde AR, Dubois SG, et al. p53+/mdm2-atypical lipomatous tumor/well-differentiated liposarcoma in young children: an early expression of Li-Fraumeni syndrome. Pediatr Dev Pathol. 2010;13:218–24.
162. Schwarzbach MH, Dimitrakopoulou-Strauss A, Mechtersheimer G, et al. Assessment of soft tissue lesions suspicious for liposarcoma by F18-deoxyglucose (FDG) positron emission tomography (PET). Anticancer Res. 2001;21:3609–14.
163. Sirvent N, Coindre JM, Maire G, et al. Detection of MDM2-CDK4 amplification by fluorescence in situ hybridization in 200 paraffin-embedded tumor samples: utility in diagnosing adipocytic lesions and comparison with immunohistochemistry and real-time PCR. Am J Surg Pathol. 2007;31:1476–89.
164. Taubert H, Wurl P, Meye A, et al. Molecular and immunohistochemical p53 status in liposarcoma and malignant fibrous histiocytoma: identification of seven new mutations for soft tissue sarcomas. Cancer. 1995;76:1187–96.
165. Weiss SW, Rao VK. Well-differentiated liposarcoma (atypical lipoma) of deep soft tissue of the extremities, retroperitoneum, and miscellaneous sites. A follow-up study of 92 cases with analysis of the incidence of "dedifferentiation". Am J Surg Pathol. 1992;16:1051–8.
166. Hisaoka M, Morimitsu Y, Hashimoto H, et al. Retroperitoneal liposarcoma with combined well-differentiated and myxoid malignant fibrous histiocytoma-like myxoid areas. Am J Surg Pathol. 1999;23:1480–92.
167. Leach FS, Tokino T, Meltzer P, et al. p53 Mutation and MDM2 amplification in human soft tissue sarcomas. Cancer Res. 1993;53:2231–4.
168. Newton Jr WA, Gehan EA, Webber BL, et al. Classification of rhabdomyosarcomas and related sarcomas. Pathologic aspects and proposal for a new classification – an Intergroup Rhabdomyosarcoma Study. Cancer. 1995;76:1073–85.
169. Davicioni E, Anderson MJ, Finckenstein FG, et al. Molecular classification of rhabdomyosarcoma–genotypic and phenotypic determinants of diagnosis: a report from the Children's Oncology Group. Am J Pathol. 2009;174:550–64.
170. Scrable H, Witte D, Shimada H, et al. Molecular differential pathology of rhabdomyosarcoma. Genes Chromosomes Cancer. 1989;1:23–35.
171. Xia SJ, Pressey JG, Barr FG. Molecular pathogenesis of rhabdomyosarcoma. Cancer Biol Ther. 2002;1:97–104.
172. Anderson J, Gordon A, Pritchard-Jones K, et al. Genes, chromosomes, and rhabdomyosarcoma. Genes Chromosomes Cancer. 1999;26:275–85.
173. Morotti RA, Nicol KK, Parham DM, et al. An immunohistochemical algorithm to facilitate diagnosis and subtyping of rhabdomyosarcoma: the Children's Oncology Group experience. Am J Surg Pathol. 2006;30:962–8.
174. Folpe AL. MyoD1 and myogenin expression in human neoplasia: a review and update. Adv Anat Pathol. 2002;9:198–203.
175. Ebauer M, Wachtel M, Niggli FK, et al. Comparative expression profiling identifies an in vivo target gene signature with TFAP2B as a mediator of the survival function of PAX3/FKHR. Oncogene. 2007;26:7267–81.
176. Bridge JA, Liu J, Weibolt V, et al. Novel genomic imbalances in embryonal rhabdomyosarcoma revealed by comparative genomic hybridization and fluorescence in situ hybridization: an Intergroup Rhabdomyosarcoma Study. Genes Chromosomes Cancer. 2000;27: 337–44.
177. Raney RB, Walterhouse DO, Meza JL, et al. Results of the Intergroup Rhabdomyosarcoma Study Group D9602 protocol, using vincristine and dactinomycin with or without cyclophosphamide and radiation therapy, for newly diagnosed patients with low-risk embryonal rhabdomyosarcoma: a report from the Soft Tissue Sarcoma Committee of the Children's Oncology Group. J Clin Oncol. 2011;29:1312–8.
178. Joshi D, Anderson JR, Paidas C, et al. Age is an independent prognostic factor in rhabdomyosarcoma: a report from the Soft Tissue Sarcoma Committee of the Children's Oncology Group. Pediatr Blood Cancer. 2004;42:64–73.
179. Arndt CA, Stoner JA, Hawkins DS, et al. Vincristine, actinomycin, and cyclophosphamide compared with vincristine, actinomycin, and cyclophosphamide alternating with vincristine, topotecan, and cyclophosphamide for intermediate-risk rhabdomyosarcoma: Children's Oncology Group study D9803. J Clin Oncol. 2009;27:5182–8.
180. Lager JJ, Lyden ER, Anderson JR, et al. Pooled analysis of phase II window studies in children with contemporary high-risk metastatic rhabdomyosarcoma: a report from the Soft Tissue Sarcoma Committee of the Children's Oncology Group. J Clin Oncol. 2006;24:3415–22.
181. Wexler LH, Ladanyi M. Diagnosing alveolar rhabdomyosarcoma: morphology must be coupled with fusion confirmation. J Clin Oncol. 2010;28:2126–8.
182. Parham DM, Barr FG. Classification of rhabdomyosarcoma and its molecular basis. Adv Anat Pathol. 2013;20:387–97.
183. Riopelle JL, Theriault JP. An unknown type of soft part sarcoma: alveolar rhabdomyosarcoma. Ann Anat Pathol (Paris). 1956;1: 88–111.
184. Tsokos M, Webber BL, Parham DM, et al. Rhabdomyosarcoma. A new classification scheme related to prognosis. Arch Pathol Lab Med. 1992;116:847–55.
185. Pinto A, Tallini G, Novak RW, et al. Undifferentiated rhabdomyosarcoma with lymphoid phenotype expression. Med Pediatr Oncol. 1997;28:165–70.
186. Gonzalez-Crussi F, Black-Schaffer S. Rhabdomyosarcoma of infancy and childhood. Problems of morphologic classification. Am J Surg Pathol. 1979;3:157–71.
187. Harms D. Alveolar rhabdomyosarcoma: a prognostically unfavorable rhabdomyosarcoma type and its necessary distinction from embryonal rhabdomyosarcoma. Curr Top Pathol. 1995;89:273–96.
188. Wang NP, Marx J, McNutt MA, et al. Expression of myogenic regulatory proteins (myogenin and MyoD1) in small blue round cell tumors of childhood. Am J Pathol. 1995;147:1799–810.
189. Wachtel M, Runge T, Leuschner I, et al. Subtype and prognostic classification of rhabdomyosarcoma by immunohistochemistry. J Clin Oncol. 2006;24:816–22.

190. Barr FG, Smith LM, Lynch JC, et al. Examination of gene fusion status in archival samples of alveolar rhabdomyosarcoma entered on the Intergroup Rhabdomyosarcoma Study-III trial: a report from the Children's Oncology Group. J Mol Diagn. 2006;8:202–8.
191. Tobar A, Avigad S, Zoldan M, et al. Clinical relevance of molecular diagnosis in childhood rhabdomyosarcoma. Diagn Mol Pathol. 2000;9:9–13.
192. Nishio J, Althof PA, Bailey JM, et al. Use of a novel FISH assay on paraffin-embedded tissues as an adjunct to diagnosis of alveolar rhabdomyosarcoma. Lab Invest. 2006;86:547–56.
193. Shapiro DN, Parham DM, Douglass EC, et al. Relationship of tumor-cell ploidy to histologic subtype and treatment outcome in children and adolescents with unresectable rhabdomyosarcoma. J Clin Oncol. 1991;9:159–66.
194. Smith LM, Anderson JR, Qualman SJ, et al. Which patients with microscopic disease and rhabdomyosarcoma experience relapse after therapy? A report from the soft tissue sarcoma committee of the children's oncology group. J Clin Oncol. 2001;19:4058–64.
195. Douglass EC, Shapiro DN, Valentine M, et al. Alveolar rhabdomyosarcoma with the t(2;13): cytogenetic findings and clinicopathologic correlations. Med Pediatr Oncol. 1993;21:83–7.
196. Lae M, Ahn EH, Mercado GE, et al. Global gene expression profiling of PAX-FKHR fusion-positive alveolar and PAX-FKHR fusion-negative embryonal rhabdomyosarcomas. J Pathol. 2007;212:143–51.
197. Williamson D, Missiaglia E, de Reynies A, et al. Fusion gene-negative alveolar rhabdomyosarcoma is clinically and molecularly indistinguishable from embryonal rhabdomyosarcoma. J Clin Oncol. 2010;28:2151–8.
198. Sorensen PH, Lynch JC, Qualman SJ, et al. PAX3-FKHR and PAX7-FKHR gene fusions are prognostic indicators in alveolar rhabdomyosarcoma: a report from the children's oncology group. J Clin Oncol. 2002;20:2672–9.
199. de Saint Aubain Somerhausen N, Fletcher CD. Leiomyosarcoma of soft tissue in children: clinicopathologic analysis of 20 cases. Am J Surg Pathol. 1999;23:755–63.
200. Ferrari A, Bisogno G, Casanova M, et al. Childhood leiomyosarcoma: a report from the soft tissue sarcoma Italian Cooperative Group. Ann Oncol. 2001;12:1163–8.
201. Hwang ES, Gerald W, Wollner N, et al. Leiomyosarcoma in childhood and adolescence. Ann Surg Oncol. 1997;4:223–7.
202. Parham DM, Alaggio R, Coffin CM. Myogenic tumors in children and adolescents. Pediatr Dev Pathol. 2012;15:211–38.
203. Akwari OE, Dozois RR, Weiland LH, et al. Leiomyosarcoma of the small and large bowel. Cancer. 1978;42:1375–84.
204. McLeod AJ, Zornoza J, Shirkhoda A. Leiomyosarcoma: computed tomographic findings. Radiology. 1984;152:133–6.
205. Bush CH, Reith JD, Spanier SS. Mineralization in musculoskeletal leiomyosarcoma: radiologic-pathologic correlation. AJR Am J Roentgenol. 2003;180:109–13.
206. Hartman DS, Hayes WS, Choyke PL, et al. From the archives of the AFIP. Leiomyosarcoma of the retroperitoneum and inferior vena cava: radiologic-pathologic correlation. Radiographics. 1992;12:1203–20.
207. Megibow AJ, Balthazar EJ, Hulnick DH, et al. CT evaluation of gastrointestinal leiomyomas and leiomyosarcomas. AJR Am J Roentgenol. 1985;144:727–31.
208. Levy AD, Remotti HE, Thompson WM, et al. Gastrointestinal stromal tumors: radiologic features with pathologic correlation. Radiographics. 2003;23:283–304.
209. Sabah M, Cummins R, Leader M, et al. Leiomyosarcoma and malignant fibrous histiocytoma share similar allelic imbalance pattern at 9p. Virchows Arch. 2005;446:251–8.
210. Ragazzini P, Gamberi G, Pazzaglia L, et al. Amplification of CDK4, MDM2, SAS and GLI genes in leiomyosarcoma, alveolar and embryonal rhabdomyosarcoma. Histol Histopathol. 2004;19:401–11.
211. Seidel C, Bartel F, Rastetter M, et al. Alterations of cancer-related genes in soft tissue sarcomas: hypermethylation of RASSF1A is frequently detected in leiomyosarcoma and associated with poor prognosis in sarcoma. Int J Cancer. 2005;114:442–7.
212. Deyrup AT, Lee VK, Hill CE, et al. Epstein-Barr virus-associated smooth muscle tumors are distinctive mesenchymal tumors reflecting multiple infection events: a clinicopathologic and molecular analysis of 29 tumors from 19 patients. Am J Surg Pathol. 2006;30:75–82.
213. Parham DM, Reynolds AB, Webber BL. Use of monoclonal antibody 1H1, anticortactin, to distinguish normal and neoplastic smooth muscle cells: comparison with anti-alpha-smooth muscle actin and antimuscle-specific actin. Hum Pathol. 1995;26:776–83.
214. Schmidt D, Thum P, Harms D, et al. Synovial sarcoma in children and adolescents. A report from the Kiel Pediatric Tumor Registry. Cancer. 1991;67:1667–72.
215. Iyengar V, Lineberger AS, Kerman S, et al. Synovial sarcoma of the heart. Correlation with cytogenetic findings. Arch Pathol Lab Med. 1995;119:1080–2.
216. Zenmyo M, Komiya S, Hamada T, et al. Intraneural monophasic synovial sarcoma: a case report. Spine (Phila Pa 1976). 2001;26:310–3.
217. Chu PG, Benhattar J, Weiss LM, et al. Intraneural synovial sarcoma: two cases. Mod Pathol. 2004;17:258–63.
218. McCarville MB, Spunt SL, Skapek SX, et al. Synovial sarcoma in pediatric patients. AJR Am J Roentgenol. 2002;179:797–801.
219. Coffin C. Synovial-based tumors and synovial sarcoma. In: Coffin CMOSP, Dehner LP, editors. Pediatric soft tissue tumors: a clinical, pathological and therapeutic approach. Baltimore, MD: Williams and Wilkins; 1997. p. 295–310.
220. Jones BC, Sundaram M, Kransdorf MJ. Synovial sarcoma: MR imaging findings in 34 patients. AJR Am J Roentgenol. 1993;161:827–30.
221. Cadman NL, Soule EH, Kelly PJ. Synovial sarcoma; an analysis of 34 tumors. Cancer. 1965;18:613–27.
222. Morton MJ, Berquist TH, McLeod RA, et al. MR imaging of synovial sarcoma. AJR Am J Roentgenol. 1991;156:337–40.
223. Berquist TH, Ehman RL, King BF, et al. Value of MR imaging in differentiating benign from malignant soft-tissue masses: study of 95 lesions. AJR Am J Roentgenol. 1990;155:1251–5.
224. Folpe AL, Schmidt RA, Chapman D, et al. Poorly differentiated synovial sarcoma: immunohistochemical distinction from primitive neuroectodermal tumors and high-grade malignant peripheral nerve sheath tumors. Am J Surg Pathol. 1998;22:673–82.
225. Kosemehmetoglu K, Vrana JA, Folpe AL. TLE1 expression is not specific for synovial sarcoma: a whole section study of 163 soft tissue and bone neoplasms. Mod Pathol. 2009;22:872–8.
226. Fritsch MK, Bridge JA, Schuster AE, et al. Performance characteristics of a reverse transcriptase-polymerase chain reaction assay for the detection of tumor-specific fusion transcripts from archival tissue. Pediatr Dev Pathol. 2003;6:43–53.
227. Sun B, Sun Y, Wang J, et al. The diagnostic value of SYT-SSX detected by reverse transcriptase-polymerase chain reaction (RT-PCR) and fluorescence in situ hybridization (FISH) for synovial sarcoma: a review and prospective study of 255 cases. Cancer Sci. 2008;99:1355–61.
228. Oda Y, Hashimoto H, Tsuneyoshi M, et al. Survival in synovial sarcoma. A multivariate study of prognostic factors with special emphasis on the comparison between early death and long-term survival. Am J Surg Pathol. 1993;17:35–44.
229. Lieberman PH, Brennan MF, Kimmel M, et al. Alveolar soft-part sarcoma. A clinico-pathologic study of half a century. Cancer. 1989;63:1–13.

230. Pappo AS, Parham DM, Cain A, et al. Alveolar soft part sarcoma in children and adolescents: clinical features and outcome of 11 patients. Med Pediatr Oncol. 1996;26:81–4.
231. Guillou L, Lamoureux E, Masse S, et al. Alveolar soft-part sarcoma of the uterine corpus: histological, immunocytochemical and ultrastructural study of a case. Virchows Arch A Pathol Anat Histopathol. 1991;418:467–71.
232. Folpe AL, Deyrup AT. Alveolar soft-part sarcoma: a review and update. J Clin Pathol. 2006;59:1127–32.
233. Tucker JA. Crystal-deficient alveolar soft part sarcoma. Ultrastruct Pathol. 1993;17:279–86.
234. Carstens HB. Membrane-bound cytoplasmic crystals, similar to those in alveolar soft part sarcoma, in a human muscle spindle. Ultrastruct Pathol. 1990;14:423–8.
235. Sciot R, Dal Cin P, De Vos R, et al. Alveolar soft-part sarcoma: evidence for its myogenic origin and for the involvement of 17q25. Histopathology. 1993;23:439–44.
236. Heller DS, Frydman CP, Gordon RE, et al. An unusual organoid tumor. Alveolar soft part sarcoma or paraganglioma? Cancer. 1991;67:1894–9.
237. Ordonez NG. Alveolar soft part sarcoma: a review and update. Adv Anat Pathol. 1999;6:125–39.
238. Wang NP, Bacchi CE, Jiang JJ, et al. Does alveolar soft-part sarcoma exhibit skeletal muscle differentiation? An immunocytochemical and biochemical study of myogenic regulatory protein expression. Mod Pathol. 1996;9:496–506.
239. Wen MC, Jan YJ, Li MC, et al. Monotypic epithelioid angiomyolipoma of the liver with TFE3 expression. Pathology. 2010;42:300–2.
240. Pang LJ, Chang B, Zou H, et al. Alveolar soft part sarcoma: a bimarker diagnostic strategy using TFE3 immunoassay and ASPL-TFE3 fusion transcripts in paraffin-embedded tumor tissues. Diagn Mol Pathol. 2008;17:245–52.
241. Folpe AL, Goodman ZD, Ishak KG, et al. Clear cell myomelanocytic tumor of the falciform ligament/ligamentum teres: a novel member of the perivascular epithelioid clear cell family of tumors with a predilection for children and young adults. Am J Surg Pathol. 2000;24:1239–46.
242. Sawyer JR, Nicholas RW, Parham DM. A novel t(X;2)(q13;q35) in clear cell sugar tumor of bone. Cancer Genet Cytogenet. 2004;154:77–80.
243. Yamashita K, Fletcher CD. PEComa presenting in bone: clinicopathologic analysis of 6 cases and literature review. Am J Surg Pathol. 2010;34:1622–9.
244. Hornick JL, Fletcher CD. Sclerosing PEComa: clinicopathologic analysis of a distinctive variant with a predilection for the retroperitoneum. Am J Surg Pathol. 2008;32:493–501.
245. Cho HY, Chung DH, Khurana H, et al. The role of TFE3 in PEComa. Histopathology. 2008;53:236–49.
246. Hornick JL, Fletcher CD. PEComa: what do we know so far? Histopathology. 2006;48:75–82.
247. Folpe AL, Mentzel T, Lehr HA, et al. Perivascular epithelioid cell neoplasms of soft tissue and gynecologic origin: a clinicopathologic study of 26 cases and review of the literature. Am J Surg Pathol. 2005;29:1558–75.
248. Wick MR, Ritter JH, Dehner LP. Malignant rhabdoid tumors: a clinicopathologic review and conceptual discussion. Semin Diagn Pathol. 1995;12:233–48.
249. Parham DM, Weeks DA, Beckwith JB. The clinicopathologic spectrum of putative extrarenal rhabdoid tumors. An analysis of 42 cases studied with immunohistochemistry or electron microscopy. Am J Surg Pathol. 1994;18:1010–29.
250. Hsueh C, Kuo TT. Congenital malignant rhabdoid tumor presenting as a cutaneous nodule: report of 2 cases with review of the literature. Arch Pathol Lab Med. 1998;122:1099–102.
251. Abdullah A, Patel Y, Lewis TJ, et al. Extrarenal malignant rhabdoid tumors: radiologic findings with histopathologic correlation. Cancer Imaging. 2010;10:97–101.
252. Ferrari A, Orbach D, Sultan I, et al. Neonatal soft tissue sarcomas. Semin Fetal Neonatal Med. 2012;17:231–8.
253. Hollmann TJ, Hornick JL. INI1-deficient tumors: diagnostic features and molecular genetics. Am J Surg Pathol. 2011;35:e47–63.
254. Hoot AC, Russo P, Judkins AR, et al. Immunohistochemical analysis of hSNF5/INI1 distinguishes renal and extra-renal malignant rhabdoid tumors from other pediatric soft tissue tumors. Am J Surg Pathol. 2004;28:1485–91.
255. Eaton KW, Tooke LS, Wainwright LM, et al. Spectrum of SMARCB1/INI1 mutations in familial and sporadic rhabdoid tumors. Pediatr Blood Cancer. 2011;56:7–15.
256. Beckwith JB, Palmer NF. Histopathology and prognosis of Wilms tumors: results from the First National Wilms' Tumor Study. Cancer. 1978;41:1937–48.
257. Haas JE, Palmer NF, Weinberg AG, et al. Ultrastructure of malignant rhabdoid tumor of the kidney. A distinctive renal tumor of children. Hum Pathol. 1981;12:646–57.
258. Weeks DA, Beckwith JB, Mierau GW, et al. Rhabdoid tumor of kidney. A report of 111 cases from the National Wilms' Tumor Study Pathology Center. Am J Surg Pathol. 1989;13:439–58.
259. Perry A, Fuller CE, Judkins AR, et al. INI1 expression is retained in composite rhabdoid tumors, including rhabdoid meningiomas. Mod Pathol. 2005;18:951–8.
260. Douglass EC, Valentine M, Rowe ST, et al. Malignant rhabdoid tumor: a highly malignant childhood tumor with minimal karyotypic changes. Genes Chromosomes Cancer. 1990;2:210–6.
261. Biegel JA. Molecular genetics of atypical teratoid/rhabdoid tumor. Neurosurg Focus. 2006;20:E11.
262. Sawyer JR, Goosen LS, Swanson CM, et al. A new reciprocal translocation (12;22)(q24.3;q11.2-12) in a malignant rhabdoid tumor of the brain. Cancer Genet Cytogenet. 1998;101:62–7.
263. Bruch LA, Hill DA, Cai DX, et al. A role for fluorescence in situ hybridization detection of chromosome 22q dosage in distinguishing atypical teratoid/rhabdoid tumors from medulloblastoma/central primitive neuroectodermal tumors. Hum Pathol. 2001;32:156–62.
264. Gururangan S, Bowman LC, Parham DM, et al. Primary extracranial rhabdoid tumors. Clinicopathologic features and response to ifosfamide. Cancer. 1993;71:2653–9.
265. Jayaram A, Finegold MJ, Parham DM, et al. Successful management of rhabdoid tumor of the liver. J Pediatr Hematol Oncol. 2007;29:406–8.
266. Gross E, Rao BN, Pappo A, et al. Epithelioid sarcoma in children. J Pediatr Surg. 1996;31:1663–5.
267. Sugarbaker PH, Auda S, Webber BL, et al. Early distant metastases from epithelioid sarcoma of the hand. Cancer. 1981;48:852–5.
268. Hornick JL, Dal Cin P, Fletcher CD. Loss of INI1 expression is characteristic of both conventional and proximal-type epithelioid sarcoma. Am J Surg Pathol. 2009;33:542–50.
269. Hanna SL, Kaste S, Jenkins JJ, et al. Epithelioid sarcoma: clinical, MR imaging and pathologic findings. Skeletal Radiol. 2002;31:400–12.
270. Sakamoto A, Jono O, Hirahashi M, et al. Epithelioid sarcoma with muscle metastasis detected by positron emission tomography. World J Surg Oncol. 2008;6:84.
271. Mirra JM, Kessler S, Bhuta S, et al. The fibroma-like variant of epithelioid sarcoma. A fibrohistiocytic/myoid cell lesion often confused with benign and malignant spindle cell tumors. Cancer. 1992;69:1382–95.
272. Perrone T, Swanson PE, Twiggs L, et al. Malignant rhabdoid tumor of the vulva: is distinction from epithelioid sarcoma possible? A pathologic and immunohistochemical study. Am J Surg Pathol. 1989;13:848–58.

273. Arber DA, Kandalaft PL, Mehta P, et al. Vimentin-negative epithelioid sarcoma. The value of an immunohistochemical panel that includes CD34. Am J Surg Pathol. 1993;17:302–7.
274. Gerharz CD, Moll R, Meister P, et al. Cytoskeletal heterogeneity of an epithelioid sarcoma with expression of vimentin, cytokeratins, and neurofilaments. Am J Surg Pathol. 1990;14:274–83.
275. Cordoba JC, Parham DM, Meyer WH, et al. A new cytogenetic finding in an epithelioid sarcoma, t(8;22)(q22;q11). Cancer Genet Cytogenet. 1994;72:151–4.
276. Raoux D, Peoc'h M, Pedeutour F, et al. Primary epithelioid sarcoma of bone: report of a unique case, with immunohistochemical and fluorescent in situ hybridization confirmation of INI1 deletion. Am J Surg Pathol. 2009;33:954–8.
277. Chase DR, Enzinger FM. Epithelioid sarcoma. Diagnosis, prognostic indicators, and treatment. Am J Surg Pathol. 1985;9:241–63.
278. Prat J, Woodruff JM, Marcove RC. Epithelioid sarcoma: an analysis of 22 cases indicating the prognostic significance of vascular invasion and regional lymph node metastasis. Cancer. 1978;41:1472–87.
279. Spillane AJ, Thomas JM, Fisher C. Epithelioid sarcoma: the clinicopathological complexities of this rare soft tissue sarcoma. Ann Surg Oncol. 2000;7:218–25.
280. Fisher C. Epithelioid sarcoma of Enzinger. Adv Anat Pathol. 2006;13:114–21.
281. Hisaoka M, Ishida T, Kuo TT, et al. Clear cell sarcoma of soft tissue: a clinicopathologic, immunohistochemical, and molecular analysis of 33 cases. Am J Surg Pathol. 2008;32:452–60.
282. Lucas DR, Nascimento AG, Sim FH. Clear cell sarcoma of soft tissues. Mayo Clinic experience with 35 cases. Am J Surg Pathol. 1992;16:1197–204.
283. Meis-Kindblom JM. Clear cell sarcoma of tendons and aponeuroses: a historical perspective and tribute to the man behind the entity. Adv Anat Pathol. 2006;13:286–92.
284. Stacy GS, Nair L. Magnetic resonance imaging features of extremity sarcomas of uncertain differentiation. Clin Radiol. 2007;62:950–8.
285. Davis IJ, Kim JJ, Ozsolak F, et al. Oncogenic MITF dysregulation in clear cell sarcoma: defining the MiT family of human cancers. Cancer Cell. 2006;9:473–84.
286. Jones RL, Constantinidou A, Thway K, et al. Chemotherapy in clear cell sarcoma. Med Oncol. 2011;28:859–63.
287. Dabska M. Parachordoma: a new clinicopathologic entity. Cancer. 1977;40:1586–92.
288. Gleason BC, Fletcher CD. Myoepithelial carcinoma of soft tissue in children: an aggressive neoplasm analyzed in a series of 29 cases. Am J Surg Pathol. 2007;31:1813–24.
289. Huang CC, Cheng SM. Clinical and radiological presentations of pelvic parachordoma. Rare Tumors. 2012;4:e5.
290. Antonescu CR, Zhang L, Chang NE, et al. EWSR1-POU5F1 fusion in soft tissue myoepithelial tumors. A molecular analysis of sixty-six cases, including soft tissue, bone, and visceral lesions, showing common involvement of the EWSR1 gene. Genes Chromosomes Cancer. 2010;49:1114–24.
291. Hornick JL, Fletcher CD. Myoepithelial tumors of soft tissue: a clinicopathologic and immunohistochemical study of 101 cases with evaluation of prognostic parameters. Am J Surg Pathol. 2003;27:1183–96.
292. Tirabosco R, Mangham DC, Rosenberg AE, et al. Brachyury expression in extra-axial skeletal and soft tissue chordomas: a marker that distinguishes chordoma from mixed tumor/myoepithelioma/parachordoma in soft tissue. Am J Surg Pathol. 2008;32:572–80.
293. Lae ME, Roche PC, Jin L, et al. Desmoplastic small round cell tumor: a clinicopathologic, immunohistochemical, and molecular study of 32 tumors. Am J Surg Pathol. 2002;26:823–35.
294. Gerald WL, Miller HK, Battifora H, et al. Intra-abdominal desmoplastic small round-cell tumor. Report of 19 cases of a distinctive type of high-grade polyphenotypic malignancy affecting young individuals. Am J Surg Pathol. 1991;15:499–513.
295. Levy AD, Arnaiz J, Shaw JC, et al. From the archives of the AFIP: primary peritoneal tumors: imaging features with pathologic correlation. Radiographics. 2008;28:583–607. quiz 621–582.
296. Zhang WD, Li CX, Liu QY, et al. CT, MRI, and FDG-PET/CT imaging findings of abdominopelvic desmoplastic small round cell tumors: correlation with histopathologic findings. Eur J Radiol. 2011;80:269–73.
297. de Alava E, Ladanyi M, Rosai J, et al. Detection of chimeric transcripts in desmoplastic small round cell tumor and related developmental tumors by reverse transcriptase polymerase chain reaction. A specific diagnostic assay. Am J Pathol. 1995;147:1584–91.
298. Ordonez NG. Desmoplastic small round cell tumor: I: a histopathologic study of 39 cases with emphasis on unusual histological patterns. Am J Surg Pathol. 1998;22:1303–13.
299. Alaggio R, Rosolen A, Sartori F, et al. Spindle cell tumor with EWS-WT1 transcript and a favorable clinical course: a variant of DSCT, a variant of leiomyosarcoma, or a new entity? Report of 2 pediatric cases. Am J Surg Pathol. 2007;31:454–9.
300. Zhang PJ, Goldblum JR, Pawel BR, et al. Immunophenotype of desmoplastic small round cell tumors as detected in cases with EWS-WT1 gene fusion product. Mod Pathol. 2003;16:229–35.
301. Sawyer JR, Tryka AF, Lewis JM. A novel reciprocal chromosome translocation t(11;22)(p13;q12) in an intraabdominal desmoplastic small round-cell tumor. Am J Surg Pathol. 1992;16:411–6.
302. Al Balushi Z, Bulduc S, Mulleur C, et al. Desmoplastic small round cell tumor in children: a new therapeutic approach. J Pediatr Surg. 2009;44:949–52.
303. Pawel BR, Hamoudi AB, Asmar L, et al. Undifferentiated sarcomas of children: pathology and clinical behavior – an Intergroup Rhabdomyosarcoma study. Med Pediatr Oncol. 1997;29:170–80.
304. Kawamura-Saito M, Yamazaki Y, Kaneko K, et al. Fusion between CIC and DUX4 up-regulates PEA3 family genes in Ewing-like sarcomas with t(4;19)(q35;q13) translocation. Hum Mol Genet. 2006;15:2125–37.
305. Choi EY, Thomas DG, McHugh JB, et al. Undifferentiated small round cell sarcoma with t(4;19)(q35;q13.1) CIC-DUX4 fusion: a novel highly aggressive soft tissue tumor with distinctive histopathology. Am J Surg Pathol. 2013;37:1379–86.
306. Machado I, Cruz J, Lavernia J, et al. Superficial EWSR1-negative undifferentiated small round cell sarcoma with CIC/DUX4 gene fusion: a new variant of Ewing-like tumors with locoregional lymph node metastasis. Virchows Arch. 2013;463:837–42.
307. Italiano A, Sung YS, Zhang L, et al. High prevalence of CIC fusion with double-homeobox (DUX4) transcription factors in EWSR1-negative undifferentiated small blue round cell sarcomas. Genes Chromosomes Cancer. 2012;51:207–18.
308. Kajtar B, Tornoczky T, Kalman E, et al. CD99-positive undifferentiated round cell sarcoma diagnosed on fine needle aspiration cytology, later found to harbour a CIC-DUX4 translocation: a recently described entity. Cytopathology. 2014;25:129–32.

Malignant Bone Tumors

4

Bruce R. Pawel and Rakhee Kisan Sansgiri

Introduction

There are few areas in tumor diagnosis where communication between clinician, radiologist, and pathologist is more critical than in the field of malignant bone tumors. Benign, reactive lesions may look alarming under the microscope, and without considering clinical and imaging features they may be overdiagnosed as malignant. Distinguishing these entities and excluding other benign lesions requires knowledge of age, symptoms, and most importantly skeletal location and radiographic appearance. Knowledge of specific bony location (e.g., diaphyseal, metaphyseal, or epiphyseal) affects the final diagnosis, as many tumors prefer specific sites. Furthermore, the incidence of a given diagnosis varies depending on age, with some being rare in infants and others more unusual in older children. Perhaps most central to establishing a correct diagnosis is correlation with radiographic imaging (see below). In brief, benign tumors tend to grow slowly and develop a sclerotic margin, whereas malignant neoplasms typically display rapid growth, destruction of the surrounding bone, and often extension into soft tissues. It is thus advisable for pathologists signing out bone tumors to develop a general understanding of major radiographic features and to work closely with radiological and surgical colleagues in evaluating these cases.

In the following sections, the imaging and pathologic features of malignant bone tumors affecting children will be discussed. Benign tumors will only be mentioned in the context of differential diagnosis.

B.R. Pawel, M.D. (✉)
Pathology and Laboratory Medicine, Perelman School of Medicine at the University of Pennsylvania, 34th Street and Civic Center Blvd, 5NW11, Philadelphia, PA 19104, USA

The Children's Hospital of Philadelphia, Philadelphia, PA, USA
e-mail: pawelb@email.chop.edu

R.K. Sansgiri, M.D.
St. Jude Children's Research Hospital, Memphis, TN, USA

Overview of Diagnostic Imaging Approaches

Plain Films

Radiographic diagnoses of bone tumors are based upon the parameters of tumor location and size, presence of soft tissue involvement and/or a periosteal reaction, the pattern of bone destruction, margination, matrix characteristics, and multiplicity. Patient demographics and clinical characteristics such as age, gender, systemic symptoms, local pain or swelling must be taken into account, and pertinent laboratory tests and the presence of underlying tumor predisposing conditions such as Paget's disease or treatment with radiation therapy must also be considered [1].

Imaging techniques differ in their individual strengths, which must be considered during analysis. Plain radiography is the first step in the diagnosis of bone tumors and is regarded as the gold standard for lesion detection. Advanced imaging techniques such as computed tomography (CT), magnetic resonance imaging (MRI), positron emission tomography (FDG/PET) and bone scans supplement plain radiography in detecting additional lesions, determining lesional characteristics, establishing lesional relationships with surrounding structures, and guiding biopsy or treatment strategies [1].

Plain Film Radiography

The nature of a lesion is defined in terms of its rate of growth or aggressiveness: slow-growing lesions are often benign or nonaggressive, and fast-growing lesions are more likely to be malignant or aggressive. Plain film imaging can detect certain lesional characteristics that indicate aggressiveness, which is valuable in distinguishing lesions that need further work-up or biopsy from those that can be safely followed. Conventional radiography remains the initial imaging modality of choice, as it offers the best spatial resolution for characterization of lesional margins, periosteal reaction, and matrix calcification,

D.M. Parham et al. (eds.), *Pediatric Malignancies: Pathology and Imaging*,
DOI 10.1007/978-1-4939-1729-7_4, © Springer Science+Business Media New York 2015

features that indicate aggressiveness. Radiography is cost effective and easily accessible. It also provides reliable information regarding the nature, progression, location, and accessibility of the lesion for biopsy [2].

Margins: The appearance of tumor margins on radiography reflects the balance of tumor osteoclastic activity with the background trabeculated normal osteoblastic activity. Slow growing tumors are usually non-aggressive and appear well marginated with geographic or sclerotic margins. Sclerosis, the osseous reaction to a lesion, implies that sufficient time has elapsed for native bone to respond to the lesion. Fast-growing, aggressive tumors appear as poorly defined lesions with a moth-eaten or permeative pattern of destruction with indistinct margins. With continued growth, these lesions may show an expansion and local break in the cortex [2].

Zone of transition: Because of the ample time for osseous reaction in slow-growing tumors, there is a narrow zone of transition with a sharp and distinct border between tumor and normal bone. When fast-growing tumors infiltrate surrounding bone, they lack clearly defined margins and have a wide zone of transition.

Periosteal reaction: The periosteal reaction is usually single-layered in non-aggressive lesions and multilayered (also termed onion-skinned, lamellated, spiculated, or sunburst) in aggressive lesions. Rapidly growing lesions penetrate through the cortex, causing its separation of the periosteum and formation of lamellated new bone. If the periosteum significantly elevates, it can break and form an acute angle termed Codman's triangle. Codman's triangle is seen in malignant bone tumors as well as other rapidly growing lesions (e.g., aneurysmal bone cyst) or reactive processes (e.g., osteomyelitis, subperiosteal hematoma).

Matrix: Malignant osteoid matrix (seen in osteosarcoma) forms amorphous, cloud-like haphazard densities. Mature osteoid or organized bone, as seen in osteoblastoma, shows a more orderly trabeculated arrangement. Chondroid matrix forms dense arcs and rings of calcifications or focal stippled or flocculent densities.

Magnetic Resonance Imaging (MRI)

If a bone malignancy is suspected in children, magnetic resonance imaging (MRI) can help establish its size, extent, and relationship to neurovascular structures, the bony physis, and joint and muscle compartments. MRI can also guide the most appropriate site for biopsy and aids in determining candidacy for limb-sparing surgery. MRI also identifies any potential skip lesions, which can impart a significantly worse outcome [3]. MRI sequences typically comprise non-contrast T1-weighted (T1W), fat-saturated T2-weighted (T2W), short T1 inversion recovery (STIR), and fat-saturated post-contrast T1W images in at least three planes. Axial and sagittal or coronal T1W and T2W sequences are acquired through the entire bone from joint to joint, and axial gradient echo sequences are acquired through the tumor. Sagittal or coronal scans and T2W sequences are used to evaluate joint involvement, identify skip metastasis, and define the soft tissue portion of the tumor. STIR and post-contrast enhanced sequences help to distinguish tumor from edema and to determine areas of tumor necrosis preferably avoided in tissue biopsy. Determination of tumor extension across the physis into the epiphyses contributes to surgical planning. Evaluation of calcification, ossification, cortical destruction, and periosteal changes is limited on MRI and best evaluated on plain films [1, 2].

Tumor size is a predictor of outcome in patients with osteosarcoma and Ewing sarcoma. MRI-based absolute tumor volume predicts overall survival ($p = 0.018$) and event free survival ($p = 0.036$) in pediatric osteosarcoma of the extremities [4]. Similarly, tumor size at diagnosis predicts patient outcome in Ewing sarcoma; smaller tumors are associated with increased disease-free survival [5].

Computed Tomography

Computed tomography (CT) mimics plain film findings but may better depict matrix calcification, cortical destruction, and cystic or fatty foci. It is particularly useful for the analysis of the spine, sacrum, or other regions of anatomical complexity. CT detection of lung lesions has particular importance in pediatric bone tumors, as approximately 15–20 % of children with osteosarcoma show detectable lung metastasis at presentation [6]. High resolution CT chest examination plays an important role in the staging and follow up of these patients.

Bone Scans

^{99m}Technitium methyldiphosphonate (^{99}Tc MDP) is a radiotracer taken up in sites of osteoblastic activity. This agent lacks specificity but helps to detect primary and early metastatic bone disease, which show areas of increased radiotracer uptake.

Positron Emission Tomography

Fluorine-18 fluorodeoxyglucose positron emission tomography (^{18}F-FDG PET) utilizes a biologically active radiotracer, FDG (an analogue of glucose), which undergoes radioactive decay by positron emission as it is metabolized. The concentration (measured as standardized uptake value)

of the tracer in the tissues yields an estimate of metabolic activity in terms of regional glucose uptake. It is typically imaged using a three-dimensional computer analysis. This assessment helps guide biopsy site selection by detecting metabolically active portions within the tumor, and it can be used to assess tumor response to treatment. Costelloe et al. [7] found that a high maximum standardized uptake value (SUV_{max}) of osteosarcoma before and after chemotherapy ($p=0.008$ and $p=0.009$, respectively) and an increase in total lesion glycolysis ($p=0.016$) after chemotherapy were associated with worse progression-free survival. These investigators also found that a high SUV_{max} after chemotherapy was associated with poor overall survival ($p=0.035$). PET is typically fused with CT imaging for a combination of anatomic and metabolic information.

After tumor diagnosis, accurate staging is essential to plan appropriate therapy. A chest CT is performed to detect pulmonary metastases, and a ^{99m}Tc bone scan is typically obtained to detect bone metastases. PET and PET-CT show good sensitivity in detecting distant metastasis, excepting pulmonary nodules <5 mm in size, which are below the limit of spatial resolution of current PET scanners. PET and PET-CT may also be superior to CT and MRI for detecting skeletal metastases when no abnormal activity is seen on ^{99m}Tc bone scan [8]. PET-CT can accurately delineate margins of viable tumor, which can often be difficult to differentiate from anatomic distortion or peritumoral edema with MRI, and so it is therefore a helpful adjunct to MRI in surgical planning [2–6].

Osteosarcoma

Osteosarcoma is the most common primary bone malignancy of children and adolescents, with a frequency of 4.4:1,000,000 [9]. In younger age groups, there is a slight female predominance; however, males are more commonly affected after age 15 [9]. Osteosarcoma is defined by the production of bone and immature bone matrix (osteoid) by malignant mesenchymal cells, which must be demonstrated to establish the diagnosis. There are several subtypes of osteosarcoma, as will be discussed in this section.

Imaging Features

By far the most common subtype, conventional osteosarcoma is a high grade malignancy that occurs at all ages. Its incidence peaks during adolescence, corresponding to the period of greatest physiologic growth, and it is quite rare in preschool children and infants [10]. It can occur in nearly any bone as a primary site (and rarely as a primary in soft tissue), but most commonly it arises in long bones, particularly the distal femur, proximal tibia, and proximal humerus. In these sites, it usually arises from the medullary cavity of the metaphysis, and at diagnosis it often extends into soft tissue outside of the bone. Osteosarcomas occasionally arise from the diaphysis, whereas epiphyseal origin is vanishingly rare [11]. Osteosarcoma can also arise in the head and neck, most frequently in the jaw bones [12], and in the flat bones of the axial or appendicular skeleton [13]. Rarely it presents in multiple sites, either synchronously or metachronously [14]. The most common presenting symptom is pain, which often begins insidiously but progresses with time.

Fig. 4.1 Plain film radiograph of conventional high grade osteosarcoma of the femur in a 14 year old girl. Note the osteoid matrix of the large soft tissue mass and Codman's triangle (*arrow*)

Plain-film radiography: The tumor is usually located eccentrically within the metaphysis or metadiaphysis (Fig. 4.1). Density of the tumor varies from lytic to sclerotic, with the majority of tumors displaying a mixed lytic-sclerotic pattern [15]. There is usually a permeative pattern of bone destruction and a wide zone of transition. Matrix is visible in 90 % of cases, with cloud-like osteoid production. Ninety percent of cases show cortical destruction and an associated soft tissue mass. The accompanying aggressive periosteal reaction may have a sunburst, interrupted, hair-on-end, or lamellated pattern, and a Codman's triangle can be present [15]. Lung metastases may be ossified.

Computed tomography (CT): CT is superior to plain film radiography for showing marrow involvement and defining osteoid matrix, which can be difficult to detect on MRI in predominantly lytic lesions. CT is rarely necessary in the evaluation of

Fig. 4.2 MRI images of same tumor shown in Fig. 4.1. (**a**) Coronal T1W fat-saturated image: the intramedullary extent of the tumor is well delineated. The lesion is hypointense to marrow (*arrows*). The center of the tumor is dark due to dense calcification. (**b**) Post-contrast T1W fat-saturated image demonstrating enhancement of the intramedullary tumor and soft-tissue component. The central calcification (*straight arrow*) and necrotic area (*curved arrow*) lack enhancement. (**c**) Short tau inversion recovery (STIR) coronal sequence shows the tumor to be very heterogenous. Surrounding soft tissue edema appears as bright signal

the primary tumor but aids in staging of pulmonary metastases and guiding minimally invasive biopsies (CT-guided biopsy). It is superior to plain film radiography at depicting the low attenuation of central necrosis in soft tissues.

Magnetic resonance imaging (MRI): MRI is useful for soft tissue and marrow evaluation, surgical or biopsy planning, and restaging after chemotherapy (Fig. 4.2a–c). Osteoid appears as a low signal on all sequences, whereas non-osteoid, solid portions of the tumor appear isointense to skeletal muscle on T1W sequences. Fluid-sensitive sequences show heterogeneous high-signal features in both the soft tissue and bony masses [15]. High-signal peritumoral edema in bone and soft tissue may exaggerate the size of the mass. Post-contrast images reveal intense, heterogenous enhancement of the soft tissue and involved marrow, which may help differentiate viable regions from low-intensity necrotic regions.

Bone scintigraphy: Triple-phase, whole-body ^{99m}Tc bone scintigraphy can help determine sites of bony metastases, polyostotic involvement, and intraosseous tumor extent. Lesions must be at least 1 cm in diameter to be detected by bone scan. Blood flow, blood pool, and delayed images reveal intense radiotracer uptake. Bone scans may show ossified lymph nodes or calcified lung metastases.

PET-CT: On ^{18}F-FDG PET-CT, conventional osteosarcoma appears as a highly ^{18}F-FDG–avid lesion. Tumor aggressiveness correlates with ^{18}F-FDG uptake, measured by tumor-to-background (T/BG) ratio, SUV, or kinetic modeling techniques [16].

Radiologic differential diagnosis: Ewing sarcoma arises more often in the diaphysis than osteosarcoma. When malignant fibrous histiocytoma arises from bone, it forms a permeative, aggressive metaphyseal lesion that may be difficult to differentiate from lytic osteosarcoma on imaging [17].

Pathologic Features

As current treatment regimens utilize presurgical chemotherapy, it is unusual to encounter a resection specimen that has not been altered by treatment. Grossly, conventional osteosarcomas typically form large destructive tumors that transect the cortex, extend into soft tissue, and contain variable degrees of necrosis, calcification and hemorrhage (Fig. 4.3). Even without presurgical treatment, necrosis may be extensive.

Histologically, diagnosis of conventional osteosarcoma requires two fundamental elements: atypical mesenchymal

cells and tumoral (as opposed to reactive) osteoid or bone. Osteoid may be quite focal. The prominence of these features varies by patient and by microscopic field, a fact important to consider with small biopsies. Usually, conventional osteosarcoma is a straightforward diagnosis. Most typically, malignant mesenchymal cells are dense and mitotically active, with hyperchromatism, cytologic atypia, and pleomorphism (Fig. 4.4). Tumor cells may be spindled, round, or polymorphic; giant cells, markedly pleomorphic cells (monstrocellular cells), and atypical mitotic figures are common. Osteoid comprises a pink, dense, amorphous material abutting tumor cells, and fibrosis and atypical chondroid matrix are also common. Distinction of osteoid from other types of collagenous matrix can be difficult and subjective. In general, a fibrillar matrix is not osteoid but rather non-osteoidal collagen. Occasionally cartilage may dominate, and demonstration of osteoid production may require careful searching [18]. Tumoral osteoid is often wispy and lace-like but may appear as larger deposits with bone production (Fig. 4.5).

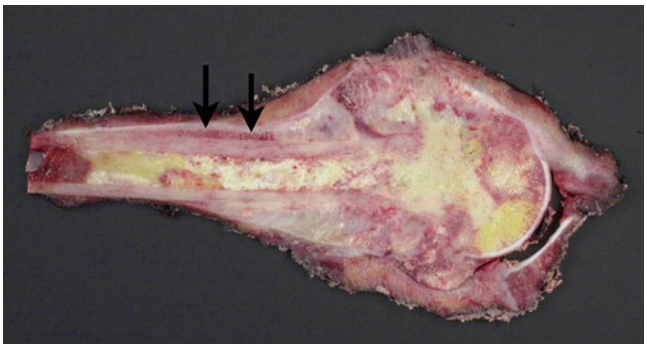

Fig. 4.3 Cut section of osteosarcoma of the femur. The destructive tumor arises from the metaphysis, with extensive involvement of the marrow cavity and extension into soft tissue. Note the elevation of the periosteum (*arrows*)

In the sclerosing osteosarcoma variant, abundant osteoid matrix totally envelopes tumor cells, giving them the appearance of benign intralacunar osteocytes. The decreased cellularity obscures the malignant nature of the lesion, especially in limited biopsy material [18]. Close attention to the tumor interface with surrounding bone can be helpful in difficult cases, as the leading edges of the tumor often show increased cellularity with atypical cells [18], but such areas may not be present in limited biopsy material. The background reveals variable degrees of hemorrhage, tumoral necrosis and calcification.

Depending upon the predominant matrix component, conventional osteosarcomas have historically been placed into categories of osteoblastic (predominant osteoid and bone production), chondroblastic (predominant chondroid production) or fibroblastic (spindle cells with only focal matrix production) (Fig. 4.6). However, the value of these descriptive categories is debatable, as there can be significant variation in different areas of a given tumor, and moreover, these histologic subtypes appear to have no prognostic significance [9].

Rare types of osteosarcoma that present difficulties in diagnosis include epithelioid and osteoblastoma-like tumors. Epithelioid osteosarcoma contains large round to polyhedral undifferentiated cells that resemble epithelial cells and produce little osteoid (Fig. 4.7). They may have prominent nucleoli and on occasion can be cohesive, mimicking an epithelial malignancy or angiosarcoma, so that careful search for osteoid becomes necessary to establish the diagnosis [18]. Cytokeratin positivity makes this distinction even more problematic (see below). Osteoblastoma-like osteosarcoma contains broad bony trabeculae and osteoblastic rimming that mimics osteoblastoma; atypical osteoblasts may also be present. However, it shows infiltration of surrounding bone and atypical mitoses [18].

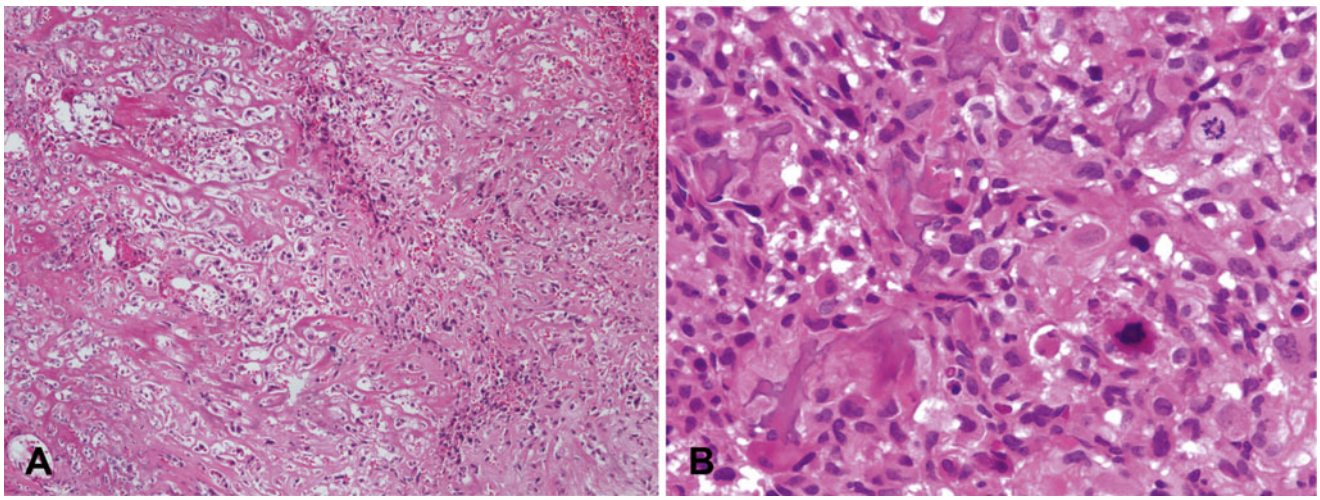

Fig. 4.4 Osteosarcoma, conventional type. (**a**) Atypical spindle cells enmeshed in lace-like osteoid. (**b**) High grade features of conventional osteosarcoma; Pleomorphic hyperchromatic spindle cells with atypical mitotic figures. Note the tumoral osteoid in *lower left* of the figure

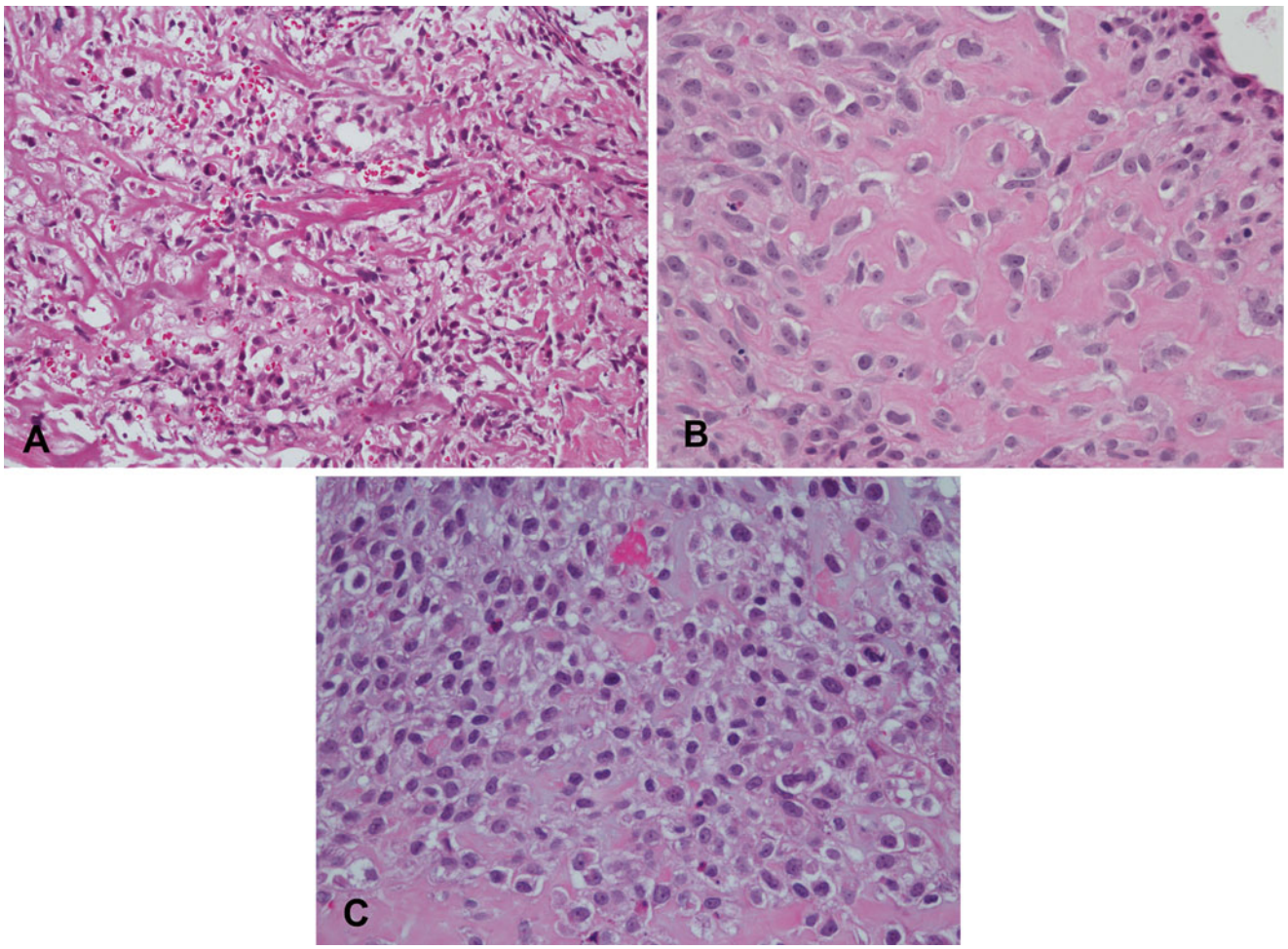

Fig. 4.5 Variable appearances of osteoid matrix in osteosarcoma. (**a**) Lace-like osteoid. (**b**) Coarser deposits. (**c**) Non-uniform deposition with subtle lace-like deposits at top of field and coarser deposits at the bottom

Immunohistochemical stains: In most cases a firm diagnosis of conventional osteosarcoma only requires routine H&E staining. Immunohistochemistry has limited utility and is mainly used to exclude tumors with better defined and more specific immunohistochemical profiles. The only consistently positive stain in general clinical use is vimentin, and smooth muscle actin may be positive as well [11]. Immunohistochemistry is most helpful in biopsies of high grade primary bone tumors with cellular pleomorphism, necrosis, and hemorrhage, but lacking tumoral osteoid or bone. Such tumors usually represent osteosarcoma, as few other primary bone tumors of childhood have these features [19] CD99 is helpful in ruling out Ewing sarcoma, as the staining pattern in osteosarcoma tends to be cytoplasmic and granular, as opposed to membranous. Rarely osteosarcomas stain with cytokeratin, which can be a pitfall in distinguishing them from synovial sarcoma, angiosarcoma, and metastatic carcinoma [20].

Diagnostic molecular genetics: No specific translocations or mutations define osteosarcoma, so that molecular cytogenetic studies mainly exclude other entities. Osteosarcomas usually exhibit very complex numerical and structural chromosomal aberrations. Some are recurring but none are consistent enough to be helpful in diagnosis [21]. Common abnormalities include loss of chromosomes 9, 13, and 17, gain of chromosome 1, partial loss of 6q, and chromosomal rearrangements of 11, 19, and 20 [22]. Li-Fraumeni syndrome and hereditary retinoblastoma syndrome markedly increase risk for developing osteosarcoma and, respectively, result in loss of *RB1* on chromosome 13q and *TP53* on chromosome 17p. A significant percentage of sporadic osteosarcomas also show alterations of these tumor suppressor genes [23].

Prognostic and post-treatment issues: According to SEER, the overall 1994–2003 5-year survival rate in children and adolescents was 61.6 %, with distant hematogenous metastases (most commonly lung) or local disease recurrence associated with much poorer survival [9, 24]. Pelvis or vertebral tumors also have adverse prognostic significance [9, 25].

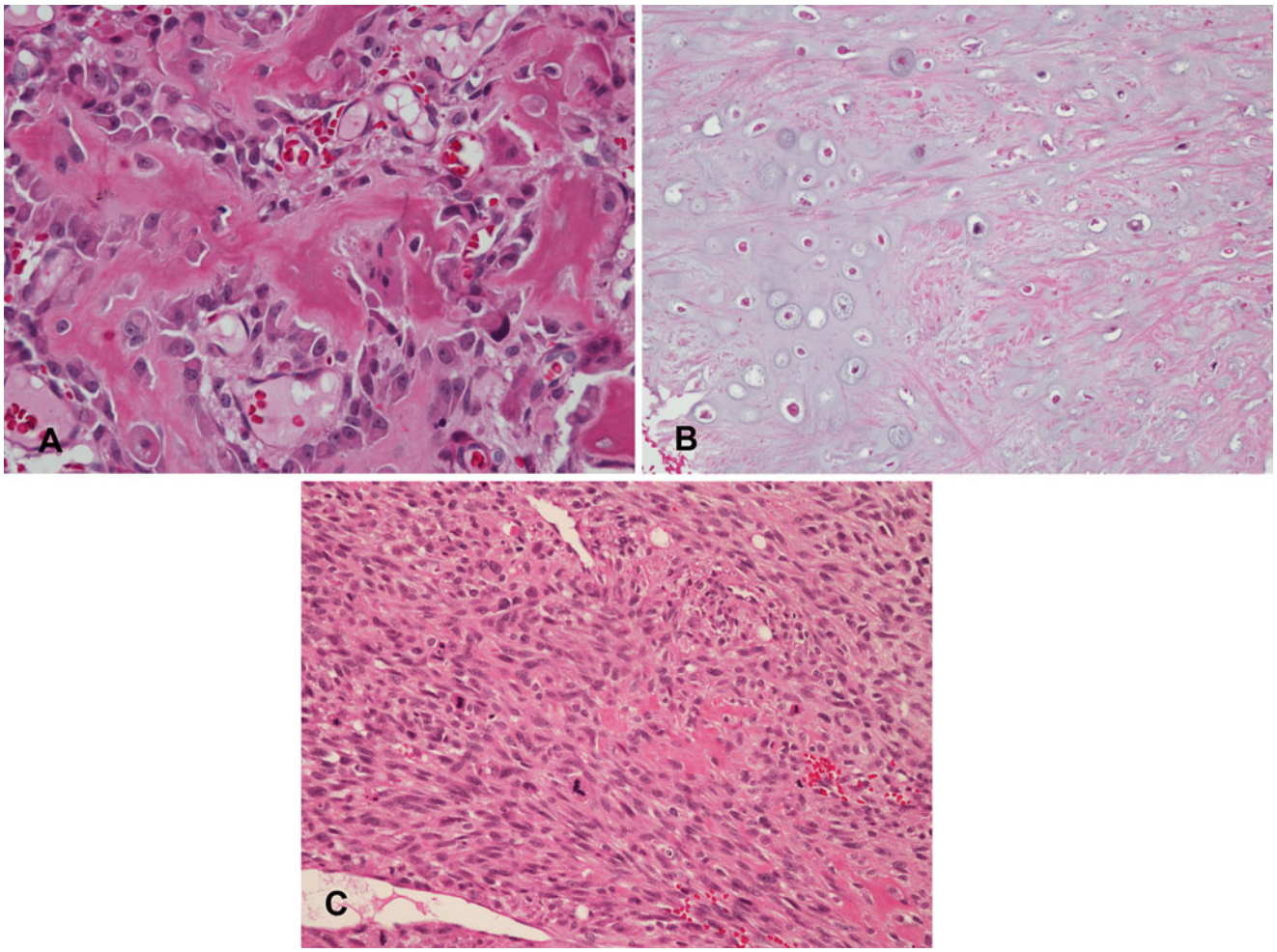

Fig. 4.6 Subtypes of conventional osteosarcoma. (**a**) Osteoblastic osteosarcoma with "normalization" characterized by solid ribbons of osteoid and minimal nuclear atypia, mimicking an osteoblastoma. Other areas of this tumor showed high grade features (not shown). (**b**) Chondroblastic osteosarcoma with atypical cartilage. Foci of malignant osteoid production were identified in other areas (not shown). (**c**) Fibroblastic osteosarcoma. Note the single focus of osteoid production in the center of the field

Pathologic examination of the definitive (post-chemotherapy) resection specimen for margin status and degree of necrosis plays an important role in clinical care. As these specimens are often large and require extensive decalcification and fixation, proper handling to ensure good histologic detail and preservation of important margins is not trivial. In our institution, such specimens are handled in the following manner: Upon receipt in the pathology laboratory, the fresh specimen is photographed and X-rayed, and when necessary, orientation is confirmed with surgical personnel. The entire specimen is inked. The specimen is then frozen at −70 °C. Depending on tumor location, the frozen specimen is sequentially sectioned along the longitudinal axis most likely to demonstrate the greatest tumor area. We obtain band saw sections at approximately 5 mm intervals, usually yielding up to 25–30 slabs. The slabs are then fixed and decalcified. Afterwards one or more slabs having the greatest tumor area is mapped, photocopied, and completely submitted along with bone and soft tissue margins (Fig. 4.8). Using the grid map, the

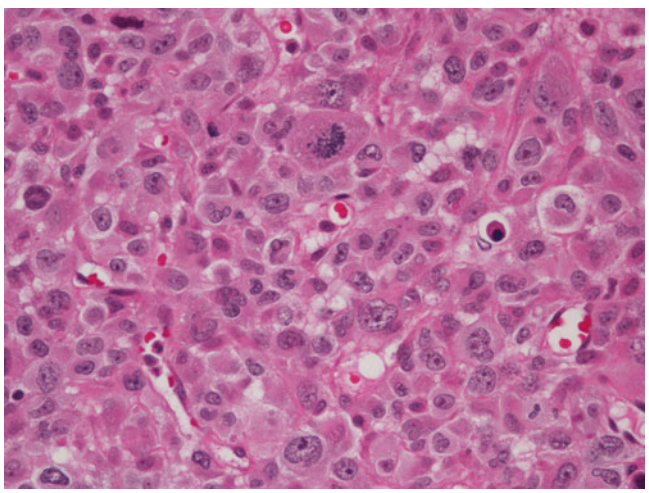

Fig. 4.7 Epithelioid osteosarcoma. Atypical plump cells contain abundant eosinophilic cytoplasm, vesicular nuclei, prominent nucleoli, and an atypical mitosis. Osteoid production in this tumor (not shown) only became evident following chemotherapy

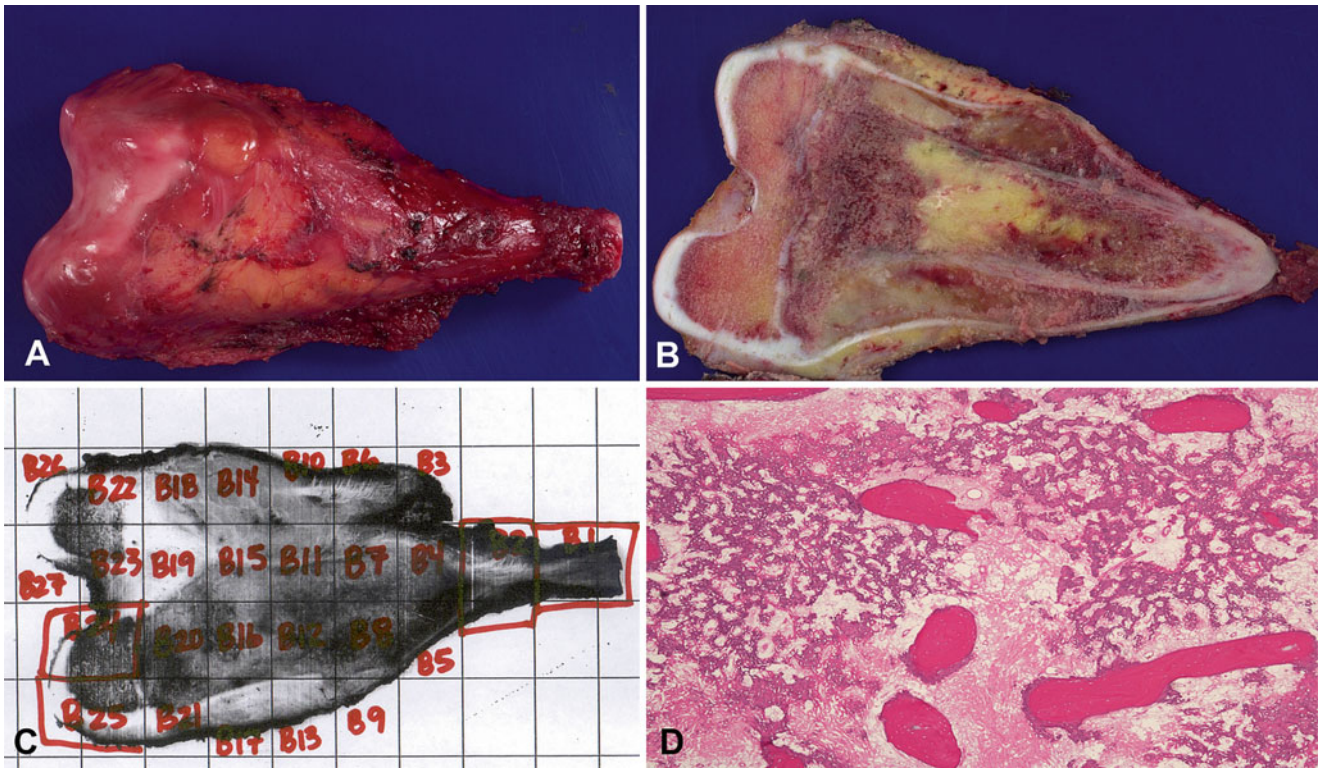

Fig. 4.8 Osteosarcoma, management of post-chemotherapy specimen. (**a**) Limb-salvage resection of distal femur tumor. (**b**) Appearance of central tumor slab following freezing of the specimen; note soft tissue and medullary components of the treated tumor. (**c**) Grid map of the tumor slab, with each labeled rectangle associated with a unique block taken for histologic examination. (**d**) A microscopic section taken from one of the labeled blocks, demonstrating complete tumor necrosis

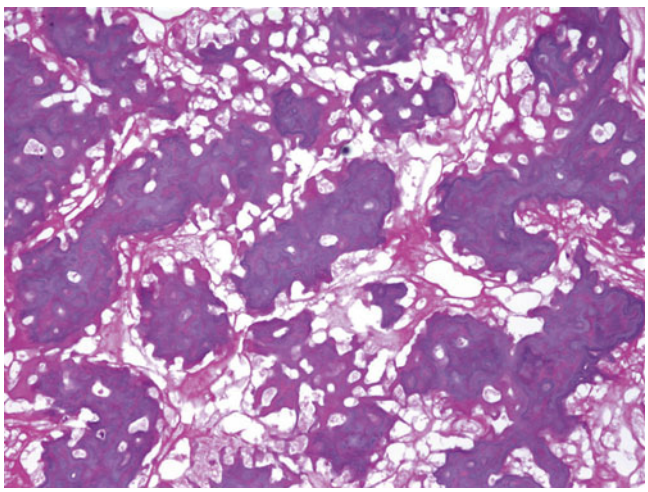

Fig. 4.9 Osteosarcoma, post treatment. There is a favorable tumor response with a residual meshwork of acellular osteoid

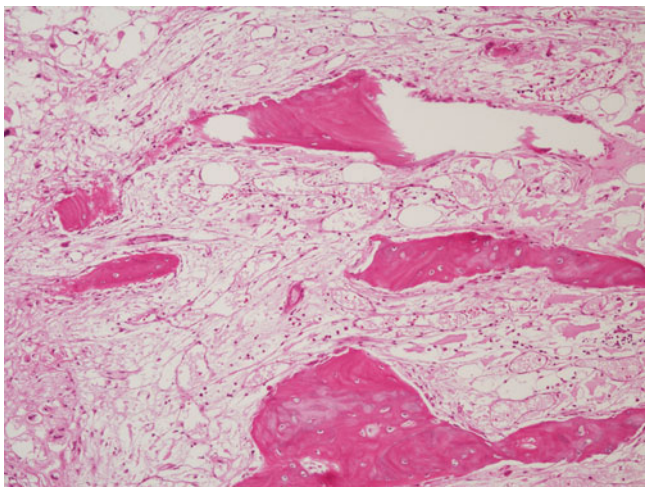

Fig. 4.10 Osteosarcoma, post treatment: Favorable tumor response with loose myxoid tissue occupying the site of the previous tumor bed. Residual atypical tumor cells are not present

pathologist examines each block and evaluates necrosis, expressed as a percentage of the total tumor surface area. Positive margins at time of definitive surgery are associated with a poor prognosis [24]. With effective chemotherapy, extirpation of malignant cells in osteoblastic and chondroblastic areas leaves a background of acellular matrix, often containing empty lacunae or pyknotic "ghost" cells (Fig. 4.9). Fibroblastic areas tend to be replaced by bland granulation and myxoid tissue (Fig. 4.10) [26]. Using current COG protocols, patients are stratified to either "favorable" or "standard" responses, the forming having necrosis >90 %. Unfortunately, such assessments involve a high level of subjectivity. Large areas of the

tumor bed composed of either sheets of tumor cells or expanses of acellular matrix are usually straightforward. However, post-chemotherapy specimens that contain foci of chemoresistant cells are typically less cellular than before therapy. Scattered pleomorphic cells with smudgy nuclei (considered to be viable for purposes of grading) [27] often persist in microscopic fields that are otherwise necrotic. In these situations, assignment of a particular percentage necrosis becomes inherently imprecise, and the literature gives little practical guidance. For additional information, the reader is advised to consult the excellent reference by Raymond et al. [28].

Small Cell Osteosarcoma

Small cell osteosarcoma is rare, accounting for less than 2 % of osteosarcomas. These lesions are small blue cell tumors that demonstrate osteoid production (sometimes focal) but otherwise have features suggestive of Ewing sarcoma. Like conventional pediatric osteosarcoma, it usually arises in long bones and most commonly occurs in the second decade. It may have a slightly worse prognosis than conventional osteosarcoma, although its relative infrequency and controversial diagnostic criteria have raised questions about its behavior.

Imaging Features

Small cell osteosarcoma is an intramedullary, permeative lytic lesion with ill-defined margins that is associated with cortical destruction, aggressive periosteal reaction, and a soft tissue mass [29].

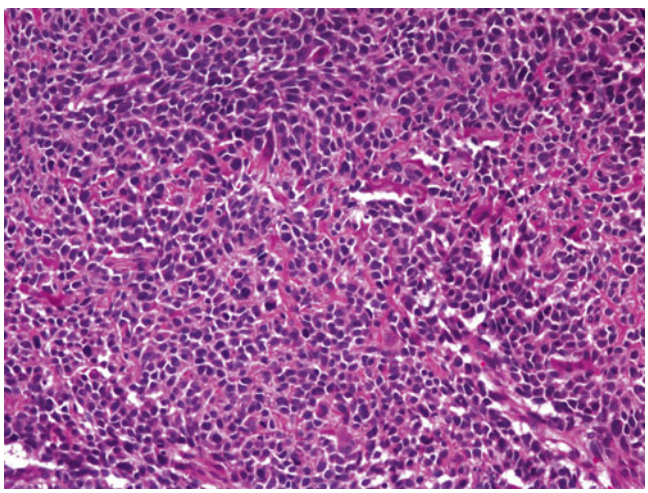

Fig. 4.11 Small cell osteosarcoma. Undifferentiated tumor cells with hyperchromatism and minimal cytoplasm, mimicking Ewing sarcoma. Subtle tumoral osteoid matrix is present in the background

Pathologic Features

Small cell osteosarcoma is composed of sheets of undifferentiated small round cells with hyperchromatic nuclei and minimal pleomorphism, similar to Ewing sarcoma (Fig. 4.11). At least focal osteoid production must be identified to establish the diagnosis [30]. Differential diagnosis can be problematic, as tumoral osteoid may be difficult to separate from the non-osteoidal matrix that may be seen in Ewing sarcoma. Tumor cell spindling favors a diagnosis of osteosarcoma, as does lack of strong, perimembranous CD99 staining. However, Ewing sarcomas may occasionally demonstrate areas of mild spindling, and CD99 positivity has also been described in small cell osteosarcoma, further complicating distinction between the two entities [31]. Most, if not all small cell osteosarcomas lack fusion transcripts for *EWSR1-FLI1* or *EWSR1-ERG*, and although the matter is not entirely settled, some investigators have argued that small cell tumors which harbor these translocations should be considered Ewing sarcomas, regardless of whether or not they produce osteoid [18].

Telangiectatic Osteosarcoma

Telangiectatic osteosarcoma is a rare (4 % of osteosarcomas) high grade subtype of osteosarcoma, with similar demographics regarding age and tumor location [32]. Approximately a quarter of patients present with pathologic fracture. Originally thought to have a worse prognosis than conventional osteosarcoma, survival figures with modern chemotherapeutic regimens are now comparable [33].

Imaging Features

Plain-film radiography: Classic telangiectatic osteosarcoma appears as a geographic area of bone destruction with endosteal scalloping, a wide zone of transition, and marked aneurysmal bony expansion. Its radiographic appearance mimics that of an aneurysmal bone cyst (Fig. 4.12a, b). Osteoid matrix may be subtly visible as small foci in the periphery of the lesion, but most of the lesion is hemorrhagic or necrotic, with multiple hemorrhagic fluid levels [33–36]. Identification of matrix precludes other differential diagnoses such as Ewing sarcoma, aneurysmal bone cyst, and lymphoma [36]. In the 40 patients with telangiectatic osteosarcoma analyzed by Murphey et al. [34], subtle radiographic findings included cortical interruption (78 %), soft tissue mass (19 %), and aggressive periosteal reaction (72 %).

Computed tomography: CT typically shows heterogeneous areas of low attenuation in the center of a soft tissue mass

Fig. 4.12 Eight year old girl with telangiectatic osteosarcoma of the distal femur. (**a**) AP and (**b**) lateral X-rays show an expansile lucent lesion and Codman triangle (*arrows*) indicating aggressiveness. Note cortical destruction, also a sign of aggressiveness. (**c**) T1W coronal MRI shows the expansile lesion invading the distal epiphysis. The bright foci within the tumor are likely due to blood products. (**d**) Coronal contrast-enhanced T1W MR image showing numerous rim enhancing cystic spaces typical of telangiectatic osteosarcoma. (**e**) T2W axial MR image shows numerous fluid-fluid levels (*arrows*) within cystic spaces

that replaces the normal medullary cavity. Cortical interruption and extension of the mass into the adjacent soft tissues is better visualized on CT than on plain films. In a retrospective CT study of 40 patients with telangiectatic osteosarcoma, fluid levels occurred in 48 % and osteoid matrix in 85 % of cases [34]. Post-contrast tumoral enhancement may be seen in the septa surrounding blood cavities. On CT, an intraosseous or soft-tissue osteoid matrix within nodular or septal regions helps distinguish telangiectatic osteosarcoma from aneurysmal bone cyst. Telangiectatic osteosarcoma is associated with aggressive growth features, i.e., cortical destruction and soft tissue extension. In contrast, aneurysmal bone cysts cause marked expansile remodeling of bone and cortical thinning but lack true soft tissue involvement [34].

Magnetic resonance imaging: MRI is the best modality to evaluate the soft-tissue component. Generally, telangiectatic osteosarcoma has heterogeneous signal intensity on both T1W and T2W images (Fig. 4.12c–e). T1W images show isointense or hyperintense signal to skeletal muscle [33, 36]. Low signal on T1W may represent calcifications. T2W images are ideal to demonstrate associated fluid levels. In a study by Murphey et al. fluid levels were more often detected by MRI (89 %) than CT and represented hemorrhage [34]. Postgadolinium-enhanced

images show peripheral nodular enhancement [36], which helps to distinguish this neoplasm from aneurysmal bone cyst, which has thin peripheral septa (usually 2–3 mm thickness) often seen as enhancing structures that lack nodularity.

Bone scintigraphy: The typical bone scintigraphic finding of telangiectatic osteosarcoma is the "doughnut sign," which is due to peripheral uptake in the solid portions of the lesion and central photopenic areas in the fluid components [34].

Pathologic features

The gross appearance of telangiectatic osteosarcoma is similar to aneurysmal bone cyst, with medullary based grossly apparent cysts containing blood and blood clots and lacking a fleshy or fibrotic component (Fig. 4.13). Histologically, the architectural resemblance to aneurysmal bone cyst is maintained, with fibrous septa of variable sizes surrounding zones of hemorrhage and blood clot. Septa are often lined by bland spindle and giant cells, but unlike aneurysmal bone cysts they usually contain conspicuous anaplastic, hyperchromatic, mitotically active, and markedly pleomorphic cells. These cells produce variable amounts of osteoid, often lace-like and limited in amount (Fig. 4.14a, b). Osteoclast-like giant cells may be numerous [18].

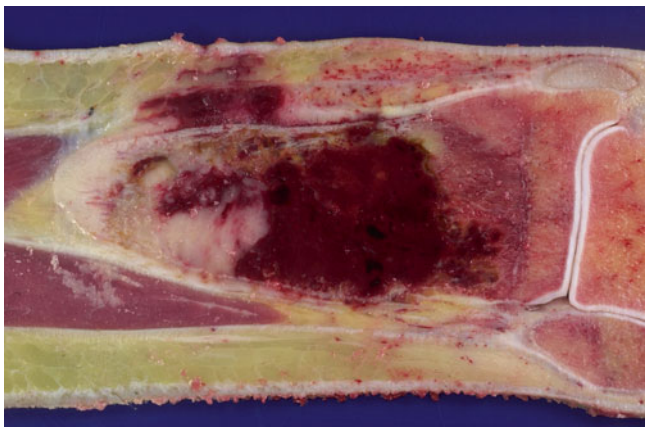

Fig. 4.13 Telangiectatic osteosarcoma arising in distal tibia. Tumor is extensively hemorrhagic and extends into soft tissue

Low-grade Central Osteosarcoma

Low-grade central osteosarcoma accounts for less than 2 % of osteosarcomas and has a favorable prognosis with complete surgical resection [37]. It only occurs in long bones. Histologically, it resembles parosteal osteosarcoma, with bony trabeculae separated by a hypocellular fibrous stroma containing minimally to moderately atypical spindle cells. Mitotic activity is always present but may be low. Cytologic atypia, infiltration, and permeation distinguish low-grade central osteosarcoma from benign processes such as fibrous dysplasia and chondromyxoid fibroma [37]. Few studies have investigated the molecular genetics of this rare neoplasm. In one study of six patients, comparative genomic hybridization showed recurrent gains at 12q13-14, showing genetic as well as histologic relatedness to parosteal osteosarcoma [38].

Parosteal Osteosarcoma

Surface osteosarcomas arise from the periosteum or cortex, with minimal or no involvement of the underlying medullary cavity. The three major types are parosteal osteosarcoma, periosteal osteosarcoma, and high grade surface osteosarcoma. Parosteal osteosarcoma is a low grade tumor that

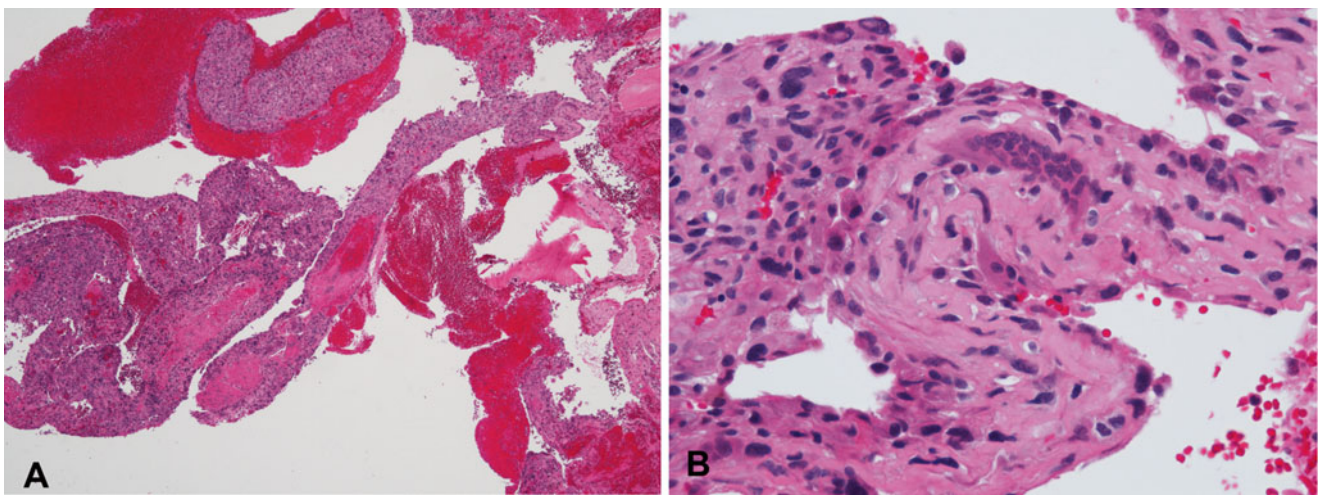

Fig. 4.14 Telangiectatic osteosarcoma. (**a**) Membranous septa admixed with blood. (**b**) Membranous septum with atypical tumor cells (*left*) and osteoclast-like giant cells (*right*)

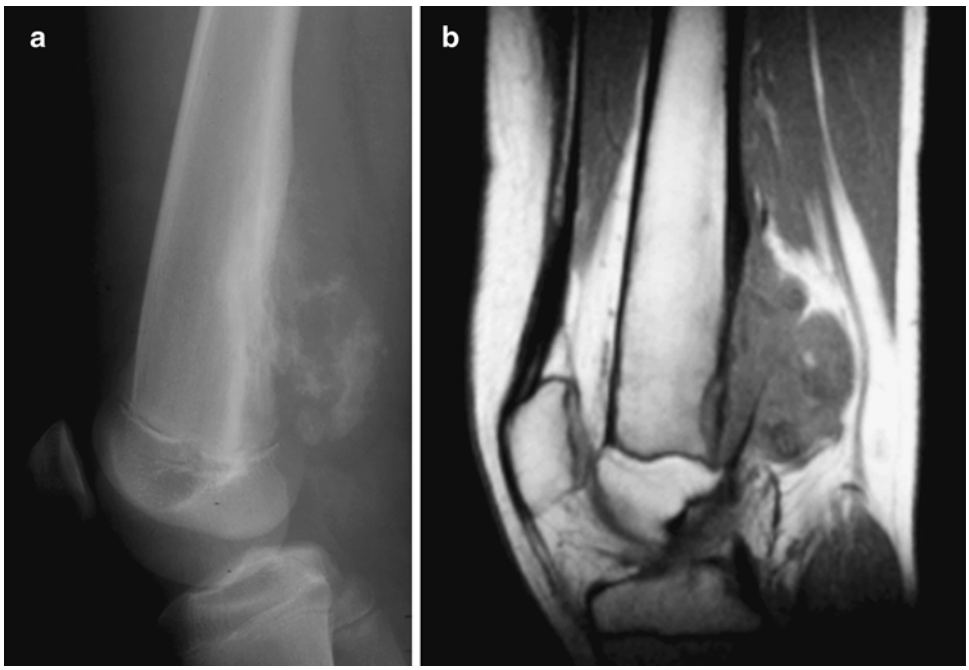

Fig. 4.15 Parosteal osteosarcoma of the distal right femur in a 14 year old boy. (**a**) Lateral radiograph demonstrates a lobulated, exophytic calcified soft-tissue mass arising from the surface of the distal femur. The radiographic appearance and anatomic location are typical of parosteal osteosarcoma. (**b**) Sagittal non-contrast-enhanced MR images shows the lobulated soft tissue mass causing cortical erosion and thickening without involvement of the medullary canal

accounts for 4 % of osteosarcomas in general but is rare in childhood. Most cases occur in young adults [39]. The most common site is the distal posterior femur, with occasional examples in other long bones. Origin in flat bones is exceptional. With total resection, the prognosis of these slow growing tumors is excellent, although there is a 10 % risk of distant metastatic disease [18]. Unlike conventional osteosarcoma, these tumors tend to be painless and usually only have symptoms of a mass or restriction of movement [18].

Imaging Features

Plain-film radiography: Parosteal osteosarcoma has an osseous fusiform configuration along the length of the bone. Its tendency to wrap around the bony circumference as it enlarges creates a cauliflower-like appearance contiguous with the cortical surface (Fig. 4.15a) [40, 41]. It may be separated from the underlying cortical bone by a radiolucent cleft. Cortical thickening without aggressive periosteal reaction may also be seen. The bone is more mature at the center of the lesion than the periphery.

Computed tomography: CT features mimic those of radiography but are more sensitive at identifying occasional soft tissue involvement. CT may also determine bone maturity at the center of lesion versus the periphery. Most parosteal osteosarcomas are low grade, but high grade foci may appear on CT or MRI as non-mineralized soft tissue components with or without fluid levels, measuring larger than 1 cm [40]. Such foci represent dedifferentiation into telangiectatic osteosarcoma, spindle cell sarcoma, or high-grade surface osteosarcoma, which have prognoses similar to that of conventional osteosarcoma.

Magnetic resonance imaging: MRI reveals a heterogeneous appearance with low-signal tumoral bone and high-signal peripheral soft tissue (Fig. 4.15b). Involvement of the cortex and marrow causes a high signal on fluid sensitive sequences and may enhance with contrast [15, 42].

99m Tc MDP scan: Elevated radiotracer activity within the tumor reflects the biological behavior of the tumor and may be valuable in detecting synchronous lesions or metastasis.

Radiographic differential diagnosis: Myositis ossificans has denser peripheral ossification than parosteal osteosarcoma and is not attached to the cortex. In addition, the bone in myositis ossificans is more mature at the periphery than the center. Continuity of cortex and marrow into the stalk of the osteochondroma differentiates it from parosteal osteosarcoma.

Pathologic and Genetic Features

Grossly, parosteal osteosarcomas form lobulated, hard masses fixed to the underlying cortex. A minor degree of marrow inva-

sion may be seen in up to 25 % of cases. Histologically, these tumors contain well formed parallel bony trabeculae immersed in a hypocellular, collagenous stroma (Fig. 4.16). These bony trabeculae mimic normal bone and sometimes have osteoblastic rimming. A cartilage cap may also be present, mimicking a sessile osteochondroma (Fig. 4.17). Unlike conventional osteosarcoma, stromal spindle cells show only minimal to moderate cytologic atypia, often with deceptively bland elongated nuclei and few mitoses. Up to one half of these tumors demonstrate cartilaginous differentiation. High grade spindle cell areas, referred to as dedifferentiation, occur in 15 % of cases. Dedifferentiation more commonly occurs in recurrent lesions and has a prognosis similar to conventional osteosarcoma [43].

Differential diagnosis includes low grade central osteosarcoma, osteochondroma, and parosteal osteoma. Central osteosarcomas have much greater medullary involvement. Cartilage caps are common in parosteal osteosarcomas, creating confusion with osteochondromas. However, osteochondromas lack the collagenous spindle cell stroma of parosteal osteosarcomas but instead resemble normal growing bone with fatty or hematopoietic marrow [18]. Correlation with imaging findings is imperative, as evidence of cortical-medullary continuity strongly favors osteochondroma. Parosteal osteomas occasionally involve the long bones, but unlike parosteal osteochondromas they lack spindle cell proliferation [44].

As opposed to conventional osteosarcomas, parosteal osteosarcomas do not display a wide variety of chromosomal gains and losses. Instead, the most common aberration is the presence of one or more supernumerary ring chromosomes, with amplification of 12q13-15 [39].

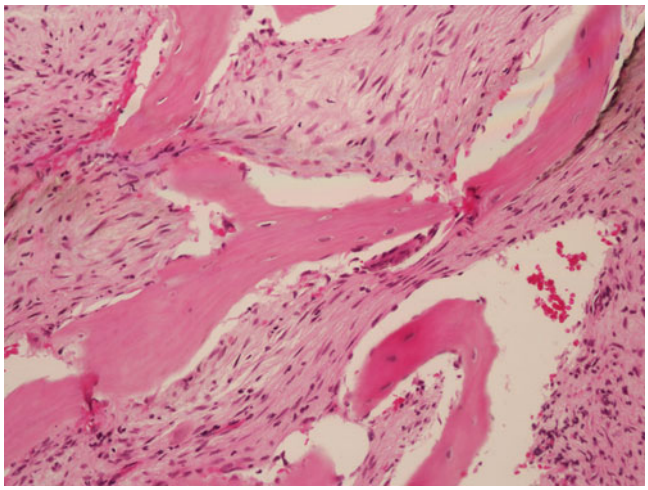

Fig. 4.16 Parosteal osteosarcoma. Parallel oriented trabeculae of woven bone lacking osteoblastic rimming, with a moderately cellular fibrotic background

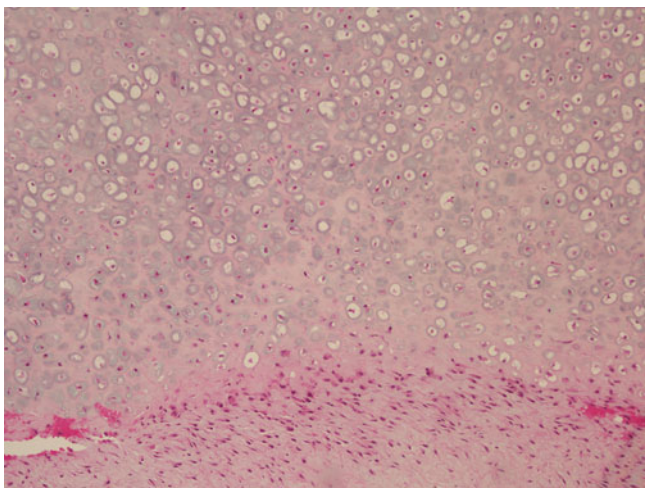

Fig. 4.17 Parosteal osteosarcoma. This section of peripheral cartilaginous cap consists of thick, low grade atypical cartilage

Periosteal Osteosarcoma

Periosteal osteosarcoma is an intermediate grade surface osteosarcoma characterized by its mainly cartilaginous matrix. Less common than parosteal osteosarcoma, it accounts for fewer than 2 % of all osteosarcomas. Most cases occur in adolescents and young adults. The metaphyseal–

Fig. 4.18 Periosteal osteosarcoma of the distal tibial diaphysis in a 15 year old male. (**a**) Lateral radiographic view of the distal tibia showing a broad based mass causing erosion of the thickened tibial diaphyseal cortex. (**b**) T1W fat-saturated post contrast MRI image shows the thickened cortex to be hypointense. There is some enhancement of the soft tissue component and a sunburst type periosteal pattern is present. No intramedullary extension of the tumor is seen

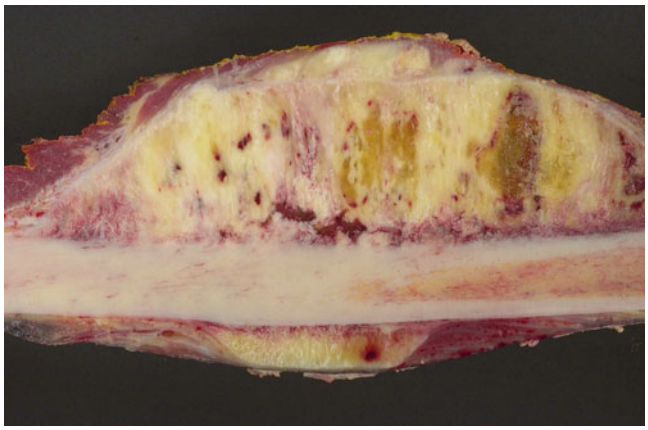

Fig. 4.19 Periosteal osteosarcoma. Bisected femoral shaft demonstrating surface location and sunburst appearance

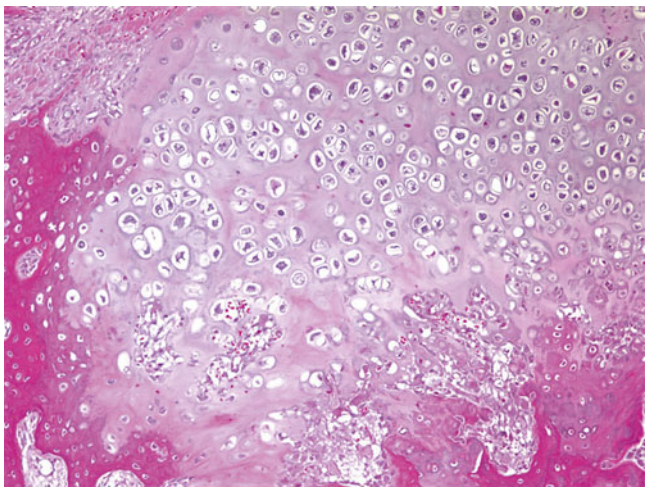

Fig. 4.20 Periosteal osteosarcoma. Lobule of malignant cartilage with associated bone formation

diaphyseal regions of long bones such as the tibia and femur are most commonly involved [45], but involvement of the flat bones is rare. Disease-free survival after adequate treatment is >80 %, with most recurrences and deaths occurring within 3 years of diagnosis [46].

Imaging Features

Plain-film radiography: Periosteal osteosarcoma forms a broad-based soft tissue mass causing extrinsic erosion of a thickened underlying diaphyseal cortex. A perpendicular sunburst-type periosteal reaction extends into the soft tissue component, typically without intramedullary involvement (Fig. 4.18a) [47]. The zoning pattern is typical of surface osteosarcoma, with more mature and organized bone at the center than the periphery. The cortex appears variegated and may be thickened, scalloped, or irregular and permeative. There is no true aggressive periosteal reaction, but cortical thickening may resemble the periosteal elevation of Codman's triangle. Because these lesions are chondroblastic, matrix ossification is not prominent [47].

Computed tomography: CT findings mimic radiographic ones, although CT better delineates cartilaginous areas, soft tissue involvement, and zoning of bone maturity. Perpendicular periosteal reaction forms low-attenuation rays.

Magnetic resonance imaging: MRI is useful in evaluating the true extent of the tumor. Cartilage and cortex appear as low signal on T1W and as high signal on T2W sequences (Fig. 4.18b). Low-signal osteoid matrix appears as rays perpendicular to the cortex. High signal contrast enhancement of the cortex or the marrow indicates tumoral involvement of these regions [47].

Pathologic Findings

Grossly, periosteal osteosarcoma arises from the bony surface as a fusiform or rounded mass that may partly or entirely involve the circumference (Fig. 4.19). A sunburst appearance results from calcified spicules that arise from the cortical surface. Glistening white-gray cartilaginous differentiation is usually prominent. Histologically, chondroblastic areas predominate and contain anaplastic spindle cells with focal enchondral ossification (Fig. 4.20) unlike periosteal chondroma. Diagnostic tumoral osteoid must be present but may be relatively inconspicuous, similar to intermediate grade chondroblastic osteosarcoma. The juxtacortical portion of the tumor is usually densely ossified. Whether or not tumor can extend into the underlying medullary cavity is controversial. Some contend it is common [45], while others feel that medullary involvement indicates conventional chondroblastic osteosarcoma with cortical destruction and periosteal spread [46]. The evidence suggests that predominantly surface chondroblastic osteosarcomas with medullary involvement show more aggressive clinical behavior [45].

High-Grade Surface Osteosarcoma

High grade surface osteosarcoma is a high grade osteosarcoma arising from the surface of the bone. Extremely rare (<1 % of all osteosarcomas), it has the clinical presentation, demographic distribution, and prognosis of conventional osteosarcoma. The most common site of involvement is the midshaft of the femur [48].

Imaging Features

Plain-film radiography: High-grade surface osteosarcoma appears as an osteoid matrix present in a soft tissue mass. Distortion of fat planes around the soft tissue mass and scalloping or permeative destruction of the underlying cortex may occur [15, 49]. Periosteal reaction is common and tends to be aggressive. High grade surface osteosarcomas typically involve the entire circumference of the bone and may involve the medullary canal.

Computed tomography: CT findings mimic radiographic ones and improve visualization of the osteoid matrix and soft tissue involvement.

Magnetic resonance imaging: MRI shows a soft tissue mass containing variable amounts of low-signal osteoid matrix, giving an overall inhomogeneous signal on fluid-sensitive sequences. Periosteal reaction and surrounding edema in the adjacent cortex are visible. Soft tissue enhances avidly on contrast administration.

Pathologic findings

Grossly, high grade surface osteosarcomas are attached to the underlying cortex and frequently have a variegated appearance imparted by intermixed zones of hard matrix production and softer hemorrhage and necrosis. The latter soft areas are not typical of lower grade surface tumors [50]. Histologically, these tumors are indistinguishable from conventional osteosarcomas and have chondroblastic, fibroblastic, and osteoblastic variants [48, 51]. If significant medullary involvement is present, there is a possibility that the lesion originated from a conventional osteosarcoma that broke through the cortex and developed a dominant surface mass. However, both are high grade lesions treated in a similar fashion.

Ewing Sarcoma

Ewing sarcoma (ES) is the second most common primary malignancy of bone in childhood. Although first described as a primary undifferentiated bone tumor, it also occurs in soft tissue and may exhibit variable degrees of neuroectodermal differentiation, designated "primitive neuroectodermal tumor" (PNET). Ewing sarcomas and PNETs involving either bone or soft tissue share identical recurrent translocations. No longer biologically distinct, these entities have now been subsumed into the category of "Ewing's sarcoma family of tumors" (ESFT's) [52]. ESFTs are most common in whites, rare in African and African-American children, and slightly more common in males than females [53]. They most commonly affect adolescents but occur at any age, even infancy [54]. Usually they arise from the diaphysis of long bones or the pelvis, but any bone can be involved. [55]. ESFTs are clinically aggressive, and prior to the advent of chemotherapy nearly all patients died of their disease. With current treatment regimens, the overall survival of patients with localized disease is 75 %. However, one quarter of patients have metastatic disease at diagnosis and a poor prognosis [56]. Tumors commonly metastasize to lung; other sites include bone marrow and other bones. Although pain with or without pathologic fracture is the most common presenting symptom, patients may show signs and symptoms mimicking infection [55].

Imaging Features

Plain-film radiography: The tumor originates in the medullary cavity, invades the Haversian system, and extends into the subperiosteal areas (Fig. 4.21a). In a study of 64 patients with Ewing sarcoma (ES), Peersman et al. found that a mixed sclerotic-lytic pattern of permeative lytic cortical destruction and a wide zone of transition were the most common patterns (40 %) [57]. Reinus et al. found cortical thickening in 58 of 274 (21 %) patients with ES [58]. Cortical violation and a soft tissue mass are frequently seen. Extension into the subperiosteal region can cause an aggressive lamellated or sunburst periosteal reaction and a Codman's triangle. The tumor cannot produce new bone or cartilaginous matrix, but reactive bone is formed. Soft tissue extension of the tumor will not contain bone [59, 60].

Computed Tomography: CT shows cortical disruption and soft tissue extension more clearly than plain films. Chest CT is important to detect lung metastases [61].

Magnetic resonance imaging: MRI is more sensitive than CT in detecting bone marrow and soft tissue infiltration, and aids in pinpointing the site for bone biopsy [57, 62]. MRI can show cortical tumoral involvement because of its prolonged T1 and T2 relaxation times [57]. MRI also shows skip lesions. The tumor appears isointense or hypointense to skeletal muscle on T1W images and homogenously hyperintense on T2W images (Fig. 4.21b). Reactive bone may form areas of low signal within the marrow. Any associated marrow or soft tissue edema or periosteal reaction appears as a high signal on STIR sequences (Fig. 4.21c). Post-contrast images show avid but inhomogeneous enhancement (Fig. 4.21d). Low signal central areas within the tumor may represent necrosis. Dynamic contrast enhanced MRI or diffusion-weighted MRI may indicate the extent of tumor necrosis [63]. MRI is also used for restaging and evaluating response to treatment. Signs of response to therapy include a decrease in tumor size, maturation of the periosteal reaction, and bony sclerosis [63].

Fig. 4.21 Ten year old boy with Ewing sarcoma of the ulna. (**a**) AP radiograph shows a permeative, medullary process with wide zone of transition in the proximal and mid ulna. Note the lamellar, irregular, periosteal reaction (*arrows*) typical of Ewing sarcoma. (**b**) Coronal TIW MR image demonstrates the medullary tumor as hypointense to muscle (*arrow*). (**c**) On STIR MR imaging the tumor is hyperintense and the soft tissue component (a typical feature of Ewing sarcoma) is evident (*arrow*). (**d**) Post-contrast axial MR image shows moderate enhancement of the medullary and soft-tissue components of the tumor

Positron emission tomography: An increased rate of glycolysis in ES causes increased FDG avidity, thereby facilitating tumor detection and making the biologically active tumor more conspicuous than the surrounding tissue. Hawkins et al. [64] found that the mean standardized uptake value (SUV) for ES was approximately 5.3 ($n = 14$). The SUV of ES, both before and after neoadjuvant therapy, predicts patient outcome [64–67]. In addition, qualitative evaluation of FDG accumulation within a large heterogeneous tumor helps identify active areas most suitable for targeted biopsies.

FDG PET is used in staging ES, as it is more sensitive than a bone scan (88 % vs. 37 %) for detecting bone marrow disease and the osteoclast-mediated response to osseous metastasis [65]. As biochemical changes in the tumor precede morphological changes [57, 68], PET-CT can often indicate tumoral regression or progression earlier than CT and MRI. Also, FDG PET is superior to bone scintigraphy in assessing the chemotherapy response of bone metastases [66].

Bone scintigraphy: Scintigraphy with ^{99m}Tc-MDP shows increased uptake on a three-phase bone scan (angiographic, blood pool, and delayed). However, bone scan can miss very small degrees of metastasis or bone marrow disease and is not sensitive enough to detect the local extent of disease or skip metastasis. Metastases appear as scattered foci of increased uptake in axial skeleton with red marrow. Photopenic foci due to necrosis often occur with aggressive lesions.

Pathologic Features and Differential Diagnosis

As with osteosarcoma, gross specimens of Ewing sarcoma are generally altered by presurgical treatment. Although the

Fig. 4.22 Ewing sarcoma. (**a**) Bisected humerus with diaphyseal tumor and soft tissue extension. (**b**) Chest wall resection and right lung lobectomy (fixed and post-treatment) with extensively hemorrhagic and necrotic tumor. This case demonstrates the inherent difficulty in determining origin from a rib or from the adjacent soft tissues of the chest wall

tumor may be localized to bone, invasion into surrounding soft tissues is frequent and often massive, masking exact origin of tumor from soft tissue or bone (particularly those in chest wall) (Fig. 4.22). By mapping slab grids of decalcified tumor similar to osteosarcoma, chemosensitivity can be evaluated and correlates with patient outcome [69, 70]. However, the inherent subjectivity in such assessments is magnified by the tendency of Ewing tumor beds to shrink as a response to treatment. Unlike osteosarcomas, Ewing sarcomas do not leave behind devitalized matrix, so that determining tumor boundaries for evaluating tumor necrosis can be quite difficult, raising questions as to the reproducibility of such efforts.

Histologically, Ewing sarcoma can be considered the prototype of the "small round blue cell tumor" of childhood. The classic microscopic appearance is of non-matrix producing sheets of uniform undifferentiated small cells with no particular architectural pattern except for occasional rosettes (Fig. 4.23a–d). The typical Ewing sarcoma cell is small (diameter less than twice that of an endothelial cell) and round to oval with minimal to no spindling. It has a high nuclear to cytoplasmic ratio with relatively little cytoplasm and a nucleus with powdery to finely dispersed chromatin. Nucleoli are usually not prominent. Cytoplasm may be cleared or eosinophilic. Most tumors contain cytoplasmic glycogen demonstrable with periodic acid-Schiff (PAS) stains, historically part of the routine diagnostic workup. However, a few lack stainable cytoplasmic glycogen, and many non-Ewing sarcomas contain it. Cytologic pleomorphism is usually minimal, and mitotic activity can be variable. Indeed, many of these tumors display surprisingly low mitotic rates, considering their aggressiveness. Commonly, scanning discloses a mixture of so-called "light" and "dark" cells. The dark cells possibly represent effete cells undergoing degenerative changes and having more hyperchromatic and dense nuclei (Fig. 4.24). Extensive necrosis is not unusual in pre-treatment biopsies.

Although the great majority of Ewing sarcomas have "classic" features, variations may cause diagnostic uncertainty (Fig. 4.25a–c). "Adamantinoma-like" Ewing sarcomas display a nested growth pattern with desmoplasia and peripheral palisading akin to true adamantinomas and accounted for 5 % of ESFT in one large series. Rare cases with abundant matrix (sclerosing pattern), extensive spindling reminiscent of synovial sarcoma (spindle cell sarcoma-like pattern), and high mitotic activity, more pleomorphism, nuclear enlargement, and prominent nucleoli (atypical Ewing sarcoma) were also encountered [71]. CD99- and translocation-positive cases with rhabdoid-like, epithelioid, or hemangioendotheliomatous features also occur [72, 73]. These rare cases broaden the morphologic spectrum of Ewing sarcomas and underscore the importance of molecular testing for Ewing associated fusions, but to date have bestowed no prognostic significance [52].

Immunohistochemically, the vast majority of Ewing sarcomas express cytoplasmic vimentin and caveolin-1 and membranous CD99 (Fig. 4.26) [74]. CD99 is highly sensitive but lacks specificity, as it is also expressed in lymphomas and some rhabdomyosarcomas, mesenchymal chondrosarcomas, rhabdoid tumors, and synovial sarcomas. Nuclear or granular cytoplasmic CD99 expression does not support a diagnosis of Ewing sarcoma. Most (75–91 %) Ewing sarcomas express nuclear FLI-1 [71, 75], a finding that is also not entirely specific and seen in some lymphomas. Up to 20 % of Ewing sarcomas display focal cytokeratin positivity [76], and rare cases with epithelial membrane antigen and desmin positivity have been described [77]. Neuronal markers such as neuron-specific enolase (NSE), synaptophysin, CD56, S-100, and neurofilament protein are variably positive, especially in PNET.

Ultrastructurally, Ewing sarcoma cells appear undifferentiated, contain few organelles, and show abundant cytoplasmic glycogen. Dense core neurosecretory granules and dendritic processes are occasional, especially in PNET. Unlike lymphomas, Ewing sarcoma cells contain primitive intercellular junctions [55]. This can be a helpful cytological feature, as intraoperative touch imprints typically contain cohesive cells in a clean background and differ from the singly dispersed cells and lymphoglandular bodies of lymphomas.

Given the undifferentiated nature of Ewing sarcoma, differential diagnosis with other undifferentiated malignan-

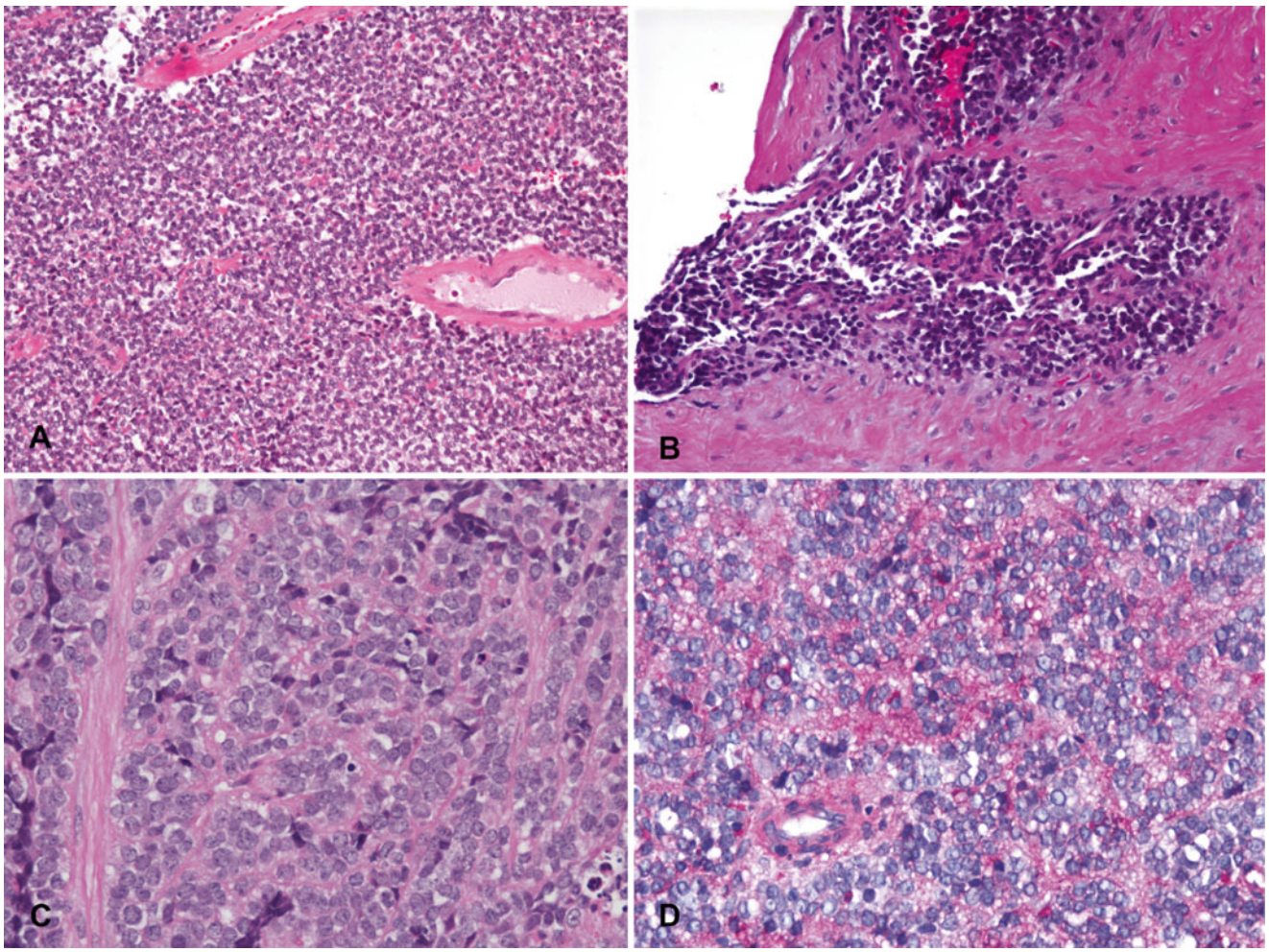

Fig. 4.23 Ewing sarcoma. (**a**) Typical appearance of sheets of undifferentiated "small round blue cells" with no particular architectural pattern. (**b**) Invasion into surrounding soft tissue. (**c**) Typical cytologic features of monotonous round cells with fine chromatin, inconspicuous nucleoli and sparse cytoplasm. (**d**) PAS stain demonstrating abundant cytoplasmic glycogen

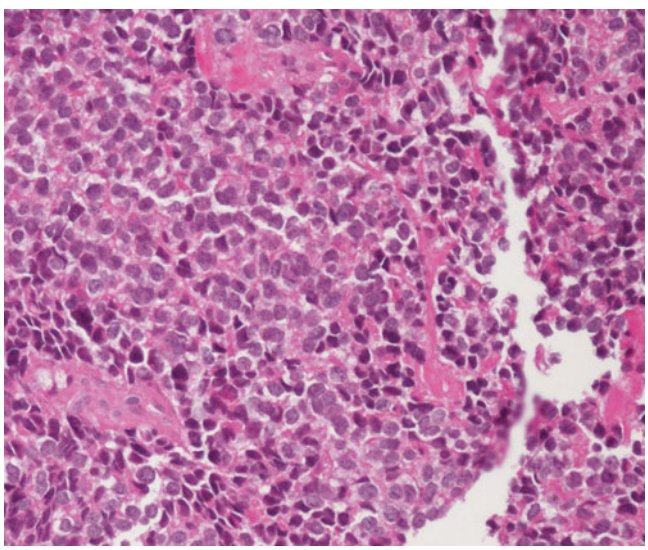

Fig. 4.24 Ewing sarcoma. The lesion contains alternating "light" and "dark" cells

cies can be challenging and requires judicious application of ancillary techniques. Particularly challenging is its distinction from lymphoblastic lymphoma of bone, metastatic undifferentiated neuroblastoma, metastatic rhabdomyosarcoma, small cell osteosarcoma, and mesenchymal chondrosarcoma. Both Ewing sarcoma and lymphoblastic lymphoma may display perimembranous CD99 positivity and lack CD45 staining, but lymphoblastic lymphoma can be diagnosed by its expression of TdT and more general markers of B- or T-cell lineage. When enough fresh tissue is available, flow cytometry can be very helpful. Small cell osteosarcoma must be diagnosed if tumoral osteoid is present. A recent report suggests that small cell osteosarcomas and mesenchymal chondrosarcomas are negative for FLI-1 [75]. In general, tumors that lack strong perimembranous staining for CD99 should not be considered Ewing sarcoma in the absence of confirmatory molecular data, as only 1 % of proven Ewing sarcomas have been found to lack it [72]. CD99 staining is particularly helpful in ruling out meta-

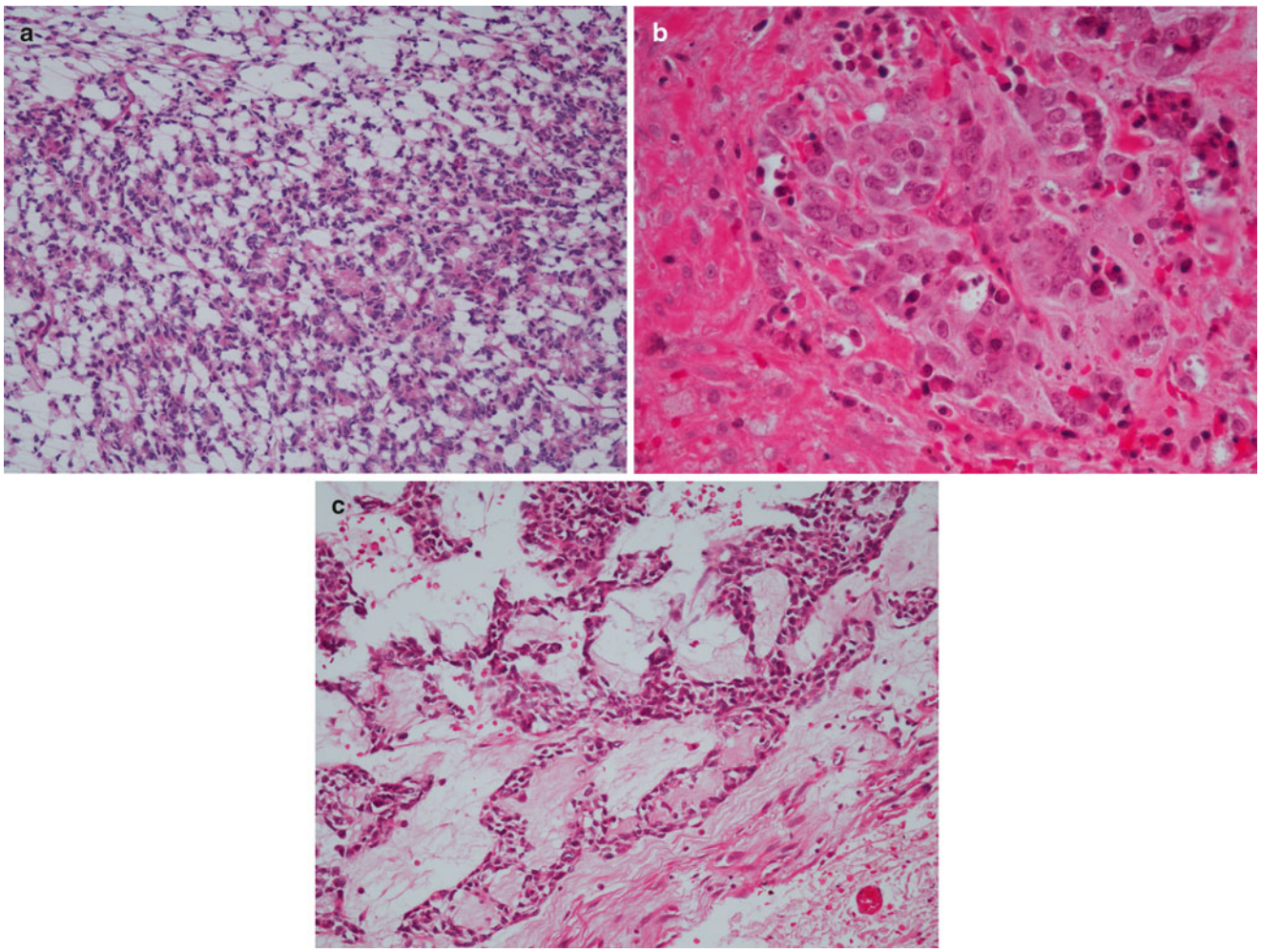

Fig. 4.25 Ewing sarcoma histologic variants. (**a**) Primitive neuroectodermal tumor pattern with neuroepithelial rosettes. (**b**) Large cell variant. (**c**) Adamantinoma-like variant

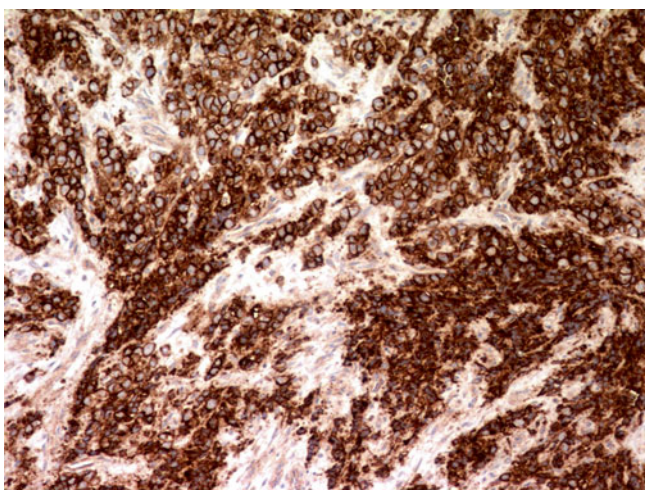

Fig. 4.26 Ewing sarcoma. Immunohistochemistry for CD99 displays strong and uniform perimembranous staining

static neuroblastoma, as neuroblastomas should be negative, and likewise myogenin can be used to exclude metastatic rhabdomyosarcoma, as Ewing sarcoma does not express that antigen. Unlike neuroblastoma and rhabdomyosarcoma, Ewing sarcoma is typically (but not always) CD56-negative [78, 79].

Diagnostic molecular genetics: The great majority of Ewing sarcomas harbor *EWSR1* translocations, which can be demonstrated with both fluorescence in situ hybridization (FISH) and reverse transcription-polymerase chain reaction (RT-PCR) [80]. FISH has become more commonly used than RT-PCR, as it is widely available, applicable to paraffin embedded formalin fixed tissue, and does not require specific primers for each possible translocation partner. This is of particular importance in Ewing sarcoma, as it has the greatest variety of fusion patterns of any translocation-associated pediatric sarcoma [81].

The most common Ewing sarcoma translocation is t(11;22)(q24;q12), which involves the *EWSR1* gene on chromosome 22 and the *FLI1* gene on chromosome 11 and is present in approximately 85–90 %. *FLI1* is a highly regulated, lineage-restricted member of the ETS family of transcription factors [82]. Breakpoints vary among the four introns of *EWSR1* and the six introns of *FLI1*, resulting in variably sized fusion transcripts, a factor to be considered when interpreting RT-PCR [83]. Most commonly *EWSR1* exon 7 fuses to *FLI1* exon 6 and is designated Type 1, followed by fusion of *EWSR1* exon 7 to *FLI1* exon 5, designated Type 2. Although previous retrospective studies indicated that type 1 fusions bestowed a better prognosis than Type 2 fusions, recent experience suggests a similar outcome regardless of fusion subtype[84–86]. Approximately 5–10 % of ES carry the second most common translocation, t(21;22), in which *EWSR1* fuses with *ERG*. *ERG* is also in the ETS family of transcription factors and is closely related to *FLI1*. An impressive number of uncommon *EWSR1* translocations to other ETS transcription family members has also been described, including: t(2;22) which fuses *EWSR1* to *FEV*, t(7;22) which fuses *EWSR1* to *ETV1*, and t(17;22) which fuses *EWSR1* to *E1AF*. In addition to *EWSR1* fusions, rare Ewing sarcoma translocations involve the *FUS* gene on chromosome 16 (*FUS-ERG* and *FUS-FEV*) [87, 88]. *EWSR1* has been described as a fusion partner with non-ETS genes such as *SP3*, *ZNF278*, and *POU5F1* [82, 83]. Small cell undifferentiated tumors that do not express CD99 may have gene fusions that do not involve EWSR1, and their relatedness to ES is unclear. All told, variant fusions (i.e., neither *EWSR1-FLI1* nor *EWSR1-ERG*) account for up to 4–9 % of cases histologically defined as Ewing sarcoma [83].

Since cryptic fusions involving *EWSR1* may not be always detected by FISH, many investigators recommend both FISH and RT-PCR [89]. However, it is clearly impracticable to test for all possible fusion combinations by RT-PCR. Since there are many variant fusions not detectable by standard molecular diagnostic methods, negative molecular testing does not necessarily rule out the diagnosis of Ewing sarcoma if the tumor otherwise has a typical phenotype. In such cases, when other diagnostic entities have been excluded, some experts recommend a diagnosis of "undifferentiated round cell sarcoma with features of Ewing sarcoma/PNET" [74], but soft tissue lesions of this type are being treated as non-Ewing sarcomas by COG. Positive break apart FISH for *EWSR1* must also be interpreted cautiously and in the context of other clinical and pathologic data, as other tumors, such as desmoplastic small round cell tumor, clear cell sarcoma, extraskeletal myxoid chondrosarcoma, myxoid liposarcoma, and angiomatoid fibrous histiocytoma, harbor *EWSR1* fusions.

Chondrosarcoma

Malignant bone tumors of cartilaginous origin are rare in childhood; the majority of pediatric chondroid malignancies are chondroblastic osteosarcomas. Pediatric chondrosarcoma does occur, with some cases arising de novo and others with syndromic multiple hereditary exostoses (MHE) or Ollier's disease. The rate of malignant transformation in MHE is estimated to be as great as 5–28 %; with the higher figures likely due to selection bias at tertiary centers with more problematic cases. Malignant sporadic osteochondromas are considerably rarer. The most common site for chondrosarcoma in children is the femur, followed by the pelvis, humerus, and head and neck [90]; approximately 90 % of affected children are 10 years of age or older.

Mesenchymal chondrosarcoma is the most common intraosseous chondrosarcoma in children. Common locations include the craniofacial bones (up to 50 %), ribs and chest wall, sacrum and spine, and lower extremities [91]. They also arise in extraosseous locations, including the meninges. The tumor is highly malignant, with a poorer prognosis than conventional chondrosarcoma. The clinical course is often prolonged, local recurrence is common, and distant metastases may occur decades after initial diagnosis [92]. The overall survival at 10 years has ranged from 21 to 67 % [91]. Although radical surgery with the goal of obtaining clear margins is the mainstay of treatment, adjuvant chemotherapy is also commonly employed [91].

Clear cell chondrosarcoma, which favors the proximal humeral and femoral epiphyses, affects a younger age group (ages 25–50) than conventional chondrosarcoma, but is still quite rare in childhood [93].

Imaging Features

Plain-film radiography: Chondrosarcoma appears as a geographic, expansile, lytic mass with cortical and endosteal thinning and scalloping (Fig. 4.27a). Typically, there is no periosteal reaction, sclerotic margin, or cortical breakthrough. Matrix calcification is typically amorphous or has a ring-and-arc pattern characteristic of calcified chondroid. It is seen in 60 %–78 % of lesions [94–96].

Computed tomography: For detecting chondroid matrix calcifications and the depth of cortical or endosteal scalloping (Fig. 4.27b, c) [95, 96], CT outperforms plane radiography.

Magnetic resonance imaging: Chondrosarcoma is often heterogeneous on MRI, with an overall low signal on T1W images and a low to intermediate signal on T2W images (Fig. 4.27d) representing focal chondroid calcification, cys-

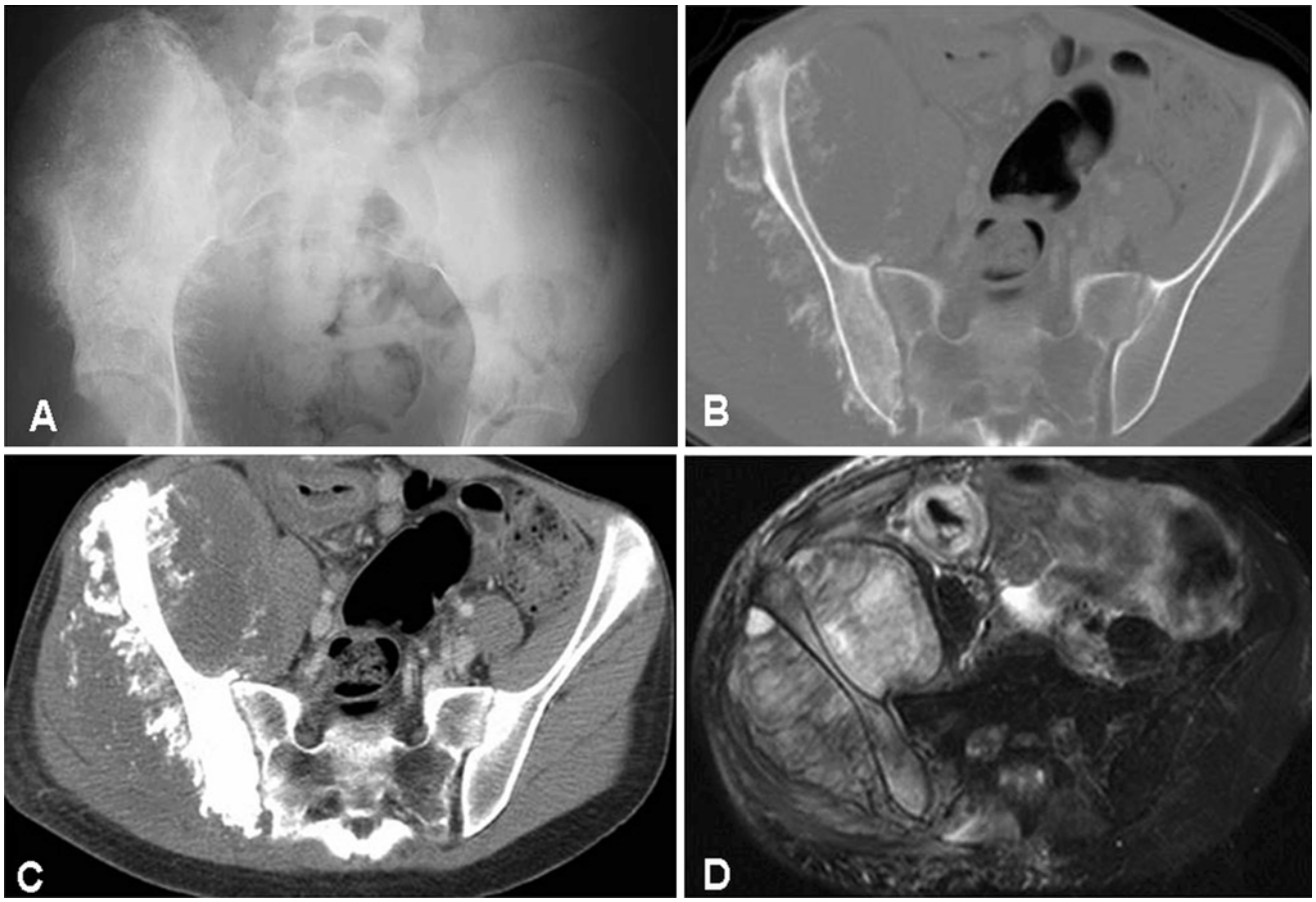

Fig. 4.27 Conventional chondrosarcoma of the right iliac bone of a 15 year old female. (**a**) Frontal radiograph of the pelvis shows soft tissue calcification surrounding the sclerotic appearing right iliac bone. (**b**) Axial CT image through the pelvis in the bone algorithm showing chondroid matrix in a large, ill defined soft tissue mass centered around the right iliac bone. (**c**) Axial CT image through the pelvis in the soft tissue algorithm demonstrates the soft-tissue component to better advantage. (**d**) Axial T2W MRI image shows a large heterogenous mass with mixed intensity. Note that underlying cortex is intact

tic changes, and intratumoral hemorrhage [93]. MRI identified a soft tissue mass in 25 of 33 chondrosarcoma patients in one study [94]. Post-contrast T1W fat-saturated sequences appear variable, depending on tumor grade. Low-grade lesions show peripheral and septal enhancement around lobulated cartilage, with a few areas of peripheral contrast puddling. High-grade lesions have a more generalized enhancement around central areas of necrosis [97].

Positron emission tomography: ^{18}FDG-PET uptake in chondrosarcoma depends upon tumor grade; it is highest in grade III and lowest in grade I tumors. Tumor SUV was 3.38 ± 1.61 for grade I ($n = 15$), 5.44 ± 3.06 for grade II ($n = 13$), and 7.10 ± 2.61 for grade III ($n = 3$) in the Brenner et al. study [98]. PET cannot differentiate between benign or low grade malignant cartilaginous tumors. High pretreatment SUV predicts a high-grade chondrosarcoma and helps to optimize the biopsy approach. FDG PEt also helps to stage and assess treatment response. PET sensitively detects high-grade lung metastasis, but it is relatively insensitive for low-grade metastasis [98].

Bone scintigraphy: ^{99m}Tc bone scintigraphy reflects the increased physiological activity of conventional chondrosarcoma and appears as heterogenous uptake, greater than that seen in enchondroma [94].

Radiologic differential diagnosis: In pediatrics, the major differential diagnosis for chondrosarcoma is an enchondroma, which is centrally located within the metaphyses and also produces endosteal scalloping and chondroid matrix calcifications.

Clear cell chondrosarcoma appears as a well-marginated lytic lesion that may contain a chondroid matrix and has an appearance strikingly similar to chondroblastoma [93]. However, chondroblastoma is more common in a younger age group, before the closure of physeal plates.

Mesenchymal chondrosarcoma contains two distinct components: a well-differentiated cartilaginous and a high-grade noncartilaginous component. CT, radiographs, and MRI of the cartilaginous component may resemble enchondroma or low-grade chondrosarcoma, with a lobulated, highly intense signal typical of cartilage, whereas the non-

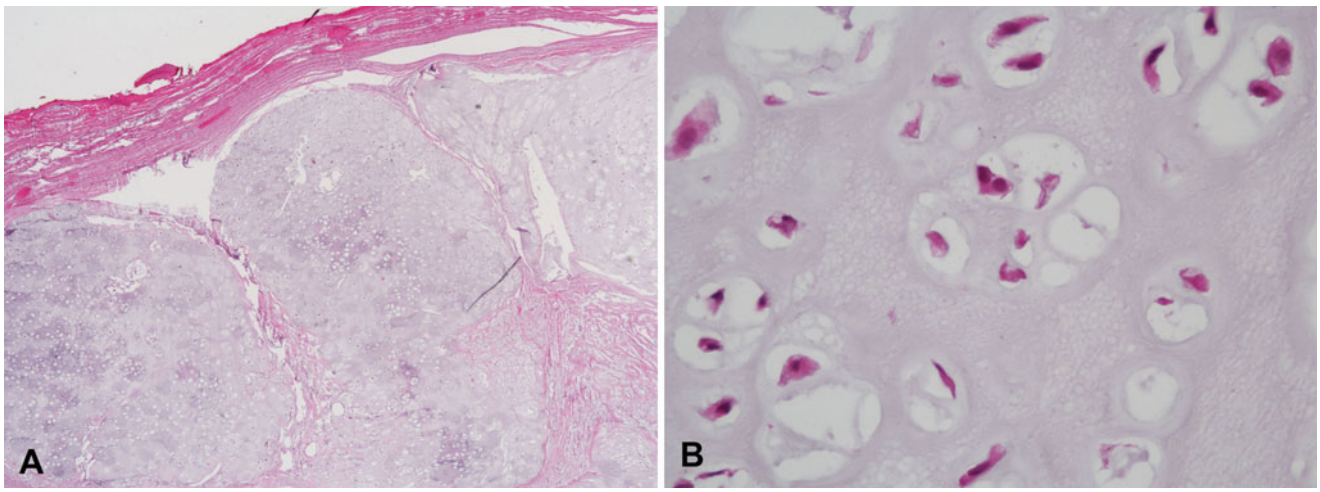

Fig. 4.28 Chondrosarcoma. (**a**) Conventional low grade chondrosarcoma arising from the rib in a patient with multiple hereditary exostoses. (**b**) High power photomicrograph demonstrating mild cytologic atypia. Radiographic correlation would be necessary to differentiate this tumor from a benign osteochondroma

chondroid component appears dark on all sequences. There is peripheral contrast enhancement of the tumor, with pudding in some nodular regions. MRI of the noncartilaginous component may depict a soft tissue mass without any matrix, in some cases with osseous invasion. The soft tissue appears inhomogeneously T1W hypointense and heterogeneously hyperintense on fluid-sensitive sequences.

Pathologic and Molecular Genetic Features

Conventional adult-type chondrosarcoma (Fig. 4.28a, b) usually occurs as a low to intermediate grade tumor containing cartilage with increased cellularity, entrapped bone, mucoid/myxoid degenerative changes, and chondrocytes with open chromatin [99]. However, these features do not reliably distinguish pediatric chondrosarcomas from cellular enchondromas (which are much more common), or peripheral chondrosarcomas from the cartilaginous caps of osteochondromas, particularly in the setting of MHE [100]. Although nuclear pleomorphism and mitotic activity are consistent with high grade adult chondrosarcoma, these features are not present in the lower grade malignancies more likely seen in children. Correlation with clinical and radiographic features is therefore critical for diagnosis. Histologic features shared by low grade chondrosarcomas and benign osteochondromatous cartilage caps include nodularity, cystic changes, irregular calcifications and even necrosis [100]. Measuring of the thickness of the cartilaginous caps of osteochondromas, both radiographically and pathologically, is used as a criterion to determine the biologic potential of a lesion, with thicknesses greater than 2 cm highly associated with malignant transformation.

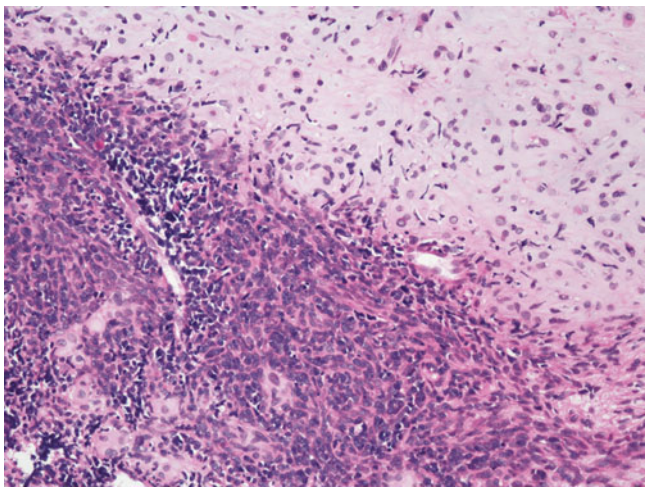

Fig. 4.29 Mesenchymal chondrosarcoma. Note sharp demarcation between undifferentiated small round cell component and mature cartilaginous component

Mesenchymal chondrosarcoma histologically shows a biphasic appearance, with islands of well differentiated cartilage alternating with sheets of undifferentiated small round or spindled cells [91]. Usually the demarcation between the two elements is abrupt; however, in some cases they are intermingled (Fig. 4.29). Hemangiopericytoma-like areas and foci of ossification, osteoid, osteoclastic giant cells, and calcification may be present. Myxoid zones, with cords of tumor cells often in "Indian-file" arrangement, may also be seen. Mitotic activity is typically low.

Immunohistochemically, mesenchymal chondrosarcoma typically expresses vimentin and usually expresses CD99 (two-thirds of cases). The cartilaginous portions stain with S-100 in 82 % of cases [91]. Small biopsies that contain only the undif-

ferentiated small or spindle cell population mimic other small round blue cell tumors, many of which may be CD99-positive. Negative FLI1 staining is helpful to rule out Ewing sarcoma [75]. Immunohistochemical staining for Sox9, a master regulator of cartilage development may also have application for this purpose. Nearly all (95 %) mesenchymal chondrosarcomas display nuclear Sox9 positivity in both the undifferentiated and cartilaginous components [101, 102], whereas it is negative in Ewing sarcomas, lymphoblastic lymphomas, diffuse large B cell lymphomas, and small cell osteosarcomas.

Until recently molecular genetic data for mesenchymal chondrosarcomas has been limited and variable. The translocation der(13;21)(q10;q10) has been noted in two tumors [103], but it is unclear whether this is characteristic. A recurrent fusion of the *HEY* and *NCO2* genes was recently detected by genome wide screening of mesenchymal chondrosarcomas [104]. It was found in all tested mesenchymal chondrosarcomas and in no other chondrosarcoma types or other sarcomas.

Clear cell chondrosarcoma contains large cells with distinct cytoplasmic membranes, abundant clear to faintly granular cytoplasm, and central round nuclei with prominent nucleoli. Mitoses are rare. The tumor has a lobulated architectural arrangement with variable amounts of hyaline cartilage, osteoid, and woven bone. Aneurysmal bone cyst-like areas and foci of conventional chondrosarcoma may be present. Given its usual epiphyseal location, it may be confused with chondroblastoma. This can be a difficult pathological diagnosis. Smaller cells with limited amounts of cytoplasm and grooved nuclei (as opposed to centrally located hyperchromatic nuclei with prominent nucleoli) favor a diagnosis of chondroblastoma. Significant amounts of reactive bone formation are not a feature of chondroblastoma [105].

Primary Lymphoma of Bone

Primary lymphoma of bone is unusual compared to other primary bone tumors. In adults, approximately 7 % of all malignant bone tumors are lymphomas [106]; however the percentage in children is likely lower, given the frequency of pediatric Ewing sarcoma and osteosarcoma. For all intents and purposes, the term "primary lymphoma of bone" is synonymous with primary non-Hodgkin lymphoma of bone. Primary involvement of bone by Hodgkin lymphoma is vanishingly rare; as bone involvement is almost always associated with progression of systemic disease. In children, bone is the primary site for approximately 2–9 % of all lymphomas [107]. Although children of all ages can be affected, pediatric primary bone lymphoma most often occurs during adolescence. Practically any bone can be involved, most commonly femur, pelvis and tibia. Symptoms are nonspecific and include localized bone pain and an occasional palpable mass, sometimes with systemic signs and symptoms [107]. The most common subtypes of primary pediatric bone lymphoma are diffuse large B cell lymphoma (DLBCL), lymphoblastic lymphoma, and Burkitt lymphoma [108]. DLBCL occurs most commonly (>50 % of primary bone lymphomas) and shows marked male predilection [109]. DLBCL patients often lack symptoms for months to years after disease onset. Anaplastic large cell lymphoma rarely presents as a primary bone tumor and also has a male predilection [110]. As compared to adults, pediatric primary bone lymphoma generally has a very favorable prognosis [108].

Imaging Features

Plain-film radiography: The radiographic appearance of primary bone lymphoma is variable, nonspecific, and often near normal [111, 112]. The appearance of the primary site ranges from a focal lytic lesion with geographic margins, to a mixed lytic-sclerotic lesion, to an area of permeative lytic destruction with a non-calcified soft tissue mass [107, 111–113]. The lytic-destructive pattern occurred in ~70 % of 237 cases; sequestra were seen in 28 (11 %) of 246 cases in one study [113, 114]. A mixed lytic-sclerotic pattern, though uncommon, is sometimes seen in Hodgkin disease or following radiation or chemotherapy in originally lytic lesions [111]. Intramedullary tumor extension may produce bony expansion and cortical destruction. Periosteal reaction occurs in 60 % of cases and tends to be multilamellated [111].

Computed tomography: CT outperforms radiography in detecting sequestra and subtle cortical breaks [111, 113, 114] and is used to evaluate the chest, abdomen, and pelvis for lymphadenopathy and visceral involvement.

Magnetic resonance imaging: Intramedullary involvement is well depicted on MRI, which shows permeative destructive lesions with serpiginous tumor located between areas of normal marrow. Tumor is isointense to muscle on T1W images and hyperintense on T2W images. It shows significant, diffuse, homogenous post gadolinium enhancement [107, 111, 113, 115, 116]. Peritumoral edema and reactive marrow changes also produce high intensity on T2W and STIR images. There is often little or no cortical disruption. The soft tissue component of the tumor, well depicted on MRI, may be disproportionately larger than the osseous component or small and circumferential. Tumors are often accompanied by tumoral angiogenesis, and dynamic contrast enhanced MRI may be superior in showing marrow involvement. In one study, 31 % of 29 primary lymphomas of bone [116], tumors appeared non-aggressive on MRI. They appear either normal, exhibit intraosseous linear cortical signal abnormalities, or cause thickened cortical bone without a soft tissue mass. A unique feature shared by small round cell tumors like lymphoma is a soft tissue mass without cortical destruction, which results from tumor cells permeating small cortical vascular channels [117].

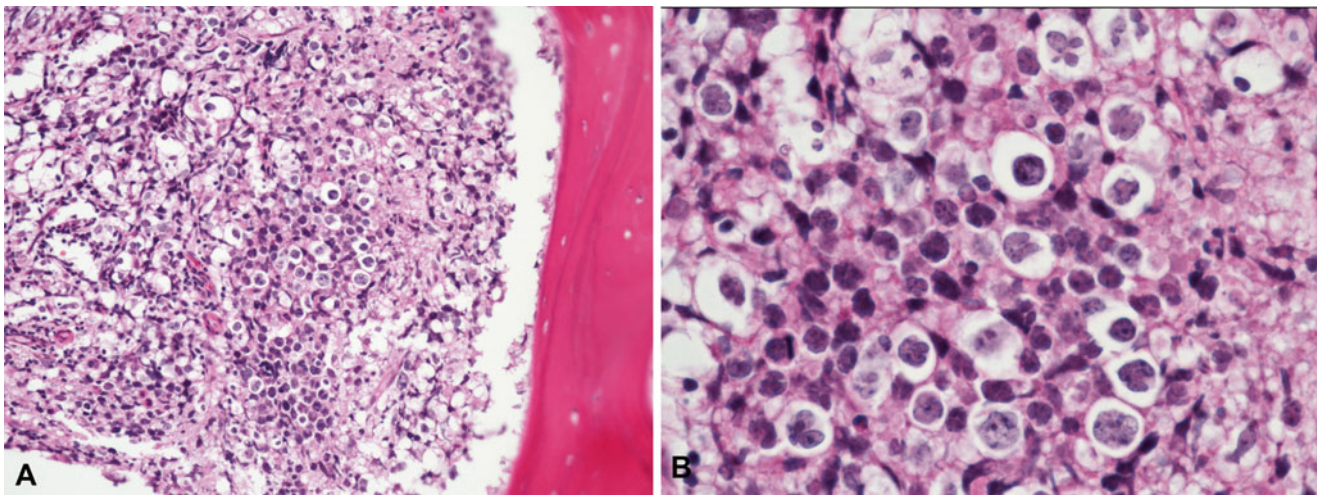

Fig. 4.30 Diffuse large B cell lymphoma arising in femur. (**a**) Low power photomicrograph. (**b**) Atypical centroblastic cells with lobated nuclei and perinuclear clearing, with reactive cells with the background

Bone scintigraphy: In a retrospective study of 237 patients with primary lymphoma of bone, Mulligan et al. found increased ^{99m}Tc radiotracer uptake in 98 %, with markedly increased activity in 64 % [113]. A central photopenic area that represents tumor necrosis may be present. Gallium scans show increased uptake throughout the lesion. However, for evaluating patients with lymphoma, gallium and ^{99m}Tc bone scans have largely been replaced by PET imaging [118, 119].

Positron emission tomography: ^{18}F-FDG PET shows increased FDG avidity at sites of primary bone lymphoma involvement. PET is significantly superior to standard staging modalities such as CT and ^{99m}Tc bone scan [120] and can determine response to treatment [121]. This may lead to changes in therapy regimens [122].

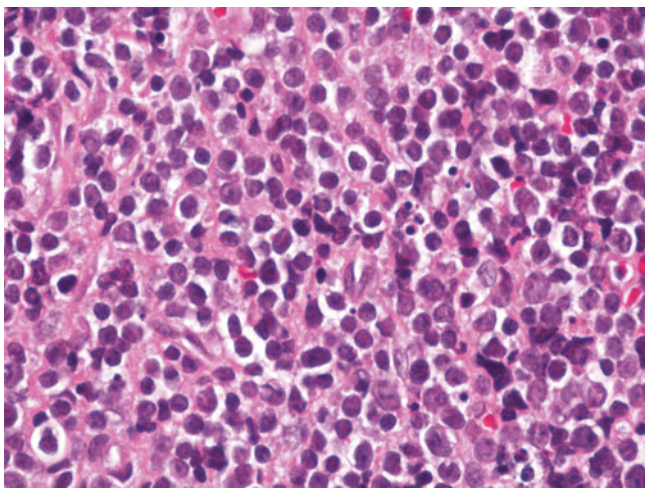

Fig. 4.31 Lymphoblastic lymphoma. Sheets of undifferentiated small cells, essentially indistinguishable on routine staining from the appearance of Ewing sarcoma. This tumor demonstrated nuclear positivity for TdT

Pathology and Molecular Genetics

Diffuse large B cell lymphoma occurs as a single or multifocal lesion, composed of tumor cells in a para or intratrabecular location. The most common histological pattern shows monomorphic or pleomorphic centroblastic tumor cells, with poorly defined cytoplasmic borders, round to irregular to multilobated nuclei, fine chromatin, ample cytoplasm, and inconspicuous to small nucleoli (Fig. 4.30a, b). Unlike typical centroblasts, perimembranous nucleoli are absent [109]. Mitoses may be present, along with necrosis and reactive histiocytes, T cells, and neutrophils. Immunohistochemistry reveals CD79a, PAX5, and CD20 expression; CD34 and TdT are negative. Most DLBL, but not all, express CD10 [109].

Given the common presence of an inflammatory background with or without necrosis, these tumors can resemble chronic osteomyelitis, especially given their indolent nature and often long-standing history of vague symptoms. A high index of suspicion for the presence of atypical cells decrease the likelihood of misdiagnosis.

For an in depth discussion of the morphologic, immunohistochemical, and molecular genetic features of lymphoblastic lymphoma, Burkitt lymphoma, and anaplastic large cell lymphoma, the reader is directed to the chapter in this book on hematopoietic neoplasms. Emphasized here is that lymphoblastic lymphoma can occasionally present as a solitary bone tumor, closely mimicking Ewing sarcoma (Fig. 4.31). Distinction of the two entities is critical, given their markedly different clinical behavior and modes of treatment. Wide surgical extirpation with possible amputation is part of the treatment of Ewing sarcoma but would be inappropriate for lymphoblastic lymphoma. Differentiating between them can

be challenging on small biopsies, as both contain delicate small cells that are prone to crush artifact, both may be extensively necrotic, and both usually express CD99. Generally lymphoblastic lymphomas display finer chromatin, less cytoplasm and more nuclear irregularity than Ewing sarcomas, but there is sufficient overlap to render these features unreliable in individual cases. Moreover, the immature cells of lymphoblastic lymphomas may not express CD20, CD3, or CD45. Useful stains in separating the two include TdT, CD43, and CD79a, which are negative in Ewing sarcoma [123]. Detection of an *EWS/ETS* fusion or *EWS* rearrangement supports a diagnosis of Ewing sarcoma, and T-cell receptor or immunoglobulin gene rearrangements support a diagnosis of lymphoma [123].

Angiosarcoma

Despite the ubiquity of cutaneous and soft tissue vascular lesions in children, primary vascular neoplasms of the skeleton are rare, and malignant examples are even more unusual. In a series of 77 pediatric patients with bony vascular lesions, only 7 (9 %) had hemangioendotheliomas and 5 (6 %) had angiosarcomas [124]. Most pediatric hemangioendotheliomas are epithelioid types. Although considered in the 2002 WHO fascicle on bone and soft tissue tumors to be a subset of angiosarcoma [125], the entity of "hemangioendothelioma" is poorly defined, with no clear consensus for these neoplasms that occupy an intermediate position between clearly benign (hemangioma) and clearly malignant (angiosarcoma) [126]. In over one-half of children with hemangioendothelioma, multiple bones and/or viscera are involved [124], and multifocal involvement is common in angiosarcoma.

Imaging Features

Plain-film radiography: Angiosarcoma appears as a predominantly lytic destructive lesion with an incomplete or absent sclerotic margin [127–130]. Clustering of multiple lytic lesions in one anatomic location is highly indicative of osseous vascular tumors. Low-grade tumors can show honeycombing or a hole-within-a-hole appearance and often lead to bony expansion [127, 129]. High-grade lesions often have an associated soft tissue mass with cortical breakthrough.

There are no specific imaging characteristics for bony epithelioid hemangioendothelioma [131]. As the disease is low-grade, plain radiographs reveal an expansile area of osteolytic destruction with occasional honeycombing. There is no periosteal reaction or peritumoral stromal calcification. Destruction of the cortex and tumor extension into the surrounding tissues is rare.

Angiography: Dense, well-circumscribed areas of enhancement with early draining veins and shunting are seen [127–130].

Computed tomography: CT findings of angiosarcoma mimic those of radiography and demonstrate varying tumor aggressiveness, depending on the tumor grade. CT may reveal a soft tissue mass of muscle attenuation, which enhances significantly on post-contrast images. Computed angio-tomography may reveal large feeding vessels [130, 131].

CT of epithelioid hemangioendothelioma typically reveals a lytic lesion without matrix mineralization, and osseous expansile remodeling. These lesions can be localized in the cortical or medullary bone. Calcification is rare, and periosteal reaction is rare in the absence of pathologic fracture [131]. Cortical disruption and extension into soft tissues can be present. Joint invasion is a common feature. Homogeneous enhancement is present at contrast material-enhanced CT.

Magnetic resonance imaging: MRI of angiosarcoma shows nonspecific T1W and T2W signal with varying degrees of contrast enhancement, depending on tumor grade [127–129]. The tumor may demonstrate prominent peripheral vascularity. Central necrosis within the tumor is fairly common, along with bright enhancement of the soft tissue mass, often appearing hyperintense on T2WI with prominent flow voids [127].

Generally, epithelioid hemangioendothelioma shows signal intensity that is isointense/hypointense to muscle on T1W and hyperintense on T2W images. The presence of signal intensity higher than muscle on T1W may represent hemorrhage. Hemangioendothelioma may appear on MRI as a lobulated, expansile lesion with irregular margins and intense, homogenous, post gadolinium enhancement [132].

Bone scintigraphy: A ^{99m}Tc-MDP bone scan shows increased tumor radiotracer uptake.

Positron emission tomography: ^{18} FDG PET/CT findings in primary angiosarcoma of bone have not been widely reported. Huang et al. reported a patient with increased FDG uptake in angiosarcoma of the rib [133].

Pathologic Features

Epithelioid hemangioendothelioma histologically contains highly cellular sheets of epithelioid and spindled cells disposed in cords and nests, lacking a lobular growth pattern and embedded in an extracellular myxoid matrix. The tumor cells have abundant cytoplasm and may display cytoplasmic vacuoles with engulfed erythrocytes, consistent with angiogenic differentiation (Fig. 4.32a, b). Nuclei have atypical features with prominent nucleoli. Mitotic activity is generally low, without atypical mitotic figures. Infiltration by lymphocytes, plasma cells, and eosinophils is common. Clinical and histologic overlap with epithelioid hemangioma exists, and pathologists disagree whether they can always be distinguished [134]. Epithelioid hemangiomas have less

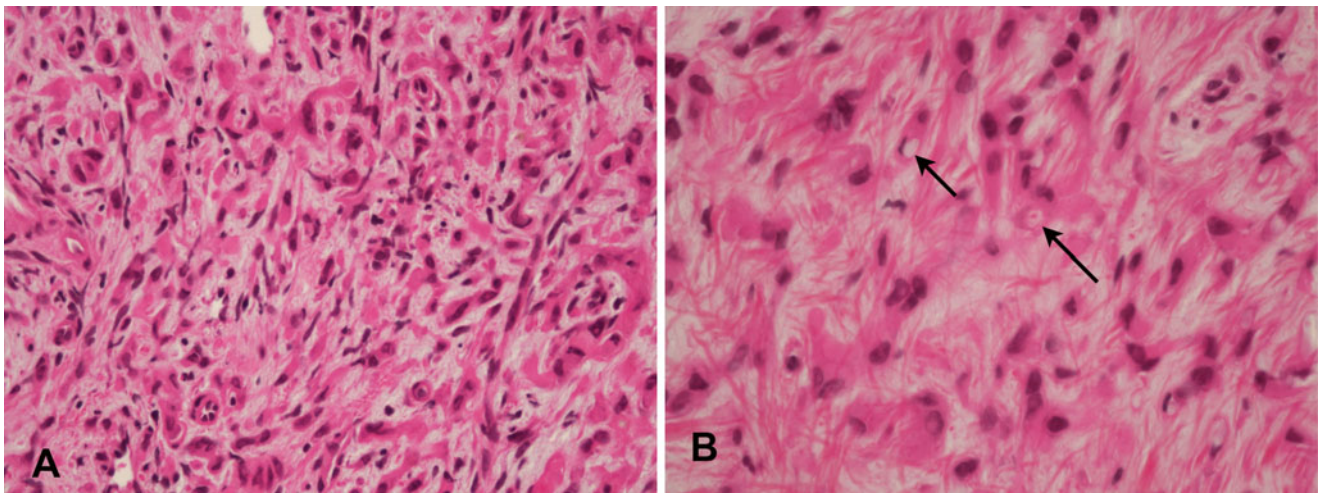

Fig. 4.32 Epithelioid hemangioendothelioma. (**a**) Cords of atypical epithelioid cells with abundant eosinophilic cytoplasm. (**b**) Higher power photomicrograph revealing cytoplasmic vacuoles (*arrows*)

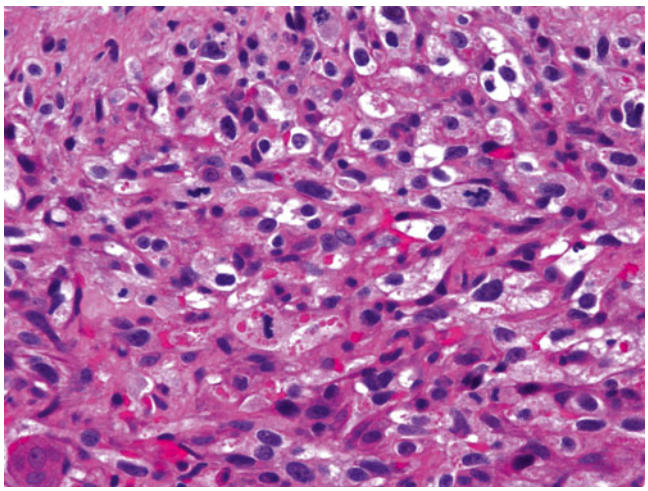

Fig. 4.33 Angiosarcoma. The section shows markedly atypical spindle cells associated with high mitotic activity and extravasated erythrocytes

solid growth and pleomorphism and better formed vascular channels than hemangioendotheliomas [124], and they lack background ground substance and areas of necrosis.

Angiosarcoma of bone varies in histologic appearance. Like hemangioendothelioma, most at least partially contain epithelioid cells, some having intracytoplasmic vacuoles, as well as infiltrating granulocytes, but they differ from lower grade lesions by their greater cytologic atypia, increased mitotic activity with atypical forms, necrosis, and disorganized architecture (Fig. 4.33). Tumoral hemorrhage with iron deposition may occur, and intratumoral reactive bone formation is common [125]. By immunohistochemistry they show vimentin expression and variable vascular marker staining. CD31 is most uniformly expressed, and many express CD34, Factor VIII-related antigen, and D2-40. Epithelioid vascular tumors may also express cytokeratins and EMA, a factor to note in their distinction from metastatic carcinoma.

Primary Fibrosarcoma of Bone

Rare in adults, fibrosarcoma of bone is even more unusual in children. Histiocytoma of Bone in adults, fibrosarcoma of bone is even more unusual in children. Closely related, and with no demonstrable difference in clinical behavior, is malignant fibrous histiocytoma (MFH). Although previously well accepted, the existence of MFH as an entity has been challenged by soft tissue pathologists, with some viewing MFH as a type of fibrosarcoma [135]. An MFH diagnosis has been applied to both bone and soft tissue tumors that demonstrate a pleomorphic, spindle cell pattern with storiform areas and a fibrohistiocytic immunophenotype [136]. However, with more specific immunohistochemical and molecular markers, many appear to be variants of other, better defined sarcomas. Despite this, a subset of spindle cell bone tumors that cannot be further classified still remains and has been variously labeled as undifferentiated high grade pleomorphic sarcoma or MFH.

Imaging

Plain-film radiology: The tumor is lytic and has a geographic or permeative destructive pattern and a wide zone of transition (Fig. 4.34a, b) [137]. Periosteal reaction is commonly absent but can be very aggressive in MFH. The underlying bone may show a prior lesion, such as a serpiginous bone infarct, a mixed lytic-sclerotic Paget's disease, or radiation necrosis [138].

Fig. 4.34 Twelve young girl with malignant fibrohistiocytoma of bone. (**a**) Anterior-posterior radiograph shows a largely lytic, aggressive lesion with a wide zone of transition (*arrow*). (**b**) Lateral radiograph demonstrates a Codman triangle (*arrow*). (**c**) T1W coronal image shows the tumor to be isointense to muscle. (**d**) STIR coronal image shows the tumor to be hyperintense and (**e**) post-contrast axial image demonstrates diffuse, fairly intense, tumor enhancement and cortical destruction (*arrows*)

Magnetic Resonance Imaging: MRI features of the tumor are nonspecific, with a signal that is isointense to muscle on T1 W imaging, hyperintense on fluid sensitive sequences, and avidly enhancing on post contrast sequences (Fig. 4.34c–e). MR imaging can define the extent and anatomic relationship of the tumor to adjacent structures and assists in biopsy site selection.

Radiological differential diagnosis: Primary lymphoma of bone and chondrosarcoma may mimic the imaging appearance of MFH.

Pathologic Features

Primary fibrosarcoma of bone is composed of spindle cells with a herringbone or fascicular pattern. Collagen production is variable but usually more evident in low to intermediate grade lesions [139]. Lower grade lesions may resemble desmoplastic fibroma of bone, which lacks atypia and significant mitotic activity. Higher grade lesions are more cellular and overlap with MFH, characterized by cellular populations of spindle cells arranged in a storiform pattern, variably containing histiocytes, osteoclastic giant cells, foam

cells, lymphocytes, and pleomorphic cells. Most MFH's of bone are high grade. Before diagnosing MFH, one must exhaustively search for tumoral osteoid to exclude fibroblastic osteosarcomas, especially with limited biopsy material.

Immunostains generally only show vimentin and occasional actin expression and are non-reactive for most antigens, which are tested to exclude other lesions such as synovial sarcomas and spindle cell rhabdomyosarcomas. Also worth consideration is angiomatoid fibrous histiocytoma, a soft tissue tumor that rarely presents as a primary bone lesion [140]. In addition to the classical features described in the soft tissue chapter, this lesion can contain hyalinized matrix that mimics osteosarcoma [141]. Demonstration of the *EWSR1-ATF* or *EWSR1-CREB1* fusions associated with angiomatoid fibrous histiocytoma assist in diagnosis.

Adamantinoma

Adamantinoma is a rare low grade malignancy of uncertain histogenesis. It typically involves the tibia but occasionally occurs in other sites, such as the ulna. It accounts for <1 % of all bone tumors [142]. Occasional lesions may synchronously coexist in the ipsilateral tibia and fibula. It is most common in young adults but has been diagnosed in 3-year-old patients. It has an indolent nature and often a protracted clinical course.

Imaging Features

Plain-film Radiography: Adamantinoma appears as a well-marginated, expansile, eccentric, lytic cortical lesion with a narrow zone of transition [143–145]. It is usually oriented longitudinally along the diaphyseal cortex of the tibia, has an average length of 10 cm, and typically lacks a significant periosteal reaction. It is often multilocular, with sclerosis and lysis giving it a soap-bubble appearance [143, 146, 147].

Computed tomography: CT provides better delineation of the cortical nature of the tumor and assists in evaluating cortical destruction and surrounding sclerosis. CT can identify pericystic sclerotic bony septa and the presence of soft tissue involvement, but not intraosseous tumoral extension [150, 151].

Magnetic resonance imaging: MRI is important for detecting satellite lesions, evaluating soft tissue and intramedullary tumor involvement, and establishing regional staging [145]. On MRI, the tumor shows isointensity to muscle on T1W, hyperintensity on T2W, and homogeneous, intense post-gadolinium enhancement. Van der Woude et al. described three appearances on MRI of 22 patients: multiple small nodules in one or more foci (45 %), a lobulated, solitary focus (41 %), and a mixed pattern consisting of both small nodules and a dominant lobulated nodule (14 %) [148].

Bone scintigraphy: Few studies have evaluated adamantinomas by nuclear medicine techniques. Usui et al. reported increased intratumoral blood flow, blood pooling, and accumulation of intralesional ^{99m}Tc-MDP in a three-phase bone scan of a tibial adamantinoma [149]. These findings may simulate those of a stress fracture [150].

Radiographic differential diagnosis: Adamantinoma must be differentiated from osteofibrous dysplasia, a benign tibial lesion with sclerotic margins, periosteal reaction, and less circumferential cortical involvement than adamantinoma [147, 151].

Pathology and Molecular Genetics

Classic adamantinoma is a biphasic tumor composed of intermingled osteofibrous and epithelial components. The epithelial component appears variable, with basaloid, tubular, squamoid and spindle cell features; tubular and basaloid patterns are most common [142]. The epithelial components typically coexpress cytokeratin, EMA, and vimentin; vimentin is expressed in tumor mesenchyme. In basaloid tumors, epithelioid nests centrally contain cells with a stellate architecture and may display peripheral basal palisading, reminiscent of gnathic ameloblastoma [152]. The tubular pattern comprises thin cords of discohesive epithelial cells resembling glands or vessels. The squamoid pattern shows focal squamous differentiation, sometimes with overt keratinization. In the spindle cell pattern, a predominant fascicular or herring-bone pattern contains clefts lined by simple epithelium [152]. All patterns contain rare mitoses, minimal nuclear atypia, and a background osteofibrous component with spindle cells disposed in a storiform arrangement [153].

Osteofibrous dysplasia-like foci often occur at the periphery of these tumors, named "osteofibrous dysplasia-like adamantinoma" or "differentiated adamantinoma." Overall they resemble osteofibrous dysplasia with additional, inconspicuous epithelial nests [154]. These overlapping lesions engender diagnostic and taxonomic confusion and lack a clear consensus regarding diagnostic criteria and classification. Cytogenetic studies of osteofibrous dysplasia and adamantinoma indicate a close relationship, as trisomies of 7, 8, and 12 occur commonly in both [154]. Although osteofibrous dysplasia-like adamantinoma may recur as classic adamantinoma, there is little evidence supporting their malignancy, provided sampling error is excluded [154].

Skeletal Metastasis

Unlike bone malignancies in adults, most bone tumors in children are primary in nature, and when bone metastases occur, they usually originate from embryonal tumors or primary bone sarcomas elsewhere in the skeleton [155]. Another

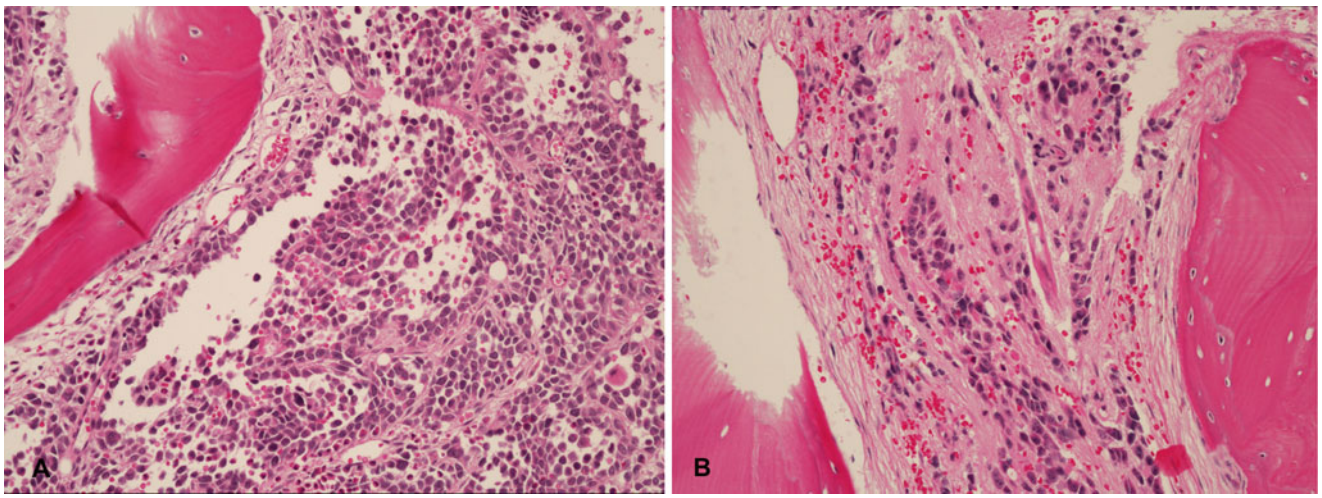

Fig. 4.35 Pediatric tumors metastatic to bone. (**a**) Alveolar rhabdomyosarcoma, with classic alveolar architecture. (**b**) Neuroblastoma with abundant pink fibrillary neuropil in the background

distinction is that bone metastases from childhood malignancies such as neuroblastoma commonly occur at the time of initial diagnosis, whereas in adults bone metastases tend to occur later. The most common symptom of metastatic disease to the bone is pain. Pathologic fracture may also occur but is initially rare. Any bone may be involved, most commonly the spine, ribs, skull, femur and pelvis [155]. Excluding leukemias, lymphomas, and metastatic primary bone tumors, the most common pediatric bony metastases are from neuroblastoma, rhabdomyosarcoma, germ cell tumors, Wilms tumor, retinoblastoma, and nasopharyngeal carcinoma, in that order [155]. Histologically, these tumors resemble their primaries (Fig. 4.35a, b). Neuroblastoma and alveolar rhabdomyosarcoma may present as bone marrow metastatic disease in the absence of a clear primary site, even in the face of exhaustive clinical and radiographic investigation.

Imaging Features

Skeletal metastases can be blastic, lytic, or mixed in nature. Langerhan cell histiocytosis and multifocal osteomyelitis may resemble skeletal metastasis in children. Tc99 bone scan and FDG-PET-CT help assess metastatic disease and aid in staging of bone tumors.

References

1. Domb BG, Tyler W, Ellis S, McCarthy E. Radiographic evaluation of pathological bone lesions: current spectrum of disease and approach to diagnosis. J Bone Joint Surg Am. 2004;86-A Suppl 2:84–90. Epub 2005/02/05.
2. Miller TT. Bone tumors and tumorlike conditions: analysis with conventional radiography. Radiology. 2008;246(3):662–74. Epub 2008/01/29.
3. Leavey PJ, Day MD, Booth T, Maale G. Skip metastasis in osteosarcoma. J Pediatr Hematol Oncol. 2003;25(10):806–8. Epub 2003/10/07.
4. Kaste SC, Liu T, Billups CA, Daw NC, Pratt CB, Meyer WH. Tumor size as a predictor of outcome in pediatric non-metastatic osteosarcoma of the extremity. Pediatr Blood Cancer. 2004;43(7):723–8. Epub 2004/09/25.
5. Miller SL, Hoffer FA, Reddick WE, Wu S, Glass JO, Gronemeyer SA, et al. Tumor volume or dynamic contrast-enhanced MRI for prediction of clinical outcome of Ewing sarcoma family of tumors. Pediatr Radiol. 2001;31(7):518–23. Epub 2001/08/07.
6. Rasalkar DD, Chu WC, Lee V, Paunipagar BK, Cheng FW, Li CK. Pulmonary metastases in children with osteosarcoma: characteristics and impact on patient survival. Pediatr Radiol. 2011;41(2):227–36. Epub 2010/09/04.
7. Costelloe CM, Macapinlac HA, Madewell JE, Fitzgerald NE, Mawlawi OR, Rohren EM, et al. 18F-FDG PET/CT as an indicator of progression-free and overall survival in osteosarcoma. J Nucl Med. 2009;50(3):340–7. Epub 2009/03/05.
8. Benz MR, Tchekmedyian N, Eilber FC, Federman N, Czernin J, Tap WD. Utilization of positron emission tomography in the management of patients with sarcoma. Curr Opin Oncol. 2009;21(4):345–51. Epub 2009/05/05.
9. Mirabello L, Troisi RJ, Savage SA. Osteosarcoma incidence and survival rates from 1973 to 2004: data from the surveillance, epidemiology, and end results program. Cancer. 2009;115(7):1531–43. Epub 2009/02/07.
10. Kager L, Zoubek A, Dominkus M, Lang S, Bodmer N, Jundt G, et al. Osteosarcoma in very young children: experience of the Cooperative Osteosarcoma Study Group. Cancer. 2010;116(22):5316–24. Epub 2010/07/31.
11. Raymond AK. Conventional osteosarcoma. In: Fletcher CDM, editor. World Health Organization classification of tumours pathology and genetics of tumours of soft tissue and bone. Lyon: IARC Press; 2002. p. 264–70.
12. Fernandes R, Nikitakis NG, Pazoki A, Ord RA. Osteogenic sarcoma of the jaw: a 10-year experience. J Oral Maxillofac Surg. 2007;65(7):1286–91. Epub 2007/06/20.
13. Duffaud F, Digue L, Baciuchka-Palmaro M, Volot F, Perles-Daniel C, Garbe L, et al. Osteosarcomas of flat bones in adolescents and adults. Cancer. 2000;88(2):324–32. Epub 2000/01/21.
14. Corradi D, Wenger DE, Bertoni F, Bacchini P, Bosio S, Goldoni M, et al. Multicentric osteosarcoma: clinicopathologic and radio-

graphic study of 56 cases. Am J Clin Pathol. 2011;136(5):799–807. Epub 2011/10/28.
15. Murphey MD, Robbin MR, McRae GA, Flemming DJ, Temple HT, Kransdorf MJ. The many faces of osteosarcoma. Radiographics. 1997;17(5):1205–31. Epub 1997/10/06.
16. Howman-Giles R. Primary bone tumors. In: Charron M, editor. Pediatric PET imaging. Berlin: Springer; 2006. p. 267.
17. Naka T, Fukuda T, Shinohara N, Iwamoto Y, Sugioka Y, Tsuneyoshi M. Osteosarcoma versus malignant fibrous histiocytoma of bone in patients older than 40 years. A clinicopathologic and immunohistochemical analysis with special reference to malignant fibrous histiocytoma-like osteosarcoma. Cancer. 1995;76(6):972–84. Epub 1995/09/15.
18. Klein MJ, Siegal GP. Osteosarcoma: anatomic and histologic variants. Am J Clin Pathol. 2006;125(4):555–81. Epub 2006/04/22.
19. Dehner LP. Skeletal system. In: Stocker JT, editor. Pediatric pathology. 3rd ed. Philadelphia: Wolters Kluwer, Lippincott Williams & Wilkins; 2011. p. 1190–270.
20. Okada K, Hasegawa T, Yokoyama R, Beppu Y, Itoi E. Osteosarcoma with cytokeratin expression: a clinicopathological study of six cases with an emphasis on differential diagnosis from metastatic cancer. J Clin Pathol. 2003;56(10):742–6. Epub 2003/09/30.
21. Sandberg AA, Bridge JA. Updates on the cytogenetics and molecular genetics of bone and soft tissue tumors: osteosarcoma and related tumors. Cancer Genet Cytogenet. 2003;145(1):1–30. Epub 2003/07/30.
22. Hayden JB, Hoang BH. Osteosarcoma: basic science and clinical implications. Orthop Clin North Am. 2006;37(1):1–7. Epub 2005/11/29.
23. Marina N, Gebhardt M, Teot L, Gorlick R. Biology and therapeutic advances for pediatric osteosarcoma. Oncologist. 2004;9(4):422–41. Epub 2004/07/22.
24. Rodriguez-Galindo C, Shah N, McCarville MB, Billups CA, Neel MN, Rao BN, et al. Outcome after local recurrence of osteosarcoma: the St. Jude Children's Research Hospital experience (1970–2000). Cancer. 2004;100(9):1928–35.
25. Isakoff MS, Barkauskas DA, Ebb D, Morris C, Letson GD. Poor survival for osteosarcoma of the pelvis: a report from the Children's Oncology Group. Clin Orthop Relat Res. 2012;470(7):2007–13. Epub 2012/02/23.
26. Abdul-Karim FW, Bauer TW, Kilpatrick SE, Raymond KA, Siegal GP. Recommendations for the reporting of bone tumors. Association of directors of anatomic and surgical pathology. Hum Pathol. 2004;35(10):1173–8. Epub 2004/10/20.
27. Coffin CM, Lowichik A, Zhou H. Treatment effects in pediatric soft tissue and bone tumors: practical considerations for the pathologist. Am J Clin Pathol. 2005;123(1):75–90. Epub 2005/03/15.
28. Raymond AK, Chawla SP, Carrasco CH, Ayala AG, Fanning CV, Grice B, et al. Osteosarcoma chemotherapy effect: a prognostic factor. Semin Diagn Pathol. 1987;4(3):212–36. Epub 1987/08/01.
29. Kransforf MJ. Osseous tumors. In: Davies AM, editor. Imaging of bone tumors and tumor-like lesions. Berlin: Springer; 2009. p. 251–306.
30. Nakajima H, Sim FH, Bond JR, Unni KK. Small cell osteosarcoma of bone. Review of 72 cases. Cancer. 1997;79(11):2095–106.
31. Bishop JA, Shum CH, Sheth S, Wakely Jr PE, Ali SZ. Small cell osteosarcoma: cytopathologic characteristics and differential diagnosis. Am J Clin Pathol. 2010;133(5):756–61. Epub 2010/04/17.
32. Matsuno T. Telangiectatic osteosarcoma. In: Fletcher CDM, editor. World Health Organization classification of tumours pathology and genetics of tumours of soft tissue and bone. Lyon: IARC Press; 2002. p. 271–2.
33. Weiss A, Khoury JD, Hoffer FA, Wu J, Billups CA, Heck RK, et al. Telangiectatic osteosarcoma: the St. Jude Children's Research Hospital's experience. Cancer. 2007;109(8):1627–37. Epub 2007/03/14.
34. Murphey MD, wan Jaovisidha S, Temple HT, Gannon FH, Jelinek JS, Malawer MM. Telangiectatic osteosarcoma: radiologic-pathologic comparison. Radiology. 2003;229(2):545–53.
35. Fechner R. Tumors of the bones and joints. In: Rosai J, editor. Atlas of tumor pathology. Washington, DC: Armed Forces Institute of Pathology; 1993. p. 51–4.
36. Discepola F, Powell TI, Nahal A. Telangiectatic osteosarcoma: radiologic and pathologic findings. Radiographics. 2009;29(2):380–3. Epub 2009/03/28.
37. Antonescu CR, Huvos AG. Low-grade osteogenic sarcoma arising in medullary and surface osseous locations. Am J Clin Pathol. 2000;114(Suppl):S90–103. Epub 2002/05/09.
38. Tarkkanen M, Bohling T, Gamberi G, Ragazzini P, Benassi MS, Kivioja A, et al. Comparative genomic hybridization of low-grade central osteosarcoma. Mod Pathol. 1998;11(5):421–6. Epub 1998/06/10.
39. Unni KK. Parosteal osteosarcoma. In: Fletcher CDM, editor. World Health Organization classification of tumours pathology and genetics of tumours of soft tissue and bone. Lyon: IARC Press; 2002. p. 279–81.
40. Rajiah P, Ilaslan H, Sundaram M. Imaging of primary malignant bone tumors (nonhematological). Radiol Clin North Am. 2011;49(6):1135–61. Epub 2011/10/26.
41. Jelinek JS, Murphey MD, Kransdorf MJ, Shmookler BM, Malawer MM, Hur RC. Parosteal osteosarcoma: value of MR imaging and CT in the prediction of histologic grade. Radiology. 1996;201(3):837–42. Epub 1996/12/01.
42. Donmez FY, Tuzun U, Basaran C, Tunaci M, Bilgic B, Acunas G. MRI findings in parosteal osteosarcoma: correlation with histopathology. Diagn Interv Radiol. 2008;14(3):142–52. Epub 2008/09/25.
43. Sheth DS, Yasko AW, Raymond AK, Ayala AG, Carrasco CH, Benjamin RS, et al. Conventional and dedifferentiated parosteal osteosarcoma. Diagnosis, treatment, and outcome. Cancer. 1996;78(10):2136–45.
44. Bertoni F, Unni KK, Beabout JW, Sim FH. Parosteal osteoma of bones other than of the skull and face. Cancer. 1995;75(10):2466–73. Epub 1995/05/15.
45. Cesari M, Alberghini M, Vanel D, Palmerini E, Staals EL, Longhi A, et al. Periosteal osteosarcoma: a single-institution experience. Cancer. 2011;117(8):1731–5. Epub 2011/04/08.
46. Rose PS, Dickey ID, Wenger DE, Unni KK, Sim FH. Periosteal osteosarcoma: long-term outcome and risk of late recurrence. Clin Orthop Relat Res. 2006;453:314–7. Epub 2006/08/15.
47. Murphey MD, Jelinek JS, Temple HT, Flemming DJ, Gannon FH. Imaging of periosteal osteosarcoma: radiologic-pathologic comparison. Radiology. 2004;233(1):129–38. Epub 2004/08/31.
48. Okada K, Unni KK, Swee RG, Sim FH. High grade surface osteosarcoma: a clinicopathologic study of 46 cases. Cancer. 1999;85(5):1044–54. Epub 1999/03/26.
49. Wold LE, Unni KK, Beabout JW, Pritchard DJ. High-grade surface osteosarcomas. Am J Surg Pathol. 1984;8(3):181–6. Epub 1984/03/01.
50. Wold LE. High grade surface osteosarcoma. In: Fletcher CDM, editor. World Health Organization classification of tumours pathology and genetics of tumours of soft tissue and bone. Lyon: IARC Press; 2002. p. 284–5.
51. Staals EL, Bacchini P, Bertoni F. High-grade surface osteosarcoma: a review of 25 cases from the Rizzoli Institute. Cancer. 2008;112(7):1592–9. Epub 2008/02/27.
52. Parham DM. Neuroectodermal and neuroendocrine tumors principally seen in children. Am J Clin Pathol. 2001;115(Suppl):S113–28. Epub 2002/05/08.

53. Balamuth NJ, Womer RB. Ewing's sarcoma. Lancet Oncol. 2010;11(2):184–92. Epub 2010/02/16.
54. van den Berg H, Dirksen U, Ranft A, Jurgens H. Ewing tumors in infants. Pediatr Blood Cancer. 2008;50(4):761–4. Epub 2007/07/20.
55. Hameed M. Small round cell tumors of bone. Arch Pathol Lab Med. 2007;131(2):192–204. Epub 2007/02/08.
56. Ludwig JA. Ewing sarcoma: historical perspectives, current state-of-the-art, and opportunities for targeted therapy in the future. Curr Opin Oncol. 2008;20(4):412–8. Epub 2008/06/06.
57. Peersman B, Vanhoenacker FM, Heyman S, Van Herendael B, Stam M, Brys P, et al. Ewing's sarcoma: imaging features. JBR-BTR. 2007;90(5):368–76. Epub 2007/12/19.
58. Reinus WR, Gilula LA, Shirley SK, Askin FB, Siegal GP. Radiographic appearance of Ewing sarcoma of the hands and feet: report from the Intergroup Ewing Sarcoma Study. Am J Roentgenol. 1985;144(2):331–6. Epub 1985/02/01.
59. Pahade J, Sekhar A, Shetty SK. Imaging of malignant skeletal tumors. Cancer Treat Res. 2008;143:367–422. Epub 2008/07/16.
60. Heare T, Hensley MA, Dell'Orfano S. Bone tumors: osteosarcoma and Ewing's sarcoma. Curr Opin Pediatr. 2009;21(3):365–72. Epub 2009/05/08.
61. Franzius C, Daldrup-Link HE, Sciuk J, Rummeny EJ, Bielack S, Jurgens H, et al. FDG-PET for detection of pulmonary metastases from malignant primary bone tumors: comparison with spiral CT. Ann Oncol. 2001;12(4):479–86. Epub 2001/06/12.
62. Steinbach LS. MRI in the detection of malignant infiltration of bone marrow – a commentary. Am J Roentgenol. 2007;188(6): 1443–5. Epub 2007/05/23.
63. Furth C, Amthauer H, Denecke T, Ruf J, Henze G, Gutberlet M. Impact of whole-body MRI and FDG-PET on staging and assessment of therapy response in a patient with Ewing sarcoma. Pediatr Blood Cancer. 2006;47(5):607–11. Epub 2005/11/02.
64. Hawkins DS, Schuetze SM, Butrynski JE, Rajendran JG, Vernon CB, Conrad 3rd EU, et al. [18F] Fluorodeoxyglucose positron emission tomography predicts outcome for Ewing sarcoma family of tumors. J Clin Oncol. 2005;23(34):8828–34. Epub 2005/11/30.
65. Volker T, Denecke T, Steffen I, Misch D, Schonberger S, Plotkin M, et al. Positron emission tomography for staging of pediatric sarcoma patients: results of a prospective multicenter trial. J Clin Oncol. 2007;25(34):5435–41. Epub 2007/12/01.
66. Franzius C, Sciuk J, Brinkschmidt C, Jurgens H, Schober O. Evaluation of chemotherapy response in primary bone tumors with F-18 FDG positron emission tomography compared with histologically assessed tumor necrosis. Clin Nucl Med. 2000;25(11):874–81. Epub 2000/11/18.
67. Bredella MA, Caputo GR, Steinbach LS. Value of FDG positron emission tomography in conjunction with MR imaging for evaluating therapy response in patients with musculoskeletal sarcomas. Am J Roentgenol. 2002;179(5):1145–50. Epub 2002/10/22.
68. Gyorke T, Zajic T, Lange A, Schafer O, Moser E, Mako E, et al. Impact of FDG PET for staging of Ewing sarcomas and primitive neuroectodermal tumours. Nucl Med Commun. 2006;27(1):17–24. Epub 2005/12/13.
69. Wunder JS, Paulian G, Huvos AG, Heller G, Meyers PA, Healey JH. The histological response to chemotherapy as a predictor of the oncological outcome of operative treatment of Ewing sarcoma. J Bone Joint Surg Am. 1998;80(7):1020–33. Epub 1998/08/11.
70. Lin PP, Jaffe N, Herzog CE, Costelloe CM, Deavers MT, Kelly JS, et al. Chemotherapy response is an important predictor of local recurrence in Ewing sarcoma. Cancer. 2007;109(3):603–11. Epub 2006/12/21.
71. Folpe AL, Goldblum JR, Rubin BP, Shehata BM, Liu W, Dei Tos AP, et al. Morphologic and immunophenotypic diversity in Ewing family tumors: a study of 66 genetically confirmed cases. Am J Surg Pathol. 2005;29(8):1025–33. Epub 2005/07/12.
72. Llombart-Bosch A, Machado I, Navarro S, Bertoni F, Bacchini P, Alberghini M, et al. Histological heterogeneity of Ewing's sarcoma/PNET: an immunohistochemical analysis of 415 genetically confirmed cases with clinical support. Virchows Arch. 2009;455(5):397–411. Epub 2009/10/21.
73. Machado I, Noguera R, Mateos EA, Calabuig-Farinas S, Lopez FI, Martinez A, et al. The many faces of atypical Ewing's sarcoma. A true entity mimicking sarcomas, carcinomas and lymphomas. Virchows Arch. 2011;458(3):281–90.
74. Tsokos M, Alaggio RD, Dehner LP, Dickman PS. Ewing sarcoma/peripheral primitive neuroectodermal tumor and related tumors. Pediatr Dev Pathol. 2012;15(1 Suppl):108–26. Epub 2012/05/11.
75. Lee AF, Hayes MM, Lebrun D, Espinosa I, Nielsen GP, Rosenberg AE, et al. FLI-1 distinguishes Ewing sarcoma from small cell osteosarcoma and mesenchymal chondrosarcoma. Appl Immunohistochem Mol Morphol. 2011;19(3):233–8. Epub 2010/11/19.
76. Gu M, Antonescu CR, Guiter G, Huvos AG, Ladanyi M, Zakowski MF. Cytokeratin immunoreactivity in Ewing's sarcoma: prevalence in 50 cases confirmed by molecular diagnostic studies. Am J Surg Pathol. 2000;24(3):410–6. Epub 2000/03/15.
77. Collini P, Sampietro G, Luksch R, Migliorini L, Boracchi P, Scopsi L. Differentiation in paediatric peripheral primitive neuroectodermal tumours of bone. A critical contribution to its assessment. Virchows Arch. 1998;432(6):505–13. Epub 1998/07/22.
78. Somers GR, Shago M, Zielenska M, Chan HS, Ngan BY. Primary subcutaneous primitive neuroectodermal tumor with aggressive behavior and an unusual karyotype: case report. Pediatr Dev Pathol. 2004;7(5):538–45. Epub 2004/11/18.
79. Mechtersheimer G, Barth T, Ludwig R, Staudter M, Moller P. Differential expression of leukocyte differentiation antigens in small round blue cell sarcomas. Cancer. 1993;71(1):237–48. Epub 1993/01/01.
80. Gulley ML, Kaiser-Rogers KA. A rational approach to genetic testing for sarcoma. Diagn Mol Pathol. 2009;18(1):1–10. Epub 2009/02/14.
81. Sankar S, Lessnick SL. Promiscuous partnerships in Ewing's sarcoma. Cancer Genet. 2011;204(7):351–65. Epub 2011/08/30.
82. Wang L, Bhargava R, Zheng T, Wexler L, Collins MH, Roulston D, et al. Undifferentiated small round cell sarcomas with rare EWS gene fusions: identification of a novel EWS-SP3 fusion and of additional cases with the EWS-ETV1 and EWS-FEV fusions. J Mol Diagn. 2007;9(4):498–509. Epub 2007/08/11.
83. Barr FG, Womer RB. Molecular diagnosis of ewing family tumors: too many fusions… ? J Mol Diagn. 2007;9(4):437–40. Epub 2007/07/27.
84. Barr FG, Meyer WH. Role of fusion subtype in Ewing sarcoma. J Clin Oncol. 2010;28(12):1973–4. Epub 2010/03/24.
85. Le Deley MC, Delattre O, Schaefer KL, Burchill SA, Koehler G, Hogendoorn PC, et al. Impact of EWS-ETS fusion type on disease progression in Ewing's sarcoma/peripheral primitive neuroectodermal tumor: prospective results from the cooperative Euro-E.W.I.N.G. 99 trial. J Clin Oncol. 2010;28(12):1982–8.
86. van Doorninck JA, Ji L, Schaub B, Shimada H, Wing MR, Krailo MD, et al. Current treatment protocols have eliminated the prognostic advantage of type 1 fusions in Ewing sarcoma: a report from the Children's Oncology Group. J Clin Oncol. 2010; 28(12):1989–94. Epub 2010/03/24.
87. Shing DC, McMullan DJ, Roberts P, Smith K, Chin SF, Nicholson J, et al. FUS/ERG gene fusions in Ewing's tumors. Cancer Res. 2003;63(15):4568–76. Epub 2003/08/09.
88. Ng TL, O'Sullivan MJ, Pallen CJ, Hayes M, Clarkson PW, Winstanley M, et al. Ewing sarcoma with novel translocation t(2;16) producing an in-frame fusion of FUS and FEV. J Mol Diagn. 2007;9(4):459–63. Epub 2007/07/11.
89. Newby R, Rowe D, Paterson L, Farquharson MA, MacDuff E, Coupe A, et al. Cryptic EWSR1-FLI1 fusions in Ewing sarcoma:

potential pitfalls in the diagnostic use of fluorescence in situ hybridization probes. Cancer Genet Cytogenet. 2010;200(1):60–4. Epub 2010/06/02.
90. Huvos AG, Marcove RC. Chondrosarcoma in the young. A clinicopathologic analysis of 79 patients younger than 21 years of age. Am J Surg Pathol. 1987;11(12):930–42.
91. Shakked RJ, Geller DS, Gorlick R, Dorfman HD. Mesenchymal chondrosarcoma: clinicopathologic study of 20 cases. Arch Pathol Lab Med. 2012;136(1):61–75. Epub 2012/01/03.
92. Nakashima Y. Mesenchymal chondrosarcoma. In: Fletcher CDM, editor. World Health Organization classification of tumours pathology and genetics of tumours of soft tissue and bone. Lyon: IARC Press; 2002. p. 255–6.
93. Collins MS, Koyama T, Swee RG, Inwards CY. Clear cell chondrosarcoma: radiographic, computed tomographic, and magnetic resonance findings in 34 patients with pathologic correlation. Skeletal Radiol. 2003;32(12):687–94. Epub 2003/10/08.
94. Murphey MD, Flemming DJ, Boyea SR, Bojescul JA, Sweet DE, Temple HT. Enchondroma versus chondrosarcoma in the appendicular skeleton: differentiating features. Radiographics. 1998;18(5):1213–37. quiz 44-5. Epub 1998/09/25.
95. Murphey MD, Walker EA, Wilson AJ, Kransdorf MJ, Temple HT, Gannon FH. From the archives of the AFIP: imaging of primary chondrosarcoma: radiologic-pathologic correlation. Radiographics. 2003;23(5):1245–78. Epub 2003/09/17.
96. Geirnaerdt MJ, Hermans J, Bloem JL, Kroon HM, Pope TL, Taminiau AH, et al. Usefulness of radiography in differentiating enchondroma from central grade 1 chondrosarcoma. Am J Roentgenol. 1997;169(4):1097–104. Epub 1997/10/06.
97. Geirnaerdt MJ, Hogendoorn PC, Bloem JL, Taminiau AH, van der Woude HJ. Cartilaginous tumors: fast contrast-enhanced MR imaging. Radiology. 2000;214(2):539–46. Epub 2000/02/15.
98. Brenner W, Conrad EU, Eary JF. FDG PET imaging for grading and prediction of outcome in chondrosarcoma patients. Eur J Nucl Med Mol Imaging. 2004;31(2):189–95. Epub 2004/05/08.
99. Eefting D, Schrage YM, Geirnaerdt MJ, Le Cessie S, Taminiau AH, Bovee JV, et al. Assessment of interobserver variability and histologic parameters to improve reliability in classification and grading of central cartilaginous tumors. Am J Surg Pathol. 2009;33(1):50–7. Epub 2008/10/15.
100. de Andrea CE, Kroon HM, Wolterbeek R, Romeo S, Rosenberg AE, De Young BR, et al. Interobserver reliability in the histopathological diagnosis of cartilaginous tumors in patients with multiple osteochondromas. Mod Pathol. 2012;25(9):1275–83. Epub 2012/05/05.
101. Wehrli BM, Huang W, De Crombrugghe B, Ayala AG, Czerniak B. Sox9, a master regulator of chondrogenesis, distinguishes mesenchymal chondrosarcoma from other small blue round cell tumors. Hum Pathol. 2003;34(3):263–9. Epub 2003/04/04.
102. Fanburg-Smith JC, Auerbach A, Marwaha JS, Wang Z, Rushing EJ. Reappraisal of mesenchymal chondrosarcoma: novel morphologic observations of the hyaline cartilage and endochondral ossification and beta-catenin, Sox9, and osteocalcin immunostaining of 22 cases. Hum Pathol. 2010;41(5):653–62. Epub 2010/02/09.
103. Naumann S, Krallman PA, Unni KK, Fidler ME, Neff JR, Bridge JA. Translocation der(13;21)(q10;q10) in skeletal and extraskeletal mesenchymal chondrosarcoma. Mod Pathol. 2002;15(5):572–6. Epub 2002/05/16.
104. Wang L, Motoi T, Khanin R, Olshen A, Mertens F, Bridge J, et al. Identification of a novel, recurrent HEY1-NCOA2 fusion in mesenchymal chondrosarcoma based on a genome-wide screen of exon-level expression data. Gene Chromosome Canc. 2012;51(2):127–39. Epub 2011/10/29.
105. Forest M. Chondrosarcoma: variants. In: Forest M, editor. Orthopedic surgical pathology. Edinburgh: Churchill Livingstone; 1988. p. 268–80.
106. Unni KK. Malignant lymphoma. In: Fletcher CDM, editor. World Health Organization classification of tumours pathology and genetics of tumours of soft tissue and bone. Lyon: IARC Press; 2002. p. 306–8.
107. Glotzbecker MP, Kersun LS, Choi JK, Wills BP, Schaffer AA, Dormans JP. Primary non-Hodgkin's lymphoma of bone in children. J Bone Joint Surg Am. 2006;88(3):583–94. Epub 2006/03/03.
108. Lones MA, Perkins SL, Sposto R, Tedeschi N, Kadin ME, Kjeldsberg CR, et al. Non-Hodgkin's lymphoma arising in bone in children and adolescents is associated with an excellent outcome: a Children's Cancer Group report. J Clin Oncol. 2002;20(9):2293–301. Epub 2002/05/01.
109. Zhao XF, Young KH, Frank D, Goradia A, Glotzbecker MP, Pan W, et al. Pediatric primary bone lymphoma-diffuse large B-cell lymphoma: morphologic and immunohistochemical characteristics of 10 cases. Am J Clin Pathol. 2007;127(1):47–54. Epub 2006/12/06.
110. Bakshi NA, Ross CW, Finn WG, Valdez R, Ruiz R, Koujok K, et al. ALK-positive anaplastic large cell lymphoma with primary bone involvement in children. Am J Clin Pathol. 2006;125(1):57–63. Epub 2006/02/18.
111. Krishnan A, Shirkhoda A, Tehranzadeh J, Armin AR, Irwin R, Les K. Primary bone lymphoma: radiographic-MR imaging correlation. Radiographics. 2003;23(6):1371–83. discussion 84–7, Epub 2003/11/15.
112. Vlychou M, Athanasou NA. Radiological and pathological diagnosis of paediatric bone tumours and tumour-like lesions. Pathology. 2008;40(2):196–216. Epub 2008/01/19.
113. Mulligan ME, McRae GA, Murphey MD. Imaging features of primary lymphoma of bone. Am J Roentgenol. 1999;173(6):1691–7. Epub 1999/12/10.
114. Mulligan ME, Kransdorf MJ. Sequestra in primary lymphoma of bone: prevalence and radiologic features. Am J Roentgenol. 1993;160(6):1245–8. Epub 1993/06/01.
115. Furman WL, Fitch S, Hustu HO, Callihan T, Murphy SB. Primary lymphoma of bone in children. J Clin Oncol. 1989;7(9):1275–80. Epub 1989/09/01.
116. Heyning FH, Kroon HM, Hogendoorn PC, Taminiau AH, van der Woude HJ. MR imaging characteristics in primary lymphoma of bone with emphasis on non-aggressive appearance. Skeletal Radiol. 2007;36(10):937–44. Epub 2007/06/15.
117. Hicks DG, Gokan T, O'Keefe RJ, Totterman SM, Fultz PJ, Judkins AR, et al. Primary lymphoma of bone. Correlation of magnetic resonance imaging features with cytokine production by tumor cells. Cancer. 1995;75(4):973–80. Epub 1995/02/15.
118. Israel O, Mekel M, Bar-Shalom R, Epelbaum R, Hermony N, Haim N, et al. Bone lymphoma: 67Ga scintigraphy and CT for prediction of outcome after treatment. J Nucl Med. 2002;43(10):1295–303. Epub 2002/10/10.
119. Bar-Shalom R, Israel O, Epelbaum R, Haim N, Ben-Arush M, Ben-Shachar M, et al. Gallium-67 scintigraphy in lymphoma with bone involvement. J Nucl Med. 1995;36(3):446–50. Epub 1995/03/01.
120. Moog F, Bangerter M, Diederichs CG, Guhlmann A, Merkle E, Frickhofen N, et al. Extranodal malignant lymphoma: detection with FDG PET versus CT. Radiology. 1998;206(2):475–81. Epub 1998/02/11.
121. Park YH, Choi SJ, Ryoo BY, Kim HT. PET imaging with F-18 fluorodeoxyglucose for primary lymphoma of bone. Clin Nucl Med. 2005;30(2):131–4. Epub 2005/01/14.
122. Moog F, Kotzerke J, Reske SN. FDG PET can replace bone scintigraphy in primary staging of malignant lymphoma. J Nucl Med. 1999;40(9):1407–13. Epub 1999/09/24.
123. Lucas DR, Bentley G, Dan ME, Tabaczka P, Poulik JM, Mott MP. Ewing sarcoma vs lymphoblastic lymphoma. A comparative immunohistochemical study. Am J Clin Pathol. 2001;115(1):11–7. Epub 2001/02/24.

124. Bruder E, Perez-Atayde AR, Jundt G, Alomari AI, Rischewski J, Fishman SJ, et al. Vascular lesions of bone in children, adolescents, and young adults. A clinicopathologic reappraisal and application of the ISSVA classification. Virchows Arch. 2009;454(2):161–79. Epub 2008/12/25.
125. Roessner A. Angiosarcoma. In: Fletcher CDM, editor. World Health Organization classification of tumours pathology and genetics of tumours of soft tissue and bone. Lyon: IARC Press; 2002. p. 322–3.
126. Verbeke SL, Bertoni F, Bacchini P, Sciot R, Fletcher CD, Kroon HM, et al. Distinct histological features characterize primary angiosarcoma of bone. Histopathology. 2011;58(2):254–64. Epub 2011/02/18.
127. Wenger DE, Wold LE. Malignant vascular lesions of bone: radiologic and pathologic features. Skeletal Radiol. 2000;29(11):619–31. Epub 2001/02/24.
128. Lomasney LM, Martinez S, Demos TC, Harrelson JM. Multifocal vascular lesions of bone: imaging characteristics. Skeletal Radiol. 1996;25(3):255–61. Epub 1996/04/01.
129. Murphey MD, Fairbairn KJ, Parman LM, Baxter KG, Parsa MB, Smith WS. From the archives of the AFIP. Musculoskeletal angiomatous lesions: radiologic-pathologic correlation. Radiographics. 1995;15(4):893–917. Epub 1995/07/01.
130. Choi JJ, Murphey MD. Angiomatous skeletal lesions. Semin Musculoskelet Radiol. 2000;4(1):103–12. Epub 2000/11/04.
131. Larochelle O, Perigny M, Lagace R, Dion N, Giguere C. Best cases from the AFIP: epithelioid hemangioendothelioma of bone. Radiographics. 2006;26(1):265–70. Epub 2006/01/19.
132. Kabukcuoglu F, Kabukcuoglu Y, Livaoglu A, Ozagari A, Armagan R, Kuzgun U. Epithelioid hemangioendothelioma of bone. Acta Orthop Traumatol Turc. 2006;40(4):324–8. Epub 2006/10/26. Kemikte yerlesim gosteren epiteloid hemanjiyoendotelyoma.
133. Huang Y. Primary epithelioid angiosarcoma of the rib: a case report. Ann Nucl Med. 2009;22:101–7.
134. Evans HL, Raymond AK, Ayala AG. Vascular tumors of bone: a study of 17 cases other than ordinary hemangioma, with an evaluation of the relationship of hemangioendothelioma of bone to epithelioid hemangioma, epithelioid hemangioendothelioma, and high-grade angiosarcoma. Hum Pathol. 2003;34(7):680–9. Epub 2003/07/23.
135. Fletcher CDM. Pleomorphic malignant fibrous histiocytoma/undifferentiated high grade pleomorphic sarcoma. In: Fletcher CDM, editor. World Health Organization classification of tumours pathology and genetics of tumours of soft tissue and bone. Lyon: IARC Press; 2002. p. 120–2.
136. Antonescu CR, Erlandson RA, Huvos AG. Primary fibrosarcoma and malignant fibrous histiocytoma of bone – a comparative ultrastructural study: evidence of a spectrum of fibroblastic differentiation. Ultrastruct Pathol. 2000;24(2):83–91. Epub 2000/05/16.
137. Murphey MD, Gross TM, Rosenthal HG. From the archives of the AFIP. Musculoskeletal malignant fibrous histiocytoma: radiologic-pathologic correlation. Radiographics. 1994;14(4):807–26. quiz 27–8, Epub 1994/07/01.
138. Min WK, Kim SY, Oh CW, Kim SJ, Park TI, Koo KH. Malignant fibrous histiocytoma arising in the area of total hip replacement. Joint Bone Spine. 2008;75(3):319–21. Epub 2007/11/06.
139. Kahn LB. Fibrosarcoma of bone. In: Fletcher CDM, editor. World Health Organization classification of tumours pathology and genetics of tumours of soft tissue and bone. Lyon: IARC Press; 2002. p. 289–90.
140. Somers GR, Viero S, Nathan PC, Teshima I, Pereira C, Zielenska M. Association of the t(12;22)(q13;q12) EWS/ATF1 rearrangement with polyphenotypic round cell sarcoma of bone: a case report. Am J Surg Pathol. 2005;29(12):1673–9. Epub 2005/12/06.
141. Mangham DC, Williams A, Lalam RK, Brundler MA, Leahy MG, Cool WP. Angiomatoid fibrous histiocytoma of bone: a calcifying sclerosing variant mimicking osteosarcoma. Am J Surg Pathol. 2010;34(2):279–85. Epub 2010/01/22.
142. Hogendoorn PC. Adamantinoma. In: Fletcher CDM, editor. World Health Organization classification of tumours pathology and genetics of tumours of soft tissue and bone. Lyon: IARC Press; 2002. p. 332–4.
143. Szendroi M, Antal I, Arato G. Adamantinoma of long bones: a long-term follow-up study of 11 cases. Pathol Oncol Res. 2009;15(2):209–16. Epub 2008/12/03.
144. Kahn LB. Adamantinoma, osteofibrous dysplasia and differentiated adamantinoma. Skeletal Radiol. 2003;32(5):245–58. Epub 2003/04/08.
145. Camp MD, Tompkins RK, Spanier SS, Bridge JA, Bush CH. Best cases from the AFIP: adamantinoma of the tibia and fibula with cytogenetic analysis. Radiographics. 2008;28(4):1215–20. Epub 2008/07/19.
146. Levine SM, Lambiase RE, Petchprapa CN. Cortical lesions of the tibia: characteristic appearances at conventional radiography. Radiographics. 2003;23(1):157–77. Epub 2003/01/21.
147. Van Rijn R, Bras J, Schaap G, van den Berg H, Maas M. Adamantinoma in childhood: report of six cases and review of the literature. Pediatr Radiol. 2006;36(10):1068–74. Epub 2006/08/15.
148. Van der Woude HJ, Hazelbag HM, Bloem JL, Taminiau AH, Hogendoorn PC. MRI of adamantinoma of long bones in correlation with histopathology. Am J Roentgenol. 2004;183(6):1737–44. Epub 2004/11/18.
149. Usui K, Yamamoto W, Shuke N, Aburano T, Yamanaka Y, Tokusashi Y, et al. Scintigraphic findings of tibial adamantinoma on a three-phase bone scan. Clin Nucl Med. 2000;25(12):1057–8. Epub 2000/12/29.
150. Imran MB, Othman SA. Bilateral tibial adamantinomas simulating stress fractures on scintigraphy. Clin Nucl Med. 2011;36(9):788–90. Epub 2011/08/10.
151. Czerniak B, Rojas-Corona RR, Dorfman HD. Morphologic diversity of long bone adamantinoma. The concept of differentiated (regressing) adamantinoma and its relationship to osteofibrous dysplasia. Cancer. 1989;64(11):2319–34.
152. Deyrup AT, Montag AG. Epithelioid and epithelial neoplasms of bone. Arch Pathol Lab Med. 2007;131(2):205–16. Epub 2007/02/08.
153. Forest M. Adamantinoma. In: Forest M, editor. Orthopedic surgical pathology. Edinburgh: Churchill Livingstone; 1988. p. 385–95.
154. Gleason BC, Liegl-Atzwanger B, Kozakewich HP, Connolly S, Gebhardt MC, Fletcher JA, et al. Osteofibrous dysplasia and adamantinoma in children and adolescents: a clinicopathologic reappraisal. Am J Surg Pathol. 2008;32(3):363–76. Epub 2008/02/28.
155. Leeson MC, Makley JT, Carter JR. Metastatic skeletal disease in the pediatric population. J Pediatr Orthop. 1985;5(3):261–7. Epub 1985/05/01.

Tumors of Lymphoid and Hematopoietic Tissues

5

Vasiliki Leventaki, Joseph D. Khoury, and Stephan D. Voss

Introduction

Normal Anatomy and Development

Lymph nodes are an integral component of the adaptive immune system. Normally, they are encapsulated ovoid structures with a rubbery consistency and a homogeneous light tan cut surface. On a microanatomic level, the lymph node is divided into four compartments: cortex, paracortex, hilum, and sinusoids (Fig. 5.1a). The cortex contains lymphoid follicles comprised primarily of B-cells. Stimulated lymphoid follicles consist of a germinal center immediately surrounded by a mantle zone and an outer marginal zone. The cells of the germinal center exhibit morphologic and functional zonation (Fig. 5.1b). The paracortex, also referred to as the interfollicular area, is generally rich in T-cells that are associated with histiocytes, interdigitating reticulum cells, and high endothelial venules. Histologic prominence of the lymph node hilar area varies by anatomic location and is most evident in nodes of the inguinal and pelvic areas. The hilum contains variable amounts of lymphoplasmacytoid cells and fibroconnective tissue. Lymph node sinusoids are vascular structures that channel lymphatic flow from the capsule towards efferent hilar lymphatics. They contain varying numbers of histiocytes.

V. Leventaki, M.D.
St. Jude Children's Research Hospital, Memphis, TN, USA

J.D. Khoury, M.D.
The University of Texas M.D. Anderson Cancer Center, Houston, TX, USA

S.D. Voss, M.D., Ph.D. (✉)
Department of Radiology, Boston Children's Hospital, 300 Longwood Avenue, Boston, MA 02115, USA
e-mail: stephan.voss@childrens.harvard.edu

Lymph Node Sampling and Tissue Handling

Excisional and core biopsies are generally most suitable for de novo evaluation of an enlarged lymph node. Fine needle aspiration cytology is often fraught with sampling limitations and does not permit evaluation of the lymph node architecture. In most clinical practices, lymph node samples are submitted either without fixative or in a nutrient-rich medium. Ideally, triage of tissue material from a patient with unexplained lymphadenopathy should be based on evaluation of a touch preparation. If neoplasia is a consideration, lymph node tissue should be handled in the following priority order: (1) formalin fixation for histologic evaluation (paraffin-embedded tissue may be also used for immunohistochemistry, fluorescence or colorimetric in situ hybridization, and molecular testing); (2) unfixed tissue in nutrient-rich media for immunophenotyping by flow cytometry; and (3) unfixed tissue in nutrient-rich media for cytogenetic analysis.

Overview of Diagnostic Imaging Approaches

Conventional Radiography/Fluoroscopy

Conventional radiographs (x-rays) are still commonly obtained as the initial imaging study in patients with disorders of the lymphoid system. Despite the emergence of sophisticated cross-sectional and functional imaging techniques, radiographs remain attractive for the initial evaluation, and they are inexpensive, rapid, and relatively easy to perform. They can be done without sedation and can be accomplished at far lower radiation doses than computed tomography (CT). Although many disorders will not be evident radiographically, the presence of primary intrathoracic tumors, mediastinal and/or paraspinal masses, intra-abdominal masses and destructive bone lesions can all be detected radiographically. The presence of calcifications in lymphoid masses may be helpful in establishing a differential diagnosis. For the evaluation of children with suspected

D.M. Parham et al. (eds.), *Pediatric Malignancies: Pathology and Imaging*,
DOI 10.1007/978-1-4939-1729-7_5, © Springer Science+Business Media New York 2015

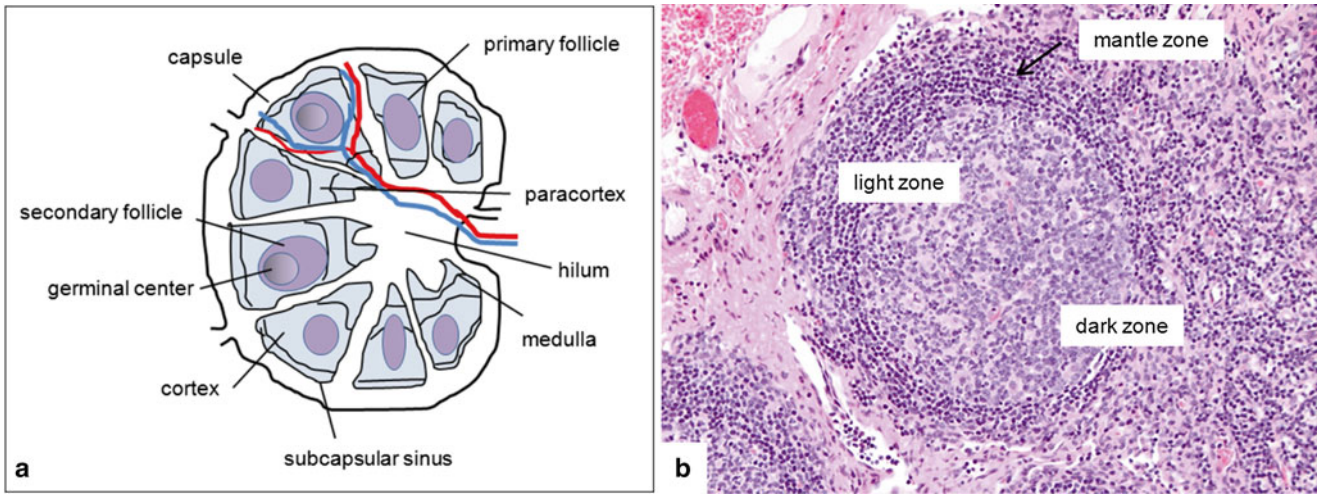

Fig. 5.1 Basic structure of normal lymph node. (**a**) Schematic representation of the anatomy of a lymph node with the cortical, paracortical, and medullary regions. The cortex contains multiple follicles including primary follicles and secondary follicles with germinal centers. (**b**) A secondary follicle with germinal center (GC) and well-defined mantle zone. In the GC, a loosely associated network of follicular dendritic cells, follicular helper T-cells, and centrocytes forms the light zone, whereas a dense area of dividing centroblasts can be recognized as a dark zone

abdominal conditions, radiographs of the abdomen should be the initial examination of choice to assess for acute obstruction or bowel perforation.

Historically, fluoroscopy was the primary modality used to evaluate the gastrointestinal tract and the upper airway. With the emergence of cross-sectional imaging, fluoroscopy is now rarely used for the primary evaluation of suspected lymphoid lesions. However, children with poorly characterized symptoms and physical exam findings may undergo fluoroscopic evaluation to assess the intestinal tract, and the radiologist should be aware of the imaging findings associated with lymphoid lesions involving the GI tract. Mucosa-based processes such as esophagitis, gastritis, or duodenitis are diagnosed almost exclusively by endoscopy nowadays. However, esophageal and intestinal strictures may benefit from further delineation by fluoroscopy, which can be performed safely and effectively. Current fluoroscopic techniques generally employ very low radiation doses due to advances in pulsed fluoroscopy, image intensifier sensitivity, and improved automatic dose rate controls [1]. Both water-soluble contrast or barium enteric contrast agents used in conjunction with fluoroscopy are considered safe even in immunocompromised children. While there are few contraindications to fluoroscopic evaluation of the intestinal tract, contrast enemas are generally avoided in neutropenic patients and barium enteric contrast should be avoided when bowel stricture or perforation are suspected.

Ultrasound

Ultrasound is an excellent technique for evaluating the child with a lymphoid system disease. With the availability of an array of high and low frequency transducers, ultrasound can be used to evaluate both superficial and deeper structures and is particularly useful in evaluating lymph nodes in the neck and axilla as well as the abdominal visceral organs [2]. Diagnostic ultrasound is relatively quick, inexpensive, and does not utilize ionizing radiation. In the hands of a skilled operator, ultrasound can also be used to evaluate even the most anxious child and does not usually require sedation. In contrast to adults, ultrasound images in children are usually of very high quality due to the relative paucity of intra-abdominal fat and other attenuating soft tissues seen in older patients and adults.

Color and pulse wave Doppler as well as the increasing availability of three-dimensional imaging techniques allow dynamic flow and vascularity to be assessed. This can be helpful in distinguishing between hyperemic/inflamed lymphoid tissue and normal tissue. The use of microbubble ultrasound contrast agents is still experimental and not routinely available for use in children [3]. The use of sonoelastography to measure the compressibility and elasticity of tissues—initially used in the evaluation of the liver—is presently under evaluation to determine tissue characteristics of superficial lymphoid structures in an effort to discriminate benign from neoplastic nodal enlargement [4].

Computed Tomography

Since its emergence in the 1970s, the use of CT has become routine in the evaluation of patients with suspected abnormalities of the lymphoid system. With the development of multiple detector row and ultrafast CT imaging techniques,

examinations of the entire body can now be performed in under one minute and, depending on the area of interest, even young children may be evaluated without the need for sedation.

CT scanning is routinely performed in transaxial cross-sections with multiplanar reconstructions being rapidly generated from the axial image data. With the use of multidetector helical CT scanners and isotropic imaging acquisition techniques, the reconstructed images have no discernible loss of resolution or contrast as compared to source transaxial data. The use of contrast agents (both intravenous and enteric) in pediatric CT scanning depends on the condition being evaluated. For assessment of the mediastinum and lymphoid tissues, the presence of contrast is considered helpful, if not essential, to better characterize lymph nodes relative to adjacent vascular structures. In addition, the use of contrast-enhanced CT scanning remains the standard of care to accurately measure the size of lymphoid tumors to determine response to therapy [5, 6]. Although concerns regarding reactions to iodinated intravenous contrast agents are frequently raised, the rate of adverse reactions, including acute allergic or anaphylactoid reactions, asthmatic reactions, and vasovagal reactions, are exceedingly rare [7]. The presence of a prior contrast reaction does, however, predict subsequent recall-type allergic reactions, and clinicians and radiologists should be aware of the increased potential for adverse events in these patients and provide appropriate premedication as indicated. Awareness by radiologists and clinicians of guidelines for the use of iodinated contrast agents is important so that imaging protocols can be modified as needed [8].

Over the past 10 years, there has been a heightened awareness of the potential risk posed by CT scanning from ionizing radiation doses used [9]. When comparing the effective dose for a pediatric chest CT to a chest radiograph, some estimates indicate the CT scan is the equivalent of tens to hundreds of chest radiographs [10]. While it is clear that the use of multiple CT scanning phases and the need for multiple sequential CT examinations increases the relative radiation risk, a more extensive discussion of the radiation risk estimates associated with CT scanning in pediatric patients is beyond the scope of this chapter and can be reviewed in a number of recent publications [11–14]. It is reasonable to conclude that opinions vary widely and uncertainty about the absolute risk of cancers associated with ionizing radiation in the diagnostic CT dose range remains [15]. Nonetheless, the principle that guides the use of CT scanning in pediatric patients is adherence to the ALARA (*a*s *l*ow *a*s *r*easonably *a*chievable) guidelines, which seek to balance the relative risk of exposure to ionizing radiation against the potential benefit from the diagnostic information obtained. Namely, every effort should be made to adjust the CT doses to the patient's body size and clinical indications and to minimize scanning of body regions that are not involved or not suspected as harboring disease.

Most major manufacturers now have new dose-reducing automatic tube current modulation technologies as well as iterative image reconstruction algorithms that allow scans to be performed at much lower doses and for the doses to be adjusted dynamically, accounting for the differing tissue densities being imaged [16]. While the technical parameters used in CT scanning are ultimately the responsibility of the radiologist, clinicians ordering CT scans should be aware of these considerations in determining the need for CT and whether the clinical indications warrant the particular examination being ordered.

Magnetic Resonance Imaging

Magnetic resonance imaging (MRI), in contrast to the *transmission* technologies such as conventional radiography, fluoroscopy, and CT, belongs to the group of *emission* technologies. MRI consists of dynamic interactions between a strong external magnetic field, the application of radiofrequency waves, and subsequent reception of low level radiofrequency (RF) emissions from hydrogen nuclei within the body [17]. Once the patient is placed in a magnetic field, the hydrogen nuclei become aligned in the orientation of the magnetic field. When they are bombarded with radiofrequency pulses, the hydrogen nuclei absorb the RF energy. Once the RF waves are turned off, the hydrogen nuclei begin to release the absorbed energy ("decay") in a manner that is related to the tissue characteristics within which the nuclei are residing. This allows exquisitely detailed images of the body's soft tissues to be acquired. There are a number of factors that can influence the signal and image quality obtained during MRI, but these are beyond the scope of this review. In general, in order to acquire a diagnostically useful image, contrast between normal tissues and diseased tissues is needed. Such contrast differences are an inherent reflection of the different tissue environments within which the protons live. Depending on the clinical indication, the MRI pulse sequences can be tailored to address specific clinical questions.

For evaluating the patient with abnormalities of the lymphoid system, characterization of normal and diseased lymph nodes can usually be accomplished well using standard T1- and T2-weighted imaging techniques in axial and at least one orthogonal (coronal or sagittal) imaging plane. The use of gadolinium-based contrast agents can be helpful in further characterizing tissue abnormalities. In some instances, the presence of iron or hemosiderin deposition may be helpful in rendering a differential diagnosis and gradient echo or T2-weighted images, which are sensitive to the local magnetic field inhomogeneities induced by the presence of paramagnetic compounds such as iron, can be utilized [18, 19].

Pediatric whole-body MRI techniques with rapid scanning sequences can now be accomplished typically in 30 min or less and have been advocated for staging and screening patients with abnormalities of the lymphoid system [20, 21]. The use of parallel imaging techniques and the ability to simultaneously receive RF information using multiple receiver coils allows for more rapid imaging and improved temporal and spatial resolution. The increased ability to perform rapid MRI studies for a wide variety of pediatric indications is particularly important for young children in whom an MRI examination of 30 min or more may require sedation in order to minimize patient motion.

The use of diffusion-weighted imaging has recently gained attention for body imaging techniques [22–24]. Diffusion-weighted imaging was initially developed for characterizing sites of brain ischemia in neuroradiologic applications. For oncologic purposes, the ability to evaluate tissue density and tumor cellularity based on changes in the restricted diffusion of water molecules within a particular region, has been helpful in characterizing and evaluating effects of therapy [24]. While diffusion-weighted imaging may aid in detecting small lymph nodes, it has not yet been able to reliably distinguish between neoplastic and non-neoplastic lymph node processes [25, 26].

The use of MR contrast agents includes both positive and negative contrast agents. Gadolinium (Gd)-based agents rely on the paramagnetic effects of Gd, which causes both T1 and T2 relaxation time shortening. The Gd ion itself is toxic and is only provided in the form of a gadolinium chelate. The pattern of tissue uptake and excretion may vary depending on the chelate used, but most commercially available Gd-based MR contrast agents are administered intravenously and are primarily excreted through the genitourinary tract. Iron- and iron oxide-based contrast agents have been specifically advocated for evaluation of the lymphoid system [19]. These agents rely on the T2 shortening effects of iron. Normal cells of the macrophage and reticuloendothelial cell lineage will typically scavenge the iron-based nanoparticles, and the use of these contrast agents has been shown in several pilot studies to be helpful in distinguishing lymph nodes involved by tumor from normal lymph nodes. Despite the potential appeal of this class of contrast agents, they have not received universal clinical acceptance.

The use of Gd-based chelates is relatively safe, although patients with underlying acute or chronic renal insufficiency have been shown to be at risk of developing nephrogenic systemic fibrosis (NSF) [27]. NSF is characterized by progressive tissue fibrosis that may be limited. On occasion, NSF may be progressive with involvement of other tissues such as the heart, lungs, and esophagus resulting in significant pathology and potentially death. Although the risk of developing NSF seems to relate to the doses of Gd chelate used and the degree of renal insufficiency, the majority of patients with renal insufficiency do not develop NSF. Nonetheless, the evaluation of renal function prior to the intended use of Gd-based contrast agents is needed in order to minimize this potential risk.

Nuclear Medicine/Positron Emission Tomography

Functional imaging techniques in nuclear medicine are commonly used in evaluating patients with abnormalities of the lymphoid system. Although these techniques provide less anatomic and morphologic information than either CT or MRI, there is often valuable metabolic and functional information to be gathered from specific nuclear medicine techniques. As with MRI, nuclear medicine imaging relies on emission data following injection with a radiopharmaceutical agent to generate an image [28]. Depending on the pharmaceutical and isotope utilized, the agent localizes to target organs and tissues and is visualized using highly specialized detector cameras used to acquire and display images of the whole body or selected body regions. Cameras are configured to acquire both 2-D planar as well as multiplanar tomographic images and can be placed at various angles and positions to optimize image quality and lesion conspicuity.

Positron emission tomography (PET) utilizes positron-emitting radiopharmaceuticals. Following radionuclide decay in situ, emitted positrons annihilate upon contact with electrons near the point of tissue localization releasing two 511 keV photons traveling in opposite directions. These high-energy photons can be imaged using coincidence detection techniques to permit precise identification of the initial site of radiopharmaceutical localization and positron decay. Similarly, single photon emission computed tomography (SPECT) applies tomographic rather than planar imaging techniques to gamma particle emitting radiopharmaceuticals allowing multiplanar acquisition and projection images to be generated. These can be fused to CT and/or MRI images, which in some instances may be simultaneously acquired to allow anatomical and functional co-localization.

A wide variety of radiopharmaceuticals is available, although the main agents used in routine evaluation of children with lymphoid disorders include ^{99m}Tc labeled methylenediphosphonate (MDP), ^{67}Ga, and ^{18}F-fluorodeoxyglucose (FDG). ^{99m}Tc-MDP localizes to areas of bone turnover and is useful in assessing osteoblastic metastatic disease as well as sites of lytic bony disease. Historically, ^{67}Ga, whic binds to transferrin receptors expressed on lymphoid cells, was used to evaluate patients with lymphoma. The use of gallium scanning has been essentially replaced by FDG PET imaging, and the latter has become standard of care in the evaluation of patients with lymphoma [29, 30] as well as a variety

of other non-neoplastic lymphoid disorders [31]. FDG PET imaging relies on the presence of ^{18}F-fluorine as a positron-emitting radiotracer that is incorporated into the glucose analog fluorodeoxyglucose. FDG accumulates at relatively high levels in metabolically active lesions including lymphoid malignancies and inflammatory disorders, providing a very sensitive means of evaluating patients with abnormalities of the lymphoid system. Nearly all PET imaging is currently performed with integrated PET/CT scanners. This allows areas of FDG uptake at sites of concern to be fused to simultaneously acquired CT images to afford better anatomic correlation and coregistration of uptake sites. In addition, areas of background or physiologic uptake such as brown fat can be accurately identified using co-registered PET/CT images.

Other nuclear medicine imaging techniques include the use of ^{99m}Tc-HMPAO or ^{111}In-oxine labeled leukocytes for inflammatory imaging, although this technique is now less frequently used with the advent of FDG PET imaging. Nuclear medicine plays an important complimentary role in providing a functional characterization of patients with disorders of the lymphoid system. In many diseases, functional imaging is crucial for disease staging, response assessment, and in certain instances disease surveillance. Increasingly, however, the use of nuclear medicine techniques is closely integrated with simultaneously acquired cross-sectional imaging examinations (e.g., CT or MRI), requiring careful assessment of both the functional and anatomic imaging data for diagnostic evaluation [29, 30, 32].

Benign Causes of Lymphadenopathy

In clinical practice, infectious and reactive etiologies are nearly always in the differential diagnosis of lymphadenopathy in a young patient [33]. The most common sites for lymphadenitis requiring imaging evaluation are the cervical, axillary, and inguinal regions. Clinically, lymphadenitis is associated with pain, tenderness, and focal lymph node enlargement [34, 35]. The most common causes of infectious lymphadenitis are summarized in Table 5.1.

Various infectious and reactive etiologies are often associated with broad histologic patterns of lymphadenopathy that include follicular, paracortical, sinusoidal, and mixed patterns [36]. While a more detailed discussion of the pathophysiologic causes that underlie these patterns is beyond the scope of this textbook, a summary of the most common etiologies associated with the various histologic patterns is listed in Table 5.2. Progressive transformation of germinal centers (PTGC) is a term used to describe a well-defined histologic pattern of follicular changes often associated with reactive lymphadenopathy. PTGC is characterized by follicles of varying sizes exhibiting disruption of the germinal center by encroaching mantle zone lymphocytes. The etiology and pathogenesis of isolated PTGC remain poorly understood. While the vast majority of PTGC changes are seen in benign reactive lymph nodes, recognition of this change is important since it is also often seen in the vicinity of nodular lymphocyte predominant Hodgkin lymphoma.

Table 5.1 Most common infectious lymphadenitis

Etiology	Common anatomic site	Histology	Diagnosis
Viral			
Epstein-Barr virus (EBV)-infectious mononucleosis	Cervical lymphadenopathy and splenomegaly	Interfollicular infiltrate with numerous immunoblasts (EBV positive)	Monospot test, and serology studies
Cytomegalovirus	Localized or generalized lymphadenopathy	Florid follicular hyperplasia and hyperplasia of monocytoid B-cells	Presence of CMV inclusions on infected cultured cells
Herpes simplex virus	Localized or multifocal lymphadenopathy	Interfollicular hyperplasia with necrotic areas with neutrophils and karyorrhectic debris	Presence of cells with glass-like inclusions in the areas of necrosis
Bacterial			
Bartonella henselae (Cat-scratch disease)	Regional lymphadenopathy following a skin lesion	Stellate necrotizing granulomas with palisading epithelioid histiocytes	Warthin-Starry stain, PCR, and serology
Common bacteria (streptococcal or staphylococcal)	Cervical lymphadenopathy	Follicular hyperplasia, and microabscesses in the lymph node	Aerobic and anaerobic tissue cultures
Mycobacterium tuberculosis	Supraclavicular and cervical lymph nodes	Ceseating granulomas with epitheliod histiocytes and multinucleated giant cells	Ziehl-Neelsen stain, cultures and PCR
Nontuberculous Mycobacteria (MAI, *M. kansasii, M. scofulaceum, M. malmoense*)	Unilateral cervical lymph nodes	Ceseating granulomas with epitheliod histiocytes and multinucleated giant cells	Ziehl-Neelsen stain, PAS + MAI and PCR
Protozoal			
Toxoplasma	Unilateral or bilateral lymph nodes	Florid follicular hyperplasia, monocytoid B-cells and clusters of epithelioid histiocytes surrounding germinal center	Characteristic cervical histologic changes and serology

Table 5.2 Common reactive lymphadenopathies

Pattern	Histologic findings	Entity
Follicular	Numerous reactive follicles; GC with irregular shape and size Tingible body macrophages; BCL2 is negative in GC	Follicular hyperplasia Autoimmune disorders Castlemans disease, hyaline vascular type Progressive transformation of germinal centers
Sinusoidal	Prominent expansion of sinuses Histiocytic hyperplasia Plasma cell proliferation Monocytoid B-cells	Sinus histiocytosis with massive lymphadenopathy (Rosai Dorfman disease) Storage disease Whipple disease Vascular transformation of sinuses Hemophagocytic syndrome
Interfollicular mixed	Interfollicular expansion T-cell predominance Immunoblasts increased in the interfollicular areas Plasma cells, macrophages Mixed population	Dermatopathic lymphadenopathy Kimura's disease Systemic lupus erythematous Kicuchi's lymphadenitis Inflammatory pseudotumor
Diffuse	Effacement of architecture Mixed population Immunoblastic proliferation	Drug-induced lymphadenophathy Viral lymphadenitis

Lymphoproliferative Disorders and Neoplasms Associated with Immune Deficiency

Lymphoproliferative Disorders and Neoplasms Associated with Primary Immunodeficiency Diseases

Primary immunodeficiencies (PID) are a rare and heterogeneous group of diseases caused by congenital defects affecting the innate and/or adaptive immunity, with impact on the humoral and/or cell-mediated immunity. The most updated classification for PID provided by the International Union of Immunodeficiencies Studies recognizes eight categories [37]: (1) combined immunodeficiencies: e.g., severe common immunodeficiency (SCID); (2) predominantly antibody deficiencies: e.g., X-linked agammaglobulinemia (XLA), common variable immunodeficiency (CVID); (3) well-defined syndromes with immunodeficiency: e.g., Wiskott-Aldrich syndrome, DNA repair defects; (4) diseases of immune dysregulation: e.g., autoimmune lymphoproliferative syndrome (ALPS), familial hemophagocytic lymphohistiocytosis; (5) congenital defects of phagocyte number, function or both: e.g., chronic granulomatous disease, severe congenital neutropenia; (6) defects in innate immunity: e.g., deficiencies impairing the interferon gamma/interleukin 12 axis; (7) autoinflammatory disorders: e.g., familial Mediterranean fever; and (8) complement deficiencies. More than 120 distinct genes have been identified, with abnormalities that account for more than 150 different forms of PID [38].

Patients with PID have a higher than usual risk of developing lymphoid malignancies, and these represent the second leading cause of death in this group [39]. The incidence of lymphoproliferative disease ranges from 1.4 to 24 % depending of the type of the PID. The diseases commonly associated with lymphoproliferative disorders or neoplasms include ataxia-telangiectasia, Wiscott-Aldrich syndrome, Nijmegen breakage syndrome, CVID, XLA, and autoimmune lymphoproliferative syndrome. In these patients, lymphoma is diagnosed at a median age of 7.1 years [39].

The pathogenesis of lymphoproliferative diseases in PIDs involves multiple mechanisms rooted in defects in DNA damage response (e.g., ataxia-telangiectasia and Wiscott-Aldrich syndrome) and immune deregulation that characteristically results in abnormal response to viral infections such as Epstein-Barr virus (EBV), hepatitis B or C viruses, and human papillomavirus [40]. The inability to eliminate infection is speculated to create an inflammatory environment that can eventually promote tumor development and growth by promoting and sustaining the acquisition of oncogenic somatic mutations [39].

Lymphoid proliferations associated with PID are heterogeneous and range in spectrum from reactive hyperplasia to non-Hodgkin and Hodgkin lymphoma. The most common presentation is at extranodal sites; namely, the gastrointestinal tract, lungs, and central nervous system. In patients with XLA and SCID, non-neoplastic lesions include a polymorphous lymphoid proliferation with plasmablasts, immunoblasts and Reed-Sternberg-like cells that result from primary EBV infection. Patients with CVID can present with lymphoid hyperplasia in the gastrointestinal tract or with lymph node follicular hyperplasia and expansion of paracortical

Table 5.3 Most common primary immunodeficiencies associated with lymphoproliferative disorders

Type of deficiency	Gene defect	Pathogenesis	Abnormality	Lymphoproliferative disease
CVID, autosomal (predominantly antibody deficiency)	*ICOS, CD19, BAFFR*	Defects in B-cell maturation and differentiation	Reduced B cells; low IgG and IgA	GI tract and lungs (HHV8 implicated in granulomatous interstitial lung disease), increased risk of B cell, extranodal NHL
SCID (combined immunodeficiency)	X-linked, γ chain mutations; JAK3, AR; ADA, AR	Abnormal interleukin signaling in XSCID and JAK3 mutations; accumulation of dATP in defective ADA	Low or absent T-cells and NK cells and nonfunctional B cells	Fulminant primary EBV Infection, lymphadenopathy, hepatosplenomegaly. Lymphoma development not well documented
Hyper IgM syndrome, X-linked (predominantly antibody deficiency)	CD40/CD40L ligand mutation	Defective B cell and dendritic cell signaling; CD40L required for isotype class-switching from IgM to IgG or IgA	Low or absent IgG, IgA; normal or increased IgM, cytopenias	Predominantly abdominal adenopathy; lack germinal of centers. Lymphoma development not well documented
Ataxia-telangiectasis, AR (well-defined syndromes with immunodeficiency)	AT gene mutation (11q22–23), encodes for protein kinase	Defective DNA repair and deregulation of cell division and apoptosis, abnormal function and development of lymphocytes	IgA, IgE, IgG2 decreased; progressive decrease in T-cells; normal B cell numbers	T-cell acute lymphoblastic leukemia/lymphoma in children; T-prolymphocytic leukemia in young adults; Hodgkin lymphoma-like lymphoproliferative disorders
X-linked lymphoproliferative syndrome (well-defined syndromes with immunodeficiency)	SH2D1A mutations (Xq25), that encodes for SAP protein	Uncontrolled T-cell proliferation; underlying mechanisms is not yet entirely understood	B cells normal or reduced. Defective lysis and polarization following EBV infection	Fulminant IM; extranodal B cell NHL, particularly of the terminal ileum
Autoimmune lymphoproliferative syndrome (well-defined syndromes with immunodeficiency)	Defects in the Fas/FasL signaling	Defects in apoptotic pathway	Autoimmune cytopenias, adenopathy and splenomegaly	Increased risk for HL, including NLPHL
Wiskott-Aldrich, AR (well-defined syndromes associated with immunodeficiency)	WAS mutation (Xp11.22–23)	Abnormal cytoskeletal architecture of hematopoietic cells	Decrease in T-cells, normal B cells; decreased IgM	7 % develop NHL; CNS involvement has been reported in this setting; Lymphomatoid granulomatosis

areas by immunoblasts infected by EBV. In patients with ALPS, lymphadenopathy results from follicular hyperplasia with or without progressive transformation of germinal centers. Overt lymphomas generally have clonal IgH rearrangement whereas non-neoplastic or polymorphous lymphocytic proliferations may show either oligoclonal or monoclonal IgH rearrangements. The presence of clonality in patients with PID does not always indicate the presence of lymphoma and correlation with clinical and imaging findings is particularly important.

The lymphomas that can occur in patients with PID are generally classified like those that arise in non-immunosuppressed patients. Diffuse large B-cell lymphoma is the most common type, followed by Burkitt lymphoma. Lymphomatoid granulomatosis involving the lungs shows T-cell background infiltrate and neoplastic B-cells, and is most commonly seen in patients with Wiscott-Aldrich syndrome. Classical Hodgkin lymphoma is less common than diffuse large B-cell lymphoma in PID patients and has been reported in patients with ataxia-telangiectasia syndrome and Wiscott-Aldrich syndrome. Peripheral T-cell lymphoma is rare and has been described in patients with ALPS. The EBV virus has been demonstrated to be present in most of the cases [41]. A summary of the most common PID types associated with lymphoproliferative disorders and neoplasms is listed in Table 5.3.

Imaging Features

Imaging features associated with PID vary by the type and severity of the immunodeficiency. Patients with XLA do not produce immunoglobulin but do have normal T-cell function and normal thymic development. Radiographically, this disorder is most frequently associated with the sequelae of recurrent pulmonary infections such as bronchiectasis, pulmonary parenchymal scarring and heterogeneous or mosaic patterns of lung aeration and attenuation (Fig. 5.2). Bacterial infection can also occur at other sites such as the sinuses and genitourinary tract; however, these are not as commonly encountered as pulmonary infections [42]. Patients with *IgA deficiency* develop pulmonary and GI infections and may have underlying allergic and autoimmune disorders. In comparison to XLA, the imaging findings are less severe and bronchiectasis,

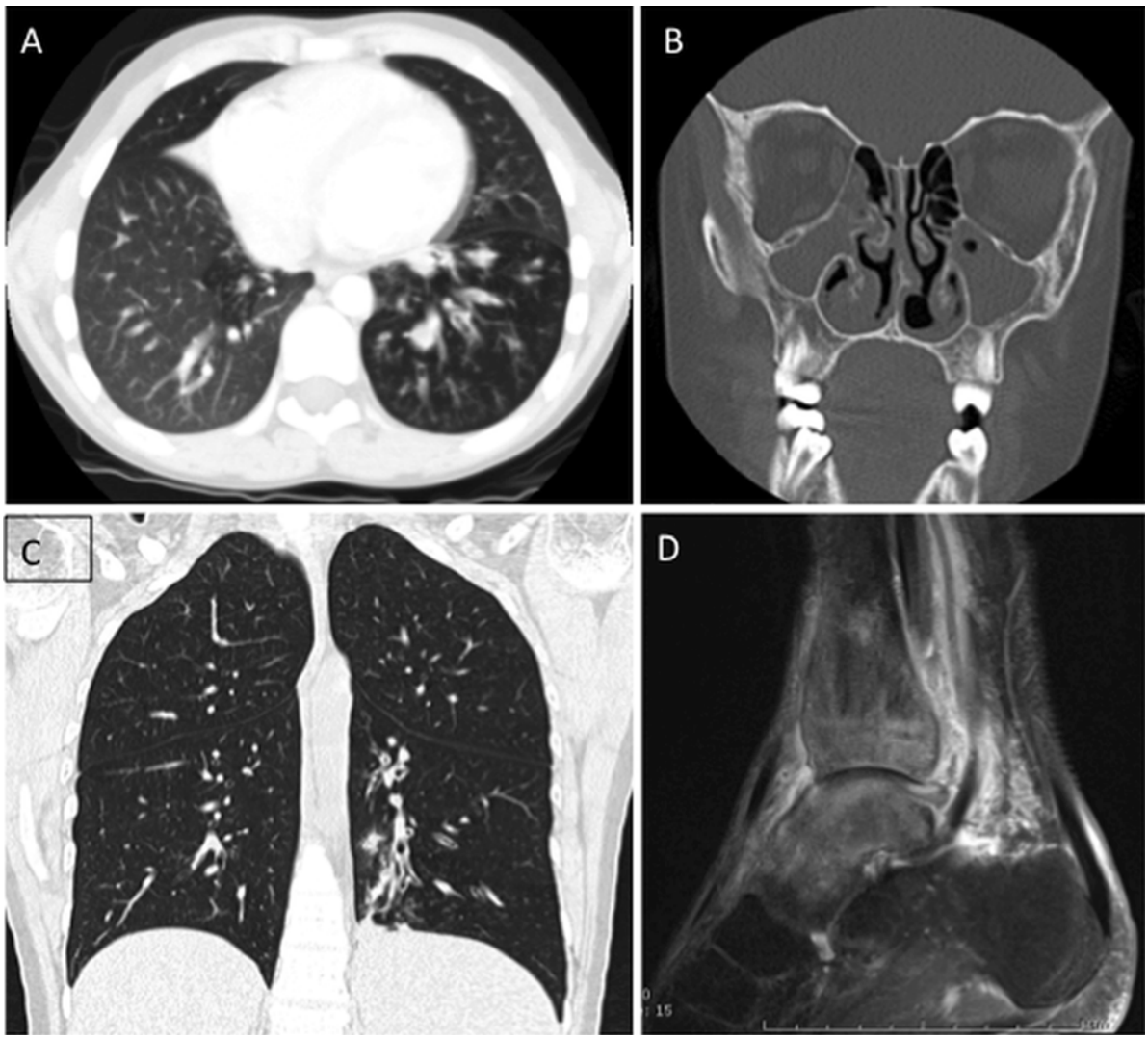

Fig. 5.2 X-linked agammaglobulinemia. Three examples of findings in patients with XLA. 9-year-old with chronic cough and sinus infection with chest CT showing mosaic lung attenuation and air trapping in the left lower lobe (**a**) and near complete opacification of the maxillary sinuses (**b**). Chest CT in a 32-year-old patient with XLA and respiratory symptoms shows left lower lobe bronchial wall thickening, bronchiectasis, and evolving consolidation (**c**). Ankle MRI (**d**) in a 30-year-old patient with XLA revealed osteomyelitis and tenosynovitis related to chronic infection

for example, is less common. Patients with CVID, as with XLA, may also have recurrent infections, bronchiectasis, and bronchial wall thickening. In contrast to the other PID, patients with CVID may also develop lymphadenopathy and splenomegaly in addition to a more generalized lymphoproliferative process (Fig. 5.3), presumably because of varying degrees of associated T-cell functional abnormalities [42, 43].

DiGeorge syndrome (DGS) and SCID are the most severe of the PID syndromes. *DiGeorge syndrome*, also known as thymic hypoplasia, results in primary T-cell deficiency secondary to abnormal thymic development [42]. Patients with DGS have other findings including hypertelorism and micrognathia, which may be apparent radiologically. Other associated anomalies include a host of cardiovascular anomalies such as abnormalities of the aortic arch and tetralogy of Fallot. Apart from the narrow mediastinum resulting from absent thymic tissue, there are no other specific imaging findings to indicate the diagnosis of DGS. *Severe combined immunodeficiency* syndrome results from absent T- and B-cell function, as well as diminished natural killer cell function. As with DGS, the combination of deficiencies in both humoral and cellular immunity in patients with SCID leads to recurrent and severe opportunistic infections [43].

Patients with Wiskott-Aldrich syndrome and ataxia telangiectasia have a high incidence of developing malignancy, particularly leukemia and lymphoma [44, 45] (Fig. 5.4). In addition, patients with ataxia telangiectasia are at an

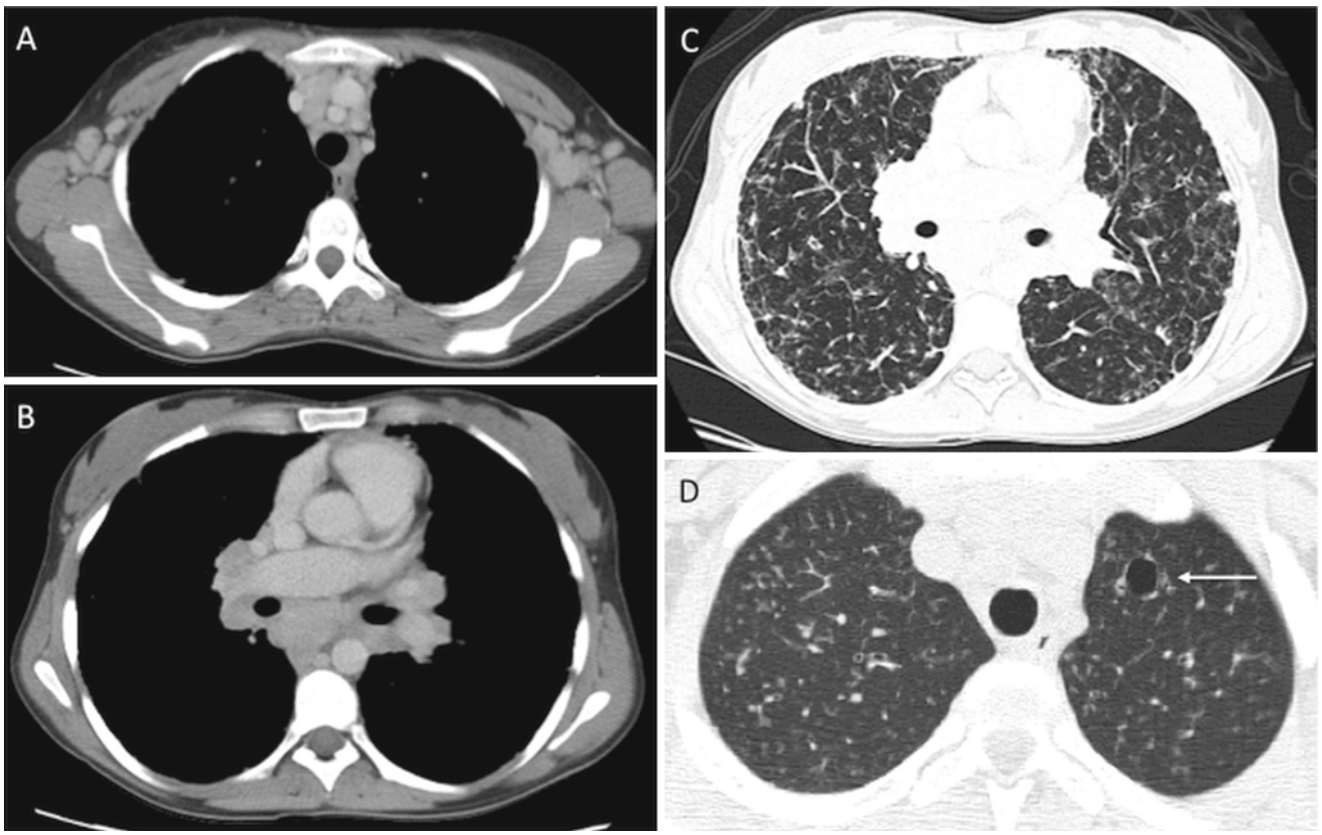

Fig. 5.3 Common Variable Immunodeficiency (CVID) (**a**–**c**) and Hyper-IgE syndrome (**d**). Chest CT in a 26-year-old patient with CVID (**a**–**c**) shows axillary (**a**) and mediastinal/hilar lymphadenopathy (**b**), in addition to extensive parenchymal lung disease (**c**), with ground glass opacities, reticular thickening and areas of air trapping related CVID. Chest CT in patient with hyper-IgE syndrome reveals a small pneumatocele (*arrow*), characteristic of this disease, in the left upper lobe, as well as background diffuse nodular opacities consistent with underlying infection

increased risk of radiation-induced malignancy, which creates unique challenges for surveillance imaging studies. Because imaging examinations in these populations of patients are aimed at screening for malignancy or characterizing active or chronic sites of infection, the results are often nonspecific, prompting multiple follow-up imaging evaluations. As such, techniques that require repeated exposure to ionizing radiation (i.e., CT) should be used judiciously [46].

Lymphoid Neoplasms Associated with Human Immunodeficiency Virus Infection

Human immunodeficiency virus (HIV) infection and the associated acquired immune deficiency syndrome (AIDS) occur infrequently in children and often as the result of in utero transmission. A distinct group of lymphoid neoplasms arise in the setting of HIV infection. These include lymphomas that are seen in HIV-negative patients such as Burkitt lymphoma, diffuse large B-cell lymphoma, and Hodgkin lymphoma. In addition, HIV patients are affected by lymphomas that are only rarely seen outside the setting of HIV: primary effusion lymphoma and plasmablastic lymphoma. The introduction of highly active antiretroviral therapy (HAART) has resulted in a dramatic decrease in the incidence of high grade lymphomas in HIV patients.

Most patients present with advanced stage disease and extranodal involvement. Extranodal sites usually include the gastrointestinal tract, central nervous system (CNS), liver and bone marrow, as well as more unusual sites such as oral mucosa and body cavities. Lymph nodes can also be involved. Epstein-Barr virus is identified in approximately 40 % of HIV-associated lymphomas, but this percentage varies significantly between the different types of lymphomas. Distinction between neoplasia and infection on imaging studies may be difficult occasionally; for example, CNS involvement by toxoplasmosis is a rare complication in pediatric HIV patients and can be difficult to distinguish from lymphoma [47].

Post-transplant Lymphoproliferative Disorders

Post-transplant lymphoproliferative disorders (PTLD) are lymphoid or plasma cell disorders that develop in a recipient of a

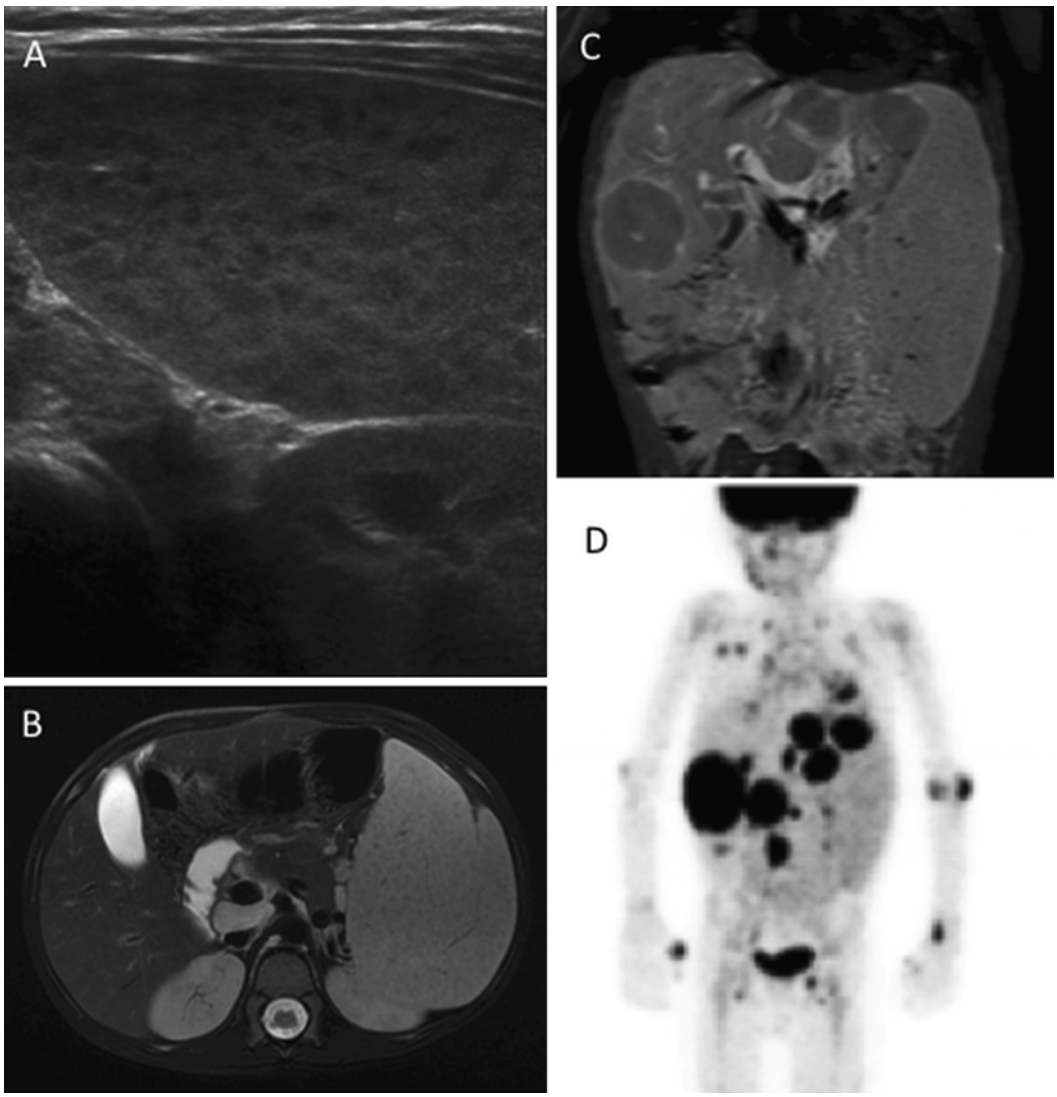

Fig. 5.4 A 6-year old with ataxia telangiectasia initially presented with splenomegaly. Ultrasound showed diffuse splenic enlargement with innumerable hypoechoic lesions, concerning for lymphoproliferative disease (**a**). Over the next 2 months subsequent MRI confirmed splenic involvement (**b**), in addition to showing multifocal hepatic involvement (**c**). Biopsy revealed large cell lymphoma. FDG PET shows extensive abnormality of the abdomen, lungs, and skeleton (**d**)

solid organ or allogeneic stem cell transplant as a result of iatrogenic immunosuppression. The spectrum of PTLD is clinically and histologically variable. Three broad categories of PTLD are recognized: (1) early lesions (infectious mononucleosis-like and plasmacytic hyperplasia); (2) polymorphic PTLD; and (3) monomorphic PTLD. The latter includes lymphomas that also occur in non-immunosuppressed patients such as Hodgkin lymphoma and plasma cell myeloma. When compared to the adult population, the incidence of PTLD in children is higher, especially following solid organ transplant. The risk for development of PTLD is significantly associated with the occurrence of primary EBV infection after transplantation [48, 49].

Imaging of PTLD patients is directed at establishing the extent of involvement and should include cross-sectional imaging, either CT or MRI, of the entire torso as well as FDG PET imaging to establish the overall extent of disease [50]. Both CT and PET can be used to monitor response to therapy and/or immunomodulation. FDG PET has been shown to be superior to conventional imaging techniques in the early evaluation of PTLD response to therapy [50].

Routine screening for PTLD (e.g., EBV serologic studies or quantitative assessment of viral RNA) facilitates early diagnosis and treatment by reduction of immunosuppression. Lymph nodes as well as extranodal sites (tonsil, gastrointestinal tract, lungs, spleen and liver can be involved (Fig. 5.5). In solid organ transplant recipients, PTLD may affect the allograft itself and needs to be differentiated from rejection or infection. Detection

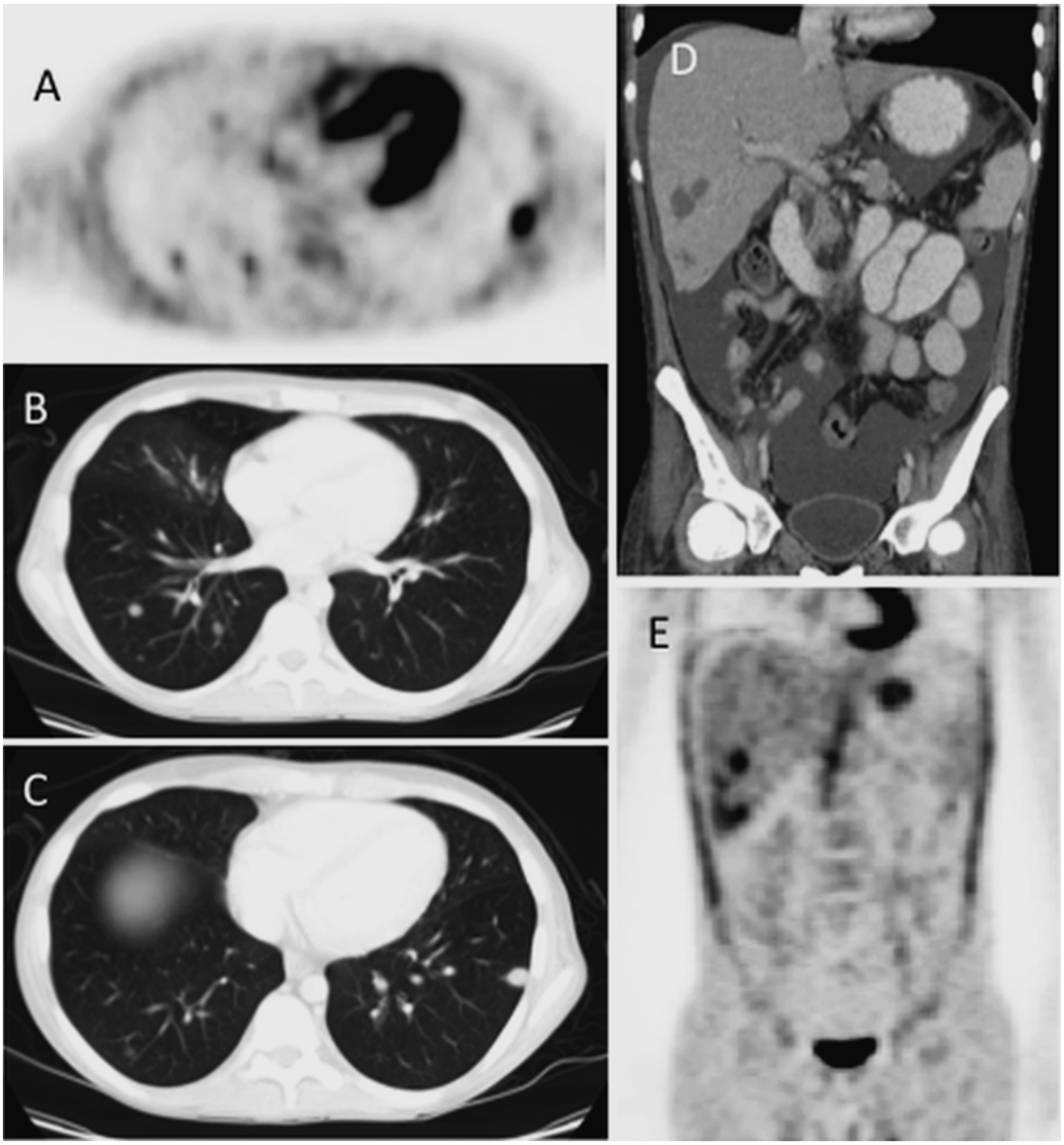

Fig. 5.5 PTLD involving lung and liver: 16-year old with AML s/p BMT with development of pulmonary PTLD. FDG-PET (**a**) and Chest CT (**b**, **c**) show multiple FDG avid lung lesions. Abdominal CT (**d**) and accompanying FDG-PET (**e**) show multiple hepatic lesion as well as ascites, all consistent with multi-focal sites of PTLD involvement

of EBV-encoded RNA in the lesion generally favors PTLD. Early lesions, including infectious mononucleosis-like PTLD are more frequent in children and usually involve tonsils and adenoids. They have a good prognosis and respond to reduction of immunosuppressive treatment. However, the polymorphous PTLD is the most common type affecting pediatric transplant recipients. Some cases of polymorphic PTLD and most cases of monomorphic PTLD require additional treatment that includes monoclonal antibodies against B-cell antigens (e.g., rituximab), chemotherapy, and more recently cellular immunotherapy (EBV-specific cytotoxic T-cell immunity).

Overview and Classification of Lymphoid Tumors

Lymphoma represents the third most common pediatric malignancy [51]. Lymphoid malignancies comprise 11 % of total cancers diagnosed in children and 13 % in adolescents and young adults (15–39 years) [52]. The classification of lymphoid neoplasms has undergone a bewildering series of changes over the course of several decades. Those classifications have been universally supplanted by the World Health Organization (WHO) classification. Distinct entities in the WHO classification

Table 5.4 Common lymphoid neoplasms in children and young adolescents

Precursor lymphoid neoplasms
B-lymphoblastic leukemia/lymphoma, NOS
B-lymphoblastic leukemia/lymphoma with recurrent genetic abnormalities
T-lymphoblastic leukemia/lymphoma, NOS
Mature B-cell neoplasms
Nodal marginal zone lymphoma
Extranodal marginal zone lymphoma of mucosa-associated lymphoid tissue (MALT lymphoma)
Pediatric follicular lymphoma
Diffuse large B-cell lymphoma, NOS
Lymphomatoid granulomatosis
Primary mediastinal (thymic) large B-cell lymphoma
ALK positive large B-cell lymphoma
Burkitt lymphoma
Mature T-cell neoplasms
Epstein-Barr virus (EBV) positive T-cell lymphoproliferative disease of childhood
Systemic EBV + T-cell lymphoproliferative disease of childhood
Hydroa vacciniform-like lymphoma
Extranodal NK/T-cell lymphoma, nasal type
Enteropathy associated T-cell lymphoma
Hepatosplenic T-cell lymphoma
Subcutaneous panniculitis-like T-cell lymphoma
Primary cutaneous gamma-delta T-cell lymphoma
Peripheral T-cell lymphoma, NOS
Anaplastic large cell lymphoma
ALK positive
ALK negative
Hodgkin lymphoma
Nodular lymphocytic predominant Hodgkin lymphoma
Classical Hodgkin lymphoma
Nodular sclerosis
Mixed cellularity
Lymphocyte-rich
Lymphocyte-depleted
Immunodeficiency –associated lymphoproliferative disorders
Lymphoproliferative diseases associated with primary immunodeficiency
Lymphomas associated with HIV infection
Post-transplant lymphoproliferative disorders
Plasmacytic hyperplasia and infectious-mononucleosis-like PTLD
Polymorphic PTLD
Monomorphic PTLD
Classical Hodgkin lymphoma PTLD
Histiocytic neoplasms
Langerhans cell histiocytosis
Disseminated Juvenile xanthogranuloma

are defined on the basis of morphologic, immunophenotypic, molecular, and clinical features. Lymphoid neoplasms in the current WHO classification that generally affect children and adolescents are summarized in Table 5.4.

Precursor T and B Neoplasms

Together, precursor T and B neoplasms represent the most common malignancies in childhood. These neoplasms are derived from precursor lymphoid cells (lymphoblasts) arrested at an early stage of differentiation. B lymphoblastic leukemia/lymphoma accounts for approximately 85 % of cases while T lymphoblastic leukemia/lymphoma accounts for the remaining 15 % [53].

Lymphoid precursor neoplasms may either involve the bone marrow and blood (lymphoblastic *leukemia*) or exhibit a predominantly tissue-based distribution (lymphoblastic *lymphoma*). An arbitrary cutoff of ≥25 % blasts in the blood and/or bone marrow is used to define lymphoblastic leukemia. Since such a distinction has no known diagnostic or prognostic relevance, the current WHO classification employs the term lymphoblastic leukemia/lymphoma.

The prognosis of patients with precursor T and B neoplasms is based on many parameters that include molecular and cytogenetic features in addition to response to induction chemotherapy. In general, patients with T lymphoblastic leukemia/lymphoma tend to have worse outcomes than those with B lymphoblastic leukemia/lymphoma.

T Lymphoblastic Leukemia/Lymphoma

Clinical Features and Epidemiology

T lymphoblastic leukemia/lymphoma is a neoplasm of lymphoid progenitors committed to the T lineage. The disease commonly affects males in the second decade of life, and whites are more commonly affected than Asians or African Americans [54]. Patients with ataxia-telangiectasia have an increased predisposition to developing T lymphoblastic leukemia/lymphoma [45]. Up to 85 % of children and adolescents with T lymphoblastic leukemia/lymphoma present with a mediastinal mass and/or lymphadenopathy without leukemia [55, 56]. The majority of patients have symptoms of mediastinal involvement, including pain, facial swelling, and respiratory compromise. Depending on the size of the mediastinal mass, there may be a significant compression of the airway, cardiac, and central vascular structures.

Imaging Features

Patients with T lymphoblastic leukemia/lymphoma and a large mediastinal mass often have their initial disease suspected based on chest radiograph (Fig. 5.6a, b). These rapidly proliferating tumors can enlarge quickly and present one of the few oncologic emergencies one may encounter in the imaging suite [57]. The presence of a pericardial effusion may result in cardiac tamponade. Care should be taken with

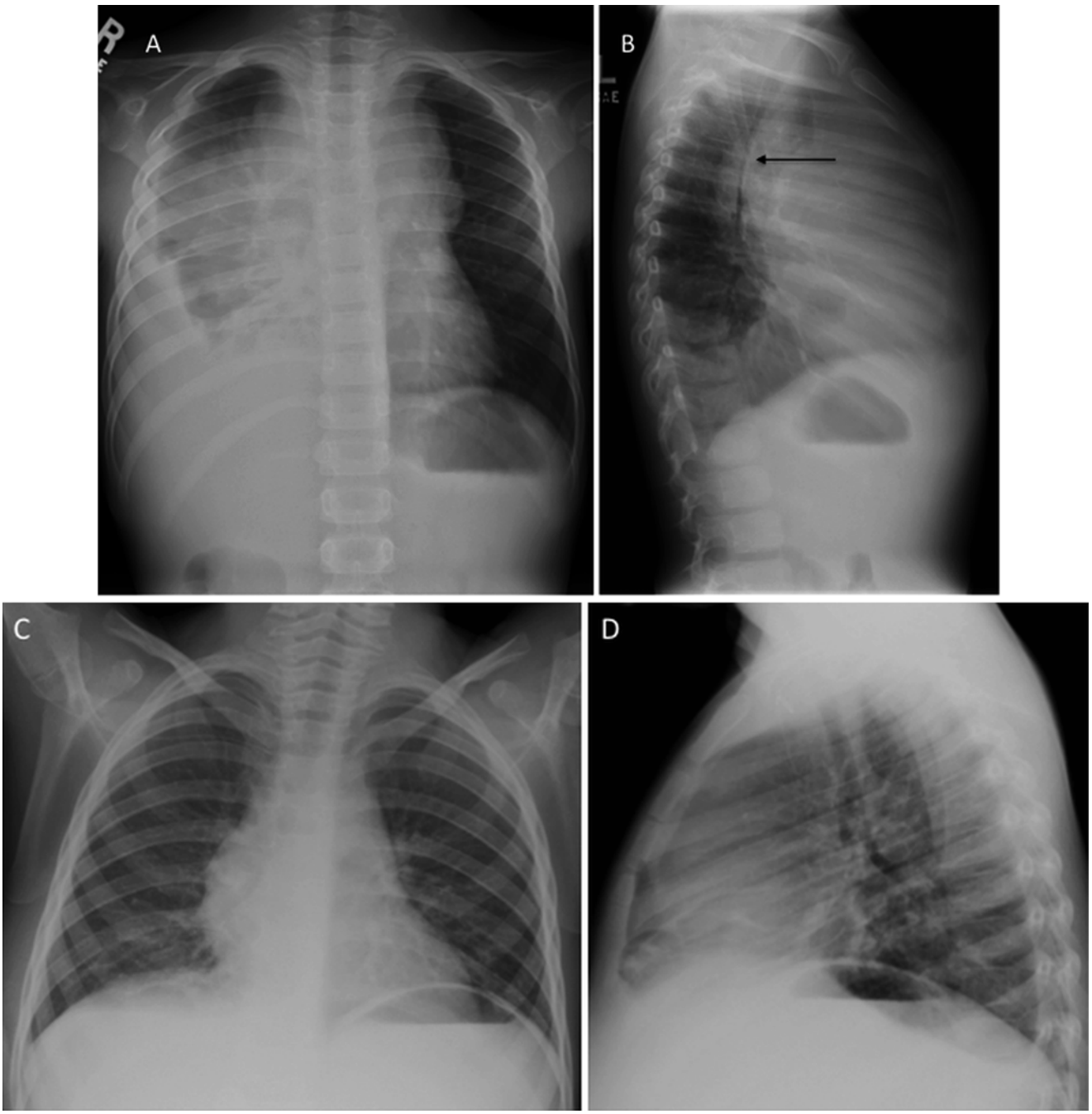

Fig. 5.6 T-lymphoblastic lymphoma: 5-year old with wheezing, fatigue, and pallor. AP and lateral CXR at diagnosis shows large mediastinal mass with significant tracheal narrowing evident on the lateral projection arrows and a large right pleural effusion (**a**, **b**). The patient could not lie flat for biopsy; pleural fluid aspirate showed T-Cell ALL. After just 6 days of therapy mediastinal mass has nearly resolved and effusions are gone (**c**, **d**)

supine positioning of these patients and with sedation given the increased risk of respiratory compromise and impaired venous return.

Once appropriate therapy is instituted, patients with Tlymphoblastic leukemia/lymphoma typically have a rapid shrinkage in their mediastinal mass and improvement in their symptoms (Fig. 5.6c, d). There is no clear prognostic role for CT characterization of the mediastinal mass apart from establishing the extent of disease and sites of disease of involvement that may require urgent intervention. CT scans at the time of diagnosis may demonstrate extensive abdominal visceral involvement and intra-abdominal lymphadenopathy (Fig. 5.7). Some studies have shown that early resolution of the mediastinal mass, either by chest radiograph [58] or by

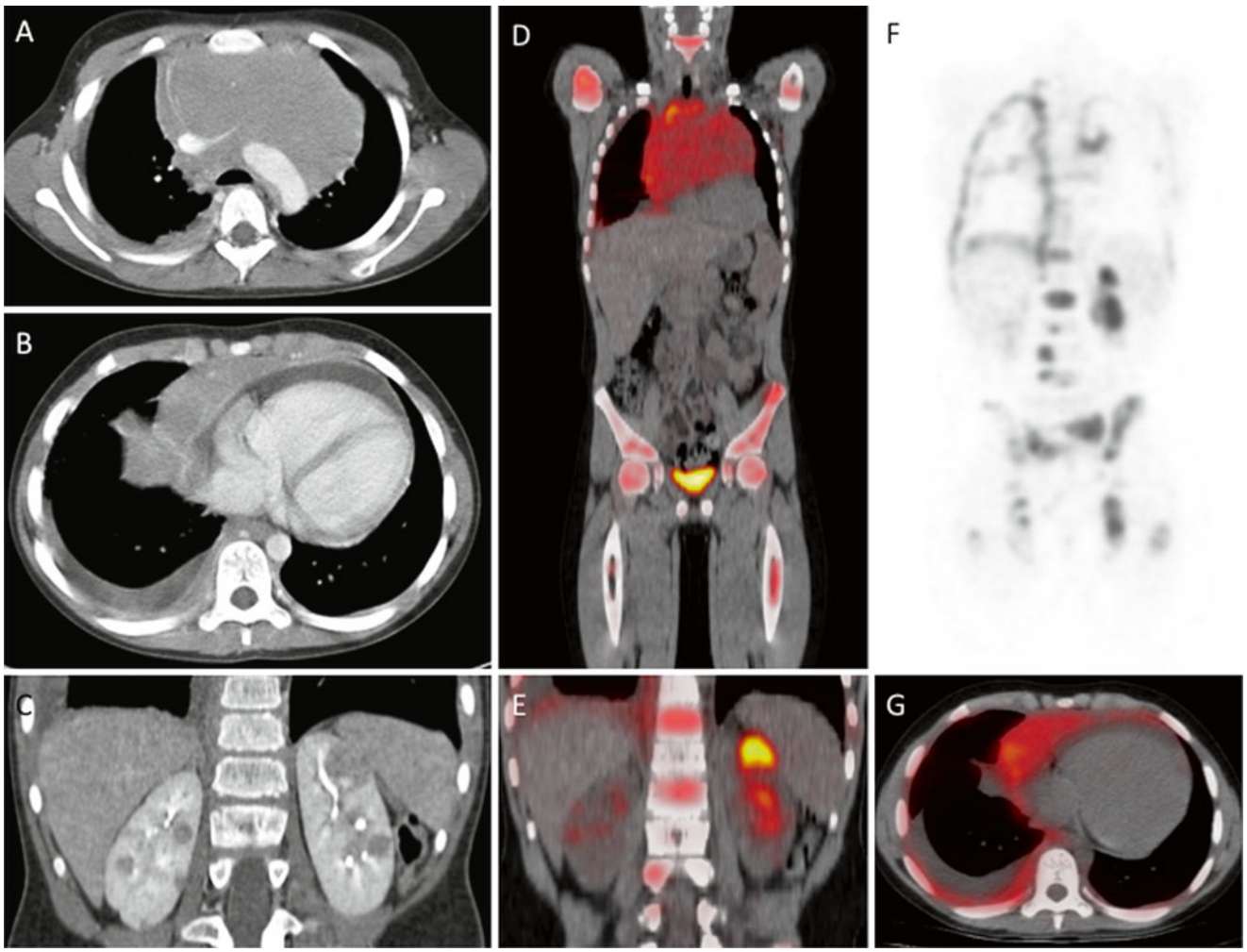

Fig. 5.7 T-lymphoblastic lymphoma, CT and FDG PET: 10-year old with T-ALL, mediastinal mass compressing major vessels (**a**), pleural effusion and pericardial effusion (**b**) and extensive visceral (bilateral renal (**c**) and bony disease (**e**, **f**). FDG PET/CT confirms multifocal sites of involvement by metabolically active tumor and in particular shows the extent of bone involvement (**d**–**g**)

CT [59] is associated with improved outcome, presumably reflecting patients with more chemosensitive disease.

Although these rapidly dividing tumors are quite metabolically active and typically FDG avid (Fig. 5.7), staging and post-treatment evaluation by FDG PET imaging is not used frequently in patients with precursor lymphoid neoplasms.

Pathology

The neoplastic cells have scant to moderate cytoplasm, irregular nuclear contours, and a dispersed chromatin pattern. The latter is best appreciated on Wright-Giemsa-stained preparations. A similar pattern is noted on hematoxylin-and-eosin-stained tissue sections. Characteristically, the neoplastic cells have high rates of mitosis and apoptosis with frequent areas of increased background macrophages imparting a so-called starry-sky pattern (Fig. 5.8).

Immunohistochemistry or flow cytometry immunophenotyping demonstrates expression of one or more T lineage markers including CD1a, CD2, CD3, CD4, CD7 and CD8 (Fig. 5.9). Of these, CD3 is regarded as the *bona fide* T lineage-specific marker. In addition, the neoplastic cells are often positive for CD34, TdT, and CD99. It should be noted that CD99 expression may be positive in other small round cell tumors that are usually part of the differential diagnosis [60]. T-LBL can be further subclassified into groups representing stages of T-cell maturation and differentiation (Table 5.5). Early T-cell precursor (ETP) acute lymphoblastic leukemia/lymphoma represents approximately 15 % of precursor T neoplasms and is characterized by high frequency of relapses following standard chemotherapy [61]. This recently described entity is characterized by CD3 expression (cytoplasmic ± surface using flow

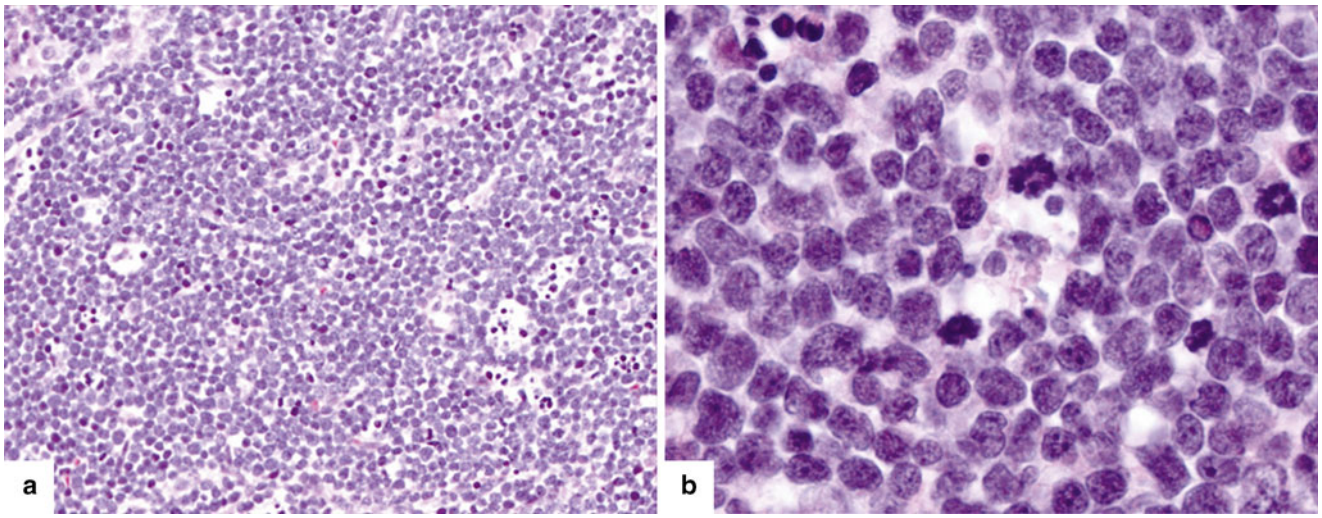

Fig. 5.8 (**a**) Precursor T-cell ALL diffusely involving the lymph node with numerous mitoses and tingible-body macrophages imparting a "starry-sky" appearance. (**b**) The blasts have characteristic features including small to intermediate size, scant amount of cytoplasm, irregular nuclear membranes, finely dispersed chromatin, and inconspicuous nucleoli

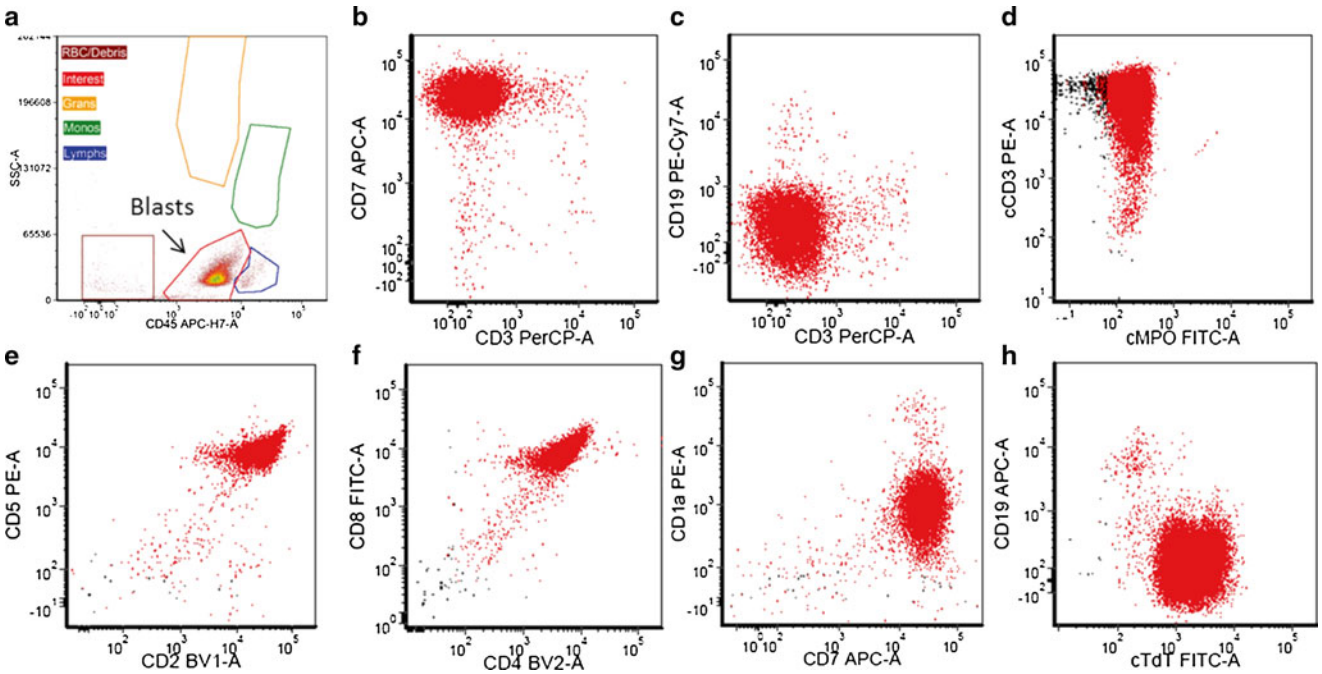

Fig. 5.9 Precursor T-cell ALL immunopheotype. The patient is a 14-year-old male with diffuse lymphadenopathy. A core biopsy reveals a diffuse infiltrate of mononuclear cells with blast morphology. Flow cytometry was performed on a cell suspension that showed increased blasts defined by dim CD45 expression and low side scatter (SSC-A) properties (**a**). The blasts expressed bright CD7 (**b**), and they were negative for CD19 (**c**). They also expressed cytoplasmic CD3 that confirmed T-cell lineage, while they were negative for MPO (**d**). The blasts also expressed CD2, CD5 (**e**), and were double positive for CD4 and CD8 (**f**). They were also positive for CD1a (**g**) and TdT (**h**), and negative for B-cell (CD19) and myeloid (MPO) antigens

Table 5.5 T-ALL Immunophenotype associated with T-cell maturation and differentiation

Stage	Immunophenotype
Pre-thymic stage	Common lymphoid progenitor cell (pro-T) expressing CD34, TdT and HLA-DR and are negative for cytoplasmic CD3 (cCD3)
Subcupsular cortical stage	Early T-cell precursors (pre-T) that express CD2, cCD3, CD7, TdT and are double negative (CD4- and CD8-). TCR gene at germ line configuration
Cortical stage	Common thymocyte phenotype: CD1a, CD2, cCD3, CD7, TdT and double positive for CD4 and CD8. TCR gene rearrangement identified
Medullary stage	Mature medullary thymocytes loose expression of TdT and CD1a, and express both cytoplasmic and surface CD3 and either CD4 or CD8 (single positive thymocytes)

Table 5.6 B-ALL with recurrent genetic abnormalities (2008 WHO classification)

Translocation	Fusion product	Frequency (%)	Prognosis	Immunophenotype
t(9;22)(q34;q11.2)	*BCR-ABL1*	2–4 % in children	Poor	CD25+, CD117−, CD13+, CD33+, CD10+, CD19+, TdT+, CD34+, CD9+
t(v;11q23) t(4;11)(q21;q23) t(19;11)(p13;q23) t(9;11)(p22;q23)	*MLL* *AF4-MLL* *ENL-MLL* *AF9-MLL*	Most common Also seen in T-ALL Common in AML	Poor	CD19+, CD10−,CD24−, CD15/65+, CD9+
t(12;21)(p13;q22)	*TEL-AML1 (ETV6-RUNX1)*	25 % of cases, common in children	Favorable	CD34+, CD13+, CD9−
Hyperdiploidy >50 chromosomes (most common +21, +X, +14, +4)		25 % of cases, common in children	Favorable	CD34+, CD45−
Hypodiploidy <46 chromosomes	−	<45 chromosomes 1 %	Poor	
t(5;14)(q31;q32)	*IL3-IGH@*	<1 %	Unknown	Eosinophilia
t(1;19)(q23;p13.3)	*E2A-PBX1 (TCF3-PBX1)*	6 %	Improved with current intensive therapies	CD9 + strong, CD34−, cμ heavy chain

BCR breakpoint cluster region, *ABL1* abelson murine leukemia viral oncogene holog 1, *MLL* mixed lineage leukemia, *AF4* AF4/FMR2 family, member 1, *ENL* MLLT1 myeloid/lymphoid/leukemia or mixed lineage leukemia translocated to 1, *AF9* ALL-1 fused gene from chromosome 9, *TEL (ETV6)* translocation, ETS, leukemia, *AML1 (RUNX1)* acute myeloid leukemia 1 gene (RUNT-related transcription factor), *IL-3* interleukin 3, *IGH@* immunoglobulin heavy chain, *E2A (TCF3)* immunoglobulin enhancer-binding factor E12/E47 (transcription factor 3), *PBX1* pre-B leukemia transcription factor 1

cytometry), lack of expression of CD1a, and aberrant expression of stem cell myeloid markers (CD34, CD33, CD13, and CD117).

B Lymphoblastic Leukemia/Lymphoma

Clinical Features and Epidemiology

B lymphoblastic leukemia/lymphoma, in contrast to its T counterpart, usually has limited tissue involvement at presentation [56, 62]. The majority of patients present with peripheral blood and bone marrow disease, with skin, testes, and lymph nodes being among the most common sites of extramedullary involvement. Various molecular/cytogenetic B lymphoblastic leukemia/lymphoma groups are recognized in the WHO classification (Table 5.6).

Imaging Features

Extensive thoracic or abdominal involvement is uncommon with B lymphoblastic leukemia/lymphoma. Accordingly, the use of FDG PET imaging for staging is generally not indicated. Typically, the initial staging evaluation is directed by symptoms and physical exam findings. For example, the presence of a testicular mass noted by ultrasound might prompt additional evaluation (Fig. 5.10).

Pathology

The morphologic features of B lymphoblastic leukemia/lymphoma are identical to those of T lymphoblastic leukemia/lymphoma. The B-cell lineage is defined by the expression of CD19 and one or more of the following markers: CD79a, cytoplasmic CD22 and/or CD10 (Fig. 5.11). In addition, the neoplastic cells are often positive for CD34 and TdT. PAX5 is a highly specific B-cell marker that is expressed in virtually all cases of B lymphoblastic leukemia/lymphoma [63]. It should be noted that the neoplastic cells of B lymphoblastic leukemia/lymphoma might be negative for CD20 and CD45 by immunohistochemistry. B lymphoblastic leukemia/lymphoma can be further subclassified into groups representing stages of B-cell maturation and differentiation (Table 5.7).

Mature B-Cell Neoplasms

Lymphomas account for approximately 15 % of all childhood malignancies, but their incidence varies in different age groups being low in children younger than 5 years and highest in adolescents between 14 and 19 years of age [64]. Mature B-cell neoplasms are broadly divided into two categories: Hodgkin lymphoma and non-Hodgkin lymphoma (NHL).

Hodgkin Lymphoma

Clinical Features and Epidemiology

Hodgkin lymphomas account for nearly 9 % of all childhood cancers and usually occur in adolescents. They are unusual in children under the age of 5 years. Hodgkin lymphomas are primary nodal malignancies characterized by relatively few

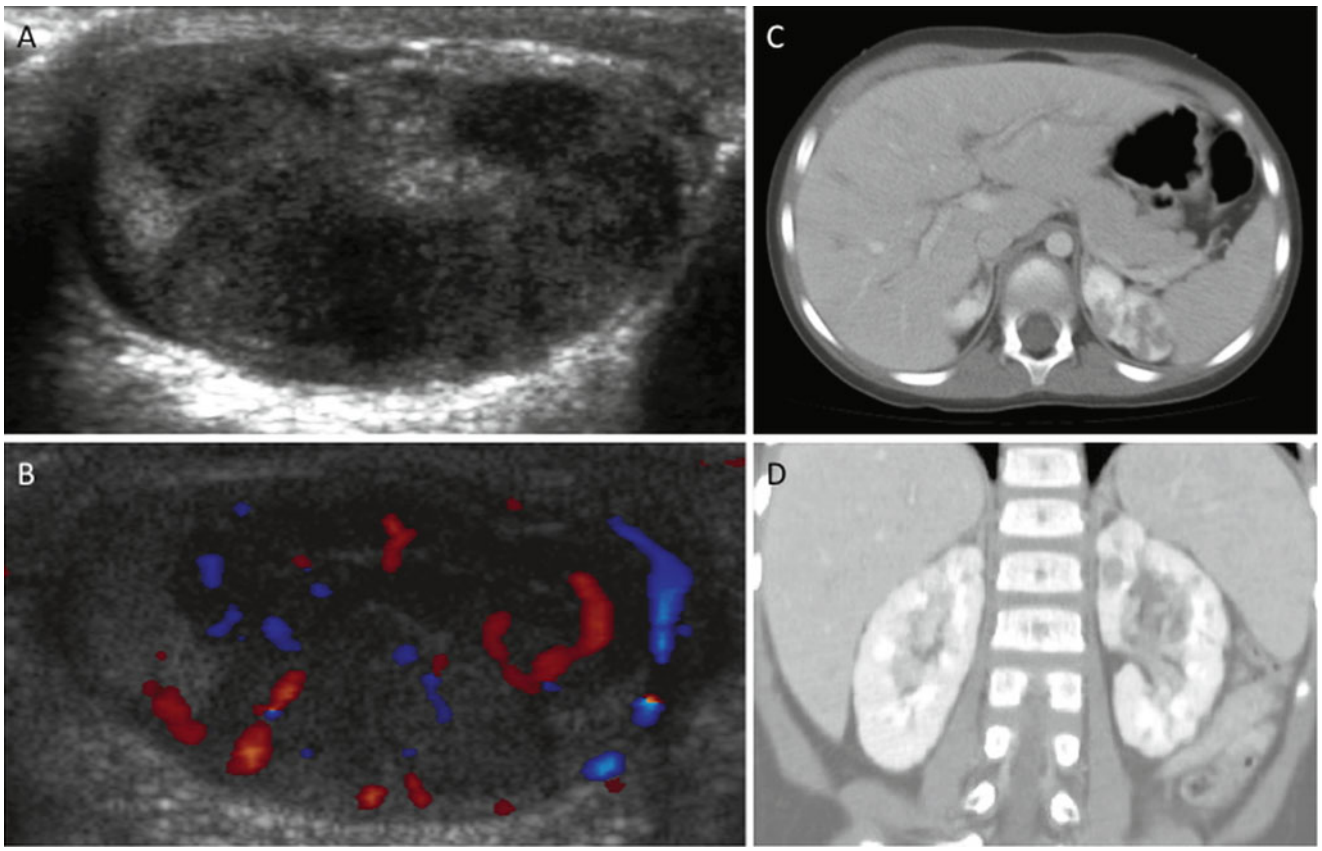

Fig. 5.10 Pre-B lymphoblastic lymphoma: 4-year-old with bilateral asymmetric, nontender testicular enlargement detected by pediatrician at a routine check-up. (**a**, **b**) US showed multifocal testicular masses with increased color Doppler flow (b). (**c**, **d**) CT showed additional bilateral renal involvement, L>R. Biopsy revealed pre-B cell lineage lymphoblastic lymphoma; bone marrow had <5 % blasts

dispersed monoclonal lymphoid cells, most commonly of B-cell lineage, surrounded by a sizeable heterogeneous population of inflammatory cells. The WHO classification divides Hodgkin lymphomas into two broad groups with distinct differences in clinical features and behavior as well as in immunophenotype: classical Hodgkin lymphoma (CHL) and nodular lymphocyte predominant Hodgkin lymphoma (NLPHL).

Classical Hodgkin lymphoma (CHL) accounts for nearly 95 % of all Hodgkin lymphomas. Four subtypes of CHL are recognized: nodular sclerosis, mixed cellularity, lymphocyte-rich, and lymphocyte-depleted. The most common sites of involvement with CHL include the mediastinum and cervical lymph nodes. The nodular sclerosis subtype is more common in developed countries and less commonly associated with EBV, whereas the mixed cellularity subtype is more common in developing countries and is frequently associated with EBV. Nodular lymphocyte predominant Hodgkin lymphoma (NLPHL) comprises approximately 5 % of Hodgkin lymphomas. The most common sites of involvement include cervical, axillary, and inguinal lymph nodes, with only rare involvement of the bone marrow, mediastinum, or spleen [65].

Therapy selection and prognostic stratification of Hodgkin lymphoma is based on pathologic and imaging staging studies, which include bilateral bone marrow biopsies and PET/CT scans [66]. The current staging system for Hodgkin lymphoma is based on the Ann Arbor staging classification system (Table 5.8). The staging system accounts for the absence (A) or presence (B) of systemic symptoms including night sweats, weight loss, and fever. The presence extranodal extension of disease (other than to bone marrow and liver, which would result in stage 4 disease) is annotated with the letter E [67].

Imaging Considerations

In Hodgkin lymphoma, chest radiographs are often the first examination to suggest the possibility of malignancy. These are usually obtained for vague upper respiratory or constitutional symptoms including fever, night sweats, and cough. A mediastinal mass is present in more than two thirds of patients at the time of diagnosis (Fig. 5.12). These findings typically prompt further evaluation by CT or

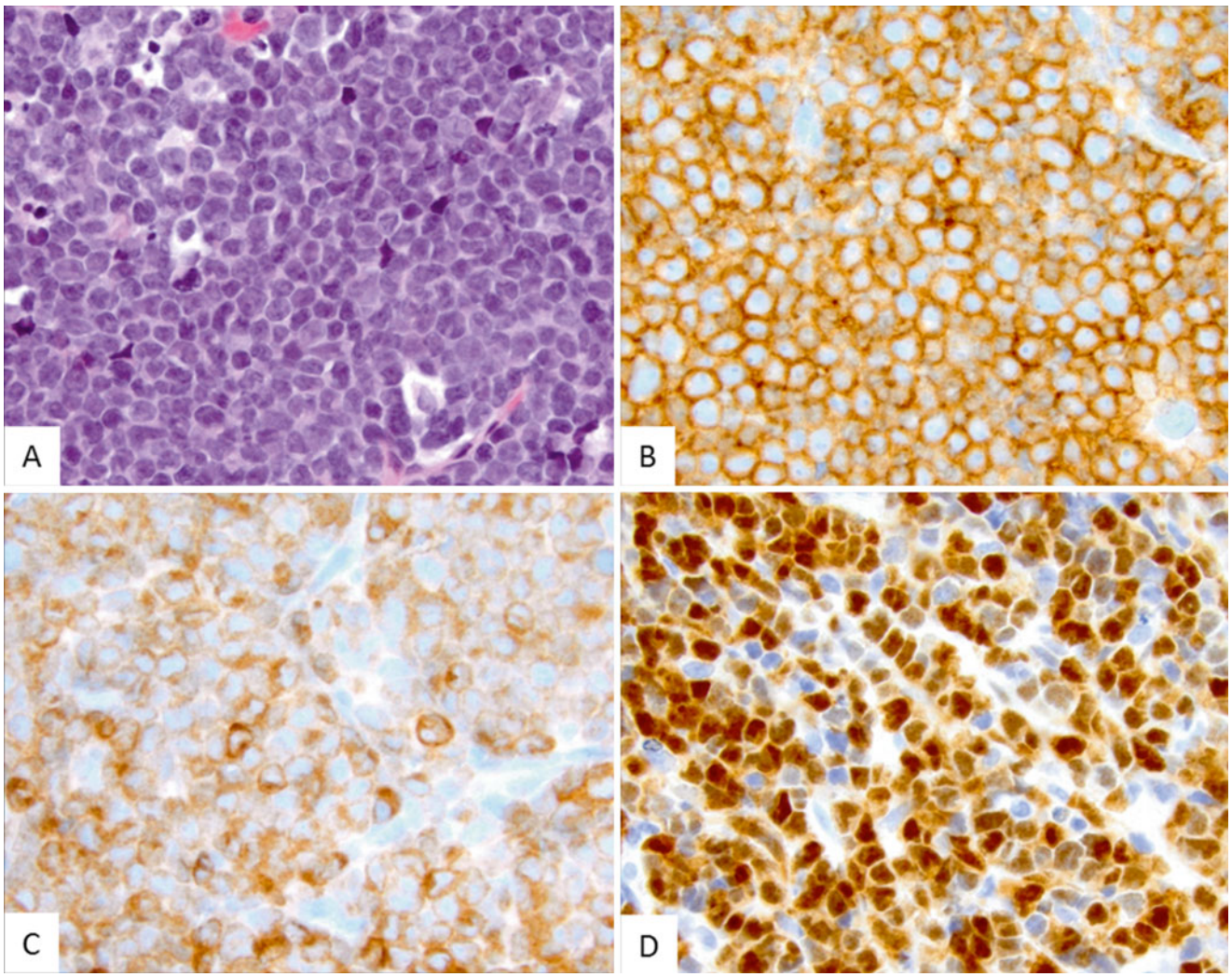

Fig. 5.11 This case of precursor B-cell ALL reveals a neoplastic infiltrate that is morphologically identical to precursor T-cell ALL. (**a**) Immunohistochemical stains showed that the blasts expressed characteristic B-cell markers being positive for CD19 (**b**) and PAX5 (**c**), as well as for TdT (**d**)

Table 5.7 B-ALL Immunophenotype associated with B-cell maturation and differentiation

Stage	Immunophenotype
Pro-B stage	Early precursor B-ALL: CD10, CD19, cytoplasmic CD79a, cytoplasmic CD22, and TdT
Intermediate stage	Common B-ALL is characterized by expression of CD10, CD19, HLA-DR and heavy chain gene rearrangement
Pre-B stage	At this stage the cells express CD19, surface CD22, and cytoplasmic μ chains. Heavy chain and light chain gene rearrangement. At this stage TdT and CD34 are not expressed

MRI. The diagnostic and staging examination should encompass all of the potential sites of lymph node involvement and should begin at the level of the skull base/Waldeyer ring and extend through the inguinal region. At the time of the staging, it is important to be aware of the potential for airway and vascular compression due to large neck and mediastinal masses. Indeed, it may be clinically contraindicated to place a patient supine for CT evaluation due to the presence of a large mediastinal mass and obvious airway narrowing that is apparent radiographically, although in some instances imaging can be accomplished with the patient prone (Fig. 5.13). The presence of greater than 50 % tracheal luminal narrowing poses a significant risk to sedation and anesthesia and should be a major consideration in the staging and diagnostic evaluation [68]. In addition to characterizing the extent of disease, the imaging evaluation should also help identify easily accessible lymph nodes for diagnostic sampling.

By imaging alone, it is not possible to distinguish between the subsets of Hodgkin lymphoma. One exception is nodular

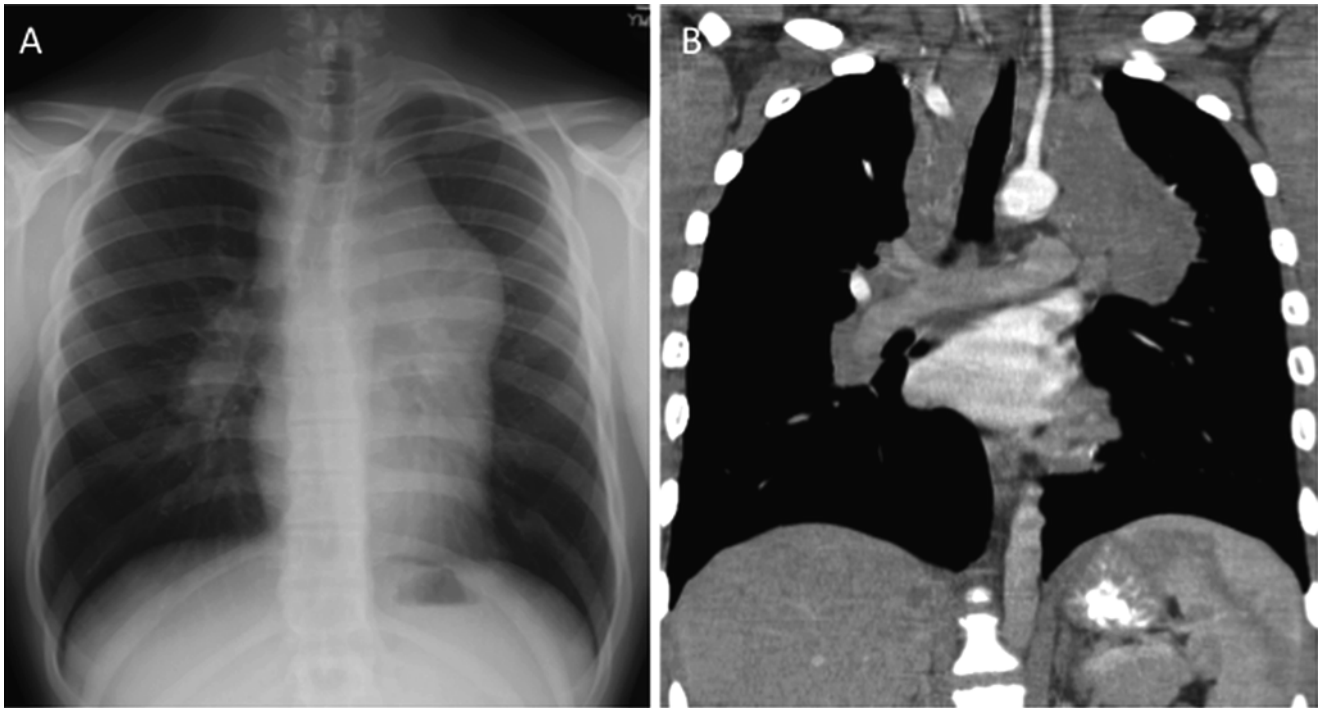

Fig. 5.12 Hodgkin lymphoma: 17-year old presented to the emergency room with chest pain and airway symptoms. (**a**) CXR shows a large mediastinal mass and rightward tracheal deviation. (**b**) Coronal CT image confirms extensive mediastinal, paratracheal, and hilar nodal involvement. Biopsy confirmed nodular sclerosis classical Hodgkin lymphoma

lymphocyte predominant Hodgkin lymphoma, which may be suggested by the presence of localized disease. Indeed, it is not uncommon for a single site of NLPHL to be completely removed at the time of surgical excisional biopsy. In Hodgkin lymphoma, hematogenously spread metastatic disease to the lung is uncommon, and is seen in less than 5 % of the patients [69]. It is not uncommon for pulmonary disease to be present; however, this is usually seen in association with ipsilateral hilar or mediastinal nodal involvement and likely reflects contiguous extension as opposed to hematogenous spread. This may be important in determining the stage of the patient, since true hematogenous spread resulting in pulmonary parenchymal nodules would indicate stage 4 disease (Fig. 5.14a, b), whereas a localized mediastinal disease with ipsilateral contiguous parenchymal involvement via peribronchovascular lymphatics would be considered stage 2-E (2-extension) disease (Fig. 5.14c, d). Pericardial and pleural effusions may be seen in Hodgkin lymphoma. It is also important for the radiologist to be alert for the presence of cardiophrenic lymph nodes and to distinguish these from upper abdominal lymph node involvement. Involvement of the abdominal viscera is relatively unusual. Liver involvement, when present, is almost always associated with splenic involvement. Isolated splenic involvement occurs in 30–40 % of the patients with Hodgkin lymphoma [69]. Often, the extent of splenic involvement may be difficult or impossible to determine by CT and is only suggested by FDG PET imaging [70]. Bone marrow involvement in Hodgkin lymphoma is rare and bone marrow aspiration has been almost completely replaced by FDG PET imaging for the purpose of staging the bone marrow for tumor involvement [71] (see below discussion).

Imaging modalities used in staging: CT scanning is still the imaging modality of choice for staging children with Hodgkin lymphoma, although several recent studies have advocated the use of MRI for this purpose [32]. FDG PET imaging is considered standard of care in the staging of children with suspected Hodgkin lymphoma [72]. Hodgkin lymphoma is typically a metabolically active tumor (Fig. 5.15) and FDG PET has increased sensitivity for detecting small sites of hypermetabolic lymph node involvement that may influence disease staging, particularly in areas difficult to characterize by cross-sectional imaging, such as the hepatic hilum and retroperitoneum, and visceral sites of involvement such as the spleen. The ability to co-register simultaneously acquired PET/CT images has further advanced the use of PET imaging in pediatric Hodgkin lymphoma staging [72] (Fig. 5.16). The overall consensus from multiple studies is that FDG PET imaging combined with co-registered, simultaneously acquired cross-sectional imaging, either by CT or

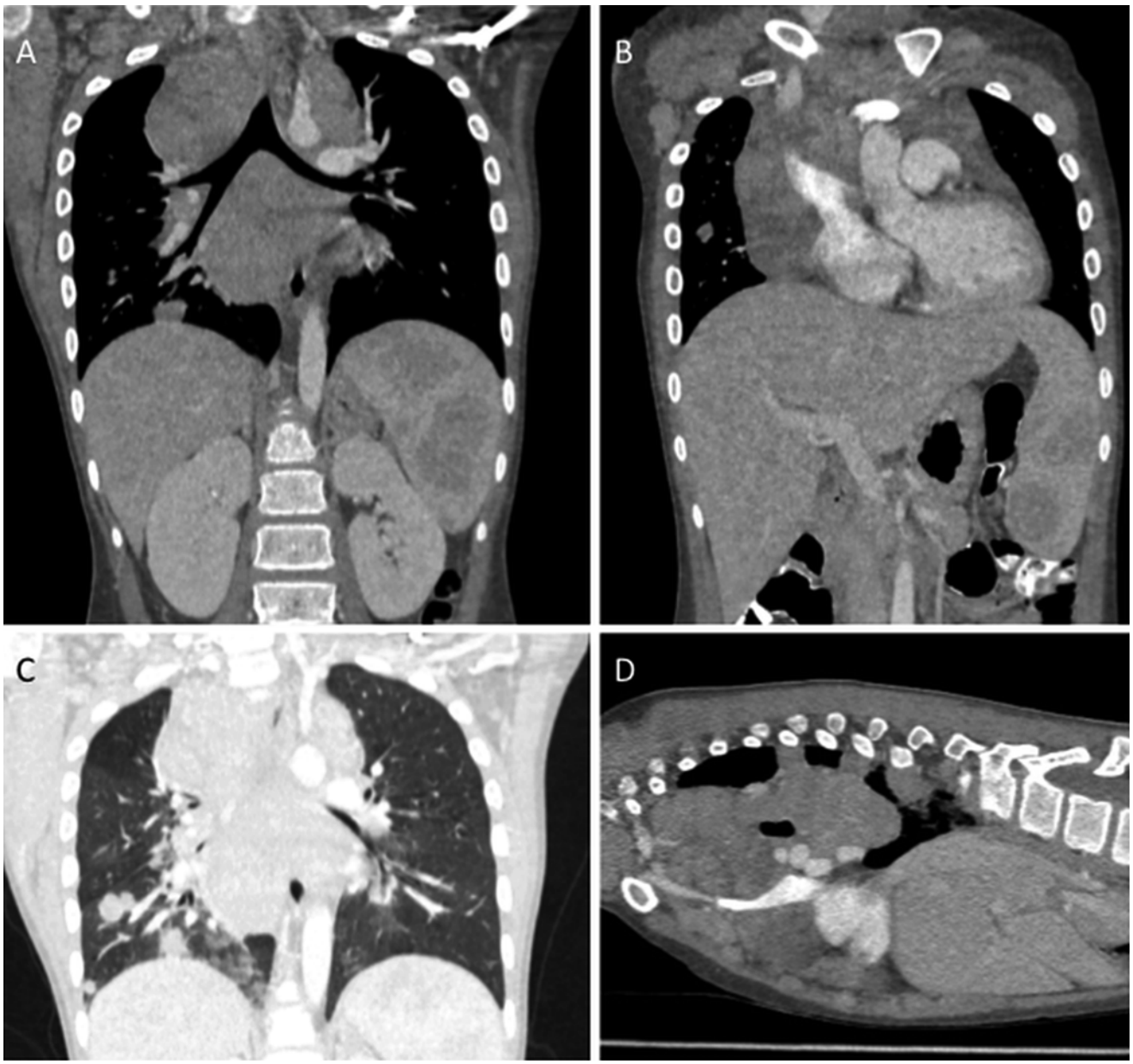

Fig. 5.13 Patient with HL and CT images at diagnosis showing extensive mediastinal, hilar, subcarinal, and splenic involvement (**a**, **b**). CT images reviewed under lung windows show parenchymal lung nodules and heterogeneous lung attenuation, with attendant compression of the bronchi. The imaging was performed prone (**d**) based on clinical concern for airway and vascular compression, which the CT confirms, showing significant SVC narrowing (**b**) and tracheal compression (**a**, **c**)

by MRI, provides the greatest sensitivity and specificity for staging the patient with suspected lymphoma [72–75]. The combined images retain the sensitivity of FDG PET at identifying sites of radiographically occult disease, while at the same time, improving the specificity of the PET imaging, allowing sites of background or physiologic uptake to be accurately localized and distinguished from malignancy.

At the time of diagnosis, diffuse homogeneous low-level bone marrow uptake is commonly seen and should not be interpreted as diffuse marrow involvement. Rather, this likely represents reactive marrow hyperplasia secondary to the underlying Hodgkin lymphoma [71], and is readily distinguishable from the focal areas of FDG uptake seen in patients with bone marrow involvement by lymphoma (Fig. 5.17). Based on imaging, there are no specific or characteristic FDG PET features to distinguish between the different forms of Hodgkin lymphoma and biopsy is required to make this distinction.

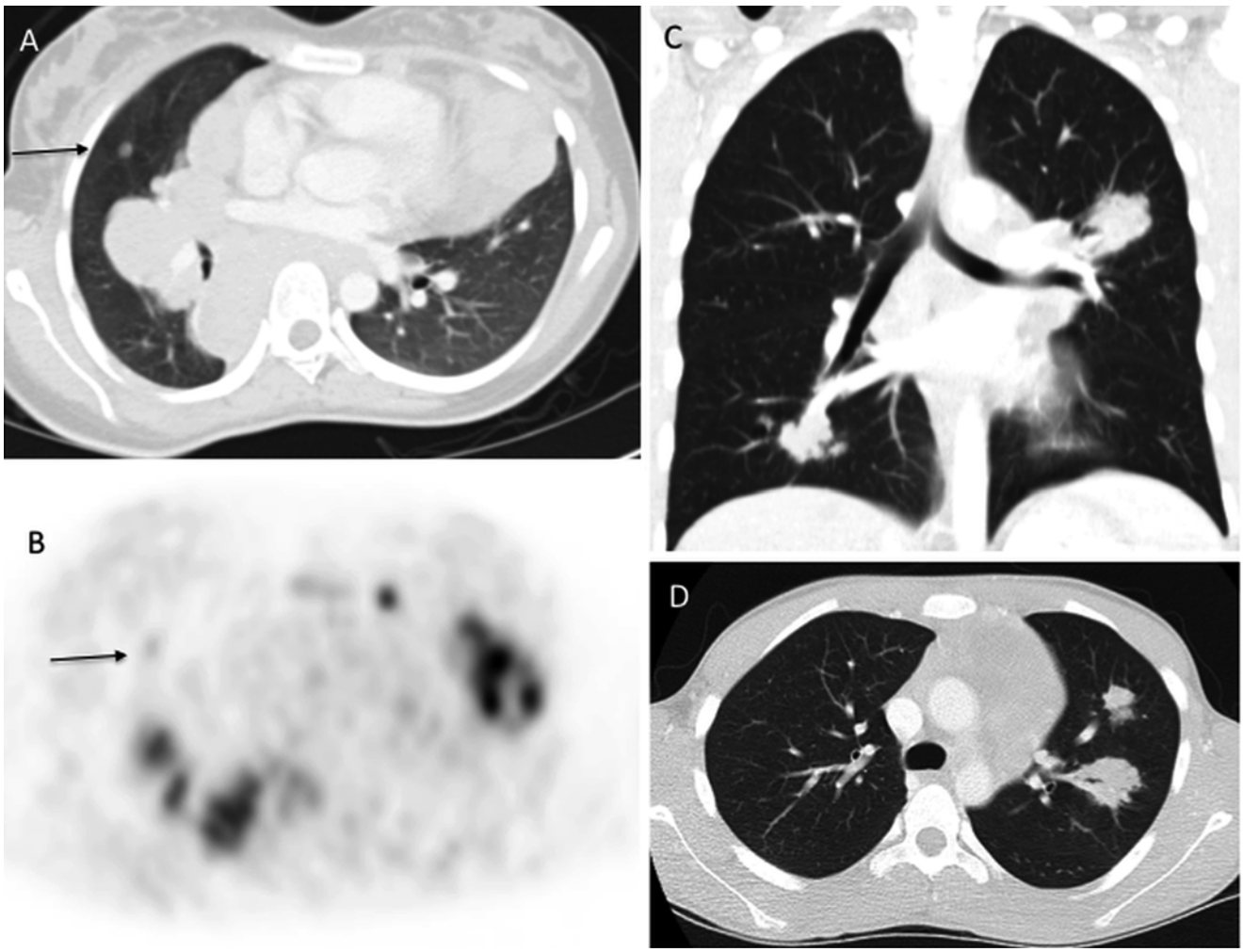

Fig. 5.14 Lung nodules in HL. (**a**, **b**) CT (a) and FDG PET (b) focal parenchymal lung nodule (*arrows*) that is FDG avid and distinct from the more centrally located mediastinal mass. This is in contrast to the parenchymal abnormalities shown by CT in (**c**) and (**d**) that extend from sites of mediastinal and hilar involvement, consistent with local extension along peribronchovascular lymphatics, rather than hematogenously spread disease

The use of bone scintigraphy in Hodgkin lymphoma is rarely performed, and has been replaced by FDG PET imaging [71]. The use of intravenous contrast agents for either CT or MRI evaluation is still considered necessary in the staging evaluation of Hodgkin lymphoma patients, even when hypermetabolic FDG PET avid disease is present. The presence of contrast allows for a more accurate measurement of disease at the time of diagnosis (Fig. 5.18), which has been shown to be important in response assessment [6] and in terms of providing accurate measurement to establish the presence of bulky disease. Furthermore, the presence of vascular invasion or thrombosis is also difficult to detect in the absence of contrast agent administration.

Chest radiographs are often still required by clinical protocols for determining the presence of mediastinal bulk disease, and typically are obtained at the time of initial disease presentation. Many clinical protocols still require an upright PA chest radiograph to determine the maximal transthoracic diameter of the mediastinal mass, with bulk disease being defined as a mediastinal mass greater than 1/3 the transthoracic diameter [76], as measured at the level of T5/T6. The Ann Arbor staging system is still used to classify patients with childhood Hodgkin lymphoma (Table 5.8). The Cotswold modification of the Ann Arbor staging system incorporates CT imaging criteria and specifies that lymph nodes detected by CT that are greater than 10 cm in transaxial diameter are to be considered sites of bulk disease [76], although different pediatric cooperative groups use different size cut-offs for determining bulk disease (e.g., the Children's Oncology Group considers lymph nodes masses >6 cm as indicative of bulk disease).

Response assessment: Patients with Hodgkin lymphoma typically enjoy greater than 90 % 5-year overall survival, with even higher rates for patients with low stage disease [69, 77]. As a

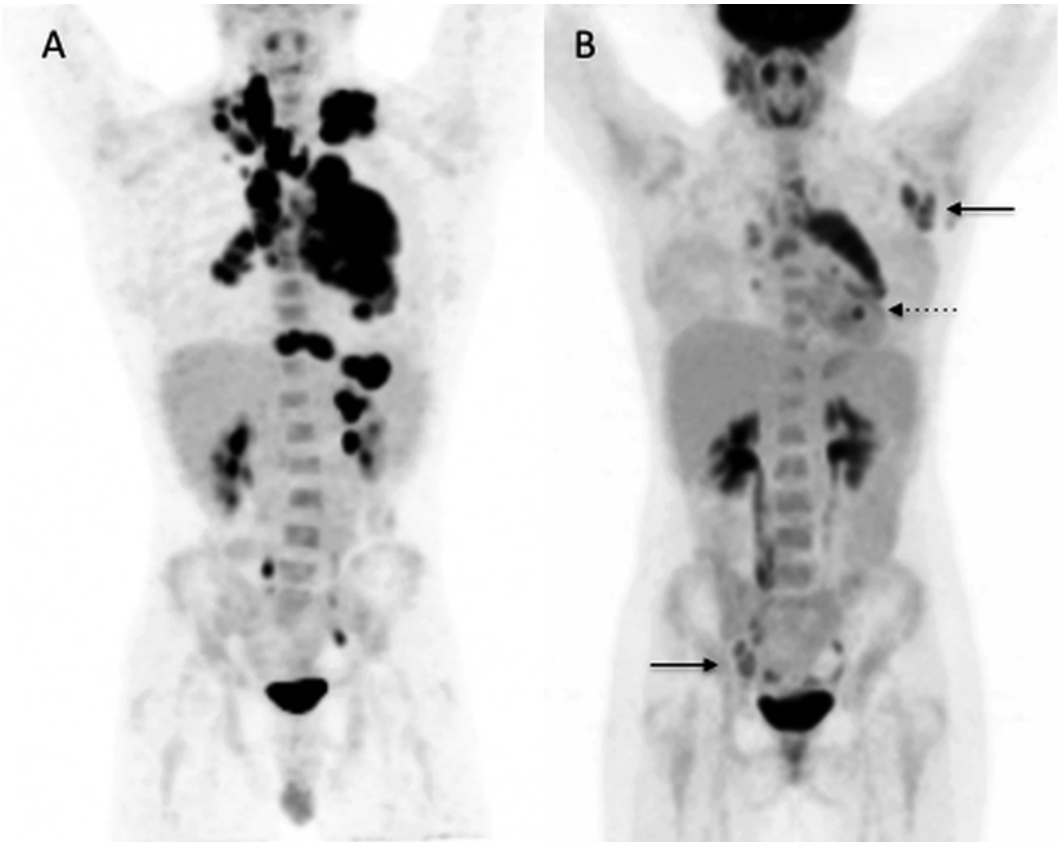

Fig. 5.15 FDG PET in Hodgkin Lymphoma. Two patients showing intensely FDG avid disease. (**a**) This patient has supraclavicular, hilar, and mediastinal disease with separate foci of disease in diaphragmatic nodes. (**b**), This patient, in addition to having mediastinal and hilar disease, also has FDG avid lesions in the left axilla and in the right iliac chain (*arrows*), as well as the left lower lobe of the lung (*dashed arrow*), emphasizing the importance of PET in identifying multifocal sites of disease involvement

result, objective measures of treatment response have gained increasing attention in an effort to develop early, objective, and prospectively evaluable end points to identify patients who are responding early to therapy, in an effort to predict which patients will have a durable response to therapy [29, 78]. There is some evidence to suggest that a brisk early response to chemotherapy may be a determinant of tumor chemosensitivity and predict an overall good outcome [78–80]. The ability to monitor changes in metabolic activity within the mediastinal mass using FDG PET imaging has provided a valuable surrogate for assessing early response to therapy [72, 75]. There have been multiple studies both in adult and pediatric patients showing that patients with early responses to therapy based on decreases in FDG PET uptake have improved event free and overall survival as compared to those who have residual PET abnormalities after the initial two cycles of therapy [81, 82]. These results have led to implementation of a response-based treatment paradigm where early interim FDG PET scanning could be an excellent prognostic indicator for predicting chemosensitivity of the tumor and ultimately clinical outcome (Fig. 5.19). Subsequent studies, evaluating both change in size of the mediastinal mass and change in the metabolic activity, have suggested that outcomes will likely be best predicted by a combination of factors including resolution of FDG uptake and significant change in size of the patient's sites of disease involvement as measured by CT and/or MRI [5, 6].

In an effort to arrive at a consensus regarding definitions of disease and treatment response in adult patients with lymphoma, an international team of experts reviewed the available data to arrive at the so-called international harmonization project criteria for determining PET and CT responses in lymphoma [83, 84]. These are shown in Table 5.9, based on a revision of previous malignant lymphoma response criteria and have been recently updated as the Lugano Classification [85, 86]. Although these proposals for classification, staging, and response assessment have not yet been validated in pediatric patients, the main challenge that remains for clinicians and diagnostic imagers is developing objective criteria for assessing FDG PET response. There have been a number of proposals aimed at distinguishing residual low-level neoplastic FDG activity from background uptake [72]. The use of standardized uptake value measurements is still considered

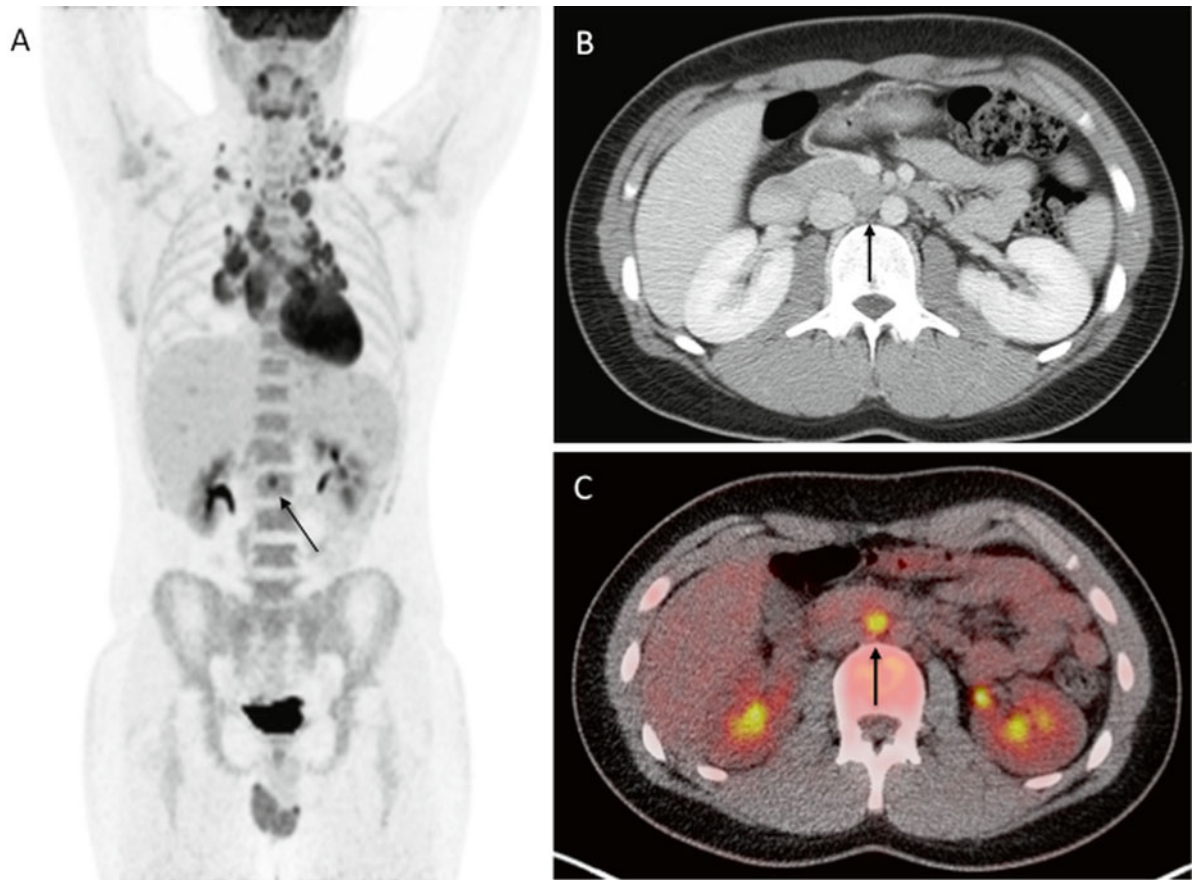

Fig. 5.16 Impact of FDG-PET on disease staging: (**a**) Coronal FDG PET MIP image showing extensive mediastinal disease and bilateral supraclavicular disease. In addition, a tiny focus of uptake below the diaphragm (*arrows*) localized to an aortocaval node on the fused PET/CT image (**c**). With the benefit of the PET images for review, the small aortocaval lymph node could be readily identified on the diagnostic CT obtained earlier (*arrow*) (**b**)

experimental and has not been universally accepted. The criteria receiving the greatest acceptance have been based on a 5-point scale, with uptake greater than mediastinal blood pool, but less than liver, considered to be background, with uptake greater than the liver considered suspicious for residual activity [85–87]. These criteria must, however, be validated in larger treatment trials.

Surveillance: Also at issue is the use of imaging for disease surveillance and the frequency with which surveillance should be performed. In a study of over 200 pediatric patients with intermediate and high risk lymphoma, it was found that the sole predictor of overall survival in these patients was time to relapse [88]. Those patients who relapsed within the first year after completing therapy had lower overall survival than those patients who had relapses after the first year. Furthermore, relapses that occurred beyond 1 year off therapy, whether they were detected by physical exam, laboratory findings or routine surveillance imaging (Fig. 5.20), were equally likely to have a good clinical outcome. Based on this, it was proposed that routine surveillance CT imaging beyond 1 year after therapy be eliminated, since it is unlikely to impact overall survival and adds additional cost and radiation exposure to patients who are likely to have an overall good outcome [88–91].

Pathology

Classical Hodgkin Lymphoma

The lymph node architecture is often effaced in classical Hodgkin lymphoma. The neoplastic Hodgkin-Reed-Sternberg (HRS) cells are typically large and dispersed among background inflammatory cells, which include variable numbers of small lymphocytes, plasma cells, eosinophils and histiocytes. Reed-Sternberg cells are binucleated neoplastic cells with round to oval nuclear contours, a prominent eosinophilic nucleolus within each of the nuclei, and abundant amphophilic or basophilic cytoplasm. Neoplastic cells without characteristic Reed-Sternberg features are referred to as Hodgkin cells (Fig. 5.21).

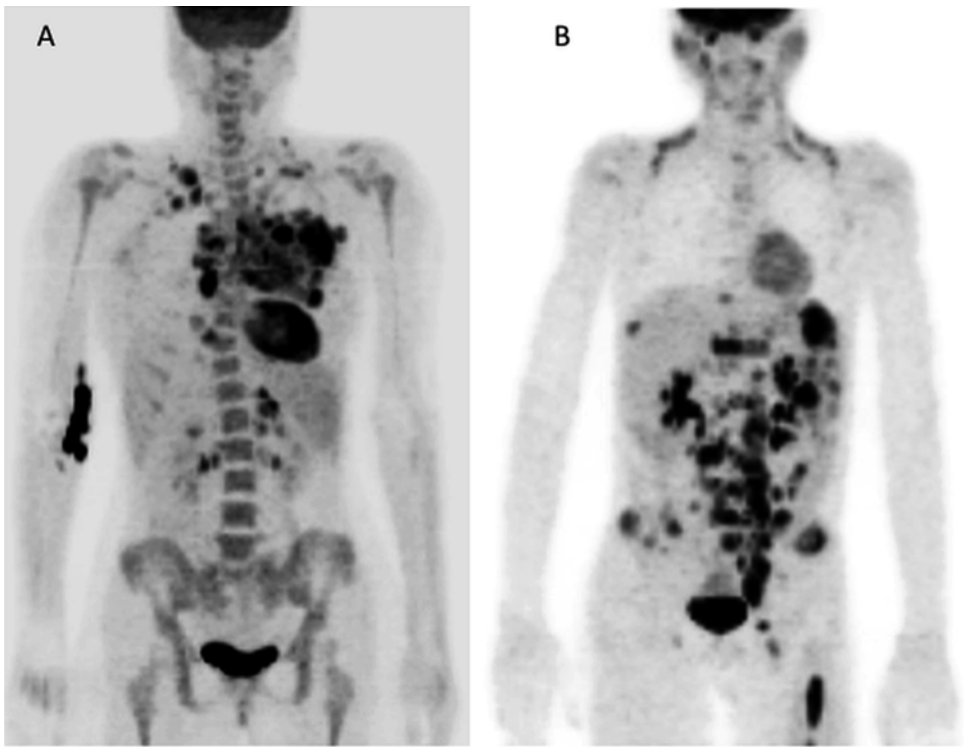

Fig. 5.17 Bone marrow involvement in HL. Two examples of bone marrow signal abnormalities on PET scans of patients with HL. In (**a**) diffuse low level uptake throughout the bone marrow is commonly seen at the time of diagnosis (see also Fig. 5.16) and felt to be related to non-specific inflammatory changes in the bone marrow. This is in contrast to intense focal bone marrow uptake (**b**), seen in the vertebral bodies, pelvis, and left femur, related to lymphomatous involvement of the bone marrow

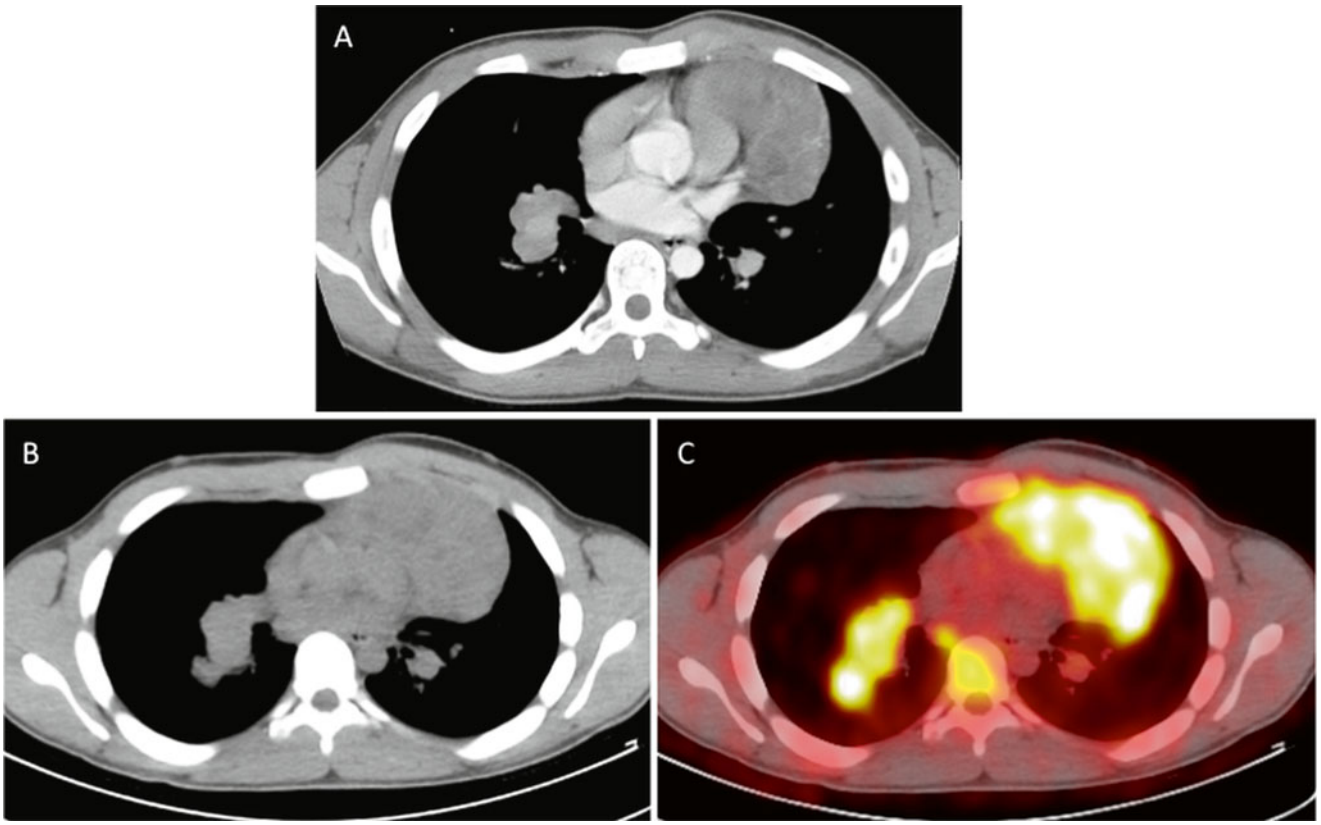

Fig. 5.18 Comparison of contrast-enhanced versus non-contrast CT/Ac: Contrast enhanced (**a**), non-enhanced (**b**) and fused PET/CT (**c**) show the importance of IV contrast in defining the boundary between normal structures and sites of disease, allowing accurate measurements to be made

Table 5.8 Lymphoma staging—Hodgkins lymphoma

Ann Arbor classification for staging
Stage I:
Involvement of single lymph node region (I) or localized involvement of a single extralymphatic organ or site (IE)
Stage II:
Involvement of two or more lymph node regions on the same side of the diaphragm (II), or localized contiguous involvement of a single extralymphatic organ or site and its regional lymph node(s), with involvement of one or more lymph node regions on the same side of the diaphragm (IIE)
Stage III:
Involvement of lymph node regions on both sides of the diaphragm (III)
These may also be accompanied by localized contiguous involvement of an extralymphatic organ or site (IIIE), by involvement of the spleen (IIIS), or both (IIIE + S)
Stage IV:
Disseminated (multifocal) involvement of one or more extralymphatic organs or tissues, with or without associated lymph node involvement, or
Isolated extralymphatic organ involvement, with distant (non-regional) nodal involvement
"A" Symptoms: Lack of "B" symptoms
"B" Symptoms: at least one of the following:
Unexplained weight loss >10 %
Unexplained recurrent fever >38°
Drenching night sweats

Nodular sclerosis classical Hodgkin lymphoma is characterized by a nodular growth pattern formed by thick collagen bands that partially or completely encase nodular areas of tumor and result in a thickened lymph node capsule. In this variant, HRS cells may occasionally retract from surrounding tissues in formalin-fixed material forming lacunar cells (Fig. 5.22). The syncytial variant of nodular sclerosis CHL refers to cases with prominent aggregates of HRS cells often associated with increased histiocytes and necrosis. *Mixed cellularity classical Hodgkin lymphoma* is characterized by effacement of the lymph node architecture with a diffuse infiltrate of HRS cells in a mixed inflammatory background without nodular collagen fibrosis. The histiocytes in the mixed inflammatory background may show epithelioid features and may form loose clusters or granulomas (Fig. 5.23). Reed-Sternberg cells are more commonly seen in this variant. *Lymphocyte-rich classical Hodgkin lymphoma* is uncommon in children. It is characterized by a nodular or, less commonly, diffuse growth pattern in which the inflammatory infiltrate consists almost exclusively of small lymphocytes. Residual germinal centers with HRS cells localized to the mantle zone are a feature that has been described in lymphocyte-rich CHL. *Lymphocyte-depleted classical Hodgkin lymphoma* is the rarest of the CHL subtypes and seldomly encountered in the pediatric age group. This subtype is characterized by an enriched HRS population and/or depletion of non-neoplastic inflammatory cells.

By immunohistochemistry, HRS cells in the various subtypes of CHL share similar immunophenotypic features. Nearly all cases are positive for CD30, MUM1/IRF4, and PAX5. Immunoreactivity for PAX5 by HRS cells is typically weak in comparison to non-neoplastic background B-cells. Nearly 80 % of cases are positive for CD15, while CD20 positivity is seen in nearly 20 % of cases. Lack of CD45 (LCA, leukocyte common antigen) expression is seen in all cases, and loss of OCT2 and/or BOB1 expression can be demonstrated in most cases (Fig. 5.24). An association exists between CHL and Epstein-Barr virus (EBV), but the prevalence of such an association varies by subtype and epidemiologic factors. It should be noted that while a mature B-cell at the germinal center stage of differentiation is believed to be the cell of origin in the vast majority of CHL cases, rare cases of demonstrable peripheral T-cell derivation have been reported.

Nodular Lymphocyte Predominant Hodgkin Lymphoma

A nodular growth pattern, with or without a diffuse component, is characteristic of NLPHL. The neoplastic cells—known as LP cells (for lymphocyte predominant; formerly, L&H cells for *l*ymphocytic and/or histiocytic)—are large, with distinctively multilobated nuclei with prominent nuclear membrane folds, chromatin clearing, and multiple basophilic nucleoli. The LP cells have been also called "popcorn" cells. They are typically scattered in nodular arrangements within a background that is rich in small lymphocytes and histiocytes, as well as follicular dendritic cells (FDC) (Fig. 5.25). Adjacent lymph nodes or lymph nodes that are partially involved by NLPHL may occasionally exhibit reactive follicular hyperplasia with PTCG.

LP cells are usually positive for CD20, CD79a, CD45, and BCL6, and they are negative for CD30 and CD15. Characteristically, background small lymphocytes consist predominantly of B-cells and CD4+/CD57+ T-cells that express markers of germinal center T-cells. Another feature of NLPHL is the presence of expanded nodular meshworks of FDC that may be highlighted using CD21, CD23, and CD35.

Prognosis

In the general population, approximately 60 % of patients present with localized disease (Ann Arbor stage I or II). The clinical stage and the response following two courses of chemotherapy evaluated by FDG-PET studies are the most important prognostic factors in CHL. Patients with low stage disease (stage IA and IIA) have a long-term survival between

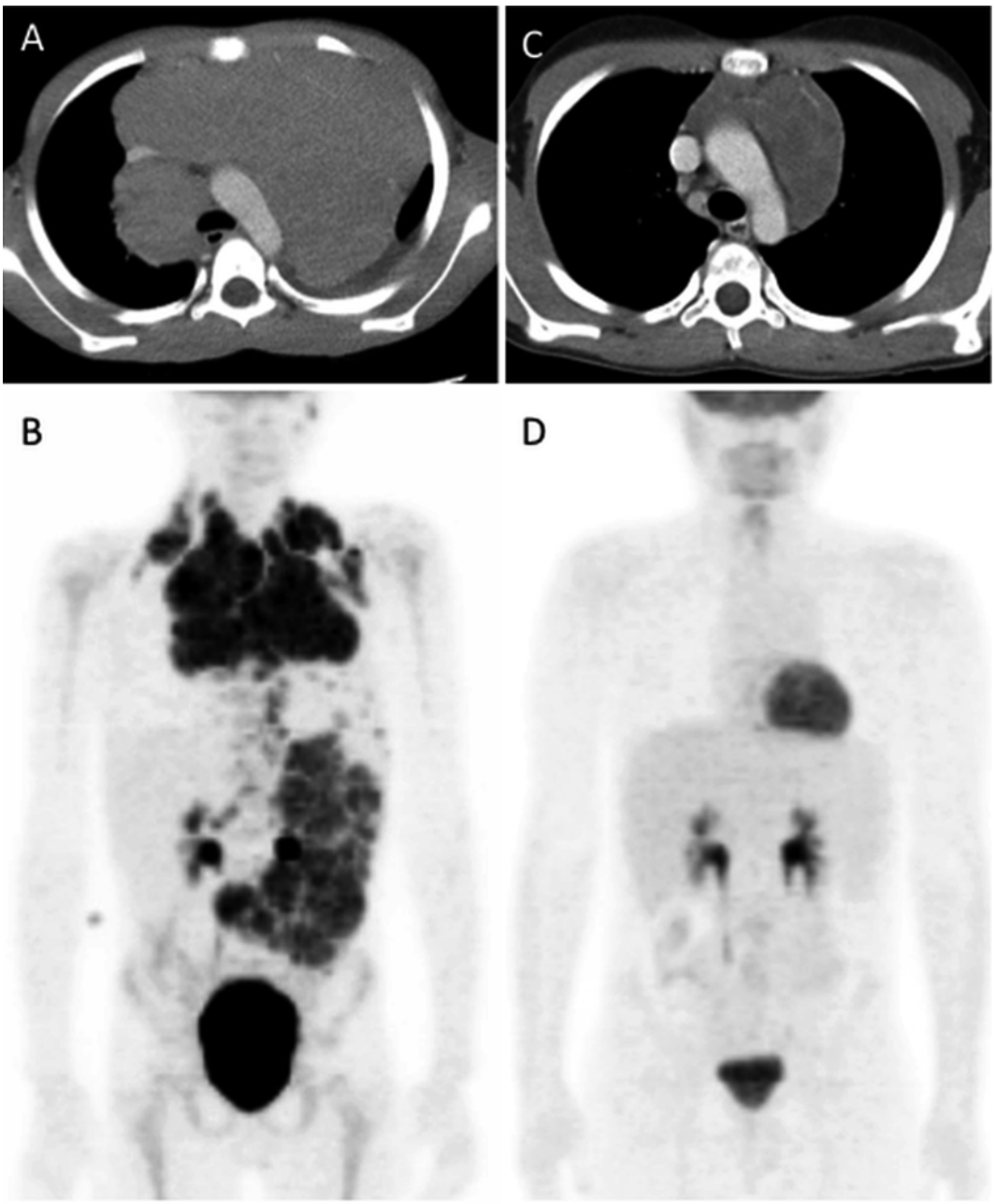

Fig. 5.19 PET versus CT response. This patient had extensive disease at baseline (**a**, **b**), with a complete metabolic response to therapy after 2 cycles of treatment (**d**). Although there has been >70 % shrinkage of the mediastinal mass, there is still residual "disease" seen on CT (**c**) and—depending on the response criteria being used—this patient may not be considered to be in CR, emphasizing the challenge of using both anatomic and metabolic criteria for response

80 and 95 %, while patients presenting at a higher stage (stage III and IV) with B symptoms have a cure rate of 60–65 % [92]. Patients with NLPHL generally have a favorable prognosis, and the disease is responsive to therapy even after relapse. In some institutions, patients with stage I disease, especially if young, are not treated following resection of involved lymph nodes. Over 80 % of patients are alive at 10 years.

Non-Hodgkin Lymphomas

Non-Hodgkin lymphomas in children are represented predominantly by mature aggressive B-cell lymphomas, most commonly Burkitt lymphoma followed by diffuse large B-cell lymphoma occurring in older children. Low grade indolent B-cell lymphomas are less frequent in children

compared to adults. The difference in incidence, prognosis and response to treatment for the different groups of B-cell lymphomas between children and adults support possible difference in the pathogenesis [93].

Table 5.9 Summary of new Harmonization Project Criteria for PET and CT in determining response in lymphoma

Response	Criteria
CR	FDG-PET completely negative
	Residual lymph nodes/nodal masses allowed, if FDG-negative
	Bone marrow biopsy negative
	Splenic/liver involvement must disappear
	No new sites of disease
PR	FDG positivity should be present in at least one previously involved site
	Regression of measurable disease; no new sites of disease
	≥50 % decrease in SPD of 6 dominant LNs/nodal masses
	≥50 % reduction in splenic/hepatic nodules, if present
	Even if CR by other criteria, positive bone marrow biopsy is considered PR
SD	Failure to achieve PR, but not meeting PD criteria
PD/relapse	Any lesion increased in size by ≥50 % from nadir
	Any new lesion
	PET should be positive in new/progressed lesions if ≥1.5 cm

Notes: New criteria include PET in definition of CR. PET considered positive if uptake is greater than mediastinal blood pool (lesions >2 cm), or above local background (lesions <2 cm)

From an imaging standpoint, the staging and response assessment of patients with NHL lymphoma are very different from the Ann Arbor system used in patients with Hodgkin lymphoma [55]. In childhood NHL, the St. Jude staging system (Table 5.10) is still widely used. Depending on the type of lymphoma, e.g., T-lymphoblastic leukemia/lymphoma, FDG PET imaging may not be indicated for staging or response assessment. Otherwise, the imaging evaluation is similar to that utilized for Hodgkin lymphoma patients and should include cross-sectional imaging either by CT or by MRI, and FDG PET imaging as indicated [94]. For patients with primary bone lymphomas, MRI may also be required to further assess the sites of skeletal involvement. For lymphomas primarily involving the cutaneous and subcutaneous tissues, there is very little role for imaging.

Diffuse Large B-Cell Lymphoma

Clinical Features

Diffuse large B-cell lymphoma (DLBCL) is a heterogeneous category of mature B-cell neoplasms characteristically comprised of large transformed mature B cells that grow in a diffuse pattern. It represents approximately 10 % of NHL of childhood [95]. Most children with DLBCL present with localized disease involving extranodal sites. Mediastinal large B-cell lymphoma is a rare but distinct variant of DLBCL

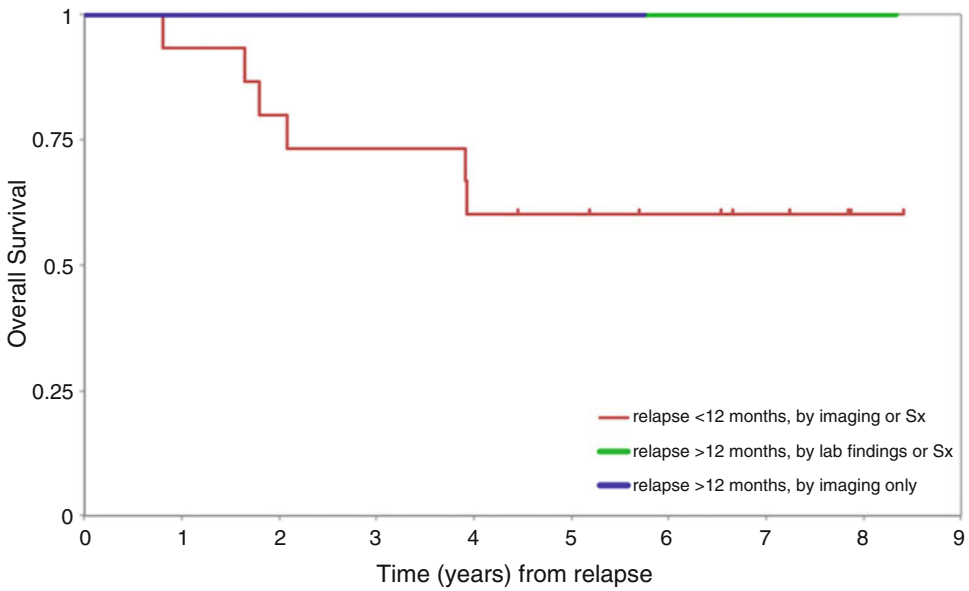

Fig. 5.20 Overall survival in HL following relapse, based on method of relapse detection: 216 patients were enrolled on the multi-institutional Children's Oncology Group Trial 9425 from 1997 to 2001. 25 patients relapsed. When patients were grouped based on method of relapse detection; (1) Relapse within the first 12 months, detected either by imaging, Sx or clinical findings (*red line*); (2) Relapse beyond 12 months, detected by Sx or clinical findings (*green line*); or (3) Relapse beyond 12 months, detected by imaging only, with no Sx or clinical findings (*blue line*)]. Six patients died, all of them within the first year off therapy, independent of the method of detection, showing that the most important predictor of survival was time to relapse. Surveillance imaging beyond 1 year after completing therapy had no impact on outcome (reproduced with permission [88])

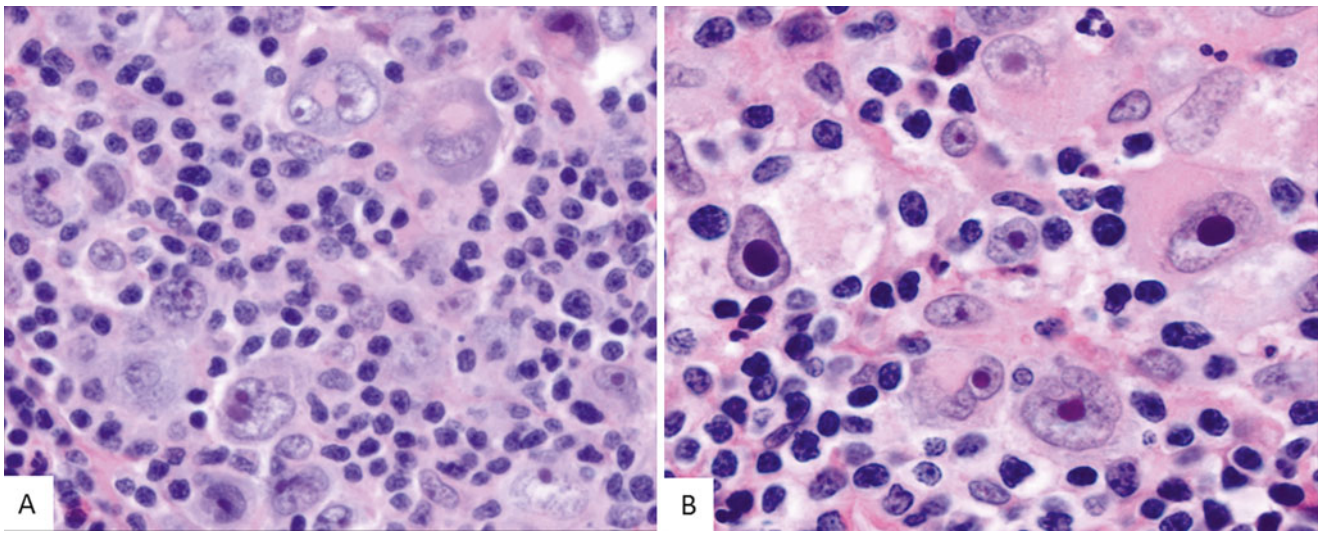

Fig. 5.21 The neoplastic cell of classical Hodgkin lymphoma. (**a**) The Reed-Sternberg (RS) cells are giant cells with binucleated or multinucleated nuclei with macronuclei present in the separate nuclei or nuclear lobes. (**b**) The Hodgkin cells represent the mononuclear variant of the RS cells with prominent large nucleoli

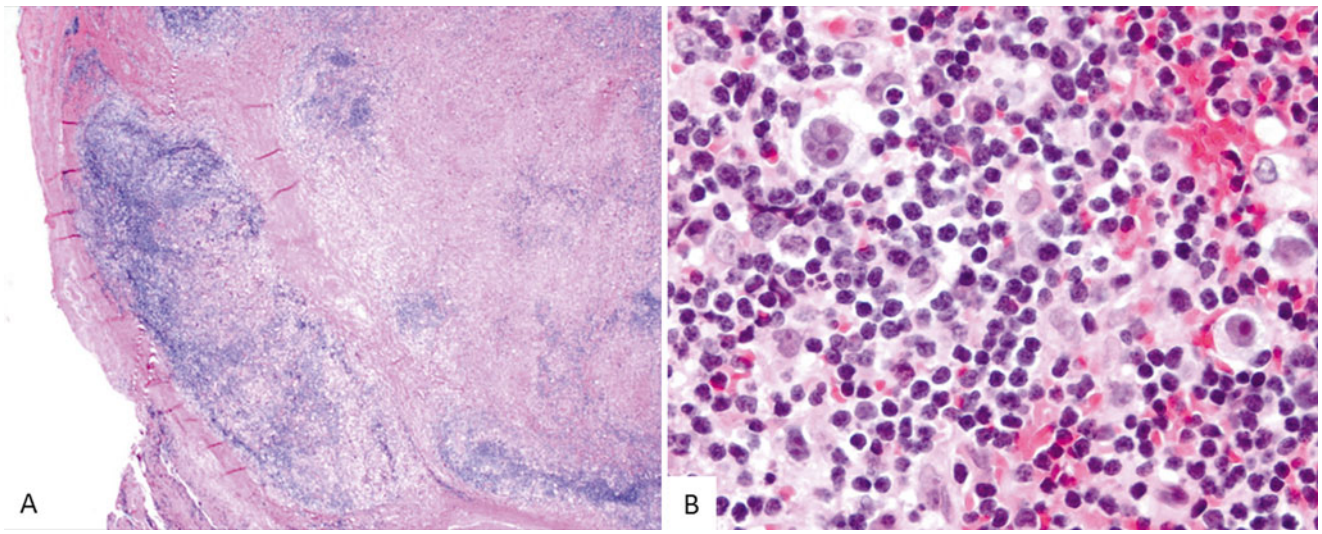

Fig. 5.22 Classical Hodgkin lymphoma, nodular sclerosis (NS) subtype. (**a**) A lymph node involved by CHL with neoplastic nodules surrounded by broad collagen bundles. (**b**) Neoplastic cells are identified in the nodules including lacunal cells that are considered characteristic of this subtype of CHL. The lacunar cells are only identified in formalin-fixed tissues due to retraction artifact

that arises from mature thymic B-cells and is generally associated with worse outcomes compared to non-mediastinal DLBCL [96].

Imaging Features

DLBCL commonly presents with localized disease. Anterior mediastinal or cervical/supraclavicular lymphadenopathy may be present and is more characteristic of DLBCL than other NHL subtypes. The mediastinal mass may appear somewhat more diffuse and aggressive by imaging, but is not specifically distinguishable from mediastinal masses present in other lymphoid malignancies such as Hodgkin lymphoma [97]. In some patients DLBCL tends to be associated with aggressive clinical features such as pericardial and malignant pleural effusions (Fig. 5.26). In addition, pulmonary parenchymal involvement and bone involvement, which are unusual in Hodgkin lymphoma, are more commonly seen in DLBCL. A characteristic of DLBCL is renal involvement [98].

Because of the difficulty in establishing the extent of visceral involvement by CT scanning alone, the use of PET-CT has increased the sensitivity with which sites of tumor involvement outside of the mediastinum are detected. The use of FDG PET imaging for response assessment, while not

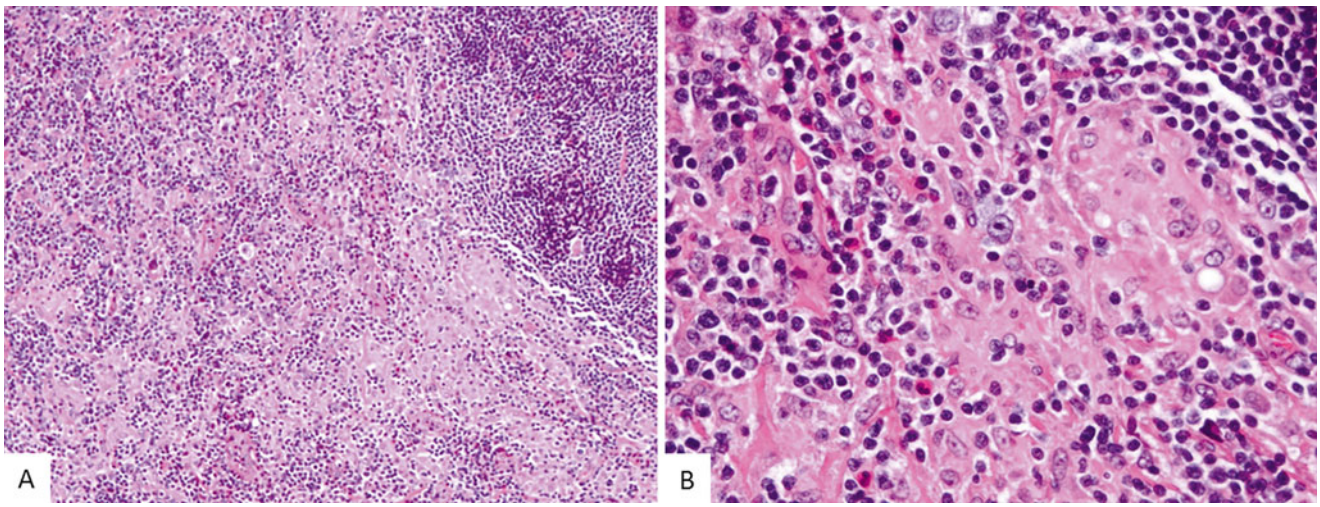

Fig. 5.23 Classical Hodgkin lymphoma, mixed cellularity (MC) subtype. (**a**) The MC subtype show a diffuse pattern sparing residual follicles. (**b**) The neoplastic cells are mixed with a significant number of epitheliod histiocytes, small lymphocytes and eosinophils

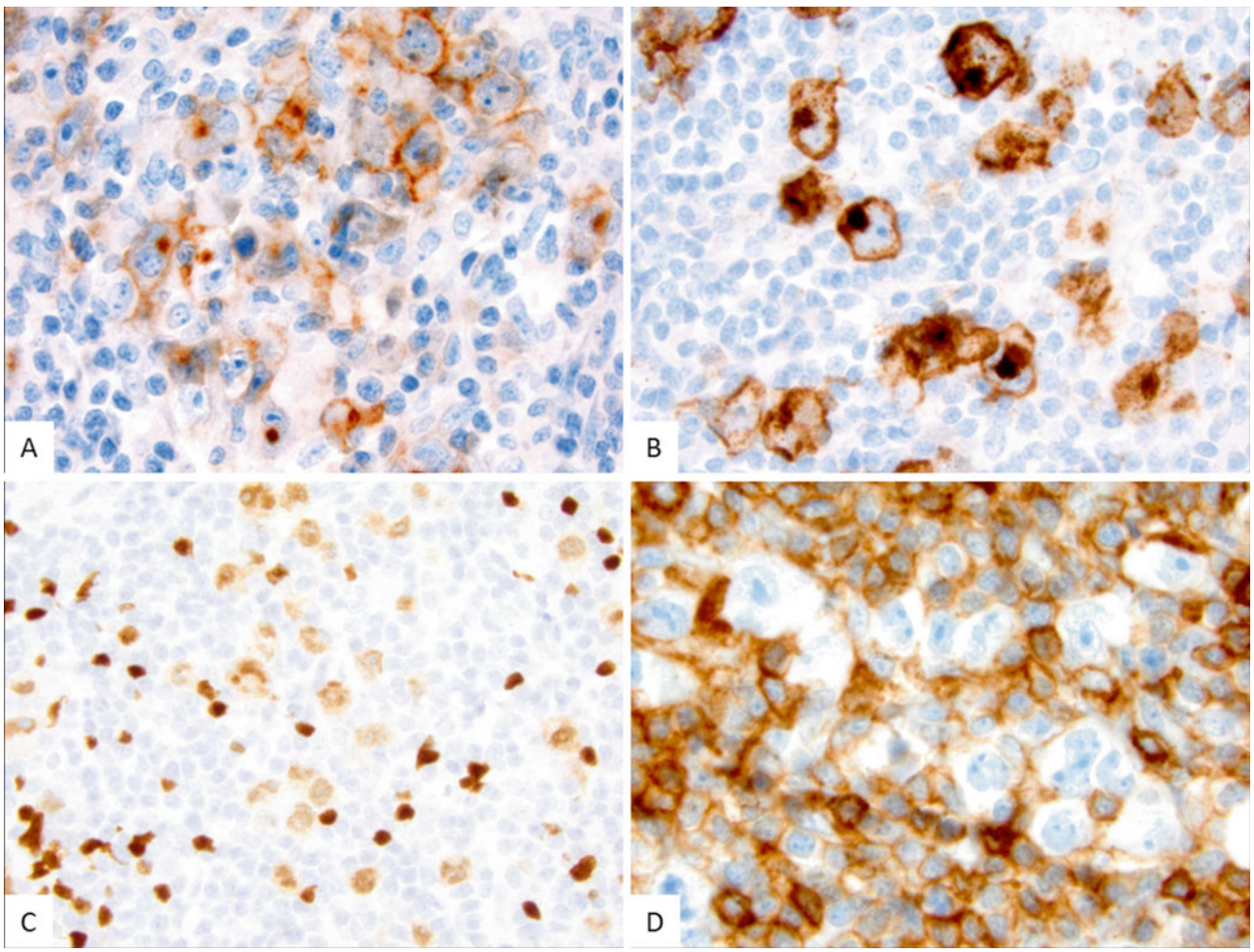

Fig. 5.24 The HRS cells show characteristic immunophenotype including the membrane-associated and cytoplasmic (Golgi-type) CD30 (**a**) and CD15 (**b**). The neoplastic cells are positive for PAX5 (**c**) with expression weaker than the small B lymphocytes, and lack CD45 (**d**)

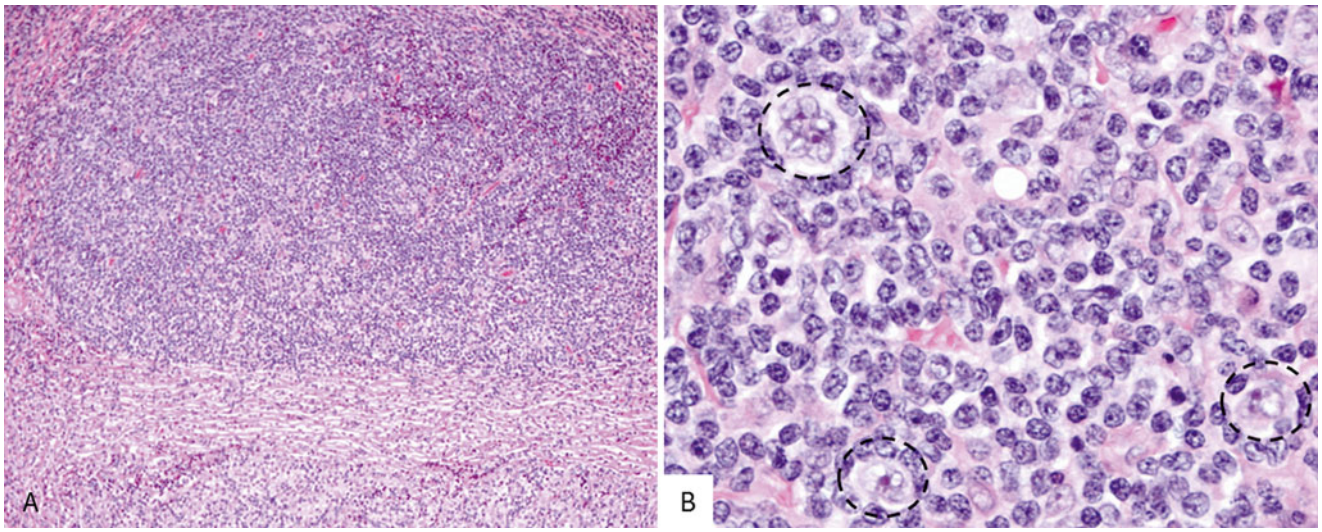

Fig. 5.25 (**a**) Nodular lymphocyte predominant classical Hodgkin lymphoma involving the lymph node in nodular pattern. (**b**) The neoplastic nodules are large with a variable number of neoplastic L&H cells (*circled*) in a background of small lymphocytes. The neoplastic L&H cells are large with nuclear lobation, vesicular chromatin, and peripherally located small nucleoli

Table 5.10 Lymphoma staging—non-Hodgkin lymphoma

St. Jude classification
Localized
Stage I:
A single tumor (extranodal) or single anatomic area (nodal) with the exclusion of mediastinum or abdomen
Stage II:
A single tumor (extranodal) with regional node involvement
Two or more nodal areas on the same side of the diaphragm
Two single (extranodal) tumors with or without regional node involvement on the same side of the diaphragm
A primary gastrointestinal tumor, usually in the ileocecal area, with or without involvement of associated mesenteric nodes only, grossly completely resected
Disseminated
Stage III:
Two single tumors (extranodal) on opposite sides of the diaphragm
Two or more nodal areas above and below the diaphragm
All primary intra-thoracic tumors (mediastinal, pleural, thymic)
All extensive primary intra-abdominal disease
All paraspinal or epidural tumors, regardless of other tumor site(s)
Stage IV:
Any of the above with initial CNS and/or bone marrow involvement (based on Murphy, Seminars in Oncology (1980) 7; 332–339)

specifically validated in the setting of pediatric NHL [40], can be helpful to assess response to therapy and evaluate sites of suspicious disease recurrence.

Pathology

The morphologic features of DLBCL are variable. In the pediatric population, the centroblastic, immunoblastic, T-cell/histiocyte rich, and anaplastic variants are most commonly seen (Fig. 5.27). Plasmablastic lymphoma, a rare variant of DLBCL, is seldomly seen in children but should be considered in the setting of immunodeficiency. ALK-positive large B-cell lymphoma is another variant characterized by t(2;17)(p23;q23) resulting in *ALK-CLTC* fusion leading to aberrant cytoplasmic expression of the ALK protein.

The neoplastic cells in DLBCL typically express the B-cell markers CD19, CD20, CD22, and PAX5, and most cases are positive for BCL6 expression. Based on gene expression profiling data, two biologically distinct subtypes of DLBCL have been recognized; they are referred to as germinal center B-cell like (GCB) and activated B-cell like (ABC). These subtypes have distinct pathogenic features and are associated with different clinical outcomes [99]. The GCB subtype is defined commonly on the basis of CD10 and/or BCL6 expression while the ABC subtype is defined on the basis of MUM1/IRF4 expression [100]. The majority of DLBCL in children (83 %) are of the GCB subtype, positive for CD10 and BCL6 [101]. In addition, childhood DLBCL tends to be associated with high proliferation index, frequent *MYC* alterations, and infrequent BCL2 expression [102].

Prognosis

Risk stratification using the international prognostic index (including age, performance status, LDH levels, Ann Arbor stage, and extranodal involvement) effectively predicts outcome with conventional chemotherapy in adult patients with DLBCL. However, additional studies are required to assess whether prognostic markers of DLBCL used in the adult population are predictive of outcomes in the pediatric group.

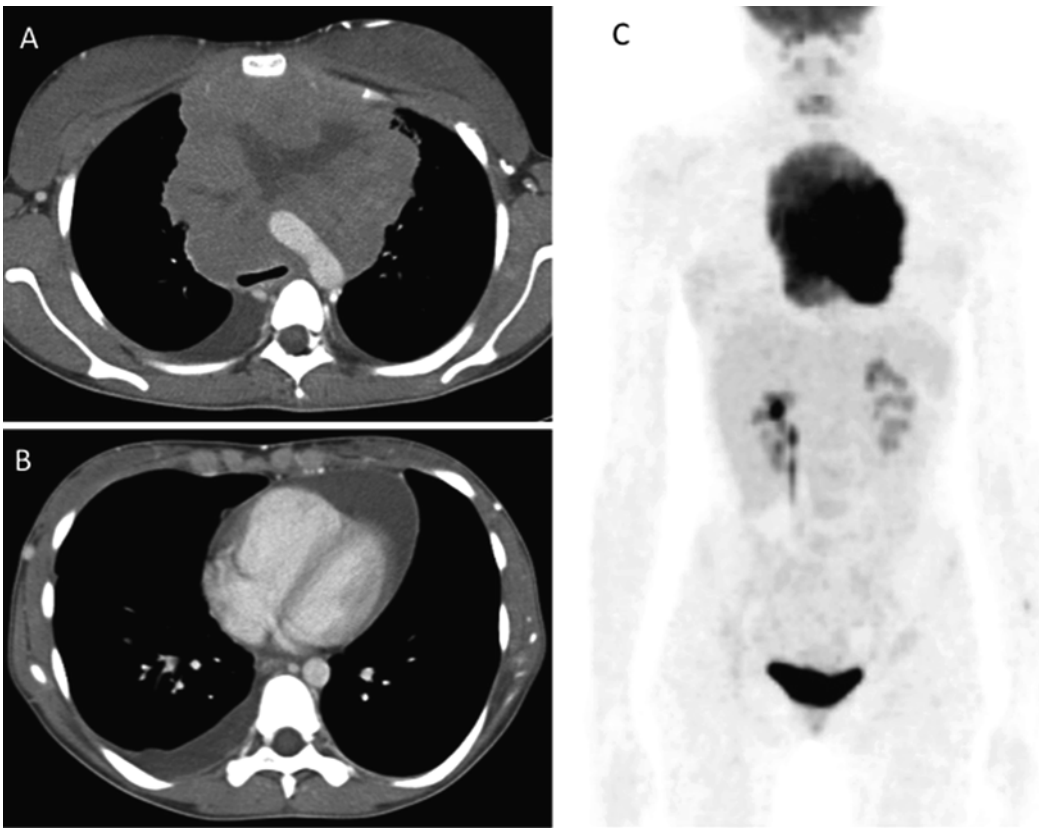

Fig. 5.26 Diffuse large B-cell lymphoma: CT (**a**, **b**) and PET (**c**) showing aggressive appearing FDG-avid large mediastinal mass with anterior chest wall invasion and accompanying pleural and pericardial effusions

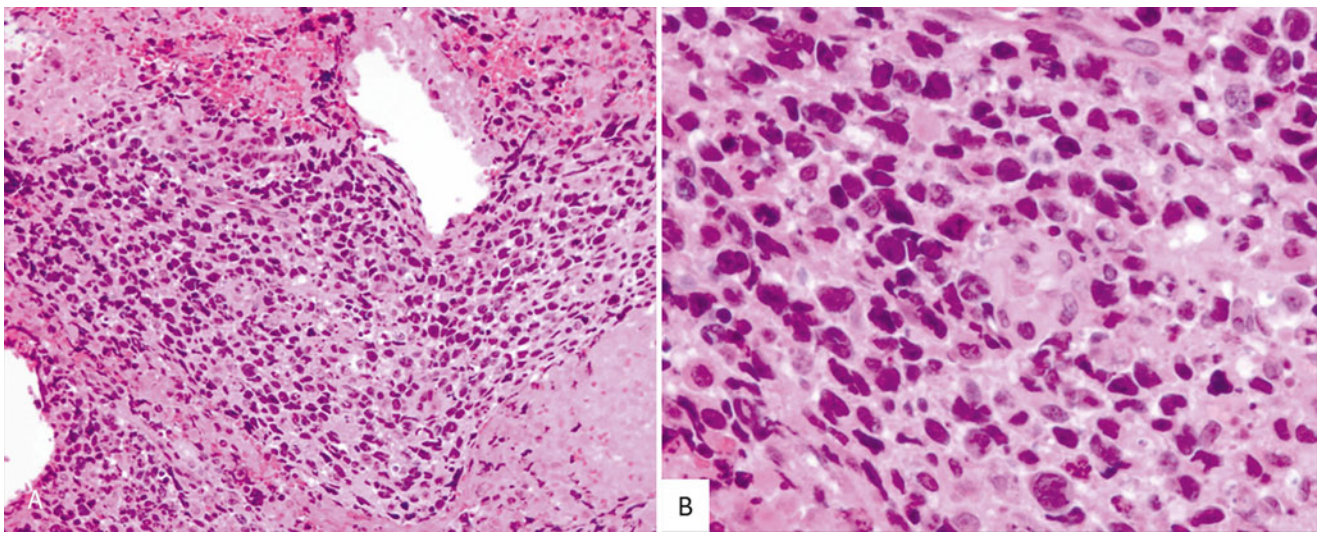

Fig. 5.27 Diffuse large B-cell lymphoma involving bone. (**a**) Sheets of large non-cleaved cells associated with tumor necrosis. (**b**) High power view of the diffuse large B-cell lymphoma composed of large neoplastic cells with irregular nuclear membrane and moderate amounts of eosinophilic cytoplasm. Imaging studies did not identify any other anatomic site involved by tumor. This case represents a primary bone diffuse large B-cell lymphoma

Burkitt Lymphoma

Clinical Features

Burkitt lymphoma (BL) is a highly aggressive mature B-cell malignancy with characteristic morphologic, immunophenotypic and cytogenetic findings, and accounts for 30 % of childhood lymphomas. Three clinical variants/forms have been identified: (1) the *endemic form,* common in children in equatorial Africa, with frequent involvement of the jaw and kidneys; (2) the *sporadic form*; and, (3) the *immunodeficiency-associated form* observed mainly in the setting of HIV infection.

Imaging Features

The sporadic form of BL typically presents with intra-abdominal visceral disease involvement, often with accompanying widespread extranodal involvement [56]. The initial evaluation, either by radiography, ultrasound or CT, is usually directed at characterizing the extent of abdominal involvement as part of assessing initial presenting abdominal symptoms. Peritoneal, abdominal viscera, visceral, and bowel wall involvement are common (Fig. 5.28a, b). Patients with bowel wall involvement characteristically present with intussusception. Occasionally, the diagnosis is made surgically following resection of an intussuscepted segment of bowel refractory to hydrostatic or air-enema reduction. More commonly, however, the presence of extensive intra-abdominal disease is noted on CT imaging (Fig. 5.28c–e). Abdominal involvement and isolated lymphadenopathy are less common in the endemic form of BL.

The presence of pleural effusions and ascites may also be present, with disease confirmation by cytologic examination. Testicular and isolated lymph node involvement is uncommon, whereas CSF involvement is identified in many patients. The use of diagnostic imaging either by FDG PET or by MRI is not sufficient to exclude bone marrow or CSF involvement. The use of PET imaging, however, has been advocated to evaluate the extent of disease in patients with BL [103, 104], although the rapid response to therapy that is commonly observed in these patients has limited the more widespread and systematic use of PET imaging at the time of diagnosis. There is currently no role for routine follow-up PET imaging to assess response to therapy in the absence of specific clinical concerns [103].

Pathology

Histologically, the tumor is composed of medium-sized lymphocytes with moderate amounts of cytoplasm and round nuclei with several small nucleoli. Mitotic figures and apoptotic cells are typically abundant, and elevated numbers of reactive histiocytes with ingested cellular debris are scattered in the background imparting a "starry sky" pattern. The neoplastic cells in BL express B-cell markers and are typically positive for CD10 and BCL6 and negative for BCL2 (Fig. 5.29). Virtually 100 % of the neoplastic cells express the proliferation marker Ki-67.

Burkitt lymphoma is characterized by chromosomal translocations involving the *MYC* gene at chromosome 8q24 leading to MYC overexpression. The *IGH* gene at 14q32 is the most frequent breakpoint partner (75–85 % of cases), with t(2;8) and t(8;22) variant translocations utilizing the *IGK* and *IGL* enhancers seen in the remainder of cases. Given the wide range of breakpoints, *MYC* alterations are usually best detected by conventional cytogenetics or FISH. Alterations involving the ARF/MDM2-MDM4/p53 pathway have been reported in pediatric Burkitt lymphomas, including *TP53* mutations in ~30 % of sporadic BL [105]. The genetic alterations and gene expression profiles of pediatric BL appear to be similar to those of adult BL.

Marginal Zone Lymphoma

Clinical Features

Both nodal and extranodal marginal zone lymphoma (MZL) can occur in the pediatric age group, although their incidence is markedly lower than that observed among older patients. Most cases are nodal MZL that arise in males with a median age of 16 years who present with localized lymphadenopathy often involving the head and neck region [106]. Extranodal marginal zone lymphoma is rare in children and adolescents [107]. The most common sites of involvement include skin, soft tissue, conjunctiva and parotid. Most of the patients present with localized disease.

Pathology

Histologically, MZL is composed of small lymphocytes with monocytoid and centrocyte-like features as well as varying degrees of plasmacytic differentiation (Fig. 5.30). Nodal MZL is frequently associated with PTGC. The neoplastic cells are positive for CD19 and CD20, and in up to 70 % of cases can show aberrant CD43 coexpression. CD5, CD10, and CD103 expression is typically absent, and, unlike splenic MZL, most nodal MZL cases are negative for IgD. In situ hybridization studies for Epstein-Barr virus are usually negative [106].

Extranodal MZL arising in pediatric patients resembles its counterpart in older individuals. Namely, the neoplasm is characterized by a dense infiltrate of small lymphocytes including monocytoid forms surrounding reactive lymphoid follicles with architectural distortion and glandular destruction (lymphoepithelial lesions).

Immunoglobulin heavy and light chain genes are clonally rearranged with somatic hypermutation of variable regions indicating a post-germinal center memory B-cell origin. Translocations that have commonly been associated with MALT lymphoma in adults, namely t(14;18)(q32;q21) leading to *IGH-MALT1* fusion, are also found in pediatric MALT lymphoma but at a lower frequency [108].

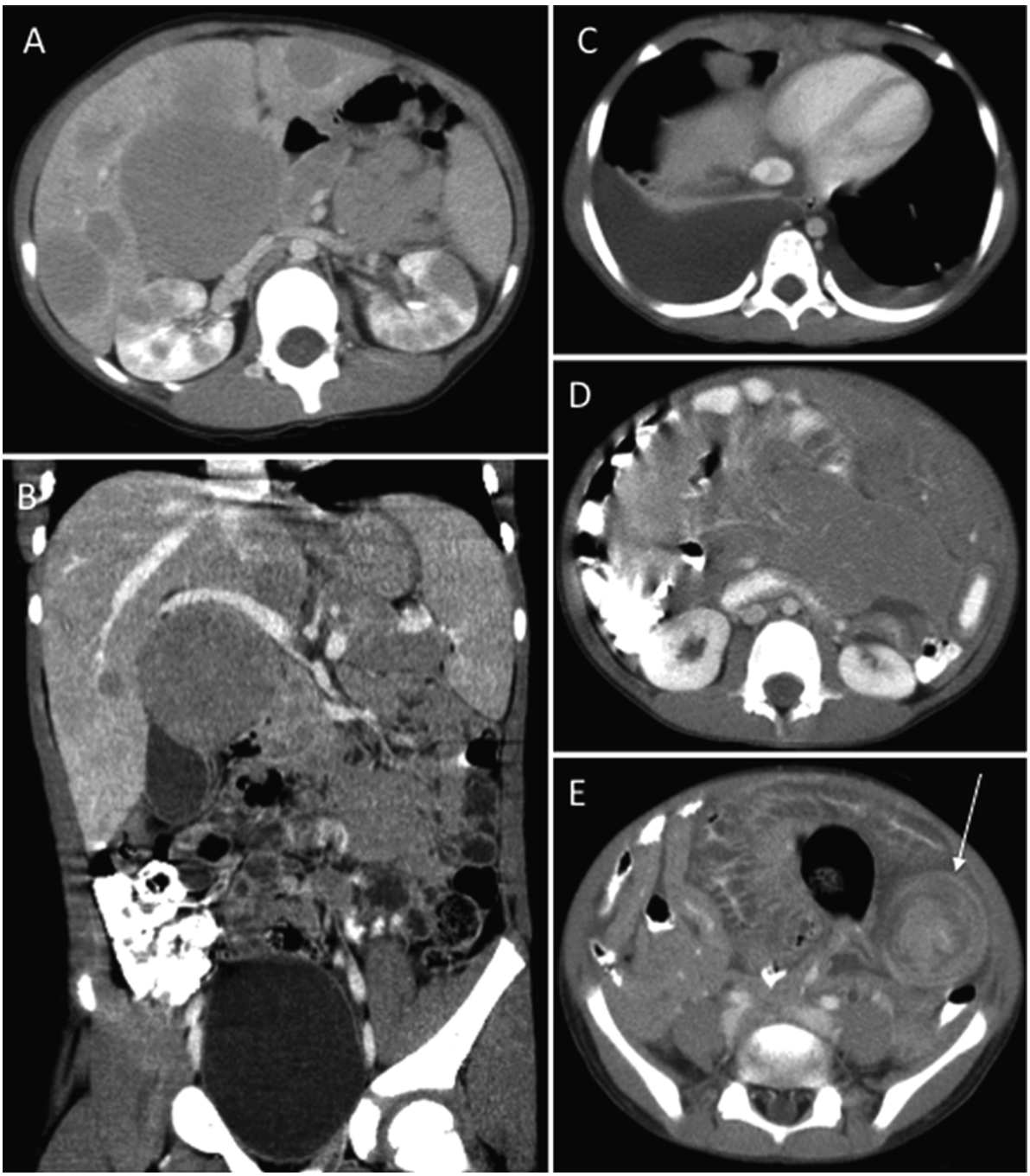

Fig. 5.28 Burkitt Lymphoma: two examples of Burkitt lymphoma. The patient in (**a**) and (**b**) has multifocal visceral involvement of liver, kidneys and retroperitoneum, whereas the patient in **c**–**e** presented with large pleural effusions, lung lesions, in addition to extensive bowel wall thickening, mesenteric nodal involvement, and small bowel intussusception (**e**, *arrow*)

Follicular Lymphoma

Clinical Features

Follicular lymphoma (FL), the most common low-grade lymphoma in adults in the United States, represents 2 % of NHL in children [98]. Pediatric FL most likely represents a genetically distinct entity unrelated to adult FL, and the t(14;18), which is characteristic of the latter, is uncommon in pediatric cases [109]. The median age at presentation is 8–12 years, and males are more commonly affected than females by a ratio of 4:1. Pediatric FL usually presents as localized disease (stage I and II) [110]. The tonsils and lymph nodes of the head and neck are most commonly involved; however, cases of other extranodal involvement have been described (gastrointestinal tract, skin, testes, and parotid gland) [111]. Unlike adult FL patients, bone marrow involvement is rare in pediatric FL.

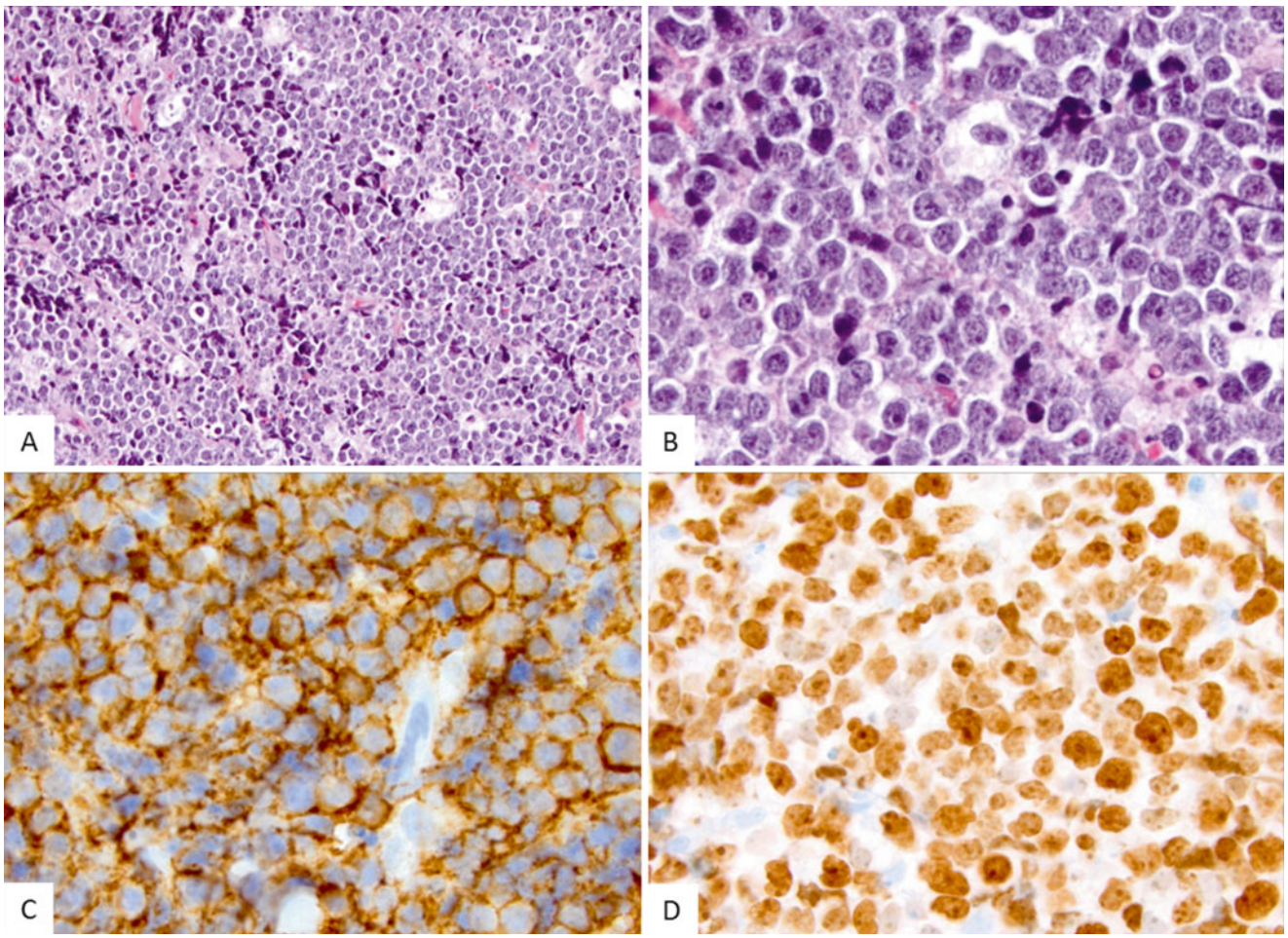

Fig. 5.29 Burkitt lymphoma, morphologic and immunophenotypic characteristics. (**a**) A low power view shows soft tissue with diffuse monomorphous lymphoid infiltrate with "starry-sky" pattern. (**b**) The tumor cells are intermediate in size with round to oval nuclei and inconspicuous nucleoli and small amounts of cytoplasm. The neoplastic cells are positive for CD20 (**c**) and show >99 % proliferation index by Ki-67 stain (**d**)

Imaging Features

There are no distinguishing imaging features to discriminate pediatric FL from other types of NHL. Depending on the symptoms or exam findings at the time of presentation, the initial site of disease involvement may be discovered incidentally or based on localizing exam findings (Fig. 5.31). Once the diagnosis is established, staging should include CT of the neck, chest, abdomen, and pelvis [112]. PET scanning may increase the sensitivity with which sites of distant disease are noted, although this is unusual in pediatric FL. When treatment is complete, routine off-treatment surveillance can be accomplished either by physical exam or by focused imaging of the original site(s) of disease, as indicated clinically. There is no evidence to support a high frequency of surveillance imaging or for FDG PET imaging in the routine surveillance of pediatric FL. Post-therapy PET imaging may be helpful in distinguishing scar tissue from residual neoplasm [113].

Pathology

Histologically, FL is comprised of a heterogeneous population of centrocytes (small cleaved cells) and centroblasts (large noncleaved cells) in a predominantly follicular growth pattern. Grading is based on the overall number of centroblasts relative to centrocytes. In grade 1 and 2 FL centrocytes are predominant, while in grade 3 FL centroblasts exceed 15 per high-power-field on microscopic evaluation. Grade 3 is further subdivided into 3A and 3B on the basis of whether centrocytes are present or absent, respectively. Pediatric FL are typically grade 3A. Notably, a diffuse large B-cell component does not portend an aggressive clinical course as it does in adult FL; rather, a favorable outcome with few relapses has been reported in children treated according to the NHL-BFM protocol [110].

The neoplastic B-cells of pediatric FL express CD19, CD20, and the germinal center markers CD10 and BCL6. Most cases lack BCL2 expression. The CD21 and CD23

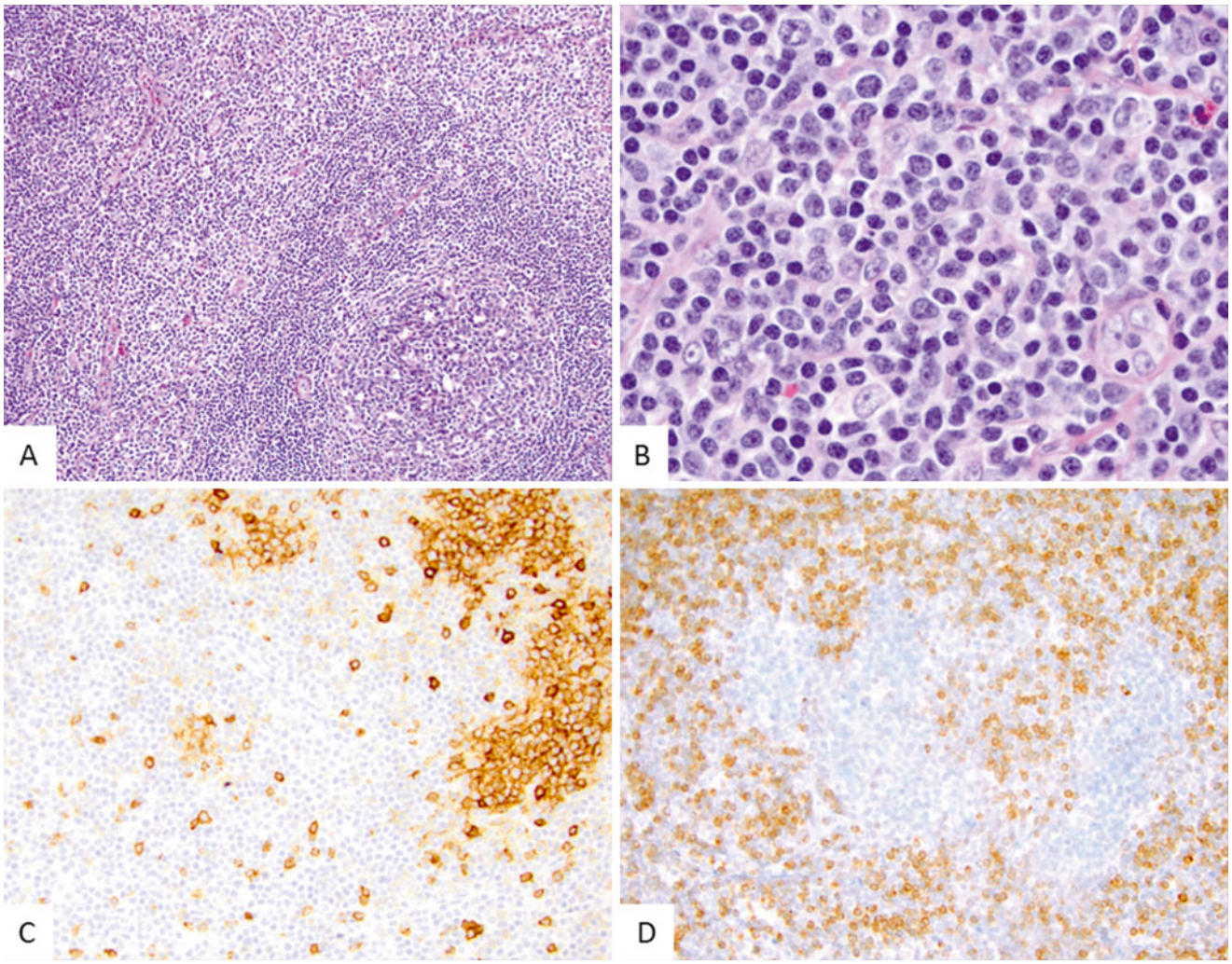

Fig. 5.30 Nodal marginal zone lymphoma. (**a**) A low power view demonstrates distorted lymph node architecture including interfollicular expansion and variably expanded and often ill-defined follicles with irregular mantle zones. (**b**) There is a heterogeneous infiltrate in the interfollicular regions that is composed of small cleaved cells admixed with plasma cells and monocytoid B cells. (**c**) The neoplastic cells disrupt the germinal centers and are positive for CD20 (not shown), but negative for CD10 (shown) that highlights the residual germinal center B-cells. (**d**) The neoplastic cells are positive for Bcl-2 (shown) with aberrant co-expression of CD43 (not shown). The disrupted, irregular germinal center is negative for Bcl-2

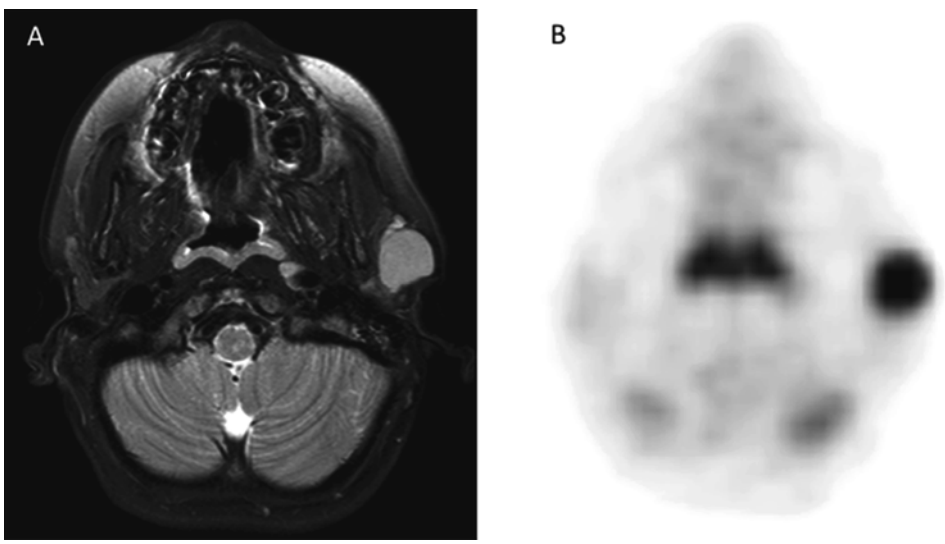

Fig. 5.31 Follicular lymphoma of the parotid. Five-year old with palpable parotid mass. MRI shows a mildly T2 hyperintense focal lesion in the left parotid (**a**). Staging FDG PET shows intense FDG uptake in the lesion (**b**); no other sites of disease were seen

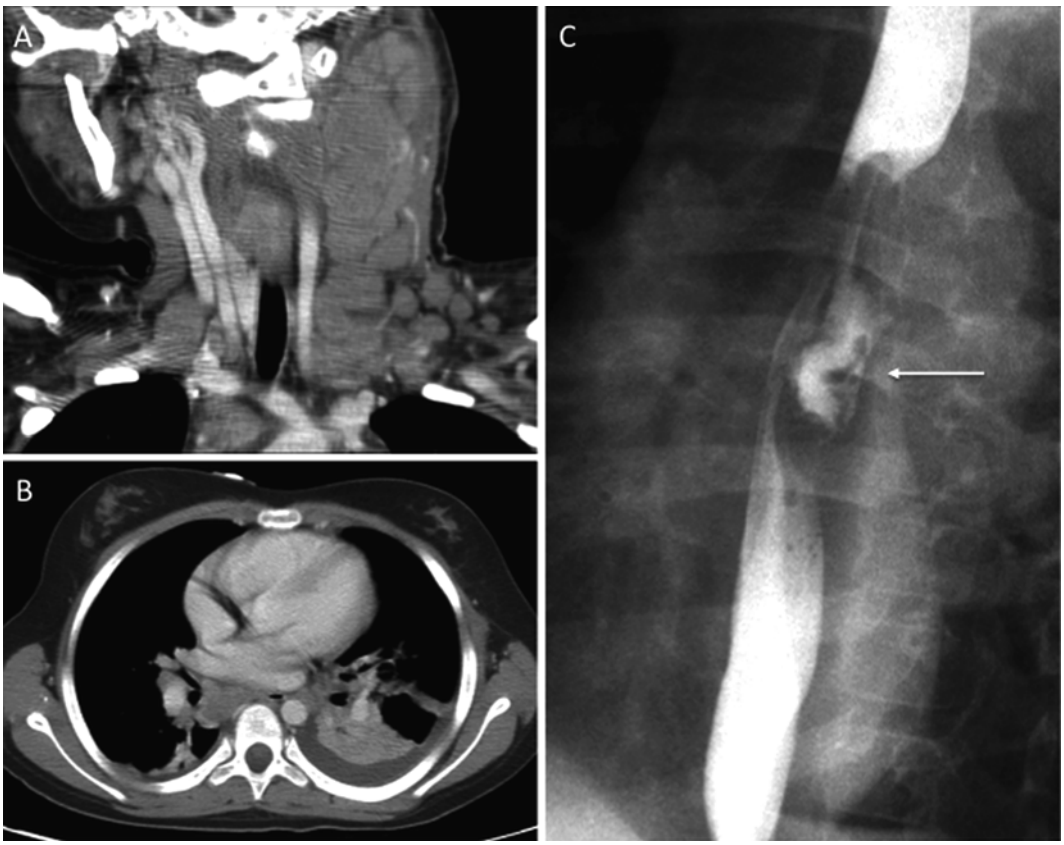

Fig. 5.32 Anaplastic large cell lymphoma (ALCL), with varied presentations of disease. (**a**, **b**)11-year-old patient with ALCL presented with bulky neck and mediastinal disease and pleural effusions. The 5-year-old patient in (**c**) presented with dysphagia. (**c**) Barium swallow shows a large esophageal ulcer (*arrow*) which subsequent biopsy confirmed as ALCL

antigens can be used to highlight the follicular dendritic cell meshworks that correlate with the follicular growth pattern observed in most cases of pediatric FL. The proliferation index assessed by Ki-67 antigen can be high, ranging from 40 to 95 %.

The presence of the t(14;18) *IGH-BCL2* translocation that is considered the hallmark of the adult follicular lymphoma is commonly absent in pediatric cases. However, rearrangements involving the *IGH* locus, some leading to *IGH-IRF4* fusion, have been described in pediatric FL [110, 114].

Anaplastic Large Cell Lymphoma

Clinical Features

Anaplastic large cell lymphoma (ALCL) is a T-cell lymphoma characterized by CD30-positive neoplastic cells that are usually large and have abundant cytoplasm with pleomorphic nuclei. Although rare, making up only about 15 % of pediatric NHL, ALCL is the most common mature T-cell neoplasm in children [115]. The majority of cases that arise among young individuals are ALK-positive ALCL characterized by balanced translocations involving the *ALK* (*anaplastic lymphoma kinase*) gene at chromosome 2p23 with one of several possible partner genes, most commonly the *NPM1* gene at 5q35 encoding the nucleophosmin protein. Patients with ALK-positive ALCL often present with lymphadenopathy and/or extranodal masses, B-type symptoms, and advanced stage (III and IV). The most commonly involved extranodal sites include skin, bone, soft tissues, lung, and liver. Central nervous system and bone marrow involvement are uncommon in ALK-positive ALCL [114]. ALK-positive ALCL must be distinguished from primary cutaneous ALCL and other T-cell or B-cell lymphomas with similar features and CD30 expression. Primary cutaneous ALCL is almost always ALK negative and is rare in children.

Imaging Features

There are no specific imaging findings associated with ALCL to distinguish it from other forms of lymphoma, although ALCL frequently presents with extensive multifocal disease and can involve the lung, skin and bone, GI tract, and abdominal viscera [97] (Fig. 5.32). A mediastinal mass may be seen in up to 40 % of the patients and

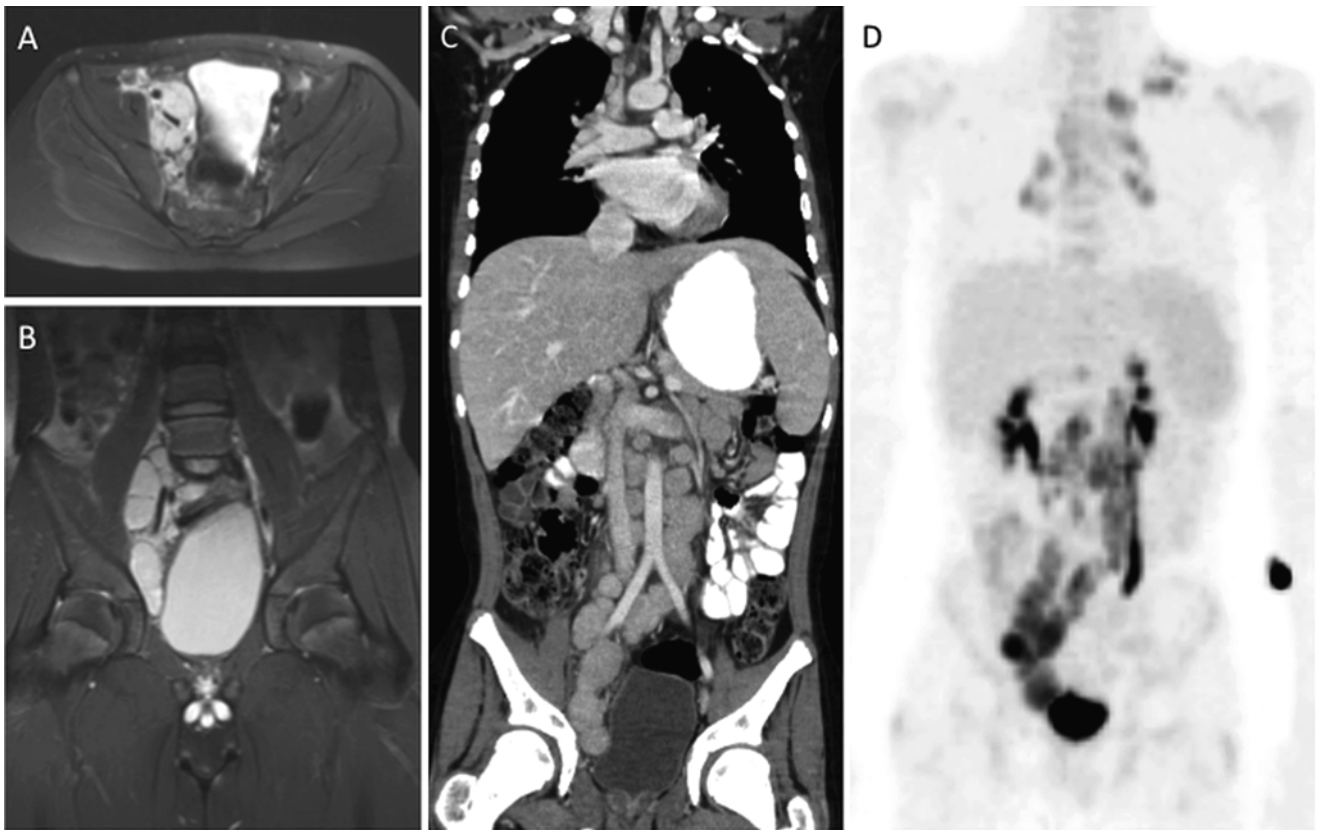

Fig. 5.33 ALCL with FDG PET: 12-year-old presented initially with right leg/groin pain. (**a**, **b**) MRI showed diffuse pelvic lymph node enlargement. (**c**) CT confirmed extensive adenopathy in chest, abdomen and pelvis, all of which was FDG avid (**d**)

is often associated with pericardial and pleural effusion. When a mediastinal mass is present, it may be difficult to distinguish ALCL from Hodgkin lymphoma and diffuse large B-cell lymphoma. PET imaging, together with CT and/or MRI should be used for initial staging (Fig. 5.33) and can be helpful in monitoring response to therapy [115]. Experimental therapies targeting ALK can show dramatic disease response, which may be best demonstrated by FDG PET imaging [117] (Fig. 5.34). As with other NHL, disease surveillance involves a combination of clinical examination and focused imaging to evaluate for the presence of disease at original sites of tumor involvement. There is no evidence to indicate that routine surveillance by FDG PET imaging improves outcome in ALCL.

Pathology

Typically, lymph node involvement by ALCL is predominantly sinusoidal in pattern and leads to partial or complete effacement of nodal architecture. Among the pleomorphic neoplastic cells of ALCL, a variable proportion with a horseshoe-shaped or kidney-shaped nucleus and abundant eosinophilic cytoplasm is often identified. Such cells have been referred to as *hallmark cells* and can be recognized in all morphologic variants of ALCL, including the lymphohistiocytic and small cell variants.

The neoplastic cells of ALCL are strongly positive for CD30. Although most cases are negative for CD3 expression, the majority express other T-cell associated antigens including CD2, CD5 and CD7. A subset of ALCL has a "null cell" immunophenotype, although a T-cell lineage can be established at a molecular level. Most cases are positive for the cytotoxic antigens granzyme B, TIA1, and perforin. The pattern of ALK expression by immunohistochemistry can often foretell the underlying translocation type, and cases with the NPM1-ALK fusion protein exhibit a cytoplasmic and nuclear staining pattern (Fig. 5.35).

Histiocytic and Dendritic Cell Neoplasms

The World Health Organization classifies neoplasms of histiocytes and dendritic cells according to their putative normal counterparts: histiocytic sarcoma, tumors derived from Langerhans cells (Langerhans cell histiocytosis, Langerhans cell sarcoma), interdigitating dendritic cell sarcoma, and disseminated juvenile xanthogranuloma (JXA).

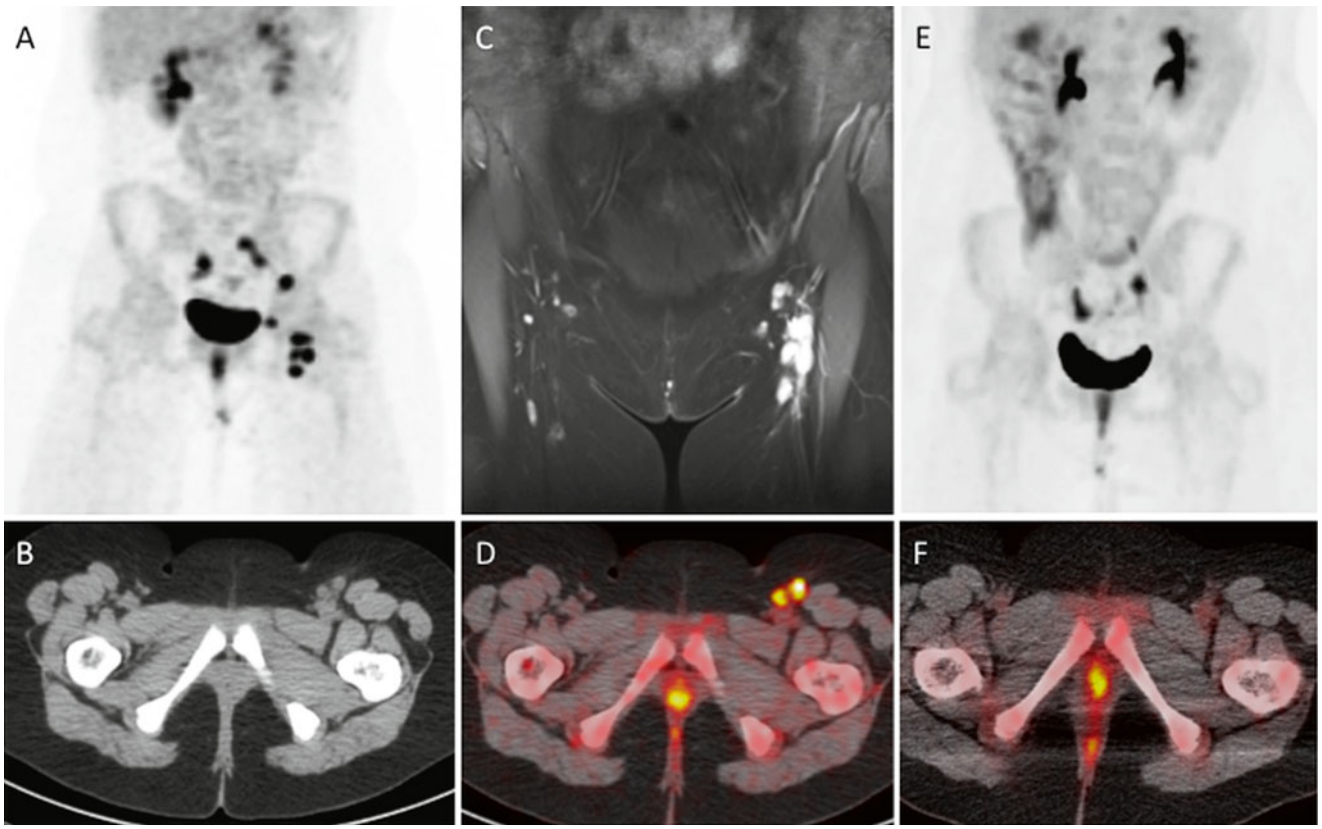

Fig. 5.34 ALCL and ALK targeted therapy: 12-year old with recurrent ALCL being treated with experimental phase 1 agent targeted at the ALK kinase. FDG PET/CT (**a**, **b**, **d**) and MRI (**c**) at baseline (**a**–**d**) showing extensive left inguinal and external iliac chain nodal disease. After just one 4 weeks cycle of ALK-targeted crizotinib, there has been both a complete anatomic (**f**) and metabolic (**e**) response, with resolution of the nodal disease seen at baseline

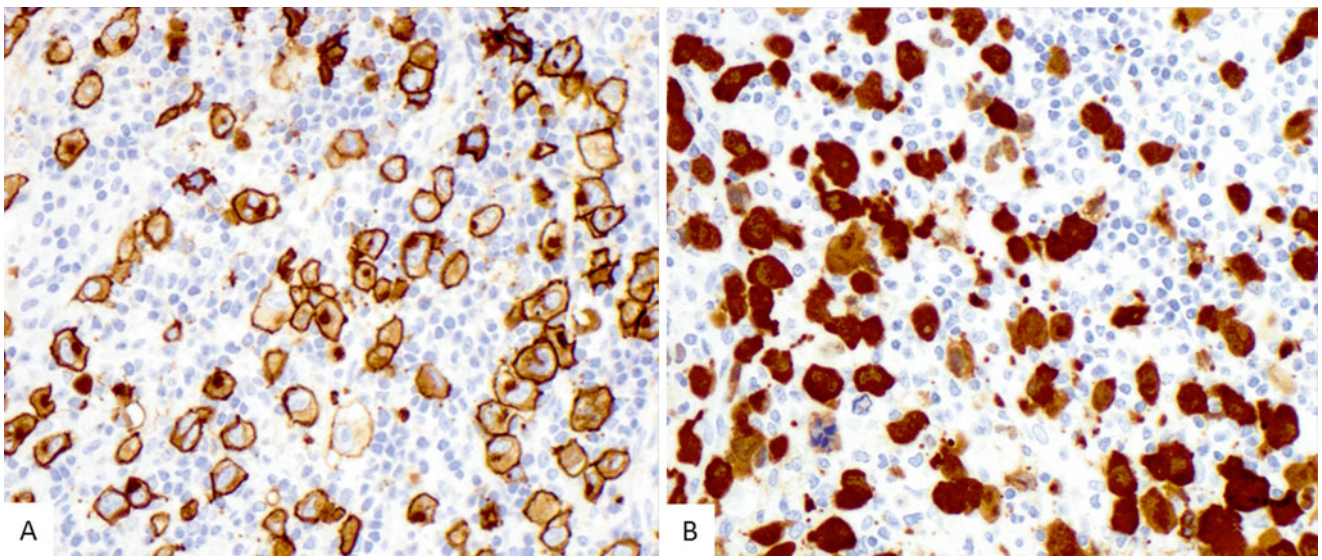

Fig. 5.35 Anaplastic large cell lymphoma, ALK positive. (**a**) CD30 immunostain highlights the neoplastic cells of anaplastic large cell lymphoma. (**b**) ALK immunostain shows the characteristic nuclear and cytoplasmic staining that is associated with the t(2;5) translocation resulting in the aberrant expression of NPM1-ALK fusion protein

Langerhans Cell Histiocytosis

Clinical Features

Langerhans cell histiocytosis (LCH) is a rare group of disorders characterized by the clonal proliferation of neoplastic Langerhans cells. The disease has a wide range of clinical presentations ranging from localized to multifocal and disseminated, and it includes the entities formerly known as Letterer-Siwe syndrome (characterized by early age at diagnosis, hepatosplenomegaly, lymphadenopathy, and pulmonary involvement), Hand-Schüller-Christian syndrome (occurring in older children and associated with osteolytic bone lesions, diabetes insipidus, and a more indolent course) and eosinophilic granuloma (associated with lung involvement, osteolytic lesions, and presentation in older children and young adults) [118].

The disorder affects up to 6 per million children per year with a male-to-female ratio of 2:1. Most patients are diagnosed between 1 and 15 years of age, with a peak incidence between 1 and 4 years [119]. Disease localized to a single site is generally benign, even without treatment. The most common sites involved are bone (skull, femur, vertebra, pelvic bones, and ribs), lymph nodes, skin and lung [120]. Multisystem (disseminated) disease commonly affects infants and is often associated with constitutional symptoms, cytopenias, skin and bone lesions, and hepatosplenomegaly [121]. Patients with LCH have been stratified into high-risk and low-risk categories, with the former including liver, lung, hematopoietic system, and spleen involvement as well as onset before 2 years of age [122].

Imaging Features

Staging evaluation is aimed at establishing the extent of disease, and most clinical protocols and practitioners require patients to undergo skeletal survey to assess for osteolytic bone lesions [120]. Depending on the clinical presentation and physical exam findings, additional imaging may include CT scan of the chest or torso, CT or MRI of the brain to assess for the presence of a focal pituitary lesion and to characterize any sites of palpable abnormality around the skull (Fig. 5.36). For bone imaging, in practice conventional radiographs are still routinely obtained and have high sensitivity for detecting lytic bone lesions (Fig. 5.37). Radiographs may not detect sites of bone marrow involvement or visceral lesions and recent studies have shown increased sensitivity of MRI and FDG PET at identifying both radiographically occult and metabolically active lesions [123, 124]. ^{99m}Tc-MDP bone scintigraphy is not recommended routinely since purely lytic lesions may not elicit sufficient surrounding bone activity to render them visible.

Several recent studies have advocated the use of FDG PET imaging to assess for active osseous and intramedullary bone lesions, to identify occult sites of soft tissue involvement and potentially as a means of monitoring response to therapy (Fig. 5.38) [123–125]. It remains to be determined whether FDG PET/CT can replace conventional imaging and clinical examination in evaluating patients with LCH.

Once the diagnosis and extent of disease have been established, follow-up imaging should be directed at characterizing response of original sites of disease to therapy. The prognostic value of FDG PET response to therapy in LCH has not been established.

Pathology

Regardless of anatomic site and clinical features, the morphologic features of LCH tend to be uniform and distinctive. The neoplastic cells are generally large (10–15 μm), with irregular nuclear contours resulting in grooved/folded nuclei

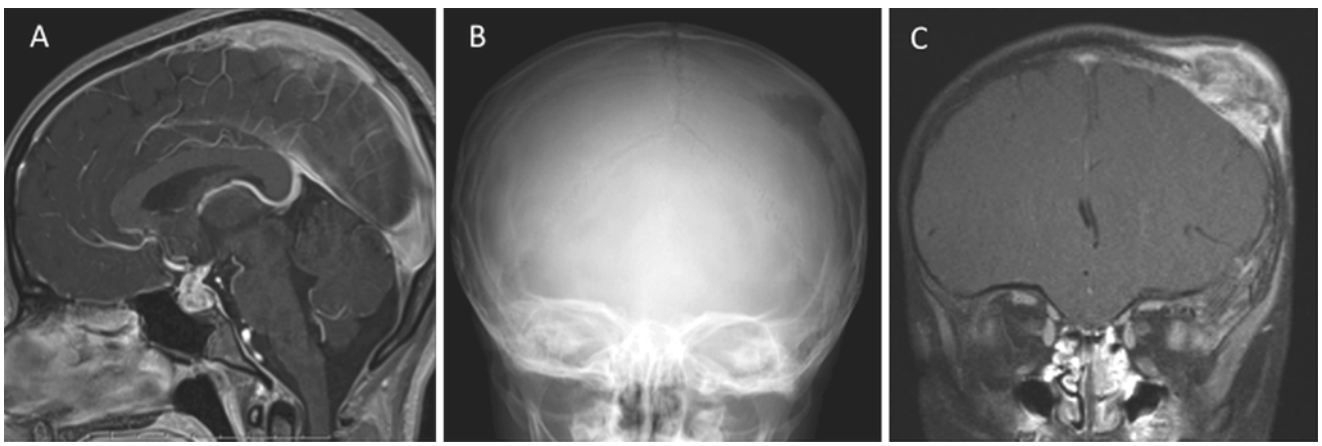

Fig. 5.36 Langerhans cell histiocytosis (LCH): 2 examples of LCH at presentation. (**a**) 15-year old presented with headache and panhypopituitarism. Contrast enhanced MRI shows diffuse enlargement of the pituitary stalk and gland; skeletal survey revealed lytic bone lesions elsewhere. (**b**, **c**) 3-year old with palpable skull mass. Skeletal survey showed left parietal lytic skull lesion (**b**); MRI revealed a large associated soft tissue mass and intracranial extension (**c**)

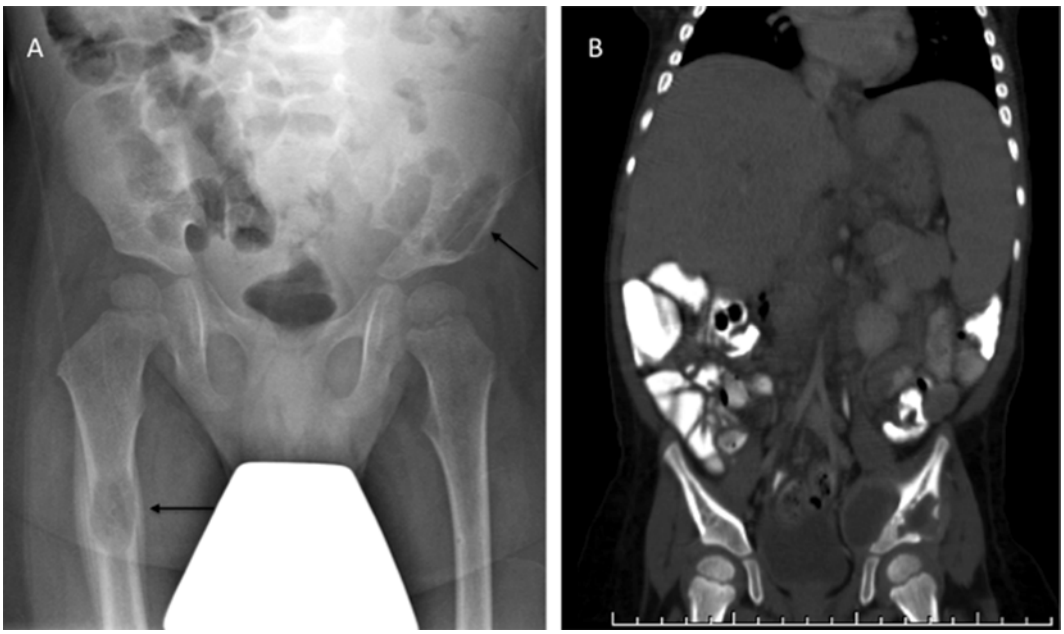

Fig. 5.37 LCH: 20-month old with limp and leg pain. Radiographs showed lytic lesions involving the right femur and left iliac bone (**a**, *arrows*). CT (**b**) shows the lytic pelvic lesion and associated soft tissue mass, in addition to revealing hepatosplenomegaly

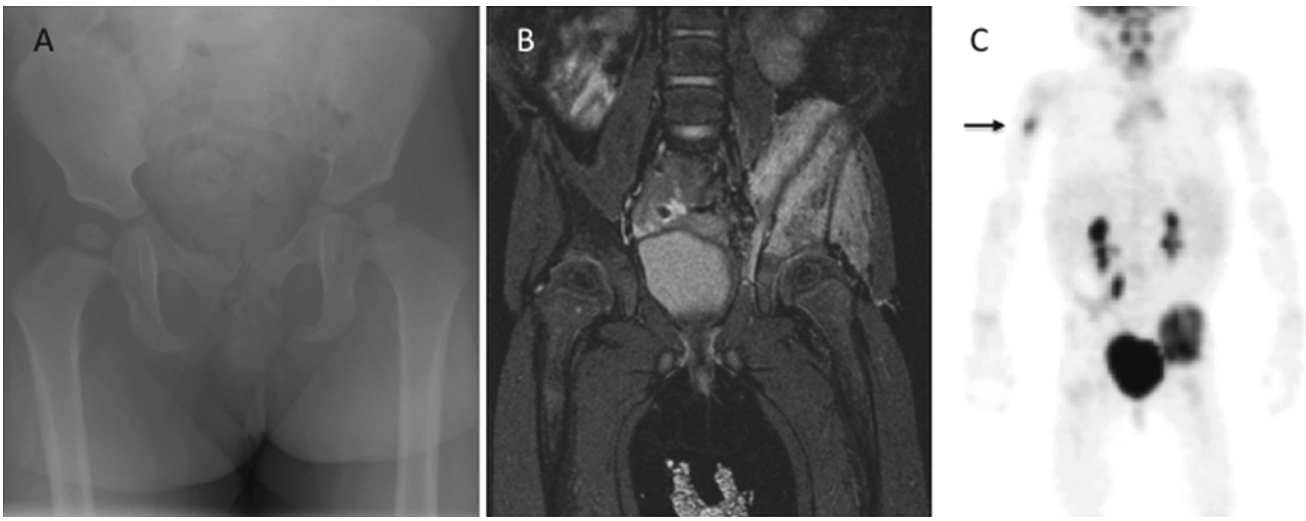

Fig. 5.38 Sixteen-month old with LCH, who initially presented with left hip pain. Radiographs were normal (**a**). MRI shows a large left iliac crest lesion (**b**). Staging FDG PET (**c**) demonstrated the iliac crest lesion to be intensely FDG avid. In addition, a clinically occult focus of FDG-avid disease in the right humerus (*arrow*) was also demonstrated by PET

("coffee-bean" shape) (Fig. 5.39a). The nuclear chromatin is dispersed and nucleoli are often inconspicuous. The neoplastic cells of LCH cells do not have dendritic morphology and show a moderate to abundant, slightly eosinophilic cytoplasm. The identification of Birbeck granules by electron microscopy is pathognomonic of LCH.

Eosinophils are often but not invariably present and may occasionally form abscesses with central necrosis and Charcot-Leyden crystals. Neutrophils and small lymphocytes may be intermixed, while plasma cells are usually sparse. In the lymph node, LCH involvement is usually sinusoidal and paracortical in distribution, with sparing of the follicles. In the spleen, LCH involvement is usually localized to the red pulp, while in the liver there is infiltration of large bile ducts and occasionally progressive sclerosing cholangitis.

The immunophenotype of LCH cells recapitulates that of normal Langerhans cells. The neoplastic cells are typically positive for CD1a, langerin (CD207), and S-100 (Fig. 5.39b–d).

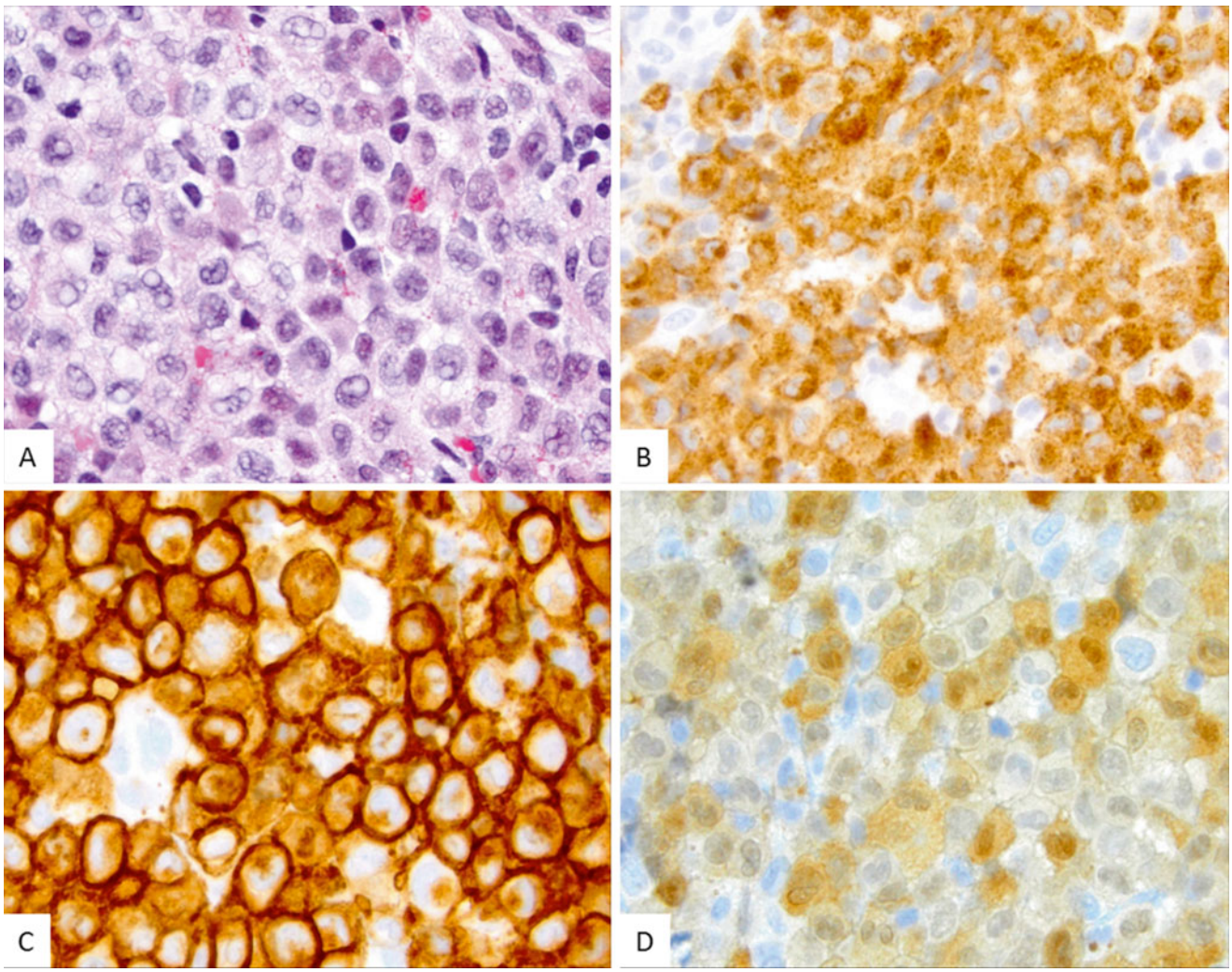

Fig. 5.39 Langerhans cell histiocytosis, skin. (**a**) Clusters of LCH cells in the dermis with eosinophils. The LCH cells are positive for langerin (CD207) (**b**) and (**c**) CD1a. (**d**) The S100 stains the neoplastic cells in both the cytoplasm and the nucleus

Disseminated Juvenile Xanthogranuloma

Clinical Features

Solitary dermal juvenile xanthogranuloma (JXG) is a benign, self-limiting non-Langerhans cell histiocytosis that arises most commonly in infants and children and presents as solitary or multiple yellowish cutaneous nodules [126]. The disseminated (deep and visceral) form is a rare disease that usually (50 %) occurs during the first year of life. A subset of JXG that occurs in older children and adults and usually involves bone and lungs is termed Erdheim-Chester disease. A possible relation between disseminated JXG and Langerhans cell histiocytosis has been suggested on the basis of rare case reports describing patients with JXG and coexisting or antecedent Langerhans cell histiocytosis [127, 128]. Some disseminated JXG cases may be associated with hematologic malignancies, most commonly juvenile myelomonocytic leukemia [129, 130].

Sites of involvement by disseminated JXG include skin, mucosal surfaces (respiratory and gastrointestinal tract), kidneys, lungs, soft tissue, central nervous system, lymph nodes, and, rarely, bone. The clinical presentation is variable and depends on the site(s) of involvement. Infiltration by neoplastic cells may result in liver and/or bone marrow failure, which has been associated with macrophage activation syndrome leading to cytopenias and liver damage or even death. Involvement of the CNS and pituitary gland by disseminated JXG can results in diabetes insipidus, seizures, hydrocephalus, and mental changes mimicking LCH.

Pathology

The neoplastic cells of JXG are small and oval shaped cells with eosinophilic cytoplasm and elongated nuclei lacking nuclear atypia. The neoplastic cells may be associated with pale foamy histiocytes, Touton giant cells, and foreign body giant cells, as well as neutrophils, lymphocytes, eosinophils, and (rarely) mast cells (Fig. 5.40). The histiocytes may contain pleomorphic nuclei, particularly in disseminated cases. Deep lesions tend to be more cellular and monotonous with fewer Touton giant cells.

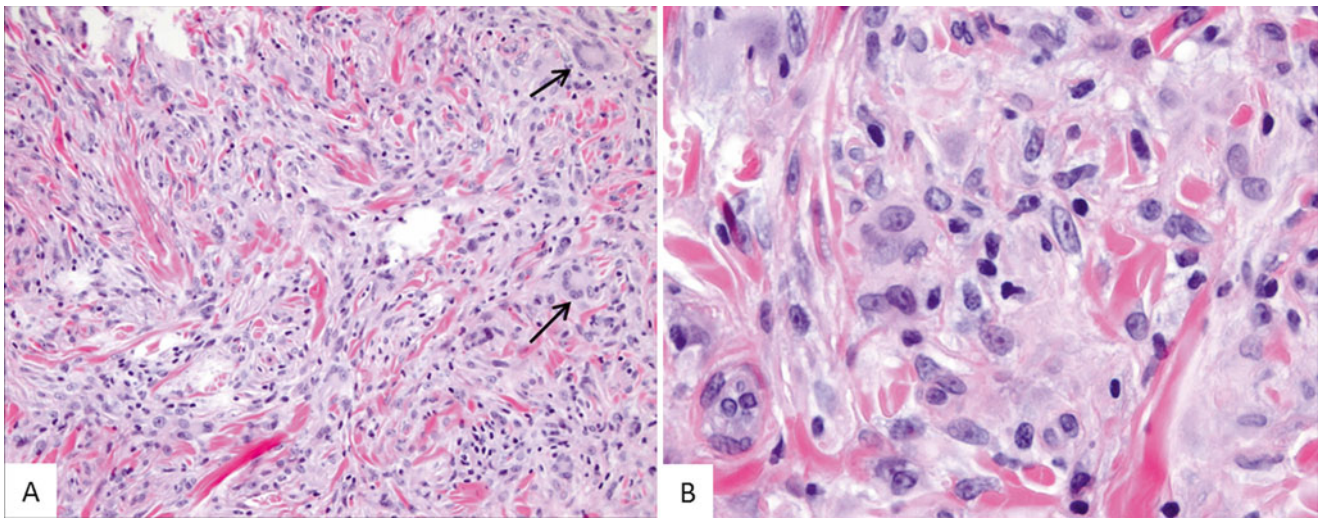

Fig. 5.40 Juvenile xanthogranuloma, skin. (**a**) Dominant histiocytic infiltrate in the dermis with spindle cell component and occasional Touton-type giant cells (*arrows*). (**b**) High power view shows the bland cytological feature of the histiocytes without significant atypia

Electron microscopy examination of the lesions shows no specific ultrastructural features and demonstrates histiocytes with short processes and abundant cytoplasm with mitochondria, rough endoplasmic reticulum, ribosomes, lysosomes, and phagolysosomes, with occasional comma-shaped dense bodies. The absence of Birbeck bodies excludes LCH.

Immunophenotypic studies are helpful in differentiating JXA from LCH and other histiocytoses. In disseminated JXA, the neoplastic cells are positive for factor XIIIa, CD68 (coarse granular pattern), CD163, CD14, lysozyme, and vimentin. Fascin, CD4, and S-100 are variably positive. CD1a and langerin (CD207) stains are typically negative.

Myeloid Sarcoma

Clinical Features

Myeloid sarcoma (granulocytic sarcoma; extramedullary leukemia; chloroma) is an extramedullary proliferation of neoplastic immature myeloid cells that disrupts the local tissue architecture. Myeloid sarcoma can be a presenting feature of acute myeloid leukemia (AML) or may arise subsequently during the disease course, including relapse, in approximately 10 % of cases [131, 132]. Myeloid sarcoma is associated with certain recurrent cytogenetic abnormalities in AML, most commonly t(8;21), inv(16), and rearrangements involving chromosome 11q23 [132].

Imaging Features

Myeloid sarcoma can involve any body part, but most typically occur in and around the orbits and subcutaneous tissues, in the sinuses, brain, spine, chest, and abdominal cavities, as well as involving the thyroid and salivary glands (Fig. 5.41) [132, 133]. When involving the brain or spinal cord, myeloid sarcoma is typically isointense or mildly hyperintense to the cerebral cortex/gray matter, but it shows intense and homogeneous enhancement following contrast injection. While the imaging features are not specific and should be confirmed by biopsy, the presence of a new mass in a patient with a prior history of myeloid malignancy should raise concern for the presence of myeloid sarcoma.

Pathology

Histologic examination of the tumor lesions shows sheets of mononuclear cells, with or without maturation. The neoplastic cells (blasts) have round to folded nuclei, usually with fine nuclear chromatin and occasional prominent nucleoli, and scant to moderate granular cytoplasm. Touch imprint preparations and cytochemical stains for myeloperoxidase and/or nonspecific esterase can be helpful for initial assessment and proper specimen processing.

Immunophenotype by flow cytometry and/or immunohistochemistry demonstrates expression of myeloid or myelomonocytic markers such as CD4, CD13, CD33, CD34, CD43, CD45, CD117, lysozyme, and myeloperoxidase (Fig. 5.42). In pediatric cases, a panel of immunohistochemical studies can be very useful especially for differentiating from small round blue cell tumors. In such cases, the expression of CD45, CD117, myeloperoxidase, and lysozyme is particularly important in distinguishing myeloid sarcoma from lymphoblastic leukemia/lymphoma and other neoplasms such as Ewing sarcoma family tumors, rhabdomyosarcoma, Wilms tumor, and neuroblastoma [134].

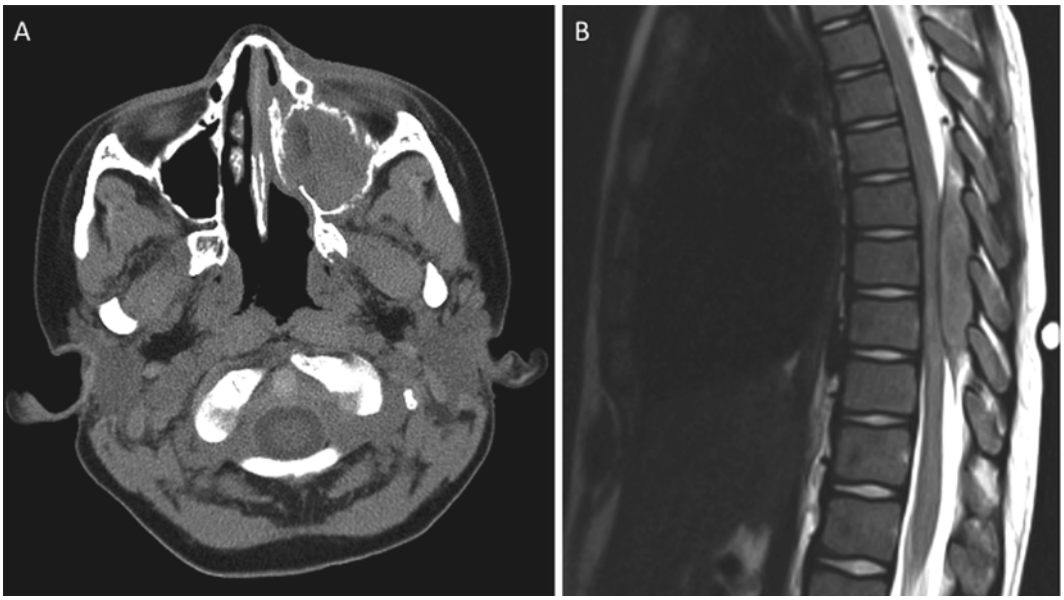

Fig. 5.41 Myeloid sarcoma: (**a**) 6-year old presenting with left infraorbital/maxillary sinus mass, peripheral blasts, and acute myeloid leukemia (AML). Biopsy of the sinus mass showed myeloid sarcoma (aka chloroma). (**b**) 10-year old with history of AML presented with back pain and progressive lower extremity paraplegia. Spine MRI revealed an intradural extramedullary mass, found at resection to be myeloid sarcoma

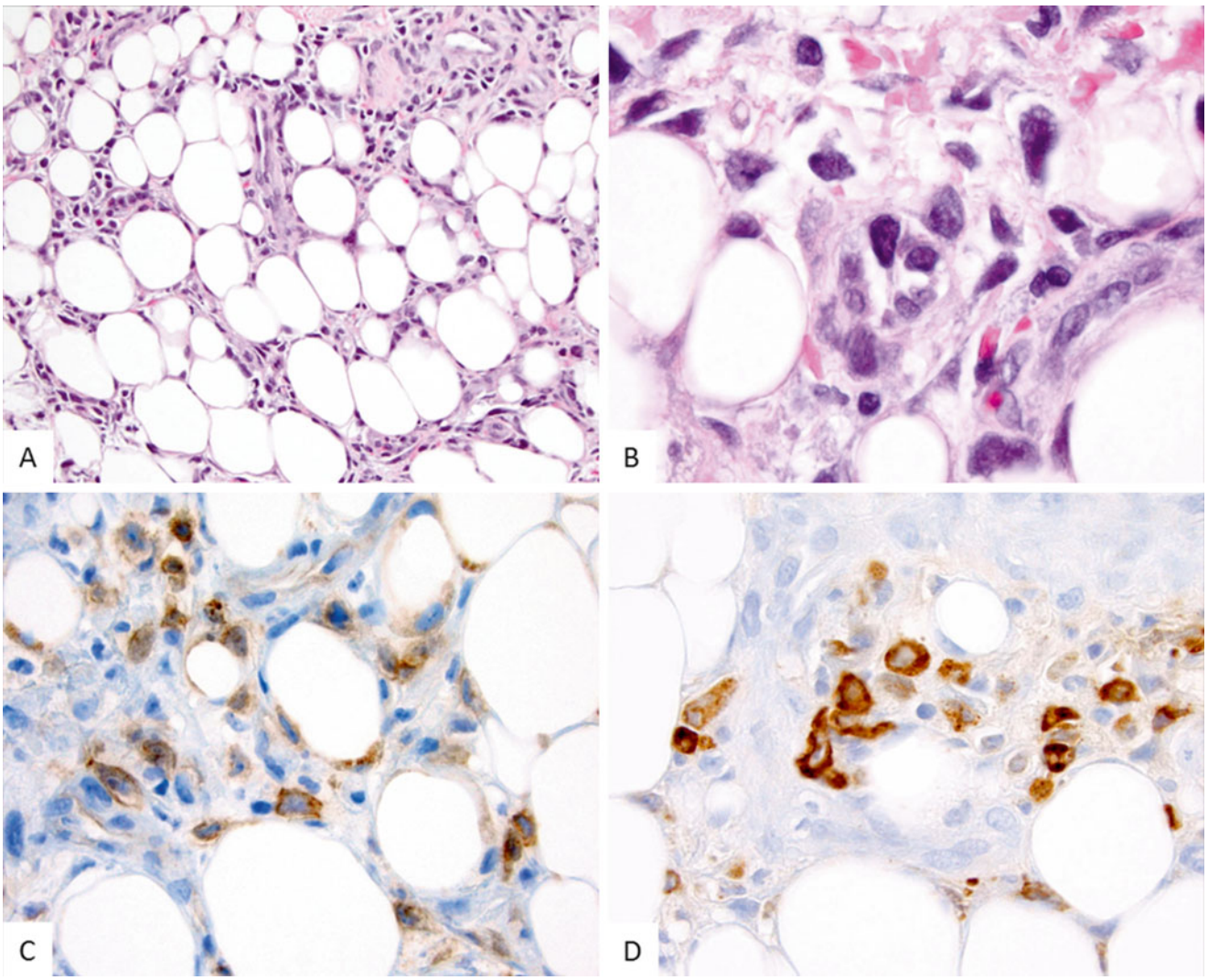

Fig. 5.42 Myeloid sarcoma, skin. (**a**, **b**) This is a patient with a history of refractory acute myeloid leukemia status post bone marrow transplant presenting with multiple skin nodules that show atypical mononuclear infiltrate in the deep dermis and subcutaneous fat. The mononuclear cells show aberrant co-expression of immature myeloid markers including CD34 (not shown) CD117 (**c**) and MPO (**d**)

Conclusion

There are a large and varied number of tumors involving lymphoid and hematopoietic tissues. A comprehensive radiologic imaging evaluation, together with a thorough histopathologic characterization of the type, lineage, and extent of the hematolymphoid disease, is necessary both to establish a diagnosis and to determine the extent of malignant involvement. This information, when integrated with the clinical situation, can be used to guide treatment, assess response to therapy, evaluate potential sites of relapse, and develop strategies for monitoring disease recurrence during periods of off-treatment surveillance.

References

1. Nickoloff EL. AAPM/RSNA physics tutorial for residents: physics of flat-panel fluoroscopy systems: survey of modern fluoroscopy imaging: flat-panel detectors versus image intensifiers and more. Radiographics. 2011;31:591–602.
2. Navarro OM. Soft tissue masses in children. Radiol Clin North Am. 2011;49:1235–59. vi–vii.
3. McCarville MB. Contrast-enhanced sonography in pediatrics. Pediatr Radiol. 2011;41 Suppl 1:S238–42.
4. Dudea SM, Botar-Jid C, Dumitriu D, et al. Differentiating benign from malignant superficial lymph nodes with sonoelastography. Med Ultrason. 2013;15:132–9.
5. Kostakoglu L, Schoder H, Johnson JL, et al. Interim [(18)F]fluorodeoxyglucose positron emission tomography imaging in stage I-II non-bulky Hodgkin lymphoma: would using combined positron emission tomography and computed tomography criteria better predict response than each test alone? Leuk Lymphoma. 2012;53:2143–50.
6. Schwartz CL, Friedman DL, McCarten K, et al. Predictors of early response and event-free survival in Hodgkin lymphoma (HL): PET versus CT imaging. J Clin Oncol. 2011;29:8006.
7. Callahan MJ, Poznauskis L, Zurakowski D, et al. Nonionic iodinated intravenous contrast material-related reactions: incidence in large urban children's hospital-retrospective analysis of data in 12,494 patients. Radiology. 2009;250:674–81.
8. ACR Manual on Contrast Media, Version 9, in Radiology ACo, editor. American College of Radiology; 2013
9. Brenner DJ, Hall EJ. Computed tomography – an increasing source of radiation exposure. N Engl J Med. 2007;357:2277–84.
10. Mettler Jr FA, Huda W, Yoshizumi TT, et al. Effective doses in radiology and diagnostic nuclear medicine: a catalog. Radiology. 2008;248:254–63.
11. Brenner DJ. Slowing the increase in the population dose resulting from CT scans. Radiat Res. 2010;174:809–15.
12. Pearce MS, Salotti JA, Little MP, et al. Radiation exposure from CT scans in childhood and subsequent risk of leukaemia and brain tumours: a retrospective cohort study. Lancet. 2012;380:499–505.
13. Mathews JD, Forsythe AV, Brady Z, et al. Cancer risk in 680,000 people exposed to computed tomography scans in childhood or adolescence: data linkage study of 11 million Australians. BMJ. 2013;346:f2360.
14. Krille L, Zeeb H, Jahnen A, et al. Computed tomographies and cancer risk in children: a literature overview of CT practices, risk estimations and an epidemiologic cohort study proposal. Radiat Environ Biophys. 2012;51:103–11.
15. Nievelstein RA, Quarles van Ufford HM, Kwee TC, et al. Radiation exposure and mortality risk from CT and PET imaging of patients with malignant lymphoma. Eur Radiol. 2012;22:1946–54.
16. McCollough CH, Bruesewitz MR, Kofler Jr JM. CT dose reduction and dose management tools: overview of available options. Radiographics. 2006;26:503–12.
17. Pooley RA. AAPM/RSNA physics tutorial for residents: fundamental physics of MR imaging. Radiographics. 2005;25:1087–99.
18. Weissleder R, Elizondo G, Wittenberg J, et al. Ultrasmall superparamagnetic iron oxide: an intravenous contrast agent for assessing lymph nodes with MR imaging. Radiology. 1990;175:494–8.
19. Pandharipande PV, Mora JT, Uppot RN, et al. Lymphotropic nanoparticle-enhanced MRI for independent prediction of lymph node malignancy: a logistic regression model. Am J Roentgenol. 2009;193:W230–7.
20. Kwee TC, Takahara T, Vermoolen MA, et al. Whole-body diffusion-weighted imaging for staging malignant lymphoma in children. Pediatr Radiol. 2010;40(10):1592–602.
21. Vermoolen MA, Kwee TC, Akkerman EM, et al. Whole-body MRI, including diffusion-weighted imaging, compared to FDG-PET for staging Hodgkin's lymphoma – initial experience. Pediatr Radiol. 2010;40:1097.
22. Punwani S, Taylor SA, Saad ZZ, et al. Diffusion-weighted MRI of lymphoma: prognostic utility and implications for PET/MRI? Eur J Nucl Med Mol Imaging. 2013;40:373–85.
23. Koh DM, Collins DJ. Diffusion-weighted MRI in the body: applications and challenges in oncology. Am J Roentgenol. 2007;188:1622–35.
24. Padhani AR, Liu G, Koh DM, et al. Diffusion-weighted magnetic resonance imaging as a cancer biomarker: consensus and recommendations. Neoplasia. 2009;11:102–25.
25. Mir N, Sohaib SA, Collins D, et al. Fusion of high b-value diffusion-weighted and T2-weighted MR images improves identification of lymph nodes in the pelvis. J Med Imaging Radiat Oncol. 2010;54:358–64.
26. Roy C, Bierry G, Matau A, et al. Value of diffusion-weighted imaging to detect small malignant pelvic lymph nodes at 3T. Eur Radiol. 2010;20:1803–11.
27. Kaewlai R, Abujudeh H. Nephrogenic systemic fibrosis. Am J Roentgenol. 2012;199:W17–23.
28. Treves ST. Pediatric nuclear medicine/PET. Seacus, NJ: Springer; 2007.
29. Kelly KM, Hodgson D, Appel B, et al. Children's Oncology Group's 2013 blueprint for research: Hodgkin lymphoma. Pediatr Blood Cancer. 2013;60:972–8.
30. Kostakoglu L, Cheson BD. State-of-the-art research on lymphomas: role of molecular imaging for staging, prognostic evaluation, and treatment response. Front Oncol. 2013;3:212.
31. Zhuang H, Yu JQ, Alavi A. Applications of fluorodeoxyglucose-PET imaging in the detection of infection and inflammation and other benign disorders. Radiol Clin North Am. 2005;43:121–34.
32. Vermoolen MA, Kersten MJ, Fijnheer R, et al. Magnetic resonance imaging of malignant lymphoma. Expert Rev Hematol. 2011;4:161–71.
33. Oguz A, Karadeniz C, Temel EA, et al. Evaluation of peripheral lymphadenopathy in children. Pediatr Hematol Oncol. 2006;23:549–61.
34. Twist CJ, Link MP. Assessment of lymphadenopathy in children. Pediatr Clin North Am. 2002;49:1009–25.
35. Rosado FG, Stratton CW, Mosse CA. Clinicopathologic correlation of epidemiologic and histopathologic features of pediatric bacterial lymphadenitis. Arch Pathol Lab Med. 2011;135:1490–3.
36. Monaco SE, Khalbuss WE, Pantanowitz L. Benign non-infectious causes of lymphadenopathy: a review of cytomorphology and differential diagnosis. Diagn Cytopathol. 2012;40:925–38.

37. Chapel H. Classification of primary immunodeficiency diseases by the International Union of Immunological Societies (IUIS) Expert Committee on Primary Immunodeficiency 2011. Clin Exp Immunol. 2012;168:58–9.
38. International Union of Immunological Societies Expert Committee on PrimaryI, Notarangelo LD, Fischer A, et al. Primary immunodeficiencies: 2009 update. J Allergy Clin Immunol. 2009;124: 1161–78.
39. Filipovich AH, Mathur A, Kamat D, et al. Primary immunodeficiencies: genetic risk factors for lymphoma. Cancer Res. 1992; 52:5465s–7.
40. Terasawa T, Lau J, Bardet S, et al. Fluorine-18-fluorodeoxyglucose positron emission tomography for interim response assessment of advanced-stage Hodgkin's lymphoma and diffuse large B-cell lymphoma: a systematic review. J Clin Oncol. 2009;27:1906–14.
41. Ng SB, Khoury JD. Epstein-Barr virus in lymphoproliferative processes: an update for the diagnostic pathologist. Adv Anat Pathol. 2009;16:40–55.
42. Hollingsworth CL. Thoracic disorders in the immunocompromised child. Radiol Clin North Am. 2005;43:435–47.
43. Yin EZ, Frush DP, Donnelly LF, et al. Primary immunodeficiency disorders in pediatric patients: clinical features and imaging findings. Am J Roentgenol. 2001;176:1541–52.
44. Cotelingam JD, Witebsky FG, Hsu SM, et al. Malignant lymphoma in patients with the Wiskott-Aldrich syndrome. Cancer Invest. 1985;3:515–22.
45. Taylor AM, Metcalfe JA, Thick J, et al. Leukemia and lymphoma in ataxia telangiectasia. Blood. 1996;87:423–38.
46. Notarangelo L, Casanova JL, Conley ME, et al. Primary immunodeficiency diseases: an update from the International Union of Immunological Societies Primary Immunodeficiency Diseases Classification Committee Meeting in Budapest, 2005. J Allergy Clin Immunol. 2006;117:883–96.
47. Safriel YI, Haller JO, Lefton DR, et al. Imaging of the brain in the HIV-positive child. Pediatr Radiol. 2000;30:725–32.
48. Boyle GJ, Michaels MG, Webber SA, et al. Posttransplantation lymphoproliferative disorders in pediatric thoracic organ recipients. J Pediatr. 1997;131:309–13.
49. Webber SA, Naftel DC, Fricker FJ, et al. Lymphoproliferative disorders after paediatric heart transplantation: a multi-institutional study. Lancet. 2006;367:233–9.
50. von Falck C, Maecker B, Schirg E, et al. Post transplant lymphoproliferative disease in pediatric solid organ transplant patients: a possible role for [18F]-FDG-PET(/CT) in initial staging and therapy monitoring. Eur J Radiol. 2007;63:427–35.
51. Gurney JG, Davis S, Severson RK, et al. Trends in cancer incidence among children in the U.S. Cancer. 1996;78:532–41.
52. Jaglowski SM, Linden E, Termuhlen AM, et al. Lymphoma in adolescents and young adults. Semin Oncol. 2009;36:381–418.
53. Pui CH, Robison LL, Look AT. Acute lymphoblastic leukaemia. Lancet. 2008;371:1030–43.
54. Morton LM, Wang SS, Devesa SS, et al. Lymphoma incidence patterns by WHO subtype in the United States, 1992–2001. Blood. 2006;107:265–76.
55. Sandlund JT, Downing JR, Crist WM. Non-Hodgkin's lymphoma in childhood. N Engl J Med. 1996;334:1238–48.
56. Gross TL, Perkins SL. Malignant non-Hodgkin lymphomas in children. In: Pizzo PA, Poplack DG, editors. Principles and practice of pediatric oncology. Philadelphia, PA: Lippincott Williams & Wilkins; 2011. p. 663–82.
57. Anghelescu DL, Burgoyne LL, Liu T, et al. Clinical and diagnostic imaging findings predict anesthetic complications in children presenting with malignant mediastinal masses. Paediatr Anaesth. 2007;17:1090–8.
58. Shepherd SF, A'Hern RP, Pinkerton CR. Childhood T-cell lymphoblastic lymphoma-does early resolution of mediastinal mass predict for final outcome? The United Kingdom Children's Cancer Study Group (UKCCSG). Br J Cancer. 1995;72:752–6.
59. Termuhlen AM, Smith LM, Perkins SL, et al. Disseminated lymphoblastic lymphoma in children and adolescents: results of the COG A5971 trial: a report from the Children's Oncology Group. Br J Haematol. 2013;162:792–801.
60. Khoury JD. Ewing sarcoma family of tumors. Adv Anat Pathol. 2005;12:212–20.
61. Zhang J, Ding L, Holmfeldt L, et al. The genetic basis of early T-cell precursor acute lymphoblastic leukaemia. Nature. 2012;481:157–63.
62. Cairo MS, Raetz E, Lim MS, et al. Childhood and adolescent non-Hodgkin lymphoma: new insights in biology and critical challenges for the future. Pediatr Blood Cancer. 2005;45:753–69.
63. Oschlies I, Burkhardt B, Chassagne-Clement C, et al. Diagnosis and immunophenotype of 188 pediatric lymphoblastic lymphomas treated within a randomized prospective trial: experiences and preliminary recommendations from the European childhood lymphoma pathology panel. Am J Surg Pathol. 2011;35:836–44.
64. Hochberg J, Waxman IM, Kelly KM, et al. Adolescent non-Hodgkin lymphoma and Hodgkin lymphoma: state of the science. Br J Haematol. 2009;144:24–40.
65. Khoury JD, Jones D, Yared MA, et al. Bone marrow involvement in patients with nodular lymphocyte predominant Hodgkin lymphoma. Am J Surg Pathol. 2004;28:489–95.
66. Carbone A, Spina M, Gloghini A, et al. Classical Hodgkin's lymphoma arising in different host's conditions: pathobiology parameters, therapeutic options, and outcome. Am J Hematol. 2011;86:170–9.
67. Bradley AJ, Carrington BM, Lawrance JA, et al. Assessment and significance of mediastinal bulk in Hodgkin's disease: comparison between computed tomography and chest radiography. J Clin Oncol. 1999;17:2493–8.
68. Shamberger RC. Preanesthetic evaluation of children with anterior mediastinal masses. Semin Pediatr Surg. 1999;8:61–8.
69. Metzger ML, Krasin MJ, Hudson MM, et al. Hodgkin Lymphoma. In: Pizzo PA, Poplack DG, editors. Principles and practice of pediatric oncology. Philadelphia, PA: Lippincott, Williams and Wilkens; 2011. p. 638–62.
70. Paes FM, Kalkanis DG, Sideras PA, et al. FDG PET/CT of extranodal involvement in non-Hodgkin lymphoma and Hodgkin disease. Radiographics. 2010;30:269–91.
71. Purz S, Mauz-Korholz C, Korholz D, et al. [18F] Fluorodeoxyglucose positron emission tomography for detection of bone marrow involvement in children and adolescents with Hodgkin's lymphoma. J Clin Oncol. 2011;29:3523–8.
72. Kluge R, Kurch L, Montravers F, et al. FDG PET/CT in children and adolescents with lymphoma. Pediatr Radiol. 2013;43:406–17.
73. Furth C, Denecke T, Steffen I, et al. Correlative imaging strategies implementing CT, MRI, and PET for staging of childhood Hodgkin disease. J Pediatr Hematol Oncol. 2006;28:501–12.
74. Furth C, Steffen IG, Amthauer H, et al. Early and late therapy response assessment with [18F]fluorodeoxyglucose positron emission tomography in pediatric Hodgkin's lymphoma: analysis of a prospective multicenter trial. J Clin Oncol. 2009;27:4385–91.
75. Gallamini A, Fiore F, Sorasio R, et al. Interim positron emission tomography scan in Hodgkin lymphoma: definitions, interpretation rules, and clinical validation. Leuk Lymphoma. 2009;50:1761–4.
76. Lister TA, Crowther D, Sutcliffe SB, et al. Report of a committee convened to discuss the evaluation and staging of patients with Hodgkin's disease: Cotswolds meeting. J Clin Oncol. 1989;7: 1630–6.
77. Freed J, Kelly KM. Current approaches to the management of pediatric Hodgkin lymphoma. Paediatr Drugs. 2010;12:85–98.
78. Metzger ML, Hudson MM. Balancing efficacy and safety in the treatment of adolescents with Hodgkin's lymphoma. J Clin Oncol. 2009;27:6071–3.

79. Metzger ML, Hudson MM, Krasin MJ, et al. Initial response to salvage therapy determines prognosis in relapsed pediatric Hodgkin lymphoma patients. Cancer. 2010;116:4376–84.
80. Metzger ML, Weinstein HJ, Hudson MM, et al. Association between radiotherapy vs no radiotherapy based on early response to VAMP chemotherapy and survival among children with favorable-risk Hodgkin lymphoma. JAMA. 2012;307:2609–16.
81. Hutchings M. How does PET/CT help in selecting therapy for patients with Hodgkin lymphoma? Hematol Am Soc Hematol Educ Program. 2012;2012:322–7.
82. Kostakoglu L, Gallamini A. Interim 18F-FDG PET in Hodgkin lymphoma: would PET-adapted clinical trials lead to a paradigm shift? J Nucl Med. 2013;54:1082–93.
83. Cheson BD, Pfistner B, Juweid ME, et al. Revised response criteria for malignant lymphoma. J Clin Oncol. 2007;25:579–86.
84. Juweid ME, Stroobants S, Hoekstra OS, et al. Use of positron emission tomography for response assessment of lymphoma: consensus of the Imaging Subcommittee of International Harmonization Project in Lymphoma. J Clin Oncol. 2007;25:571–8.
85. Barrington SF, Mikhaeel NG, Kostakoglu L, et al. Role of imaging in the staging and response assessment of lymphoma: consensus of the international conference on Malignant Lymphomas Imaging Working Group. J Clin Oncol. 2014. pii: JCO.2013.53.5229. PMID: 25113771, [Epub ahead of print].
86. Cheson BD, Fisher RI, Barrington SF, et al. Recommendations for initial evaluation, staging, and response assessment of Hodgkin and non-Hodgkin lymphoma: the Lugano classification. J Clin Oncol. 2014. pii: JCO.2013.54.8800. PMID: 25113753, [Epub ahead of print].
87. Meignan M, Gallamini A, Itti E et al. Report on the Third International Workshop on Interim Positron Emission Tomography in Lymphoma held in Menton, France, 26–27 September 2011 and Menton 2011 consensus. Leuk Lymphoma 2012;53:1876-81.
88. Voss SD, Chen L, Constine LS, et al. Surveillance computed tomography imaging and detection of relapse in intermediate- and advanced-stage pediatric Hodgkin's lymphoma: a report from the Children's Oncology Group. J Clin Oncol. 2012;30:2635–40.
89. Voss SD. Surveillance imaging in pediatric hodgkin lymphoma. Curr Hematol Malig Rep. 2013;8:218–25.
90. Rathore N, Eissa HM, Margolin JF, et al. Pediatric Hodgkin lymphoma: are we over-scanning our patients? Pediatr Hematol Oncol. 2012;29:415–23.
91. Friedmann AM, Wolfson JA, Hudson MM, et al. Relapse after treatment of pediatric Hodgkin lymphoma: outcome and role of surveillance after end of therapy. Pediatr Blood Cancer. 2013;60:1458–63.
92. Venkataraman G, Mirza MK, Eichenauer DA, et al. Current status of prognostication in classical Hodgkin lymphoma. Br J Haematol. 2014;165:287–99.
93. Deffenbacher KE, Iqbal J, Sanger W, et al. Molecular distinctions between pediatric and adult mature B-cell non-Hodgkin lymphomas identified through genomic profiling. Blood. 2012;119:3757–66.
94. Toma P, Granata C, Rossi A, et al. Multimodality imaging of Hodgkin disease and non-Hodgkin lymphomas in children. Radiographics. 2007;27:1335–54.
95. Burkhardt B, Oschlies I, Klapper W, et al. Non-Hodgkin's lymphoma in adolescents: experiences in 378 adolescent NHL patients treated according to pediatric NHL-BFM protocols. Leukemia. 2011;25:153–60.
96. Gerrard M, Waxman IM, Sposto R, et al. Outcome and pathologic classification of children and adolescents with mediastinal large B-cell lymphoma treated with FAB/LMB96 mature B-NHL therapy. Blood. 2013;121:278–85.
97. Reiter A, Ferrando AA. Malignant lymphomas and lymphadenopathies. In: Orkin SH, Fisher DE, Look AT, et al., editors. Oncology of infancy and childhood. Philadelphia: Elsevier; 2009. p. 417–508.
98. Reiter A, Klapper W. Recent advances in the understanding and management of diffuse large B-cell lymphoma in children. Br J Haematol. 2008;142:329–47.
99. Morin RD, Gascoyne RD. Newly identified mechanisms in B-cell non-Hodgkin lymphomas uncovered by next-generation sequencing. Semin Hematol. 2013;50:303–13.
100. Hans CP, Weisenburger DD, Greiner TC, et al. Confirmation of the molecular classification of diffuse large B-cell lymphoma by immunohistochemistry using a tissue microarray. Blood. 2004; 103:275–82.
101. Oschlies I, Klapper W, Zimmermann M, et al. Diffuse large B-cell lymphoma in pediatric patients belongs predominantly to the germinal-center type B-cell lymphomas: a clinicopathologic analysis of cases included in the German BFM (Berlin-Frankfurt-Munster) Multicenter Trial. Blood. 2006;107:4047–52.
102. Miles RR, Raphael M, McCarthy K, et al. Pediatric diffuse large B-cell lymphoma demonstrates a high proliferation index, frequent c-Myc protein expression, and a high incidence of germinal center subtype: Report of the French-American-British (FAB) international study group. Pediatr Blood Cancer. 2008;51: 369–74.
103. Sandlund JT. Burkitt lymphoma: staging and response evaluation. Br J Haematol. 2012;156:761–5.
104. Karantanis D, Durski JM, Lowe VJ, et al. 18F-FDG PET and PET/CT in Burkitt's lymphoma. Eur J Radiol. 2010;75:e68–73.
105. Leventaki V, Rodic V, Tripp SR, et al. TP53 pathway analysis in paediatric Burkitt lymphoma reveals increased MDM4 expression as the only TP53 pathway abnormality detected in a subset of cases. Br J Haematol. 2012;158:763–71.
106. Taddesse-Heath L, Pittaluga S, Sorbara L, et al. Marginal zone B-cell lymphoma in children and young adults. Am J Surg Pathol. 2003;27:522–31.
107. Rizzo KA, Streubel B, Pittaluga S, et al. Marginal zone lymphomas in children and the young adult population; characterization of genetic aberrations by FISH and RT-PCR. Mod Pathol 23: 866–73
108. Rizzo KA, Streubel B, Pittaluga S, et al. Marginal zone lymphomas in children and the young adult population; characterization of genetic aberrations by FISH and RT-PCR. Mod Pathol. 2010;23:866–73.
109. Lorsbach RB, Shay-Seymore D, Moore J, et al. Clinicopathologic analysis of follicular lymphoma occurring in children. Blood. 2002;99:1959–64.
110. Oschlies I, Salaverria I, Mahn F, et al. Pediatric follicular lymphoma – a clinico-pathological study of a population-based series of patients treated within the Non-Hodgkin's Lymphoma–Berlin-Frankfurt-Munster (NHL-BFM) multicenter trials. Haematologica. 2010;95:253–9.
111. Setty BA, Termuhlen AM. Rare pediatric non-hodgkin lymphoma. Curr Hematol Malig Rep. 2010;5:163–8.
112. Hayashi D, Lee JC, Devenney-Cakir B, et al. Follicular non-Hodgkin's lymphoma. Clin Radiol. 2010;65:408–20.
113. Hofman MS, Hicks RJ. Imaging in follicular NHL. Best Pract Res Clin Haematol. 2011;24:165–77.
114. Salaverria I, Philipp C, Oschlies I, et al. Translocations activating IRF4 identify a subtype of germinal center-derived B-cell lymphoma affecting predominantly children and young adults. Blood 118:139–47
115. Lowe EJ, Gross TG. Anaplastic large cell lymphoma in children and adolescents. Pediatr Hematol Oncol. 2013;30:509–19.
116. Le Deley MC, Reiter A, Williams D, et al. Prognostic factors in childhood anaplastic large cell lymphoma: results of a large European intergroup study. Blood. 2008;111:1560–6.
117. Mosse YP, Lim MS, Voss SD, et al. Safety and activity of crizotinib for paediatric patients with refractory solid tumours or anaplastic large-cell lymphoma: a Children's Oncology Group phase 1 consortium study. Lancet Oncol. 2013;14:472–80.

118. Favara BE, Feller AC, Pauli M, et al. Contemporary classification of histiocytic disorders. The WHO Committee on Histiocytic/Reticulum Cell Proliferations. Reclassification Working Group of the Histiocyte Society. Med Pediatr Oncol. 1997;29:157–66.
119. Alston RD, Tatevossian RG, McNally RJ, et al. Incidence and survival of childhood Langerhans cell histiocytosis in Northwest England from 1954 to 1998. Pediatr Blood Cancer. 2007;48:555–60.
120. Degar BA, Fleming MD, Rollins BJ. Histocytoses. In: Orkin SH, Fisher DE, Look AT, et al., editors. Oncology of infancy and childhood. Philadelphia, PA: Saunders Elsevier; 2009. p. 963–88.
121. Gadner H, Grois N, Arico M, et al. A randomized trial of treatment for multisystem Langerhans' cell histiocytosis. J Pediatr. 2001;138:728–34.
122. Gadner H, Grois N, Potschger U, et al. Improved outcome in multisystem Langerhans cell histiocytosis is associated with therapy intensification. Blood. 2008;111:2556–62.
123. Mueller WP, Melzer HI, Schmid I, et al. The diagnostic value of 18F-FDG PET and MRI in paediatric histiocytosis. Eur J Nucl Med Mol Imaging. 2013;40:356–63.
124. Phillips M, Allen C, Gerson P, et al. Comparison of FDG-PET scans to conventional radiography and bone scans in management of Langerhans cell histiocytosis. Pediatr Blood Cancer. 2009;52:97–101.
125. Kaste SC, Rodriguez-Galindo C, McCarville ME, et al. PET-CT in pediatric Langerhans cell histiocytosis. Pediatr Radiol. 2007;37:615–22.
126. Janssen D, Harms D. Juvenile xanthogranuloma in childhood and adolescence: a clinicopathologic study of 129 patients from the kiel pediatric tumor registry. Am J Surg Pathol. 2005;29:21–8.
127. Hoeger PH, Diaz C, Malone M, et al. Juvenile xanthogranuloma as a sequel to Langerhans cell histiocytosis: a report of three cases. Clin Exp Dermatol. 2001;26:391–4.
128. Yu H, Kong J, Gu Y, et al. A child with coexistent juvenile xanthogranuloma and Langerhans cell histiocytosis. J Am Acad Dermatol. 2010;62:329–32.
129. Zvulunov A, Barak Y, Metzker A. Juvenile xanthogranuloma, neurofibromatosis, and juvenile chronic myelogenous leukemia. World statistical analysis. Arch Dermatol. 1995;131:904–8.
130. Aparicio G, Mollet J, Bartralot R, et al. Eruptive juvenile xanthogranuloma associated with relapsing acute lymphoblastic leukemia. Pediatr Dermatol. 2008;25:487–8.
131. Reinhardt D, Creutzig U. Isolated myelosarcoma in children-update and review. Leuk Lymphoma. 2002;43:565–74.
132. Dusenbery KE, Howells WB, Arthur DC, et al. Extramedullary leukemia in children with newly diagnosed acute myeloid leukemia: a report from the Children's Cancer Group. J Pediatr Hematol Oncol. 2003;25:760–8.
133. Guermazi A, Feger C, Rousselot P, et al. Granulocytic sarcoma (chloroma): imaging findings in adults and children. Am J Roentgenol. 2002;178:319–25.
134. Klco JM, Welch JS, Nguyen TT, et al. State of the art in myeloid sarcoma. Int J Lab Hematol. 2011;33:555–65.

Tumors of the Central Nervous System

6

Kar-Ming Fung, Zhongxin Yu, and Kalliopi Petropoulou

Normal Anatomy and Development

Knowledge of normal neuroanatomy and neurodevelopment is critical to proper diagnosis. A few normal structures may be mistaken as tumor particularly on frozen sections.

The external granular layer (Fig. 6.1a) is a layer of small neurons that covers the external surface of fetal/infant cerebellum. It is quite prominent at the time of birth but is almost completely regressed by the ninth postnatal month. It should not be misinterpreted as medulloblastoma or lymphocytic infiltration in younger infants. The internal granular layer is also composed of small neurons. Without a size comparison, these cells may be mistaken for medulloblastoma or other small blue cell tumors in minute specimens or cytologic preparations. Conversely medulloblastoma cells, particularly those with smaller nuclei, can be mistaken as internal granular cells. Purkinje cells are rather large and should not be mistaken as rhabdoid cells (Fig. 6.1b). Other normal structures that can be mistaken for neoplastic tissue include the posterior pituitary and the pineal gland which may be mistaken as glial neoplasm and normal choroid plexus being mistaken as choroid plexus papilloma. These misinterpretations are likely to be committed when the specimen is minute and communication between the pathologist and the neurosurgeon is poor.

K.-M. Fung, M.D., Ph.D. (✉) • Z. Yu, M.D.
Department of Pathology, University of Oklahoma Health Sciences Center, BMSB 451, 940 Stanton Young Blvd., Oklahoma City, OK 73104, USA
e-mail: karming-fung@ouhsc.edu

K. Petropoulou, M.D.
Department of Radiology, State University of New York (SUNY) Upstate, Syracuse, NY 13210, USA

Overview and Classification

Tumor of the CNS is not uncommon in the pediatric age group and some of these entities occur only rarely in adults (Table 6.1). While meningiomas are very common in adults, it is uncommon in children and almost nonexistent in infants. The most common pediatric tumors in descending order of frequency are pilocytic astrocytoma, diffuse astrocytomas, medulloblastomas, and craniopharyngiomas. Ependymal neoplasms and schwannomas are the most frequent infratentorial tumors. Most tumors occur in the brain with a supratentorial-to-infratentorial ratio of approximately 2-to-1. Malignant CNS neoplasms represent 16.6 % of all malignancies in the pediatric age group. In general, the incidence is higher in males than females and among white compared to black children. The incidence is 36.2 per million between infancy and 7 years of age and 21.0 per million between 7 and 10 years of age. As a group, they are the second most frequent malignancy and most common solid tumor in pediatric patients. About 2,200 new cases are diagnosed annually in the United States. Among CNS malignancies, astrocytic tumors account for 52 %, while medulloblastoma and primitive neuroectodermal tumor (PNET), other gliomas, and ependymomas accounted for 21, 15, and 9 %, respectively [2].

In contrast to adults, there is a high occurrence of malignancies in the cerebellum and brain stem in young children. About 40 % of all thalamic tumors arise in patients under 18 years old and account for 2–5 % of all intracranial tumors in children [3]. About two third or pediatric thalamic tumors are high grade in histology [4]. Tumor of the spinal cord represents about 9.9 % and extramedullary tumors are slightly more common than intramedullary tumors [5]. Astrocytomas are most common and comprise 70 % of tumors arising in the spinal cord of children. In contrast, ependymoma is the most common spinal cord tumor in adults [6]. Although hemangioblastoma is common in adults [6], it is uncommon in children other than those affected by von Hippel Lindau syndrome. Myxopapillary ependymoma and paraganglioma

D.M. Parham et al. (eds.), *Pediatric Malignancies: Pathology and Imaging*,
DOI 10.1007/978-1-4939-1729-7_6, © Springer Science+Business Media New York 2015

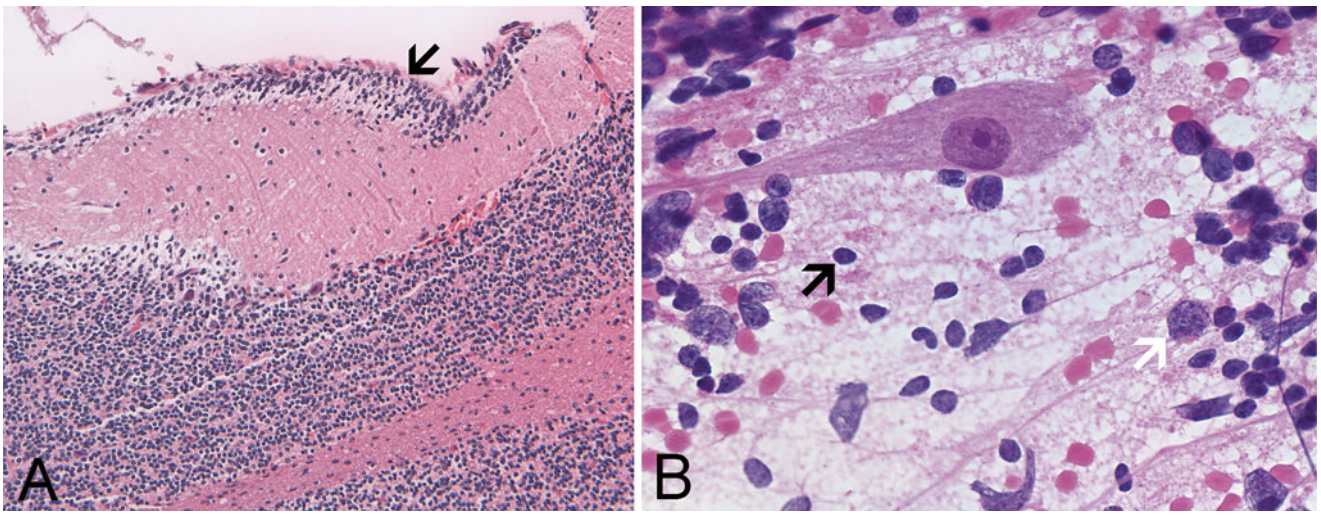

Fig. 6.1 Normal anatomy: (**a**) The external granular layer (*arrow*) is a transient structure that is present in infants, and much less commonly, toddlers. It should not be mistaken as evidence of meningitis or neoplastic changes. (**b**) In this cytologic preparation, the large cell is a Purkinje cell. The smaller cells (*black arrow*) are internal granular cells. They are monotonous and almost always appear in form of naked nuclei. Medulloblastoma cells, for comparison here, are larger and more variable in size (*white arrow*)

Table 6.1 WHO classification and grades of tumors

Tumor	I	II	III	IV
Astrocytic tumors				
Subependymal giant cell astrocytoma[a]	■			
Pilocytic astrocytoma[a]	■			
Pilomyxoid astrocytom[a] a		■		
Diffuse astrocytoma[b]		■		
Pleomorphic xanthoastrocytoma		■		
Anaplastic astrocytoma			■	
Glioblastoma[a]				■
Giant cell glioblastoma				■
Gliosarcoma				■
Gliomatosis cerebri[b]			■	
Oligodendroglial tumors				
Oligodendroglioma		■		
Anaplastic oligodendroglioma			■	
Oligoastrocytic tumors				
Oligoastrocytoma		■		
Anaplastic oligoastrocytoma			■	
Ependymal tumors				
Subependymoma	■			
Myxopapillary ependymoma[a]	■			
Ependymoma[a]		■		
Anaplastic ependymoma[a]			■	
Choroid plexus tumors				
Choroid plexus papilloma[a]	■			
Atypical choroid plexus papilloma[a]		■		
Choroid plexus carcinoma[a]			■	
Other neuroepithelial tumors				
Astroblastoma[c, d]				
Angiocentric glioma[c]	■			
Choroid glioma of the third ventricle		■		

Table 6.1 (continued)

Tumor	I	II	III	IV
Neuronal and mixed neuronal-glial tumors				
Gangliocytoma[a]	■			
Ganglioglioma[a]	■			
Anaplastic ganglioglioma[a]			■	
Desmoplastic infantile astrocytoma and ganglioglioma[a]	■			
Dysembryoplastic neuroepithelioma[a]	■			
Central neurocytoma		■		
Extraventricular neurocytoma		■		
Cerebellar liponeurocytoma		■		
Paraganglioma of the spinal cord	■			
Papillary glioneuronal tumor[b]	■			
Rosette-forming glioneuronal tumor of the fourth ventricle[b]	■			
Dysplastic gangliocytoma of the cerebellum (lhermitte-Duclos disease)[b, e]	■			
Pineal tumors				
Pineocytoma[a]	■			
Pineal parenchymal tumor of intermediate differentiation[a]		■	■	
Pineoblastoma[a]				■
Papillary tumor of the pineal region[b]		■	■	
Embryonal tumors				
Medulloblastoma[a]				■
CNS primitive neuroectodermal tumor (PNET)[a]				■
Atypical teratoid/rhabdoid tumor[a]				■
Tumors of the cranial and paraspinal nerves				
Schwannoma	■			
Neurofibroma[a]	■			
Perineurioma	■	■	■	
Malignant peripheral nerve sheath tumor (MPNST)[b]		■	■	■

(continued)

Table 6.1 (continued)

Tumor	I	II	III	IV
Meningeal tumors				
Meningioma	■			
Atypical meningioma		■		
Anaplastic/malignant meningioma			■	
Hemangiopericytoma		■		
Anaplastic hemangiopericytoma			■	
Hemangioblastoma	■			
Tumors of sellar region				
Craniopharyngioma[a]	■			
Granular cell tumor of the neurohypophysis	■			
Pituicytoma	■			
Spindle cell oncocytoma of the adenohypophysis	■			
Miscellaneous tumors of the CNS				
Primary malignant lymphoma of the CNS[d]				
Histiocytic tumors[a, d]				
CNS germ cell tumors[a, d]				

[a]These tumors are common in children. Some of them, such as medulloblastoma and pilocytic astrocytoma, occur mostly in infants and children. Others, such as glioblastoma, are also common in adults
[b]These tumors can be seen in the second decade of life but are uncommon in younger patients. They also have significant incidence in adults
[c]The incidence of these tumors is very small. However, cases have been reported in the pediatric age group
[d]WHO has not established a grading system for these tumors
[e]As per WHO, it is not clear whether this is neoplastic or hamartomatous. If neoplastic, it corresponds histologically to WHO grade I
Modified from the WHO classification of tumors of the central nervous system [1]

(rare in children) are two entities that are mostly limited to the filum terminale.

The incidence of congenital brain tumors is reported to be 11 per million live births with medulloblastoma as the most frequent one in one study [7]. In another study, teratoma is the most frequent followed in descending order by glioblastoma, intracranial lipoma, choroid plexus papilloma, craniopharyngiomas, and others [8].

Overview of Diagnostic Imaging Approach

While computed tomography (CT) provides excellent demonstration of acute intracranial hemorrhage or calcifications, the superb soft tissue resolution and direct multiplannar imaging capability of magnetic resonance imaging (MRI) make it the modality of choice. Different excitation and relaxation sequences with or without gadolinium provide a comprehensive delineation of tumors in terms of extent and relationship with surrounding tissue. Fluid attenuation with image recovery (FLAIR) and T2-weighted sequences provide valuable estimation on the extent of edema and differentiation of solid from cystic components. Gradient echo sequences are sensitive to susceptibility artifact and can detect tiny amounts of blood products and, though slightly less effectively, calcification in the brain parenchyma and tumor bed. CT, however, remains a key modality in evaluation of the bony calvarium.

Proton magnetic resonance spectroscopy (MRS) detects important metabolites like choline, creatine, *N-acetyl-aspartate* (NAA), lactate, and lipid which form the major peaks and shed light on the tumor composition. Choline reflects membrane turn over; creatine reflects energy metabolism; NAA is a marker of neuronal cells; lactate is detected in necrotic tumor or ischemic/infarcted brain; and a lipid peak reflects myelin breakdown and necrosis. Tumors almost invariably are associated with decreased NAA/creatine ratio, increased choline/creatine ratio, and increased lactate. Increased choline/NAA ratio is often seen in cellular tumor due to the increase in cell membranes. Increased lactate peak is suggestive of necrosis and tumor aggressiveness [9, 10]. While MRS is useful in separating residual tumor from post radiation changes and from tumor progression with necrosis, it is sensitive but not specific and must be interpreted in conjunction with MRI. For example, pilocytic astrocytoma typically shows an elevated lactate peak [11] which is otherwise a hallmark of more aggressive tumors such as glioblastoma.

Diffusion based MRI techniques include diffusion-weighted imaging (DWI) which evaluates microscopic water diffusion within tissues and thus provides information on the degree of cellularity of a lesion. DWI distinguishes reliably between cystic and solid masses when both are hyperintense on T2-weighted sequences. The most notable example is the differentiation of an arachnoid cyst from epidermoid. DWI has also proven helpful in distinguishing brain tumors with necrosis from abscess. DWI along with the calculated apparent diffusion coefficient (ADC) maps have recently been utilized to assess tumor cellularity in an attempt to differentiate between different brain tumors [12, 13]. Diffusion tensor imaging (DTI) demonstrates the relation between tumor and adjacent white matter tracts that may be infiltrated or displaced by tumor. DTI is a useful tool for stereotactic surgical planning.

Perfusion-weighted imaging (PWI) can be performed either with CT or with MRI. CT perfusion though is deemed inappropriate for children because of the involved radiation exposure. Perfusion weighted imaging of a brain tumor reflects the degree of angiogenesis and abnormal neovascularity with leaky vessels. Different perfusion techniques are available and include dynamic susceptibility contrast enhanced (DSC), arterial spin label (ASL), and dynamic contrast enhanced (DCE) techniques. DSC echo planar imaging is utilized most commonly to acquire data from which maps of relative cerebral blood flow (rCBF), relative cerebral volume (rCBV), and mean transit time (MTT) are calculated. rCBV is the most useful parameter in the evaluation of brain tumors [14] because increased angiogenesis and neovascularity are features of tumors with higher aggressiveness. Currently, the most common application of perfusion

MRI is to define the area of the tumor with highest perfusion (CBV) and thus the highest histologic grade [15] for biopsy. PWI may also help in distinguishing between post-radiation injuries from tumor recurrence [16].

Intraoperative Consultation, Immunohistochemistry, and Molecular Pathology

Cytologic preparation and frozen section are the two arms in intraoperative diagnosis. The authors prefer to do a squash preparation by pressing a piece of representative tissue about 1 mm cube in volume between two microscopic glass slides and then smear. After the squash, the two slides should be separated momentarily to let air in before smearing in order to produce a smooth smear. Methanol is the preferred fixative, and it is extremely important to put the slides immediately into the methanol without delay in order to avoid air dry artifacts. The authors turn hematoxylin-stained slides blue with tap water rather than ammonium water in order to preserve nuclear details and avoid washout of necrotic debris and macrophages. Routine hematoxylin and eosin stain is sufficient in most circumstances. Toluidine blue is a good adjunct in demonstrating the metachromatic mucoid substances in glioma and Romanowsky-type stains such as DiffQuick are helpful when lymphoma is suspected.

Most diagnostic procedures with the exception of cytogenetics can be performed on formalin fixed paraffin embedded sections. Collection of fresh and snap frozen tissue, however, is often required by research protocols. Immunohistochemistry and special stains (Table 6.2) remain the most frequently

Table 6.2 Common immunohistochemical markers and special stains

Immunohistochemistry	Properties and applications
Ki-67 and PHH3	*Summary*: Ki67 is a non-histone protein that is present in all phases of cell cycle except Go and the early G0-G1 transitional phase. Phosphohistone-H3 (PHH3) is a histone associated with condensed chromatin during mitosis *Application*: Ki67 is useful for estimation of overall proliferation and PHH3 is useful for highlighting mitotic figures [240]. The immunoreactivities are in the nuclei
Olig2	*Summary*: Olig1 and Olig2 are transcription factors that regulate oligodendroglial development [241, 242] *Application*: Olig2 has been shown to be widely expressed in gliomas that include both astrocytic and oligodendroglial tumors [182, 243–246]. Similar to other transcription factors, the immunoreactivities are in the nuclei
Glial fibrillary acidic protein (GFAP)	*Summary*: this is a class III intermediate filament of 55 kDa. GFAP is expressed in mature astrocytes. It may co-express with other intermediate such as vimentin *Application*: in gliomas, GFAP are often positive in tumors with glial differentiation. Oligodendroglioma also expression GFAP so it is not a useful marker in separating these two entities. GFAP is usually extensively expressed in ependymal tumors
Synaptophysin	*Summary*: Synaptophysin is an acidic, *N*-glycosylated integral membrane glycoprotein of 38–42 kDa that is expressed in the CNS *Application*: it is expressed in tumors with neuroendocrine differentiation including medulloblastomas and central neurocytomas. However, weak to moderate expressions have been described in gliomas including pilocytic astrocytomas [134] and oligodendrogliomas
NeuN	*Summary*: NeuN, for neuronal nuclei, is a neuronal nuclear antigen is expressed predominantly in the nuclei and some minor cytoplasmic expression and is a marker for mature neurons *Application*: it is a good tool for demonstration of mature neuronal phenotypes and to detected scattered neurons that are entrapped within an infiltrating glioma [247, 248]
Epithelial membrane antigen (EMA)	*Summary*: this is a group of high molecular mass molecules with a high carbohydrate content. They are widely expressed by many epithelial cells *Application*: EMA is expressed by meningiioma, ependymoma, and AT/RT. The expression, however, is not very consistent and therefore the absence of immunoreactivity does not rule out a meningioma or ependymoma
BAF47	*Summary*: this antibody is specific for the gene product of *hSNF5/INI1* (*SMARCB1*) gene *Application*: immunoreactivity can be detected in normal cells. In tumors of the central nervous system, this gene is mutated or deleted in AT/RT and therefore not expressed in these tumors (i.e., negative staining indicates positive result indicating deletion or mutation) [92, 93]
Special Stain	*Properties and applications*
Periodic acid Schiff (PAS) stain with diastase digestion	*Application*: this is useful in demonstration of eosinophilic granular bodies particularly when they are scant
Luxol fast blue	*Application*: Luxol fast blue can be combined with other stain for detection of demyelination. Luxol fast blue-PAS is a good combination as this stain demonstrate macrophages as well
Masson's trichrome	*Application*: this is a useful stain in separating collagenous/desmoplastic component from the glial component
Reticulin	*Application*: reticulin deposition is typically found around individual cells in schwannoma, pleomorphic xanthoastrocytomas, and desmoplastic infantile ganglioglioma/astrocytoma

used special studies followed by fluorescence in situ hybridization (FISH) and other molecular techniques.

Electron microscopy still has a minor role in the diagnosis of ependymal tumors, meningeal tumors, and a few other tumors. The use of molecular pathology has gained impressive momentum, and the details will be discussed with their relevant entities.

Non-neoplastic Tumor-Like Mimickers

The first important step in oncologic pathology is to rule out non-neoplastic mimickers. Detailed clinical and imaging studies are invaluable in recognizing these mimickers.

The bulk of these mimickers are related to inflammation with or without histiocytic infiltration, infection, and infarction. While a demyelinating process is a common tumor mimicker in adults in western countries, this is uncommon in the pediatric age group, particularly among boys. Other common tumor mimickers include abscess and local extension of infection from middle ear infection, tuberculosis in the form of tuberculoma, toxoplasmosis, and other parasites such as neurocysticercosis and echinococcosis, granulomatous inflammation other than tuberculosis, and infarction. The other entities that would lead to surgical intervention include vascular lesions, heterotopia, and ectopia such as hypothalamic hamartoma. Although radiation necrosis is a common mimicker of genuine neoplasm in adults, it is rather uncommon as a surgical specimen in pediatric patients.

Conversely, it should be noted that substantial histiocytic infiltration and inflammation can pose diagnostic challenges particularly in cases of germ cell tumors and lymphoma, although primary CNS lymphoma is rare in the pediatric group.

Tumors with Features of the Developing Central Nervous System

This is a family of tumors with morphological and molecular phenotypes recapitulating embryonal stages of the developing CNS. These tumors are highly cellular, highly aggressive tumors that occur most frequently, if not exclusively, in infants and children. Some may occur as congenital tumors. Specific genetic aberrations are common and often provide in-depth understanding in the biology.

In the WHO classification, there are three major groups: medulloblastoma and its variants including desmoplastic/nodular medulloblastoma, medulloblastoma with extensive nodularity, anaplastic medulloblastoma, large cell neuroblastoma; CNS primitive neuroectodermal tumor including CNS neuroblastoma, CNS ganglioneuroblastoma, medulloepithelioma, ependymoblastoma; and atypical teratoid/rhabdoid tumor (AT/RT).

Medulloblastoma and Its Variants

Definition: Medulloblastoma is a malignant, invasive embryonal tumor of the cerebellum.

Clinical features: Medulloblastoma is the most common malignant brain tumor of childhood. It occurs predominantly in children with a peak age at presentation of 7 years; it is the most frequent malignant tumor of the CNS in children with an estimated annual incidence of 5 per million children under 15 years of age. About 10 % appear in adults and occur almost exclusively in young adults between 20 and 40 years of age. There is no definitive sex predilection. While dissemination through the cerebrospinal fluid (CSF) is a rule, metastasis outside the CNS is uncommon and most frequent involves bone followed by lymph nodes [17].

Phenotypically, medulloblastoma recapitulates the embryonal CNS but morphologic features and phenotypic markers indicative of further differentiation such as glial, neuronal, photoreceptor, myogenic, and melanotic differentiation can be seen in some cases. While most cases are sporadic, medulloblastoma is associated with a short list of hereditary cancer syndrome (Tables 6.3 and 6.4). Variants of medulloblastoma include the two with improved prognosis, namely desmoplastic medulloblastoma and medulloblastoma with extensive nodularity, and the two variant with worse prognosis, namely anaplastic medulloblastoma and large cell medulloblastoma. Most medulloblastomas arise in the midline. Hemispheric tumors tend to arise in older patients (adolescents and young adults) many of these tumors are desmoplastic medulloblastomas [18] However, molecular advancements have revolutionized our understanding of these tumor well beyond their histopathology (see below). Rare cases of maturation of medulloblastoma after therapy have been reported [19].

Imaging findings: Over 75 % of medulloblastomas [18] occur at the vermis at the level of posterior vellum medullaris and protrude into the fourth ventricle. Although usually solid, a cystic component is not uncommon. The solid part is isodense or slightly hyperdense to the gray matter on CT. On MRI (Fig. 6.2), medulloblastomas are almost isointense to gray matter on T1-weighted images and hypointense on T2-weighted images likely due to their high cellularity. The potential association of the tumor with a cystic component, hemorrhage or calcification may result in a heterogeneous appearance. Contrast enhancement is variable and some cases have no enhancement at all. Because medulloblastoma has high cellularity it would be expected to have a relatively low ADC value but this observation is not universal [20]. Leptomeningeal dissemination presents as diffuse meningeal enhancement with or without enhancing nodules in the subarachnoid space of the brain or spinal cord [21]. Medulloblastoma encountered in older patients may originate in the cerebellar hemisphere and have a more heterogeneous appearance especially on MRI [22].

Table 6.3 Hereditary cancer syndromes associated with medulloblastoma

Syndrome	locus/gene	Features
Turcot syndrome (Type 2) [249]	*APC*, 5q21-q22	*Autosomal dominant Medulloblastoma tumor risk*: 20 %
Faconi anemia subtype D1 [250, 251]	*BRCA2*, 13q12.3	*Medulloblastoma tumor risk*: high
Nevoid basal cell carcinoma syndrome/Gorlin syndrome [252–255]	*PTCH*, 9q22.3	*Autosomal dominant Medulloblastoma tumor risk*: 4 %
Li-Fraumeni syndrome [256]	*TP53*, 17p13.1	*Autosomal dominant Medulloblastoma tumor risk*: 10 %
Rubinstein-Taybi syndrome[a] [257]	*CREBBP*, 16P13.3	*Medulloblastoma tumor risk*: rare
Coffin-Siris syndrome[a] [258, 259]	*ARID1A, AR1D1B, SMARCA4, SMARCB1, SMARCE1*	*Medulloblastoma tumor risk*: rare
Megalencephaly and perisylvian polymicrogyria with postaxial polydactyly and hydrocephalus syndrome [260]	*Unbalanced der(5)t(5;20) translocation*[b]	*Medulloblastoma tumor risk*: uncertain
DICER1 syndrome or Pleuropulmonary blastoma family tumor and dysplasia syndrome (PPB-FTDS) [261]	*DICER1*, 14q32.13	*Medulloblastoma tumor risk*: about 1 %

[a]These syndromes are rare, only three cases and eight cases are reported for Rubinstein-Taybi syndrome and Coffin-Siris syndrome respectively
[b]Based on the study of two cases

Classic medulloblastoma: Clinical manifestations are cerebellar symptoms and those resulted from increased intracranial pressure and hydrocephalus secondary to obstruction. These include truncal ataxia, gait disturbance, lethargy, headache, and morning vomiting.

Surgical specimens of medulloblastoma are typically composed of small pieces of pale, semitranslucent tissue with the consistency of sticky soft glue with no suggestion of necrosis. Disseminated translucent coating of the cerebellum (the so-called sugar coating) can be well appreciated in autopsy cases.

Cytologically, medulloblastoma is composed of hyperchromatic, small blue cells with a thin rim of cytoplasm, and slightly crumbled nuclei (Fig. 6.3) without prominent nucleoli. As stated previously, smears of internal granular layer should not be mistaken for medulloblastoma cells (Fig. 6.1a). Medulloblastoma cells are larger than internal granular cells and a comparison of size between different cells on the smear would help to avoid this pitfall (Fig. 6.1b). In smears with prominent nuclei and significant increase in amount of cytoplasm, the differential diagnoses of large cell/anaplastic medulloblastoma and AT/RT must be entertained. Histologically (Fig. 6.3a–c), classic medulloblastoma is a small blue cell tumor composed of carrot-shaped cells with hyperchromatic nuclei. Occasionally, Homer Wright rosettes and palisading ribbons of tumor cell nuclei reminiscent of a picket fence can be seen. Both necrosis and endothelial proliferation are uncommon, but small areas of pseudopalisading necrosis can occur. One of the salient features of the developing CNS is high rate of cell proliferation and apoptosis. These features are often, but not always, well reflected in medulloblastomas as they typically contain mitoses and apoptotic bodies, albeit, atypical mitosis are rather uncommon.

Superficial spread along the cerebellar surface and Virchow-Robin spaces should not be mistaken as persistent external granular layer. The age of the patient can be a useful hint. Invasion of the leptomeninges may trigger fibrotic reactive changes. These areas, when being examined out of context, particularly as frozen section, may suggest a sarcoma or entities other than medulloblastomas.

Large cell medulloblastoma and anaplastic medulloblastoma: Although large cell medulloblastoma and anaplastic medulloblastoma are different subtype in the WHO classification, they have significant overlapping histopathologic features. About 2–4 % of medulloblastomas are large cell medulloblastomas. Large cell medulloblastomas have anaplastic features including large, round, vesicular nuclei with prominent nucleoli, and nuclear wrapping is a common feature (Fig. 6.3d–f). Necrosis and apoptotic cells, often in the form of small clusters, are common. The prominent nucleoli can be efficiently identified on cytologic preparations. Although AT/RT also has large and prominent nucleoli, rhabdoid cells can be usually found to confirm the diagnosis.

Imaging findings: All types of medulloblastomas share similar signal characteristics and variable enhancement on conventional MRI. Anaplastic medulloblastomas have been found to have increased ADC values and rim enhancement attributed to central necrosis [23].

Desmoplastic/nodular medulloblastoma: This variant has an increased tendency to occur at a hemispheric location and typically in adolescent and young adults. Histologically (Fig. 6.4), the salient features are "pale islands" (or nodules) of reticulin free tumor with reduced cellularity, decreased nuclear-to-cytoplasmic ratio, negligible mitotic rate, and high apoptotic rate surrounded by a densely packed, highly proliferative, hyperchromatic tumor reminiscent of classic medulloblastoma that contains a dense reticulin network. These islands represent regions of more mature phenotype.

Table 6.4 Hereditary tumor syndrome involving tumor of the nervous system[a]

Syndrome	Pathology	Genetics	Study
Tuberous sclerosis	*Nervous system*: cortical hamartomas (tubers), subependymal hamartoma and subependymal giant cell tumor *Extraneural*: adenoma sebaceum and other manifestations of skin, retinal astrocytoma, renal angiolipoma, cardiac rhabdomyoma and other systemic manifestations	*Inheritance*: autosomal dominant *Prevalence*: between 1 in 5,000 and 100,000 Gene: *TSC1* gene (tuberin) on chromosome 9q34 and *TSC2* gene on chromosome 16p13.3.	van Slegtenhorst et al. [262]
Neurofibromatosis type 1 (NF1)	*Nervous system*: Neurofibromas and malignant peripheral nerve sheath tumor of the peripheral nerve, gliomas of the brain *Extraneural*: multiple café-au-lait spots, rhabdomyosarcoma, phaeochromocytoma, carcinoid tumor, juvenile chronic myeloid leukemia, bone lesions and other manifestations	*Inheritance*: autosomal dominant *Prevalence*: 1 in 3,000–4,000 of the general population *Gene*: *NF1* gene (neurofibromin) on chromosome 17q2	Pollack and Mulvihill [263]; Von Deimling et al. [264]
Neurofibromatosis type 2 (NF2)	*Nervous system*: bilateral vestibular schwannomas, peripheral schwannomas, meningiomas and meningioangiomatosis, ependymomas, astrocytomas, glial hamartoma, and cerebral calcifications *Extraneural*: posterior lens opacity	*Inheritance*: autosomal dominant *Prevalence*: 1 in 50,000 of the general population *Gene*: *NF2* gene (merlin) on chromosome 22q12	Pollack and Mulvihill [263]
Von Hippel–Lindau disease	*Nervous system*: haemangioblastoma of the retina and CNS *Extraneural*: renal cysts and renal cell carcinoma, pancreatic cysts, islet cell tumors, phaeochromocytoma, and other manifestations	*Inheritance*: autosomal dominant *Prevalence*: 1 in 36,000 to 1 in 45,500 of the general population *Gene*: *VHL* gene is located on chromosome 3p25.3	Maddock et al. [265]
Naevoid basal cell carcinoma syndrome (Gorlin syndrome)	*Nervous system*: Medulloblastoma *Extraneural*: multiple basal cell carcinoma and keratocyst of the jaw. Abnormal ribs and other skeletal abnormalities, epidermal cysts, ovarian cysts and other features	*Inheritance*: autosomal dominant *Incidence*: 1 in 57,000 of the general population *Gene*: human homologue of the *Drosophilia* segment polarity gene patched (*PTCH*) on chromosome 9q22.3	Hahn et al. (1996) [255]; Vorechovsky et al. [266]
Cowden disease	*Nervous system*: dysplastic gangliocytoma of the cerebellum (Lhermitte–Duclos disease). Other pathological changes include megalencephaly and heterotopic gray matter. Meningiomas and medulloblastomas have also been described *Extraneural*: verrucous skin changes, papules and fibromas of oral mucosa, multiple facial trichilemmomas, hamartomas polyps of the colon, thyroid tumor and breast cancer	*Inheritance*: Autosomal dominant *Gene*: *PTEN/MMAC1* gene on chromosome 10q23.	Sutphen et al. [267]; Robinson and Cohen [268]
Turcot syndrome (type 1)	*Nervous system*: usually glioblastoma *Extraneural*: Café-au-lait spots. Small number of large colorectal polyps and high incidence of colorectal carcinoma. Some patients are associated with hereditary non-polyposis colorectal carcinoma syndrome (HNPCC)	*Inheritance*: autosomal dominant *Gene*: several genes involved in mismatch repair including *hMLH1* at chromosome 3p21, *hMLH2* at 2p16, *hMSH3* at 5q11-q13, *hMSH6/GTBP* at 2p16, *hPMS1* at 2q32 and *hPMS2* at 7p22	Cavenee et al. [269]
Turcot syndrome (type 2)	*Nervous system*: usually medulloblastoma *Extraneural*: associated with familial adenomatous polyposis syndrome (FAP). Patient has innumerable adenomatous colorectal polyposis and high incidence of colorectal carcinoma	*Inheritance*: autosomal dominant *Gene*: *APC* gene on chromosome 5q21 that is associated with familial adenomatous polyposis syndrome (FAP)	Hamilton et al. [247], [249]; Cavenee et al. [269]
Cobbs syndrome (Cutaneous angiomatosis multiple cavernous angiomas)	*Nervous system*: multiple intracranial cavernous haemangiomas *Extraneural*: some patients also have haemangiomas in the skin and other organs	*Inheritance*: autosomal dominant transmission has been shown in many cases Gene: the gene has not been identified but appears to be present on chromosome 7q11, 7p, and 3q	Laberge-le Couteulx et al. [270]
Sturge-Weber syndrome (Encephalofacial angiomatosis or Encephalotrigerminal angiomatosis)	*Nervous system*: meningeal haemangioma and meningeal hypervascularity, calcification in the cortical layer under the hypervascular meninges *Extraneural*: choroid haemangioma, angiomatosis of the skin and mucosa of face and neck	*Inheritance and gene*: unknown	

(continued)

Table 6.4 (continued)

Syndrome	Pathology	Genetics	Study
Rhabdoid predisposition syndrome	*Nervous system*: a typical rhabdoid tumor, choroids plexus carcinoma *Extraneural*: renal and extra-renal malignant rhabdoid tumor	*Inheritance*: the pattern of inheritance has not been confirmed as the number of reported pedigrees are limited *Gene*: mutation or deletion of the *hSN5/INI1* gene on chromosome 22q11.2	Sevenet et al. [267]; Taylor et al. [271]
Retinoblastoma (RB) gene deletion syndrome	*Nervous system*: retinoblastoma in the retina with or without PNET in the pineal gland (pineoblastoma) *Extraneural*: increased incidence of second malignancy, multiple congenital abnormalities and mental retardation	*Inheritance*: autosomal dominant *Gene*: *RB1* gene on chromosome 13q14.2	Sopta et al. [272]; Pratt et al. [273]
Li–Fraumeni syndrome	*Nervous system*: astrocytic tumor, oligodendroglioma, medulloblastoma, supratentorial PNET, and choroid plexus tumor *Extraneural*: tumor in various organs including the breast, lung, stomach, colon, pancreas, skin and others	*Inheritance*: autosomal dominant *Gene*: *TP53* on chromosome 17p13 and checkpoint kinase 2 (*hCKh2*) gene on chromosome 22q12	Tachibana et al. [274]

[a]Please refer to Table 6.3 for hereditary tumor syndromes associated with medulloblastoma

Desmoplastic/nodular medulloblastoma carries a better prognosis. This diagnosis should be made when the tumor is predominantly or exclusively composed of this nodular pattern. Medulloblastoma with only focal nodular pattern should not be classified as desmoplastic/nodular medulloblastoma.

Imaging findings: Desmoplastic medulloblastoma often presents as a cerebellar hemisphere mass that is isointense to gray matter on T2-weighted images and demonstrates moderate enhancement. The mass may extend to the overlying meninges resulting in moderate meningeal enhancement [22, 24].

Medulloblastoma with extensive nodularity: These tumors were previously designated as "cerebellar neuroblastoma." They typically occur in infants and are associated with good prognosis. Histologically, it is characterized by an expanded lobular architecture with large separated by elongated reticulin-free zones of variable thickness. These areas contain streaming small cells resembling the cells of a central neurocytoma. Maturation into tumors dominated by ganglion cells has been reported [19].

Imaging findings: The tumor has been described as an extensively nodular, grape-like mass [21] These tumors most often are located off midline, reveal isointense signal on T2W sequences and enhance on post-contrast imaging [25].

Melanotic and myogenic differentiation: Medulloblastomas mimic embryonal tissues in being able to differentiate along different phenotypes. Aside from glial and neuronal (including photoreceptors) features, occasional medulloblastomas have myogenic differentiation (previously termed medullomyoblastoma) and others have melanotic differentiation (previously melanocytic medulloblastoma). The former is composed of primitive neuroectodermal cells with rhabdomyoblastic cells, and the latter is characterized by primitive neuroectodermal cells with intracytoplasmic melanin. A case of medulloblastoma with melanotic and myogenic features has been reported [26]. These cases are rare and no specific imaging findings have been published.

Molecular pathology of medulloblastoma: A consortium of genetic abnormalities is associated with medulloblastoma. A multiparameter approach based on histology subtype, metastatic status, and genetic profile has recognized that medulloblastoma is composed of four distinct molecular groups with different risks: *WNT*/Wingless group, Sonic Hedgehog group, Group 3, and Group 4 [27–31], In general, the prognosis of group 3 and 4 is less favorable. A fifth group that can be designated as "not otherwise specified" may be included for rare tumors that cannot be assigned to a group in the 4-tier classification. Among the *WNT*/Wingless and Sonic Hedgehog groups, tumors with different features can be further separated into different risk groups [27, 32].

Immunohistochemistry and electron microscopy: Medulloblastoma and its variants are at least focally, if not diffusely, positive for synaptophysin. It is also positive for class III β-tubulin or microtubule-associated protein 2 [33, 34]. Positive immunoreactivity is often intense in Homer Wright rosettes and pale islands of desmoplastic/nodular medulloblastomas. Occasional immunoreactivity for neurofilament proteins, markers specific for photoreceptors such as S-antigen, and interphotoreceptor retinoid-binding protein can be demonstrated [33–35]. GFAP-positive cells may represent reactive cells, and possible focal tumor cell staining may be difficult to ascertain. In one study, about 10 % of the GFAP positive cells were found to be genuinely neoplastic [36]. Medulloblastomas has high Ki67 labeling index and apoptotic index among tumors of the CNS [37, 38]. The Ki67 labeling index can easily exceed 30 % but areas with neuronal development such as the pale islands have much lower labeling. Mutation of *CTNNB1*, an important gene in the *WNT* pathway, is associated with nuclear accumulation of β-catenin [36] that can be demonstrated by immunohistochemistry and, as per one study, is present in about 10 % of medulloblastomas [39].

Fig. 6.2 MR-medulloblastoma. (**a**) Axial FSE T2W MR image shows a mass expanding and completely obliterating the fourth ventricle. The intermediate hyperintense signal reflects the high cellularity of medulloblastoma. Peritumoral edema is also evident. (**b**) Axial post-contrast, T1W MR image demonstrates heterogenous, predominantly minimal tumor enhancement. (**c**, **d**) Sagittal FSE T2W MR images demonstrate drop metastases (*arrows*) in the form of nodules (3-year-old male)

Ultrastructually, tumor cells may contain neurosecretory granules (dense core granules), synapses, and Intermediate filaments but no specific diagnostic structures [40].

Differential diagnoses: Ependymoma, AT/RT, medulloepithelioma, embryonal tumor with abundant neuropil and true rosettes (ETANTR), and metastatic small blue cell tumors can histologically mimic medulloblastomas particularly on small specimens for intraoperative consultation. Cytologically, ependymoma nuclei are more monotonous, round, and do not have the crumbled appearance. Histologically, perivascular rosettes and ependymal canals, when present, are good diagnostic clue. Immunohistochemistry for GFAP is often diffusely positive in ependymoma but only patchy or in the form of reactive astrocytes in medulloblastoma. Ependymoma can be positive for epithelial membrane antigen (EMA), but medulloblastoma is typically negative. A substantial number of AT/RT has a small cell component resembling medulloblastoma but careful search particularly on the cytologic preparation at intraoperative consultation almost always identify rhabdoid cells. Immunohistochemistry for BAF47 is negative in AT/RT but positive in most other tumors including medulloblastoma.

Prognostic indicators: The prognosis of medulloblastoma and its variants in children is dependent on multiple factors including

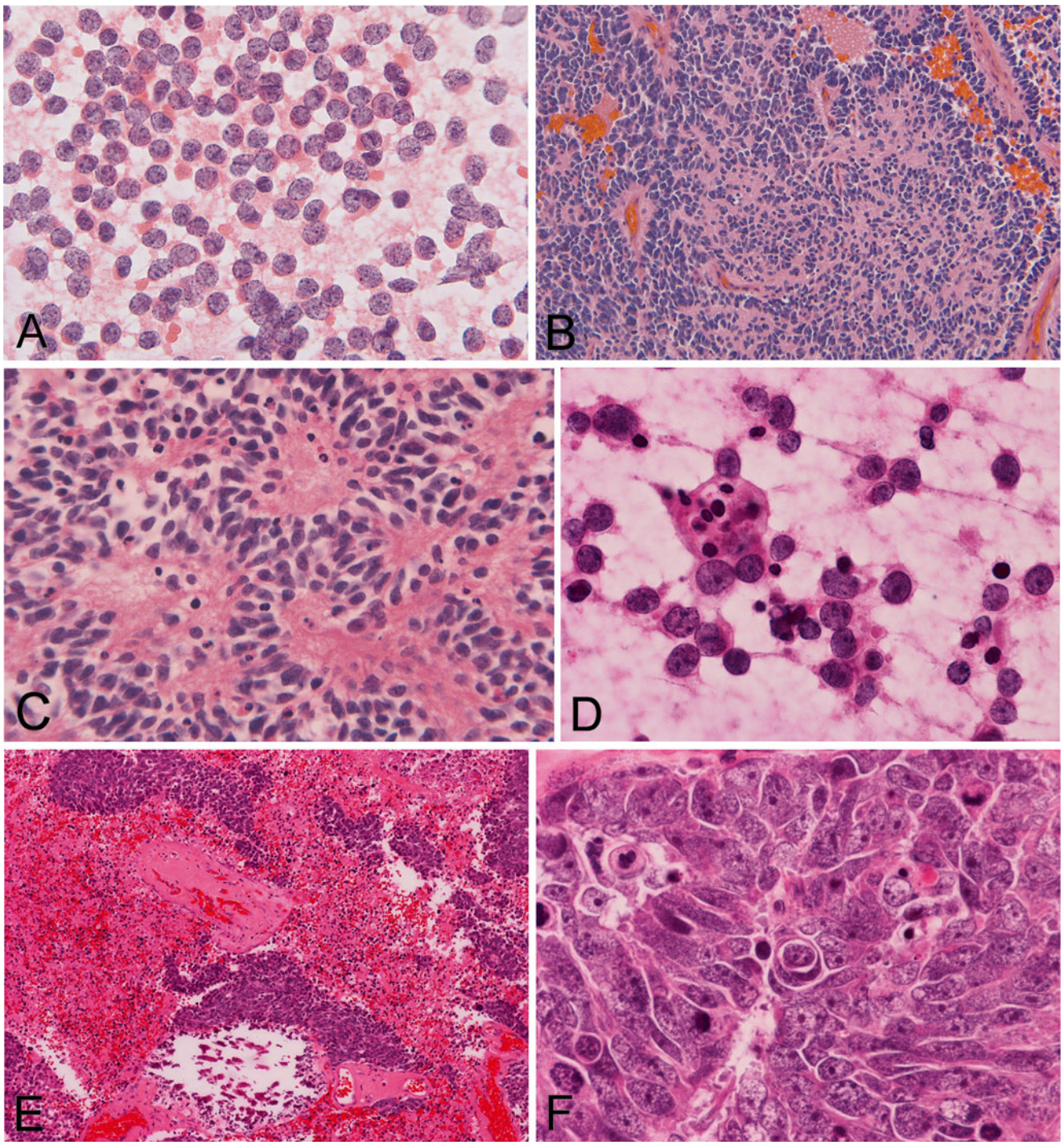

Fig. 6.3 Medulloblastoma and large cell medulloblastoma: (**a**–**c**) are taken from a medulloblastoma. (**a**) On cytologic preparations, the nuclei are hyperchromatic and slightly crumbled. (**b**) Histologically, areas with small amount of neuropils are usually present. (**c**) Homer Wright rosette as illustrated here is not always present. (**d**–**f**) are taken from a large cell medulloblastoma. (**d**) The nucleoli are distinct and apoptotic bodies are present. (**e**) Extensive necrosis is a common feature. (**f**) The nuclei are large and pleomorphic. Nucleoli are distinct and nuclear warping is a typical feature. Mitotic figures and apoptotic bodies are common

age, completeness of surgical resection, and metastatic status at presentation. The overall 5-year survival rate is about 60–80 % [28, 41]. Histologic correlation with clinical behavior is not always accurate. The recently proposed stratification into four groups as discussed above seems to be a good way for prognostic purposes. High expression of *hTERT* [42], high expression of *ERBB-2* [43], high *MYC* mRNA expression, and low *TrkC* mRNA expression [44, 45] are associated with poor clinical outcome. In general, better prognosis is noted in tumors associated with the *WNT* pathway.

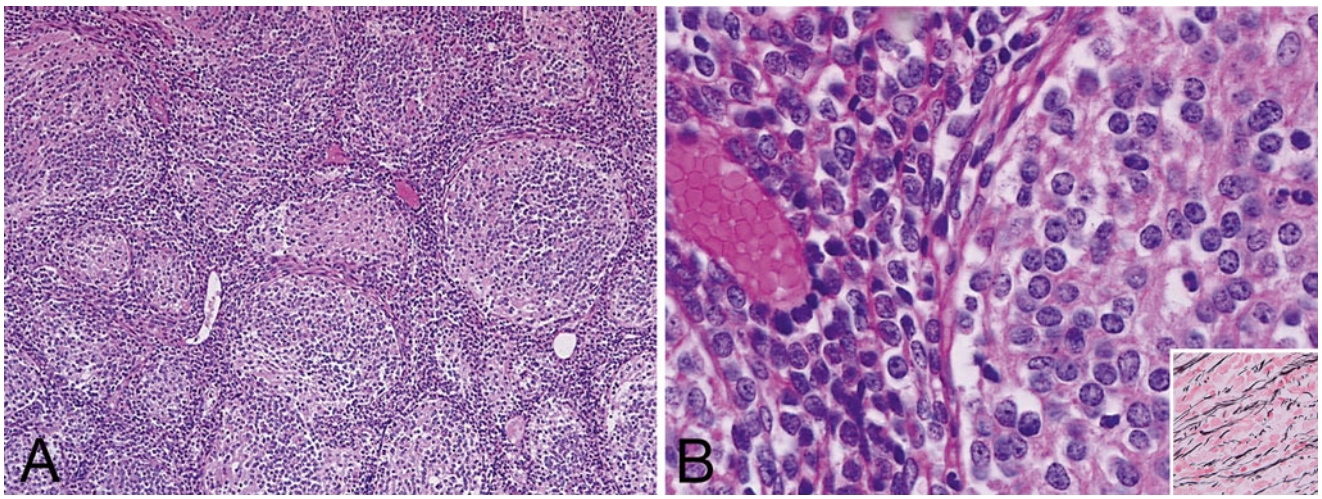

Fig. 6.4 Desmoplastic medulloblastoma: (**a**) The salient features are "pale islands" surrounded by densely packed hyperchromatic cells. (**b**) The pale nodules have lower nuclear cytoplasmic ratio than the surrounding densely packed areas. Reticulin substances could be demonstrated in the dense packed areas (Inset)

Primitive Neuroectodermal Tumor (PNET)

This is a collection of tumors characterized by undifferentiated or poorly differentiated neuroepithelial cells resembling the embryonal neuroectoderm (neuroepithelium) that occurs outside the posterior fossa. Histologically, some of them are indistinguishable from medulloblastoma. Morphologic differentiation along neuronal, glial, and ependymal lineage can occur.

Medulloepithelioma

Definition: Medulloepithelioma of the CNS [46, 47] is a rare and highly aggressive tumor that phenotypically recapitulates a very early stage, the neurotube stage, of the developing nervous system. Please refer to the discussion of ETANTR for the genetic relationship between medulloepithelioma, ependymoblastoma, and ETANTR.

Clinical features: Medulloepithelioma occurs almost exclusively in infancy and early childhood with half of them occurring before 2 years of age [47]. Some may occur as congenital tumors. Medulloepithelioma has a sinister reputation of dissemination through the neuroaxis and therefore initial treatment always includes irradiation of the entire neural axis. Dissemination through the cerebral spinal fluid (CSF) is a grave sign with median survival of 10 months [46, 47]. Over half of these cases arise in the lateral ventricles, many also arise in the posterior fossa and rare examples can be found in uncommon locations such as the cauda equine [47] and ciliary body [48]. Some cases of medulloepitheliomas arising in ciliary bodies have been associated with pleuropulmonary blastoma [48]. Although the CNS is a favored site, the so-called peripheral medulloepitheliomas have been described outside the CNS [49, 50]. In addition, medulloepithelioma components can also be found in immature teratomas arising in the ovaries and testicles [51, 52]. The prognosis of teratomas with medulloepithelioma component is far more favorable than medulloblastomas occurring in the central nervous system [51, 52].

Imaging findings: The tumor is usually large at the time of presentation. The features on CT and MRI are variable. On MRI these tumors are usually well circumscribed, hypointense or isointense on T1, hyperintense on T2, and non-enhancing at presentation [47, 53]. Enhancement occurs with tumor progression. The tumor may include cysts and calcifications which contribute to the variability of the mass on imaging.

Histopathology: The histopathologic picture is highly distinctive. The tumor is composed of tubular or papillary structures formed by mitotically active, hyperchromatic, pleomorphic, epithelial cells supported by basement membrane material (Fig. 6.5). The tumor cells have very high nuclear to cytoplasmic ratio. Other areas are composed of sheets of primitive cells with no specific pattern formation. Some tumors may differentiate along neuronal, astrocytic, ependymal, oligodendroglial and, on rare occasions, mesenchymal lineage [54, 55]. Rare cases can be pigmented (contain melanin pigmentation) [56].

Extensive primitive lateral cell junctions (zonulae adherents) and basal lamina, both reflecting the epithelial phenotype of the neuroepithelium, are demonstrated at the ultrastructural level [57].

Molecular pathology and genetics: Due to the rarity of these cases, the understanding on genetic changes is limited. Amplification of *hTERT* gene has been identified in this rare tumor [42]. Amplifications at 19q13.42 involving the *C19MC* cluster, a feature shared by ependymoblastoma and ETANTR has been demonstrated [58] and serve as a useful diagnostic tool.

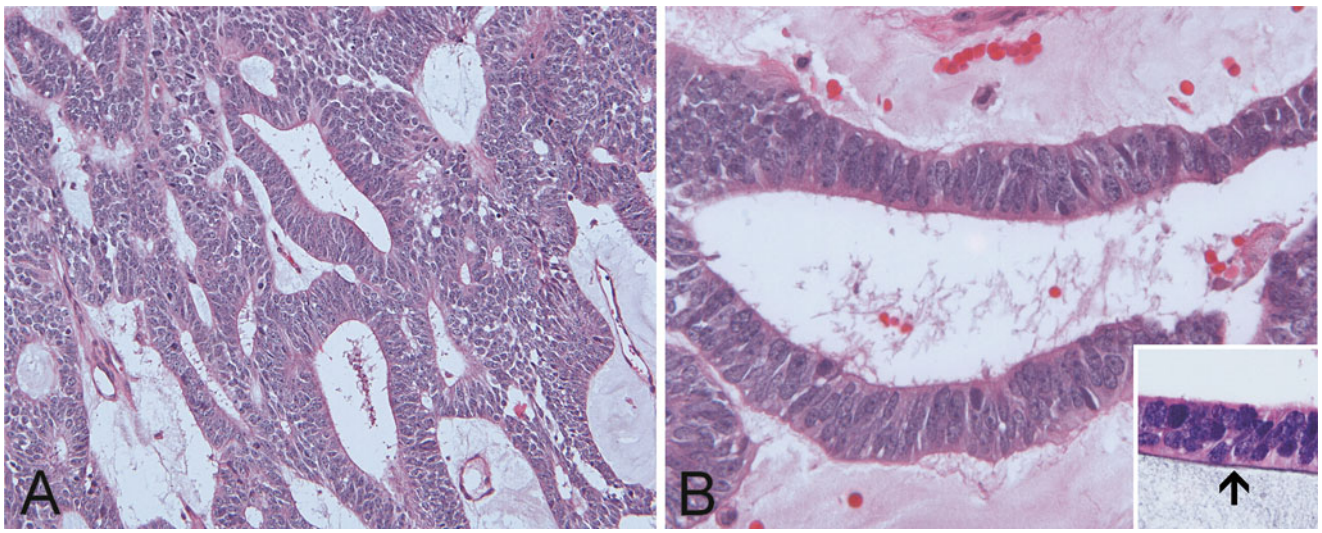

Fig. 6.5 Medulloepithelioma: (**a**) In contrast to medulloblastoma, the tumor cells have an epithelial growth pattern and cytology. (**b**) Stratified epithelial cells with a basement membrane on one side can be demonstrated by Jones stain (inset)

Electron microscopy and immunohistochemistry: On immunohistochemistry, medulloepithelioma is positive for nestin, vimentin, two intermediate filaments that are expressed in the primitive neuroectoderm. These tumors are also positive for synaptophysin, neurofilament, glial fibrillary acidic protein, and microtubule associated proteins, markers that are found in neural tissue [59, 60]. Medulloepithelioepitheliomas also express cytokeratin and EMA, which reflects the epithelial phenotype of the primitive neuroectoderm [59]. Immunohistochemistry shows diffuse immunoreactivity for LIN28A in these tumors [61].

Differential diagnosis: The histologic pattern of medulloepithelioma is very distinct and allows separation from medulloblastoma and primitive neuroectodermal tumors easily even though these tumors share a very similar, if not identical, immunohistochemical profile.

Supratentorial Primitive Neuroectodermal Tumor (PNET)

Definition: This is a collection of poorly differentiated or undifferentiated neuroepithelial tumors with morphologic resemblance to medulloblastoma. These tumors have the capacity to differentiate. Cerebral neuroblastomas and ganglioneuroblastomas refer to these tumors with only neuronal or ganglionic differentiation, respectively.

Clinical features: The majority of these tumors occur in children, adolescent, and young adults with a mean age of 5.5 years. The cerebrum is the most common site but they may occur in the suprasellar region and spinal cord. Clinical manifestation ranges from seizure to visual and endocrine problems in cases with suprasellar involvement.

Imaging findings: The tumor usually presents as a sizable, heterogeneous mass with sharp, irregular margins. The heterogeneity is the result of the presence of cysts due to tumor necrosis, or hemorrhage. The solid component appears iso-to hypointense compared to gray matter on T1- and T2-weighted MR images and demonstrates variable enhancement. The surrounding edema is insignificant for the size of the mass. Leptomeningeal spread and dissemination through cerebral spinal fluid manifesting as leptomeningeal enhancement is common [62].

Macroscopic pathology and histopathology: The tumors are soft and well demarcated. Hemorrhages and cysts may be present. Histologically, the classic picture is that of a small blue cell tumor with cytologic features reminiscent of a medulloblastoma, but the cells may be larger than classic medulloblastomas. Tumor cells may arrange in parallel streams, palisade, and in single files. There is a fibrillary cytoplasmic background and Homer-Wright rosettes are often found. Morphologic evidence of neuronal differentiation may be found in neuroblastomas and dominate the histologic picture in ganglioneuroblastoma. Rich vascular network may be present. Calcifications are common. This combination makes heterogeneity of morphology in supratentorial PNETs a rule.

Immunohistochemistry and electron microscopy: The immunohistochemical profile is similar to that of medulloblastoma and these tumor express synaptophysin, class III ß-tubulin, neurofilament proteins, S100, and Leu-7 (CD56). GFAP may occasionally be detected in the small tumor cells [63, 64]. No specific findings of diagnostic value are demonstrated by electron microscopy.

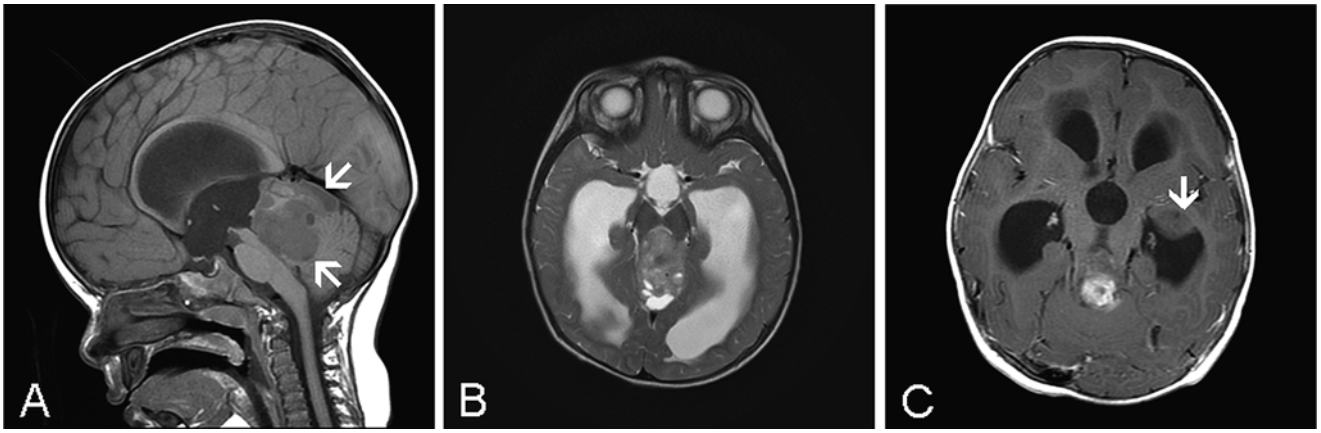

Fig. 6.6 MR-AT/RT. (**a**) Sagittal T1W MR image demonstrates a midline, heterogeneous mass invading the vermis (*arrows*). The mass is compressing the aqueduct and causes hydrocephalus. (**b**) Axial FSE-T2W MR image demonstrates mostly intermediate hyperintensity. (**c**) Axial T1W post-contrast MR image shows that only part of the tumor enhances. A non-enhancing lesion in the lateral ventricle (*arrow*) is likely the result of intraventricular seeding (13 month-old male)

Molecular pathology and cytogenetics: In contrast to medulloblastoma, isochromosome 17 has only been rarely reported. The genetic profile of supratentorial PNET and medulloblastoma is also different [65, 66]. The genetic mechanisms on tumorigenesis between medulloblastoma and supratentorial PNET is likely to be different.

Differential diagnosis: The supratentorial location and heterogeneous histopathologic picture open this entity to a long list of differential diagnoses including ependymoma, central neurocytoma, and oligodendroglioma.

Ependymoblastoma

Definition: This is an extremely rare, malignant, embryonal tumor featured by distinctive multilayered rosettes. Please refer to the discussion of ETANTR for its relationship with ETANTR and medulloepithelioma.

Overview: These tumors are seen predominantly in neonates and young children and often occur as large, supratentorial tumors that are close to the ventricles. Neither clinical manifestations nor radiographic features are specific. The incidence is uncertain due to its rarity and congenital examples have been described [67].

Macroscopic pathology and histopathology: These tumors are typically well circumscribed but leptomeningeal invasion and widespread CSF dissemination are common. Histologically, the tumor is featured by highly cellular, densely packed, primitive appearing small blue cells harboring occasional ependymal rosettes and tubules. However, it lacks the high grade pleomorphism that would otherwise qualify these tumors as anaplastic ependymomas. Endothelial proliferations are lacking. Ultrastructural features of ependymal differentiation including apical surfaces bearing cilia and microvilli projecting into a lumen, interconnected adjacent cells by zonulae adherents, and basal lamina-lined labyrinth have been demonstrated [68, 69]. Immunohistochemically, these tumors are positive for S100, vimentin, and GFAP [69–71]. Amplifications at 19q13.42 involving the *C19MC* cluster [58] and immunoreactivity for LIN28A [61], two features shared by ependymoblastoma and ETANTR, has been demonstrated and serve as a useful diagnostic tool.

Imaging findings: At present there no specific features described that would reliably distinguish ependymoblastoma from PNET.

Atypical Teratoid/Rhabdoid Tumor (AT/RT)

Definition: This is a highly malignant tumor that occurs predominantly in infants and young children, featured by neoplastic rhabdoid cells without and with non-rhabdoid elements, most often primitive neuroectodermal neoplastic component, and typically associated with inactivation (deletion or mutation) of *hSNF5/SMARCB1/INI1*.

Clinical features: Most tumors occur in children under 6 years of age with a male predominance. AT/RTs comprise about 1–2 % of pediatric brain tumors [72] but are estimated to represent about 10 % of tumors in infants [73]. Rare adult cases have been reported [74–78]. AT/RTs are slightly more common in supratentorial than infratentorial locations. Depending on the location of the tumor and the age of the patient, the clinical presentations can be variable and include nonspecific symptoms (e.g. lethargy, vomiting, headache, failure to thrive) and/or to focal manifestations (e.g. sixth and seventh cranial nerve palsy).

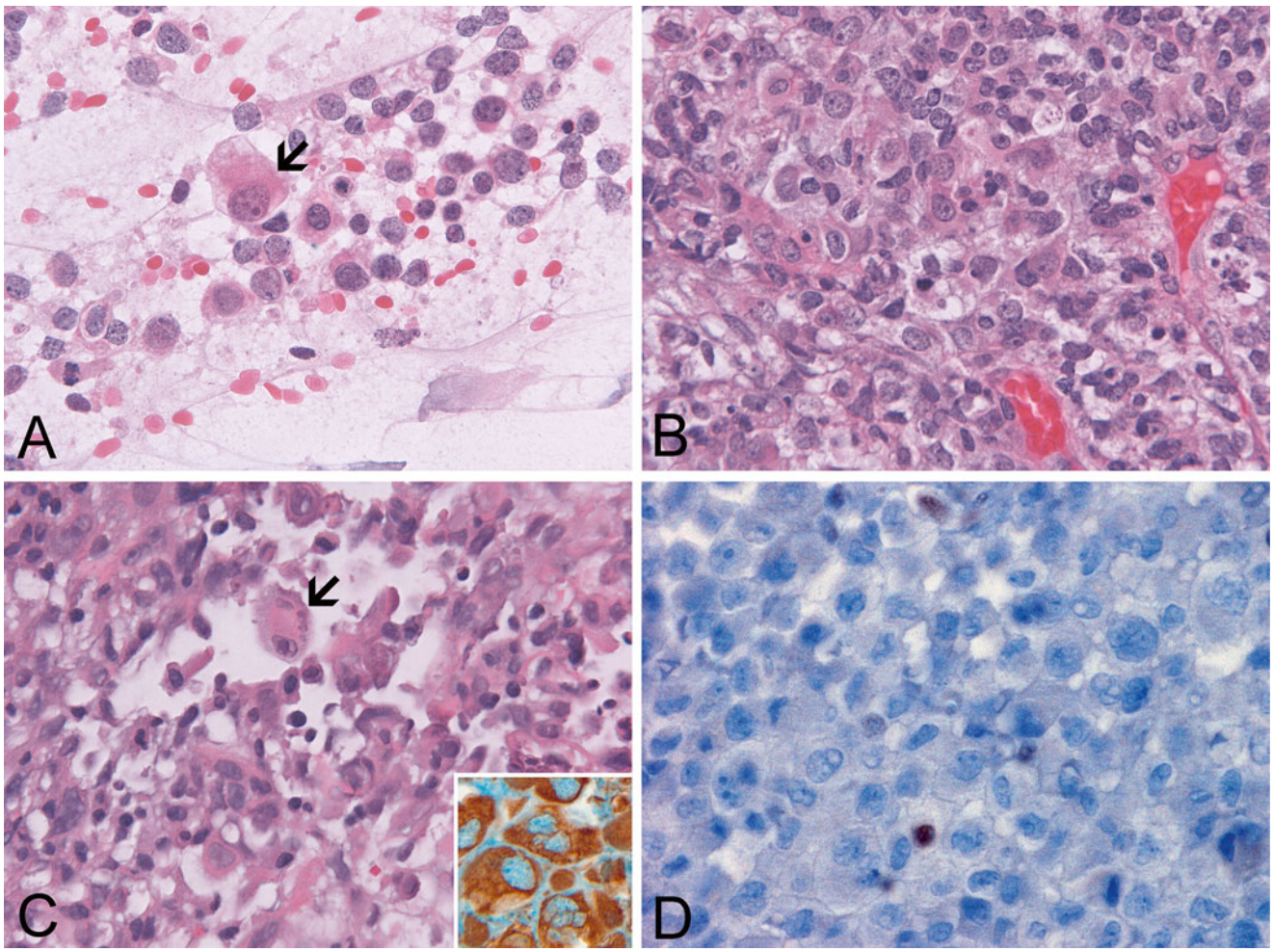

Fig. 6.7 Atypical teratoid rhabdoid tumor: (**a**) A cytologic preparation with a large rhabdoid cells containing a cytoplasmic inclusion-like body (*arrow*). A range of rhabdoid changes can be seen in the rest of the cells. (**b**) and (**c**) are taken from the same tumor but different areas. Note that the rhaboid changes (arrow) are more common in (**c**). The rhabdoid cells have strong cytoplasmic immunoreactivity for vimentin (inset in (**c**)). (**d**) AT/RT is non-immunoreactive for BAF47 (INI1). Occasional positive cells, most likely entrapped non-neoplastic cells, can be found, which serves as an internal positive control

Imaging findings: AT/RT usually present as a large, lobulated, heterogeneous mass sharing many similarities to supratentorial PNET although the solid component may be iso- to slightly hyperintense on T2-weighted sequences (Fig. 6.6). Cystic necrosis is common. Enhancement of the solid component is usually avid albeit often inhomogeneous [79]. The tumor can arise in the intratentorial as well as supratentorial compartment. When infratentorial, the tumor may involve the cerebellopontine angle [80]. Cerebrospinal dissemination is common and can be detected with post-contrast MRI manifested as enhancement along the leptomeninges and/or drop metastasis.

Macroscopic pathology and histopathology: Typically, AT/RTs are large, well-demarcated, necrotic and hemorrhagic. Fragments that are submitted as surgical specimens are soft and have a consistency similar to that of medulloblastoma.

Microscopically, AT/RTs are heterogeneous and the amount of rhabdoid cells can range from abundant to scant [81]. Tumors with *hSNF5/SMARCB1/INI1* inactivation but no rhabdoid cells have been described [82, 83]. The salient feature is large neoplastic cells with abundant cytoplasm that displaces the nuclei to an eccentric location. Commonly, a round inclusion-like amphopilic to slightly eosinophilic round body will occupy the bulk of the cytoplasm. Artifactual cytoplasmic vacuoles are common. Nuclei are large and have vesicular chromatin with prominent eosinophilic nucleoli. Multinucleated tumor cells are not uncommon. During intraoperative consultation, cytologic evaluation effectively identifies rhabdoid cells (Fig. 6.7a).

The classic rhabdoid changes can range from subtle to obvious and vary in different tumors and different parts of the same tumor. Histologically, rhabdoid cells do not exhibit a particular growth pattern; instead, the tumor cells are often jumbled up and give a picture reminiscent of a jigsaw puzzle (Fig. 6.7b–c).

The presence of non-rhabdoid elements, most frequently small cell component reminiscent of medulloblastomas and supratentorial PNETs are often present. These components may dominate the histologic picture, which makes identification of rhabdoid cells difficult. Mesenchymal differentiation is less common and epithelial differentiation is rare. When the epithelial component represents the dominant component, the diagnosis of choroid plexus carcinoma must be entertained.

Molecular pathology: Deletion of chromosome 22q was the first genetic aberrations identified [84, 85] and *hSNF5/SMARCB1/INI1*, a chromatin remodeling complex which functions as a tumor suppressor gene, was later identified as the critical gene [86]. While homozygous or heterozygous deletion is demonstrated in most AT/RTs, point mutations without structural abnormality of chromosome 22 can be demonstrated in a number of tumors. Fluorescent in situ hybridization (FISH) is an efficient way to demonstrate these deletions. Germline mutations have been well documented [87] and sequencing may be required to detect them. Patients with familial AT/RTs are more likely to have extensive disease and more likely to die of their disease than patients with sporadic AT/RTs [88]. Other than rare exceptions [89], deletion and mutation of *hSNF5/SMARCB1/INI1* are typically absent in adult composite rhabdoid tumors [90]. It should be noted that *hSNF5/SMARCB1/INI1*-deficient tumors do not always have rhabdoid histology [83], while primitive neuroectodermal tumor with *hSNF5/SMARCB1/INI1* with no rhabdoid features also behave aggressively [82].

Immunohistochemistry and electron microscopy: The protein product of *hSNF5/SMARCB1/INI1* is demonstrated by immunohistochemistry for BAF47, a 47 kDa BRG1-associated factor (BAF) as nuclear immunoreactivity [91]. This protein is present in practically all normal tissue but tumor cells with deleted or mutated *hSNF5/SMARCB1/INI1* are negative (Fig. 6.7d). Initially, this lack of immunoreactivity was demonstrated in AT/RT and other primary rhabdoid tumors of infancy and childhood occurring outside the CNS [92–95] but not composite rhabdoid tumors in adult [90]. Subsequently, a variety of *INI1*-deficient tumors other than primary childhood rhabdoid tumors characterized by negative BAF47 immunoreactivity have been demonstrated [96]. These tumors include medullary carcinoma of the kidney, epithelioid sarcoma, epithelioid malignant peripheral nerve sheath tumor, myoepithelial carcinoma, extraskeletal myxoid chondrosarcoma [96], and pediatric undifferentiated soft tissue sarcomas that lacks rhabdoid features [97] and meningiomas [98, 99]. Rare cases of AT/RT with intact *hSNF5/SMARCB1/INI1* and mRNA but no protein expression [100] and retained protein expression with nonsense mutation of *hSNF5/SMARCB1/INI1* have also been described. Under appropriate clinical and histopathologic circumference, a lack of immunoreactivity for BAF47 still offers a firm confirmation of AT/RT and other primary rhabdoid tumor of childhood and remains an important tool in the correct diagnosis of AT/RT in the CNS [81].

On immunohistochemistry, AT/RTs are characteristically immunoreactive for EMA and vimentin. The cytoplasmic inclusion-like bodies are composed of whorls of bundles of intermediate filaments [85, 101]. Strong immunoreactivity for vimentin is seen in practically every rhabdoid cells (Fig. 6.7c inset). Many AT/RTs are also immunoreactive for smooth muscle actin, GFAP, and cytokeratin. Neurofilament, synaptophysin, and chromogranin are less likely to be positive and most cases are negative for desmin [85, 102]. Markers for germ cell tumors (placental alkaline phosphatase, α-fetoprotein, and β-human chorionic gonadotropin) are negative [85, 102]. Patchy staining for S100 and rare positive cells for HMB-45 have been described [102]. Ependymal differentiation has been recently documented in one case [103].

Differential diagnosis: The common mimickers of AT/RT include large cell/anaplastic medulloblastoma, anaplastic ependymomas, and choroid plexus carcinoma. Identification of rhabdoid cells is key to the diagnosis. In histologically challenging cases, immunohistochemistry for BAF47 or molecular studies on *hSNF5/SMARCB1/INI1* should be performed [81]. Primary rhabdomyosarcoma is a rare entity in the CNS, and such tumors are positive for desmin and other myogenic markers such as myogenin and have intact *hSNF5/SMARCB1/INI1* (positive nuclear immunoreactivity for BAF47 on immunohistochemistry).

Miscellaneous Tumors with Morphologic Features of the Primitive Neuroectoderm

Tumor with primitive neuroectoderm is a heterogeneous group of tumor. The following entities are not, or not yet, included in the current WHO classification.

Embryonal Tumor with Abundant Neuropil and True Rosettes (ETANTR) and Embryonal Tumor with Multilayered Rosettes (ETMR)

Embryonal tumor with abundant neuropil and true rosettes (ETANTR), also known as neuroblastic brain tumor containing abundant neuropil and true rosettes and embryonal tumor with abundant neuropils and ependymoblastic rosettes, is a newly recognized entity [104]. This rare tumor occurs mostly in infants and childrens and is more common in girls than boys. Most often, it is a supratentorial hemispheric mass that is well demarcated on imaging studies. The prognosis is poor. This tumor is characterized by a distinct microscopic picture of true ependymoblastic rosette formation in a background of neuropil. The rosettes are formed by circumferentially arranged pseudo-stratified embryonal cells around a central

lumen with limiting membrane. Homer Wright rosettes and perivascular pseudorosettes can be present. Mitosis and apoptosis are frequent [104]. The morphologic features overlap with medulloepithelioma, ependymoblastoma, medulloblastoma, and PNETs. The rich neuropil background distinguishes ETANTR from these tumors. Neurocytic differentiation [105], rhabdomyoblastic and melanotic differentiation [106] as well as rare sarcomatous-like areas have been described. Amplification in chromosome 19q12.42 has been documented in a few cases. The undifferentiated cells are negative for synaptophysin and neurofilaments but the neuropil is strongly positive. Immunohistochemistry for GFAP essentially show a reactive astrocyte pattern [104].

Recent genetic studies, however, show that medulloepithelioma, ETANTR, and ependymoblastoma share similar molecular features and probably comprise the spectrum of a single clinicopathological entity [58]. These entities also share similar overall poor prognosis [58]. An umbrella term of embryonal tumor with multilayered rosettes (ETMR) has been proposed for these tumors [107].

Imaging findings: Limited literature regarding the imaging features this tumor describe T1 hypointensity, T2 iso to hyperintensity and heterogeneous enhancement [108]. The tumor, therefore, shares very similar features with PNET and AT/RT.

Tumors with Features of Glial and Neuronal Tissue

Glial neoplasm comprises the bulk of this group in both adult and pediatric populations. However, tumors with glial-neuronal differentiation such as ganglioglioma and dysembryoplastic neuroepithelial tumors are far more common in the pediatric population. In addition, several molecular alterations that are useful in adult tumors—deletion of chromosome 1p and 19q, mutations of isocitrate dehydrogenase 1 and 2 gene (*IDH 1, IDH 2*), and epigenetic silencing of the *MGMT* (O6-methylguanine–DNA methyltransferase) gene—are uncommon to rare in pediatric gliomas. In contrast, V600E mutation of *BRAF* has been shown to have high mutation frequency in pleomorphic xanthoastrocytoma, gangliogliomas and extra-cerebellar pilocytic astrocytomas and is a diagnostic adjunct of these tumors that are often seen in pediatric patients [109].

Astrocytic and Oligodendroglial Tumors

Although the full spectrum of astrocytic, oligodendroglial, and mixed oligoastrocytic tumors can be seen in pediatric patients, the incidence is different from that of adults. In general, astrocytic tumors and ependymomas are common in children but oligodendrogliomas are rare [5].

Pilocytic Astrocytoma and Pilomyxoid Astrocytoma Definition

Pilocytic astrocytoma is a WHO grade I tumor characterized by a well-circumscribed, biphasic astrocytic tumor with densely packed fibrillary areas and loosely packed area with spongy and/or microcystic areas accompanied by Rosenthal fibers and eosinophilic granular bodies/hyaline droplets. Pilomyxoid astrocytoma is closely related to pilocytic astrocytoma and is currently regarded as a subtype of pilocytic astrocytoma. This is a WHO grade II tumor featured by prominent mucoid matrix and angiocentric arrangement of tumor cells typically without Rosenthal fibers or eosinophilic granular bodies/hyaline droplets.

Pilocytic Astrocytoma

Clinical features: Pilocytic astrocytoma is a clinically indolent tumor with excellent prognosis that occurs predominantly in children and, less commonly, in young adults.

It is the most common pediatric glial tumor and constitutes 18.2 % of all brain tumors and 11.2 % of all spinal tumors [5]. The incidence exceeds the combined incidence of diffuse astrocytoma, anaplastic astrocytoma, and glioblastoma in pediatric patients. Over 75 % of patients are under the age of 20 and the peak incidence is between 8 and 13 years. They tend to occur along the midline with the cerebellum as the most common site. Other primary sites include the optic nerve-chiasma-hypothalamus axis, thalamus and basal ganglia, cerebral hemispheres, brainstem. Pilocytic astrocytoma represents 11 % of the tumors arising in spinal cord of children [5] and its incidence is only second to ependymomas. About 15 % of patient with type 1 neurofibromatosis (NF1) develop pilocytic astrocytoma with optic nerve as the preferred site. About 45 % of gliomas associated with NF1 are pilocytic astrocytomas [110]. Malignant transformation is extremely rare and changes over time are typically regressive in nature [111–113].

Seizure in cerebellar tumors is uncommon. In contrast, cerebellar tumors cause clumsiness, worsening headache, nausea, vomiting, and manifestations of hydrocephalus are common. Visual defects and hypothalamic dysfunctions are often present tumors arising in the optic nerve-chiasma-hypothalamic axis which are often associated with NF1 [4].

Imaging findings: Cerebellar pilocytic astrocytoma is typically a well-circumscribed mass with rather homogenous enhancement when solid. A cyst with an enhancing nodule formation is common [114, 115] and an important finding that distinguishes pilocytic astrocytoma from other glial tumors particularly those occurring outside the cerebellum (Fig. 6.8). In contrast to astrocytomas that diffusely enlarge the pons, pilocytic astrocytomas of the brainstem are usually exophytic, enhance, and contain cysts [116].

Fig. 6.8 MR-pilocytic astrocytoma. (**a**) Axial FSE-T2W MR image demonstrates a large, well-circumscribed mass with mixed cystic and solid component. Mild midline shift is also present. (**b**) Axial T1W post-contrast MR image shows rim enhancement of the cystic component (*arrow*). Patchy enhancement is also present in the solid component (*arrowhead*). (**c**) Axial gradient recalled echo (GRE) MR image reveals susceptibility artifact suggestive of blood byproducts (10-year old male). Note that the tumor illustrated here arises from an uncommon location for pilocytic astrocytoma

Macroscopic pathology and histopathology: Pilocytic astrocytoma is typically well circumscribed and often associated with intra- or paratumoral cysts. The long, hair-like cytoplasmic processes (pilo-) and slightly elongated, bland nuclei, and mucoid materials are well appreciated in cytologic preparations (Fig. 6.9a). The cytoplasmic processes tend to form a mesh on the smeared/squashed preparations. The histologic picture of pilocytic astrocytoma characteristically varies in different parts of the tumor (Fig. 6.9b–f). Alternating densely packed fibrillary and loosely packed areas featured by spongy, microcystic areas are histologic signatures. The densely packed area contains bipolar cells with elongated, coarse cytoplasmic processes. Rosenthal fibers are eosinophilic, hyalinized elongated intracytoplasmic curvy structures common in these dense areas (Fig. 6.9c). The loosely packed areas often contain microcyst in a mucoid background. Eosinophilic granular bodies (Fig. 6.9f) and hyaline droplets are important diagnostic features of pilocytic astrocytomas and are typically found in loosely packed areas. The density of eosinophilic granular bodies can be quite variable. They can be demonstrated with PAS stain with diastase pretreatment. Areas with perinuclear halo reminiscent of oligodendrogliomas are not uncommon. Focal calcifications may be present.

Pilocytic astrocytoma is richly vascularized. Perivascular chronic inflammatory cell infiltration is common. Hyalinized glomeruloids of blood vessels are characteristic of pilocytic astrocytoma (Fig. 6.9e). These blood vessels contain fenestrations and vesicles in the endothelial cells [117]. Endothelial proliferation similar to those seen in glioblastoma can be present in pilocytic astrocytoma but, in contrast to glioblastomas, maturation is often present and a spectrum of blood vessels ranging from plump endothelial cells to vessels with hyalinized vessel wall and thin endothelial cells would be seen. These features probably contribute to contrast enhancement on imaging studies.

Pilocytic astrocytomas involving optic nerve often invade into the subarachnoid space to form a collar-like structure around the optic nerve that has been enlarged by tumor (Fig. 6.10).

Rare mitosis, hyperchromatic nuclei, increased pleomorphism, and infarct-like necrosis, are compatible with the diagnosis of pilocytic astrocytoma. Increased cellularity, nuclear atypia, and occasional mitoses are not indications of malignancy [113]. In long standing cases, degenerative atypia featured by enlarged and hyperchromatic nuclei with smudgy chromatin and nuclear pseudoinclusions. Occasionally, an infiltrative growth pattern can be seen at the periphery of the tumor. Although pilocytic astrocytomas frequently invade the leptomeninges, subarachnoid dissemination is rare and survival rate of these cases are comparable to those without dissemination [118].

Anaplastic (malignant) pilocytic astrocytoma refers to pilocytic astrocytomas with multiple mitoses, endothelial proliferation, and palisading necrosis. It is not uncommon that these are recurrent tumor after radiation [112, 113].

Pilomyxoid Astrocytoma

Clinical features: This is a WHO grade II tumor [119, 120]. This uncommon tumor occurs predominantly in children with a median age of 10 months but rare cases have been reported in adolescents [121, 122] and adults. In contrast to pilocytic astrocytoma, the suprasellar and hypothalamic/chiasmatic region is the preferred location and tumors may occur in other part of the brain and spinal cord. Clinical symptoms are related to the location of the tumor with visual and hypothalamic/pituitary symptoms as major manifestations. Dissemination through CSF may occur. Progression of a rare case of pilomyxoid astrocytoma in the spinal cord to glioblastoma has been reported [123, 124].

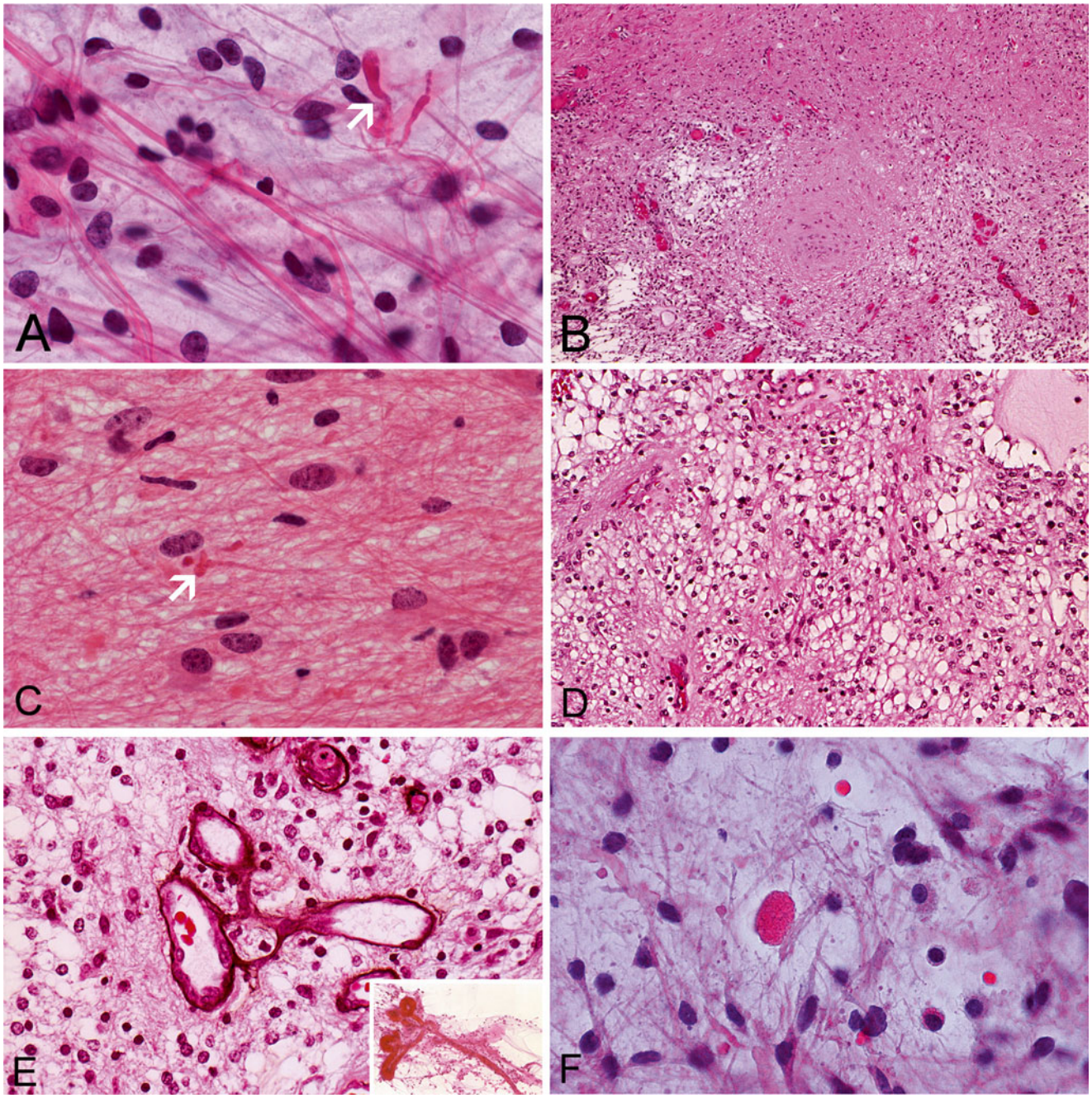

Fig. 6.9 Pilocytic astrocytoma: (**a**) Squash preparation shows bipolar tumor cells with long, coarse, hair-like process and occasional Rosenthal fiber (*arrow*) in a mucoid background. The nuclei are small, monotonous, and lack pleomorphism. (**b**) The alternating densely packed, loosely packed pattern is shown in this image. (**c**) Rosenthal fibers, elongated cytoplasmic processes and bland nuclei are shown in densely packed area. (**d**) Areas with perinuclear halo mimicking oligodendroglioma can be found. (**e**) Complex glomeruloid blood vessels are common in pilocytic astrocytoma. The outline is well illustrated by Jones stain here. This type of glomeruloid vessels can appear as a multi-headed, club shape structure on cytologic preparation (inset in (**e**)). (**f**) Eosinophilic granular bodies are often found in loosely packed areas

Imaging findings: Pilomyxoid astrocytomas are well-circumscribed tumors, hypointense on T1-weighted imaging, and hyperintense on T2-weighted imaging reflecting the mucoid component (Fig. 6.11). In contrast to pilocytic astrocytoma, pilomyxoid astrocytoma tends to occur as a solid suprasellar mass with enhancing and non-enhancing areas and occasional leptomeningeal dissemination [125].

Macroscopic pathology and histopathology: Surgical specimens typically appear gelatinous. Histologically, this tumor is composed of a mucoid, hypocellular mucoid neoplastic growth in a "cobweb" pattern punctuated by perivascular palisading arrangement of tumor cells around blood vessels reminiscent of ependymomas (Fig. 6.12). In contrast to pilocytic astrocytoma, pilomyxoid astrocytomas do not have

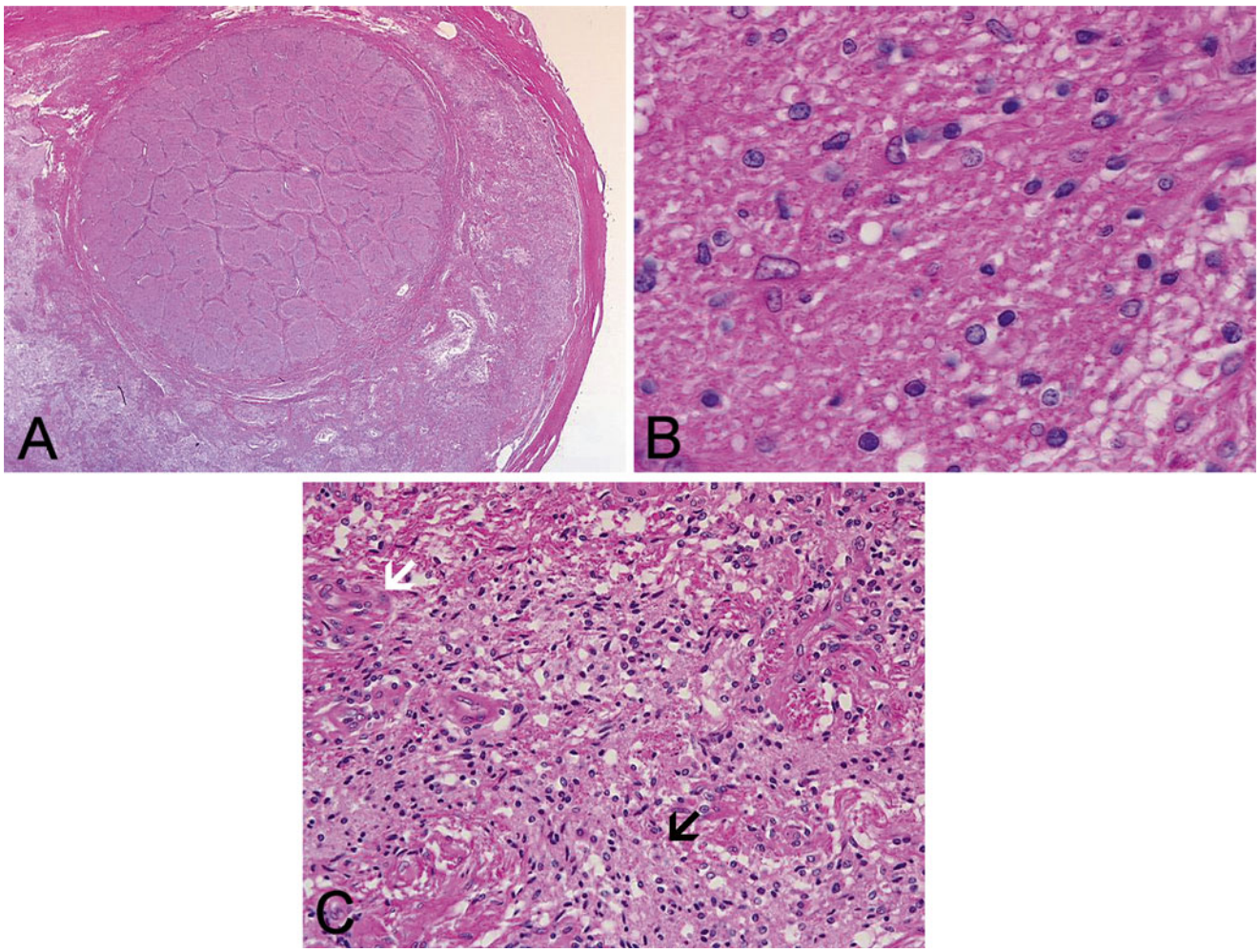

Fig. 6.10 Optic nerve glioma: (**a**) The optic nerve is infiltrated and expanded by an astrocytoma. Note that the fibrous septa within the optic nerve are preserved but the subarachnoid space around the optic nerve is expanded by the tumor. (**b**) The tumor has low grade nuclei. (**c**) The expanded subarachnoid space is composed of a mixture of tumor (*black arrow*) and reactive meningothelial cells (*white arrow*) which appears slightly more eosinophilic

biphasic growth pattern and lack Rosenthal fibers, eosinophilic granular bodies, or calcifications [119]. The neoplastic cells are monotonous, small spindle cells with bland nuclei and the cells palisading around blood vessels have similar morphology. The mucoid background is positive for Alcian blue. Features worrisome of poor prognosis such as necrosis, mitoses, and vascular proliferation are not uncommon in pilomyxoid astrocytoma [119, 126].

Pilocytic-Pilomyxoid Spectrum

Pilocytic astrocytoma and pilomyxoid astrocytoma have significant overlap in clinical and radiographic features, histologic features [126], and genetic aberrations [127]. Tumors with intermediate features are typically found in older patients, and cases of "maturation" of pilomyxoid astrocytoma into pilocytic astrocytoma [126] have been documented. Pilocytic astrocytoma and pilomyxoid astrocytoma are probably related entities along a common spectrum, and the pure form represents the two extremes of this spectrum.

Differential diagnosis: It is important to distinguish classic WHO grade I pilocytic astrocytoma from WHO grade II pilomyxoid astrocytoma, diffuse astrocytoma and oligodendroglioma, and ependymoma. The palisading perivascular arrangement in pilomyxoid astrocytoma can suggest ependymoma particularly when the specimen is small and the mucoid, hypocellular background can suggest dysembryoplastic neuroepithelial tumor (DNET). The clear cell component may suggest oligodendroglioma but pilocytic astrocytoma is typically heterogeneous in histopathology, and areas with typical morphology are generally found. Eosinophilic granular bodies are a useful feature in recognition of pilocytic astrocytomas.

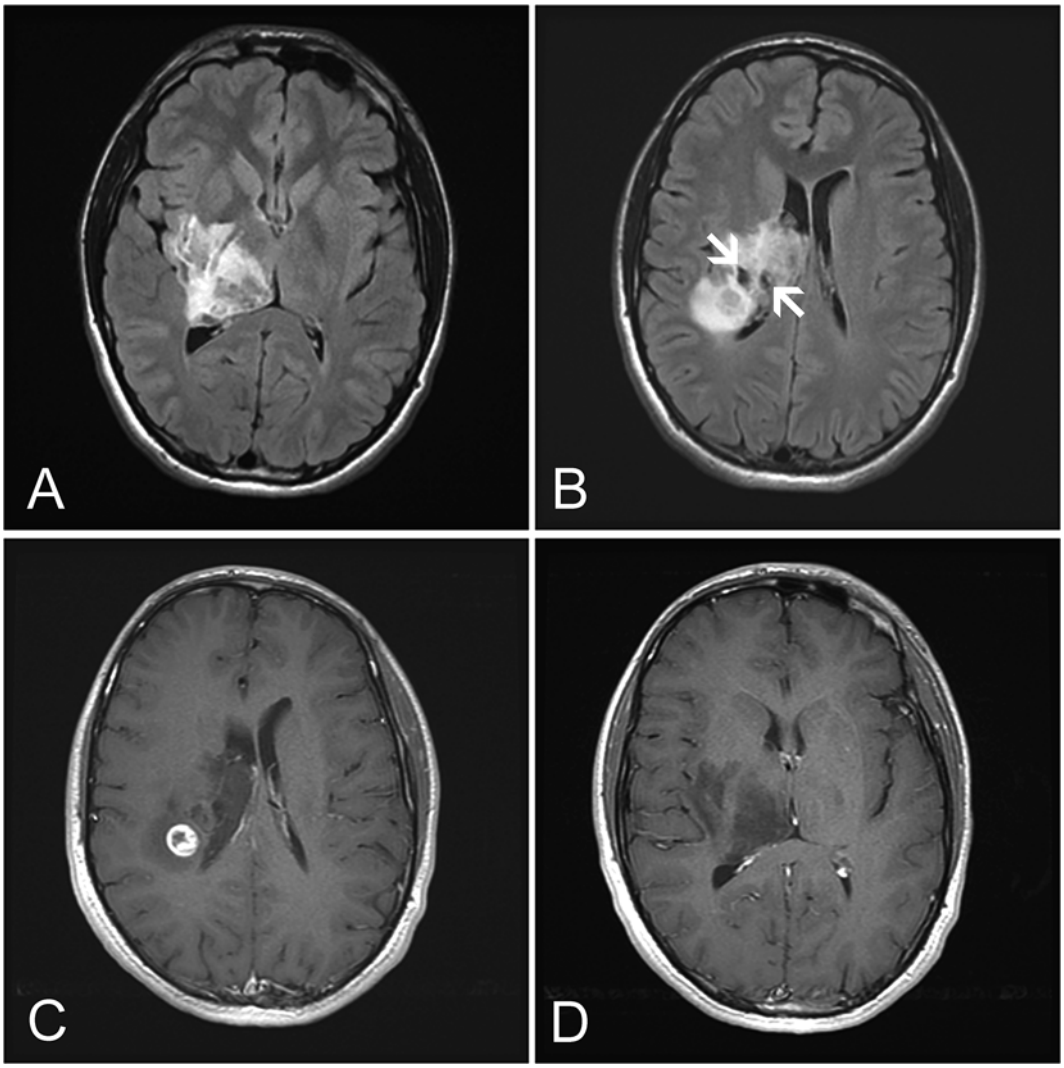

Fig. 6.11 MR-pilomyxoid astrocytoma**.** (**a**) Axial FLAIR MR images show (**a**) an infiltrating tumor involving the basal ganglia and thalamus. (**b**) A cystic component is present (*arrows*) and there is extension into the corona radiata. Axial T1W post-contrast enhanced MR images show (**c**) nodular enhancement in some areas while (**d**) enhancement is not found in other areas (adolescent male)

Immunohistochemistry and Molecular Pathology of Pilocytic-Pilomyxoid Spectrum

Immunohistochemistry: The immunohistochemical profile of pilomyxoid and pilocytic astrocytomas are very similar. The astrocytic cells are reactive for GFAP, Olig2, and S100 [128]. Rosenthal fibers are composed of α B-crystallin [129] and are often, but not always, negative for GFAP. Eosinophilic granular bodies are immunoreactive for α-1-antichymotrypsin and α-1-antitrypsin [130]. The Ki67 labeling index is usually under 1 % for most pilocytic astrocytoma [131], but a Ki67 labeling index of up to 18 % [132] has been reported. The range of Ki67 labeling varies from <1 % to 10 % in one small study [128]. Immunohistochemistry for synaptophysin varying from weak to strong has been documented in slightly less than half of the cases in a large study [133].

Cytogenetics and molecular pathology: Patients affected by neurofibromatosis 1 (NF1) has a high tendency to develop bilateral pilocytic astrocytoma in the optic nerve [134]. Mutation of *TP53* is usually absent in pilocytic astrocytoma [132]. No diagnostic ultrastructural features specific for pilomyxoid astrocytoma have been described [135]. BRAFKIAA1549 fusion can occur in up to 80 % of pilocytic astrocytoma [136–138] but are uncommon in other WHO grade II pediatric astrocytomas and oligodendrogliomas. The fusion gene may act as an adjunct in separating pilocytic astrocytoma from other WHO grade II pediatric astrocytomas and oligodendrogliomas. Tumors with fusion genes occur more commonly in the posterior fossa [133, 139] and behave less aggressively [138]. Point mutation leading to *BRAF* V600E substitution is less common (about 9 % of pilocytic astrocytomas) [109]

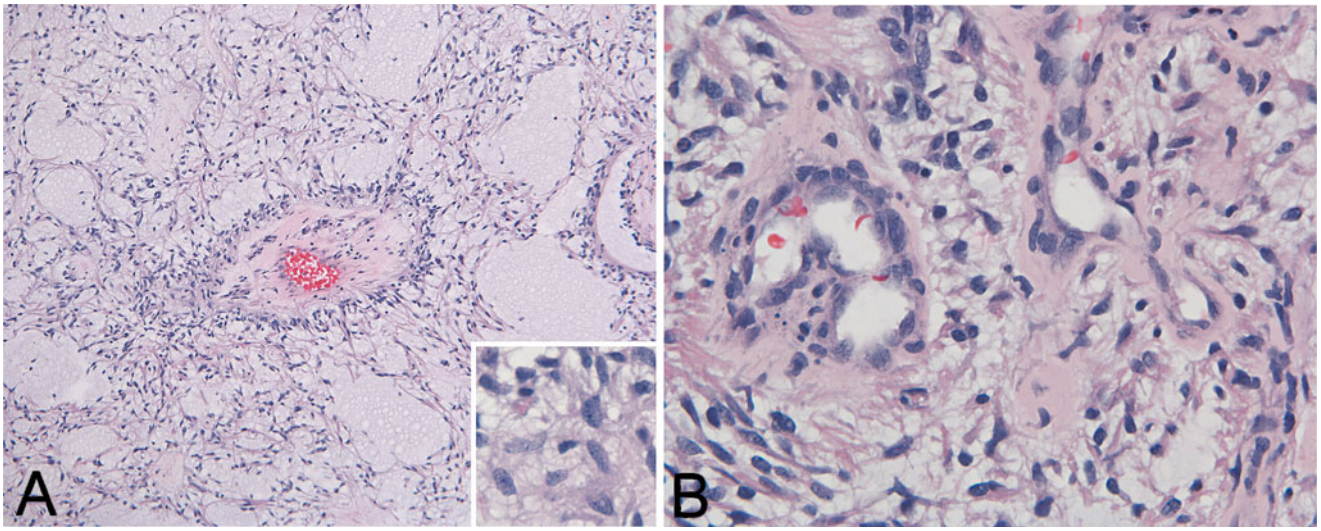

Fig. 6.12 Pilomyxoid astrocytoma: (**a**) Angiocentric arrangement of tumor cells scattered within a background with diffuse mucoid changes are the salient features. The tumor cells lack high grade pleomorphic changes (inset). (**b**) Endothelial proliferation is not uncommon in pilomyxoid astrocytomas (Images are courtesy of Dr. Gregory Fuller)

and often occurs in tumor outside the posterior fossa. Heterozygous PTEN/10q and homozygous p16 deletions have been demonstrated in 32 and 20 % of anaplastic pilocytic astrocytoma, respectively, but not in classic pilocytic astrocytoma or recurrent pilocytic astrocytoma [139]. Mutation of *IDH1* and *IDH2* [140] and other genetics changes in diffuse astrocytomas are uncommon in pilocytic astrocytomas [139].

Diffuse Astrocytoma, Anaplastic Astrocytoma, and Glioblastoma

Diffuse Astrocytoma and Anaplastic Astrocytoma

Definition: Diffuse astrocytoma, WHO grade II, is a slow growing tumor containing cells with features of highly differentiated astrocytes. Anaplastic astrocytoma, WHO grade III, is the aggressive form of astrocytoma.

Clinical features: Both tumors tend to occur in white matter area and are most common in supratentorial locations. Diffuse astrocytomas occur most commonly in young adults with some of the cases seen in adolescent and children. These tumors have an intrinsic tendency to progress to anaplastic astrocytoma or glioblastoma. Anaplastic astrocytoma is a tumor of adults and is far less common in pediatric patients.

The incidence of diffuse astrocytoma and anaplastic astrocytoma in pediatric brain is 6.2 % and 4.4 %, respectively, and that in the spinal cord is 9.5 % and 3.4 %, respectively [5]. In contrast to pilocytic astrocytomas, diffuse astrocytomas and anaplastic astrocytomas occur more frequently in the cerebral hemispheres with new onset seizure frequently seen. Other manifestations are resulted from increased intracranial pressure such as headache, nausea, vomiting, personality change, speech difficulties, and other nonspecific symptoms. Locations of the tumors dictate the nature of focal neurologic signs and symptoms.

Imaging findings: Diffuse astrocytoma appears as an ill-defined, homogeneous, non-enhancing mass that is hypointense on T1-weighted sequences and hyperintense on T2-weighted sequences. The tumor grows along the white matter tracts in the hemispheres or the infratentorial brain and may cross the corpus callosum or progress along the long tracts in the cerebral peduncles. Anaplastic astrocytoma is iso- to hypointense on T1-weighted sequences with a variable hypo- to hyperintense appearance on T2-weighted sequences. These tumors may be associated with substantial edema that is best demonstrated by FLAIR images.

Macroscopic pathology and histopathology: Gross pathology of these tumors is best appreciated, unfortunately, in untreated autopsy cases, a rare case scenario currently. In surgical specimens, tumors typically consist of small fragments or lumps of gray, tan soft tissue. Lower grade tumors tend to be more mucoid and thus have a gel-like consistency.

The histopathologic changes of classic diffuse astrocytoma and anaplastic astrocytoma are similar to those arising in adults. Diffuse astrocytomas of WHO grade II are featured by infiltrating low-grade neoplastic astrocytes (Fig. 6.13). A variable amount of mucoid background is present (Fig. 6.14). Pediatric cases often tend to be fibrillary, but gemistocytic and protoplasmic patterns can also be encountered. Mucoid substance is common in the background and it can vary from little to intermediate (Fig. 6.14a, b) to substantial and accompanied by microcyst formation.

Although anaplastic astrocytoma (WHO grade III) has many features similar to diffuse astrocytoma, these tumors have increased cellularity, distinct nuclear atypia and mitotic figures. However, by definition no endothelial proliferation or necrosis should be present.

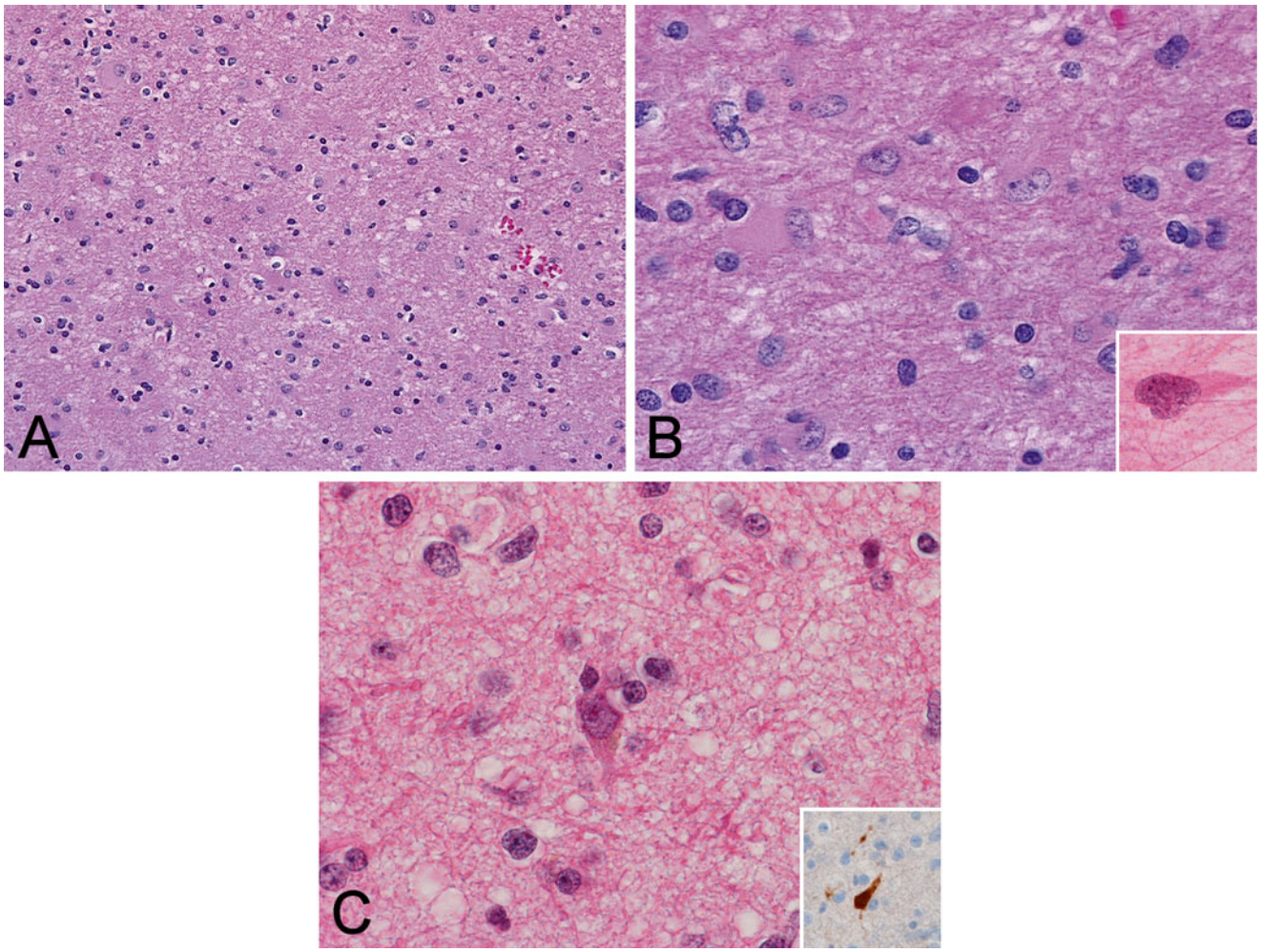

Fig. 6.13 Astrocytoma: (**a**) The cellularity is only mildly increased. (**b**) Note that the neoplastic astrocytes have enlarged nuclei as compared to the normal astrocytes in the same field. Enlarged nucleoli are not common features (inset is cytologic preparation). (**c**) Entrapped neurons are common and easily demonstrated by immunohistochemistry for neurofilament proteins (inset)

While the number of mitoses is an important criterion of malignancy, one or two mitotic figures in a large (resection) specimen unaccompanied by other features indicative of malignancy is not sufficient for a diagnosis of anaplastic astrocytoma. On the other hand, even one mitotic figure in a small stereotactic biopsy should raise the concern of an anaplastic astrocytoma.

Glioblastoma

Definition: Glioblastoma is a WHO grade IV tumor predominantly with astrocytic differentiation and histologically characterized by high-grade histology, endothelial proliferation and/or necrosis.

Clinical features: Although glioblastoma is the most common malignant brain tumor in adults, its incidence is far less common in the pediatric age group. Pediatric glioblastomas comprises about one-tenth of all glioblastoma. It may appear as a second tumor due to prior radiation treatment for other malignancies such as acute leukemia. The clinical manifestations are similar to those of diffuse astrocytoma and anaplastic astrocytoma but the clinical history is usually shorter. Rare congenital glioblastomas can occur [8]. Secondary glioblastoma (arising from a preexisting low-grade glioma) is extremely rare in children.

Imaging findings: Glioblastoma often presents as a heterogeneous mass with areas of cystic necrosis and hemorrhage. The solid component may be hypo- to isointense on T1-weighted sequences and moderately to significantly hyperintense on T2-weighted sequences. Surrounding edema is usually significantly. The enhancement is usually avid but inhomogeneous, or the so-called dirty looking and the tumor may extend to the leptomeninges resulting in leptomeningeal spread and drop metastasis (Fig. 6.15).

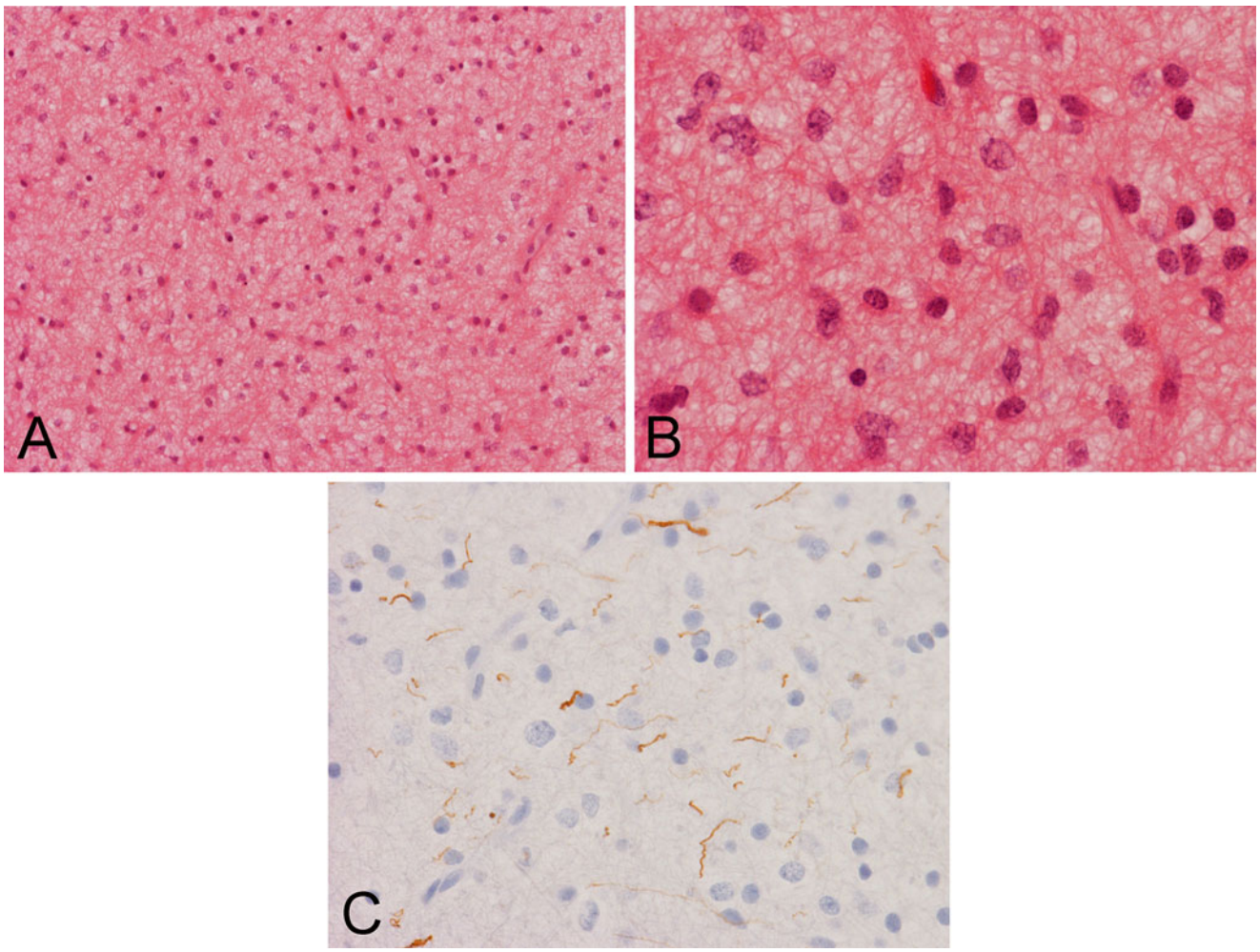

Fig. 6.14 Astrocytoma, brainstem: (**a**) and (**b**)**,** In contrast to Fig. 6.12, this tumor is composed exclusively of neoplastic astrocytes with processes that form a mesh work with mucoid fluid in the background. (**c**) The infiltrative nature is best testified by the entrapped axons as demonstrated by immunohistochemistry for neurofilament proteins

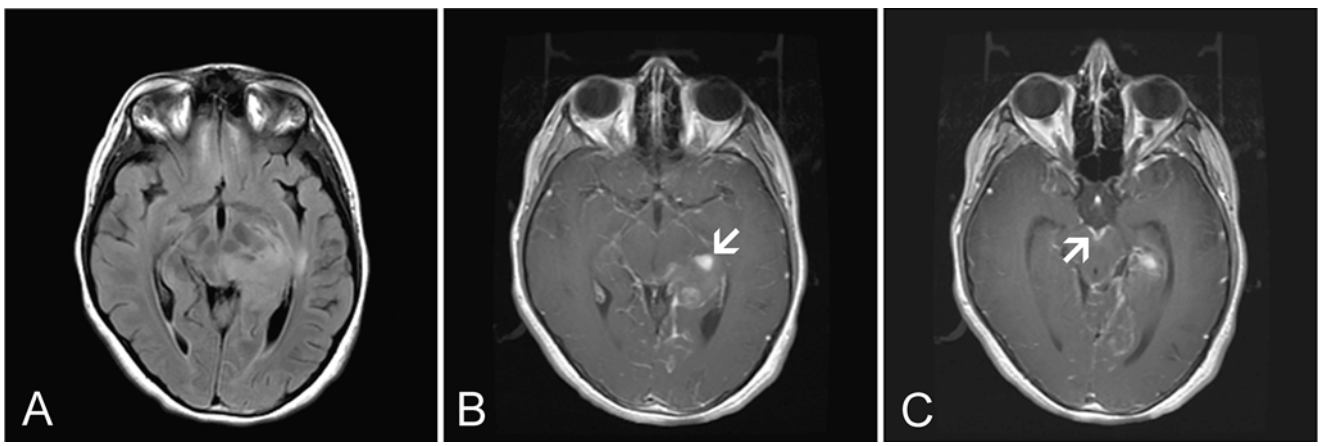

Fig. 6.15 MR-glioblastoma with CSF seeding**.** (**a**) Axial FLAIR MR image demonstrates an infiltrative, poorly defined mass involving the thalamus and temporal lobe. (**b**) Axial post-contrast enhanced T1W MR image shows inhomogeneous enhancement of the tumor. (**c**) Leptomeningeal enhancement consistent with tumor seeding (*arrow*)

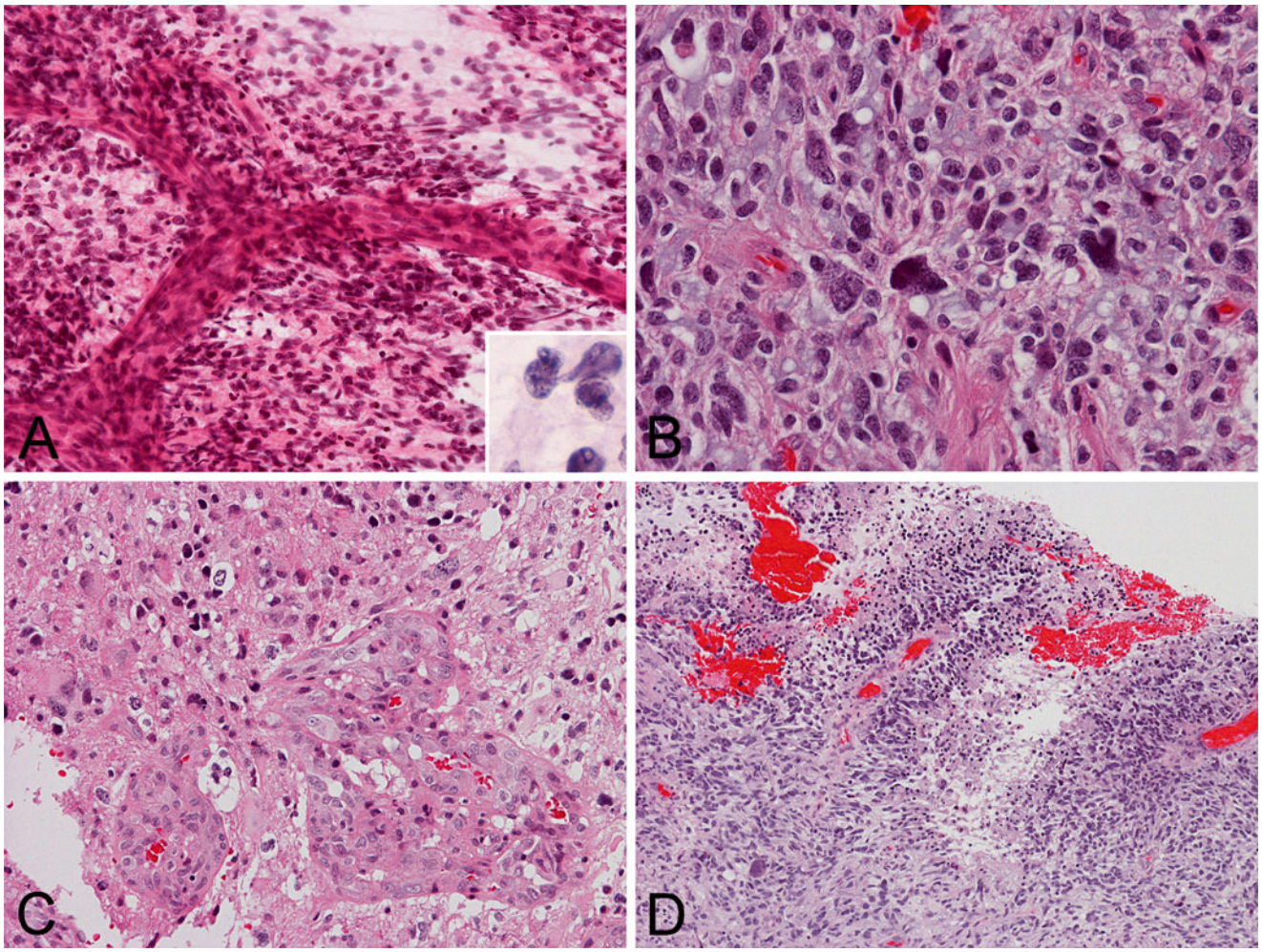

Fig. 6.16 Glioblastoma: (**a**) Tumor cells are large and atypical. Note the blood vessels with endothelial proliferation giving a tree-trunk like appearance on cytologic preparations. High grade nuclear features are shown in the inset. (**b**) Tumor cells are large and, bizarre cells can be present. (**c**) Endothelial prolilferation and (**d**) pseudopalisading necrosis are diagnostic features

Macroscopic pathology and histopathology: Glioblastoma typically arises in cerebral hemispheres and may present as a large mass. It is one of the few tumors that infiltrate across the midline through the corpus callosum to form the so-called butterfly tumor. Glioblastoma is usually poorly delineated, but genuinely multifocal tumors are rare. The size of surgical specimens varies, and gross areas of opacity corresponding to necrotic tumor generally offer a clue to the diagnosis.

In cytologic preparation, glioblastoma shares characteristics of other glial tumors with neoplastic cells having signature long cytoplasmic processes. In general, glioblastomas do not smear out as evenly as diffuse astrocytoma, and the preparation typically appears clumpy (Fig. 6.16). Tumor cell nuclei may range from medium size to large and anaplastic. Tumor cells often contain less cytoplasm than lower grade gliomas. The combination of these features may suggest other high grade tumors such as atypical teratoid/rhabdoid tumors in pediatric patients. Vessels with endothelial proliferation typically appear as thick tree-trunk-like structures with clubbing ends. The amount of necrosis can be significant, and small biopsy specimens may not contain viable tissue.

On histologic sections, the tumor is composed of neoplastic glial cells with nuclear features similar to those seen in cytologic preparations. Endothelial proliferation and/or necrosis are hallmarks of glioblastoma. Glioblastoma is notorious for having multiple tissue patterns such as glandular, ribbon-like epithelial structures suggestive of an epithelial tumor, lipid rich epithelioid cells [141], granular cells, gemistocytic cells, small cell, multinucleated giant cells, and oligodendroglioma components.

Immunohistochemistry and Molecular Pathology of Astrocytoma, Anaplastic Astrocytoma, and Glioblastoma

Astrocytoma, anaplastic astrocytomas, and glioblastomas share many common phenotypic features. These tumors are positive of GFAP and olig2. Molecular aberrations that are often found in glioblastoma include loss of heterozygosity of chromosome 10q, amplification of *EGFR*, $p16^{INK4a}$ deletion, *PTEN,* and p53 mutations. In contrast to glioblastomas of adults, *TP53* is rarely mutated in pediatric cases. Mutations of *IDH1* and *IDH2* are uncommon in pediatric cases.

Differential Diagnosis of Astrocytoma, Anaplastic Astrocytoma, and Glioblastoma

Highly cellular glioblastomas may closely mimic medulloblastoma particularly when the expression of synaptophysin is patchy. Molecular features such as EGFR amplification, loss of heterozygosity of chromosome 10q in glioblastoma, isochromosome 17 and *c-Myc* ampliation are helpful adjuncts. Comprehensive analysis of the genetic profile can also help to resolve this diagnostic dilemma [32].

Glioblastoma can mimic AT/RT, but immunohistochemistry for BAF47 and FISH for the loss of chromosome 22q generally resolve this situation. In addition, EMA is frequently expressed in AT/RT but not glioblastoma.

Pleomorphic xanthoastrocytoma contains bizarre, enlarged, and lipidized cells. Its differentiation from glioblastoma will be discussed in the section on pleomorphic xanthoastrocytoma. *BRAF* mutation is seen in slightly more than half of all cases of pleomorphic xanthoastrocytoma and is a good diagnostic help [109].

Oligodendroglioma and Anaplastic Oligodendroglioma

Definition: Oligodendroglioma (WHO grade II) and anaplastic oligodendroglioma (WHO grade III) are composed of neoplastic cells morphologically resembling oligodendroglia.

Clinical features: Both are rare in the pediatric age group. Oligodendrogliomas of WHO grade II or III occur predominantly in adults. Uncommon cases can be seen in the second decade but they are almost nonexistent during infancy and childhood. Clinical presentation is similar to other hemispheric brain tumors and is generally nonspecific.

Macroscopic pathology and histopathology: The frontal lobe is the most common site in adults and tumor arises from the cortex and white matter. Histologically, oligodendroglioma is characterized by solid sheets of tumor cells with perinuclear halo giving the so-called fried-egg cytology and a network of delicate blood vessels embedded in between. Calcifications are common. Anaplastic oligodendrogliomas have features of aggressive tumors including increased cellularity, pleomorphism, and mitotic activity, microvascular proliferation and necrosis. The tumor cells also tend to have amphophilic or eosinophilic cytoplasm rather than clear cytoplasm. In contrast to adult cases, mutations of *IDH 1* and *IDH 2*, deletion of 1p and 19q are uncommon in pediatric cases [142, 143].

Oligoastrocytoma and Anaplastic Oligoastrocytoma

Oligoastrocytoma (WHO grade II) and anaplastic oligodendroglioma (WHO grade III) are tumors composed of a mixture of both neoplastic oligodendroglial cells and astrocytic cells. Similar to oligodendroglioma, they are rare in the pediatric age group.

Pleomorphic Xanthoastrocytoma

Definition: Pleomorphic xanthoastrocytoma (PXA) (WHO grade II) is a tumor of relatively favorable prognosis and occur most frequently in children and young adult. Histologically these tumors are characterized by large, lipidized, pleomorphic cells.

Clinical features: PXA is uncommon and accounts for less than 1 % of all gliomas. The symptoms usually reflect the location of the tumor. Since PXA typically occurs in a superficial location, seizure is a commonly associated symptom.

Imaging findings: This tumor is slow growing and is usually not associated with substantial peritumoral edema. Typically tumors present as a well-circumscribed mass involving the surface of the cerebral hemispheres, particularly the temporal lobes. It can vary from a solid to cystic tumor with a mural nodule. On MRI, these tumors usually demonstrate hypointense or mixed-signal intensity on T1-weighted images and hyperintense or mixed signals on T2-weighted images. The solid areas of the tumor, including mural nodules, enhance after administration of contrast agent [144].

Macroscopic pathology and histopathology: PXA is typically superficial tumor attached to the leptomeninges with or without a cyst formation associated with a mural module. The histologic signature of PXA is the large, pleomorphic, lipidized cells with eccentrically located, bizarre, and often multinucleated nuclei. The cytoplasm of these tumor cells demonstrates a characteristic fine bubbly, lipidized xanthomatous cytoplasm. The histopathology of PXA is often heterogeneous. Areas composed predominantly of spindle to epithelioid cells without large pleomorphic cells can pose a diagnostic challenge (Fig. 6.17). Xanthomatous changes in these cells are usually subtle. Eosinophilic granular bodies are often present. Occasional association with cortical dysplasia has also been described [145, 146].

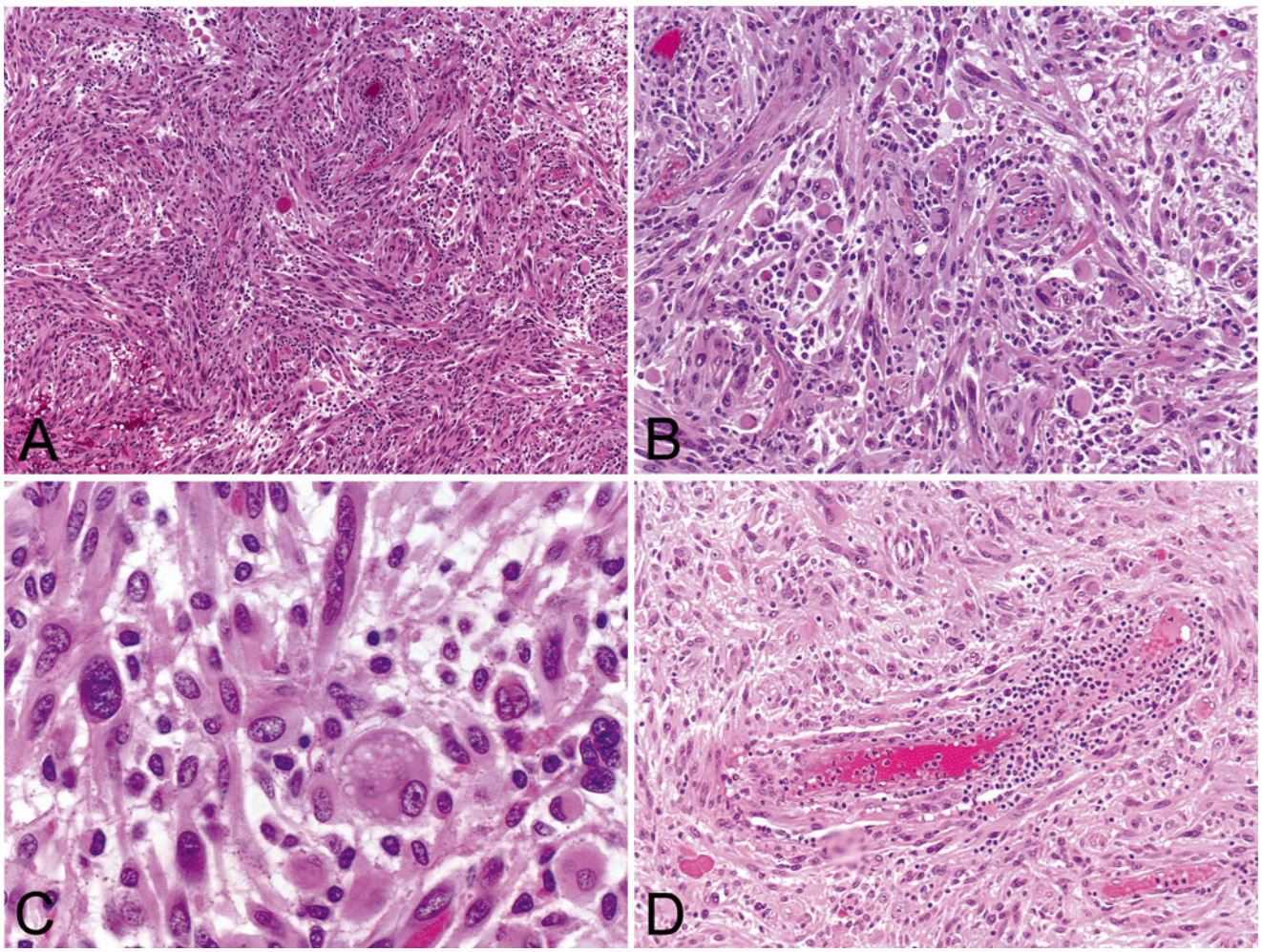

Fig. 6.17 Pleomorphic xanthoastrocytoma. (**a**, **b**) Pleomorphic xanthoastrocytoma often contains an intermixed pattern of spindle cells and large, lipidized, pleomorphic cells. The spindle cell component can be overwhelming and constitute a diagnostic challenge. (**c**) The large, pleomorphic cells often have eccentrically located nuclei and lipidized cytoplasm. (**d**) Perivascular lymphocytic infiltration is common

Despite the presence of pleomorphic cells, neither necrosis nor mitoses are features of PXA. Their presence should raise a strong suspicion of more aggressive behavior. WHO recommends the use of the term "pleomorphic xanthoastrocytoma with anaplastic features" in PXA with five or more mitoses per ten high-powered fields and/or necrosis [147, 148].

Eosinophilic granular bodies are important diagnostic features and their search is well facilitated by PAS stain with diastase pretreatment. Deposition of reticulin fibers around individual tumor cells is another diagnostic feature which reflects the possible origin of PXA from subpial glial cells. While markers for glial differentiation are typically positive in PXA, immuno reactivities for neuronal markers such as neurofilament, synaptophysin can be demonstrated in a small subset of PXA [147]. These findings suggest biphenotypic differentiation in some PXA, a finding that is confirmed by ultrastructural studies [147, 149] and p53. The latter does not appear to have prognostic value [150].

Molecular genetics: The recent demonstration of mutation of *BRAF* mutations [109, 151] in PXA represents an important adjunct of diagnosis as well as a predictive marker for potential target therapy. Like other pediatric tumors, mutation of isocitrate dehydrogenase 1 and 2 genes (*IDH1, IDH2*) is uncommon in PXA [151].

Prognostic features: The overall 5- and 10-year survival rate is about 72 and 61 %, respectively. About 20 % of PXS will progress to higher grade tumor [147].

Gliomatosis Cerebri

Gliomatosis cerebri (WHO grade III) is an uncommon, extensively infiltrative diffuse glioma. As the extent of involvement comprises part of the WHO diagnostic criteria, correlation of pathologic changes with neuroimaging studies is mandatory. Gliomatosis cerebri is most common in the fifth and sixth decade but it can be seen in all age groups. It can be seen in

adolescents and young adults but it is rare. Due to the variable and extensive involvement, the clinical manifestation has a broad spectrum including seizures, headache, cranial nerve dysfunction, dementia, lethargy, and others.

Gliomatosis cerebri is characterized by diffuse infiltration without enlargement of the involved areas. It should involve at least three cerebral lobes. Involvement across midline and deep gray matter with extension to the brainstem are common. Grossly, the involved area is usually enlarged and firm. Histologically, astrocytic phenotype is most common and the extent of infiltration is variable among different areas. The classic histology is that of infiltrating small glial cells with elongated, fusiform nuclei. Nuclear atypia is common but mitotic figures are not abundant. In stereotactic biopsies obtained from an area with low density of infiltrating tumor cells, recognition of the scattered atypical cells can be challenging but important for a correct diagnosis. Immunohistochemistry for GFAP and S100 in tumor cells is variable. Ki67 labeling can vary from less than 1 % to about 30 %. Immunohistochemistry for Ki67 is a helpful adjunct in identifying infiltrating atypical cells particularly those with subtle changes.

Imaging findings: Gliomatosis cerebri is a diffuse process involving central and peripheral structures in more than one cerebral lobe. Expansion of the involved brain structures may be seen with preservation of the brain architecture. The tumor reveals hypo- to isointense signal on T1-weighted sequences, increased signal intensity on T2-weighted sequences and, very rarely, scant enhancement. Perfusion MR imaging is a useful adjunct [152].

Leptomeningeal Neurogliomatosis

This is a rare [153, 154] disseminated glial or glial-neuronal lesion that is found predominantly in children and adolescents. This lesion has also been known as leptomeningeal oligodendrogliomatois. However, since some of these cells are immunoreactive for neuronal markers the term leptomeningeal neurogliomatosis has been adopted. In at least 1 study, the tumors showed period of stability but about one fifth of the cases had anaplastic progression. Radiographically, they appear as leptomeningeal enhancement within the spinal cord/brain along the subpial surface with cystic or nodular lesion. Histologically (Fig. 6.18), the tumor is composed of infiltrating oligodendroglioma-like cells with low mitotic rate in a desmoplastic to myoid background. The cellularity can vary from high to low. These tumors may have ganglion/ganglioid cells and intraparenchymal component. The tumor cells are positive for olig2, S100, GFAP, and synaptophysin and negative for NeuN, EMA. There is no *IDH1* mutation as detected by immunohistochemistry for R132H mutation. Co-deletion of chromosome deletion of chromosome 1p, and 19q have been demonstrated in only a minor subset of cases [154, 155]. Histologically, this is a challenging diagnosis and one of the differential diagnoses is chronic meningitis [156].

Mixed-Glial Neuronal and Neuronal Tumors

Tumors with mixed-glial neuronal and neuronal tumor comprise a family of neoplasms with a high incidence in pediatric patients and young adults. Mixed glial-neuronal tumors have a broad array of histologic feature but are essentially variation on the same theme in which recognition of neoplastic glial and neuronal components is the key to the diagnosis.

Ganglioglioma and Gangliocytoma

Definition: Ganglioglioma contains neoplastic glial cells and neuronal (ganglionic) cells while gangliocytoma contains only neoplastic neuronal cells. While gangliocytoma and most ganglioglioma are of WHO grade I, anaplastic ganglioglioma (WHO grade III) has anaplastic features in their glial component.

Clinical features: Gangliogliomas are uncommon but not rare tumors. Although gangliogliomas can occur in any age, the majority arise in children and young adults. While they can be found anywhere in the CNS including the optic nerve, the majority occur in the temporal lobe. For those that occurred in the cerebral hemispheres, seizure is the most common presentation. Less common symptoms include headaches, vomiting, ataxia, and others.

Imaging findings: Ganglioglioma is typically a well-circumscribed mass without excessive edema in surrounding tissue or mass effect (Fig. 6.19). It can be cystic and contain a mural nodule. It appears hypointense on T1-weighed images, hyperintense on T2-weighted images, and enhances. Foci of calcification are common. Due to their slow growth rate, superficially located tumors may have scalloping effects on the calvarium [157].

Macroscopic pathology and histopathology: Grossly, ganglioglioma can be rather rubbery and particularly unamenable to adequate cytologic preparation. Histologically, the histopathology is heterogeneous. The spectrum varies from a predominantly neuronal tumor (gangliocytoma) to a ganglioglioma with predominantly glial component mimicking a glioma. The distribution of neoplastic neuronal and glial component varies considerably [158, 159]. A thorough examination is often required to recognize both neoplastic glial and neuronal components. The distribution of ganglionic cells is typically uneven and clustering is the rule. Cytologically, ganglionic cells resemble normal neurons, or large ganglionic cells with bizarre shape, abnormal Nissl substance, and occasionally vacuolation (Fig. 6.20). Binucleation of ganglionic cells (Fig. 6.20A) can be seen in about 60 % of cases [159]. Increased reticulin deposition around ganglionic cells is frequent. The glial component is also heterogeneous. It can vary

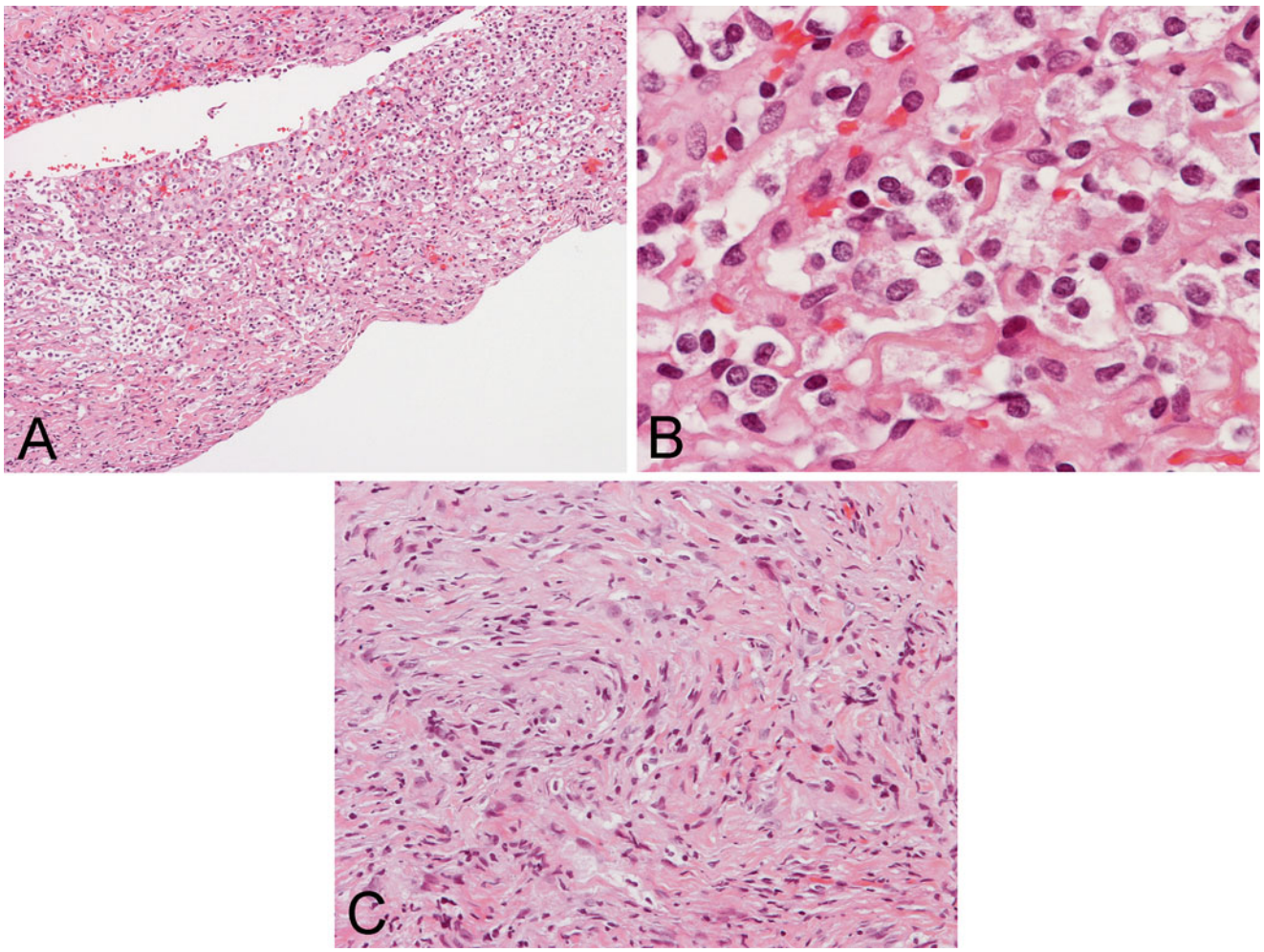

Fig. 6.18 Spinal leptomeningeal neurogliomatosis. (**a**) The typical area appears as an infiltrating tumor in a fibrous background. (**b**) On higher magnification, the tumor cells have perinuclear halo and round, monotonous nuclei resembling oligodendrogliocytes. (**c**) The amount of fibrosis can be quite variable and this image is taken from the same specimen in (a) and (b) and has a fibroblastic appearance suggestive of fibroblastic meningioma

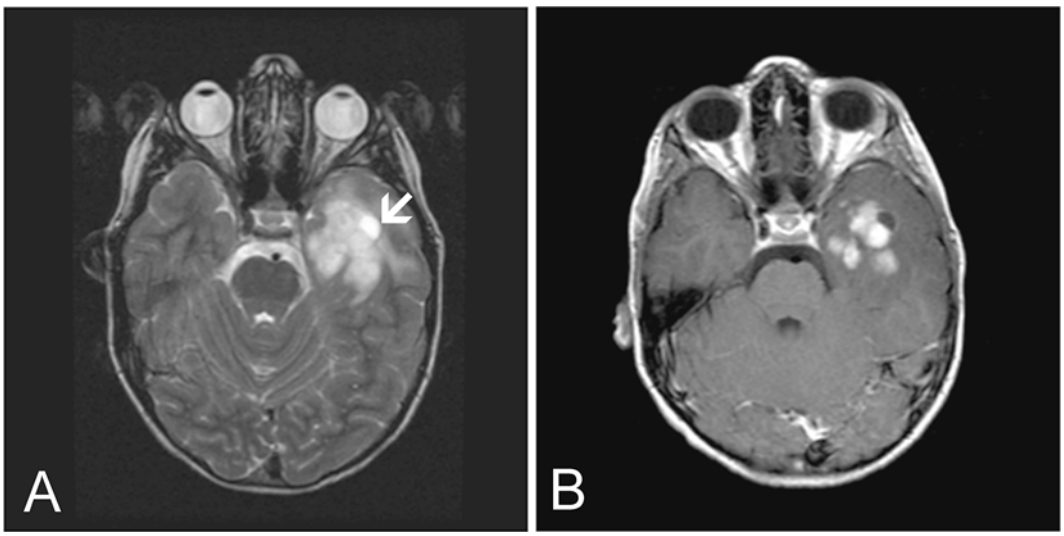

Fig. 6.19 MR-ganglioglioma. (**a**) Axial FSE-T2W MR image demonstrate a lobulated mass in the left temporal lobe with a small cystic component (*arrow*). (**b**) Axial post-contrast T1W MR image shows vivid enhancement of the solid component (8-year-old male)

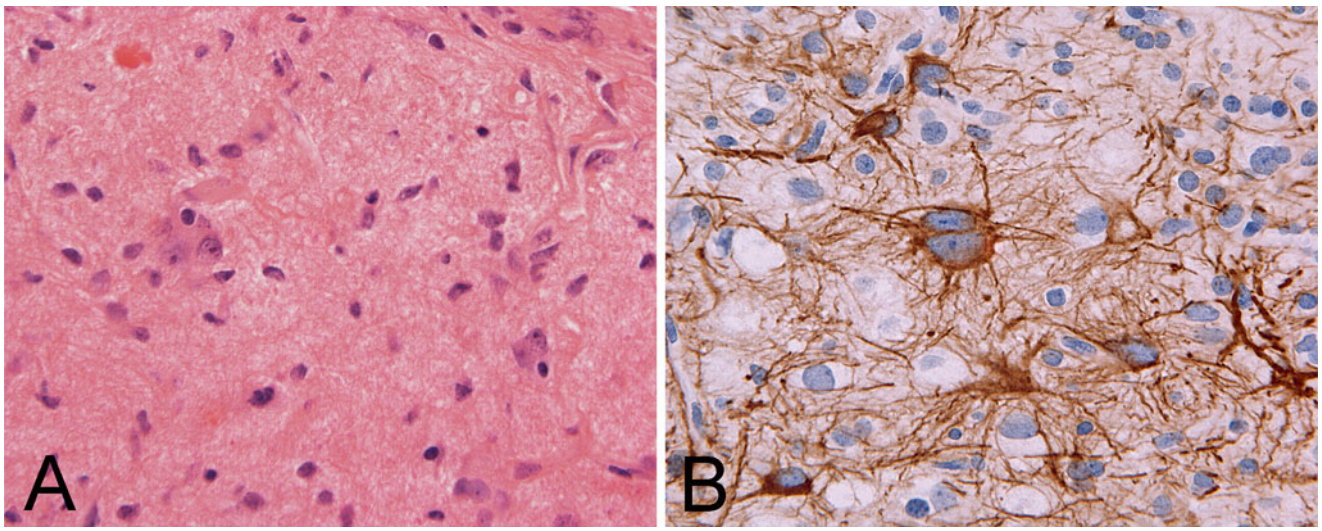

Fig. 6.20 Ganglioglioma: (**a**) Typical ganglioglioma is composed of a mixture of larger neurons and smaller neoplastic glial cells. The neurons often have dysplastic features, such as binucleation. (**b**) Immunohistochemistry for neurofilament proteins highlights the binucleated bizaare multipolar neurons within a background of proliferating glial cells

from low cellularity with only a few spindle cells to a cellularity closely resembling an astrocytic neoplasm. Calcifications, eosinophilic granular bodies, Rosenthal fibers, extensive perivascular lymphocytic infiltrations, and prominent capillary network are other common features. Mitotic figures are absent or rare, and necrosis should be absent. When a malignant component of anaplastic ganglioglioma is identified, it almost always involves the glial component.

Molecular pathology and Immunohistochemistry: *BRAF* V600E mutation has recently been demonstrated in ganglioglioma [160] and may represent a negative prognostic factor [161]. When the neuronal component is not obvious, immunohistochemistry for synaptophysin, neurofilament proteins, and NeuN are helpful adjuncts to highlight it. Neurofilament protein immunostain has the additional benefit of demonstrating the abnormal shape and processes of the ganglionic cells (Fig. 6.20b). Ganglionic cells typically demonstrate cytoplasmic surface immunoreactivity for synaptophysin [158]. Although CD34 are negative in adult neurons, it is positive in ganglionic cells in about three quarter of cases [162]. Silver-positive neurofibrillary tangles have been demonstrated in rare cases [163].

Associated lesions: Most gangliogliomas are sporadic, but about 5 % are associated with congenital abnormalities. In particular, cortical dysplasia has been demonstrated in about half the cases in one study [159].

Differential diagnosis: The major challenge in the diagnosis of ganglioglioma is to distinguish ganglioma with only focal ganglionic component from glioma. By the same token, it is also important not to mistake entrapped neurons in gliomas, particularly astrocytomas.

Dysplastic Gangliocytoma of the Cerebellum/ Lhermitte-Duclos Disease

Dysplastic gangliocytoma of the cerebellum/Lhermitte-Duclos disease is part of the PTEN hamartoma tumor syndrome that includes Bannayan–Riley–Ruvalcaba syndrome, and possibly Proteus syndrome, and Cowden syndrome [164, 165]. The disease is characterized by germline mutations of *PTEN*. Lhermitte-Duclos disease is usually discovered in the third or fourth decade and rarely seen in children. Radiographically, the lesion is a non-enhancing cerebellar mass with or without involvement of the vermis. It is hypointense on T1-weighted and hyperintense on T2-weighted sequences with alternating striations that follow the outline of the folia [166].

It is not certain whether this entity is a hamartoma, neoplastic growth, or a reaction to dysembryogenetic events. The signature gross feature is regional thickening of cerebellar folia with an unusual firmness but with preserved architecture. Histologically, it has the so-called inside-out architecture of the cerebellum. A layer of myelinated fibers with large diameter myelinated axons replaces the molecular layer. The internal granular layer is replaced by intermediate sized to large dysplastic neurons with some of them vaguely reminiscent to Purkinje cells. Scattered cells reminiscent of granule cells may be found in molecular layer or subpial locations. In some cases, granule cells persist in the deeper layer of the affected cortex. The native white matter of the folia is atrophic and rarefied.

Desmoplastic Infantile Ganglioglioma and Astrocytoma

Definition: Desmoplastic infantile ganglioglioma (DIG) and astrocytoma (DIA) (WHO grade I) are rare, slow growing, superficially located large, typically cystic tumor with desmoplastic changes that are often attached to the dura.

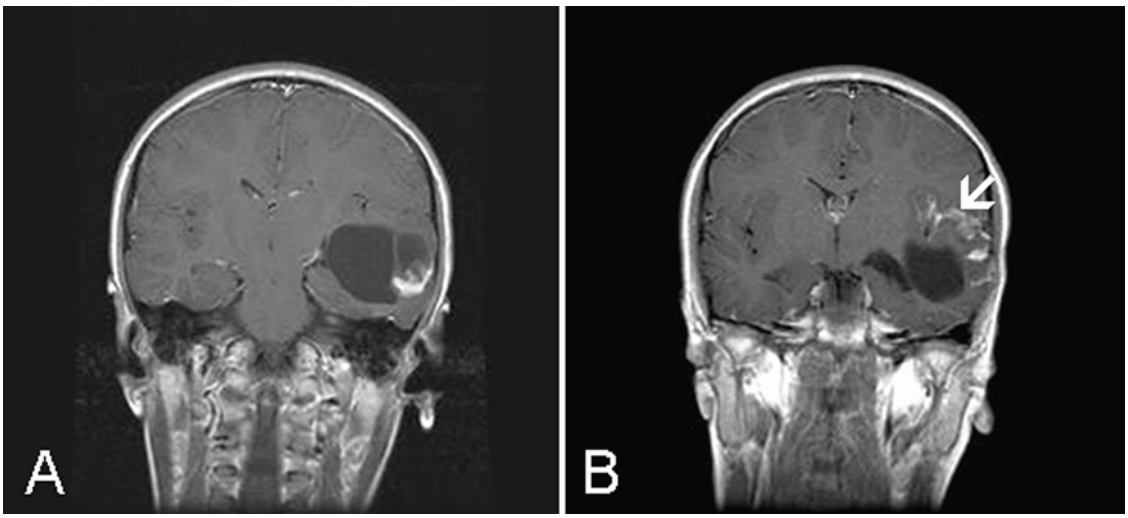

Fig. 6.21 MR-desmoplastic infantile ganglioglioma: post-contrast T1W coronal MR images demonstrate (**a**) a cystic mass with an enhancing, peripheral, solid component and (**b**) leptomeningeal enhancement (*arrow*) (9-year-old girl)

Clinical features: These tumors are seen almost exclusively within the first 2 years of life with exceptional cases in older children and young adults. Manifestations of increased cranial pressure and hydrocephalus are most common. Seizure and focal motor signs are only occasional.

Imaging findings: Imaging studies typically demonstrate a well-circumscribed, large, hypointense, uni- or multiloculated cystic mass with a superficially located nodule. The solid component reveals low signal intensity on T2-weighted sequences likely due to desmoplasia (Fig. 6.21). On post-contrast images, enhancement of the peripherally located nodule is avid [167].

Macroscopic pathology and histopathology: The tumor is often rubbery tough and cytologic preparation is often difficult to make. The peripherally located solid component often attaches to the leptomeninges and dura. Hemorrhage and necrosis should not be present. Histologically (Fig. 6.22) these tumors are sharply demarcated from the adjacent cortex. DIG contains both ganglionic and astrocytic component while DIA contains only astrocytic component. The desmoplastic component is featured by a mixture of collagen fibers, fibroblast like spindle cells and pleomorphic neuroepithelial cells with eosinophilic cytoplasm. These cells may arrange in whorls or fascicles. The ganglionic cells vary from small neuron to large, atypical ganglionic cells. Isolated ganglionic cells surrounded by desmoplastic changes are not uncommon. The collagenous deposition is well demonstrated by trichrome stain and reticulin deposition around individual cells is another diagnostic feature. Islands of poorly differentiated neuroepithelial cells with features of small blue cells reminiscent of primitive neuroectodermal tumor and without desmoplastic changes can be present and sometime as a prominent component. A non-desmoplastic cortical component can be found in the tumor adjacent to the cortex. While mitosis can be seen in the poorly differentiated component, they are not readily seen in the desmoplastic and cortical components.

Molecular pathology and immunohistochemistry: *BRAF* V600E mutation has been demonstrated in a small number of these tumors [168]. The ganglionic component can be demonstrated by neuronal markers including neurofilament proteins and synaptophysin. The fibroblast-like cells in the desmoplastic leptomeningeal component are often positive for vimentin and GFAP and also focally for smooth muscle actin. The astrocytic component is demonstrated by immunohistochemistry for GFAP.

Differential diagnosis: Tumors with the poorly differentiated component dominating the picture may raise a concern for primitive neuroectodermal tumor. The desmoplastic component, the spindle cells, and the large pleomorphic cells often raise a possibility of sarcoma. Both of situations are particularly challenging during intraoperative consultations.

Prognostic features: Despite the presence of poorly differentiated component, complete resection appears is an effective treatment. A rare case with anaplastic changes and dissemination through the CSF has been reported [169].

Dysembryoplastic Neuroepithelial Tumor (DNET)

Definition: Dysembryoplastic neuroepithelial tumor (DNET) (WHO grade 1) is a benign glial-neuronal tumor with a complex columnar and multinodular architecture and often associated with cortical dysplasia.

Clinical features: DNET is usually seen in infants, children, adolescent and young adults, and drug-resistant partial seizure is the most common presentation. Surgical treatment would lead to a cure and recurrence is uncommon.

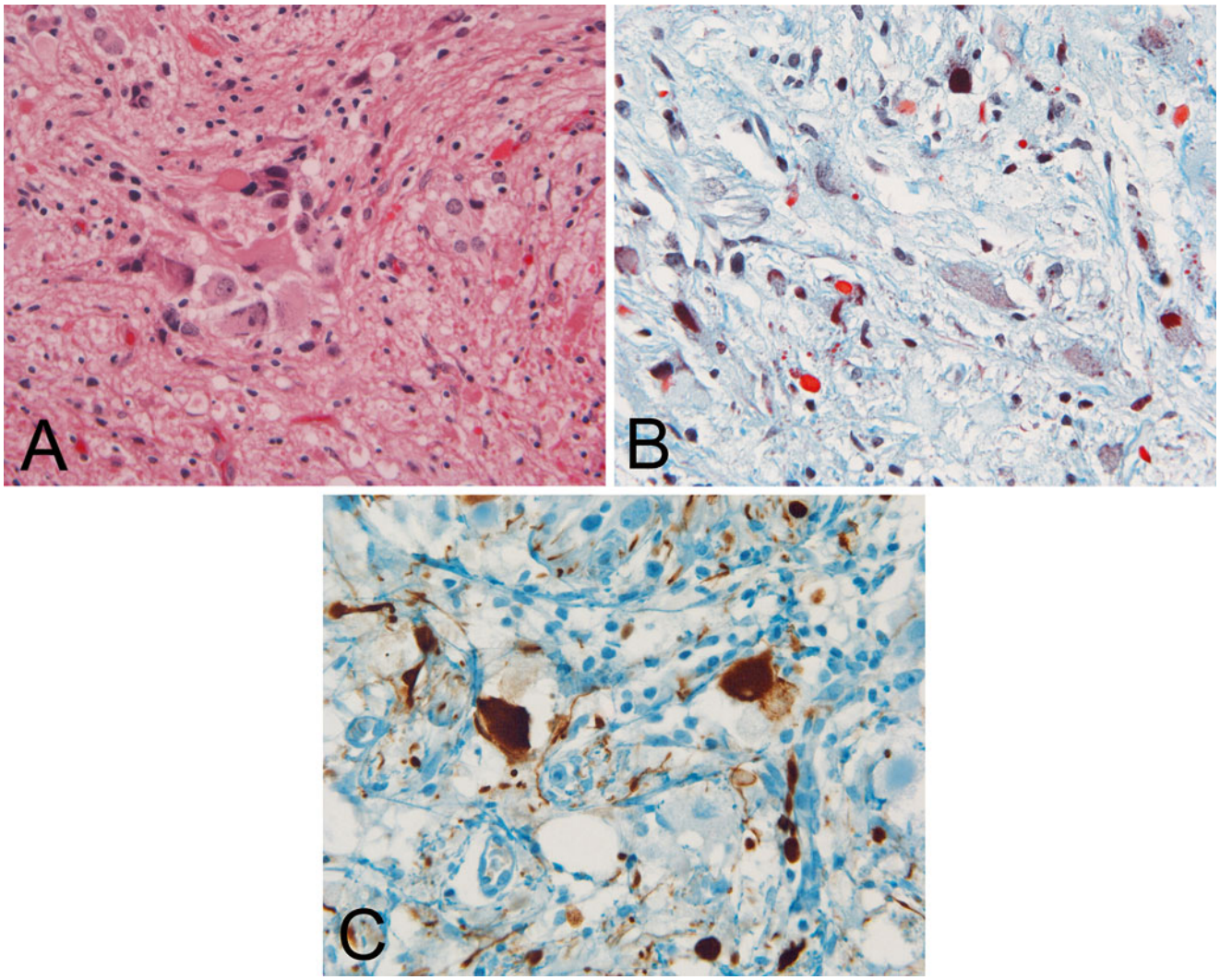

Fig. 6.22 Desmoplastic infantile ganglioglioma. (**a**) Note the large ganglionic cells cluster surrounded by a fibrillary component containing collagen fibers. (**b**) Note the ganglionic cells standing out in the collagenous background as demonstrated here with trichrome stain. (**c**) The neuronal component is well demonstrated by immunohistochemistry for neurofilament proteins

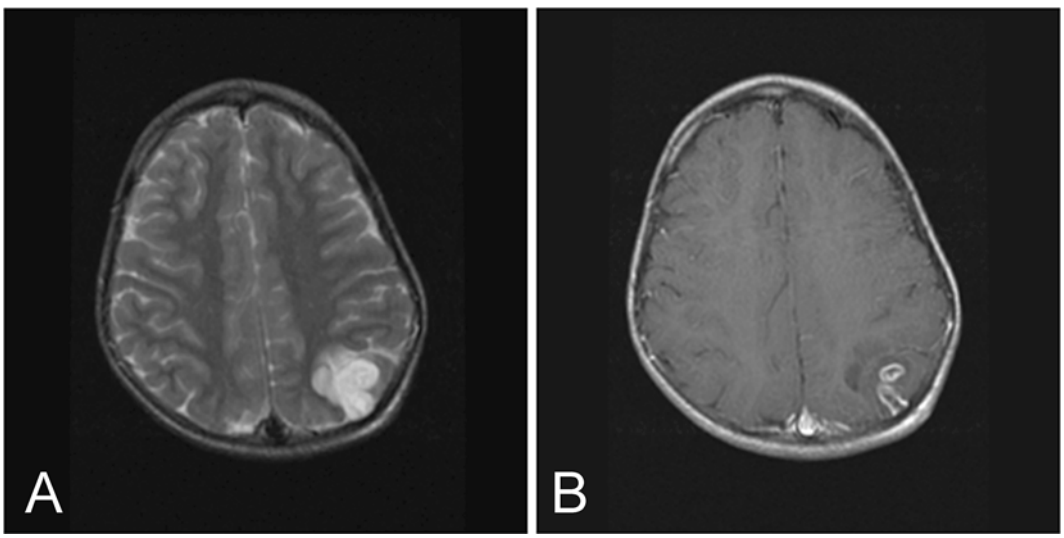

Fig. 6.23 MR-dysembryoplastic neuroepithelial tumor. (**a**) Axial FSE-T2W MR image demonstrates a cortically based, hyperintense mass in the left parietal lobe. (**b**) Axial post-contrast T1W MR image shows the tumor has focal enhancement. Only minimal edema is present around the tumor (10-year- old male). Note that the tumor illustrated here arises in an unusual location for this type of tumor

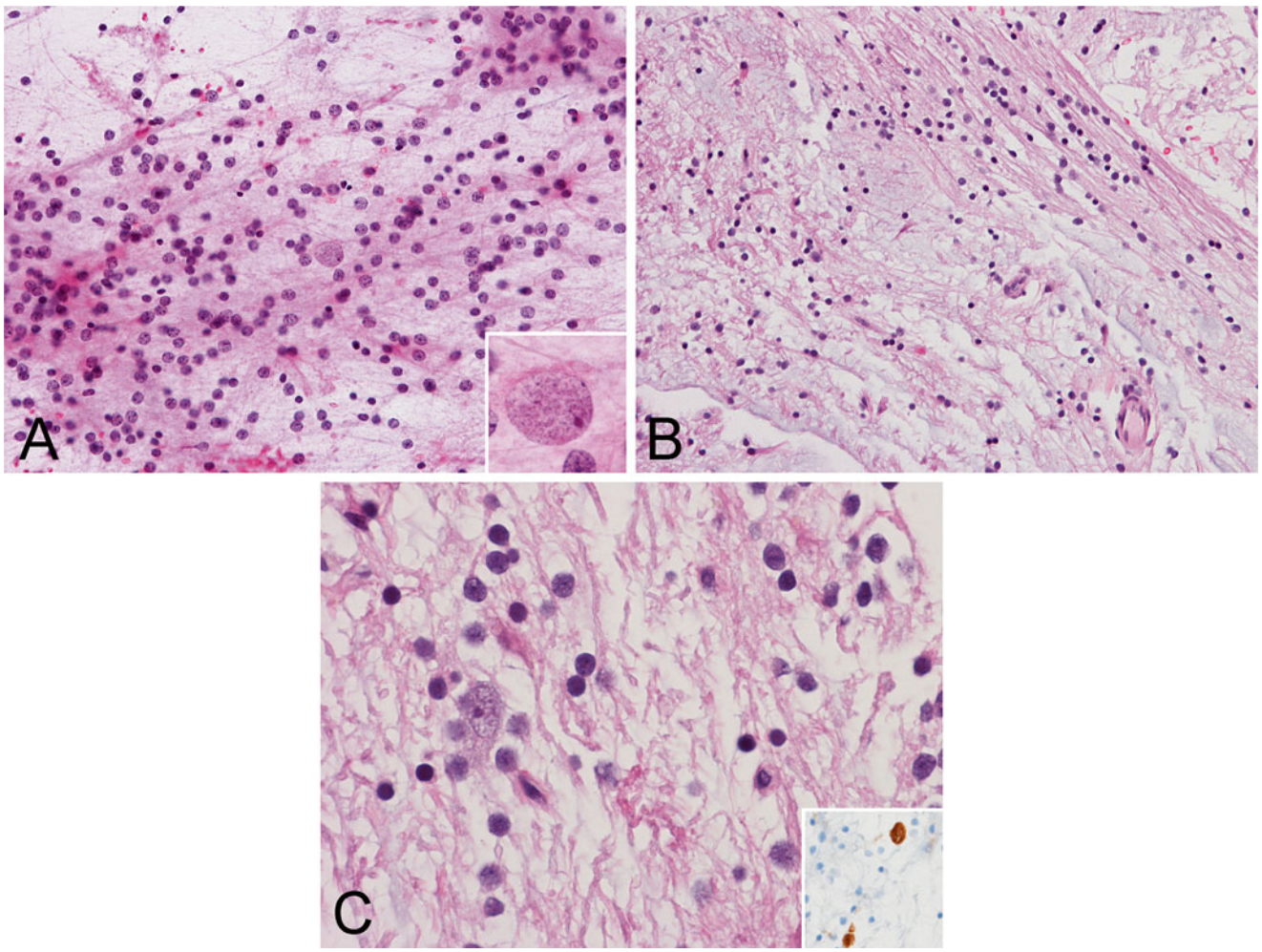

Fig. 6.24 Dysembryoplastic neuroepithelial tumor. (**a**) Cytologic preparation shows a meshwork of fine fibrillary neuropil-like processes. A naked nucleus from a neuronal cell is present and appears "floating" in the fibrillary background (inset). (**b**) This image is obtained from an area with substantial mucoid changes. (**c**) A ganglionic cell is shown here. Often these neurons are low in number but well demonstrated by immunohistochemistry to neuronal markers such as neurofilament proteins (Inset)

Imaging findings: This tumor typically presents as a well-circumscribed cortically based lesion without mass effect or peritumoral edema (Fig. 6.23). The size can vary from subcentimeter to several centimeters. These tumors are isointense or hypointense on T1-weighted images and hyperintense on T2-weighted images. A pseudocystic or multicystic appearance may be seen. If the tumor enhances the enhancement pattern is nodular [170].

Macroscopic pathology and histopathology: Surgical specimens of DNET typically consist of soft mucoid fragments. Cytologic preparation and frozen section would often demonstrate a mucoid background with small round, oligodendroglial-like cells and occasional neurons (Fig. 6.24). It should be noted that the amount of mucoid changes can be quite variable. The simple form of DNET contains the "specific glioneuronal element" featured by columnar alignment of small, oligodendrocyte-like cells along bundled axons and delicate capillaries in a mucoid background. Microcyst formation is common in cases that are markedly mucoid. In addition to the "specific glioneuronal element" the complex form of DNET contains sharply delineated nodular glial proliferations reminiscent of pilocytic astrocytoma, astrocytoma, oligodendroglioma or oligoastrocytoma. Cortical dysplasia can be found in the cortex surrounding the tumor.

Molecular pathology and immunohistochemistry: Neuronal cells are positive for CD34 in about 30 % of cases and *BRAF* (V600E) mutation has been demonstrated in about 25 % of the cases [171].

Papillary Glioneuronal Tumor

Papillary glioneuronal tumor (WHO grade I) is an uncommon tumor of young adult and adolescents that is uncommon in children and infants. It is typically seen in the cerebral hemispheres particularly the temporal lobe and the typical manifestation is seizure and headache. In the small number of reported cases, these tumors occur as cystic periventricular

lesion with mural nodules, enhancing borders, and septations [172, 173]. The tumor can be solid or cystic and shows the typical biphasic architecture. Histologically, hyalinized blood vessels form the backbone of the pseudopapillary architecture that is covered by a single or pseudostratified layer of small, cuboidal cells that has scant cytoplasm and round nuclei. In between the papillary structures are solid sheets of oligodendrogliocyte-like or neurocytic clear cells, medium sized "ganglioid" neurons, and large ganglionic cells in variable proportions. Minigemistocytes are occasionally present in the solid interpapillary areas. Rosenthal material and eosinophilic granular bodies can be found at the periphery of the tumor where they interface with the surrounding parenchyma. Perivascular glial cells are strongly positive for GFAP and Olig2. Solid areas are positive for synaptophysin and NeuN, but only larger ganglion-like cells are positive for neurofilament proteins. Microvascular proliferation and necrosis are generally absent. Mutations of *IDH1* and *IDH2*, deletion of chromosome 1p and 19q are not identified [174].

Rosette-Forming Glioneuronal Tumor of the Fourth Ventricle

Rosette-forming glioneuronal tumor of the fourth ventricle (WHO grade I) is a recently recognized uncommon benign tumor [175]. The lesion presents as well-defined mass with heterogeneous enhancement in fourth ventricle with cystic and solid components, potentially with hemorrhage and calcifications [176, 177]. It is essentially a tumor of young adults. Occasional cases can be seen in adolescents but are rare in children and infants. Due to its location, hydrocephalus is a typical manifestation [177]. Histologically, these tumors are biphasic. The superficial features mimic dysembryoplastic neuroepithelial tumor with a pilocytic astrocytoma-like growth pattern [178]. The tumor contains perivascular pseudorosettes lined by delicate cells with delicate cell process radiating towards the vessel. In between these pseudorosettes are monotonous small neurocytic cells that form neurocytic rosettes characterized by a core of eosinophilic neuropils rimmed by neurocytic cells.

Central Neurocytoma and Cerebellar Liponeurocytoma

Central neurocytoma (WHO grade II) is commonly seen in young adults but uncommon in adolescents and children. They occur most frequently as intraventricular tumor in the lateral and/or third ventricle. Extraventricular tumors can occur. Central neurocytoma present as a well marginated, lobulated mass, often with cystic changes and hemorrhage. On MR imaging the lesion is isointense on T1-weighted, hyperintense on T2-weighted sequences and shows inhomogeneous moderate enhancement [176, 179].

Histologically, neurocytoma is composed of monotonous round to polygonal cells with centrally located nuclei and formation of neuropil islands [180]. Calcifications are seen in half of the cases. With all these features considered, they can be mistaken as oligodendroglioma. The neuronal differentiation is best testified by strong and diffuse staining for synaptophysin in both tumor cells and neuropils. NeuN is often positive [181]. It should be noted that central neurocytoma can also be focally positive for Olig2 [182]. Ultrastructural examination shows a neuronal tumor with distinctive features [180].

Cerebellar liponeurocytoma is essentially a tumor of older adults. Histologically, it is similar to central neurocytoma, but a lipomatous component is present. Gene expression studies suggest that it is related to central neurocytoma [183].

Spinal Paraganglioma

This is a tumor of older adults and is rarely seen in the pediatric age group. They occur typically at the cauda equina and they are histologically identical to paraganglioma arising in other part of the body. On MR imaging, spinal paraganglioma appears as a well-marginated mass, isointense on T1-weighted images, iso to hyperintense on T2-weighted sequences, with avid enhancement following contrast administration. Hemorrhage may be seen within the mass [6].

Ependymal Family of Tumors

In the current WHO classification, ependymal tumors are found in grade I (subependymoma and myxopapillary ependymoma), grade II (ependymoma), and grade III (anaplastic ependymoma) categories. Together, they comprise one of the most frequent tumors in the pediatric age group.

Subependymoma

Subependymoma is a benign, slow growing glial neoplasm typically attached to the ventricular wall. It is almost unknown to the pediatric age group. Subependymoma is most often encountered in the fourth ventricle followed by the lateral ventricle typically as a well-circumscribed hypo to isointense on T1-weighted and relatively hyperintense on T2-weighted sequences mass without enhancement [176]. Histologically, it is characterized by clusters of bland appearing neoplastic glial cells embedded within a dense background of fibrillary matrix of glial processes reminiscent of bouquet of flowers scattered within a lawn. Microcystic changes are common. Because of their slow growing, subependymoma is an uncommon surgical specimen but they can present as incidental finding in autopsy.

Ependymoma and Anaplastic Ependymoma

Definition: Ependymoma (WHO grade II) and anaplastic ependymoma (WHO grade III) are tumors with phenotypic features of ependymal cells and are typically found in areas with ependymal cells. While ependymoma is slow-growing and indolent, anaplastic ependymoma is aggressive.

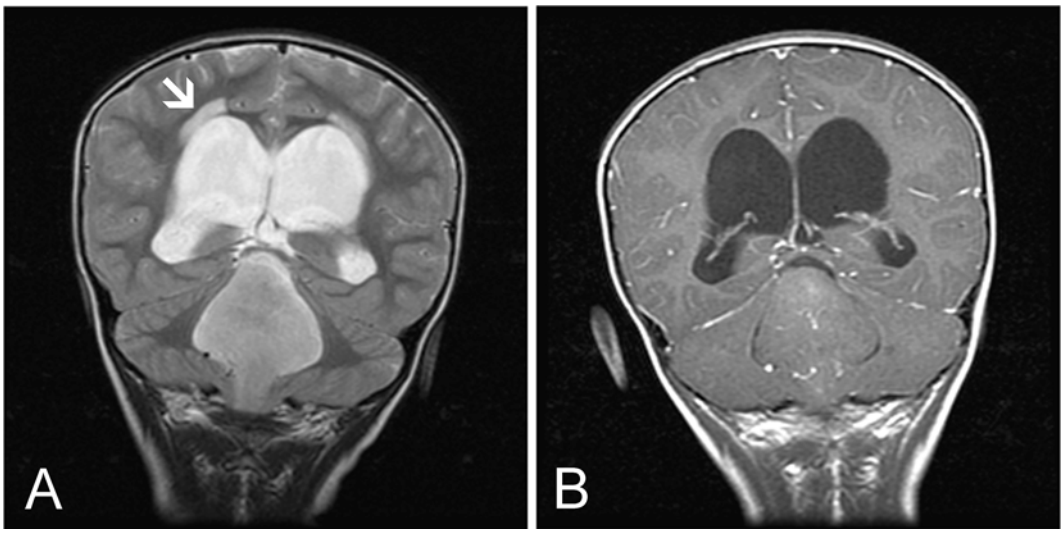

Fig. 6.25 MR-ependymoma. (**a**) Coronal FSE-T2W MR image demonstrates a large, well-demarcated mass of intermediate to high signal intensity that filled and dilated the fourth ventricle causing hydrocephalus and CSF edema (*arrow*). (**b**) Coronal T1W post-contrast MR image show minimal enhancement of the tumor (5-year-old male)

Incidence: Ependymoma is a childhood tumor and comprises up to 6–12 % of all pediatric intracranial tumors and up to 30 % of intracranial tumors in children younger than 3 years old. In contrast to those arising in adult patients, pediatric ependymomas and anaplastic ependymomas occur more commonly in the posterior fossa than in spinal cord. Interestingly, rare congenital cases have been described [8].

Clinical features: With its typical association with the ventricular lining and involvement of the fourth ventricle, symptoms are typically caused by hydrocephalus and increased intracranial pressure. Head enlargement secondary to hydrocephalus can be seen in patients under 2 years of age. Tumors arising in the posterior fossa can also cause cerebellar ataxia, visual disturbance, and other symptoms. As surgical resection remains the mainstay of treatment for ependymoma, correct recognition of these entities particularly during intraoperative consultation is crucial.

Imaging findings: Ependymoma in younger children occurs most frequently in the posterior fossa as a well-circumscribed intraventricular mass with variable enhancement. Associated ventricular obstruction and hydrocephalus are common. This tumor commonly demonstrates cystic change and calcification. Intraventricular ependymomas may insinuate and even exit through the foramina of Luschka and Magenti. Spinal dissemination may occur. Intratumoral hemorrhage can rapidly expand the tumor leading to compression of the brain stem that requires urgent neurosurgical intervention. The tumor reveals hypo to isointense signal characteristics on T1-weighted imaging and iso to hyperintense signal on T2-weighted sequences (Fig. 6.25). The presence of calcifications and hemorrhage is associated with "blooming artifact" on MRI while both are readily demonstrated on CT [176, 184]. Ependymomas in older children or young adults are often supratentorial. Supratentorial tumors may be intraventricular or intraparenchymal. While they share common imaging features with infratentorial ependymomas, they tend to be larger in size [184].

Macroscopic pathology and histopathology: These tumors can occur in any location along the ventricular lining. Rare extraneural ependymoma can be found in the sacrococcygeal area where the filum inserts. When compared to diffuse astrocytomas, ependymomas are well circumscribed. Necrosis and hemorrhage are uncommon. Ependymomas can also fill the fourth ventricle and extend through the foramina of Luschka and Magendie into the subarachnoid space. Both ependymoma and anaplastic ependymoma have a tendency for craniospinal dissemination through the CSF.

Classic ependymomas (Fig. 6.26) typically have a well-delineated interface with the surrounding parenchymal tissue. Ependymomas are characterized by a moderately cellular proliferation with small to moderately sized, monotonous, nuclei with "salt and pepper" speckling of the chromatin and small nucleoli. Mitotic activities are not readily seen. These cells typically arrange in a perivascular pseudorosettes around a blood vessel associated with a signature paucinuclear zone around the blood vessel.

In addition, true ependymal rosettes or ependymal canals featured by ependymal cells in circular arrangement forming a lumen can be seen but are not common features. Focal papillary changes can also be seen (see below). Secondary changes including myxoid background, calcifications, hemorrhage, and hyalinization of blood vessels can also occur.

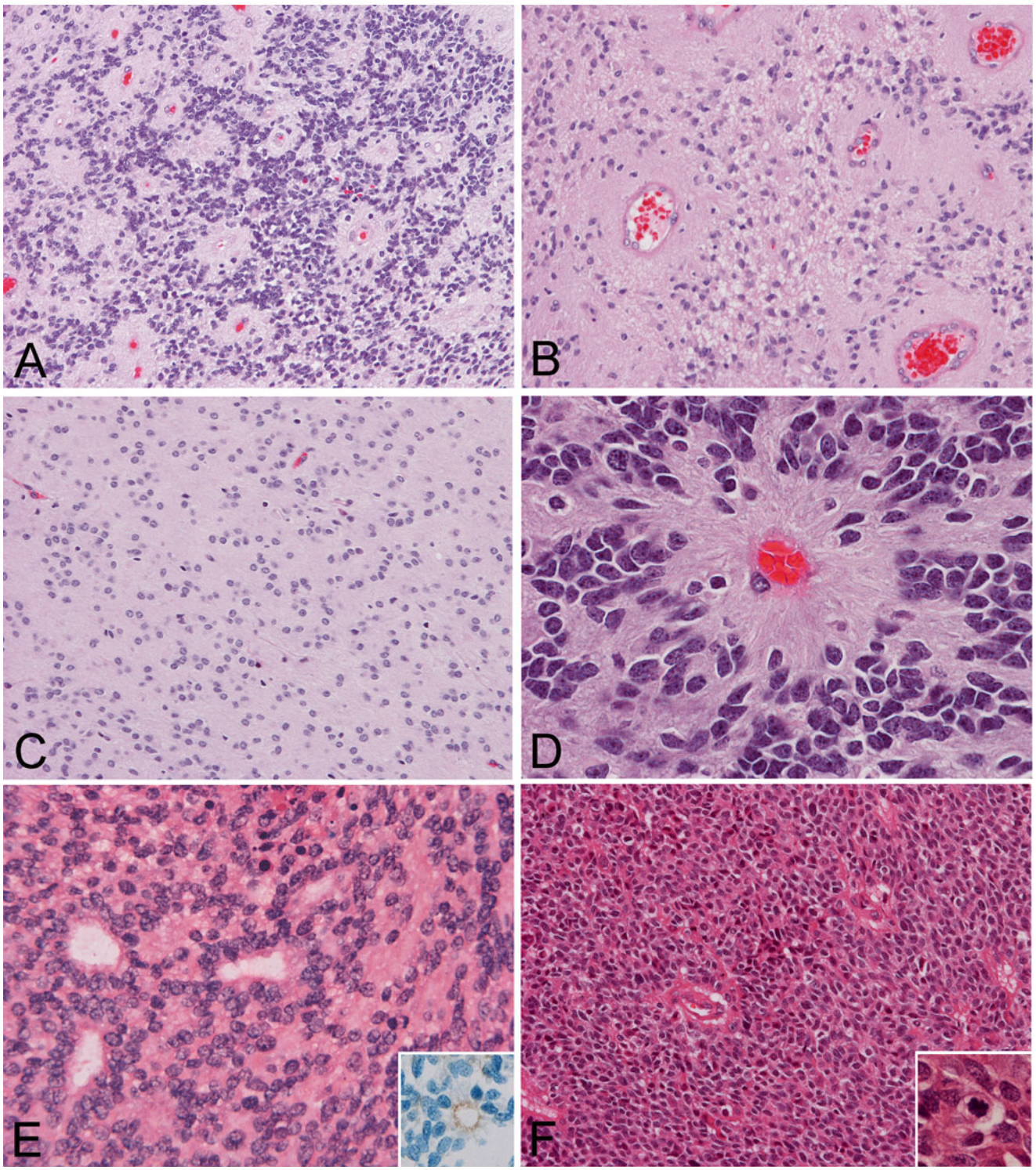

Fig. 6.26 Ependymoma: (**a**) and (**b**) show two ependymomas with significant variation in cellularity. Note that the perivascular pseudorosettes can be well appreciated. (**c**) is obtained from the same case as (**b**) in a location where perivascular pseudorosettes are subtle. (**d**) is a classic perivascular pseudorosettes in ependymoma. (**e**) shows ependymal canals in an ependymoma. These structures are reminiscent of the central canal of spinal cord. Immunohistochemistry for epithelial membrane antigen would demonstrate positive immunoreactivity at the luminal border of these canals (inset in (**e**)). (**f**) shows a cellular ependymoma. Note the increase in cellularity in comparison to classic ependymoma and increase in mitotic figure (Inset). Necrosis is not readily seen in this tumor

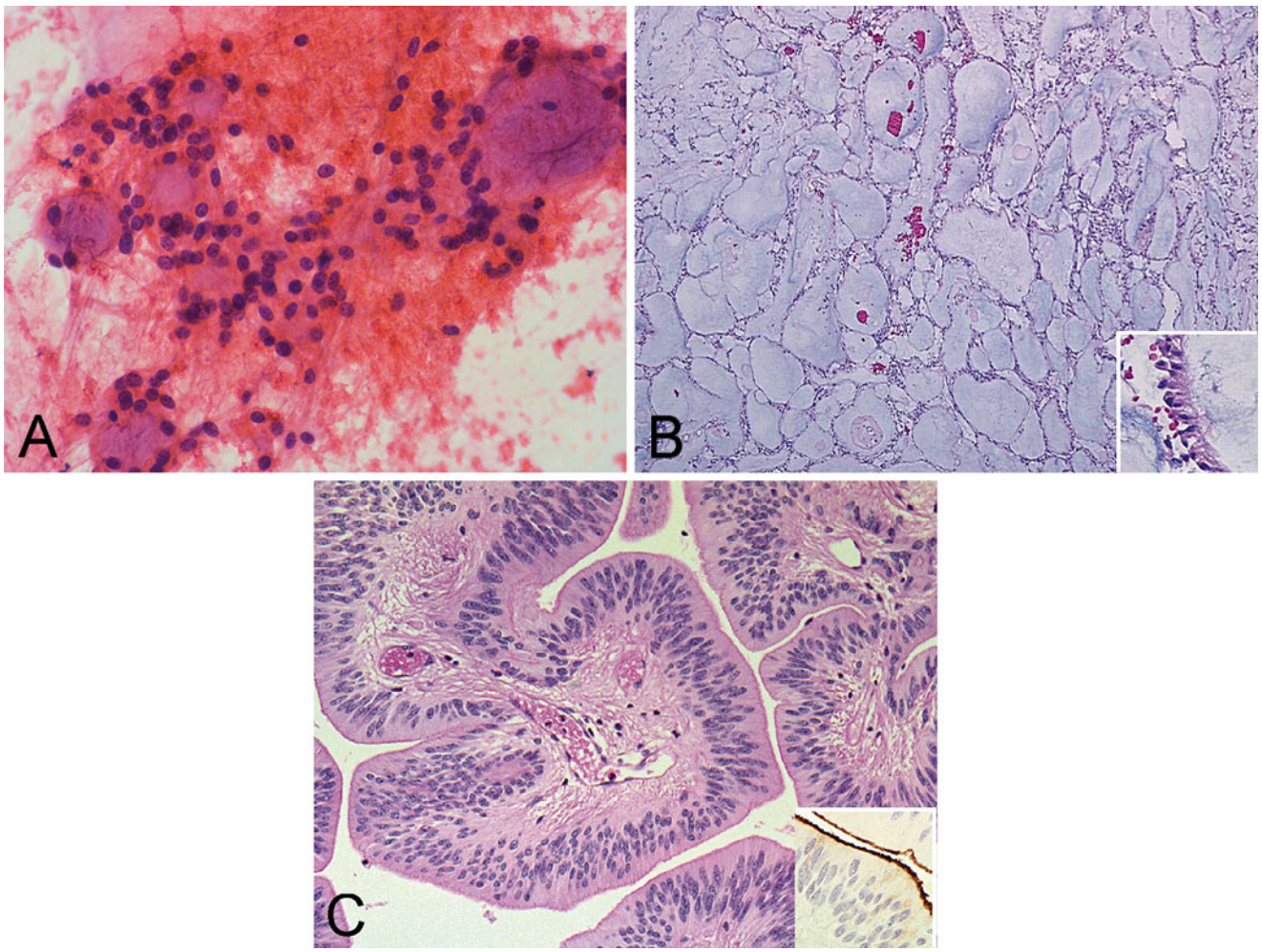

Fig. 6.27 Myxopapillary ependymoma and papillary ependymoma: (**a**) is a cytologic preparation of a myxopapillary ependymoma. Note the large globes of myxoid substance and the monotonous nuclei. (**b**) is myxopapillary ependymoma. Note the attenuated ependymal cells in inset. (**c**) is a papillary ependymoma. Note that there are no myxoid changes in comparison to myxopapillary ependymoma and no basement membrane in comparison to choroid plexus papilloma. EMA immunoreactivity can often be demonstrated at the luminal border but not cytoplasm of the lining cells (inset in (**c**))

Mitotic figures and necrosis are typically absent in ependymoma. However, occasional mitoses and occasional non-palisading, geographic foci of necrosis are allowed in ependymoma. It should also be noted that histologic features of ependymoma do not always faithfully reflect the biological potential of an ependymoma. Anaplastic ependymomas are characterized by cellular pleomorphism, brisk mitotic activity and high proliferative index, pseudopalisading necrosis, and microvascular proliferation.

Variants of ependymoma: *Cellular ependymoma* is characterized by a substantial increase in cellularity without increase in mitotic rate or other features of anaplastic changes; they are often extraventricular. While papillary formations can be identified focally in classical ependymoma, they are characteristically extensive in *papillary ependymoma* (Fig. 6.27c). The finger-like projections are covered by a layer of ependymal cells with characteristic fibrillary processes extending to the fibrovascular stalk and lacking a basement membrane, a critical feature that distinguishes these tumors from choroid plexus tumors. *Clear cell ependymoma* is often a supratentorial tumors of young patients and are associated with extraneural metastases and early recurrence [185]. *Tanycytic ependymoma* usually involve the spinal cord and are characterized by tumor cells arranged in poorly intertwined fascicles of variable width. Nuclei maintain the classic "salt and pepper" speckling of ependymoma and provide a diagnostically helpful feature.

Immunohistochemistry and electron microscopy: Ependymomas and anaplastic ependymomas are typically immunoreactive for GFAP. Cytokeratin can be focally positive but is usually not as extensive as choroid plexus

tumors. EMA is typically positive at the luminal surface of the ependymal canals or areas with papilla formation. Intracytoplasmic immunoreactivities are far less common and often appear as dot like immunoreactivity. Ependymomas are also positive for S100, vimentin, and rare cases express thyroid transcription factor-1 (TTF-1) [186]. Ki67 labeling index for ependymoma is low and in the range of 2–5 %; a higher level might be indicative of a more adverse biology.

Ependymal tumors possess highly diagnostic ultrastructural features including microvilli (9 + 2 cilia, with their basal blepharoplasts), zonulae adherents (long "zipper' like" and extensive junctional complexes), and luminal cilia. These electron microscopic features are particularly helpful in distinguishing clear cell ependymoma from mimicking tumors such as gliomas under some circumstances.

Differential diagnosis: Classic ependymoma is usually not a diagnostic challenge. However, the cellularity of an ependymoma may be high enough to suggest a small blue cell tumor such as medulloblastoma. On the other extreme, the cellularity may be low enough to suggest a pilocytic astrocytoma. A small intraoperative biopsy may become a diagnostic challenge particularly when it is obtained from the posterior fossa of a child. Clear cell ependymoma is particularly easy to be confused with other tumors with clear cell features such as oligodendroglioma and central neurocytoma. Tanycytic astrocytoma may be confused with pilocytic astrocytoma.

Molecular genetics: Although multiple genetic aberrations have been demonstrated in ependymoma, no definitive genetic pathways have been related to biological behavior of ependymomas [187].

Myxoependymoma

Myxopapillary ependymoma (WHO grade I) is seen predominantly in young adults and sometime children. It arises almost exclusively in the most distal part of the spinal cord including the conus medullaris, cauda equine, and filum terminale. Incomplete resection is associated with late recurrence and distant metastases. Back pain is a common presentation.

Radiographically, the tumor is typically a mass around the filum terminale that is isointense, occasionally hyperintense, to the spinal cord on T1-weighted sequences and hyperintense on T2-weighted sequences [6].

Grossly, myxoependymoma is well demarcated and does not invade surrounding structures. Histologically, tumors display a characteristic pattern with lobules of myxoid material lined by a thin and attenuated layer of ependymal cells that lacks nuclear atypia (Fig. 6.27a, b). These tumors are positive for GFAP, EMA, and S100 but negative for cytokeratin.

Miscellaneous Neuroepithelial Tumors and Tumor-Like Lesions

Astroblastoma

Astroblastoma is a rare glial tumor that has not been assigned a WHO grade. It occurs mainly in cerebral hemispheres of children, adolescents, and young adults and its biological behavior is variable. Radiographically, astroblastoma usually present as a large, supratentorial tumor with solid and cystic components. The solid component has been described as "bubbly" in appearance and is mostly isointense on T2-sequences with inhomogeneous enhancement [188]. The cystic component demonstrates peripheral enhancement. The tumor may calcify. Astroblastomas are well-circumscribed, non-calcifying, often cystic changes, and associated with little edema [189]. Histologically, they are well delineated and have a pushing margin. The tumor is characterized by perivascular arrangement of tumor cells similar to that of ependymoma. In contrast to ependymoma where fine perivascular cytoplasmic processes are seen, astroblastoma has stout columnar cells anchoring to the blood vessels with broad processes. The blood vessels are often sclerotic. The tumor cells are reactive for GFAP, S100, and vimentin. Limited reactivities for EMA [190] cytokeratin have also been reported. In general, tumors with low-grade histology have better prognosis than high-grade tumors. Comparative genomic hybridization [190] and cytogenetic studies [191] reveal change that are not typical for ependymoma and argue against astroblastoma being a variant of ependymoma.

Angiocentric Glioma

Angiocentric glioma (WHO grade I) [192] is a rare tumor that is mostly found in children, adolescents, and young adults. Tumors are located superficially in the cerebral hemispheres and on MRI appear as a well-defined, non-enhancing mass that is hypointense on T1-weighted images and hyperintense on T2-weighted sequences [193]. Epilepsy is the most common presentation. In general, surgical treatment is effective for these tumors although a rare case of recurrence and malignant progression in an adult [192] and a case with combined features of angiocentric glioma and glioblastoma [194] have been reported. Histologically, the tumor is characterized by mono- or multilayered sleeves of monomorphic, bipolar spindle cells with radial arrangement reminiscent of pseudorosettes of ependymomas. The tumor cells extend lengthwise along blood vessels and may aggregate beneath the pia-arachnoid in horizontal streams. Areas with solid growth may also be present. The nuclei are generally bland in appearance. Eosinophilic intracytoplasmic density abutting the nuclei can be seen and these structures are immunoreactive for EMA and these structures correspond ultrastructurally to microlumens.

Perivascular tumor cells are variably positive for GFAP. The major differential diagnosis is ependymoma. Cortical dysplasia has been reported to be associated with this entity [195]. The *IDH1 R132H* mutation has not been demonstrated in three cases studied [196].

Chordoid Glioma

Chordoid glioma (WHO grade II) is a tumor of adulthood and are rarely seen in adolescence. This is a slow growing, noninvasive glial tumor that occurs in the third ventricle. On imaging, the lesion has been described as a well defined, oblong mass located in the anterior third ventricle or hypothalamus. The tumor is usually isointense on T1W sequences, iso to slightly hyperintense on T2W sequences and exhibits uniform dense enhancement. Cystic changes may be observed in the center of the mass [197]. Histologically, it is composed of epithelioid GFAP-positive glial cells arranged in cords and islands embedded within a mucinous background. Lymphoplasmacytic infiltration is typical [197].

Hypothalamic Neuronal Hamartoma

The majority of cases occur as a mass hanging from the floor of the third ventricle. They may be sporadic or associated with syndromes such as Pallister-Hall (congenital hypothalamic hamartoblastoma syndrome). Precocious puberty is the most common clinical manifestation. On MRI the lesion presents as an exophytic or pedunculated, well-circumscribed, nonenhancing mass in the region of the tuber cinereum. It is isointense on T1-weighted sequences and slightly hyperintense on T2-weighted sequences [198]. Histologically, these hamartomas contain neurons of variable size similar to neurons in the adjacent normal tuber cinereum and hypothalamic nuclei. Typically lesions are composed of abnormally distributed but cytologically normal neurons and glia, including fibrillary astrocytes and oligodendrocytes [199].

Choroid Plexus Tumors

Definition: The choroid plexus give rise to choroid plexus papilloma (WHO grade I), atypical choroid plexus papilloma (WHO grade II), and choroid plexus carcinoma (WHO grade III).

Clinical features: Although choroid plexus tumor is an uncommon tumor, it is common in children and represents 10–20 % of tumors within the first year of life. Choroid plexus papilloma has been reported to be associated with Aicardi syndrome [200–202] and Li-Fraumeni syndrome [203]. In the pediatric age group, the lateral ventricles are the most common sites followed by the fourth ventricle and the cerebellar pontine angle. Due to their location, manifestations of CSF blockage and hydrocephalus are common. Choroid plexus papilloma, although benign, can produce drop metastases. Choroid plexus carcinoma is one of the very few carcinomas that occurs almost exclusively in children under 3 years of age and often results in malignant invasion and metastases. This entity has been associated with rhabdoid predisposition syndrome and proposed to represent AT/RT [204]. However, as the spectrum of INI1-deficient tumors is expanding [82, 83] such an association remains to be confirmed.

Imaging findings: On MRI (Fig. 6.28) choroid plexus papilloma typically appears as a well delineated, lobulated, intraventricular mass that is isointense on T1-weighted imaging,

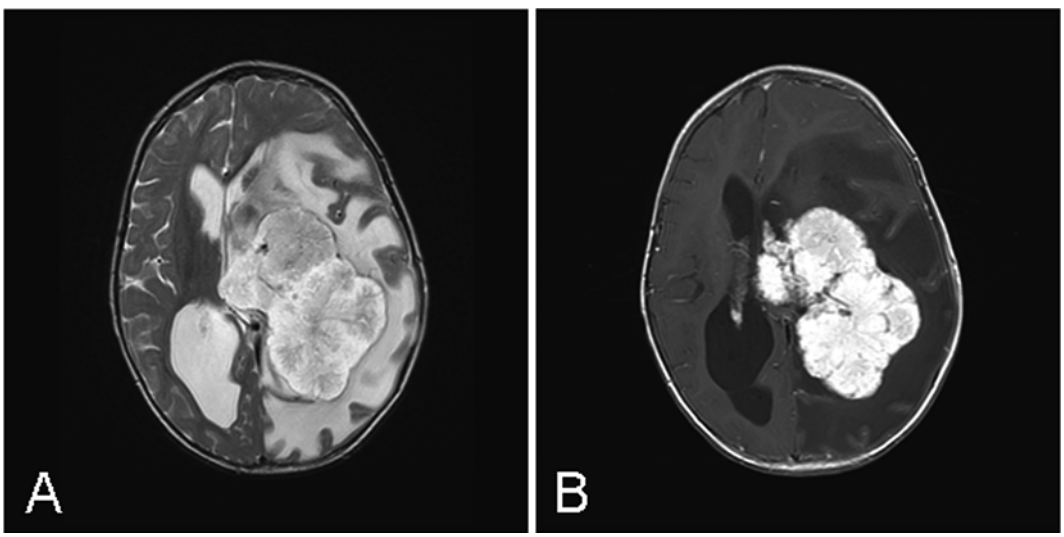

Fig. 6.28 MR-choroid plexus papilloma. (**a**) Axial FSE-T2W MR image demonstrates a large, well-defined mass arising from the left lateral ventricle. The tumor has mixed, intermediate intensity and increased signal intensity. (**b**) Axial post-contrast T1W MR image shows the mass has vivid enhancement. Significant edema is also present in the surrounding brain (15-month-old male)

iso- to hyperintense on T2-weighted sequences and enhances avidly on post-contrast imaging. Occasionally there may be T2-weighted hyperintensity in the surrounding brain parenchyma due to edema [176]. Leptomeningeal dissemination may occur [205].

Macroscopic pathology and histopathology: Choroid plexus papillomas are cauliflower-like exophytic growths that are well-circumscribed from the ventricular wall. Histologically, choroid plexus papilloma appears as papillary proliferation with a fibrovascular core lined by a single layer of monotonous cuboidal to columnar epithelium with a basement membrane. Mitotic figures are typically absent. Some tumors may have focal necrosis, increased cellularity, pleomorphism, brain invasion, and focal loss of papillary arrangement.

Atypical choroid plexus papilloma: On imaging, atypical choroid plexus papilloma is indistinguishable from typical choroid plexus papilloma. Mitotic figures are extremely rare in choroid plexus papilloma and when the mitotic rate is over two or more per ten randomly selected high powered fields, a diagnosis of atypical choroid plexus papilloma can be established [206]. Up to two of the following features may be present in atypical choroid plexus papilloma but their presence is not required for the diagnosis: increased cellularity, nuclear pleomorphism, areas of solid growth (blurring of the papillary pattern), and areas of necrosis.

Choroid plexus carcinoma: These are malignant tumor with at least four of the five following features: mitotic rate of over five per ten high powered fields, increased cellularity, increased nuclear pleomorphism, solid growth pattern (solid sheets of tumor cells), and necrosis. Diffuse brain invasion is also common, but it is not a required diagnostic criterion [206]. Spinal dissemination may be present at the time of diagnosis. On MRI studies, choroid plexus carcinoma may have more irregular margins than papillomas but they share the same signal characteristics. Therefore, MRI cannot reliably distinguish between these two choroid plexus malignancies [176].

Immunohistochemistry: Choroid plexus papillomas are positive for vimentin and podoplanin (D2-40) [207]. It should be noted that podoplanin is also positive in glioblastoma, and anaplastic astrocytomas. These tumors are positive for cytokeratins and often, but now always, positive for cytokeratin 7 and negative for cytokeratin 20. Choroid plexus papillomas are variably positive for S100, synaptophysin [208, 209], transthyretin, synaptophysin, and EMA. Although GFAP is negative in normal choroid plexus, it is positive in choroid plexus papilloma.

Differential diagnosis: In the pediatric age group, choroid plexus carcinoma needs to be distinguished from other high grade tumors such as medulloblastoma and AT/RT. Endolymphatic sac tumor is an uncommon tumor associated with von Hippel-Lindau syndrome and is mostly seen in adults. These tumors morphologically recapitulate the features of choroid plexus papilloma and are a close mimicker of choroid plexus papilloma. Rare pediatric cases have been reported [210, 211]. In contrast to choroid plexus papilloma, bone invasion is common in endolymphatic sac tumors. EAAT-1 and Kir7.1 are positive in choroid plexus papilloma but negative in endolymphatic sac tumors [212].

Tumor of the Pineal Region

Clinical presentation of different kinds of pineal lesion is very similar. About half of pineal parenchymal tumors occur in children [213]. It includes manifestations due to increase in intracranial pressure, changes in mental status, or due to compression of tectum and associated midbrain structures (Parinaud syndrome), brainstem, and cerebellum.

Pineocytoma

Pineocytoma (WHO grade I) occurs mainly in adults but it can also be seen in the pediatric age group. Pineocytoma usually presents as round, well-demarcated mass on imaging. Histologically, it is moderately cellular tumor consists of small, monotonous, mature cells with round to oval nuclei containing finely dispersed chromatin and without prominent nucleoli resembling pineocytes. Mitotic figures are typically rare or absent. One of the diagnostic features is short, conspicuous club shaped cytoplasmic processes that are further demonstrated by immunohistochemistry for neurofilament proteins or silver stains. Pineocytomatous rosette is another diagnostic feature. The tumor cells are strongly positive for synaptophysin, neurofilament proteins and variably for other neuronal markers and markers of photoreceptors such as S-antigen. Ultrastructural features of normal pineocytes can also be found in pineocytomas.

Pineal Parenchymal Tumor of Intermediate Differentiation

Depending on histologic features, pineal parenchymal tumor of intermediate differentiation (PPTID) is of WHO grade II or III. It is most common in young adults but it occurs in all ages including childhood. Dissemination through the CSF is limited to a small number of cases. On MRI, pineocytoma and pineal parenchymal tumor of intermediate differentiation share similar features. Both present as well demarcated masses, hypo to isointense on T1-weighted images and

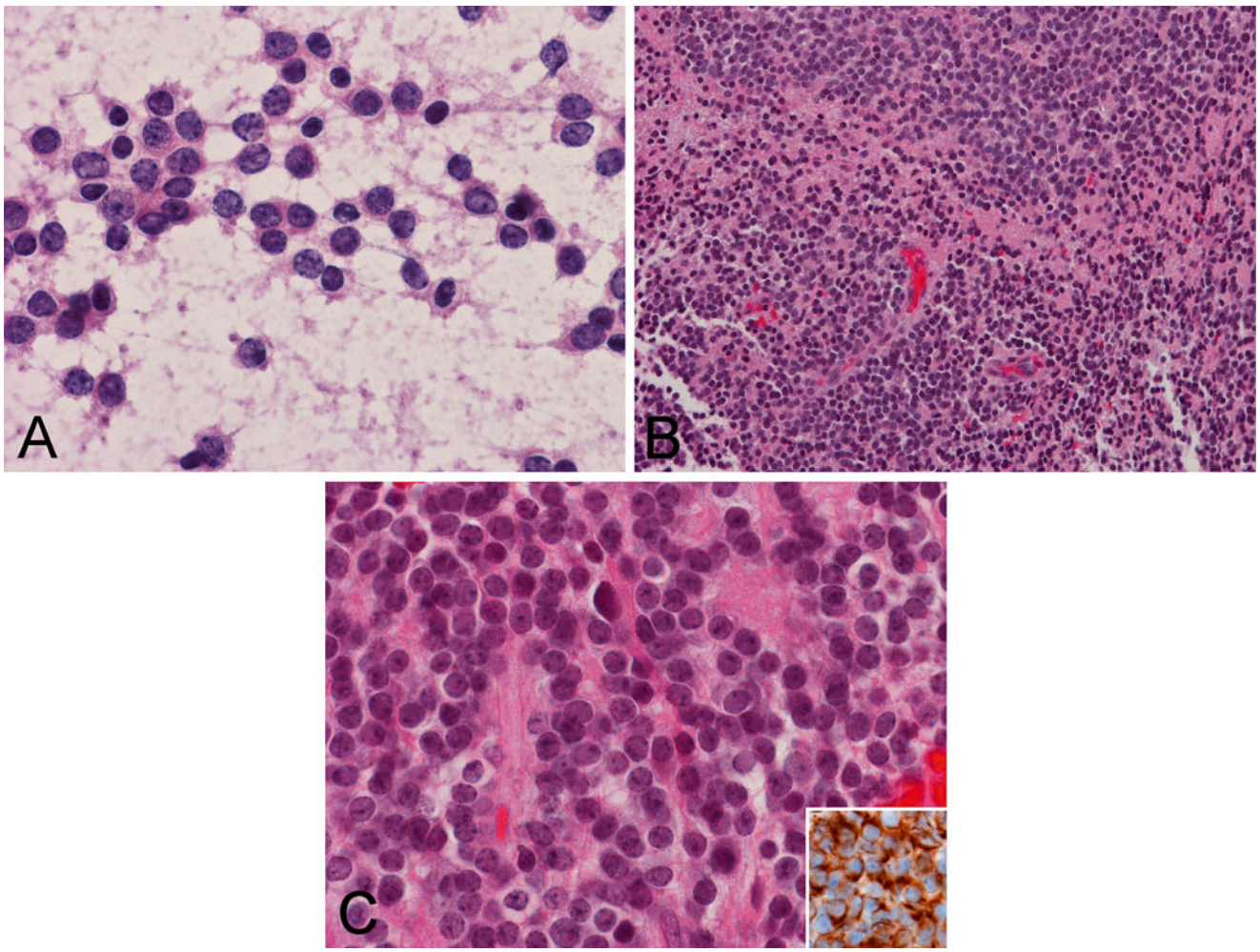

Fig. 6.29 Pineal parenchymal tumor of intermediate differentiation. What is shown here is a WHO grade II tumor. (**a**) On cytologic smear preparation, the tumor is composed of small blue cells with minimal cytoplasm. The nuclei have a "salt and pepper" appearance, a typical feature of neuroendocrine tumor. (**b**) The tumor cells are packed in solid sheets without specific pattern of arrangement. (**c**) Close view of the tumor showing monotonous, round nuclei with small islands of neuropils. The tumor cells are strongly positive for neurofilament proteins (Inset)

hyperintense on T2-weighted sequences. Homogenous, avid enhancement is seen on post-contrast imaging. Pineoblastoma presents as a large mass with signal characteristics similar to the more benign tumors of pineal tissue origin although enhancement may be in homogenous and areas of necrosis may be present. CSF dissemination may occur [214].

Histologically, it varies from neurocytoma-like solid sheets of tumor cells to lobulated arrangement with moderate to high cellularity (Fig. 6.29). There is mild to moderate atypia and low to moderate mitotic activity. Occasionally Homer Wright rosettes or giant tumor cells can be seen. The less aggressive tumors (WHO grade II) have mitoses less than six per ten high powered fields and strong neurofilament protein staining. Grade III tumors has either six or more mitoses per ten high powered fields or fewer than six mitoses but without immunoreactivity for neurofilament proteins [215].

Pineoblastoma

Pineoblastoma (WHO grade IV) represents the most primitive of pineal parenchymal tumor [216]. It is a highly aggressive primitive embryonal tumor that is seen mostly in the first two decades of life followed by young adults and older adults. Pineoblastoma can occur in patients with bilateral retinoblastoma as what has been designated "trilateral retinoblastoma" and these tumors are usually associated with *RB1* gene mutation [217]. Due to its aggressiveness interval between initial presentation and diagnosis can be short. On MRI, it is hypo- to isointense on T1-weighted images with heterogeneous enhancement (Fig. 6.30). In general, pineal germinoma and pineoblastoma has lower ADC value and higher Choline/NAA ratio than pineal glioma and teratoma [218]. Cranial spinal dissemination through CSF is not

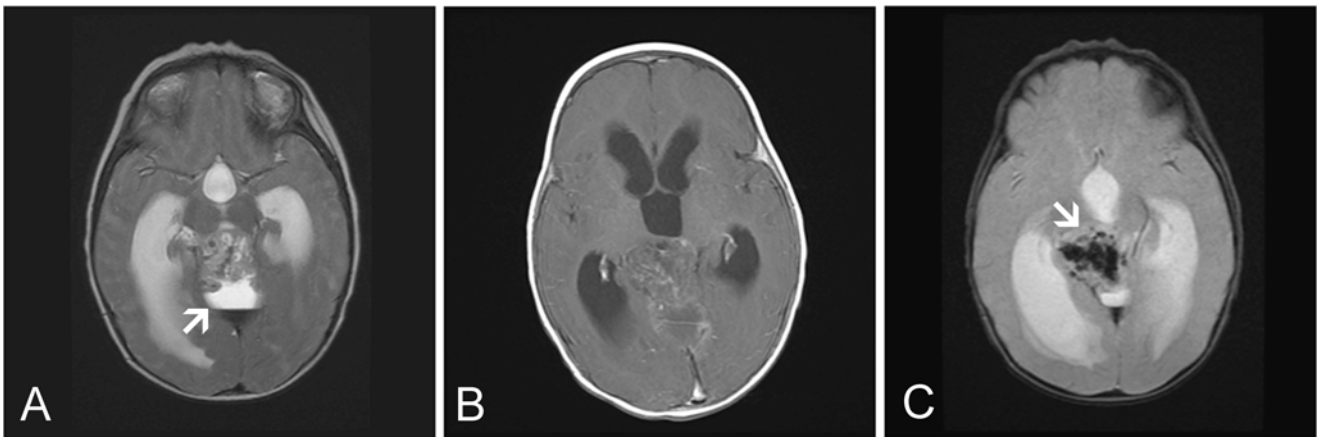

Fig. 6.30 MR-pineoblastoma. (**a**) Axial Sequence MR image shows a large solid and cystic pineal mass causing obstructive hydrocephalus. A fluid–fluid level (*arrow*) is likely due to hemorrhage in the posterior aspect of the mass. (**b**) Axial T1W post-contrast enhanced MR image shows the mass is poorly defined and has heterogeneous enhancement. (**c**) Axial GRE MR image shows additional areas of hemorrhage in the solid component of the mass (*arrow*) (8-month-old female)

uncommon. Surgical specimens are usually composed of fragments of friable tissue. Histologically, they are comparable to PNETs and medulloblastomas and are composed of solid sheets of small blue cells with minimal amount of cytoplasm. Although Homer Wright rosettes and Flexner-Wintersteiner rosettes may be present, pineocytomatous rosette is lacking. These tumors are mitotically active and often necrotic. These tumors are immunoreactive for synaptophysin and variably with S-100 antigen but non-reactive for neurofilament proteins [215]. The major differential diagnoses of pineoblastoma include germ cell tumor, atypical teratoid/rhabdoid tumor, pineal parenchymal tumor of intermediate differentiation, and medulloblastoma.

Papillary Tumor of the Pineal Region

Papillary tumor of the pineal region is a rare tumor of WHO grade II or grade III but the criteria for distinction are not well established. The small number of reported cases includes both adults and children. In the two reported pediatric cases with radiographic studies, these tumors had solid and cystic components, obstructed the third ventricle and demonstrated moderate, inhomogeneous enhancement after administration of gadolinium [219, 220]. These tumors generally present as a relatively large (2.5–4 cm) well-circumscribed mass. Histologically, it contains fibrovascular cores lined by amphophilic to eosinophilic columnar cells. Some tumors are mitotically active. Ependymal-like differentiation such as true rosette and ependymal tubules can be found in the more densely areas. Tumor cells can also be vacuolated and contain an eosinophilic PAS-positive cytoplasmic mass. Necrosis is common. In contrast to ependymoma, immunoreactivity for GFAP is usually focal. Immunohistochemistry for cytokeratins is more likely to be positive in the papillary areas. Ultrastructural studies have demonstrated features of ependymal differentiation [221, 222].

Tumor and Tumor-Like Lesions of the Sellar Region

The sellar region is a complex structure which includes the anterior and posterior pituitary, dura, and surrounding bone. Several tumors and tumor-like lesions can arise from this area. Craniopharyngioma and germ cell tumors are more common in the pediatric age group.

Tumor and Tumor-Like Condition of the Meninges

Meningeal space occupying lesion is uncommon in children. Dural or leptomeningeal mass and neoplastic meningitis are the most common presentations. The major categories [223] of this family include meningothelial proliferations, particularly meningiomatosis and meningioma, primary melanocytic tumors, benign mesenchymal tumors and sarcomas, poorly differentiated/embryonal tumors, inflammatory tumors, secondary and metastasis of primary tumor of the CNS. Meningioma is uncommon in the pediatric age group particularly in young children. When this is compounded by the rich diversity of meningiomas and other meningeal lesions, meningeal lesions in children pose diagnostic challenges.

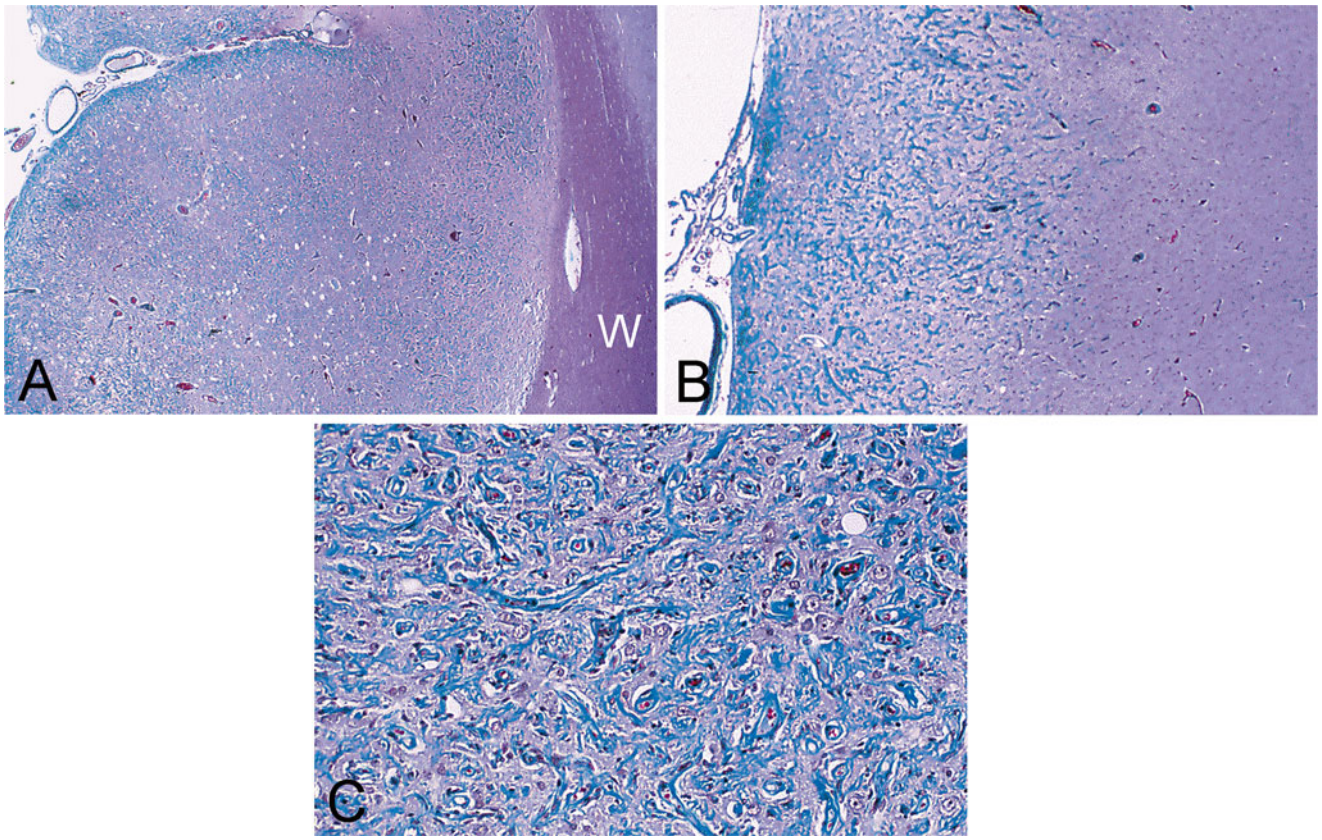

Fig. 6.31 Meningioangiomatosis. (**a**) Trichrome stain demonstrates an "en plaque" proliferation along the cerebral cortex that is well demarcated from the white matter (*W*). (**b**) At the periphery of the lesion, the lesion has an infiltrative margin that interfaces with the adjacent cortex. (**c**) The proliferation is composed of whorls of cells and the blood vessels in this particular case are markedly sclerotic (Trichrome stain)

Meningioangiomatosis

Meningioangiomatosis is believed to be hamartomatous, developmental, or reactive in nature. It typically presents as an "en plaque" leptomeningeal proliferation along the cerebral cortex with seizure as the most common manifestation [224, 225]. It can present in pediatric and adult patients; it can be sporadic or associated with neurofibromatosis type 2 (NF-2). Cases associated with NF-2 are often multifocal and clinically asymptomatic. A single case associated with sudden death has been reported [226]. In rare occasions, meningioma may arise from meningiomatosis. Although these tumors are intraparenchymal, they should not be viewed as brain invasion [227]. These tumors radiographically and pathologically mimic invasive meningiomas [227]. The meningioangiomatosis component in cases associated with meningioma appears to be neoplastic in nature in comparison to cases of pure meningioangiomatosis [227].

On MRI, meningioangiomatosis is usually plaque-like, hypo- to isointense on T1-weighted sequences, iso- to hyperintense on T2-weighted sequences, and demonstrates heterogeneous enhancement. Intratumoral calcifications are common. Gyriform hyperintensity seen on FLAIR sequences, reflects proliferating microvessels with perivascular cuffs of spindle-cell proliferation [228]. Due to its rarity meningioangiomatosis is often misdiagnosed as meningioma, vascular malformation, or other low grade tumors [228, 229].

Grossly, meningioangiomatosis appears as a firm plaque that is adhered to the brain. In contrast to meningiomas, they cannot be peeled off from the brain. An infiltrative interface with the brain parenchyma explains its firm adhesion (Fig. 6.31). Psammoma bodies can be seen. Histologically, meningiomatosis is characterized by a perivascular spindle-cell proliferation that is separated by a variable amount of brain parenchyma. In sporadic cases, vimentin is consistently positive in spindle cells but immunoreactivity for EMA and CD34 is variable [230]. The Ki67 labeling index is typically low [230, 231].

Meningioma

Meningiomas can be sporadic or associated with NF-2. These tumors are uncommon in adolescents and almost

unheard of during infancy. Seizure and increased intracranial pressure are the most frequent sign at presentation [232, 233]. However, meningiomas are the most common dural tumor in the pediatric age group. Pediatric meningiomas tend to be larger, intraparenchymal, and more aggressive [232, 233]. Clear cell meningioma (WHO grade II) and papillary meningioma (WHO grade III) are more common than the adult spectrum.

The imaging characteristics of the tumor in children are similar to those in adults. The tumor is usually large, well demarcated, isointense on T1-weighted sequences, with variable intensity on T2-sequences and avid enhancement. Meningiomas are usually extra-axial; a feature that may be reflected by the presence of a cleft of CSF on T2-weighted images. A small number of tumors are intra-axial or intraventricular. Radiation induced meningiomas may develop years after radiation of the brain [233].

The histologic grading is the same as in adult cases, pediatric meningiomas are predominantly leptomeningeal or intracerebral [234], with occasional association with meningiomatosis. These tumors should not be viewed as meningioma with brain invasion corresponding to WHO grade II [227]. Although a correlation of prognosis with WHO histologic grade exists, the correlation is not is strong as in adult cases. These tumors tend to occur in uncommon locations such as the spinal canal, posterior fossa, and ventricles [223]. Meningiomas, particularly those with high-grade histology, can pose a diagnostic challenge and must be distinguished form mimickers including other high grade tumors such as undifferentiated poorly differentiated and undifferentiated small blue cell tumor, secondary hematopoietic and histiocytic tumors, and primary CNS tumors such as AT/RT and gliosarcomas. Sarcomatoid meningioma should be carefully distinguished from bone/soft tissue sarcoma.

Leptomeningeal Tumor Dissemination ("Neoplastic Meningitis")

Widespread leptomeningeal dissemination of a primary CNS or systemic tumor typically would give rise to a meningitis-like clinical and neuroimaging picture. In some cases, a conspicuous primary tumor cannot be identified. Such dissemination includes meningeal gliomatosis, oligodendrogliomatosis, sarcomatosis, lymphomatosis, histiocytosis, and melanomatosis. In contrast to adult patients, carcinomatosis, other than those caused by choroid plexus carcinoma, is rare in pediatric patients. On the other hand, primary CNS tumors that tend to give rise to CSF dissemination including medulloblastoma/PNET, AT/RT, and less commonly ependymomas do not usually pose a diagnostic challenge as a tumor mass is almost always present.

Imaging studies play an important role in the diagnosis of disseminated tumor because a mass is not always present. The diagnosis of leptomeningeal dissemination of a primary CNS tumor requires post-contrast imaging showing enhancement of tumor coating the leptomeninges. In addition, drop metastatic lesions, manifested as enhancing nodules, can be seen along the spinal cord, predominantly along the cauda equine [235].

Miscellaneous Tumors and Tumor-Like Lesions

Intracranial germ cell tumor is a rather common tumor in the pediatric age group. They are most common in the pineal gland followed by the pituitary. A significant proportion of these tumors is seminoma dominated by a seminomatous component (Fig. 6.32). The pathologic features are similar to germ cell tumors arising in other locations (please see corresponding chapter for details). It should be noted that the pineal biopsy is usually small endoscopic specimens and granulomatous changes may mask the tumor cells (Fig. 6.32c).

Epidermoid cysts can be found in all age groups and they are most commonly seen in the cerebellopontine angle followed by para-pituitary area and other locations. A small number can be paraspinal or intraspinal and seen in the sacral region. Histology is identical to epidermoid cysts in other locations.

Chordoma and chondrosarcoma are typically tumor of adults. Other than patients with prior radiation, intracranial osteosarcoma is uncommon.

Langerhans histiocytosis is a common entity in the cranial bone in the pediatric age group but intra-axial ones are rare. Grois et al. have identified three main types: circumscribed granuloma in the meninges and choroid plexus; granulomas involving the brain parenchyma, usually as an extension from the meninges or Virchow-Robin spaces; and neurodegenerative lesions without granuloma that affects mainly the cerebellum and the brainstem [236, 237]. Isolated involvement of the CNS by juvenile granulomatosis is rare but systemic juvenile granulomatosis with involvement of the CNS is not uncommon.

Primary lymphoma of the CNS is extremely rare in the pediatric age group with non-Hodgkin B-cell lymphoma being most common. Patients with congenital or acquired immune deficiencies are associated with increased risk [238] of primary CNS lymphoma. The outcome seems to be better than in adult cases with an overall survival of 86 % [239]. Secondary involvement of the CNS by lymphoma and leukemia often takes the form of leptomeningeal involvement, which makes cytologic examination of the CSF an important diagnostic procedure.

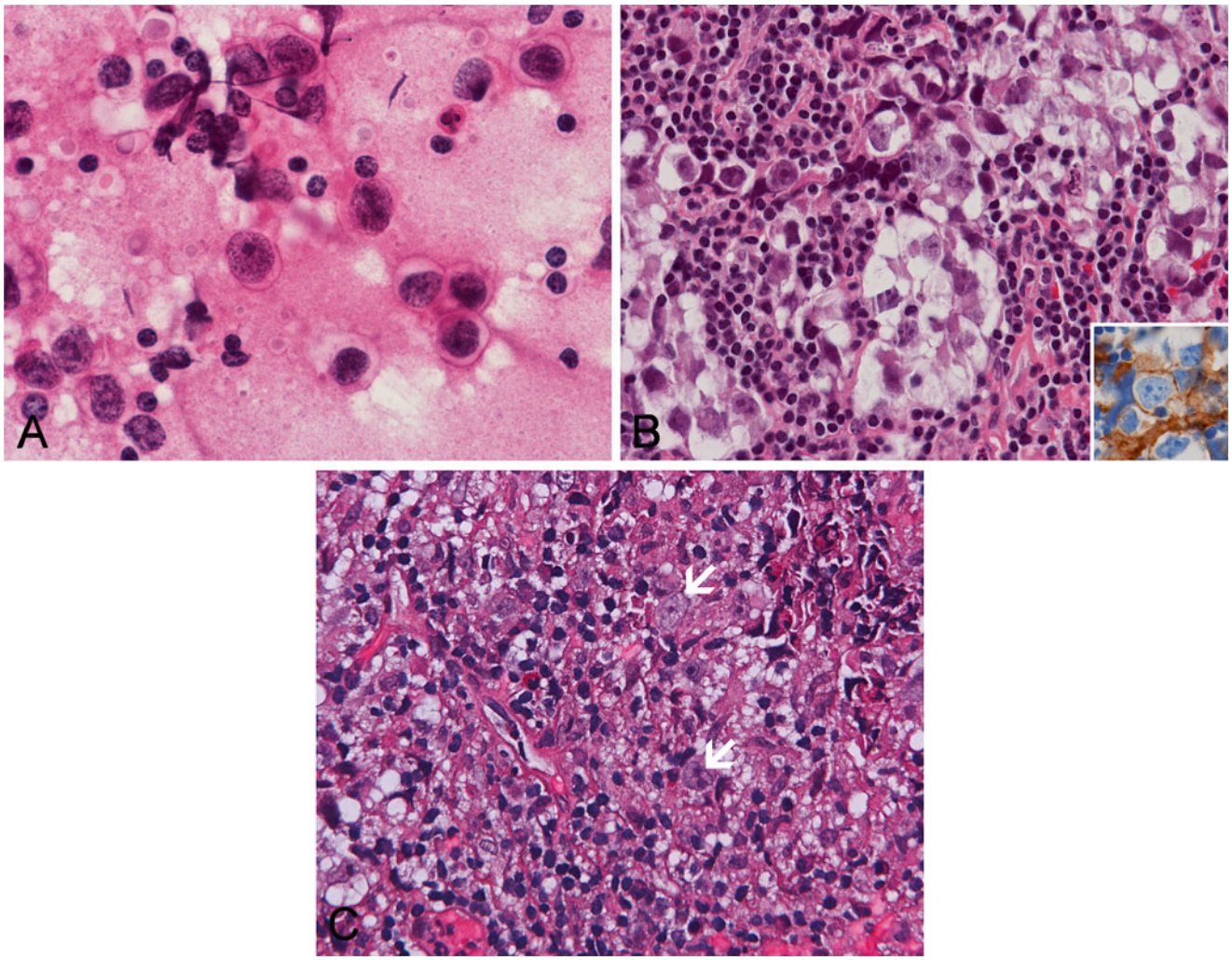

Fig. 6.32 Germinoma of pineal. (**a**) Smeared cytologic preparation shows a mixture of large tumor cells with large nuclei and prominent nucleoli admixed with small lymphocytes in the background. (**b**) A classic germinoma with small clusters of tumor cells embedded in a background of normal appearing lymphocytes. The tumor cells have large nuclei with prominent nucleoli and abundant, clear cytoplasm. The tumor cells show positive staining for placental alkaline phosphatase (inset). (**c**) Extensive granulomatous changes in this particular case raise the question of infection. The scant atypical cells (*arrows*) indicate germinoma with granulomatous changes

References

1. Louis DN, Ohgaki H, Wiesteler OD, Cavenee WK. WHO classification of tumours of the central nervous system. Lyon: International Agency for Research on Cancer; 2007.
2. Ries LAGSM, Gurney JG, Linet M, Tamra T, Young JL, Bunin GR, editors. Cancer incidence and survival among children and adolescents: United States SEER Program 1975–1995, National Cancer Institute, SEER Program. Bethesda, MD: National Institutes of Health; 1999. NIH Pub. No. 99-4649. Bethesda, MD, 1999.
3. Colosimo C, di Lella GM, Tartaglione T, et al. Neuroimaging of thalamic tumors in children. Childs Nerv Syst. 2002;18:426–39.
4. Cuccia V, Monges J. Thalamic tumors in children. Childs Nerv Syst. 1997;13:514–20. Discussion 521.
5. Rosemberg S, Fujiwara D. Epidemiology of pediatric tumors of the nervous system according to the WHO 2000 classification: a report of 1,195 cases from a single institution. Childs Nerv Syst. 2005;21:940–4.
6. Koeller KK, Rosenblum RS, Morrison AL. Neoplasms of the spinal cord and filum terminale: radiologic-pathologic correlation. Radiographics. 2000;20:1721–49.
7. Janisch W, Haas JF, Schreiber D, et al. Primary central nervous system tumors in stillborns and infants. Epidemiological considerations. J Neurooncol. 1984;2:113–6.
8. Rickert CH. Neuropathology and prognosis of foetal brain tumours. Acta Neuropathol. 1999;98:567–76.
9. Panigrahy A, Krieger MD, Gonzalez-Gomez I, et al. Quantitative short echo time 1H-MR spectroscopy of untreated pediatric brain tumors: preoperative diagnosis and characterization. AJNR Am J Neuroradiol. 2006;27:560–72.
10. Tzika AA, Vajapeyam S, Barnes PD. Multivoxel proton MR spectroscopy and hemodynamic MR imaging of childhood brain tumors: preliminary observations. AJNR Am J Neuroradiol. 1997;18:203–18.

11. Hwang JH, Egnaczyk GF, Ballard E, et al. Proton MR spectroscopic characteristics of pediatric pilocytic astrocytomas. AJNR Am J Neuroradiol. 1998;19:535–40.
12. Kan P, Liu JK, Hedlund G, et al. The role of diffusion-weighted magnetic resonance imaging in pediatric brain tumors. Childs Nerv Syst. 2006;22:1435–9.
13. Rumboldt Z, Camacho DL, Lake D, et al. Apparent diffusion coefficients for differentiation of cerebellar tumors in children. AJNR Am J Neuroradiol. 2006;27:1362–9.
14. Borja MJ, Plaza MJ, Altman N, et al. Conventional and advanced MRI features of pediatric intracranial tumors: supratentorial tumors. AJR Am J Roentgenol. 2013;200:W483–503.
15. Lefranc M, Monet P, Desenclos C, et al. Perfusion MRI as a neurosurgical tool for improved targeting in stereotactic tumor biopsies. Stereotact Funct Neurosurg. 2012;90:240–7.
16. Barajas Jr RF, Chang JS, Segal MR, et al. Differentiation of recurrent glioblastoma multiforme from radiation necrosis after external beam radiation therapy with dynamic susceptibility-weighted contrast-enhanced perfusion MR imaging. Radiology. 2009;253:486–96.
17. Liwnicz BH, Rubinstein LJ. The pathways of extraneural spread in metastasizing gliomas: a report of three cases and critical review of the literature. Hum Pathol. 1979;10:453–67.
18. Buhren J, Christoph AH, Buslei R, et al. Expression of the neurotrophin receptor p75NTR in medulloblastomas is correlated with distinct histological and clinical features: evidence for a medulloblastoma subtype derived from the external granule cell layer. J Neuropathol Exp Neurol. 2000;59:229–40.
19. Chelliah D, Mensah Sarfo-Poku C, Stea BD, et al. Medulloblastoma with extensive nodularity undergoing post-therapeutic maturation to a gangliocytoma: a case report and literature review. Pediatr Neurosurg. 2010;46:381–4.
20. Pillai S, Singhal A, Byrne AT, et al. Diffusion-weighted imaging and pathological correlation in pediatric medulloblastomas: "They are not always restricted!". Childs Nerv Syst. 2011;27:1407–11.
21. Koeller KK, Rushing EJ. From the archives of the AFIP: medulloblastoma: a comprehensive review with radiologic-pathologic correlation. Radiographics. 2003;23:1613–37.
22. Bourgouin PM, Tampieri D, Grahovac SZ, et al. CT and MR imaging findings in adults with cerebellar medulloblastoma: comparison with findings in children. AJR Am J Roentgenol. 1992;159:609–12.
23. Yeom KW, Mobley BC, Lober RM, et al. Distinctive MRI features of pediatric medulloblastoma subtypes. AJR Am J Roentgenol. 2013;200:895–903.
24. Koci TM, Chiang F, Mehringer CM, et al. Adult cerebellar medulloblastoma: imaging features with emphasis on MR findings. AJNR Am J Neuroradiol. 1993;14:929–39.
25. Fruehwald-Pallamar J, Puchner SB, Rossi A, et al. Magnetic resonance imaging spectrum of medulloblastoma. Neuroradiology. 2011;53:387–96.
26. Kalimo H, Paljarvi L, Ekfors T, et al. Pigmented primitive neuroectodermal tumor with multipotential differentiation in cerebellum (pigmented medullomyoblastoma). A case with light- and electron-microscopic, and immunohistochemical analysis. Pediatr Neurosci. 1987;13:188–95.
27. Gottardo NG, Hansford JR, McGlade JP, et al. Medulloblastoma down under 2013: a report from the third annual meeting of the International Medulloblastoma Working Group. Acta Neuropathol. 2014;127:189–201.
28. Taylor RE, Bailey CC, Robinson KJ, et al. Impact of radiotherapy parameters on outcome in the International Society of Paediatric Oncology/United Kingdom Children's Cancer Study Group PNET-3 study of preradiotherapy chemotherapy for M0-M1 medulloblastoma. Int J Radiat Oncol Biol Phys. 2004;58:1184–93.
29. Northcott PA, Korshunov A, Witt H, et al. Medulloblastoma comprises four distinct molecular variants. J Clin Oncol. 2011;29:1408–14.
30. Kool M, Korshunov A, Remke M, et al. Molecular subgroups of medulloblastoma: an international meta-analysis of transcriptome, genetic aberrations, and clinical data of WNT, SHH, Group 3, and Group 4 medulloblastomas. Acta Neuropathol. 2012;123:473–84.
31. Thompson MC, Fuller C, Hogg TL, et al. Genomics identifies medulloblastoma subgroups that are enriched for specific genetic alterations. J Clin Oncol. 2006;24:1924–31.
32. Ellison DW. Childhood medulloblastoma: novel approaches to the classification of a heterogeneous disease. Acta Neuropathol. 2010;120:305–16.
33. Katsetos CD, Del Valle L, Legido A, et al. On the neuronal/neuroblastic nature of medulloblastomas: a tribute to Pio del Rio Hortega and Moises Polak. Acta Neuropathol. 2003;105:1–13.
34. Maraziotis T, Perentes E, Karamitopoulou E, et al. Neuron-associated class III beta-tubulin isotype, retinal S-antigen, synaptophysin, and glial fibrillary acidic protein in human medulloblastomas: a clinicopathological analysis of 36 cases. Acta Neuropathol. 1992;84:355–63.
35. Korf HW, Korf B, Schachenmayr W, et al. Immunocytochemical demonstration of interphotoreceptor retinoid-binding protein in cerebellar medulloblastoma. Acta Neuropathol. 1992;83:482–7.
36. Ellison D. Classifying the medulloblastoma: insights from morphology and molecular genetics. Neuropathol Appl Neurobiol. 2002;28:257–82.
37. Schiffer D, Cavalla P, Chio A, et al. Tumor cell proliferation and apoptosis in medulloblastoma. Acta Neuropathol. 1994;87:362–70.
38. Buczynski J, Jesionek-Kupnicka D, Kordek R, et al. Apoptosis in non-astrocytic brain tumours in children. Folia Neuropathol. 2002;40:155–9.
39. Fattet S, Haberler C, Legoix P, et al. Beta-catenin status in paediatric medulloblastomas: correlation of immunohistochemical expression with mutational status, genetic profiles, and clinical characteristics. J Pathol. 2009;218:86–94.
40. Matakas F, Cervos-Navarro J, Gullotta F. The ultrastructure of medulloblastomas. Acta Neuropathol. 1970;16:271–84.
41. Packer RJ, Sutton LN, Elterman R, et al. Outcome for children with medulloblastoma treated with radiation and cisplatin, CCNU, and vincristine chemotherapy. J Neurosurg. 1994;81:690–8.
42. Fan X, Wang Y, Kratz J, et al. hTERT gene amplification and increased mRNA expression in central nervous system embryonal tumors. Am J Pathol. 2003;162:1763–9.
43. Fernandez-Teijeiro A, Betensky RA, Sturla LM, et al. Combining gene expression profiles and clinical parameters for risk stratification in medulloblastomas. J Clin Oncol. 2004;22:994–8.
44. Grotzer MA, Hogarty MD, Janss AJ, et al. MYC messenger RNA expression predicts survival outcome in childhood primitive neuroectodermal tumor/medulloblastoma. Clin Cancer Res. 2001;7:2425–33.
45. Grotzer MA, Janss AJ, Fung K, et al. TrkC expression predicts good clinical outcome in primitive neuroectodermal brain tumors. J Clin Oncol. 2000;18:1027–35.
46. Karch SB, Urich H. Medulloepithelioma: definition of an entity. J Neuropathol Exp Neurol. 1972;31:27–53.
47. Molloy PT, Yachnis AT, Rorke LB, et al. Central nervous system medulloepithelioma: a series of eight cases including two arising in the pons. J Neurosurg. 1996;84:430–6.
48. Priest JR, Williams GM, Manera R, et al. Ciliary body medulloepithelioma: four cases associated with pleuropulmonary blastoma—a report from the International Pleuropulmonary Blastoma Registry. Br J Ophthalmol. 2011;95:1001–5.
49. Donner LR, Teshima I. Peripheral medulloepithelioma: an immunohistochemical, ultrastructural, and cytogenetic study of a rare, chemotherapy-sensitive, pediatric tumor. Am J Surg Pathol. 2003;27:1008–12.
50. Bruggers CS, Welsh CT, Boyer RS, et al. Successful therapy in a child with a congenital peripheral medulloepithelioma and disruption of hindquarter development. J Pediatr Hematol Oncol. 1999;21:161–4.

51. Kleinman GM, Young RH, Scully RE. Primary neuroectodermal tumors of the ovary: a report of 25 cases. Am J Surg Pathol. 1993;17:764–78.
52. Michael H, Hull MT, Ulbright TM, et al. Primitive neuroectodermal tumors arising in testicular germ cell neoplasms. Am J Surg Pathol. 1997;21:896–904.
53. Davies RP, Lee CS. Medulloepithelioma: MRI appearances. Australas Radiol. 1988;32:503–5.
54. Auer RN, Becker LE. Cerebral medulloepithelioma with bone, cartilage, and striated muscle. Light microscopic and immunohistochemical study. J Neuropathol Exp Neurol. 1983;42:256–67.
55. Scheithauer BW, Rubinstein LJ. Cerebral medulloepithelioma. Report of a case with multiple divergent neuroepithelial differentiation. Childs Brain. 1979;5:62–71.
56. Sharma MC, Mahapatra AK, Gaikwad S, et al. Pigmented medulloepithelioma: report of a case and review of the literature. Childs Nerv Syst. 1998;14:74–8.
57. Troost D, Jansen GH, Dingemans KP. Cerebral medulloepithelioma: electron microscopy and immunohistochemistry. Acta Neuropathol. 1990;80:103–7.
58. Korshunov A, Sturm D, Ryzhova M, et al. Embryonal tumor with abundant neuropil and true rosettes (ETANTR), ependymoblastoma, and medulloepithelioma share molecular similarity and comprise a single clinicopathological entity. Acta Neuropathol. 2013;128(2):279–89.
59. Khoddami M, Becker LE. Immunohistochemistry of medulloepithelioma and neural tube. Pediatr Pathol Lab Med. 1997;17:913–25.
60. Caccamo DV, Herman MM, Rubinstein LJ. An immunohistochemical study of the primitive and maturing elements of human cerebral medulloepitheliomas. Acta Neuropathol. 1989;79:248–54.
61. Korshunov A, Ryzhova M, Jones DT, et al. LIN28A immunoreactivity is a potent diagnostic marker of embryonal tumor with multilayered rosettes (ETMR). Acta Neuropathol. 2012;124:875–81.
62. Horten BC, Rubinstein LJ. Primary cerebral neuroblastoma. A clinicopathological study of 35 cases. Brain. 1976;99:735–56.
63. Gould VE, Jansson DS, Molenaar WM, et al. Primitive neuroectodermal tumors of the central nervous system. Patterns of expression of neuroendocrine markers, and all classes of intermediate filament proteins. Lab Invest. 1990;62:498–509.
64. Rhodes RH, Cole M, Takaoka Y, et al. Intraventricular cerebral neuroblastoma. Analysis of subtypes and comparison with hemispheric neuroblastoma. Arch Pathol Lab Med. 1994;118:897–911.
65. McCabe MG, Ichimura K, Liu L, et al. High-resolution array-based comparative genomic hybridization of medulloblastomas and supratentorial primitive neuroectodermal tumors. J Neuropathol Exp Neurol. 2006;65:549–61.
66. Russo C, Pellarin M, Tingby O, et al. Comparative genomic hybridization in patients with supratentorial and infratentorial primitive neuroectodermal tumors. Cancer. 1999;86:331–9.
67. Lorentzen M, Hagerstrand I. Congenital ependymoblastoma. Acta Neuropathol. 1980;49:71–4.
68. Langford LA. The ultrastructure of the ependymoblastoma. Acta Neuropathol. 1986;71:136–41.
69. Cruz-Sanchez FF, Haustein J, Rossi ML, et al. Ependymoblastoma: a histological, immunohistological and ultrastructural study of five cases. Histopathology. 1988;12:17–27.
70. Ehret M, Jacobi G, Hey A, et al. Embryonal brain neoplasms in the neonatal period and early infancy. Clin Neuropathol. 1987; 6:218–23.
71. Mannoji H, Becker LE. Ependymal and choroid plexus tumors. Cytokeratin and GFAP expression. Cancer. 1988;61:1377–85.
72. Rickert CH, Paulus W. Epidemiology of central nervous system tumors in childhood and adolescence based on the new WHO classification. Childs Nerv Syst. 2001;17:503–11.
73. Biegel JA. Molecular genetics of atypical teratoid/rhabdoid tumor. Neurosurg Focus. 2006;20:E11.
74. Las Heras F, Pritzker KP. Adult variant of atypical teratoid/rhabdoid tumor: immunohistochemical and ultrastructural confirmation of a rare tumor in the sella tursica. Pathol Res Pract. 2010;206:788–91.
75. Raisanen J, Biegel JA, Hatanpaa KJ, et al. Chromosome 22q deletions in atypical teratoid/rhabdoid tumors in adults. Brain Pathol. 2005;15:23–8.
76. Makuria AT, Rushing EJ, McGrail KM, et al. Atypical teratoid rhabdoid tumor (AT/RT) in adults: review of four cases. J Neurooncol. 2008;88:321–30.
77. Takahashi K, Nishihara H, Katoh M, et al. Case of atypical teratoid/rhabdoid tumor in an adult, with long survival. Brain Tumor Pathol. 2011;28:71–6.
78. Samaras V, Stamatelli A, Samaras E, et al. Atypical teratoid/rhabdoid tumor of the central nervous system in an 18-year-old patient. Clin Neuropathol. 2009;28:1–10.
79. Meyers SP, Khademian ZP, Biegel JA, et al. Primary intracranial atypical teratoid/rhabdoid tumors of infancy and childhood: MRI features and patient outcomes. AJNR Am J Neuroradiol. 2006;27: 962–71.
80. Koral K, Gargan L, Bowers DC, et al. Imaging characteristics of atypical teratoid-rhabdoid tumor in children compared with medulloblastoma. AJR Am J Roentgenol. 2008;190:809–14.
81. Fleming AJ, Hukin J, Rassekh R, et al. Atypical teratoid rhabdoid tumors (ATRTs): the British Columbia's Children's Hospital's experience, 1986–2006. Brain Pathol. 2012;22:625–35.
82. Haberler C, Laggner U, Slavc I, et al. Immunohistochemical analysis of INI1 protein in malignant pediatric CNS tumors: Lack of INI1 in atypical teratoid/rhabdoid tumors and in a fraction of primitive neuroectodermal tumors without rhabdoid phenotype. Am J Surg Pathol. 2006;30:1462–8.
83. Bourdeaut F, Freneaux P, Thuille B, et al. hSNF5/INI1-deficient tumours and rhabdoid tumours are convergent but not fully overlapping entities. J Pathol. 2007;211:323–30.
84. Biegel JA, Rorke LB, Packer RJ, et al. Monosomy 22 in rhabdoid or atypical tumors of the brain. J Neurosurg. 1990;73:710–4.
85. Rorke LB, Packer RJ, Biegel JA. Central nervous system atypical teratoid/rhabdoid tumors of infancy and childhood: definition of an entity. J Neurosurg. 1996;85:56–65.
86. Roberts CW, Biegel JA. The role of SMARCB1/INI1 in development of rhabdoid tumor. Cancer Biol Ther. 2009;8:412–6.
87. Biegel JA, Zhou JY, Rorke LB, et al. Germ-line and acquired mutations of INI1 in atypical teratoid and rhabdoid tumors. Cancer Res. 1999;59:74–9.
88. Bruggers CS, Bleyl SB, Pysher T, et al. Clinicopathologic comparison of familial versus sporadic atypical teratoid/rhabdoid tumors (AT/RT) of the central nervous system. Pediatr Blood Cancer. 2011;56:1026–31.
89. Donner LR, Wainwright LM, Zhang F, et al. Mutation of the INI1 gene in composite rhabdoid tumor of the endometrium. Hum Pathol. 2007;38:935–9.
90. Perry A, Fuller CE, Judkins AR, et al. INI1 expression is retained in composite rhabdoid tumors, including rhabdoid meningiomas. Mod Pathol. 2005;18:951–8.
91. Wang W, Cote J, Xue Y, et al. Purification and biochemical heterogeneity of the mammalian SWI-SNF complex. Embo J. 1996; 15:5370–82.
92. Judkins AR, Burger PC, Hamilton RL, et al. INI1 protein expression distinguishes atypical teratoid/rhabdoid tumor from choroid plexus carcinoma. J Neuropathol Exp Neurol. 2005;64:391–7.
93. Judkins AR, Mauger J, Ht A, et al. Immunohistochemical analysis of hSNF5/INI1 in pediatric CNS neoplasms. Am J Surg Pathol. 2004;28:644–50.
94. Savage N, Linn D, McDonough C, et al. Molecularly confirmed primary malignant rhabdoid tumor of the urinary bladder: implications of accurate diagnosis. Ann Diagn Pathol. 2012;16:504–7.

95. Trobaugh-Lotrario AD, Finegold MJ, Feusner JH. Rhabdoid tumors of the liver: rare, aggressive, and poorly responsive to standard cytotoxic chemotherapy. Pediatr Blood Cancer. 2011;57:423–8.
96. Hollmann TJ, Hornick JL. INI1-deficient tumors: diagnostic features and molecular genetics. Am J Surg Pathol. 2011;35:e47–63.
97. Kreiger PA, Judkins AR, Russo PA, et al. Loss of INI1 expression defines a unique subset of pediatric undifferentiated soft tissue sarcomas. Mod Pathol. 2009;22:142–50.
98. Rieske P, Zakrzewska M, Piaskowski S, et al. Molecular heterogeneity of meningioma with INI1 mutation. Mol Pathol. 2003;56:299–301.
99. Schmitz U, Mueller W, Weber M, et al. INI1 mutations in meningiomas at a potential hotspot in exon 9. Br J Cancer. 2001;84:199–201.
100. Tsai CY, Wong TT, Lee YH, et al. Intact INI1 gene region with paradoxical loss of protein expression in AT/RT: implications for a possible novel mechanism associated with absence of INI1 protein immunoreactivity. Am J Surg Pathol. 2012;36:128–33.
101. Biggs PJ, Garen PD, Powers JM, et al. Malignant rhabdoid tumor of the central nervous system. Hum Pathol. 1987;18:332–7.
102. Burger PC, Yu IT, Tihan T, et al. Atypical teratoid/rhabdoid tumor of the central nervous system: a highly malignant tumor of infancy and childhood frequently mistaken for medulloblastoma: a Pediatric Oncology Group study. Am J Surg Pathol. 1998;22:1083–92.
103. Antonelli M, Cenacchi G, Modena P, et al. Ultrastructural evidence of ependymal differentiation in a genetically proven atypical teratoid/rhabdoid tumor. Childs Nerv Syst. 2009;25:1627–31.
104. Gessi M, Giangaspero F, Lauriola L, et al. Embryonal tumors with abundant neuropil and true rosettes: a distinctive CNS primitive neuroectodermal tumor. Am J Surg Pathol. 2009;33:211–7.
105. Dunham C, Sugo E, Tobias V, et al. Embryonal tumor with abundant neuropil and true rosettes (ETANTR): report of a case with prominent neurocytic differentiation. J Neurooncol. 2007;84:91–8.
106. Al-Hussaini M, Abuirmeileh N, Swaidan M, et al. Embryonal tumor with abundant neuropil and true rosettes: a report of three cases of a rare tumor, with an unusual case showing rhabdomyoblastic and melanocytic differentiation. Neuropathology. 2011;31:620–5.
107. Paulus W, Kleihues P. Genetic profiling of CNS tumors extends histological classification. Acta Neuropathol. 2010;120:269–70.
108. Neelima R, Easwer HV, Kapilamoorthy TR, et al. Embryonal tumor with multilayered rosettes: Two case reports with a review of the literature. Neurol India. 2012;60:96–9.
109. Schindler G, Capper D, Meyer J, et al. Analysis of BRAF V600E mutation in 1,320 nervous system tumors reveals high mutation frequencies in pleomorphic xanthoastrocytoma, ganglioglioma and extra-cerebellar pilocytic astrocytoma. Acta Neuropathol. 2011;121:397–405.
110. Rodriguez FJ, Perry A, Gutmann DH, et al. Gliomas in neurofibromatosis type 1: a clinicopathologic study of 100 patients. J Neuropathol Exp Neurol. 2008;67:240–9.
111. Burkhard C, Di Patre PL, Schuler D, et al. A population-based study of the incidence and survival rates in patients with pilocytic astrocytoma. J Neurosurg. 2003;98:1170–4.
112. Dirks PB, Jay V, Becker LE, et al. Development of anaplastic changes in low-grade astrocytomas of childhood. Neurosurgery. 1994;34:68–78.
113. Tomlinson FH, Scheithauer BW, Hayostek CJ, et al. The significance of atypia and histologic malignancy in pilocytic astrocytoma of the cerebellum: a clinicopathologic and flow cytometric study. J Child Neurol. 1994;9:301–10.
114. Fulham MJ, Melisi JW, Nishimiya J, et al. Neuroimaging of juvenile pilocytic astrocytomas: an enigma. Radiology. 1993;189:221–5.
115. Lee YY, Van Tassel P, Bruner JM, et al. Juvenile pilocytic astrocytomas: CT and MR characteristics. AJR Am J Roentgenol. 1989;152:1263–70.
116. Fisher PG, Breiter SN, Carson BS, et al. A clinicopathologic reappraisal of brain stem tumor classification. Identification of pilocystic astrocytoma and fibrillary astrocytoma as distinct entities. Cancer. 2000;89:1569–76.
117. Takeuchi H, Kubota T, Sato K, et al. Ultrastructure of capillary endothelium in pilocytic astrocytomas. Brain Tumor Pathol. 2004;21:23–6.
118. Perilongo G, Garre ML, Giangaspero F. Low-grade gliomas and leptomeningeal dissemination: a poorly understood phenomenon. Childs Nerv Syst. 2003;19:197–203.
119. Tihan T, Fisher PG, Kepner JL, et al. Pediatric astrocytomas with monomorphous pilomyxoid features and a less favorable outcome. J Neuropathol Exp Neurol. 1999;58:1061–8.
120. Fernandez C, Figarella-Branger D, Girard N, et al. Pilocytic astrocytomas in children: prognostic factors—a retrospective study of 80 cases. Neurosurgery. 2003;53:544–53. Discussion 554-545.
121. French PJ, Barlow A, Barlow P, et al. A case of pilomyxoid astrocytoma presenting with CSF rhinorrhoea in a 15-year-old. Br J Neurosurg. 2009;23:545–7.
122. Alimohamadi M, Bidabadi MS, Ayan Z, et al. Pilomyxoid astrocytoma with involvement of the sella turcica in an adolescent. J Clin Neurosci. 2009;16:1648–9.
123. Paraskevopoulos D, Patsalas I, Karkavelas G, et al. Pilomyxoid astrocytoma of the cervical spinal cord in a child with rapid progression into glioblastoma: case report and literature review. Childs Nerv Syst. 2011;27:313–21.
124. van der Wal EJ, Azzarelli B, Edwards-Brown M. Malignant transformation of a chiasmatic pilocytic astrocytoma in a patient with diencephalic syndrome. Pediatr Radiol. 2003;33:207–10.
125. Lee IH, Kim JH, Suh YL, et al. Imaging characteristics of pilomyxoid astrocytomas in comparison with pilocytic astrocytomas. Eur J Radiol. 2011;79:311–6.
126. Johnson MW, Eberhart CG, Perry A, et al. Spectrum of pilomyxoid astrocytomas: intermediate pilomyxoid tumors. Am J Surg Pathol. 2010;34:1783–91.
127. Jeon YK, Cheon JE, Kim SK, et al. Clinicopathological features and global genomic copy number alterations of pilomyxoid astrocytoma in the hypothalamus/optic pathway: comparative analysis with pilocytic astrocytoma using array-based comparative genomic hybridization. Mod Pathol. 2008;21:1345–56.
128. Amatya VJ, Akazawa R, Sumimoto Y, et al. Clinicopathological and immunohistochemical features of three pilomyxoid astrocytomas: comparative study with 11 pilocytic astrocytomas. Pathol Int. 2009;59:80–5.
129. Goldman JE, Corbin E. Rosenthal fibers contain ubiquitinated alpha B-crystallin. Am J Pathol. 1991;139:933–8.
130. Katsetos CD, Krishna L. Lobar pilocytic astrocytomas of the cerebral hemispheres: I. Diagnosis and nosology. Clin Neuropathol. 1994;13:295–305.
131. Machen SK, Prayson RA. Cyclin D1 and MIB-1 immunohistochemistry in pilocytic astrocytomas: a study of 48 cases. Hum Pathol. 1998;29:1511–6.
132. Matsumoto T, Fujii T, Yabe M, et al. MIB-1 and p53 immunocytochemistry for differentiating pilocytic astrocytomas and astrocytomas from anaplastic astrocytomas and glioblastomas in children and young adults. Histopathology. 1998;33:446–52.
133. Tihan T, Ersen A, Qaddoumi I, et al. Pathologic characteristics of pediatric intracranial pilocytic astrocytomas and their impact on outcome in 3 countries: a multi-institutional study. Am J Surg Pathol. 2012;36:43–55.
134. Lewis RA, Gerson LP, Axelson KA, et al. von Recklinghausen neurofibromatosis. II. Incidence of optic gliomata. Ophthalmology. 1984;91:929–35.
135. Fuller CE, Frankel B, Smith M, et al. Suprasellar monomorphous pilomyxoid neoplasm: an ultrastructural analysis. Clin Neuropathol. 2001;20:256–62.
136. Jeuken JW, Wesseling P. MAPK pathway activation through BRAF gene fusion in pilocytic astrocytomas; a novel oncogenic

fusion gene with diagnostic, prognostic, and therapeutic potential. J Pathol. 2010;222:324–8.
137. Tian Y, Rich BE, Vena N, et al. Detection of KIAA1549-BRAF fusion transcripts in formalin-fixed paraffin-embedded pediatric low-grade gliomas. J Mol Diagn. 2011;13:669–77.
138. Hawkins C, Walker E, Mohamed N, et al. BRAF-KIAA1549 fusion predicts better clinical outcome in pediatric low-grade astrocytoma. Clin Cancer Res. 2011;17:4790–8.
139. Rodriguez EF, Scheithauer BW, Giannini C, et al. PI3K/AKT pathway alterations are associated with clinically aggressive and histologically anaplastic subsets of pilocytic astrocytoma. Acta Neuropathol. 2011;121:407–20.
140. Cheng Y, Pang JC, Ng HK, Ding M, Zhang SF, Zheng J, Liu DG, Poon WS. HYPERLINK "/pubmed/11119125"Pilocytic astrocytomas do not show most of the genetic changes commonly seen in diffuse astrocytomas. Histopathology. 2000 Nov;37(5):437-44. PMID: 11119125.
141. Rosenblum MK, Erlandson RA, Budzilovich GN. The lipid-rich epithelioid glioblastoma. Am J Surg Pathol. 1991;15:925–34.
142. Suri V, Jha P, Agarwal S, et al. Molecular profile of oligodendrogliomas in young patients. Neuro Oncol. 2011;13:1099–106.
143. Kreiger PA, Okada Y, Simon S, et al. Losses of chromosomes 1p and 19q are rare in pediatric oligodendrogliomas. Acta Neuropathol. 2005;109:387–92.
144. Lipper MH, Eberhard DA, Phillips CD, et al. Pleomorphic xanthoastrocytoma, a distinctive astroglial tumor: neuroradiologic and pathologic features. AJNR Am J Neuroradiol. 1993;14:1397–404.
145. Lach B, Duggal N, DaSilva VF, et al. Association of pleomorphic xanthoastrocytoma with cortical dysplasia and neuronal tumors. A report of three cases. Cancer. 1996;78:2551–63.
146. Im SH, Chung CK, Kim SK, et al. Pleomorphic xanthoastrocytoma: a developmental glioneuronal tumor with prominent glioproliferative changes. J Neurooncol. 2004;66:17–27.
147. Giannini C, Scheithauer BW, Burger PC, et al. Pleomorphic xanthoastrocytoma: what do we really know about it? Cancer. 1999;85:2033–45.
148. Pahapill PA, Ramsay DA, Del Maestro RF. Pleomorphic xanthoastrocytoma: case report and analysis of the literature concerning the efficacy of resection and the significance of necrosis. Neurosurgery. 1996;38:822–8. Discussion 828-829.
149. Hirose T, Giannini C, Scheithauer BW. Ultrastructural features of pleomorphic xanthoastrocytoma: a comparative study with glioblastoma multiforme. Ultrastruct Pathol. 2001;25:469–78.
150. Martinez-Diaz H, Kleinschmidt-DeMasters BK, Powell SZ, et al. Giant cell glioblastoma and pleomorphic xanthoastrocytoma show different immunohistochemical profiles for neuronal antigens and p53 but share reactivity for class III beta-tubulin. Arch Pathol Lab Med. 2003;127:1187–91.
151. Dougherty MJ, Santi M, Brose MS, et al. Activating mutations in BRAF characterize a spectrum of pediatric low-grade gliomas. Neuro Oncol. 2010;12:621–30.
152. Yang S, Wetzel S, Law M, et al. Dynamic contrast-enhanced T2*-weighted MR imaging of gliomatosis cerebri. AJNR Am J Neuroradiol. 2002;23:350–5.
153. Armao DM, Stone J, Castillo M, et al. Diffuse leptomeningeal oligodendrogliomatosis: radiologic/pathologic correlation. AJNR Am J Neuroradiol. 2000;21:1122–6.
154. Rodriguez FJ, Perry A, Rosenblum MK, et al. Disseminated oligodendroglial-like leptomeningeal tumor of childhood: a distinctive clinicopathologic entity. Acta Neuropathol. 2012;124:627–41.
155. Schniederjan MJ, Alghamdi S, Castellano-Sanchez A, et al. Diffuse leptomeningeal neuroepithelial tumor: 9 pediatric cases with chromosome 1p/19q deletion status and IDH1 (R132H) immunohistochemistry. Am J Surg Pathol. 2013;37:763–71.
156. Ko MW, Turkeltaub PE, Lee EB, et al. Primary diffuse leptomeningeal gliomatosis mimicking a chronic inflammatory meningitis. J Neurol Sci. 2009;278:127–31.
157. Koeller KK, Henry JM. From the archives of the AFIP: superficial gliomas—radiologic-pathologic correlation. Armed Forces Institute of Pathology. Radiographics. 2001;21:1533–56.
158. Miller DC, Lang FF, Epstein FJ. Central nervous system gangliogliomas. Part 1: pathology. J Neurosurg. 1993;79:859–66.
159. Prayson RA, Khajavi K, Comair YG. Cortical architectural abnormalities and MIB1 immunoreactivity in gangliogliomas: a study of 60 patients with intracranial tumors. J Neuropathol Exp Neurol. 1995;54:513–20.
160. Donson AM, Kleinschmidt-Demasters BK, Aisner DL, et al. Pediatric brainstem gangliogliomas show BRAF mutation in a high percentage of cases. Brain Pathol. 2013;24(2):173–83.
161. Dahiya S, Haydon DH, Alvarado D, et al. BRAF (V600E) mutation is a negative prognosticator in pediatric ganglioglioma. Acta Neuropathol. 2013;125:901–10.
162. Blumcke I, Giencke K, Wardelmann E, et al. The CD34 epitope is expressed in neoplastic and malformative lesions associated with chronic, focal epilepsies. Acta Neuropathol. 1999;97:481–90.
163. Soffer D, Umansky F, Goldman JE. Ganglioglioma with neurofibrillary tangles (NFTs): neoplastic NFTs share antigenic determinants with NFTs of Alzheimer's disease. Acta Neuropathol. 1995;89:451–3.
164. Blumenthal GM, Dennis PA. PTEN hamartoma tumor syndromes. Eur J Hum Genet. 2008;16:1289–300.
165. Pilarski R, Burt R, Kohlman W, et al. Cowden syndrome and the PTEN hamartoma tumor syndrome: systematic review and revised diagnostic criteria. J Natl Cancer Inst. 2013;105:1607–16.
166. Shin JH, Lee HK, Khang SK, et al. Neuronal tumors of the central nervous system: radiologic findings and pathologic correlation. Radiographics. 2002;22:1177–89.
167. Tenreiro-Picon OR, Kamath SV, Knorr JR, et al. Desmoplastic infantile ganglioglioma: CT and MRI features. Pediatr Radiol. 1995;25:540–3.
168. Koelsche C, Sahm F, Paulus W, et al. BRAF V600E expression and distribution in desmoplastic infantile astrocytoma/ganglioglioma. Neuropathol Appl Neurobiol. 2014;40:337–44.
169. De Munnynck K, Van Gool S, Van Calenbergh F, et al. Desmoplastic infantile ganglioglioma: a potentially malignant tumor? Am J Surg Pathol. 2002;26:1515–22.
170. Fernandez C, Girard N, Paz Paredes A, et al. The usefulness of MR imaging in the diagnosis of dysembryoplastic neuroepithelial tumor in children: a study of 14 cases. AJNR Am J Neuroradiol. 2003;24:829–34.
171. Chappe C, Padovani L, Scavarda D, et al. Dysembryoplastic neuroepithelial tumors share with pleomorphic xanthoastrocytomas and gangliogliomas BRAF (V600E) mutation and expression. Brain Pathol. 2013;23:574–83.
172. Stosic-Opincal et al. Papillary glioneuronal tumor. AJR Am J Roentgenol. 2005;185(1):265–7.
173. Xiao H et al. Papillary glioneuronal tumor: radiological evidence of a newly established tumor entity. J Neuroimaging. 2011;21(3): 297–302.
174. Agarwal S, Sharma MC, Singh G, et al. Papillary glioneuronal tumor: a rare entity—report of four cases and brief review of literature. Childs Nerv Syst. 2012;28:1897–904.
175. Rosenblum MK. The 2007 WHO classification of nervous system tumors: newly recognized members of the mixed glioneuronal group. Brain Pathol. 2007;17:308–13.
176. Smith AB, Smirniotopoulos JG, Horkanyne-Szakaly I. From the radiologic pathology archives: intraventricular neoplasms: radiologic-pathologic correlation. Radiographics. 2013;33:21–43.
177. Marhold F, Preusser M, Dietrich W, et al. Clinicoradiological features of rosette-forming glioneuronal tumor (RGNT) of the fourth

ventricle: report of four cases and literature review. J Neurooncol. 2008;90:301–8.
178. Komori T, Scheithauer BW, Hirose T. A rosette-forming glioneuronal tumor of the fourth ventricle: infratentorial form of dysembryoplastic neuroepithelial tumor? Am J Surg Pathol. 2002;26: 582–91.
179. Kerkovsky M, Zitterbart K, Svoboda K, et al. Central neurocytoma: the neuroradiological perspective. Childs Nerv Syst. 2008; 24:1361–9.
180. Kubota T, Hayashi M, Kawano H, et al. Central neurocytoma: immunohistochemical and ultrastructural study. Acta Neuropathol. 1991;81:418–27.
181. Preusser M, Laggner U, Haberler C, et al. Comparative analysis of NeuN immunoreactivity in primary brain tumours: conclusions for rational use in diagnostic histopathology. Histopathology. 2006;48:438–44.
182. Preusser M, Budka H, Rossler K, et al. OLIG2 is a useful immunohistochemical marker in differential diagnosis of clear cell primary CNS neoplasms. Histopathology. 2007;50:365–70.
183. Horstmann S, Perry A, Reifenberger G, et al. Genetic and expression profiles of cerebellar liponeurocytomas. Brain Pathol. 2004; 14:281–9.
184. Yuh EL, Barkovich AJ, Gupta N. Imaging of ependymomas: MRI and CT. Childs Nerv Syst. 2009;25:1203–13.
185. Fouladi M, Helton K, Dalton J, et al. Clear cell ependymoma: a clinicopathologic and radiographic analysis of 10 patients. Cancer. 2003;98:2232–44.
186. Zamecnik J, Chanova M, Kodet R. Expression of thyroid transcription factor 1 in primary brain tumours. J Clin Pathol. 2004;57:1111–3.
187. Yao Y, Mack SC, Taylor MD. Molecular genetics of ependymoma. Chin J Cancer. 2011;30:669–81.
188. Bell JW, Osborn AG, Salzman KL, et al. Neuroradiologic characteristics of astroblastoma. Neuroradiology. 2007;49:203–9.
189. Port JD, Brat DJ, Burger PC, et al. Astroblastoma: radiologic-pathologic correlation and distinction from ependymoma. AJNR Am J Neuroradiol. 2002;23:243–7.
190. Brat DJ, Hirose Y, Cohen KJ, et al. Astroblastoma: clinicopathologic features and chromosomal abnormalities defined by comparative genomic hybridization. Brain Pathol. 2000;10:342–52.
191. Jay V, Edwards V, Squire J, et al. Astroblastoma: report of a case with ultrastructural, cell kinetic, and cytogenetic analysis. Pediatr Pathol. 1993;13:323–32.
192. Wang M, Tihan T, Rojiani AM, et al. Monomorphous angiocentric glioma: a distinctive epileptogenic neoplasm with features of infiltrating astrocytoma and ependymoma. J Neuropathol Exp Neurol. 2005;64:875–81.
193. Osborn AG, Salzman KL, Thurnher MM, et al. The new World Health Organization classification of central nervous system tumors: what can the neuroradiologist really say? AJNR Am J Neuroradiol. 2012;33:795–802.
194. Lu JQ, Patel S, Wilson BA, et al. Malignant glioma with angiocentric features. J Neurosurg Pediatr. 2013;11:350–5.
195. Marburger T, Prayson R. Angiocentric glioma: a clinicopathologic review of 5 tumors with identification of associated cortical dysplasia. Arch Pathol Lab Med. 2011;135:1037–41.
196. Raghunathan A, Olar A, Vogel H, et al. Isocitrate dehydrogenase 1 R132H mutation is not detected in angiocentric glioma. Ann Diagn Pathol. 2012;16:255–9.
197. Pomper MG, Passe TJ, Burger PC, et al. Chordoid glioma: a neoplasm unique to the hypothalamus and anterior third ventricle. AJNR Am J Neuroradiol. 2001;22:464–9.
198. Mittal S, Mittal M, Montes JL, et al. Hypothalamic hamartomas. Part 1. Clinical, neuroimaging, and neurophysiological characteristics. Neurosurg Focus. 2013;34:E6.
199. Coons SW, Rekate HL, Prenger EC, et al. The histopathology of hypothalamic hamartomas: study of 57 cases. J Neuropathol Exp Neurol. 2007;66:131–41.
200. Frye RE, Polling JS, Ma LC. Choroid plexus papilloma expansion over 7 years in Aicardi syndrome. J Child Neurol. 2007;22:484–7.
201. Taggard DA, Menezes AH. Three choroid plexus papillomas in a patient with Aicardi syndrome. A case report. Pediatr Neurosurg. 2000;33:219–23.
202. Trifiletti RR, Incorpora G, Polizzi A, et al. Aicardi syndrome with multiple tumors: a case report with literature review. Brain Dev. 1995;17:283–5.
203. Gozali AE, Britt B, Shane L, et al. Choroid plexus tumors; management, outcome, and association with the Li-Fraumeni syndrome: the Children's Hospital Los Angeles (CHLA) experience, 1991–2010. Pediatr Blood Cancer. 2012;58:905–9.
204. Schittenhelm J, Nagel C, Meyermann R, et al. Atypical teratoid/rhabdoid tumors may show morphological and immunohistochemical features seen in choroid plexus tumors. Neuropathology. 2011;31:461–7.
205. Irsutti M, Thorn-Kany M, Arrue P, et al. Suprasellar seeding of a benign choroid plexus papilloma of the fourth ventricle with local recurrence. Neuroradiology. 2000;42:657–61.
206. Jeibmann A, Hasselblatt M, Gerss J, et al. Prognostic implications of atypical histologic features in choroid plexus papilloma. J Neuropathol Exp Neurol. 2006;65:1069–73.
207. Shibahara J, Kashima T, Kikuchi Y, et al. Podoplanin is expressed in subsets of tumors of the central nervous system. Virchows Arch. 2006;448:493–9.
208. Kepes JJ, Collins J. Choroid plexus epithelium (normal and neoplastic) expresses synaptophysin. A potentially useful aid in differentiating carcinoma of the choroid plexus from metastatic papillary carcinomas. J Neuropathol Exp Neurol. 1999;58:398–401.
209. Carlotti Jr CG, Salhia B, Weitzman S, et al. Evaluation of proliferative index and cell cycle protein expression in choroid plexus tumors in children. Acta Neuropathol. 2002;103:1–10.
210. Ferreira MA, Feiz-Erfan I, Zabramski JM, et al. Endolymphatic sac tumor: unique features of two cases and review of the literature. Acta Neurochir (Wien). 2002;144:1047–53.
211. Kupferman ME, Bigelow DC, Carpentieri DF, et al. Endolymphatic sac tumor in a 4-year-old boy. Otol Neurotol. 2004;25:782–6.
212. Schittenhelm J, Roser F, Tatagiba M, et al. Diagnostic value of EAAT-1 and Kir7.1 for distinguishing endolymphatic sac tumors from choroid plexus tumors. Am J Clin Pathol. 2012;138:85–9.
213. Al-Hussaini M, Sultan I, Abuirmileh N, et al. Pineal gland tumors: experience from the SEER database. J Neurooncol. 2009;94:351–8.
214. Smith AB, Rushing EJ, Smirniotopoulos JG. From the archives of the AFIP: lesions of the pineal region—radiologic-pathologic correlation. Radiographics. 2010;30:2001–20.
215. Jouvet A, Saint-Pierre G, Fauchon F, et al. Pineal parenchymal tumors: a correlation of histological features with prognosis in 66 cases. Brain Pathol. 2000;10:49–60.
216. Dahiya S, Perry A. Pineal tumors. Adv Anat Pathol. 2010; 17:419–27.
217. Plowman PN, Pizer B, Kingston JE. Pineal parenchymal tumours: II. On the aggressive behaviour of pineoblastoma in patients with an inherited mutation of the RB1 gene. Clin Oncol (R Coll Radiol). 2004;16:244–7.
218. Tong T, Zhenwei Y, Xiaoyuan F. MRI and 1H-MRS on diagnosis of pineal region tumors. Clin Imaging. 2012;36:702–9.
219. Buffenoir K, Rigoard P, Wager M, et al. Papillary tumor of the pineal region in a child: case report and review of the literature. Childs Nerv Syst. 2008;24:379–84.
220. Abela L, Rushing EJ, Ares C, et al. Pediatric papillary tumors of the pineal region: to observe or to treat following gross total resection? Childs Nerv Syst. 2013;29:307–10.

221. Cykowski MD, Wartchow EP, Mierau GW, et al. Papillary tumor of the pineal region: ultrastructural study of a case. Ultrastruct Pathol. 2012;36:68–77.
222. Jouvet A, Fauchon F, Liberski P, et al. Papillary tumor of the pineal region. Am J Surg Pathol. 2003;27:505–12.
223. Perry A, Dehner LP. Meningeal tumors of childhood and infancy. An update and literature review. Brain Pathol. 2003;13:386–408.
224. Wiebe S, Munoz DG, Smith S, et al. Meningioangiomatosis. A comprehensive analysis of clinical and laboratory features. Brain. 1999;122(Pt 4):709–26.
225. Kim NR, Choe G, Shin SH, et al. Childhood meningiomas associated with meningioangiomatosis: report of five cases and literature review. Neuropathol Appl Neurobiol. 2002;28:48–56.
226. Wixom C, Chadwick AE, Krous HF. Sudden, unexpected death associated with meningioangiomatosis: case report. Pediatr Dev Pathol. 2005;8:240–4.
227. Perry A, Kurtkaya-Yapicier O, Scheithauer BW, et al. Insights into meningioangiomatosis with and without meningioma: a clinicopathologic and genetic series of 24 cases with review of the literature. Brain Pathol. 2005;15:55–65.
228. Yao Z, Wang Y, Zee C, et al. Computed tomography and magnetic resonance appearance of sporadic meningioangiomatosis correlated with pathological findings. J Comput Assist Tomogr. 2009;33:799–804.
229. Arcos A, Serramito R, Santin JM, et al. Meningioangiomatosis: clinical-radiological features and surgical outcome. Neurocirugia (Astur). 2010;21:461–6.
230. Wang Y, Gao X, Yao ZW, et al. Histopathological study of five cases with sporadic meningioangiomatosis. Neuropathology. 2006;26:249–56.
231. Prayson RA. Meningioangiomatosis. A clinicopathologic study including MIB1 immunoreactivity. Arch Pathol Lab Med. 1995;119:1061–4.
232. Thuijs NB, Uitdehaag BM, Van Ouwerkerk WJ, et al. Pediatric meningiomas in The Netherlands 1974–2010: a descriptive epidemiological case study. Childs Nerv Syst. 2012;28:1009–15.
233. Mehta N, Bhagwati S, Parulekar G. Meningiomas in children: a study of 18 cases. J Pediatr Neurosci. 2009;4:61–5.
234. Legius E, Vles JS, Casaer P, et al. Intraparenchymal meningioma in a 14-month-old infant: case report. Brain Dev. 1985;7:622–4.
235. Rippe DJ, Boyko OB, Friedman HS, et al. Gd-DTPA-enhanced MR imaging of leptomeningeal spread of primary intracranial CNS tumor in children. AJNR Am J Neuroradiol. 1990;11:329–32.
236. Grois N, Prayer D, Prosch H, et al. Neuropathology of CNS disease in Langerhans cell histiocytosis. Brain. 2005;128:829–38.
237. Grois N, Prosch H, Waldhauser F, et al. Pineal gland abnormalities in Langerhans cell histiocytosis. Pediatr Blood Cancer. 2004;43:261–6.
238. Schabet M. Epidemiology of primary CNS lymphoma. J Neurooncol. 1999;43:199–201.
239. Abla O, Weitzman S, Blay JY, et al. Primary CNS lymphoma in children and adolescents: a descriptive analysis from the International Primary CNS Lymphoma Collaborative Group (IPCG). Clin Cancer Res. 2011;17:346–52.
240. Fukushima S, Terasaki M, Sakata K, et al. Sensitivity and usefulness of anti-phosphohistone-H3 antibody immunostaining for counting mitotic figures in meningioma cases. Brain Tumor Pathol. 2009;26:51–7.
241. Lu QR, Yuk D, Alberta JA, et al. Sonic hedgehog-regulated oligodendrocyte lineage genes encoding bHLH proteins in the mammalian central nervous system. Neuron. 2000;25:317–29.
242. Zhou Q, Wang S, Anderson DJ. Identification of a novel family of oligodendrocyte lineage-specific basic helix-loop-helix transcription factors. Neuron. 2000;25:331–43.
243. Yokoo H, Nobusawa S, Takebayashi H, et al. Anti-human Olig2 antibody as a useful immunohistochemical marker of normal oligodendrocytes and gliomas. Am J Pathol. 2004;164:1717–25.
244. Otero JJ, Rowitch D, Vandenberg S. OLIG2 is differentially expressed in pediatric astrocytic and in ependymal neoplasms. J Neurooncol. 2011;104:423–38.
245. Mokhtari K, Paris S, Aguirre-Cruz L, et al. Olig2 expression, GFAP, p53 and 1p loss analysis contribute to glioma subclassification. Neuropathol Appl Neurobiol. 2005;31:62–9.
246. Ligon KL, Alberta JA, Kho AT, et al. The oligodendroglial lineage marker OLIG2 is universally expressed in diffuse gliomas. J Neuropathol Exp Neurol. 2004;63:499–509.
247. Wolf HK, Buslei R, Schmidt-Kastner R, et al. NeuN: a useful neuronal marker for diagnostic histopathology. J Histochem Cytochem. 1996;44:1167–71.
248. Koperek O, Gelpi E, Birner P, et al. Value and limits of immunohistochemistry in differential diagnosis of clear cell primary brain tumors. Acta Neuropathol. 2004;108:24–30.
249. Hamilton SR, Liu B, Parsons RE, et al. The molecular basis of Turcot's syndrome. N Engl J Med. 1995;332:839–47.
250. Hirsch B, Shimamura A, Moreau L, et al. Association of biallelic BRCA2/FANCD1 mutations with spontaneous chromosomal instability and solid tumors of childhood. Blood. 2004;103:2554–9.
251. Offit K, Levran O, Mullaney B, et al. Shared genetic susceptibility to breast cancer, brain tumors, and Fanconi anemia. J Natl Cancer Inst. 2003;95:1548–51.
252. Evans DG, Farndon PA, Burnell LD, et al. The incidence of Gorlin syndrome in 173 consecutive cases of medulloblastoma. Br J Cancer. 1991;64:959–61.
253. Schofield D, West DC, Anthony DC, et al. Correlation of loss of heterozygosity at chromosome 9q with histological subtype in medulloblastomas. Am J Pathol. 1995;146:472–80.
254. Aszterbaum M, Rothman A, Johnson RL, et al. Identification of mutations in the human PATCHED gene in sporadic basal cell carcinomas and in patients with the basal cell nevus syndrome. J Invest Dermatol. 1998;110:885–8.
255. Hahn H, Wicking C, Zaphiropoulous PG, et al. Mutations of the human homolog of Drosophila patched in the nevoid basal cell carcinoma syndrome. Cell. 1996;85:841–51.
256. Malkin D, Li FP, Strong LC, et al. Germ line p53 mutations in a familial syndrome of breast cancer, sarcomas, and other neoplasms. Science. 1990;250:1233–8.
257. Taylor MD, Mainprize TG, Rutka JT, et al. Medulloblastoma in a child with Rubenstein-Taybi syndrome: case report and review of the literature. Pediatr Neurosurg. 2001;35:235–8.
258. Rogers L, Pattisapu J, Smith RR, et al. Medulloblastoma in association with the Coffin-Siris syndrome. Childs Nerv Syst. 1988;4:41–4.
259. Fleck BJ, Pandya A, Vanner L, et al. Coffin-Siris syndrome: review and presentation of new cases from a questionnaire study. Am J Med Genet. 2001;99:1–7.
260. Osterling WL, Boyer RS, Hedlund GL, et al. MPPH syndrome: two new cases. Pediatr Neurol. 2011;44:370–3.
261. Slade I, Bacchelli C, Davies H, et al. DICER1 syndrome: clarifying the diagnosis, clinical features and management implications of a pleiotropic tumour predisposition syndrome. J Med Genet. 2011;48:273–8.
262. van Slegtenhorst M, de Hoogt R, Hermans C, Nellist M, Janssen B, Verhoef S, et al. Identification of the tuberous sclerosis gene TSC1 on chromosome 9q34. Science. 1997;277(5327):805–8.
263. Pollack IF, Mulvihill JJ. Neurofibromatosis 1 and 2. Brain Pathol. 1997;7(2):823–36.
264. von Deimling A, Fimmers R, Schmidt MC, Bender B, Fassbender F, Nagel J, et al. Comprehensive allelotype and genetic anaysis of

466 human nervous system tumors. J Neuropathol Exp Neurol. 2000;59(6):544–58.
265. Maddock IR, Moran A, Maher ER, Teare MD, Norman A, Payne SJ, et al. A genetic register for von Hippel-Lindau disease. J Med Genet. 1996;33(2):120–7
266. Vorechovsky et al. (1997) et al. Patched (ptch)-associated preferential expression of smoothened (smoh) in human basal cell carcinoma of the skin. Cancer Res. 1997;57(21):4731–5.
267. Sutphen R, Diamond TM, Minton SE, Peacocke M, Tsou HC, Root AW. Severe Lhermitte-Duclos disease with unique germline mutation of PTEN. Am J Med Genet. 1999;82(4):290–3.
268. Robinson S, Cohen AR. Cowden disease and Lhermitte-Duclos disease: characterization of a new phakomatosis. Neurosurgery. 2000;46(2):371–83.
269. Cavenee WK, Burger PC, Leung SY, van Meir EG. Turcot syndrome. In: Louis DN, Ohgaki H, Wiestler OD, Cavenee WK, editors. WHO classification of tumours of the central nervous system. Lyon, France: International Agency for Research on Cancer (IARC); 2007. p. 229–31.
270. Laberge-le Couteulx S, Jung HH, Labauge P, Houtteville JP, Lescoat C, Cecillon M, et al. Truncating mutations in CCM1, encoding KRIT1, cause hereditary cavernous angiomas. Nat Genet. 1999;23(2):189–93.
271. Taylor MD, Gokgoz N, Andrulis IL, Mainprize TG, Drake JM, Rutka JT. Familial posterior fossa brain tumors of infancy secondary to germline mutation of the hSNF5 gene. Am J Hum Genet. 2000;66(4):1403–6.
272. Sopta M, Gallie BL, Gill RM, Hamel PA, Muncaster M, Zacksenhaus E, et al. The retinoblastoma protein and the cell cycle. Semin Cancer Biol. 1992;3(3):107–13.
273. Pratt CB, Raimondi SC, Kaste SC, Heaton DM, Mounce KG, Mandrell B, et al. Outcome for patients with constitutional 13q chromosomal abnormalities and retinoblastoma. Pediatr Hematol Oncol. 1994;11(5):541–7.
274. Tachibana I, Smith JS, Sato K, Hosek SM, Kimmel DW, Jenkins RB. Investigation of germline PTEN, p53, p16(INK4A)/p14(ARF), and CDK4 alterations in familial glioma. Am J Med Genet. 2000;92(2):136–41.

Pediatric Cancer in the Head and Neck

7

Zhongxin Yu, David M. Parham,
and Marcia Komlos Kukreja

Overview of Head and Neck Malignancies

Head and neck malignancies typically occur in adults, often as a result of tobacco and/or alcohol exposure [1, 2]. More recently, oncogenic human papillomavirus (HPV) exposure related to oral sex has been related to a rise in head and neck cancers among nonsmokers [3]. These factors and others make the head and neck region a major focus for adult oncology. In children, the situation differs, as head and neck cancers fortunately are quite rare. However, more typical cancers of childhood such as embryonal rhabdomyosarcoma show a predilection for this anatomic region, as do unusual neoplasms such as NUT-translocation carcinoma and melanotic neuroectodermal tumor. Infections may also give rise to juvenile head and neck cancers; among these are oncogenic HPV infections, usually acquired at birth, and Epstein-Barr virus (EBV) infections, which may initiate poorly differentiated nasopharyngeal carcinomas. In the following section we also discuss pediatric thyroid cancers, which may arise secondary to irradiation, autoimmune stimulation, or an inherited propensity for cancer.

For the purposes of discussion, the central nervous system and eyes are excluded, and the head and neck region may be conveniently divided into the nose, oral cavity, salivary glands, ear, and larynx. In addition, it contains a bilobate thyroid gland, four parathyroid glands, and various ganglia, paraganglia, and lymphatic related structures. All of these regions are housed within a skeletal or connective tissue framework, supplied by neurovascular structures, and mobilized by a complex series of muscles, including the tongue. Any of these structures may become the site of origin of a pediatric cancer.

Embryologic development of the head and neck proceeds by an intricate orchestration of signals among the neural tube, adjacent neuroectoderm, cephalic mesoderm, proximal endoderm (the primitive pharynx), and the vestigial gills that comprise the branchial arches and pharyngeal pouches. The posterior pharyngeal endoderm invaginates to form thyroglossal duct, which in turn elongates to form the thyroid. Similarly, a laryngotracheal diverticulum forms just distal to the thyroglossal duct and gives rise to the tracheobronchial tree. The branchial arches and pharyngeal pouches, respectively, give rise to the mandible, pharyngeal tonsils, ears, parathyroid glands, thymus, and C-cells of the thyroid. Malformations and perturbations of these various processes may give rise to the premalignant soil from whence pediatric cancers arise.

Imaging of Head and Neck Tumors

Imaging has an important role in diagnosis, staging, treatment, and posttreatment follow-up in pediatric head and neck cancer. When interpreting imaging studies for a suspected mass, some clinical findings should be taken into consideration, including age of the child, location of the mass, how long the mass has been present, and if there is a known syndrome associated with neoplasms [4]. Ultrasound is widely used as the initial evaluation technique of a superficial neck mass in the pediatric population given its availability, sedation being not needed, and the absence of ionizing radiation. Ultrasound can frequently differentiate a solid from a cystic mass. Color Doppler ultrasound allows assessment of vascularity within a

Z. Yu, M.D.
Department of Pathology, University of Oklahoma Health Sciences Center, Oklahoma, OK, USA

D.M. Parham, M.D. (✉)
Department of Pathology and Laboratory Medicine, Children's Hospital Los Angeles, 4650 Sunset Blvd., #43, Los Angeles, CA 90027, USA

Department of Pathology and Laboratory Medicine, University of Southern California, Los Angeles, CA, USA
e-mail: daparham@chla.usc.edu

M.K. Kukreja, M.D.
Department of Radiology, Baylor College of Medicine, Texas Children's Hospital, Houston, TX, USA

D.M. Parham et al. (eds.), *Pediatric Malignancies: Pathology and Imaging*,
DOI 10.1007/978-1-4939-1729-7_7,

mass and is helpful in distinguishing lymph nodes from congenital lesions such as vascular malformations. For deeper lesions and further characterization of superficial masses, computed tomography (CT) [5] and magnetic resonance imaging (MRI) are the preferred imaging modalities. In head and neck malignancies, CT is useful to evaluate for bony involvement as well as to evaluate for the presence of calcifications within a mass. Current CT scans allow very quick imaging of the neck and can usually be performed without sedation unless the patient is too young to cooperate. Radiation should be minimized and intravenous contrast is mandatory in the evaluation of a neck mass with CT. Images are acquired axially and coronal and sagittal reformations are usually performed. MRI is frequently better for characterization of the primary cancer and its relationship to adjacent structures. Both T1- and T2-weighted images are usually performed; however T2 images and postgadolinium fat-suppressed images are especially important when evaluating a neck mass. MRI is also important in evaluating for the presence of intracranial extension of a cervical or skull base mass. Since MRI of the neck requires more time to be performed, sedation is frequently needed in the pediatric population, especially in patients under the age of 6 or 7. [^{18}F]Fluorodeoxyglucose ([^{18}F]FDG) positron emission tomography [6] provides whole-body functional imaging and has a role in staging head and neck malignancies and monitoring response to treatment. PET and PET-CT are commonly used in childhood head and neck malignancies, predominantly in staging and follow-up of lymphoma [7]. It may also have a role in soft-tissue sarcomas [7]. Plain radiographs have very limited role in the evaluation of head and neck malignancies.

Nasal Tumors

Nasopharyngeal Carcinoma

Definition: Nasopharyngeal carcinoma is a malignant epithelial tumor that arises in the nasopharyngeal mucosa and shows evidence of squamous differentiation by light or electron microscopy or tested by immunohistochemistry. It is subclassified into three groups: keratinizing squamous cell carcinoma, nonkeratinizing carcinoma, and basaloid squamous cell carcinoma [8].

Clinical features and epidemiology: Nasopharyngeal carcinoma is rare in the pediatric population but relatively common among tumors in that location. It has a remarkable geographic and ethnic distribution, with high incidence in Southeast Asia and northern Africa [9, 10]. While infection with EBV is known to be an essential risk factor, cofactors including HLA type, genetics, and environment are thought to play an important role, especially in low-incidence populations such as the USA [11, 12]. In high-incidence populations most patients are middle-aged adults, but in other populations there is a bimodal age-incidence curve with an early peak around ages 15–24 years and a second peak later in life around ages 65–79 years [13]. In pediatrics, the tumors are more commonly of undifferentiated histology and associated with EBV infection, frequently occur in African American population, and often present with advanced loco-regional disease manifesting as cervical lymphadenopathy [14–16].

Imaging features: Nasopharyngeal carcinoma in children presents as an asymmetric mass in the posterior nasopharynx and may extend into the posterior choana and nasal cavity (Fig. 7.1a). The tumor may also extend into the adjacent parapharyngeal space and pterygopalatine fossa, features concerning for malignancy. Invasion of the central skull base is common [17, 18]. Mastoid opacification frequently occurs as a secondary finding [17]. Lymphadenopathy is also common at the time of diagnosis [17, 18]. The lateral retropharyngeal nodes are the most frequently affected, followed by high level II and high level V lymph nodes [17]. On MRI, the nasopharyngeal mass is usually iso- or slightly hyperintense to adjacent muscle on T1-weighted images and hyperintense compared to muscle on T2-weighted images. Enhancement on contrast-enhanced images is usually present [18] (Fig. 7.1b). It may be difficult to distinguish from benign adenoid hypertrophy, the most common nasopharyngeal "mass" in children. Some imaging features, including asymmetry and involvement of skull base and adjacent regions, are useful in differentiating NPC from adenoid hypertrophy. Differential diagnosis also includes lymphoma and sarcomas, which can have a similar appearance (Fig. 7.1c) but are more common in younger children while NPC is more common in adolescents [18].

Gross and microscopic features: Nasopharyngeal carcinoma usually arises from the lateral wall of the nasopharynx, especially the fossa of Rosenmüller. Grossly, it may form a smooth bulge or nodule in the mucosa, with or without surface ulceration. Sometimes there is no visible lesion found, and the diagnosis is made by random biopsy in suspicious areas [19].

Microscopically, there are three distinctive subtypes: keratinizing squamous cell carcinoma (SCC), non-keratinizing carcinoma, and basaloid SCC. Keratinizing SCC resembles the usual well-differentiated SCC arising in other locations. There is obvious squamous differentiation with intercellular bridges and abundant keratinization at the light microscopic level. This type of tumor often occurs in an older age group and may not be associated with EBV infection.

Non-keratinizing carcinoma, which represents the large majority of nasopharygeal carcinoma, is associated with EBV infection in practically all cases. It may be subclassified

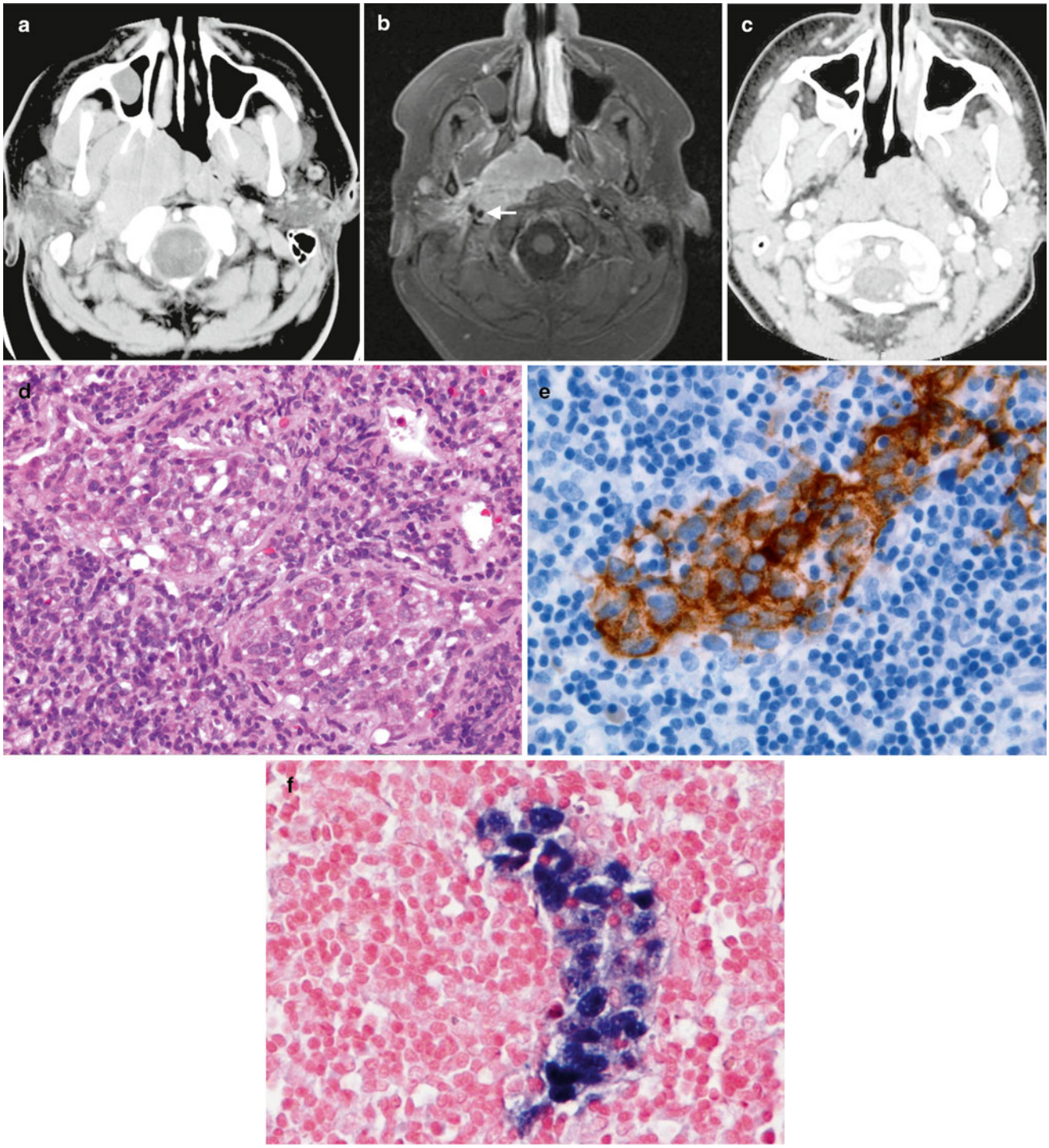

Fig. 7.1 (**a**, **b**) *Nasopharyngeal carcinoma*. (**a**) Contrast-enhanced CT in a teenage boy demonstrating an asymmetric enhancing right nasopharyngeal with extension into the retropharyngeal soft tissues. A right maxillary retention cyst or mucosal polyp is incidentally noted. (**b**) Axial T1W postcontrast MRI image in the same patient shows the enhancing nasopharyngeal mass as well as delineates better the involvement of adjacent structures. Encasement of the carotid sheath vessels can be appreciated (*arrow*). (**c**) Contrast-enhanced CT image in a 12-year-old girl with an asymmetric enhancing nasopharyngeal mass similar in appearance to a nasopharyngeal carcinoma but confirmed by biopsy to be lymphoma. (**d**) *Nasopharyngeal carcinoma*, *nonkeratinizing undifferentiated subtype*. The tumor cells form irregular islands intimately intermingled with inflammatory infiltrates. The tumor cells are relatively large with scant, lightly eosinophilic cytoplasm and indistinct cell borders, vesicular nuclei, and prominent nucleoli. Keratin formation is difficult to be identified on routine H&E-stained section. (**e**) *Nasopharyngeal carcinoma*, *metastatic to the neck lymph node*. Immunohistochemical stains with pan-cytokeratin AE1/AE3 antibody shows uniform strong reactivity in the tumor cells (*brown color*), but no staining in surrounding lymphocytes. (**f**) *Nasopharyngeal carcinoma*, *metastatic to the neck lymph node*. EBV in situ hybridization for EBER shows positive nuclear reaction in tumor cells (*blue color*)

into differentiated and undifferentiated types, the latter accounting for majority of cases. This subclassification is generally considered unnecessary, because it lacks clinical significance and lesions may show heterogeneity in different areas in the same biopsy or in different biopsies taken at different time intervals [20, 21]. However, a recent study showed worse prognosis with differentiated histology [22].

Tumor cells in non-keratinizing carcinoma typically form solid sheets or irregular islands intimately intermingled with variable numbers of inflammatory infiltrates rich in lymphocytes. Sometimes the lymphocytes may dominate the entire lesion and obscure the epithelial nature of the cells, mimicking a lymphoma. Undifferentiated subtype cells exhibit a syncytial appearance with scant, lightly eosinophilic cytoplasm and indistinct cell borders, vesicular nuclei, and prominent nucleoli (Fig. 7.1d), whereas differentiated subtype cells demonstrate some level of cellular stratification or pavement arrangement, often described as resembling transitional cell carcinoma of the bladder. Tumors may have focal or extensive spindle cell morphology or form papillary fronds. Other occasional finds include scattered spherical amyloid globules [23], epithelioid granulomas [24], and prominent infiltration by eosinophils and plasma cells [25].

The basaloid variant is the rarest type of NPC, as only a few cases are reported in the literature [26, 27]. This type of tumor is morphologically identical to neoplasms occurring in other head and neck sites but show a lower clinical aggressiveness. The tumors were composed of two types of cells, basaloid and squamous cells. The basaloid cells are small with hyperchromatic nuclei, inconspicuous nucleoli, and scant cytoplasm. The cells form closely packed solid sheets, irregular islands, nests, or cords, occasionally with peripheral palisading. A component of conventional SCC foci is invariably present in the basaloid variant, and the junction between the squamous and basaloid cells may be abrupt. Careful examination of the entire specimen to find the areas with conventional SCC may aid diagnosis. Another feature of basaloid SCC is the presence of stromal hyalinization with small cystic spaces containing PAS and Alcian blue-positive material. Comedo-type necrosis is frequent.

Immunohistochemistry and other special stains: The tumor cells show uniform strong reactivity for pan-cytokeratin AE1/AE3, cytokeratin 5/6, and p63, focal or weak reactivity for low-molecular-weight cytokeratins and EMA, and no reactivity for cytokeratins 7 and 20 [28–30] (Fig. 7.1e). Most tumors, especially non-keratinizing carcinoma, show a positive nuclear reaction for EBV-encoded early RNA (EBER) by in situ hybridization [31–33] (Fig. 7.1f). High-level expression of ERCC1 may be associated with more aggressive clinical behavior [22].

Molecular diagnostic features and cytogenetics: Although of no diagnostic value, rearrangement and deletion on chromosome 3 have been consistently noted in nasopharyngeal carcinoma [34–37].

Prognostic features: The mainstay of treatment for nasopharyngeal carcinoma is concomitant chemotherapy and radiation, with or without neoadjuvant chemotherapy. Progressive improvement has been reported both from endemic and non-endemic areas. The outcome in pediatric patients is usually better than that of adults, and the presence of metastatic disease in cervical lymph nodes at diagnosis apparently does not adversely affect prognosis. Development of therapy-related complications including second malignancy is of special concern in long-term survivors [16, 38–41].

NUT Midline Carcinoma

Definition: NUT midline carcinoma is a rare aggressive subset of poorly differentiated SCC, genetically defined by rearrangement of the *Nuclear Protein in Testis* [42] gene at chromosome 15q13 [43].

Clinical features and epidemiology: NMC is a newly described carcinoma commonly occurring in children and young adults, with a median age of 16 years (range 0.1–78) at the time of diagnosis [5, 44–46]. The majority of tumors arise in the midline structures in head and neck or in the thorax, and nearly one-half of the cases present with either lymph node or distant metastases [45, 46]. Rarely, the tumors arise in salivary glands, liver and pancreas, testis, and bladder [44, 47–50]. None of the cases tested to date have been associated with EBV or HPV infection [51].

Imaging features: Imaging appearance of NUT midline carcinoma is nonspecific, and very few case reports are present in the imaging literature. Imaging features include heterogeneous low density on CT and heterogeneous but predominant T1 hypointensity and T2 hyperintensity on MRI with heterogeneous enhancement [52]. Metastasis may occur in any part of the body and metastatic intraspinal and intracranial involvement have been described [52, 53]. The intracranial lesion may demonstrate restricted diffusion [52]. Intralesional calcification has also been reported [52]. NMC has been shown to be avid on PET imaging [52, 54].

Molecular genetics: NUT midline carcinoma is a genetically defined neoplasm caused by chromosomal rearrangement of the gene encoding *NUT* at 15q13. Approximately two-thirds have a translocation t(15;19)(q13;p13.1) involving *NUT* and *BRD4*, resulting in a *BRD4-NUT* fusion oncogene [43, 55]. Less common tumors have a different rearrangement involving *NUT*, of which t(9;15)(q34.2;q13) with *BRD3-NUT* fusion gene is the most common variant [55]. There is no significant

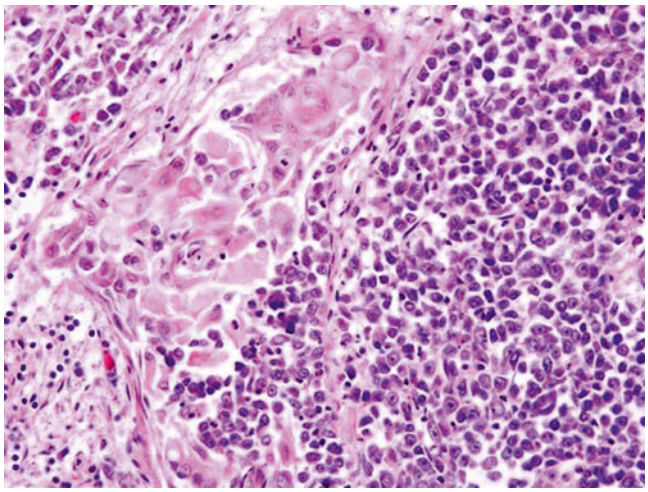

Fig. 7.2 *NUT midline carcinoma*. The tumor is typically composed of poorly differentiated, uniform round, oval, or spindle-shaped tumor cells (*right half* of the picture) with occasional abrupt squamous differentiation with minimal keratinization (*left half* of the picture)

association between translocation type (*BRD4-NUT*, *BRD3-NUT*, or *NUT* variant) and outcome, although some studies suggest that NUT-variant cancers may be associated with longer survival [44, 46].

Gross and microscopic features: The histology of NUT midline carcinoma mimics many tumors arising in these locations. Most tumors have poorly differentiated carcinoma morphology with uniform round, oval, or spindle-shaped tumor cells arranged in sheets, islands, or ribbons, with or without desmoplastic stroma. The tumor cells often have high nuclear-to-cytoplasm ratios with inconspicuous cytoplasm, dense chromatin, and absent nucleoli. Occasional cases show abrupt squamous differentiation with minimal keratinization (Fig. 7.2). Sometimes neuroendocrine structures mimic neuroblastoma or Ewing's sarcoma/primitive neuroectodermal tumor (PNET). Apparent chondroid differentiation has been described [47]. The tumor often shows brisk mitoses, apoptosis, and focal necrosis.

NUT midline carcinoma is often confused with similar, poorly differentiated carcinoma features, such as poorly differentiated SCC, Ewing's sarcoma/PNET, nasopharyngeal carcinoma, and pancreatoblastoma [51, 56].

Immunohistochemistry and other special stains: Immunohistochemical staining with a monoclonal antibody against NUT has been proven highly sensitive and specific for the diagnosis of NUT midline carcinoma [57]. In addition, the tumors express cytokeratin and p63, in keeping with squamous cell differentiation [56]. Occasionally, there is negative staining for keratins including a pan-keratin cocktail, Cam5.2, and/or AE1/AE3 [58]. The tumor is in general negative for sarcoma, melanoma, and lymphoma markers.

Molecular diagnostic features and cytogenetics: NUT midline carcinoma can be diagnosed by conventional cytogenetics with characteristic t(15;19). Since the discovery of *NUT* rearrangement and its partner genes, reverse transcriptase (RT)-PCR and fluorescence in situ hybridization (FISH) have been used for the diagnoses but are largely replaced by NUT immunohistochemistry (see above). Nonetheless, they remain the gold standard for confirming the diagnosis.

Prognostic features: All NUT midline carcinomas show aggressive behavior with early locoregional invasion and distant metastases. They are often initially responsive to chemotherapy and radiation but invariably recur and do not respond to subsequent therapeutic interventions. The overall survival at 1 and 2 years after diagnosis has been 30 and 19 %, respectively, and the average survival is less than 1 year [46].

Esthesioneuroblastoma (Olfactory Neuroblastoma)

Definition: Esthesioneuroblastoma, also called olfactory neuroblastoma, is a malignant neuroendocrine tumor arising from the olfactory mucosa of sinonasal tract and frequently invading into the orbits and skull base.

Clinical features and epidemiology: Esthesioneuroblastoma is an uncommon tumor, accounting for approximately 3–6 % of all sinonasal malignancy [59, 60]. It usually occurs in adults between the ages of 40 and 70 years (mean 53) [61] but is rare in children; only 10 % of reported cases in English literature are in the pediatric population [62]. Most pediatric patients are adolescents, with slight male predominance (1.5:1). Patients usually present with a nasopharyngeal polypoid mass that may cause unilateral nasal obstruction, local swelling, facial pain, and recurrent epistaxis. The tumor may protrude into the orbit and cause proptosis, ophthalmoplegia, and even visual loss, or extend via the cribriform plate into the cranium. The resultant frontal lobe lesion mimics a brain tumor [63, 64]. Occasional patients may present with Cushing syndrome or hyponatremia due to ectopic ACTH or ADH production [6, 65, 66]. Pediatric esthesioneuroblastoma seems to have a more aggressive presentation than in adults [67]. There is no evidence of EBV infection [68].

Imaging features: Esthesioneuroblastoma and its imaging characteristics have been well described in the adult literature. Because these are rare tumors in the pediatric population, there is paucity of literature focusing on imaging of this tumor in children. Typically, esthesioneuroblastoma demonstrates a large aggressive-appearing nasal mass with common extension into the paranasal sinuses and erosion of the cribriform plate and orbital wall, with

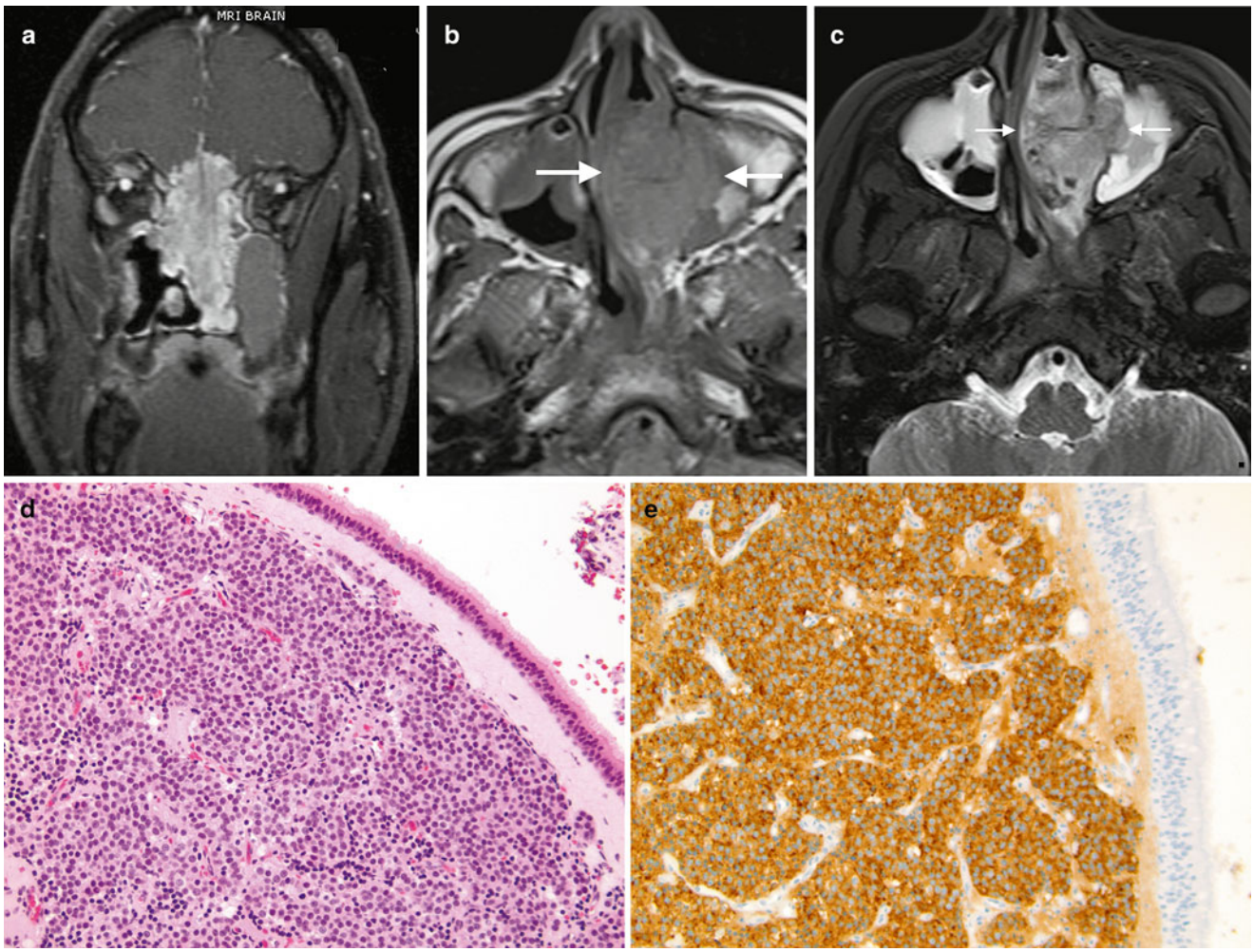

Fig. 7.3 (**a**) *Esthesioneuroblastoma*. Coronal T1W postcontrast MRI image in an adult patient demonstrates the common appearance of esthesioneuroblastoma, with a large nasal mass extending into the ethmoid sinuses and causing erosion of the cribriform plate, with orbital and intracranial extension. Image courtesy of Dr. Nicholas Weisman, Yale New Haven Hospital. (**b**, **c**) 14-year-old girl with left nasal esthesioneuroblastoma (**b**) Non-contrast-enhanced T1W axial MRI shows that the tumor is isointense to muscle and infiltrates the left maxillary sinus. (**c**) Axial T2W MRI shows the tumor to be slightly hyperintense to muscle. Mucoperiosteal thickening of both maxillary sinuses is present. Images courtesy of Dr. Beth McCarville, St Jude Children's Research Hospital, Memphis, TN. (**d**) *Esthesioneuroblastoma*. The tumor is located in the subepithelial region of the nasal mucosa. It is composed of nests of primitive small round blue cells invested by fibrovascular stroma. (**e**) *Esthesioneuroblastoma*. The tumor cells show strong expression of synaptophysin demonstrated by immunohistochemical stain

intracranial and/or orbital extension (Fig. 7.3a). On CT, they are usually homogenous, enhancing masses which cause bone remodeling. As mentioned, they can involve the nasal cavity and the paranasal sinuses. On MRI, esthesioneuroblastoma has intermediate signal on T1 and T2 (Fig. 7.3a–c) and enhances with gadolinium. In tumors with intracranial extension, peripheral cysts can be present at the margins of the intracranial mass and are helpful in suggesting the diagnosis of esthesioneuroblastoma [69]. Erosion of the paranasal sinuses is common. In contrast to neuroblastoma in other locations, metaiodobenzylguanidine (MIBG) scans have been shown to be negative in a series of patients with esthesioneuroblastoma [67].

Gross and microscopic features: Esthesioneuroblastoma is a small round blue cell tumor that resembles neuroblastoma arising from adrenal gland or sympathetic chain. Grossly, tumors form a red-gray, highly vascularized, polypoid mass, commonly located in the roof of the nasal fossa. Sizes range from <1 cm up to large masses involving the nasal cavity and intracranial region.

Microscopically, esthesioneuroblastoma has a lobular architecture composed of nests of cells invested by fibrovascular stroma. The cellular components consist of small- to medium-sized primitive cells with high nuclear-to-cytoplasmic ratio, uniform round nuclei with dispersed coarse "salt and pepper"-appearing chromatin, and

inconspicuous nucleoli (Fig. 7.3d). The background often has a neurofibrillary appearance with occasional Homer Wright-type rosettes, which are nearly pathognomonic in the nasal cavity when containing true neuropil [70]. The stroma between the tumor lobules is fibrotic and often contains a prominent vascular proliferation that may obscure the histology of the underlying neoplastic process [71]. Uncommon findings include occasional calcification, melanin-containing cells, ganglion cells, and divergent differentiation with rhabdomyoblasts or epithelial islands [70]. Ganglioneuroblastic transformation after chemotherapy has been reported [72].

Immunohistochemistry and other special stains: In keeping with their neuroblastic differentiation, esthesioneuroblastomas show strong immunoreactivity for neuroendocrine marks including synaptophysin (Fig. 7.3e), chromogranin, CD56, neuron-specific enolase [73], neurofilament protein, and calretinin [74]. S-100 protein is usually expressed in the sustentacular cells at the periphery of the tumor lobules. A few esthesioneuroblastomas may focally express cytokeratin or p63, but they usually show negative immunoreaction to EMA [75, 76]. In general, esthesioneuroblastomas show negative immunoreactivity to HMB45, desmin, myogenin, CD99, and leukocyte common antigen, unless heterologous elements are present (see above).

Molecular diagnostic features and cytogenetics: Molecular genetic data is sparse for esthesioneuroblastoma. Several recent studies have demonstrated extremely complex genetic changes, but none has been sufficiently recurrent to be helpful in diagnosis [77–79]. The constant absence of t(11;22) or *EWS* rearrangement [80–82] indicates that esthesioneuroblastoma is not related to Ewing's sarcoma.

Prognostic features: In pediatrics, the first line of treatment for esthesioneuroblastoma is a combination of chemotherapy and radiotherapy. The most important predictors of outcome are tumor stage, treatment modality, lymph node status, and age at diagnosis. The prognosis is better in children in comparison to adult patients [67], with overall 5-year survival rates of 45.6 % in adults and 88.9 % in children [61, 67]. Lymph node metastasis, which occurs in approximately 23 % of the cases, has been considered as an important prognostic factor; therefore an elective neck treatment has been recommended [83–85].

Sarcomas Affecting the Nasal Area

Sarcomas arising in nasal area are rare and account for no more than 5 to 10 % of all malignant tumors in head and neck region. Compared to adults, children have a somewhat higher proportion of sarcomas in the head and neck and about 40 % of all rhabdomyosarcoma arise in the region. Among head and neck rhabdomyosarcoma, 35–50 % arise in the sinonasal and nasopharyneal areas [86, 87]. The majority in the sinonasal region are alveolar type and have worse prognosis than tumors in other head and neck areas [86]. Other rare sarcomas in the sinonasal region include fibrosarcoma, leiomyosarcoma, malignant fibrous histiocytoma, angiosarcoma, and malignant peripheral nerve sheath tumor (MPNST). The morphology, immunohistochemistry, and molecular features of sinonasal sarcomas are similar to the same tumors occurring in other parts of the body.

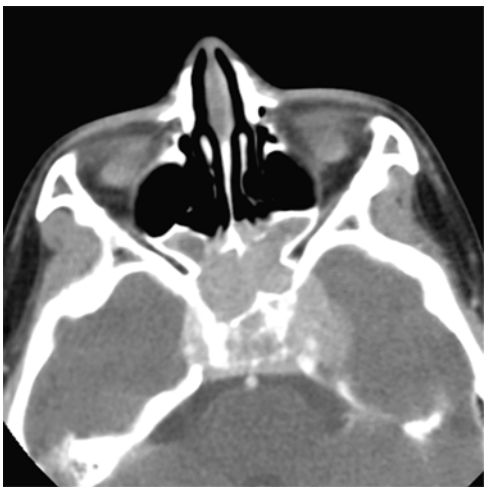

Fig. 7.4 *Rhabdomyosarcoma*. Contrast-enhanced CT image of a young girl shows a large mass centered in the sphenoid sinus with intracranial extension and bony destruction of the skull base

Imaging features: Rhabdomyosarcoma in the paranasal regions is often advanced and locally invasive. Imaging usually demonstrates a poorly defined enhancing mass commonly with bony destruction and intracranial extension (Fig. 7.4). CT is useful to demonstrate the degree of bony erosion. When in the nasal soft tissues, rhabdomyosarcoma may present as a relatively small soft-tissue mass without bony destruction. The absence of bony erosion is also common in rhabdomyosarcoma in other head and neck regions. MRI is especially useful in the evaluation of intracranial extension as well as on follow-up of these tumors.

Oral Cavity and Salivary Gland Carcinomas in Children

Salivary glands are exocrine organs and comprise three paired major glands (the parotid, submandibular, and sublingual), and numerous minor widely distributed throughout the mouth and oropharynx. The global annual incidence of malignant

salivary gland tumors ranges from 0.4 to 0.9 cases per 100,000 population [88, 89]. The peak incidence of salivary gland carcinomas is in the sixth and seventh decades [90, 91]. From 1973 to 2006, Sultan et al. identified 12,834 cases of salivary gland carcinomas reported to the Surveillance, Epidemiology, and End Results (SEER) database, of which only 263 cases (2 %) occurred in children and adolescents (<20 years) [92]. Mucoepidermoid carcinoma is the most common primary salivary gland malignancy in both adults and children and often presents as a secondary cancer in pediatric patients with a history of nonsalivary cancer. Sialoblastoma is unique to pediatrics as most tumors present congenitally or during early infancy. Acinar cell carcinoma and adenoid cystic carcinomas are very rare in the pediatric population and may act similarly to those occurring in adults [93].

Mucoepidermoid Carcinoma

Definition: Mucoepidermoid carcinoma is a malignant glandular epithelial tumor arising from the large ducts of both major and minor salivary glands. It is principally composed of three types of cells, mucinous, squamous, and intermediate, that display columnar, clear cell and oncocytoid features.

Clinical features and epidemiology: Although rare, mucoepidermoid carcinoma is the most common malignant salivary gland tumor in childhood. Many pediatric patients have a history of chemotherapy or radiation for a nonsalivary malignancy [94]. Most tumors arise in the major salivary glands, predominantly in the parotid. Occasionally, the tumors occur in minor salivary glands, most commonly in the palate. Rarely, the tumor may occur in the trachea, nasal cavity, and other locations [95]. Most patients present with an isolated, painless, and slow-growing mass. The clinical and pathologic features are similar in pediatric and adult populations.

Imaging features: Diagnosis of mucoepidermoid carcinoma may be difficult based on imaging alone, and tissue diagnosis is usually needed. On computed tomography, these tumors frequently appear as well-defined masses with moderate enhancement (Fig. 7.5a). Magnetic resonance can be useful in evaluating soft-tissue masses in the salivary glands, since it has better tissue resolution. The mass is usually hyperintense to the adjacent gland on T2-weighted images, and however hypointense compared to the adjacent lymph nodes [96]. Differential diagnosis includes vascular malformations as well as pleomorphic adenoma, the most common salivary gland tumor in children. Pleomorphic adenomas tend to have higher signal intensity on T2-weighted MR images compared to mucoepidermoid carcinoma [97]. Other malignancies such as adenoid cystic carcinoma, acinic cell carcinoma, and lymphoma may have similar imaging findings to mucoepidermoid carcinoma. Imaging features of atypical infection may also overlap.

Gross and microscopic features: Grossly, mucoepidermoid carcinoma is firm, often cystic, and tan with well-defined or infiltrated margin. Microscopically, it is principally composed of three types of cells: mucin producing, squamous (epidermoid), and intermediate. Mucus cells vary in shape and contain abundant foamy cytoplasm that stains positively with mucin stains. Squamous cells are usually polygonal shaped and show intercellular bridges and occasional keratinization. Intermediate cells are basaloid in appearance and believed to be able to differentiate into the other two cell types [98]. Some tumors also show variable numbers of clear cells or lymphoid infiltrates.

Mucoepidermoid carcinoma can be divided into low-, intermediate-, and high-grade types. Low-grade tumors consist of well-differentiated mucin-producing cells which produce well-formed glandular structures or cystic spaces (Fig. 7.5b). High-grade tumors have a more cellular appearance and are composed largely of squamous and intermediate cells with minimal mucinous cells (Fig. 7.5c). The intermediate-grade tumor usually has more intermediate and squamous cells than the low-grade lesion, with occasional cysts and intracystic proliferation of intermediate or squamous cells. There is usually no marked nuclear atypia, brisk mitosis, or extensive necrosis in any grade of this tumor.

Immunohistochemistry and other special stains: Sialomucin content of mucin-producing mucoepidermoid carcinoma cells is demonstrated by mucicarmine or Alcian blue staining (Fig.7.5d). This special stain is particularly useful in high-grade tumors, in which the mucin-producing cells are usually sparse. Cytokeratin, especially high-molecular cytokeratin, and p63 may be used to identify squamous cells [99].

Molecular diagnostic features and cytogenetics: A nonrandom t(11;19) reciprocal translocation with a *CRTC1-MAML2* fusion oncogene is frequently identified in mucoepidermoid carcinoma by conventional cytogenetics, FISH, and reverse transcription polymerase chain reaction [99]. However, this translocation may be found in some benign salivary tumors such as Warthin's tumour and clear cell hidradenoma, so that interpretation must be performed in the context of histopathology.

Prognostic features: Treatment of mucoepidermoid carcinoma includes surgery or radiation, or both. The most important prognostic factors are the tumor grade and stage. Tumors in children have a better prognosis. One study showed that the 5-year survival rate in pediatric mucoepidermoid carcinoma

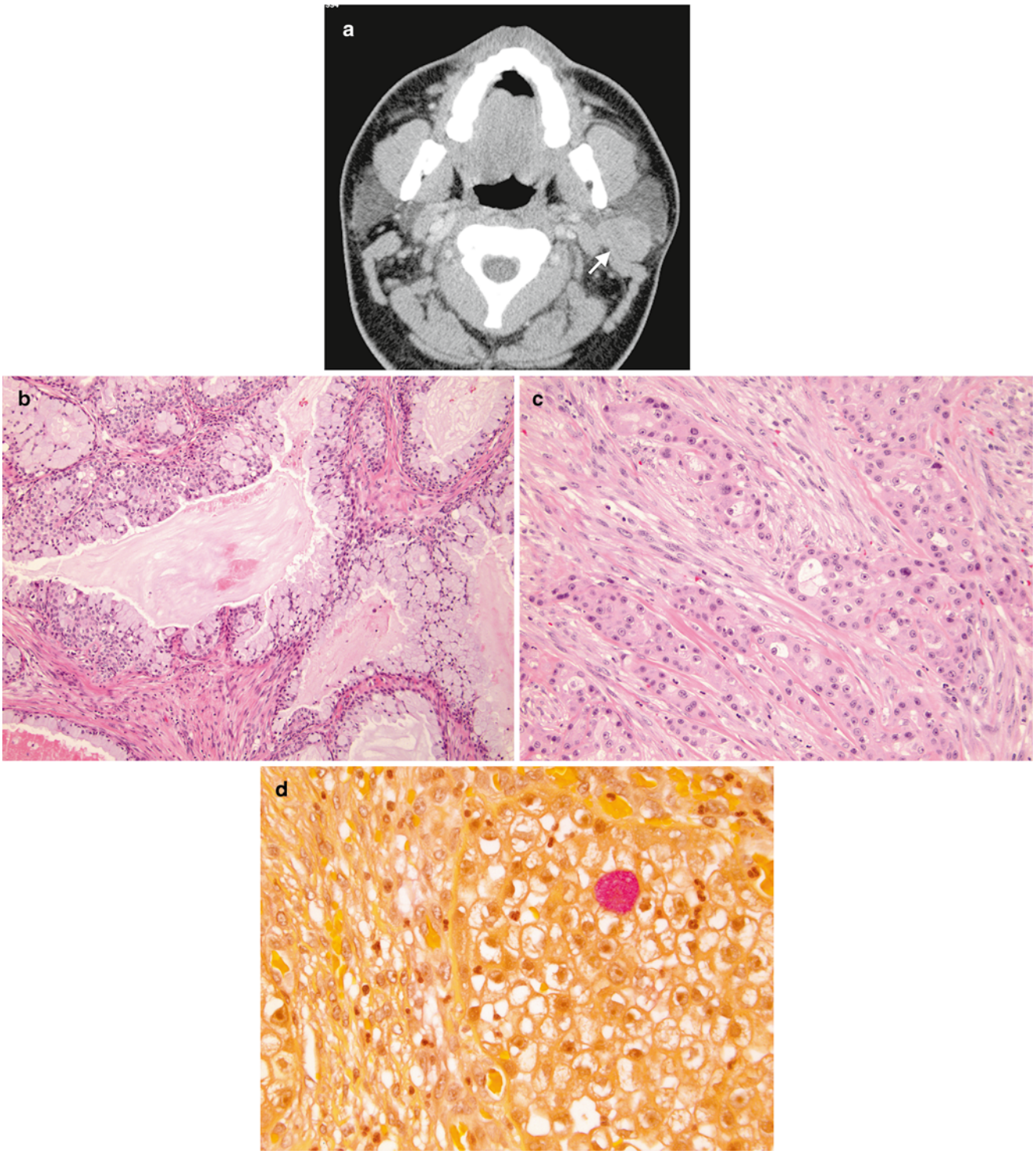

Fig. 7.5 (**a**) *Mucoepidermoid carcinoma*, *left parotid gland*. Postcontrast CT image demonstrates a moderately enhancing, well-circumscribed mass within the posterior aspect of the left parotid gland (*arrow*). Biopsy confirmed mucoepidermoid carcinoma. (**b**) *Mucoepidermoid carcinoma*, *low grade*. The tumor consists predominately of well-differentiated mucin-producing cells with well-formed glandular structures and cystic spaces. (**c**) *Mucoepidermoid carcinoma*, *high grade*. The tumor is composed of solid sheets of squamous and intermediate cells with minimal mucinous cells. (**d**) *Mucoepidermoid carcinoma*, *high grade*. The mucus cell contains abundant foamy cytoplasm that stains positively with mucicarmine special stain (*pink color*)

was 93.7 %, and survival rate did not differ in patients with secondary tumors [94]. Mucoepidermoid carcinoma with *CRTC1-MAML2* may have a better prognosis [100].

Sialoblastoma

Definition: Sialoblastoma is a rare, malignant epithelial salivary gland neoplasm that usually present at birth and recapitulates the primitive salivary anlage [101].

Clinical features and epidemiology: Most sialoblastomas present congenitally or during early infancy. Some patients may be diagnosed by prenatal ultrasound. Occasional children may be diagnosed after the age of 2 years. Most patients present with respiratory difficulty shortly after birth. The male-to-female ratio is 2:1. The tumor commonly arises in the parotid or submandibular gland. Originally considered as a benign neoplasm, sialoblastomas have documented locoregional recurrence and distant metastases and so are included among malignant epithelial salivary gland neoplasms. The simultaneous occurrence of hepatoblastoma has been reported [73, 102, 103].

Imaging features: Very few case reports describe the imaging features of sialoblastoma. CT shows a mass which is usually hypoattenuating compared to adjacent muscle. On MR, this tumor has been demonstrated to have isointense signal to muscle on T1-weighted images and an intermediate-to-high signal intensity on T2-weighted images [21]. On contrast-enhanced T1-weighted images sialoblastoma usually demonstrates heterogeneous contrast enhancement [21]. Intralesional hemorrhage and necrosis have also been described [104].

Gross and microscopic features: Grossly, sialoblastoma is a firm, smooth, polypoid mass measuring 2–7 cm in greatest dimension [105]. Microscopically, tumors have a biphasic pattern: basaloid epithelial cells that form ductules or bud-like structures and solid organoid nests, and relatively hypocellular spindle cell stroma (Fig. 7.6). The basaloid epithelial cells have scanty cytoplasm, round-to-oval nuclei, single or few nucleoli, and relatively fine chromatin pattern. More mature cuboidal epithelial cells with squamous differentiation can be seen, and some form solid squamous nests or duct structures resembling sialometaplasia. The mitotic rate within sialoblastomas is highly variable and may increase with subsequent recurrences [106]. Significant necrosis and marked pleomorphism are uncommon in this tumor.

Immunohistochemistry and other special stains: Sialoblastomas show diffuse and widespread reactivity for salivary gland amylase. The epithelial components express p63, cytokeratin, EMA, CK5/6, CK7, and S-100. There is no expression for CK20. The stroma spindle cells show focal reactivity to smooth muscle actin [101, 107].

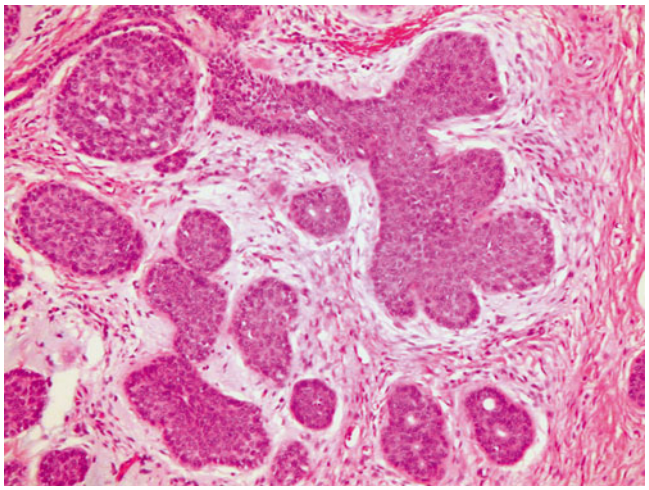

Fig. 7.6 *Sialoblastoma*. The tumor has a biphasic pattern: basaloid epithelial cells with squamous features that form solid organoid nests with focal ductule-like structures, and relatively hypocellular spindle cell stroma (picture courtesy Deborah Perry, M.D., Children's Hospital & Medical Center, University of Nebraska Medical Center College of Medicine)

Molecular diagnostic features and cytogenetics: One case report of a sialoblastoma showed clonal chromosome aberrations with a complex karyotype [106].

Prognostic features: Surgery is the treatment of choice. There is limited prognostic data on this tumor due to its rarity. One study has suggested that the presence of anaplastic basaloid tumor cells, minimal stroma, and broad pushing to infiltrative periphery may be related to more aggressive behavior [105].

HPV-Related Carcinoma

HPV has become a considerable concern in cancer epidemiology and is linked to carcinomas of the head and neck and male and female genitalia. In children, HPV-associated neoplasms primarily arise in the context of congenital infections presumably acquired around the time of labor and delivery. These lesions primarily affect the mouth, pharynx, and larynx and may give rise to solitary or multiple papillomas. Juvenile oropharyngeal papillomas usually are benign lesions comprising a layer of HPV-infected stratified squamous epithelium overlying a fibrous core. They show variable degrees of dysplasia and atypia, as well as koilocytosis. HPV types 6 and 11 predominate in these lesions [108, 109]. The tumors may be aspirated into the lungs and cause bronchial based lesions. Rarely they give rise to well-differentiated squamous cell carcinomas, with cervical nodal metastasis [110].

A rising health care concern is the increasing incidence of oral cancers among younger nonsmoking adults, primarily as a result of sexual exposures to oncogenic HPV types 16 and 18 [3, 111]. Sites affected include the tongue and tonsils [112, 113]. Although adolescents are reportedly not affected by metastatic cancers, we have seen oral in situ carcinomas in our dental clinic.

Imaging features: Masses within the oral cavity and larynx are frequently diagnosed by direct visualization and laryngoscopy. Imaging plays an important role in evaluation of the submucosal involvement, involvement of deep soft tissues and bone, as well as in evaluation for distant metastases [118]. Squamous papillomas can be solitary or multiple. The multiple form is also known as juvenile laryngotracheal papillomatosis. Computed tomography demonstrates nodules within the larynx and tracheobronchial tree and lungs. CT is important in evaluating the extent of these lesions and degree of tracheal and lung involvement. The possibility of malignant transformation of papilloma makes follow-up by CT important in these patients [114]. Squamous cell carcinoma of the oral cavity may appear as homogeneous or heterogeneous masses with variable contrast enhancement. Contrast enhancement may predominate along its margins [115]. On MRI, SCC has predominantly low-to-intermediate T1 signal and intermediate-to-high T2 signal. Delineation of soft tissue involvement is better demonstrated with MRI. A significant percentage of SCC of the oral cavity present with lymph node metastases.

Melanotic Neuroectodermal Tumor of Infancy

Clinical features and epidemiology: Melanotic neuroectodermal tumor of infancy is a rare neoplasm of neural crest origin that presents in the first year of life in 95 % of cases, typically involves the mandible or maxilla, and has similarities to neuroblastoma and Ewing's sarcoma histologically but is genetically unique [116]. The tumor may present congenitally, and occasionally can involve sites outside of the jaw, such as the leptomeninges, genitourinary system, and the extremities. Like neuroblastoma, plasma and urine catecholamine metabolites may be elevated. Other names that have been applied to this tumor in the past are retinal anlage tumor and progonoma. Although the majority (greater than 90 %) behave in a benign fashion, there are recorded cases of metastases and fatal outcome [117].

Imaging features: About 70 % of MNTI arise in the maxilla, followed by 11 % in the skull and 6 % in the mandible. Skull lesions generally arise around the sutures with about 50 % occurring near the anterior fontanelle. Parenchymal brain involvement, when present, results from direct tumor extension, although there are reports of MNTI arising in the third ventricle and cerebellar vermis. Tumors generally compress adjacent structures rather than infiltrating them. In the mandible and maxilla they may cause tooth displacement, bone destruction, expansion, or remodeling.

Plain-film radiography: Initial radiographs may show a well-marginated, non-aggressive, radiolucent lesion with or without irregular margins in the skull or facial bones [118, 119]. When tumors arise in the mandible or maxilla, the differential includes developmental cysts, odontogenic lesions, infection, fibrous dysplasia, and vascular malformations. In contrast to benign lesions, MTNI grow rapidly resulting in bone destruction, a finding that can narrow the differential to more aggressive lesions. Occasionally a faint spiculated or sunburst appearance may be present [120].

Computed tomography: CT can accurately define the extent of the lesion and aid in surgical planning [119]. Tumors appear expansile with a well-defined soft-tissue component that may be slightly hyperdense on non-contrast-enhanced images due to melanin content. The tumors generally enhance after administration of contrast material. Maxillary lesions may cause "floating teeth" while calvarial lesions may show spiculation and hyperostosis [116, 120].

Magnetic resonance imaging (*MRI*): On MRI, maxillary and calvarial tumors may appear variably hyperintense on T1-weighted and hypointense on T2-weighted images depending on the amount of melanin within the tumor. The tumor may also contain areas that are hypointense on both T1- and T2-weighted images due to calcification and hyperostosis (Fig. 7.7a–c). After administration of contrast material, MTNI typically demonstrate intense enhancement in non-calcified areas. On diffusion-weighted MRI, cellular areas of tumor will demonstrate restricted diffusion. Sinovenous involvement, which is sometimes associated with this tumor, is best assessed with magnetic resonance angiography [118, 119].

Gross and microscopic features: Ranging in size from 1 to 10 cm, these tumors are gray-black and firm to palpation, reflecting the presence of pigment and a prominent stromal component. Histologically, nests of tumor cells are surrounded by dense fibrous stroma (Fig. 7.7d, e). The cellular nests are composed of primitive small neuroblast-like cells with hyperchromatic nuclei and little cytoplasm. These cells may form neuroblastic type rosettes, and in some cases may be associated with neuropil. Mitoses are absent to rare. Larger, melanin-containing cells are present, either interspersed with the neuroblast-like cells or present at the periphery of the nests [117, 121].

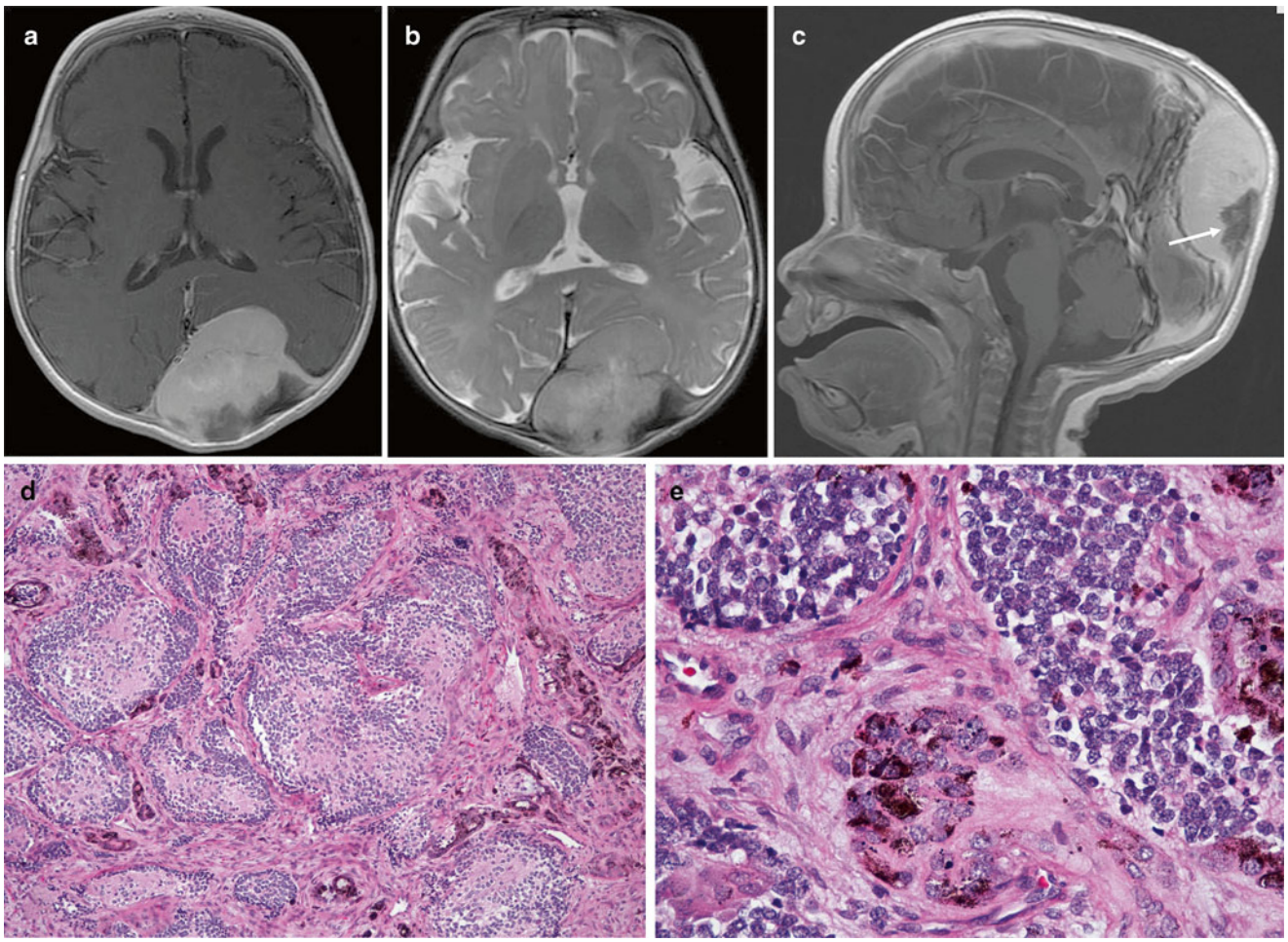

Fig. 7.7 (**a**–**e**) *Melanotic neuroectodermal tumor of infancy arising in a 5-month-old male*. (**a**) Axial T1W postcontrast MRI image shows the extra axial tumor to be homogenously enhancing. (**b**) Axial T2W MRI image shows the tumor to be predominantly isointense to white matter, and causing mass effect on the underlying parenchyma. (**c**) Sagittal postcontrast T1W MRI image shows contrast enhancement of the tumor except in the area of spiculated hyperostosis, a feature typical of MNTI. (**d**) Nested, neuroblastoma-like pattern with pigmented cells in the peripheral fibroblastic stroma. (**e**) Higher power view of D, demonstrating coarse melanin granules at the periphery of the small cell nests

Immunohistochemical and other special stains: The large cells of melanotic neuroectodermal tumors stain immunohistochemically with melan-A, HMB-45, vimentin, cytokeratin AE1/AE3, and epithelial membrane antigen but are negative with S-100. Cytoplasmic melanin can be demonstrated with the Fontana stain. The neuroblast-like cells stain with neural markers such as NSE and CD56, and have variable staining for chromogranin, synaptophysin, and GFAP. Occasional cases have shown positivity with desmin and muscle-specific actin, and may even show focal myogenin positivity [121, 122]. CD99 is generally not expressed, although one of the eight cases in one study had membranous staining [123]. Cases subjected to electron microscopic examination have shown the small cells to share the ultrastructural features of dense core neurosecretory granules and dendritic processes with neuroblastoma, whereas the larger cells contain melanosomes [124].

Molecular diagnostic features and cytogenetics: Molecular genetic data is sparse for this rare neoplasm, and the diagnosis rests largely upon its biphasic light microscopic appearance and polyphenotypic immunohistochemical profile. Unlike Ewing's sarcoma, these tumors lack a t(11;22) translocation [116], and unlike neuroblastoma none of these tumors have shown evidence of MYCN amplification or 1p deletion [124].

Lymphoma/Leukemia of the Oral Cavity

Pediatric lymphomas have a well-known tendency to first appear as enlarged cervical lymph nodes or neck masses and are more extensively discussed in the chapter on hematopoietic and lymphoid tumors. Of particular note, however, in a discussion of pediatric head and neck tumors is the tendency of both Burkitt lymphomas and monoblastic

leukemias to present as jaw masses. Gnathic Burkitt lymphomas have been well described in the original literature of the endemic, EBV-associated form of the disease discovered in sub-Saharan Africa by Burkitt in 1952 [125]. For a fascinating history of the association between Burkitt lymphoma and EBV, the reader is referred to reference [126]. Outside of this setting, Burkitt lymphoma of the jaw is distinctly rare [127].

The head and neck, particularly the oral cavity and jaw, comprise a relatively common site for myeloid sarcomas. Monoblastic leukemias of the jaw tend to occur in young patients and are usually associated with 11p23 translocations involving the *MLL* gene [128]. Other leukemias may also present in this manner [129], and the leukemia may be first discovered by histological examination of soft tissues associated with an extracted tooth. The gingival tissues appear to be one of the preferred sites for extramedullary leukemias, which may present prior to leukemic manifestations of the disease.

Imaging features: Burkitt lymphoma in the head and neck typically affects the mandible or maxilla. On radiographs and CT, these appear as poorly defined lytic lesions with displacement of tooth buds [130]. The differential diagnosis for a lytic lesion involving the mandible/maxilla is however broad and include more common entities such as infection, benign cysts, Langerhans cell histiocytosis, and sarcomas.

Sarcomas of the Oral Cavity/Salivary Glands

A number of pediatric sarcomas show a predilection for the head and neck and have a particular propensity to arise in or near the mouth or salivary glands. The most common by far is embryonal rhabdomyosarcoma, which can affect soft tissues adjacent to the parotid gland [121]. Diagnosis may be accomplished by fine-needle aspiration [131]. Rarely, alveolar rhabdomyosarcoma also occurs in these regions [131, 132], but confirmation of fusion status via FISH, RT-PCR, or karyotyping is advisable to avoid over-treatment. Following radiation and chemotherapy, 5-year overall survival of parotid region rhabdomyosarcomas approaches 85 % [121].

Among pediatric non-rhabdomyosarcomatous soft-tissue sarcomas (NRSTS), epithelioid sarcoma [133], alveolar soft part sarcoma [134, 135], myofibrosarcoma [136], and synovial sarcoma [137, 138] share a propensity to occur in the head and neck, particularly in and about the oral cavity. The prognosis of these lesions generally depends on the adequacy of excision. Synovial sarcomas respond well to chemotherapy [139, 140].

Among bony sarcomas, osteosarcomas may occur in the jaw, where they appear to have clinicopathological characteristics distinct from those arising in extremities [141]. Most occur in the mandible. In children, they generally show an osteoblastic morphology and tend to be large and of high grade [54]. In spite of these features, they have a better outcome than extremity osteosarcomas [54].

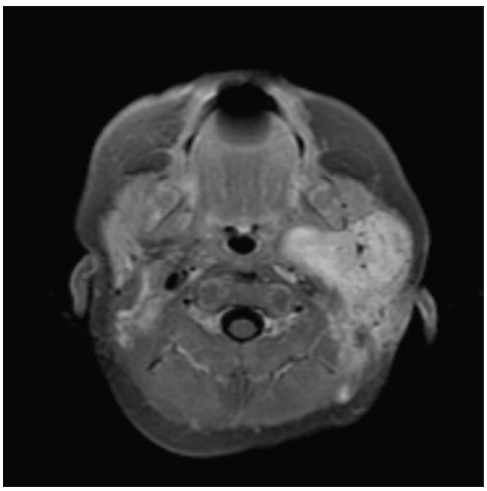

Fig 7.8 *Rhabdomyosarcoma, left parotid gand*. Axial T1W postcontrast MRI image demonstrates a large infiltrative enhancing mass involving the left parotid gland and extending into the deep cervical soft tissues and parapharyngeal space

Imaging features: Rhabdomyosarcomas in the head and neck usually present as a soft-tissue mass which may cause bone destruction or remodeling. The absence of bone involvement is fairly common, however, for smaller lesions. CT is the modality of choice to evaluate for bony involvement. On MRI the mass tends to be hypointense on T1, and of low, intermediate, or high signal intensity on T2 depending on the cellularity. Contrast enhancement is variable; however, postcontrast imaging is helpful for evaluation of intracranial extension of disease [4] (Fig. 7.8). The presence of associated metastatic lymphadenopathy is common at presentation and imaging of cervical lymph nodes should be included in the initial evaluation.

Osteosarcomas of the head and neck most frequently affect the mandible and maxilla and frequently present with swelling and pain. On CT, they tend to have an aggressive osteolytic appearance with tumor matrix mineralization and a soft-tissue component [142, 143] (Fig. 7.9). An osteolytic lesion without tumor matrix mineralization is less common but can occur. CT is excellent in demonstrating tumor calcification, cortical involvement, and soft-tissue involvement as well as intramedullary extension. Periosteal reaction tends to be less pronounced than in long bone osteosarcoma [142]. MRI can be useful in evaluating adjacent structures and follow-up posttreatment. Cervical lymphadenopathy at presentation is uncommon [142].

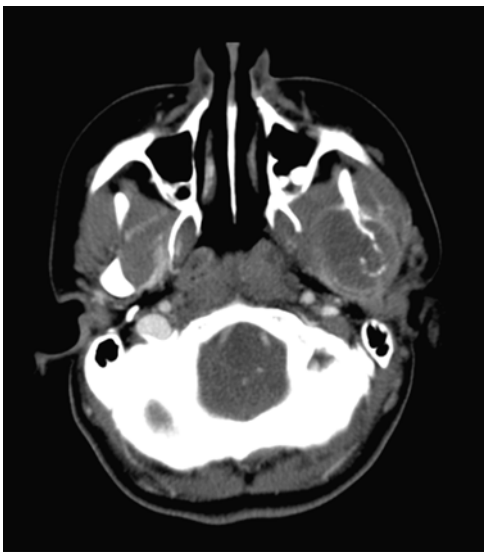

Fig 7.9 *Osteosarcoma of the mandible*. Contrast-enhanced CT image shows a fairly large, mostly rim-enhancing, mass involving the left mandibular ramus and condyle with intermixed calcific densities, bony destruction, and associated soft-tissue mass. The margins of the mass are difficult to distinguish from the surrounding musculature on CT and may be better delineated on MRI

Ear Tumors

Paragangliomas

Paragangliomas are more extensively discussed elsewhere in this text (see Tumors of Adrenal Gland and Extraadrenal Paraganglia). However, special mention must be made of the jugulotympanic paragangliomas that occur in the region of the ear or the glomus jugulare. These lesions may bulge against the tympanic membrane or into the jugular vein. Those in the ear cause problems with hearing, balance, or tinnitus, and those in the jugular region may extensively invade the base of the skull [144]. These lesions have a wide age range that includes children; fortunately they have a low metastatic rate, less than 5 % [145].

Imaging features: Paragangliomas (glomus tumors) may be confined to the middle ear (glomus tympanicum) or involve the region of the jugular bulb (glomus jugulare) with or without involvement of the middle ear due to destruction of the jugular plate (glomus jugulotympanicum). These are very rare in the pediatric population. On CT, the glomus jugulare or jugulotympanicum is a poorly defined soft-tissue mass with permeative bone destruction and avid diffuse contrast enhancement [146, 147]. A hyperintense mass on T2-weighted images is characteristic on MRI, with internal foci of hypointensity which represent high-flow vessels. Unenhanced T1-weighted images show their characteristic "salt-and-pepper" appearance. The "pepper" represents the hypointense foci caused by the signal void of large feeding vessels, whereas the "salt" is secondary to subacute hemorrhage or slow-flow vessels within the tumor [146, 147]. On angiography, this tumor is hypervascular, with rapid tumor blush and early draining veins. The glomus tympanicum has a characteristic appearance on CT which demonstrates a focal soft-tissue mass with flat base in the region of the cochlear promontory. The ossicular chain is usually spared and bone erosion is rarely present. These are frequently small tumors measuring up to 2 cm; however bone destruction may be present when the tumor is large. On T2-weighted images, these lesions may vary in signal intensity [146, 147]. Contrast-enhanced T1-weighted MR images usually demonstrate a strongly enhancing mass lesion within the middle ear.

Gross and microscopic features: Microscopically, jugulotympanic paragangliomas resemble those in other locations and contain epithelioid cells arranged in zellballen separated by rich vascular arcades and surrounded by sustentacular cells (Fig. 7.10a). They tend to be more vascular than other lesions, and they may show significant degrees of sclerosis. At times, they have a small cell, neuroblastoma-like configuration. Immunostains for neuroendocrine markers such as chromogranin and synaptophysin confirm the diagnosis. Immunostain for S-100 protein is positive in sustentacular cells, but negative in tumor cells (Fig. 7.10b). On occasion [148], rhomboid intracytoplasmic crystals that resemble those of alveolar soft part sarcoma are seen by electron microscopy.

Rhabdomyosarcoma of the Ear

Of all tumors arising in the ear, rhabdomyosarcomas head the list and often grow as invasive masses that expand into the middle ear of the external auditory canal. They usually affect younger patients (less than 5 years of age), who may present with purulent or bloody discharge associated with an external ear mass, sometimes with cranial nerve palsy [149].

Imaging features: CT and MRI both have a role in the evaluation of rhabdomyosarcoma of the middle ear and temporal bone. CT demonstrates the extensive bony destruction associated with these tumors, as well as involvement of the middle ear ossicles (Fig. 7.11a). MRI may better delineate the soft-tissue mass and the extent of disease, specifically the degree of intracranial involvement [146, 150]. The mass demonstrates nonspecific low-to-intermediate T1 and predominant high T2 signal on MRI, with intense enhancement with gadolinium [146, 150] (Fig. 7.11b). MRI is also useful in evaluating for recurrent disease. Obstructive secretions may be present in the mastoids. There may be invasion of adjacent structures, including external auditory canal, internal auditory canal, intracranial compartment, and temporomandibular fossa [151]. The facial canal may be involved [151]. It is diffi-

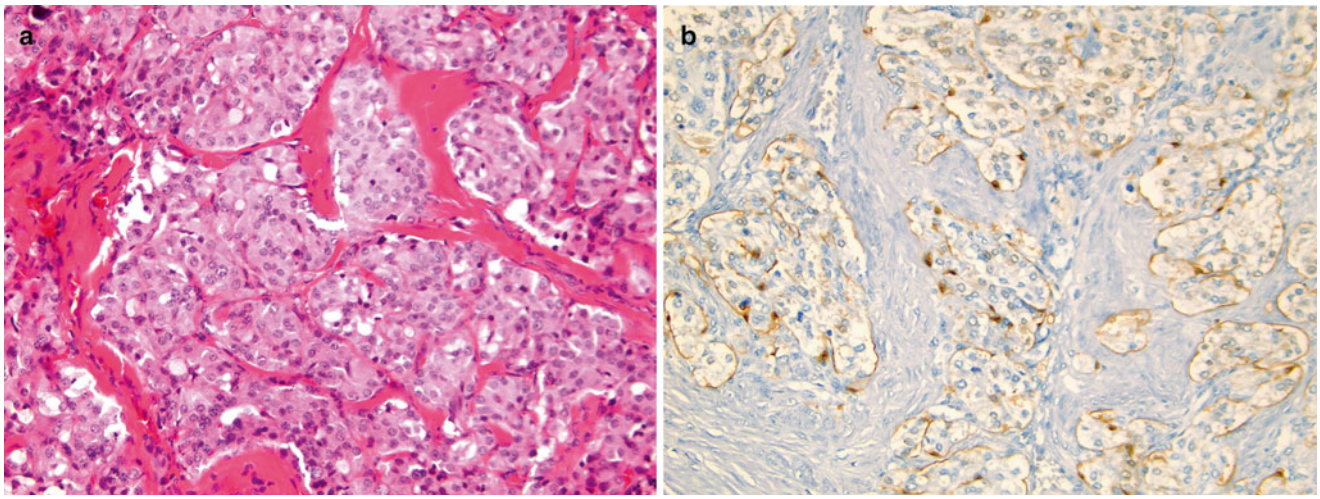

Fig. 7.10 (**a**, **b**) *Paraganglioma*. (**a**) The tumor contains epithelioid cells arranged in *zellballen* pattern and separated by rich vascular arcades. (**b**) S100 immunostaining reveals a network of sustentacular cells surrounding neuroendocrine cell clusters

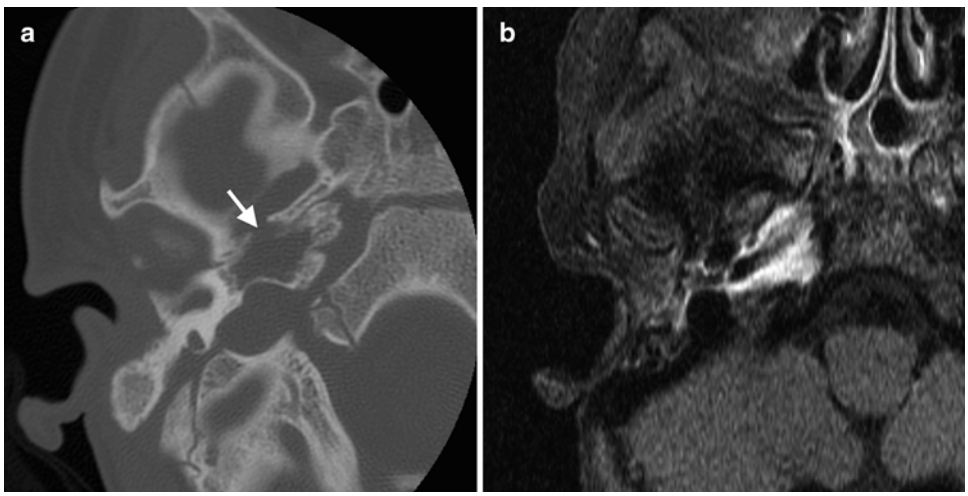

Fig. 7.11 (**a**, **b**) *Rhabdomyosarcoma of the temporal bone*. (**a**) CT of the temporal bone in a 4-year-old girl demonstrates an irregular destructive lesion involving the right petrous apex (*arrow*). There is erosion of the carotid canal (not shown). (**b**) Axial T1W postcontrast image in the same patient shows marked enhancement in the region of bone destruction, with encasement of the internal carotid artery

cult to differentiate rhabdomyosarcoma from Langerhans cell hystiocytosis and other aggressive entities on imaging; however rhabdomyosarcoma should always be considered when an aggressive-appearing middle ear/temporal bone lesion is found in a child.

Essentially all aural rhabdomyosarcomas are embryonal or botryoid lesions. In the series of Raney et al. [149], no alveolar rhabdomyosarcomas were found. As such, they will contain a condensed, subepithelial "cambium" layer of cells if botryoid, and they display a variety of cellular densities and cytodifferentiation patterns if embryonal (see the chapter on soft tissue sarcomas for more information). One must particularly beware of overdiagnosis of myxoid lesions, which may resemble chronic otitis. Myogenin and/or desmin stains should be confirmatory.

Survival of patients with aural rhabdomyosarcomas is generally good, particularly in patients with low-stage disease [149, 152]. In the most recent COG review, overall survival approached 90 % [152].

Thyroid Cancers

Papillary and Follicular Carcinoma

Clinical features and epidemiology: Although more common in adults, epithelial thyroid cancers as a group comprise the majority of adult-type carcinomas in children [153, 154]. Primarily, this has been due to the carcinogenic effect of radiation on the pediatric thyroid gland, as witnessed by the

childhood epidemics of thyroid cancer that followed the accident at the Chernobyl nuclear plant and the atomic bomb at Hiroshima [155–157]. Similar effects have been seen with the indiscriminate use of radiation for acne therapy or its rational use for lymphoma [158–161]. Adolescent autoimmune disease and chronic inflammation of the thyroid also have an associated risk of thyroid cancer [162–164], and it may occur in the setting of cancer susceptibility syndromes and inherited mutations [42, 165, 166]. In general, pediatric patients are adolescents, but thyroid cancer has been reported in children as young as newborn [167].

Clinically, the most common presentation of pediatric thyroid cancer is an otherwise asymptomatic cervical mass, generally found to be a cold nodule on ^{123}I nuclear scanning (see below). However, patients may present with hyperthyroidism and a hot nodule, and adolescent females in particular may have a history of Hashimoto's disease or Graves' disease [162, 168, 169]. The greatest challenge from a clinical and pathological standpoint is discrimination of carcinoma from adenoma or a hyperplastic goiter, which may form nodules of alarming proportions. These can be a particular challenge for cytological diagnosis when they contain excessive hemorrhage or colloid, and drainage or repeated aspiration may be required to obtain an adequate cytological specimen.

Another challenge for pediatric pathologists is the relative infrequency of childhood thyroid carcinoma, so that consultation is usually advisable with general cytopathologists or surgical pathologists who have more familiarity with these neoplasms on cytological preparations or frozen sections, both of which can present diagnostic challenges [see below]. Cytological diagnosis of thyroid carcinoma is beyond the purview of this text, but for additional information the reader can consult references [170, 171]. Cytological examination is usually performed prior to thyroid excision, but with inconclusive results frozen sections may be requested. In this instance, touch preparations of the thyroid nodule may be useful, but the cells look much different when stained with Romanowsky stains like Diff-Quik rather than Papanicolaou stains. Hematoxylin and eosin staining of the intraoperative touch preparation is thus recommended.

Imaging features: On ultrasound, papillary carcinoma appears as a solid hypoechoic nodule which frequently contains calcifications and internal vascularity (Fig. 7.12a, b). These findings, however, are not specific and a biopsy is mandatory. Follicular carcinoma has been described as a hypo- or isoechoic nodule. Ultrasound can also demonstrate an ill-defined mass, extraglandular extension, or lymph node enlargement, helpful clues for diagnosis of a thyroid malignancy [172]. CT and MR imaging is helpful in assessing patients with a suspected thyroid malignancy. They are useful to evaluate for the extraglandular extension (Fig. 7.12a) and also important in assessing for cervical and mediastinal lymph nodal metastases. On CT and MRI, papillary carcinoma may present as a well- or ill-defined mass, multiple nodules, or a diffuse infiltration of the gland [172]. Follicular carcinoma more often presents as a solitary lesion. Of the thyroid malignancies, papillary carcinoma has the highest incidence of cervical lymph node metastases [173]. Regarding metastatic lymph nodes, studies have shown that a lymph node larger than 13 mm or presence of a cystic lymph node in the setting of papillary carcinoma strongly indicates metastasis [174]. In a large number of cases, lymph node metastasis in the neck may precede the diagnosis of a thyroid mass. These metastatic lymph nodes are more common in the paratracheal and supraclavicular areas, followed by jugular and retropharyngeal regions. Distant metastasis to lung and bone is more common than lymphatic spread in follicular carcinoma [175]. Many papillary carcinomas concentrate radioiodine; consequently, iodinated radionuclides may be used both in the imaging evaluation and treatment of patients with thyroid cancers. ^{131}I is particularly useful following thyroidectomy in which it is valuable in identifying recurrent/residual disease in the thyroidectomy bed, as well as in detecting distant metastases. Iodinated contrast is contraindicated in the evaluation of differentiated thyroid carcinoma because iodine may compete with ^{131}I and therefore interfere with radioactive iodine treatment and diagnostic scans in these patients. Treatment is therefore recommended to be delayed after administration of iodinated contrast [175].

Gross and microscopic features: Of the two major pathological types of epithelial thyroid cancer, papillary carcinoma is far more common than follicular carcinoma. When the latter histological pattern is encountered, the follicular variant of papillary carcinoma should be rigorously excluded, as it has a propensity to occur in juveniles. Typically, papillary fronds of tumor are lined by rows of epithelial cells with clear nuclei resembling the kernels of an ear of corn. The nuclei are referred to as "Orphan Annie" nuclei because of their resemblance to the eyes of the cartoon character, but this has become an anachronism with the progressive decline of newspapers, few of which continue to print this once popular syndicated strip (Fig. 7.12c, d). Scattered laminated, calcified microspherites comprise another characteristic feature, and their appearance in areas of fibrosis or metastasis indicates the need for additional sections if diagnostic tumor is not present. Unfortunately, "Orphan Annie" nuclei are not seen with frozen sections, and microspherites are often absent. In the follicular variant of papillary carcinoma, papillae are absent, but follicles lined by cells with large "Orphan Annie" nuclei should be present at least focally.

Follicular carcinomas in children also present diagnostic challenges, particularly in their distinction from the relatively more common adenomas and hyperplasias. As a rule, follicular carcinoma in children is of low grade, so that diagnosis requires careful examination of the entire capsule. In low-grade follicular carcinoma, either complete capsular penetration or vascular

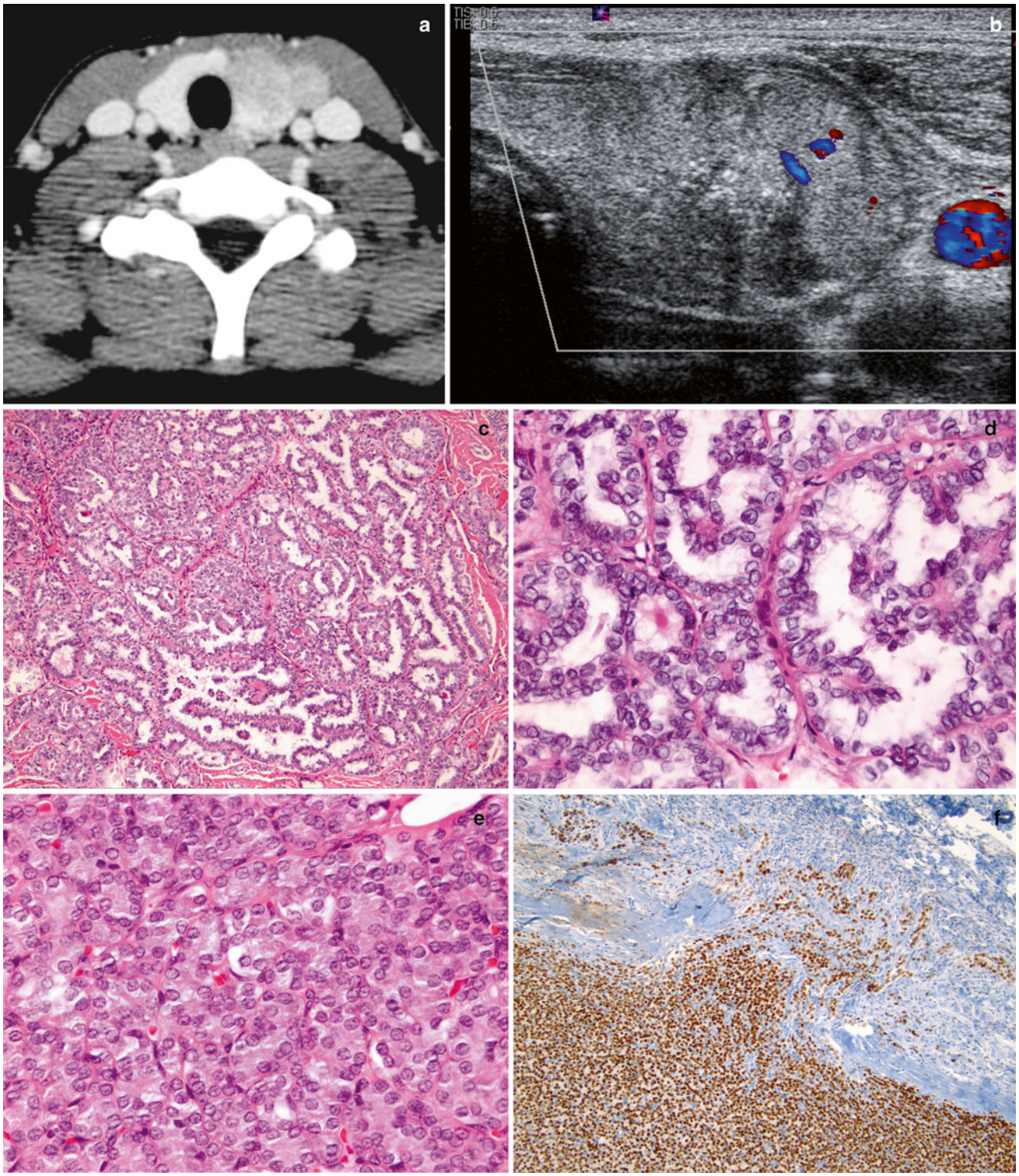

Fig. 7.12 (**a**, **b**) *Papillary thyroid carcinoma*. (**a**) Contrast-enhanced CT in a 16-year-old girl with a palpable left neck mass. An ill-defined mass is demonstrated within the left thyroid lobe with extension into the adjacent cervical soft tissues and presence of perithyroid lymph node. (**b**) Transverse ultrasound image in the same patient at the level of the left thyroid lobe before biopsy demonstrates similar ill-defined large thyroid lesion with mild internal vascularity. (**c**, **d**) *Papillary thyroid carcinoma*. (**c**) At lower magnification, the papillary fronds are obvious; they are lined by rows of epithelial cells with clear nuclei resembling the kernels of an ear of corn. (**d**) At higher magnification, the nuclei appear empty, also referred to as "Orphan Annie" nuclei because of their resemblance to the eyes of the cartoon character. Occasionally there are nuclear grooves. (**e**, **f**) *Follicular thyroid carcinoma*. (**e**) The tumor cells have a follicular arrangement; in contrast to papillary thyroid carcinoma, the nuclei in follicular thyroid carcinoma do not have a clearing or "Orphan Annie" appearance. (**f**) TTF-1 immunohistochemical stain highlights complete capsular penetration (tumor cells are stained *brown*; capsular tissue are stained *pale blue*)

invasion should be identified (Fig. 7.12e, f). Complete capsular penetration implies that tumor should be clearly present in the adjacent parenchyma. Vascular invasion may be easily missed unless one realizes that capsular vessels have a circumferential, parallel orientation. Thus, any tumors that invade the capsule and extend in a longitudinal fashion likely involve a vessel. In this instance, recuts and/or CD31 stains should clarify the presence of intravascular tumor.

For handling, reporting, and staging of thyroid carcinoma, the reader is advised to follow the College of American Pathologists checklist [176]. Items to be reported in this document include the type of the surgical procedure, the integrity, size, and weight of the specimen, the laterality, size, histological type and grade of the tumor(s), and the invasion status.

Immunohistochemistry and other special stains: In general, ancillary studies are not necessary for diagnosis of pediatric thyroid carcinoma. However, for metastatic lesions, thyroglobulin immunostains are extremely useful. Of note, neoplastic thyroid follicles in metastatic locations in extrathyroidal locations may appear benign but should be considered malignant. In these and other equivocal situations, thyroglobulin stains indicate an intrathyroidal location, which may be fibrotic and degenerate. Although "lateral aberrant thyroid" has been reported as a pathological curiosity in the older literature [177, 178], in modern practice these lesions are regarded as metastases [179].

Molecular diagnostic features and cytogenetics: Although the majority of non-medullary thyroid carcinomas are sporadic, many of which harbor somatic point mutations or gene rearrangement. More than 70 % of papillary carcinoma contains a point mutation in *BRAF* or *RAS*, *or* gene rearrangements with fusion genes involving *RET* or *NTRK1* with various partner genes such as *PTC*-1, -2, and -3 [180]. There is an association between the types of molecular alteration and the tumor morphology and prognosis. *BRAF* mutation is the most common molecular alteration detected in classical and aggressive variants of adult tumors, and is associated with more aggressive clinical behaviors. In pediatrics and in patients with a history of exposure to ionizing radiation, there is a higher prevalence of *RET*/*PTC* mutations and lower prevalence of *BRAF* mutations, which may in part explain the decreased aggressiveness of papillary carcinoma in children [171]. Tumors associated with *RET*/*PTC* mutations often have classical or solid morphology and have been frequently described in microcarcinomas, suggesting that they are an early genetic event in tumorigenesis. Point mutation in *RAS*, including *NRAS*, *HRAS*, and *KRAS*, may be seen in both papillary and follicular thyroid carcinomas. An additional common mutation is *PAX8*/*PPARγ* rearrangement, which is most commonly, although not exclusively, identified in follicular type carcinoma. Detection of the point mutations may be accomplished by PCR-based analysis, while identification of gene rearrangement can be achieved by RT-PCR or FISH [180].

Prognostic features: If treated appropriately, pediatric thyroid carcinoma has an excellent outcome, with a 5-year survival of 98 % for papillary variant and 96 % for follicular carcinoma [181]. The critical task for the pathologist is to avoid overdiagnosis, as total thyroid ablation and lifelong hormone replacement are indicated.

Medullary Thyroid Carcinoma

Clinical features and epidemiology: Medullary thyroid carcinoma is a rare and unusual cancer in children. It typically arises in the setting of multiple endocrine neoplasia type 2 (MEN2), along with pheochromocytoma, paraganglioma, an inherited form of Hirschsprung disease, and intestinal ganglioneuromatosis. These lesions are caused by autosomal dominant mutations in the *RET* protooncogene, which encodes the signal transduction protein merlin. Children of patients with MEN2 can be monitored by serum calcitonin level. Significant elevations of this hormone indicate the need for prophylactic thyroidectomy, so that the disease can be excised in a premalignant or non-metastatic stage. This also avoids the need for neck dissection to remove involved lymph nodes, but the patients require lifelong hormone replacement following the operation. Thyroids removed in this fashion often contain aggregates of C-cells, which are derived from fusion of the ultimobranchial body (the fifth pharyngeal pouch) with the developing thyroid. Under the influence of the mutant *ret*, the C-cells undergo clonal expansion and form small nodules that are best visualized by routine H&E stain and calcitonin immunohistochemistry [182, 183].

Imaging features: Ultrasound of medullary thyroid carcinoma usually shows a solid, hypoechoic mass with internal vascularity [175]. On CT and MRI, medullary carcinoma may be solitary or multifocal, the latter being more frequent in inherited forms. When a single mass is present, it tends to be well defined and have a relatively benign appearance on CT and MRI. A more infiltrative appearance has been correlated with familial forms. Punctate calcifications, extraglandular spread, and lymph node and distant metastasis may be present [184]. The lymph nodes are not usually cystic as in papillary carcinoma. ^{131}I MIBG (metaiodobenzylguanidine) and somatostatin analog ^{111}In pentetreotide have been used to evaluate primary and metastatic medullary thyroid carcinoma, since these tumors do not concentrate iodine. Iodinated contrast is therefore not contraindicated in these tumors.

Gross and microscopic features: Medullary carcinoma comprises a neuroendocrine cancer and as such has features of

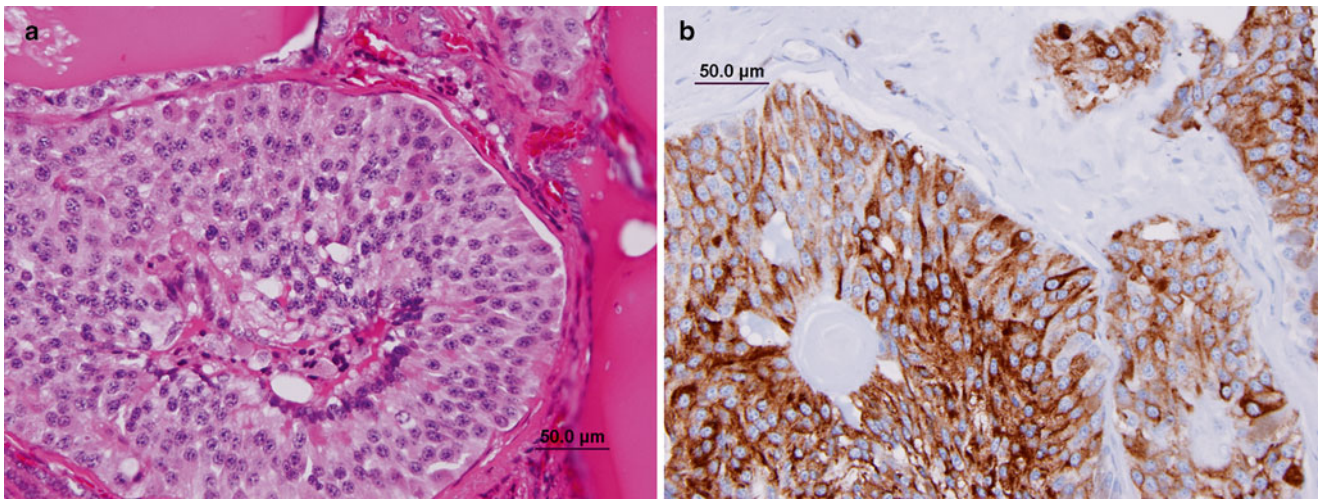

Fig. 7.13 (**a**) *Medullary thyroid carcinoma*. The tumor contains small cells arranged in a zellballen pattern, with balls of cells subdivided by a rich arborization of capillary-sized blood vessels. The tumor cells have even, round, monotonous nuclei with smooth nuclear membranes and granular "salt-and-pepper" chromatin. (**b**) The tumor cells show strong positivity for calcitonin immunostains, a useful feature for diagnosis of this tumor

similar lesions arising in other organs, such as islet cell carcinoma and pheochromocytoma. It typically contains small cells arranged in a *zellballen* pattern, with balls of cells subdivided by a rich arborization of capillary-sized blood vessels (Fig. 7.13a). These arcades of vessels may subtend the tumor cells into a trabecular or insular pattern, or the cells may form patternless sheets. Cytological features of the tumor cells include even, round, monotonous nuclei with smooth nuclear membranes and granular "salt-and-pepper" chromatin. In comparison, the cytoplasm is relatively inconspicuous and may be eosinophilic, amphophilic, purple, or clear. Cellular boundaries are indistinct. Mitoses may be prominent.

One peculiar feature of medullary thyroid carcinoma, less commonly seen in other neuroendocrine cancers, is the presence of amyloid within the interstitium. This substance possesses a bright pink, fibrillary quality and may resemble dense collagen at first glance. However, unlike collagen it stains with Congo red or thioflavin T and forms dense fibrillary pleated sheets on ultrastructural examination. Calcitonin polymers form this material in medullary carcinoma [185, 186], rather than the excess gamma globulin seen in other amyloid-producing diseases.

Immunohistochemistry and other special stains: As mentioned above, calcitonin immunostains are the most effective method to confirm the diagnosis of C-cell neoplasia (Fig. 7.13b). In addition, medullary carcinomas stain with neuroendocrine markers such as synaptophysin, chromogranin, NSE, and CD56, but the latter two immunostains are relatively unreliable in excluding other pediatric small-cell neoplasms.

Prognostic features: The prognosis is excellent for MEN2 patients who undergo prophylactic thyroidectomy. Genetic studies can confirm the presence of the mutation to ensure that periodic serum calcitonin levels are checked for this purpose. Otherwise, medullary carcinoma has a 96 % 5-year overall survival but only 86 % 15- and 30-year survivals [181].

Acknowledgment The section on Melanotic Neuroectodermal Tumor of Infancy was written by Dr. Bruce R. Pawel and Dr. Rakhee Kisan Sansgiri.

References

1. Zhou J, Michaud DS, Langevin SM, McClean MD, Eliot M, Kelsey KT. Smokeless tobacco and risk of head and neck cancer: evidence from a case-control study in New England. Int J Cancer. 2013;132(8):1911–7. Epub 2012/09/19. doi: 10.1002/ijc.27839, PubMed PMID: 22987222; PubMed Central PMCID: PMC3552089.
2. Hashibe M, Hunt J, Wei M, Buys S, Gren L, Lee YC. Tobacco, alcohol, body mass index, physical activity, and the risk of head and neck cancer in the prostate, lung, colorectal, and ovarian (PLCO) cohort. Head Neck. 2012. Epub 2012/06/20. doi: 10.1002/hed.23052. PubMed PMID: 22711227.
3. Dufour X, Beby-Defaux A, Agius G, Lacau St Guily J. HPV and head and neck cancer. Eur Ann Otorhinolaryngol Head Neck Dis. 2012;129(1):26–31. Epub 2011/09/29. doi: 10.1016/j.anorl.2011.05.004, PubMed PMID: 21944953.
4. Robson CD. Imaging of head and neck neoplasms in children. Pediatr Radiol. 2010;40(4):499–509. doi: 10.1007/s00247-009-1526-9, PubMed PMID: 20225112.
5. Engleson J, Soller M, Panagopoulos I, Dahlen A, Dictor M, Jerkeman M. Midline carcinoma with t(15;19) and BRD4-NUT fusion oncogene in a 30-year-old female with response to docetaxel and radiotherapy. BMC Cancer. 2006;6:69.
6. Galioto S, Di Petrillo A, Pastori M, Arecchi A. Metastatic esthesioneuroblastoma secreting adrenocorticotropic hormone in pediatric patients. J Craniofac Surg. 2011;22(5):1924–9.
7. Jadvar H, Connolly LP, Fahey FH, Shulkin BL. PET and PET/CT in pediatric oncology. Semin Nucl Med. 2007;37(5):316–31. doi: 10.1053/j.semnuclmed.2007.04.001, PubMed PMID: 17707239.
8. Barnes L, Eveson JW, Reichart P, et al., editors. World Health Organization classification of tumors: pathology and genetics of head and neck tumors. Lyon: IARC Press; 2005.

9. Chang ET, Adami HO. The enigmatic epidemiology of nasopharyngeal carcinoma. Cancer Epidemiol Biomarkers Prev. 2006;15(10):1765–77.
10. Ablashi DV, Levine PH, Prasad U, Pearson GR. Fourth international symposium on nasopharyngeal carcinoma application of field and laboratory studies to the control of NPC. Cancer Res. 1983;43(5):2375–8.
11. Shanmugaratnam K. Nasopharyngeal carcinoma: epidemiology, histopathology and aetiology. Ann Acad Med. 1980;9(3):289–95.
12. Nam JM, McLaughlin JK, Blot WJ. Cigarette smoking, alcohol, and nasopharyngeal carcinoma: a case-control study among U.S. whites. J Natl Cancer Inst. 1992;84(8):619–22.
13. Bray F, Haugen M, Moger TA, Tretli S, Aalen OO, Grotmol T. Age-incidence curves of nasopharyngeal carcinoma worldwide: bimodality in low-risk populations and aetiologic implications. Cancer Epidemiol Biomarkers Prev. 2008;17(9):2356–65.
14. Cannon T, Zanation AM, Lai V, Weissler MC. Nasopharyngeal carcinoma in young patients: a systematic review of racial demographics. Laryngoscope. 2006;116(6):1021–6.
15. Richey LM, Olshan AF, George J, Shores CG, Zanation AM, Cannon T, et al. Incidence and survival rates for young blacks with nasopharyngeal carcinoma in the United States. Arch Otolaryngol Head Neck Surg. 2006;132(10):1035–40.
16. Sultan I, Casanova M, Ferrari A, Rihani R, Rodriguez-Galindo C. Differential features of nasopharyngeal carcinoma in children and adults: a SEER study. Pediatr Blood Cancer. 2010;55(2):279–84.
17. Stambuk HE, Patel SG, Mosier KM, Wolden SL, Holodny AI. Nasopharyngeal carcinoma: recognizing the radiographic features in children. Am J Neuroradiol. 2005;26(6):1575–9. PubMed PMID: 15956532.
18. Yabuuchi H, Fukuya T, Murayama S, Sakai S, Okamura J, Fukuda T, et al. CT and MR features of nasopharyngeal carcinoma in children and young adults. Clin Radiol. 2002;57(3):205–10. doi: 10.1053/crad.2001.0731, PubMed PMID: 11952316.
19. Sham JS, Wei WI, Kwan WH, Chan CW, Choi PH, Choy D. Fiberoptic endoscopic examination and biopsy in determining the extent of nasopharyngeal carcinoma. Cancer. 1989;64(9):1838–42.
20. Shanmugaratnam K, Chan SH, de-The G, Goh JE, Khor TH, Simons MJ, et al. Histopathology of nasopharyngeal carcinoma: correlations with epidemiology, survival rates and other biological characteristics. Cancer. 1979;44(3):1029–44.
21. Brown JJ, Berry GJ, Moretto J, Keating WF, Fee Jr WE. Validity of clinic biopsy specimens in classifying histopathologic characteristics of recurrent nasopharyngeal carcinoma. Arch Otolaryngol Head Neck Surg. 1997;123(9):950–5.
22. Cheung F, Chan O, Ng WT, Chan L, Lee A, Pang SW. The prognostic value of histological typing in nasopharyngeal carcinoma. Oral Oncol. 2012;48(5):429–33.
23. Prathap K, Looi LM, Prasad U. Localized amyloidosis in nasopharyngeal carcinoma. Histopathology. 1984;8(1):27–34.
24. Chen CL, Su IJ, Hsu MM, Hsu HC. Granulomatous nasopharyngeal carcinoma: with emphasis on difficulty in diagnosis and favorable outcome. J Formos Med Assoc. 1991;90(4):353–6.
25. Zong YS, Lin H, Choy DT, Sham JS, Wei W, Chan KH, et al. Nasopharyngeal carcinoma and lymphoinfiltration. Oncology. 1991;48(4):290–6.
26. Wan SK, Chan JK, Lau WH, Yip TT. Basaloid-squamous carcinoma of the nasopharynx. An Epstein-Barr virus-associated neoplasm compared with morphologically identical tumors occurring in other sites. Cancer. 1995;76(10):1689–93.
27. Roy C, Choudhury KB, Basu S. Basaloid squamous cell carcinoma of nasopharynx: an extremely rare variety of tumour of nasopharynx. J Indian Med Assoc. 2011;109(5):343–4.
28. Franchi A, Moroni M, Massi D, Paglierani M, Santucci M. Sinonasal undifferentiated carcinoma, nasopharyngeal-type undifferentiated carcinoma, and keratinizing and nonkeratinizing squamous cell carcinoma express different cytokeratin patterns. Am J Surg Pathol. 2002;26(12):1597–604.
29. Guo C, Pan ZG, Li DJ, Yun JP, Zheng MZ, Hu ZY, et al. The expression of p63 is associated with the differential stage in nasopharyngeal carcinoma and EBV infection. J Transl Med. 2006;4:23.
30. Friedrich RE, Bartel-Friedrich S, Lobeck H, Niedobitek G, Arps H. Epstein-Barr virus DNA, intermediate filaments and epithelial membrane antigen in nasopharyngeal carcinoma. Anticancer Res. 2000;20(6D):4909–16.
31. Hsiao JR, Jin YT, Tsai ST. EBER1 in situ hybridization as an adjuvant for diagnosis of recurrent nasopharyngeal carcinoma. Anticancer Res. 1998;18(6B):4585–9.
32. Hwang TZ, Jin YT, Tsai ST. EBER in situ hybridization differentiates carcinomas originating from the sinonasal region and the nasopharynx. Anticancer Res. 1998;18(6B):4581–4.
33. Inoue H, Sato Y, Tsuchiya B, Nagai H, Takahashi H, Kameya T. Expression of Epstein-Barr virus-encoded small nuclear RNA 1 in Japanese nasopharyngeal carcinomas. Acta Otolaryngol Suppl. 2002;547:113–7.
34. Sheu JJ, Lee CH, Ko JY, Tsao GS, Wu CC, Fang CY, et al. Chromosome 3p12.3-p14.2 and 3q26.2-q26.32 are genomic markers for prognosis of advanced nasopharyngeal carcinoma. Cancer Epidemiol Biomarkers Prev. 2009;18(10):2709–16.
35. Zhou W, Feng X, Li H, Wang L, Zhu B, Liu W, et al. Inactivation of LARS2, located at the commonly deleted region 3p21.3, by both epigenetic and genetic mechanisms in nasopharyngeal carcinoma. Acta Biochim Biophys Sin. 2009;41(1):54-62.
36. Yi HM, Li H, Peng D, Zhang HJ, Wang L, Zhao M, et al. Genetic and epigenetic alterations of LTF at 3p21.3 in nasopharyngeal carcinoma. Oncol Res. 2006;16(6):261–72.
37. Zeng Z, Zhou Y, Zhang W, Li X, Xiong W, Liu H, et al. Family-based association analysis validates chromosome 3p21 as a putative nasopharyngeal carcinoma susceptibility locus. Genet Med. 2006;8(3):156–60.
38. Jenkin RD, Anderson JR, Jereb B, Thompson JC, Pyesmany A, Wara WM, et al. Nasopharyngeal carcinoma–a retrospective review of patients less than thirty years of age: a report of Children's Cancer Study Group. Cancer. 1981;47(2):360–6.
39. Lombardi F, Gasparini M, Gianni C, De Marie M, Molinari R, Pilotti S. Nasopharyngeal carcinoma in childhood. Med Pediatr Oncol. 1982;10(3):243–50.
40. Ozyar E, Selek U, Laskar S, Uzel O, Anacak Y, Ben-Arush M, et al. Treatment results of 165 pediatric patients with non-metastatic nasopharyngeal carcinoma: a Rare Cancer Network study. Radiother Oncol. 2006;81(1):39–46.
41. Chen CL, Hsu MM. Second primary epithelial malignancy of nasopharynx and nasal cavity after successful curative radiation therapy of nasopharyngeal carcinoma. Hum Pathol. 2000;31(2):227–32.
42. Khan A, Smellie J, Nutting C, Harrington K, Newbold K. Familial nonmedullary thyroid cancer: a review of the genetics. Thyroid. 2010;20(7):795–801. Epub 2010/05/15. doi: 10.1089/thy.2009.0216, PubMed PMID: 20465534.
43. French CA, Miyoshi I, Kubonishi I, Grier HE, Perez-Atayde AR, Fletcher JA. BRD4-NUT fusion oncogene: a novel mechanism in aggressive carcinoma. Cancer Res. 2003;63(2):304–7.
44. French CA, Kutok JL, Faquin WC, Toretsky JA, Antonescu CR, Griffin CA, et al. Midline carcinoma of children and young adults with NUT rearrangement. J Clin Oncol. 2004;22(20):4135–9.
45. Stelow EB. A review of NUT midline carcinoma. Head Neck Pathol. 2011;5(1):31–5.
46. Bauer DE, Mitchell CM, Strait KM, Lathan CS, Stelow EB, Luer SC, et al. Clinicopathologic features and long-term outcomes of NUT midline carcinoma. Clin Cancer Res. 2012;18(20):5773–9.
47. den Bakker MA, Beverloo BH, van den Heuvel-Eibrink MM, Meeuwis CA, Tan LM, Johnson LA, et al. NUT midline carci-

noma of the parotid gland with mesenchymal differentiation. Am J Surg Pathol. 2009;33(8):1253–8.
48. Shehata BM, Steelman CK, Abramowsky CR, Olson TA, French CA, Saxe DF, et al. NUT midline carcinoma in a newborn with multiorgan disseminated tumor and a 2-year-old with a pancreatic/hepatic primary. Pediatr Dev Pathol. 2010;13(6):481–5.
49. Ziai J, French CA, Zambrano E. NUT gene rearrangement in a poorly-differentiated carcinoma of the submandibular gland. Head Neck Pathol. 2010;4(2):163–8.
50. Tanaka M, Kato K, Gomi K, Yoshida M, Niwa T, Aida N, et al. NUT midline carcinoma: report of 2 cases suggestive of pulmonary origin. Am J Surg Pathol. 2012;36(3):381–8.
51. French CA. Pathogenesis of NUT midline carcinoma. Annu Rev Pathol. 2012;7:247–65.
52. Polsani A, Braithwaite KA, Alazraki AL, Abramowsky C, Shehata BM. NUT midline carcinoma: an imaging case series and review of literature. Pediatr Radiol. 2012;42(2):205–10. doi: 10.1007/s00247-011-2272-3, PubMed PMID: 22033856.
53. Nelson BA, Lee EY, French CA, Bauer DE, Vargas SO. BRD4-NUT carcinoma of the mediastinum in a pediatric patient: multidetector computed tomography imaging findings. J Thorac Imaging. 2010;25(3):W93–6. doi: 10.1097/RTI.0b013e3181b5d84d, PubMed PMID: 20395873.
54. Huh WW, Holsinger FC, Levy A, Palla FS, Anderson PM. Osteosarcoma of the jaw in children and young adults. Head Neck. 2012;34(7):981–4. Epub 2011/08/20. doi: 10.1002/hed.21850, PubMed PMID: 21853501.
55. French CA, Ramirez CL, Kolmakova J, Hickman TT, Cameron MJ, Thyne ME, et al. BRD-NUT oncoproteins: a family of closely related nuclear proteins that block epithelial differentiation and maintain the growth of carcinoma cells. Oncogene. 2008;27(15):2237–42.
56. Fang W, French CA, Cameron MJ, Han Y, Liu H. Clinicopathological significance of NUT rearrangements in poorly differentiated malignant tumors of the upper respiratory tract. Int J Surg Pathol. 2013;21(2):102–10.
57. Haack H, Johnson LA, Fry CJ, Crosby K, Polakiewicz RD, Stelow EB, et al. Diagnosis of NUT midline carcinoma using a NUT-specific monoclonal antibody. Am J Surg Pathol. 2009;33(7):984–91.
58. Evans AG, French CA, Cameron MJ, Fletcher CD, Jackman DM, Lathan CS, et al. Pathologic characteristics of NUT midline carcinoma arising in the mediastinum. Am J Surg Pathol. 2012;36(8):1222–7.
59. Broich G, Pagliari A, Ottaviani F. Esthesioneuroblastoma: a general review of the cases published since the discovery of the tumour in 1924. Anticancer Res. 1997;17(4A):2683–706.
60. Turner JH, Reh DD. Incidence and survival in patients with sinonasal cancer: a historical analysis of population-based data. Head Neck. 2012;34(6):877–85.
61. Jethanamest D, Morris LG, Sikora AG, Kutler DI. Esthesioneuroblastoma: a population-based analysis of survival and prognostic factors. Arch Otolaryngol Head Neck Surg. 2007;133(3):276–80.
62. Kumar M, Fallon RJ, Hill JS, Davis MM. Esthesioneuroblastoma in children. J Pediatr Hematol Oncol. 2002;24(6):482–7.
63. Cohen ZR, Marmor E, Fuller GN, DeMonte F. Misdiagnosis of olfactory neuroblastoma. Neurosurg Focus. 2002;12(5):e3.
64. Hamilton AE, Rubinstein LJ, Poole GJ. Primary intracranial esthesioneuroblastoma, (olfactory neuroblastoma). J Neurosurg. 1973;38(5):548–56.
65. Josephs L, Jones L, Marenette L, McKeever P. Cushing's syndrome: an unusual presentation of olfactory neuroblastoma. Skull Base. 2008;18(1):73–6.
66. Plasencia YL, Cortes MB, Arencibia DM, Damaso TM, Contreras IL, Pino AO, et al. Esthesioneuroblastoma recurrence presenting as a syndrome of inappropriate antidiuretic hormone secretion. Head Neck. 2006;28(12):1142–6.
67. Bisogno G, Soloni P, Conte M, Podda M, Ferrari A, Garaventa A, et al. Esthesioneuroblastoma in pediatric and adolescent age. A report from the TREP project in cooperation with the Italian Neuroblastoma and Soft Tissue Sarcoma Committees. BMC Cancer. 2012;12(117):1471–2407.
68. Wang SL, Li SH, Chen WT, Chai CY. Absence of Epstein-Barr virus in olfactory neuroblastoma. Pathology. 2007;39(6):565–6.
69. Som PM, Lidov M, Brandwein M, Catalano P, Biller HF. Sinonasal esthesioneuroblastoma with intracranial extension: marginal tumor cysts as a diagnostic MR finding. Am J Neuroradiol. 1994;15(7):1259–62. PubMed PMID: 7976934.
70. Faragalla H, Weinreb I. Olfactory neuroblastoma: a review and update. Adv Anat Pathol. 2009;16(5):322–31.
71. Gaudin PB, Rosai J. Florid vascular proliferation associated with neural and neuroendocrine neoplasms. A diagnostic clue and potential pitfall. Am J Surg Pathol. 1995;19(6):642–52.
72. Bates T, Plessis DD, Polvikoski T, Sloan P, McQueen A, Meikle D, et al. Ganglioneuroblastic transformation in olfactory neuroblastoma. Head Neck Pathol. 2012;6(1):150–5.
73. Stones DK, Jansen JC, Griessel D. Sialoblastoma and hepatoblastoma in a newborn infant. Pediatr Blood Cancer. 2009;52(7):883–5.
74. Wooff JC, Weinreb I, Perez-Ordonez B, Magee JF, Bullock MJ. Calretinin staining facilitates differentiation of olfactory neuroblastoma from other small round blue cell tumors in the sinonasal tract. Am J Surg Pathol. 2011;35(12):1786–93.
75. Frierson Jr HF, Ross GW, Mills SE, Frankfurter A. Olfactory neuroblastoma. Additional immunohistochemical characterization. Am J Clin Pathol. 1990;94(5):547–53.
76. Bourne TD, Bellizzi AM, Stelow EB, Loy AH, Levine PA, Wick MR, et al. p63 Expression in olfactory neuroblastoma and other small cell tumors of the sinonasal tract. Am J Clin Pathol. 2008;130(2):213–8.
77. Holland H, Koschny R, Krupp W, Meixensberger J, Bauer M, Kirsten H, et al. Comprehensive cytogenetic characterization of an esthesioneuroblastoma. Cancer Genet Cytogenet. 2007;173(2):89–96.
78. Guled M, Myllykangas S, Frierson Jr HF, Mills SE, Knuutila S, Stelow EB. Array comparative genomic hybridization analysis of olfactory neuroblastoma. Mod Pathol. 2008;21(6):770–8.
79. Weiss GJ, Liang WS, Izatt T, Arora S, Cherni I, Raju RN, et al. Paired tumor and normal whole genome sequencing of metastatic olfactory neuroblastoma. PLoS One. 2012;7(5):23.
80. Argani P, Perez-Ordonez B, Xiao H, Caruana SM, Huvos AG, Ladanyi M. Olfactory neuroblastoma is not related to the Ewing family of tumors: absence of EWS/FLI1 gene fusion and MIC2 expression. Am J Surg Pathol. 1998;22(4):391–8.
81. Mezzelani A, Tornielli S, Minoletti F, Pierotti MA, Sozzi G, Pilotti S. Esthesioneuroblastoma is not a member of the primitive peripheral neuroectodermal tumour-Ewing's group. Br J Cancer. 1999;81(4):586–91.
82. Kumar S, Perlman E, Pack S, Davis M, Zhang H, Meltzer P, et al. Absence of EWS/FLI1 fusion in olfactory neuroblastomas indicates these tumors do not belong to the Ewing's sarcoma family. Hum Pathol. 1999;30(11):1356–60.
83. Koka VN, Julieron M, Bourhis J, Janot F, Le Ridant AM, Marandas P, et al. Aesthesioneuroblastoma. J Laryngol Otol. 1998;112(7):628–33.
84. Ferlito A, Rinaldo A, Rhys-Evans PH. Contemporary clinical commentary: esthesioneuroblastoma: an update on management of the neck. Laryngoscope. 2003;113(11):1935–8.
85. Demiroz C, Gutfeld O, Aboziada M, Brown D, Marentette LJ, Eisbruch A. Esthesioneuroblastoma: is there a need for elective neck treatment? Int J Radiat Oncol Biol Phys. 2011;81(4):15.
86. Ahmed AA, Tsokos M. Sinonasal rhabdomyosarcoma in children and young adults. Int J Surg Pathol. 2007;15(2):160–5.

87. Turner JH, Richmon JD. Head and neck rhabdomyosarcoma: a critical analysis of population-based incidence and survival data. Otolaryngol Head Neck Surg. 2011;145(6):967–73.
88. Koivunen P, Suutala L, Schorsch I, Jokinen K, Alho OP. Malignant epithelial salivary gland tumors in northern Finland: incidence and clinical characteristics. Eur Arch Otorhinolaryngol. 2002;259(3):146–9.
89. Pinkston JA, Cole P. Incidence rates of salivary gland tumors: results from a population-based study. Otolaryngol Head Neck Surg. 1999;120(6):834–40.
90. Eveson JW, Cawson RA. Salivary gland tumours. A review of 2410 cases with particular reference to histological types, site, age and sex distribution. J Pathol. 1985;146(1):51–8.
91. Fitzpatrick PJ, Theriault C. Malignant salivary gland tumors. Int J Radiat Oncol Biol Phys. 1986;12(10):1743–7.
92. Sultan I, Rodriguez-Galindo C, Al-Sharabati S, Guzzo M, Casanova M, Ferrari A. Salivary gland carcinomas in children and adolescents: a population-based study, with comparison to adult cases. Head Neck. 2011;33(10):1476–81.
93. Baker SR, Malone B. Salivary gland malignancies in children. Cancer. 1985;55(8):1730–6.
94. Vedrine PO, Coffinet L, Temam S, Montagne K, Lapeyre M, Oberlin O, et al. Mucoepidermoid carcinoma of salivary glands in the pediatric age group: 18 clinical cases, including 11 second malignant neoplasms. Head Neck. 2006;28(9):827–33.
95. Brandwein MS, Ivanov K, Wallace DI, Hille JJ, Wang B, Fahmy A, et al. Mucoepidermoid carcinoma: a clinicopathologic study of 80 patients with special reference to histological grading. Am J Surg Pathol. 2001;25(7):835–45.
96. Rahbar R, Grimmer JF, Vargas SO, Robson CD, Mack JW, Perez-Atayde AR, et al. Mucoepidermoid carcinoma of the parotid gland in children: a 10-year experience. Arch Otolaryngol Head Neck Surg. 2006;132(4):375–80. doi: 10.1001/archotol.132.4.375, PubMed PMID: 16618905.
97. Som PM, Biller HF. High-grade malignancies of the parotid gland: identification with MR imaging. Radiology. 1989;173(3):823–6. doi: 10.1148/radiology.173.3.2813793, PubMed PMID: 2813793.
98. Bell D, El-Naggar AK. Molecular heterogeneity in mucoepidermoid carcinoma: conceptual and practical implications. Head Neck Pathol. 2013;7(1):23–7.
99. Sams RN, Gnepp DR. P63 expression can be used in differential diagnosis of salivary gland acinic cell and mucoepidermoid carcinomas. Head Neck Pathol. 2013;7(1):64–8.
100. Ellis GL. What's new in the AFIP fascicle on salivary gland tumors: a few highlights from the 4th Series Atlas. Head Neck Pathol. 2009;3(3):225–30.
101. Dehner LP, Valbuena L, Perez-Atayde A, Reddick RL, Askin FB, Rosai J. Salivary gland anlage tumor ("congenital pleomorphic adenoma"). A clinicopathologic, immunohistochemical and ultrastructural study of nine cases. Am J Surg Pathol. 1994;18(1):25–36.
102. Siddiqi SH, Solomon MP, Haller JO. Sialoblastoma and hepatoblastoma in a neonate. Pediatr Radiol. 2000;30(5):349–51.
103. Cheng YK, Chu WC, Law LW, Ting YH, Leung TY. A fetus with a huge neck mass and a large abdominal circumference–a rare case of sialoblastoma and hepatoblastoma. Prenat Diagn. 2012;32(9):915–7. Epub 2012/06/20. doi: 10.1002/pd.3927, PubMed PMID: 22711473.
104. Yekeler E, Dursun M, Gun F, Kilincaslan H, Ucar A, Genchellac H, et al. Sialoblastoma: MRI findings. Pediatr Radiol. 2004;34(12):1005–7. doi: 10.1007/s00247-004-1286-5, PubMed PMID: 15278323.
105. Williams SB, Ellis GL, Warnock GR. Sialoblastoma: a clinicopathologic and immunohistochemical study of 7 cases. Ann Diagn Pathol. 2006;10(6):320–6.
106. Mertens F, Wahlberg P, Domanski HA. Clonal chromosome aberrations in a sialoblastoma. Cancer Genet Cytogenet. 2009;189(1):68–9. doi: 10.1016/j.cancergencyto.2008.10.005, Epub 2009/01/27 S0165-4608(08)00582-7 [pii]. PubMed PMID: 19167616.
107. Brandwein M, Al-Naeif NS, Manwani D, Som P, Goldfeder L, Rothschild M, et al. Sialoblastoma: clinicopathological/immunohistochemical study. Am J Surg Pathol. 1999;23(3):342–8.
108. Draganov P, Todorov S, Todorov I, Karchev T, Kalvatchev Z. Identification of HPV DNA in patients with juvenile-onset recurrent respiratory papillomatosis using SYBR Green real-time PCR. Int J Pediatr Otorhinolaryngol. 2006;70(3):469–73. Epub 2005/09/03. doi: 10.1016/j.ijporl.2005.07.018, PubMed PMID: 16137771.
109. Somers GR, Tabrizi SN, Borg AJ, Garland SM, Chow CW. Juvenile laryngeal papillomatosis in a pediatric population: a clinicopathologic study. Pediatr Pathol Lab Med. 1997;17(1):53–64. Epub 1997/01/01. PubMed PMID: 9050060.
110. Gelinas JF, Manoukian J, Cote A. Lung involvement in juvenile onset recurrent respiratory papillomatosis: a systematic review of the literature. Int J Pediatr Otorhinolaryngol. 2008;72(4):433–52. Epub 2008/02/19. doi: 10.1016/j.ijporl.2007.12.003, PubMed PMID: 18281102.
111. Schlecht NF, Burk RD, Nucci-Sack A, Shankar V, Peake K, Lorde-Rollins E, et al. Cervical, anal and oral HPV in an adolescent inner-city health clinic providing free vaccinations. PLoS One. 2012;7(5):e37419. Epub 2012/05/25. doi: 10.1371/journal.pone.0037419, PubMed PMID: 22624027. PubMed Central PMCID: PMC3356254.
112. El-Mofty SK, Lu DW. Prevalence of human papillomavirus type 16 DNA in squamous cell carcinoma of the palatine tonsil, and not the oral cavity, in young patients: a distinct clinicopathologic and molecular disease entity. Am J Surg Pathol. 2003;27(11):1463–70. Epub 2003/10/25. PubMed PMID: 14576481.
113. Elango KJ, Suresh A, Erode EM, Subhadradevi L, Ravindran HK, Iyer SK, et al. Role of human papilloma virus in oral tongue squamous cell carcinoma. Asian Pac J Cancer Prev. 2011;12(4):889–96. Epub 2011/07/28. PubMed PMID: 21790221.
114. Aggunlu L, Erbas G. Recurrent respiratory papillomatosis with lung involvement. Diagn Interv Radiol. 2009;15(2):93–5. Epub 2009/06/12. PubMed PMID: 19517378.
115. Som P, Curtin HD. Head and neck imaging. 5th ed. St. Louis: Elsevier; 2011. 3080 p.
116. Khoddami M, Squire J, Zielenska M, Thorner P. Melanotic neuroectodermal tumor of infancy: a molecular genetic study. Pediatr Dev Pathol. 1998;1(4):295–9. Epub 1999/08/27. PubMed PMID: 10463291.
117. Kapadia SB, Frisman DM, Hitchcock CL, Ellis GL, Popek EJ. Melanotic neuroectodermal tumor of infancy. Clinicopathological, immunohistochemical, and flow cytometric study. Am J Surg Pathol. 1993;17(6):566–73.
118. George JC, Edwards MK, Jakacki RI, Kho-Duffin J. Melanotic neuroectodermal tumor of infancy. Am J Neuroradiol. 1995;16(6):1273–5. Epub 1995/06/01. PubMed PMID: 7677023.
119. Mirich DR, Blaser SI, Harwood-Nash DC, Armstrong DC, Becker LE, Posnick JC. Melanotic neuroectodermal tumor of infancy: clinical, radiologic, and pathologic findings in five cases. Am J Neuroradiol. 1991;12(4):689–97. Epub 1991/07/01. PubMed PMID: 1652883.
120. Haque S, McCarville MB, Sebire N, McHugh K. Melanotic neuroectodermal tumour of infancy: CT and MR findings. Pediatr Radiol. 2012;42(6):699–705. Epub 2012/03/21. doi: 10.1007/s00247-011-2339-1, PubMed PMID: 22430481. PubMed Central PMCID: PMC3526662.
121. Walterhouse DO, Pappo AS, Baker KS, Parham DM, Anderson JR, Donaldson SS, et al. Rhabdomyosarcoma of the parotid region occurring in childhood and adolescence. A report from the Intergroup Rhabdomyosarcoma Study Group. Cancer. 2001;92(12):3135–46. Epub 2001/12/26. PubMed PMID: 11753993.
122. Ellison DA, Adada B, Qualman SJ, Parham DM. Melanotic neuroectodermal tumor of infancy: report of a case with myogenic

differentiation. Pediatr Dev Pathol. 2007;10(2):157–60. Epub 2007/03/24. doi: 10.2350/06-07-0138.1, PubMed PMID: 17378694.
123. Barrett AW, Morgan M, Ramsay AD, Farthing PM, Newman L, Speight PM. A clinicopathologic and immunohistochemical analysis of melanotic neuroectodermal tumor of infancy. Oral Surg Oral Med Oral Pathol Oral Radiol Endod. 2002;93(6):688–98. Epub 2002/07/27. doi: S107921040200032X [pii]. PubMed PMID: 12142876.
124. Parham DM. Neuroectodermal and neuroendocrine tumors principally seen in children. Am J Clin Pathol. 2001;115(Suppl):S113–28. Epub 2002/05/08. PubMed PMID: 11993686.
125. Burkitt DP. The discovery of Burkitt's lymphoma. Cancer. 1983;51(10):1777–86. Epub 1983/05/15. PubMed PMID: 6299496.
126. Thorley-Lawson DA, Allday MJ. The curious case of the tumour virus: 50 years of Burkitt's lymphoma. Nat Rev Microbiol. 2008;6(12):913–24. Epub 2008/11/15. doi: 10.1038/nrmicro2015, PubMed PMID: 19008891.
127. Bilodeau E, Galambos C, Yeung A, Potluri A, Collins B. Sporadic Burkitt lymphoma of the jaw: case report and review of the literature. Quintessence Int. 2012;43(4):333–6. Epub 2012/04/26. PubMed PMID: 22532948.
128. Ishii E, Eguchi M, Matsuzaki A, Zaizen Y, Yoshidomi S, Kimura N, et al. Granulocytic sarcoma in infant with MLL rearrangement preceding acute monoblastic leukemia with t(10;11)(p11;q23). Leukemia. 1995;9(11):1970–4. Epub 1995/11/01. PubMed PMID: 7475292.
129. Arul AS, Verma S, Ahmed S. A clinical and fine needle aspiration cytology study of gingiva in acute leukemia. Dent Res J (Isfahan). 2012;9(1):80–5. Epub 2012/03/01. doi: 10.4103/1735-3327.92954, PubMed PMID: 22363368. PubMed Central PMCID: PMC3283984.
130. Anavi Y, Kaplinsky C, Calderon S, Zaizov R. Head, neck, and maxillofacial childhood Burkitt's lymphoma: a retrospective analysis of 31 patients. J Oral Maxillofac Surg. 1990;48(7):708–13. PubMed PMID: 2358947.
131. Valencerina Gopez E, Dauterman J, Layfield LJ. Fine-needle aspiration biopsy of alveolar rhabdomyosarcoma of the parotid: a case report and review of the literature. Diagn Cytopathol. 2001;24(4):249–52. Epub 2001/04/04. PubMed PMID: 11285621.
132. De M, Banerjee A, Graham I, Dempster J. Alveolar rhabdomyosarcoma of the parotid gland. J Laryngol Otol. 2001;115(2):155–7. Epub 2001/04/26. PubMed PMID: 11320838.
133. Nayak JV, Teot LA, Vyas Y, Snyderman CH, Toh EH, Deleyiannis FW. Head and neck epithelioid sarcoma in a child: diagnostic dilemma and anterolateral thigh free flap reconstruction. Int J Pediatr Otorhinolaryngol. 2008;72(5):719–24. Epub 2008/03/19. doi: 10.1016/j.ijporl.2008.01.032, PubMed PMID: 18346795.
134. Kim HS, Lee HK, Weon YC, Kim HJ. Alveolar soft-part sarcoma of the head and neck: clinical and imaging features in five cases. Am J Neuroradiol. 2005;26(6):1331–5. Epub 2005/06/16. PubMed PMID: 15956492.
135. Hunter BC, Devaney KO, Ferlito A, Rinaldo A. Alveolar soft part sarcoma of the head and neck region. Ann Otol Rhinol Laryngol. 1998;107(9 Pt 1):810–4. Epub 1998/09/28. PubMed PMID: 9749554.
136. Smith DM, Mahmoud HH, Jenkins 3rd JJ, Rao B, Hopkins KP, Parham DM. Myofibrosarcoma of the head and neck in children. Pediatr Pathol Lab Med. 1995;15(3):403–18. Epub 1995/05/01. PubMed PMID: 8597827.
137. Sharif MA, Mushtaq S, Mamoon N, Khadim MT, Asghar Z. Biphasic synovial sarcoma of oral cavity. J Coll Physicians Surg Pak. 2008;18(11):713–5. Epub 2008/11/06. doi: 11.2008/JCPSP.713715, PubMed PMID: 18983797.
138. Wang H, Zhang J, He X, Niu Y. Synovial sarcoma in the oral and maxillofacial region: report of 4 cases and review of the literature. J Oral Maxillofac Surg. 2008;66(1):161–7. Epub 2007/12/18. doi: 10.1016/j.joms.2007.05.007, PubMed PMID: 18083434.
139. Canter RJ, Qin LX, Maki RG, Brennan MF, Ladanyi M, Singer S. A synovial sarcoma-specific preoperative nomogram supports a survival benefit to ifosfamide-based chemotherapy and improves risk stratification for patients. Clin Cancer Res. 2008;14(24):8191–7. Epub 2008/12/18. doi: 10.1158/1078-0432.CCR-08-0843, PubMed PMID: 19088035. PubMed Central PMCID: PMC2779709.
140. Chen Y, Yang Y, Wang C, Shi Y. Adjuvant chemotherapy decreases and postpones distant metastasis in extremity stage IIB/III synovial sarcoma patients. J Surg Oncol. 2012;106(2):162–8. Epub 2012/02/03. doi: 10.1002/jso.23061, PubMed PMID: 22297839.
141. Nissanka EH, Amaratunge EA, Tilakaratne WM. Clinicopathological analysis of osteosarcoma of jaw bones. Oral Dis. 2007;13(1):82–7. Epub 2007/01/24. doi: 10.1111/j.1601-0825.2006.01251.x, PubMed PMID: 17241435.
142. Lee YY, Van Tassel P, Nauert C, Raymond AK, Edeiken J. Craniofacial osteosarcomas: plain film, CT, and MR findings in 46 cases. Am J Roentgenol. 1988;150(6):1397–402. doi: 10.2214/ajr.150.6.1397, PubMed PMID: 3259385.
143. Gadwal SR, Gannon FH, Fanburg-Smith JC, Becoskie EM, Thompson LD. Primary osteosarcoma of the head and neck in pediatric patients: a clinicopathologic study of 22 cases with a review of the literature. Cancer. 2001;91(3):598–605. PubMed PMID: 11169944.
144. Ma CY, Ji T, Wu YQ, Ow A. A jugulotympanic paraganglioma with craniocervical extension. Int J Oral Maxillofac Surg. 2012;41(2):221–4. Epub 2011/11/29. doi: 10.1016/j.ijom.2011.10.020, PubMed PMID: 22119569.
145. Johnstone PA, Foss RD, Desilets DJ. Malignant jugulotympanic paraganglioma. Arch Pathol Lab Med. 1990;114(9):976–9. Epub 1990/09/01. PubMed PMID: 2167653.
146. De Foer B, Kenis C, Vercruysse JP, Somers T, Pouillon M, Offeciers E, et al. Imaging of temporal bone tumors. Neuroimaging Clin N Am. 2009;19(3):339–66. doi: 10.1016/j.nic.2009.06.003, PubMed PMID: 19733312.
147. Caldemeyer KS, Mathews VP, Azzarelli B, Smith RR. The jugular foramen: a review of anatomy, masses, and imaging characteristics. Radiographics. 1997;17(5):1123–39. doi: 10.1148/radiographics.17.5.9308106, PubMed PMID: 9308106.
148. Horvath KK, Ormos J, Ribari O. Crystals in a jugulotympanic paraganglioma. Ultrastruct Pathol. 1986;10(3):257–64. Epub 1986/01/01. PubMed PMID: 3012841.
149. Raney Jr RB, Lawrence Jr W, Maurer HM, Lindberg RD, Newton Jr WA, Ragab AH, et al. Rhabdomyosarcoma of the ear in childhood. A report from the Intergroup Rhabdomyosarcoma Study-I. Cancer. 1983;51(12):2356–61. Epub 1983/06/15. PubMed PMID: 6342748.
150. Mena JC, Borne JA. Case 3: temporal bone rhabdomyosarcoma. Am J Roentgenol. 1998;171(3):873. 7–9, doi: 10.2214/ajr.171.3.9725346, PubMed PMID: 9725346.
151. Sbeity S, Abella A, Arcand P, Quintal MC, Saliba I. Temporal bone rhabdomyosarcoma in children. Int J Pediatr Otorhinolaryngol. 2007;71(5):807–14. doi: 10.1016/j.ijporl.2007.02.002, PubMed PMID: 17346806.
152. Hawkins DS, Anderson JR, Paidas CN, Wharam MD, Qualman SJ, Pappo AS, et al. Improved outcome for patients with middle ear rhabdomyosarcoma: a children's oncology group study. J Clin Oncol. 2001;19(12):3073–9. Epub 2001/06/16. PubMed PMID: 11408504.
153. Desandes E, Lacour B, Belot A, Molinie F, Delafosse P, Tretarre B, et al. Cancer Incidence and Survival in Adolescents and Young Adults in France, 2000-2008. Pediatr Hematol Oncol. 2013. Epub 2013/02/01. doi: 10.3109/08880018.2012.762569. PubMed PMID: 23363314.
154. Holmes Jr L, Hossain J, Opara F. Pediatric thyroid carcinoma incidence and temporal trends in the USA (1973–2007): race or shifting diagnostic paradigm? ISRN Oncol. 2012;2012:906197. Epub 2012/04/25. doi: 10.5402/2012/906197, PubMed PMID: 22530151; PubMed Central PMCID: PMCPMC3317016.

155. Kazakov VS, Demidchik EP, Astakhova LN. Thyroid cancer after Chernobyl. Nature. 1992;359(6390):21. Epub 1992/09/03. doi: 10.1038/359021a0, PubMed PMID: 1522879.
156. Baverstock KF. Thyroid cancer in children in Belarus after Chernobyl. World Health Stat Q. 1993;46(3):204–8. Epub 1993/01/01. PubMed PMID: 8017079.
157. Socolow EL, Hashizume A, Neriishi S, Niitani R. Thyroid carcinoma in man after exposure to ionizing radiation. A summary of the findings in Hiroshima and Nagasaki. N Engl J Med. 1963;268:406–10. Epub 1963/02/21. doi: 10.1056/nejm196302212680803, PubMed PMID: 13989805.
158. Albright EC, Allday RW. Thyroid carcinoma after radiation therapy for adolescent acne vulgaris. JAMA. 1967;199(4):280–1. Epub 1967/01/23. PubMed PMID: 4224873.
159. Refetoff S, Harrison J, Karanfilski BT, Kaplan EL, De Groot LJ, Bekerman C. Continuing occurrence of thyroid carcinoma after irradiation to the neck in infancy and childhood. N Engl J Med. 1975;292(4):171–5. Epub 1975/01/23. doi: 10.1056/nejm197501232920402, PubMed PMID: 122783.
160. Weshler Z, Krasnokuki D, Peshin Y, Biran S. Thyroid carcinoma induced by irradiation for Hodgkin's disease. Report of a case. Acta Radiol Oncol Radiat Phys Biol. 1978;17(5):383–6. Epub 1978/01/01. PubMed PMID: 726946.
161. McDougall IR, Coleman CN, Burke JS, Saunders W, Kaplan HS. Thyroid carcinoma after high-dose external radiotherapy for Hodgkin's disease: report of three cases. Cancer. 1980;45(8):2056–60. Epub 1980/04/15. PubMed PMID: 7370951.
162. Mauras N, Zimmerman D, Goellner JR. Hashimoto thyroiditis associated with thyroid cancer in adolescent patients. J Pediatr. 1985;106(6):895–8. Epub 1985/06/01. PubMed PMID: 3839014.
163. Pacini F, Mariotti S, Formica N, Elisei R, Anelli S, Capotorti E, et al. Thyroid autoantibodies in thyroid cancer: incidence and relationship with tumour outcome. Acta Endocrinol (Copenh). 1988;119(3):373–80. Epub 1988/11/01. PubMed PMID: 3188810.
164. Okayasu I, Fujiwara M, Hara Y, Tanaka Y, Rose NR. Association of chronic lymphocytic thyroiditis and thyroid papillary carcinoma. A study of surgical cases among Japanese, and white and African Americans. Cancer. 1995;76(11):2312–8.
165. Ni Y, He X, Chen J, Moline J, Mester J, Orloff MS, et al. Germline SDHx variants modify breast and thyroid cancer risks in Cowden and Cowden-like syndrome via FAD/NAD-dependant destabilization of p53. Hum Mol Genet. 2012;21(2):300–10. Epub 2011/10/08. doi: 10.1093/hmg/ddr459, PubMed PMID: 21979946; PubMed Central PMCID: PMCPMC3276278.
166. Moses W, Weng J, Kebebew E. Prevalence, clinicopathologic features, and somatic genetic mutation profile in familial versus sporadic nonmedullary thyroid cancer. Thyroid. 2011;21(4):367–71. Epub 2010/12/31. doi: 10.1089/thy.2010.0256, PubMed PMID: 21190444; PubMed Central PMCID: PMCPMC3070337.
167. Mills SE, Allen Jr MS. Congenital occult papillary carcinoma of the thyroid gland. Hum Pathol. 1986;17(11):1179–81. Epub 1986/11/01. PubMed PMID: 3770736.
168. Shapiro SJ, Friedman NB, Perzik SL, Catz B. Incidence of thyroid carcinoma in Graves' disease. Cancer. 1970;26(6):1261–70. Epub 1970/12/01. PubMed PMID: 5536634.
169. Kraimps JL, Bouin-Pineau MH, Mathonnet M, De Calan L, Ronceray J, Visset J, et al. Multicentre study of thyroid nodules in patients with Graves' disease. Br J Surg. 2000;87(8):1111–3. Epub 2000/08/10. doi: 10.1046/j.1365-2168.2000.01504.x, PubMed PMID: 10931060.
170. Cibas ES, Ali SZ. The Bethesda system for reporting thyroid cytopathology. Am J Clin Pathol. 2009;132(5):658–65. Epub 2009/10/23. doi: 10.1309/ajcpphlwmi3jv4la, PubMed PMID: 19846805.
171. Monaco SE, Pantanowitz L, Khalbuss WE, Benkovich VA, Ozolek J, Nikiforova MN, et al. Cytomorphological and molecular genetic findings in pediatric thyroid fine-needle aspiration. Cancer Cytopathol. 2012;120(5):342–50. Epub 2012/05/19. doi: 10.1002/cncy.21199, PubMed PMID: 22605559.
172. Loevner LA, Kaplan SL, Cunnane ME, Moonis G. Cross-sectional imaging of the thyroid gland. Neuroimaging Clin N Am. 2008;18(3):445–61. vii, doi: 10.1016/j.nic.2008.05.001, PubMed PMID: 18656027.
173. Mafee M, Valvassori GE, Becker M. Imaging of the head and neck. 2nd ed. New York: Thieme; 2004. 866 p.
174. Takashima S, Sone S, Takayama F, Wang Q, Kobayashi T, Horii A, et al. Papillary thyroid carcinoma: MR diagnosis of lymph node metastasis. Am J Neuroradiol. 1998;19(3):509–13. PubMed PMID: 9541309.
175. Sohn SY, Choi JH, Kim NK, Joung JY, Cho YY, Park SM, et al. The impact of iodinated contrast agent administered during preoperative computed tomography scan on body iodine pool in patients with differentiated thyroid cancer preparing for radioactive iodine treatment. Thyroid. 2014. Epub 2013/12/04. doi: 10.1089/thy.2013.0238. PubMed PMID: 24295076.
176. Ghossein R, Asa SL, Barnes L, Chan J, et al. Protocol for the examination of specimens from patients with carcinomas of the thyroid gland. 2012. College of American Pathologists (CAP) Cancer Protocol. www.cap.org/cancerprotocol.
177. Schrager V. Lateral aberrant thyroids. Surg Gynecol Obstet. 1906;3:465–75.
178. Lahey FH, Ficarra BJ. The lateral aberrant thyroid. Surg Gynecol Obstet. 1946;82:705–11. Epub 1946/06/01. PubMed PMID: 20983141.
179. Rabinov CR, Ward PH, Pusheck T. Evolution and evaluation of lateral cystic neck masses containing thyroid tissue: "lateral aberrant thyroid" revisited. Am J Otolaryngol. 1996;17(1):12–5. Epub 1996/01/01. PubMed PMID: 8801808.
180. Hassell LA, Gillies EM, Dunn ST. Cytologic and molecular diagnosis of thyroid cancers: is it time for routine reflex testing? Cancer Cytopathol. 2012;120(1):7–17. Epub 2011/09/02. doi: 10.1002/cncy.20186, PubMed PMID: 21882358.
181. Hogan AR, Zhuge Y, Perez EA, Koniaris LG, Lew JI, Sola JE. Pediatric thyroid carcinoma: incidence and outcomes in 1753 patients. J Surg Res. 2009;156(1):167–72. Epub 2009/07/28. doi: 10.1016/j.jss.2009.03.098, PubMed PMID: 19631341.
182. Perry A, Molberg K, Albores-Saavedra J. Physiologic versus neoplastic C-cell hyperplasia of the thyroid: separation of distinct histologic and biologic entities. Cancer. 1996;77(4):750–6. Epub 1996/02/15. PubMed PMID: 8616768.
183. Albores-Saavedra JA, Krueger JE. C-cell hyperplasia and medullary thyroid microcarcinoma. Endocr Pathol. 2001;12(4):365–77. Epub 2002/03/27. PubMed PMID: 11914470.
184. Ganeshan D, Paulson E, Duran C, Cabanillas ME, Busaidy NL, Charnsangavej C. Current update on medullary thyroid carcinoma. Am J Roentgenol. 2013;201(6):W867–76. doi: 10.2214/AJR.12.10370, PubMed PMID: 24261394.
185. Das DK, Mallik MK, George SS, Sheikh ZA, Pathan SK, Haji BE, et al. Secretory activity in medullary thyroid carcinoma: a cytomorphological and immunocytochemical study. Diagn Cytopathol. 2007;35(6):329–37. Epub 2007/05/15. doi: 10.1002/dc.20637, PubMed PMID: 17497663.
186. Reches M, Porat Y, Gazit E. Amyloid fibril formation by pentapeptide and tetrapeptide fragments of human calcitonin. J Biol Chem. 2002;277(38):35475–80. Epub 2002/07/04. doi: 10.1074/jbc.M206039200, PubMed PMID: 12095997.

Malignancies of the Pediatric Lower Respiratory Tract

8

R. Paul Guillerman, Esben Vogelius, Alfredo Pinto-Rojas, and David M. Parham

Introduction

Masses of the lungs and lower airways in children have a wide differential diagnosis. Nonneoplastic etiologies are most common and can be congenital, inflammatory, infectious, vascular, or posttraumatic. For example, congenital pulmonary airway malformations (CPAM), granulomatous diseases, abscesses, infarctions, and hematomas can all present as masses. Additionally, pneumonia in childhood can be associated with a round, mass-like consolidation that simulates a neoplasm [1]. Secondary (metastatic) neoplasms involving the lungs are far more common than primary lung neoplasms in children [2].

Evidence-based evaluation of neoplastic masses of the lungs in children is handicapped by the rarity of the disease entities and the paucity of associated literature. The literature is largely composed of case reports, small case series, and reviews. Hartman and Shochat in 1982 summarized 230 cases of primary neoplasms of the lungs in children [3]. Subsequently, Hancock et al. incorporated an additional 153 cases for a review in 1993 [4]. Long-term, single-center reviews by Cohen and Kaschula [2] and subsequently Dishop and Kuruvilla [5] and Yu et al. [6] have contributed further cases to the literature.

R.P. Guillerman, M.D. (✉)
Department of Pediatric Radiology, Texas Children's Hospital, Baylor College of Medicine, 6701 Fannin Street, Suite 470, Houston, TX 77030, USA
e-mail: rpguille@texaschildrens.org

E. Vogelius, M.D.
Cleveland Clinic, Cleveland, OH, USA

A. Pinto-Rojas, M.D.
University of Calgary, Calgary, AB, Canada T2N 1N4

D.M. Parham, M.D.
Children's Hospital Los Angeles, Los Angeles, CA, USA

University of Southern California, Los Angeles, CA, USA

The largest series remains that of Hancock et al. [4]. They reviewed 383 total cases of pediatric primary neoplasms of the lungs from multiple centers. Of these they found 76 % (291/383) to be malignant and 24 % (92/383) to be benign. This preponderance of malignant tumors becomes even greater (88 %, 339/383) if the 48 cases of inflammatory myofibroblastic tumor (IMT), also known as inflammatory pseudotumor, are reclassified as low-grade malignancies per the revised WHO criteria [7].

Benign Tumors

Before being reclassified as a low-grade malignancy, IMT was regarded as the most commonly encountered primary benign neoplasm of the lung in children. The second most common entity was the hamartoma followed by benign neurogenic tumors and leiomyomas [4]. A subsequent series reported the most common benign neoplasm to be the squamous papilloma [5]. Other rarer benign entities include mucous cell adenoma, granular cell tumor, benign teratoma, hemangioma, lymphangioma, chondroma, juvenile xanthogranuloma, lipoblastoma, immature mesenchymal hamartoma, and solitary fibrous tumor [5].

Malignant Tumors

Secondary

Secondary (metastatic) malignant tumors are reported to be five times as common as primary neoplasms [2]. A wide variety of tumors can metastasize to the lungs. Lung metastases are most common in Wilms tumor and osteosarcoma [8]. They can also be seen in Ewing sarcoma, rhabdomyosarcoma, lymphoma/leukemia, hepatocelluar carcinoma, hepatoblastoma, and neuroblastoma. The mechanism of spread is typically hematological dissemination, resulting in well-defined pulmonary nodules. However, lymphatic spread giving a reticular or

D.M. Parham et al. (eds.), *Pediatric Malignancies: Pathology and Imaging*,
DOI 10.1007/978-1-4939-1729-7_8,

miliary pattern can also be seen, notably in lymphoma/leukemia and neuroblastoma [8]. Pulmonary infiltration in the setting of leukemia can demonstrate ill-defined margins more typical of an inflammatory process.

Cavitation can be seen with Wilms tumor, Hodgkin lymphoma, and osteosarcoma metastases which can lead to pneumothorax. Osteosarcoma metastases can also demonstrate a calcified or ossified matrix which is a relatively specific finding [8].

Primary

Primary malignant tumors of the lower respiratory tract are far less common than metastases but will constitute the predominant focus of the remainder of this chapter.

Pleuropulmonary blastoma (PPB) is likely the most common primary malignancy of the lung in childhood. Analysis is somewhat limited by the wide variety of terminologies previously used to refer to this entity. PPB accounted for about 20 % of pediatric primary lung malignancy in the series of Hancock et al. [4]. It is predominantly seen in children less than 6 years of age. It has a varied appearance ranging from cystic to solid. The cystic form is indistinguishable from the more common large cyst form of CPAM by gross inspection or imaging [9].

Bronchogenic carcinoma was reported as the second most common primary lung malignancy by Hancock et al., accounting for 16.8 % of cases [4]. This number may be contaminated by inclusion of older case reports and older patients. More recent single-center experience reports a proportion below 10 % [2, 5, 6]. There are no specific imaging findings of bronchogenic carcinoma but it tends to present at a late stage with poor prognosis (90 % mortality) [10].

Bronchial carcinoid tumor was the next most common primary malignancy of the lower respiratory tract in children and the most common endobronchial tumor, accounting for 16.5 % of pediatric primary lung malignancy in the series of Hancock et al. [4]. Bronchial carcinoids are typically a single endobronchial lesion with variable calcification and enhancement. Uptake of octreotide on somatostatin receptor scintingraphy is specific to this diagnosis [11].

Bronchial mucoepidermoid carcinoma (MEC) was the fourth most common pediatric primary malignancy of the lower respiratory tract and second most common endobronchial tumor, accounting for 13 % of cases in the series of Hancock et al. [4]. The mass was typically of low grade and demonstrated a good prognosis. MEC and other salivary gland tumors were previously referred to as bronchial adenomas.

Other primary malignancies of the lower respiratory tract account for less than 10 % of tumors and include bronchopulmonary fibrosarcoma, rhabdomyosarcoma, leiomyosarcoma, solitary fibrous tumor, plasmacytoma, and immature teratoma [5].

Diagnostic Imaging Modalities

Chest Radiography (CXR)

Chest radiography remains the most common initial imaging modality for evaluation of lung masses secondary to its wide availability, low cost, and relatively low associated radiation dose [12].

Computed Tomography (CT)

Chest CT is used to investigate suspicious or persistent abnormalities seen on CXR, or to detect disease occult on CXR. Compared to CXR, CT is much more sensitive for detecting small lesions and calcifications, and better at defining anatomic relationships and mass effect on critical structures such as the airway and great vessels. Due to its greater sensitivity for small lesions and precision for measuring the size of lesions, CT is routinely used in follow-up of treated malignancy [1]. While CT is highly sensitive, it lacks specificity and cannot reliably differentiate between benign and malignant lung nodules [13, 14]. Correlation with clinical history and serial imaging follow-up improves the specificity. CT is also useful for guiding tissue sampling.

Modern multidetector volumetric CT scanners allow rapid image acquisition, so that the entire chest of a child can be covered in a few seconds or even less than a second, resulting in less motion artifact and less need for sedation. These scanners also permit high-resolution multiplanar image reconstructions and 3D renderings to better depict anatomy for treatment planning. The dose of ionizing radiation from CT is typically much higher than from CXR, but can be reduced by judicious technique and new image reconstruction algorithms [1]. To better characterize tumors and evaluate the mediastinal/hilar structures, intravenous contrast is typically administered for chest CT scans of primary thoracic tumors for initial staging, therapy response assessment, and relapse surveillance. However, chest CT scans performed to detect and follow up lung metastases from extrathoracic tumors can be performed without intravenous contrast without loss of sensitivity [15].

Magnetic Resonance Imaging (MRI)

MRI currently has a limited role in the evaluation of pulmonary malignancy. While there is no associated ionizing radiation exposure, it has a number of disadvantages. It typically requires a relatively long exam time, requiring sedation in infants and most young children. The evaluation of the lung parenchyma is limited by respiratory motion and by the

intrinsically low signal. There may be an adjuvant role for MRI in evaluation of tumors with known or suspected neural foraminal, pericardial, or chest wall extension [12].

Positron Emission Tomography (PET)

Combined fluorodeoxyglucose (FDG)-PET/CT demonstrates increased sensitivity for the detection of small lesions when compared to stand-alone FDG-PET but not when compared to CT. However, there may be a limited role for FDG-PET/CT in adding specificity to the interpretation of small lung nodules or lymph nodes seen by CT [16].

Diagnostic Imaging Strategy

While it is difficult to construct a rigid algorithm for assessing such a heterogeneous group of rare tumors, general imaging guidelines have been proposed [17]. CXR and laboratory analysis remain the initial investigations of choice. If there are suspicious imaging findings, persistent symptoms, or persistent nonspecific radiographic abnormalities, CT should be obtained to detect and define an underlying mass or other causes. Detection of a mass suggestive of neoplasm should prompt biopsy or excision. This approach, in conjunction with increased clinical awareness of these rare but potentially morbid or even fatal conditions, may expedite the diagnosis without unnecessary testing [17].

Normal Lung Development and Malformations

Embryonic lung begins as a foregut diverticulum extending just caudal to the thyroglossal duct during the fourth week of embryogenesis. The growing lung extends into mesenchyme of the upper coelomic cavity, and by epithelial-mesenchymal interaction it forms a progressively complex structure that passes through successive histological phases corresponding to embryo-fetal development. These stages—pseudoglandular, canalicular, saccular, and alveolar—produce a progressively thinner interstitium, an increasingly greater vasculature, and a larger potential air volume. During this process, portions of the original bronchopulmonary diverticulum may pinch off and form bronchogenic cysts, which have tumorlike compressive effects. A variety of malformations including CPAMs are thought to result from in utero bronchial obstruction and resultant lack of proper epithelial-mesenchymal interaction. Type 1 CPAM, a relatively proximal malformation, contains mucinous goblet cells and may give rise to adenocarcinoma in situ and bronchioloalveolar carcinoma [18]. Of note, bronchial malformations often induce striated muscle development rather than the expected smooth muscle, a phenomenon that is recapitulated in pleuropulmonary blastomas (see below).

Specific Neoplasms

Epithelial Malignancies

Unlike lung cancer in adults, epithelial malignancies are extremely rare in children. There are occasional examples, such as the carcinomas that may arise in type 1 CPAM and the epithelial malignancies related to *NUT* fusion genes or human papillomavirus (HPV) infections.

NUT Midline Carcinoma

NUT midline carcinomas are also discussed in the head and neck chapter (Chap. 7).

Definition

Poorly differentiated aggressive carcinoma associated with characteristic rearrangement of the nuclear protein in testes (*NUT*) promoter gene.

Clinical Features and Epidemiology

The largest series of NUT midline carcinomas details 22 cases [19]. No clear gender predilection was present, and the average age of diagnosis was 25 years, although a 78-year-old patient was also affected. The reported age range may suffer from referral bias, as younger patients with undifferentiated carcinoma are more likely to undergo chromosomal analysis/FISH [20]. The presenting symptoms were nonspecific and depended on the primary site of tumor or metastases. Survival was poor with a reported mean survival of 9.5 months [19].

Imaging Features

NUT carcinomas originate from the head, neck, or chest in the majority of cases [19]. Less common origins include the salivary glands [21] and below the diaphragm. Primary sites in the liver, the bladder [22], iliac bone [23], and extremity soft tissues have been reported [24]. The tumor is midline in 70 % of cases [24]. Imaging descriptions of the

tumor are rare. Apart from the midline location, imaging features are nonspecific. On CT, it has been described as heterogeneously low in attenuation with areas of central necrosis. Small areas of central calcification have been reported [24]. On MRI, it appears hypointense on T1-weighted images and mildly hyperintense on T2-weighted images, and enhances heterogeneously with contrast. Both the primary tumor and metastases appear to be FDG-avid on PET. Metastases are frequently widespread. The lungs are the most common site of metastases but metastases to the liver, kidney, brain, spinal cord, and subcutaneous soft tissues have also been reported [24].

Molecular Genetics

NUT midline carcinoma was first described in 1991 by Kubonishi in a patient with suspected thymic carcinoma [25]. On chromosomal analysis the patient was found to have a novel translocation of chromosomes 15 and 19. The site on chromosome 15 was later identified as the *NUT* promoter gene (15q14) that encodes a polypeptide in spermatids, but whose function is unknown. The classic translocation seen in greater than two-thirds of cases occurs with the *BRD4* gene on chromosome 19 that may be involved in chromatin regulation and possibly needed for epithelial differentiation [19]. The translocation can also involve the *BRD3* or other genes and the tumor then referred to as variant NUT midline carcinoma.

Pathology

NUT midline carcinomas typically comprise patternless sheets of primitive, undifferentiated tumor cells, from whence obvious squamous differentiation may abruptly arise [22] (Fig. 8.1). They should be considered Ewing-like small-cell malignancies that lack an *EWS* fusion and strongly express cytokeratin. Immunohistochemical demonstration of nuclear *NUT* expression or FISH testing that indicates *NUT* rearrangement is diagnostic but usually requires use of a specialized center. Because of the multiple fusion partners, RT-PCR is less helpful as a diagnostic tool.

Prognostic Features

With few exceptions, NUT carcinomas are highly lethal malignancies. Most patients die within weeks, as metastases are typically present at diagnosis, and bulky intrathoracic growth produces superior vena cava compression. No association of outcome with fusion type has been demonstrated to date [22].

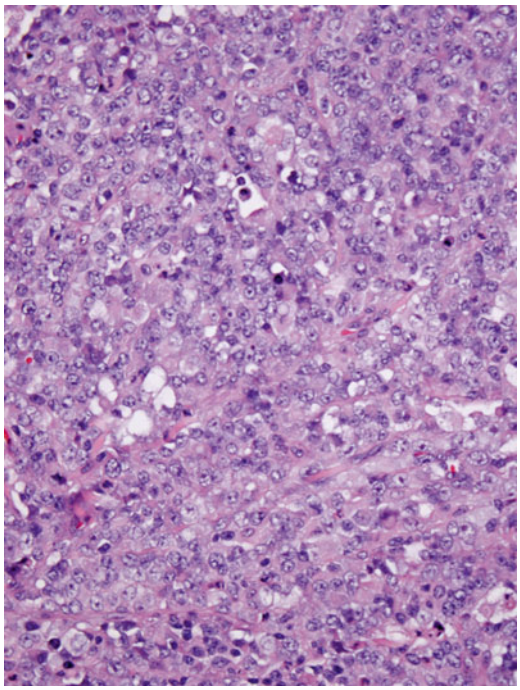

Fig. 8.1 NUT midline carcinoma. Histology consists of an undifferentiated neoplasm with vague epithelioid features

Squamous Cell Carcinoma (SCC)

HPV-related squamous cell carcinomas are discussed in the head and neck chapter (Chap. 7).

Definition

Type of bronchogenic malignancy of the lung.

Clinical Features and Epidemiology

Squamous cell carcinoma (SCC) is a common malignancy in adults, accounting for 44 and 25 % of primary malignancies of the lung of men and women, respectively [26]. In adults there is a strong association with smoking.

Bronchogenic carcinoma is much less common in children than in adults, accounting for 7–17 % of primary pediatric pulmonary malignancies [4, 5]. When seen in children, SCC is often associated with recurrent respiratory papillomatosis (RRP).

RRP is caused by the human papillomavirus (HPV) transmitted primarily via vaginal delivery [27]. RRP is usually isolated to the larynx (>95 % of cases). The distal trachea is affected in less than 5 % of cases and the pulmonary parenchyma is affected in less than 1 % of cases [28]. While pulmonary involvement is uncommon, papillomas are the most

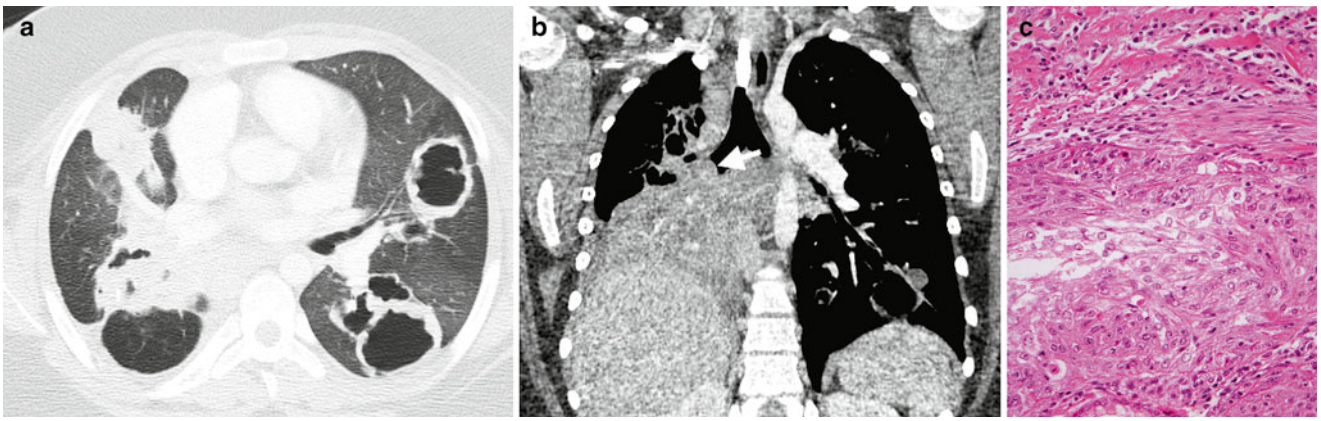

Fig. 8.2 Recurrent respiratory papillomatosis. Axial (**a**) and coronal (**b**) contrast-enhanced chest CT images from a 13-year-old male demonstrate multiple thick-walled cavitary lung lesions and an endobronchial papilloma (*arrow*) occluding the bronchus intermedius with post-obstructive atelectasis of the right middle and lower lobes. Histology (**c**) of another case shows a well-differentiated squamous carcinoma invading the underlying tissues of the bronchial submucosa and inciting adjacent fibrosis

common primary benign tumor of the lower respiratory tract in children (accounting for up to 40 %) [5]. Distal dissemination may be caused by aerogenous embolization of papilloma particles and can be precipitated by tracheotomy or other airway procedures [29]. Juvenile-onset RRP has a bimodal peak at 2 and 10 years of age [30]. No clear sex predilection has been identified.

RRP undergoes malignant transformation into SCC in less than 1 % of cases [28]. Transformation can occur with or without a history of smoking or radiation, and is most frequently observed in males in the third and fourth decades of life.

Imaging Features

RRP can present as a single or, more commonly, multiple masses predominantly affecting the airway and posterior lower lobes [29]. The masses may be solid or cavitary with a thin or thick wall and either air or fluid contents (Fig. 8.2). An air-fluid level is a nonspecific finding that may be seen in the setting of superimposed infection or hemorrhage. Benign lesions may demonstrate increased FDG uptake on PET imaging and simulate malignancy [30]. Findings that suggest malignant transformation include lesion growth, thoracic lymphadenopathy, or distal metastases.

Associated findings include atelectasis, consolidation, and bronchiectasis secondary to airway obstruction and recurrent superimposed infections [29].

Molecular Genetics

Respiratory papillomatosis is usually caused by low-risk HPV types 6 and 11. Certain HPV types, particularly types 16 and 18, are more likely to transform into carcinoma, similar to uterine cervical cancers. With HPV16-associated lesions, transformation is related to genetic polymorphisms or deletions, but aggressiveness of low-risk HPV11-associated lesions does not relate to intratypic variants but rather to the interaction of multiple genetic factors [31].

Pathology

The pathological features of HPV-related carcinomas are discussed in the head and neck chapter (Chap. 7) (Fig. 8.2). Juvenile papillomas from the upper respiratory tract may be aspirated into the bronchial passages. From there, they may act similar to metastatic lesions, as malignant transformation may produce a well-differentiated squamous carcinoma.

Prognostic Features

RRP associated with HPV 11 demonstrates a more aggressive course and worse prognosis [32].

Endobronchial Tumors

Bronchial Carcinoid

Definition

Malignant neuroendocrine tumor of endodermal origin arising from Kulchitsky cells.

Clinical Features and Epidemiology

Neuroendocrine and salivary gland tumors of the tracheobronchial tree were previously referred to as bronchial adenomas [1]. This potentially confusing terminology has fallen

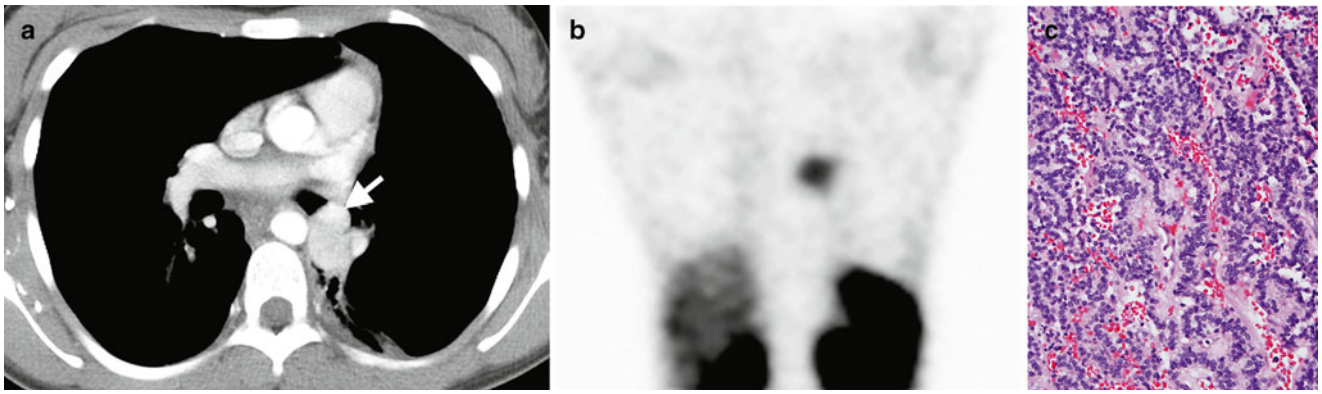

Fig. 8.3 Bronchial carcinoid. An axial contrast-enhanced chest CT image (**a**) from a 13-year-old female shows a hyper-enhancing lobular soft-tissue mass with a "tip of the iceberg" endobronchial component (*arrow*) involving the distal left mainstem bronchus. A coronal image (**b**) from an In-111 octreotide SPECT scan shows radiopharmaceutical uptake by the mass. Histology (**c**) of another case demonstrates uniform cells with round nuclei, forming cords and festoons

out of favor secondary to the variable glandular component and malignant potential of these tumors [33].

Bronchial carcinoid is the most common malignant endobronchial tumor and the second most common primary malignancy of the lower respiratory tract in children (after PPB) [5]. Carcinoids are most commonly seen in the gastrointestinal tract, with only 10–32 % occurring in the tracheobronchial tree [34, 35]. The average age of presentation of bronchial carcinoid is 45–56 years [34, 35]. This is a decade younger than the average age of presentation for other lung malignancies, but carcinoid is still uncommon in the pediatric age range. When it occurs in children, it tends to affect older children and adolescents with the youngest reported patient being 8 years of age [34]. There is no known smoking association, or sex or racial predilection.

Presentation is varied. Post-obstructive atelectasis and pneumonitis are common [35]. Nonspecific respiratory symptoms and signs, including pleuritic pain, dyspnea, cough, wheeze, and hemoptysis, are also seen. The tumor is incidentally detected in up to half of patients. Carcinoid tumors can synthesize a variety of neuroamines and peptides leading to more specific presentations. Overproduction of adrenocorticotropic hormone (ACTH) leads to Cushing syndrome in up to 4 % of patients. Overproduction of serotonin leading to carcinoid syndrome is rare in bronchial carcinoid outside of the setting of metastatic disease (2–5 %). Up to 4 % of carcinoid tumors are associated with other endocrine neoplasias [34]. The most common association is with pituitary tumors, seen in half of this patient subset.

In addition to imaging, detection and follow-up of lesions can be aided by serum and urine 5-hydroxyindolacetic acid (5-HIAA), a serotonin metabolite that is relatively specific though not sensitive for the diagnosis [34].

Imaging Features

The typical appearance of a bronchial carcinoid is that of a single round or lobulated mass that is at least partially endobronchial [35, 36]. The mass is typically 2–5 cm in size. Endoscopy can underestimate the size of the mass as the endobronchial component can represent just the "tip of the iceberg." The mass is seen within the main, lobar, and segmental bronchi in 80 % of cases with a preference for branching sites (Fig. 8.3). The remaining 20 % of bronchial carcinoids are peripheral in location and indistinguishable from intraparenchymal pulmonary masses [35].

In up to 30 % of cases, bronchial carcinoids demonstrate calcification that is best appreciated on CT. The masses demonstrate high signal intensity on T2-weighted MRI images and typically exhibit homogeneous avid enhancement [35]. However, heterogeneous or minimal enhancement does not exclude the entity. Bronchial carcinoids demonstrate octreotide uptake on somatostatin receptor scintingraphy in greater than 86 % of cases [35, 37] (Fig. 8.3).

Associated findings include post-obstructive atelectasis or pneumonitis, bronchiectasis, and mucous plugging. Local or distal recurrence occurs in up to a fifth of cases with 15 % presenting with metastases [35]. Metastases are most commonly seen in the liver, bone, adrenals, and brain.

Molecular Genetics

In the current molecular model [38], bronchial carcinoids originate from bronchial Kulchitsky-type neuroendocrine cells. These cells are capable of producing precursor lesions such as diffuse idiopathic pulmonary cell hyperplasia or tumorlets. Small invasive foci break through the basal lamina and invade locally, producing small lesions termed tumorlets, which are by definition <5 mm in diameter. The most common chromosomal aberrations in pulmonary carcinoids include −11p, +19p, −13q, +19q, +17q. −11p, −6q, +16p, +2-p, and −3p, although these occur at a frequency of <25 % in typical lesions. However, as bronchial carcinoids assume atypical features and undergo carcinomatous transformation, the frequency of these changes rises to as high as 75 % for

−3p and −13q. Approximately 18 % show sporadic mutations and loss of heterozygosity of *MEN1*, the multiple endocrine neoplasia 1 gene.

Pathology

Pulmonary carcinoids generally contain a uniform population of monotonous round cells with regular, central nuclei, granular chromatin, inconspicuous nuclei, and a relatively high nuclear-to-cytoplasmic ratio. The cytoplasm is generally lightly eosinophilic but on occasion is more abundant and resembles that of rhabdoid cells. Rarely, it is clear, and melanin or mucus may be present. Some tumors show marked nuclear pleomorphism, a feature not reliable in predicting behavior. The cells usually grow in an organoid or trabecular pattern, forming nests or cords, but sometimes they form spindle cells or rosettes. The intervening stroma is vascular and collagenous and is capable of producing amyloid, hyaline, bone, or cartilage (Fig. 8.3).

Atypical carcinoids are characterized by the presence of focal necrosis or conspicuous mitotic activity (2–10 mitoses/2 mm^2) [33].

Prognostic Features

Prognostic factors in bronchial carcinoids include stage and the presence of atypical features (atypical carcinoid). Pediatric bronchial carcinoids generally have an excellent long-term outcome with adequate surgery and lymph node excision. Long-term follow-up is required, as relapse may occur years after the initial excision, but usually can be successfully treated with additional surgery [39].

Mucoepidermoid Carcinoma

Definition

Malignant salivary-type neoplasm arising from the mucous cells of the submucosa.

Clinical Features and Epidemiology

Mucoepidermoid carcinoma comprises 0.1–0.2 % of malignant lung tumors and 2.5–7.3 % of endobronchial tumors [34]. While it is even more unusual in children, it is likely the second most common endobronchial malignancy [34]. The tumor has a wide age range of 3–78 years, with half of cases occurring in patients younger than 30. The tumor may be more common in Caucasians and has a 3:2 male-to-female ratio [33].

Obstructive airway symptoms and signs are a common presentation and include wheezing and recurrent pneumonia. Up to 25 % of patients are asymptomatic and the tumor is incidentally discovered [34].

Fig. 8.4 Mucoepidermoid carcinoma. A coronal contrast-enhanced chest CT image from a 12-year-old male depicts a partially calcified endobronchial mass (*arrow*) occluding the left upper lobe bronchus with associated left upper lobe collapse

Mucoepidermoid carcinoma is graded by histology similar to other salivary-type neoplasms into low, intermediate, and high grades. Higher grades have a higher rate of metastasis and worse prognosis [40].

Imaging Features

The typical appearance is a single round, lobulated or polypoid mass occurring in a proximal lobar bronchus [41] (Fig. 8.4). A more peripheral mass with the same histology should raise concern for metastatic salivary gland neoplasm [34]. The mass is typically 1–4 cm in size and often extends beyond the lumen of the bronchus. Calcification is seen in up to half of cases. Grades are indistinguishable by imaging.

These endobronchial tumors frequently cause airway obstruction with associated findings of atelectasis, bronchiectasis, and mucous plugging. Post-obstructive pneumonitis is seen in up to a third of cases [42].

Lymph node extension and distal metastasis are infrequent, being seen in less than 10 % of cases [42].

Molecular Genetics

The molecular genetic features of mucoepidermoid carcinoma are discussed in the head and neck chapter.

Pathology

The pathological features of mucoepidermoid carcinoma are discussed in the head and neck chapter.

Prognostic Features

Pediatric mucoepidermoid carcinomas of the lung are generally low-grade, low-stage lesions with excellent patient survival following excision. In a recent SEER survey [43], all 14 patients survived. In a recent Egyptian study of radiographic features [44], overall survival of patients with salivary gland-type tumors of the lung was affected by the presence of mediastinal/hilar lymphadenopathy, suspected metastatic disease, and primary tumor heterogeneity. Higher FDG uptake on PET was associated with nodal metastasis. The mean survival time for pulmonary mucoepidermoid carcinoma was 4.4 years. In a recent Chinese study [45], prognostic factors for pulmonary mucoepidermoid carcinoma included age, grade, lymph node metastasis, and stage. Lower age had a positive effect on outcome, with 80 % survival in patients <60 years old.

Mesenchymal Tumors

Pleuropulmonary Blastoma

Definition

Pleuropulmonary blastoma (PPB) is a rare primitive mesenchymal, embryonal type neoplasm of the lung and pleura of young children.

Clinical Features and Epidemiology

PPB has been previously termed pulmonary embryoma, pulmonary blastoma, mesenchymal cystic hamartoma, and sarcoma arising in congenital cystic malformations [5]. PPB was described as a tumor distinct from adult pulmonary blastoma in 1988 by Manivel et al. [46]. PPB is a rare neoplasm with approximately 25–50 cases occurring annually in the USA, 500–600 cases reported in the literature, and 370 centrally reviewed cases in the International Pleuropulmonary Registry (Personal communication, Dr. Yoav Messinger, on July 17, 2013). In spite of its rarity, it is likely the most common primary malignancy of the lung in children. Epidemiological data is largely derived from the largest reported case series of 50 patients from the Registry [47]. The average age of presentation is 38 months with the cystic types presenting earlier and rarely presenting at more than 6 years of age. Prenatal presentation of cystic PPB has been reported [48].

There is no apparent sex or racial predilection. About 40 % of patients with PPB or their relatives manifest certain other dysplasias and neoplasms as part of the PPB Family Tumor Dysplasia Syndrome (PPB-FTDS). Conditions associated with PPB-FTDS include PPB, cystic nephroma, pineoblastoma, pituitary blastoma, embryonal rhabdomyosarcoma (especially of the uterine cervix), medulloblastoma, nasal chondromesenchymal hamartoma, ciliary body medulloepithelioma, multinodular goiter, intestinal juvenile hamartomatous polyp, and ovarian stromal sex-cord tumor (especially Sertoli-Leydig tumors) [49–51]. The clinical presentation of PPB ranges from an incidental finding in an asymptomatic patient to nonspecific respiratory or systemic symptoms, such as respiratory distress, fever, chest pain, cough, anorexia, and malaise [47].

Imaging Features

PPB has been categorized into three main types based on gross morphology. Type I is entirely cystic, type II is mixed cystic and solid, and type III is entirely solid [52]. Age of presentation, malignant behavior, and mortality increase with type number. If untreated, progression of type I to type II and III can occur. CPAMs do not transform into PPB [47]. Type I PPB may also spontaneously regress, leading to categorization as type Ir PPB for type I-regressed PPB [49].

Types I and Ir PPB appear as an air-filled unilocular or multilocular thin-walled cyst with delicate septations, and are indistinguishable from the more common large cyst form of CPAM (Fig. 8.5). Findings that favor type I PPB over large-cyst CPAM include the presence of multifocal or bilateral cysts or spontaneous pneumothorax [47–49, 53]. Type II and III PPB usually appear as a large, heterogeneously enhancing mass in the hemithorax with associated mediastinal mass effect and pleural effusion and lack of chest wall invasion [9] (Fig. 8.6). PPB is slightly more common in the right hemithorax than the left, and bilateral tumors may be synchronous or metachronous [54].

Aggressive local invasion of the bronchi, great vessel, and heart is unusual but has been reported [54, 55]. Metastases occur in 11 % and 55 %, respectively, of types II and III cases [49]. The most common location for distal metastasis is the brain, followed by bone. Cerebral metastases are much more frequent in PPB than in other childhood sarcomas [56]. Metastases to the liver, adrenal glands, and ovary have also been reported [47, 49].

Molecular Genetics

Comparative genomic hybridization identifies aberrations (amplifications, gains, losses) in PPB tumors, with DNA gains involving chromosome 8q being the most frequent abnormality. Losses of 9p and 11q are also reported [57]. The sites of gains and losses may contain oncogenes or tumor suppressor genes, respectively.

Children with PPB-FTDS discussed above frequently have heterozygous, germline loss-of-function mutations in the *DICER1* gene that codes for a protein involved in microRNA (miRNA) processing. Loss of DICER 1 function in the epithelium of the developing lung may alter the regulation of diffusible factors that results in mesenchymal proliferation and sarcomatous transformation [58]. DICER1

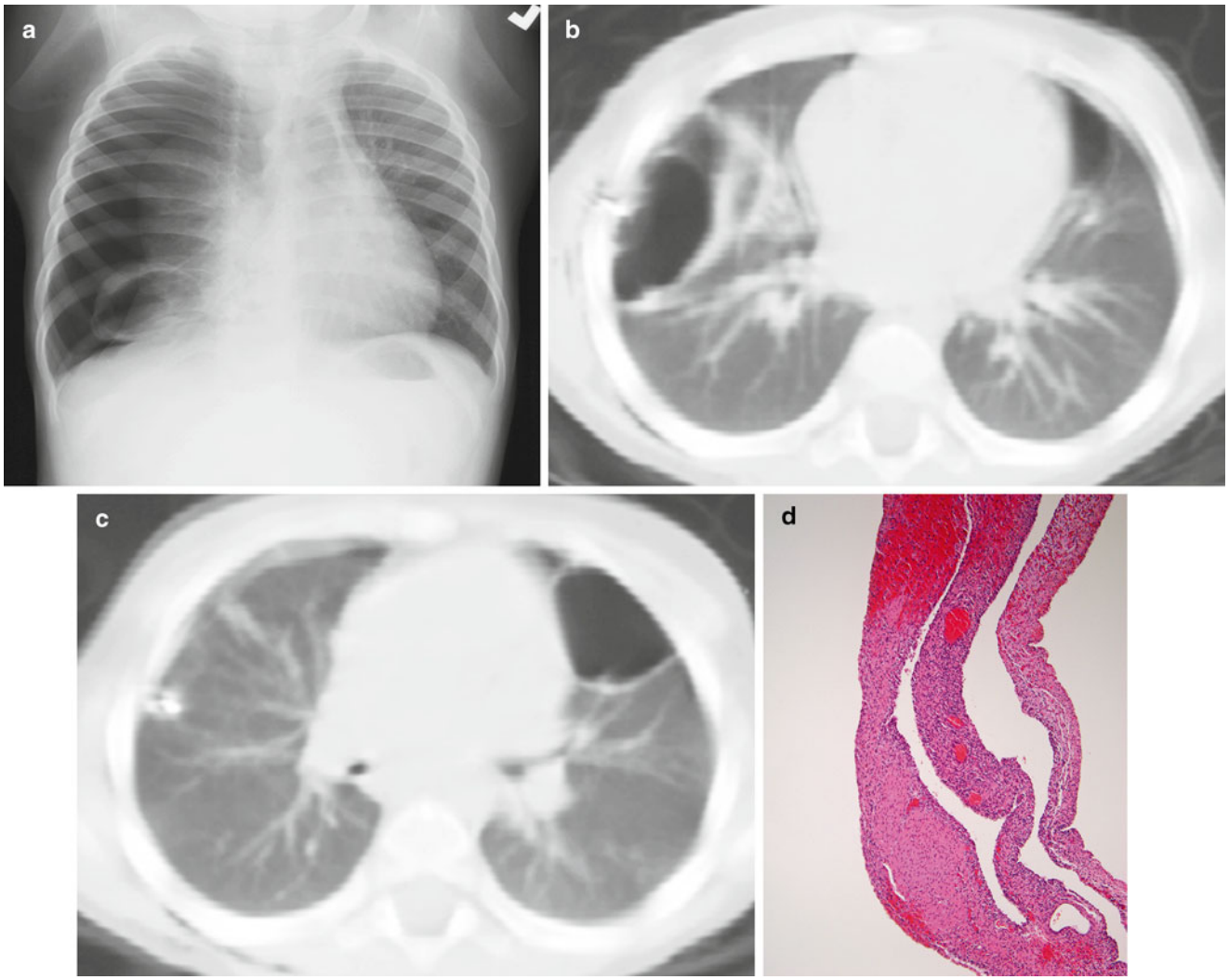

Fig. 8.5 Type I (cystic) pleuropulmonary blastoma. A chest radiograph (**a**) from a 2-year-old presenting with respiratory distress demonstrates a right pneumothorax, right lung collapse, and a cystic lesion of the right lower lung. Axial chest CT images (**b**, **c**) obtained after right chest tube placement and pneumothorax evacuation demonstrate bilateral air-filled, thin-walled cystic lung lesions. Histology (**d**) of another case shows large spaces lined by thin septa, some containing nodules of primitive blastemal cells

mutations are inherited by an autosomal dominant mechanism with variable expressivity, and are thought to be present in 60–70 % of cases of PPB [49].

Pathology

PPB is composed of a malignant mesenchymal component but no malignant epithelial component. It is postulated that PPB originates in mesenchymal elements resembling fetal lung at 10–16 weeks of gestation. Three types (I, II, and III) based on gross morphology are described [59].

A unilocular or multilocular cyst with thin fibrous septa characterizes type I PPB. The cysts are lined by ciliated epithelium with small subepithelial "buds" containing aggregates of primitive mesenchymal cells or nodules of immature cartilage (Fig. 8.5). These small, round-to-spindled, subepithelial mesenchymal cells may display rhabdomyoblastic differentiation. In type Ir (regressed cystic), the small primitive mesenchymal cells are not seen, and the wall or septa of the cyst may be hyalinized or necrotic.

In type II PPB, cystic and plaque-like areas mingle with solid areas with overgrowth of rhabdomyoblasts, spindle cell sarcoma, or blastematous elements. Type III PPB consists of a solid tumor with mixed sarcomatous (fibrosarcoma, rhabdomyosarcoma, pleomorphic undifferentiated sarcoma) and blastematous features (Fig. 8.6). Foci of muscle and chondroid differentiation are frequent, as are foci of anaplasia with giant bizarre pleomorphic tumor cells (Fig. 8.6a). Malignant epithelium is not seen, differentiating PPB from pulmonary blastoma. Immunohistochemical staining is variable from one tissue type to another. Myogenin, desmin, and MyoD1 are useful for the identification of rhabdomyoblasts [49].

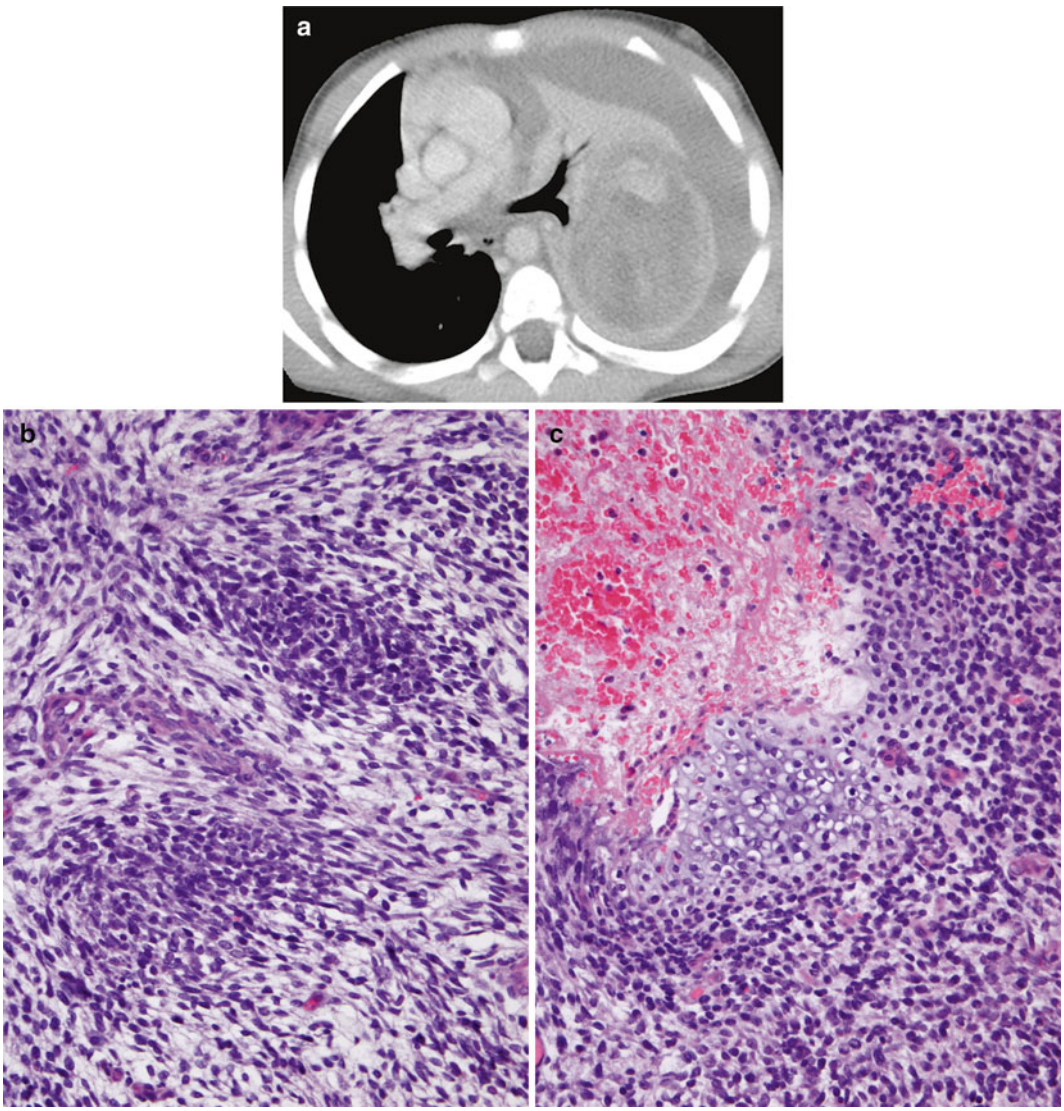

Fig. 8.6 Type III (solid) pleuropulmonary blastoma. An axial contrast-enhanced chest CT image (**a**) from a 3-year-old male reveals a large, heterogeneously enhancing left pulmonary mass with a large left pleural effusion and rightward mediastinal shift from mass effect. Histology (**b**) of another case demonstrates primitive blastemal cells arranged in an organoid pattern. A small bar of hyaloid cartilage is revealed in an additional histologic section (**c**)

As was mentioned, PPB is histologically and clinically distinct from pulmonary blastoma, a rare subtype of malignant biphasic sarcomatoid carcinoma typically seen in adults. However, a recent case report of a neonate described histology distinct from PPB and more similar to adult PB [60]. PB is occasionally reported in adolescents [61].

Prognostic Features

Overall survival rate is estimated at 90 % for type I and 40–60 % for types II and III [49]. Progression of type I to type II and III is well recognized. Tumors do not regress from type III to type II or from type II to type I. Local recurrence develops in fewer than 15 % of type I but is seen in over 45 % of types II and III [49]. Recurrence can affect the ipsilateral or contralateral lung [47]. Sex, tumor side, tumor size, preexisting lung cysts, and extent of surgical resection at the time of diagnosis do not impact prognosis, whereas incomplete resection and extrapulmonary involvement at diagnosis result in a significantly worse prognosis [62].

Fetal Interstitial Lung Tumor (FLIT)

Definition

Tumefactive lesion presenting in utero or early infancy with a solid appearance on imaging and gross inspection and a prominent immature interstitium on histology that resembles immature fetal lung at 20–24 weeks gestational age.

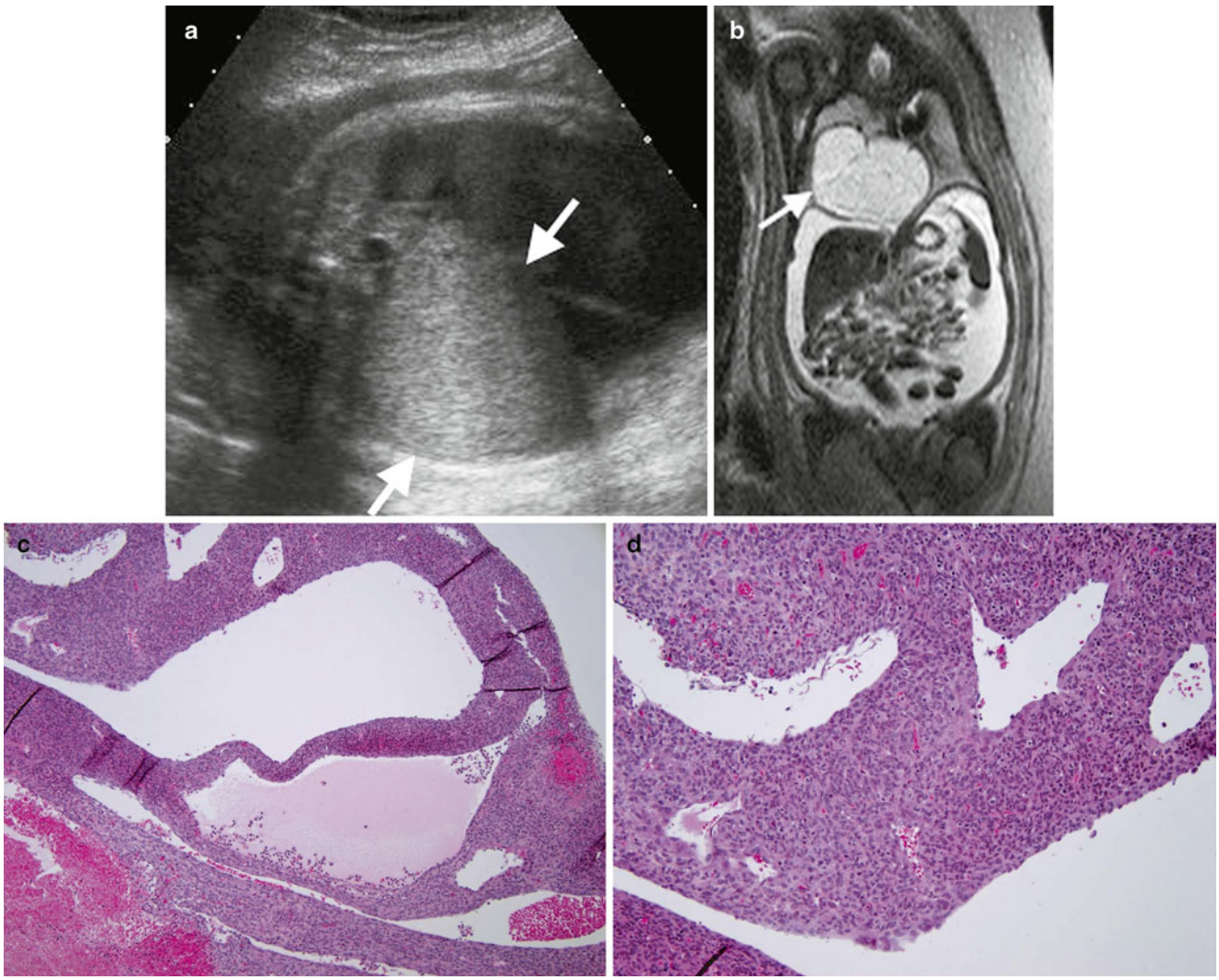

Fig. 8.7 Fetal lung interstitial tumor. Prenatal ultrasound (**a**) at 36 weeks gestation shows a large, well-circumscribed, solid hyperechoic mass arising from the right lung (*arrows*). T2-weighted fetal MRI image (**b**) at 36 weeks gestation shows the high signal intensity mass compressing the adjacent lung and everting the diaphragm, with associated hydrops and large-volume ascites from inferior vena cava compression. Histology (**c**) of another case shows primitive mesenchymal cells that line spaces resembling alveoli. An additional histologic section (**d**) demonstrates constituent cells that are primitive and lack obvious differentiation

Clinical Features and Epidemiology

FLIT is a rare tumor recently described in a series of ten cases [63]. All were discovered before 3 months of age. Two were detected by prenatal ultrasound and one of these was further evaluated by prenatal MRI [64]. In the patient that underwent MRI, the tumor was not seen at routine second trimester prenatal ultrasound but was first noted in late third trimester as a large pulmonary mass causing hydrops, prompting ex utero intrapartum treatment (EXIT procedure) at 37 weeks gestational age. This late gestational growth and late onset of hydrops would be atypical for a CPAM or PPB [64]. The other patients presented with respiratory symptoms, two in the immediate postpartum period [63].

Imaging Features

The tumors are well circumscribed, unifocal, and confined within a single lobe. The tumors have been reported in all lobes, with the right lower lobe being the most common location [63]. The tumors usually appear solid, with small cysts occasionally observed. On prenatal ultrasound, the tumors are hyperechoic compared to normal lung parenchyma (Fig. 8.7). The tumors are predominantly low in attenuation on CT. The single case examined by MRI appeared heterogeneously hyperintense on T2-weighted images, with mass effect compressing the heart and inferior vena cava leading to fetal hydrops (Fig. 8.7). The solid nature of a FLIT can resemble a type 3 CPAM, sequestration, or congenital peribronchial myofibroblastic tumor.

Although rapid growth can be observed, no locally recurrent or metastatic FLIT has been described to date, even in the setting of an incompletely resected lesion [63].

Molecular Genetics

No genetic aberrations have been reported. The one child in the defining series who underwent testing for *DICER1* mutations associated with PPB tested negative [63].

Pathology

Grossly, FLIT manifests as a well-circumscribed solid-to-spongy mass. A fibrous interface demarcates the tumor from adjacent normal lung. Histopathology shows immature airspace-like structures with uniform expansion of immature vimentin-positive interstitial mesenchymal cells with abundant cytoplasmic glycogen (Fig. 8.7). The histology resembles lung arrested in development at 20–24 weeks gestation. The interstitial cells have monotonous, round-to-oval contours and round-to-oval nuclei with a prominent rim of clear-to-pale eosinophilic cytoplasm and well-defined cell borders. Nuclear hyperchromasia, mitoses, or atypia are not identified. Occasional isolated foci of cartilage, similar to that seen in small bronchioles, may be noted [63]. The interstitial cells contain PAS-positive cytoplasm and express vimentin, focal smooth muscle actin, and focal desmin. The epithelial lining of the air spaces is positive for cytokeratin, EMA, and TTF-1.

Prognostic Features

Prognosis is favorable. Resolution of respiratory symptoms and no local recurrence or metastatic disease is expected after resection, even without chemotherapy. In the Dishop et al. series [63], lobectomy or wide resection was performed with complete excision in eight of ten cases. No metastases and no recurrence were reported [63].

Leiomyoma and Leiomyosarcoma

Definition

Spectrum of benign-to-malignant tumors of smooth muscle origin.

Clinical Features and Epidemiology

Primary leiomyoma and leiomyosarcoma of the lung are very rare [10]. An association between human immunodeficiency virus (HIV) infection and both benign and malignant smooth muscle tumors has been noted [65]. While HIV was initially thought to be causative, subsequent studies have shown marked expression of clonal Epstein-Barr virus (EBV) within the tumor cells that is not seen in non-HIV-associated smooth muscle tumors or normal muscle [66]. This is similar to the association of EBV with tumors in patients undergoing solid organ transplant [67]. The causal mechanism of tumorigenesis is not entirely known. The frequency of tumors in the pediatric HIV population is considerably lower than in adults, and no specific age or sex predilection has been noted [65].

Presentation usually consists of nonspecific respiratory signs and symptoms [10]. Given the frequent immunosuppression of these patients, infection is often the initial consideration and definitive diagnosis can be considerably delayed [66].

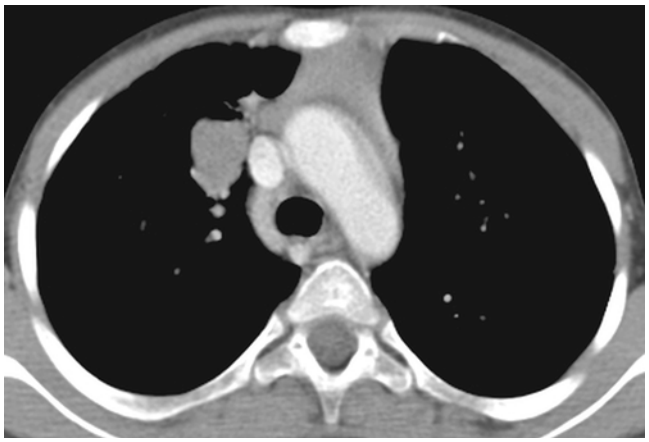

Fig. 8.8 EBV-related smooth muscle tumor. An axial contrast-enhanced chest CT image from an 11-year-old HIV + male shows a well-defined solid mass in the right suprahilar peribronchial region

Imaging Features

The tumors have a propensity for the gastrointestinal tract and tracheobronchial tree and typically present as single or multiple well-defined solid masses [68] (Fig. 8.8). Metastases are most frequently observed in the lungs, although brain metastases have also been described [65].

Molecular Genetics

The molecular mechanism for development of EBV-related smooth muscle tumors is unclear, but there may be a relationship with expression of the EBV receptor CD21 [69]. Clonality studies indicate that multifocality of these lesions is caused by infection of multiple cells and not metastasis [70].

Pathology

EBV-related smooth muscle tumors consist of spindle cells with a smooth muscle phenotype, i.e., abundant cytoplasmic microfilaments (smooth muscle actin), elongated cells with squared-off nuclei, and expression of actin, desmin, and h-caldesmon. The tumor cells appear well differentiated with mild atypia and a variable amount of myxoid stroma. Mitotic activity can vary from none to 18/10 hpfs. Some cases contain intratumoral lymphocytes, and small round cell foci may be seen [70].

Prognostic Features

EBV-related smooth muscle tumors appear to be less aggressive than sporadic leiomyosarcomas, although recurrence is reported. Surgical excision, chemotherapy, cessation of immunotherapy (in transplant patients), or a combination thereof are standard treatment options. Because of their relatively indolent behavior, some prefer the term "smooth muscle tumor of uncertain malignant potential" [70].

Inflammatory Myofibroblastic Tumor (IMT)

Definition

A low-grade myofibroblastic tumor of borderline malignant potential occurring at a variety of sites in younger patients.

Clinical Features and Epidemiology

IMT has been referred to by a variety of names including inflammatory pseudotumor and plasma cell granuloma [7]. The current nomenclature emphasizes the dominant fibrous and muscular components of this tumor.

IMT is a rare neoplasm accounting for only 0.4–1 % of primary lung tumors [71]. However, in the largest series to date of primary pediatric lung tumors it accounted for 12.5 % (48/383) of tumors, having a similar incidence to malignant lesions such as carcinoid, mucoepidermoid carcinoma, and pleuropulmonary blastoma [4]. The tumor also accounted for the majority (52 %) of benign primary tumors of the lung in this series, although it has since been reclassified as low grade or borderline malignant [4].

IMT has a wide age distribution ranging from 1 to 77 years with an average age of presentation of 29.5 years [71]. In children, this tumor tends to occur above 5 years of age [5]. There is no sex or racial predilection [5].

IMT can occur at a variety of sites. The abdomen is the most common, followed by the lung (22 %) [72]. The presentation depends largely on the site of tumor. Presentations of pulmonary IMT range from asymptomatic to respiratory symptoms to the constellation of fever, weight loss, anemia, thrombocytosis, and polyclonal hyperglobulinemia with elevated ESR [72].

Imaging Features

The imaging appearance is typically a well-circumscribed solitary pulmonary mass [71]. Upper lobe predominance has been described [73]. The mass ranges widely in size from 1 to 36 cm with an average size of 3 cm [7]. A majority (83 %) are parenchymal with the remainder (17 %) being endobronchial [4] (Fig. 8.9). They can be homogeneously or heterogeneously low in attenuation, and calcification or cavitation are rarely seen [71]. There is aggressive local invasion of the chest wall in 5–10 % [7]. On MRI, they are typically hypointense on T1-weighted images and variably hyperintense on T2-weighted images. They demonstrate mild heterogeneous enhancement after contrast administration that is typically more pronounced in the delayed phases [71].

There is a high incidence of local recurrence, especially with incompletely resected tumors [72]. Metastases are rare but have been documented to the lung, brain, liver, and bone. A recent series reported a 25 % incidence of developing CNS metastases [73].

Molecular Genetics

Up to 56 % of these patients demonstrate increased cytoplasmic expression of the receptor tyrosine kinase protein anaplastic lymphoma kinase (ALK) encoded by the *ALK1* gene on chromosome 2p, secondary to translocations and fusions with a variety of partner genes. When over-expressed, *ALK1* is associated with an increased rate of local recurrence, decreased metastatic disease, and overall improved prognosis. Partner genes in *ALK1* fusions include *TPM3, TPM4, CLTC, RANBP2*, and *ATIC* [72]. These genetic rearrangements appear to be more common in tumors of children than those of adults [74]. They overlap somewhat with similar fusions found in anaplastic large cell lymphoma [75].

Pathology

IMT is a spindle cell lesion containing variable amounts of inflammatory cells, particularly eosinophils, lymphocytes, and plasma cells (hence the former name of "plasma cell granuloma")

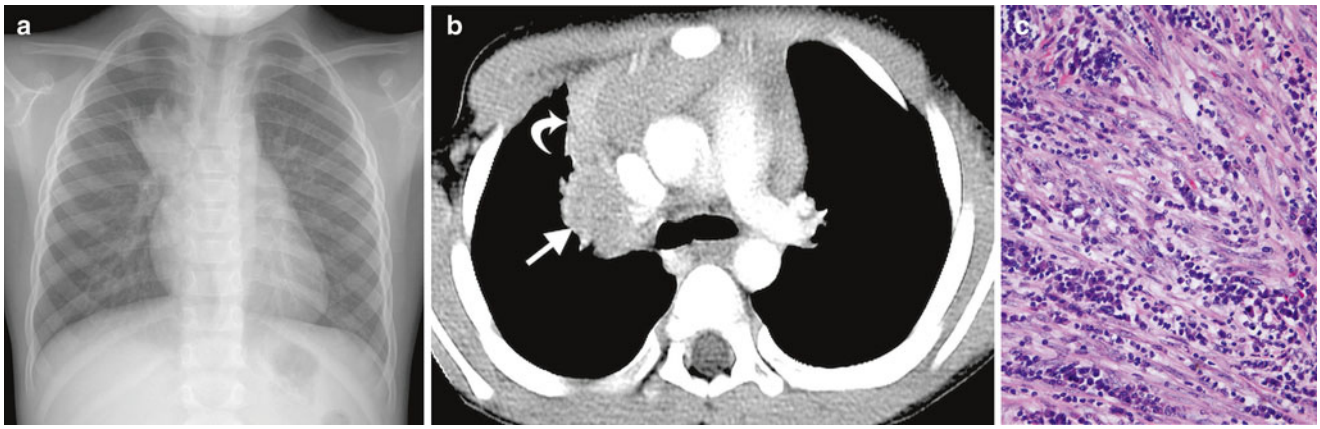

Fig. 8.9 Inflammatory myofibroblastic tumor. A chest radiograph (**a**) from a 4-year-old male shows a right suprahilar mass and volume loss of the right upper lobe. An axial contrast-enhanced chest CT image (**b**) reveals a low-attenuation non-calcified mass (*straight arrow*) along the region of the central right upper lobe bronchus with associated anterior right upper lobe atelectasis (*curved arrow*). Histology (**c**) of another case reveals a mixture of spindle cells and inflammatory cells, particularly plasma cells

(Fig. 8.9). The constituent tumor cells contain moderate amounts of cytoplasm with tapered cellular margins. They display variable eosinophilia, but not to the extent of rhabdomyosarcoma. Because of RNA content, a purplish tint may be apparent. The nuclei appear oval to elongated and show mild-to-moderate degrees of pleomorphism. The mitotic rate is variable and can be fairly brisk, and atypical mitoses may be seen. Occasional ganglion cell-like elements may be present [72].

Depending on a degree on the relative content of inflammatory cells, IMTs form three patterns: inflammatory, hemangiopericytomatous, and fibrous. The first pattern displays relatively a more fascicular arrangement with a diffuse inflammatory infiltrate. The hemangiopericytomatous pattern shows relatively loose cellularity enmeshed in a staghorn, granulation tissue-like vascularity. The fibrous pattern exhibits scar-like features, with more abundant collagen and relatively sparse inflammation.

Like most myofibroblastic lesions, IMTs express vimentin, actin, and occasionally desmin. Anti-α-smooth muscle actin shows strongest expression among the actin subtypes. ALK1 immunostaining, the best method for detecting the presence of *ALK1* fusions, is present in the majority of cases [76]. In ALK1-negative cases, FISH testing may indicate *ALK1* rearrangement [73]. ALK1-negative tumors may be associated with aneuploidy and more aggressive behavior [77].

Prognostic Features

IMTs usually act in a relatively indolent fashion, although about one-fourth recur, depending on site, adequacy of excision, and multinodularity. When over-expressed *ALK1* may be associated with an increased rate of local recurrence, decreased metastatic disease, and overall improved prognosis. Metastases are rare, occurring in <2 % of patients. Metastatic disease is associated with fusion negativity, with specific fusions such as *ALK1-RANBP2*, and with round cell cytology. Size, cellularity, and histological features are not predictive of outcome [72].

Congenital Peribronchial Myofibroblastic Tumor (CPMT)

Definition

A locally invasive tumor of the pluripotent mesenchyme surrounding the developing bronchi.

Clinical Features and Epidemiology

Congenital peribronchial myofibroblastic tumor (CPMT) has been previously described as massive congenital malformation of lung, hamartoma of lung, bronchopulmonary leiomyosarcoma, and primary bronchopulmonary fibrosarcoma [78]. The cellular nature of the tumor has led to confusion with malignant congenital pulmonary tumors. The current terminology is preferred to emphasize the benign histology of this lesion. The tumor is thought to develop at approximately 12 weeks of gestational age and have various degrees of smooth muscle and cartilaginous differentiation [79].

CPMT is very rare with approximately 25 cases reported in the literature [5] and the largest case series detailing 11 patients [80]. The mass is typically detected in the neonatal period, and prenatal detection has also been reported [80].

Although histologically benign, high mortality is reported predominantly secondary to nonimmune hydrops fetalis (55 % mortality). No sex or racial predilection, or syndromic, genetic, or maternal associations have been identified [78].

Imaging Features

CPMT typically appears as a large solitary well-defined pulmonary mass. Any lobe can be involved. The tumors are typically 5–7 cm in diameter and occupy much of the involved hemithorax, exerting mass affect with mediastinal shift [78]. Mass effect leads to hydrops fetalis in 36 % of cases [80]. Polyhydramnios is observed in 27 % of cases, presumably secondary to compression of the esophagus [80]. The tumor is heterogeneously hyperechoic on ultrasound [80], and heterogeneous but without cystic areas or calcification on CT [78]. The appearance on MRI has not been described. No local recurrence or metastasis has been reported [80].

Molecular Genetics

The genetics of CPMT are not well described. Some have complex karyotypic rearrangements [81]. A few cases published as CPMT show the t(12;15) and *TEL-TRK3* fusion of infantile fibrosarcoma [82], suggesting that, like cellular mesoblastic nephroma, at least some examples comprise visceral examples of this soft-tissue neoplasm, and the cellular features and typical age support this notion.

Pathology

CPMT typically occurs as a peribronchial mass containing interlacing fascicles of myofibroblastic cells. Tumor may also infiltrate interlobular septa and the subpleural region. The cells show a partial smooth muscle phenotype, such as smooth muscle actin expression and submicroscopic cytoplasmic microfilaments, which led to its early description as "leiomyosarcoma of lung." Although it has bland cytological features, mitotic activity can be brisk, and rare atypical forms may be seen, along with geographic necrosis. Some lesions have a minor cartilaginous component that increases markedly after birth [81]. One lesion to consider in the differential diagnosis is myofibroma, a benign mesenchymal disorder thought to be the most common fibrous tumor of infancy. In its visceral form, it often affects the lung and acts similar to a malignant neoplasm, although multifocality rather than metastasis likely accounts for the aggressive behavior [83].

Prognostic Features

In general, patients survive CPMT following surgical extirpation. However, some die in the prenatal or neonatal period as a result of fetal hydrops or respiratory failure [81].

References

1. Guillerman RP, McCarville ME, Kaste SC, Shulkin BL, Voss SD. Imaging studies in the diagnosis and management of pediatric malignancies. In: Poplack PD, Pizzo PA, editors. Principles and practice of pediatric oncology. Baltimore: Lippincott, Williams and Wilkins; 2011. p. 216–78.
2. Cohen MC, Kaschula RO. Primary pulmonary tumors in childhood: a review of 31 years' experience and the literature. Pediatr Pulmonol. 1992;14:222–32.
3. Hartman GE, Shochat SJ. Primary pulmonary neoplasms of childhood: a review. Ann Thorac Surg. 1983;36:108–19.
4. Hancock BJ, Di Lorenzo M, Youssef S, et al. Childhood primary pulmonary neoplasms. J Pediatr Surg. 1993;28:1133–6.
5. Dishop MK, Kuruvilla S. Primary and metastatic lung tumors in the pediatric population: a review and 25-year experience at a large children's hospital. Arch Pathol Lab Med. 2008;132:1079–103.
6. Yu DC, Grabowski MJ, Kozakewich HP, et al. Primary lung tumors in children and adolescents: a 90-year experience. J Pediatr Surg. 2010;45:1090–5.
7. Yousem S, Tazelaar H, Manabe T, et al. Inflammatory myofibroblastic tumor. In: Travis WD, Brambilla E, Muller-Hermelink HK, Harris CC, editors. World Health Organization classification of tumours: pathology and genetics of tumors of the lung, pleura, thymus, and heart. Lyon: IARC Press; 2004. p. 105–6.
8. McCahon E. Lung tumours in children. Paediatr Respir Rev. 2006;7:191–6.
9. Naffaa LN, Donnelly LF. Imaging findings in pleuropulmonary blastoma. Pediatr Radiol. 2005;35:387–91.
10. Lal DR, Clark I, Shalkow J, et al. Primary epithelial lung malignancies in the pediatric population. Pediatr Blood Cancer. 2005;45:683–6.
11. Roby BB, Drehner D, Sidman JD. Pediatric tracheal and endobronchial tumors: an institutional experience. Arch Otolaryngol Head Neck Surg. 2011;137:925–9.
12. Newman B. Thoracic neoplasms in children. Radiol Clin North Am. 2011;49:633–64.
13. McCarville MB, Lederman HM, Santana VM, et al. Distinguishing benign from malignant pulmonary nodules with helical chest CT in children with malignant solid tumors. Radiology. 2006;239:514–20.
14. Rosenfield NS, Keller MS, Markowitz RI, et al. CT differentiation of benign and malignant lung nodules in children. J Pediatr Surg. 1992;27:459–61.
15. Kuhns LR, Roubal S. Should intravenous contrast be used for chest CT in children with nonlymphomatous extrathoracic malignancies? Pediatr Radiol. 1995;25 Suppl 1:S184–6.
16. Kleis M, Daldrup-Link H, Matthay K, et al. Diagnostic value of PET/CT for the staging and restaging of pediatric tumors. Eur J Nucl Med Mol Imaging. 2009;36:23–36.
17. Weldon CB, Shamberger RC. Pediatric pulmonary tumors: primary and metastatic. Semin Pediatr Surg. 2008;17:17–29.
18. Lantuejoul S, Nicholson AG, Sartori G, et al. Mucinous cells in type 1 pulmonary congenital cystic adenomatoid malformation as mucinous bronchioloalveolar carcinoma precursors. Am J Surg Pathol. 2007;31:961–9.
19. French CA. NUT midline carcinoma. Cancer Genet Cytogenet. 2010;203:16–20.
20. Stelow EB, French CA. Carcinomas of the upper aerodigestive tract with rearrangement of the nuclear protein of the testis (NUT) gene (NUT midline carcinomas). Adv Anat Pathol. 2009;16:92–6.
21. den Bakker MA, Beverloo BH, van den Heuvel-Eibrink MM, et al. NUT midline carcinoma of the parotid gland with mesenchymal differentiation. Am J Surg Pathol. 2009;33:1253–8.

22. French CA, Kutok JL, Faquin WC, et al. Midline carcinoma of children and young adults with NUT rearrangement. J Clin Oncol. 2004;22:4135–9.
23. Mertens F, Wiebe T, Adlercreutz C, et al. Successful treatment of a child with t(15;19)-positive tumor. Pediatr Blood Cancer. 2007;49: 1015–7.
24. Polsani A, Braithwaite KA, Alazraki AL, et al. NUT midline carcinoma: an imaging case series and review of literature. Pediatr Radiol. 2012;42:205–10.
25. Kubonishi I, Takehara N, Iwata J, et al. Novel t(15;19)(q15;p13) chromosome abnormality in a thymic carcinoma. Cancer Res. 1991;51:3327–8.
26. Hammar SP, Brambilla C, Pugatch B, Geisinger K, Fernandez EA, Vogt P, Petrovitchev N, Matsuno Y, Aisner S, Rami-Porta R, Capelozzi VL, Schmidt R, Carvalho L, Petersen I, Gazdar A, Meyerson M, Hanash SM, Jen J, Harris CC. Squamous cell carcinoma. In: Travis WD, Brambilla E, Muller-Hermelink HK, Harris CC, editors. WHO classification of tumours: pathology and genetics of tumors of the lung, pleura, thymus, and heart. Lyon: IARC Press; 2004. p. 26–30.
27. Cook JR, Hill DA, Humphrey PA, et al. Squamous cell carcinoma arising in recurrent respiratory papillomatosis with pulmonary involvement: emerging common pattern of clinical features and human papillomavirus serotype association. Mod Pathol. 2000;13: 914–8.
28. Katz SL, Das P, Ngan BY, et al. Remote intrapulmonary spread of recurrent respiratory papillomatosis with malignant transformation. Pediatr Pulmonol. 2005;39:185–8.
29. Williams SD, Jamieson DH, Prescott CA. Clinical and radiological features in three cases of pulmonary involvement from recurrent respiratory papillomatosis. Int J Pediatr Otorhinolaryngol. 1994;30:71–7.
30. Pipavath SN, Manchanda V, Lewis DH, et al. 18F FDG-PET/CT findings in recurrent respiratory papillomatosis. Ann Nucl Med. 2008;22:433–6.
31. Gall T, Kis A, Tatar TZ, et al. Genomic differences in the background of different severity in juvenile-onset respiratory papillomatoses associated with human papillomavirus type 11. Med Microbiol Immunol. 2013;202(5):353–63.
32. Rabah R, Lancaster WD, Thomas R, et al. Human papillomavirus-11-associated recurrent respiratory papillomatosis is more aggressive than human papillomavirus-6-associated disease. Pediatr Dev Pathol. 2001;4:68–72.
33. Beasley MB, Thunnissen FB, Hasleton PS, Barbareschi M, Pugatch B, Geisinger K, Brambilla E, Gazdar A, Travis WD. Carcinoid tumour. In: Travis WD, Brambilla E, Muller-Hermelink HK, Harris CC, editors. World Health Organization classification of tumours: pathology and genetics of tumors of the lung, pleura, thymus, and heart. Lyon: IARC Press; 2004. p. 59–62.
34. Al-Qahtani AR, Di Lorenzo M, Yazbeck S. Endobronchial tumors in children: institutional experience and literature review. J Pediatr Surg. 2003;38:733–6.
35. Jeung MY, Gasser B, Gangi A, et al. Bronchial carcinoid tumors of the thorax: spectrum of radiologic findings. Radiographics. 2002;22:351–65.
36. Chong S, Lee KS, Chung MJ, et al. Neuroendocrine tumors of the lung: clinical, pathologic, and imaging findings. Radiographics. 2006;26:41–57. discussion 57–8.
37. Hervas Benito I, Bello Arques P, Loaiza JL, et al. Somatostatin receptor scintigraphy in pediatric bronchial carcinoid tumor. Rev Esp Med Nucl. 2010;29:25–8.
38. Swarts DR, Ramaekers FC, Speel EJ. Molecular and cellular biology of neuroendocrine lung tumors: evidence for separate biological entities. Biochim Biophys Acta. 1826;2012:255–71.
39. Rizzardi G, Marulli G, Calabrese F, et al. Bronchial carcinoid tumours in children: surgical treatment and outcome in a single institution. Eur J Pediatr Surg. 2009;19:228–31.
40. Brandwein MS, Ivanov K, Wallace DI, et al. Mucoepidermoid carcinoma: a clinicopathologic study of 80 patients with special reference to histological grading. Am J Surg Pathol. 2001;25:835–45.
41. Kim TS, Lee KS, Han J, et al. Mucoepidermoid carcinoma of the tracheobronchial tree: radiographic and CT findings in 12 patients. Radiology. 1999;212:643–8.
42. Wu M, Wang Q, Xu XF, et al. Bronchial mucoepidermoid carcinoma in children. Thorac Cardiovasc Surg. 2011;59:443–5.
43. Neville HL, Hogan AR, Zhuge Y, et al. Incidence and outcomes of malignant pediatric lung neoplasms. J Surg Res. 2009;156: 224–30.
44. Elnayal A, Moran CA, Fox PS, et al. Primary salivary gland-type lung cancer: imaging and clinical predictors of outcome. Am J Roentgenol. 2013;201:W57–63.
45. Xi JJ, Jiang W, Lu SH, et al. Primary pulmonary mucoepidermoid carcinoma: an analysis of 21 cases. World J Surg Oncol. 2012;10:232.
46. Manivel JC, Priest JR, Watterson J, et al. Pleuropulmonary blastoma. The so-called pulmonary blastoma of childhood. Cancer. 1988;62:1516–26.
47. Priest JR, McDermott MB, Bhatia S, et al. Pleuropulmonary blastoma: a clinicopathologic study of 50 cases. Cancer. 1997;80: 147–61.
48. Miniati DN, Chintagumpala M, Langston C, et al. Prenatal presentation and outcome of children with pleuropulmonary blastoma. J Pediatr Surg. 2006;41:66–71.
49. Priest JR. Pleuropulmonary blastoma. In: Schneider DT, Brecht IB, Olson TA, Ferrari A, editors. Rare tumors in children and adolescents, pediatric oncology. Berlin: Springer; 2012. p. 213–21.
50. Priest JR, Watterson J, Strong L, et al. Pleuropulmonary blastoma: a marker for familial disease. J Pediatr. 1996;128:220–4.
51. Schultz KA, Pacheco MC, Yang J, et al. Ovarian sex cord-stromal tumors, pleuropulmonary blastoma and DICER1 mutations: a report from the International Pleuropulmonary Blastoma Registry. Gynecol Oncol. 2011;122:246–50.
52. Dehner LP. Pleuropulmonary blastoma is THE pulmonary blastoma of childhood. Semin Diagn Pathol. 1994;11:144–51.
53. Oliveira C, Himidan S, Pastor AC, et al. Discriminating preoperative features of pleuropulmonary blastomas (PPB) from congenital cystic adenomatoid malformations (CCAM): a retrospective, age-matched study. Eur J Pediatr Surg. 2011;21:2–7.
54. Goel P, Panda S, Srinivas M, et al. Pleuropulmonary blastoma with intrabronchial extension. Pediatr Blood Cancer. 2010;54:1026–8.
55. Priest JR, Andic D, Arbuckle S, et al. Great vessel/cardiac extension and tumor embolism in pleuropulmonary blastoma: a report from the International Pleuropulmonary Blastoma Registry. Pediatr Blood Cancer. 2011;56:604–9.
56. Priest JR, Magnuson J, Williams GM, et al. Cerebral metastasis and other central nervous system complications of pleuropulmonary blastoma. Pediatr Blood Cancer. 2007;49:266–73.
57. de Krijger RR, Claessen SM, van der Ham F, et al. Gain of chromosome 8q is a frequent finding in pleuropulmonary blastoma. Mod Pathol. 2007;20:1191–9.
58. Hill DA, Ivanovich J, Priest JR, et al. DICER1 mutations in familial pleuropulmonary blastoma. Science. 2009;325:965.
59. Dehner LPWJ, Watterson J, Priest JR. Pleuropulmonary blastoma. A unique intrathoracic-pulmonary neoplasm of childhood. Perspect Pediatr Pathol. 1995;18:214–26.
60. Reichman M, Kovanlikaya A, Mathew S, et al. Pulmonary blastoma in a neonate: a lesion distinct from pleuropulmonary blastoma with unique cytogenetic features. Pediatr Radiol. 2010;40:366–70.
61. Agrawal D, Lahiri TK, Lakhotia S, et al. Pulmonary blastoma in a young adult. Indian J Chest Dis Allied Sci. 2012;54:189–92.
62. Indolfi P, Bisogno G, Casale F, et al. Prognostic factors in pleuropulmonary blastoma. Pediatr Blood Cancer. 2007;48:318–23.
63. Dishop MK, McKay EM, Kreiger PA, et al. Fetal lung interstitial tumor (FLIT): a proposed newly recognized lung tumor of infancy

to be differentiated from cystic pleuropulmonary blastoma and other developmental pulmonary lesions. Am J Surg Pathol. 2010;34:1762–72.
64. Lazar DA, Cass DL, Dishop MK, et al. Fetal lung interstitial tumor: a cause of late gestation fetal hydrops. J Pediatr Surg. 2011;46:1263–6.
65. Chadwick EG, Connor EJ, Hanson IC, et al. Tumors of smooth-muscle origin in HIV-infected children. JAMA. 1990;263:3182–4.
66. McClain KL, Leach CT, Jenson HB, et al. Association of Epstein-Barr virus with leiomyosarcomas in children with AIDS. N Engl J Med. 1995;332:12–8.
67. Lee ES, Locker J, Nalesnik M, et al. The association of Epstein-Barr virus with smooth-muscle tumors occurring after organ transplantation. N Engl J Med. 1995;332:19–25.
68. Balsam D, Segal S. Two smooth muscle tumors in the airway of an HIV-infected child. Pediatr Radiol. 1992;22:552–3.
69. Suzuki K, Urushihara N, Fukumoto K, et al. A case of Epstein-Barr virus-associated pulmonary leiomyosarcoma arising five year after a pediatric renal transplant. Pediatr Transplant. 2011;15:E145–8.
70. Parham DM, Alaggio R, Coffin CM. Myogenic tumors in children and adolescents. Pediatr Dev Pathol. 2012;15:211–38.
71. Takayama Y, Yabuuchi H, Matsuo Y, et al. Computed tomographic and magnetic resonance features of inflammatory myofibroblastic tumor of the lung in children. Radiat Med. 2008;26:613–7.
72. Coffin CM, Hornick JL, Fletcher CD. Inflammatory myofibroblastic tumor: comparison of clinicopathologic, histologic, and immunohistochemical features including ALK expression in atypical and aggressive cases. Am J Surg Pathol. 2007;31:509–20.
73. Siminovich M, Galluzzo L, Lopez J, et al. Inflammatory myofibroblastic tumor of the lung in children: anaplastic lymphoma kinase (ALK) expression and clinico-pathological correlation. Pediatr Dev Pathol. 2012;15:179–86.
74. Gleason BC, Hornick JL. Inflammatory myofibroblastic tumours: where are we now? J Clin Pathol. 2008;61:428–37.
75. Gascoyne RD, Lamant L, Martin-Subero JI, et al. ALK-positive diffuse large B-cell lymphoma is associated with Clathrin-ALK rearrangements: report of 6 cases. Blood. 2003;102:2568–73.
76. Cook JR, Dehner LP, Collins MH, et al. Anaplastic lymphoma kinase (ALK) expression in the inflammatory myofibroblastic tumor: a comparative immunohistochemical study. Am J Surg Pathol. 2001;25:1364–71.
77. Coffin CM, Patel A, Perkins S, et al. ALK1 and p80 expression and chromosomal rearrangements involving 2p23 in inflammatory myofibroblastic tumor. Mod Pathol. 2001;14:569–76.
78. Travis W, Dehner LP, Manabe T, et al. Congenital peribronchial myofibroblastic tumor. In: Travis WD, Brambilla E, Mυller-Hermelink HK, Harris CC, editors. World Health Organization classification of tumours: pathology and genetics of tumors of the lung, pleura, thymus, and heart. Lyon: IARC Press; 2004. p. 102–3.
79. Alobeid B, Beneck D, Sreekantaiah C, et al. Congenital pulmonary myofibroblastic tumor: a case report with cytogenetic analysis and review of the literature. Am J Surg Pathol. 1997;21:610–4.
80. Horikoshi T, Kikuchi A, Matsumoto Y, et al. Fetal hydrops associated with congenital pulmonary myofibroblastic tumor. J Obstet Gynaecol Res. 2005;31:552–5.
81. Huppmann AR, Coffin CM, Hoot AC, et al. Congenital peribronchial myofibroblastic tumor: comparison of fetal and postnatal morphology. Pediatr Dev Pathol. 2011;14:124–9.
82. Steelman C, Katzenstein H, Parham D, et al. Unusual presentation of congenital infantile fibrosarcoma in seven infants with molecular-genetic analysis. Fetal Pediatr Pathol. 2011;30:329–37.
83. Koujok K, Ruiz RE, Hernandez RJ. Myofibromatosis: imaging characteristics. Pediatr Radiol. 2005;35:374–80.

Gastrointestinal, Pancreatic and Hepatic Malignancies in Children

9

Alexander J. Towbin, Jon M. Rowland, and David M. Parham

The gastrointestinal tract, liver, and pancreas are uncommon sites for primary malignant neoplasms in the pediatric population. None of the individual malignant neoplasms of these sites represented more than 2 % of cancer diagnoses in children between 0 and 19 years of age in the SEER database [1]. This is in marked contrast to the frequency of malignant neoplasms of these sites in adulthood.

Gastrointestinal Tract

Lymphoma is the most common pediatric gastrointestinal tract malignancy, accounting for approximately 75 % of malignancies in most series. This is followed by neuroendocrine tumors (NET), adenocarcinoma, and sarcoma [2–4]. Carcinomas and a variety of rare neoplasms can occur in the gastrointestinal tract but are not addressed in this chapter. Lymphoma is discussed in another chapter.

Neuroendocrine Tumors

Gastroenteropancreatic neuroendocrine tumors (NETs) are thought to arise from neuroendocrine cells found in the pancreas and gastrointestinal tract. Similar neoplasms are found throughout the body, particularly the thymus and bronchial tree, which share embryologic origins with the gastrointestinal tract. Widespread bodily distribution and variable behavior at multiple sites have led to a complex mixture of terms for tumor classification, staging, and grading. Traditionally, gastrointestinal NETs were referred to as carcinoid tumors and pancreatic NET as islet cell tumors. Gastrointestinal NETs will be discussed below while pancreatic NETs will be discussed in the section on the pancreas.

Clinical Features and Epidemiology

Gastroenteropancreatic NETs account for 36 % of all NETs in the pediatric age group. They occur most commonly in the appendix [5]. Overall, NETs are identified in 0.085–0.169 % of histologically examined appendiceal specimens [6]. These tumors appear to be more common in females and occur at a mean age at diagnosis of 10.5–14.6 years [7–10].

As a rule, appendiceal NETs are incidentally discovered at appendectomy, so that most laboratory tests are performed after diagnosis. Tests included in the diagnostic work-up include: urine 5-HIAA, plasma levels of chromogranin A, serotonin, and carcinoembryonic antigen (CEA).

Imaging Features

Appendiceal NET is typically first diagnosed as acute appendicitis due to the typical clinical signs and symptoms as well as the typical imaging findings (Figs. 9.1 and 9.2). The imaging findings of acute appendicitis are not discussed; instead, we focus on the findings more typical of appendiceal NET.

Ultrasound: Because of the small size of most appendiceal NETs, they are not often seen by ultrasonography. Larger tumors appear as asymmetric appendiceal wall thickening. Tumors with calcifications may appear as an echogenic focus with posterior acoustic shadowing [11], but these lesions can be difficult to distinguish from fecaliths.

CT: Due to its small size and location at the tip of the appendix, an appendiceal NET is rarely identified on preoperative CT. If it is seen, the tumor appears as diffuse wall thickening. Occasionally calcification within the tumor mimics an appendicolith [11]. CT can also be used to identify metastatic

A.J. Towbin, M.D. (✉)
Neil D. Johnson Chair of Radiology Informatics, Department of Radiology, Cincinnati Children's Hospital Medical Center, 3333 Burnet Avenue, MLC 5031, Cincinnati, OH 45229, USA
e-mail: alexander.towbin@cchmc.org

J.M. Rowland, M.D., Ph.D.
UCSF Benioff Children's Hospital Oakland, Oakland, CA, USA

D.M. Parham, M.D.
Children's Hospital Los Angeles, University of Southern California, Los Angeles, CA, USA

D.M. Parham et al. (eds.), *Pediatric Malignancies: Pathology and Imaging*,
DOI 10.1007/978-1-4939-1729-7_9, © Springer Science+Business Media New York 2015

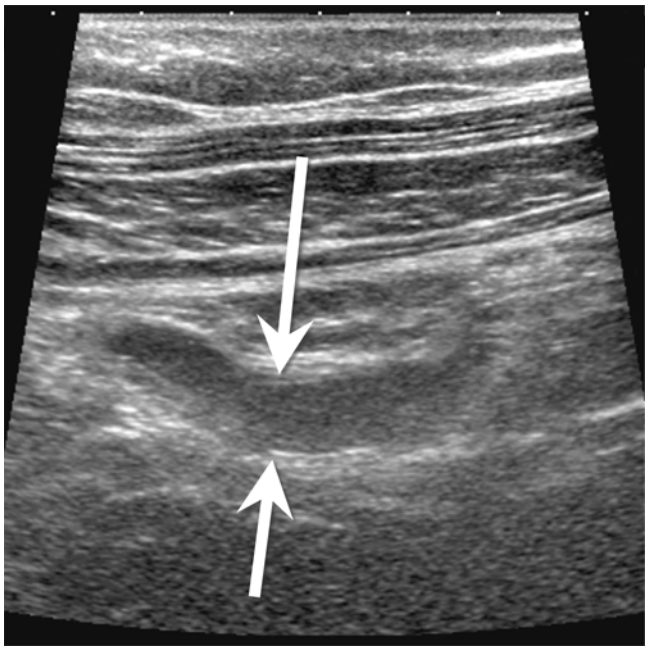

Fig. 9.1 A 17-year-old female with appendiceal carcinoid. Transverse ultrasound shows an enlarged appendix (*arrows*) with surrounding echogenic fat. No discrete mass was identified even though at resection a 5 mm carcinoid was present in the mid portion of the appendix

Fig. 9.2 A 12-year-old female with appendiceal carcinoid. Axial contrast enhanced CT shows a dilated appendix (*arrow*) with a mildly thickened and hyper-enhancing wall. There is a considerable amount of surrounding free fluid. No discrete mass was identified in the appendix by imaging even though at resection a 10 mm carcinoid was present

disease in lymph nodes and elsewhere. An irregular soft issue mass near the root of the mesentery is characteristic of metastatic NET [11].

Nuclear medicine: Both Indium-111 octreotide and Iodine-131 meta-iodobenzylguanidine can be used to identify metastatic sites of disease.

Pathology

Gross and microscopic features: Grossly, gastrointestinal NETs form well circumscribed round lesions in the submucosa or muscular layer. The cut surface appears red to tan, reflecting an abundant microvasculature, or sometimes yellow because of high lipid content. In the majority of cases, the tumor is located at the tip of the appendix and is <1 cm in diameter (Fig. 9.3a). Tumor size (>2.0 cm) has been correlated with nodal metastasis but not with poor outcome [12].

Morphologically, well-differentiated NETs display a characteristic "organoid" arrangement, with solid/nesting, trabecular, or gyriform patterns (Fig. 9.3b). The cells are relatively uniform and contain round to oval nuclei, coarsely stippled chromatin, and finely granular cytoplasm.

The College of American Pathologists (CAP) protocol grades well-differentiated appendiceal NETs as either G1 [<2 mitoses/10 high power fields (HPF)] or G2 (2–10 mitoses/10 HPF) [13–16]. G1 tumors represent "carcinoids," and G2 tumors are "atypical carcinoids." Tumors with >10 mitoses/10 HPF comprise poorly differentiated neuroendocrine carcinomas.

Immunohistochemistry and other special stains: NET cells produce abundant neurosecretory granules, reflected by strong and diffuse immunohistochemical expression of neuroendocrine markers such as synaptophysin and chromogranin. Some tumors may secrete specific peptide hormones or bioamines such as insulin, glucagon, somatostatin, vasoactive intestinal peptide (VIP), serotonin, and gastrin, which may produce clinically evident hormonal syndromes.

Molecular diagnostic features and cytogenetics: There are limited data about molecular genetics of appendiceal carcinoids.

Prognosis

Because most appendiceal NETs are incidentally discovered, they are initially treated with surgical resection. The size of the tumor is a key indicator of survival. Patients with tumors <2 cm have an overall excellent survival, whereas patients with tumors >3 cm have a significantly worse long-term outcome [17]. Other factors that lead to decreased survival include lymph node metastases and moderate to poor tumor cell differentiation [17].

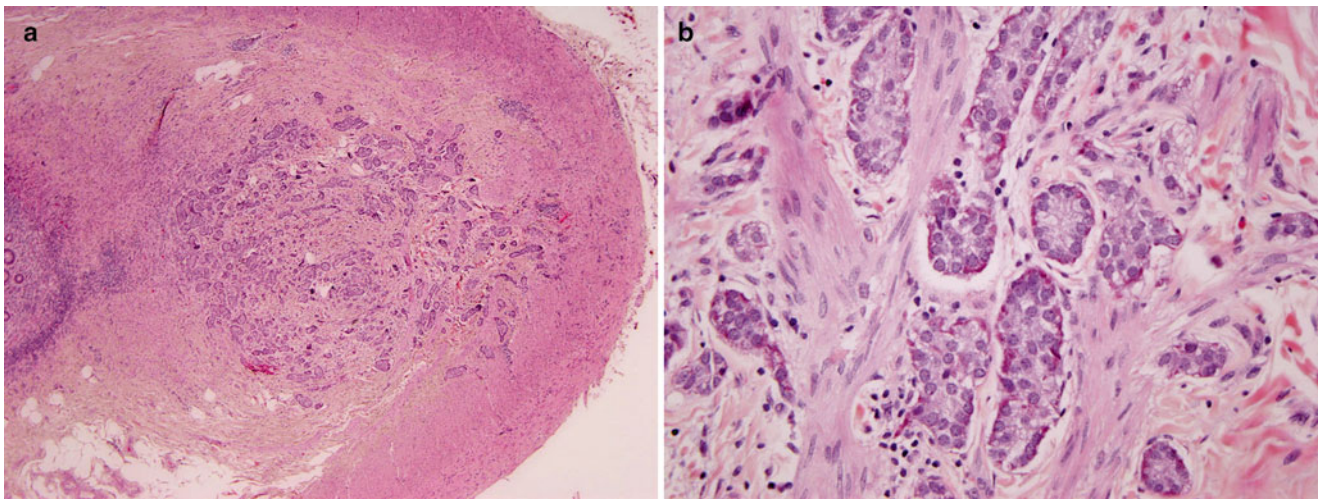

Fig. 9.3 Appendiceal carcinoid. (**a**) A poorly circumscribed, non-encapsulated neoplasm arises from the tip of the appendix and invades the muscularis propria. (**b**) The lesion contains nest of neuroendocrine cells invading smooth muscle. The cells contain basal nuclei and pink granules

Gastrointestinal Stromal Tumor (GIST)

Clinical Features and Epidemiology

Gastrointestinal stromal tumors are the most common mesenchymal tumor of the gastrointestinal tract in adults but are rare in children [18]. Isolated institutional reports estimate that pediatric GISTs account for about 2 % of all non-rhabdomyosarcomatous soft tissue sarcomas and 2 % of all GISTs [19, 20].

Pediatric GIST occurs with a median age at presentation of approximately 13 years with females representing over 70 % of cases [21, 22]. The vast majority occur in the stomach. Multifocal gastric tumors and lymph node metastases are more common in children [23].

While pediatric patients with GIST can be asymptomatic, they usually present with signs and symptoms of chronic GI bleeding such as anemia, weakness, or syncope [23]. Other possible symptoms include acute abdominal pain, bowel obstruction, or abdominal distension.

Imaging Features (Figs. 9.4 and 9.5)

Ultrasound: On ultrasound, GIST can appear as a hypoechoic mass. Because GISTs are usually exophytic and project into the abdominal cavity, it is difficult to determine the organ of origin on ultrasound.

CT: On CT, a GIST appears as a well circumscribed mass arising from the outer wall of the gastrointestinal tract (Fig. 9.4a). Mucosal ulceration can be visible on the luminal surface of the tumor. After contrast administration (Fig. 9.4a), the mass can have variable enhancement. Calcification can also be present.

MRI: GIST has a variable appearance on MRI. It typically is isointense to the gastric wall on T1-W images and after contrast administration, the mass enhances (Fig. 9.4b). On T2-W images, GIST appears hypointense or isointense to the gastric wall (Fig. 9.4c).

PET-CT: PET-CT is useful in the setting of GIST because tumors are FDG avid (Fig. 9.4d). PET-CT, therefore, can detect multifocal tumor and distant metastases. It is also useful in detecting lymph node metastases [24].

Genetics

GIST can present in childhood either as a sporadic tumor or in the setting of a genetic syndrome. About 10 % of pediatric patients with GIST have a predisposition syndrome, such as Carney triad, Carney–Stratakis dyad, familial GISTs, or neurofibromatosis (NF) type 1.

The Carney triad is the most common entity predisposing pediatric patients to GIST. It is a sporadic syndrome that also includes paragangliomas and pulmonary chondromas (Fig. 9.5a–c). Carney triad GIST tends to occur in the antrum or lesser curvature of the stomach [23]. Patients with Carney triad are usually female (85 %) with a mean age at presentation of 20 years [23].

Other syndromes such as the Carney–Stratakis dyad and familial GIST syndrome are less common. The Carney–Stratakis dyad is an autosomal dominant cancer predisposition syndrome characterized by paragangliomas, GIST, and other tumors [23]. GIST in patients with Carney–Stratakis dyad tends to be multifocal and arise from the stomach. The median age at presentation is 19 years. With familial GIST syndrome, an autosomal dominant disorder, there is an activating mutation in the KIT or platelet-derived growth factor α (*PDGFRA*) gene [23]. Patients with familial GIST syndrome usually do not present with a tumor until they are in their mid-40s.

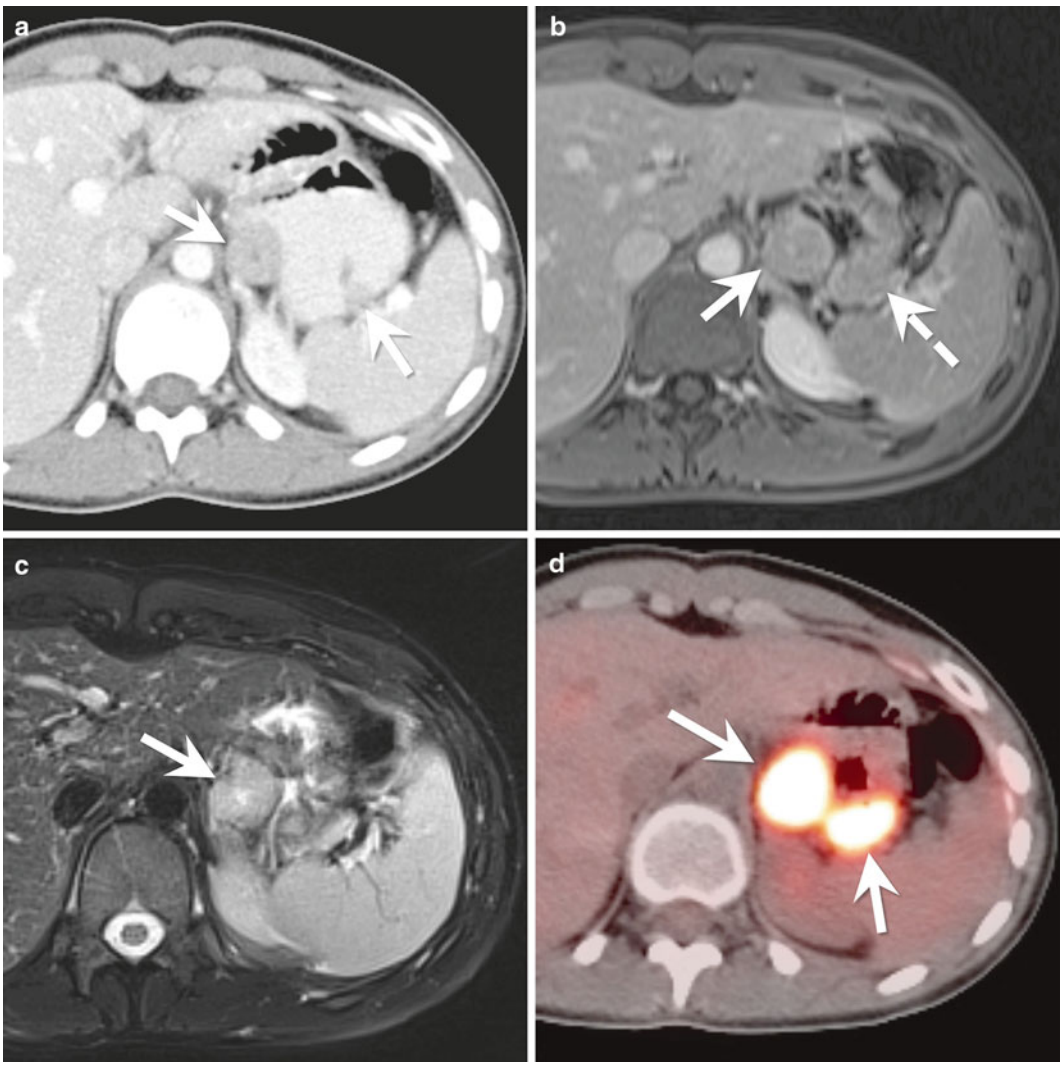

Fig. 9.4 A 14-year-old female with a gastrointestinal stromal tumor (GIST). (**a**) Axial contrast enhanced CT of the abdomen shows two exophytic masses (*arrows*) arising from the gastric antrum. The masses enhance less than the liver but more than the paraspinal musculature. (**b**) Axial T1-W post-contrast MR image of the upper abdomen shows the dominant mass (*arrow*) arising from the gastric antrum. The mass is isointense to the nearby liver. The smaller mass (*dashed arrow*) is not visible as a discrete mass on the MRI but instead appears as an area of gastric thickening. (**c**) On the axial T2-W MR image, the dominant mass (*arrow*) is hyperintense compared to the liver. (**d**) Axial image from a fused PET/CT shows intense FDG uptake in both gastric masses (*arrows*)

Pathology

Gross and microscopic features: GISTs arise from myenteric ganglion cells. They contain spindle cells, epithelioid cells, or a mixture of both (Fig. 9.6a). Pediatric GISTs are predominantly the epithelioid type [25]. Grossly they can range from small nodules to large masses.

Immunohistochemistry and other special stains: More than 95 % of GISTs express CD117 (c-Kit) on immunohistochemical stains (Fig. 9.6b), even in pediatric tumors that frequently lack mutations in this gene. DOG1 staining may be useful for patients with negative CD117 stains [26].

Molecular diagnostic features and cytogenetics: Large-scale chromosome changes have been identified in pediatric GISTs. Unlike adult tumors, *KIT* or *PDGF* mutations are infrequent. It is recommended that mutational analysis of tumor tissue be performed, as specific treatment guidelines are available for patients with *KIT* or *PDGFR* mutations. Mutations in the succinate dehydrogenase gene (*SDH*) are common in pediatric GISTs lacking *KIT*/*PDGFR* abnormalities [25, 27].

Prognosis and Treatment

Surgery is the mainstay of therapy for non-metastatic tumors. The goal of surgery is complete resection without violation

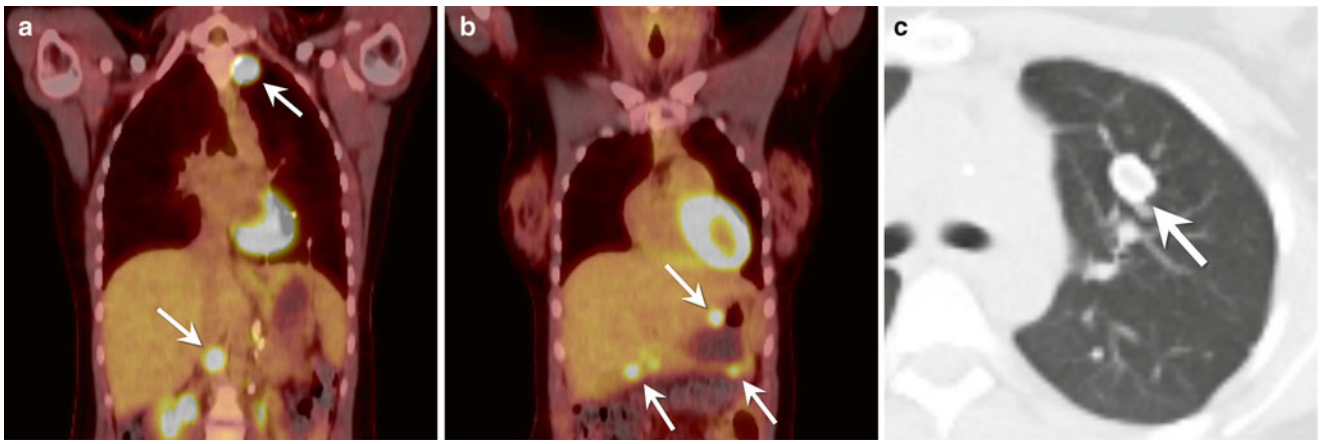

Fig. 9.5 A 17-year-old female with Carney syndrome. (**a**) Coronal fused image from a PET/CT through the chest and upper abdomen shows increased FDG uptake in two paragangliomas (*arrows*). (**b**) Coronal fused image from a PET/CT through the chest and upper abdomen (more anterior to the image in part (**a**)) shows increased FDG uptake in multiple gastrointestinal stromal tumors (*arrows*) in the wall of the stomach and proximal duodenum. (**c**) Axial CT image of the chest shows a pulmonary chondroma (*arrow*) in the left upper lobe. The mass has a peripheral rim of calcification

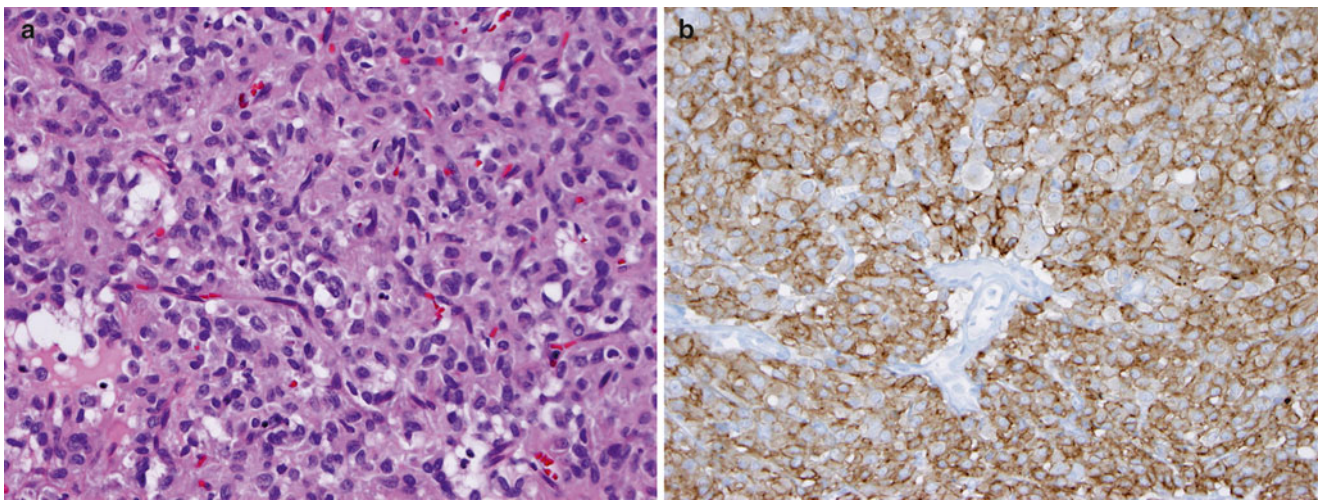

Fig. 9.6 Gastric GIST. (**a**) The lesion demonstrates epithelioid features and contains groups of cells with round to oval nuclei and modest amounts of lightly eosinophilic cytoplasm, separated by a rich vascular stroma. (**b**) The lesion strongly expresses c-kit, with membranous accentuation (CD117 immunostain)

of the tumor pseudocapsule [23]. Due to the high incidence of nodal involvement, lymph node resection is recommended. Imatinib is not usually given to pediatric patients because it lacks the efficacy seen in adults [23].

The most common prognostic system for GIST in adults utilizes tumor size, location and mitotic rate. The outcome in pediatric GIST appears more difficult to predict than that of adults. Although pediatric GIST is prone to lymph node metastasis and local recurrences, the clinical course is usually indolent [19]. In Carney triad, there may be a long time interval (up to 26 years) between the GIST diagnosis and second tumors [21].

Pancreas

Pancreatic malignancies are distinctly rare in childhood with an overall incidence of 0.018 cases per 100,000 children [28]. There were 58 cases of malignant pancreatic neoplasms in patients under 20 years of age reported to the SEER registry between 1973 and 2004 [28]. These consisted of 31 exocrine tumors (ten solid pseudopapillary neoplasm, ten pancreatoblastomas, seven ductal adenocarcinomas, and four acinar cell carcinomas), 19 NETs, and 5 sarcomas. This discussion will be restricted to solid pseudopapillary neoplasm, pancreatoblastoma, and pancreatic NET.

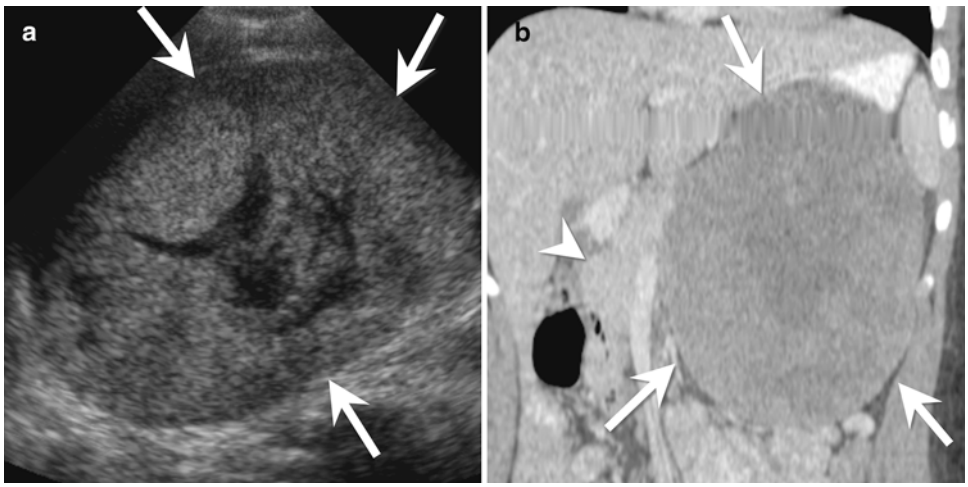

Fig. 9.7 A 15-year-old female with a solid pseudopapillary neoplasm of the pancreas. (**a**) *Transverse* ultrasound image of the upper abdomen shows a large heterogeneous mass (*arrows*). The mass is mostly solid with a central cystic area. (**b**) Coronal contrast-enhanced CT shows a large, mildly heterogeneous mass (*arrows*) arising from the tail of the pancreas. The mass enhances less than the remainder of the pancreas (*arrowhead*)

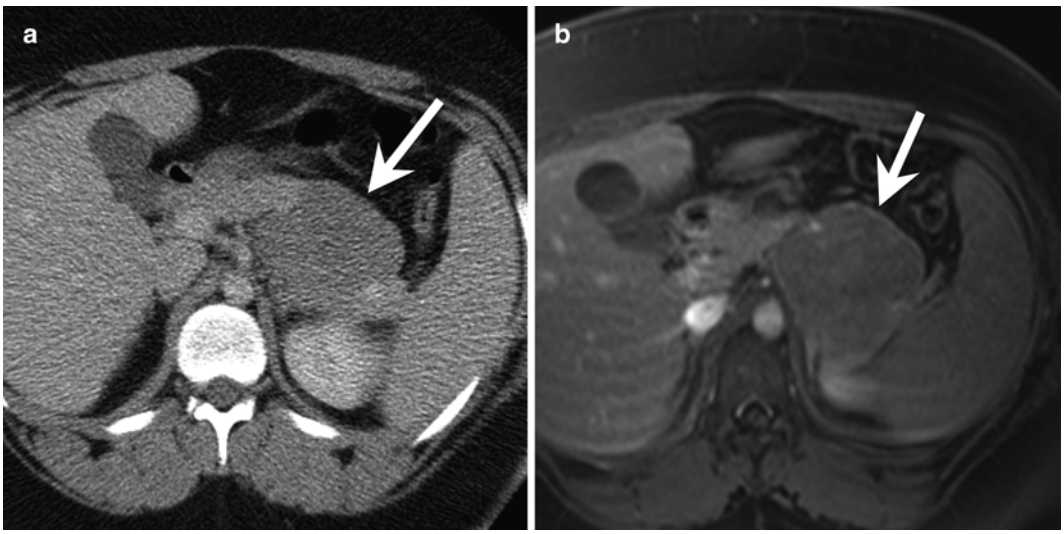

Fig. 9.8 A 15-year-old female with a solid pseudopapillary neoplasm. (**a**) Axial contrast-enhanced CT shows a mass (*arrow*) arising from the tail of the pancreas. The mass enhances less than the background pancreas. (**b**) Axial T1-W post-contrast MRI shows the hypoenhancing mass (*arrow*) arising from the tail of the pancreas

Solid Pseudopapillary Neoplasm (SPN)

Solid pseudopapillary neoplasm (SPN) has been called many names, including solid and papillary epithelial neoplasm, papillary-cystic neoplasm, papillary cystic tumor of the pancreas, and Frantz tumor.

Clinical Features and Epidemiology

SPN account for only 1–2 % of all pancreatic tumors, but they are the most common pediatric pancreatic neoplasms, representing over 50 % of the total [29–34]. SPNs are found almost exclusively in young women. In one large review of SPNs, more than 90 % of patients were female, and 85 % were under 30 years of age [35]. Patients with SPN typically present with nonspecific abdominal complaints and a palpable abdominal mass [36]. Other signs and symptoms can include gastrointestinal obstruction, jaundice, or pancreatitis.

Imaging Features (Figs. 9.7 and 9.8)

SPNs are partially cystic and partially solid masses arising from the pancreas. The tumors are usually large at diagnosis and compress adjacent structures [37].

Ultrasound: On ultrasound, a SPN appears as a large heterogeneous mass, usually well demarcated with an echogenic rim. SPNs can have variable internal characteristics. Most commonly, they have a complex internal architecture with echogenic solid components and hypoechoic cystic components (Fig. 9.7a) [37].

CT: On CT, SPNs have a hypodense rim. The solid component of the tumor is isodense to the remainder of the pancreas, while the cystic component has a density slightly greater than water [37]. Fluid-debris levels are present in up to 20 % of tumors, and calcifications can be seen in one-third of cases [37]. After the administration of contrast, SPNs enhance mildly in their solid portions. The fluid and debris do not enhance (Figs. 9.7b and 9.8a).

MRI: MR imaging shows a pancreatic mass with a hypointense capsule on T1-W and T2-W images. There is often internal high signal on T1-W images due to intratumoral hemorrhage [37]. Compared with the pancreas, the solid portions of the mass are hypointense to isointense on T1-W images and slightly hyperintense on T2-W images [37]. The enhancement pattern of SPNs on MRI resembles that seen on CT, with early peripheral, heterogeneous enhancement that gradually diffuses with time (Fig. 9.8b) [37].

Pathology

Gross and microscopic features: Grossly, SPNs form large, circumscribed tumors with degenerative and hemorrhagic change [37]. The tumors measure of 6–10 cm and occur throughout the pancreas, though some studies report a predilection for the head or tail [37]. Histologically, the tumor contains merging solid, pseudopapillary, and cystic regions (Fig. 9.9) [37]. Solid sheets of uniform, epithelial cells may resemble endocrine tumors. Characteristic perivascular pseudopapillae frequently contain pools of mucinous material. Hemorrhage and/or necrosis are common features.

Immunohistochemistry and other special stains: Immunohistochemistry reveals a complex array of reactive antibodies including CD56, CD10, nuclear beta-catenin, alpha-1 antitrypsin, progesterone receptors, and synaptophysin [38, 39]. Ultrastructural studies also document acinar, ductal, and endocrine features [40].

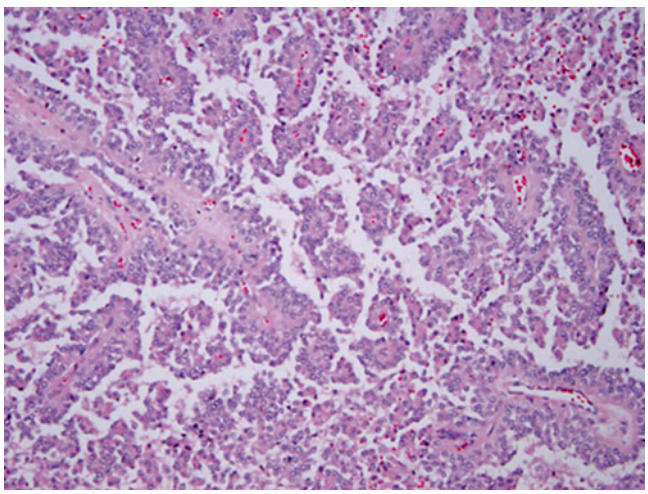

Fig. 9.9 Solid pseudopapillary neoplasm of pancreas. The neoplasm contains papillary fronds that are lined by poorly differentiated cells and appear to float in the plane of section

Molecular diagnostic features and cytogenetics: Mutations of the beta-catenin gene *CNNB1*, nuclear accumulation of beta-catenin protein, and alterations in the Wnt-signaling pathway are commonly found in SPN [38, 41–43]. The accumulation of protein products of chromosome 11q genes, such as cyclin D1, CD56, and FLI-1, is also characteristic [44]. Allelic loss on chromosome 5q22.1 was frequently found by Min Kim et al. [42]. Between chromosomes 13 and 17 resulting in a loss of 13q14 → qter and 17p11 → pter was described in one SPN.

Prognosis and Treatment

SPNs are usually slow-growing tumors with a benign clinical course [37]. Because of the potential for aggressive behavior, they should be completely resected if possible. Nearly 85 % are confined to the pancreas, and 95 % of these are cured with resection [37]. Metastases develop in 7–16 %, usually in older women and most commonly occur in the liver [37].

Pancreatoblastoma

Clinical Features and Epidemiology

Pancreatoblastoma, the most common pancreatic tumor in young children, typically occurs in children between 1 and 8 years of age (mean age 5 years), but it also has been reported in adolescents [45]. Overall, it accounts for 0.2 % of pancreatic tumors [37] and is more common in children of Asian descent and males (M:F = 1.14:1 to 2.7:1) [37, 45]. Pancreatoblastoma has been associated with Beckwith–Wiedemann syndrome and familial adenomatous polyposis (FAP).

Patients present with a large abdominal mass, abdominal distension, and upper abdominal pain. On laboratory examination, serum α-fetoprotein (AFP) is elevated in up to 33–70 % of patients [37, 45]. Other elevated serum tests can include α-1-antitrypsin and lactate dehydrogenase. Tumor hormones can cause endocrine syndromes such as Cushing syndrome and the syndrome of inappropriate antidiuretic hormone [45].

Pancreatoblastoma most commonly occurs in the head of the pancreas, although it can occur at any site [45]. The liver is the most common site of metastasis, followed by the lungs and regional lymph nodes [45]. Metastases are present in 35 % of patients at diagnosis [45].

Imaging (Fig. 9.10)

On imaging, the mass is often very large with a mean diameter of 7–18 cm [45]. Because of the large size, it can be difficult to determine the organ or origin.

Fig. 9.10 A 6-year-old male with pancreatoblastoma. (**a**) Axial contrast-enhanced CT shows a large mass (*arrow*) arising from the pancreatic head. The mass is hypodense compared to the pancreas and contains multiple enhancing vessels. Metastatic disease is present, involving the liver (*dashed arrows*) and retroperitoneal lymph nodes (*arrowhead*)

Ultrasound: At ultrasound, pancreatoblastoma appears as a heterogeneous, well-circumscribed mass with cystic and solid components [37]. The cystic structures are hypoechoic with internal septa. When solid components are present, they appear hypoechoic to the normal pancreas.

CT: On CT, pancreatoblastoma appears as a well to partially circumscribed mass arising from the pancreas [37]. The tumor has a heterogeneous appearance with hypodense cystic areas and enhancing septa. Small punctate or curvilinear calcifications may be present (Fig. 9.10) [37].

MRI: On MRI, pancreatoblastoma is hypointense to isointense on T1-W images and hyperintense on T2-W images. Due to internal necrosis, the mass has a heterogeneous appearance.

Pathology

Gross and microscopic features: Grossly, pancreatoblastomas are partially encapsulated, large (mean diameter = 10.6 cm), solitary masses [46]. Microscopic examination shows a cellular tumor with a variety of patterns, including prominent acinar differentiation and lesser degrees of endocrine and ductal differentiation (Fig. 9.11). Often, bands of spindled stromal cells separate solid and lobular sheets of epithelial cells. Endocrine differentiation has been observed in only a few instances. Squamoid corpuscles, a characteristic feature, may range from clusters of nondescript cells to clear squamous cells with keratinization.

Immunohistochemistry and other special stains: Immunohistochemical stains highlight acinar differentiation with trypsin and chymotrypsin expression. Squamous corpuscles show a characteristic epithelial immunoprofile: keratins 8, 18, 19, and EMA are positive, whereas cytokeratin in negative or heterogeneously positive [47]. Immunohistochemical staining may demonstrate focal endocrine differentiation via chromogranin, synaptophysin, and neuron-specific enolase expression.

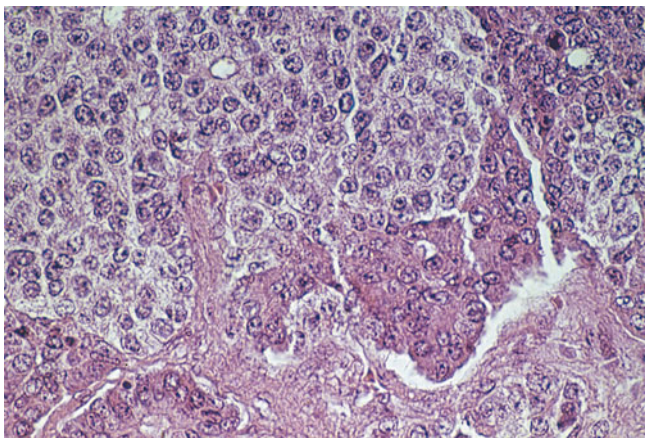

Fig. 9.11 Pancreatoblastoma. This tumor contains a mélange of primitive, eosinophilic acinar epithelium and amphophilic neuroendocrine cells

Molecular diagnostic features and cytogenetics: Genetic alterations are not well defined in pancreatoblastoma. Allelic loss of 11p has been reported [48].

Prognosis and Treatment

Surgical resection remains the mainstay of therapy for pancreatoblastoma. Primary resection may not be possible in patients with large tumors involving major blood vessels or adjacent organs. In these patients and those with metastases, neoadjuvant chemotherapy is often the first line of treatment [45]. Pancreatoblastomas have a high recurrence rate. After resection, patients are monitored with serial imaging and serum AFP levels.

Pancreatic Neuroendocrine Tumors

Clinical Features and Epidemiology

Pancreatic NETs are rare tumors in children and typically occur in middle aged adults. They may be asymptomatic or present with a hormone secretion syndrome. The latter tumors are said to be functioning or hyperfunctioning [37], whereas all other tumors are either nonfunctioning or clinically silent. Insulinomas are the most common subtype followed by gastrinomas [37].

The clinical presentation of pancreatic NET depends on tumor function. Insulinomas can present with symptoms of hypoglycemia that resolve with glucose [37]. In young

children, hypoglycemia can cause behavioral problems, seizures, or coma [37]. Gastrinomas cause Zollinger-Ellison syndrome or diarrhea. Nonfunctioning pancreatic neuroendocrine tumors present later, often with symptoms due to mass effect.

Imaging (Figs. 9.12 and 9.13)

Pancreatic neuroendocrine tumors vary in their location in the pancreas depending on the type of tumor. Insulinomas occur more commonly in the body and tail of the pancreas, whereas gastrinomas and nonfunctioning tumors are more common in the head (Fig. 9.12) [37].

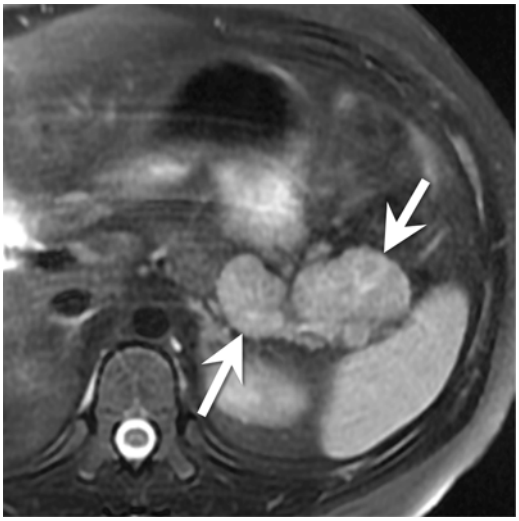

Fig. 9.12 An 11-year-old male with a pancreatic neuroendocrine tumor (secreting adrenocorticotropic hormone (ACTH)). Axial T2-W MRI of the upper abdomen shows a bilobed mass (*arrows*) arising from the pancreatic tail. The mass is hyperintense compared to the remainder of the pancreas

Ultrasound: Insulinomas are typically small round or ovoid tumors that appear hypoechoic with a hyperechoic rim. Larger pancreatic NETs are usually heterogeneous with foci of cystic change, hemorrhage, and necrosis. There can be small echogenic areas of calcification on ultrasound [37].

CT: On CT, insulinomas are small tumors that avidly enhance during the arterial phase. The larger tumors are heterogeneous with enhancing solid portions and non-enhancing cystic areas [37]. Larger tumors are more likely to be associated with liver metastases.

MRI: Insulinomas are hyperintense on T1-W and T2-W images (Fig. 9.13). They avidly enhance on the arterial phase of imaging.

Nuclear medicine: Somatostatin receptor imaging can be useful to localize a tumor; however, only 60–75 % of pancreatic NET express somatostatin receptors.

Pathology

Gross and microscopic features: Grossly, pancreatic neuroendocrine tumors are round or ovoid tumors. Small tumors are solid and homogeneous, while larger tumors have an incomplete fibrous pseudocapsule and contain cysts, necrosis, or hemorrhage [37].

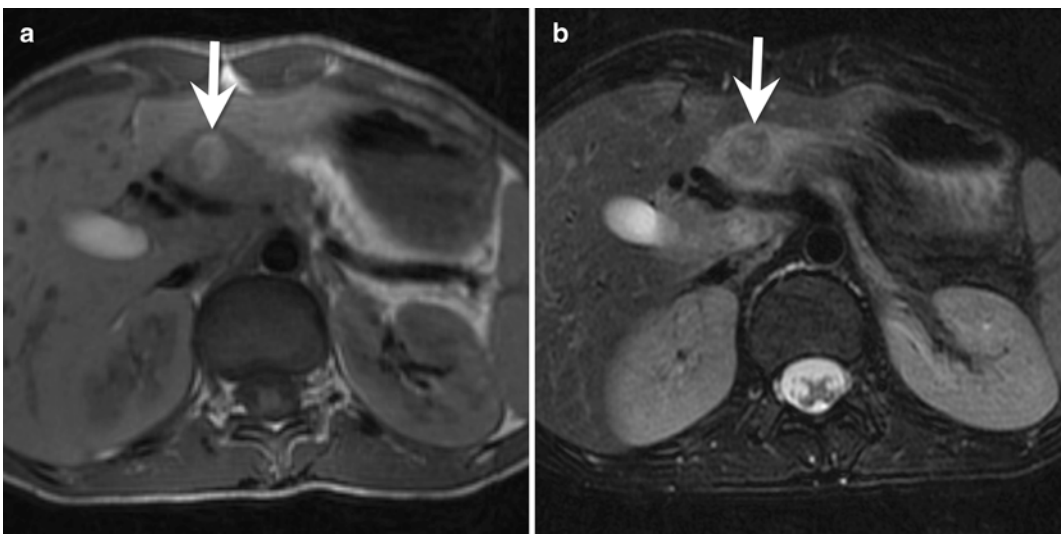

Fig. 9.13 A 15-year-old female with a poorly functioning pancreatic neuroendocrine tumor (insulinoma). (**a**) Axial T1-W MRI shows a hyperintense, circular mass (*arrow*) in the neck of the pancreas. (**b**) The mass (*arrow*) is hypointense to the pancreas on T2-W images. There was peripheral enhancement on post-contrast images (not shown). Histologically, this insulinoma has a trabecular pattern

Histologically, pancreatic NETs contain sheets or nests of monomorphic cells arranged in one of three patterns: the trabecular pattern with or without a gyriform arrangement, the acinar or glandular pattern, or the medullary or solid pattern (Fig. 9.13a) [37]. The intervening stroma is variable and can contain numerous blood vessels. Insulinomas characteristically contain amyloid that shows green birefringence when stained with Congo red [37].

Immunohistochemistry and other special stains: Pancreatic NETs generally show strong reactivity with antibodies to synaptophysin and chromogranin A. Detection of one or more peptide hormones in tumor tissue is common, even in nonfunctioning tumors. Expression of cytokeratin 19 has been associated with poor outcome in several studies [49, 50] but not in others [51].

Molecular diagnostic features and cytogenetics: Familial inherited syndromes, such as the multiple endocrine neoplasia (MEN) 1, von Hippel-Lindau, NF1, or tuberous sclerosis, may be associated with pancreatic NETs. In sporadic pancreatic NET tumors, losses of chromosome 1 and 11q and gain on 9q have been identified [52].

Prognosis and Treatment

Surgical excision can cure both non-metastatic pancreatic NET and its associated clinical syndrome [37]. For tumors with metastatic disease at presentation, the optimal therapeutic approach and outcome are not clear. In one study of 19 pediatric patients with pancreatic NET, there was a 50 % 5-year survival rate [28].

Liver

The liver is the third most common site of origin for solid abdominal tumors in children, following the kidney and adrenal gland [53]. Hepatic tumors account for 0.3–2 % of all pediatric tumors [54]. This chapter discusses the more common malignant tumors hepatoblastoma, hepatocellular carcinoma (HCC), fibrolamellar HCC, and undifferentiated embryonal sarcoma (UES).

Overview of Imaging Approaches

When evaluating children with a suspected liver mass, ultrasound is often the first imaging study performed. Ultrasound has several advantages compared to other modalities, including lack of ionizing radiation, ability to provide real-time information, and performance without sedation or general anesthesia. It is used to help localize the tumor and define its internal structure. Doppler sonography can be used to determine the relationship of the tumor to adjacent vasculature, the patency of the vessels, and the presence of biliary obstruction.

CT is frequently used for additional evaluation of pediatric liver masses and has many advantages including ease of access, rapid imaging time (possibly obviating sedation), capacity for high-quality multiplanar and 3D reconstruction, ease of interpretation, and superior spatial resolution. Perhaps its greatest disadvantage is the use of ionizing radiation [55].

When evaluating liver tumors, it is helpful to determine the enhancement pattern of the mass during the hepatic arterial and portal venous phase of imaging. Because obtaining images in different phases of enhancement requires additional imaging, using CT for multiphase imaging can double the radiation dose delivered to the patient. This has led to some disagreement on the optimal CT protocol for liver tumor evaluation. Some groups propose performing multiphase imaging, while others image only in the portal venous phase of enhancement.

The concern over the radiation dose delivered by CT has led many pediatric radiologists to recommend MRI as the modality of choice to characterize liver masses. MRI's advantages include its lack of ionizing radiation, its capacity for imaging in multiple planes and in multiple phases of contrast enhancement, and its superior contrast resolution. MRI's biggest disadvantage is its long scan time, requiring sedation or anesthesia for young children and infants.

Recently, the hepatocyte-specific contrast agents gadoxetate disodium (Eovist/Primovist; Bayer HealthCare, Leverkusen, Germany) and gadobenate dimeglumine (Multihance; Bracco Diagnostics, Princeton, New Jersey) have been developed for MR imaging. These gadolinium-based contrast agents are bound by functioning hepatocytes and partially excreted by the biliary system [56]. Hepatocyte-specific contrast agents have proven useful in characterizing pediatric liver masses [57, 58].

Hepatoblastoma

Hepatoblastoma is an embryonal tumor arising from hepatocytes that resemble the fetal and embryonic liver [59].

Clinical Features and Epidemiology

Hepatoblastoma, the most common primary hepatic malignancy in childhood, accounts for between 65 and 80 % of all pediatric liver tumors [59–61]. It primarily occurs in young children and peaks during infancy (median age at diagnosis of 18 months) [59]. Hepatoblastoma is rare in older children; 90–95 % of new cases occur before 4 years of age [59, 62].

During the past 20 years, the incidence of hepatoblastoma has increased approximately 4 % per year, faster than for any other childhood cancer [63]. Currently, its

overall incidence is 10.5 cases per million in children <1 year of age and 5.4 cases per million in children 1–4 years of age [63].

There are many known risk factors for hepatoblastoma including male gender, very low birth weight (<1,500 g), and genetic syndromes such as FAP, Beckwith–Wiedemann syndrome, hemihypertrophy, and trisomy 18 [63].

Patients with hepatoblastoma usually present with a palpable abdominal mass. Non-specific symptoms such as anorexia and weight loss may occur [60, 64]. Serum AFP is elevated in 90 % of patients, although a small subset of tumors with a worse prognosis does not express it [62, 64].

Imaging Features (Figs. 9.14, 9.15, and 9.16)

Imaging is used for diagnosis and staging of hepatoblastoma. The combination of the clinical and imaging findings in a child between 6 months and 3 years of age is essentially diagnostic of hepatoblastoma [65]. Hepatoblastoma can present with a solitary mass, a dominant mass with satellite lesions, or as multifocal disease [65].

Radiography: Abdominal radiography shows hepatomegaly and displacement of loops of bowel. Occasionally calcifications can be identified in the right upper quadrant [64].

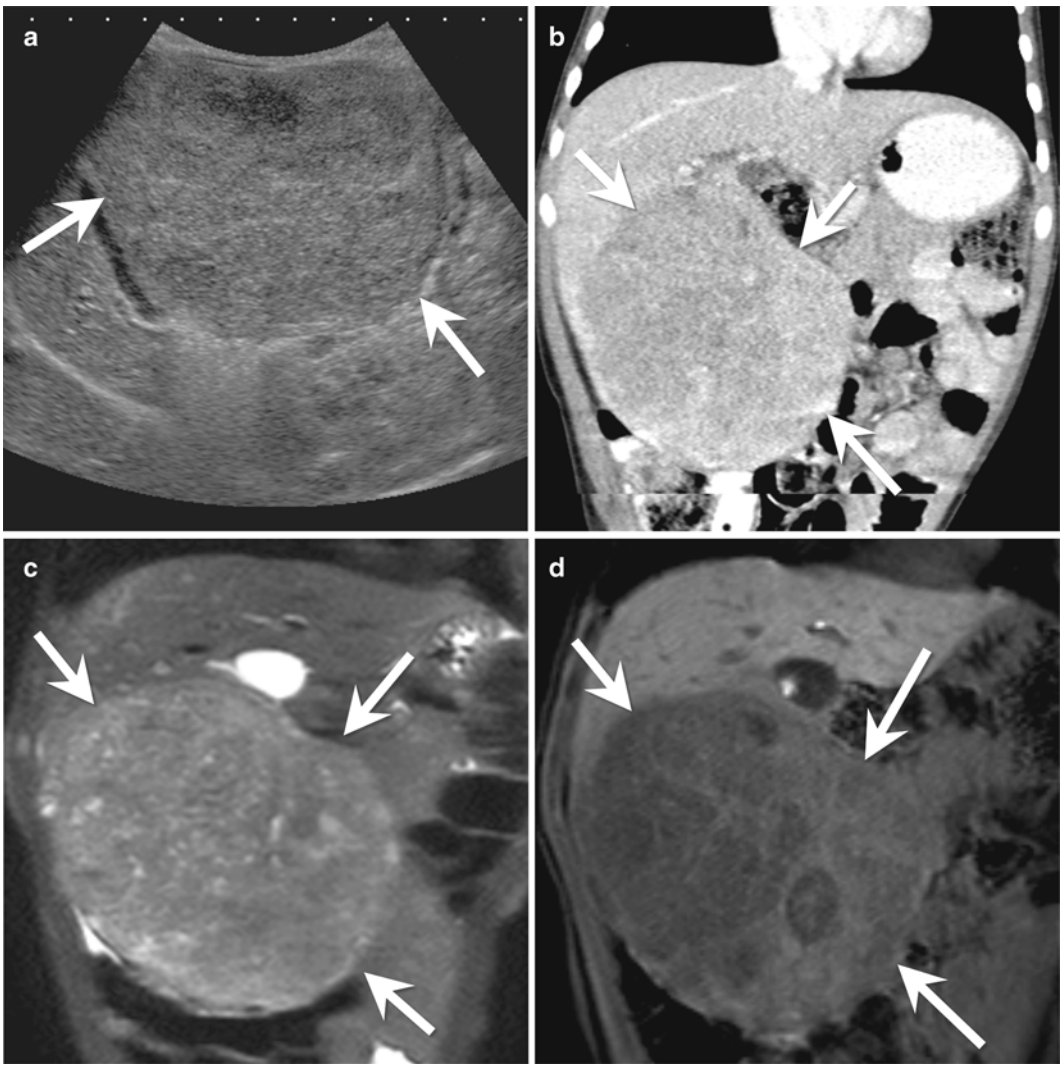

Fig. 9.14 An 18-month-old male with hepatoblastoma. (**a**) Longitudinal ultrasound of the liver shows a large mass (*arrows*) arising from the inferior aspect of the right lobe of the liver. The mass is heterogeneous with similar echogenicity to the background liver. (**b**) Coronal contrast-enhanced CT shows a large, pedunculated mass (*arrows*) arising from segments 5 and 6 of the liver. The mass is overall hypodense compared to the background liver. (**c**) Coronal T2-W image of the liver shows the heterogeneous appearance of the mass (*arrows*). (**d**) Coronal Liver Acquisition with Volume Acquisition (LAVA) image of the liver in the hepatocyte phase after contrast administration shows minimal enhancement of septations within the mass (*arrows*). The background liver is bright due to retention of the hepatocyte specific contrast agent

Fig. 9.15 A 4-month-old male with a mixed epithelial hepatoblastoma. (**a**) Longitudinal ultrasound image of the liver shows a large heterogeneous mass (*arrows*) arising from the liver. The mass has small areas of calcification with posterior acoustic shadowing (*arrowhead*). (**b**) Axial contrast-enhanced CT of the abdomen shows the large mass (*arrows*) arising from the left lobe of the liver. The mass has a central stellate area of low density. (**c**) Axial T1-W and (**d**) axial T2-W images of the liver show the large heterogeneous mass (*arrows*). The mass is hypointense to the background liver on the T1-W image and slightly hyperintense to the liver on the T2-W image

Ultrasound: Ultrasound is often used as the first imaging test in a patient with hepatoblastoma. It can confirm the presence of a mass, localize the mass to the liver, and evaluate its vascular supply [65]. The tumor is usually hyperechoic compared to the background liver and shows a heterogeneous echotexture (Figs. 9.14a and 9.15a) [65]. Calcifications appear as hyperechoic foci with posterior acoustic shadowing (Fig. 9.15a). Necrosis and internal hemorrhage appear as anechoic intratumoral foci [65]. Color Doppler interrogation assists in evaluating the patency of the hepatic veins, inferior vena cava, and portal veins.

CT: Generally, hepatoblastoma appears as a well-defined, hypodense mass of the liver (Fig. 9.14b, c; Figs. 9.15b and Fig. 9.16a, b) [64]. Calcifications are present in approximately 50 % of tumors [64]. The calcifications are usually small and fine in epithelial tumors and coarse in mixed mesenchymal-epithelial tumors [65].

After the administration of contrast, the tumor enhances to a lesser degree than the background liver [64, 65]. During the arterial phase of enhancement, there may be septa or a peripheral rim of enhancement [64, 65].

Metastases are present in 20 % of patients at diagnosis and almost always occur in the lungs. Because of this, a chest CT should be performed at diagnosis [65].

MRI: The MRI appearance of hepatoblastoma varies with histologic subtype. Epithelial tumors have a homogeneous

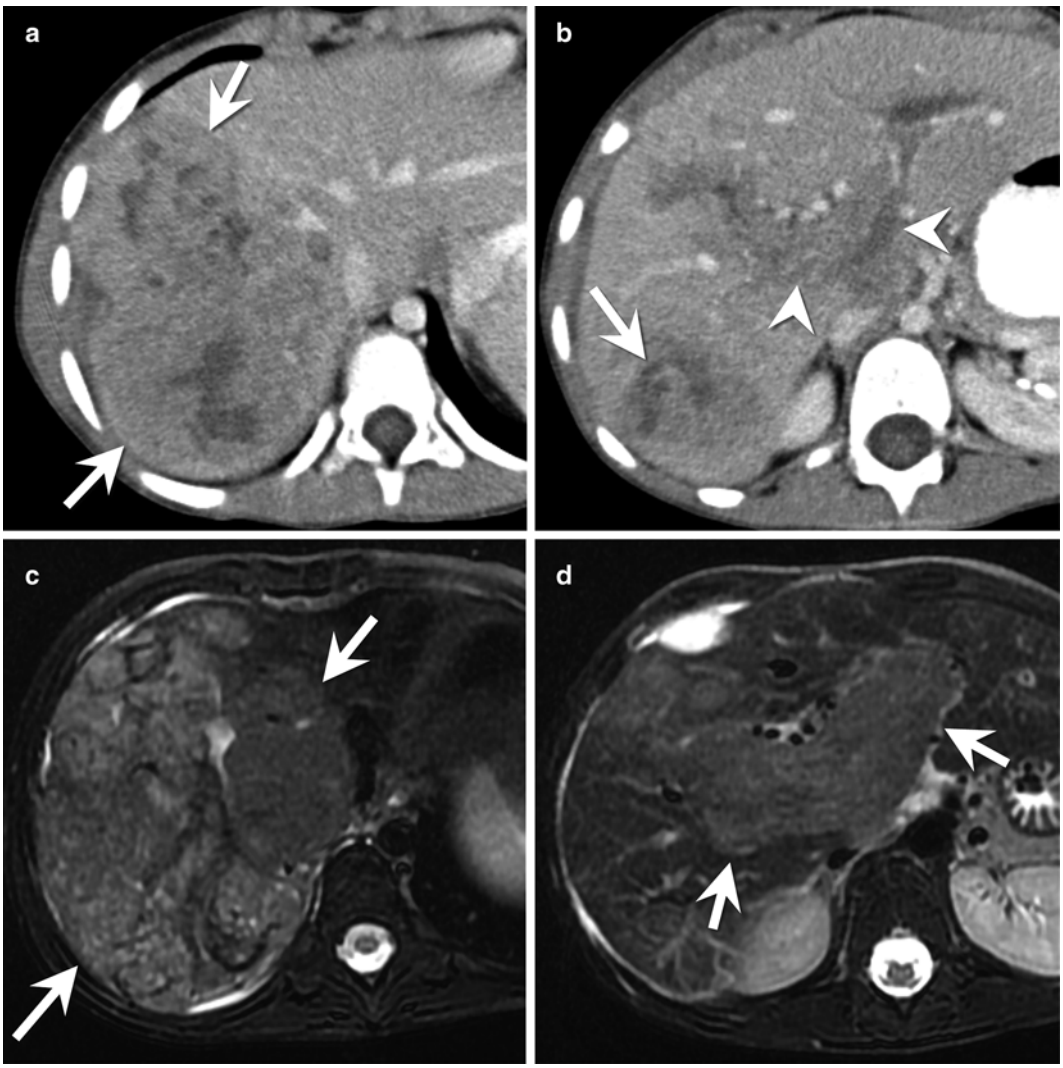

Fig. 9.16 A 6-year-old female with a mixed epithelial hepatoblastoma. (**a**) Axial contrast-enhanced CT shows a heterogeneous mass (*arrow*) within segment 7 of the liver. The mass has an irregular contour with capsular retraction along its lateral margin. (**b**) Axial contrast-enhanced CT image several centimeters inferior to the mass shown in part (**a**) shows enlargement and enhancement of the main portal vein as well as its major branches (*arrowheads*) consistent with tumor thrombus. A portion of the main tumor mass (*arrow*) is present in the posterior right lobe. (**c**) Axial T2-W MR shows a large, heterogeneous mass in the posterior section of the right hepatic lobe. (**d**) Axial T2-W MR image several centimeters inferior to the mass shown in part (**c**) shows enlargement and abnormal signal within the portal vein and its major branches (*arrows*) consistent with tumor thrombus

appearance and are hypointense on T1-W images (Fig. 9.15c) and hyperintense on T2-W imaging (Figs. 9.15d and 9.16c) [65]. Mixed epithelial-mesenchymal tumors are heterogeneous due to hemorrhage, necrosis, fibrosis, calcification, cartilage, and septa [65]. The variable composition of these tumors imparts a heterogeneous appearance on T1 and T2-W images. Septa appear hypointense on both T1 and T2-W images.

Post-contrast images are performed in the hepatic arterial and portal venous phases. The tumor enhances to a lesser degree than the background liver. Post-contrast imaging also defines the vascular anatomy and determines the presence of vascular invasion. Tumor thrombosis appears as an enhancing mass enlarging the involved vessel (Fig. 9.16d). This differs from bland thrombosis, which neither enhances nor enlarges vessels.

With hepatocyte-specific contrast agents, hepatoblastomas [57, 58] can have a variable appearance during the hepatocyte phase of imaging (Fig. 9.14d). Most tumors are hypointense during the hepatocyte phase, but a small number variably retain contrast [58]. It is not yet known if contrast retention occurs more commonly in certain histologic subtypes.

Pathology

Gross and microscopic features: Grossly, hepatoblastoma usually appears as a well-defined liver mass. About 60 % occur in the right lobe [66]. The tumor may have a variegated appearance due to its mixed histologic composition and areas of hemorrhage, necrosis, or calcification [64].

Histologically, hepatoblastoma is classified into two broad types with multiple distinct patterns (Table 9.1) (Figs. 9.17, 9.18, 9.19, and 9.20) [64]. The epithelial type of hepatoblastoma occurs most commonly and comprises multiple subtypes including fetal, embryonal, small cell undifferentiated, and rhabdoid (Fig. 9.17) [60]. Nearly one-third of hepatoblastomas are well differentiated epithelial tumors with pure fetal histology (Fig. 9.18) [64]. These tumors are composed of small cuboidal cells arranged in thin trabeculae and containing varying amounts of glycogen and lipid. Like fetal liver, these characteristics impart an alternating light–dark pattern at low-power microscopy. More poorly differentiated epithelial tumors contain both fetal and embryonal components (Fig. 9.17). Embryonal tumors contain small, round, blue cells with less cytoplasm than fetal cells, often arranged in epithelial rosettes. The most poorly differentiated epithelial hepatoblastoma, the small cell undifferentiated tumor (Fig. 9.19), totally lacks recognizable hepatocytic differentiation and fails to express INI1 [64]. At times, these lesions exhibit a rhabdoid phenotype, with cytoplasmic inclusions and positivity for epithelial and mesenchymal markers (see Chap. xx, Renal for further discussion).

Table 9.1 Histological subtypes of hepatoblastoma [Data from Cynthia E. Herzog, Richard J. Andrassy, Farzin Eftekhari: Childhood Cancers: Hepatoblastoma, The Oncologist 2000; 5:445–453]

Pure epithelial 56 %
Pure fetal 31 %
Fetal/embryonal 19 %
Macrotrabecular 3 %
Small cell undifferentiated/rhabdoid 3 %
Mixed epithelial mesenchymal (including teratoid) 44 %

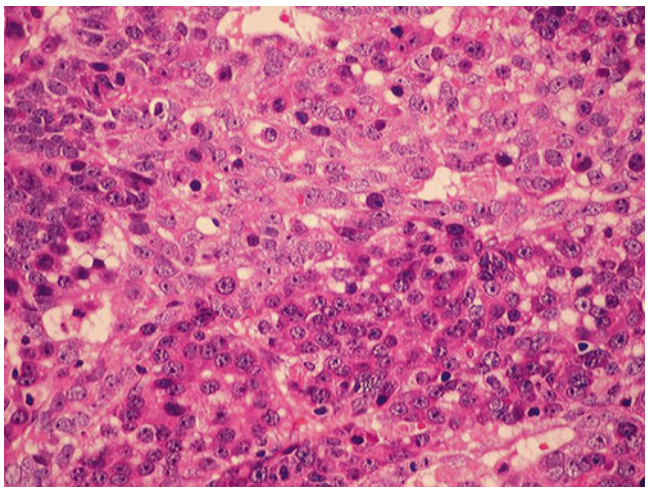

Fig. 9.17 Hepatoblastoma, mixed embryonal-fetal type. Primitive embryonal hepatocytes with brightly pink cytoplasm intermingle with fetal hepatocytes with more abundant, lightly eosinophilic cytoplasm

Mixed epithelial and mesenchymal hepatoblastomas comprise the second large histologic type and account for 44 % of tumors [64]. Most mixed tumors contain fibrous, cartilaginous, and osteoid-like material in addition to epithelium. Teratoid tumors contain other differentiated tissues, such as respiratory epithelium or muscle (Fig. 9.20) [64]. Mixed epithelial and mesenchymal tumors typically have a more heterogeneous appearance.

Immunohistochemistry and other special stains: Biomarkers used for hepatoblastoma immunohistochemistry include β-catenin, E-cadherin, and cyclin D1 [67]. Hepatoblastomas show membranous expression of β-catenin in fetal cells and diffuse nuclear and cytoplasmic staining in embryonal cells.

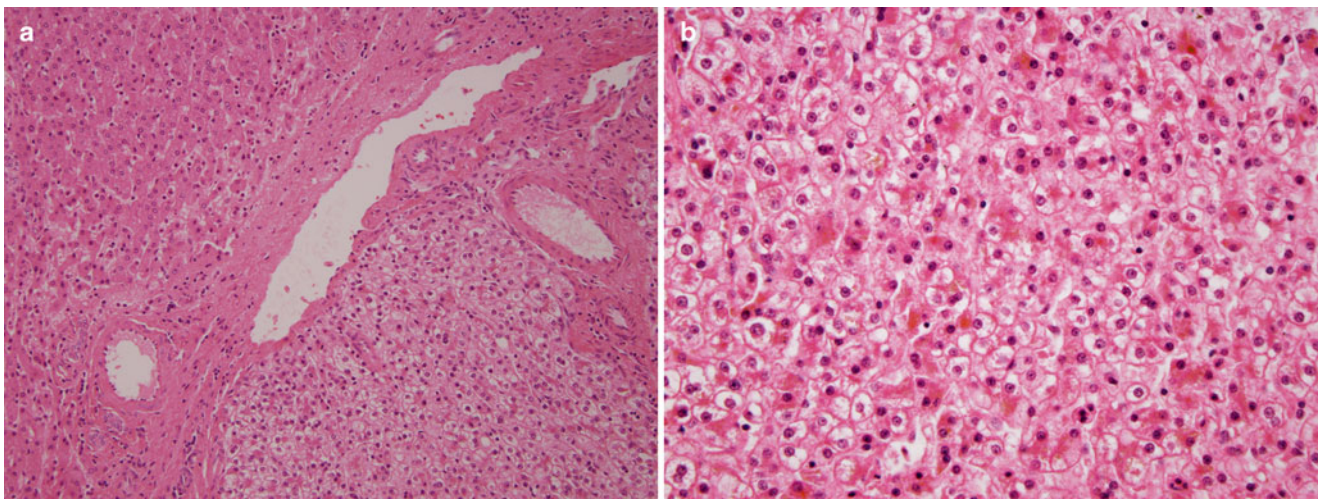

Fig. 9.18 Pure fetal hepatoblastoma. (**a**) The neoplasm (*lower right*) is separated from normal liver (*upper left*) by a fibrous capsule with prominent vessels. In contradistinction from the normal liver, the neoplastic hepatocytes form clusters lacking distinct sinusoids. (**b**) At higher power, the fetal hepatocytes are very well differentiated and contain small, round nuclei with even chromatin. Cytoplasmic bile pigment is focally evident

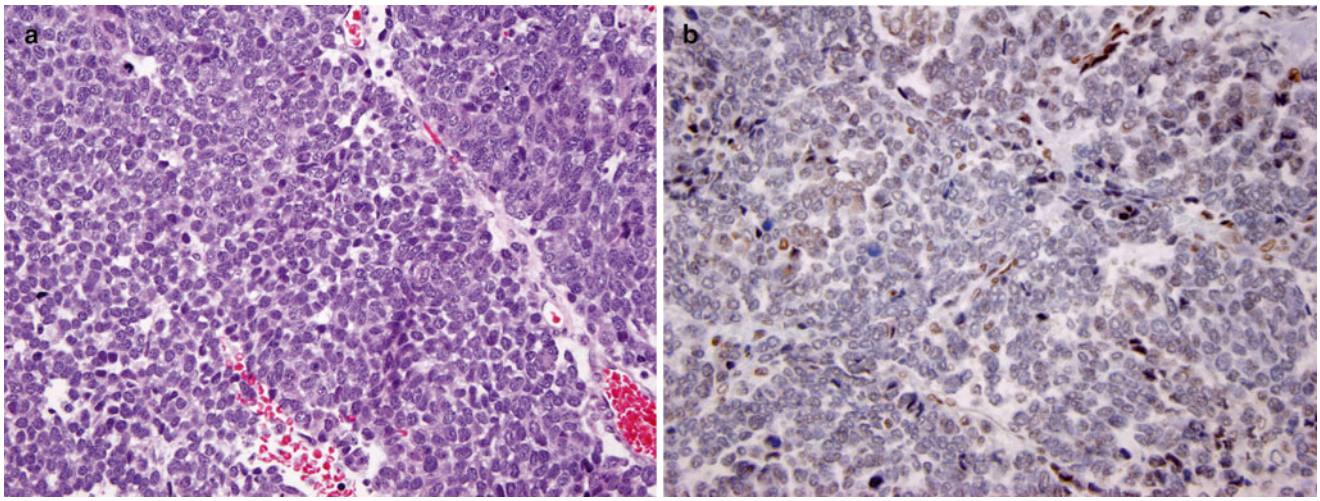

Fig. 9.19 Small cell hepatoblastoma. (**a**) This small blue cell neoplasm lacks any obvious hepatocytic differentiation. (**b**) The tumor cells lack INI1 expression, whereas staining is present in endothelial cells (BAF-47 immunostain)

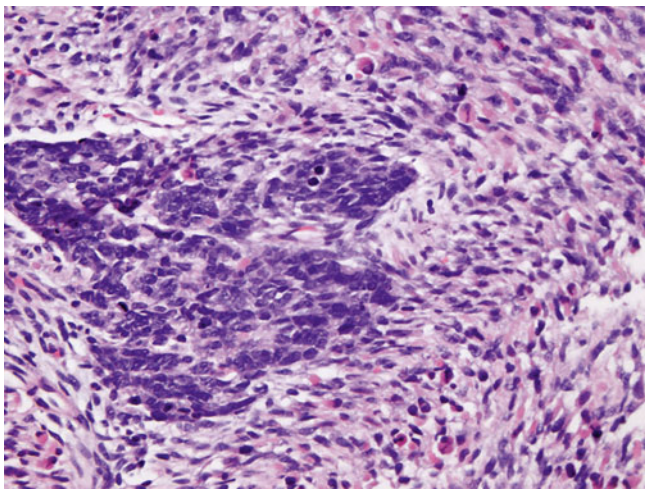

Fig. 9.20 Teratoid hepatoblastoma. This tumor contains both primitive fetal hepatocytes that stained with HepPar (not shown) and well differentiated rhabdomyoblasts. Rhabdomyosarcoma was considered as a possible diagnosis, but serum AFP was elevated

Table 9.2 Definitions of PRETEXT staging [Data from Roebuck DJ, 2007]

PRETEXT stage	Definition
I	Has the following characteristics: • Tumor involves one liver section • Three contiguous sections of the liver are free of tumor
II	Has the following characteristics: • Tumor is present in one or two sections of the liver • Two contiguous sections of the liver are free of tumor
III	Has the following characteristics: • Tumor is present in two or three sections of the liver • No two contiguous sections of the liver are free of tumor
IV	Tumor involving all for sections of the liver

Poorly dedifferentiated cells show strong nuclear expression. Decreased E-cadherin expression is associated with dedifferentiation, infiltration, and metastases. With abnormal expression, E-cadherin either shows heterogeneous membrane staining or a complete absence. When it occurs, cyclin D1 expression is limited to the nucleus. One recent study showed that cyclin D1 expression was more common in mixed epithelial mesenchymal tumors than pure fetal ones. Cyclin D1 expression is correlated with an increased recurrence risk.

Molecular diagnostic features and cytogenetics: The most characteristic cytogenetic findings in hepatoblastoma are structural rearrangements and gain or loss of whole chromosomes, most commonly additions of chromosomes, 2, 8, and 20 and loss of chromosome 18. Unbalanced translocations may involve a breakpoint on chromosome 1q12 or 1q24. Gene mutations that affect the Wnt signaling pathway include *CTNNB1*, *APC*, *AXIN1*, and *AXIN2* [68–70]. Other genetic changes in hepatoblastoma include upregulated expression, epigenetic silencing, and altered micro-RNA expression [71].

Prognosis and Treatment

Accurate staging is essential for risk stratification and treatment planning. Currently, European hepatoblastoma trials rely on the pretreatment extent of disease (PRETEXT) staging system and this system is being investigated in the United States by the Children's Oncology Group (COG). In this staging system, cross sectional imaging (CT or MRI) is used to define the location and extent of tumor by counting the number of involved anatomic sections (Table 9.2) [72, 73]. Complete PRETEXT staging also includes other criteria,

Table 9.3 Current SIOPEL risk stratification of hepatoblastoma [Data from von Schweinitz D, 2012; Roebuck DJ, 2007]

Stratum 1	PRETEXT I, II, or III tumor that is confined to the liver
Stratum 2	Patients with one or more of the following characteristics: • Age >5 years • PRETEXT IV • Multifocal disease • Serum AFP >120,000 ng/mL
Stratum 3	Patients with one or more of the following characteristics: • Metastases • Serum AFP <100 ng/mL Tumor with small cell undifferentiated histology

Table 9.4 Current COG staging and risk stratification of hepatoblastoma [Data from von Schweinitz D, 2012; Malogolowkin MH, 2012]

Stage I	Complete gross resection of tumor at diagnosis with clear margins
Stage II	Complete gross resection at diagnosis with microscopic residual disease at the resection margin
Stage III	Has one of the following characteristics: • Tumor biopsied at diagnosis • Gross total resection with nodal involvement or tumor spill • Incomplete resection with gross intrahepatic disease
Stage IV	Metastases at diagnosis
Very low risk	Has all of the following characteristics: • COG stage I tumor • Pure fetal histology
Low risk	Has all of the following characteristics: • COG stage I or II tumor • Any histology besides pure fetal or small cell undifferentiated
Intermediate risk	Has one of the following characteristics: • COG stage III tumors of any histology • COG stage I or II tumors with small cell undifferentiated histology
High risk	Has one of the following characteristics: • COG stage IV tumors of any histology • Serum AFP <100 ng/mL

such as involvement of the vessels, extrahepatic disease, and distant metastases [73]. Currently, there are differences between the International Childhood Liver Tumor Strategy Group (SIOPEL) and Children's Oncology Group (COG) as to how additional criteria are defined, although this is beyond the scope of this chapter [65, 72, 73].

Once the PRETEXT staging is performed, the patient can be risk stratified. The most recent risk stratification methods used by SIOPEL (Table 9.3) and COG (Table 9.4) take additional clinical factors into account besides the extent of disease. Factors that infer a worse prognosis include patients older than 5 years of age, multifocal or PRETEXT IV tumor, serum AFP levels <100 ng/mL or >1,200,000 ng/mL, small cell undifferentiated histology, and metastatic disease [74]. The best prognosis occurs with a PRETEXT I, II, or III tumor with pure fetal histology; these patients have a 100 % cure rate with surgery alone [75].

Table 9.5 Predisposition factors for hepatocellular carcinoma [Data from Meyers, 2007; Chung, 2011; Litten, 2008]

Chronic viral hepatitis B or C
Glycogen storage disease
Tyrosinemia
Hemochromatosis
α_1-antitrypsin deficiency
Autoimmune hepatitis
Primary sclerosing cholangitis
Extrahepatic biliary atresia
Progressive familial intrahepatic cholestasis
Wilson disease
Alagille syndrome
Neurofibromatoses 1 and 2
Ataxia-telangiectasia
Fanconi anemia

Patients with hepatoblastoma are treated with either upfront surgical resection or neoadjuvant chemotherapy followed by resection [76]. Patients treated in this manner have a five-year survival rate of 80–90 % [77]. Unresectable liver tumors make up 10–20 % of all hepatoblastomas in cooperative trials [77]. After neoadjuvant chemotherapy followed by liver transplantation, these patients have an overall survival of 82–100 %.

Hepatocellular Carcinoma

Hepatocellular carcinoma (HCC) is a primary hepatocyte malignancy that more typically occurs in adults but has a different behavior in children.

Clinical Features and Epidemiology

Even though HCC is the second most common primary pediatric liver malignancy, it rarely occurs in children. In western countries, HCC accounts for less than 25 % of hepatic malignancies and has a prevalence of 0.5–1 cases per 1 million [64]. It is more frequent in countries where hepatitis B infection is endemic. In these regions, HCC is the most common pediatric liver malignancy and occurs with a prevalence of 2.1 cases per million [64].

Unlike hepatoblastoma, HCC occurs in older children and adolescents; the majority occurs in patients older than 10 years of age [59]. The male-to-female ratio is 1.8–2:1 [64].

Preexisting liver disease is only present in 30–50 % of pediatric patients who develop HCC [64, 78]. Cirrhosis is much less common in pediatric HCC patients than adult ones and occurs in 20–25 % [62]. Other predisposing conditions are listed in Table 9.5.

Patients with HCC usually present with a large abdominal mass, abdominal pain, fever, weight loss, and anorexia [64]. Serum AFP levels are elevated in 70–80 % [64, 79].

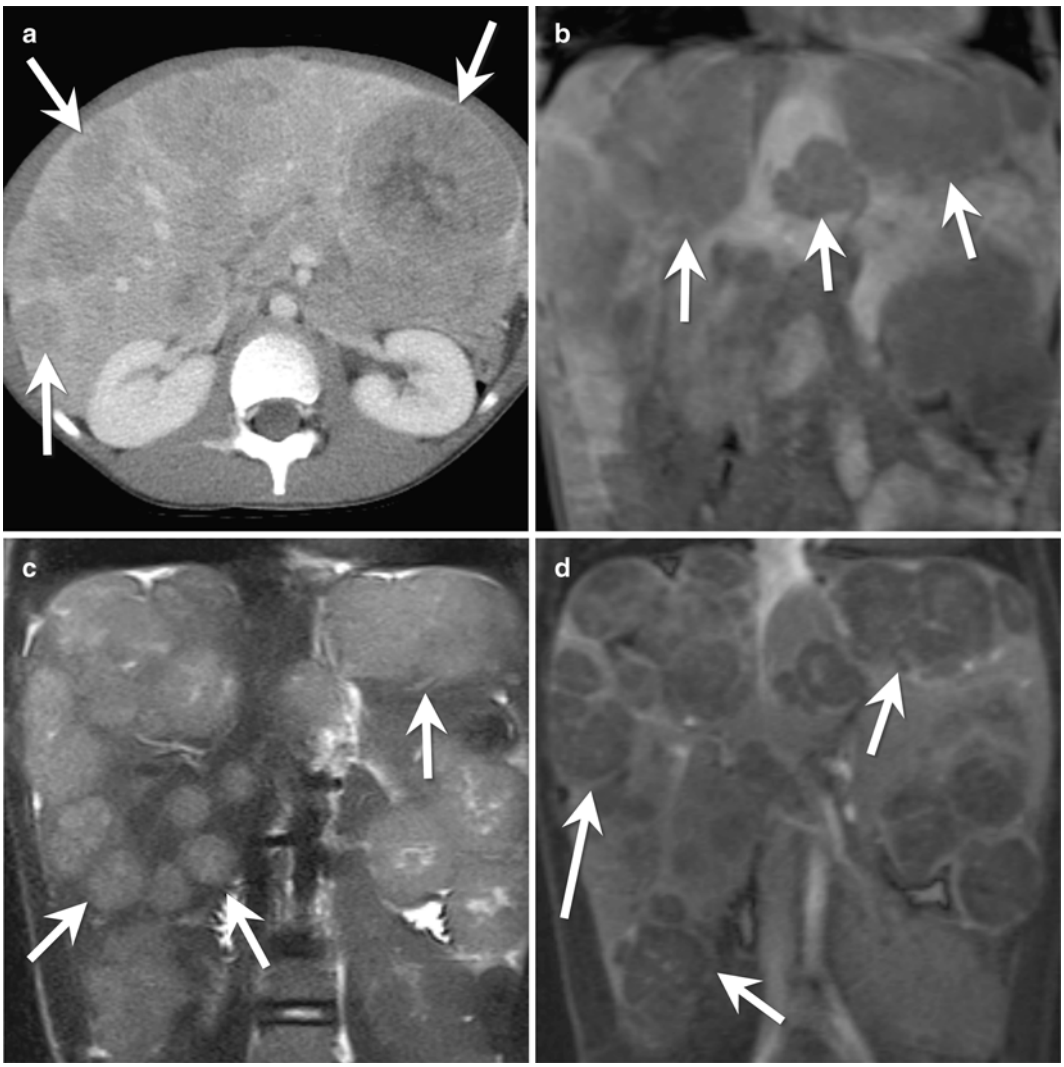

Fig. 9.21 A 7-year-old with hepatocellular carcinoma. (**a**) Axial contrast-enhanced CT of the liver shows multiple hepatic masses (*arrows*) throughout the liver. The masses are slightly hypodense compared to background liver. (**b**) Coronal T1-W, (**c**) coronal T2-W, and (**d**) coronal T1-W post contrast MRI shows multiple hepatic masses (*arrows*) throughout the liver. The masses are hypointense on T1-W images, hyperintense on T2-W images, and enhance less than the background liver

Imaging Features (Fig. 9.21)

There are three patterns of tumor growth in HCC: a solitary mass, multinodular tumor, and diffuse infiltrative tumor [64]. Multifocal tumors occur more frequently than in hepatoblastoma. Metastatic disease is present in 25–50 % of patients at the time of diagnosis and most commonly occurs in the lungs [66, 79].

Ultrasound: On ultrasound, small tumors are usually hypoechoic compared to the background liver, while larger tumors are heterogeneous due to hyperechoic regions representing fat or hemorrhage and anechoic areas representing necrosis [64]. Color Doppler interrogation is useful to evaluate the patency of the portal vein, hepatic veins, and inferior vena cava [64].

CT: On non-contrast-enhanced CT, HCC appears as a hypodense mass with either a well-defined or poorly defined border [64]. Larger masses can be heterogeneous due to internal hemorrhage, necrosis, fat, or calcification [64].

HCC appears hyperintense on the arterial phase of enhancement [64, 79]. It has a variable enhancement pattern on the portal venous phase of imaging, appearing hypodense, isodense, or mildly hyperdense (Fig. 9.21a) [64, 79]. The portal venous phase of imaging is useful to evaluate the portal vein, hepatic veins, and inferior vena cava for tumor invasion. Chest CT is used to evaluate for pulmonary metastases.

MRI: HCC can have a variable appearance on T1-W images although it is most commonly hypointense to isointense

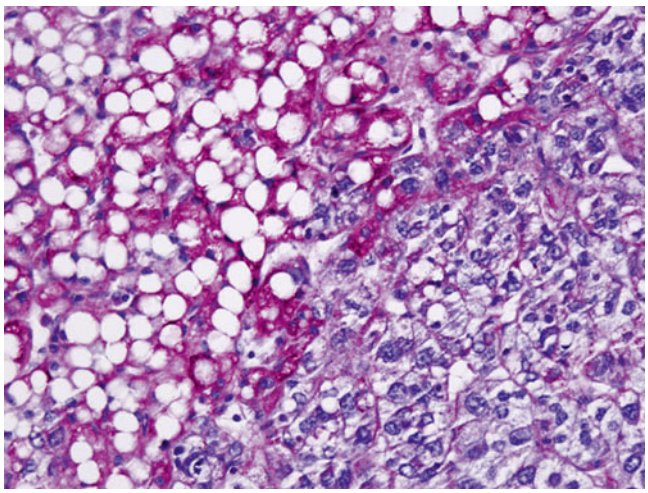

Fig. 9.22 Hepatocellular carcinoma. This lesion arose in a child with fatty liver disease of indeterminate origin. It contains large hepatocytes with irregular nuclei and clear cytoplasm. There are occasional multinucleated cells and a fine, arcuate vasculature. The adjacent liver contains PAS-positive glycogen and large fat globules (PAS stain)

compared to the liver. HCC is typically slightly hyperintense compared to the normal liver on T2-W images. The enhancement pattern on MRI is similar to the pattern seen on CT (Fig. 9.21b–d). With hepatocyte specific contrast agents, HCC usually appears hypointense compared to the liver on the hepatocyte phase of imaging; however, well-differentiated HCC can appear hyperintense [57].

Pathology

Gross and microscopic features: Grossly, HCC forms a soft tan or yellow–white mass with areas of hemorrhage or necrosis [64, 79]. Vascular invasion of the portal or hepatic veins occurs in nearly 75 % of cases [80]. The neoplasm may be separated from the adjacent liver by a grossly evident fibrous capsule [81].

Most HCC show evidence of hepatocytic differentiation, with sinusoids and canaliculi (Fig. 9.22) [82]. Some tumors exhibit marked nuclear pleomorphism, atypical mitotic figures, and tumor giant cells, making it difficult to identify a hepatocellular in origin. Others contain cells that so closely resemble normal liver that identification of malignancy is challenging. The cytoplasm may contain Mallory's hyaline, hyaline or fibrillary globules, or bile pigment.

Immunohistochemistry and other special stains: Among antigens that show some reactivity in HCC, HepPar1 (carbamoyl phosphate synthetase 1) and Glypican 3 are reasonably sensitive and specific markers of hepatocellular differentiation, whereas AFP is not as sensitive. CEA and CD10 are useful markers of canalicular structures, not found in cholangiocarcinomas or neoplasms metastatic to liver. CD34 reacts with the vascular network within HCC but generally not with sinusoidal vessels in normal liver, making it useful in distinguishing between HCC and benign lesions [83]. Reticulin stains can be useful in separating the sinusoidal pattern of normal liver from the non-sinusoidal pattern of well-differentiated HCC.

Molecular diagnostic features and cytogenetics: Unlike adult tumors, the *c-met* gene is mutated in pediatric tumors [84]. Loss of heterozygosity on chromosome 13q is much higher in pediatric HCC, whereas adult HCC has higher levels of cyclin D1 [84].

Prognosis and Treatment

Patients with HCC have an overall survival rate of 10–30 % [64, 66]. Survival is dependent on tumor resection, but two-thirds of patients have unresectable disease at diagnosis due to multifocality, large size, vascular invasion, or metastases [64]. Access to liver transplantation for pediatric HCC is restricted, because most children present with a large tumor burden [78, 84]. Children who undergo transplantation have a survival rate between 63 and 83 % [84, 85].

The response of pediatric HCC to chemotherapy appears better than in adults [78, 86]. When given preoperative chemotherapy, 30–50 % show some response [78]. Other strategies to treat HCC, such as radiofrequency ablation, transarterial chemoembolization and Yttrium-90 radioembolization, are limited in pediatric hospitals.

Fibrolamellar Hepatocellular Carcinoma

Fibrolamellar HCC (FLC) is a rare variant of HCC. It differs from typical HCC in its clinical features, imaging and histologic appearance.

Clinical Features and Epidemiology

FLC is a rare tumor, comprising 0.85 % of all primary liver malignancies and 0.9–3 % of all cases of HCC [87–89]. It is more common in adolescents and young adults, in whom it accounts for 13–22 % of all HCC [90]. The overall age-adjusted incidence of FLC is 0.02 per 100,000. The tumor has a unimodal age distribution with a peak incidence near 25 years of age [91]. There is no gender predilection, although FLC is more common in Caucasians [91].

Patients with FLC typically present with an abdominal mass and vague, nonspecific symptoms such as abdominal pain, weight loss, or malaise [92]. Occasionally, patients present with gynecomastia or jaundice [64]. Most patients do not have underlying liver disease [92]. On laboratory evaluation, serum B12, serum unsaturated B12-binding capacity, and serum neurotensin are elevated, whereas serum AFP is usually normal [87, 88, 92].

Fig. 9.23 An 11-year-old male with fibrolamellar hepatocellular carcinoma. Axial contrast-enhanced CT shows a large mass (*arrows*) in the right lobe of the liver. The mass is heterogeneous with a central stellate scar (*arrowhead*)

Imaging Features (Fig. 9.23)

FLC occurs as a solitary mass. A central stellate scar resembling focal nodular hyperplasia (FNH) is present in 33–60 % [88]. It is more common in the left lobe of the liver [92]. Lymph node metastases are common.

Ultrasound: On ultrasound, FLC appears as a solitary, well circumscribed mass with a heterogeneous echotexture [64, 88]. If a central scar is present, it appears hyperechoic. Shadowing echogenic calcifications can be present [64, 88].

CT: On CT, FLC has a heterogeneous appearance and a lobular contour [88, 91]. Calcifications, present in 35–68 % of tumors, tend to be centrally located, small, and fewer than 3 in number [91]. Most tumors are heterogeneous but mostly hypodense on non-enhanced CT. On the hepatic arterial phase of enhancement, the tumor is hyperdense compared to the background liver in 80 % of cases [91]. The central scar does not enhance and can appear either stellate or amorphous [64, 91]. Lack of enhancement of the central scar helps to differentiate FLC from FNH (Fig. 9.23) [64, 88]. On the portal venous phase of imaging, the enhancement pattern of FLC is variable.

MRI: On T1-W images, FLC is usually hypointense but can be isointense, while on T2-W images, the mass is slightly hyperintense or isointense [64]. Central scars are hypointense on all sequences [91] and help to distinguish FLC from FNH, where the scar is hyperintense on T2-W images. Like CT, the central scar does not enhance on MRI [64].

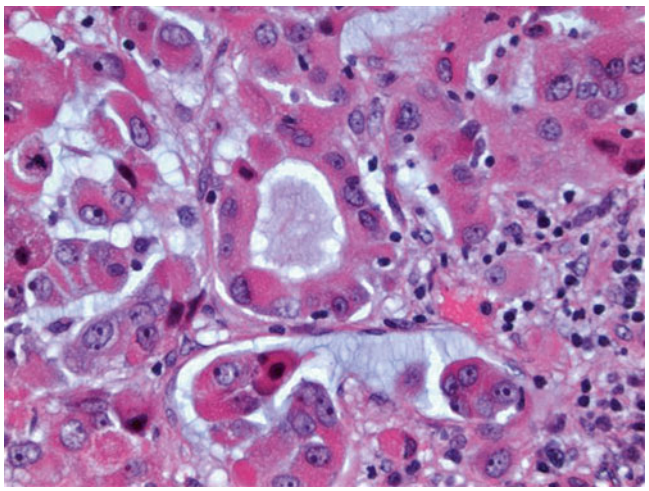

Fig. 9.24 Fibrolamellar carcinoma. The lesion contains cells with abundant, well-defined, glassy, brightly eosinophilic cytoplasm. Sinusoid differentiation is evident

Pathology

Gross and microscopic features: Grossly, FLC is a pale-tan to yellow tumor. A central scar is often present [91]. The tumor is usually solitary and non-encapsulated [64]. Central calcifications are visible in 35–55 %.

Histologically, FLC contains large polygonal cells with prominent nucleoli, arranged in cords surrounded by a meshwork of lamellated collagen fibers (Fig. 9.24) [92]. The tumor cells contain coarse granular eosinophilic cytoplasm [64, 91], with an abundance of swollen mitochondria producing the granularity [64, 92]. Many cases contain hyaline droplets; isolated tumor cells may contain pale bodies [92].

Immunohistochemistry and other special stains: FLC may express high molecular weight cytokeratin 7 and EMA, similar to bile ductules, and HepPar1, similar to hepatocytes. Most show a canalicular pattern of CEA expression. Glypican expression is found in about one-half. Positive cytokeratin 7 and EMA staining helps to separate this lesion from HCC, whereas glypican expression tends to be stronger in FLC. Neuroendocrine differentiation may occasionally be seen [92].

Molecular diagnostic features and cytogenetics: Overall, FLC has fewer genetic alterations compared to HCC; yet, 64 % still have karyotypic findings [92]. FLC shares many alterations with HCC, some as gains in 1q and 8q and loss in 18q [92].

Prognosis and Treatment

While FLC was initially thought to have a better prognosis than HCC, the difference may have been related to the

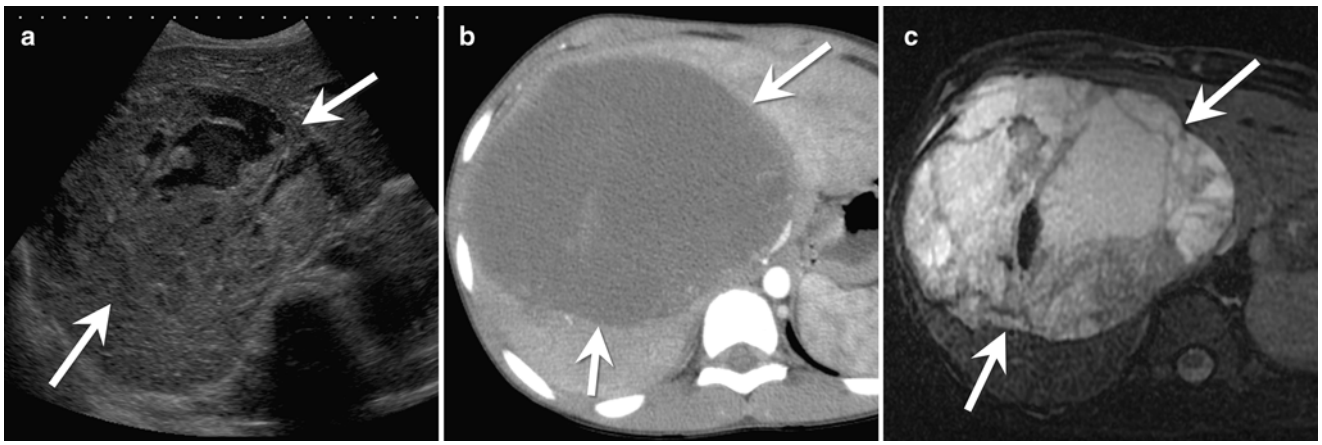

Fig. 9.25 An 11-year-old male with undifferentiated embryonal sarcoma. (**a**) Transverse ultrasound of the liver shows a large heterogeneous mass (*arrows*) in the right lobe of the liver. The mass is mostly solid and slightly hperechoic compared to the remainder of the liver. There is a small anechoic cystic component. (**b**) Axial contrast-enhanced CT of the abdomen shows a large hypodense mass (*arrows*) within the liver. The mass has mostly fluid density although there are several strandy areas of enhancement within the mass. (**c**) Axial T2-W images shows a hyperintense mass (*arrows*). The mass has mostly fluid signal although there is internal complexity

patients' younger ages and lack of underlying liver disease [92]. When patients with FLC are compared to patients with HCC without underlying liver disease, there is no significant difference in outcome [87, 91]. The overall 5-year survival rate for patients with FLC is 45 % [87]. Resection is the mainstay of treatment and the only chance for cure. Five-year survival for resectable FLC is 75 % vs. practically nil for unresectable tumors, which show a median survival of 12–14 months [91, 92].

Prognostic factors predicting worse survival include multiple tumors, vascular invasion, tumors larger than 5 cm, serum AFP greater than 2,000 μg/mL, positive resection margins, and positive lymph nodes [89, 91]. Relapse rates are high, ranging from 36 to 100 %. The median time for relapse is 10–33 months, but aggressive surgical and medical treatment helps to prolong survival [87]. While relapses typically are intrahepatic in HCC, FLC typically relapses in extrahepatic locations, including regional lymph nodes, peritoneum, and lungs [89].

Undifferentiated Embryonal Sarcoma (UES)

UES of the liver is a rare, malignant hepatic neoplasm of mesenchymal origin [93] and is also known as fibromyxoid sarcoma, malignant mesenchymoma, and embryonal sarcoma [94].

Clinical Features and Epidemiology

UES is the third most common pediatric hepatic malignancy [94], accounting for 9–13 % and occurring in patients between 5 and 10 years of age [95]. Males and females are equally affected [93]. Patients present with an abdominal mass, abdominal pain, nausea, anorexia, intermittent fever, or headache [93, 96]. Occasionally patients present with abdominal pain after mild trauma. In these patients, the mass may be first diagnosed as a hematoma [95].

There are no reliable laboratory evaluations to help diagnoses UES. Serum AFP is usually normal [93, 96].

Imaging Features (Figs. 9.25 and 9.26)

UES usually arises in the right lobe of the liver [93]. Metastases typically involve the lungs, pleura, and peritoneum [64]. The imaging appearance of UES reflects its solid, cystic, and mucoid composition [64].

Ultrasound: On ultrasonography, UES typically forms a solid hepatic mass [64, 93, 96]. That is isoechoic to hyperechoic compared to the background liver. It has small anechoic spaces corresponding to foci of necrosis, hemorrhage, and cystic degeneration (Fig. 9.25a) [64].

CT: On CT, the mass appears cystic with near water density [64, 93, 96]. Calcifications are rare [64]. Septa of varying thickness and foci of peripheral soft tissue are often present (Fig. 9.25b) [64, 93]. Central hyperdense foci and fluid-debris levels represent hemorrhage [64]. During the arterial phase, UES is hypodense, but it may show internal or peripheral enhancement on more delayed images (Fig. 9.26a, b) [64, 93, 96].

MRI: UES demonstrates fluid signal on both T1 and T2-W images. A hypointense rim caused by the fibrous pseudocapsule surrounds tumor on both sequences [64]. Foci of T1 hyperintensity and T2 hypointensity represent intratumoral hemorrhage. T2-W images outline septa and fluid-

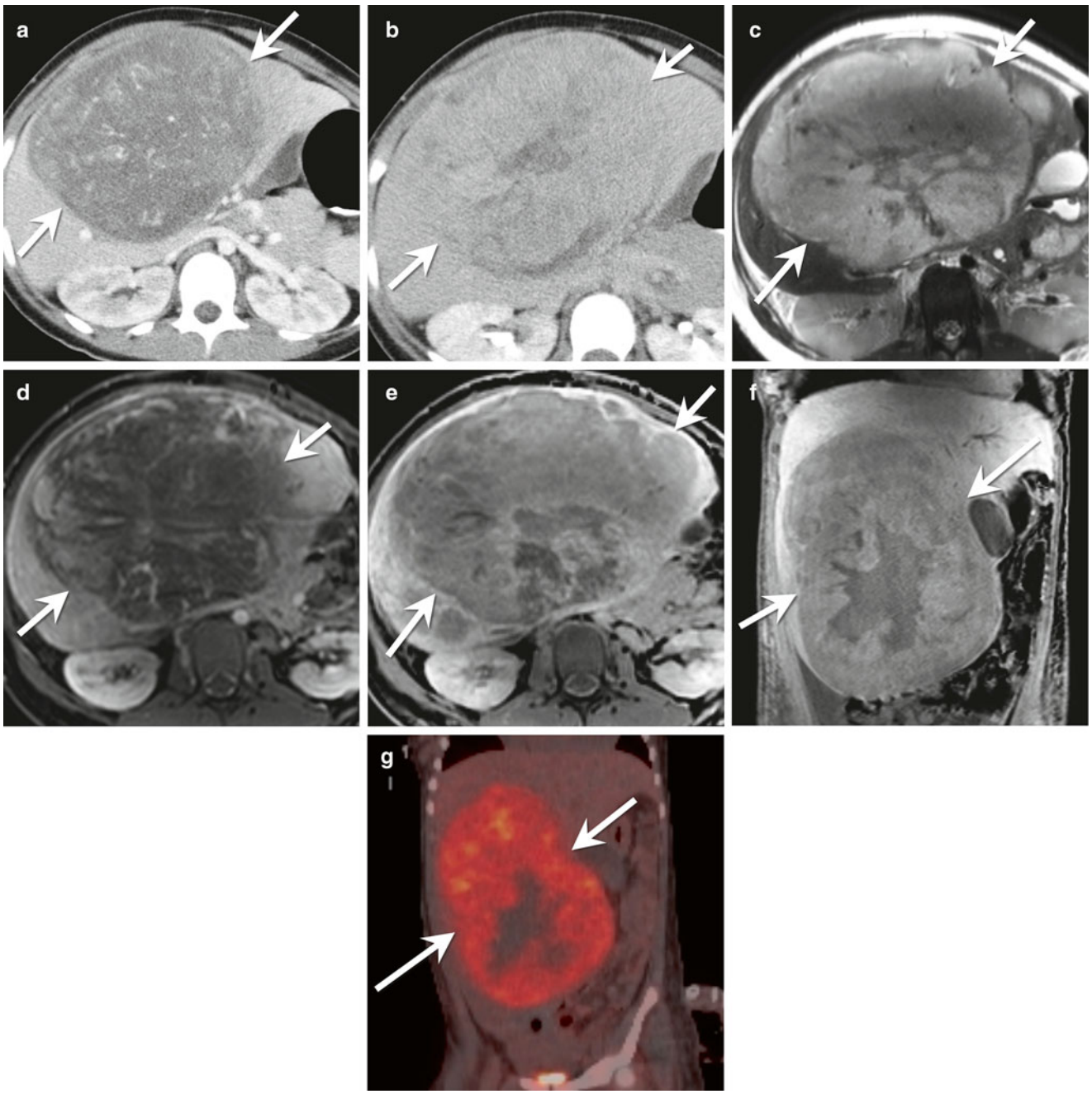

Fig. 9.26 A 12-year-old female with undifferentiated embryonal sarcoma. (**a**) Axial contrast-enhanced CT of the abdomen obtained in the portal venous phase of imaging shows a hypodense mass (*arrows*) in the central liver. The mass has mostly fluid density although there are whispy areas of enhancement throughout the mass. (**b**) Axial contrast-enhanced CT of the abdomen obtained in a delayed phase of imaging shows interval delayed enhancement of the majority of the mass (*arrows*). The mass is now mostly isodense to the remainder of the liver. (**c**) Axial T2-W image of the liver shows a large hyperintense mass (*arrows*). The mass is heterogeneous with a central area of low signal intensity. (**d**) Axial T1-W post-contrast image of the liver obtained in the portal venous phase of imaging shows the large mass (*arrows*) in the central liver. The mass enhances less than the remainder of the liver. There are large vessels coursing through the mass. (**e**) Axial and (**f**) coronal T1-W post-contrast image of the liver obtained in the hepatocyte phase of imaging shows the large mass (*arrows*) arising from the inferior aspect of the right lobe of the liver. There has been mild delayed enhancement of the mass although it remains hypointense compared to the background liver. There is a central, cystic area of the mass that does not enhance. (**g**) Coronal fused PET/CT of the abdomen shows FDG uptake within the majority of the large hepatic mass (*arrows*). There is no FDG uptake in the cystic portion of the mass

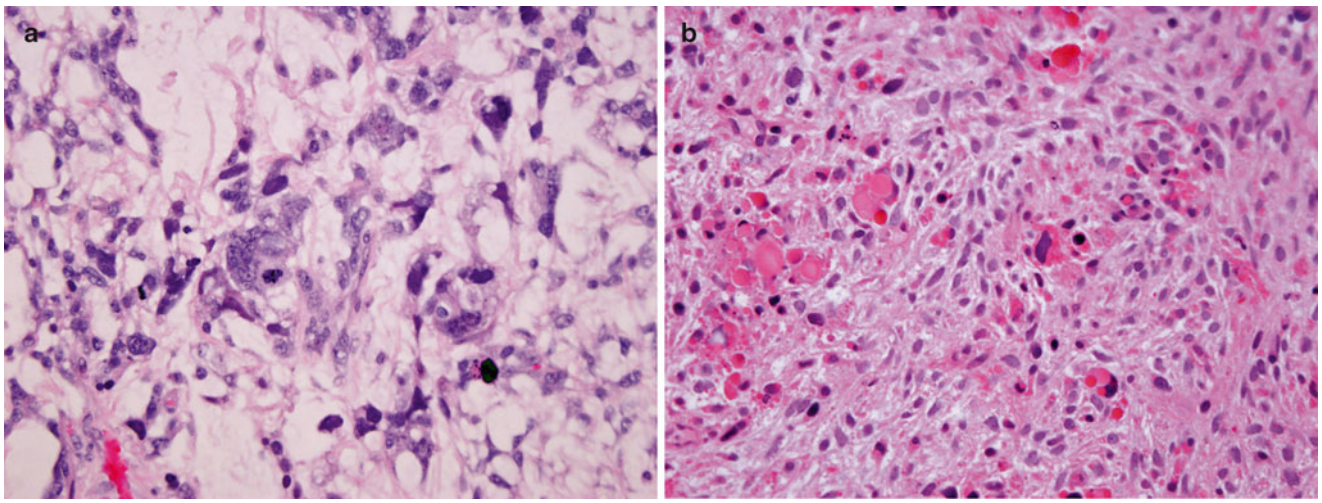

Fig. 9.27 Undifferentiated embryonal sarcoma of liver. (**a**) Large tumor cells with markedly pleomorphic nuclei are separated by a myxoid stroma. (**b**) Abundant, bright-pink hyaline globules are evident

debris levels (Figs. 9.25c and 9.26c) [64]. Heterogeneous enhancement, best seen in the late portal venous phase, occurs in the peripheral and solid portions of UES following contrast administration, (Fig. 9.26d) [64, 93, 96]. If hepatocyte specific contrast agents are used, the mass appears hypointense compared to the background liver (Fig. 9.26e, f) [57].

PET/CT: There have been few reports of the use of PET/CT in patients with UES. In these patients, the tumor shows patchy or diffuse FDG uptake.

Pathology

UES may occur sporadically or arise from mesenchymal hamartoma. It shows several features of mesenchymal hamartoma, including a predilection for the right lobe of the liver, presence of cystic changes, benign duct elements, loose myxoid stroma, immature mesenchymal cells, and shared immunohistochemical and cytogenetic findings [94].

Gross and microscopic features: UES is typically a large tumor and has a mean diameter of 14 cm [64]. A fibrous pseudocapsule separates it from the adjacent liver [94]. The neoplasm demonstrates a variegated cut surface, with a mixture of grey–white firm tumor, cystic gelatinous areas, and foci of hemorrhage or necrosis [64].

UES contains hypocellular and hypercellular arrays of undifferentiated mesenchymal cells surrounding benign appearing bile ducts (Fig. 9.27a). The cellular regions frequently feature multinucleated giant cells and marked pleomorphism [93]. Intracellular PAS-positive, diastase-resistant hyaline globules occur commonly (Fig. 9.27b). Abnormal mitoses are common, and the mitotic rate is usually high.

Immunohistochemistry and other special stains: Like mesenchymal hamartoma, UES expresses vimentin and alpha-1 antitrypsin [94]. Hyaline globules may show reactivity with alpha-1 antitrypsin antibodies, and they stain positively with PASD. Ki-67 stains demonstrate an elevated proliferation index [93]

Molecular diagnostic features and cytogenetics: Both mesenchymal hamartomas and their associated UES frequently harbor rearrangements of band 19q13.4, including the translocation t(11;19)(q13;q13.4). The breakpoint at 11q13 occurs in the *MALAT1* gene, also known as *ALPHA*, which is rearranged in renal tumors harboring the t(6;11)(p21;q13) translocation. A number of human carcinomas overexpress noncoding *MALAT1* transcripts. The breakpoint at 19q13.4 has been called MHLB1, for Mesenchymal Hamartoma of the Liver Breakpoint [97–99].

Prognosis and Treatment

Historically, the median survival of UES has been less than 1 year [96]. Currently, UES is treated with neoadjuvant chemotherapy followed by resection. This has led to markedly improved survival, and the disease is now considered curable [64, 93, 100]. It has been treated with soft tissue sarcoma protocols by the COG.

References

1. Howlader N, Noone AM, Krapcho M, Aminou R, Altekruse SF, Kosary CL, et al. SEER cancer statistics review (Vintage 2009 Publications). Bethesda, MD: National Cancer Institute; 2012. [updated August 20, 2012 cited 2013], Available from: http://seer.cancer.gov/csr/1975_2009_pops09/.

2. Ladd AP, Grosfeld JL. Gastrointestinal tumors in children and adolescents. Semin Pediatr Surg. 2006;15(1):37–47. Epub 2006/02/07.
3. Bethel CA, Bhattacharyya N, Hutchinson C, Ruymann F, Cooney DR. Alimentary tract malignancies in children. J Pediatr Surg. 1997;32(7):1004–8. Discussion 8–9. Epub 1997/07/01.
4. Skinner MA, Plumley DA, Grosfeld JL, Rescorla FJ, West KW, Scherer LR. Gastrointestinal tumors in children: an analysis of 39 cases. Ann Surg Oncol. 1994;1(4):283–9. Epub 1994/07/01.
5. Sarvida ME, O'Dorisio MS. Neuroendocrine tumors in children and young adults: rare or not so rare. Endocrinol Metab Clin North Am. 2011;40(1):65–80. vii. Epub 2011/02/26.
6. Doede T, Foss HD, Waldschmidt J. Carcinoid tumors of the appendix in children: epidemiology, clinical aspects and procedure. Eur J Pediatr Surg. 2000;10(6):372–7. Epub 2001/02/24.
7. Corpron CA, Black CT, Herzog CE, Sellin RV, Lally KP, Andrassy RJ. A half century of experience with carcinoid tumors in children. Am J Surg. 1995;170(6):606–8. Epub 1995/12/01.
8. Moertel CG, Weiland LH, Nagorney DM, Dockerty MB. Carcinoid tumor of the appendix: treatment and prognosis. New Eng J Med. 1987;317(27):1699–701. Epub 1987/12/31.
9. Parkes SE, Muir KR, al Sheyyab M, Cameron AH, Pincott JR, Raafat F, et al. Carcinoid tumours of the appendix in children 1957–1986: incidence, treatment and outcome. British J Surg. 1993;80(4):502–4. Epub 1993/04/01.
10. Spunt SL, Pratt CB, Rao BN, Pritchard M, Jenkins JJ, Hill DA, et al. Childhood carcinoid tumors: the St Jude Children's Research Hospital experience. J Pediatr Surg. 2000;35(9):1282–6. Epub 2000/09/22.
11. Pickhardt PJ, Levy AD, Rohrmann Jr CA, Kende AI. Primary neoplasms of the appendix: radiologic spectrum of disease with pathologic correlation. Radiographics. 2003;23(3):645–62. Epub 2003/05/13.
12. Groth SS, Virnig BA, Al-Refaie WB, Jarosek SL, Jensen EH, Tuttle TM. Appendiceal carcinoid tumors: predictors of lymph node metastasis and the impact of right hemicolectomy on survival. J Surg Oncol. 2011;103(1):39–45. Epub 2010/10/30.
13. Washington MK, Tang LH, Berlin J, Branton PA, Burgart LJ, Carter DK, et al. Protocol for the examination of specimens from patients with neuroendocrine tumors (carcinoid tumors) of the stomach. Arch Pathol Lab Med. 2010;134(2):187–91. Epub 2010/02/04.
14. Washington MK, Tang LH, Berlin J, Branton PA, Burgart LJ, Carter DK, et al. Protocol for the examination of specimens from patients with neuroendocrine tumors (carcinoid tumors) of the small intestine and ampulla. Arch Pathol Lab Med. 2010;134(2):181–6. Epub 2010/02/04.
15. Washington MK, Tang LH, Berlin J, Branton PA, Burgart LJ, Carter DK, et al. Protocol for the examination of specimens from patients with neuroendocrine tumors (carcinoid tumors) of the colon and rectum. Arch Pathol Lab Med. 2010;134(2):176–80. Epub 2010/02/04.
16. Washington MK, Tang LH, Berlin J, Branton PA, Burgart LJ, Carter DK, et al. Protocol for the examination of specimens from patients with neuroendocrine tumors (carcinoid tumors) of the appendix. Arch Pathol Lab Med. 2010;134(2):171–5. Epub 2010/02/04.
17. Landry CS, Woodall C, Scoggins CR, McMasters KM, Martin 2nd RC. Analysis of 900 appendiceal carcinoid tumors for a proposed predictive staging system. Arch Surg. 2008;143(7):664–70. Discussion 70. Epub 2008/07/23.
18. Benesch M, Wardelmann E, Ferrari A, Brennan B, Verschuur A. Gastrointestinal stromal tumors (GIST) in children and adolescents: a comprehensive review of the current literature. Pediatr Blood Cancer. 2009;53(7):1171–9. Epub 2009/06/06.
19. Agaram NP, Laquaglia MP, Ustun B, Guo T, Wong GC, Socci ND, et al. Molecular characterization of pediatric gastrointestinal stromal tumors. Clin Cancer Res. 2008;14(10):3204–15. Epub 2008/05/17.
20. Cypriano MS, Jenkins JJ, Pappo AS, Rao BN, Daw NC. Pediatric gastrointestinal stromal tumors and leiomyosarcoma. Cancer. 2004;101(1):39–50. Epub 2004/06/29.
21. Benesch M, Leuschner I, Wardelmann E, Thielen M, Schmid I, Kontny U, et al. Gastrointestinal stromal tumours in children and young adults: a clinicopathologic series with long-term follow-up from the database of the Cooperative Weichteilsarkom Studiengruppe (CWS). Eur J Cancer. 2011;47(11):1692–8. Epub 2011/04/14.
22. Pappo AS, Janeway K, Laquaglia M, Kim SY. Special considerations in pediatric gastrointestinal tumors. J Surg Oncol. 2011;104(8):928–32. Epub 2011/11/10.
23. Janeway KA, Pappo A. Treatment guidelines for gastrointestinal stromal tumors in children and young adults. J Pediatr Hematol Oncol. 2012;34 Suppl 2:S69–72. Epub 2012/05/02.
24. Gong N, Wong CS, Chu YC. Is lymph node metastasis a common feature of gastrointestinal stromal tumor? PET/CT correlation. Clin Nucl Med. 2011;36(8):678–82. Epub 2011/07/01.
25. Janeway KA, Kim SY, Lodish M, Nose V, Rustin P, Gaal J, et al. Defects in succinate dehydrogenase in gastrointestinal stromal tumors lacking KIT and PDGFRA mutations. Proc Natl Acad Sci U S A. 2011;108(1):314–8. Epub 2010/12/22.
26. Simon S, Grabellus F, Ferrera L, Galietta LJ, Schwindenhammer B, Muehlenberg T, et al. DOG1 regulates growth and IGFBP5 in gastrointestinal stromal tumors. Cancer Res. 2013;73:3661–70. Epub 2013/04/12.
27. Miettinen M, Wang ZF, Sarlomo-Rikala M, Osuch C, Rutkowski P, Lasota J. Succinate dehydrogenase-deficient GISTs: a clinicopathologic, immunohistochemical, and molecular genetic study of 66 gastric GISTs with predilection to young age. Am J Surg Pathol. 2011;35(11):1712–21. Epub 2011/10/15.
28. Perez EA, Gutierrez JC, Koniaris LG, Neville HL, Thompson WR, Sola JE. Malignant pancreatic tumors: incidence and outcome in 58 pediatric patients. J Pediatr Surg. 2009;44(1):197–203. Epub 2009/01/23.
29. Shorter NA, Glick RD, Klimstra DS, Brennan MF, Laquaglia MP. Malignant pancreatic tumors in childhood and adolescence: the memorial Sloan-Kettering experience, 1967 to present. J Pediatr Surg. 2002;37(6):887–92. Epub 2002/05/31.
30. Grosfeld JL, Vane DW, Rescorla FJ, McGuire W, West KW. Pancreatic tumors in childhood: analysis of 13 cases. J Pediatr Surg. 1990;25(10):1057–62. Epub 1990/10/01.
31. Jaksic T, Yaman M, Thorner P, Wesson DK, Filler RM, Shandling B. A 20-year review of pediatric pancreatic tumors. J Pediatr Surg. 1992;27(10):1315–7. Epub 1992/10/01.
32. Dall'igna P, Cecchetto G, Bisogno G, Conte M, Chiesa PL, D'Angelo P, et al. Pancreatic tumors in children and adolescents: the Italian TREP project experience. Pediatr Blood Cancer. 2010;54(5):675–80. Epub 2009/12/10.
33. Park M, Koh KN, Kim BE, Im HJ, Kim DY, Seo JJ. Pancreatic neoplasms in childhood and adolescence. J Pediatr Hematol Oncol. 2011;33(4):295–300. Epub 2011/04/06.
34. Ellerkamp V, Warmann SW, Vorwerk P, Leuschner I, Fuchs J. Exocrine pancreatic tumors in childhood in Germany. Pediatr Blood Cancer. 2012;58(3):366–71. Epub 2011/06/18.
35. Papavramidis T, Papavramidis S. Solid pseudopapillary tumors of the pancreas: review of 718 patients reported in English literature. J Am Coll Surg. 2005;200(6):965–72. Epub 2005/06/01.
36. Frost M, Krige JE, Bornman PC, Panieri E, Beningfield SJ, Wainwright H. Solid pseudopapillary epithelial neoplasm: a rare but curable pancreatic tumour in young women. S Afr J Surg. 2011;49(2):75–6. 8–81.

37. Chung EM, Travis MD, Conran RM. Pancreatic tumors in children: radiologic-pathologic correlation. Radiographics. 2006; 26(4):1211–38. Epub 2006/07/18.
38. Abraham SC, Klimstra DS, Wilentz RE, Yeo CJ, Conlon K, Brennan M, et al. Solid-pseudopapillary tumors of the pancreas are genetically distinct from pancreatic ductal adenocarcinomas and almost always harbor beta-catenin mutations. Am J Pathol. 2002;160(4):1361–9. Epub 2002/04/12.
39. Notohara K, Hamazaki S, Tsukayama C, Nakamoto S, Kawabata K, Mizobuchi K, et al. Solid-pseudopapillary tumor of the pancreas: immunohistochemical localization of neuroendocrine markers and CD10. Am J Surg Pathol. 2000;24(10):1361–71. Epub 2000/10/07.
40. Lieber MR, Lack EE, Roberts Jr JR, Merino MJ, Patterson K, Restrepo C, et al. Solid and papillary epithelial neoplasm of the pancreas. Am J Surg Pathol. 1987;11(2):85–93. Epub 1987/02/01.
41. Tanaka Y, Kato K, Notohara K, Hojo H, Ijiri R, Miyake T, et al. Frequent beta-catenin mutation and cytoplasmic/nuclear accumulation in pancreatic solid-pseudopapillary neoplasm. Cancer Res. 2001;61(23):8401–4. Epub 2001/12/04.
42. Min Kim S, Sun CD, Park KC, Kim HG, Lee WJ, Choi SH. Accumulation of beta-catenin protein, mutations in exon-3 of the beta-catenin gene and a loss of heterozygosity of 5q22 in solid pseudopapillary tumor of the pancreas. J Surg Oncol. 2006;94(5): 418–25. Epub 2006/09/13.
43. Shi C, Daniels JA, Hruban RH. Molecular characterization of pancreatic neoplasms. Adv Anat Pathol. 2008;15(4):185–95. Epub 2008/06/27.
44. Tiemann K, Heitling U, Kosmahl M, Kloppel G. Solid pseudopapillary neoplasms of the pancreas show an interruption of the Wnt-signaling pathway and express gene products of 11q. Mod Pathol. 2007;20(9):955–60. Epub 2007/07/17.
45. Glick RD, Pashankar FD, Pappo A, Laquaglia MP. Management of pancreatoblastoma in children and young adults. J Pediatr Hematol Oncol. 2012;34 Suppl 2:S47–50. Epub 2012/05/02.
46. Klimstra DS, Wenig BM, Adair CF, Heffess CS. Pancreatoblastoma. Am J Surg Pathol. 1995;19(12):1371–89. Epub 1995/12/01.
47. Nishimata S, Kato K, Tanaka M, Ijiri R, Toyoda Y, Kigasawa H, et al. Expression pattern of keratin subclasses in pancreatoblastoma with special emphasis on squamoid corpuscles. Pathol Int. 2005;55(6):297–302. Epub 2005/06/10.
48. Kerr NJ, Chun YH, Yun K, Heathcott RW, Reeve AE, Sullivan MJ. Pancreatoblastoma is associated with chromosome 11p loss of heterozygosity and IGF2 overexpression. Med Pediatr Oncol. 2002;39(1):52–4. Epub 2002/07/13.
49. Schmitt AM, Anlauf M, Rousson V, Schmid S, Kofler A, Riniker F, et al. WHO 2004 criteria and CK19 are reliable prognostic markers in pancreatic endocrine tumors. Am J Surg Pathol. 2007;31(11):1677–82. Epub 2007/12/07.
50. La Rosa S, Rigoli E, Uccella S, Novario R, Capella C. Prognostic and biological significance of cytokeratin 19 in pancreatic endocrine tumours. Histopathology. 2007;50(5):597–606. Epub 2007/03/31.
51. Deshpande V, Fernandez-del Castillo C, Muzikansky A, Deshpande A, Zukerberg L, Warshaw AL, et al. Cytokeratin 19 is a powerful predictor of survival in pancreatic endocrine tumors. Am J Surg Pathol. 2004;28(9):1145–53. Epub 2004/08/19.
52. Oberg K. Genetics and molecular pathology of neuroendocrine gastrointestinal and pancreatic tumors (gastroenteropancreatic neuroendocrine tumors). Curr Opin Endocrinol Diabetes Obes. 2009;16(1):72–8. Epub 2009/01/01.
53. Kochin IN, Miloh TA, Arnon R, Iyer KR, Suchy FJ, Kerkar N. Benign liver masses and lesions in children: 53 cases over 12 years. IMAJ. 2011;13(9):542–7. Epub 2011/10/14.
54. von Schweinitz D. Management of liver tumors in childhood. Semin Pediatr Surg. 2006;15(1):17–24. Epub 2006/02/07.
55. Pearce MS, Salotti JA, Little MP, McHugh K, Lee C, Kim KP, et al. Radiation exposure from CT scans in childhood and subsequent risk of leukaemia and brain tumours: a retrospective cohort study. Lancet. 2012;380(9840):499–505. Epub 2012/06/12.
56. Ringe KI, Husarik DB, Sirlin CB, Merkle EM. Gadoxetate disodium-enhanced MRI of the liver: part 1, protocol optimization and lesion appearance in the noncirrhotic liver. AJR Am J Roentgenol. 2010;195(1):13–28. Epub 2010/06/23.
57. Meyers AB, Towbin AJ, Serai S, Geller JI, Podberesky DJ. Characterization of pediatric liver lesions with gadoxetate disodium. Pediatr Radiol. 2011;41(9):1183–97. Epub 2011/06/28.
58. Meyers AB, Towbin AJ, Geller JI, Podberesky DJ. Hepatoblastoma imaging with gadoxetate disodium-enhanced MRI: typical, atypical, pre- and post-treatment evaluation. Pediatr Radiol. 2012;42(7):859–66. Epub 2012/03/16.
59. Litten JB, Tomlinson GE. Liver tumors in children. Oncologist. 2008;13(7):812–20. Epub 2008/07/23.
60. Hadzic N, Finegold MJ. Liver neoplasia in children. Clin Liver Dis. 2011;15(2):443–62. vii–x. Epub 2011/06/22.
61. Venkatramani R, Furman WL, Fuchs J, Warmann SW, Malogolowkin MH. Current and future management strategies for relapsed or progressive hepatoblastoma. Paediatr Drugs. 2012;14(4):221–32. Epub 2012/06/19.
62. Meyers RL. Tumors of the liver in children. Surg Oncol. 2007;16(3):195–203. Epub 2007/08/24.
63. Spector LG, Birch J. The epidemiology of hepatoblastoma. Pediatr Blood Cancer. 2012;59(5):776–9. Epub 2012/06/14.
64. Chung EM, Lattin Jr GE, Cube R, Lewis RB, Marichal-Hernandez C, Shawhan R, et al. From the archives of the AFIP: pediatric liver masses—radiologic-pathologic correlation. Part 2. Malignant tumors. Radiographics. 2011;31(2):483–507.
65. McCarville MB, Roebuck DJ. Diagnosis and staging of hepatoblastoma: imaging aspects. Pediatr Blood Cancer. 2012;59(5): 793–9. Epub 2012/06/09.
66. Agarwala S. Primary malignant liver tumors in children. Indian J Pediatr. 2012;79(6):793–800. Epub 2012/03/03.
67. Purcell R, Childs M, Maibach R, Miles C, Turner C, Zimmermann A, et al. Potential biomarkers for hepatoblastoma: results from the SIOPEL-3 study. Eur J Cancer. 2012;48(12):1853–9. Epub 2011/12/06.
68. Oda H, Imai Y, Nakatsuru Y, Hata J, Ishikawa T. Somatic mutations of the APC gene in sporadic hepatoblastomas. Cancer Res. 1996;56(14):3320–3. Epub 1996/07/15.
69. Taniguchi K, Roberts LR, Aderca IN, Dong X, Qian C, Murphy LM, et al. Mutational spectrum of beta-catenin, AXIN1, and AXIN2 in hepatocellular carcinomas and hepatoblastomas. Oncogene. 2002;21(31):4863–71. Epub 2002/07/09.
70. Koch A, Weber N, Waha A, Hartmann W, Denkhaus D, Behrens J, et al. Mutations and elevated transcriptional activity of conductin (AXIN2) in hepatoblastomas. J Pathol. 2004;204(5):546–54. Epub 2004/11/13.
71. Tomlinson GE, Kappler R. Genetics and epigenetics of hepatoblastoma. Pediatr Blood Cancer. 2012;59(5):785–92. Epub 2012/07/19.
72. von Schweinitz D. Hepatoblastoma: recent developments in research and treatment. Semin Pediatr Surg. 2012;21(1):21–30. Epub 2012/01/18.
73. Roebuck DJ, Aronson D, Clapuyt P, Czauderna P, de Ville de Goyet J, Gauthier F, et al. PRETEXT: a revised staging system for primary malignant liver tumours of childhood developed by the SIOPEL group. Pediatr Radiol. 2007;37(2):123–32.
74. Maibach R, Roebuck D, Brugieres L, Capra M, Brock P, Dall'Igna P, et al. Prognostic stratification for children with hepatoblastoma: the SIOPEL experience. Eur J Cancer. 2012;48(10):1543–9. Epub 2012/01/17.

75. Malogolowkin MH, Katzenstein HM, Meyers RL, Krailo MD, Rowland JM, Haas J, et al. Complete surgical resection is curative for children with hepatoblastoma with pure fetal histology: a report from the Children's Oncology Group. J Clin Oncol. 2011;29(24):3301–6. Epub 2011/07/20.
76. Malogolowkin MH, Katzenstein HM, Krailo M, Meyers RL. Treatment of hepatoblastoma: the North American cooperative group experience. Front Biosci (Elite Ed). 2012;4:1717–23. Epub 2011/12/29.
77. Meyers RL, Tiao GM, Dunn SP, McGahren 3rd ED, Langham Jr MR. Surgical management of children with locally advanced hepatoblastoma. Cancer. 2012;118(16):4090–1. Author reply 4–5. Epub 2012/07/05.
78. Ismail H, Broniszczak D, Kalicinski P, Markiewicz-Kijewska M, Teisseyre J, Stefanowicz M, et al. Liver transplantation in children with hepatocellular carcinoma. Do Milan criteria apply to pediatric patients? Pediatr Transplant. 2009;13(6):682–92.
79. Das CJ, Dhingra S, Gupta AK, Iyer V, Agarwala S. Imaging of paediatric liver tumours with pathological correlation. Clin Radiol. 2009;64(10):1015–25. Epub 2009/09/15.
80. Albacete RA, Matthews MJ, Saini N. Portal vein thromboses in malignant hepatoma. Ann Intern Med. 1967;67(2):337–48. Epub 1967/08/01.
81. Okuda K, Musha H, Nakajima Y, Kubo Y, Shimokawa Y, Nagasaki Y, et al. Clinicopathologic features of encapsulated hepatocellular carcinoma: a study of 26 cases. Cancer. 1977;40(3):1240–5. Epub 1977/09/01.
82. Edmondson HA, Steiner PE. Primary carcinoma of the liver: a study of 100 cases among 48,900 necropsies. Cancer. 1954;7(3):462–503. Epub 1954/05/01.
83. Coston WM, Loera S, Lau SK, Ishizawa S, Jiang Z, Wu CL, et al. Distinction of hepatocellular carcinoma from benign hepatic mimickers using Glypican-3 and CD34 immunohistochemistry. Am J Surg Pathol. 2008;32(3):433–44. Epub 2008/02/28.
84. Beaunoyer M, Vanatta JM, Ogihara M, Strichartz D, Dahl G, Berquist WE, et al. Outcomes of transplantation in children with primary hepatic malignancy. Pediatr Transplant. 2007;11(6):655–60. Epub 2007/08/01.
85. Kosola S, Lauronen J, Sairanen H, Heikinheimo M, Jalanko H, Pakarinen M. High survival rates after liver transplantation for hepatoblastoma and hepatocellular carcinoma. Pediatr Transplant. 2010;14(5):646–50. Epub 2010/03/30.
86. Schmid I, Haberle B, Albert MH, Corbacioglu S, Frohlich B, Graf N, et al. Sorafenib and cisplatin/doxorubicin (PLADO) in pediatric hepatocellular carcinoma. Pediatr Blood Cancer. 2012;58(4):539–44. Epub 2011/09/17.
87. Maniaci V, Davidson BR, Rolles K, Dhillon AP, Hackshaw A, Begent RH, et al. Fibrolamellar hepatocellular carcinoma: prolonged survival with multimodality therapy. Eur J Surg Oncol. 2009;35(6):617–21. Epub 2009/01/16.
88. Yen JB, Chang KW. Fibrolamellar hepatocellular carcinoma: report of a case. Chang Gung Med J. 2009;32(3):336–9. Epub 2009/06/17.
89. Stipa F, Yoon SS, Liau KH, Fong Y, Jarnagin WR, D'Angelica M, et al. Outcome of patients with fibrolamellar hepatocellular carcinoma. Cancer. 2006;106(6):1331–8. Epub 2006/02/14.
90. Cruz O, Laguna A, Vancells M, Krauel L, Medina M, Mora J. Fibrolamellar hepatocellular carcinoma in an infant and literature review. J Pediatr Hematol Oncol. 2008;30(12):968–71. Epub 2009/01/10.
91. Smith MT, Blatt ER, Jedlicka P, Strain JD, Fenton LZ. Best cases from the AFIP: fibrolamellar hepatocellular carcinoma. Radiographics. 2008;28(2):609–13. Epub 2008/03/20.
92. Ward SC, Waxman S. Fibrolamellar carcinoma: a review with focus on genetics and comparison to other malignant primary liver tumors. Semin Liver Dis. 2011;31(1):61–70. Epub 2011/02/24.
93. Boybeyi O, Karnak I, Orhan D, Akcoren Z, Tanyel FC. Undifferentiated (embryonal) sarcoma of the liver: an intriguing diagnosis in a child. Eur J Pediatr Surg. 2009;19(5):328–30. Epub 2009/02/27.
94. Shehata BM, Gupta NA, Katzenstein HM, Steelman CK, Wulkan ML, Gow KW, et al. Undifferentiated embryonal sarcoma of the liver is associated with mesenchymal hamartoma and multiple chromosomal abnormalities: a review of eleven cases. Pediatr Develop Pathol. 2011;14(2):111–6. Epub 2010/10/12.
95. Ida S, Okajima H, Hayashida S, Takeichi T, Asonuma K, Baba H, et al. Undifferentiated sarcoma of the liver. Am J Surg. 2009;198(1):e7–9. Epub 2009/03/03.
96. Crider MH, Hoggard E, Manivel JC. Undifferentiated (embryonal) sarcoma of the liver. Radiographics. 2009;29(6):1665–8. Epub 2009/12/05.
97. Lauwers GY, Grant LD, Donnelly WH, Meloni AM, Foss RM, Sanberg AA, et al. Hepatic undifferentiated (embryonal) sarcoma arising in a mesenchymal hamartoma. Am J Surg Pathol. 1997;21(10):1248–54. Epub 1997/10/23 22:23.
98. O'Sullivan MJ, Swanson PE, Knoll J, Taboada EM, Dehner LP. Undifferentiated embryonal sarcoma with unusual features arising within mesenchymal hamartoma of the liver: report of a case and review of the literature. Pediatr Develop Pathol. 2001;4(5):482–9. Epub 2002/01/10.
99. Sawyer JR, Roloson GJ, Bell JM, Thomas JR, Teo C, Chadduck WM. Telomeric associations in the progression of chromosome aberrations in pediatric solid tumors. Cancer Genet Cytogenet. 1996;90(1):1–13. Epub 1996/08/01.
100. May LT, Wang M, Albano E, Garrington T, Dishop M, Macy ME. Undifferentiated sarcoma of the liver: a single institution experience using a uniform treatment approach. J Pediatr Hematol Oncol. 2012;34(3):e114–6. Epub 2012/01/06.

Malignant Renal Tumors

10

Bahig M. Shehata, Mina M. Naguib, Jenny Lin, and Geetika Khanna

Overview and Classification

Renal tumors account for approximately 6–7 % of all pediatric cancers, with Wilms' tumor being the most common malignancy [1, 2]. Current classification and staging criteria for renal tumors, aided by advances in molecular and cytogenetic abnormalities, have allowed accurate diagnostic, staging, and therapeutic protocols [2], elucidated new categories of renal neoplasms, and created more inclusive classification (Table 10.1) [2, 3].

Overview of Imaging Features

The imaging evaluation of a suspected pediatric renal mass should always begin with ultrasound. Sonography is readily available, can be performed without sedation and intravenous contrast, and does not expose the child to ionizing radiation. If a renal mass is identified on ultrasound, further evaluation of the renal vessels and inferior vena cava (IVC) with both gray scale and color Doppler images are required to detect vascular extension, present in up to 10 % of cases [4]. Further evaluation with contrast enhanced computed tomography (CT) or magnetic resonance imaging (MRI) is also required for local staging of the mass prior to any intervention, as per the guidelines of the Children's Oncology Group (COG). Either modality can be used, depending on institutional availability and expertise [5].

In keeping with the As Low As Reasonably Achievable (ALARA) principle regarding ionizing radiation exposure, pre-contrast and multiphase contrast enhanced CT images are not required for diagnosis or staging of pediatric renal tumors [6]. A single-phase study in the portal venous phase (approximately 50 s after contrast injection) sufficiently stages a renal tumor and delineates relevant anatomy. Multiplanar CT reconstructions or multiplanar scanning with MRI can confirm the renal origin of the mass and assess its relationship to vital structures such as the renal vessels. If a partial nephrectomy is being considered, multiphase images are helpful to determine the relationship of the mass to the renal vessels and collecting system. A CT of the chest is required in all malignant renal tumors to evaluate for potential lung metastasis.

Wilm's Tumor

Definition

Wilms' tumor (*syn:* nephroblastoma), a malignant neoplasm originating from nephrogenic blastemal cells, is the second most common malignant, solid extracranial tumor in children [1, 7, 8]. It is a traditional blastematous tumor, exhibiting various stages of embryonic development and multiple lines of differentiation.

Clinical Features and Epidemiology

In children ranging from 0 to 15 years of age, Wilms' tumor occurs in seven to ten cases per million annually (1 in 10,000 children) and accounts for approximately 95 % of renal tumors, and comprises 6–7 % of all pediatric tumors [7, 9, 10]. It is the fifth most common pediatric tumor and the second most common intraabdominal tumor in children [11].

G. Khanna, M.D., M.S. (✉)
Radiology, St. Louis Children's Hospital,
Washington University School of Medicine – MIR,
510 S. Kingshighway, Box 8131, St. Louis,
MO 63110, USA
e-mail: khannag@mir.wustl.edu

B.M. Shehata • M.M. Naguib • J. Lin
Department of Pathology and Pediatrics,
Emory University School of Medicine, Pediatric Pathologist,
Children's Healthcare of Atlanta,
1405 Clifton Road, Atlanta, GA 30322, USA

D.M. Parham et al. (eds.), *Pediatric Malignancies: Pathology and Imaging*,
DOI 10.1007/978-1-4939-1729-7_10,

Table 10.1 Summary of the pediatric renal tumors described in this chapter

Classification for pediatric renal tumors
Nephroblastic tumors
Nephroblastoma (Wilms' tumor)
Favorable histology
Anaplasia (diffuse or focal)
Nephrogenic rests and nephroblastomatosis
Cystic nephroma and cystic partially differentiated nephroblastoma
Mesoblastic nephroma
Cellular
Classic
Mixed
Clear cell sarcoma
Rhabdoid tumor
Renal epithelial tumors of childhood
Translocation-associated tumors
Renal cell carcinoma associated with Xp11.2 translocations (*TFE3*)
Other translocation-associated tumors
Papillary renal cell carcinoma
Renal medullary carcinoma
Oncocytic renal neoplasms after neuroblastoma
Chromophobe renal cell carcinoma
Rare tumors
Primitive neuroectodermal tumors (PNET)
Primary rhabdomyosarcoma of the kidney
Primary synovial sarcoma

Wilms' tumor predominantly arises in young children. Greater than 80 % of Wilms' tumors are found in children younger than 5 years old, with an average age of 3.5 years [1]. Rarely, 0.16 % of Wilms' tumors are seen in neonates, and on very few occasions it occurs in adults [7].

Wilms' tumor statistics vary with respect to ethnicities. In the USA, there is a lower incidence in Hispanic/Latino compared with non-Hispanic children (RR=0.78, 95 % confidence interval=[0.64, 0.95]) [9]. The incidences in Chinese and American black children are 2.5 per million and 10.9 per million, respectively [7]. In Britain, the incidence is lower among Asian children than Caucasian children (RR=0.51, $p<0.05$) but higher among West Indian children (RR=2.55, $p<0.05$) [9].

Wilms' tumor has a slightly greater propensity to occur in girls (9.7 per million) than boys (8.4 per million). Data has shown that the age at diagnosis is significantly higher for girls than boys. The Wilms' tumor population in Europe shows similar trends with a 0.9 ratio of boys to girls (median age for girls 3 years; for boys 2 years). In Asia, a higher reported percentage of boys developed Wilms' tumor [9].

More than 90 % of Wilms' tumors present as an asymptomatic abdominal mass. Most are contained within a single lesion, 6 % present as bilateral tumors, and 12 % have multifocal disease within a single kidney. If abdominal pain (20–40 %) exists at diagnosis, there is a risk of rupture and bleeding [1, 12]. Gross hematuria (5–25 %) indicates tumor invasion into the collecting system or ureter [1, 12]. Rare cases have been reported at extrarenal sites, such as in the perirenal, inguinal, or gonadal areas, perhaps as a component of "monodermal" teratoma [8]. The average birth weight of patients with Wilms' tumors is greater than controls [7].

Symptoms present in less than 10 % of Wilms' tumor patients as a result of vascular invasion or pressure from surrounding organs. Patients with vascular invasion may present with ascites, congestive heart failure, hepatomegaly, or varicocele. Symptoms caused by tumor-induced hormones include hypertension (25 %), hypercalcemia, erythrocytosis, and von Willebrand's disease [1, 10, 12].

Ninety percent of Wilms' tumors are sporadic, and the rest occur as part of overgrowth and non-overgrowth syndromes [8]. Overgrowth syndromes include Beckwith–Wiedemann, isolated hemihypertrophy, Perlman, Sotos', and the Simpson–Golabi–Behmel syndromes. Non-overgrowth syndromes include WAGR (WT, aniridia, genitourinary anomalies, mental retardation) and Denys–Drash syndromes [1, 10]. Familial cases have an earlier age of onset and an increased incidence of bilateral disease [10].

Imaging Features

Wilms' tumor typically appears as a heterogeneous mass arising from the renal parenchyma. The normal renal parenchyma is distorted and displaced around the mass, resulting in a characteristic "claw sign" that helps confirm its renal origin [13]. On sonography, a small WT may appear uniformly isoechoic; however, more often areas of necrosis, hemorrhage, and calcification create a heterogeneous echo texture. On power Doppler evaluation, the mass typically shows decreased perfusion as compared to the normal vascular renal parenchyma. Evaluation of the renal vein with both gray scale and color Doppler evaluation is essential to exclude venous thrombus, which can be present in up to 11.3 % of WT [14]. On CT or MRI, WT typically appear heterogeneous in attenuation/signal intensity and show decreased enhancement as compared to the normal renal parenchyma (Fig. 10.1a). Intracaval extension of the tumor thrombus can be identified with a sensitivity of 84.6–96.0 % on CT (Fig. 10.1b) [15]. The presence and level of tumor thrombus in the IVC determines the surgical approach and need for preoperative chemotherapy, so the renal vein and IVC should be carefully evaluated for any filling defects. Potential pitfalls in the evaluation of the renal vein and IVC include contrast mixing artifacts and extrinsic compression of the vessels caused by a large WT.

Though microscopic extension of WT through the renal capsule is impossible to detect on imaging, gross infiltration

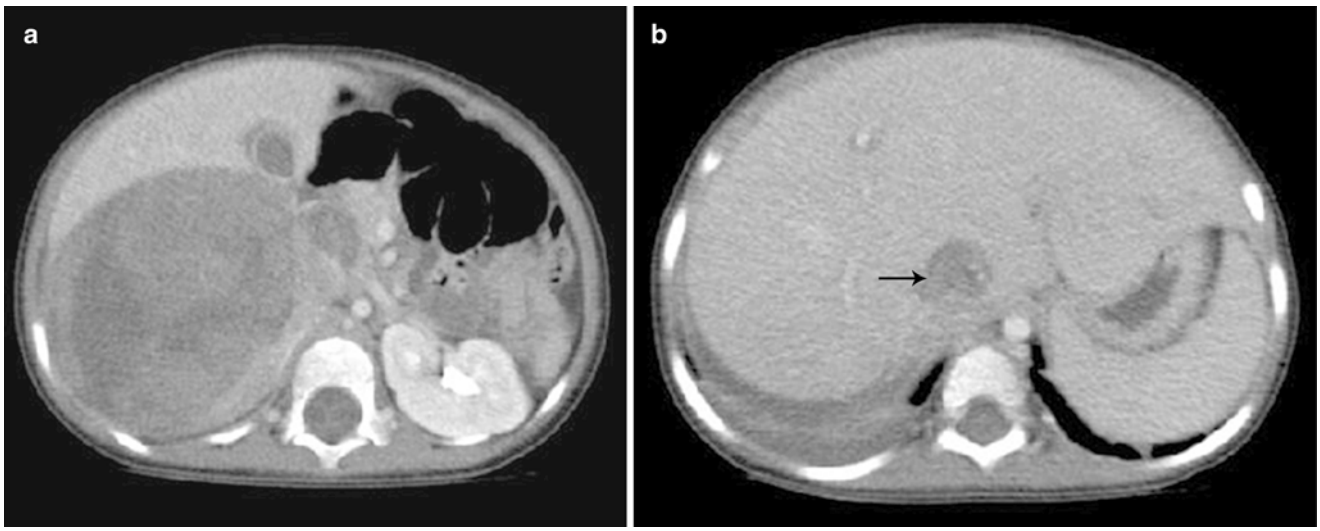

Fig. 10.1 Wilms' tumor with IVC thrombus. (**a** and **b**) Axial contrast enhanced CT images from a 4-year-old show a large heterogeneous mass in the right renal fossa with tumor thrombus distending the inferior vena cava (**b**) (*arrow*)

into adjacent structures such as the liver and psoas muscle should be evaluated on imaging. Wilms' tumor can rupture preoperatively upstaging the child to stage III with increased risk of intraabdominal recurrence. Signs of preoperative tumor rupture include ascites beyond the cul-de-sac, extracapsular perinephric fluid, and peritumoral fat stranding [16]. The regional lymph nodes, lung, and liver, common sites of metastatic disease in WT, should be carefully evaluated. Enlarged lymph nodes should be noted, though current imaging techniques have limited accuracy in detection of nodal metastasis, necessitating sampling during nephrectomy [5]. The contralateral kidney should be carefully evaluated for a contralateral WT or nephrogenic rest, as WT can be bilateral in approximately 10 % of cases [17]. Differentiation of WT from a nephrogenic rest is limited by imaging, though the former tends to inhomogeneous as compared to the homogeneous appearance of rests [18].

Pathology

Gross and Microscopic Features

The majority of Wilms' tumors form isolated, well-demarcated masses separated from the adjacent kidney (Fig. 10.2) [1, 8]. Rarely, a botryoid variant of Wilms' tumor is seen, characterized by polypoid mass occupying the renal pelvis (Fig. 10.3). After preoperative chemotherapy, significant amounts of necrosis or hemorrhage can occur. Cystic lesions require careful inspection for nodular solid areas [8].

Histology is an important prognostic indicator for Wilms' tumor. Certain histologies, particularly anaplastic Wilms' tumors, show higher risks of tumor recurrence or chemotherapy resistance [1]. Traditional Wilms' tumors contain varying amounts of three basic histological components—blastemal, epithelial, and stromal cells—which vary widely in relative proportions (Fig. 10.4) [7, 8]. If one component

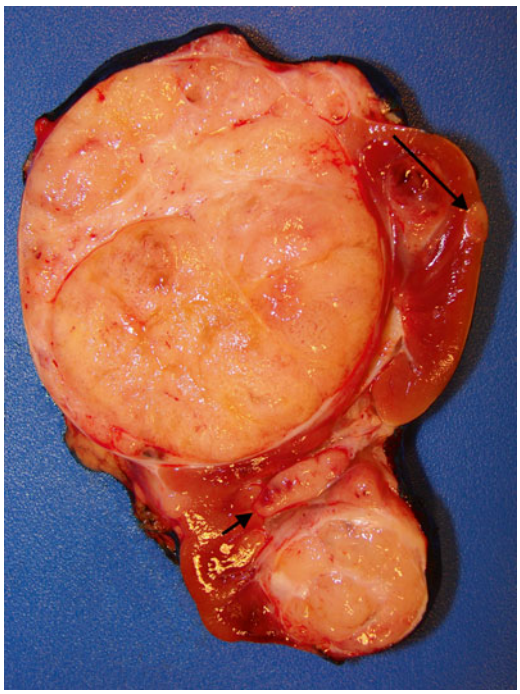

Fig. 10.2 Multifocal Wilms' tumor with renal sinus invasion (*short arrow*) and perilobar nephrogenic rest (*long arrow*)

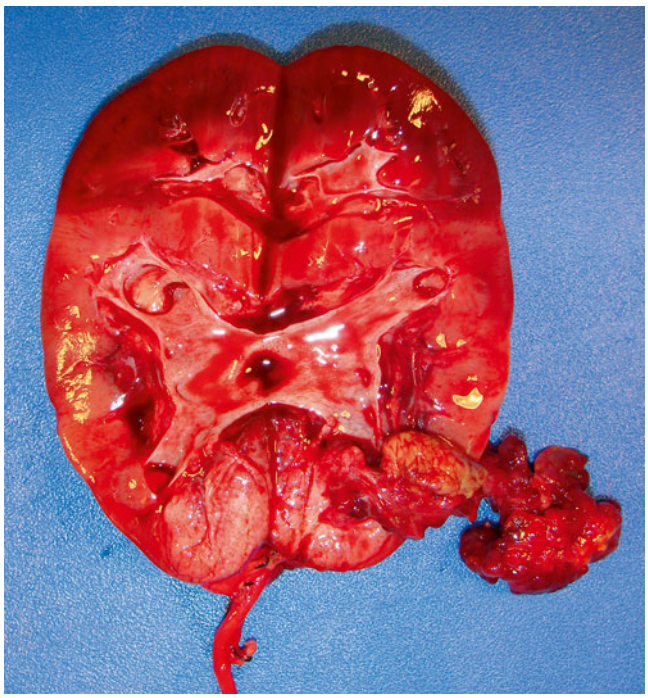

Fig. 10.3 Botryoid variant of Wilms' tumor, figure shows tumor arising in the lower pole of the kidney with a polypoid mass attached to the original tumor with a pedicle

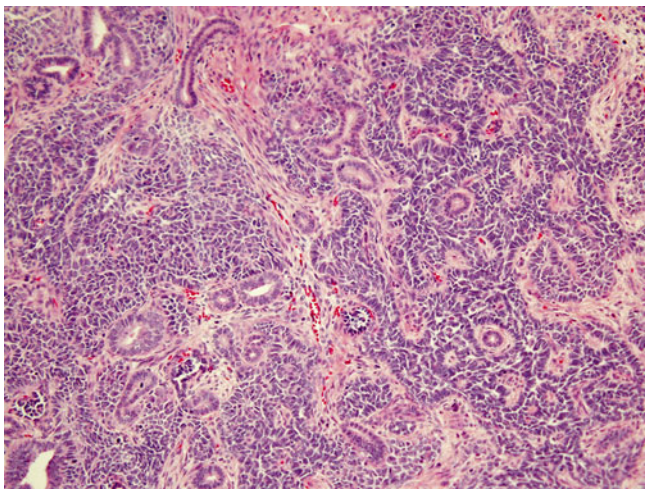

Fig. 10.4 Triphasic Wilms' showing epithelial, blastemal, and stromal components

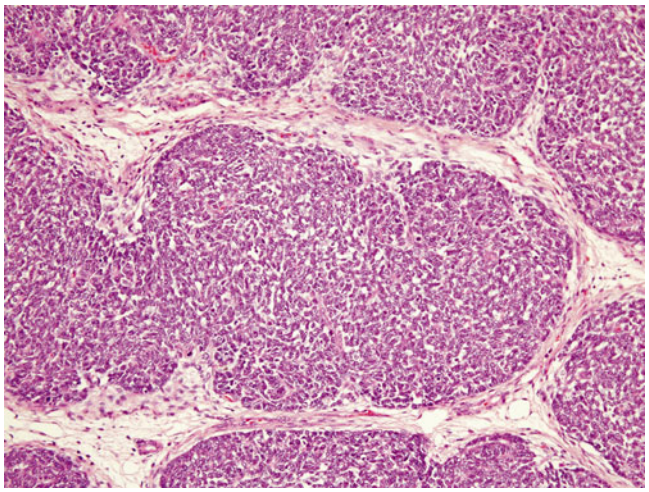

Fig. 10.5 Blastemal predominant Wilms' tumor. The tumor is composed of primitive small cells arranged in a serpentine pattern and separated by fibrovascular networks

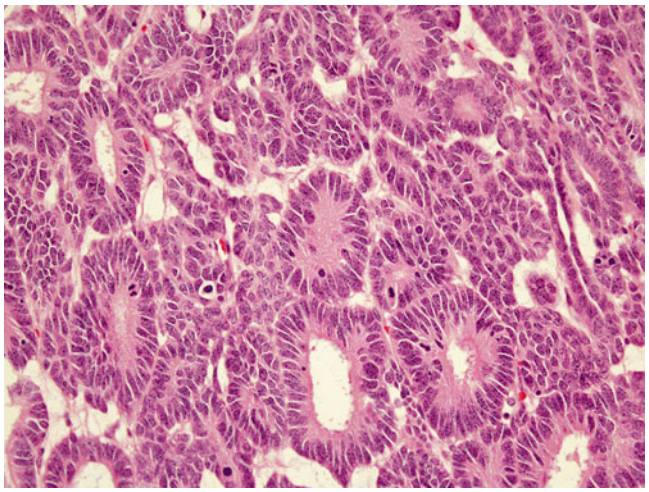

Fig. 10.6 Epithelial predominant Wilms' composed of rosette-like tubules lined by columnar epithelium with occasional mitotic figures

comprises >2/3 of a tumor, it is referred to as predominant for that specific cell type [7].

Blastemal predominant Wilms' tumors are generally more aggressive, i.e., higher stage, but usually respond to stage-specific therapy [10]. They contain sheets of small, round-to-ovoid cells with irregular nuclei, small nucleoli, and little cytoplasm, usually with mitotic figures, apoptotic bodies, and closely packed, overlapping nuclei with diffuse chromatin (Fig. 10.5) [8]. On occasion, rosette formation may resemble neuroblastoma. Growth patterns lack prognostic significance and include diffuse, serpentine, nodular, and basaloid features [7, 8].

Epithelial predominant Wilms' tumor is less aggressive but may be resistant to therapy with advanced stage [10]. It is composed of rosette-like and glomeruloid tubules lined by low columnar cells with hyperchromatic nuclei and papillary intratubular invaginations (Fig. 10.6) [7, 8]. Mucinous and squamous epithelium, neural structures, and neuroendocrine cells may also be seen [7]. With epithelial predominant Wilms' tumor, one should exclude metanephric adenoma (MA), a rare benign tumor that accounts for

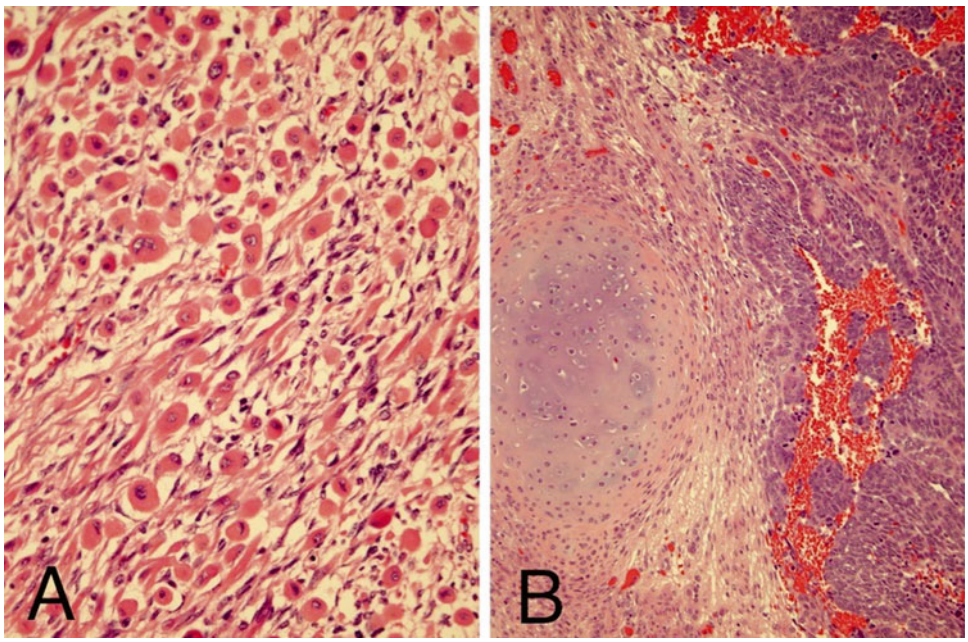

Fig. 10.7 Stromal component of Wilms' showing skeletal muscle differentiation (**a**) and cartilaginous differentiation (**b**)

~0.2–1 % of all kidney tumors [19]. MAs occur at all ages, ranging 5–80 but most commonly 40–60 years old [8, 20]. Up to 12 % of MA patients have polycythemia [21]. They are purely epithelial lesions lacking stroma and containing densely packed uniform ovoid cells with even, lymphocyte-like nuclei forming a tubular pattern, pink to clear cytoplasm and frequent psammoma bodies. Unlike Wilms' tumors, MAs contain extremely rare to absent mitoses [21], and show little or no compression of adjacent renal tissue. Metanephric adenofibromas contain both stromal and epithelial components but occur extremely rarely (only 25 cases in the NWTS series [22, 23]).

Stromal predominant Wilms' tumors, like epithelial-predominant ones, show poor clinical responses to chemotherapy [10]. They may contain hypocellular, sparse regions of immature stellate cells in a myxoid background and dense areas of primitive spindled mesenchymal cells. Other stromal cell types include smooth and striated muscle (Fig. 10.7a), adipose tissue, cartilage (Fig. 10.7b), bone, and osteoid, with muscle representing the most common differentiated stromal cell type [7, 8]. It is important in bone forming lesions to consider ossifying renal tumor of infancy, an extremely rare pediatric renal neoplasm with a benign clinical course [23]. With stromal lesions, one should also consider metanephric stromal tumor (MST), an extremely rare, entirely stromal lesion in the spectrum of metanephric neoplasms. Most MSTs occur in the first decade of life [8, 25, 26]. Characteristic concentric "onion skin" rings are observed surrounding entrapped renal tubules or blood vessels. These rings or collarettes are the most defining histological characteristic of MST.

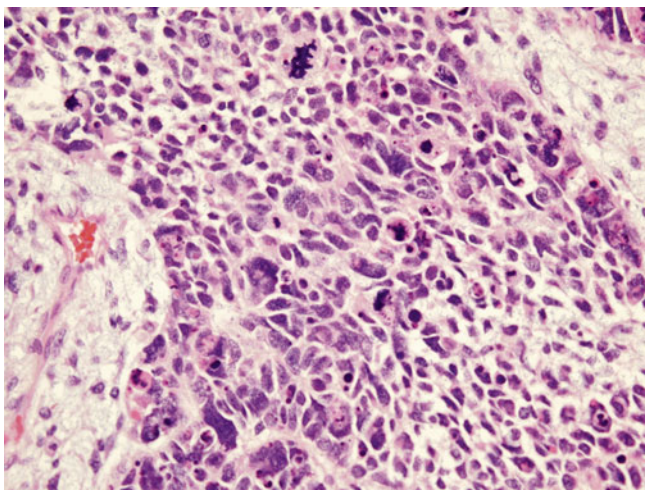

Fig. 10.8 Anaplastic Wilms' showing a multipolar mitotic figure and large anaplastic cells

Anaplasia is the major unfavorable histological variant of Wilms' tumors and accounts for 5–10 % of unilateral Wilms' tumors [1, 8, 10]. It rarely occurs in children under 2 but peaks at about 5 years of age [7, 11]. It is more common in African-American that Caucasian patients [11]. Anaplasia is defined by atypical multipolar mitotic figures, hyperchromatism, and enlarged tumor nuclei at least three times the size of adjacent ones (Fig. 10.8). Anaplasia may be focal or diffuse. With focal anaplasia, only one or two isolated intrarenal foci show anaplastic changes. Diffuse anaplasia occurs in extrarenal or multiple intrarenal locations. In stages higher than stage I, diffuse anaplasia has a significantly worse prognosis and is chemotherapy-resistant [7, 8].

Immunohistochemistry and Other Special Stains

Immunohistochemistry has a minor role in diagnosis of nephroblastomas, since the major diagnostic tool lies in tumor morphology. However, it can be helpful with needle core biopsies containing small round cell tumor. WT1, the most helpful marker, is expressed by nuclei of both blastemal and primitive epithelial cells. Primitive renal blastema also shows diffuse and strong but nonspecific positivity for CD56. Nuclear p53 expression has been reported in most anaplastic Wilms' tumors [8].

Molecular Diagnostic Features and Cytogenetics

Various genes have been implicated in hereditary and syndromic Wilms' tumor. One to 3 % of patients have a family history of inherited tumors [1, 9]. Genetically inherited cases tend to have an earlier onset and increased bilaterality [10]. Two familial genes have been specified: *FWT1* at 17q12-q21 and *FWT2* at 19q13 [10]. About 10 % of Wilms' tumor patients show associated congenital abnormalities and syndromes. Mutations of Wilms' tumor 1 (*WT1*), a tumor suppressor gene located at 11p13, occur in the Wilms' tumor, aniridia, genitourinary anomalies, mental retardation (WAGR), and Denys–Drash (DDS) syndromes (Fig. 10.9) [9]. *WT1* encodes a transcription factor important in gonadal development, ureteric budding, and nephrogenesis [1]. WAGR and DDS patients have increased risk of bilateral tumors, younger age, and renal dysfunction [10]. *WT1* mutations also occur in about 2 % of sporadic tumors [10].

Aniridia is a non-overgrowth syndrome found in 1.1 % of Wilms' tumor patients. It is caused by a defect in the *PAX6* gene located at 11p13 adjacent to *WT1*. About 40–70 % of aniridia patients have a contiguous *WT1* deletion causing Wilms' tumor [1, 10]. In addition, more than half of tumors with *WT1* mutations have coexisting ones in the beta-catenin gene (*CTNNB1*), suggesting involvement of the Wnt/beta-catenin pathway, and mutations in this gene are found in 5–15 % of Wilms' tumors overall [9, 10].

Loss of heterozygosity (LOH) of the Wilms' tumor 2 (*WT2*) gene locus located on chromosome 11p15 has been identified in up to 40 % of sporadic cases and 1–8 % of Beckwith–Wiedemann syndrome (BWS) patients [9]. BWS patients with hemihypertrophy have a 4–10 % chance of developing Wilms' tumors, 21 % of them bilateral [1, 10]. Specific genes located within the *WT2* domain include *H19* and insulin-like growth factor 2 (*IGF2*) [10]. Differential DNA methylation of these two genes reveals biallelic expression of *IGF2* in 26–77 % and hypermethylation of *H19* in 26–75 % of Wilms' tumors without LOH [9].

Wilms' tumors show LOH at chromosomes 16q and 1p in 20 % and 10 % of cases, respectively. LOH at these locations increases the risk of tumor relapse and mortality [1, 10]. Lesions that have LOH at both 16q and 1p show an even greater propensity for relapse and mortality, with the relapse-free rate dropping to 74.9 % (in combination) from 80.4 % (1p alone) and 82.5 % (16q alone) [27]. LOH at 11q occurs in 20 % of Wilms' tumors and is three to four times more common in anaplastic ones [10].

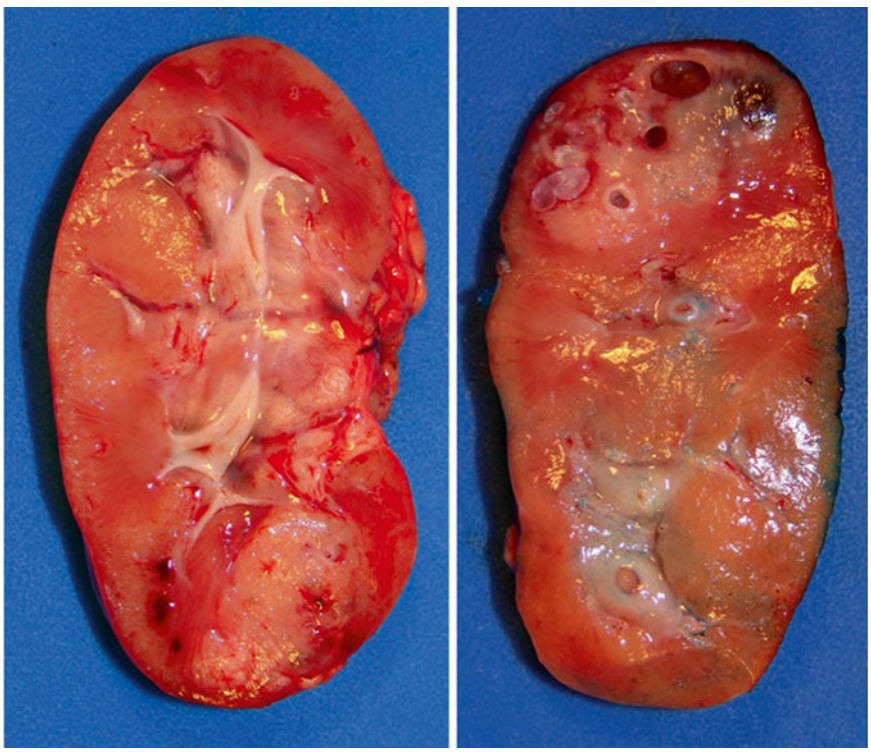

Fig. 10.9 Bilateral Wilms', nephrectomy in a patient with Denys–Drash syndrome

The Wilms' tumor gene on the X chromosome (*WTX*) on Xq11.1 is activated in up to one third of Wilms' tumors, affecting the single X in males or the active X in females as a "single hit," or monoallelic, event. *WTX* is thought to be involved in the Wnt/beta-catenin signaling pathway [1, 10].

Prognostic Features

Although survival for patients diagnosed with Wilms' tumor was once under 30 %, more than 90 % of children now have excellent outcomes [1, 11]. This marked improvement is due to adherence to protocol-based therapy that includes specific surgical approaches, enhancements in chemotherapy, and refined radiation therapy [11].

Histopathology is a major prognostic indicator, especially after preoperative chemotherapy. Blastemal Wilms' tumors are highly aggressive, and more than 75 % of this subtype present at stage III or IV. Blastema is generally responsive to chemotherapy but is associated with a high relapse rate [7, 10]. Substantial reduction in size subsequent to chemotherapy is a good prognostic indicator [7], but persistent viability after chemotherapy of a blastemal lesion indicates a poor prognosis [8]. Diffusely anaplastic tumors are resistant to chemotherapy but with complete excision have better prognosis [1]. Epithelial predominant tumors are less aggressive, and more than 80 % present at stage I. Although more resistant to chemotherapy, epithelial and stromal-predominant subtypes have a good prognosis after complete resection [1, 7].

Wilms' tumor metastasizes most commonly to the lungs and less commonly to the liver. About 12 % of patients show hematogenous metastases at diagnosis, 80 % extending to the lungs. Lymph node involvement indicates distant metastases but is difficult to assess [1, 7, 8, 11]. About 20 % of favorable histology tumors relapse after therapy [11], but patients are usually curable if there is no liver or mediastinal metastasis. However, repeated relapses indicate a very poor prognosis [7].

LOH for chromosomes 1p and 16q in stage I and II Wilms' tumors confers a significantly worse prognosis and is now used to stratify Wilms' tumor patients into different levels of risk and treatment [11].

Nephrogenic Rests and Nephroblastomatosis

Nephrogenic rests (NRs), abnormally persistent clusters of embryonal renal parenchyma tissue beyond 36 weeks of gestation, are known precursors of Wilms' tumors (WT) [28–30]. Multifocal or diffuse lesions are called nephroblastomatosis. Based on their topographic location with respect to the renal lobe, nephrogenic rests are separated into perilobar nephrogenic rests (PLNR), found at the periphery of the lobe (often subcapsular), and intralobar nephrogenic rests (ILNR), present anywhere within the kidney [8, 31, 32]. Both of these subtypes can be further classified as dormant, sclerosing, hyperplastic, or neoplastic (development into WT), depending on their eventual fate [29–32].

Nephrogenic rests are often clinically asymptomatic and are usually discovered incidentally in conjunction with Wilms' tumor [30]. Higher than average birth weight significantly correlates with NR diagnosis, especially PLNR. A small percentage of patients with NRs have associated syndromes or genetic abnormalities. WAGR and Denys–Drash syndromes are strongly associated with ILNR, along with other genital anomalies like hypospadias and cryptorchidism. Overgrowth syndromes like BWS and hemihypertrophy (HH) have a higher prevalence of PLNR but a slight correlation with ILNR. PLNRs also occur in Perlman syndrome, and trisomies 13 and 18 [29, 33].

The subtypes and various fates of NRs can be histologically distinguished based on their location, gross features, and morphologic appearance. Perilobar nephrogenic rests are predominantly composed of well circumscribed blastemal tissue (Fig. 10.2; long arrow), while ILNRs are primarily composed of stromal or epithelial tissue with irregular margins that often interdigitate with surrounding normal interstitial tissue. PLNRs usually present with multiple lesions that well demarcated from adjacent kidney, while ILNRs mostly occur as isolated or few foci that often blend with adjacent kidney [7, 30].

The pathogenesis of NRs is undoubtedly linked to that of Wilms' tumor, with perhaps over ten genes involved. Many studies have reported similar LOH in both NRs and adjacent Wilms' tumors [34–37]. Since PLNR is positioned in the periphery of the renal lobe, their genetic dysregulation likely occurs later in development than ILNR, following lobar pattern establishment. The deeper location of ILNR within the renal lobe supports an earlier developmental abnormality [29].

Imaging Features of Nephrogenic Rests

Recent advancements in imaging technology have greatly facilitated the detection of small renal tumors and nephrogenic rests. Both contrast enhanced CT and contrast enhanced MRI can detect nephrogenic rests as small as 4–5 mm, so routine intraoperative exploration of the contralateral kidney is no longer recommended [38].

Because US is widely available and relatively inexpensive, it is the primary imaging method for screening patients at risk of nephrogenic rests. On US, NR lesions are typically homogeneous and hypoechoic or isoechoic to normal kidney tissue. As nephrogenic rests are relatively less vascular than normal renal parenchyma, use of power Doppler imaging can aid in the detection of nephrogenic rests. Ultrasonography

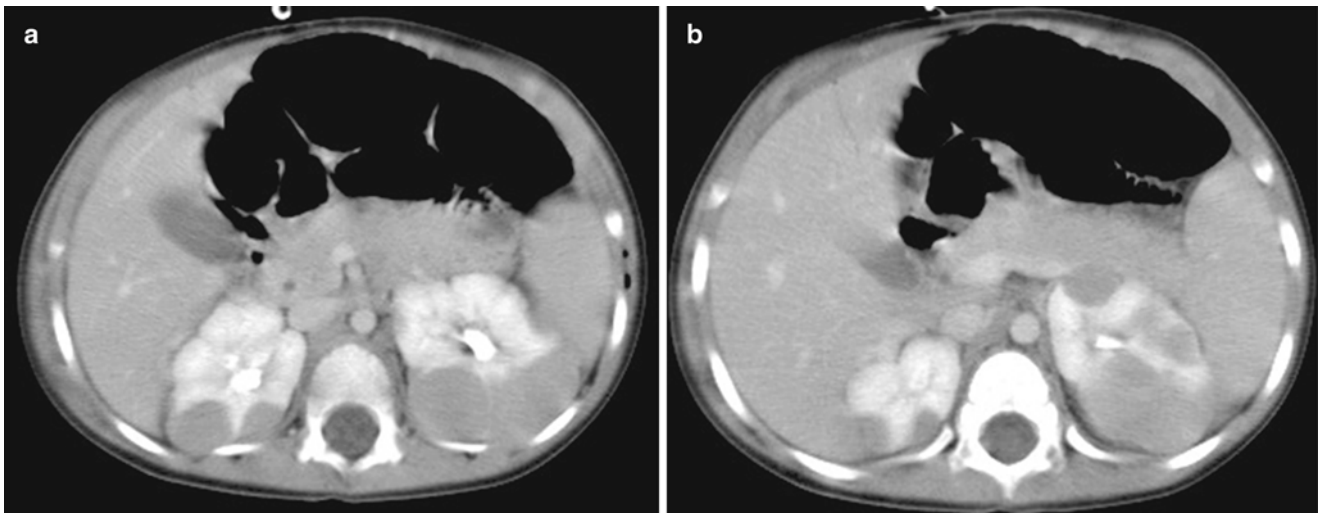

Fig. 10.10 Bilateral Wilms' tumor (nephroblastomatosis). (**a** and **b**) Axial contrast enhanced CT images of the abdomen in a 3-year-old show bilateral hypodense lesions consistent with nephroblastomatosis

can detect NR as small as 8 mm, but has a lower sensitivity than CT or MRI [18, 39, 40]. On CT, nephrogenic rests are most evident on post contrast images as homogeneous lesions that enhance less than the normal renal parenchyma. On MR, hyperplastic rests are relatively T2 hyperintense compared to normal renal parenchyma, while sclerotic rests are relatively hypointense on T2 weighted images [39]. As on CT, nephrogenic rests enhance less than normal renal parenchyma on post contrast MR images.

Imaging differentiation of nephrogenic rests from Wilms' tumor can be difficult. While nephrogenic rests tend to have a more homogeneous appearance on all imaging modalities, heterogeneity favors Wilms' tumor. Both tumor and hyperplastic rests tend to be bright on T2-weighted images [39]. The size of the lesion per se is not reliable for differentiation, as nephrogenic rests up to 5 cm in diameter have been reported [18].

The presence of multiple bilateral nephrogenic rests is referred to as nephroblastomatosis (Fig. 10.10a, b) [41]. A specific subtype of nephroblastomatosis is diffuse hyperplastic perilobar nephroblastomatosis (DHPLN), characterized by a rind of nephroblastic tissue surrounding the renal parenchyma (Fig. 10.11). On imaging the kidneys are diffusely enlarged but maintain their normal reniform shape. The nephroblastic rind is confined to the periphery of the kidney, has homogeneous attenuation/signal intensity, and enhances less than the normal kidney.

Nephroblastomatosis should be distinguished from renal lymphoma, which can also result in bilateral renal masses. Children with nephroblastomatosis are younger (<5 years of age) and lack the extensive retroperitoneal lymphadenopathy usually seen in patients with lymphomatous involvement of the kidneys.

Fig. 10.11 Diffuse nephroblastomatosis showing overgrowth of perilobar nephroblastic tissue

Cystic Nephroma and Cystic Partially Differentiated Nephroblastoma

Cystic nephroma (CN) and cystic partially differentiated nephroblastoma (CPDN) are two uncommon benign renal tumors macroscopically characterized by multilocular cysts. The two entities are well demarcated from the rest of the kidney and have no solid components except for septa composed of fibrous tissue. A distinction is drawn between CN and CPDN in that the former contains only mature septal elements such as tubules while the latter contains embryonal elements or blastema in the cyst walls [7, 8].

For CN and CPDN, there exist four criteria that characterize the lesion. First, the entity is composed entirely of cysts and their septa. The lesion is discrete from the surrounding

renal parenchyma and well demarcated. The septa are the only solid component of the tumor and completely encase the cysts without any solid expanding nodules. Finally, the cysts are lined by flattened, cuboidal, or hobnail epithelium [42].

Cystic nephroma is distinguished by its fibrous septa that is well differentiated and contains only mature elements such as tubules. Also, mature tissue such as heterologous skeletal muscle can also be seen in CN.

Cystic partially differentiated nephroblastoma macroscopically and microscopically resembles CN but contains various immature septal elements. Usually this difference is characterized by poorly differentiated blastemal cells in the septa that may contain other embryonal cell types such as stroma or epithelia comprising poorly differentiated glomeruli, cartilage, fibrous tissue, mesenchyme, fat, tubules, or striated muscle intermixed with blastemal cells [42].

CPDN shows no excessive mitotic activity or evidence of contiguous extension or vascular involvement. The "partially differentiated" term is derived from the mixture of undifferentiated blastemal tissue with partially or well-differentiated renal tissue [43]. Cystic nephroma does not present with this spectrum of differentiation.

CN is benign,as tumor-related death or metastasis has not been previously reported. Local recurrence of the lesion after resection has been reported, most probably due to outgrowth from residual tissue and not malignancy [44].

Cystic partially differentiated nephroblastomas have an equally favorable prognosis with 100 % survival in some studies. This applies to stage 1 and 2 CPDN, which are both successfully treated with complete resection of the tumor and varying amounts of chemotherapy [45]. However, one study has reported two cases in which CPDNs undertook a more aggressive course and lead to death [43]. The more aggressive potential of CPDN may be due to the malignant potential of the poorly differentiated tissue present in the septa. The extremely favorable prognosis of CN and CPDN provides additional separation from Wilms' tumor, which has a less favorable prognosis.

Imaging Features of Cystic Tumors

Cystic nephroma and cystic partially differentiated nephroblastoma are relatively uncommon benign lesions that are indistinguishable on imaging [46]. They are typically solitary, multilocular lesions sharply demarcated from an otherwise normal remaining kidney. The masses are usually large, averaging 8–10 cm in size, and involve only part of the kidney. These are multicystic lesions, and with no solid nodules, that may protrude into the renal pelvis/ureter. On sonography, the mass consists of multiple anechoic cystic areas separated by septations (Fig. 10.12a, b). These cystic areas can vary in size from microscopic to 4 cm in diameter. The microcystic areas may mimic solid areas due to the closely packed septations. On CT and MRI, CN and CPDN typically appear as well circumscribed, multicystic masses that have variable enhancement of septations on the post contrast images. The septations are typically hypointense on precontrast T1 and T2 weighted images due to fibrous tissue in them. The differential diagnosis of a multilocular cystic renal mass in a child includes cystic Wilms' tumor or renal cell carcinoma; clear cell sarcoma; cystic variants of mesoblastic nephroma; and segmental

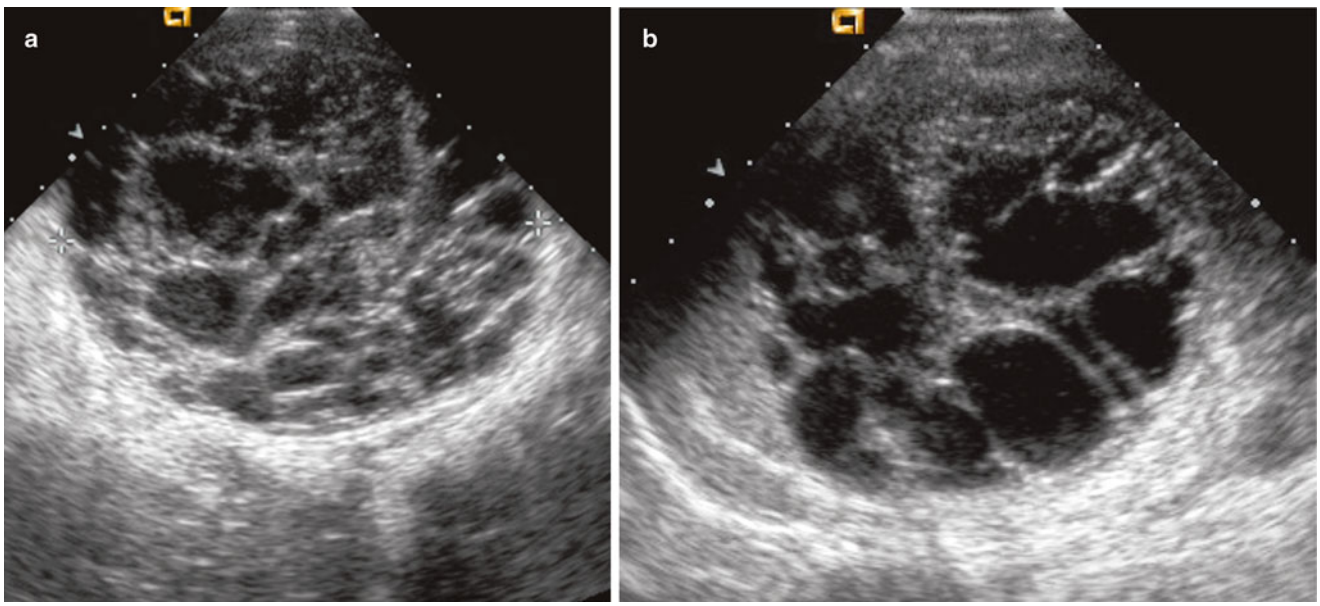

Fig. 10.12 Multilocular cystic nephroma. (**a** and **b**) Sonographic images from a 9 month old show a multiloculated cystic mass arising from the left kidney. No solid components are noted. Pathology confirmed a multilocular cystic nephroma

forms of multicystic dysplastic kidney. The presence of solid components within a cystic mass should make one consider a diagnosis other cystic nephroma/cystic partially differentiated nephroblastoma. If a cystic pulmonary lesion is identified in a child with a multicystic renal mass, this should lead one to consider a DICER 1 mutation with cystic nephroma and coexistent pleuropulmonary blastoma [47].

Mesoblastic Nephroma

Definition

Mesoblastic nephroma (MN), also known as congenital mesoblastic nephroma (CMN), is a mesenchymal rare renal neoplasm most commonly diagnosed prenatally or in early infancy. This spindle cell neoplasm can be classified as either classic or cellular or mixed pattern [7, 8].

Clinical Features and Epidemiology

Incidence and Prevalence

Although CMN only represents less than 5 % of all pediatric renal neoplasms, it is the most common congenital renal tumor, with over 90 % of patients diagnosed before age 1 and almost no patients presenting after the age of 3. The cellular variant represents approximately 40–60 % of CMN, with the classical and mixed subtypes constituting the remaining percentage with about an equal prevalence [8, 48].

Population Features

The majority of renal tumors diagnosed within the first 6 months of life are CMN, so it must be included in the differential diagnosis of any infant with a renal mass. Because its incidence drops off significantly after early childhood, diagnosis of any spindle cell tumor as CMN must be questioned in patients older than 3 years. There does not appear to be any definitive gender predisposition, but some studies report a slight male prevalence [49, 50]. The general median age of diagnosis is approximately 20–35 days, with the cellular type (median: 3–4 months) being diagnosed at a significantly older age than the classic (median: 7 days) or mixed (median: 2 months) variants [49, 50].

Presenting Symptoms and Signs

Most patients present with an asymptomatic abdominal mass discovered upon physical examination or after imaging analysis. Other symptoms include abdominal swelling and protrusion, abdominal pain, hypertension, hypercalcemia, and hematuria [48, 50, 51]. These tumors may cause polyhydramnios during pregnancy, requiring preterm delivery in a reported 71 % of CMN associated fetuses [48].

Imaging Features

Mesoblastic nephroma presents as a solitary unilateral mass with variable cystic/solid mass in the neonate, typically within the first 3 months of life [52]. Mesoblastic nephroma has been detected in utero on prenatal sonography as a heterogeneous renal mass as early as 26 weeks. These masses can be associated with polyhydramnios and premature labor [53]. The classic and cellular subtypes of CMN differ in their imaging appearances. Classic CMN presents as a uniform soft tissue mass with minimal, predominantly peripheral, enhancement seen on post contrast CT or MRI. However, the cellular variant of CMN can have a more heterogeneous appearance and can vary from a predominantly cystic to mixed solid and cystic mass (Fig. 10.13a, b). Areas of cystic change, necrosis, and hemorrhage can be seen on all imaging modalities in cellular CMN, corresponding to its pathologic appearance.

Pathology

Gross and Microscopic Features

Grossly, the tumor is usually solid but rarely can have a prominent cystic appearance. Congenital mesoblastic nephroma tend to be firm pale to tan-colored lesions (Fig. 10.14), with the cellular variant being softer and more likely to demonstrate necrosis or hemorrhage than the classic variant. The mixed subtype shows both characteristics. The tumor often infiltrates normal adjacent renal parenchyma and perinephric fat. As previously mentioned, the cellular type is usually much larger in volume than the mixed or classic types [7, 8, 48].

Histologically, classic CMN demonstrates morphology similar to that of uterine leiomyoma and infantile fibromatosis; it contains bundled spindle cells, infrequent mitosis, and absence of necrosis (Fig. 10.15a). The spindle cells lie within collagenous stroma, show an interlacing fascicular pattern, and infiltrate surrounding renal parenchyma as finger-like projections. The cellular variant has a more malignant appearance, with an increased nuclear: cytoplasmic ratio, cellularity, and mitotic index and significantly more necrosis and hemorrhage (Fig. 10.15b). CMNs lack the blastemal components observed in Wilms' tumor and do not demonstrate characteristic vascular patterns, nuclear grooves, or clear cells as seen in clear cell sarcoma of the kidney [8, 51, 52]. However, they often entrap renal tubular elements, which may show atypia.

Immunohistochemistry and Other Special Stains

The most common immunohistochemical characteristic of CMN is diffuse nonspecific reactivity for vimentin and focal reactivity for smooth muscle actin [8, 51]. The tumor usually

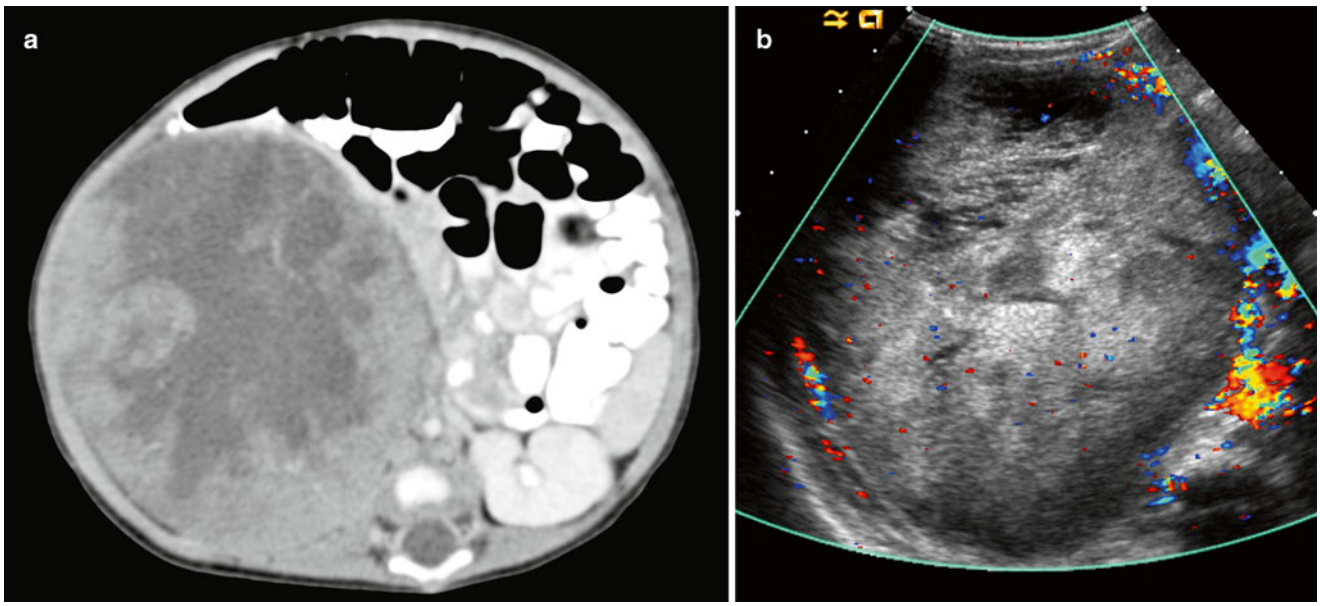

Fig. 10.13 Mesoblastic nephroma. Axial contrast enhanced CT (**a**) and color Doppler image (**b**) from a 54 day old neonate shows a heterogeneous, well circumscribed mass consistent with a cellular variant of mesoblastic nephroma

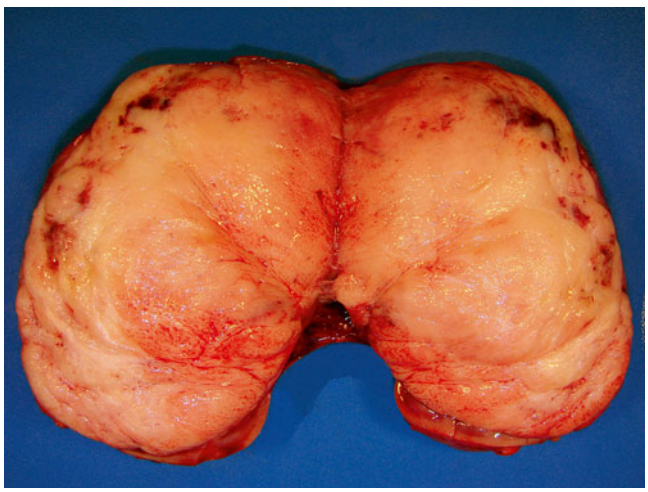

Fig. 10.14 Congenital mesoblastic nephroma showing firm, pale-colored cut surface with small cystic and hemorrhagic areas

does not show immunoreactivity for desmin, S-100, cytokeratin, AE1/AE3, epithelial membrane antigen, bcl-2, or CD99 [51, 54].

Molecular Diagnostic Features and Cytogenetics

Recent cytogenetic studies have found strong genetic correlations between the cellular variant of CMN and congenital infantile fibrosarcoma (CFS). Using RT-PCR and fluorescence in situ hybridization, a study found that five out of six cellular CMN tumors and five out of five CFS tumors tested were found with the same t(12;15)(p13;q25) translocation that resulted in a *ETV6-NTRK3* (aka *TEL-NTRK3*) gene fusion [55]. Both of these entities have also been associated with genetic polysomies at chromosomes 8, 11, 17, and 20 [55, 56], with trisomy 11 being strongly correlated with CMN. Because cellular CMN and CFS have similar histological and morphologic features and the same genetic abnormalities, these two neoplasms appear to represent the same entity, with cellular CMN being the renal variant. Additionally, it has been reported that primary bronchopulmonary fibrosarcoma (BPFS), a rare lower respiratory neoplasm affecting children and young adults, also carries the t(12;15) *ETV6-NTRK3* genetic abnormality [55, 57]. Thus, we consider CMN and BPFS as visceral variants of CFS. The same t(12;15) *ETV6-NTRK3* fusion does not appear with classic CMN, which may be found in conjunction with cellular CMN in the mixed subtype. *ETV6-NTRK3* fusion is also found in a dissimilar tumor, secretory carcinoma of the breast [55].

Prognostic Features

Mesoblastic nephroma is usually a benign neoplasm with overall good prognosis after nephrectomy. Local recurrences and metastasis to the brain, lungs, heart, bone, and liver have been reported, with the majority of these relapses being associated with the cellular variant of CMN. Overall, about 10 % of CMN tumors relapse and such recurrences almost always

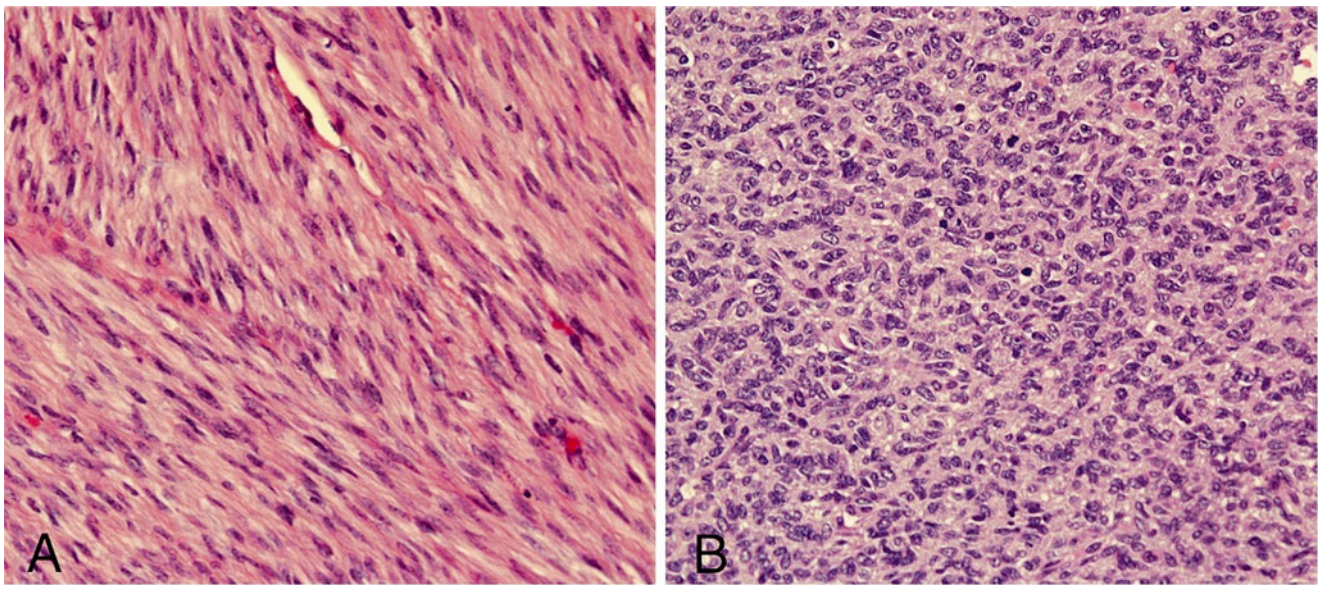

Fig. 10.15 (**a**) Classic CMN showing interlacing fascicular pattern of benign spindle cells. (**b**) Cellular variant showing sheets of round cells with increased nuclear cytoplasmic ratio and abundant mitotic figures

occur during the first year after initial diagnosis [48]. The survival overall is very high at >95 %. Late stage cellular CMN occurring in patients older than 3 years carries the worst prognosis. Adjuvant chemotherapy is not recommended after complete resection [7, 49].

Clear Cell Sarcoma of the Kidney

Definition

Clear cell sarcoma of the kidney (CCSK) is rare renal pediatric neoplasm with a generally unfavorable prognosis [58, 59]. Because of its greater tendency towards bone metastasis, the tumor has been called bone metastasizing renal tumor of childhood, and it has also been referred to as sarcomatous Wilms' tumor [7].

Clinical Features and Epidemiology

CCSK is extremely rare; only 20 new cases are reported annually in the USA [60]. Overall accounts for 3–5 % of all pediatric renal neoplasms. Nevertheless, CCSK still represents the second most common childhood renal tumor [61].

CCSK patients present at a mean age of 36 months; most are diagnosed between ages 2 and 3 years, with a large decline in incidence afterwards [60]. It is extremely uncommon during the first 6 months of life and has seldom been reported in adolescents and adults [59, 60]. Patients have a male predominance with an average ratio of 2:1 [7, 59, 60].

Clinical manifestations of CCSK include an abdominal mass or swelling, abdominal pain, constipation, decreased appetite, fever, gross hematuria, hypertension, and vomiting [59, 63]. Approximately 5 % present with metastasis, with the lymph nodes being the most common site [8, 60]. According to the National Wilms' Tumor Study (NWTS), approximately 26 % of CCSK cases present at stage I, 35 % at stage II, 34 % at stage III, and 5 % at stage IV, with negligible numbers at stage V [59, 60].

Imaging Features

Clear cell sarcoma typically presents as a large, solid but inhomogeneous renal mass with cystic/necrotic areas, that on imaging is indistinguishable from WT [64]. Foci of calcification can be present in up to 25 % of cases. This aggressive tumor can have extracapsular spread and vascular extension at the time of initial presentation, though the latter is less common than in WT cases. The most common sites of metastasis are bone, lymph nodes, lung, and liver.

Pathology

Gross and Microscopic Features

Grossly, CCSKs are large, soft, and gray-tan to white in appearance. They are uniform, fleshy, well circumscribed,

sharply demarcated, and almost always present unilaterally in the kidneys. Tumors are usually solid but may be focally cystic with necrosis and hemorrhage [7, 8, 54, 63]. The tumors often involve renal medulla and may replace and distort the entire kidney [7, 59]. Renal vein invasion occurs in approximately 5 % of cases [59, 60]. Tumors measure between 2.3 and 24 cm [60].

Perhaps the most diagnostically difficult aspect of CCSK is its histological variability: nine variations have been described [59, 60]. The classic pattern contains cords or nests of ovoid, epithelioid, and spindle shaped cells separated by consistently spaced fibrovascular septa [67, 60]. These septa characteristically feature branching or "chicken-wire" capillaries that vary in width. Tumor nuclei are uniform in shape, and their cytoplasm is clear to pale with an ill-defined cell border (Fig. 10.16) [60, 63]. Although over 90 % of CCSK predominately or focally demonstrate the classic pattern, most also present one of the other eight identified histologic variants, percentages: myxoid (50 %), sclerosing (35 %), cellular (26 %), epithelioid (13 %), palisading (11 %), spindle cell (7 %), storiform (4 %), and anaplastic (2.6 %) [60]. The different patterns are essentially varying alterations of the cord/nest or septal cell appearance, and they therefore cannot be separated as distinct biological entities.

Immunohistochemistry and Other Special Stains

Clear cell sarcoma of the kidney can only be definitely diagnosed by microscopic analysis Immunohistochemistry has limited usefulness in excluding other renal neoplasms. Almost all CCSKs are nonspecifically immunoreactive for vimentin [59, 60]. Positive expression has also been associated with NGFR, muscle specific actin, bcl-2, alpha-1-antitrypsin, and CD56 [7, 8, 54, 59, 60]. CCSKs are negative for cytokeratin, CD99, S100, desmin, WT1, von Willebrand factor, epithelial membrane antigen, CD688, and NSE [7, 59, 60, 63].

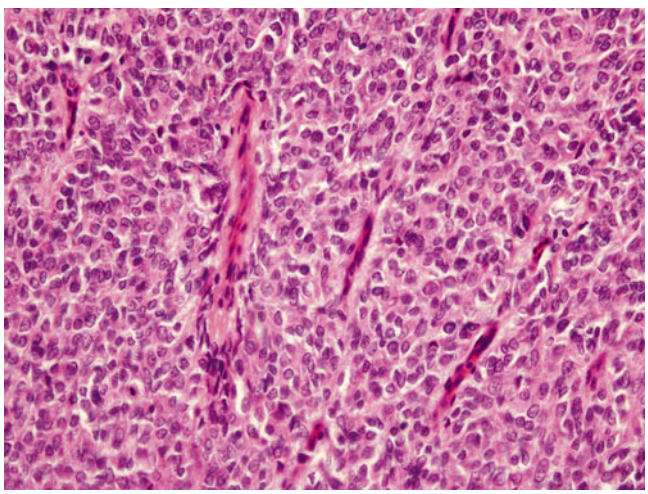

Fig. 10.16 Clear cell sarcoma, classic pattern showing cords of ovoid epithelioid cells separated by fibrovascular septa

Molecular Diagnostic Features and Cytogenetics

Various genetic abnormalities are associated with CCSK, but no common consensus has been established as to its probable underlying molecular pathogenesis. Among the most common genetic defects reported is a t(10;17)(q22;p13) that may be associated with *TP53* [58, 65]. *TP53* expression occurs with anaplastic CCSK [60], but, *TP53* mutations have not been consistently implicated among the other subtypes. One study found a rearrangement of chromosome 17 (*YWHAE*) and 10 (*FAM22*) that resulted in an *YWHAE-FAM22* transcript in some CCSK [65]. Other reports note t(1;6)(p32.3;q21) and t(2;22).

The most common loss or gain mutations in CCSK include a 1q gain and a 19p loss, with 16p loss, 10q loss, 4p loss, and 10q gain being less common [59, 65].

Studies have reported loss of imprinting in insulin-like growth factor 2 (IGF2) in CCSK comparable to Wilms' tumor [66]. One study reported an up-regulation of neural markers with simultaneous activation of Sonic hedgehog and phosphoinositide-3-kinase/Akt pathways [61].

CCSK has not been associated with genetic syndromes or familial inheritance.

Prognostic Features

Traditionally, a renal neoplasm with unfavorable prognostic outlook, recent advancements in treatment have greatly improved the overall survival of CCSK to about 70 % [63]. The addition of doxorubicin chemotherapy to existing treatment regiments greatly improved the outcome contributing to a 98 % survival rate among those diagnosed at stage 1 and an increase in the survival stage 2 or 3 patients from 30 to 70 % [60], with decreased bone metastasis to about 20 % [7]. Patient age is an important prognostic factor, with those being diagnosed at less than 2 years or greater than 4 years of age (outside of the 2–4 age median) having a lower survival rate. Tumor necrosis has been linked to lower survival rates [50].

The likelihood of relapse after initial CCSK treatment is approximately 20–40 %, with the most common sites of relapse being bone, lung, brain, and abdomen [59]. CCSK has a propensity to metastasize longer after nephrectomy than Wilms' tumor (median time 24 months), so that patient monitoring is required for longer periods of time [60].

Malignant Rhabdoid Tumor of the Kidney

Definition

Malignant rhabdoid tumor of the Kidney (RTK) is one of the most lethal pediatric neoplasms and the most lethal childhood renal tumor [67, 68]. This tumor is extremely rare and arises primarily in children less than 2 years of age. It is characterized by mutation of the *INI1* gene.

Clinical Features and Epidemiology

Rhabdoid tumor of the kidney is an extremely rare pediatric neoplasm, accounting for only about 2 % of all renal tumors in the National Wilms' Tumor Study (NWTS) [7, 68].

This neoplasm occurs almost exclusively in young children, with about 80 % of cases occurring in patients younger than 2 years of age and 95 % of cases in patients less than 3 years [2, 7]. Almost no cases are reported in children over the age of 5 [8]. The average age at presentation is approximately 17 months with a male predominance of 2:1 [68].

Children with RTK present with an abdominal mass sometimes accompanied by painful swelling, hematuria, fever, hypertension, hypercalcemia, and elevated serum levels of parathormone activity [67–70]. The majority of cases exhibit metastatic spread at the time of diagnosis, with only about 15 % of patients presenting at stage 1 or 2 (tumor limited to the kidney and not extending beyond renal capsule). The most common sites of metastasis include the lungs, abdomen, liver, brain and bone [68].

Imaging Features

Rhabdoid tumor of the kidney is a highly malignant neoplasm which presents as a large, centrally located, heterogeneous soft-tissue mass involving the renal hilum. The margins of this aggressive tumor tend to be indistinct, as opposed to WT which can form a pseudocapsule around it. It has been suggested that the presence of a subcapsular fluid collection, lobulated contour of the mass, and linear areas of calcification between the lobules should raise suspicion for a rhabdoid tumor of the kidney [71, 72]. However, these are nonspecific findings which can be seen with more common renal tumors such as WT as well. The diagnosis of a rhabdoid tumor should be considered in a young child (typically <2–3 years of age), with an aggressive appearing renal tumor. MRI of the brain is recommended in all children with rhabdoid tumor of the kidney due to the known association with synchronous or metachronous central nervous system rhabdoid tumors and the risk of brain metastasis. Other reported sites of metastasis include lung, liver, and heart [73].

Pathology

Gross and Microscopic Features

Grossly, RTKs present as large masses almost entirely replacing the kidney, with an average weight of 389 g and tumor diameter of 9.6 cm [68]. The surface of the lesion is soft, solid, and gray-pink to tan in color, often with extensive necrosis and hemorrhage [8, 68, 70]. Tumors are usually unencapsulated and show vascular invasion and infiltration into the renal parenchyma. Most of the lesions are unilateral; bilateral involvement almost always results from metastasis [68].

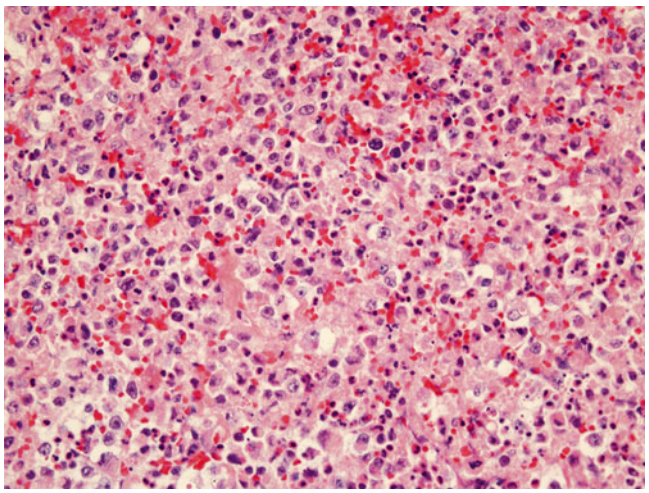

Fig. 10.17 Rhabdoid tumor, classical type composed of monomorphous noncohesive sheets of tumor cells showing vesicular nuclei, and prominent nucleoli. Note: tumor necrosis and hemorrhage

Histologically, the majority of RTK neoplasms present with "classical" morphology, but variations exist [68]. The classical type is characterized by noncohesive sheets of tumor cells showing vesicular nuclei, prominent nucleoli, and abundant eosinophilic cytoplasm containing large oval hyaline inclusions (Fig. 10.17) [7, 8, 68]. However, the presence of cytoplasmic inclusions is variable. Nuclear pleomorphism is moderate and, mitoses are numerous. Other morphologic patterns include sclerosing, epithelioid, spindled, lymphomatoid, vascular, pseudopapillary, and cystic variations [68]. The presence of multiple intratumoral patterns is not uncommon, as no single pattern (including classical) composes more than 65 % of the lesion in most cases. Transitions between patterns are often gradual, but some lesions show abrupt changes similar to collision tumors [68].

Immunohistochemistry

RTK shows strong immunopositivity for vimentin in the cytoplasmic inclusions as well as in the cytoplasm [68]. INI1 immunoreactivity is characteristically absent in the nucleus of RTK tumor cells, with such reactivity being demonstrated in the cells of almost all other pediatric renal neoplasms except for medullary carcinoma [8]. Other occasionally positive markers include alpha-1-antichymotrypsin, desmin, epithelial membrane antigen, myoglobin, neurofilaments, neuron-specific enolase, and S100 protein [7].

Molecular Diagnostic Features and Cytogenetics

Rhabdoid tumors can occur in various extra-renal sites including soft-tissue and the central nervous system. The common genetic abnormality among all rhabdoid tumors is the mutation and downregulation of the *SMARCB1/hSNF5/*

INI-1 gene found at chromosome 22q11 [74]. *SMARCB1* is a tumor suppressor gene that encodes for the SMARCB1 protein, a subunit in the SWI/SNF chromatin remolding complex that has been implicated in various processes including neural development, transcriptional regulation, and cell-cycle regulation [75]. SMARCB1 protein interaction with other proteins is implicated in many RTK pathways.

Abnormalities in genes associated with normal neural development, such as *DOCK4*, *PTN*, *PTPRK*, and *SPOCK1* [76], are commonly found in RTK of *B1*. SMARCB1 protein is necessary for normal neural development, and it interacts with proteins such as pleiotrophin (encoded by PTN), which regulates differentiation and proliferation of neural stem cells. Other neural differentiation pathways, such as the Notch pathway, are compromised in RTs, leading to the hypothesis that these neoplasms may arise in neural progenitor cells with arrested development [76].

Normal expression of *SMARCB1* plays an important role in transcriptional regulation. An intact SWI/SNF complex regulates gene expression by disrupting DNA-histone interactions and allowing transcriptional proteins (activating or repressing) more efficient access to their targets. SMARCB1 hypothetically links SWI/SNF with transcriptional regulators [76]. Proteins known to physically interact with SMARCB1 include ATP1B1, FZD7, and PTN, all of which are implicated in RT development [74, 76]. SMARCB1 also interacts with trithorax and polycomb protein families, implicated in transcriptional activation and repression respectively [76]. The balance between the two families is mediated by a direct interaction between SMARCB1 and MLL1 protein, a member in the trithorax family. MLL1 protein facilitates transcriptional activation by methylation of histone H3 lysine 4 (H3K4), while the polycomb family is responsible for transcriptional repression through methylation of histone H3 lysine 27 (H3K27). With the disruption of this interaction, the trithorax family is unable to adequately activate transcription levels resulting in an overall transcriptional repression from the polycomb family.

A marked downregulation of cyclin-dependent kinase inhibitors *CDKN1A* and/or *CDKN2A* due to a loss of interaction with *SMARCB1* gene products occurs in RTs [76]. Without this kinase inhibition, RT cells more readily proliferate. Genes implicated in tumor invasion and metastasis are also upregulated in RTs; these include *MMP12*, *NCOA3*, *RSU1*, *SPP1*, *TRFC*, and *ZNF217*. Conversely, genes associated with tumor suppression, such as *COL18A1*, *DOCK4*, *PTPRK*, and *SELENBP*, are downregulated in RTs [76].

Prognostic Features

Rhabdoid tumor of the kidney has an extremely poor prognosis, with an overall survival rate of about 23 % [76]. More than 70 % of patients present with metastasis, and over 80 % demonstrate metastatic spread within 3–4 months after diagnosis [7, 76]. Tumor stage at diagnosis is strongly correlated to survival, with the vast majority of survivors presenting at stage I or II [7]. Despite intensive chemotherapy, the survival rate has not increased, and RTK remains resistant to most forms of medicinal therapy. One study, however, has reported the successful use of ICE (isofamide, carboplatin, and etoposide) and VDCy (vincristine, doxorubicin, and cyclophosphamide) in the treatment of a stage IV RTK [70]. This patient remained recurrence free for 24 months after treatment. A higher survival rate is found among females (56.3 %) as compared to males (11.1 %) [68].

Pediatric Renal Cell Carcinoma

Definition and Overview

Pediatric renal cell carcinomas (PRCC) are rare neoplasms accounting for approximately 2–5 % of all childhood renal tumors [77, 78]. These entities although sharing the same name generally differ from adult renal cell carcinoma in their histology and cytogenetic characteristics. Conventional or pure clear cell carcinoma of the kidney (accounting for about 70–80 % of adult RCC neoplasms) is extremely uncommon in children, comprising about 6–20 % of PRCC and almost never carrying the characteristic chromosome arm 3p abnormality found in adults [79, 80]. The more common subtypes of childhood RCC include translocation-associated neoplasms (20–40 %) and papillary PRCC (30 %) [77]. Renal medullary carcinoma (RMC) associated with sickle cell trait and oncocytic RCC associated with post-neuroblastoma treatment have been described but are extremely rare. These four are described separately below. Additionally, about 25 % of PRCCs differ histologically from the aforementioned subtypes and are classified as PRCC NOS [77].

Generally, PRCC has a reported median age of anywhere from 9 to 17 years, differentiating these lesions from most other pediatric renal neoplasms, which occur earlier in life [78]. No racial or gender predominance has been consistently reported, although some indicated higher prevalence in African-Americans and in females. Unlike adult RCC, in which lesions are often found incidentally, patients with PRCC usually present with symptoms including protruding abdominal mass, abdominal pain, fever, hematuria, and weight loss, with only about 10 % presenting asymptomatically [8, 78]. Additionally, children with PRCC are more likely to be found with locally advanced disease at diagnosis as compared with adults [78]. Also, a significant number of PRCC patients present in the context of underlying syndromes such as von Hippel–Lindau disease and tuberous sclerosis or have been previously treated with chemotherapy

for another pediatric neoplasm [70]. Each subtype carries unique cytogenetic characteristics detailed below. Overall, the 5-year survival rate is approximately 30–90 % depending on the subtype and staging. Patients with lymph node (LN) metastasis (about 30 % of cases) have about a 90 % survival rate, but the rate drops to 10–15 % in cases with non-localized/non-nodal metastasis [80]. As with other pediatric lesions, PRCCs are generally treated by radical nephrectomy, with surgical impact on overall prognosis depending on disease stage [80]. Additionally, the effectiveness adjunct retroperitoneal lymphadenectomy in addition to radical nephrectomy is controversial [81, 82]. Targeted therapies have become the standard in adult RCC treatment, while the role of such therapies has not been established in children.

Translocation-Associated PRCC

Translocation-associated PRCC forms a distinct group of neoplasms occurring almost exclusively in children and adolescents. The most common translocations involve the *TFE3* gene on chromosome Xp11.2 and less commonly the *TFEB* gene on chromosome 6p21 [77, 80]. Genetic abnormalities in the *TFE3* gene can result in multiple gene fusion products, with the *ASPL-TFE3* fusion (found also in alveolar soft-part sarcoma) involving chromosome 17 [t(X;17)(p11.2;q25)] and the *PRCC-TFE3* fusion involving chromosome 1 [t(X;1p11.2;q21)] being the two most common types [77]. Other less common fusions involving this gene include *CLTC-TFE3* [t(X;17)(p11.2;q23)], *PSF-TFE3* [t(X;1)(p11.2;p34)], and *NONO-TFE3* [inv(X)(p11;q12)] [83–85]. These fusions result in increased expression of TFE3 protein [8]. *TFE3* and *TFEB* genes belong to the microphthalmia transcription factor (MiTF) family implicated in helix-loop-helix leucine zipper transcriptional function [80].

Additionally, these neoplasms can rarely occur in children who received prior chemotherapy with presentation onset ranging from 4 to 13 years after treatment. Such a correlation may be due to treatment with DNA topoisomerase II inhibitors and/or alkylating agents that may facilitate chromosomal instability [80].

Grossly, translocation associated PRCCs are usually unifocal, circumscribed neoplasms, with a tan-yellow appearance and hemorrhage and necrosis (Fig. 10.18) [77, 78]. Multifocal PRCCs are rare and usually occur in the context of other underlying syndromes including von Hippel–Lindau disease and tuberous sclerosis [77].

Generally, the microscopic features of translocation PRCCs are consistent regardless of the variant (Fig. 10.19). Papillary morphology is common with many clear cells [8, 79]. Cells are arranged in nests, tubules, and papillae with clear to markedly granular eosinophilic cytoplasm [8, 77]. The cells have distinct infiltrative borders, with entrapment of renal tubules and vascular invasion commonly observed. Prominent nucleoli and psammoma bodies are commonly present in these neoplasms [78, 84, 85]. Some trends have emerged correlating to specific translocation variants but are not consistently reliable. For example, the *ASPL-TFE3* variant tends to have more abundant cytoplasm, psammoma body formation, and prominent nucleoli than *PRCC-TFE3*, while the latter tends to present with less calcification and be more nested and compactly arranged [8, 77].

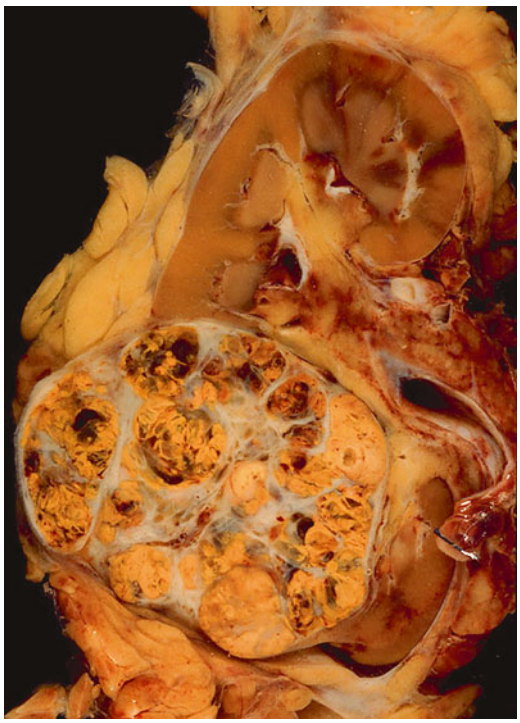

Fig. 10.18 Renal cell carcinoma showing a circumscribed neoplasm with a tan-yellow appearance, hemorrhage, and necrosis

Immunohistochemistry is important in the diagnosis of PRCCs, because a significant amount cannot be easily distinguished from other PRCC variants and even other pediatric renal neoplasms. Nuclear expression for TFE3 protein is both sensitive and specific in diagnosing all types of this PRCC variant [77]. Translocation associated PRCCs differ from adult RCC in that the former rarely stains for vimentin and various epithelial markers such as AE1/AE3, Cam 5.2, cytokeratin 7, and EMA [77, 80]. Additionally, cathepsin-K positivity has been reported [80]. Like adult RCC, translocation PRCCs stain for CD10, AMACR, and RCC antigen, while being negative for CD117. *TFEB*-RCCs can be further distinguished from other variants in that they show positivity for melanocytic markers HMB-45 and Melan-A.

The overall prognosis of translocation PRCCs is unclear with some studies reporting favorable outcome even with LN metastasis while others indicating a poor prognosis regardless of stage at presentation. However, distant metastasis is generally associated with poor prognosis, with further tumor progression being seen in 45 % of these cases [77]. The

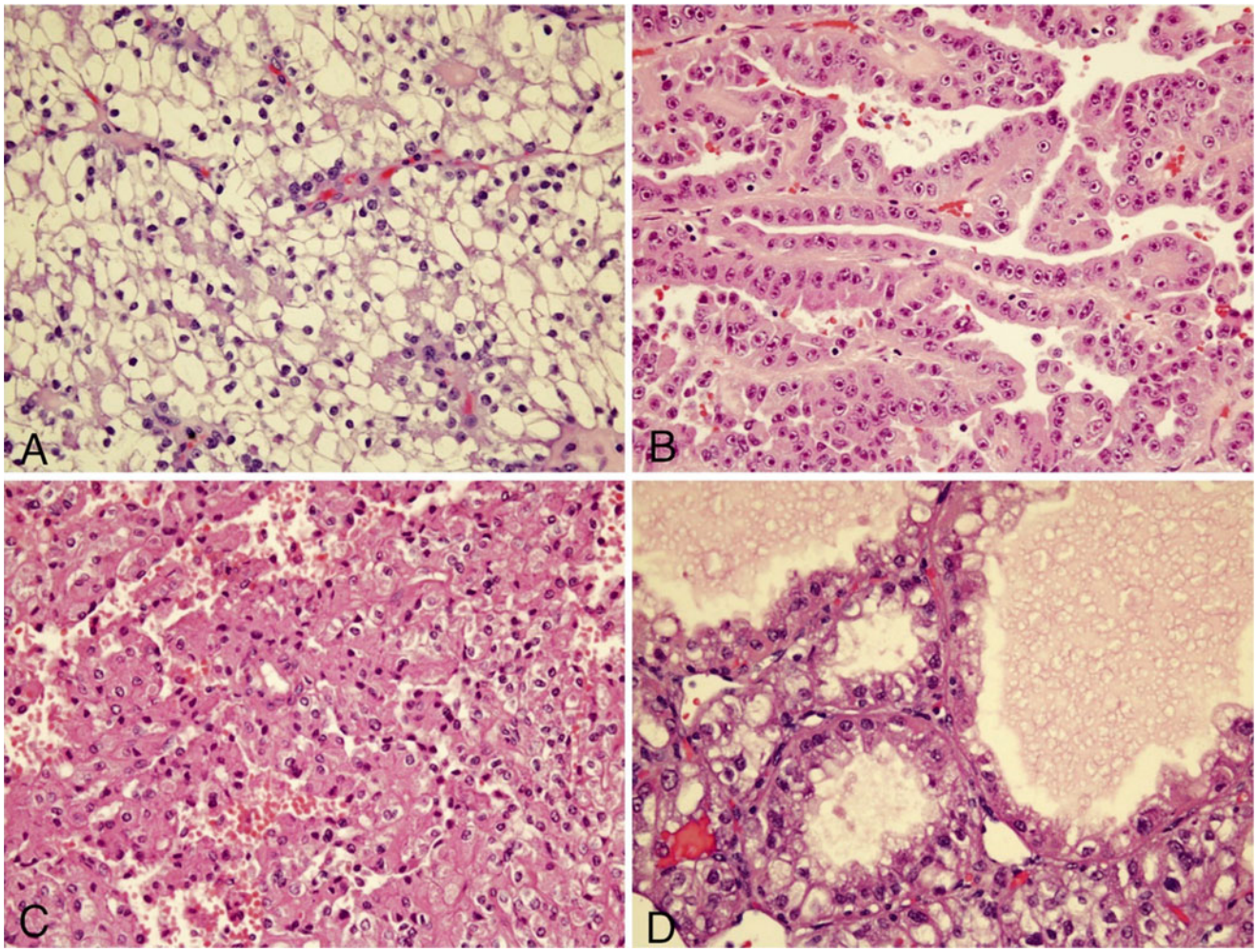

Fig. 10.19 Clear cell carcinoma, various patterns: sheets of clear cells showing well-defined cell borders (**a**), papillary configuration (**b**), showing granular eosinophilic cytoplasm (**c**), and papillary pattern with intracytoplasmic acidophilic inclusion (**d**)

TFEB variant has been reported to have a less aggressive clinical course compared with TFE3 [8]. Aside from radical or partial nephrectomy, the optimal treatment for these lesions remains undetermined. The use of antiangiogenics and targeted therapies has been reported with limited success [87–89].

Papillary PRCC

Papillary PRCC is the second most common subtype of PRCC and accounts for approximately 30 % of all cases [77]. This neoplasm is further separated into two groups, type 1 and type 2. Many patients with this lesion present in the context of preexisting tumors, which include metanephric adenoma, metanephric adenofibroma, and Wilms' tumor [77].

Papillary RCC has a similar gross presentation to translocation associated PRCCs, occurring unifocally and having circumscribed borders [77]. It has a tan yellow appearance and may be hemorrhagic [90]. Type 2 lesions tend to be larger (mean: 5.6 cm) than type 1 (mean 3.8 cm) and are also more likely to show extracapsular invasion [91].

Microscopically, cells of papillary PRCCs are arranged in papillary and tubular configurations and often contain foamy macrophages [77]. Specifically, type 1 lesions are characterized by cuboidal cells with scant cytoplasm arranged in a single layer, while type 2 lesions have a higher nuclear grade with more eosinophilic cytoplasm and are characterized by pseudostratification. These neoplasms are usually encapsulated but penetration of the surrounding fibrous pseudocapsule is not uncommon. Both subtypes of papillary PRCC can be difficult to diagnose, as type 1 has considerable histological overlap with metanephric adenoma and well-differentiated Wilms' tumor and type 2 is histologically similar to t(X;1)(p11.2;q21)-associated PRCC [77].

Immunohistochemistry can be helpful in differentiating papillary PRCC from histologically similar neoplasms.

Cytokeratin 7 is positive in 87 % of type 1 lesions and 20 % of type 2 lesions, while EMA usually stains for both types [92]. Additionally, this lesion is negative for WT1. Since epithelial differentiated Wilms' tumor and metanephric adenoma are only limitedly positive for cytokeratin 7 and EMA and positive for WT1, these stains can help separate type 1 lesions from these other neoplasms. Also, papillary PRCC is often positive for vimentin, which can be helpful in differentiating type 2 from translocation associated PRCC [77].

The genetic etiology of papillary PRCC is poorly understood, with very little being reported specifically about the pediatric variant. In the adult population, however, these lesions have multiple chromosomal aberrations, with a tendency to form trisomies [91]. Type 1 lesions show strong tendency for abnormalities in chromosome 19 while type 2 shows frequent abnormalities in chromosomes 5, 6, 8, 10, 11, 15, 18, and 22.

Like other PRCCs, the papillary variant's prognosis depends on stage at presentation. Type 2 lesions appear to have an overall more aggressive clinical course with a higher incidence of venous invasion, LN metastasis, and distant metastasis [91].

Imaging Features

Renal cell carcinoma is usually smaller in size than WT at presentation with an average size around 6 cm [93]. CT and MRI reveal a nonspecific solid intrarenal mass which enhances less than the normal kidney. Heterogeneous areas of necrosis and hemorrhage maybe present. Intratumoral calcification is seen more frequently with PRCC than with WT. Lymph node metastasis are common at the time of presentation and can be seen even with small primary tumor (Fig. 10.20a, b). Approximately 40 % of patients have lymph node or distant metastatic disease at presentation, with the most common sites of distant metastasis being lung, liver, and bone [94].

Renal Medullary Carcinoma

Renal medullary carcinoma (RMC) is an extremely rare pediatric neoplasm arising from collecting duct epithelium, associated with sickle cell trait, and characterized by a highly aggressive clinical course. Sickle cell trait is present in about 8 % of African Americans but the incidence of RMC within this population is unknown [95]. Over 80 % of RMC cases occur in African Americans with an almost 2:1 ratio of males to females. Age range at presentation is 5–51 years [96, 97]. There is a 3:1 predilection for involvement in the right kidney [97]. Patients may present with flank pain, hematuria, and abdominal mass [95, 98–100]. Widespread metastasis is extremely common at presentation.

Grossly, a poorly circumscribed tumor extensively infiltrates the renal medulla and protrudes into the renal hilum [77]. Lesions are tan to gray, firm, and lobulated, with areas of necrosis and hemorrhage common (Fig. 10.21) [101]. Tumors have an average diameter of 7.4 cm (range: 1.9–18 cm) and are not predominantly cystic. Due to its aggressive infiltration, it is often difficult to determine the original or dominant mass [77].

Microscopically, RMCs are characterized as high-grade epithelioid cells with large nuclei and prominent nucleoli. The cells are arranged in a cribriform and tubular architecture with acidophilic cytoplasm and show prominent stromal desmoplasia and neutrophils (Fig. 10.22) [77]. Other common features include the presence of chronic inflammatory infiltrate, drepanocytes, and abundant eosinophilic cytoplasm [77, 97]. This lesion shows similar histological characteristics

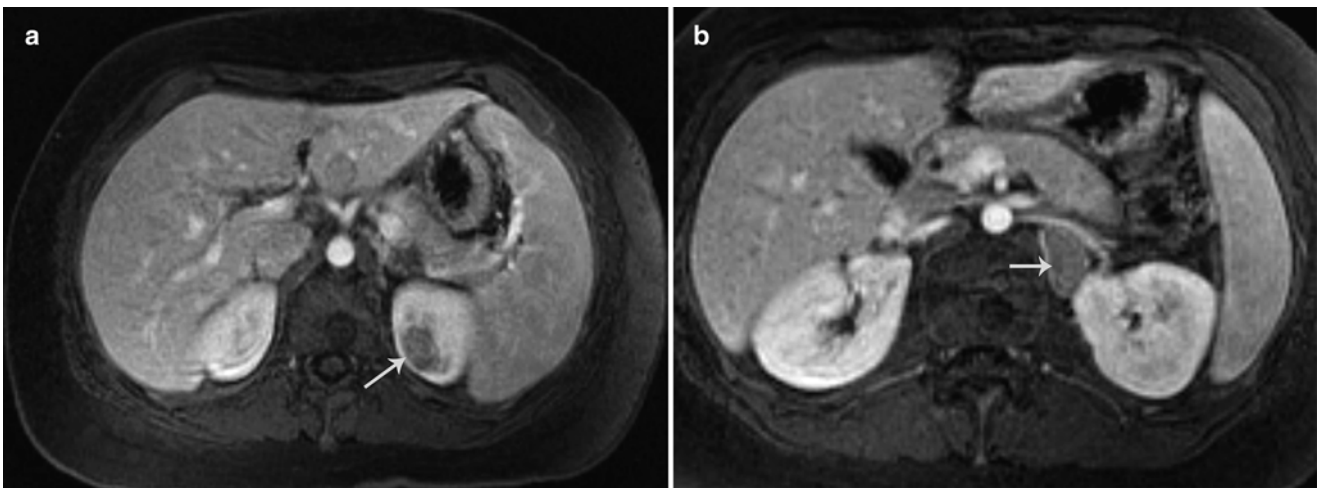

Fig. 10.20 Renal cell carcinoma. Axial post contrast MR images from a 15-year-old girl show a small renal mass at the upper pole of the right kidney (*arrow*) (**a**) and enlarged retroperitoneal lymph nodes (*arrow*) (**b**)

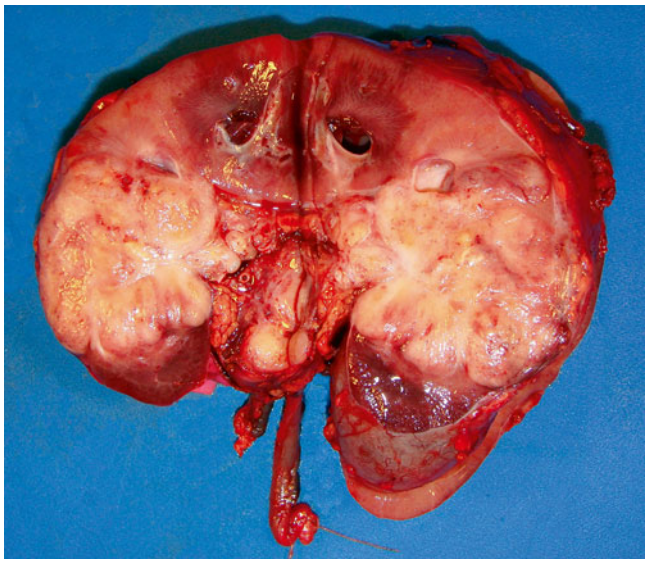

Fig. 10.21 Renal medullary carcinoma occupying the medullary portion of the kidney and extending to the hilum

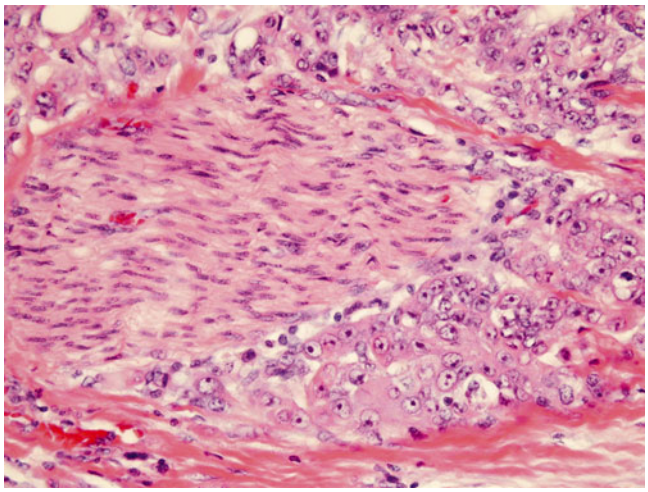

Fig. 10.22 Microscopically showing high-grade epithelioid cells mimicking rhabdoid tumor. Tumors cells show perineural invasion

to rhabdoid tumor, having similar loss of nuclear INI-1 protein positivity [97].

Immunohistochemistry is usually not needed to diagnose RMC, which expresses AE1/AE3 and EMA and does not stain for high molecular weight cytokeratin. RMC is variably positive for cytokeratin 7, CAM 5.2, and vimentin [77, 97].

No common genetic abnormalities have been reported with some studies even failing to detect losses or gains [97]. Balanced translocations reported include t(3;8)(p21;q24), t(9;22)(q34;q11), and t(10;16)(q22;q22). Monosomy for chromosome 11 has been reported, with the betaglobin gene being located on 11p [98, 102].

Prognosis is extremely poor in this neoplasm, with mortality reaching 100 % (1, 8). Approximately 50 % present at stage IV, and survival is reported beyond 16 months post diagnosis (mean: 4 months) [96, 97]. Treatment with carboplatin, paclitaxel, and high-dose-intensity MVAC chemotherapy has been reported to extend survival to up to 16 months post diagnosis [96].

Imaging Features

Renal medullary carcinoma is an aggressive malignancy, with poor prognosis that typically presents with advanced disease at presentation. A specific diagnosis of renal medullary carcinoma can be suggested on imaging due to its unique demographic features (teenagers/young adults with sickle cell trait) and characteristic imaging findings (Fig. 10.23a, b) [103]. These include a poorly circumscribed, infiltrative, hypodense mass located centrally within the kidney. Renal sinus invasion is characteristic and the infiltrative mass can result in reniform enlargement of the kidney with peripheral satellite nodules. The mass has a heterogeneous appearance due to areas of internal necrosis and hemorrhage. The right kidney is involved in approximately 70 % of renal medullary carcinoma. Regional lymphadenopathy is common at presentation. Common sites of metastatic disease include the lung, liver, pleura, and omentum [104].

Oncocytic PRCC Following Neuroblastoma

Oncocytic PRCC is an extremely rare pediatric neoplasm associated with previous neuroblastoma diagnosis. It is thought that this entity arises due to the potentially carcinogenic effects of chemotherapy and/or radiotherapy treatment [105]. However, some patients have received no chemotherapy for neuroblastoma yet still presented with oncocytic PRCC. Thus, an underlying genetic relationship between the two neoplasms may be the cause. Among the small pool of reported patients, age at neuroblastoma presentation ranged from 4 to 24 months, with subsequent oncocytic PRCC diagnosis occurring at an average of about 7–10 years post-neuroblastoma [105, 106]. Among the reported cases, a slight female predilection is noted [105].

Grossly, these lesions tend to be multifocal and occur bilaterally. Tumor size ranges from 3.5 to 8 cm (mean: 5.1 cm) [77, 105].

Microscopically, cells in oncocytic PRCC are solid and occasionally papillary in arrangement, containing abundant eosinophilic cytoplasm [77]. Cells also show oncocytoid features and cellular heterogeneity with high nuclear grade. Cell and nuclear size and shape can vary greatly, with some cells showing reticular cytoplasm [105].

Oncocytic PRCC usually does not require immunohistochemistry for diagnosis, but the lesion has been reported to be positive cytokeratins 8, 18, and 20, EMA, and vimentin, and it is negative for S-100, HMB45, and cytokeratins 7, 14, and 19.9 [77, 105].

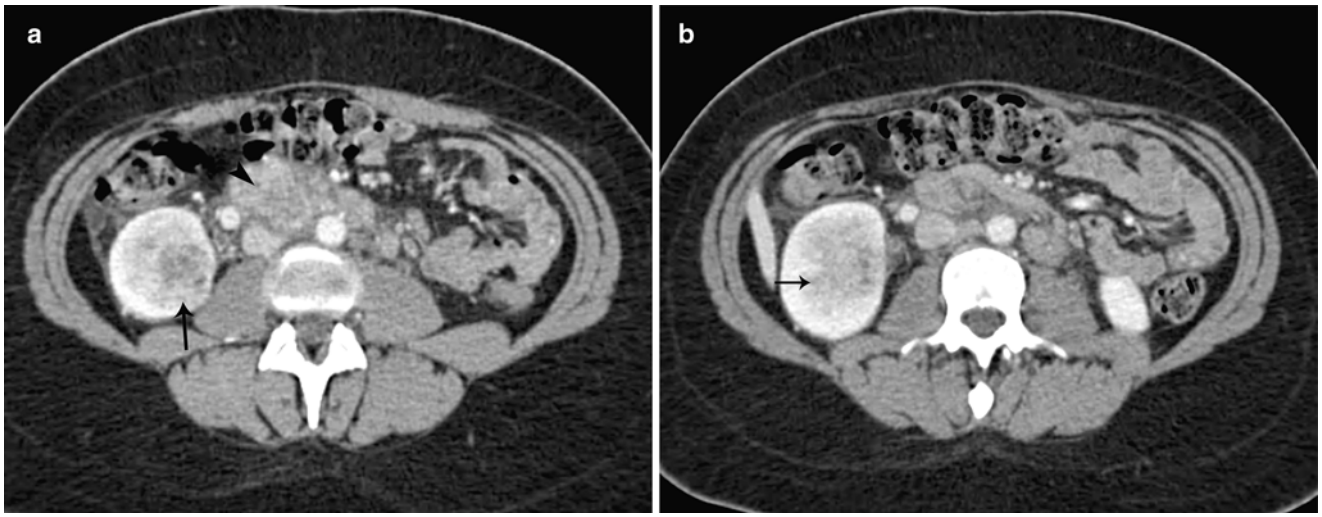

Fig. 10.23 Medullary carcinoma of kidney. (**a** and **b**) Axial contrast enhanced CT images from a 20-year-old girl with sickle cell trait show an infiltrative renal mass at the lower pole of the right kidney (*arrow*) with enlarged retroperitoneal lymph nodes (*arrowhead*)

Although the definitive cytogenetic characteristics of this neoplasm are yet to be established, the lesion is not known to demonstrate the common aberrations seen in other renal neoplasms, further supporting it as a separate entity. Cytogenetic studies of two neoplasms report monosomy 22 in both, duplication of the 7q32-36 region in one case, and multiple aberrations including monosomy 14, deletion at 3q11, and translocations at chromosomes 4 and 22 in the other [105]. Further studies are needed to support the significance of these findings.

Prognostic outlook for these patients is unclear. Partial or radical nephrectomy is used in most cases and usually clears any symptoms, with patients generally remaining recurrence free [107]. However, additional cases are needed to confirm this observation.

The imaging features of oncocytic PRCC following neuroblastoma have not been well described.

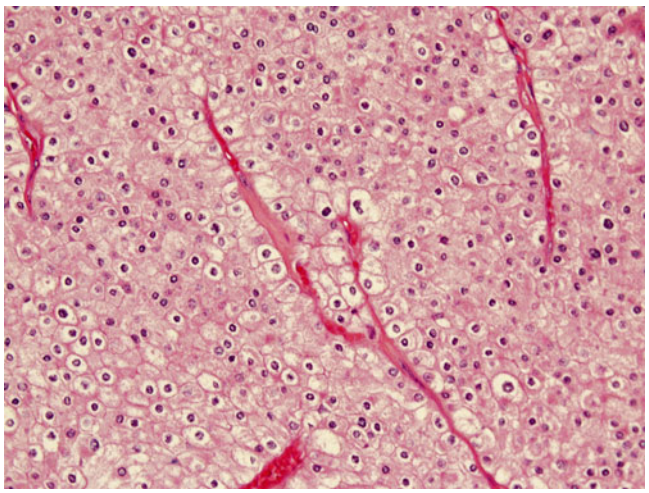

Fig. 10.24 Chromophobe renal cell carcinoma showing broad trabeculae with the tumor cells showing eosinophilic cells and some show vacuolated cytoplasm

Chromophobe RCC

Chromophobe renal cell carcinoma (CRCC) accounts for about 5 % of all renal cell carcinomas (RCC) and is extremely rare in childhood, with less than ten cases reported in the literature [108, 109]. The average age at diagnosis is during the fifth decade of life, and there is a slight predominance of females over males (52–48 %) [110]. Among the few pediatric cases the average age was 11.7 [108]. Most patients present asymptomatically, with the presence an abdominal mass, hematuria, or pain usually indicative of advanced disease. Generally metastasis is rare at presentation (6–7 % of cases) and the most common sites are the liver and lung [109].

Grossly, CRCC is usually larger than other RCC variants, with a median tumor size of 6 cm [109]. Additionally, lesions tend to be well-circumscribed and highly lobulated, and the cut surface tends to be brownish-tan. Microscopically, CRCC neoplasms present in two different histological variants: classic and eosinophilic. In the classic variant, cells are polygonal, pale and large, with abundant transparent cytoplasm. The eosinophilic variant has similar features to oncocytomas, which include a nested or alveolar architecture with granularity (Fig. 10.24). Additionally, there is a mixed variant in which neither of the two prominent variants occupies more than 80 % of the morphology. Also, some CRCC can show sarcomatoid changes, which are associated with more aggressive behavior and metastasis [111]. These lesions are characterized by positive Hale's colloidal iron staining in the cytoplasm.

The genetic features of CRCC are not fully understood. Chromosome losses at 2, 10, 13, 17, and 21 have been widely reported [109]. This variant does not show the 3p loss characteristic of nonpapillary RCCs [108]. Additionally, CRCC has been associated with Birt–Hogg–Dubé (BHD) syndrome, with over 30 % of patients with BHD presenting with CRCC. This familial syndrome is a result of inactivating mutations on the *FLCN* gene on the short arm of chromosome 17. Overall, CRCC has a good prognosis with about a 90 % survival rate at 10 years post diagnosis [112]. Interestingly, females appear to have much higher survival rates than males. Additionally, greater risk of mortality has been associated with high clinical or pathological stage and sarcomatoid differentiation [111].

The imaging features of chromophobe RCC have not been well described.

Primitive Neuroectodermal Tumors

Primitive neuroectodermal tumor (PNET) of the kidney belongs to a family of tumors that include Ewing sarcoma and Askin tumor, together comprising about 1 % of all sarcomas [113]. Specifically, PNET is a poorly differentiated neoplasm arising from the cells of the neuroectoderm that can occur anywhere in the soft tissues and rarely in the kidneys [114]. This neoplasm is malignant and must be differentiated from other round-cell tumors such as neuroblastoma and blastema-predominant Wilms' tumor.

Over 75 % of renal PNET cases occur between the ages of 10 and 39, with a median age of 24 years and a range from 4 to 66 years [115]. A slight male predominance has been reported in renal PNET but not confirmed, and it is more commonly reported among Hispanics and whites than in blacks and Asians [113]. Presenting symptoms vary and include abdominal pain, hematuria, malaise, fever, and dysuria [113, 114]. Over 50 % of these cases at presentation are a result of recurrence or metastasis [116].

Grossly, the tumors are solid and firm with necrosis and hemorrhage being commonly observed. Additionally, the lesion may be tan-yellow to gray-white in appearance and usually vary in size from about 8 to 16 cm in diameter [117]. Microscopically, most PNETs have typical features characterized by undifferentiated cells with round or ovoid hyperchromatic nuclei with minimal cytoplasm and mitotic figures [118]. Additionally, the most characteristic histological feature of PNET is the arrangement of cells forming pseudorosettes. There also exist PNETs with non-typical histology, which include those with CCSK-like, MPNST-like, rhabdoid, epithelioid, paraganglioma-like, and sclerosing morphologies [118]. Immunohistochemistry can be used to help in confirming PNET diagnosis. CD99 positivity is reported in the vast majority of lesions and further negative staining with WT-1 and CD45 can help to further separate PNET from Wilms' tumor and non-Hodgkin lymphoma respectively [113].

Over 85 % of PNET lesions show a genetic alteration with t(11;22)(q24;q12). This results in a chimeric fusion transcript of *EWS/FLI-1* gene products [119]. Additionally, about 5–10 % of PNET neoplasms have a t(21;22)(q22;q12) genetic mutation. These lesions follow a generally malignant clinical course with the majority of patients presenting with locally advanced disease and/or metastasis. The overall 5-year survival rate is reported to be between 45 and 55 % [115].

Imaging Features

Renal PNETs are large, heterogeneous tumors that may replace the entire kidney [120]. Presence of calcification, areas of internal hemorrhage or necrosis, and peripheral hypervascularity makes these tumors heterogeneous in appearance on all imaging modalities. On MR, PNETs demonstrate intermediate to high T2 signal intensity. They can show intravascular extension. Common sites of metastasis include lungs, bones, and liver.

Rhabdomyosarcoma of the Kidney

Primary rhabdomyosarcoma (RMS) of the kidney is extremely rare in the pediatric population, with fewer than ten cases reported in the literature [121]. Rhabdomyosarcomas can occur in the genitourinary tract or in the head and neck and have several histological subtypes, but only the conventional or embryonal type has been reported in pediatric renal cases [121]. Grossly, the lesions originate in the renal parenchyma and are poorly circumscribed and tan in appearance, with hemorrhage and necrosis common (Fig. 10.25). Microscopic features include cells separated by myxoid stroma with undifferentiated mesenchymal cells with ovoid

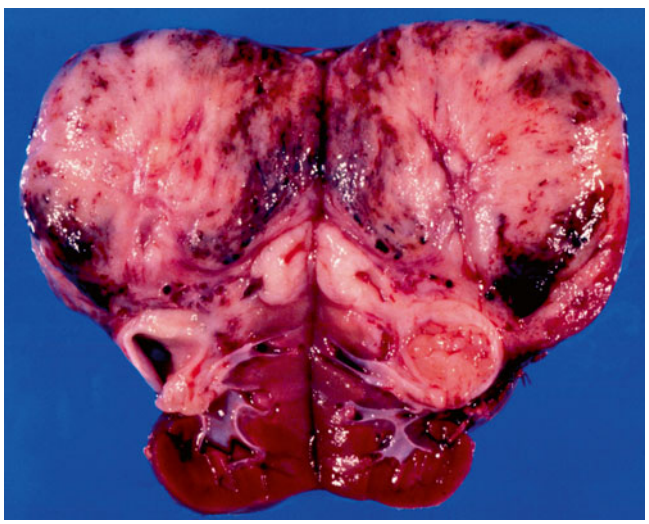

Fig. 10.25 Lesion occupying the upper pole of the renal parenchyma; it is poorly circumscribed and shows a tan cut surface, with hemorrhage and necrosis

nuclei and scant cytoplasm [122]. This tumor can be mistaken for blastemal predominant Wilms' tumor. Anaplasia was found in 67 % of cases reported in a study reviewing six renal RMS cases [121]. This prevalence greatly exceeds that of RMSs in general. Renal RMSs of the embryonal subtype are strongly immunopositive for desmin, myogenin, and MyoD1 (Fig. 10.26) [121]. Rhabdomyosarcoma of the kidney does not have any characteristic imaging findings, and the diagnosis has to be made at histopathological evaluation. It can present as a poorly enhancing, large soft tissue mass. Genetic mutations seen in embryonal RMS include LOH at 11p15.5, which is seen in Wilms' tumors and commonly associated with Beckwith–Wiedemann syndrome. Anaplasia usually carries the *PAX*/*FKHR* gene fusion. Of the cases reported, all but one were treated with radical nephrectomy. Survival rate is strongly diminished by metastasis at presentation with subsequent recurrence (survival years average: 6.5 (no metastasis or recurrence) vs. 1.1 (with) [121].

The imaging features of rhabdomyosarcoma of the kidney have not been well described.

Synovial Sarcoma

Primary renal synovial sarcoma (PRSS) is an extremely rare renal neoplasm with only about 65 cases reported in the literature in all age groups [123]. To our knowledge, two cases have been reported in the pediatric population with the youngest reported in a 13-year-old patient [124]. Generally, synovial sarcomas (SSs) account for about 10 % of all soft tissue sarcomas and can affect various regions of the body including the head and neck, bone, lung, and prostate [125]. Renal SS usually occurs in the adult population with a reported median age of 37 years [123]. Additionally, there appears to be no gender predominance. Patients often present with hematuria, flank/abdominal pain, and/or abdominal distention [126] with about 8 % demonstrating metastatic spread at diagnosis [123].

Grossly, the tumors are usually large, showing necrosis and containing cystic regions [126]. The lesions are described as tan in color and rubbery with hemorrhage and necrosis commonly observed. Microscopically, PRSS are made up of plump spindle cells with necrosis forming intersecting fascicles showing hyperchromatic nuclei [126]. Additionally, tumors cells at high power have a characteristic "rice grain" shape with minimal cytoplasm and frequent mitotic figures [126]. These lesions show immunopositivity most reliably for vimentin and bcl-2 [123].

The characteristic genetic mutation of PRSS is a translocation t(X;18)(p11;q11) resulting in an SSX-SYT gene fusion product thought to be implicated in transformation activity [123]. Two variants of the *SSX* gene (*SSX1* and *SSX2*) are most commonly implicated in PRSS with the *SSX2* variant occurring more often and also associated with a higher survival rate compared with *SSX1* [123]. Additionally, the *SSX4* variant has been rarely reported in PRSS [125]. Additionally, a translocation t(X;20)(p11;q13) has been associated with PRSS [127].

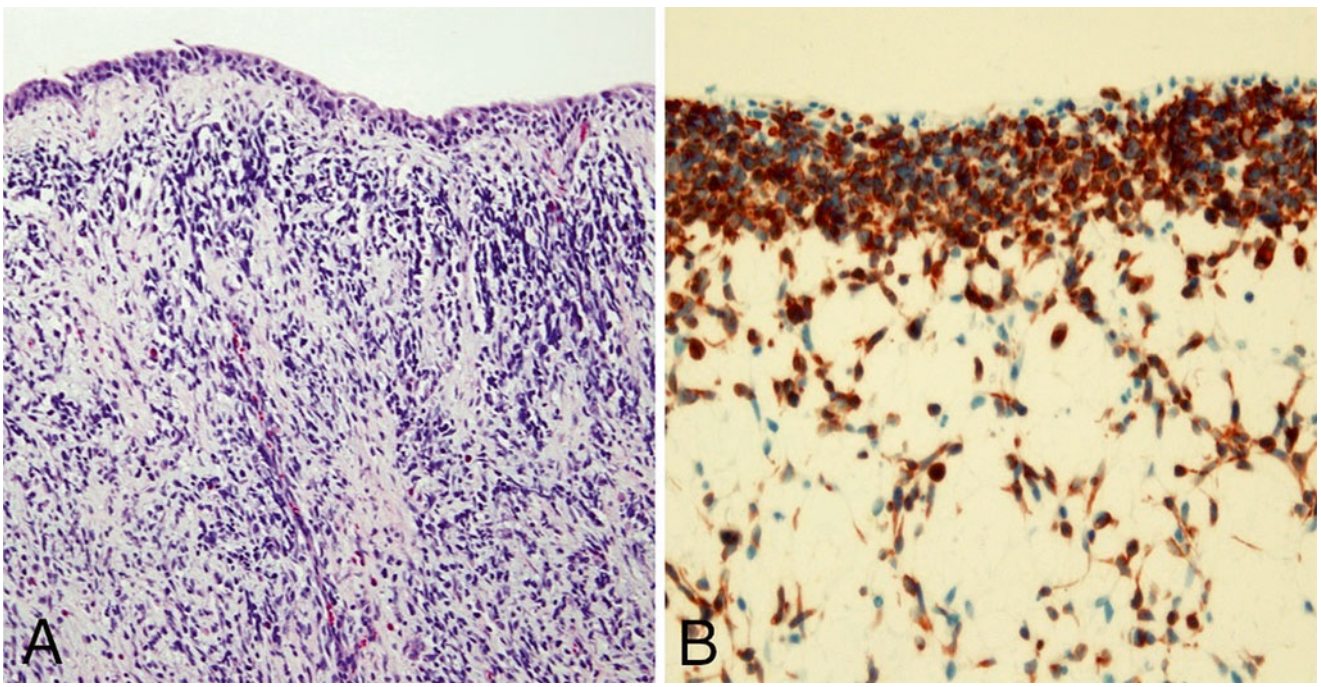

Fig. 10.26 Primary rhabdomyosarcoma of the kidney showing cambium layer (**a**) and strong positive desmin immunostain (**b**)

Synovial sarcomas in general have a poor prognostic outlook with a reported 36 % developing metastasis after nephrectomy [123]. Most common sites of metastasis include the lungs (42 %), abdominal lymph nodes and local recurrence (29 %), liver (24 %), and bone (6 %). Metastasis increases mortality with a median disease free survival of 33 months after diagnosis reported in non-metastatic patients and only 6 months for those developing metastatic disease [123].

Imaging Features

Renal synovial sarcoma appears as a large well-circumscribed heterogeneously enhancing soft-tissue mass that may extend into the renal pelvis or the perinephric region [128]. Some tumors may be predominantly cystic with enhancing septa and mural nodules. Extension into the renal vein and inferior vena cava has been described. At MR imaging, soft-tissue synovial sarcomas are heterogeneously hyperintense on T2-weighted images and hypointense on T1-weighted images with areas of hemorrhage, fluid levels, and septa [129].

References

1. Ko EY, Ritchey ML. Current management of Wilms' tumor in children. J Pediatr Urol. 2009;5(1):56–65.
2. Murphy WM, Grignon DJ, Perlman EJ. Kidney tumors in children. In: Silverberg SG, Sobin LH, editors. Tumors of the kidney, bladder, and related urinary structures. Washington, DC: American Registry of Pathology; 2004. p. 1–99.
3. Shen SS, et al. Recently described and emphasized entities of renal neoplasms. Arch Pathol Lab Med. 2007;131(8):1234–43.
4. Lall A, et al. Wilms' tumor with intracaval thrombus in the UK Children's Cancer Study Group UKW3 trial. J Pediatr Surg. 2006;41(2):382–7.
5. Servaes S, et al. Comparison of diagnostic performance of CT and MRI for abdominal staging of pediatric renal tumors: a report from the Children's Oncology Group. Pediatr Radiol. 2014 Aug 19. [Epub ahead of print].
6. Brisse HJ, et al. Imaging in unilateral Wilms tumour. Pediatr Radiol. 2008;38(1):18–29.
7. Charles AK, Vujanić GM, Berry PJ. Renal tumours of childhood. Histopathology. 1998;32(4):293–309.
8. Sebire NJ, Vujanic GM. Paediatric renal tumours: recent developments, new entities and pathological features. Histopathology. 2009;54(5):516–28.
9. Chu A, et al. Wilms' tumour: a systematic review of risk factors and meta-analysis. Paediatr Perinat Epidemiol. 2010;24(5):449–69.
10. Nakamura L, Ritchey M. Current management of wilms' tumor. Curr Urol Rep. 2010;11(1):58–65.
11. Davidoff AM. Wilms' tumor. Curr Opin Pediatr. 2009;21(3):357–64.
12. Keaney CM, Springate JE. Cancer and the kidney. Adolesc Med Clin. 2005;16(1):121–48.
13. Lowe LH, et al. Pediatric renal masses: Wilms tumor and beyond. Radiographics. 2000;20(6):1585–603.
14. Ritchey ML, et al. Renal vein involvement with nephroblastoma: a report of the National Wilms' Tumor Study-3. Eur Urol. 1990; 17(2):139–44.
15. Khanna G, et al. Evaluation of diagnostic performance of CT for detection of tumor thrombus in children with Wilms tumor: a report from the Children's Oncology Group. Pediatr Blood Cancer. 2012;58(4):551–5.
16. Khanna G, et al. Detection of preoperative Wilms tumor rupture with CT: a report from the Children's Oncology Group. Radiology. 2013;266(2):610–7.
17. Ehrlich PF. Bilateral Wilms' tumor: the need to improve outcomes. Expert Rev Anticancer Ther. 2009;9(7):963–73.
18. Rohrschneider WK, et al. US, CT and MR imaging characteristics of nephroblastomatosis. Pediatr Radiol. 1998;28(6):435–43.
19. Choueiri TK, et al. BRAF mutations in metanephric adenoma of the kidney. Eur Urol. 2012;62(5):917–22.
20. Schmelz HU, et al. Metanephric adenoma of the kidney: case report and review of the literature. Int Urol Nephrol. 2005;37(2): 213–7.
21. Davis Jr CJ, et al. Metanephric adenoma. Clinicopathological study of fifty patients. Am J Surg Pathol. 1995;19(10):1101–14.
22. Arroyo MR, et al. The spectrum of metanephric adenofibroma and related lesions: clinicopathologic study of 25 cases from the National Wilms Tumor Study Group Pathology Center. Am J Surg Pathol. 2001;25(4):433–44.
23. Hennigar RA, Beckwith JB. Nephrogenic adenofibroma. A novel kidney tumor of young people. Am J Surg Pathol. 1992;16(4): 325–34.
24. Hoglund HH, et al. Ossifying renal tumor of infancy (ORTI)—a rare diagnosis. Klin Padiatr. 2011;223(3):178–9.
25. Argani P, Beckwith JB. Metanephric stromal tumor: report of 31 cases of a distinctive pediatric renal neoplasm. Am J Surg Pathol. 2000;24(7):917–26.
26. Kacar A, et al. Metanephric stromal tumor: a challenging diagnostic entity in children. J Pediatr Surg. 2011;46(12):e7–10.
27. Grundy P, et al. Clinicopathologic correlates of loss of heterozygosity in Wilm's tumor: a preliminary analysis. Med Pediatr Oncol. 1996;27(5):429–33.
28. Argani P, Collins MH. Anaplastic nephrogenic rest. Am J Surg Pathol. 2006;30(10):1339–41.
29. Beckwith JB. Nephrogenic rests and the pathogenesis of Wilms tumor: developmental and clinical considerations. Am J Med Genet. 1998;79(4):268–73.
30. Lonergan GJ, et al. Nephrogenic rests, nephroblastomatosis, and associated lesions of the kidney. Radiographics. 1998;18(4): 947–68.
31. Beckwith JB. Precursor lesions of Wilms tumor: clinical and biological implications. Med Pediatr Oncol. 1993;21(3):158–68.
32. Beckwith JB, Kiviat NB, Bonadio JF. Nephrogenic rests, nephroblastomatosis, and the pathogenesis of Wilms' tumor. Pediatr Pathol. 1990;10(1–2):1–36.
33. Fukuzawa R, Reeve AE. Molecular pathology and epidemiology of nephrogenic rests and Wilms tumors. J Pediatr Hematol Oncol. 2007;29(9):589–94.
34. Charles AK, Brown KW, Berry PJ. Microdissecting the genetic events in nephrogenic rests and Wilms' tumor development. Am J Pathol. 1998;153(3):991–1000.
35. Hennigar RA, O'Shea PA, Grattan-Smith JD. Clinicopathologic features of nephrogenic rests and nephroblastomatosis. Adv Anat Pathol. 2001;8(5):276–89.
36. Park S, et al. Inactivation of WT1 in nephrogenic rests, genetic precursors to Wilms' tumour. Nat Genet. 1993;5(4):363–7.
37. Steenman M, et al. Comparative genomic hybridization analysis of Wilms tumors. Cytogenet Cell Genet. 1997;77(3–4):296–303.
38. Ritchey ML, et al. Fate of bilateral renal lesions missed on preoperative imaging: a report from the National Wilms Tumor Study Group. J Urol. 2005;174(4 Pt 2):1519–21. discussion 1521.
39. Gylys-Morin V, et al. Wilms tumor and nephroblastomatosis: imaging characteristics at gadolinium-enhanced MR imaging. Radiology. 1993;188(2):517–21.

40. Hausegger KA, et al. Can MR contribute to the diagnosis of nephroblastomatosis? A report of one case. Pediatr Radiol. 1991;21(7):533–5.
41. Perlman EJ, et al. Hyperplastic perilobar nephroblastomatosis: long-term survival of 52 patients. Pediatr Blood Cancer. 2006; 46(2):203–21.
42. Joshi VV, Beckwith JB. Multilocular cyst of the kidney (cystic nephroma) and cystic, partially differentiated nephroblastoma. Terminology and criteria for diagnosis. Cancer. 1989;64(2): 466–79.
43. Joshi VV, et al. Cystic partially differentiated nephroblastoma: a clinicopathologic entity in the spectrum of infantile renal neoplasia. Cancer. 1977;40(2):789–95.
44. Truong LD, et al. Renal cystic neoplasms and renal neoplasms associated with cystic renal diseases: pathogenetic and molecular links. Adv Anat Pathol. 2003;10(3):135–59.
45. Blakely ML, et al. Outcome of children with cystic partially differentiated nephroblastoma treated with or without chemotherapy. J Pediatr Surg. 2003;38(6):897–900.
46. Agrons GA, et al. Multilocular cystic renal tumor in children: radiologic-pathologic correlation. Radiographics. 1995;15(3): 653–69.
47. Bahubeshi A, et al. Germline DICER1 mutations and familial cystic nephroma. J Med Genet. 2010;47(12):863–6.
48. Bayindir P, et al. Cellular mesoblastic nephroma (infantile renal fibrosarcoma): institutional review of the clinical, diagnostic imaging, and pathologic features of a distinctive neoplasm of infancy. Pediatr Radiol. 2009;39(10):1066–74.
49. England RJ, et al. Mesoblastic nephroma: a report of the United Kingdom children's cancer and leukaemia group (CCLG). Pediatr Blood Cancer. 2011;56(5):744–8.
50. Furtwaengler R, et al. Mesoblastic nephroma—a report from the Gesellschaft fur Padiatrische Onkologie und Hamatologie (GPOH). Cancer. 2006;106(10):2275–83.
51. Gupta R, et al. Cellular mesoblastic nephroma in an infant: report of the cytologic diagnosis of a rare paediatric renal tumor. Diagn Cytopathol. 2009;37(5):377–80.
52. Chaudry G, et al. Imaging of congenital mesoblastic nephroma with pathological correlation. Pediatr Radiol. 2009;39(10):1080–6.
53. Irsutti M, et al. Mesoblastic nephroma: prenatal ultrasonographic and MRI features. Pediatr Radiol. 2000;30(3):147–50.
54. Portugal R, Barroca H. Clear cell sarcoma, cellular mesoblastic nephroma and metanephric adenoma: cytological features and differential diagnosis with Wilms tumour. Cytopathology. 2008; 19(2):80–5.
55. Rubin BP, et al. Congenital mesoblastic nephroma t(12;15) is associated with ETV6-NTRK3 gene fusion: cytogenetic and molecular relationship to congenital (infantile) fibrosarcoma. Am J Pathol. 1998;153(5):1451–8.
56. Henno S, et al. Cellular mesoblastic nephroma: morphologic, cytogenetic and molecular links with congenital fibrosarcoma. Pathol Res Pract. 2003;199(1):35–40.
57. Steelman C, et al. Unusual presentation of congenital infantile fibrosarcoma in seven infants with molecular-genetic analysis. Fetal Pediatr Pathol. 2011;30(5):329–37.
58. Brownlee NA, et al. Recurring translocation (10;17) and deletion (14q) in clear cell sarcoma of the kidney. Arch Pathol Lab Med. 2007;131(3):446–51.
59. Gooskens SL, et al. Clear cell sarcoma of the kidney: a review. Eur J Cancer. 2012;48(14):2219–26.
60. Argani P, et al. Clear cell sarcoma of the kidney: a review of 351 cases from the National Wilms Tumor Study Group Pathology Center. Am J Surg Pathol. 2000;24(1):4–18.
61. Cutcliffe C, et al. Clear cell sarcoma of the kidney: up-regulation of neural markers with activation of the sonic hedgehog and Akt pathways. Clin Cancer Res. 2005;11(22):7986–94.
62. Amin MB, et al. Clear cell sarcoma of kidney in an adolescent and in young adults: a report of four cases with ultrastructural, immunohistochemical, and DNA flow cytometric analysis. Am J Surg Pathol. 1999;23(12):1455–63.
63. Watts KE, Hansel DE, MacLennan GT. Clear cell sarcoma of the kidney. J Urol. 2011;185(1):279–80.
64. Glass RB, Davidson AJ, Fernbach SK. Clear cell sarcoma of the kidney: CT, sonographic, and pathologic correlation. Radiology. 1991;180(3):715–7.
65. O'Meara E, et al. Characterization of the chromosomal translocation t(10;17)(q22;p13) in clear cell sarcoma of kidney. J Pathol. 2012;227(1):72–80.
66. Schuster AE, et al. Genetic and genetic expression analyses of clear cell sarcoma of the kidney. Lab Invest. 2003;83(9):1293–9.
67. Desai SR, Upadhyay V. Rhabdoid tumour of the kidney: a diagnostic challenge and a fatal outcome. Pediatr Surg Int. 2000; 16(5–6):449–50.
68. Weeks DA, et al. Rhabdoid tumor of kidney. A report of 111 cases from the National Wilms' Tumor Study Pathology Center. Am J Surg Pathol. 1989;13(6):439–58.
69. Winger DI, et al. Radiology-Pathology Conference: rhabdoid tumor of the kidney. Clin Imaging. 2006;30(2):132–6.
70. Yamamoto M, et al. Treatment of stage IV malignant rhabdoid tumor of the kidney (MRTK) with ICE and VDCy: a case report. J Pediatr Hematol Oncol. 2006;28(5):286–9.
71. Han TI, et al. Rhabdoid tumour of the kidney: imaging findings. Pediatr Radiol. 2001;31(4):233–7.
72. Sisler CL, Siegel MJ. Malignant rhabdoid tumor of the kidney: radiologic features. Radiology. 1989;172(1):211–2.
73. Palmer NF, Sutow W. Clinical aspects of the rhabdoid tumor of the kidney: a report of the National Wilms' Tumor Study Group. Med Pediatr Oncol. 1983;11(4):242–5.
74. Nagata T, et al. Molecular genetic alterations and gene expression profile of a malignant rhabdoid tumor of the kidney. Cancer Genet Cytogenet. 2005;163(2):130–7.
75. Lee RS, et al. A remarkably simple genome underlies highly malignant pediatric rhabdoid cancers. J Clin Invest. 2012;122(8): 2983–8.
76. Gadd S, et al. Rhabdoid tumor: gene expression clues to pathogenesis and potential therapeutic targets. Lab Invest. 2010;90(5): 724–38.
77. Perlman EJ. Pediatric renal cell carcinoma. Surg Pathol Clin. 2010;3(3):641–51.
78. Sausville JE, et al. Pediatric renal cell carcinoma. J Pediatr Urol. 2009;5(4):308–14.
79. Soller MJ, et al. Cytogenetic findings in pediatric renal cell carcinoma. Cancer Genet Cytogenet. 2007;173(1):75–80.
80. Spreafico F, et al. Renal cell carcinoma in children and adolescents. Expert Rev Anticancer Ther. 2010;10(12):1967–78.
81. Indolfi P, et al. Local lymph node involvement in pediatric renal cell carcinoma: a report from the Italian TREP project. Pediatr Blood Cancer. 2008;51(4):475–8.
82. Selle B, et al. Population-based study of renal cell carcinoma in children in Germany, 1980–2005: more frequently localized tumors and underlying disorders compared with adult counterparts. Cancer. 2006;107(12):2906–14.
83. Argani P, et al. Primary renal neoplasms with the ASPL-TFE3 gene fusion of alveolar soft part sarcoma: a distinctive tumor entity previously included among renal cell carcinomas of children and adolescents. Am J Pathol. 2001;159(1):179–92.
84. Argani P, Ladanyi M. Translocation carcinomas of the kidney. Clin Lab Med. 2005;25(2):363–78.
85. Argani P, et al. A novel CLTC-TFE3 gene fusion in pediatric renal adenocarcinoma with t(X;17)(p11.2;q23). Oncogene. 2003;22(34): 5374–8.

86. Schafernak KT, et al. Pediatric renal cell carcinoma as second malignancy: reports of two cases and a review of the literature. Can J Urol. 2007;14(6):3739–44.
87. Joshi DD, Banerjee T. Vascular endothelial growth factor (VEGF) receptor antibody bevacizumab (avastin) induces regression of renal cell carcinoma in an adolescent resulting in residual tumorectomy. Pediatr Blood Cancer. 2008;50(4):903–4.
88. Malouf GG, et al. Targeted agents in metastatic Xp11 translocation/TFE3 gene fusion renal cell carcinoma (RCC): a report from the Juvenile RCC Network. Ann Oncol. 2010;21(9):1834–8.
89. Pwint TP, et al. An adult Xp11.2 translocation renal carcinoma showing response to treatment with sunitinib. Urol Oncol. 2011; 29(6):821–4.
90. Schultz TD, et al. Papillary renal cell carcinoma: report of a rare entity in childhood with review of the clinical management. J Pediatr Surg. 2011;46(6):e31–4.
91. Antonelli A, et al. Cytogenetic features, clinical significance and prognostic impact of type 1 and type 2 papillary renal cell carcinoma. Cancer Genet Cytogenet. 2010;199(2):128–33.
92. Delahunt B, Eble JN. Papillary renal cell carcinoma: a clinicopathologic and immunohistochemical study of 105 tumors. Mod Pathol. 1997;10(6):537–44.
93. Downey RT, et al. CT and MRI appearances and radiologic staging of pediatric renal cell carcinoma. Pediatr Radiol. 2012;42(4): 410–7. quiz 513–4.
94. Khanna G, et al. Cell carcinoma in children and adolescents: a summary of imaging findings from the Children's Oncology Group. Pediatr Radiol. 2014;44(Suppl):S136.
95. Coogan CL, et al. Renal medullary carcinoma in patients with sickle cell trait. Urology. 1998;51(6):1049–50.
96. Gangireddy V, et al. Response of metastatic renal medullary carcinoma to carboplatinum and Paclitaxel chemotherapy. Clin Genitourin Cancer. 2012;10(2):134–9.
97. Swartz MA, et al. Renal medullary carcinoma: clinical, pathologic, immunohistochemical, and genetic analysis with pathogenetic implications. Urology. 2002;60(6):1083–9.
98. Baig MA, et al. Renal medullary carcinoma. J Natl Med Assoc. 2006;98(7):1171–4.
99. Hakimi AA, et al. Renal medullary carcinoma: the Bronx experience. Urology. 2007;70(5):878–82.
100. Walsh AM, et al. Response to radiation in renal medullary carcinoma. Rare Tumors. 2011;3(3):e32.
101. Assad L, et al. Cytologic features of renal medullary carcinoma. Cancer. 2005;105(1):28–34.
102. Avery RA, et al. Renal medullary carcinoma: clinical and therapeutic aspects of a newly described tumor. Cancer. 1996;78(1):128–32.
103. Khan A, et al. Renal medullary carcinoma: sonographic, computed tomography, magnetic resonance and angiographic findings. Eur J Radiol. 2000;35(1):1–7.
104. Davidson AJ, et al. Renal medullary carcinoma associated with sickle cell trait: radiologic findings. Radiology. 1995;195(1):83–5.
105. Medeiros LJ, et al. Oncocytoid renal cell carcinoma after neuroblastoma: a report of four cases of a distinct clinicopathologic entity. Am J Surg Pathol. 1999;23(7):772–80.
106. Lack EE, Cassady JR, Sallan SE. Renal cell carcinoma in childhood and adolescence: a clinical and pathological study of 17 cases. J Urol. 1985;133(5):822–8.
107. Dhall D, et al. Pediatric renal cell carcinoma with oncocytoid features occurring in a child after chemotherapy for cardiac leiomyosarcoma. Urology. 2007;70(1):178e13–5.
108. Katzman PJ, Schwartz JI. Chromophobe renal cell carcinoma in a child: case report and review of the literature. Pediatr Dev Pathol. 2007;10(2):125–8.
109. Vera-Badillo FE, Conde E, Duran I. Chromophobe renal cell carcinoma: a review of an uncommon entity. Int J Urol. 2012;19(10):894–900.
110. Amin MB, et al. Chromophobe renal cell carcinoma: histomorphologic characteristics and evaluation of conventional pathologic prognostic parameters in 145 cases. Am J Surg Pathol. 2008; 32(12):1822–34.
111. Przybycin CG, et al. Chromophobe renal cell carcinoma: a clinicopathologic study of 203 tumors in 200 patients with primary resection at a single institution. Am J Surg Pathol. 2011;35(7): 962–70.
112. Volpe A, et al. Chromophobe renal cell carcinoma (RCC): oncological outcomes and prognostic factors in a large multicentre series. BJU Int. 2012;110(1):76–83.
113. Bartholow T, Parwani A. Renal primitive neuroectodermal tumors. Arch Pathol Lab Med. 2012;136(6):686–90.
114. Chu WC, et al. Primitive neuroectodermal tumour (PNET) of the kidney: a rare renal tumour in adolescents with seemingly characteristic radiological features. Pediatr Radiol. 2008;38(10): 1089–94.
115. Ellinger J, et al. Primitive neuroectodermal tumor: rare, highly aggressive differential diagnosis in urologic malignancies. Urology. 2006;68(2):257–62.
116. Gonlusen G, et al. Primitive neuroectodermal tumor of the kidney: a rare entity. Int Urol Nephrol. 2001;33(3):449–51.
117. Jimenez RE, et al. Primary Ewing's sarcoma/primitive neuroectodermal tumor of the kidney: a clinicopathologic and immunohistochemical analysis of 11 cases. Am J Surg Pathol. 2002;26(3):320–7.
118. Parham DM, et al. Primary malignant neuroepithelial tumors of the kidney: a clinicopathologic analysis of 146 adult and pediatric cases from the National Wilms' Tumor Study Group Pathology Center. Am J Surg Pathol. 2001;25(2):133–46.
119. de Alava E, Gerald WL. Molecular biology of the Ewing's sarcoma/primitive neuroectodermal tumor family. J Clin Oncol. 2000;18(1):204–13.
120. Kim MS, et al. Radiologic findings of peripheral primitive neuroectodermal tumor arising in the retroperitoneum. AJR Am J Roentgenol. 2006;186(4):1125–32.
121. Raney B, et al. Primary renal sarcomas in the Intergroup Rhabdomyosarcoma Study Group (IRSG) experience, 1972–2005: a report from the Children's Oncology Group. Pediatr Blood Cancer. 2008;51(3):339–43.
122. Putnam AR, Wallentine JC. Diagnostic pathology. Pediatric neoplasms. 1st ed. Salt Lake City, UT: Amirsys; 2012.
123. Iacovelli R, et al. Clinical and pathological features of primary renal synovial sarcoma: analysis of 64 cases from 11 years of medical literature. BJU Int. 2012;110(10):1449–54.
124. Scarpato KR, et al. Primary renal synovial sarcoma in a 13-year-old boy. J Pediatr Surg. 2011;46(9):1849–51.
125. Divetia M, et al. Synovial sarcoma of the kidney. Ann Diagn Pathol. 2008;12(5):333–9.
126. Argani P, et al. Primary renal synovial sarcoma: molecular and morphologic delineation of an entity previously included among embryonal sarcomas of the kidney. Am J Surg Pathol. 2000;24(8):1087–96.
127. Fisher C. Diagnostic pathology. Soft tissue tumors. Salt Lake City, UT: Amirsys; 2011.
128. Perlmutter AE, et al. Primary synovial sarcoma of the kidney. Int J Urol. 2005;12(8):760–2.
129. Zakhary MM, et al. Magnetic resonance imaging features of renal synovial sarcoma: a case report. Cancer Imaging. 2008; 8:45–7.

Germ Cell and Gonadal Tumours

11

Neil J. Sebire and Kieran McHugh

Introduction

This chapter includes the major gonadal tumours affecting boys and girls in childhood, of which by far the largest group is represented by germ cell tumours (GCT). Since paediatric GCTs may also occur at a range of extragonadal sites, and since many of the histopathological and radiological features in this age group are similar regardless of site, the majority of the chapter focuses on radiology and pathology of pediatric GCTs. Other gonadal tumour types are covered separately.

Normal Anatomy and Development

As a group, GCTs are presumed to arise from primordial germ cells, which undergo aberrant proliferation and differentiation, either at their normal site within the gonads or at aberrant, extragonadal sites, presumably a consequence of abnormal migration of germ cells during embryonic development. Human germ cells originate in the yolk sac and migrate to the gonadal ridge by around 40 days post-fertilisation, with the supporting cells of the germinal cords and mesenchymal cells becoming Sertoli/follicular cells, and interstitial stromal cells, respectively [1].

Overview and Classification

Across the entire paediatric age range, GCTs affect around one in 400,000 children, of which around half involve the ovary or testis, with the remainder being at extragonadal sites; these are most frequent in infancy, the commonest of which are sacrococcygeal teratomas. Overall, around 5 % of pediatric germ cell tumours will be intracranial in origin [2].

In general, there is an approximately biphasic distribution of GCT prevalence in childhood, with an initial peak in the first 1 or 2 years of life, (GCTs being one of the commoner types of congenital fetal tumours), with a second peak in adolescence, corresponding to the more "adult" histological types. In young children GCTs are almost always teratomas or malignanct yolk sac tumours. The majority of germ cell tumours in young children arise at extragonadal sites, most commonly the sacrococcygeal region [2, 3].

Since the underlying histological features of an individual case are generally not directly related to the anatomical site of the tumour, the histological descriptions initially will be based primarily on general histological findings with illustrative cases provided in conjunction with the radiology at a range of sites. Where there are specific associations between a particular histological tumour type and a characteristic clinical presentation, site or age, such as testicular yolk sac tumour in infancy, this will be highlighted as appropriate.

Overview of Diagnostic Imaging Approaches

In general, the radiological and histopathological features are related to both the degree of differentiation of the germ cell components and the specific lineage to which they are differentiating, resulting in a wide range of histological types; these include mature teratoma, immature teratoma, yolk sac tumour, embryonal carcinoma, choriocarcinoma,

N.J. Sebire, MD FRCPath
Great Ormond Street Hospital for Children,
Great Ormond Street, London, UK

K. McHugh, F.R.C.R., F.R.C.P.I., D.C.H. (✉)
Radiology, Great Ormond Street Hospital for Children,
Great Ormond Street, London WC1N 3JH, UK
e-mail: kieran.mchugh@gosh.nhs.uk

D.M. Parham et al. (eds.), *Pediatric Malignancies: Pathology and Imaging*,
DOI 10.1007/978-1-4939-1729-7_11, © Springer Science+Business Media New York 2015

germinoma/seminoma and gonadoblastoma, often with mixed components.

The relative distribution of these subtypes varies according to the site and age of the patient. Similarly, the clinical presentation may vary from a prenatally diagnosed mass leading to high output cardiac failure, to a simple mass lesion detected incidentally to a clinically apparent mass lesion with systemic endocrine manifestations. It should be noted that whilst many of the histological features of paediatric GCTs are similar to those in adults, as a group, the distribution, and indeed underlying biological basis for their tumorigenesis is different to most adult GCTs.

Regardless of the relatively complex histological permutations for a given tumour, virtually all GCTs manifest radiologically as similar mass lesions with varying cystic, fatty, calcific and solid components (Fig. 11.1). In general, these should be imaged first, where possible, by ultrasound examination, which allows optimal demonstration of the cystic components of the tumour and can often show abnormal tumour vascularity using Doppler evaluation of the solid-appearing components. Some lesions may appear highly cystic with minimal solid elements, and may indeed even mimic simple cysts, particularly when affecting the ovary, such as a hemorrhagic ovarian cyst (Fig. 11.2). However, on close examination almost all GCTs do contain some sonographically detectable solid components. An otherwise nondescript multilocular cystic appearance on all imaging modalities is also possible. Movement of the mass on dynamic ultrasound evaluation in relation to other organs can provide useful information for the surgeon, and as an example with pelvic or abdominal masses in girls the presence or absence of two ovaries separate from the mass can aid differential diagnosis. Plain X-rays may show a mass lesion, and may also identify calcification within the mass, but in general plain radiography plays only a minor role in the detection and depiction of these tumours.

After sonographic assessment, further detailed evaluation with cross-sectional imaging is ideally performed with magnetic resonance imaging (MRI), which will typically show cysts with varying contents, from a simple fluid signal to complex proteinaceous fluids. Conventional T1-weighted (T1W) MRI will also easily demonstrate the fatty components of GCTs as high signal foci, paralleling the signal from subcutaneous fat (the fatty components, in terms of imaging appearances, will mirror fat elsewhere on all sequences). MRI with gadolinium optimally demonstrates the solid components and septa of GCTs [4]. The relationship, and infiltrative nature when present, of the mass to other viscera will further become apparent on MRI. Similarly, MRI is the best method to assess for intraspinal tumour extension, such as can occur with sacrococcygeal teratomas for example. When MRI is unavailable then CT will also show lesion extent to good effect, albeit with an inherent irradiation burden. CT is the most sensitive modality for detecting foci of calcification, a common occurrence, within these tumours and also readily demonstrates the fatty components of these masses [4]. Malignant tumours in general have more solid components than benign lesions, but with the exception of detecting metastases with some malignant disease, imaging generally cannot predict whether a lesion is benign or malignant.

Associations of Paediatric Germ Cell Tumours

An association between pediatric GCTs and haematological malignancies has been reported, (including acute myeloid leukaemia, histiocytoses and mastocytosis), usually in association with mediastinal malignant germ cell tumours in young adult males but occasionally also with ovarian germ cell tumours. In such cases the haematological malignancy may arise concurrently or several months after the initial GCT [5]. At least a proportion of such cases, particularly those developing many months following the GCT, may be chemotherapy related [6].

For most pediatric GCTs there are no strong epidemiological associations with environmental factors [7] and no strong genetic associations reported, although both mediasinal and intracranial GCTs are more frequent in patients with Klinefelter syndrome [8]. In contrast to adult testicular GCTs which frequently demonstrate isochromosome 12p, there are no characteristic cytogenetic abnormalities in childhood cases, although chromosome 1p deletions leading to loss of heterozygosity (LOH) are reported more frequently in childhood malignant GCTs [9] and array CGH approaches have demonstrated that whilst infant teratomas show no consistent abnormality, in older children changes similar to adult cases, such as chromosome 12p gains, may be identified [10]. However, whilst molecular diagnostic testing does not currently play a major role in pediatric GCT diagnosis or prognostication, it is likely that new generation technologies may identify additional molecular relationships, previously undetectable using cytogenetic approaches [11].

General Histological Features of Germ Cell Tumours

GCTs represent neoplasms derived from primordial germ cells, which may theoretically differentiate into a wide range of recognisable mature tissue types in addition to forming specific tumour types based on proliferation of immature and abnormal germ cells. Therefore, all GCTs can, in principle, be histologically composed of either a pure population demonstrating one specific histological phenotype, or may represent a mixture of multiple different GCT components. Frankly malignant elements generally

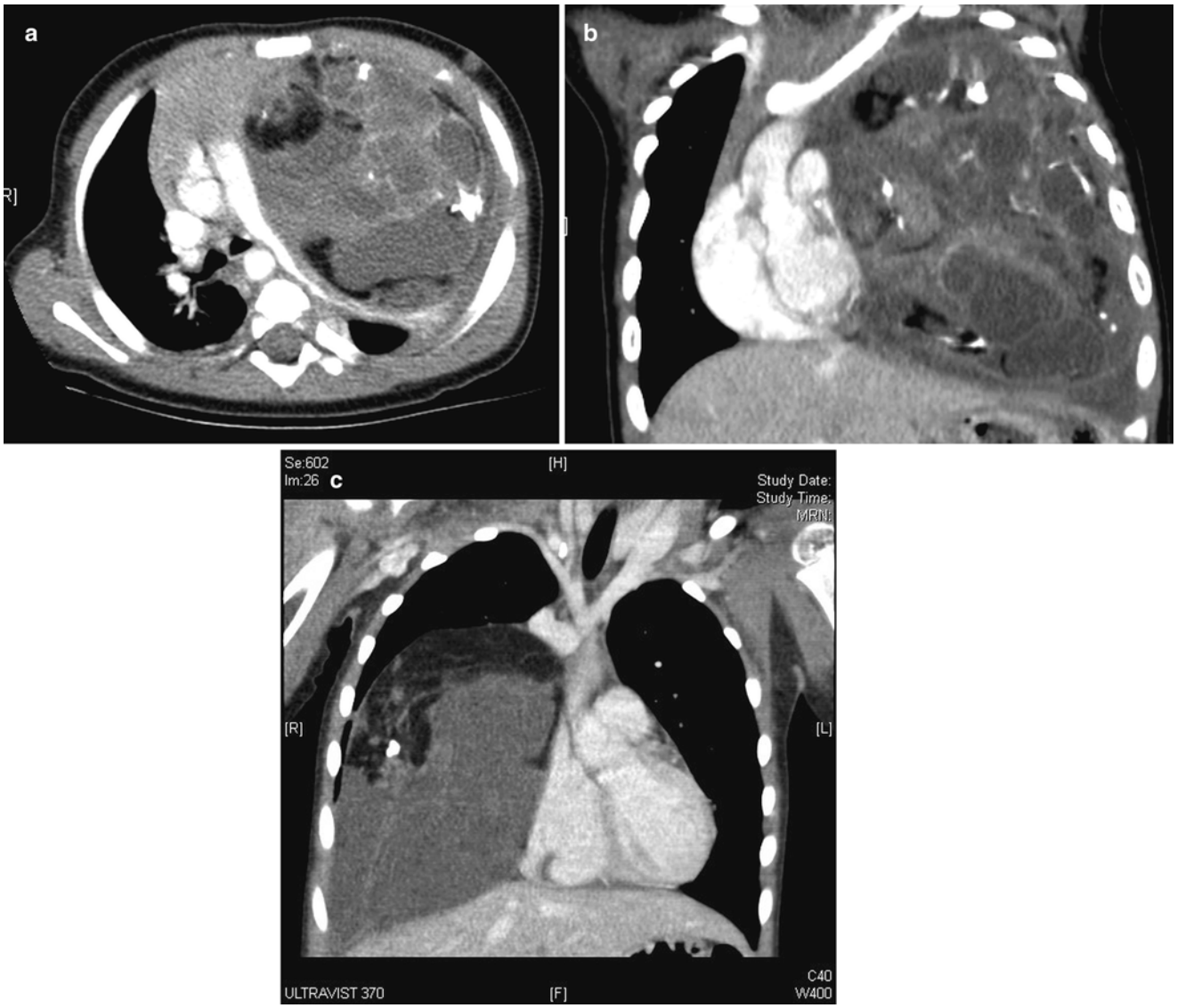

Fig. 11.1 Mediastinal teratoma. (**a**) Axial and (**b**) coronal contrast-enhanced chest CT in a 2-year-old boy shows a mixed solid, cystic, fatty and calcific lesion occupying most of the *left* chest. Narrowing and stretching of the *left* pulmonary artery is evident on the axial image. It is difficult to exclude pleural or chest wall invasion from the coronal images. (**c**) Coronal contrast-enhanced CT in another patient again showing a thoracic mass lesion with solid, calcific and fatty components

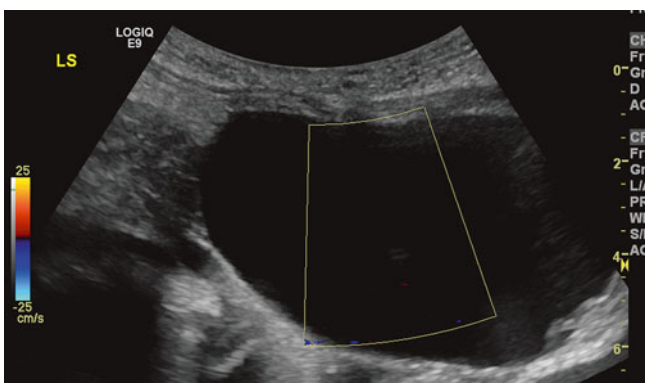

Fig. 11.2 Ovarian germ cell tumour. An ovarian GCT which appeared as a largely cystic hypovascular mass in an 8-year-old girl with only small solid components inferiorly

represent the least differentiated GCT elements and initial management is usually based on the predominant malignant element present [2, 3].

Rarely, secondary malignancies may arise within pre-existing GCTs, in which the malignant element represents secondary transformation of an underlying teratomatous element, rather than a primary malignant GCT element. This has been reported to include both a range of carcinomas and sarcomas, but when this occurs in childhood the malignant elements present are usually those recapitulating either primitive neuroectodermal tumour or rhabdomyosarcoma [12, 13].

From a practical clinical perspective, due to the potential marked heterogeneity in histological tissue composition within a GCT, of which a malignant element such as yolk

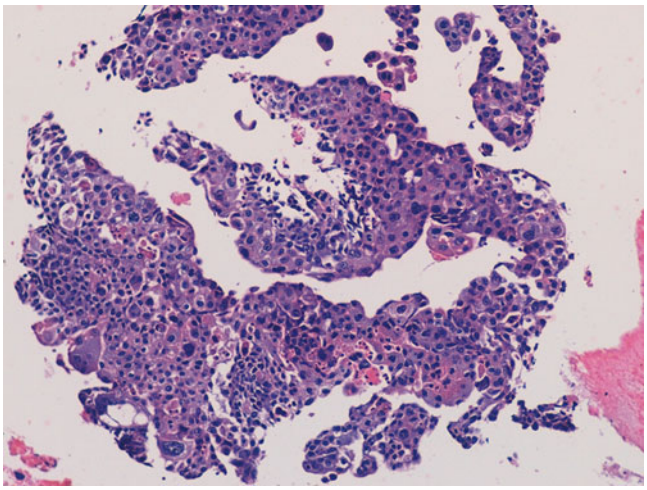

Fig. 11.3 Photomicrograph of material obtained from a thoracic/lung biopsy in a child with a large mass lesion and raised serum human chorionic gonadotropin level demonstrating irregular fragments and sheets of cells recapitulating the morphological features of trophoblast indicating a choriocarcinomatous component of a malignant mixed germ cell tumour. Original magnification 200×

sac tumour, which is overall by far the commonest malignant germ cell tumour component in childhood, may only represent a minority of the entire tumour mass. As a consequence caution must always be exercised when interpreting the results of a small image-guided biopsy (Fig. 11.3). There has been there a marked recent move in many pediatric centres towards primary diagnosis of most pediatric tumours using image-guided needle core biopsies rather than open biopsy or resection, especially in the UK and Europe. Such an approach can usually provide an adequate amount of material for diagnosis in the vast majority of cases but due to the issues of limited sampling, malignant elements of a GCT may not be sampled, and the results of such biopsies should be interpreted in light of other clinical features including the results of serum biomarkers such as alpha fetoprotein (AFP) and human chorionic gonadotropin (HCG) [14].

In addition to the wide range of specific histological subtypes which may be present in GCTs, ranging from mature through to very immature and embryonal tissue, within a given histological subtype there may also be further wide variation in specific patterns of histological appearances which are described. Therefore, GCTs can demonstrate a huge variation in their histological appearances both within a given tumour and between cases. Nevertheless, despite this apparent complexity, from a diagnostic perspective in clinical pathology practice, most of these patterns are of no relevance other than allowing correct recognition of the diagnosis. In routine practice, GCT diagnosis does not usually represent a major diagnostic difficulty in specialist laboratories [15].

Specific Histological Types of Germ Cell Tumours

Teratoma

Teratomas represent neoplasms in which there are histological tissue components recapitulating all three embryonic germ cell layers, which form recognisable structures but a histologically disorganised mass lesion. There may be a wide variation in the proportion showing differentiation towards each of the different germ cell layers and in very rare cases in childhood, monodermal teratomas may exist in which only one element appears present, the characteristic example being struma ovarii of the ovary composed of thyroid-type tissue [16].

In general, the most common elements identified in pediatric teratomas regardless of site are neural components followed by cutaneous tissue, fat, fibrous tissue, cartilage and gastrointestinal type epithelium, but with a wide range of other tissue types being described [2, 3]. Due to the large variation in elements present there is usually a mixture of cystic and solid components, corresponding to the general imaging appearances described above. Depending on the site, teratomas may locally infiltrate widely and markedly distort the normal anatomy, this being particularly the case in congenital tumours in which the teratoma is presumed to have grown in utero; in such cases surgery may be technically very difficult due to the unusual anatomy, including atypical vascular anatomy supplying, or running through, the tumour [17, 18].

In the majority of cases, all elements within a teratoma are histologically mature. Most cases of mature teratoma, provided excision is complete, behave in a benign fashion. There are some exceptions to this, however, specifically that the presence of an apparently mature teratoma within the testis of young adult may be associated with malignant behaviour [19] (Figs. 11.4, 11.5, 11.6, and 11.7).

Immature teratomas represent cases in which, in addition to any other tissues present, there is a component of immature embryonal tissue. In most cases, the majority of the tumour represents mature teratoma but with presence of immature neuroepithelial structures, the frequency and extent of which is related to the histological grading of such cases (Figs. 11.8, 11.9, and 11.10). The clinical significance of immature tissue within a teratoma appears to be related to the age of the patient and anatomical site. For example, immature elements in a congenital sacrococcygeal teratoma appear to have little significance for prognosis whereas immature tissue in the ovary of an adolescent girl is of adverse prognostic significance. The diagnosis of immature teratoma should be reserved for cases in which definite immature neuroepithelial tissue can be identified. The presence of apparently immature mesenchymal components, in isolation, is of uncertain significance, and is not usually a

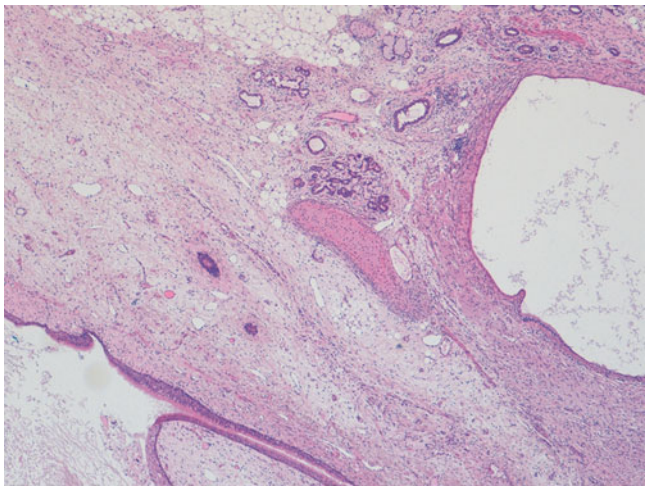

Fig. 11.4 Photomicrograph of a mature teratoma demonstrating a variety of disorganised but mature elements. There are no immature areas. Original magnification 40×

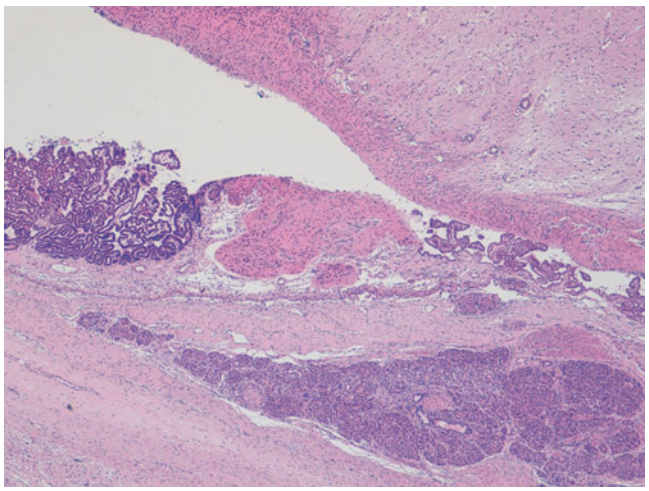

Fig. 11.6 Photomicrograph of a mature teratoma demonstrating a variety of disorganised but mature elements. There are no immature areas. Original magnification 20×

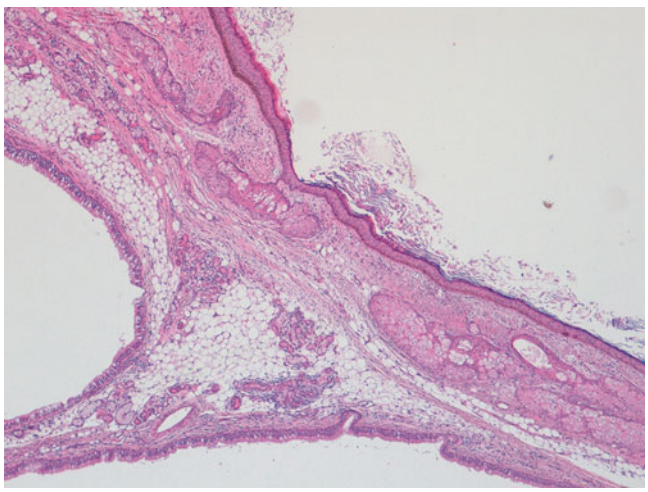

Fig. 11.5 Photomicrograph of a mature teratoma demonstrating a variety of disorganised but mature elements. There are no immature areas. Original magnification 40×

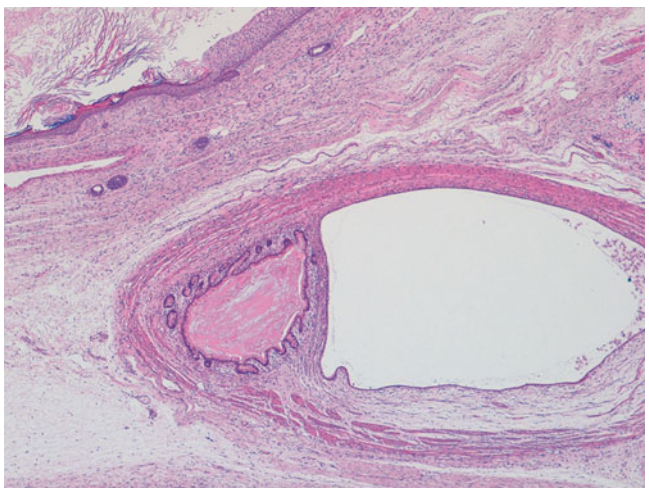

Fig. 11.7 Photomicrograph of a mature teratoma demonstrating a variety of disorganised but mature elements. There are no immature areas. Original magnification 20×

clinically relevant issue in immature teratoma of the ovary, in which immature neuroepithelial elements are almost always additionally present. The main relationship in the literature between histological grading of immature teratomas and clinical behaviour and outcome is provided for ovarian immature teratomas in young adults but such data is not available for teratomas at extragonadal sites in younger children [2, 20].

For the diagnostic pathologist, the most important aspect in the histological diagnosis of a teratomatous GCT is adequate sampling and histological assessment in order to detect any possible areas of malignant elements, almost always represented by yolk sac tumour. Therefore, it is important that the entire tumour is examined and sectioned and any atypical areas are sampled. The clinical management of GCTs in which a small focus of malignant yolk sac tumour is identified depends on the age and stage in terms of completeness of excision. Whilst the serum alpha-fetoprotein is often raised in the presence of the malignant yolk sac elements it should also be recognised that there may be cases in which serum alpha-fetoprotein is raised but despite an extensive examination of the specimen, no yolk sac tumour can be identified. In such cases, it has been suggested that the alphafetoprotein may be derived from other sources such as immature hepatic tissue [2, 3, 21].

Imaging Features

Teratomas manifest as typical GCTs with cystic and solid areas, with lesions in individual areas of the body having a propensity to invade local structures. Some important

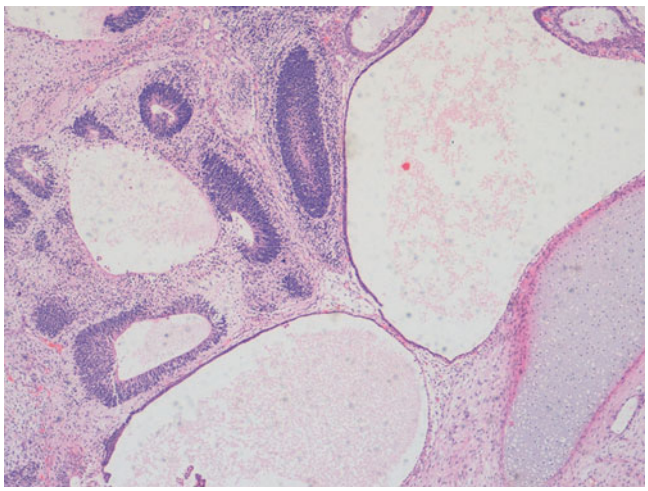

Fig. 11.8 Photomicrograph of a teratoma demonstrating mixed mature and immature elements. There are well differentiated cystic structures and an area of cartilage in the *bottom right* hand corner whereas in the *top left* area there are numerous immature neuroepithelial tubules. Original magnification 100×

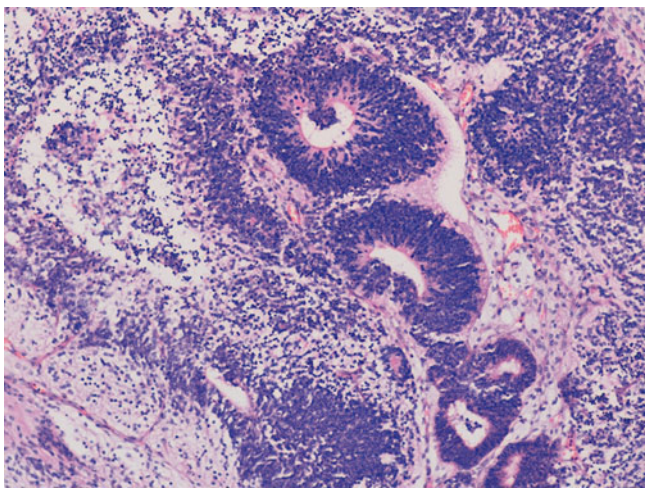

Fig. 11.9 Photomicrograph of a teratoma demonstrating mixed mature and immature elements. There are well-differentiated cystic structures and numerous immature neuroepithelial tubules. Original magnification ×200

specific radiological features of intracranial, mediastinal and sacro-coccygeal tumours are described elsewhere in this chapter.

Benign mature teratoma accounts for between 23 and 48 % of prepubertal *testicular* GCTs. These are usually found in boys under 4 years of age and appear radiologically as complex solid and cystic masses on ultrasound evaluation, often being large relative to the size of the testis. Echogenic foci may be evident as a result of calcification or fat within the lesion [22].

Most ovarian teratomas are diagnosed late in the first decade of life, with a peak age incidence at diagnosis of 10 years, or in early adolescence. The majority are benign. Most patients present as an abdominal mass (Fig. 11.11) or with pain due to torsion of the lesion (Fig. 11.12).

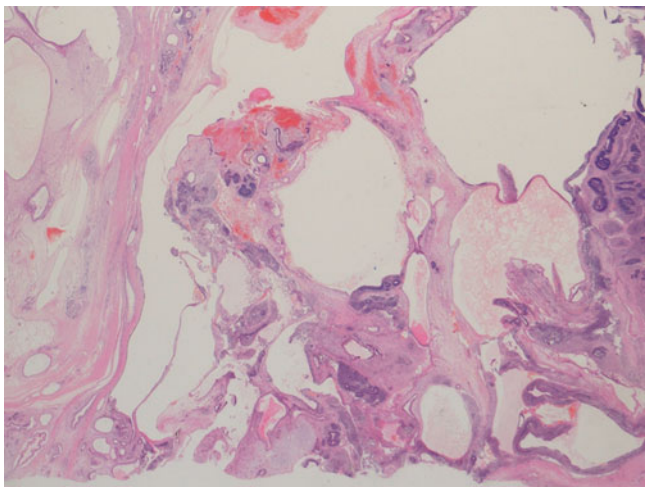

Fig. 11.10 Photomicrograph of a teratoma demonstrating numerous immature neuroepithelial tubules. Original magnification ×20

Primary abdominal and *retroperitoneal teratomas* are extremely rare and represent only 4–6 % of teratomas [23]. Although usually benign, abdominal teratomas in infants are often large and have a particular tendency to infiltrate widely such that describing them as merely retroperitoneal masses is anatomically simplistic. They have a propensity to expand anteriorly and often occupy virtually the entire abdomen such that contact with the anterior abdominal wall is common. Their large size often makes ascribing a definite organ or anatomical compartment of origin difficult. Whilst pancreatic, gastric, mesenteric and gallbladder origins are frequently described for these masses, the location may simply reflect the largest component of a tumour mass originating in the retroperitoneum or root of the mesentery. The typical radiological features of a retroperitoneal teratoma are a large, complex mass, usually with well-circumscribed cystic components, containing fat and areas of calcification [24]. The sonographic appearances of mature retroperitoneal teratoma are usually those of a mixed tumour with cystic and solid components. Calcification and characteristic adipose content or fat-fluid levels are better demonstrated on CT or MRI. Contrast enhancement of an intra-cystic solid component has been suggested as a criterion to distinguish benign from rarer malignant lesions in adults (with a sensitivity and specificity of approximately 80 %) and this may also be applicable to paediatric GCTs [25].

It is noteworthy, that vascular displacement seems to occur in a different pattern in abdominal teratomas to that seen with other infiltrative paediatric tumours such as neuroblastoma. These tumours almost invariably envelop the aorta and vena cava [26]. Mass effect can cause marked distortion

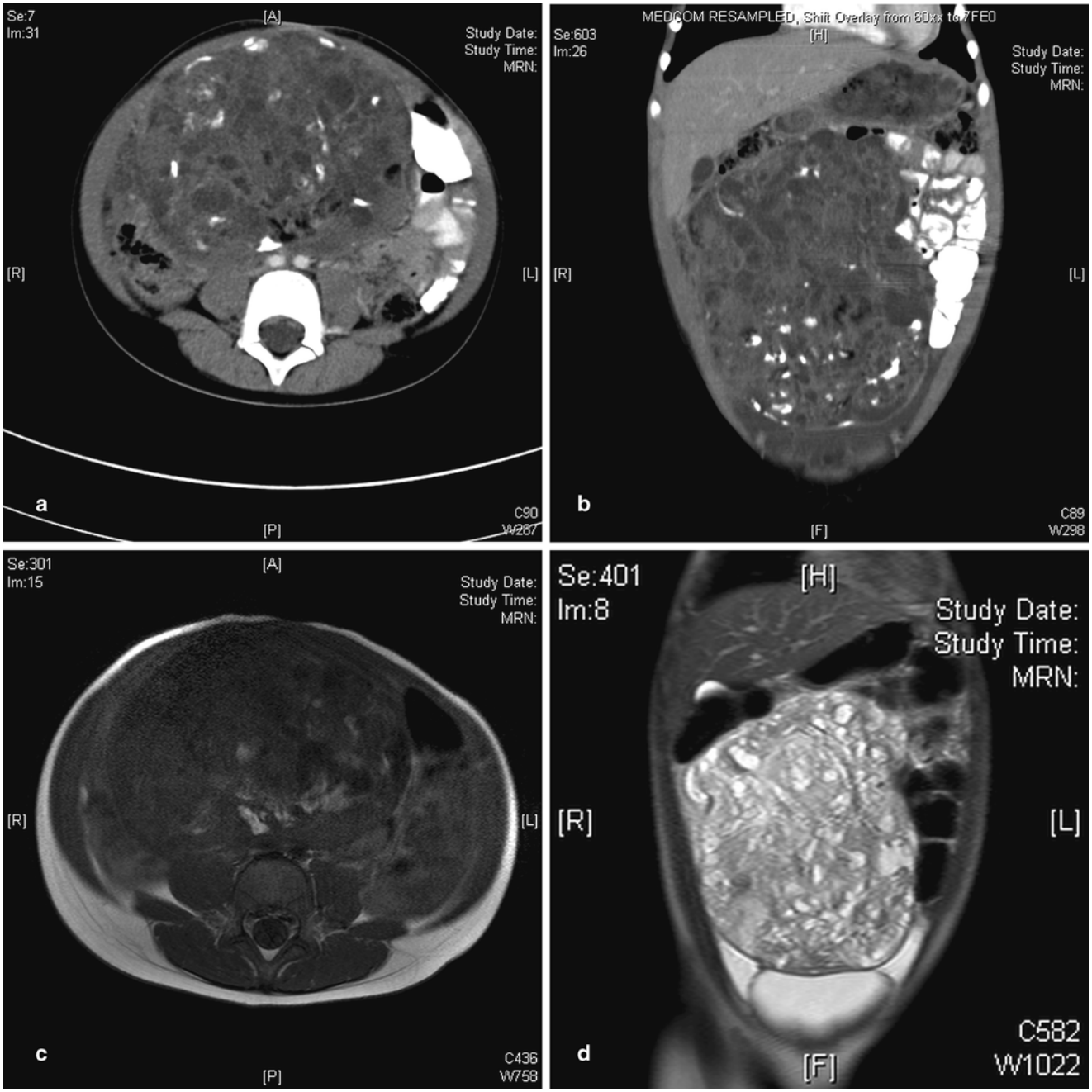

Fig. 11.11 Ovarian teratoma. (**a**) Axial CT in a 6-year-old girl showing a calcified and cystic mass occupying much of the central abdomen. (**b**) Coronal CT in the same patient shows the supero-inferior extent of the mass. (**c**) Conventional T1-weighted image in the same patient shows the fatty components of the mass posteriorly to have hyperintense signal similar to subcutaneous fat. (**d**) Coronal T2W image again shows the craniocaudal extent of this cystic mass to good effect, with some associated ascites in the lower quadrants being more obvious on this sequence

of normal anatomical relationships and compression or complete effacement of the IVC. In addition to being compressed or effaced, unusual but marked anterior displacement of the IVC away from the aorta is a surgical risk with these tumours and this should be carefully considered pre-operatively [26] (Fig. 11.13). Furthermore these masses may prove difficult to remove at surgery not only due to vascular encasement but also from being densely adherent to adjacent structures. Current CT angiographic techniques should be adequate to assess the arterial anatomy but the compressed abdominal veins can be very difficult to evaluate even with the best sonographic technique.

Seminoma/Germinoma

Seminoma and germinoma represent essentially the same neoplasm, depending upon the site and sex of the patient, being composed of sheets of uniform immature germ cells with no significant morphological differentiation towards other tissue types. Germinoma/seminoma occurs predominantly in adults and is generally rare in childhood, although is not uncommon affecting the gonads of teenagers and young adults. In younger children this diagnosis is very uncommon, particularly in its pure form, except in the context of a pineal germ cell tumour [2, 27].

Seminoma/germinomas usually present as solid masses with focal haemorrhage and necrosis and histologically demonstrate a distinctive appearance composed of sheets and nests of bland uniform cells separated by delicate fibrous septa. In most cases there is an associated significant lymphocytic inflammatory infiltrate, which in some cases may initially obscure the underlying seminomatous component. The tumour cells have a characteristic uniform appearance with open vesicular nuclei but some cases can show variable degrees of cytological pleomorphism. In small biopsies, especially with extensive lymphoid tissue present, immunohistochemical staining may be helpful in making the diagnosis [2, 3] (Fig. 11.14).

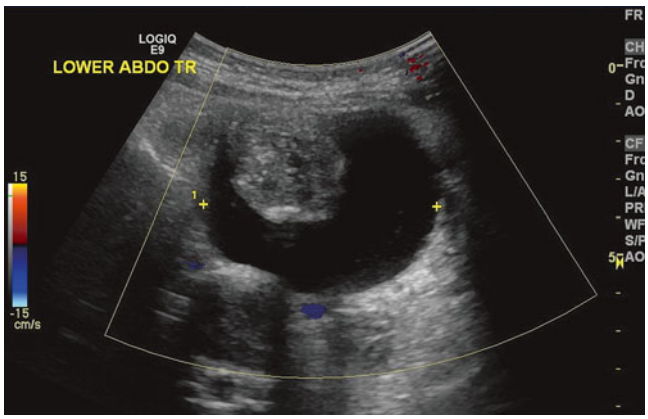

Fig. 11.12 Ovarian teratoma. A torted ovarian teratoma in an adolescent girl manifested with acute abdominal pain. Ultrasound, with Doppler evaluation, showed a mixed solid and cystic avascular mass

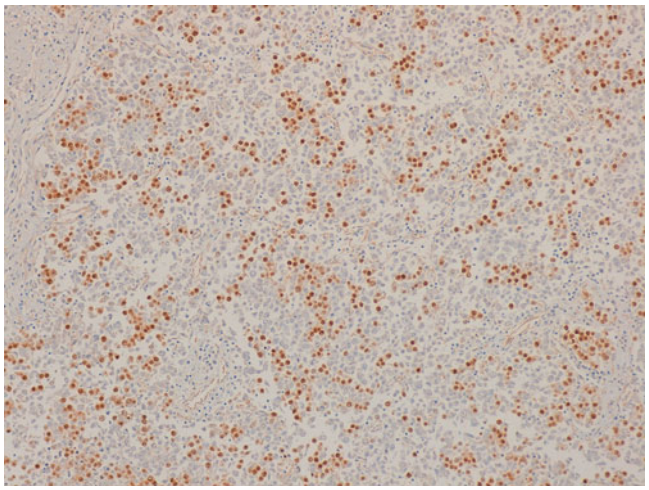

Fig. 11.14 Photomicrograph of a seminoma/germinoma immunostaining for OCT3/4 demonstrating positivity in the majority of cells. Original magnification 100×

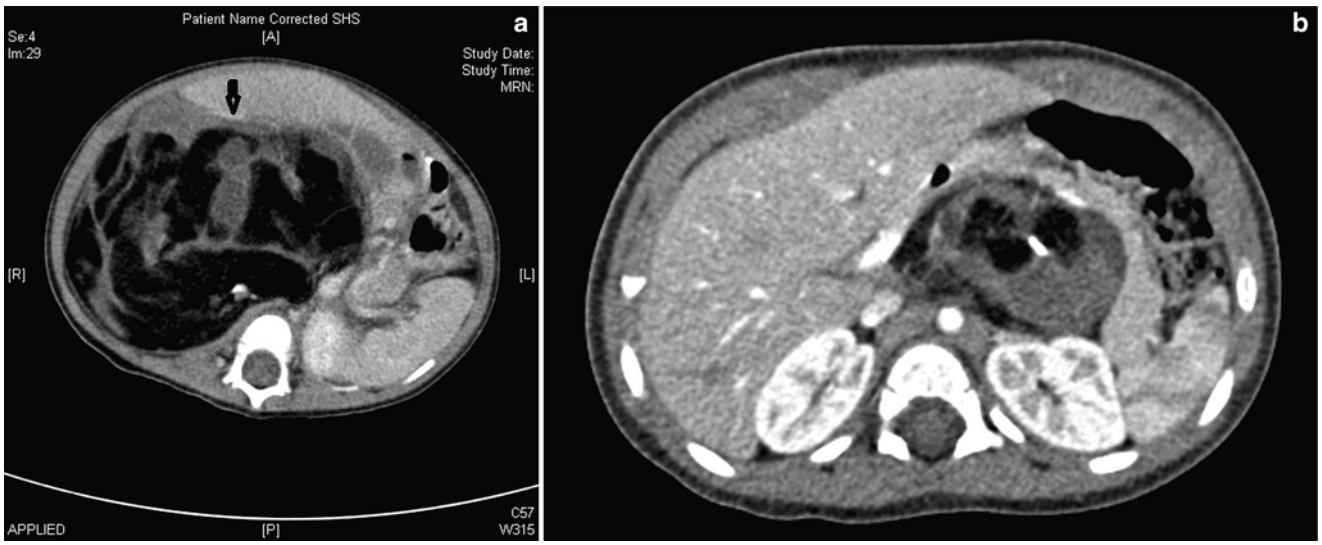

Fig. 11.13 Retroperitoneal teratoma. (**a**) Axial contrast-enhanced CT in a 6-month-old male infant shows a heterogenous, mainly fatty, retroperitoneal mass in the *right* flank crossing the midline. The unusual, and surgically hazardous, anterior displacement of the IVC (*arrow*) is highlighted here. (**b**) CT in a 5-month-old girl shows a mainly *left*-sided solid, fatty and calcific retropancreatic mass, anterior to the *left* kidney

Imaging Features

Seminoma, whilst the most common testicular tumour in adults, is very rare in childhood but when it does occur, it is the neoplasm most commonly associated with a cryptorchid testis [22]. Seminomas tend to have homogeneous, soft-tissue attenuation while the more malignant lesions frequently have large necrotic components but there is wide variation in the appearance of all these tumours.

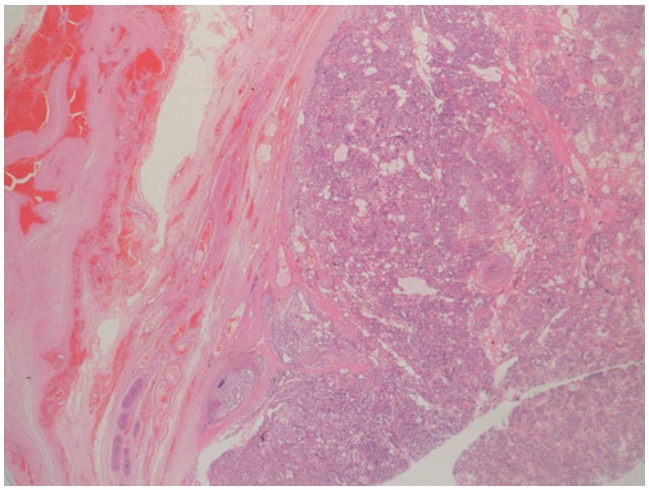

Fig. 11.15 Photomicrograph of a testicular malignant yolk sac tumour, which is confined to the testis. Original magnification 20×

Yolk Sac Tumour (Endodermal Sinus Tumour)

Yolk sac tumour represents by far the most common malignant GCT element in young children. They may occur as pure neoplasms or, more commonly, in association with other GCT elements such as teratoma. In the majority of cases they are associated with raised serum levels of alpha-fetoprotein (AFP).

Macroscopically yolk sac tumours (YST) are usually solid with areas of haemorrhage and necrosis. Microscopically, they have been reported as displaying an extremely large variety of histological patterns, which may make diagnosis difficult in some cases on small needle biopsy specimens. Histologically, there is almost always microcyst formation with intervening solid components composed of tumour cells which are relatively uniform small cells with little cytoplasm. The variant architectural features of these cystic and solid components include reticular, pseudopapillary, polyvesicular vitelline and solid patterns, in addition to areas of myxoid change and even pleomorphic sarcoma-like areas. The characteristic histological feature, which is not required for the diagnosis, is the presence of Schiller-Duval bodies, glomeruloid structures appearing to show a central blood vessel covered with tumour cells surrounded by a cyst lined by tumour cells. In most cases, in a resection specimen, the diagnosis is straightforward since a wide range of patterns are exhibited. The only variant which may cause some difficulty in diagnosis is the hepatoid pattern which usually shows solid sheets of cells with eosinophilic cytoplasm recapitulating fetal liver development [2, 3, 28] (Figs. 11.5 and 11.16).

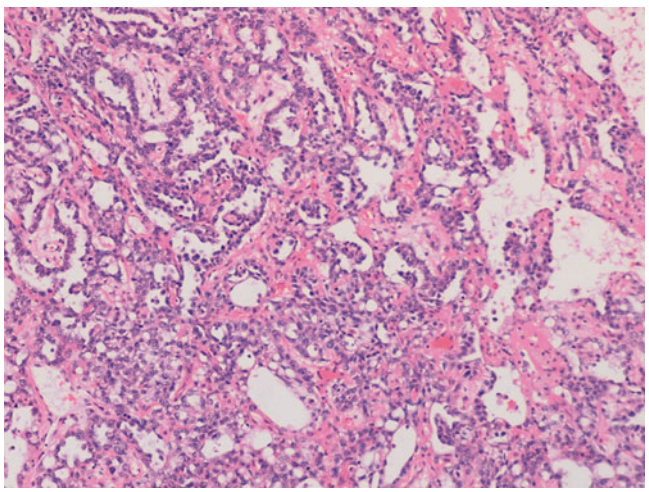

Fig. 11.16 Photomicrograph of a testicular malignant yolk sac tumour, demonstrating characteristic histological patterns. Original magnification 200×

A useful diagnostic feature in general is the presence of hyaline droplets which are present in the vast majority of yolk sac tumours and highlighted by DPAS staining. Yolk sac tumours almost always exhibit strong cytokeratin positivity, patchy expression of alpha fetoprotein, and more recently, glypican-3 immunostaining has been reported as a reliable and sensitive immunomarker for YST [29].

Imaging Features

YSTs appear on imaging similar to other GCTs, but elevated serum levels of AFP suggest the diagnosis. They tend to be more infiltrative than benign GCTs and may arise from the ovary, testis or elsewhere in the abdomen (Fig. 11.17). Testicular yolk sac tumours, which occur mainly in pre-pubertal boys, are confined to the testis (stage 1 disease) in 85 % at presentation [22] (Fig. 11.18). In the upper abdomen yolk sac tumours may mimic a primary hepatic tumour and it can be very difficult to identify the true site of origin of the lesion (Fig. 11.19). Extragonadal yolk sac tumours may occur virtually anywhere in the body, such as in the brain, mediastinum, common bile duct or thyroid gland as examples. Routine chest CT to detect or exclude pulmonary metastases is recommended at diagnosis.

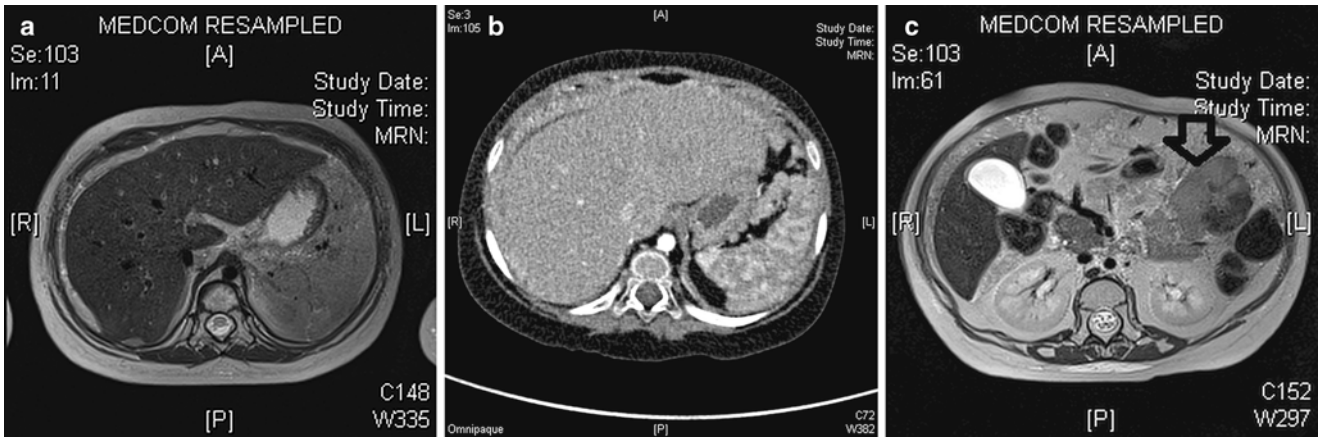

Fig. 11.17 Abdominal yolk sac tumour (YST). (**a**) Axial T2W image shows tissue similar to subcutaneous fat, albeit with some heterogeneity, peripheral to the liver parenchyma in a 3-year-old girl. (**b**) Contrast-enhanced CT shows this tissue is not adipose tissue but rather widespread infiltrating tumour tissue from a biopsy proven YST. (**c**) T2W MRI more inferiorly in the same patient shows a hypointense mass lesion in the *left* abdomen (*arrow*) which was also a component of this multifocal YST peritoneal tumour

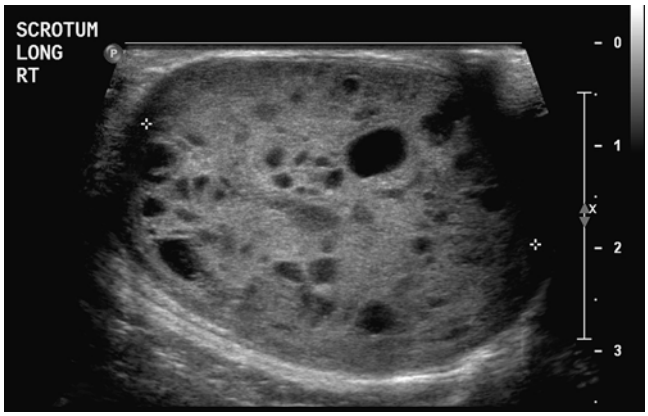

Fig. 11.18 Testicular yolk sac tumour. This tumour manifested as a cystic, and predominantly solid testicular mass, in a 4-year-old boy

Embryonal Carcinoma

Pure embryonal carcinoma almost never occurs in childhood and is rare even as a component of a mixed malignant GCT, which is the setting in which it is most commonly encountered. Histologically, embryonal carcinoma displays sheets of large pleomorphic cells with prominent nucleoli in an epithelioid pattern. Immunostaining is helpful for their recognition since they usually express cytokeratins and CD30 [2, 3].

Choriocarcinoma

Choriocarcinoma essentially does not occur in childhood as a primary GCT although it may rarely be a component of a mixed GCT in older children. It should be noted that in other GCTs such as seminoma, germinoma and embryonal carcinoma, scattered syncytiotrophoblast-like giant cells may be present but this does not designate the diagnosis of choriocarcinoma [19].

A hepatic malignancy termed "infantile choriocarcinoma of the liver" has been reported in association with maternal metastatic disease and intraplacental choriocarcinoma, representing metastatic spread from a placental gestational trophoblastic tumour [30] In young teens, at the start of the reproductive period, if pregnancy should occur, there is an increased risk of a hydatidiform molar pregnancy with potential associated risk of persistent gestational trophoblastic disease, however these gestational neoplasms do not represent GCTs. In adolescents extrauterine choriocarcinoma is extremely rare but may occur in the fallopian tube, ovary or elsewhere in the abdomen and pelvis. Ovarian choriocarcinoma accounts for less than 1 % of all ovarian tumours, and the mean age of presentation in children is 13.6 ± 6.9 years [31].

Imaging Features

A hemorrhagic mass or a hemoperitoneum may be seen with an ovarian primary. A large unilateral, hypervascular adnexal mass with multiple cystic cavities and the presence of haemorrhage associated with elevated β–HCG levels and an "empty uterus" are highly suspicious for an ovarian choriocarcinoma [31]. An MRI of the pelvis can confirm the contents of a mass to be hemorrhagic. It may nevertheless be challenging to differentiate choriocarcinoma from ectopic pregnancy in a young woman by imaging findings alone [31]. Distant hematogenous metastases may be present, however, with choriocarcinoma and help point to that diagnosis.

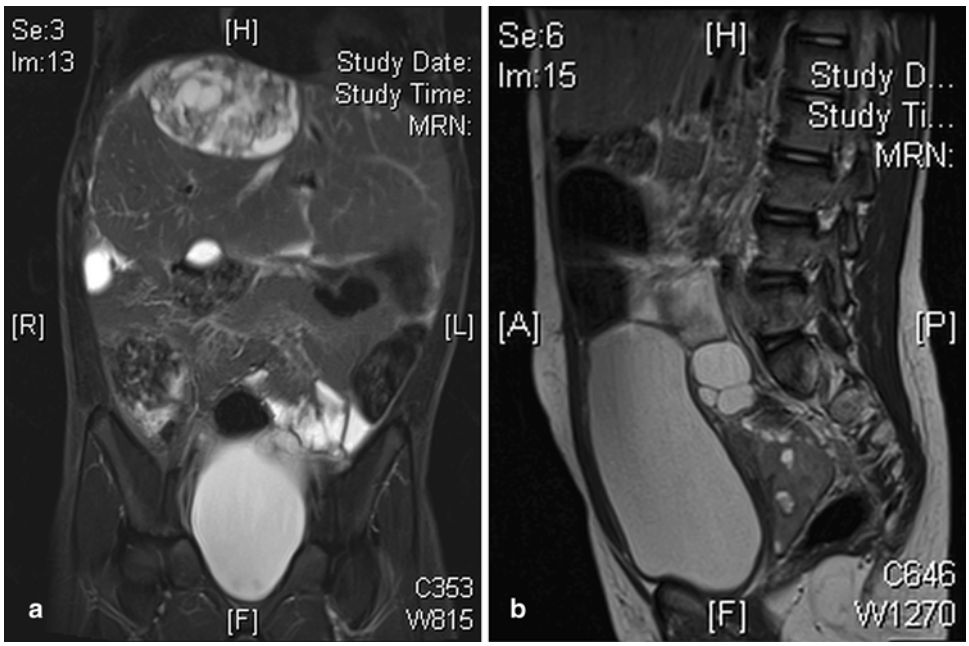

Fig. 11.19 Peritoneal tumour infiltration. This can occur with a mature teratoma or more malignant infiltrating tumours also. (**a**) An initial mature ovarian teratoma at surgery was found to have numerous small peritoneal deposits with identical pathology. Some of these enlarged over time. Coronal T2W image shows a heterogenous hyperintense mass superior to the *right* lobe of the liver. This was proven on repeated resection to be entirely mature teratomatous tissue. (**b**) Sagittal T2W image shows a cystic and solid metastatic deposit in the pouch of Douglas, posterior to a distended bladder, from a yolk sac tumour of the ovary

Issues Relating to Germ Cell Tumours at Specific Sites

Gonadal Germ Cell Tumours

GCTs arising in the gonad have different epidemiological characteristics in boys and girls. In boys there are two distinct peaks of GCT development, corresponding to distinctly different histological entities and underlying pathophysiological basis. GCTs occurring in young children represent either mature or immature teratomas or malignant yolk sac tumour. The majority of these present as asymptomatic mass lesions confined to the testis and do not show an association with intratubular precursor germ cell lesions, almost all of them in young children occurring in otherwise normal testes. Yolk sac tumour in young children does not show the characteristic cytogenetic abnormalities associated with adult testicular GCTs [28] (Figs. 11.20, 11.21, 11.22, 11.23, 11.24, 11.25, and 11.26).

Fig. 11.20 Macroscopic photograph of a testicular benign mature teratoma

In adolescent boys and young adults, the most common germ cell tumour type represents seminoma and these are often associated with precursor lesions of intratubular germ cell neoplasia unclassified (ICGNU). It should be noted that the reliable identification of ICGNU can be more difficult in both younger children and those with dysgenetic and developmentally abnormal gonads, particular in patients with disorders of sexual differentiation who are at increased risk of germ cell tumours, since they may also have associated abnormalities of normal germ cell maturity (see later section). Fetal germ cells express markers such as CD117, PLAP and OCT3/4, this expression normally being lost in early childhood. However, abnormal germ cell maturation may result in persistence of such markers even in the absence of true ICGNU development. Both disorders of sexual differentiation and cryptorchidism increase the risk of development of

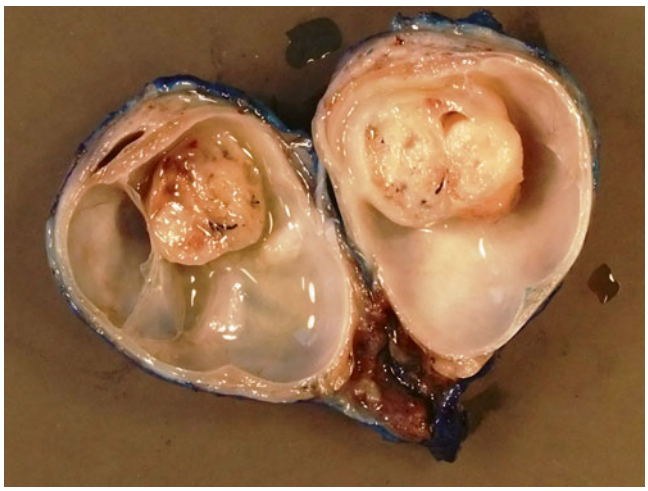

Fig. 11.21 Macroscopic photograph of a testicular benign mature teratoma

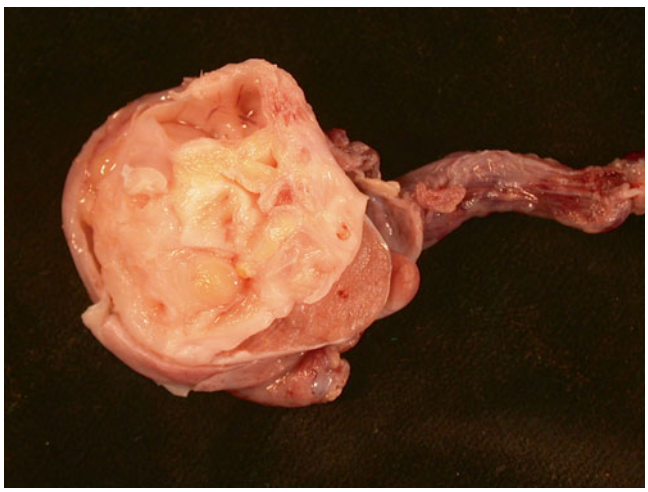

Fig. 11.22 Macroscopic photograph of a testicular benign mature teratoma

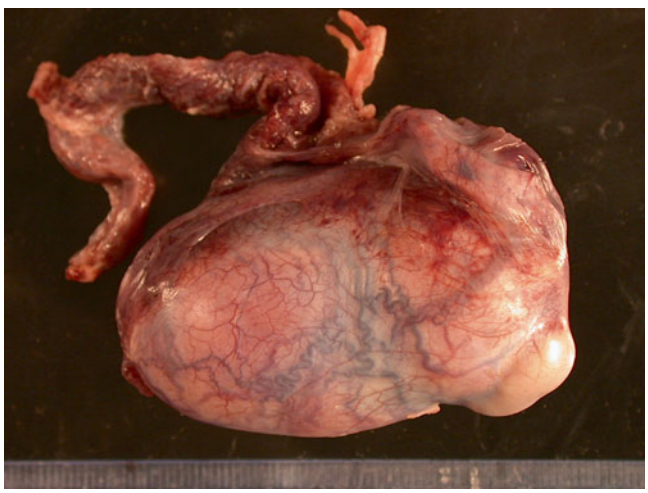

Fig. 11.23 Macroscopic photograph of a testicular malignant yolk sac tumour. The coverings are intact

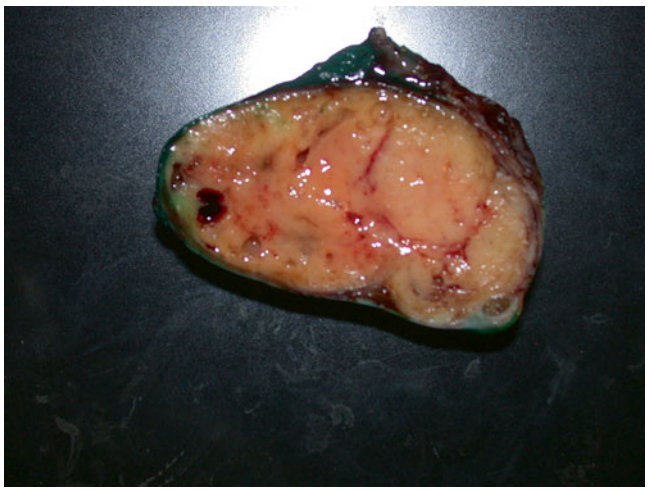

Fig. 11.24 Macroscopic photograph of a testicular malignant yolk sac tumour. The cut surface is solid and *pale yellow*

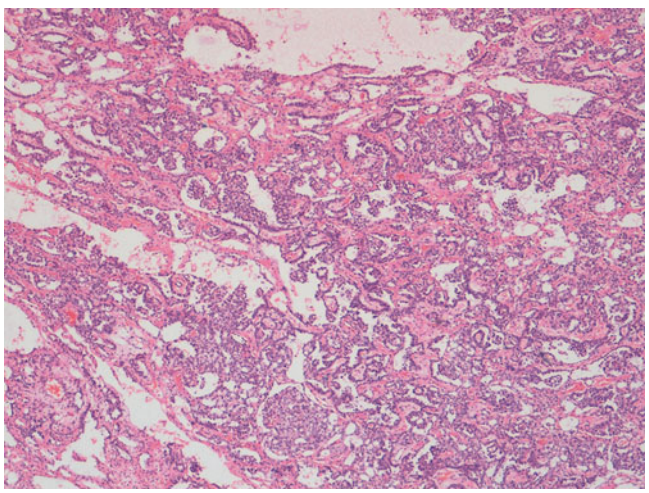

Fig. 11.25 Photomicrograph of a testicular malignant yolk sac tumour, demonstrating characteristic histological patterns. Original magnification 100×

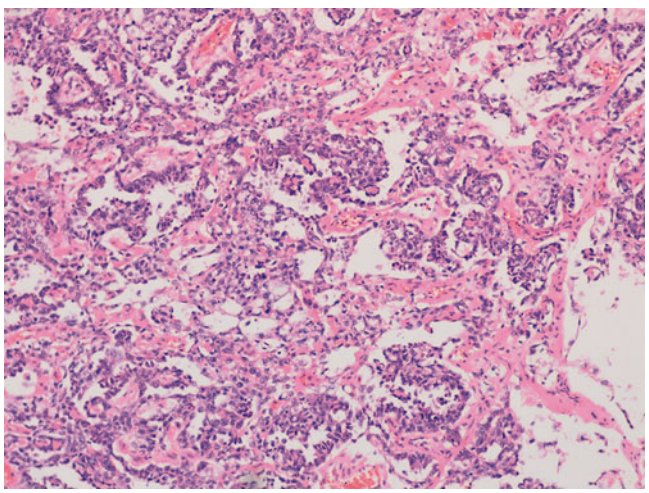

Fig. 11.26 Photomicrograph of a testicular malignant yolk sac tumour, demonstrating characteristic histological patterns. Original magnification 200×

testicular seminoma, which usually occur in adulthood, although they may affect an older child. Testicular teratomas may also occur, the majority of which appear mature histologically, but even mature teratomas can occasionally demonstrate metastatic disease. Cytogenetic analysis shows a characteristic abnormality in the majority of almost all postpubertal testicular germ cell tumours with the presence of isochromosome 12p [28].

In girls, ovarian GCTs most often occur in older children and in young adults, the vast majority of which represent mature teratomas. Ovarian GCTs in young children are rare and if they occur are usually malignant. In older children, immature teratoma of the ovary is associated with increased risk of metastatic disease and malignant behaviour, particularly in high-grade cases in which a greater amount of immature tissue is present. Ovarian immature teratoma grading requires sampling of at least 1 section per cm diameter as follows; grade 1 < 1 lpf (40×) on any slide, Grade 2 1–3 lpf (40×) on any slide, Grade 3 > 3 lpf (40×) on any slide. In some cases of ovarian teratoma, disseminated teratomatous components throughout the peritoneal cavity may occur (gliomatosis peritoneii), which are usually composed of mature glial tissue in a patient with a primary ovarian immature teratoma. Whilst usually not malignant per se, they may present management difficulties especially if extensive [19] (Figs. 11.27, 11.28, 11.29, 11.30, 11.31, 11.32, 11.33, 11.34, 11.35, 11.36, and 11.37).

Ovarian dysgerminomas almost never occur in younger children but may be encountered in teenagers and young adults. Whilst the majority of germinomas occur in genetically normal females, this tumour also occurs in dysgenetic gonads. Ovarian yolk sac tumours and embryonal carcinomas are extremely rare in childhood and have histological features similar to tumours at other sites.

Fig. 11.28 Macroscopic photograph of a predominantly cystic ovarian germ cell tumour

Fig. 11.29 Macroscopic photograph of a predominantly cystic ovarian germ cell tumour. On opening, solid areas are identified

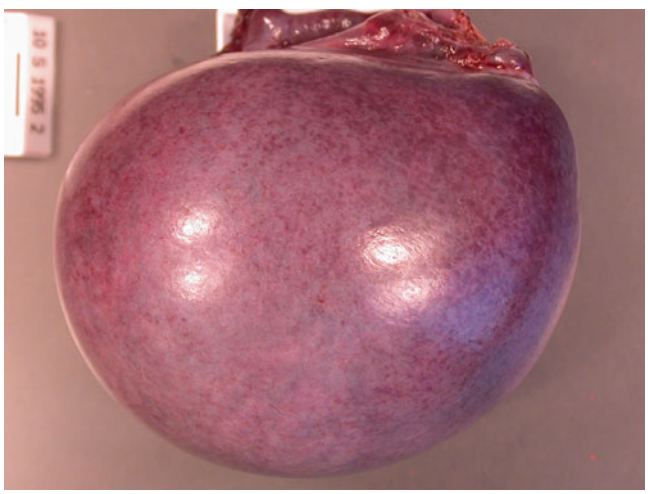

Fig. 11.27 Macroscopic photograph of a predominantly cystic ovarian germ cell tumour

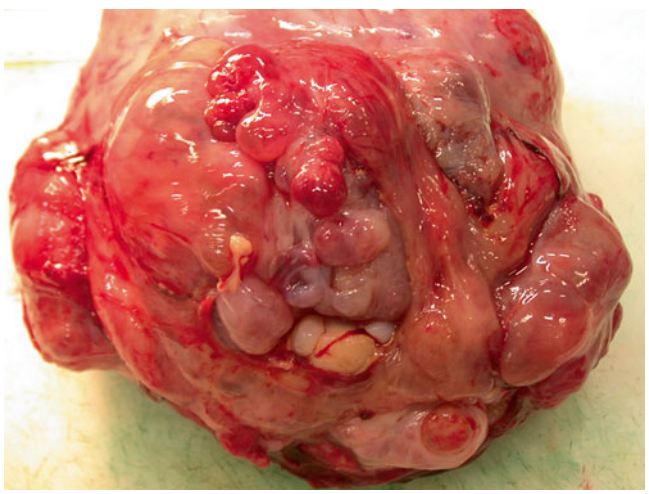

Fig. 11.30 Macroscopic photograph of a predominantly solid ovarian immature teratoma

Fig. 11.31 Macroscopic photograph of a predominantly solid ovarian immature teratoma

Fig. 11.32 Macroscopic photograph of a predominantly solid ovarian immature teratoma in which numerous cystic areas are seen on opening

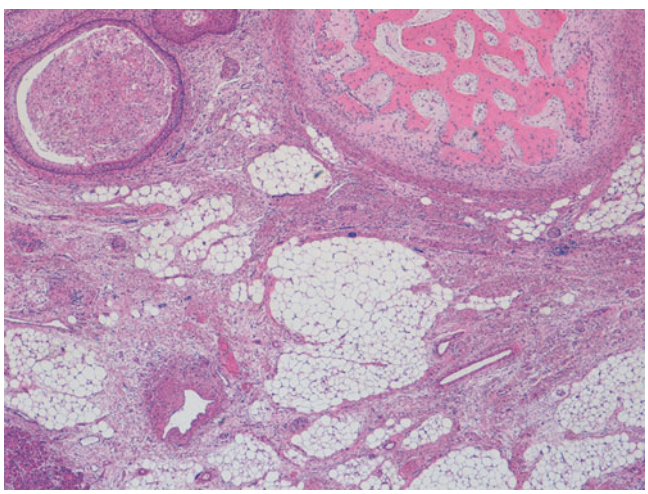

Fig. 11.33 Photomicrograph of a mature teratoma demonstrating a variety of disorganised but mature elements. There are no immature areas. Original magnification 40×

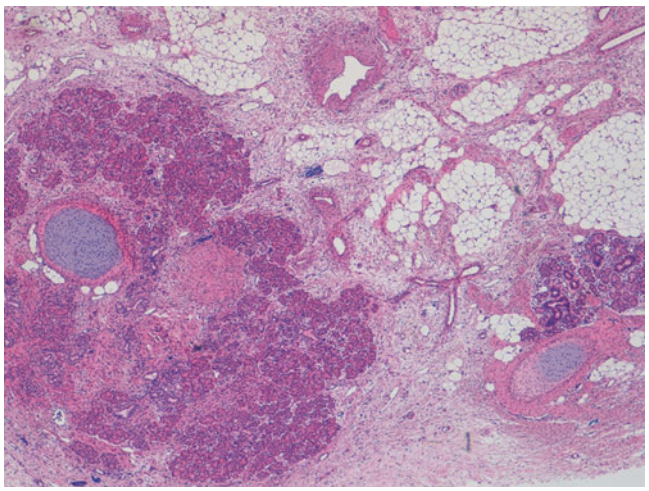

Fig. 11.34 Photomicrograph of a mature teratoma demonstrating a variety of disorganised but mature elements. There are no immature areas. Original magnification 20×

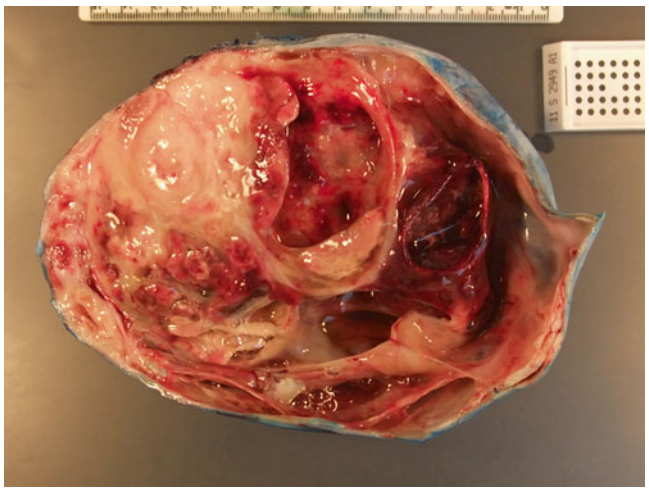

Fig. 11.35 Macroscopic photograph of a solid and cystic ovarian germ cell tumour in which a malignant neuroepithelial component was present within the solid tissue

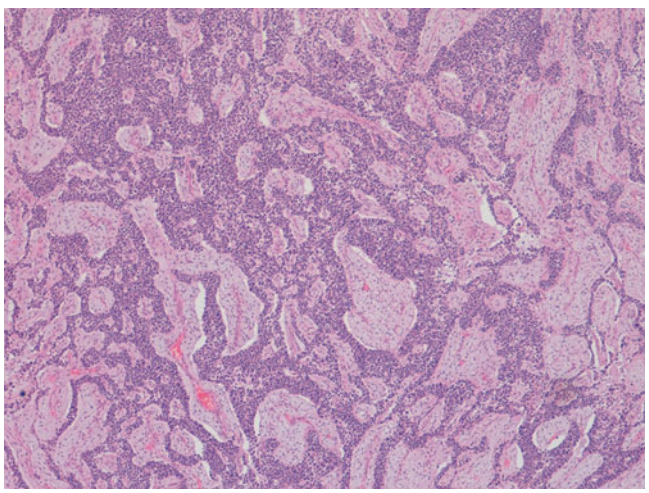

Fig. 11.36 Photomicrograph of an ovarian teratoma with a malignant neuroepithelial component. Original magnification 40×

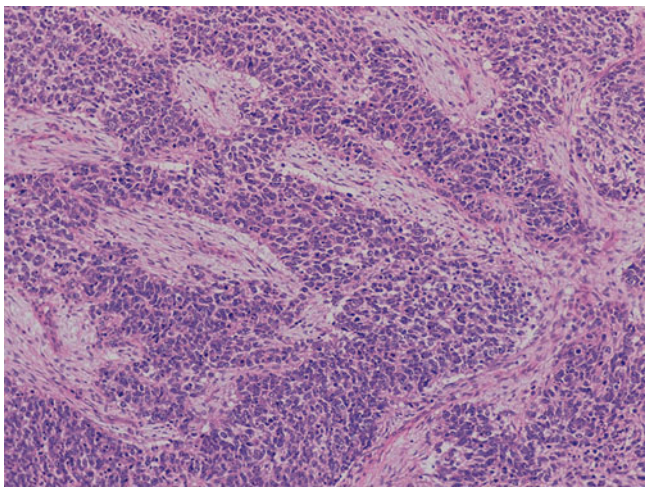

Fig. 11.37 Photomicrograph of an ovarian teratoma with a malignant neuroepithelial component. Original magnification 100×

Malignant mixed germ cell tumours of the ovary contain more than one malignant element, often dysgerminoma, and yolk sac tumour and occur rarely in younger children although precocious puberty may be an association in a minority of these cases.

Imaging Features

Most boys with *testicular tumours* present with painless testicular or scrotal enlargement. With metastatic disease, boys may present with nodal enlargement or malignant ascites. Serum AFP and HCG levels are often elevated in patients with malignant testicular GCTs (90 % of cases) [32]. The majority of testicular tumours are non-metastatic and localised to the scrotum at presentation [32]. In the remaining patients, the tumour may spread to retroperitoneal lymph nodes, lungs and liver or rarely, to bone or brain. Ultrasound is the technique of choice for the diagnosis of any testicular lesion since it can define the cystic or solid nature of a mass and its relationship to the testes. The distinction between intra- and extratesticular masses is important because the majority of intratesticular lesions are malignant, whereas most extratesticular lesions are benign (with the exception of paratesticular rhabdomyosarcoma). At sonography, CT and MRI, testicular tumours generally appear as discrete solid masses, but occasionally they present as diffuse testicular enlargement. They may be hypo- or isoechoic to normal testicular tissue on sonography. There also may be homogeneous or contain calcifications or hypoechoic areas, which may be due to the presence of haemorrhage or necrosis. Findings of extratesticular extension include reactive hydroceles and irregularity of the tunica albuginea. Scrotal skin thickening is rare. In practice, the combination of scrotal skin thickening and an intratesticular mass is more characteristic of an inflammatory process than a neoplasm.

Imaging of the chest, abdomen and pelvis are routinely performed to search for metastases. The abdomen and pelvis can be further evaluated by CT or MR. CT is necessary to evaluate the lungs. After tumour resection, ultrasound is usually sufficient for defining local scrotal recurrence, as well as assessing the status of the contralateral testis and abdomen.

The diagnosis of an *ovarian* mass usually is established by ultrasound. Ultrasound findings of ovarian malignancy include a solid mass with central necrosis and thickened irregular septa or papillary projections. Other signs of malignancy include ascites, typically containing echogenic material, and liver metastases. CT findings of malignant ovarian lesions include a cystic soft tissue mass with thick, irregular walls, low-attenuation areas due to necrosis or haemorrhage, and thickened septa. Irregular, coarse calcifications are common in both dysgerminomas and immature or malignant teratomas. On MRI, malignant ovarian tumours commonly have low to intermediate signal intensity on T1W images and intermediate or high signal intensity on T2W, with the solid areas showing variable enhancement after gadolinium administration. Fibrovascular septa may be noted. These are hypo- or isointense on T1W images and typically show marked enhancement after administration of gadolinium. Bilateral involvement may be seen in up to 15 % of ovarian dysgerminomas [33]. With malignant lesions, the staging evaluation should include CT of the chest and CT or MRI of the abdomen.

Peritoneal tumour implants appear as soft tissue nodules on the lateral peritoneal surfaces or in the ligaments and mesenteries of the abdomen. Omental implants appear as nodules or conglomerate masses (“omental cake”) beneath the anterior abdominal wall. They may enhance after intra-venous administration of iodinated contrast agents or gadolinium. Malignant ovarian neoplasms spread by contiguous extension, lymphatic spread, or haematogenous dissemination. Ovarian GCTs usually metastasise to liver, lungs or lymph nodes; metastases to bone and peritoneal surfaces are rare.

Intracranial GCT

Congenital intracranial teratomas are reported but the majority of GCTs affecting the brain occur in older children and young adults and show a male predominance. Primary intracranial GCTs are relatively common in paediatric neuropathological practice, around two thirds of cases being seminoma/germinoma, approximately 20 % being teratomas, with other malignant elements representing the minority [34, 35].

CNS GCTs are usually midline affecting third ventricle, pineal gland or suprasellar region. Intracranial teratomas are uncommon in childhood, accounting for only 2 % of primary intracranial neoplasms in children younger than 15 years. Intracranial teratomas are more common in males than females, as a result of the preponderance of pineal teratomas in males.

In general, histological findings of intracranial germ cell tumours are similar to those at other sites but it should be noted that both a granulomatous reaction and florid lymphocytic infiltrate may be associated and may even be prominent at this site. Immunohistochemical staining can be extremely useful and in particular OCT3/4 appears to be a more reliable germ cell marker than PLAP for identifying germinomatous elements in this setting [2, 3].

Symptoms and signs are variable and include pyrexia of unknown origin, hemiparesis, seizures and visual disturbance. Psychiatric symptoms, precocious puberty and even dementia are also possible [35].

Imaging Features

A heterogenous, sharply marginated, midline mass is the usual manifestation. Fat and calcium within the lesion are readily apparent on CT and MRI, but are perhaps more obvious on CT. When both fat and calcium are seen in a midline intracranial mass, a diagnosis of teratoma should be suggested (Fig. 11.38). Not all teratomas contain fat or calcium however, and some manifest merely as solid homogenous masses. The solid components show variable degrees of enhancement with gadolinium administration at MRI or iodinated contrast enhancement for CT. The masses may be very cystic or entirely solid. The tumours are usually isointense to hyperintense compared to cortical gray matter on T1W and T2W images. Subarachnoid tumour seeding is a recognised complication and is best evaluated with gadolonium-enhanced MRI. The high lipid concentration within a tumour may be apparent also at MR spectroscopy. Although most GCTs are found in the suprasellar and pineal regions, a small number (4–14 %), arise in the basal ganglia and thalami, particularly in boys in the second decade of life [36].

Mediastinal Germ Cell Tumours

Mediastinal GCTs represent around 5–10 % of paediatric GCTs and include benign teratomas, which may present either incidentally as a local mass effect or occurring congenitally, when usually clearly involving the thymus. Primary GCTs account for up to 10 % of *mediastinal* masses in children. They are second only to lymphoma as a cause of a thymic mass. These tumours are most often located in the anterior mediastinum, only 2–3 % of mediastinal GCTs occurring in the posterior mediastinum [37]. In children and adolescents mediastinal germinomas may occur and have an association with subsequent haematological malignancies [38] (Figs. 11.39, 11.40, 11.41, and 11.42).

Imaging Features

Most teratomas have well-defined margins, thick walls and some fatty tissue or calcification or both. Approximately 25 % of teratomas contain calcification [39]. Fatty tissue plus calcification in an anterior mediastinal mass almost invariably indicate a germ cell origin (Fig. 11.1). Teratomas in the mediastinum may rupture into adjacent structures such as the pleural space, pericardium, lung parenchyma or tracheobronchial tree. Up to one third of mature benign mediastinal teratomas are reported to rupture, with malignant lesions having a significantly lesser tendency to leak their contents [40]. Proteolytic or digestive enzymes and sebaceous materials within these teratomas are thought to play a role in their tendency to rupture and cause

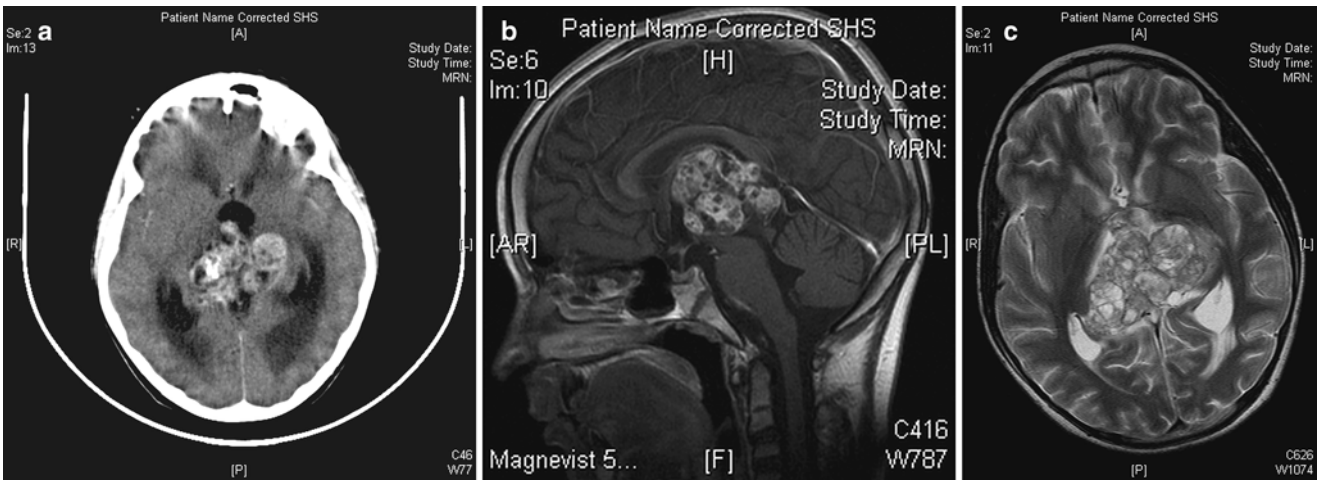

Fig. 11.38 Intracranial germ cell tumour. (**a**) Axial post-contrast enhanced CT shows an enhancing midline mass with some associated dilatation of the third and lateral ventricles. Despite enhancement of the mass, more dense attenuation in the *right* side of the lesion is clearly due to calcification. (**b**) Sagittal T1W MRI after gadolinium administration shows a heterogeneously enhancing midline mass. (**c**) Axial T2W MRI shows the heterogenous mass with the more hyperintense areas representing cystic changes within the lesion. Note that the lesional calcification cannot be appreciated on this MR image

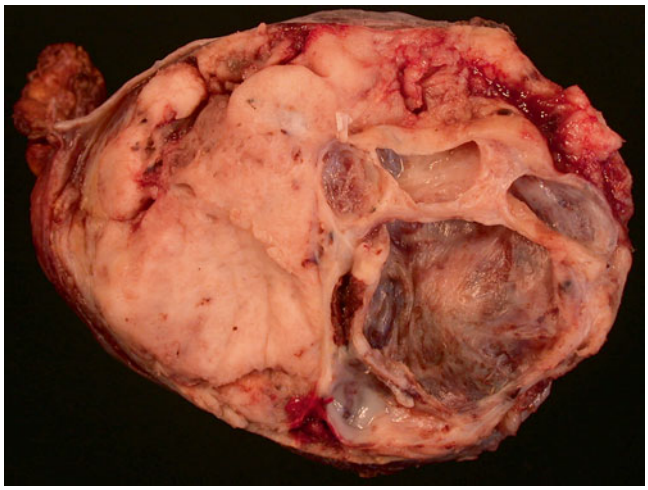

Fig. 11.39 Macroscopic photograph of mediastinal germ cell tumour demonstrating solid and cystic area

Fig. 11.40 Macroscopic photograph of a thymic teratoma demonstrating a complex solid and cystic structure

Fig. 11.41 Macroscopic photograph of a thymic teratoma demonstrating a solid and cystic structure with prominent fat

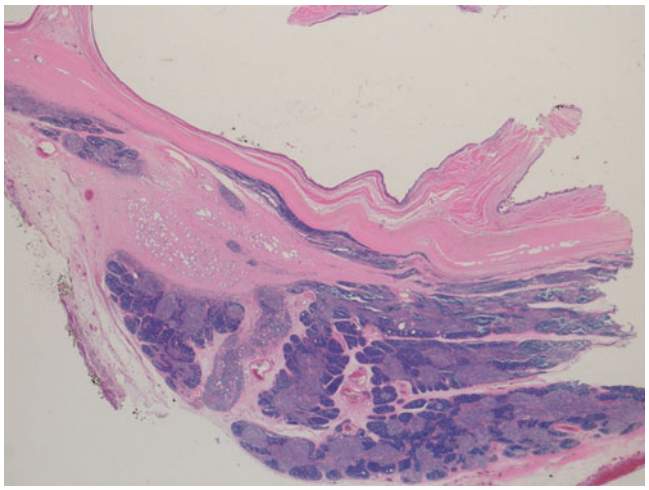

Fig. 11.42 Photomicrograph of a thymic teratoma demonstrating mature tissue with cyst formation and peripheral residual thymus. Original magnification 12.5×

adjacent non-infectious inflammation. High amylase levels have been found in pleural effusions and within the tumour contents [40]. Additional findings in ruptured tumours depend on the space into which the rupture occurs. Rupture into the lung or through the tracheobronchial tree may cause a chemical pneumonitis or fat-containing masses in the adjacent lung parenchyma. Haemoptysis with expectoration of hair or sebaceous material indicates a fistula between the tumour and the tracheobronchial tree and is said to be pathognomonic of a mature teratoma. Rupture into the pleura or pericardium results in pleural or pericardial effusions. Adjacent consolidation or atelectasis should be regarded as suspicious for rupture but can also, of course, be seen with atelectasis resulting from by any large thoracic mass. Rupture is important to recognise or suspect as inflammatory changes and adhesions secondary to extravasation of tumour contents may result in more hazardous surgery than had been thought likely from initial CT or MRI evaluation.

Sacrococcygeal Teratoma

Sacrococcygeal teratomas are congenital lesions either presenting during pregnancy or shortly after birth. The vast majority of sacrococcygeal GCTs are pure teratomas and their management and prognosis is primarily dependent upon mechanical and other complications related to their resectability. The main treatment for sacrococcygeal teratomas is complete local resection which now includes removal of the coccyx in order to minimise recurrence risk. The presence of immature tissue in these young infants is not associated with adverse prognosis in the absence of malignant elements, although recurrent and/or metastatic immature teratomas have been reported. Around one in five sacrococcygeal teratomas

will contain yolk sac tumour elements, the frequency increasing with older age at presentation, most congenital cases being composed of mature and immature teratoma only. There are no consistent chromosomal cytogenetic abnormalities in sacrococcygeal teratomas [41] (Fig. 11.43).

Four anatomical types of *sacrococcygeal teratomas* have been described based on the relative amounts of internal and external tumour:

Type I—predominantly external; limited extension into the presacral space (47 %).

Type II—similar external and intrapelvic components (34 %).

Type III—minimal external tumour; large pelvic and abdominal components (9 %).

Type IV—purely presacral tumour without an external component (10 %).

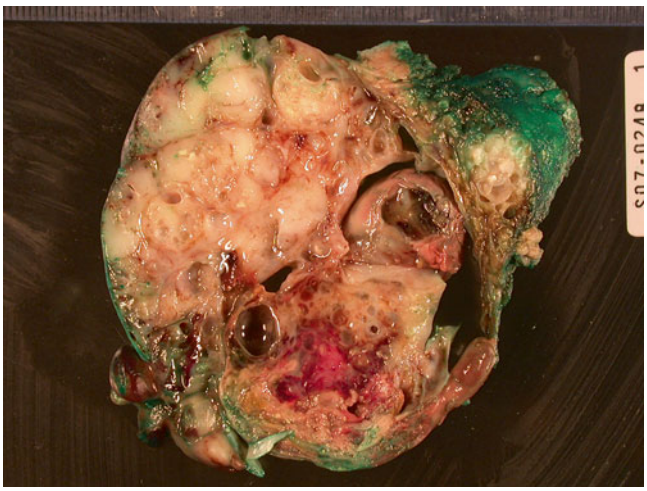

Fig. 11.43 Macroscopic photograph of a solid and cystic sacrococcygeal teratoma in which a malignant yolk sac component was present

Imaging Features

Benign mature sacrococcygeal tumours are usually cystic masses, whilst malignant tumours are typically more complex with larger areas of solid tissue easily depicted with US. Malignant sacrococcygeal teratomas appear as soft tissue masses on CT with or without fat or calcification, although MRI is, of course, preferred due to the radiation burden from CT (Fig. 11.44). The tumour, like teratomas elsewhere, displays intermediate signal intensity areas on T1W images and intermediate or high signal intensity components on T2W images and contrast-enhanced images. Tumour margins are often poorly defined, infiltration of adjacent soft tissues and intraspinal tumour extension are commonly seen. Although both CT and MR can demonstrate the extent of intrapelvic and intra-abdominal tumour, MR is better for the detection of soft-tissue extension, such as the relationship of tumour to the gluteal muscles and for the detection of intraspinal involvement. It is debated whether MR is needed in newborns because virtually all lesions then are benign. Some surgeons advocate only plain radiographs and US. After 2–3 months of age, however, when the frequency of malignant change increases, cross-sectional imaging is recommended.

Gonadal Sex Cord/Stromal Tumours

These tumours are derived from gonadal stromal supporting cells and hence essentially only affect the gonad. They include Leydig cell tumours, Sertoli cell tumours, granulosa cell tumours and thecomas/fibromas. Overall this group represents around one third of all testicular tumours in the pediatric age group and in this setting almost all cases clinically behave in a benign manner. Sex cord stromal tumours are however usually hormonally active and are

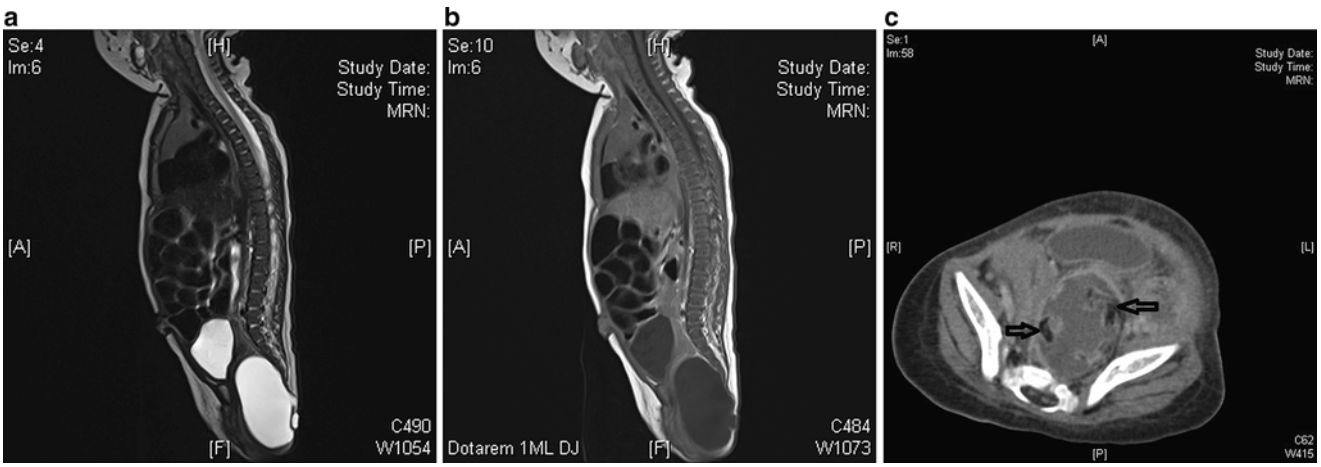

Fig. 11.44 Sacrococcygeal teratoma in a neonate. (**a**) Sagittal T2W MRI shows a predominantly cystic pre-sacral mass with no obvious solid components on this image. The more anteriorly located bladder, with similar T2 signal, is displaced superiorly. (**b**) Sagittal T1 after gadolinium administration shows only minimal, barely perceptible, enhancement of the lesion outer surface. (**c**) Axial CT (but MRI is generally preferred to evaluate lesion extent) shows a heterogenous presacral mass containing fatty low-attenuation components (*arrows*)

classically associated with isosexual precocious puberty (juvenile granulosa cell tumour) or virilisation or hirsutism (Sertoli-Leydig cell tumours) [33]. Boys are typically younger than girls at diagnosis [42] and plasma gonadotrophins are more often completely suppressed in boys than in girls [42]. Pure Leydig cell tumours are exceedingly rare in girls, who most often have Sertoli-Leydig tumours [43].

Leydig Cell Tumour

The tumour cells recapitulate normal Leydig cells and these lesions account for around 3 % of testicular tumours of childhood. The usual presentation is painless testicular enlargement but in around one third of cases hormonal effects may be present such as precocious puberty. The tumours are usually well circumscribed from surrounding testicular parenchyma, are macroscopically encapsulated and show a distinctive brown appearance on their cut surface. Histologically they are usually composed of relatively uniform medium to large polygonal cells with abundant eosinophilic cytoplasm. Crystals of Reinke can be identified in around the third of cases and Lipofuscin pigment may be prominent in 10–20 % of cases. Sex cord stromal tumours, including Leydig cell tumour, express vimentin and Inhibin [3] (Fig. 11.45).

The main differential diagnosis in childhood is to distinguish Leydig cell tumours from multinodular Leydig cell proliferation associated with adrenogenital syndrome. Leydig cell proliferation is usually bilateral, shows more marked cellular pleomorphism and pigmentation and more fibrous stroma. Furthermore, such Leydig cell hyperplasias have an interstitial rather expansile growth pattern. Malignant Leydig cell tumours are rarely reported and have much more marked cytological atypia. Malignant behaviour is associated with large size (>5 cm diameter), cytological atypia, mitoses, necrosis and vascular invasion, similar to other endocrine active tumours [3, 44].

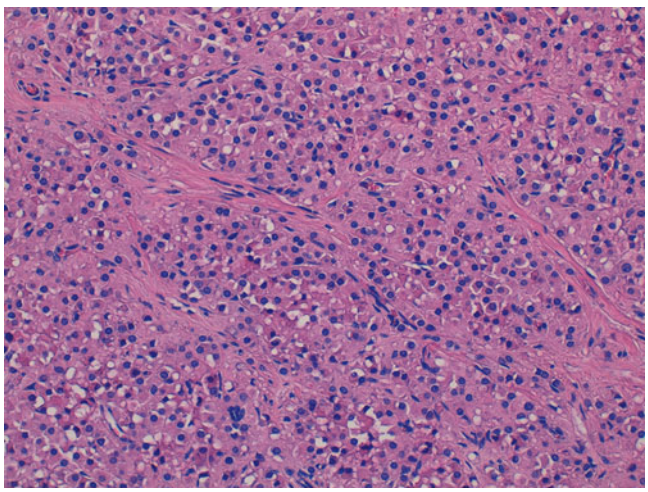

Fig. 11.45 Photomicrograph of a Leydig cell tumour demonstrating sheets of bland, plump Leydig cells with prominent eosinophilic cytoplasm. Original magnification 200×

Sertoli Cell Tumour

Sertoli cell tumours are composed of cells demonstrating histological features of Sertoli cells and are extremely rare in childhood. They may occasionally occur in conjunction with underlying genetic predispositions such as Carney and Peutz-Jeghers syndromes. Presentation is usually with a painless testicular mass.

Histologically, the tumours are generally composed of uniform cells with oval to round nuclei and pale eosinophilic cytoplasm. Few mitoses are present and the cells are usually arranged into tubules with prominent surrounding hyalinised basement membrane-like material. Sertoli cell tumours express vimentin and cytokeratin and around half of cases also express inhibin. A variant known as large cell calcifying Sertoli cell tumour has been reported in childhood and is associated with precocious puberty/gynecomastia, the average age at presentation being in the mid teens but also occuring in younger children. Around 20 % of such tumours are malignant and 40 % are bilateral. The microscopic histological features include similar nests and cords of polygonal Sertoli type cells but with more prominent nucleoli, and with the stroma showing multifocal areas of calcification [3, 45].

Imaging Features

These tumours may present simply as an enlarged hyperemic ovary on ultrasound assessment, in comparison to the normal ovary in the same child. Alternatively, the lesion may appear as solid, predominantly hypoechoic, abnormality on ultrasound [33]. On MRI they can manifest as hypointense solid lesions on T2W sequences, depending on their fibrous content. They may be indistinguishable from granulosa cell tumours [33]. Tumours affect either testis equally but appear to occur more often in the left ovary [42]. Testicular tumours are generally isointense to normal testicular tissue on T1W and hypointense on T2W images.

Granulosa Cell Tumours

Granulosa cell tumours of the testis are essentially identical to those of the ovary and have two distinct variants, adult and juvenile types. Adult type granulosa cell tumour rarely occurs in childhood. In contrast, juvenile type granulosa cell tumour is the most common congenital testicular neoplasm, comprising 5–10 % of all testicular tumours in prepubertal children. This lesion usually presents as an asymptomatic

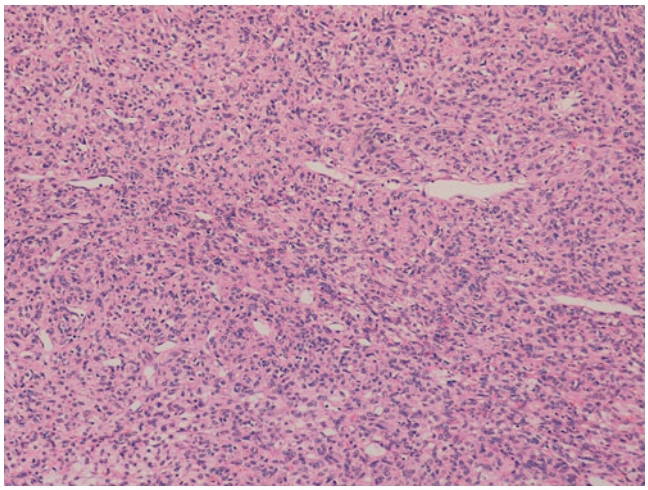

Fig. 11.46 Photomicrograph of a juvenile granulosa cell tumour demonstrating sheets of relatively monomorphic ovoid cells. In this field there is no cystic change. Original magnification 100×

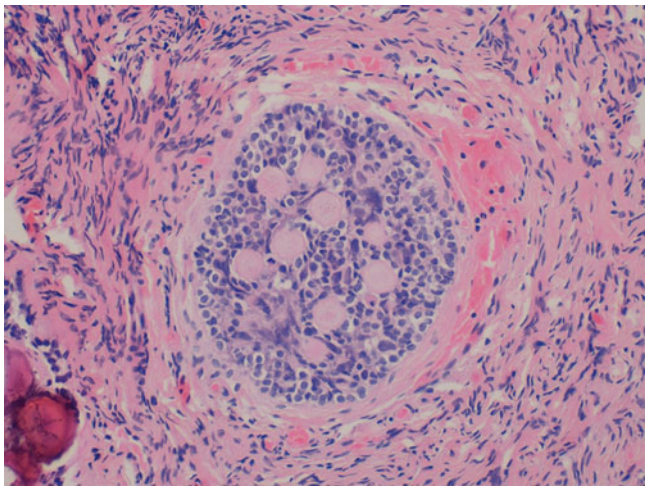

Fig. 11.47 Photomicrograph of an intra-abdominal testis demonstrating gonadoblastoma in which there is a well circumscribed lesion composed of hyalinised and focally calcified nodules surrounded by bland supporting cells. No malignant component is present in this case. Original magnification 100×

mass lesion in the first year of life, often identified at birth. These tumours may be associated with other abnormalities such as mixed gonadal dysgenesis and hypospadias [28, 46].

Histologically they are characteristically solid and cystic, with the microcystc being lined by several layers of cells with the appearance of inner granulosa cells and outer thecoma-like cells. Similar to other sex-cord stromal tumours they express vimentin, cytokeratin and inhibin on immunostaining [3] (Fig. 11.46).

Thecomas and fibromas are rare and histologically similar to their ovarian counterparts in adults. These tumours have been described as being composed of undifferentiated tissue with incompletely differentiated sex cord or stromal elements. They are extremely rare in childhood and mostly benign. Other mixed forms of sex cord stromal tumours have also been described.

Imaging Features

A testicular thecoma may present as a testicular lump or as an exophytic paratesticular lesion but these are extremely rare tumours in boys. There is an association with nevoid basal cell carcinoma syndrome (Gorlin syndrome) [47]. In an adult study in women, most ovarian fibromas and fibrothecomas were isointense to hypointense compared with myometrium on T1-weighted and T2-weighted images [48]. A capsule was noted in the majority and degenerative changes were seen with tumours over 6 cm in diameter. The maximum percentage of enhancement for fibromas and fibrothecomas was significantly lower than those for myometrium and fibroids [48]. Fibrothecomas had a higher maximum percentage of enhancement than did fibromas. Similar to other ovarian masses, the imaging manifestations of these tumours are often varied and non-specific, with a mixture of a solid enhancing mass with cystic areas being most likely.

Gonadoblastoma

Gonadoblastoma almost exclusively occurs in the dysgenetic gonads of patients with at least some Y-chromosome material, usually phenotypic females with disorders of sexual differentiation and gonadal dysgenesis. Whilst gonadoblastoma itself represents a localised benign tumour of both germ cells and other supporting cells, around half of the patients presenting with gonadoblastoma also have an associated frankly malignant germ cell tumour, usually seminoma/germinoma. In contrast to the malignant germ cell tumour components which almost always develop in adulthood, gonadoblastomas can develop in younger children and may even be present in infancy. There are a few reports of gonadoblastoma development in anatomically male children with cryptorchism, sliding testicle, hypospadias, and even normal scrotal testicles and in dysgenetic ovaries in the apparent absence of a Y chromosome [49].

These tumours contain both germ cell and sex cord stromal elements demonstrating large central germ cells similar to those of seminoma/germinoma and surrounding small cells resembling Sertoli/granulosa cells. The Sertoli-like cells usually surround hyalinised nodules or large germ cells and variable degrees of calcification may be present. The stromal cells of gonadoblastoma express inhibin and WT1 [3, 50] (Fig. 11.47).

Imaging Features

Gonadoblastomas may manifest as microscopic neoplasms, too small to be detected by diagnostic imaging. When obvious macroscopically, ovaries with gonadoblastoma development have the appearance of solid tumours in the

lower abdomen on US and CT while some cases with bloody ascites have been reported [51]. Testicular gonadoblastoma on US presents as a hyperechoic area in the central part of the affected testicle.

Gonadal Epithelial Tumours

Epithelial tumours of the ovary represent a significant category of neoplastic ovarian lesions in later adulthood. In childhood, such epithelial lesions are rare and when present affect older children. Most epithelial neoplasms are serous, followed by other miscellaneous epithelial tumours, mucinous tumours, endometroid tumours and clear cell tumours, in order of frequency [33]. Each of these tumour types is classified as benign, borderline or malignant according to the clinical behaviour of the tumour [33]. Serous and mucinous cystadenomas are the most common histological sub-types in the pediatric age range [52].

Imaging Features

Large ovarian lesions may manifest with torsion, presenting as an acute abdomen. Serous cystadenomas present as unilocular or multilocular cystic masses, typically with homogenous cystic components but without papillary excrescenses [33]. Mucinous cystadenomas are generally large multiloculated cystic masses with thin septations, and fluids of differing MRI signal intensities are seen within the locules. These locules are often small and numerous [33]. With serous cystadenofibromas, the solid component may manifest with very low signal on T2W sequences.

Secondary Testicular Tumours

In children, primary testicular lymphomas are extremely rare, occasionally occurring in younger children. In contrast, secondary involvement of the testis clinically occurs in around 5 % of childhood lymphomas. In children, the majority of testicular lymphomas therefore represent secondary involvement with Burkitt lymphoma, diffuse large B-cell lymphoma or lymphoblastic lymphoma. Such leukemic infiltrates are histologically found in 60–90 % of children at autopsy who die from complications of leukaemia, but they are clinically apparent only in about 5–10 % [28, 53].

Imaging Features

Ultrasound may show either a diffusely enlarged testis or a focal hypoechoic or heterogenous lesion. Testicular involvement is usually bilateral, but it can be unilateral or asymmetric. Involvement of the testis, as a focal lesion, is also recognised in metastatic neuroblastoma and Wilms' tumour, again most easily detected with ultrasound. In the latter situation, tumour is believed to seed down the left testicular vein.

Rarities and Paratesticular/Adnexal Tumours

Extremely rare tumours of the testis have been described in childhood including testicular carcinoid and other rare forms ovarian and testicular epithelial tumour may also occur, and other rare forms of ovarian and testicular include small cell carcinoma of hypercalcaemic type, and other uncommon epithelial neoplastic cysts.

Furthermore, whilst not gonadal or germ cell in origin, a range of paratesticular tumours may occur in childhood which may enter the clinical and radiological differential diagnosis of an apparent scrotal mass, including spindle cell rhabdomyosarcoma, adenomatoid tumour, nodular mesothelial hyperplasia, melanotic neuroectodermal tumour of infancy, desmoplastic small round cell tumour, lipoma, haemangioma, neurofibroma, granular cell tumour, and fibrous hamartoma of infancy [3].

Summary

In general, the radiological and histopathological features of gonadal and extragonadal GCTs are related to the degree of differentiation and the specific lineage to which they are differentiating, resulting in a wide range of histological types; mature teratoma, immature teratoma, yolk sac tumour, embryonal carcinoma, choriocarcinoma, germinoma/seminoma, and gonadoblastoma. The relative distribution of these subtypes varies according to the site and age of the patient. Similarly, the clinical presentation may vary from a prenatally diagnosed mass leading to high output cardiac failure, to a mass lesion in the brain, pelvis or testis, or a lesion with endocrine manifestations.

Virtually all GCTs manifest radiologically as mass lesions with varying cystic and solid components. These should be imaged first, when possible, by ultrasound. Some lesions may be very cystic with little solid components, and may mimic simple cysts, or a hemorrhagic ovarian cyst, but they all contain some solid components and that should be looked for at ultrasound evaluation. After sonographic assessment, further detailed evaluation with cross-sectional imaging is ideally done with magnetic resonance imaging (MRI), which will typically show cysts with varying contents, from simple fluid signal to complex proteinaceous fluids with different signal intensities. Conventional T1-weighted (T1W) MRI will easily demonstrate the fatty components of GCTs as high signal foci, paralleling the signal from subcutaneous fat. MRI with gadolinium demonstrates the solid components and septations best. The relationship, and infiltrative nature when present, of a mass

to other viscera will be apparent on MRI. Similarly, MRI is the best method to assess for intraspinal tumour extension. When MRI is unavailable then CT will also show lesion extent to good effect, albeit with an inherent radiation burden. CT is the most sensitive modality for detecting foci of calcification, a common occurrence, within these tumours. CT also readily demonstrates the fatty components when present.

References

1. Barber HR. Embryology of the gonad with reference to special tumors of the ovary and testis. J Pediatr Surg. 1988;10:967–72.
2. Perlman EJ. Germ cell tumors. In: Stocker JT, Askin FB, editors. Pathology of solid tumors in children. London: Chapman Hall; 1998. p. 213–34.
3. Sebire NJ, Malone M, Ashworth M, Jacques TS. Diagnostic pediatric surgical pathology. London: Elsevier; 2010.
4. McHugh K. Uncommon pediatric neoplasms. In: Husband J, Reznek R, editors. Imaging in oncology. 3rd ed. Colchester, UK: Informa UK Ltd.; 2010. p. 954–60.
5. deMent SH. Association between mediastinal germ cell tumors and hematologic malignancies: an update. Hum Pathol. 1990;21: 699–703.
6. Schneider DT, Hilgenfeld E, Schwabe D, Behnisch W, Zoubek A, Wessalowski R, Göbel U. Acute myelogenous leukemia after treatment for malignant germ cell tumors in children. J Clin Oncol. 1999;17:3226–33.
7. Chen Z, Robison L, Giller R, Krailo M, Davis M, Gardner K, Davies S, Shu XO. Risk of childhood germ cell tumors in association with parental smoking and drinking. Cancer. 2005;103: 1064–71.
8. Queipo G, Aguirre D, Nieto K, Peña YR, Palma I, Olvera J, Chavez L, Nájera N, Kofman-Alfaro S. Intracranial germ cell tumors: association with Klinefelter syndrome and sex chromosome aneuploidies. Cytogenet Genome Res. 2008;121(3–4):211–4.
9. Zahn S, Sievers S, Alemazkour K, Orb S, Harms D, Schulz WA, Calaminus G, Göbel U, Schneider DT. Imbalances of chromosome arm 1p in pediatric and adult germ cell tumors are caused by true allelic loss: a combined comparative genomic hybridization and microsatellite analysis. Genes Chromosomes Cancer. 2006;45(11): 995–1006.
10. Veltman I, Veltman J, Janssen I, Hulsbergen-van de Kaa C, Oosterhuis W, Schneider D, Stoop H, Gillis A, Zahn S, Looijenga L, Göbel U, van Kessel AG. Identification of recurrent chromosomal aberrations in germ cell tumors of neonates and infants using genomewide array-based comparative genomic hybridization. Genes Chromosomes Cancer. 2005;43:367–76.
11. Rapley EA, Turnbull C, Al Olama AA, Dermitzakis ET, Linger R, Huddart RA, Renwick A, Hughes D, Hines S, Seal S, Morrison J, Nsengimana J, Deloukas P, Rahman N, Bishop DT, Easton DF, Stratton MR, UK Testicular Cancer Collaboration. A genome-wide association study of testicular germ cell tumor. Nat Genet. 2009;41:807–10.
12. Ulbright TM, Loehrer PJ, Roth LM, Einhorn LH, Williams SD, Clark SA. The development of non-germ cell malignancies within germ cell tumors. A clinicopathologic study of 11 cases. Cancer. 1984;54:1824–33.
13. Corbett R, Carter R, MacVicar D, Horwich A, Pinkerton R. Embryonal rhabdomyosarcoma arising in a germ cell tumour. Med Pediatr Oncol. 1994;23:497–502.
14. Sebire NJ, Roebuck DJ. Pathological diagnosis of paediatric tumours from image-guided needle core biopsies: a systematic review. Pediatr Radiol. 2006;36:426–31.
15. Horton Z, Schlatter M, Schultz S. Pediatric germ cell tumors. Surg Oncol. 2007;16:205–13.
16. Rescorla FJ. Pediatric germ cell tumors. Semin Pediatr Surg. 2012;21:51–60.
17. Göbel U, Schneider DT, Calaminus G, Haas RJ, Schmidt P, Harms D. Germ-cell tumors in childhood and adolescence. GPOH MAKEI and the MAHO study groups. Ann Oncol. 2000;11:263–71.
18. Gornall P. Paediatric surgical oncology. Germ cell tumours. Eur J Surg Oncol. 1997;23:68–72.
19. Ulbright TM. Germ cell tumors of the gonads: a selective review emphasizing problems in differential diagnosis, newly appreciated, and controversial issues. Mod Pathol. 2005;S2:61–79.
20. Ulbright TM, Roth LM. Recent developments in the pathology of germ cell tumors. Semin Diagn Pathol. 1987;4:304–19.
21. Roth LM, Talerman A. Recent advances in the pathology and classification of ovarian germ cell tumors. Int J Gynecol Pathol. 2006;25:305–20.
22. Coley BD. Sonography of pediatric scrotal swelling. Sem Ultrasound CT MRI. 2007;28:297–306.
23. De Backer A, Madern G, Hazebroek FWJ. Retroperitoneal germ cell tumours. A clinical study of 12 patients. J Pediat Surg. 2005;40:1475–81.
24. Hayasaka K, Yamada T, Saitoh Y, Sakura K. CT evaluation of primary benign retroperitoneal tumour. Radiat Med. 1994;12:115–20.
25. Nobusawa H, Hashimoto T, Munechika K, et al. CT findings of primary retroperitoneal cystic tumours; special emphasis on the distinction of benignancy from malignancy. Nippon Igaku Hash Gak Zass. 1995;55:861–6.
26. Jones NM, Kiely EM. Retroperitoneal teratomas-potential for surgical misadventure. J Pediatr Surg. 2008;43(1):184–6.
27. Echevarría ME, Fangusaro J, Goldman S. Pediatric central nervous system germ cell tumors: a review. Oncologist. 2008;13:690–9.
28. Ahmed HU, Arya M, Muneer A, Mushtaq I, Sebire NJ. Testicular and paratesticular tumours in the prepubertal population. Lancet Oncol. 2010;11:476–83.
29. Kandil DH, Cooper K. Glypican-3: a novel diagnostic marker for hepatocellular carcinoma and more. Adv Anat Pathol. 2009;16: 125–9.
30. Sebire NJ, Lindsay I, Fisher RA, Seckl MJ. Intraplacental choriocarcinoma: experience from a tertiary referral center and relationship with infantile choriocarcinoma. Fetal Pediatr Pathol. 2005;24:21–9.
31. Lalwani N, Shanbhogue AKP, Bhargava P, et al. Rare, miscellaneous primary ovarian neoplasms: spectrum of cross-sectional imaging. Curr Probl Diag Radiol. 2012;41:73–80.
32. Skoog SJ. Benign and malignant pediatric scrotal masses. Pediatr Clin North Am. 1997;44:1229–50.
33. Epelman M, Chikwava KR, Chauvin N, Servaes S. Imaging of pediatric ovarian neoplasms. Pediatr Radiol. 2011;41:1085–99.
34. Sato K, Takeuchi H, Kubota T. Pathology of intracranial germ cell tumors. Prog Neurol Surg. 2009;23:59–75.
35. Packer RJ, Cohen BH, Cooney K. Intracranial germ cell tumors. Oncologist. 2000;5:312–20.
36. Barkovich AJ. In: Pediatric neuroimaging. 4th ed. Lippincott, Williams & Wilkins; 2005. p. 572.
37. Dulmet EM, Macchiarini P, Suc B, Verley JM. Germ cell tumors of the mediastinum: a 30 year experience. Cancer. 1993;72: 1894–901.
38. Domínguez Malagón H, Pérez Montiel D. Mediastinal germ cell tumors. Semin Diagn Pathol. 2005;22:230–40.
39. Alper F, Kaynar H, Kantarci M, et al. Trichoptysis caused by intrapulmonary teratoma: computed tomography and magnetic resonance imaging findings. Australas Radiol. 2005;49:53–6.
40. Sasaka K, Kurihara Y, Nakajima Y, et al. Spontaneous rupture: a complication of benign mature teratomas of the mediastinum. AJR. 1998;170:323–8.

41. Sebire NJ, Fowler D, Ramsay AD. Sacrococcygeal tumors in infancy and childhood; a retrospective histopathological review of 85 cases. Fetal Pediatr Pathol. 2004;23:295–303.
42. Olivier P, Simoneau-Roy J, Francoeur D, et al. Leydig cell tumors in children: contrasting clinical, hormonal, anatomical, and molecular characteristics in boys and girls. J Pediatr. 2012;161(6):1147–52.
43. Young RH, Scully RE. Ovarian Sertoli-Leydig cell tumors. A clinicopathological analysis of 207 cases. Am J Surg Pathol. 1985;9:543–69.
44. Rich MA, Keating MA. Leydig cell tumors and tumors associated with congenital adrenal hyperplasia. Urol Clin North Am. 2000;27:519–28.
45. Borer JG, Tan PE, Diamond DA. The spectrum of Sertoli cell tumors in children. Urol Clin North Am. 2000;27:529–41.
46. Cronjé HS, Niemand I, Bam RH, Woodruff JD. Granulosa and theca cell tumors in children: a report of 17 cases and literature review. Obstet Gynecol Surv. 1998;53:240–7.
47. Ueda M, Kanematsu A, Nishiyama H, et al. Testicular thecoma in an 11-year-old boy with nevoid basal-cell carcinoma syndrome (Gorlin syndrome). J Pediatr Surg. 2010;45:E1–3.
48. Shinagare AB, Meylaerts LJ, Laury AR, Mortele KJ. MRI features of ovarian fibroma and fibrothecoma with histopathologic correlation. Am J Roentgenol. 2012;198(3):W296–303.
49. Papaioannou G, Sebire N, McHugh K. Imaging of the unusual blastomas in childhood. Cancer Imaging. 2009;9:1–11.
50. Govan AD, Woodcock AS, Gowing NF, Langley FA, Neville AM, Anderson MC. A clinico-pathological study of gonadoblastoma. Br J Obstet Gynaecol. 1977;84:222–8.
51. Obata NH, Nakashima N, Kawai M, Kikkawa F, Mamba S, Tomoda Y. Gonadoblastoma with dysgerminoma in one ovary and gonadoblastoma with dysgerminoma and yolk sac tumor in the contralateral ovary in a girl with 46XX karyotype. Gynecol Oncol. 1995;58:124–8.
52. Hatzipantelis ES, Dinas K. Ovarian tumours in childhood and adolescence. Eur J Gynaecol Oncol. 2010;31:616–20.
53. Murphy FL, Law H, Mushtaq I, Sebire NJ. Testicular and paratesticular pathology in infants and children: the histopathological experience of a tertiary paediatric unit over a 17 year period. Pediatr Surg Int. 2007;23:867–72.

Tumors of the Adrenal Gland

12

Simon Ching-Shun Kao and Alfredo Pinto-Rojas

Introduction

During embryonic development, the neural crest, a pluripotent and highly migratory cell population arising at the junction of the neural tube and the dorsal ectoderm, gives rise to Schwann cell, neuroblast, and paraganglionic cells [1]. The "autonomic nervous system" is the system of nervous system formed by organs composed of aggregates of neural crest-derived cells that form the sympathetic ganglia, paraganglia, and the adrenal medulla. The adrenal cortex is developed from mesenchyme surrounding the adrenal medulla. Neuroblastoma, ganglioneuroblastoma, and ganglioneuroma are tumors arising from *neuroblasts*. Pheochromocytoma and paraganglioma arise from *paraganglionic cells*. Adrenal carcinoma arises from the *adrenal cortical cells*.

Diagnostic Imaging: General Principles

Diagnostic imaging plays an important part at initial diagnosis, during treatment, and after treatment of patients with adrenal and extra-adrenal tumors arising from neuroblasts, paraganglionic cells, and adrenal cortical cells [2, 3]. At initial diagnosis, irrespective of the specific tumors, radiologists need to answer questions asked by clinical colleagues: (1) Are the imaging findings supporting a diagnosis of a specific tumor derived from the neural crest or adrenal cortex? (2) What is the staging of the tumor based on imaging? (3) Can a localized primary tumor be completely excised without sacrificing any adjacent vital structures? (4) What is the best imaging modality that can provide baseline information to which subsequent response assessment can be compared during and after therapy, keeping in mind the risk of using repeated radiation-based imaging?

During treatment, radiologists need to answer whether the tumor has responded to therapy based on assessment of size (volume) and percentage of necrosis using anatomic cross-sectional imaging and/or functional data using molecular imaging. Delayed imaging may be needed to detect recurrence, metastases, and late or long-term complication of disease or therapy of disease, such as scoliosis following spinal operation or radiation therapy in the treatment of neuroblastoma with intraspinal extension and the development of a second tumor following prior therapy of a primary malignant tumor.

Even with the advent of cross-sectional imaging modalities, *plain radiography* may be the first modality based on which various tumors of the neuroblasts, paraganglionic cells, and adrenal cortical cells are diagnosed. *Ultrasound* is often the first modality of choice used in the investigation of an abdominal or neck mass in children. With proper use, this modality is useful in the determination of the site of origin of the mass and the detection of mass, calcification, intravascular extension of tumor, and presence of metastasis to organs. Either *multidetector computed tomography* (MDCT) or *magnetic resonance imaging* (MRI) is often the definitive anatomical imaging modality of choice to confirm the presence of a mass and to determine its origin, to assess the extent of infiltration of adjacent vital structures, and to help staging by finding possible lymphadenopathy and pulmonary or bony metastasis. Thin-section MDCT allows isometric voxel resolution and provides multiplanar reconstruction to facilitate diagnosis. The use of intravenous and oral contrast (in abdominal and pelvic examinations) is necessary to provide better soft tissue differentiation. MRI with conventional T1- and fat-saturated T2-weighted spin-echo images can provide superior soft tissue contrast and spatial resolution in more

S.C.-S. Kao, M.B., B.S., D.M.R.D., D.A.B.R.
Department of Radiology, Director of Pediatric Radiology Fellowship Program, University of Iowa Healthcare, 3894 JPP, 200 Hawkins Drive, Iowa City, IA 52242, USA
e-mail: simon-kao@uiowa.edu

A. Pinto-Rojas, M.D., F.R.C.R. (✉)
University of Calgary, 2888 Shaganappi Trail NW, Calgary, AB, Canada T3B 6A8
e-mail: apintoro@ucalgary.ca

D.M. Parham et al. (eds.), *Pediatric Malignancies: Pathology and Imaging*,
DOI 10.1007/978-1-4939-1729-7_12,

than one plane without the use of ionizing radiation. The use of intravenous MR contrast medium may provide further information related to the nature of the mass based on presence or absence of enhancement such as showing the areas of necrosis versus viable tumor after therapy. Detection of small lung nodule by MRI is less accurate than MDCT, which can be acquired in a much shorter time, resulting in less motion artifacts. Detection of intraspinal tumors can be performed with either MDCT or MRI visualized in three planes, but the latter is preferred. MRI is superior to MDCT in assessing marrow infiltration. Presence of metallic spinal rods may impair the imaging quality with either CT or MRI, or both. The use of coronal and sagittal short tau inversion recovery (STIR) imaging sequence has been used to obtain whole body MRI (WBMRI) screening for staging, to assess response to treatment, and to detect complications of therapy, but the experience in children is relatively limited [4–8]. Whole body diffusion-weighted imaging (WBDWI), using single-shot spin-echo echo-planar imaging and acquired in the axial plane, can provide functional information about a tumor, such as its cellularity and presence of necrosis [9]. The ultimate choice of MDCT versus MRI is often dependent on the availability of machines and local expertise. Three-dimensional segmentation [10] and reconstructions may be able to provide additional information to radiologists and surgeons not easily appreciated on two-dimensional images (Fig. 12.1). Proton 1H-MRS (MR spectroscopy) has been used to assess treatment response in children with neuroblastoma, but this technique has not been widely used at present. Various *radionuclide scintigraphy* agents have been used to locate primary tumor, to identify any metastases, and some agents have been used in therapy. Further details will be discussed under specific tumors to follow.

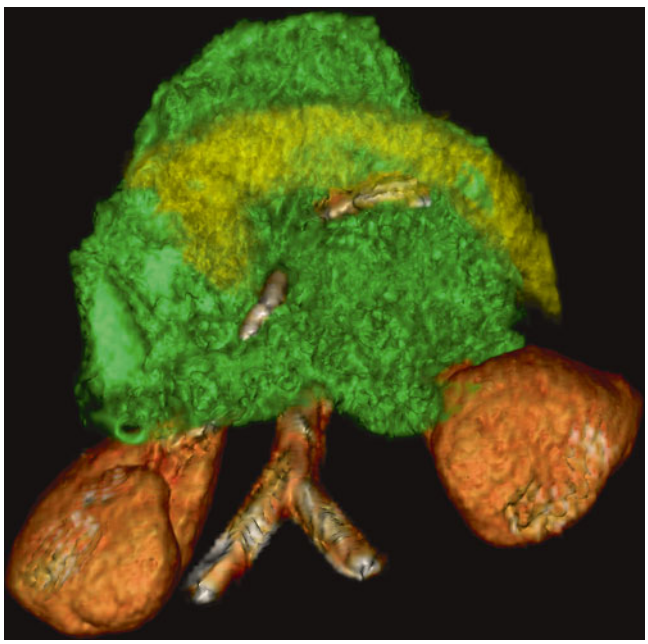

Fig. 12.1 Three-dimensional CT reconstruction of an abdominal neuroblastoma in a 4-year-old boy. Segmentation of the neuroblastoma (in *green*) from the anterior pancreas (*yellow*), the posterior kidneys (*orange-brown*), and aorta and its encased branches is displayed in three dimensions. This also allows computer calculation of the tumor volume (167 cc)

NEUROBLASTOMA AND PERIPHERAL NEUROBLASTIC TUMORS

Definition: Neuroblastoma is an embryonal cancer of the sympathetic nervous system and primarily arises early in childhood. Neuroblastoma is one of the few human malignancies known to demonstrate spontaneous regression from a poorly differentiated malignancy to a completely benign one [11]. The etiology of neuroblastoma is unknown. A subset of patients that inherit a genetic predisposition to neuroblastoma may have multifocal tumors that arise at a very early age or are detected during screening ultrasound examinations.

Clinical Features and Epidemiology

Neuroblastoma accounts for 7–10 % of all childhood cancers, and it is the most common extracranial cancer diagnosed during infancy [12]. The annual incidence of neuroblastoma is 10.5 per million in children less than 15 years of age [13, 14]. The prevalence is about one case in 7,000 live births, and there are about 700 annual new cases in the United States [15]. Mass screening for neuroblastoma at 6–12 months of age led to an increased prevalence of neuroblastoma in the screened populations but no decrease in mortality for this disease, as the tumors detected had overwhelming favorable genetic features [15]. There is no strong evidence for epidemiological differences according to ethnical origin, although African Americans are more likely to have high-risk disease with fatal outcome [16].

Neuroblastoma occurs slightly more frequently in boys than girls, and the median age at diagnosis is 17 months [14]. There is no significant geographical variation in the incidence between North America and Europe, and there are no differences between races [16]. Some patients inherit a genetic predisposition to neuroblastoma due to germline mutations, whereas most appear to be caused by sporadic mutations [17]. Cases of familial neuroblastoma may have bilateral adrenal or multifocal primary tumors [15].

Clinical presentation of neuroblastoma depends upon site of origin, disease extent, and the presence of paraneoplastic syndromes (Table 12.1). The majority (65 %) arise in the abdomen, with most arising in the adrenal gland. Additional sites of origin include the neck, chest, and pelvis. There is a concordance with age and site of disease, with infants more likely to present with thoracic and cervical primaries [16]. Approximately one-half of patients present with localized or

Table 12.1 Clinical syndromes associated with neuroblastoma (data from Park [16])

Eponym	Syndrome features
Pepper syndrome	Massive involvement of the liver by metastatic neuroblastoma
Horner syndrome	Unilateral ptosis, myosis, and anhydrosis associated with a thoracic or cervical primary tumor
Hutchinson syndrome	Limping and irritability in young child associated with metastasis of neuroblastoma to bone and bone marrow
Opsoclonus myoclonus ataxia syndrome	Myoclonic jerking and random eye movement with or without cerebellar ataxia, likely immune mediated. It may not resolve with tumor removal, and often exhibits progressive neuropsychological sequelae
Kerner–Morrison syndrome	Intractable secretory diarrhea due to tumor secretion of vasointestinal peptides
Neurocristopathy syndrome	Neuroblastoma associated with other neural crest disorders, including hypoventilation syndrome or Hirschsprung disease
Blueberry muffin syndrome	Multiple blue/purple skin marks or nodules in the skin
Raccoon eyes	Periorbital swelling and ecchymoses in neuroblastoma spread to periorbital region

regional disease, and approximately 35 % have regional lymph node spread at the time of diagnosis [16]. Patients with localized disease are often asymptomatic, with disease coincidently diagnosed after testing for unassociated medical conditions. Alternatively, a mass or abdominal distension and pain are present. An abdominal neuroblastoma may present as diarrhea owing to secretion of vasoactive intestinal peptides. Patients who have localized cervical disease arising from the superior cervical ganglion may present with Horner syndrome. Epidural or intradural extension of tumors occurs in approximately 5–15 % of neuroblastoma and may be accompanied by neurologic impairment [16].

Most neuroblastomas secrete catecholamines, whose urinary metabolites include dopamine, vanillylmandelic acid, and homovanillic acid. These analytes are useful both for diagnosis and follow-up. Because infants with neuroblastoma have a better outcome than children who are more than 1 year at diagnosis, mass screening for neuroblastoma was pioneered by Japanese investigators who demonstrated that asymptomatic tumors could be detected in infants by measurement of urine catecholamines. Subsequent studies have shown that mass screening for neuroblastoma rarely detects biologically unfavorable tumors early and has not improved the overall mortality rate [15].

Imaging Features

Neuroblastoma, ganglioneuroblastoma, and ganglioneuroma are sympathetic nervous system tumors of varying maturity derived from the primordial neural crest cells and may be found in the adrenal medulla (35–40 %) and extra-adrenal sites. In neuroblastoma and ganglioneuroblastoma, extra-adrenal sites include the retroperitoneum (30–35 %), posterior mediastinum (20 %), neck (1–5 %), and pelvis (2–3 %), in descending order of frequency [18]. Rarely, primary neuroblastoma can be found in the central nervous system (supratentorial primitive neuroectodermal tumor, see CNS Chap. 6 for detailed discussion) and within the kidney (mimicking mesoblastic nephroma [19]). In contrast, posterior mediastinum is the commonest site (41.5 %) for ganglioneuroma, followed by retroperitoneum (37.5 %), adrenal gland (21 %), and neck (8 %). The differentiation among the various histologic types by imaging is not accurate unless one finds metastases, which are only rarely reported in ganglioneuroma. In general, ganglioneuroma is found in older patients and is not as common as neuroblastoma. While the majority of neuroblastomas and ganglioneuroblastomas have irregular contours and sometimes show invasion of adjacent structures, most ganglioneuromas are round, well-demarcated, and occasionally lobulated in outline. Distant metastases from neuroblastic tumors, which may be present in 60–70 % of children at the time of presentation, are located in cortical bone (55 %), bone marrow (70 %), regional lymph nodes (30 %), liver (Pepper syndrome), skin, and rarely lung and brain [20, 21]. Patients with marrow infiltration have a better prognosis than those with cortical metastases.

Since patients can present with a large range of symptoms and signs and tumors occurring in various locations [22], the initial imaging modality may range from plain radiography to ultrasound, or other cross-sectional modalities with or without the use of ionizing radiation. It is important to be familiar with imaging findings of each modality used initially and the value of additional imaging modality to obtain further anatomical and functional information. The choice of modality also depends on physician preference and availability of local expertise and of imaging equipment or radionuclide.

Plain Radiography: Plain radiography of neuroblastic tumors may show evidence of a primary mass in the neck, posterior mediastinum (Fig. 12.2), retroperitoneum, or pelvis. Calcification can be detected in at least 30 % of neuroblastomas (Fig. 12.3). Lateral radiographs of neck tumors may show a prevertebral soft tissue mass with tracheal or pharyngeal displacement. In patients presenting with Horner's syndrome, a mass may be seen in the lower neck or superior mediastinum. Posterior mediastinal tumors may cause rib erosion or splaying, lung compression, and displacement of the paraspinal lines from the adjacent mass effect (Fig. 12.4). The pedicles may be eroded and intervertebral foramina widened from intraspinal extension. Abdominal and pelvic masses may cause displacement of air-filled bowel loops. Paravertebral widening and increased

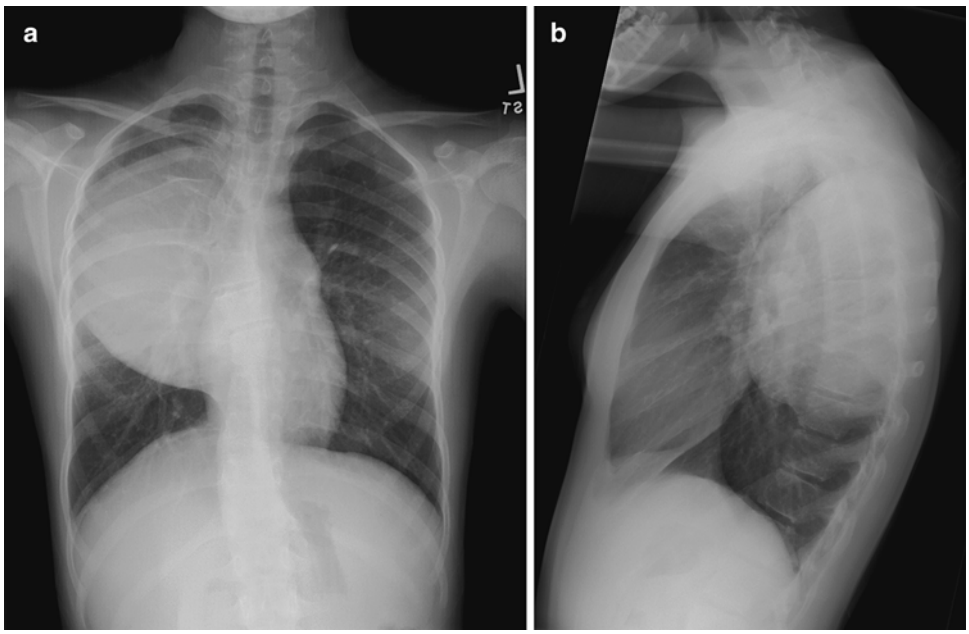

Fig. 12.2 Posterior mediastinal ganglioneuroma in a 12-year-old girl. Frontal (**a**) and lateral (**b**) views of the chest show a large soft tissue mass in the right upper posterior mediastinum with splaying of ribs. Histology of the excised mass showed a mature ganglioneuroma

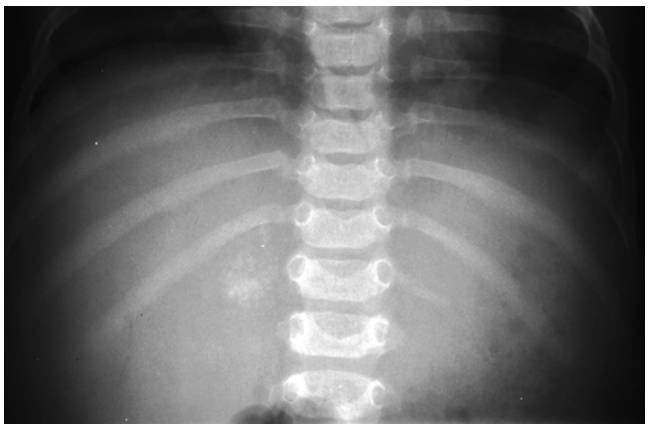

Fig. 12.3 Right adrenal calcification in a 6-month-old girl with stage IVs adrenal neuroblastoma. Plain radiograph shows amorphous calcification in the region of right adrenal gland at the last thoracic spine level

interpediculate distances from intraspinal extension may be seen. Metastases to the skull (calvaria and skull base) and periorbital region appear as lucent (and less often sclerotic) destruction and ill-defined sutural diastasis from dural involvement [21]. Long bone metastases manifest as metaphyseal lucent erosions and periosteal new bone formation. Enlarged liver shadow may be seen in metastatic neuroblastoma to liver.

Ultrasound: Sonography is able to detect primary (usually adrenal and cervical) neuroblastic tumors and metastases (such as liver) in fetuses during obstetric ultrasound evaluation, mostly after 32 gestational weeks [23, 24]. Approximately 90 % of prenatally detected neuroblastomas are adrenal in origin, and the remainder either thoracic or cervical. Two-thirds of the adrenal tumors are on the right side. While solid masses tend to increase in size with serial antenatal ultrasound examinations, the cystic or complex ones may either grow or shrink on follow-up [25]. Ultrasonography (including use of color-coded and power Doppler technique) is useful in the differentiation between neonatal adrenal hemorrhage and neuroblastic tumors affecting the adrenal glands [26, 27]. A short-term follow-up ultrasound examination in 4–6 weeks showing resolution or decrease in size of mass and cystic or calcific changes is the most important differentiating factor favoring hemorrhage (Fig. 12.5). In neuroblastomas, a network of microscopic vessels supplying the tumor shows high velocity Doppler shifts; in adrenal hemorrhages, there is either decreased or absent flow to the mass. Neuroblastic tumors that undergo spontaneous regression and histologic maturation usually occur in stage 4S tumors and resolve in 6–12 months.

A subdiaphragmatic extralobar pulmonary sequestration is an important differential diagnosis (Fig. 12.6). It is purely hyperechoic or hypoechoic, mostly on the left side, and is less frequently seen than neuroblastoma. Finding an arterial supply from the thoracic aorta and stability of size are helpful in the differentiation from neuroblastoma. Other differential diagnoses of a suprarenal mass on prenatal ultrasound include a duplex collecting system with dysplastic changes, exophytic Wilms' tumor, mesoblastic nephroma [19], retroperitoneal teratoma, liver tumor, and splenic cyst [24].

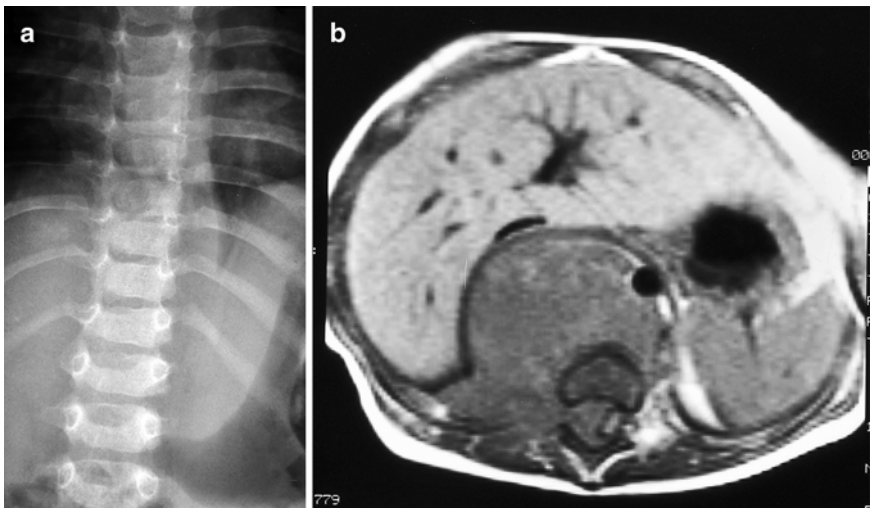

Fig. 12.4 Paravertebral soft tissue mass with displacement of the left paravertebral stripe (**a**) in a 14-month-old boy with neuroblastoma. Enhanced axial (**b**) MRI of the thoracolumbar spine show retrocrural mass and, more clearly, right intraspinal extension

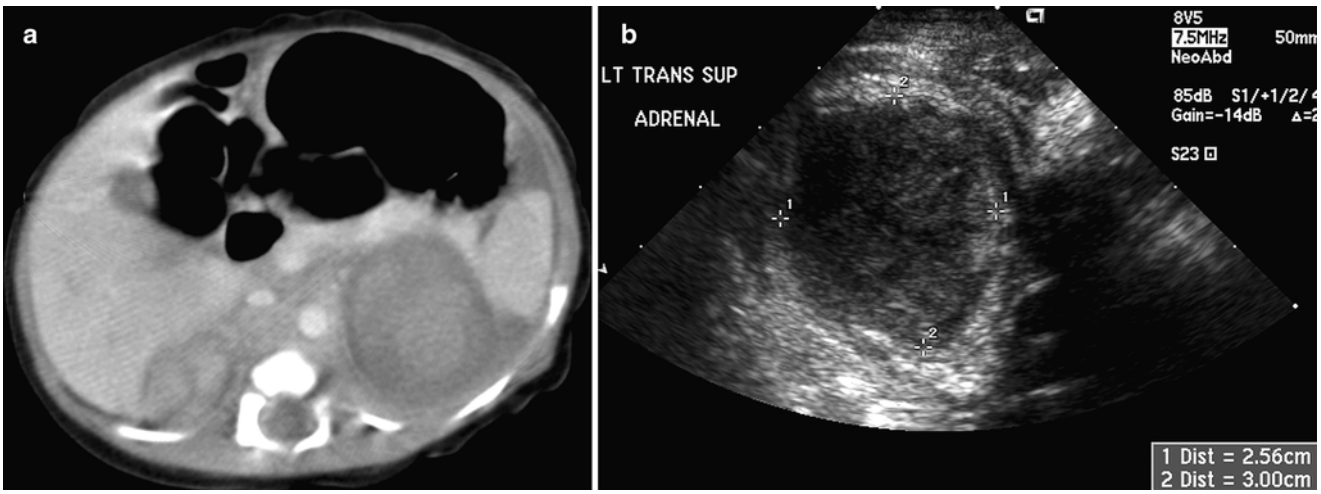

Fig. 12.5 Bilateral adrenal hemorrhage in a neonate. Contrast-enhanced axial CT scan (**a**) of the upper abdomen shows bilateral suprarenal masses with soft tissue densities. Transverse ultrasound image (**b**) shows an inhomogeneous hypoechoic mass in the suprarenal region. Both masses decrease in size on a 6-week ultrasound follow-up examinations

Neuroblastic tumors in the pediatric abdomen and pelvis appear as solid masses of varying echogenicity and heterogeneity (Fig. 12.7). Hyperechoic areas correspond to calcifications and cystic areas correspond to hemorrhage or necrosis. Calcifications may produce acoustic shadowing that limits assessment of the size and full extent of the tumor. Tumor of adrenal origin typically produces inferolateral displacement of the adjacent kidney. Hydronephrosis may be seen from obstruction of the collecting system by tumor or metastatic nodes. Real-time demonstration of differential movement between the mass and adjacent organs, such as liver and kidney, helps in the determination of the organ of origin or invasion of adjacent organ. Although ultrasonography may detect metastasis to liver and lymph nodes, or spread to pleural space, and rarely, scrotum [28, 29], it is not possible to detect extradural intraspinal extension of tumor. Duplex and color Doppler examination helps in evaluating blood vessels (aorta and inferior vena cava and their branches) that may be compressed, encased, or displaced by the tumor, or may demonstrate intravascular extension [27]. Ultrasound is also useful in follow-up, especially if an initial baseline examination is obtained.

Computed Tomography: Intravenous-enhanced CT is the most commonly used imaging modality in the assessment of origin and extent of neuroblastic tumors. Regions of coverage include chest, abdomen, pelvis, neck, and skull,

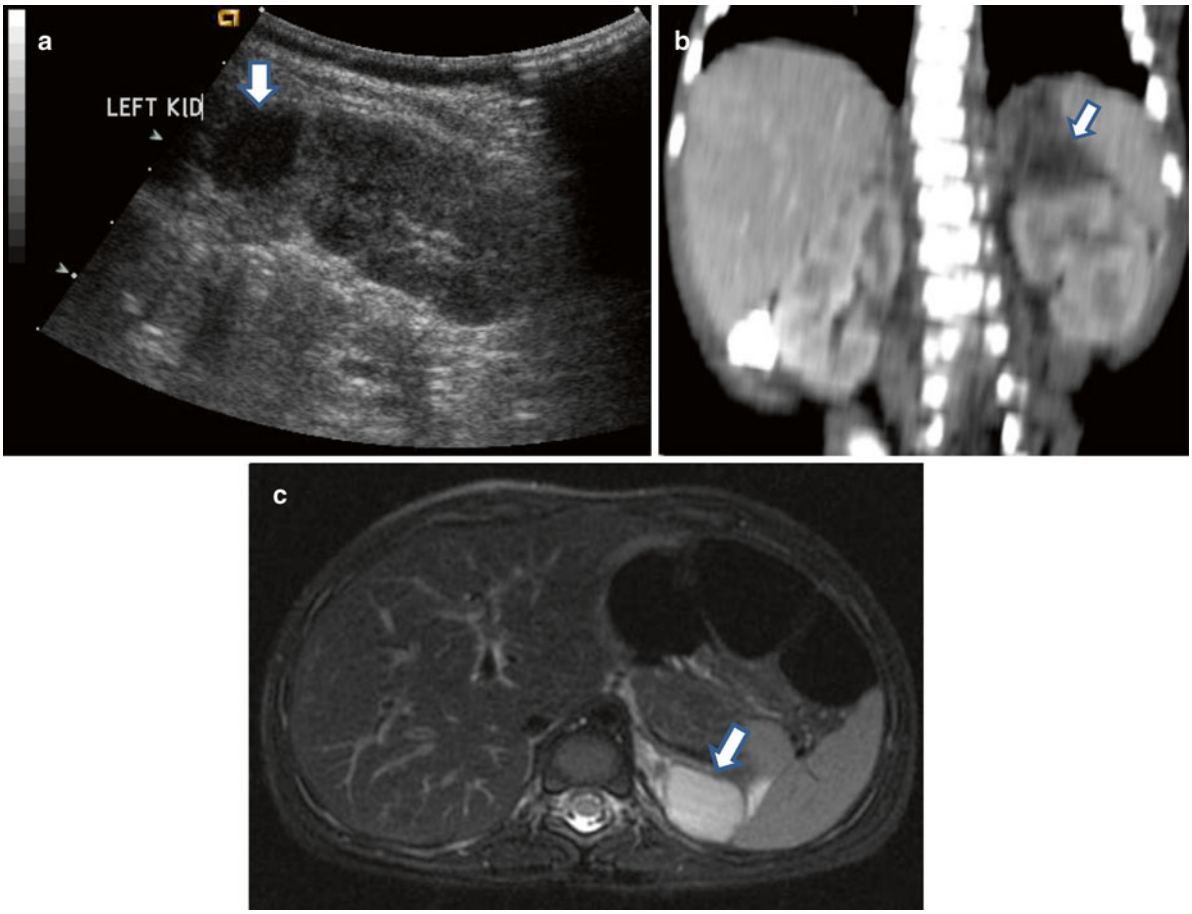

Fig. 12.6 Subdiaphragmatic extralobar pulmonary sequestration in a neonate. Antenatal ultrasound (not shown) shows a cystic mass in the retroperitoneum. Postnatal longitudinal ultrasound (**a**) of the abdomen shows a hypoechoic mass (*arrow*) just above the left kidney. Coronally reconstructed CT (**b**) of the abdomen shows a hypodense mass (*arrow*) indenting on the upper pole of left kidney. Axial T2W MR of the abdomen (**c**) shows a hyperintense mass (*arrow*) in the left suprarenal region. Histology of the excised specimen shows extralobar pulmonary sequestration

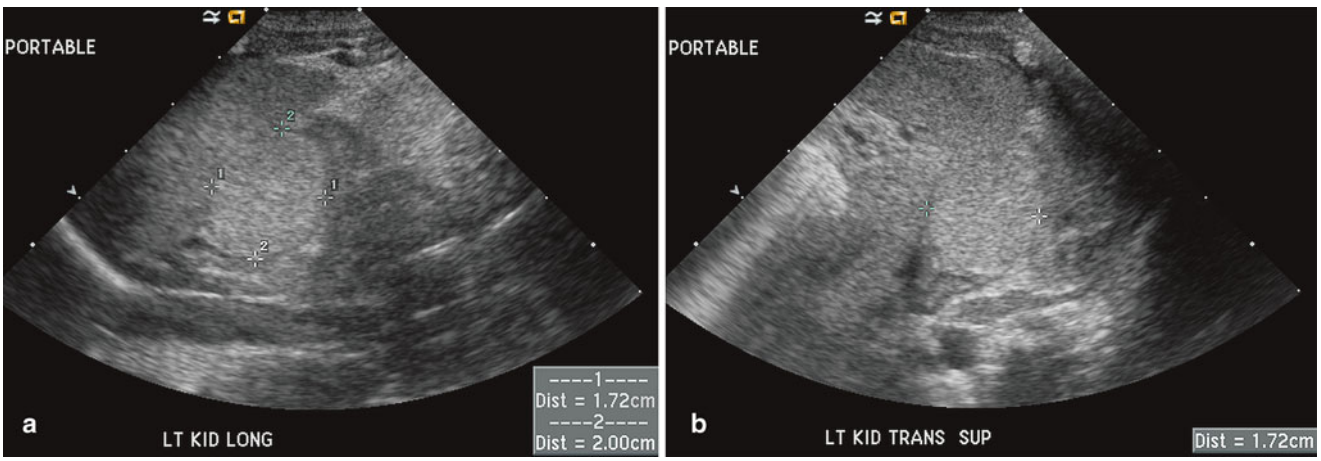

Fig. 12.7 Neuroblastic tumor in a newborn. A suprarenal mass was found incidentally on renal ultrasound performed for oliguria. Longitudinal (**a**) and transverse (**b**) ultrasound images show a uniformly echogenic mass measuring 1.7×1.7×2.0 cm in the left suprarenal fossa. The mass is MIBG avid, and it regresses spontaneously on follow-up ultrasound examination

Fig. 12.8 Right adrenal neuroblastoma in a 2-year-old girl with vascular encasement and displacement. Contrast-enhanced CT scan of the upper abdomen shows a right adrenal tumor with retroperitoneal lymphadenopathy encasing abdominal aorta and renal vasculature, anterior displacement of the inferior vena cava without intravascular invasion, and extension over the vertebral body without invasion

Fig. 12.10 Large neuroblastoma in the retroperitoneum in a 30-month-old girl. Axial CT image of the upper abdomen shows the relation of the mass to the hilar lymph nodes, right lobe of liver, both kidneys, aorta, inferior vena cava, renal vasculature, and vertebral body

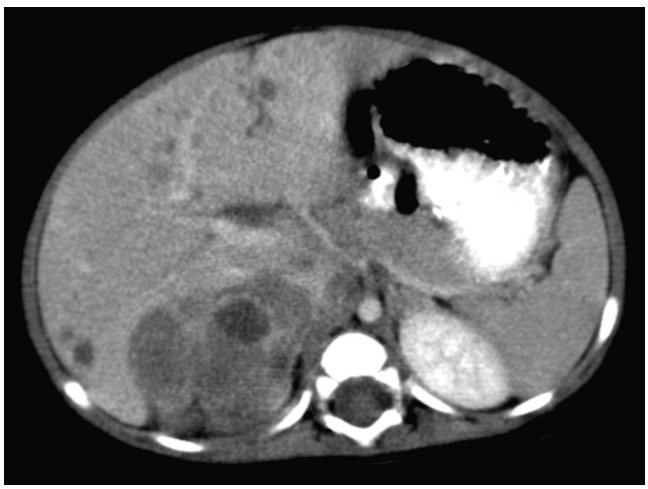

Fig. 12.9 Metastatic neuroblastoma to liver from a right adrenal neuroblastoma in a 7-month-old boy. Contrast-enhanced axial CT image of the liver shows multiple small hypodense lesions in both lobes of the liver. A right adrenal mass with hypodense necrotic or hemorrhagic areas is also seen

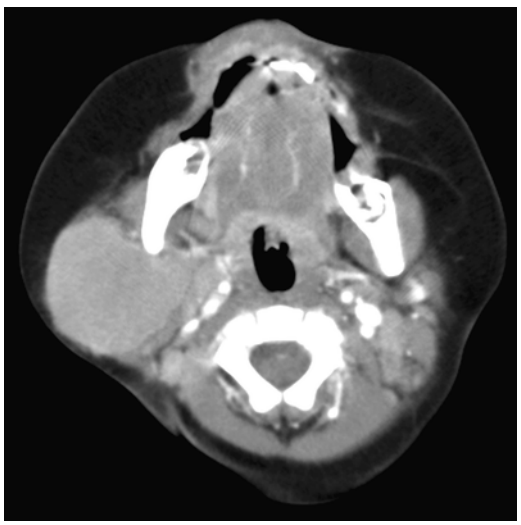

Fig. 12.11 Metastatic cervical neuroblastoma from a right adrenal neuroblastoma in a 7-month-old boy. Axial CT image of the head and neck shows a soft tissue mass in the right parotid space. Biopsy of the neck mass showed neuroblastoma. An abdominal CT showed a right adrenal neuroblastoma with liver metastases (not shown)

depending on the location of the mass at presentation. Findings suggestive of a neuroblastic tumor include calcifications hemorrhage and/or necrosis, lymphadenopathy, vascular involvement (Fig. 12.8), and metastases to liver (Fig. 12.9) and bone. Metastases to lung are infrequent (1–3 %). Most masses are heterogeneous, with fine or coarse calcifications (80–90 % of neuroblastoma and ganglioneuroblastomas and 40–60 % of ganglioneuromas). Calcifications are usually coarse, mottled, and amorphous in neuroblastomas and discrete and punctate in ganglioneuromas. Ganglioneuroma may show a delayed and progressive heterogeneous enhancement pattern [30]. Hemorrhage and/or necrosis are more common in larger tumors, appearing as area of low attenuation. Lymphadenopathy is commonly seen around the renal hilum (Fig. 12.10), liver hilum, retroperitoneum. It is less common in the neck (Fig. 12.11) and mediastinum. When the primary is large, it is often difficult to differentiate between the primary and metastatic nodes. Vascular displacement, encasement, or invasion may be seen (Fig. 12.10). In the abdomen, the aorta and the inferior vena cava and their branches are commonly involved. Right atrial extension of

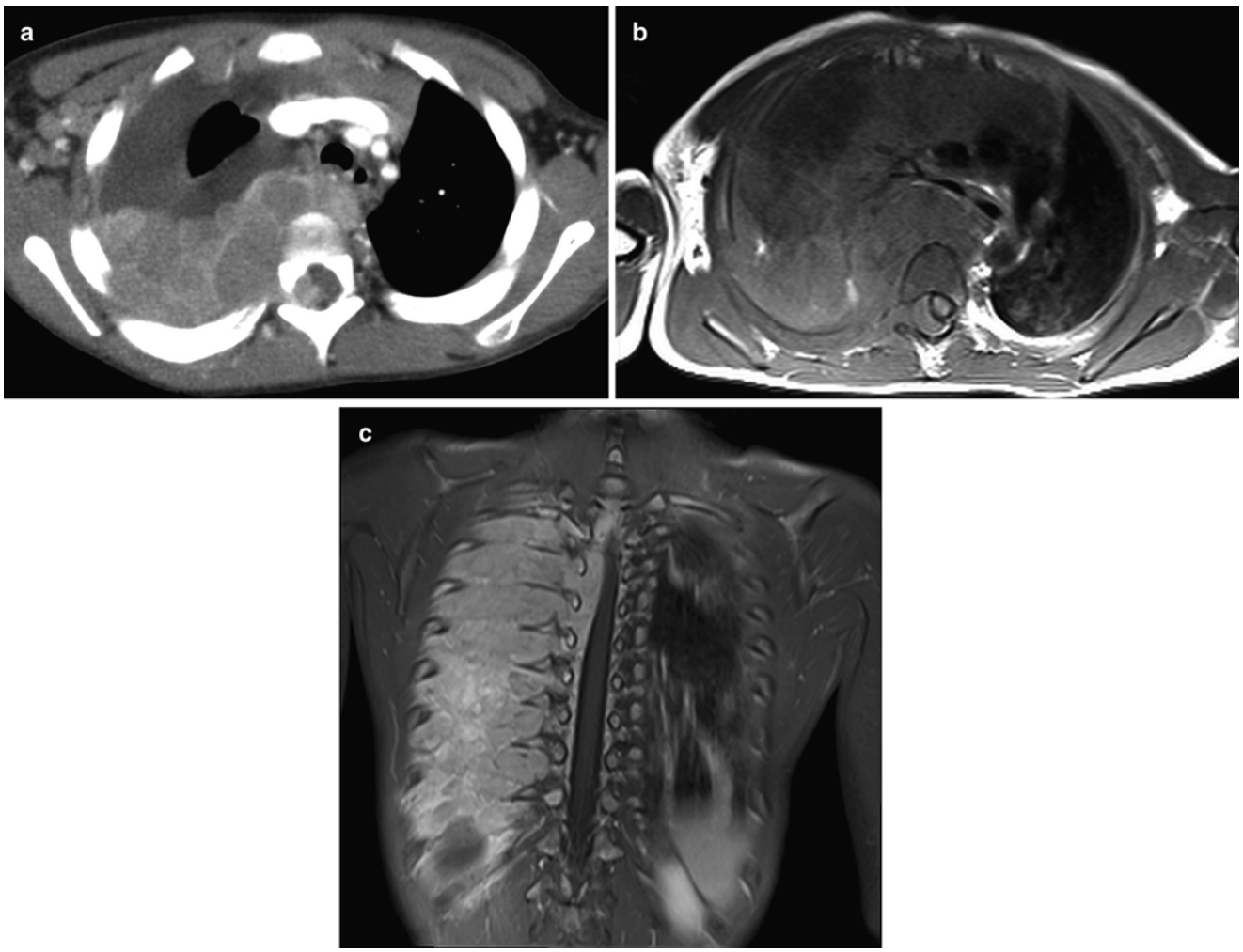

Fig. 12.12 Thoracic neuroblastoma with intraspinal extension in a 34-month-old boy. Intravenous enhanced axial CT (**a**) image shows an enhancing right posterior mediastinal mass crossing midline with intraspinal extension. Enhanced axial (**b**) MR image shows the similar finding with displacement of the spinal cord to the left. The coronal (**c**) MR image shows a large posterior mediastinal mass with extensive chest wall and intraspinal involvement through intervertebral foramina at multiple levels

tumor thrombus has been reported [31]. Tumor arising from the adrenal gland produces displacement of the adjacent kidney laterally and caudally, best demonstrated with a coronally reconstructed image. Up to 20 % of neuroblastomas have been shown to invade the renal parenchyma and these tumors tend to be extensive, of unfavorable histological features, and involve lymph nodes. CT scan was found to be sensitive and specific for showing renal parenchymal invasion [32]. Extra-adrenal retroperitoneal or posterior mediastinal masses (Fig. 12.12) may also invade the paraspinal muscles or extend into the intraspinal epidural space via the neural foramina. Paraspinal tumors may displace the kidney anteriorly. Retrocrural extension is well demonstrated by CT. Cervical neuroblastic tumors are uncommon, usually presenting as a mass in the parapharyngeal space, displacing or involving the adjacent carotid artery and jugular vein (Fig. 12.11). Pelvic neuroblastic tumors arise from the presacral space and the anteriorly located organ of Zuckerkandl (Fig. 12.13). CT

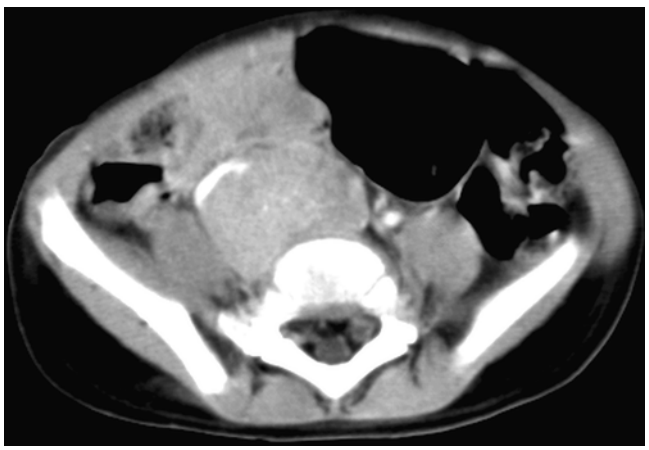

Fig. 12.13 Differentiating neuroblastoma of the organ of Zuckerkandl in a 17-month-old boy. Enhanced axial CT image of the abdomen shows a mass in the lower abdomen and upper pelvis with anterior displacement of the right iliac artery. Fine calcifications are present in the mass.

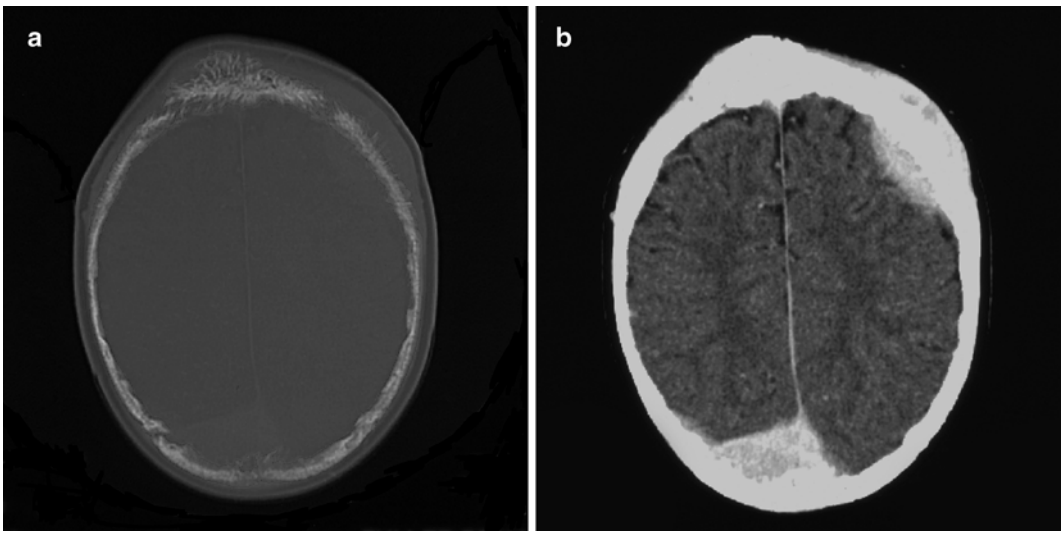

Fig. 12.14 Metastatic poorly differentiated neuroblastoma to skull with associated dural masses in a 9-year-old boy. Enhanced CT image of the skull with bone window (**a**) shows erosive skull changes close to sutures and associated enhancing dural deposits when displayed on brain window (**b**)

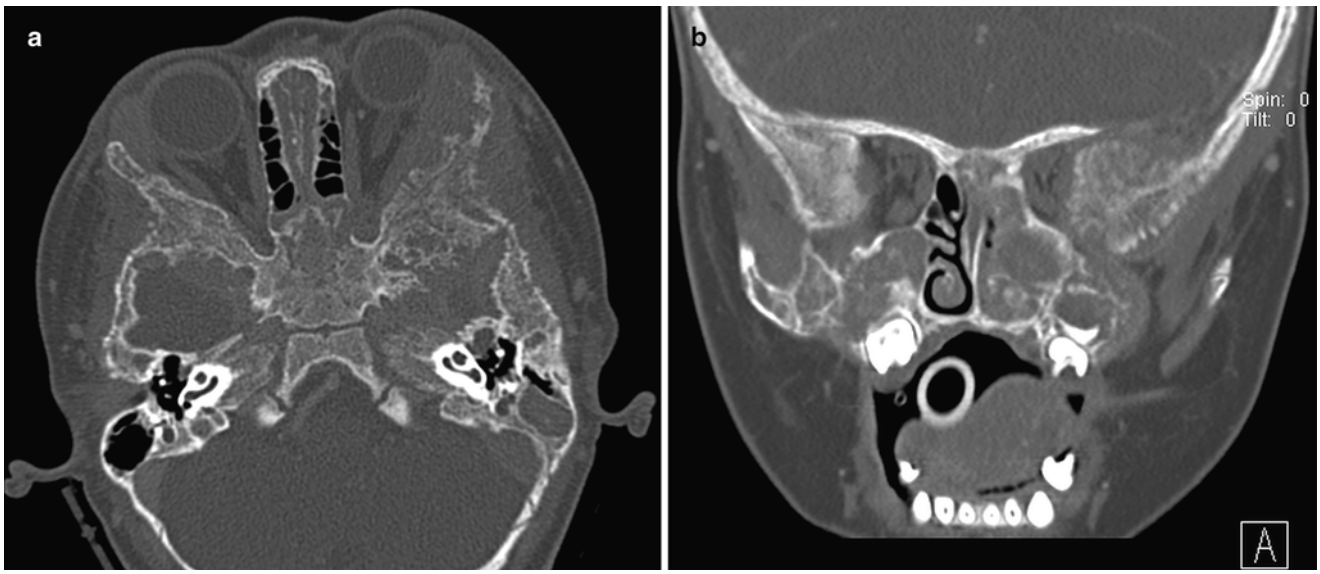

Fig. 12.15 Metastatic neuroblastoma to bilateral periorbital region in a 14-month-old girl presenting with bilateral proptosis and bruising. Axial (**a**) and coronal (**b**) CT images of the orbits show bilateral erosions of the lateral orbital walls as well as the facial and sphenoid bones

allows demonstration of bony metastases as lytic destruction or erosions. In the skull, additional dural involvement is associated with enhancing dural masses indenting underlying brain; extension into a suture is associated with sutural diastasis (Fig. 12.14). "Raccoon-eye" discoloration and proptosis may be the first presenting signs of involvement of the sphenoid bone and periorbital regions (Fig. 12.15). Rare brain metastasis can be intraventricular, leptomeningeal, or parenchymal in location [21].

Magnetic Resonance Imaging: Magnetic resonance imaging is an important imaging modality of choice because it does not utilize radiation and provides high contrast resolution for the detection, multiplanar localization, and assessment of the extent of primary tumor involvement [33]. It is superior to CT to assess marrow infiltration and intraspinal extension. MRI is useful to evaluate resectability, to detect recurrence and metastasis, and to assess response to treatment and development of complications [34]. While the coronal plane is optimal to define the origin of organ involvement, spinal canal extension, and abdominal great vessel involvement, the axial plane (Fig. 12.16a, b) is the best to assess involvement of the origins of celiac axis and superior mesenteric artery [34]. Compared to CT, T1W images provide superior anatomic resolution and T2W images provide

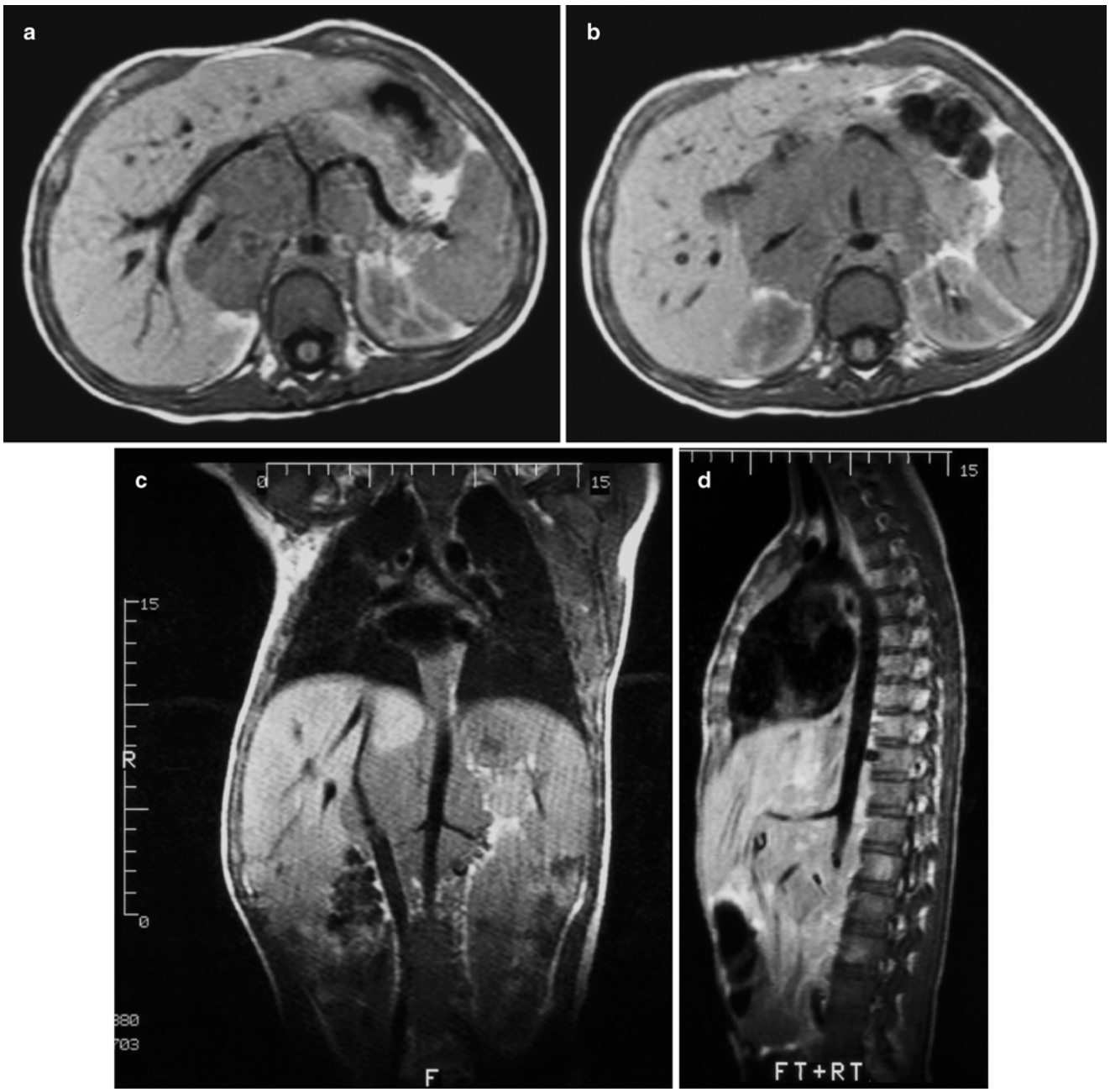

Fig. 12.16 Retroperitoneal neuroblastoma in a 13-year-old boy. Axial T1W MR images of the upper abdomen at the levels of the celiac axis (**a**) and the superior mesenteric artery (**b**) show tumor encasement of the abdominal aorta, celiac axis and its branches, the superior mesenteric artery, and the inferior vena cava. There is anterior displacement of the main portal vein. Coronal (**c**) and sagittal (**d**) images provide improved determination of vascular relationship to tumor. Encased renal vessels are noted

superior contrast differentiation from normal tissues. The multiplanar capability (especially coronal and sagittal planes, Fig. 12.16c, d) improves determination of vascular invasion and, therefore, resectability. The definition of the location of tumor mass in relation to the hemidiaphragms or crura is useful to determine the surgical approach (infra- or supradiaphragmatic). In the abdomen, the aorta and inferior vena cava are usually displaced anteriorly, and the various branches from these vessels may be encased (Fig. 12.16) or invaded (Fig. 12.17). Retroperitoneal lymphadenopathy and spread to various intra-abdominal organs may be seen. Differentiation from renal tumors, adrenal hemorrhage, and lymphoma is facilitated with the multiplanar depiction. MR imaging was found to be the single best test for detection of nodal and chest wall involvement (Figs. 12.12b, c) and intraspinal extension for thoracic neuroblastoma [35]. MR imaging

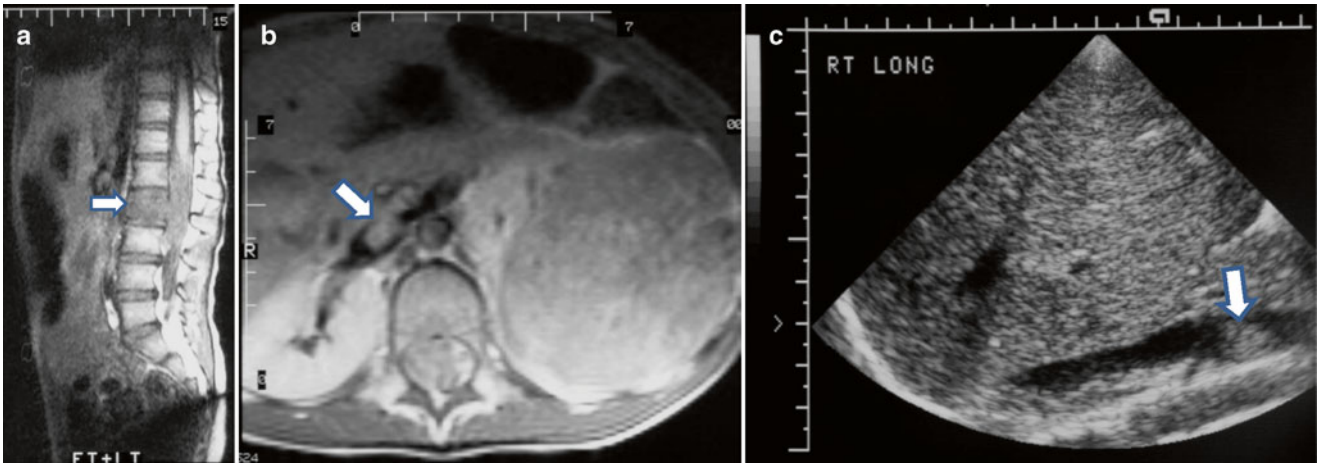

Fig. 12.17 Left neuroblastoma in a 5-year-old girl with lumbar vertebral marrow involvement and extension into inferior vena cava and spinal canal. Sagittal T1W image (**a**) shows tumor replacement of fatty marrow (*arrow*) and intraspinal extension around the conus medullaris. Axial post-contrast T1W MR (**b**) and longitudinal ultrasound (**c**) images show a large left suprarenal mass with a tumor thrombus (*arrow*) in the inferior vena cava. Intraspinal extension is also seen in (**a**) and (**b**)

shows more accuracy than CT for the detection of stage 4 disease, with sensitivities of 83 and 43 % ($p<0.01$) and specificities of 97 and 88 % ($p>0.05$), respectively [36], and it could replace the combination of CT and bone scintigraphy for overall assessment of stage 4 disease in children with neuroblastomas [36].

Without intravenous contrast, neuroblastomas and ganglioneuroblastomas are typically heterogeneous with low signal intensity on T1W images and high signal intensity on T2W images. Ganglioneuromas are typically homogeneous but with T1W and T2W signal intensities similar to other neuroblastic tumors (Fig. 12.18). Hemorrhagic areas may show increased signal intensity on T1W images; cystic areas will appear bright on T2W images. Although calcifications may appear dark, detection may be difficult as compared to CT or sonography. After administration of intravenous contrast, neuroblastoma and ganglioneuroblastoma show heterogeneous enhancement while ganglioneuromas show variable and delayed enhancement [37]. In tumors contiguous with the kidneys, the delineation of the mass from the kidney may be lost when the enhancement of the tumor and the adjacent kidney parenchyma is to the same degree. MRI provides the best multiplanar assessment of intraspinal extension (dumbbell tumors) of paraspinal neuroblastic tumors, irrespective of the level of spinal involvement (10 % abdominal and 28 % intrathoracic). The post-contrast images will depict the enhancing intraspinal epidural tumor and assess its relation to the displaced or compressed spinal cord or nerve roots at neural foramina. Dural involvement associated with cranial vault metastasis shows enhancement of the soft tissues around the bony destruction (Fig. 12.19). Involvement of bone marrow by neuroblastic tumor will appear as low signal intensity on T1W images and high signal intensity on T2W images (Fig. 12.17). Two patterns of bone marrow involvement have been described. A nodular pattern is associated with less cortical metastases and a better prognosis. A diffuse pattern is associated with cortical metastases and is less responsive to chemotherapy [38]. MRI, however, is not useful to assess marrow tumor response to treatment since signal abnormalities may persist for a long time despite good response. Liver metastases may either be nodular or diffuse in distribution. Nodular metastases to liver often result in hepatomegaly and appear dark on T1W images and bright on T2W images. MRI is superior to CT in the depiction of diffuse liver metastatic infiltration in stage IVS disease (patients under 1 year of age with metastases to liver, skin, and bone marrow) as increased signal intensity on T2W images.

Diffusion-weighted sequences show increased signal intensity (restricted diffusion) in tumors owing to the high nuclear-to-cytoplasm ratio limiting intracellular motion and the densely packed tumor cells inhibiting effective motion of the extracellular water protons. Preliminary data showed that diffusion-weighted echo-planar imaging may be able to distinguish neuroblastoma from ganglioneuroblastoma or ganglioneuroma using the apparent diffusion coefficient (ADC). Neuroblastomas were found to have a lower ADC, reflecting their small densely packed, immature cells containing little cytoplasm versus the former groups with abundant cytoplasm surrounded by more stroma [39]. The potential value of ADC in assessing therapeutic response remains to be seen. Whole body MRI (WBMRI) using a STIR sequence has shown high sensitivity but low specificity in the detection of bony metastasis and has a low positive predictive value in comparison to I-123-MIBG scintigraphy [6, 8, 40].

Nuclear Medicine: Various radionuclide scintigraphic studies have been used in the localization of primary tumor

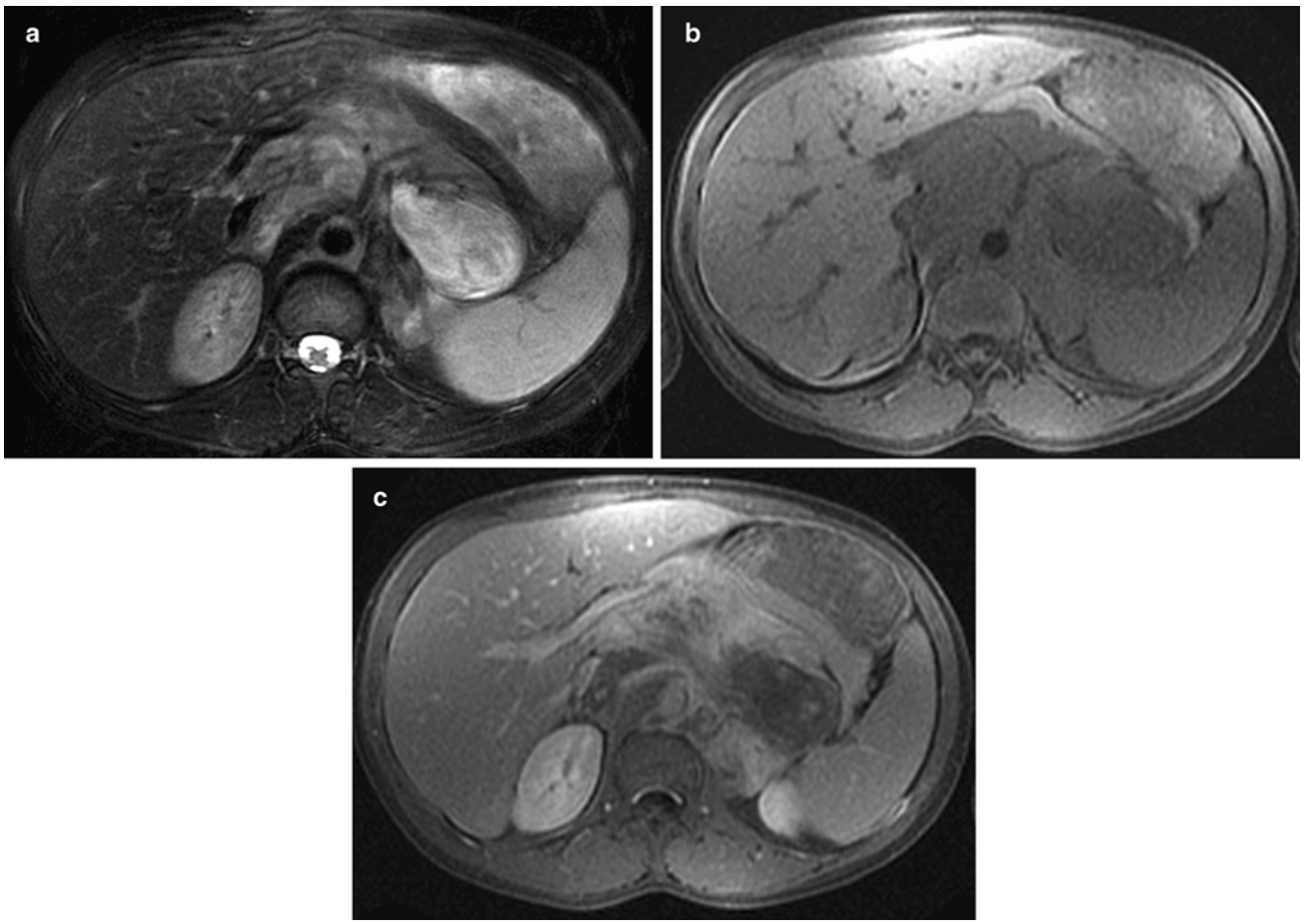

Fig. 12.18 Ganglioneuroma in a 13-year-old boy in the retroperitoneum. Fat-saturated T2W (**a**) and T1W (**b**) images of the upper abdomen showed retroperitoneal mass encasing abdominal vasculature with inhomogeneous bright and isointense signal intensities, respectively. Post-gadolinium fat-saturated T1W image (**c**) of the same region showed inhomogeneous enhancement of the tumor. Signal intensities in all sequences are indistinguishable from those with neuroblastoma. Histology showed mature ganglioneuroma

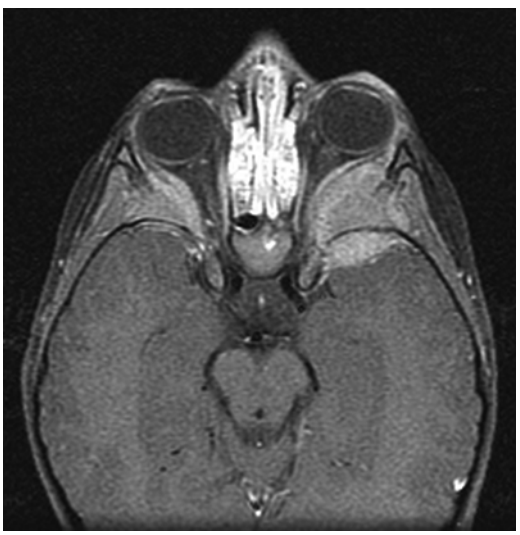

Fig. 12.19 Metastases to both lateral orbits in 3-year-old boy with a large left adrenal neuroblastoma. Enhanced MRI of the orbits shows bilateral soft tissue masses involving the lateral orbital walls and left greater wing of sphenoid bone with extradural extension into both middle cranial fossae

and surveillance of metastases in patients with neuroblastic tumors [41]. In children with bone pain, whole body ^{99m}Tc-bone scintigraphy is used to detect bony cortical metastases, manifested typically as areas of increased radionuclide uptake, corresponding to destructive lesions on plain radiography (Fig. 12.20) [42]. Occasionally, photopenic "cold" foci may appear. Bone scintigraphy increases the sensitivity detecting bony metastasis by radiographic skeletal survey from 35–70 % to 90 % [43]. Unlike ^{123}I-metaiodobenzylguanidine (MIBG) scintigraphy, bone scans can differentiate between cortical bone and bone marrow involvement, an important distinction in the staging of patients <18 months of age [41]. Involvement of the bony cortex has been shown to carry prognostic significance. Detection of bone involvement at long bone ends may be difficult owing to the relatively high normal uptake of bone-seeking agents in the growth plates in children. Over 60 % of neuroblastomas have increased uptake in the primary tumor. Even areas of tumor calcifications show increased uptake, this uptake may not correlate with extent of calcification or degree of necrosis [44]. Since up to 10 % of

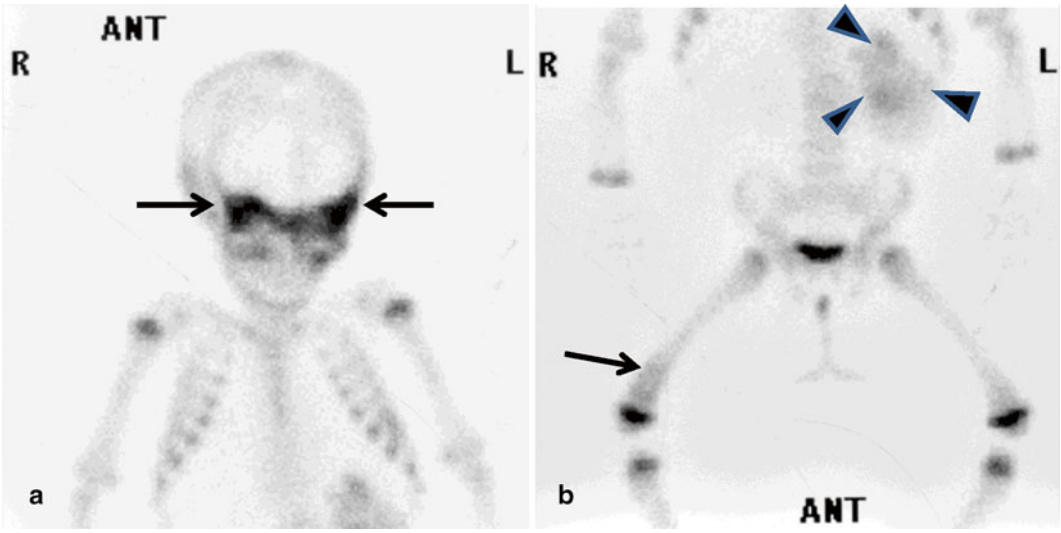

Fig. 12.20 Multiple bony metastases from retroperitoneal neuroblastoma in a 10-month-old girl. Anterior views of the body on skeletal scintigraphy (Tc-99m-MDP) shows increased uptake in (**a**) sphenoid bone (*arrows*), orbits, and (**b**) distal right femur (*arrow*). Note uptake of the radionuclide in part of the primary tumor (*arrowheads*)

MIBG scans may be negative in neuroblastoma patients, bone scintigraphy and MIBG scans are complementary to each other. After therapy, areas with increased uptake on ^{99m}Tc-bone scintigraphy may persist for an extended period of time and with variable intensity.

Radiolabeled ^{123}I-MIBG is a catecholamine analog taken up catecholamine-producing primary or metastatic tumors (bone, bone marrow, and soft tissues) and mainly excreted by the kidneys (Fig. 12.21). In addition to neuroblastic tumors, neuroendocrine tumors including pheochromocytoma and carcinoid tumors also show uptake of MIBG. MIBG is concentrated within the cytoplasm of neuroblastoma cells. Retention of MIBG is enhanced by its rapid reuptake of any MIBG that exits the tumor cells [41]. The guidelines for evaluation of the metastatic response and the extent of neuroblastoma using ^{123}I-MIBG scans had been reported, using a semiquantitative scoring system (the Curie scoring system), based on the extent of metastases in each of the 9 anatomic sectors for osteomedullary and soft tissue lesions in the body [45, 46]. This agent has superior imaging quality and radiation dose properties (shorter half-life of 13.2 h, ideal photon energy of 159 KeV for gamma camera and single-photon emission computed tomography [SPECT], and lack of a beta particle) over ^{131}I-MIBG, but there is no significant difference in survival predictability in patients with stage IV neuroblastoma by the type of scan [47]. Planar images are obtained most commonly at 24 h. The addition of 48-h delayed images and tomographic technique (SPECT) has been shown to increase the number of detected lesions and to better anatomically localize neuroblastomas [48]. Fusion of SPECT data to separately acquired anatomical imaging studies (CT or MRI) can be performed [49] (Fig. 12.22). SPECT imaging is most useful in localizing lesions near areas of physiologic uptake, such as in the retroperitoneum. Normal sites of radiotracer distribution include the nasal mucosa, salivary glands, thyroid gland, the upper chest, myocardium, liver, normal adrenal tissues (especially after contralateral adrenalectomy), and the urinary and gastrointestinal tracts , the latter two resulting in false positives. False negatives (mostly bony metastases) may be caused by pharmacological interference from some commonly prescribed and readily available over-the-counter medicines [50], and possibly tumor cell differentiation and maturation [40]. About 57 % of ganglioneuromas accumulate MIBG, and these MIBG-avid tumors usually produce increased amount of urinary catecholamines.

A recent meta-analysis of ^{123}I-MIBG scintigraphy estimated a sensitivity of 97 % in the detection of neuroblastomas [51]. Detection of presacral neuroblastic tumors may be missed when there is a full urinary bladder distended with the excreted radionuclide. This pitfall can be reduced by catheterization of the urinary bladder during imaging. ^{123}I-MIBG carries a relatively high radiation dose of 13–19 mSv. In patients with neuroblastoma presenting with Horner's syndrome secondary to sympathetic denervation, there is asymmetric loss of normal uptake by the ipsilateral salivary glands. Although results of MIBG scan correlate fairly well with bone marrow aspirates and MRI, MIBG cannot replace marrow aspirates at diagnosis and evaluation of response in children with neuroblastoma. The combined use of ^{123}I-MIBG scintigraphy and MRI has been shown to increase the sensitivity and specificity of the diagnosis of neuroblastoma [52]. Poor prognosis has been associated with MIBG-avid tumors in stage IV patients over 1 year of age at

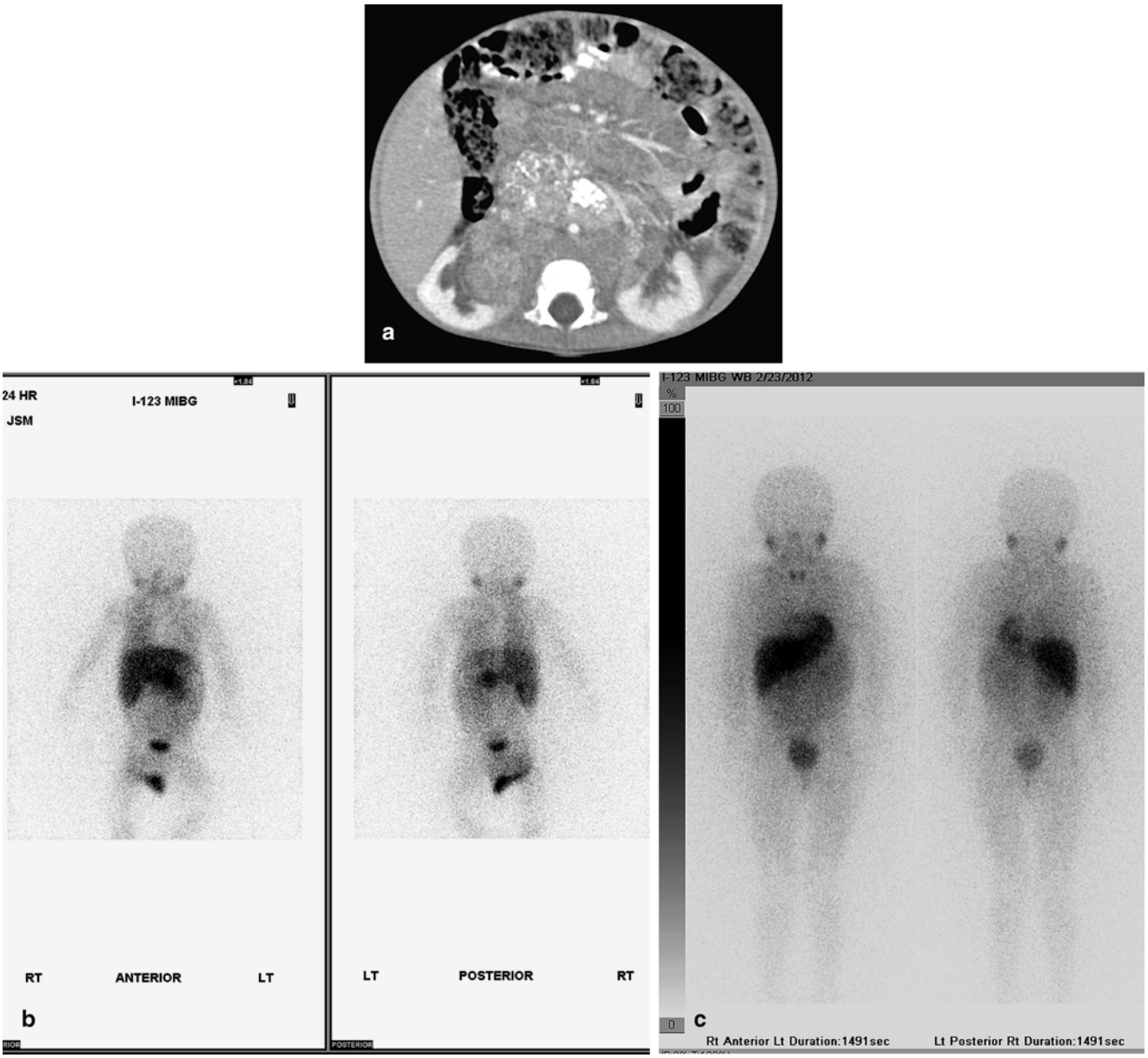

Fig. 12.21 Retroperitoneal neuroblastoma in an 11-month-old girl. Contrast-enhanced axial CT image (**a**) shows a large retroperitoneal neuroblastoma encasing abdominal vasculature and displacing kidneys. Increased uptake is present in part of the tumor shown on planar (**b**) I-123-MIBG scintigraphy. After chemotherapy and surgical treatment, follow-up axial CT (not shown) shows no residual tumor and planar I-123-MIBG scintigraphy (**c**) shows no abnormal uptake

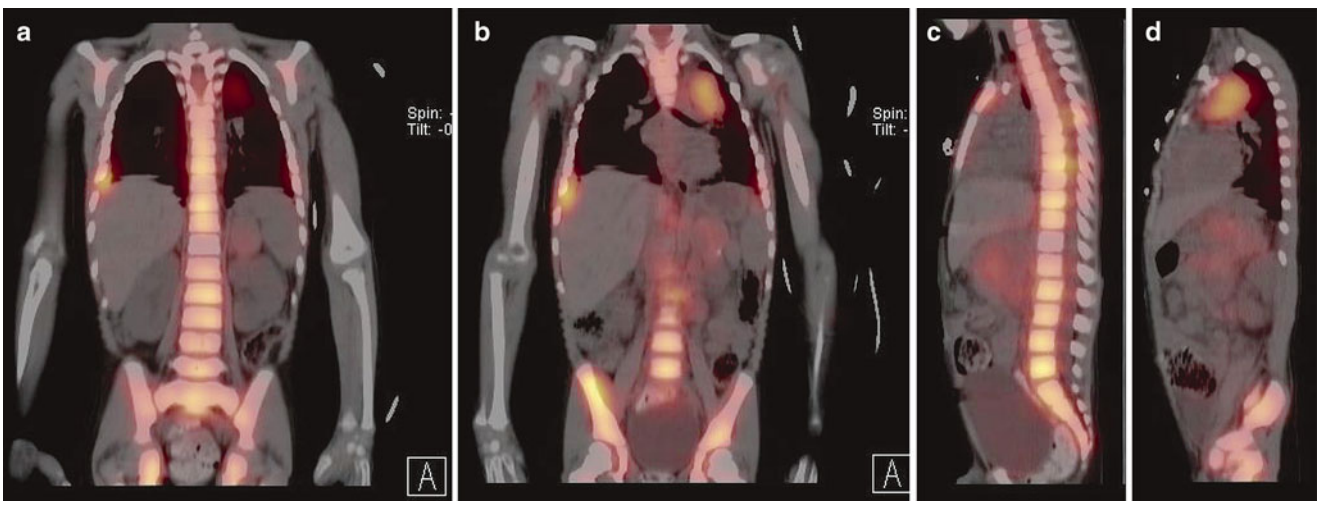

Fig. 12.22 (**a**–**d**) Extensive metastatic neuroblastoma in a 4-year-old boy. Fusion of $^{I\text{-}123}$MIBG SPECT and CT images reveals abnormal uptake in retroperitoneum, left upper mediastinum, and extensive metastases to the spine, sternum, scapula, and ribs

presentation and in those patients that remain avid after chemotherapy.

^{18}F-FDG-PET scan has been shown to be equal or superior to MIBG scintigraphy for localizing neuroblastic tumors in soft tissue and extracranial skeleton, for identifying small lesions, and for delineating the extent of disease [53, 54]. ^{18}F-FDG PET/CT may be useful in the <10 % of patients with primary neuroblastoma that are not ^{123}I-MIBG avid or when there is suspicion that disease extent exceeds what is depicted with ^{123}I-MIBG scan [55] (Fig. 12.23). Moreover, tumoral avidity (maximal standardized uptake value of the most intense soft tissue and bone-bone marrow lesion) for ^{18}F-FDG and the extent of ^{18}F-FDG-avid bone-bone marrow disease were identified as adverse prognostic factors in high-risk neuroblastoma patients undergoing high-dose ^{131}I-MIBG therapy. In a study [56] comparing the diagnostic utility of ^{123}I-MIBG (with SPECT) to ^{18}F-FDG PET (or PET-CT) scans in neuroblastomas of all stages, the investigators found

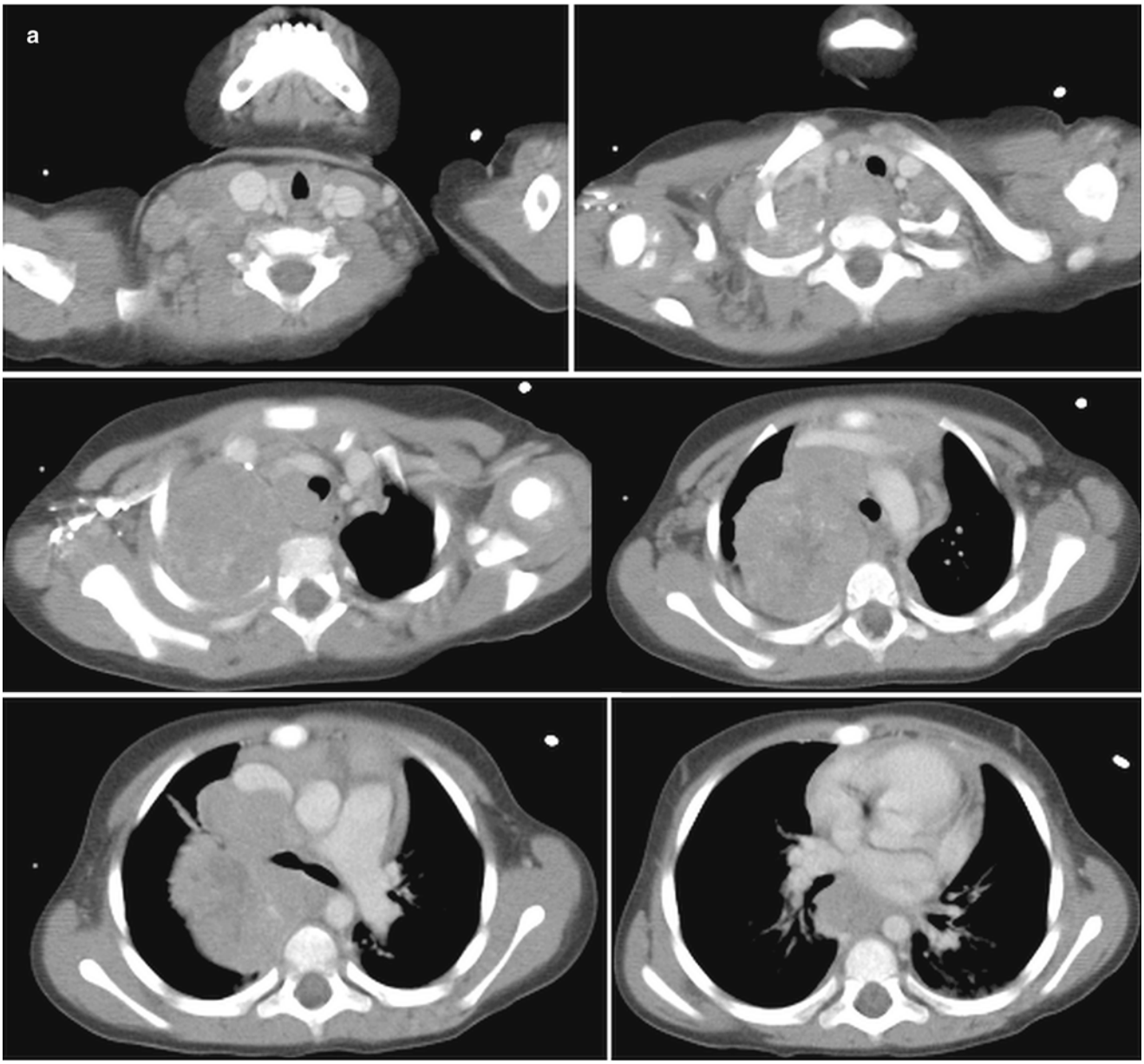

Fig. 12.23 PET-CT scan of thoracic neuroblastoma in a 35-month-old girl. Contrast-enhanced axial CT images (**a**) of the thorax show a large posterior and superior mediastinum mass. (**b**) $^{I\text{-}123}$-MIBG scan shows abnormal uptake in right lung apex and mediastinum, right supraclavicular nodes, and bone marrow. Coronal ^{18F}-FDG PET images (**c**) more clearly show areas of increased activity in the neck, both sides of mediastinum, and bone marrow of the axial and appendicular skeleton. Fusion of ^{18F}-PET images to CT images is not shown

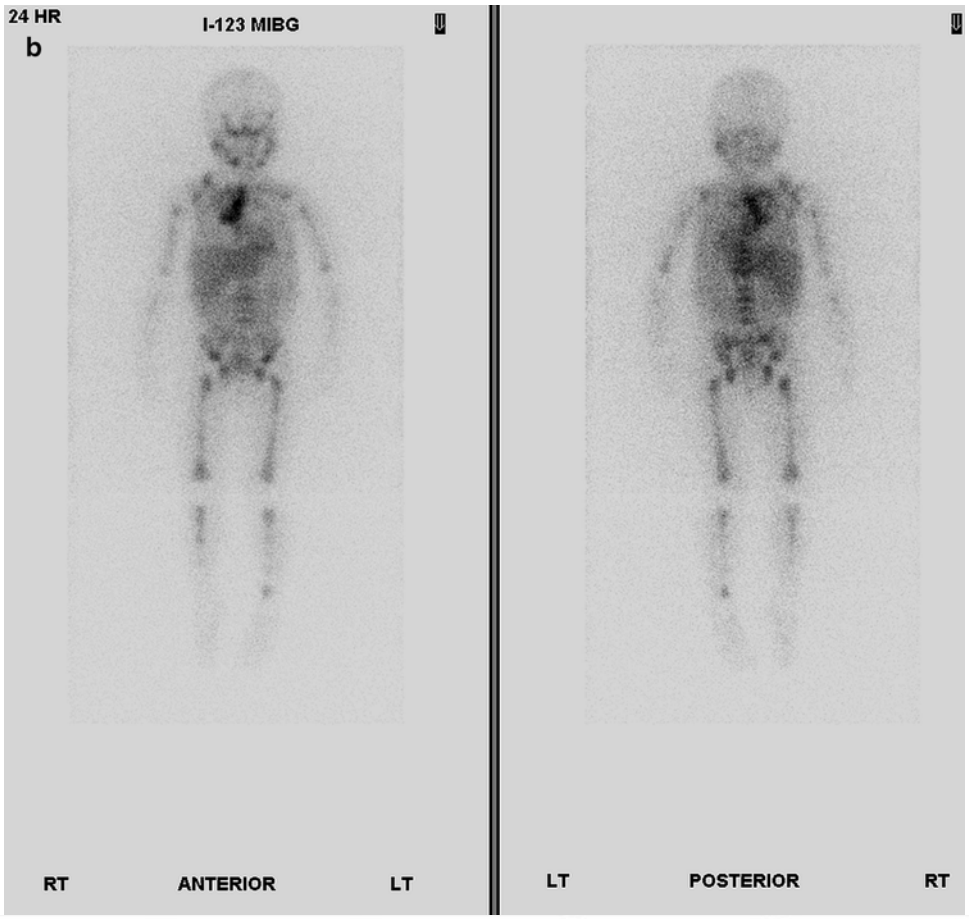

Fig. 12.23 (continued)

that ^{18}F-FDG PET was superior in the follow-up of patients with stages 1 and 2 disease because the extent of tumor was better demonstrated relative to background and when bone marrow involvement was not likely to be present. Also, $^{18F\text{-}FDG}$ PET scan better depicts disease sites in stage 3 and 4 patients when the tumor was weakly positive for ^{123}I-MIBG. Moreover, ^{18}F-FDG PET scan was useful in showing extent of disease in chest, abdomen, and pelvis when disease involvement on CT or MRI appeared more extensive than shown with ^{123}I-MIBG scan. However, ^{123}I-MIBG scan was superior in the evaluation of stage 4 neuroblastoma patients, primarily because of the better detection of bone or bone marrow metastases. Detection of these metastases with ^{18}F-FDG PET scan was often difficult owing to the normal physiologic uptake pattern in the growing skeleton and skull metastases were masked by normal brain uptake. Also, bone and bone marrow lesions could be masked or falsely interpreted as positive in patients receiving granulocyte colony-stimulating factor. In another study comparing ^{123}I-MIBG scintigraphy/SPECT and ^{18}F-FDG PET scan in pediatric neuroblastomas [57], the sensitivities were 50 and 78 % and the specificities were 75 and 92 %, respectively. The combined use of both modalities increased the sensitivity to 85 %. False positive results of each modality were due to physiological uptake or post-therapy changes, and false negative results from low uptake and small lesion size. These authors suggest that ^{18}F-FDG PET may be useful when there is a discrepancy between the ^{123}I-MIBG and morphologic imaging or when there are inconclusive findings.

Molecular Genetics

A family history is observed in about 1 % of neuroblastoma cases [58]. Germline heterozygous mutations in the homeobox gene *PHOX2B* has been described in these patients [59]. The *PHOX2B* gene, localized at chromosome 4p12, regulates development of the autonomous nervous system [58]. Mutations in *PHOX2B* are associated with other neural crest disorders such as Hirschsprung disease and Ondine curse [59], and they also occur in rare sporadic neuroblastomas.

Activating mutations in the tyrosine kinase domain of the anaplastic lymphoma kinase (*ALK*) oncogene on chromosome 2p23 account for most cases of hereditary neuroblastoma [60]. Copy number increases of *ALK* have been found in 20–25 % of primary neuroblastomas, and elevated expression of *ALK* occurs in aggressive neuroblastoma.

Associations between neuroblastic tumors and various "neuro-cardio-faciocutaneous" syndromes, including Noonan and Costello syndromes, and neurofibromatosis type (NF1), are defined by the constitutive activation of the RAS-MAPK pathway [61] and have also been reported [62]. However, germline mutations of *NF1*, *ALK*, and *PHOX2B* do not account for all familial cases of neuroblastoma. Various types of abnormal constitutional karyotypes have been observed in neuroblastoma, including copy number anomalies, balanced and unbalanced translocations, and specific chromosomal deletions [60, 63]. *NBPF1* (Neuroblastoma Break point Family) is another candidate neuroblastoma susceptibility gene [64], and *NBPF23*, another member of this gene family, is associated with neuroblastoma susceptibility [65]. Associations have also been found with single nucleotide polymorphisms at chromosome 6p22 within the putative *FLJ22536* and *FLJ44180* genes and at 2q35 within the *BARD1* genes [66, 67].

Pathology

Currently neuroblastoma tumors are classified according to the International Neuroblastoma Pathology Classification (INPC) [68–70], which distinguishes between two prognostic groups, favorable histology (FH) and unfavorable histology (UH), according to the amount of Schwannian stroma, ganglionic differentiation, the mitotic and karyorrhectic index (MKI), and the age of the patients (Table 12.2). MKI should be assigned to each of the neuroblastoma tumor categories

Table 12.2 International neuroblastoma classification (data from Shimada [69])

Age	Any age	<1.5 years	1.5 to <5 years	≥5 years
Favorable histology	Ganglioneuroma (SSD) Maturing/mature GNB, intermixed (SSR)	Neuroblastoma (SSP) PD with low/intermediate MKI Differentiating with low/intermediate MKI	Neuroblastoma (SSP) Differentiating with low MKI	GNB Nodular (composite, Schwannian stroma-rich/stroma-dominant and stroma-poor), favorable subset
Unfavorable histology	Neuroblastoma (SSP) Undifferentiated with any MKI	Neuroblastoma (SSP) PD with high MKI Differentiating with high MKI	Neuroblastoma (SSP) PD any MKI Differentiating with intermediate or high MKI	Neuroblastoma (SSP) with any subtype and any MKI GNB Nodular (composite, Schwannian stroma-rich/stroma-dominant and stroma-poor), unfavorable subset

Low MKI = <100/5,000 cells
Intermediate MKI = 100–200/5,000 cells
High MKI = >200/5,000 cells
SSD Schwannian stroma dominant, *SSP* Schwannian stroma poor, *SSR* Schwannian stroma rich: *GNB* ganglioneuroblastoma, *MKI* mitosis-karyorrhexis index, *PD* poorly differentiated

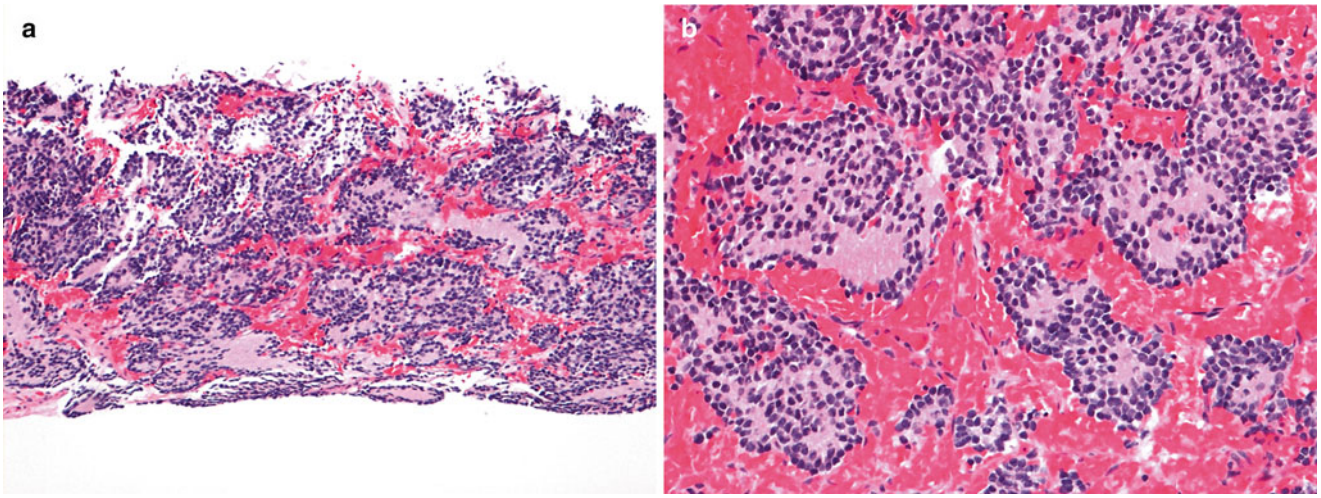

Fig. 12.24 Neuroblastoma poorly differentiated subtype (Schwannian stroma-poor). (**a**) Core biopsy shows neurites in the background and rosette formation (H-E10X). (**b**) Detail of Homer-Wright rosettes (H-E20X)

and comprises low (−<100/5,000 cells), intermediate (100–200/5,000cells), or high (>200/5,000 cells). Peripheral neuroblastic tumors are assigned to one of four basic morphological categories: neuroblastoma, nodular ganglioneuroblastoma, diffuse ganglioneuroblastoma, and ganglioneuroma [69, 71].

Neuroblastoma: Neuroblastoma (Schwannian stroma-poor) is composed of groups/nests of small dark primitive appearing tumor cells (neuroblasts) with dark nuclei, scant cytoplasm, and poorly differentiated cytoplasmic borders. The cells grow in solid sheets separated by thin fibrovascular septal tissue. S100 positive slender cells (putative Schwann cell blasts) can be detected in septa. Such tumors may be difficult to differentiate morphologically from other small round cell tumors. The neuroblastoma category consists of three subtypes, based on degree of neuroblastic differentiation: undifferentiated, poorly differentiated, and differentiating.

In undifferentiated neuroblastoma, virtually all the tumor cells are undifferentiated neuroblasts, and the tumor cannot be diagnosed without ancillary studies such as immunohistochemistry. Tumor cells may contain nucleoli, which has been found to be an unfavorable feature [72]. Neuropil is virtually absent. Neuronal markers are typically positive in only sporadic tumor cells. Poorly differentiated neuroblastoma, the most common subtype, shows ganglionic differentiation in less than 5 % of the tumor neuroblasts A variable amount of neuropil is easily recognized. Homer-Wright rosettes may be present (Fig. 12.24). In differentiating neuroblastoma, at least 5 % of the neuroblasts show definite ganglionic differentiation, and the lesion contains moderate to abundant neuropil.

Ganglioneuroblastoma-intermixed (Schwannian stroma-rich) is a tumor with mixed maturation, typically a predominant ganglioneuromatous component (>50 %), and microscopic nests of neuroblasts and neuropil showing a variable degree of differentiation with or without the presence of ganglion cells. The ganglioneuromatous component contains a Schwann cell matrix containing mature ganglion cells.

Ganglioneuroblastoma-nodular (composite Schwannian stroma-rich/stroma-dominant and stroma-poor) is a composite and multiclonal tumor characterized by the presence of one or more grossly visible often hemorrhagic/necrotic nodules (neuroblastoma nodules) coexisting with ganglioneuroblastoma-intermixed or with ganglioneuroma nodules (Fig. 12.25). *Grading should be based on the neuroblastomatous component*.

Ganglioneuroma (Schwannian stroma-dominant) is a benign tumor separated into maturing and mature subtypes. The maturing subtype is composed of predominantly ganglioneuromatous Schwann cell stroma with scattered collections of mature/maturing ganglion cells and fully mature ganglion cells. The mature subtype contains mature Schwannian stroma and ganglion cells. Neuroblasts are not present (Fig. 12.26).

Immunohistochemistry and Other Special Stains

By immunohistochemistry, neuroblastic tumors express neuronal proteins such as neuron-specific enolase (NSE), synaptophysin, Pgp9.5, NB84, and CD56. CD99 is generally negative; positive tumors should be tested for *EWS* fusions to exclude a Ewing's sarcoma. More differentiated tumors express chromogranin and neurofilaments. Schwann cell marker expression depends on the relative Schwann cell content.

Molecular Diagnostic Features and Cytogenetics

Hyperdiploid neuroblastoma (with near triploid DNA content) associates with more favorable outcomes, whereas near diploid DNA content predicts poor outcome [58]. Recurrent segmental copy number alterations, mainly deletions of chromosome 1p,3p,11q, and gain of 1q, 2p, and 17q, have

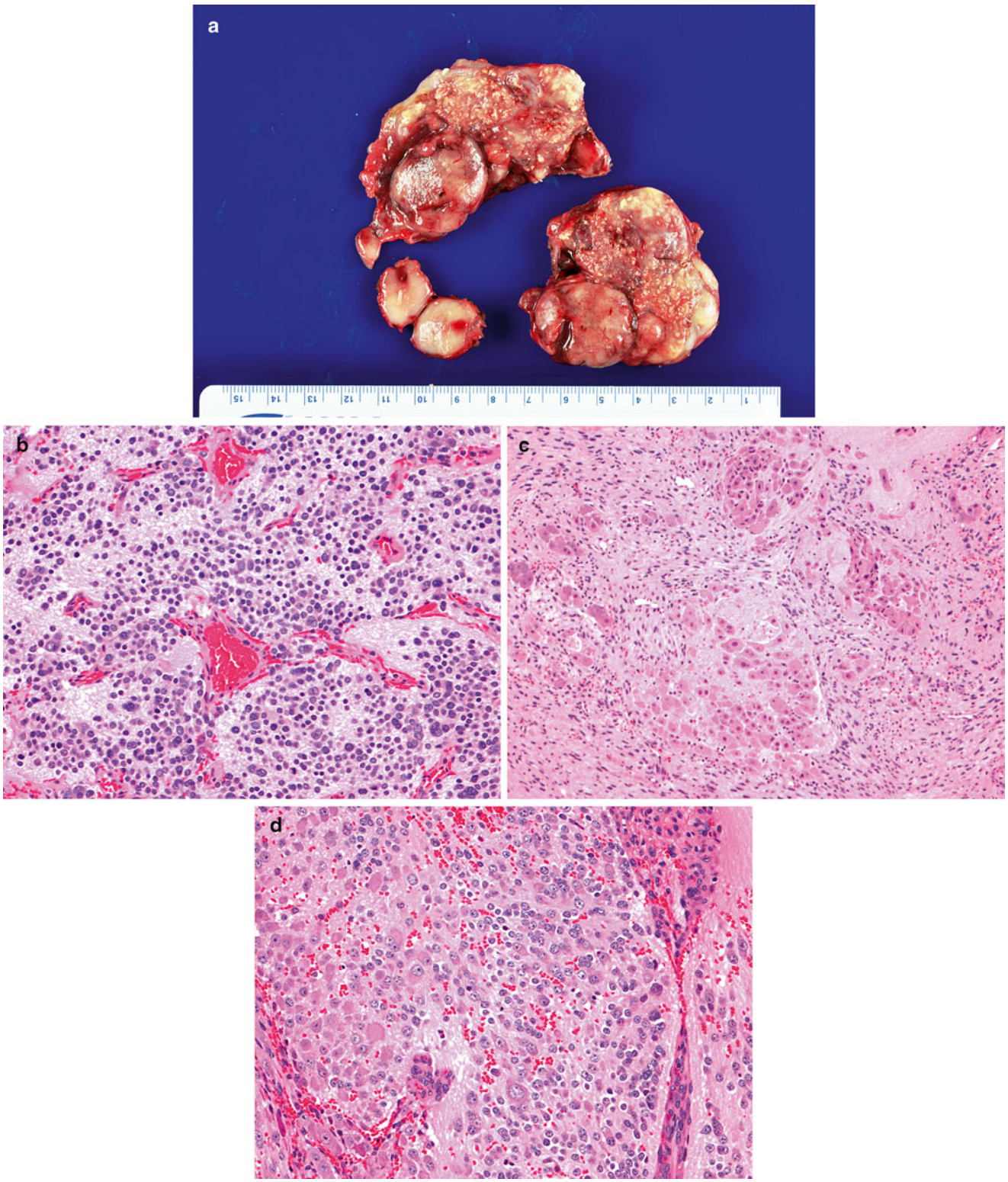

Fig. 12.25 Ganglioneuroblastoma nodular (composite Schwannian stroma-dominant/stroma-rich and stroma-poor) arising in posterior mediastinum. (**a**) Cut section shows a nodular appearance with areas of stippled calcification, nodules with a light tan appearance with foci of hemorrhage and nodules with a fibrous appearance. The lesion contains three different histological patterns: (**b**) Poorly differentiated NEUROBLASTOMA (Schwannian stroma-poor) with low MKI (H-E20X). (**c**) Intermixed ganglioneuroblastoma (Schwannian stroma-rich) with extensive Schwannian stroma development and pockets of naked neuropil containing tumor cells at various stages of neuronal differentiation (H-E10X). (**d**) Neuroblastoma (Schwannian stroma-poor) differentiating subtype containing more than 5 % of tumor cells showing neuroblastic differentiation (H-E20X)

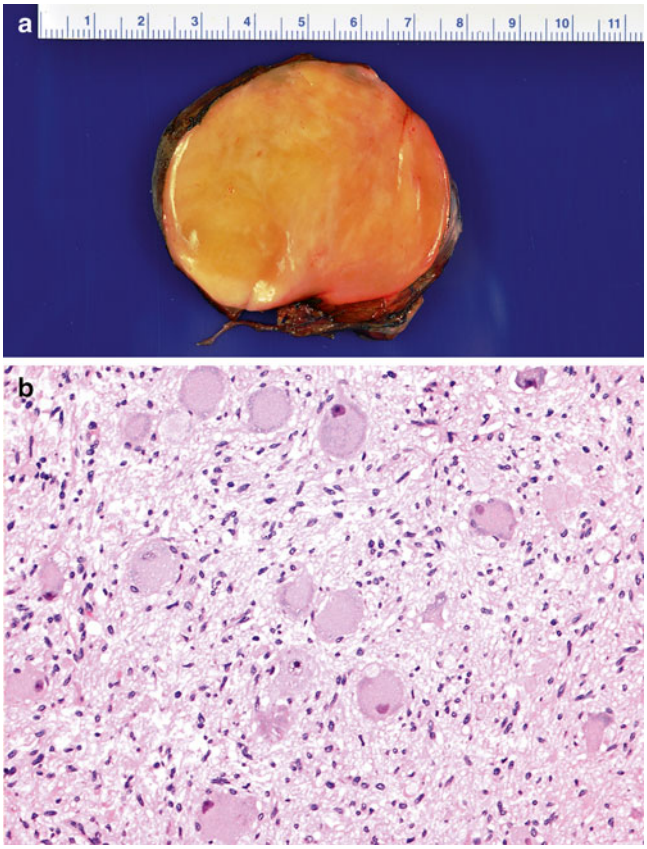

Fig. 12.26 (**a**) Posterior mediastinal tumor showing a homogeneous light tan color appearance. (**b**) Ganglioneuroma (Schwannian stroma-dominant) composed of Schwann cells and maturing/mature ganglion cells (H-EX20)

been associated with a poor outcome [58]. Loss of 1p36, seen in 25–35 % of neuroblastoma cases [73], has a strong correlation with *MYCN* amplification and advanced-stage disease, and is associated with an increased risk of disease relapse in localized tumors [73–75]. Allelic loss of 11q, present in 35–45 % of primary tumors [73], rarely occurs with MYCN amplification [76] yet remains associated with other high-risk features; may be the most common deletion event in neuroblastoma [77]. Partial gain of distal 17q, present in up to 50 % of the tumors, is associated with an adverse outcome, particularly in localized tumors without MYCN amplification [78]. Gain of 17q also correlates with a more aggressive phenotype and often with unbalanced translocations with chromosome 1 or 11 [73, 78]. The presence of segmental alterations was the strongest predictor of relapse in neuroblastoma patients in one study [58].

MYCN amplification at chromosome 2p24 is the most important genetic abnormality for risk stratification of neuroblastoma. It occurs in about one fourth of neuroblastoma cases and is associated with advanced-stage disease and rapid tumor progression [79]. Karyotypically, amplification of MYCN manifests as extrachromosomal double minutes or intra-chromosomal homogeneous staining regions. The association of *MYCN* amplification with poor outcome in patients with otherwise favorable disease patterns, such as localized or 4S disease, underscores its biological importance [15, 79].

Somatic mutations of *ALK* play a role in both familial [60] and sporadic [80] neuroblastoma. *ALK* encodes a transmembrane receptor tyrosine (RTK) that is preferentially expressed in the central and peripheral nervous system. Interestingly, the spectrum of somatic and germline ALK mutations varies [58], possibly indicating differences in ALK signaling associated with specific mutations. *ALK* mutations occur at a high frequency in advanced-stage neuroblastoma [80].

Neurotrophins and their receptors, such as the Trk family, regulate survival, growth, and differentiation of normal and neoplastic neuroblasts and play an important role in the biology and clinical behavior of neuroblastomas. High levels of Trk-A expression in neuroblastoma are associated with a favorable outcome [81], and expression of Trk-C correlates with a favorable prognosis [82, 83]. Truncated Trk-B is predominantly expressed in differentiated tumors, whereas co-expression of full-length Trk-B is associated with *MYCN* amplification, possibly as an autocrine survival pathway [81, 84].

Prognostic Features

Neuroblastoma is a heterogeneous tumor characterized by a broad spectrum of clinical behaviors ranging from spontaneous regression to fatal outcome despite aggressive therapy. Various clinical and biological factors appear to have prognostic value and have led to risk classifications for patients with newly diagnosed neuroblastoma. Most cooperative groups use a system that combines the patient's age, tumor stage, and specific biologic variables to derive low, intermediate, and high-risk categories.

The International Neuroblastoma Risk Group (INRG) classification system provides a consensus approach for pretreatment risk stratification [85] and includes stage, age, histologic category (international neuroblastoma classification Table 12.2), grade of tumor differentiation, *MYCN* status, presence/absence of 11q aberrations, and tumor cell ploidy.

Radiologists involved particularly with clinical trials should be familiar with the 2009 INRG Staging (INRGSS) System [85–87]. As distinguished from the International Neuroblastoma Staging System (INSS), which is a postoperative staging system based on the degree of operative resection (Table 12.3), the new INRGSS, based on clinical criteria and image-defined risk factors (IDRFs) in neuroblastic tumors (Table 12.4), attempts to stage patients prior to operation or other therapies [86]. The presence of these risk factors had been validated to be associated with lower complete resection rate and greater risk of operation-related complications. Imaging modalities that are important include computed tomography (CT) and/or magnetic resonance imaging (MRI), I-123-metaiodobenxylguanidine (MIBG),

Table 12.3 The original international neuroblastoma staging system (INSS) tumor stages [Brodeur]

1	Localized tumor with complete gross excision, with or without microscopic residual disease; representative ipsilateral lymph nodes negative for tumor microscopically. Nodes attached to and removed with the primary tumor may be positive
2A	Localized tumor with incomplete gross excision; representative ipsilateral nonadherent lymph nodes negative for tumor microscopically
2B	Localized tumor with or without complete gross excision, with ipsilateral nonadherent lymph nodes positive for tumor; enlarged contralateral lymph nodes negative microscopically
3	Unresectable unilateral tumor infiltrating across the midline (beyond the opposite side of the vertebral column) with or without regional lymph node involvement, or midline tumor with bilateral extension via infiltration (unresectable) or lymph node involvement
4	Any primary tumor with dissemination to distant lymph nodes, bone marrow, liver, skin, and/or other organs (except as defined for stage 4S disease)
4S	Localized primary tumor (as defined for stage 1, 2A, or 2B disease) with disseminated limited to skin, liver, and/or bone marrow (limited to infants younger than 1 year, marrow involvement of less than 10 % of total nucleated cells, and MIBG findings negative in the marrow)

Table 12.4 Image-defined risk factors (IDRFs) in neuroblastic tumors (data from Monclair [86])

Multiple body compartments (Ipsilateral tumor extension within two body compartments: (neck-chest, chest-abdomen, abdomen-pelvis)
Neck
Tumor encasing carotid and/or vertebral artery and/or internal jugular vein
Tumor extending to base of skull
Tumor compressing the trachea
Cervico-thoracic junction
Tumor encasing brachial plexus roots
Tumor encasing subclavian vessels and/or carotid and/or vertebral arteries
Tumor compressing the trachea
Thorax
Tumor encasing the aorta and/or major branches
Tumor compressing the trachea and/or principal bronchi
Lower mediastinal tumor, infiltrating the costo-vertebral junction between T9-T12
Thoraco-abdominal
Tumor encasing the aorta and/or vena cava
Abdomen/pelvis
Tumor infiltrating the portal hepatis and/or the hepaticoduodenal ligament
Tumor encasing branches of the superior mesenteric artery at the mesenteric root
Tumor encasing the origin of the celiac axis, and/or of the superior mesenteric artery
Tumor invading one or both renal pedicles
Tumor encasing the aorta and/or vena cava
Tumor encasing the iliac vessels
Pelvic tumor crossing the sciatic notch
Intraspinal tumor extension whatever the location provided that more than one third of the spinal canal in the axial plane is invaded and/or the perimedullary leptomeningeal spaces are not visible and/or the spinal cord signal is abnormal
Infiltration of adjacent organs/structures: pericardium, diaphragm, kidney, liver, duodenpancreatic block, and mesentery
Conditions to be recorded, but not considered IDRFs: multifocal primary tumors, pleural effusion, with or without malignant cells, ascites with or without malignant cells

and technetium-99m-scintigraphy. In the INRGSS based on IDRFs, four stages have been described (Table 12.5).

To increase reproducibility in staging using the INRGSS by each center, various terms have been used to define the relation between the primary tumor and vital structures. These include "separation," "contact," "encasement," "compression," "infiltration," and "renal pedicle invasion" [20] (Table 12.6).

In a consensus report from the International Neuroblastoma Risk Group Project, mandatory imaging of neuroblastic tumors includes 123-MIBG-scintigraphy (using SPECT, or SPECT-CT), an enhanced-CT or MR of the primary tumor compartment, and a chest radiograph. While one unequivocal MIBG-avid lesion at a distant site defines metastatic disease, a single equivocal lesion on MIBG scintigraphy requires confirmation by plain radiography (MRI if negative radiography). Optional imaging includes bone scintigraphy, plain radiographs for equivocal skeletal uptake, liver imaging (ultrasound, CT, or MRI) for suspected extra-abdominal primary tumors, chest CT for pleuropulmonary abnormalities, and brain imaging for neurological symptoms not due to spinal cord compression or MIBG/bone scintigraphy for uptake in skull base or orbits.

Table 12.5 International neuroblastoma risk group staging system (INRGSS; data from Monclair [86], 2009)

Tumor stage	Description
L1	Localized tumor *not* involving vital structures, as defined by the list of IDRFs, and confined to one body compartment
L2	Local-regional tumor *with* presence of one or more IDRFs
M	Distant metastatic disease (except stage MS tumor)
MS	Metastatic disease in children younger than 18 months, with metastases confined to skin, liver, and/or bone marrow

PARAGANGLIOMA/PHEOCHROMOCYTOMA

Definition: Pheochromocytomas and paragangliomas are rare neuroendocrine tumors derived from adrenal chromaffin cells or similar cells in extra-adrenal sympathetic and parasympathetic ganglia. Pheochromocytomas occur within the adrenal medulla and usually cause symptoms by secretion of catecholamines. Paragangliomas are similar tumors but non-adrenal. Head and neck paragangliomas arise from parasympathetic ganglia and are almost always nonfunctioning

Table 12.6 Terms to define relationship between primary tumor and vital structures [modified from Brisse [20]. Those in *italics* are considered IDRFs)

Separation	A visible layer, usually fat, is present between the tumor and the neighboring structure. When a tumor is separated from a vital structure, an IDRF is not present
Contact	No visible layer is present between the tumor and the neighboring structure. For an artery, <50 % circumference of the artery is in contact with the tumor. *Flattening* is used to describe a vein with decreased diameter but without luminal obliteration. When a tumor is in contact with a vital structure or is flattening a vein but without encasement, an IDRF is not present, except in renal vessels (see below)
Encasement	The tumor is surrounding (>50 % in contact with) the neighboring structure. If a tumor is encasing a vital structure, an IDRF is present. *Total* encasement means that a vital organ or vessel is completely surrounded by the tumor, including a flattened vein with obliteration of its lumen
Compression	This only applies to airways with reduced short-axis diameter and this pattern is considered an IDRF. Displacement or distortion of vital neighboring organs by tumor is not considered an IDRF unless there is total encasement or infiltration
Infiltration	This refers to involvement of vital structures other than vessels manifested by ill-defined margins between the tumor and the infiltrated structure. When a tumor infiltrates a vital structure, an IDRF is present
Invasion	This is an IDRF describing the tumor is either in contact or encasing the renal pedicle or infiltrating the spinal canal. This is based on the high risk of surgical dissection of the renal pedicle in patients with neuroblastoma

(non-chromaffin). Infra-cervical paragangliomas occur predominantly within the abdomen and less frequently in thorax and pelvis, arise from sympathetic paraganglia, and cause symptoms by catecholamine production and other paraneoplastic phenomenon.

Clinical Features and Epidemiology

Pheochromocytomas and paragangliomas are rare, occurring in 2–8 per million people and having a peak incidence in the third or fourth decade of life. They are often benign but still are associated with high morbidity and mortality secondary to mass effect and high circulating catecholamines. At least 30 % of pheochromocytomas and paragangliomas contain hereditary and germline mutations of at least ten tumor genes. In children this prevalence may be as high as 40 % [88–90].

Population-based studies indicate that approximately one-third of patients with apparently sporadic pheochromocytomas and paragangliomas possess a germline mutation in a known susceptibility gene [91]. This number rises to 79 % in patients with a positive family history of non-syndromic tumor [92] and to 54 % in patients with head and neck paragangliomas [93]. Although pheochromocytomas and paragangliomas are infrequent, they are more often associated with inherited mutations than any other tumor.

Traditionally pheochromocytomas and paragangliomas have been associated with a "rule of 10s" (10 % of sporadic are bilateral, 10 % are not associated with hypertension, 10 % are extra-adrenal, 10 % are malignant, 10 % harbor germline mutations). The last rule has been challenged, as currently 30 % overall are associated with germline mutations, and in children the prevalence may rise to 40 % [88–90]. They are associated with high morbidity and mortality secondary to mass effect and high circulating catecholamines. Catecholamine secretion leads to hypertension, stroke, and even death. Classically, episodic headaches, palpitations, diaphoresis, and anxiety are the hallmarks of a secreting pheochromocytomas and paragangliomas. Younger age, bilateral localization, and a positive family history suggest a familial syndrome (Table 12.7). Specific mutations and familial syndromes correlate with phenotypic features such as differences in tumor distribution, catecholamine production, and risk of metastasis (Table 12.7) [94, 95].

Laboratory diagnosis of these tumors is based on the demonstration of increased urinary excretion of free catecholamines and their metabolites, such as vanillylmandelic acid and metanephrines. The initial testing for pheochromocytomas/paraganglionic should always include measurements of plasma free or urinary fractionated metanephrines or both [96]. O-Methylated metabolites provide a selective biomarker for catecholamine metabolism in pheochromocytes and are not produced by neurons. Because the neuronal pathway makes by far the largest contribution to catecholamine turnover and production of norepinephrine metabolites, measurement of O-methylated metabolites thus provides superior diagnostic biomarkers compared to metabolites such as vanillylmandelic acid, the main metabolic end product of both norepinephrine and epinephrine [97].

Most reports note a higher urinary excretion or plasma concentration of dopamine in patients with evidence of malignancy. Patients with metastatic disease also tend to have lower plasma or urinary levels of epinephrine related to norepinephrine than those with apparently benign tumors [98]. Other studies have focused on differences in secretion of chromogranin or its derived peptides as potential biomarkers of malignancy [97, 98]. The differences may reflect a more immature biochemical phenotype in malignant tumors as compared to benign ones [97]. Catecholamine metabolomics suggests plasma-free methoxyamine as a candidate biomarker for malignancy and therapeutic monitoring. Methoxyamine is the primary metastatic tumor metabolite in some patients [97].

Paraganglionic cells (chromaffin cells) are specialized neural crest cells that are scattered throughout the body, including the adrenal medulla, the chemoreceptors, and cells associated with the thoracic, abdominal, and retroperitoneal

Table 12.7 Susceptibility genes pheochromocytomas and paragangliomas modified from Galan(94), Fishbein (95) Gimenez-Roqueplo (121)

Gene	Locus	Syndrome	INH	Other Clinical manifestations	Primary location	M. rate (%)
NF1	17q11.2	NF1	AD	Café au lait spots, neurofibromas, Lisch nodule, gliomas, soft tissue sarcomas, leukemias of childhood, seizure, macrocephaly, short stature, scoliosis, pseudoarthrosis	Adrenal	12
RET	10q11.2	MEN 2A	AD	Medullary thyroid cancer, hyperparathyroidism, cutaneous lichen amyloidosis	Adrenal (b)	<5
		MEN 2B		Medullary thyroid cancer, mucosal neuroma, marfanoid habitus		
VHL	3p25-26	VHL	AD	Hemangioblastoma, retinal angiomas, renal cell carcinoma (clear cell), endolymphatic sac tumors, serous cystadenoma, and neuroendocrine tumors of pancreas, papillary cystadenoma of the epididymis, and broad ligament	Adrenal	5
SDHA	5q15		AD		Any location	?
SDHB	1p36.1	PGL-4	AD	Additional neoplasms, such as renal cell carcinoma, thyroid tumor, neuroblastoma, GIST	Extra-adrenal	31–71
SDHC	1q23.3	PGL-3	AD	None	HNparagangliomas	Low
SDHD	11q23.1	PGL-1	AD;PI	None	HNparagangliomas (multifocal)	<5
SDHAF2	11q12.2	PGL-2	AD;Pi	None	HNparagangliomas multifocal	low
TMEM127	2q11.2		AD	None	Any location	low
MAX	14q23		AD;PI	None	Adrenal (b)	?

INH inheritance, *M* mortality, *AD* autosomal dominant, *PI* paternal inheritance, *HNParagangliomas* head and neck paraganglioma; *b* bilateral, *NF* neurofibromatosis, *VHL* von Hippel–Lindau

ganglia [99]. Primary tumors associated with extra-adrenal sites (paragangliomas) are found in 9–23 %, are frequently multicentric, and more likely to be malignant than pheochromocytomas. These tumors arise in widespread locations and are associated with both the parasympathetic and sympathetic systems [100]. Tumors arising from the parasympathetic system are located in the head (including pineal gland, orbit, external ear, cheek), neck (such as carotid body, jugulotemporal region, thyroid gland, larynx, trachea, nasal cavity, and nasopharynx), and anterior mediastinum (aortopulmonary). Tumors arising from the sympathetic system are mostly found in the posterior mediastinum and retroperitoneum (such as the para-aortic region, including organ of Zuckerkandl). Visceral involvement includes lung, gallbladder, duodenum, urinary bladder, prostate, and uterus [101]. About 80–95 % of paraganglioma arise within the abdomen, lying in front of or to the side of the vertebral column near the abdominal aorta or kidney. Presenting symptoms are variable, depending on the site of origin and whether the tumor is hormonally active.

Malignancy is defined by the presence of metastases. Frequent metastatic sites include regional lymph nodes, liver, bone, and lung [101–104]. Metastases are seen in 20–42 % of paragangliomas and 2–10 % of pheochromocytomas. The clinical behavior of recurrent metastases is the best predictor of prognosis. While most paragangliomas are solitary and arise sporadically, they can be multifocal and familial (such as in multiple endocrine neoplasia types IIA and IIB, neuroectodermal syndromes, and Carney's triad) in occurrence (Fig. 12.27). In children, multifocal and extra-adrenal tumors are found in up to 30–43 % of cases [105].

Imaging Features

In this section, only imaging of the adrenal (pheochromocytoma) and intra-abdominal extra-adrenal paragangliomas will be discussed. When there is clinical or laboratory suspicion of pheochromocytomas and paragangliomas, localization should combine anatomical imaging (such as ultrasound, CT, MRI, and angiography) and functional imaging (such as ^{123}I-MIBG and ^{18}FDG-PET scans) [106].

Differentiation between benign and malignant pheochromocytoma/paraganglioma by imaging is difficult to establish unless metastases (occurring at sites where chromaffin tissue is not normally present) are found. The presence of vascular or capsular invasion, although more commonly seen in malignant tumors, is not specific for malignancy [104]. Differential diagnoses of pheochromocytoma/paraganglioma include adrenal adenoma, adrenocortical carcinoma, neuroblastoma, metastases, and lymphoma.

Ultrasound: On ultrasound, pheochromocytoma/paraganglioma appears as a well-defined round or oval mass that varies from solid to mixed solid/cystic to cystic appearance. While smaller lesions are homogeneous, the larger lesions are more inhomogeneous in echotexture. Fluid in the cyst may appear anechoic or contain echogenic debris. Acute hemorrhagic lesion may appear echogenic [104]. Reported sensitivity of ultrasound in evaluating pheochromocytoma

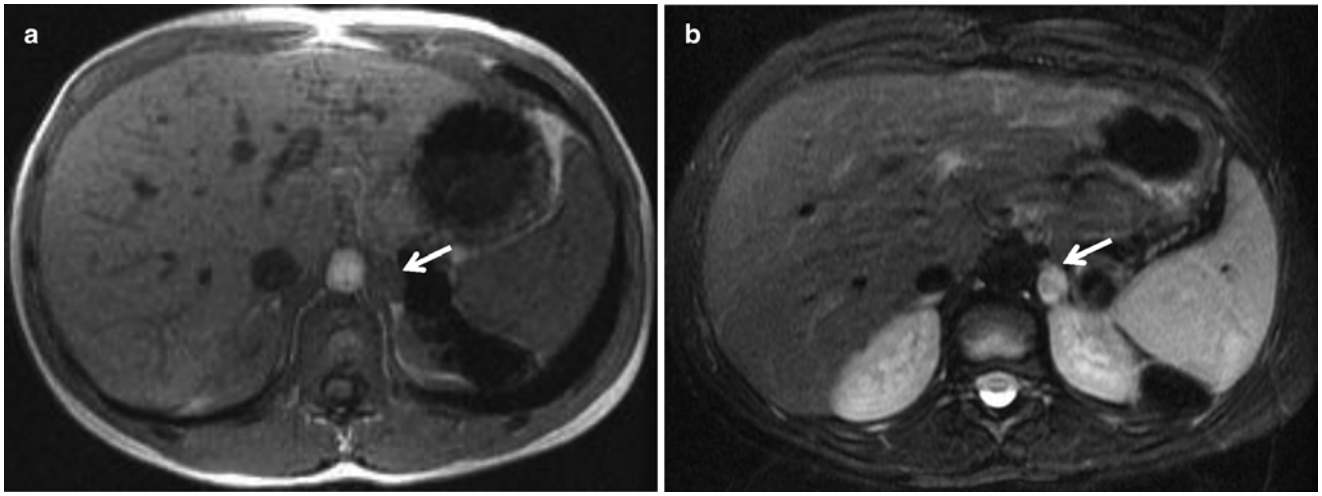

Fig. 12.27 A 10-year-old boy with von Hippel–Lindau syndrome. A small left adrenal pheochromocytoma was identified on screening MRI. Axial images of the abdomen show a small (1.1 cm × 1.2 cm) adrenal mass (*arrow*) in the superoanterior aspect of the left kidney with homogeneous low signal intensity on T1W image (**a**) and high signal intensity on fat-saturated T2W image (**b**). Histologic examination of the excised left adrenal showed a pheochromocytoma

was 83–89 % and specificity, based on early studies, was about 60 % [105].

Computed tomography: Abdominopelvic CT scan should extend from the diaphragm to the pubic symphysis to cover tumors arising from the adrenal gland, retroperitoneum (especially para-aortic, para-caval, and around renal hilum), the organ of Zuckerkandl (7–10 %), and the urinary bladder.

Localization sensitivity is 85–94 % in adrenal location and 90 % in extra-adrenal, metastatic, or recurrent tumor. The specificity is lower at 70–80 % [107]. Most pheochromocytomas are 3 cm or larger in size and may be associated with hemorrhage, necrosis, and fluid-fluid levels. In those associated with MEN syndromes, the adrenal gland tumors tend to be smaller or the adrenal glands may only appear hyperplastic. On unenhanced CT, pheochromocytoma has low to soft-tissue attenuation. About two-thirds are solid and the remainder appear cystic or complex. While small 1–2 cm tumors are usually homogeneous in density (40–50 HU), larger tumors may be inhomogeneous from hemorrhage with increased density [105]. Punctate calcifications may be seen in 10–20 %. After intravenous administration of low-osmolarity nonionic contrast medium, which is safe to use in patient not receiving adrenergic blockade, marked enhancement of the solid portion is seen owing to hypervascularity (Fig. 12.28). Hemorrhage or necrosis will appear as central hypodense areas. The washout pattern after contrast enhancement is variable. When a lesion has regions of myxoid degeneration showing low attenuation on venous phase images, delayed enhancement may be seen [108].

Magnetic resonance imaging: MRI is preferred in children to avoid radiation exposure. On MRI, pheochromocytoma is typically isointense to muscle and hypointense to liver on T1W

Fig. 12.28 Paraganglioma found in a 14-year-old boy presenting with right groin pain radiating to scrotum. Intravenous and enteral enhanced axial CT of the abdomen shows a roundish (3.5 cm × 3.8 cm × 3.7 cm) and inhomogeneously enhancing mass just in front of the abdominal aorta and inferior vena cava at the umbilical level (*arrows*). The mass was a paraganglioma on histologic examination

imaging and "light-bulb" bright (up to three times that of the liver) on T2W imaging [106, 109]. However, variability may be seen if there is necrosis or hemorrhage (Fig. 12.29a–e). In a recent study of T2-weighted appearances of 44 adrenal pheochromocytomas, the "classical" homogeneous high signal intensity ("light-bulb," isointense to cerebrospinal fluid, CSF) was only seen in 11 % [110]. Thirty-four percent appeared homogeneous, isointense, or minimally hyperintense to liver and spleen (hypointense to CSF), 16 % had a heterogeneous and marbled (swirl-like areas of mixed high and lower signal intensity) appearance, and 39 % appeared heterogeneous, with multiple high signal intensity pockets or cystic appearance.

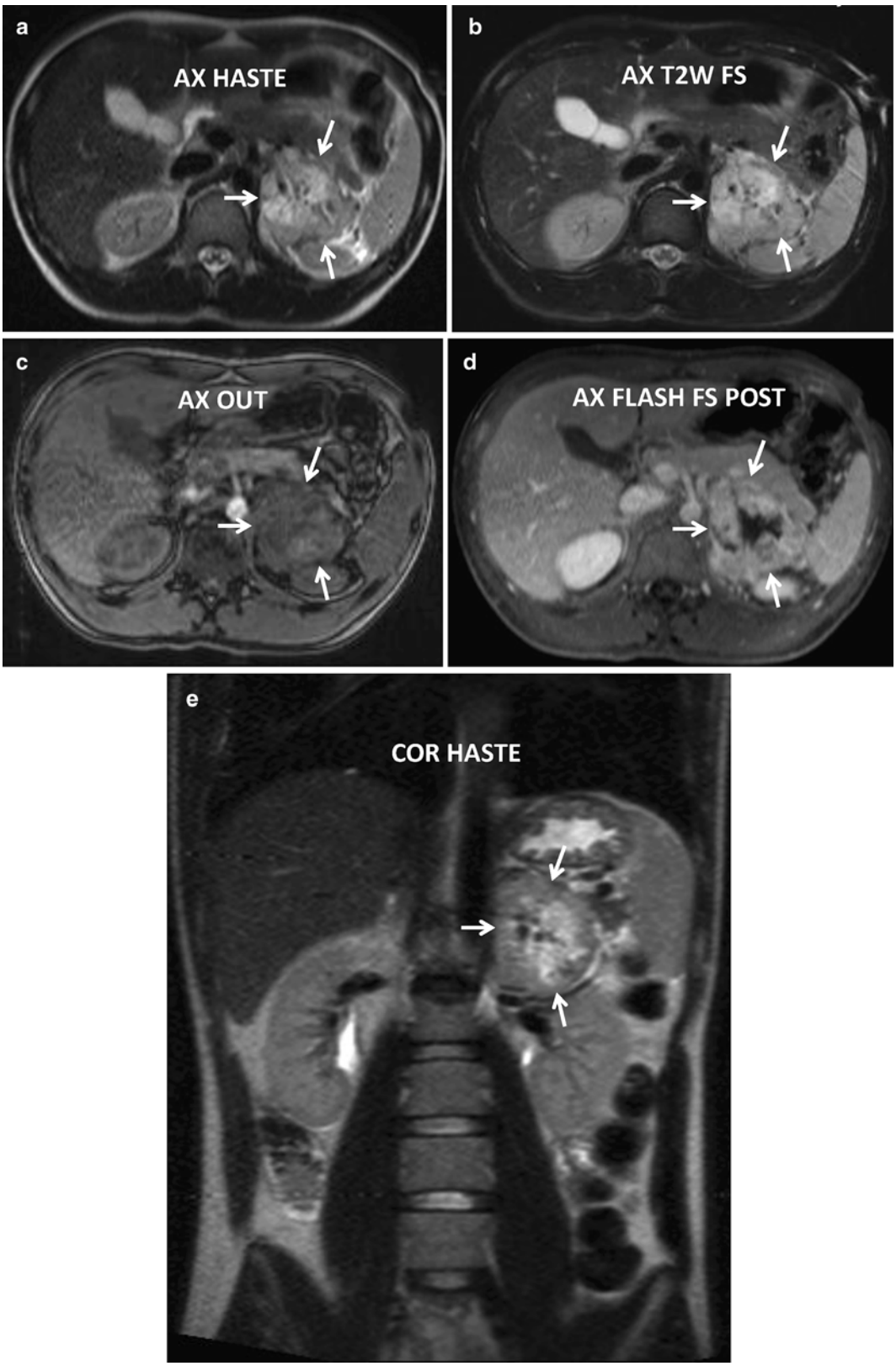

Fig. 12.29 Benign left adrenal pheochromocytoma in a 17-year-old boy presenting with 1 year history of hypertension and poor exercise tolerance. Axial (**a**–**d**) and coronal (**e**) MR images of the abdomen show a left suprarenal mass (*arrows*) with inhomogeneous low signal intensity on T1W image and high signal intensity on T2W image. The mass showed inhomogeneous enhancement with necrotic center (proved on histology). Increased radionuclide uptake was demonstrated only in left adrenal gland tumor on ^{131}I MIBG (**f**) and ^{111}In-octreotide (**g**) scintigraphy (*arrow*)

f

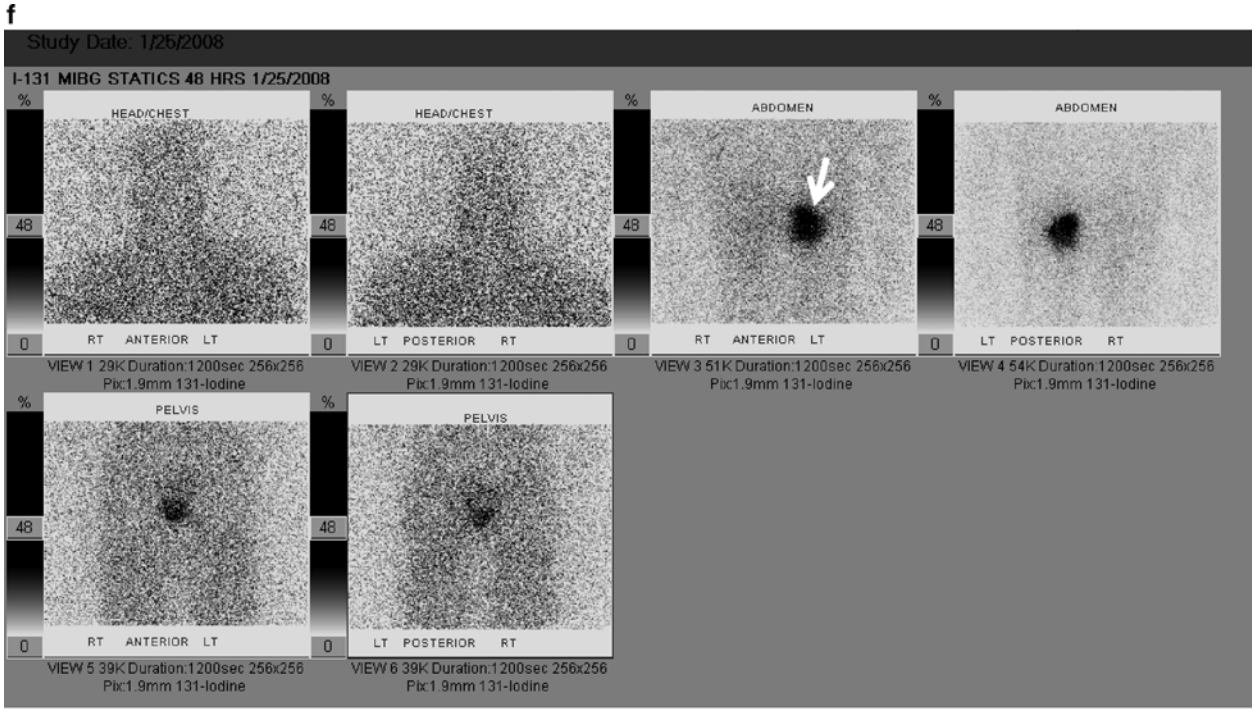

g

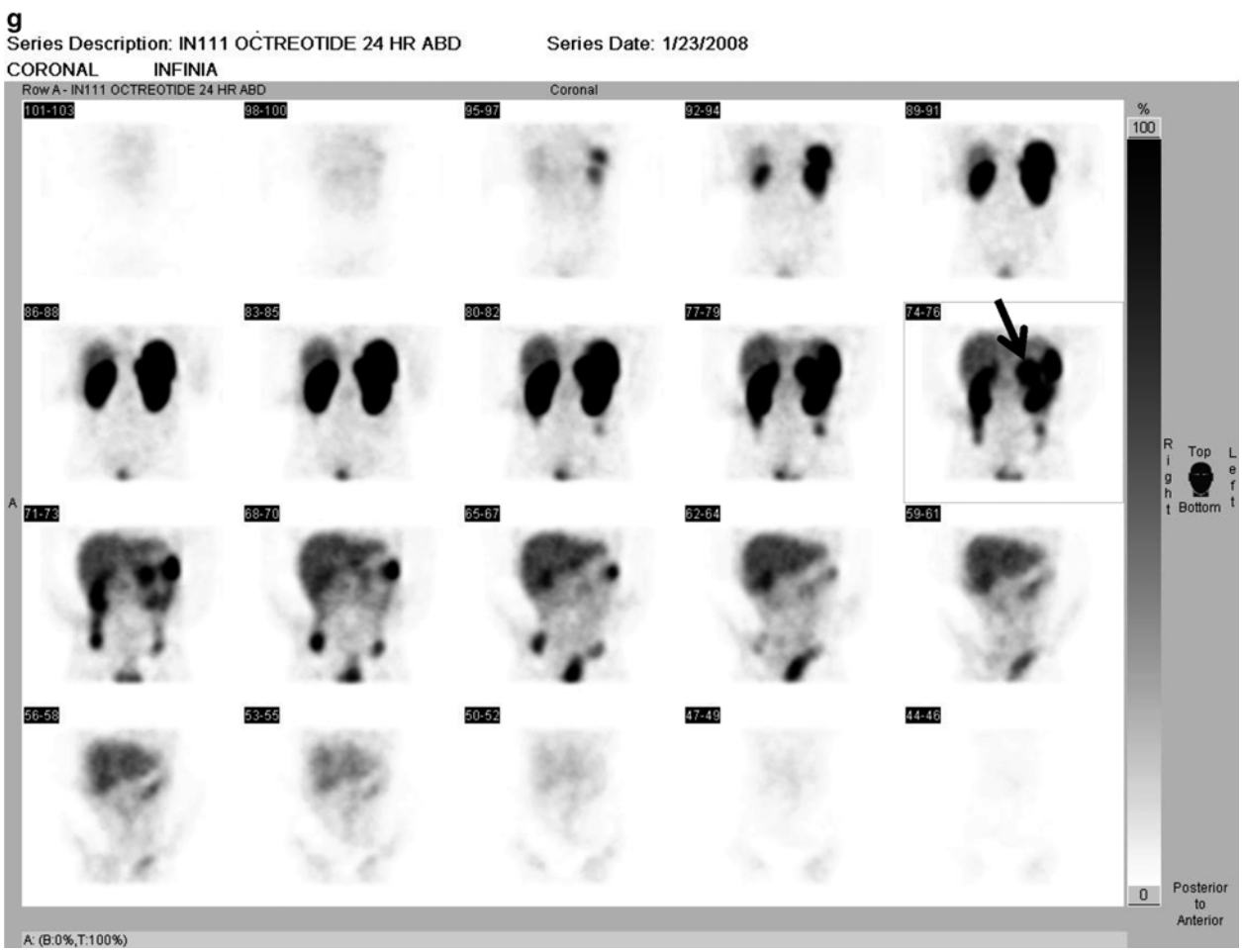

Fig. 12.29 (continued)

These percent differences in appearance on T2-weighted MR imaging may be explained by differences in criteria used to define hyperintense lesions in different series ("isointensity to CSF" in Jacques' series versus "almost isointense to fat" used in others). In one study, lesions that appeared homogeneous were smaller (mean, 4.5 cm) than those with heterogeneous appearance (mean, 6.3 cm) and nonfunctional pheochromocytomas were larger than functional lesions. Pathologic examination showed that heterogeneity correlated with increased amounts of hemorrhage, necrosis, and fibrosis. No MRI features were predictive of malignancy. Chemical shift MRI showed no loss of signal (absence of intracytoplasmic lipid) on spoiled out-of-phase gradient-recalled-echo (GRE) sequence, with few exceptions, in pheochromocytoma [109, 110]. Up to 80 % of paragangliomas show characteristic high signal intensity on T2W images. The presence of hemorrhage may reduce the signal intensity. Typically, pheochromocytoma or paraganglioma shows avid gadolinium enhancement in non-necrotic portions and a prolonged washout phase. Rarely rupture of pheochromocytoma or paraganglioma results in large retroperitoneal hematoma. The reported sensitivity of conventional MRI for adrenal disease is 93–100 and 90 % for extra-adrenal lesions. The specificity is about 50 %. On diffusion-weighted MRI, pheochromocytoma or paraganglioma has high signal intensity due to increased cellularity and diffusion restriction. However, the finding is not specific and this sequence should only be used with the routine T1W and T2W imaging.

Nuclear medicine imaging: Functional radionuclide imaging increases the sensitivity and specificity for the detection of pheochromocytoma/paraganglioma compared to anatomic imaging modalities and allows whole-body evaluation to detect extra-adrenal or metastatic disease in laboratory-positive lesions [106]. Because of excretion of radionuclides in urine, tumors close to kidneys, head of pancreas, and the urinary bladder may be obscured. ^{123}I-MIBG scintigraphy, with imaging obtained at 24 h (and 48 h, if necessary), is the most commonly used functional imaging with a sensitivity of 77–90 % and specificity of 95–100 % [107]. Coregistered fusion imaging technology using MIBG SPECT/CT or MRI is useful, particularly in the detection and three-dimensional localization of recurrence, small extra-adrenal pheochromocytomas, multifocal tumors, and metastatic disease [111, 112]. When positive, there is an increased uptake of ^{123}I-MIBG by the noradrenergic transporter system into intracytoplasmic vesicles and uptake is proportional to the number of neurosecretory granules in the tumor. The ^{123}I-MIBG uptake correlates significantly with the diameter of the tumor and plasma epinephrine levels and is significantly greater in benign, sporadic, intra-adrenal, and unilateral tumors [100]. False negatives (13–25 %) tend to be smaller in size (<1.5–2.0 cm), malignant in nature, or associated with early stages of hereditary tumor syndromes [100]. The combination of MRI and MIBG scintigraphy reached 100 % sensitivity and positive predictive value [113]. ^{131}I-MIBG has been used as a semi-selective radiation therapy agent for malignant pheochromocytomas that take up ^{131}I-MIBG (Fig. 12.29f) [114, 115].

Somatostatin receptors (predominantly types 2 and 4) are present in about three-quarters of pheochromocytomas. Octreotide is an eight-amino acid-long peptide analog of somatostatin that is metabolically stable and has high affinity for type 2 somatostatin receptors, but no affinity for type 4 receptors. ^{111}In-pentetreotide scintigraphy, with high sensitivity in localizing head and neck paragangliomas, has a lower sensitivity (25 %) and specificity in the detection of primary pheochromocytomas and paragangliomas (Fig. 12.29g) [100]. It is mainly used in the assessment of dedifferentiated or malignant tumors (MIBG or ^{18}F-fluorodopamine negative) and detection of metastases [100, 111]. When compared to MIBG scintigraphy, the lack of uptake interference by various drugs and medications makes the use of octreotide less problematic in patients with symptomatic pheochromocytoma who are on antihypertensive drugs and other medications (such as tricyclic antidepressants and nasal decongestants containing phenylpropanolamine) [107, 114].

Experience with qualitative and quantitative assessment using PET scan in the differentiation between benign and malignant adrenal masses is increasing with time [116]. PET agents that have been used include ^{18}F-FDG, ^{11}C-hydroxyephedrine, ^{11}C-epinephrine, ^{18}F-DOPA, and ^{18}F-fluorodopamine [105, 106, 111, 117–119]. These agents have high sensitivity to localize primary (both benign and malignant) and metastatic pheochromocytoma/paraganglioma and are useful in MIBG-negative cases [114]. PET/CT scan using ^{18}F-FDG, the most common agent, is of value in detecting dedifferentiated metastatic tumors and in inherited forms due to specific germline genetic defects, such as succinate dehydrogenase-related tumors [106, 120].

Angiography: Angiography is rarely performed nowadays, but will show enlargement of feeding arteries and an intense tumor blush.

Molecular Genetics

The genetic background of pheochromocytomas and paragangliomas is complex, and at least ten susceptibility genes have been identified to date [95, 121] (Table 12.7). A considerable number of patients with apparently sporadic pheochromocytomas actually have a genetic predisposition to tumor development. At least 30 % of pheochromocytomas/paragangliomas are linked to germline mutations in *VHL*, *RET*, *NF1*, *SDHA*, *SDHB*, *SDHC*, *SDHD*, *SDHAF2*, *TEM127*, and *MAX* geaes [122]. *K1F1B* and *PHD2* have also been associated with pheochromocytomas [94, 95].

Pheochromocytomas and paragangliomas have well-known associations with von Hippel–Lindau disease (VHL), neurofibromatosis 1 (NF1), and multiple endocrine neoplasia 2 (MEN2). Most VHL-associated pheochromocytomas

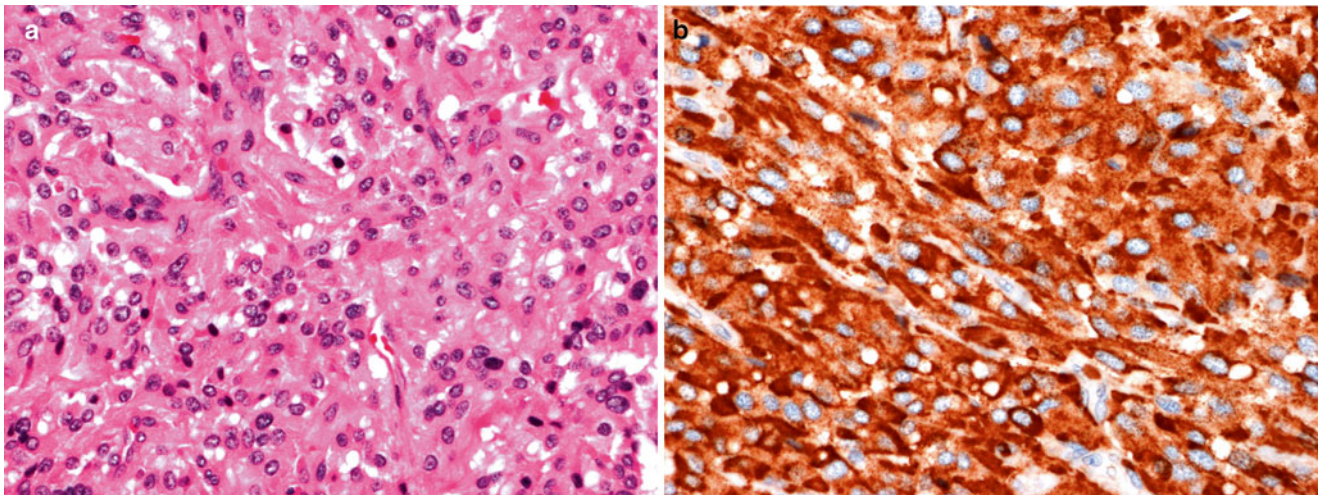

Fig. 12.30 Paragangliomas with zellballen pattern. There is a rich vascular network separating clusters of endocrine cells with round nuclei containing salt and pepper chromatin (**a**) and expressing chromogranin (**b**)

show loss of heterozygosity (LOH) of *VHL* as their second hit. NF1 is an autosomal dominant genetic disorder caused by inactivating mutations in the tumor suppressor gene *NF1*. The estimated rate of pheochromocytomas in NF1 is 5–13 % [95, 122, 123]. MEN 2 is an autosomal dominant syndrome caused by activating mutations in the *RET* proto-oncogene. There are three subtypes of MEN2, with a strong genotype-phenotype correlation [95]. More than 50 % of MEN2-associated pheochromocytomas arise bilaterally in the adrenal glands.

Germline mutations in genes encoding succinate dehydrogenase (SDH) link mitochondrial-associated genes and neural crest-derived cancers [124]. SDH is a heterotetrameric protein consisting of A, B, C, and D subunits and located in the inner mitochondrial membrane [125]. All SDH subunits are encoded by nuclear genes and subsequently transported to the mitochondria. SDH has critical role in cellular energy metabolism through its dual role in the Krebs citric acid cycle and the respiratory oxidative chain (mitochondrial complex 2). Mutations in any of the SDH complex subunit genes (*SDHA*, *SDHB*, *SDHC*, *SDHD*) and in the gene encoding the subunit cofactor SDHAF2 can lead to pheochromocytomas/paraganglionic. These mutations are inherited in an autosomal dominant fashion with incomplete penetrance. Heterozygous mutations of *SDHD*, *SDHB*, and *SDHC* predispose to head and neck paragangliomas (HNPGLs) and extra-adrenal pheochromocytomas [124, 126, 127]. Phenotype-associated *SDHD* mutations are only transmitted from the paternal gene, indicating that they are paternally imprinted [124, 128]. Although rare, *SDHAF2* mutation shows a similar paternally imprinted phenotype [129].

TMEM127, a tumor suppressor gene, has been associated with pheochromocytomas development [130]. Pheochromocytomas with *TMEM127* mutations show transcriptional alterations that are similar to those seen in tumors bearing *NF1* mutations. TMEM127 is a negative regulator of mTOR [130], and disruption of TMEM127 function could be the underlying basis for tumors with aberrant mTOR pathway.

The discovery of *MAX* germline mutations in individuals with hereditary adrenal tumors indicates a key role for the MYC-MAX-MXD1 network in the development of neural crest tumors [131]. Similar to neuroblastomas with *MYCN* amplification, malignant behavior of MAX-related pheochromocytomas indicates that MAX loss of function is correlated with metastatic potential [131].

Pathology

Pheochromocytomas and paragangliomas range from small circumscribed lesions confined to the adrenal to large hemorrhagic masses weighing several kilograms. Generally they are well circumscribed by either connective tissue or compressed cortical or medullary tissue. In many tumors, remnants of the adrenal gland can be identified at the periphery of the tumor. On section, the cut surface is yellow-tan and slightly lobular. Large lesions tend to be hemorrhagic, necrotic, and cystic and typically efface the adrenal gland. Incubation of fresh tissue with a potassium dichromate solution turns the tumor a dark brown color, due to oxidation of stored catecholamines (the chromaffin reaction).

Pheochromocytomas and paragangliomas are composed of polygonal to spindle-shaped chromaffin cells arranged into small nests and alveoli (*zellballen*) by a rich vascular network (Fig. 12.30a). Uncommonly, the dominant cell may be spindle or small. Various patterns can be found in any one tumor. The cytoplasm has a finely granular appearance best demonstrated with silver stains, due to the presence of granules containing catecholamines. The nuclei are usually round to ovoid with the stippled "salt and pepper" chromatin that is characteristic of neuroendocrine tumors. There are no histological features that reliably predict clinical behavior.

Immunohistochemistry and Other Special Stains

Neuroendocrine markers are most useful for diagnosis of pheochromocytomas and paragangliomas. Chromogranin (Fig. 12.30b) and synaptophysin are positive in chief cells, whereas S-100 is positive in sustentacular cells.

Immunostaining for SDHB has 100 % sensitivity in detecting tumors harboring *SDHB* germline mutations [132]. Immunostaining for SDHA can be used specifically to detect mutations, as revealed by loss of staining of both SDHB and SDHA [132]. Caution in the interpretation is advised, as SDH complex is located in the mitochondria; intact staining must be cytoplasmic and granular. Endothelial cells and sustentacular cells retain SDHB expression and serve as internal positive controls. The majority of SDH-deficient tumors have *SDHD* or *SDHB* mutations [132]. Immunostaining for SDHB serves to triage patients needing genetic testing for *SDH* mutations.

Molecular Diagnostic Features and Cytogenetics

Gene copy alterations in pheochromocytomas and paragangliomas are common, and gains of 1q, 11q, 12, and 19q occur in malignant pheochromocytomas [133]. Loss of 1p occurs in more than 80 %, and additional losses involve 3q22-25, 11p, 3p13-14, 4q, 2q, and 11q22-23. Gains are found on 19p, 19q, 17q24-qter, 11cen-q13, and 16p. Losses of 6q and 17p may play an important role in progression to malignancy. Gene expression profiling indicates that most genes (including genes of the catecholamine-production pathway) are downregulated in malignant pheochromocytomas and paragangliomas, suggesting a less differentiated state or concomitant loss of chromosomal material [134]. Microarray analysis reveals differences in gene expression in benign and malignant pheochromocytomas [135]. Transcriptomic and proteomic studies report a multitude of differentially expressed genes and proteins with potential diagnostic or prognostic significance [97].

Prognostic Features

The definitive diagnosis of malignancy in pheochromocytomas and paragangliomas is based on the presence of metastases. Approximately one quarter of pheochromocytomas/PGL are malignant, as defined by the metastases that most commonly occur in bone, liver, and lymph nodes. Metastasis may occur even 20 years after diagnosis, and unfortunately, there currently are no good predictors of malignancy. Proliferative markers such as Ki67 show discrepant results in predicting unfavorable behavior [97]. The Pheochromocytomas of the Adrenal gland Scaled Score (PASS) system is a graded score developed to predict the malignant potential of pheochromocytomas by quantitating histological findings such as mitoses, necrosis, and vascular density [136]. However, PASS shows high inter- and intra-observer variability, making it unreliable [137]. Some studies suggest that malignancy is associated with tumor size over 5–6 cm in diameter, increased vascular density, or expression of vascular markers such as CD32 or VEGF [138]. Germline mutation in *SDHBB* may also be a reliable predictor of malignancy [95]. The general consensus is that extra-adrenal tumor location and presence of *SDHB* mutations are both important risk factors for malignancy.

Early treatment of pheochromocytomas and paragangliomas results in a significant decrease in morbidity and mortality. It is now clear that up to 30 % of patients with apparently sporadic tumors harbor a constitutional germline mutation, so that directed genetic testing is often recommended. Detection of specific *SDH* germline mutations is useful in selecting patients for genetic counseling and predicting clinical manifestations [124].

Plasma methoxyamine shows promise as a biomarker that together with SDHB mutation status, and tumor size and location provides useful information to assess the likelihood of malignancy and manage affected patients [139].

ADRENAL CORTICAL (ADRENOCORTICAL) CARCINOMA

Definition: Adrenal cortical adenoma and carcinoma respectively comprise the primary neoplasms of the adrenal cortex. They may be further distinguished by hormonal expression, and they should be distinguished from diffuse or nodular hyperplasia, as may occur with mutations of enzymes that orchestrate corticosteroid hormone production, e.g., 21 hydroxylase deficiency. Special forms of these neoplasms occur in syndromic lesions such as Carney's syndrome, which includes pigmented adrenal cortical neoplasms in its phenotype.

Clinical Features and Epidemiology

Although rare, pediatric adrenal cortical adenoma and carcinoma show a variable prevalence that is related to population-based gene mutations. The best characterized are those occurring in Brazilian children, who exhibit founder mutations of *TP53* [140]. In certain regions of Brazil, the incidence of adrenal cortical neoplasms is at least 15 times higher than that of other countries. Worldwide, pediatric adrenal cortical neoplasms have an incidence of 0.3/million/year, 1/6th–1/7th of the adult incidence [140].

Presenting symptoms and signs of pediatric adrenal cortical neoplasms include an abdominal mass, cushingoid features, precocious puberty, and virilism. The latter symptom may be manifested by hirsutism and/or genital enlargement. Most pediatric patients have functional tumors, with virilism as the most frequent manifestation [141–144]. Less common symptoms include abdominal pain, weight loss, and features of metastatic disease. Laboratory findings include elevated blood or urine concentrations of adrenocortical hormones, with androgens being the most common followed by corticosteroids. Mixed steroid production is common, and nonsecretors may

produce hormonal precursors with low activity. Estrogen or aldosterone secretion is rare [141].

Imaging Features

When a child presents with clinical signs and symptoms of adrenocortical hyperfunction, such as virilization in girls and precocious puberty in boys, both benign and malignant adrenocortical tumors should be considered. However, differentiation between adrenal adenoma and carcinoma may be difficult [145]. Increased urinary levels of 17-ketosteroids and plasma dehydroepiandrosterone sulfate, seen in about 90 % of the cases, are essential in the diagnosis [146]. The objectives of imaging of adrenocortical tumors are to confirm the adrenal origin of tumor, assess disease staging and resectability, and aid operative planning [147]. Although some carcinomas can be <5 cm in diameter at diagnosis, all adenomas are <5 cm. Other features suggestive of malignancy include a lobulated margin, heterogeneity due to necrosis, hemorrhage, cystic areas, and/or calcium, local invasion or nodal metastasis, and vascular invasion by tumor thrombus. By imaging, only the presence of metastatic disease is definitive of malignancy.

Plain radiography: Plain radiography of the abdomen may show a soft tissue mass with or without calcification. Often a hand x-ray is obtained to assess bone age and a chest x-ray to assess for metastasis to lungs from adrenocortical carcinoma (Fig. 12.31a).

Ultrasound: Sonography may reveal a retroperitoneal mass displacing the kidney and is useful to exclude vascular invasion and extension (Figs. 12.31b and 12.32a, b). Three distinct

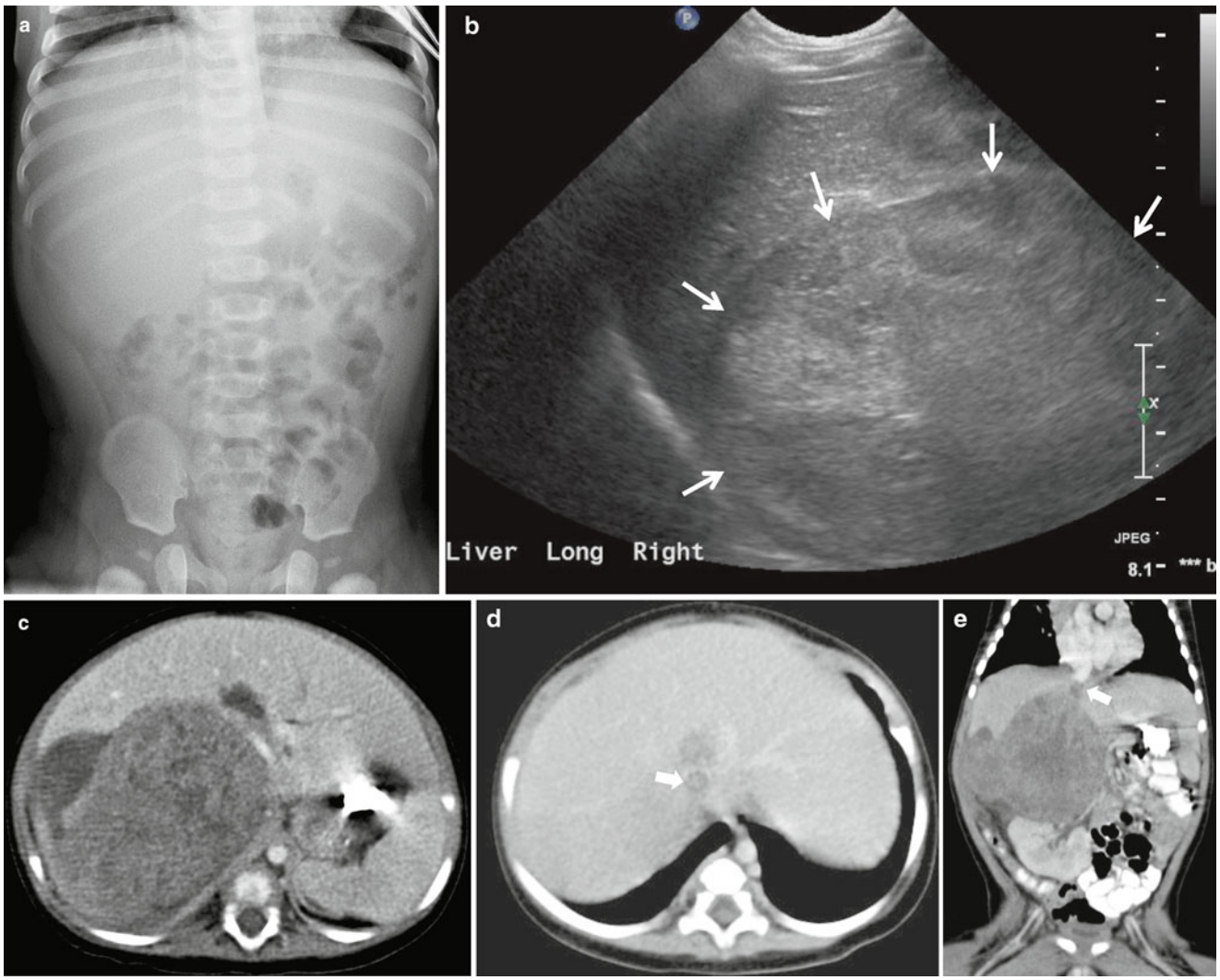

Fig. 12.31 Adrenal cortical carcinoma in a 5-month-old boy presenting with abdominal distention. Plain radiography (**a**) showed a soft tissue mass over the right upper quadrant of abdomen. (**b**) Longitudinal abdominal ultrasound image showed a large (9 cm × 6 cm × 11 cm) inhomogeneous mass (*arrows*) at right upper quadrant of abdomen displacing the liver superiorly and the right kidney (not shown) inferiorly. IV enhanced axial (**c**, **b**) and coronal (**e**) CT images confirmed a suprarenal mass with inferior vena caval extension (*arrow*). Histologic examination of the resected mass showed an adrenal cortical carcinoma with caval invasion

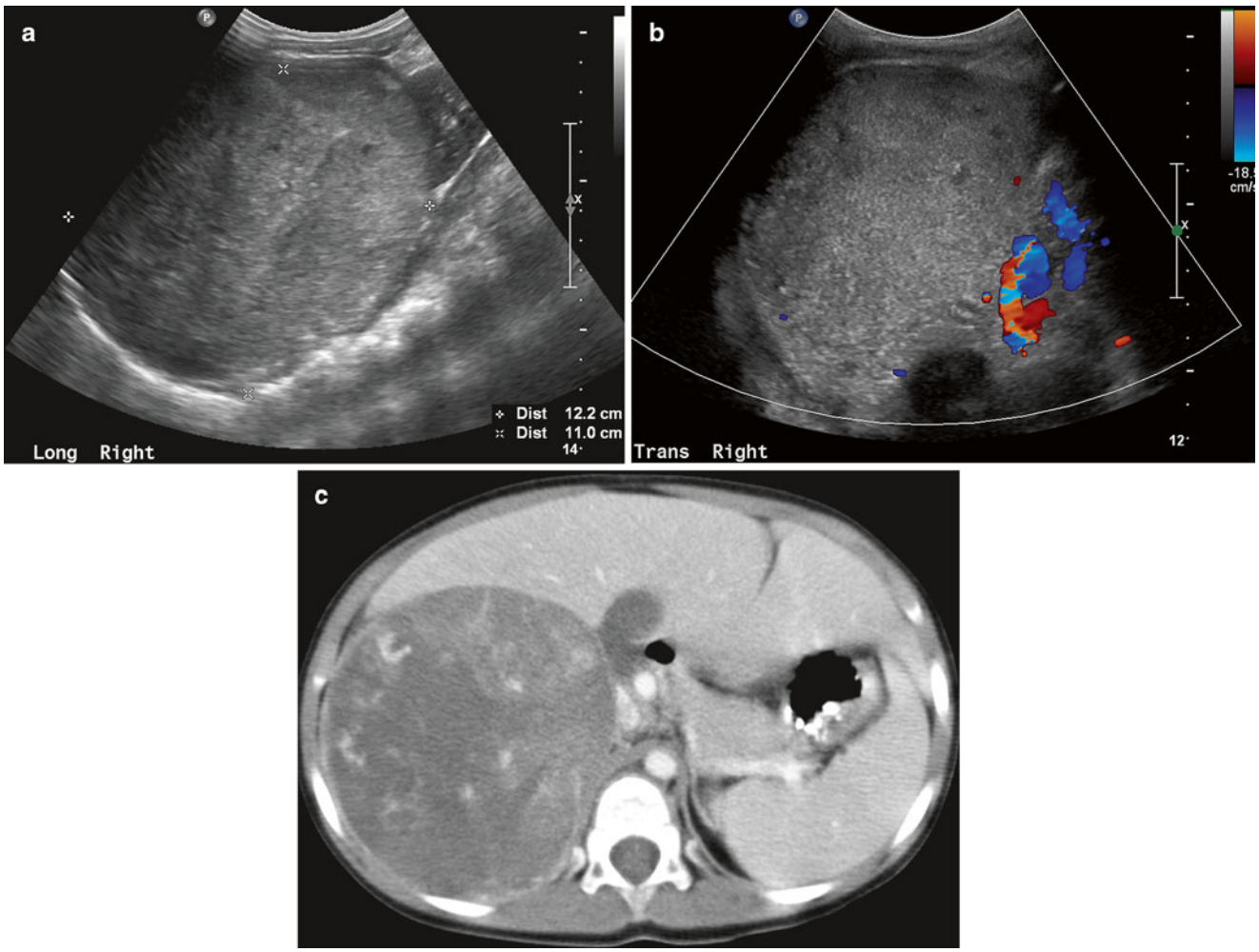

Fig. 12.32 Functional right adrenal carcinoma in a 2-year-old boy presenting with adrenarche and abdominal mass. Longitudinal (**a**) and axial (**b**) images of the upper abdomen show a large (12 cm × 11 cm) suprarenal mass (marked by cursors in (**a**)) at the right upper quadrant of abdomen with mild inhomogeneity of its echotextures. (**c**) IV enhanced axial CT scan of the abdomen showed a large mass (12 cm × 11 cm × 10 cm) in the right suprarenal region with inhomogeneous enhancement and areas of low densities due to necrosis. The liver and the gallbladder were displaced anteriorly and to the left. The inferior vena cava was deformed but not invaded. Histologic examination of the excised mass showed an adrenal carcinoma

sonographic patterns had been reported: (1) radiating echogenic fibrotic septa (scar sign) separating areas of necrosis, hemorrhage, and tumor, (2) small well-defined rounded hypoechoic mass, and (3) small well-circumscribed hyperechoic mass [148]. A complex echo pattern reflecting hemorrhage and necrosis is seen in large carcinomas. Retroperitoneal lymphadenopathy, hematoma from tumor rupture, and tumor thrombus extension into the inferior vena cava may be demonstrated.

Cross-sectional imaging: Either CT or MRI is the most commonly used anatomical imaging assessment of the adrenal tumor (Fig. 12.31c, d [149]). On unenhanced CT scan, adrenocortical carcinoma is seen as a large well-defined mass (usually over 6 cm in diameter) displacing and compressing the kidney posteriorly and the stomach and pancreas anteriorly. In many carcinomas, the margins are irregular and contents are inhomogeneous (higher than 10 HU) from necrosis, hemorrhage, or calcification (Fig. 12.32). Calcifications, seen in 19–33 % of cases, are either microscopic or coarse. Small areas of intracytoplasmic lipid or fatty regions may be seen. After IV enhancement, the carcinoma enhances heterogeneously, often peripherally with a thin rim of enhancing capsule. Relative percent washout is typically less than 40 % and a delayed (10–15 min) attenuation of more than 35 HU is suspicious for malignancy. Sites of metastasis include the liver (48–96 %), lungs (45–97 %), bones (11–33 %), and lymph nodes (25–46 %), along with direct extension and tumor thrombus formation [150]. The hepatic metastases are usually hypervascular and best seen on the arterial phase. The inferior vena cava, particularly the suprahepatic segment, is a preferred site of extension and this invasion has been reported in 9–19 % at presentation [150].

Table 12.8 Inherited tumor syndromes associated with adrenal neoplasia

Tumor	Syndrome	Chromosome locus/(genes)	Extra-adrenal features
(ACA/ACC)	Beckwith–Wiedemann	11p15.5 (*CDKN1/NSD1*, *KCNQ1*, *KCNQ10T1*, *IGF2*, and *H9*)	Exomphalos, microglossia, pancreatic islet cell hyperplasia, gigantism/hemihypertrophy, Wilms tumor, hepatoblastoma, pancreatoblastoma
ACC	Li–Fraumeni	17p13.1 (*Tp53*)	Other neoplasms, particularly breast, bone, blood, and soft tissue cancers
PPNA	Carney complex	17q23-q24 (*PRKARIA* or *PDE114A*)	Lentigines and other pigmented skin lesions, myxomas, LCCST of testis, pituitary adenomas, GIST
(ACA)	MEN1 (Wermer syndrome)	11q13 (*MEN1*)	Endocrine lesions of parathyroid, pituitary, pancreas, GI tract, skin lesions
Adrenal incidentaloma	Familial adenomatous polyposis	5q21-22 (*APC*) 1p34.1 (*MUTYH*)	Colonic polyps, congenital hypertrophy of retinal pigment epithelium, jaw cysts, benign bone tumors

ACA adrenocortical adenoma, *ACC* adrenocortical carcinoma, *PPNA* primary pigmented nodular adenoma, *LCCST* large-cell calcifying Sertoli cell tumor, *GIST* gastrointestinal stromal tumor

On MRI, adrenal cortical carcinomas are typically heterogeneous and isointense or slightly hypointense to normal liver on T1W images, and heterogeneous with intermediate to high signal intensity (compared to normal liver) on T2W images. The heterogeneity seen on T2W images is due to hemorrhage or necrosis. On STIR images, the tumor is isointense to water [149]. In some tumors, an area may be seen that is hypointense on T1W images, and hyperintense on T2W and STIR images, resembling the "central scar" described in liver tumors. A functional adrenal carcinoma may contain small areas of intracytoplasmic lipids resulting in areas of loss of signal on chemical shift imaging. After intravenous contrast, adrenal carcinomas show avid enhancement with slow washout. Inferior vena cava and right atrial extension of tumor can be diagnosed [151]. MR spectroscopy may be useful to differentiate among adrenal adenoma, pheochromocytoma, carcinoma, and metastases [150].

Nuclear medicine imaging: Adrenal scintigraphy using iodocholesterol analogs has not been used widely because it is time-consuming and is associated with high radiation dose. Although experience in using FDG-PET is limited, it has been found to be helpful in distinguishing adrenal carcinomas from adenomas with high density (>10 and <43 HU) or delayed contrast washout values on CT [152]. The combined use of FDG-PET and CT improves the sensitivity, specificity, positive predictive value, and negative predictive value for carcinoma versus adenoma [153]. ^{11C}-metomidate-PET (metomidate binds to adrenal ^{11}C-hydroxylase) is a newer method for adrenal imaging, including detection of potential metastatic disease [154].

Molecular Genetics

Non-neuroblastic pediatric adrenal tumors are rare and may be associated with a genetic predisposition (Table 12.8). Childhood adrenocortical carcinoma occurs with Beckwith–Wiedemann syndrome (BWS) and Li–Fraumeni syndrome (LFS), and it has been reported in patients with multiple endocrine neoplasia 1 (MEN1), familial adenomatous polyposis coli (FAP), and NF1).

LFS results from germline mutations in the *TP53* tumor suppressor gene, which encodes p53. Adrenal tumor-associated *TP53* mutations predominantly occur in infants and toddlers; 68 % of children present in the first 4 years of life and 92 % of patients present in pediatric age group [142]. This predilection suggests that the adrenal tissue of children is most permissive for p53-driven malignant transformation [142].

One of the highest incidences of adrenal cortical carcinoma in children has been found in southern Brazil [140] and is associated with a distinctive germline mutation of *TP53* [143]. This mutation appears to be due to a founder effect, and it segregates with tumor development in LFS and LFS-like families, although its penetrance is lower than that of most other LFS-causing *TP53* mutations [144].

Pathology

Adrenocortical carcinomas are large invasive lesions, many exceeding 20 cm in diameter and 400 gm in weight. In some cases they may exceed 1 kg. Adrenal cortical carcinoma tends to efface the normal adrenal gland and invade surrounding soft tissue organs, with a strong tendency to invade the adrenal vein, vena cava, and lymphatics (Fig. 12.33a). Metastases to regional and periaortic nodes and to lungs are common. The cut surface is variegated and poorly demarcated, containing areas of necrosis, hemorrhage, and cystic change.

Adrenocortical carcinomas may be composed of well-differentiated cells or bizarre monstrous giant cells that may be difficult to distinguish from undifferentiated metastatic carcinoma. Between these two extremes lie cancers with moderate degree of anaplasia, some predominantly composed of spindle cells. The cytomorphologic features of adrenal cortical neoplasia resemble fetal adrenal cortex. Cells are larger than adult cortical cells, have abundant eosinophilic cytoplasm, and are sometimes cytomegalic [155] (Fig. 12.33b).

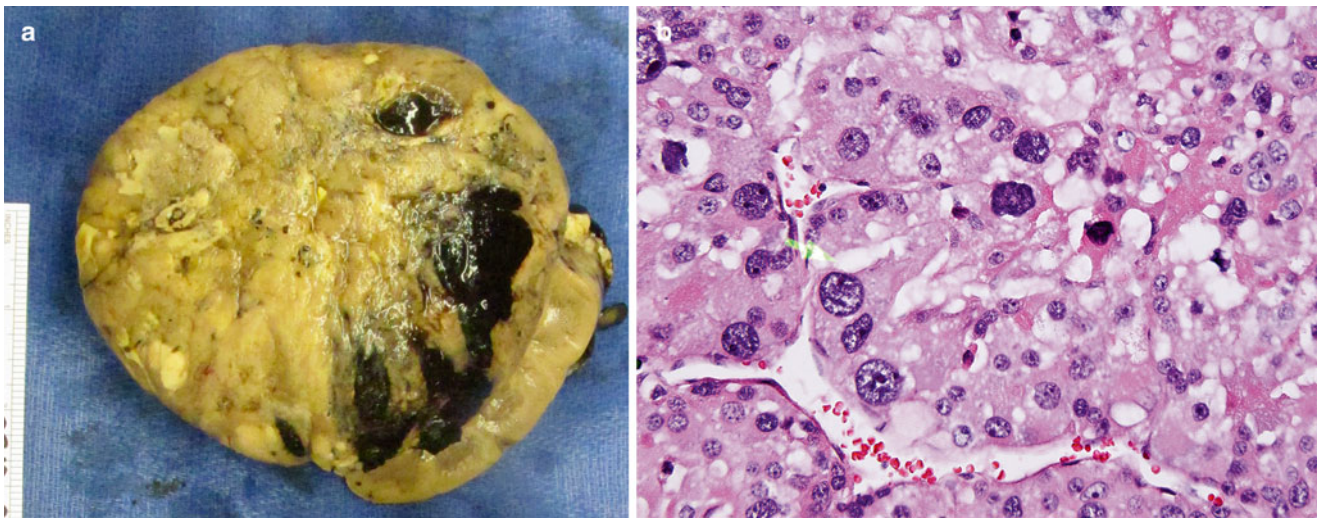

Fig. 12.33 Adrenal cortical carcinoma, with compression of adjacent kidney (**a**). The lesion contains neoplastic adrenal cortical cells forming a sinusoidal pattern and containing large atypical cells (**b**)

Immunohistochemical and Special Stains

Adrenal cortical carcinoma is immunoreactive with vimentin, melan-A, inhibin A, and calretinin. Inhibin A is particularly useful in differentiating adrenal certical neoplasm from similar neoplasms such as renal cell carcinoma or hepatocellular carcinoma, often diagnostic considerations because of location.

Molecular Diagnostics and Cytogenetics

Adrenocortical adenoma/carcinoma in children probably reflects a biological continuum between benign and malignant tumors [156, 157]. The biologic, molecular, and epidemiological differences between childhood and adult adrenal cortical carcinoma suggest that pediatric and adult adrenal cortical carcinoma may represent genetically and biologically distinct entities with convergent pathology [142]. Because at birth the fetal zone begins massive apoptosis and postnatal regression, it is postulated that dysregulation of apoptosis-related genes plays a complex role in the biology and in the pathogenesis of neoplasia [158].

Loss of p53 function may cooperate with additional genetic insults such as IGF2 dysregulation in pediatric ACC, as both are common genetic abnormalities in malignant adrenocortical neoplasms [159].

Prognosis

Histological scoring systems to discriminate between adrenal cortical carcinoma and adenoma have been proposed by different authors [160, 161]. In childhood ACTs, however, standard histopathological approaches have been uniformly reliable in predicting biological behavior [157].

A combination of gross and microscopic features has been used to predict adrenocortical neoplasia behavior.

Table 12.9 Adrenocortical tumors: risk groups based on tumor location and weight (data from Dehner [155])

Risk group	Site	Weight (g)
Low	Any cortical neoplasm confined to the adrenal cortex	<200
Intermediate	Any cortical neoplasm confined to the adrenal gland	200–400
	Any cortical neoplasm confined to the adrenal gland with microscopic invasion into surrounding tissues, completely resected and no evidence of metastases	<400
High	Any cortical neoplasm with direct gross invasion into adjacent organs like the liver, spleen, or kidney or with metastatic spread	>400

Features associated with an increased probability of malignant clinical behavior include tumor weight (>400gm), tumor size (>10.5 cm), vena cava invasion, capsular invasion, extension into periadrenal soft tissue, confluent necrosis, severe nuclear atypia, >15 mitotic figures/20 high power fields, and the presence of atypical mitotic figures [162]. Vena cava invasion, necrosis, and increased mitotic activity (>15mitotic figures/20 high power fields) independently suggest malignant clinical behavior in multivariate analysis [162]. However, correlation of histological features to prognosis in adrenal cortical neoplasms in children has been unreliable in most studies. Dehner et al. [155] proposed use of three risk groups based on tumor location and weight as an alternative means of predicting the clinical behavior of pediatric adrenocortical neoplasma (Table 12.9).

Immunoreactivity is not useful to predict prognosis. Use of proliferation markers such as Ki67 as predictors of outcome is controversial because of inter- and intra-observer variability [163]. DNA ploidy is also controversial [155, 164].

Adrenocortical tumor demonstrates chromosomal imbalances gains and especially high-level amplification is almost exclusive to adrenocortical carcinoma. The number of karyotypic imbalances may have a predictive value for overall survival in pediatric tumors [165].

References

1. Ariel IM. Tumors of the peripheral nervous system. CA Cancer J Clin. 1983;33:282–99.
2. Ilias I, Sahdev A, Reznek RH, et al. The optimal imaging of adrenal tumours: a comparison of different methods. Endocr Relat Cancer. 2007;14:587–99.
3. Balassy C, Navarro OM, Daneman A. Adrenal masses in children. Radiol Clin North Am. 2011;49:711–27, vi.
4. Darge K, Jaramillo D, Siegel MJ. Whole-body MRI in children: current status and future applications. Eur J Radiol. 2008;68: 289–98.
5. Ley S, Ley-Zaporozhan J, Schenk JP. Whole-body MRI in the pediatric patient. Eur J Radiol. 2009;70:442–51.
6. Goo HW. Whole-body MRI, of neuroblastoma. Eur J Radiol. 2010;75:306–14.
7. Chavhan GB, Babyn PS. Whole-body MR imaging in children: principles, technique, current applications, and future directions. Radiographics. 2011;31:1757–72.
8. Siegel MJ, Acharyya S, Hoffer FA, et al. Whole-body MR imaging for staging of malignant tumors in pediatric patients: results of the American College of Radiology Imaging Network 6660 Trial. Radiology. 2013;266:599–609.
9. Koh DM, Blackledge M, Padhani AR, et al. Whole-body diffusion-weighted MRI: tips, tricks, and pitfalls. AJR Am J Roentgenol. 2012;199:252–62.
10. Deglint HJ, Rangayyan RM, Ayres FJ, et al. Three-dimensional segmentation of the tumor in computed tomographic images of neuroblastoma. J Digit Imaging. 2007;20:72–87.
11. Benard J, Raguenez G, Kauffmann A, et al. MYCN-non-amplified metastatic neuroblastoma with good prognosis and spontaneous regression: a molecular portrait of stage 4S. Mol Oncol. 2008; 2:261–71.
12. Gurney JG, Ross JA, Wall DA, et al. Infant cancer in the U.S.: histology-specific incidence and trends, 1973 to 1992. J Pediatr Hematol Oncol. 1997;19:428–32.
13. Stiller CA, Parkin DM. International variations in the incidence of neuroblastoma. Int J Cancer. 1992;52:538–43.
14. Maris JM. Recent advances in neuroblastoma. N Engl J Med. 2010;362:2202–11.
15. Brodeur GM. Neuroblastoma: biological insights into a clinical enigma. Nat Rev Cancer. 2003;3:203–16.
16. Park JR, Eggert A, Caron H. Neuroblastoma: biology, prognosis, and treatment. Hematol Oncol Clin North Am. 2010;24:65–86.
17. Eng C. Cancer: a ringleader identified. Nature. 2008;455:883–4.
18. Lonergan GJ, Schwab CM, Suarez ES, et al. Neuroblastoma, ganglioneuroblastoma, and ganglioneuroma: radiologic-pathologic correlation. Radiographics. 2002;22:911–34.
19. Garnier S, Maillet O, Haouy S, et al. Prenatal intrarenal neuroblastoma mimicking a mesoblastic nephroma: a case report. J Pediatr Surg. 2012;47:e21–3.
20. Brisse HJ, McCarville MB, Granata C, et al. Guidelines for imaging and staging of neuroblastic tumors: consensus report from the International Neuroblastoma Risk Group Project. Radiology. 2011;261:243–57.
21. D'Ambrosio N, Lyo JK, Young RJ, et al. Imaging of metastatic CNS neuroblastoma. AJR Am J Roentgenol. 2010;194:1223–9.
22. Chu CM, Rasalkar DD, Hu YJ, et al. Clinical presentations and imaging findings of neuroblastoma beyond abdominal mass and a review of imaging algorithm. Br J Radiol. 2011;84:81–91.
23. Lee JY, Cho JY. Prenatal and postnatal imaging findings of congenital adrenal neuroblastoma. J Diagn Med Sonogr. 2004;20: 138–43.
24. Houlihan C, Jampolsky M, Shilad A, et al. Prenatal diagnosis of neuroblastoma with sonography and magnetic resonance imaging. J Ultrasound Med. 2004;23:547–50.
25. Nuchtern JG. Perinatal neuroblastoma. Semin Pediatr Surg. 2006;15:10–6.
26. Deeg KH, Bettendorf U, Hofmann V. Differential diagnosis of neonatal adrenal haemorrhage and congenital neuroblastoma by colour coded Doppler sonography and power Doppler sonography. Eur J Pediatr. 1998;157:294–7.
27. Baun J, Garcia K. Prenatal diagnosis of neuroblastoma: color doppler imaging may increase accuracy. J Diagn Med Sonogr. 2004; 20:134–7.
28. Yamashina M, Kayan H, Katayama I, et al. Congenital neuroblastoma presenting as a paratesticular tumor. J Urol. 1988;139: 796–7.
29. Gallagher BL, Vibhakar R, Kao S, et al. Bilateral testicular masses: an unusual presentation of neuroblastoma. Urology. 2006;68:672. e615–77.
30. Ichikawa T, Ohtomo K, Araki T, et al. Ganglioneuroma: computed tomography and magnetic resonance features. Br J Radiol. 1996;69:114–21.
31. Day DL, Johnson R, Cohen MD. Abdominal neuroblastoma with inferior vena caval tumor thrombus: report of three cases (one with right atrial extension). Pediatr Radiol. 1991;21:205–7.
32. Albregts AE, Cohen MD, Galliani CA. Neuroblastoma invading the kidney. J Pediatr Surg. 1994;29:930–3.
33. Nour-Eldin NE, Abdelmonem O, Tawfik AM, et al. Pediatric primary and metastatic neuroblastoma: MRI findings: pictorial review. Magn Reson Imaging. 2012;30:893–906.
34. Dietrich RB, Kangarloo H, Lenarsky C, et al. Neuroblastoma: the role of MR imaging. AJR Am J Roentgenol. 1987;148:937–42.
35. Slovis TL, Meza MP, Cushing B, et al. Thoracic neuroblastoma: what is the best imaging modality for evaluating extent of disease? Pediatr Radiol. 1997;27:273–5.
36. Siegel MJ, Ishwaran H, Fletcher BD, et al. Staging of neuroblastoma at imaging: report of the radiology diagnostic oncology group. Radiology. 2002;223:168–75.
37. Zhang Y, Nishimura H, Kato S, et al. MRI of ganglioneuroma: histologic correlation study. J Comput Assist Tomogr. 2001;25: 617–23.
38. Mehta K, Haller JO, Legasto AC. Imaging neuroblastoma in children. Crit Rev Comput Tomogr. 2003;44:47–61.
39. Gahr N, Darge K, Hahn G, et al. Diffusion-weighted MRI for differentiation of neuroblastoma and ganglioneuroblastoma/ganglioneuroma. Eur J Radiol. 2011;79:443–6.
40. Mueller WP, Coppenrath E, Pfluger T. Nuclear medicine and multimodality imaging of pediatric neuroblastoma. Pediatr Radiol. 2013;43:418–27.
41. Sharp SE, Gelfand MJ, Shulkin BL. Pediatrics: diagnosis of neuroblastoma. Semin Nucl Med. 2011;41:345–53.
42. Krishnamurthy G. Neuroblastoma: role of bone imaging. J Postgrad Med. 2004;50:260–1.
43. Howman-Giles RB, Gilday DL, Ash JM. Radionuclide skeletal survey in neuroblastoma. Radiology. 1979;131:497–502.
44. Bousvaros A, Kirks DR, Grossman H. Imaging of neuroblastoma: an overview. Pediatr Radiol. 1986;16:89–106.
45. Matthay KK, Edeline V, Lumbroso J, et al. Correlation of early metastatic response by 123I-metaiodobenzylguanidine scintigraphy with overall response and event-free survival in stage IV neuroblastoma. J Clin Oncol. 2003;21:2486–91.

46. Matthay KK, Shulkin B, Ladenstein R, et al. Criteria for evaluation of disease extent by ^{123}I-metaiodobenzylguanidine scans in neuroblastoma: a report for the International Neuroblastoma Risk Group (INRG) Task Force. Br J Cancer. 2010;102:1319–26.
47. Naranjo A, Parisi MT, Shulkin BL, et al. Comparison of ^{123}I-metaiodobenzylguanidine (MIBG) and ^{131}I-MIBG semi-quantitative scores in predicting survival in patients with stage 4 neuroblastoma: a report from the Children's Oncology Group. Pediatr Blood Cancer. 2011;56:1041–5.
48. Rufini V, Fisher GA, Shulkin BL, et al. Iodine-123-MIBG imaging of neuroblastoma: utility of SPECT and delayed imaging. J Nucl Med. 1996;37:1464–8.
49. Rozovsky K, Koplewitz BZ, Krausz Y, et al. Added value of SPECT/CT for correlation of MIBG scintigraphy and diagnostic CT in neuroblastoma and pheochromocytoma. AJR Am J Roentgenol. 2008;190:1085–90.
50. Solanki KK, Bomanji J, Moyes J, et al. A pharmacological guide to medicines which interfere with the biodistribution of radiolabelled meta-iodobenzylguanidine (MIBG). Nucl Med Commun. 1992;13:513–21.
51. Jacobson AF, Deng H, Lombard J, et al. ^{123}I-meta-iodobenzylguanidine scintigraphy for the detection of neuroblastoma and pheochromocytoma: results of a meta-analysis. J Clin Endocrinol Metab. 2010;95:2596–606.
52. Pfluger T, Schmied C, Porn U, et al. Integrated imaging using MRI and ^{123}I metaiodobenzylguanidine scintigraphy to improve sensitivity and specificity in the diagnosis of pediatric neuroblastoma. AJR Am J Roentgenol. 2003;181:1115–24.
53. Kushner BH, Yeung HW, Larson SM, et al. Extending positron emission tomography scan utility to high-risk neuroblastoma: ^{18}F fluorodeoxyglucose positron emission tomography as sole imaging modality in follow-up of patients. J Clin Oncol. 2001;19:3397–405.
54. Kushner BH. Neuroblastoma: a disease requiring a multitude of imaging studies. J Nucl Med. 2004;45:1172–88.
55. Papathanasiou ND, Gaze MN, Sullivan K, et al. ^{18}F-FDG PET/CT and ^{123}I-metaiodobenzylguanidine imaging in high-risk neuroblastoma: diagnostic comparison and survival analysis. J Nucl Med. 2011;52:519–25.
56. Sharp SE, Shulkin BL, Gelfand MJ, et al. ^{123}I-MIBG scintigraphy and ^{18}F-FDG PET in neuroblastoma. J Nucl Med. 2009;50:1237–43.
57. Melzer HI, Coppenrath E, Schmid I, et al. ^{123}I-MIBG scintigraphy/SPECT versus ^{18}F-FDG PET in paediatric neuroblastoma. Eur J Nucl Med Mol Imaging. 2011;38:1648–58.
58. Janoueix-Lerosey I, Schleiermacher G, Delattre O. Molecular pathogenesis of peripheral neuroblastic tumors. Oncogene. 2010;29:1566–79.
59. Gaultier C, Trang H, Dauger S, et al. Pediatric disorders with autonomic dysfunction: what role for PHOX2B? Pediatr Res. 2005;58:1–6.
60. Mosse YP, Laudenslager M, Longo L, et al. Identification of ALK as a major familial neuroblastoma predisposition gene. Nature. 2008;455:930–5.
61. Bentires-Alj M, Kontaridis MI, Neel BG. Stops along the RAS pathway in human genetic disease. Nat Med. 2006;12:283–5.
62. Denayer E, de Ravel T, Legius E. Clinical and molecular aspects of RAS related disorders. J Med Genet. 2008;45:695–703.
63. Satge D, Moore SW, Stiller CA, et al. Abnormal constitutional karyotypes in patients with neuroblastoma: a report of four new cases and review of 47 others in the literature. Cancer Genet Cytogenet. 2003;147:89–98.
64. Vandepoele K, Staes K, Andries V, et al. Chibby interacts with NBPF1 and clusterin, two candidate tumor suppressors linked to neuroblastoma. Exp Cell Res. 2010;316:1225–33.
65. Diskin SJ, Hou C, Glessner JT, et al. Copy number variation at 1q21.1 associated with neuroblastoma. Nature. 2009;459:987–91.
66. Maris JM, Mosse YP, Bradfield JP, et al. Chromosome 6p22 locus associated with clinically aggressive neuroblastoma. N Engl J Med. 2008;358:2585–93.
67. Capasso M, Devoto M, Hou C, et al. Common variations in BARD1 influence susceptibility to high-risk neuroblastoma. Nat Genet. 2009;41:718–23.
68. Peuchmaur M, d'Amore ES, Joshi VV, et al. Revision of the International Neuroblastoma Pathology Classification: confirmation of favorable and unfavorable prognostic subsets in ganglioneuroblastoma, nodular. Cancer. 2003;98:2274–81.
69. Shimada H, Ambros IM, Dehner LP, et al. Terminology and morphologic criteria of neuroblastic tumors: recommendations by the International Neuroblastoma Pathology Committee. Cancer. 1999;86:349–63.
70. Shimada H, Ambros IM, Dehner LP, et al. The International Neuroblastoma Pathology Classification (the Shimada system). Cancer. 1999;86:364–72.
71. Umehara S, Nakagawa A, Matthay KK, et al. Histopathology defines prognostic subsets of ganglioneuroblastoma, nodular. Cancer. 2000;89:1150–61.
72. Wang LL, Suganuma R, Ikegaki N, et al. Neuroblastoma of undifferentiated subtype, prognostic significance of prominent nucleolar formation, and MYC/MYCN protein expression: a report from the Children's Oncology Group. Cancer. 2013;119(20):3718–26.
73. Maris JM, Hogarty MD, Bagatell R, et al. Neuroblastoma. Lancet. 2007;369:2106–20.
74. Attiyeh EF, London WB, Mosse YP, et al. Chromosome 1p and 11q deletions and outcome in neuroblastoma. N Engl J Med. 2005;353:2243–53.
75. Caron H, van Sluis P, de Kraker J, et al. Allelic loss of chromosome 1p as a predictor of unfavorable outcome in patients with neuroblastoma. N Engl J Med. 1996;334:225–30.
76. Plantaz D, Vandesompele J, Van Roy N, et al. Comparative genomic hybridization (CGH) analysis of stage 4 neuroblastoma reveals high frequency of 11q deletion in tumors lacking MYCN amplification. Int J Cancer. 2001;91:680–6.
77. George RE, Attiyeh EF, Li S, et al. Genome-wide analysis of neuroblastomas using high-density single nucleotide polymorphism arrays. PLoS One. 2007;2:e255.
78. Schleiermacher G, Michon J, Huon I, et al. Chromosomal CGH identifies patients with a higher risk of relapse in neuroblastoma without MYCN amplification. Br J Cancer. 2007;97:238–46.
79. Seeger RC, Brodeur GM, Sather H, et al. Association of multiple copies of the N-myc oncogene with rapid progression of neuroblastomas. N Engl J Med. 1985;313:1111–6.
80. Chen Y, Takita J, Choi YL, et al. Oncogenic mutations of ALK kinase in neuroblastoma. Nature. 2008;455:971–4.
81. Brodeur GM, Nakagawara A, Yamashiro DJ, et al. Expression of TrkA, TrkB and TrkC in human neuroblastomas. J Neurooncol. 1997;31:49–55.
82. Ryden M, Sehgal R, Dominici C, et al. Expression of mRNA for the neurotrophin receptor trkC in neuroblastomas with favourable tumour stage and good prognosis. Br J Cancer. 1996;74:773–9.
83. Yamashiro DJ, Nakagawara A, Ikegaki N, et al. Expression of TrkC in favorable human neuroblastomas. Oncogene. 1996;12:37–41.
84. Nakagawara A, Azar CG, Scavarda NJ, et al. Expression and function of TRK-B and BDNF in human neuroblastomas. Mol Cell Biol. 1994;14:759–67.
85. Cohn SL, Pearson AD, London WB, et al. The International Neuroblastoma Risk Group (INRG) classification system: an INRG Task Force report. J Clin Oncol. 2009;27:289–97.
86. Monclair T, Brodeur GM, Ambros PF, et al. The International Neuroblastoma Risk Group (INRG) staging system: an INRG Task Force report. J Clin Oncol. 2009;27:298–303.

87. McCarville MB. Imaging neuroblastoma: what the radiologist needs to know. Cancer Imaging. 2011;11(Spec No A):S44–7.
88. Chen H, Sippel RS, O'Dorisio MS, et al. The North American Neuroendocrine Tumor Society consensus guideline for the diagnosis and management of neuroendocrine tumors: pheochromocytoma, paraganglioma, and medullary thyroid cancer. Pancreas. 2010;39:775–83.
89. Barontini M, Levin G, Sanso G. Characteristics of pheochromocytoma in a 4- to 20-year-old population. Ann N Y Acad Sci. 2006; 1073:30–7.
90. Gimenez-Roqueplo AP, Favier J, Rustin P, et al. Mutations in the SDHB gene are associated with extra-adrenal and/or malignant phaeochromocytomas. Cancer Res. 2003;63:5615–21.
91. Neumann HP, Erlic Z, Boedeker CC, et al. Clinical predictors for germline mutations in head and neck paraganglioma patients: cost reduction strategy in genetic diagnostic process as fall-out. Cancer Res. 2009;69:3650–6.
92. Cascon A, Pita G, Burnichon N, et al. Genetics of pheochromocytoma and paraganglioma in Spanish patients. J Clin Endocrinol Metab. 2009;94:1701–5.
93. Burnichon N, Rohmer V, Amar L, et al. The succinate dehydrogenase genetic testing in a large prospective series of patients with paragangliomas. J Clin Endocrinol Metab. 2009;94:2817–27.
94. Galan SR, Kann PH. Genetics and molecular pathogenesis of pheochromocytoma and paraganglioma. Clin Endocrinol (Oxf). 2013;78:165–75.
95. Fishbein L, Nathanson KL. Pheochromocytoma and paraganglioma: understanding the complexities of the genetic background. Cancer Genet. 2012;205:1–11.
96. Pacak K, Eisenhofer G, Ahlman H, et al. Pheochromocytoma: recommendations for clinical practice from the First International Symposium. October 2005. Nat Clin Pract Endocrinol Metab. 2007;3:92–102.
97. Eisenhofer G, Tischler AS, de Krijger RR. Diagnostic tests and biomarkers for pheochromocytoma and extra-adrenal paraganglioma: from routine laboratory methods to disease stratification. Endocr Pathol. 2012;23:4–14.
98. van der Harst E, de Herder WW, de Krijger RR, et al. The value of plasma markers for the clinical behaviour of phaeochromocytomas. Eur J Endocrinol. 2002;147:85–94.
99. Rha SE, Byun JY, Jung SE, et al. Neurogenic tumors in the abdomen: tumor types and imaging characteristics. Radiographics. 2003;23:29–43.
100. van der Harst E, de Herder WW, Bruining HA, et al. [^{123}I] metaiodobenzylguanidine and [^{111}In]octreotide uptake in begnign and malignant pheochromocytomas. J Clin Endocrinol Metab. 2001;86:685–93.
101. Lee KY, Oh YW, Noh HJ, et al. Extraadrenal paragangliomas of the body: imaging features. AJR Am J Roentgenol. 2006;187: 492–504.
102. Ellison DA, Parham DM. Tumors of the autonomic nervous system. Am J Clin Pathol. 2001;115(Suppl):S46–55.
103. Atalabi OM, Lee EY. Abdominal paraganglioma in a pediatric patient. Pediatr Radiol. 2008;38:592.
104. Leung K, Stamm M, Raja A, et al. Pheochromocytoma: the range of appearances on ultrasound, CT, MRI, and functional imaging. AJR Am J Roentgenol. 2013;200:370–8.
105. Ilias I, Pacak K. Current approaches and recommended algorithm for the diagnostic localization of pheochromocytoma. J Clin Endocrinol Metab. 2004;89:479–91.
106. Forssell-Aronsson E, Schüller E, Ahlman H. Advances in the diagnostic imaging of pheochromocytomas. Rep Med Imag. 2011;4:19–37.
107. Jiang L, Schipper ML, Li P, et al. ^{123}I-labeled metaiodobenzylguanidine for diagnosis of neuroendocrine tumors. Rep Med Imag. 2009;2:79–89.
108. Johnson PT, Horton KM, Fishman EK. Adrenal mass imaging with multidetector CT: pathologic conditions, pearls, and pitfalls. Radiographics. 2009;29:1333–51.
109. Elsayes KM, Narra VR, Leyendecker JR, et al. MRI of adrenal and extraadrenal pheochromocytoma. AJR Am J Roentgenol. 2005;184:860–7.
110. Jacques AE, Sahdev A, Sandrasagara M, et al. Adrenal phaeochromocytoma: correlation of MRI appearances with histology and function. Eur Radiol. 2008;18:2885–92.
111. Ilias I, Yu J, Carrasquillo JA, et al. Superiority of 6-[^{18}F]-fluorodopamine positron emission tomography versus [^{131}I]-metaiodobenzylguanidine scintigraphy in the localization of metastatic pheochromocytoma. J Clin Endocrinol Metab. 2003;88: 4083–7.
112. Meyer-Rochow GY, Schembri GP, Benn DE, et al. The utility of metaiodobenzylguanidine single photon emission computed tomography/computed tomography (MIBG SPECT/CT) for the diagnosis of pheochromocytoma. Ann Surg Oncol. 2010;17:392–400.
113. Lumachi F, Tregnaghi A, Zucchetta P, et al. Sensitivity and positive predictive value of CT, MRI and ^{123}I-MIBG scintigraphy in localizing pheochromocytomas: a prospective study. Nucl Med Commun. 2006;27:583–7.
114. Shapiro B, Gross MD, Shulkin B. Radioisotope diagnosis and therapy of malignant pheochromocytoma. Trends Endocrinol Metab. 2001;12:469–75.
115. Grogan RH, Mitmaker EJ, Duh QY. Changing paradigms in the treatment of malignant pheochromocytoma. Cancer Control. 2011;18:104–12.
116. Boland GW, Dwamena BA, Jagtiani Sangwaiya M, et al. Characterization of adrenal masses by using FDG PET: a systematic review and meta-analysis of diagnostic test performance. Radiology. 2011;259:117–26.
117. Taieb D, Sebag F, Barlier A, et al. ^{18}F-FDG avidity of pheochromocytomas and paragangliomas: a new molecular imaging signature? J Nucl Med. 2009;50:711–7.
118. Brink I, Schaefer O, Walz M, et al. Fluorine-18 DOPA PET imaging of paraganglioma syndrome. Clin Nucl Med. 2006;31:39–41.
119. Levine DS, Metzger DL, Nadel HR, et al. Novel use of F-DOPA PET/CT imaging in a child with paraganglioma/pheochromocytoma syndrome. Pediatr Radiol. 2011;41:1321–5.
120. Waguespack SG, Rich T, Grubbs E, et al. A current review of the etiology, diagnosis, and treatment of pediatric pheochromocytoma and paraganglioma. J Clin Endocrinol Metab. 2010;95:2023–37.
121. Gimenez-Roqueplo AP, Dahia PL, Robledo M. An update on the genetics of paraganglioma, pheochromocytoma, and associated hereditary syndromes. Horm Metab Res. 2012;44:328–33.
122. Burnichon N, Vescovo L, Amar L, et al. Integrative genomic analysis reveals somatic mutations in pheochromocytoma and paraganglioma. Hum Mol Genet. 2011;20:3974–85.
123. Walther MM, Reiter R, Keiser HR, et al. Clinical and genetic characterization of pheochromocytoma in von Hippel-Lindau families: comparison with sporadic pheochromocytoma gives insight into natural history of pheochromocytoma. J Urol. 1999;162:659–64.
124. Pasini B, Stratakis CA. SDH mutations in tumorigenesis and inherited endocrine tumours: lesson from the phaeochromocytoma-paraganglioma syndromes. J Intern Med. 2009;266:19–42.
125. Sun F, Huo X, Zhai Y, et al. Crystal structure of mitochondrial respiratory membrane protein complex II. Cell. 2005;121: 1043–57.
126. Baysal BE, Ferrell RE, Willett-Brozick JE, et al. Mutations in SDHD, a mitochondrial complex II gene, in hereditary paraganglioma. Science. 2000;287:848–51.
127. Astuti D, Latif F, Dallol A, et al. Gene mutations in the succinate dehydrogenase subunit SDHB cause susceptibility to familial pheochromocytoma and to familial paraganglioma. Am J Hum Genet. 2001;69:49–54.

128. Heutink P, van der Mey AG, Sandkuijl LA, et al. A gene subject to genomic imprinting and responsible for hereditary paragangliomas maps to chromosome 11q23-qter. Hum Mol Genet. 1992; 1:7–10.
129. Bayley JP, Kunst HP, Cascon A, et al. SDHAF2 mutations in familial and sporadic paraganglioma and phaeochromocytoma. Lancet Oncol. 2010;11:366–72.
130. Qin Y, Yao L, King EE, et al. Germline mutations in TMEM127 confer susceptibility to pheochromocytoma. Nat Genet. 2010;42:229–33.
131. Comino-Mendez I, Gracia-Aznarez FJ, Schiavi F, et al. Exome sequencing identifies MAX mutations as a cause of hereditary pheochromocytoma. Nat Genet. 2011;43:663–7.
132. Barletta JA, Hornick JL. Succinate dehydrogenase-deficient tumors: diagnostic advances and clinical implications. Adv Anat Pathol. 2012;19:193–203.
133. Sandgren J, Andersson R, Rada-Iglesias A, et al. Integrative epigenomic and genomic analysis of malignant pheochromocytoma. Exp Mol Med. 2010;42:484–502.
134. Brouwers FM, Elkahloun AG, Munson PJ, et al. Gene expression profiling of benign and malignant pheochromocytoma. Ann N Y Acad Sci. 2006;1073:541–56.
135. Eisenhofer G, Bornstein SR, Brouwers FM, et al. Malignant pheochromocytoma: current status and initiatives for future progress. Endocr Relat Cancer. 2004;11:423–36.
136. Thompson LD. Pheochromocytoma of the Adrenal gland Scaled Score (PASS) to separate benign from malignant neoplasms: a clinicopathologic and immunophenotypic study of 100 cases. Am J Surg Pathol. 2002;26:551–66.
137. Wu D, Tischler AS, Lloyd RV, et al. Observer variation in the application of the Pheochromocytoma of the Adrenal Gland Scaled Score. Am J Surg Pathol. 2009;33:599–608.
138. Szalat A, Fraenkel M, Doviner V, et al. Malignant pheochromocytoma: predictive factors of malignancy and clinical course in 16 patients at a single tertiary medical center. Endocrine. 2011;39: 160–6.
139. Eisenhofer G, Lenders JW, Siegert G, et al. Plasma methoxytyramine: a novel biomarker of metastatic pheochromocytoma and paraganglioma in relation to established risk factors of tumour size, location and SDHB mutation status. Eur J Cancer. 2012;48:1739–49.
140. Custodio G, Komechen H, Figueiredo FR, et al. Molecular epidemiology of adrenocortical tumors in southern Brazil. Mol Cell Endocrinol. 2012;351:44–51.
141. Rodriguez-Galindo C, Figueiredo BC, Zambetti GP, et al. Biology, clinical characteristics, and management of adrenocortical tumors in children. Pediatr Blood Cancer. 2005;45:265–73.
142. Wasserman JD, Zambetti GP, Malkin D. Towards an understanding of the role of p53 in adrenocortical carcinogenesis. Mol Cell Endocrinol. 2012;351:101–10.
143. Ribeiro RC, Sandrini F, Figueiredo B, et al. An inherited p53 mutation that contributes in a tissue-specific manner to pediatric adrenal cortical carcinoma. Proc Natl Acad Sci U S A. 2001;98:9330–5.
144. Garritano S, Gemignani F, Palmero EI, et al. Detailed haplotype analysis at the TP53 locus in p.R337H mutation carriers in the population of Southern Brazil: evidence for a founder effect. Hum Mutat. 2010;31:143–50.
145. Martinez Leon MI, Romero Chaparro S, Weil Lara B. et al. Adrenocortical tumors in children: imaging adenomas and carcinomas. Radiologia. 2012;54:342–9.
146. Ribeiro RC, Michalkiewicz EL, Figueiredo BC, et al. Adrenocortical tumors in children. Braz J Med Biol Res. 2000;33:1225–34.
147. Daneman A, Chan HS, Martin J. Adrenal carcinoma and adenoma in children: a review of 17 patients. Pediatr Radiol. 1983;13:11–8.
148. Prando A, Wallace S, Marins JL, et al. Sonographic findings of adrenal cortical carcinomas in children. Pediatr Radiol. 1990;20:163–5. discussion 169.
149. Ribeiro J, Ribeiro RC, Fletcher BD. Imaging findings in pediatric adrenocortical carcinoma. Pediatr Radiol. 2000;30:45–51.
150. Bharwani N, Rockall AG, Sahdev A, et al. Adrenocortical carcinoma: the range of appearances on CT and MRI. AJR Am J Roentgenol. 2011;196:W706–14.
151. Godine LB, Berdon WE, Brasch RC, et al. Adrenocortical carcinoma with extension into inferior vena cava and right atrium: report of 3 cases in children. Pediatr Radiol. 1990;20:166–8. discussion 169.
152. Groussin L, Bonardel G, Silvera S, et al. ^{18}F-Fluorodeoxyglucose positron emission tomography for the diagnosis of adrenocortical tumors: a prospective study in 77 operated patients. J Clin Endocrinol Metab. 2009;94:1713–22.
153. Lacroix A. Approach to the patient with adrenocortical carcinoma. J Clin Endocrinol Metab. 2010;95:4812–22.
154. Allolio B, Fassnacht M. Clinical review: adrenocortical carcinoma: clinical update. J Clin Endocrinol Metab. 2006;91:2027–37.
155. Dehner LP, Hill DA. Adrenal cortical neoplasms in children: why so many carcinomas and yet so many survivors? Pediatr Dev Pathol. 2009;12:284–91.
156. West AN, Neale GA, Pounds S, et al. Gene expression profiling of childhood adrenocortical tumors. Cancer Res. 2007;67:600–8.
157. Assie G, Guillaud-Bataille M, Ragazzon B, et al. The pathophysiology, diagnosis and prognosis of adrenocortical tumors revisited by transcriptome analyses. Trends Endocrinol Metab. 2010;21:325–34.
158. Lorea CF, Moreno DA, Borges KS, et al. Expression profile of apoptosis-related genes in childhood adrenocortical tumors: low level of expression of BCL2 and TNF genes suggests a poor prognosis. Eur J Endocrinol. 2012;167:199–208.
159. Simon DP, Hammer GD. Adrenocortical stem and progenitor cells: implications for adrenocortical carcinoma. Mol Cell Endocrinol. 2012;351:2–11.
160. Hough AJ, Hollifield JW, Page DL, et al. Prognostic factors in adrenal cortical tumors. A mathematical analysis of clinical and morphologic data. Am J Clin Pathol. 1979;72:390–9.
161. Weiss LM. Comparative histologic study of 43 metastasizing and nonmetastasizing adrenocortical tumors. Am J Surg Pathol. 1984;8:163–9.
162. Wieneke JA, Thompson LD, Heffess CS. Adrenal cortical neoplasms in the pediatric population: a clinicopathologic and immunophenotypic analysis of 83 patients. Am J Surg Pathol. 2003;27: 867–81.
163. Sasano HNY, Moriya T, Suzuki T. Adrenal cortex. In: Lloyd R, editor. Endocrine pathology: differential diagnosis and molecular advances. New York: Springer; 2010. p. 261–79.
164. Bugg MF, Ribeiro RC, Roberson PK, et al. Correlation of pathologic features with clinical outcome in pediatric adrenocortical neoplasia. A study of a Brazilian population. Brazilian Group for Treatment of Childhood Adrenocortical Tumors. Am J Clin Pathol. 1994;101:625–9.
165. Loncarevic IF, Hering A, Posorski N, et al. Number of genomic imbalances correlates with the overall survival for adrenocortical cancer in childhood. Pediatr Blood Cancer. 2008;51:356–62.

Malignant Skin Tumors in Children

13

Isabel Colmenero, M. Beth McCarville,
and Miguel Reyes-Múgica

Overview and Classification

Primary skin malignancies are uncommon in children, and both benign and metastatic tumors surpass them in frequency. However, the resulting low index of suspicion may lead to a delay in diagnosis and treatment. Underlying factors associated with skin malignancies in children include giant congenital melanocytic nevi, xeroderma pigmentosum, albinism, Gorlin syndrome, immunodeficiency disorders, radiotherapy, and bone marrow and solid organ transplantation, among others [1–3].

The most prevalent primary malignant tumor of the skin in children and adolescents is malignant melanoma (MM), representing around 74 % of the cases [4], and its incidence has rapidly increased in adults and adolescents in the past decades [5]. All other malignant tumors of the pediatric skin are very uncommon and will be grouped in the nonmelanoma skin cancer (NMSC) category, which is mainly represented by basal cell carcinoma (BCC) and squamous cell carcinoma (SCC).

Non-epidermal tumors such as soft tissue malignant neoplasms, leukemias, and lymphomas may rarely primarily involve the skin. These tumors are discussed in other sections of this book. Skin metastasis will be briefly discussed at the end of this chapter.

I. Colmenero, M.D.
Birmingham Children's Hospital,
Steelhouse Ln, Birmingham, West Midlands, UK

M.B. McCarville, M.D.
St. Jude Children's Research Hospital, Memphis, TN, USA

M. Reyes-Múgica, M.D. (✉)
Children's Hospital of Pittsburgh, UPMC, University of Pittsburgh
School of Medicine, One Children's Hospital Drive,
4401 Penn Avenue, Pittsburgh, PA 15224, USA
e-mail: Miguel.Reyes@chp.edu

Genetic Conditions Related to Cutaneous Malignant Tumors

Xeroderma Pigmentosum

Xeroderma pigmentosum (XP) refers to a set of autosomal recessive disorders characterized by defects in the cellular repair of UV-induced DNA damage. XP cells have defects in seven of the proteins of the nucleotide excision repair pathway and in DNA polymerase η (eta) and show hypersensitivity to UV radiation damage. XP cancers feature characteristic "UV signature" mutations [6].

The prevalence of XP is about one in 1 million in Western countries, and it is more common in Japan (1 in 100,000). Affected patients suffer extreme photosensitivity, experience degenerative changes in sun-exposed skin and eyes, and show predisposition to early onset cancers. Numerous freckle-like, hyperpigmented macules appear on sun-exposed skin in all patients, usually starting between 1 and 2 years [7, 8] (Fig. 13.1).

Patients with XP under 20 years of age have a greater than 1,000-fold increased risk of developing skin cancer (BCC, SCC, or MM) [7]; multiple, simultaneous primary skin cancers are common in these patients. The median age of onset of NMSC reported in patients with XP is 8 years. MM develops in about 5 % of XP patients [9], with an estimated median age of onset of 19 years [7], although one study reports that up to 40 % of XP-associated melanomas occur in children under 12 years of age [10]. Children affected by XP must be followed very closely and observe extreme sun protection.

Familial Atypical Mole Melanoma Syndrome

Familial atypical mole melanoma syndrome (FAMMS), sometimes called dysplastic nevus syndrome, or familial cutaneous melanoma syndrome, is characterized by familial

D.M. Parham et al. (eds.), *Pediatric Malignancies: Pathology and Imaging*,
DOI 10.1007/978-1-4939-1729-7_13, © Springer Science+Business Media New York 2015

MM in the setting of atypical moles. Components of the syndrome include a family history of cutaneous MM in two or more first-degree relatives, early age of diagnosis, and the presence of numerous (usually more than 100) often clinically atypical melanocytic nevi, and these are usually 5–10 mm in diameter, variegated from tan to dark brown, and round or oval with irregular, ill-defined borders. They often feature a central elevation within a flat lesion. Early in childhood, the nevi may appear relatively normal, but the atypical nevus phenotype is fully apparent at puberty in most patients [1].

The genetic susceptibility to develop MM in these patients is caused by germ line mutations in the CDKN2A, but rare cases of families carrying mutations in the CDK4 gene have also been described. Through alternative splicing, CDKN2A encodes two distinct protein products, p16 and p14ARF, that exert inhibitory effects on cell growth through distinct pathways involving the retinoblastoma and p53 proteins [11]. The prevalence of germ line CDKN2A mutations among familial melanoma kindreds varies widely, ranging from 20 % in Australia, to 45 % in North America and 57 % in Europe [12].

The lifetime cumulative risk of MM in patients with very strong FAMMS pedigree approaches 100 % [13]. Children with FAMMS should undergo a thorough skin examination every 6–12 months, use sunscreen daily, and avoid significant sun exposure [14].

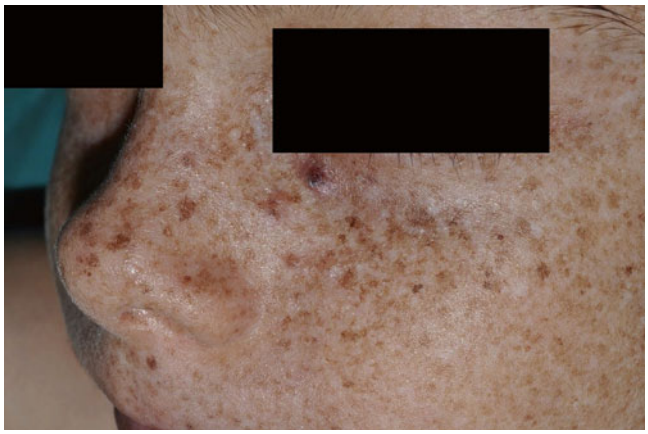

Fig. 13.1 Multiple hyperpigmented macules and a basal cell carcinoma in a patient with xeroderma pigmentosum (Courtesy of Dr. A. Torrelo, Madrid)

Nevoid Basal Cell Carcinoma Syndrome

The nevoid basal cell carcinoma syndrome (NBCCS), or Gorlin syndrome, is an autosomal dominant genodermatosis resulting from heterozygous mutations in PTCH1, PTCH2, SUFU, or other as yet unknown genes [15–18]. NBCCS is transmitted as an autosomal dominant trait with complete penetrance and variable expressivity [17].

NBCCS is characterized by numerous BCC and epidermal cysts of skin, odontogenic keratocysts in the jaws, palmar and plantar pits, calcified dural folds, various neoplasms or hamartomas (ovarian fibromas, medulloblastoma, lymphomesenteric cysts, fetal rhabdomyomas, etc.), and various stigmata of maldevelopment (rib and vertebral abnormalities, Sprengel anomaly, enlarged head circumference, cleft lip and/or palate, cortical defects of bones, etc.) (Fig. 13.2). Diagnosis of NBBCC requires two major or one major and two minor clinical criteria (Table 13.1) [19]. BCCs may arise at various stages of the syndrome; most often they appear between puberty and 35 years of age [20], but patients as young as 4 years old have been reported [21]. Different histological subtypes of BCC, even affecting the same patient, have been described [22]. Documented histological patterns include infundibulocystic, nodular, superficial,

Fig. 13.2 Clinical features of the nevoid basal cell nevus syndrome. (**a**) Pigmented basal cell carcinoma, (**b**) palmar pits, and (**c**) falx cerebri calcification (Courtesy of Dr. A. Torrelo, Madrid)

Table 13.1 Diagnostic criteria for NBCCS [19]

Major criteria
1. More than two BCCs or one under age of 20 years
2. Odontogenic keratocysts
3. Three or more palmar pits
4. Bilamellar calcification of falx cerebri
5. Bifid, fused, or splayed ribs
6. First-degree relative with NBCCS
Minor criteria
1. Macrocephaly adjusted for height
2. Frontal bossing, cleft lip/palate, hypertelorism
3. Sprengel deformity, pectus, syndactyly of digits
4. Bridging of sella turcica, hemivertebrae, flame-shaped radiolucencies
5. Ovarian fibroma
6. Medulloblastoma
Two major or one major and two minor criteria are necessary to diagnose NBCCS

NBCCS Nevoid basal cell carcinoma syndrome; *BCC* Basal cell carcinoma

pigmented, and many others [23]. The appearance of odontogenic keratocysts and new BCCs continues throughout life. Medulloblastomas appear before the age of 4 years, while ovarian fibromas usually develop after puberty. A rare case with the simultaneous occurrence of two solid tumors commonly seen in the pediatric age, rhabdomyosarcoma and Wilms tumor, has also been described [24]. Therapeutic radiation should be avoided whenever possible due to the high occurrence of BCC in the radiation field. Limitation of sun exposure reduces the appearance of skin cancers.

Malignant Melanoma

Pediatric MM is generally defined as melanoma occurring in patients ranging in age from in utero to 21 years, although the upper limits of the cutoff age vary from 13 to 21 years in published reports. Pediatric melanoma can be subdivided into several groups including congenital (in utero to birth), neonatal or infantile (birth to 1 year), childhood (1 year to puberty), and adolescent melanoma (puberty to 21) [25]. In children, as in adults, most melanomas develop de novo. In children, atypical, amelanotic, and nodular melanomas are more common [26].

Epidemiology

MM is the most common skin cancer of childhood, followed by BCC and SCC. It accounts for <3 % of all cancers seen in children, and the incidence in children and adolescents accounts for only 1 % of all new cases diagnosed in the United States annually. The incidence of pediatric melanoma in the United States appears to have increased from 1973 to 2001 at a rate of 2.9 % per year and 46 % per year of age [27, 28]. The incidence of pediatric MM is higher in older children. A review of the National Cancer Institute Registry for melanoma patients aged 1–19 found that 3.8 % were between 1 and 4 years old, 5.7 % were 5 and 9 years old, 17.3 % were 10 and 14 years old, and 73 % were 15 and 19 years old [27–29].

Whites are more likely to develop MM than any other racial-ethnic group. However, there is a proportionately higher incidence of melanoma in nonwhite children less than 10 years of age [27]. There is an apparent female predominance, and the female-to-male ratio increases with age during adolescence and young adulthood. Melanoma can present at any site; however, the extremity is the most common primary site of disease in patients under 20 years of age, followed by trunk and head and neck [30].

Pathogenesis and Genetics

The exact etiology of MM in children remains unclear. It is likely that there is interplay of both inherited and environmental factors.

MM development has been linked to germ line mutations in genes encoding *CDKN2A*, *CDK4*, and *MCIR* as well as to somatic mutations in proto-oncogenes *B-RAF*, *N-RAS*, *KIT* and tumor suppressor genes *CDKN2A*, *p53*, and *PTEN*. Somatic mutations in *B-RAF* are the most common genetic alterations in MM, occurring in up to 66 % of cases. There are at least 30 documented mutations of *B-RAF* that activate the MAPK pathway. The most common *B-RAF* mutation is V600E [31]. Targeting these mutations with specific inhibitors offers an exciting new therapeutic approach for these tumors.

Uribe et al. [32] recently described a pediatric-specific pathogenetic finding. Higher levels of microsatellite instability (MSI) and LOH were found in pediatric melanoma as compared with adult melanoma, although the differences did not reach statistical significance. Increased allelic loss at 11q23 was found in pediatric melanoma, postulated to be related to its early onset. The higher MSI found in pediatric MM could increase the rate of spontaneous mutations in both oncogenes and tumor suppressor genes, leading to tumorigenesis. Increased loss of heterozygosity (LOH) involving *TP53*, *RB1*, and *BRCA1* in both adult and pediatric melanoma possibly reflects inactivation of these genes and a role in melanoma pathogenesis [25].

Risk Factors

Most of the predisposing factors shown in Table 13.2 lead to melanomas in adulthood, although they may have been present since childhood [32]. In addition to the already mentioned inherited tumor syndromes such as XP and FAMMS,

Table 13.2 Predisposing factors for malignant melanocytic skin tumors in children

• Impaired DNA repair, especially xeroderma pigmentosum (XP)
• Familial atypical mole syndrome (FAMM)
• Immunosuppression
• Previous malignant disease
• Congenital melanocytic nevus, especially giant nevus
• Melanoma in the family
• Large number of common melanocytic nevi
• Several atypical melanocytic nevi
• Light skin, red or blond hair, and/or light eyes
• Freckles and/or actinic lentigines (sun spots)
• Tendency to sunburn when exposed to UV light
• Intermittent intensive exposure to UV light

significant predisposing conditions include congenital melanocytic nevi, immune dysfunction (either immunodeficiency or immunosuppression), and a previous history of another malignancy [27, 29, 33]. Immunosuppression secondary to a hematologic, infectious, or acquired disorder (e.g., organ or bone marrow transplant) increases the pediatric risk of melanoma by three- to sixfold [34].

Congenital Melanocytic Nevi (CMN)

Figure 13.3 represent benign proliferations of melanocytes that present at birth or within the first few months of life [35, 36]. Krengel et al. [37] have proposed a system that offers an objective and reproducible classification.

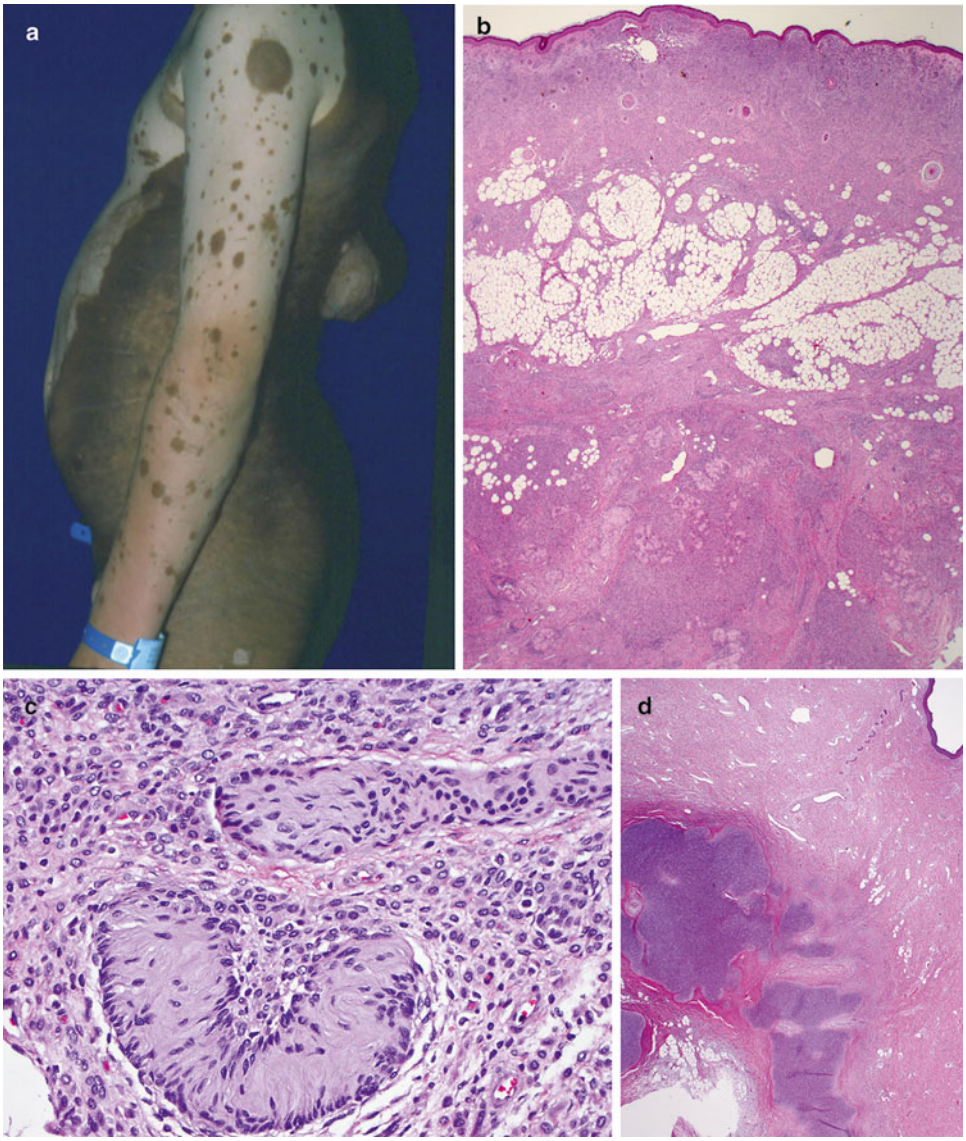

Fig. 13.3 Giant congenital melanocytic nevus of the "bathing-trunk" type with multiple "satellite" nevi and a nodular malignant melanoma in the back (**a**). On low power, the nevus cells replace the entire dermal compartments and extend through the subcutaneous tissue and underlying fascia (**b**). The so-called neurotization is represented by the formation of Wagner-Meissner bodies, or *lames foliacées* (**c**). Hyaline cartilage is a common heterologous component seen within giant congenital nevi (**d**)

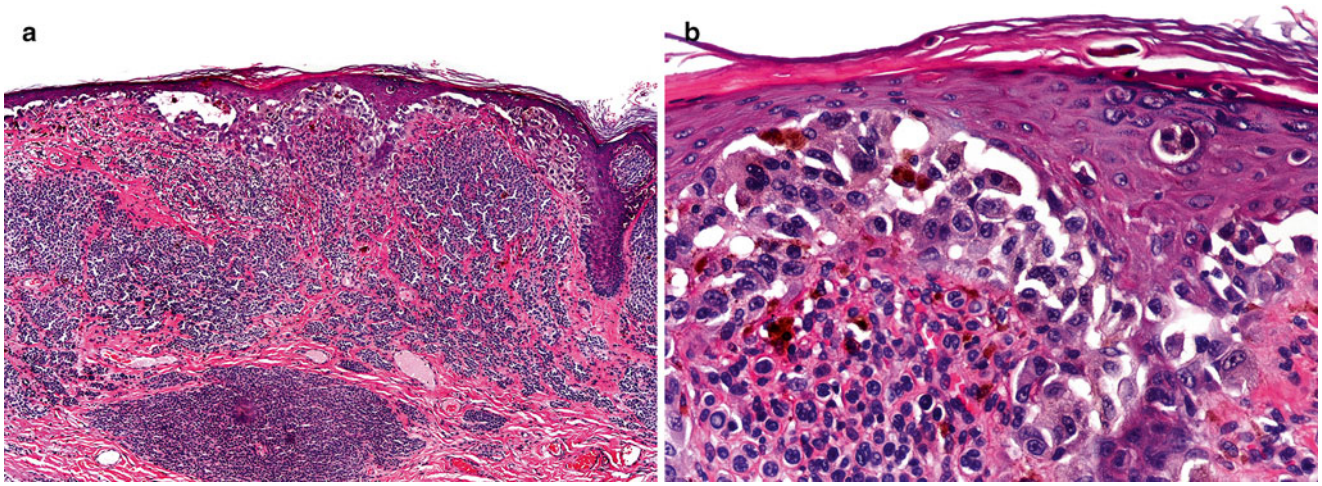

Fig. 13.4 (**a**) Malignant melanoma arising in the dermoepidermal juntion in a medium size CMN. (**b**) High power magnification of the juntional area

Giant CMN are larger than 20 cm in final size. In neonates, giant CMN can be alternatively defined as being larger than the palm of the patient at birth [38]. Giant CMNs are rare and occur in approximately one in 20,000 births [39]. They cause significant distress for the patients and their families, due to their marked cosmetic effects and purported malignant potential. Giant CMN are most commonly found on the posterior trunk ("bathing trunk nevi") and are characterized by a verrucous surface, significant pigmentation, color variation within the dominant background color, and irregular margins. They are accompanied by smaller "satellite" nevi (Fig. 13.3a). As the infant grows, the lesion often acquires increased terminal hairs, variegated colors, and a more irregular surface. Changes may also occur at puberty [40]. Giant congenital nevi have a peculiar histological appearance (*vide infra*) and frequently show an extensive and deep involvement of the entire dermis and subcutaneous tissue, sometimes going even deeper into fascial planes. They may feature significant "neurotization," represented by formations that recapitulate the neural crest origin of these cells, with Masson or Wagner-Meissner bodies, also known as *lames folliacées*. Heterologous elements may also be found, probably indicative of the multipotential differentiation capabilities of the neural crest elements from which they form (Fig. 13.3b–d). In addition, deep tissues underlying these congenital nevi frequently feature poorly developed muscle and vascular elements, resulting in decreased or altered strength and other local symptoms (MRM, unpublished observations). Medium-size congenital nevi are defined as those >1.5 cm but <20 cm in diameter. They occur in about 0.6 % of newborns. Small congenital nevi are defined as those <1.5 cm in diameter. They are seen in about 1 % of newborns. Small CMNs usually present as solitary, well-demarcated, light tan to dark brown uniformly colored macules or slightly raised papules. They can occur in any cutaneous location and be clinically indistinguishable from the so-called common acquired nevi [41].

According to published figures, small and medium-sized CMN carry a lifetime risk of malignant transformation of 2–5 %, while giant CMN carry a 4.5–10 % lifetime risk [42, 43]. However, there is ample variation of this estimated risk, and in general there is a tendency to exaggerate it. A systematic review of the literature published by Krengel et al. [44] showed an overall risk of melanoma of 0.7 %. Melanomas developing in small to medium-sized CMN generally begin to appear around puberty, and their incidence increases throughout adult life. In these nevi, MM develops at the dermoepidermal junction as melanoma in situ. Malignant transformation of giant CMN generally occurs in the deep dermal component of the lesion rather than in the dermoepidermal junction [25] (Fig. 13.4). Higher risk of malignant transformation correlates with larger lesional diameter, increasing number of satellite nevi, and location on the posterior axis [45].

CMN may exhibit distinctive histologic features that help in distinguishing them from common acquired melanocytic nevi. Nevertheless, these features are not entirely pathognomonic for their diagnosis, but they are suspicious for congenital onset in the absence of documentation of the presence of the nevus at birth.

Histologic features, which are shared by small and giant congenital nevi (Fig. 13.3), include (1) the presence of nevomelanocytes within the lower two thirds of the dermis and within the subcutaneous tissue; (2) nevomelanocytes splaying or extending between the collagen bundles of the reticular dermis as single cells, or cords of cells; (3) extension of nevomelanocytes around and within hair follicles, sebaceous glands, eccrine apparatus, vessel walls, and

nerves; (4) a perivascular and perifollicular distribution of nevomelanocytes simulating an inflammatory reaction such as figurate erythema; and (5) arrector pili that may be enlarged, distorted, and infiltrated by nevomelanocytes [41, 46–48].

The optimal management of congenital nevi is controversial. It is generally accepted that complete excision of the entire lesion in early childhood decreases the risk of malignancy, but this is difficult to accomplish in giant CMN, the lesion of highest risk. An alternative option is close monitoring by physical examination with serial follow-up and prompt excision if the lesion develops suspicious changes [34].

Additional complications associated with congenital melanocytic nevi, especially in patients with either giant or multiple nevi, include the spectrum of lesions described under the heading of neurocutaneous melanocytosis (NCM), which encompass proliferations of neural crest-derived melanocytic elements within the meninges and/or the brain, frequently accompanied by Dandy-Walker malformations, cysts of the IV ventricle, and other malformations of the central nervous system. Patients with this spectrum of disorders have variable outcomes depending on a number of factors, particularly the degree of CSF obstruction and the presence of associated CNS symptoms [37].

Clinical Presentation

MMs in prepubertal children are so rare that they are not usually suspected. Clinical findings of MM in children, particularly in adolescents, are similar to those seen in adults. Atypical morphological features are more frequently seen in children. Congenital MMs are also very rarely seen, can present de novo [49], in neonates with giant CMN [50], and may be secondary to transplacental metastasis from an affected mother [51].

In an early series of 125 patients with pediatric melanoma, the most common clinical presentations included increasing size of a mole, bleeding, color change, itching, palpable adenopathy, and palpable subcutaneous mass [52]. Compared with adult melanoma, a significant proportion of pediatric MM are amelanotic (50 %) or have a nodular configuration (30 %), and present at a greater median thickness (3.5 mm) [53].

The ABCDE clinical rule (Asymmetry, Border irregularity, Color variability, Diameter >6 mm, and Evolution) that is often used in identifying potential adult melanomas may be difficult to apply to pediatric skin lesions, because common pediatric lesions such as Spitz or benign nevi can have these features. Pediatric patients are also more likely to present with amelanotic lesions, not a common feature in adult melanoma [53] (Fig. 13.5).

Fig. 13.5 Amelanotic melanoma presenting de novo in the leg of an infant (Courtesy Dr. A. Lassaletta, Madrid)

Most patients (>80 %) present with localized disease at diagnosis; the remainder have either regional lymph node disease (10–15 %) or distant metastasis (1–3 %). Any organ may be involved by metastasis, including lung, liver, lymph nodes, subcutaneous tissue, and brain [30].

Histopathology

The histopathological criteria used for adult patients should also be used for pediatric melanomas (Table 13.3). The most useful features distinguishing MM from nevi are large size (>7 mm), ulceration, high mitotic rate (>4 mitoses/mm^2), mitoses in the lower third of the lesion, asymmetry, poorly demarcated lateral borders, lack of so-called maturation, finely divided melanin, and marked nuclear pleomorphism [54, 55].

Melanoma in children is classified in three groups [19], as per the following sections:

Conventional melanoma. Most melanomas in children can be included in this group. Of the four classical histologic subtypes (superficial spreading, nodular, acral-lentiginous, and lentigo maligna), superficial spreading melanoma is the most common type in both pediatric and adult patients [34] (Fig. 13.6). Young patients appear to have a greater frequency of nodular melanoma. Melanomas of glabrous skin are exceedingly rare in childhood. Lentigo malignant melanoma does not occur in childhood, suggesting that sun exposure

Table 13.3 Histological features of malignant melanoma

Histopathology
• Asymmetry • Ill-defined borders • Lack of maturation • Atypia of melanocytes (variable) • Mitotic figures may be present • Irregular pagetoid spread • Lentiginous junctional proliferation • Ulceration and/or "consumption of the epidermis" • Predominance of solitary units of melanocytes • Marked confluence of melanocytes along the dermal-epidermal junction • Marked dyscohesion of melanocytes • Lichenoid inflammatory reaction may be present • Fibrosis and dermal regression may be present
Immunophenotype
• Positive for S100, Melan-A, HMB-45, tyrosinase
Variants
• Common MM (superficial spreading, nodular, acral lentiginous) • Small cell melanoma • Spitzoid Melanoma
Differential diagnosis
• Spitz nevi • Atypical spitzoid neoplasm • Reed nevi • Proliferative nodule in CMN • Acquired or congenital nevi with pagetoid melanocytosis and lentiginous melanocytic proliferation

MM Malignant melanoma; *CMN* Congenital melanocytic nevus

plays a less important role in the development of melanoma in young people [56].

Small-cell melanoma. These tumors may appear de novo or develop in a congenital nevus, are frequently localized in the scalp, show striking Breslow thickness, and are associated with a fatal outcome in most patients. Small-cell MMs are comprised of monomorphous cells arranged in sheets or in organoid configurations. The high cellular density, lack of maturation, and high mitotic rate are the clues to recognize this lesion [54, 55] (Fig. 13.7).

Spitzoid melanoma. Some melanomas may exhibit features suggesting a Spitz nevus, such as large epithelioid cells and spindle cells arranged in fascicles, epidermal hyperplasia, wedge-shaped configuration, and epidermal clefting surrounding intraepidermal nests. Although most of these lesions also show unequivocal features of a malignant melanocytic neoplasm (Fig. 13.8), some of them may represent extreme difficulty under the microscope, and require additional molecular analyses for definitive discrimination (*vide infra*).

Differential Diagnosis

Pagetoid melanocytosis and lentiginous melanocytic proliferations are commonly observed in acquired or congenital nevi developing in children, particularly in the glabrous skin. These changes must not be overinterpreted, unless architectural disorder and cytological atypia are prominent.

The main differential diagnoses of MM in children are Spitz nevus, atypical spitzoid neoplasms, nevus of Reed, and proliferative nodules in CMN.

Spitz Nevus

Spitz nevi (SN) are benign proliferation of large spindled, oval, or large round (epithelioid) melanocytes that begin in the epidermis and evolve into compound or intradermal stages [19].

SN usually present as a single, dome-shaped papule or nodule with a diameter of 6 mm or less (Fig. 13.9), but larger lesions are not uncommon. Most examples occur on the face and head in children or lower extremities in young adults, particularly women. Their color may vary from nonpigmented through pink to red-brownish and even black. SN commonly appear suddenly and grow rapidly for a period, after which they plateau and remain stable. However, color changes, bleeding, and pruritus may occur. Unusual variants include grouped or agminated [57–60], disseminated SN [61], and eruptive [62].

The classic SN (Fig. 13.10) is dome shaped and symmetric with abrupt attenuation of the junctional nests at the lateral borders of the lesion. The nevus is composed of variable proportions of spindle and epithelioid nevomelanocytes, plump and with abundant cytoplasm, featuring a centrally located vesicular nucleus, often with prominent nucleolus. The proliferating cells sometimes show bizarre shapes, and multinucleated cells may be present. The cytoplasm of the epithelioid cells may have a ground glass appearance, and melanin is usually absent. If present, melanin is symmetrically distributed and absent at the deepest level of the lesion.

A common feature in SN is the presence of Kamino bodies, which are eosinophilic and globular deposits of basement membrane material found within the epidermis, usually above dermal papillae and present in variable numbers from case to case [63]. SN usually features a compound histological pattern, although junctional and intradermal lesions are not uncommon. Compound SN are symmetric, well circumscribed, and often wedge-shaped, with large nests of nevomelanocytes in the epidermis and in the underlying dermis. The proliferating cells are relatively uniform in size and shape, typically oriented perpendicular to the epidermis. Artifactual clefting around the nests is usually seen. Pagetoid spread of nevomelanocytes can be present, mainly in the lower half of the epidermis. This process is usually confined to the center of the lesion, but it can be quite marked in developing junctional SN in young children [64]. SN show "maturation," traditionally defined as progressive reduction of melanocytic nests and cellular size from the top to the bottom. Nevomelanocytes in the dermis are mostly nested or arranged in fascicles and

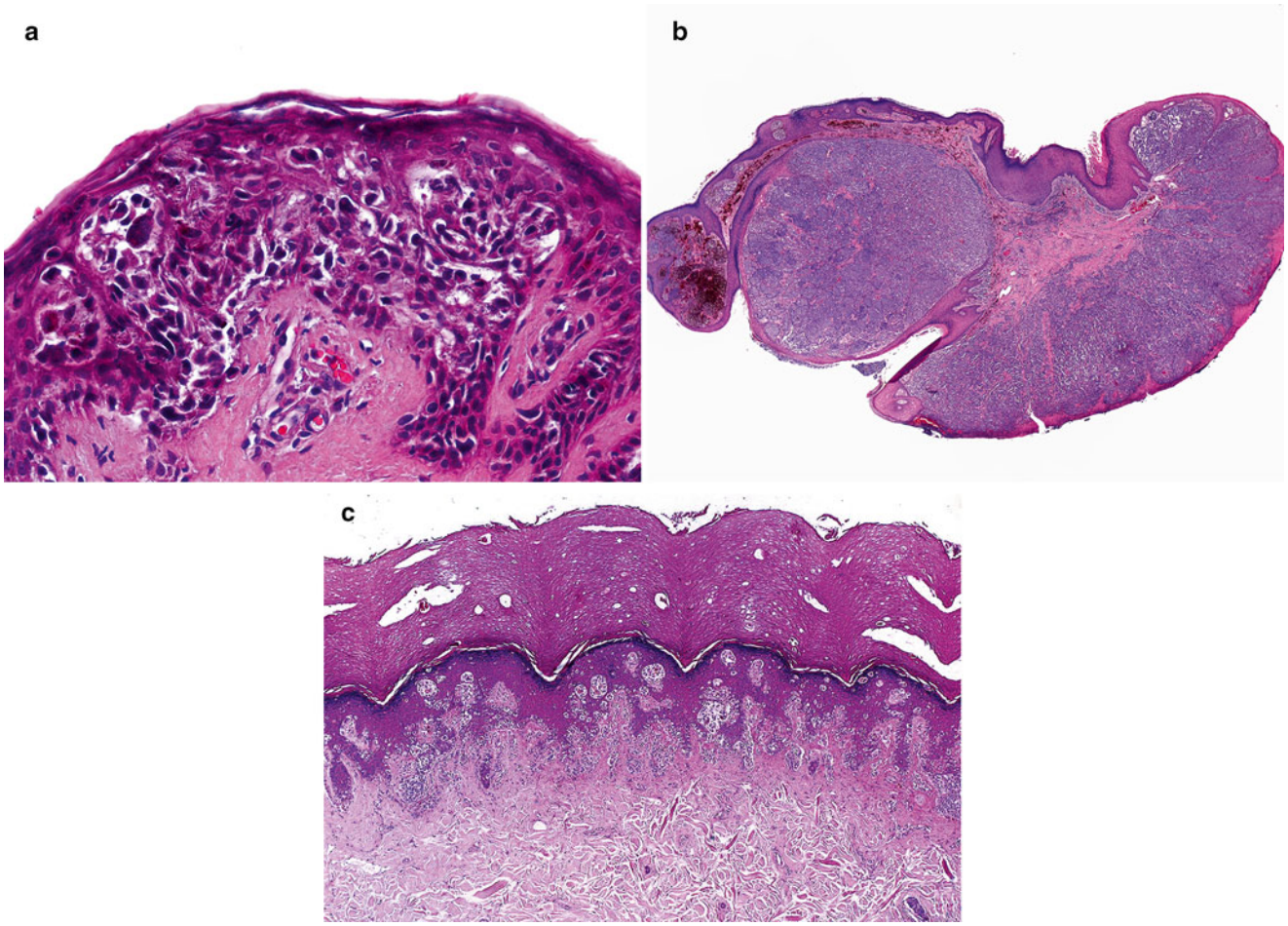

Fig. 13.6 Conventional or adult type malignant melanomas in childhood. (**a**) Superficial spreading melanoma. (**b**) Nodular melanoma. (**c**) Acral lentiginous melanoma (Courtesy Prof. L. Requena, Madrid)

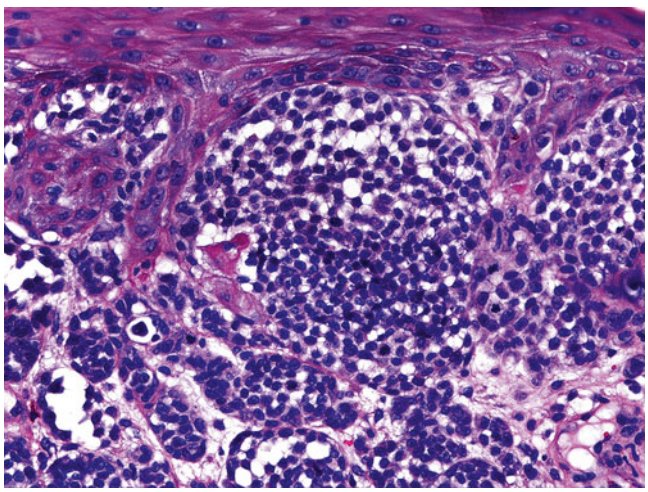

Fig. 13.7 Small-cell melanoma, containing monomorphous cells arranged in sheets

do not form sheets. There are often single cells infiltrating between collagen bundles in the reticular dermis at the base of the lesion. Non-atypical mitotic figures may be seen, but they are usually not numerous, occur in the mid- to upper portion of the lesion, and are more prevalent in the compound type of SN compared with the junctional and intradermal SN [65]. Some authors suggest a cutoff number of up to 2 mitoses per lesion for benign SN [66]. However, numerous mitoses can be present in rapidly growing SN and recurrent, regressing, or traumatized ones [67].

The epidermis associated with SN is acanthotic, hyperplastic, hypergranulotic, and hyperkeratotic. Perfectly symmetric epidermal hyperplasia with expansion at the center and attenuation at the periphery is a feature of SN, whereas there is usually "consumption of the epidermis" in spitzoid MM.

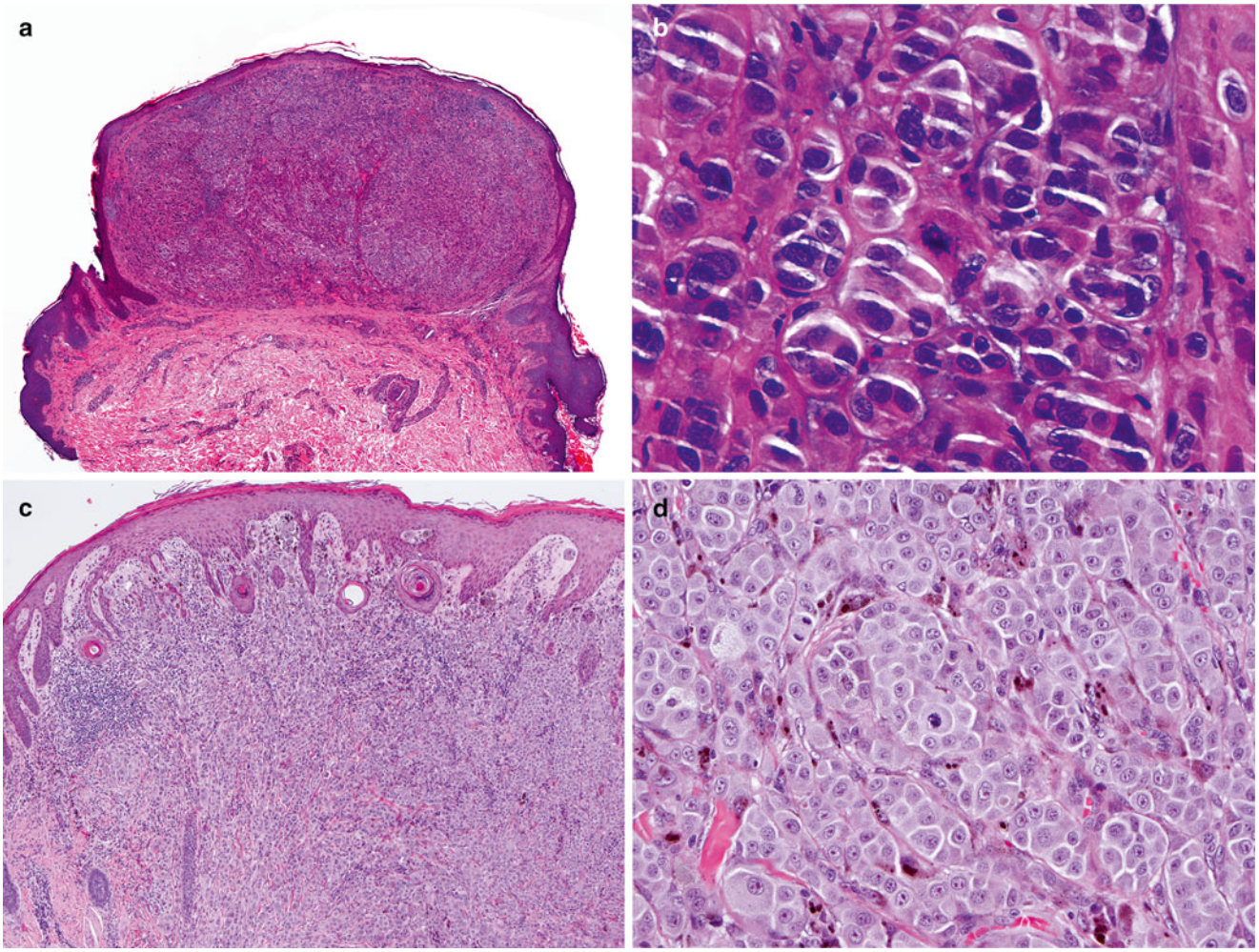

Fig. 13.8 Spitzoid melanoma. (**a**) A symmetric and well-delimited lesion that mimics a Spitz nevus at low power magnification. (**b**) The melanocytes have an epithelioid appearance, but there is no "maturation" and mitotic figures are present at the deepest part of the tumor. (**c**) Low power view of another example with epithelioid elements filling the dermal compartment. (**d**) The cells are highly atypical and feature increased mitotic activity (Courtesy Prof. L. Requena, Madrid)

Fig. 13.9 Typical Spitz nevus presenting as a dome-shaped pink papule on the leg. These lesions may be clinically misdiagnosed as hemangiomas

Lymphocytic inflammatory infiltrates are often seen around vessels and at the base of the lesion but not admixed with the nevomelanocytes. Blood vessels may be dilated and prominent. Variants of SN include desmoplasic, angiomatoid, myxoid, plexiform, and rosette-like types.

There are only a few histological differences between SN in children and in adults. Kapur et al. [68] compared 27 features in specimens obtained from both children and adults. The adult lesions were significantly more likely to be intradermal, and to display dermal fibroplasia, but otherwise to show histological similarity to their pediatric counterparts. Requena and colleagues found hyalinization to be the only histologic parameter of statistical significance more frequently encountered in adults than in children [65].

Although distinction between SN and spitzoid MM cannot be reliably made on the basis of immunohistochemistry,

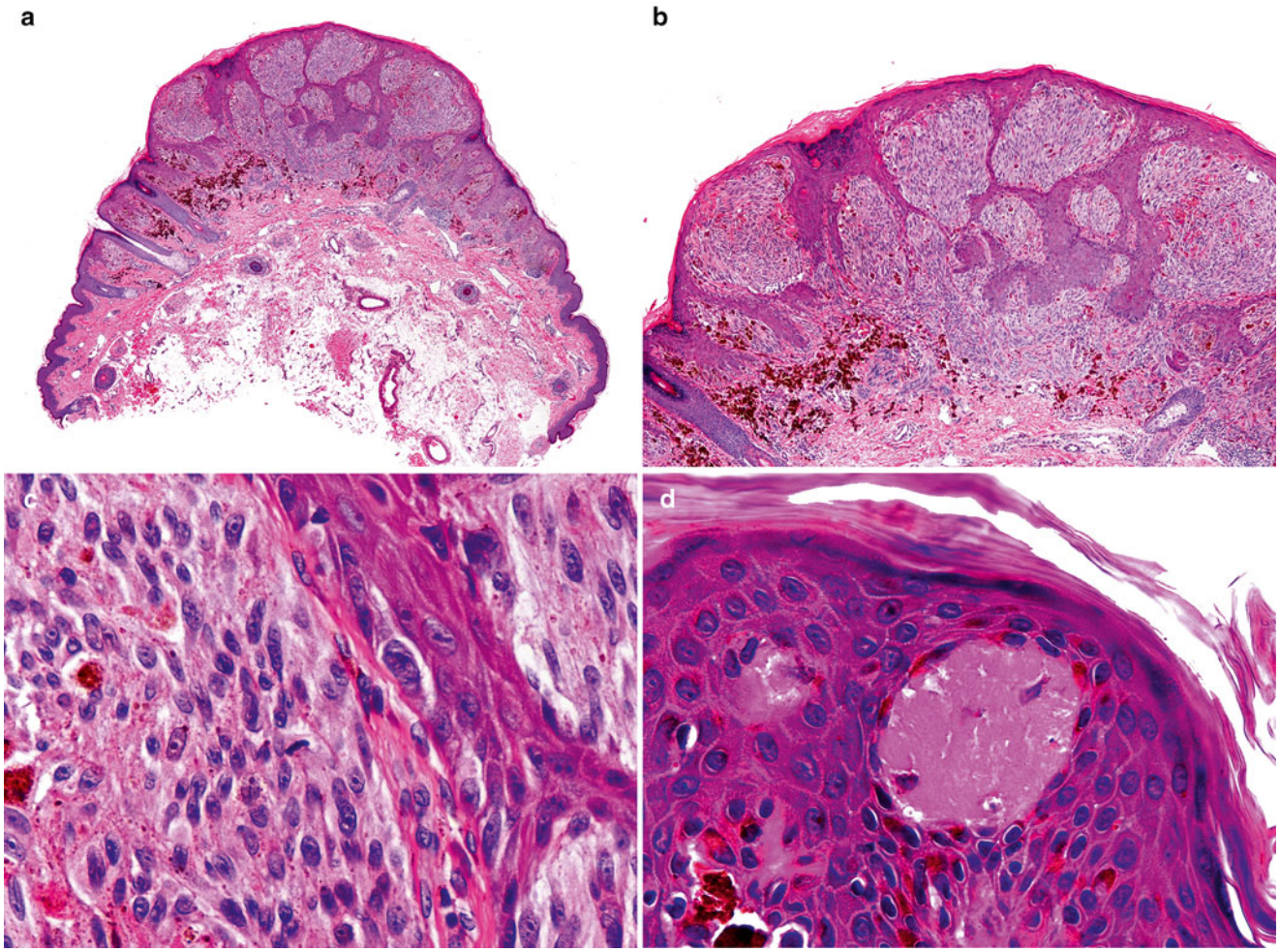

Fig. 13.10 Histological features of the Spitz nevus. (**a**) A well-circumscribed lesion (**b**) composed of spindle and epithelioid cells (**c**) with some superficial mitotic figures and (**d**) Kamino bodies

some stains may be useful in distinguishing spitzoid melanocytic neoplasms from nonmelanocytic tumors. HMB-45 and tyrosinase diminish toward the base of SN, in contrast with the diffuse pattern seen in spitzoid MM. MIB-1 staining is higher in MM than in SN (29.7 and 4.0 %, respectively). As S100 and Melan A are diffusely expressed in both SN and spitzoid MM, they are only useful in differentiating SN from nonmelanocytic tumors [69–73].

CGH and FISH are promising ancillary tests, and a large body of literature on this topic is rapidly accumulating [74]. The sensitivity and specificity of these techniques is improving fast although there are still some pitfalls, including false positive and false negative results, and the fact that some histologically "borderline" lesions show "borderline" cytogenetic features as well. Among the newer and most useful approaches is the use of a FISH probe set including 9p21, 6p25, 11q13, and 8q24, which has recently been demonstrated to reach a sensitivity of 94 % and a specificity of 98 % [75].

Atypical Spitzoid Neoplasms

This is a poorly defined and likely heterogeneous group with morphological overlap between melanoma and Spitz nevi. In contrast to classic SN, atypical spitzoid neoplasms (ASN) exhibit more worrisome features, such as size >1 cm in diameter, ulceration, increased cellularity or prominent confluence of nevomelanocytes in the dermis, extension into dermis or subcutaneous fat, dermal mitoses, cytological atypia, and lack of "maturation" at the base. Using some of the histological criteria noted above in conjunction with clinical characteristics, Spatz et al. [76] developed a grading system that stratified ASN into low-, intermediate-, and

Table 13.4 Grading system for risk of metastasis in atypical spitzoid neoplasms

Parameter	Score
Age (years)	
0–10	0
11–17	1
Diameter (mm)	
0–10	0
>10	1
Involvement of subcutaneous fat	
Absent	0
Present	2
Ulceration	
Absent	0
Present	2
Mitotic activity (mm^2)	
0–5	0
6–8	2
≥9	5

Total score and risk for metastasis: 0–2, low risk; 3–4, intermediate risk; 5–11, high risk. From Spatz et al. [76]

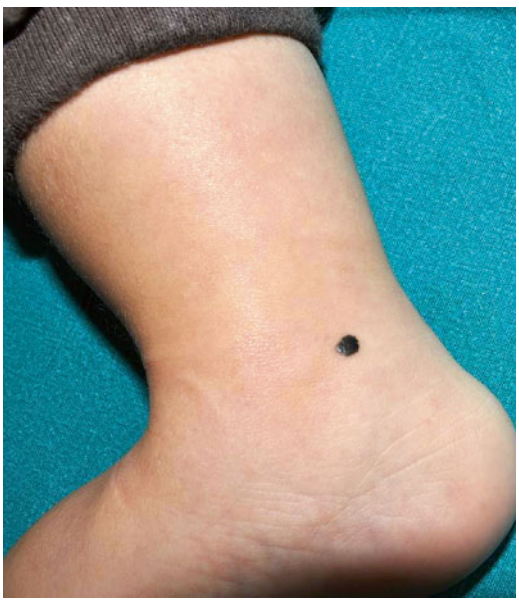

Fig. 13.11 Nevus of Reed. A sharply circumscribed black papule on the leg of a child (Courtesy Dr. A. Torrelo, Madrid)

high-risk groups based on total accumulated atypical features (Table 13.4).

Although ASN have generally been reported to have a good prognosis, well-documented cases of metastasis and death exist [77–79]. Because the malignant potential of these lesions is uncertain if the thickness is >1 mm, many clinicians and patients make decisions to treat them as if they were melanomas with excision and, often, a sentinel lymph node biopsy [80]. Newer genetic alterations are being described

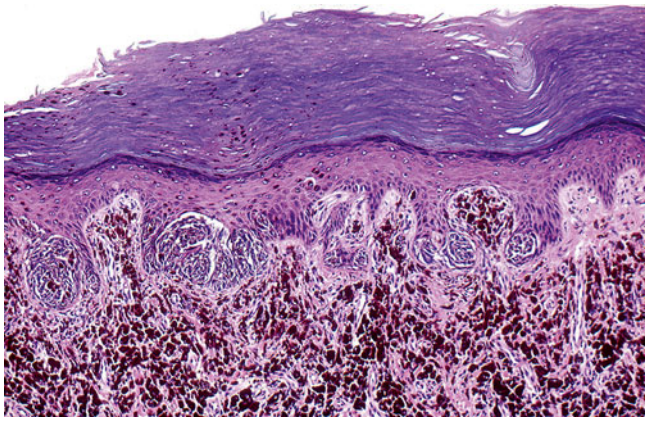

Fig. 13.12 Histological features of the nevus of Reed. A junctional spindle cell neoplasm with vertically oriented nests and numerous dermal melanophages

that will contribute to an improved understanding of these neoplasm. Among them, there is recent description of an autosomal dominant tumor syndrome with high penetrance for melanocytic tumors and distinct clinical and phenotypical features associated with germ line mutations of the *BAP1* gene [81]. Individuals affected by these ASN show *BRAF* mutations and loss of *BAP1* expression, changes also seen in 28 % (from a total of 32 cases studied) of sporadic ASN [82].

Nevus of Reed

The nevus of Reed (NR) is a melanocytic proliferation histologically characterized by non-atypical, uniform, heavily pigmented spindled melanocytes [83, 84]. Although NR is a benign tumor, its natural history remains incompletely studied, and the lesion can be histologically or clinically misinterpreted as melanoma [84].

NR presents as a well-circumscribed, uniformly dark-brown or black lesion, averaging 3–5 mm in diameter (Fig. 13.11). Histologically, NR is symmetrical and shows a sharp lateral circumscription. The nevomelanocytes are arranged in vertical nests at the dermo-epidermal junction but can be seen above the dermal/epidermal junction, associated with confluence of the nests. The proliferation of nevomelanocytes may extend into the papillary dermis. Occasional mitoses may be found. Epithelioid nevomelanocytes are seen in a minority of cases. Commonly, the epidermis is slightly hyperplastic and shows marked hyperpigmentation of the basal keratinocytes. Kamino bodies can be observed in about half of the cases. An inflammatory infiltrate composed of lymphocytes and histiocytes with many melanophages is found within the papillary dermis [47, 84, 85] (Fig. 13.12).

There is significant controversy as to whether the NR represents a separate clinical entity or a variant of the classical Spitz nevus.

Fig. 13.13 Proliferative nodule arising within a giant congenital melanocytic nevus (Courtesy Dr. A. Torrelo, Madrid)

Proliferative Nodules in CMN

Proliferative nodules (PN) in congenital melanocytic nevi are defined as atypical melanocytic proliferations that predominantly manifest in the neonatal period within a pre-existing giant CMN [19]. The vast majority of atypical nodular proliferations developing in CMN are biologically benign and must be differentiated from MM arising in the deep dermal component of CMN.

PN present clinically as one or more dark brown to black plaques or nodules above a giant CMN (Fig. 13.13). The lesions may become lighter and show regression after years. In some cases, a palpable mass can be found deeply in the skin. Features that favor a benign lesion include blending of these cellular aggregates with the surrounding

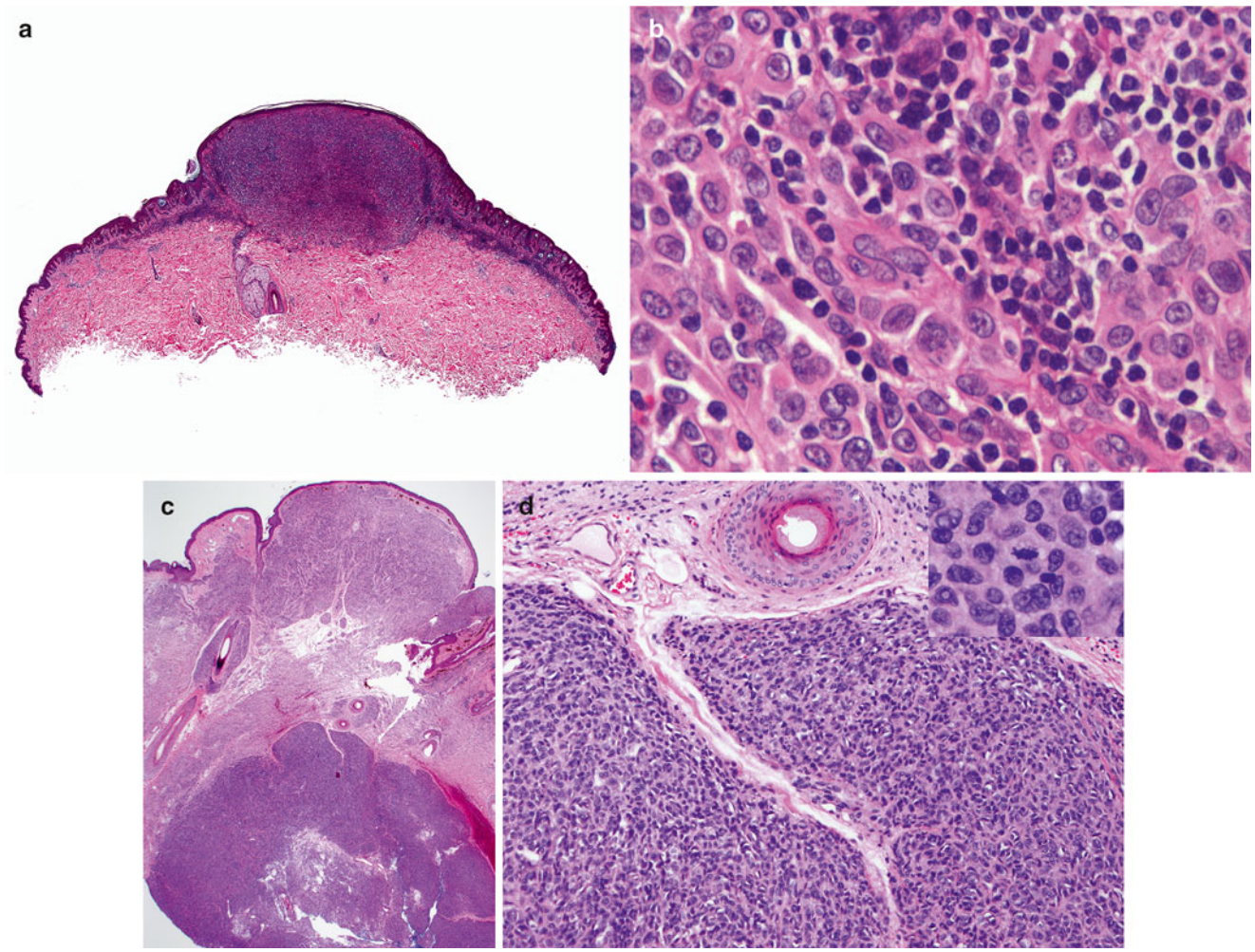

Fig. 13.14 Histological features of a proliferative nodule in a congenital melanocytic nevus. (**a**) Low power view. (**b**) The epithelioid non-atypical melanocytes merge with the smaller nevomelanocytes that can be recognized around the nodule. (**c**) An atypical proliferative nodule, sharply demarcated and with an expansile appearance, underlying an area of conventional giant congenital melanocytic nevus. (**d**) Cells in the atypical proliferative nodule show a compact arrangement and do not blend with the adjacent nevus cells. Mitoses are increased (*inset*)

nevomelanocytes, low mitotic rate, absence of uniform high-grade cytologic atypia, and absence of inflammatory infiltrates or necrosis (Fig. 13.14a, b) [41].

Atypical PN appear sharply demarcated, show an expansile pattern of growth, and feature epidermal effacement, pleomorphism, and higher mitotic activity. They feature an increased Ki67 and PHH3 staining compared to non-atypical PN and the adjacent nevus cells surrounding the nodule. On this basis, some authors consider them as lesions intermediate between PN and MM. However, they show the same pattern of *BRAF* and *NRAS* mutations seen in PN and surrounding nevus cells [86] (Fig. 13.14c, d).

Prognosis and Treatment

Pediatric melanoma patients appear to have better prognosis than adults with melanoma even when matched for stage. Although this has not been thoroughly studied, it is conceivable that differences in clinical behavior reflect distinct tumor biology [27, 87].

Clinical characteristics associated with poor prognosis include male gender, earlier age at diagnosis, and head-and-neck location of primary tumor.

A sizable number of pediatric patients with melanoma present with evidence of nodal or distant metastatic disease (approximately 10–20 % depending on the age) [27]. However, unlike adults, a comprehensive staging system has not been established for melanoma in children and adolescents, making direct comparison of prognoses difficult.

There is no current consensus for appropriate staging workup in cases of pediatric melanomas. For patients with a localized, thin melanoma (<1 mm) without ulceration, no routine laboratory tests are warranted. The pursuit of sentinel lymph node biopsy (SLNB) for higher-risk tumors (e.g., >1 mm thick or 0.76–1 mm thick with ulceration or Clark level IV–V invasion) remains controversial as in adult melanomas.

A randomized controlled trial of 1,269 adult patients showed that SLNB does not improve overall survival compared to observation [88]. The therapeutic benefits of immediate complete lymph node dissection (CLND) and interferon alpha-2b for those with histologically positive SLN have not been substantiated by trials in the pediatric population. SLNB appears to be well tolerated by the pediatric patient. In contrast, CLND produces a much higher rate of complications in children [89] and its potential lifelong morbidity should be considered carefully prior to therapy.

Pigmented lesions clinically suspicious for melanoma should always be narrowly excised for complete and accurate histological diagnosis. Definitive resection for melanoma should follow the guidelines established for adult melanomas (www.nccn.org):

- Melanoma in situ: 0.5 cm margin.
- <1.0 mm: 1 cm margin.
- 1.01–2.0 mm thick: 1 or 2 cm margin depending on anatomic constraints.
- ≥2.0 mm thick: 2 cm margin.

Once the diagnosis of melanoma has been confirmed microscopically, staging and surgical treatment can be undertaken. Additional therapies, including immunotherapy, chemotherapy, and radiation therapy can be considered depending on extent of disease.

Imaging of Patients with Melanoma

Although the primary skin malignancy cannot be imaged, diagnostic imaging plays an important role in staging children with melanoma. It is important to balance the potential benefit of cross-sectional imaging in these children with the negative effects of added radiation exposure or the need for sedation. The most recent guidelines of the National Comprehensive Cancer Network (NCCN) clarified that routine cross-sectional imaging is not indicated for patients with stage I and II melanoma and should be used only to assess specific signs and symptoms in these patients. In stage III patients, investigators have also shown a low yield for CT and PET-CT. However, when sentinel node biopsy is positive the yield of imaging increases. Therefore, the NCCN now recommends that patients with clinically positive nodes or in-transit nodes and all stage IV patients should undergo baseline imaging for staging [90].

When sentinel node biopsy is indicated lymphoscintigraphy can identify the draining nodal basin and direct surgical dissection of the sentinel node [91, 92]. Sentinel node lymphoscintigraphy is performed by injecting small aliquots of ^{99m}Tc labeled, filtered, sulfur colloid intradermally within 0.5–1.0 cm of the skin lesion or surgical scar. Immediately following injection, dynamic imaging with a digital gamma camera is performed to assess flow of the radioisotope in draining lymphatics. Transverse and anterior-posterior (AP) planar, static, transmission images of the nodal basin are then obtained to accurately localize the depth and location of the sentinel node. Transmission images obtained with a Co-57 flood source allow definition of the body contour and further enable sentinel node localization (Fig. 13.15a, b) [93]. When lymphoscintigraphy is performed with a single-photon emission computed tomography-computed tomography (SPECT-CT) scanner, it is possible to co-register and fuse the SPECT nuclear

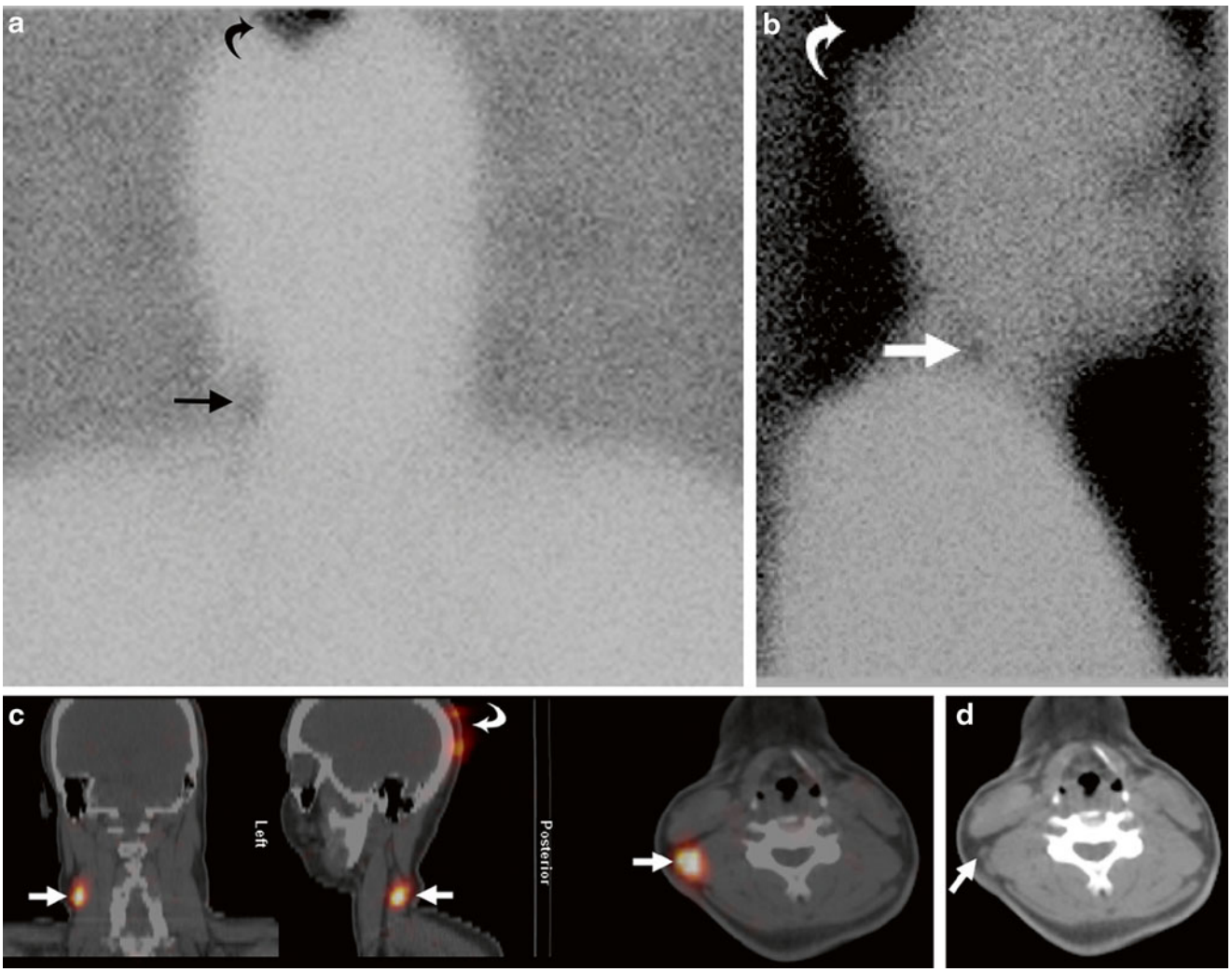

Fig. 13.15 Twenty-year-old male with AJCC stage IIIC melanoma, scalp primary site. (**a**) Anterior-posterior and (**b**) lateral projection transmission images obtained during lymphoscintigraphy show the scalp injection site (*curved arrows*) and the sentinel node in the right lower neck (*straight arrows*). (**c**) Coronal, sagittal, and axial fused images (*left* to *right*) and (**d**) CT only image obtained with single-photon emission computed tomography-computed tomography show activity near the injection site (*curved arrow*) and accurately localize the focus of activity to a small right posterior cervical node (*straight arrows*)

images with low-dose, attenuation correction CT images. SPECT-CT images can be reconstructed in the axial, coronal, and sagittal planes (Fig. 13.15c, d). Investigators have found that SPECT-CT sentinel node imaging provides superior anatomic localization and reduces false positives due to contamination when compared to conventional planar lymphoscintigraphy [94].

The use of magnetic resonance imaging (MRI) or CT to assess for metastatic disease will depend on the clinical index of suspicion, the structure of interest and, in part, the age of the patient and need for sedation. Because melanoma can metastasize anywhere in the body, PET-CT offers the important advantage of assessing the entire body in one imaging session (Fig. 13.16a–c). The role of PET-CT in assessing melanoma patients, however, remains controversial. Some investigators have found that PET-CT has no patient-relevant benefit [95] while others have shown that in high-risk patients PET-CT can reveal nodal disease, unsuspected distant metastatic disease, and metastatic sites not included in conventional cross-sectional imaging [96, 97]. More recently, investigators have shown that diffusion weighted whole body MRI compares favorably to PET-CT and may be a reliable alternative that could avoid exposure to ionizing radiation making it particularly attractive in children [98].

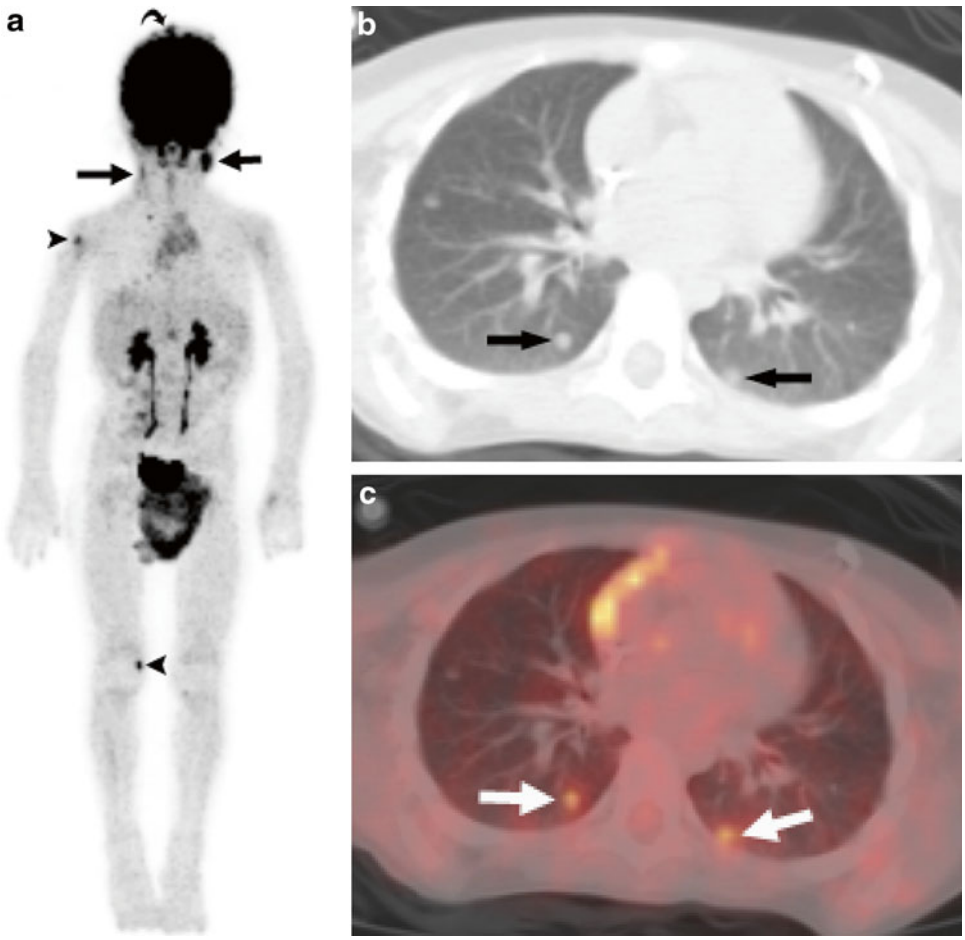

Fig. 13.16 Three-year-old boy with AJCC stage IV melanoma. (**a**) Whole body maximum intensity projection PET-CT image obtained at diagnosis shows abnormal FDG uptake in the primary right scalp lesion (*curved arrow*), bilateral cervical nodes (*straight arrows*), proximal right humerus and distal left femur (*arrow heads*). FDG activity over the pelvis and thighs is in a diaper. (**b**) Low-dose, attenuation correction axial CT image showing small pulmonary metastases (*arrows*). (**c**) Fused PET-CT axial image shows that the pulmonary metastases are FDG avid (*arrows*)

Nonmelanoma Skin Cancer (NMSC)

NMSC arises from the epidermis or adnexal epithelium. In adults BCC and SCC typically arise after long periods of recurrent exposition to ultraviolet light. In contrast, in children the presence of a malignant epithelial tumor should prompt a detailed search for predisposing factors (Table 13.5).

Table 13.5 Predisposing factors for NMSC in children

Basal cell carcinoma	Squamous cell carcinoma
• Nevoid basal cell carcinoma syndrome	• Xeroderma pigmentosum
• Bazex-Dupré-Christol syndrome	• Epidermolysis bullosa
• Xeroderma pigmentosum	• Hidrotic ectodermal dysplasia
• Rothmund-Thompson syndrome	• Albinism
• Albinism	• Fanconi anemia
• Immunodeficiency	• Dyskeratosis congenita
• Immunosuppression	• Erythropoietic porphyria
• Chemotherapy	• Immunodeficiency
• Ionizing radiation	• Immunosuppression
• Arsenic exposure	• Epidermodysplasia verruciformis
• Nevus sebaceous	• Burn scars
	• Chronic infections with sinus tracts
	• Chemotherapy
	• Ionizing radiation
	• Arsenic exposure

Basal Cell Carcinoma

BCC represents a group of malignant cutaneous tumors characterized by the presence of lobules, columns, bands, or cords of basaloid cells ("germinative cells") [19].

The occurrence of BBC in children is an uncommon event. Although some sporadic cases of BBC in children have been described [99], most of them are associated with different predisposing conditions such as albinism [100, 101], Bazex syndrome [102], NBCCS [103], nevus sebaceous [104], solid organ transplants [105], XP [106, 107], or radiotherapy [108–110].

BCC has been documented in children under 4 years of age [21] and even some congenital cases have been reported. The pathogenesis of BCC in children has not been established. Ultraviolet radiation exposure may

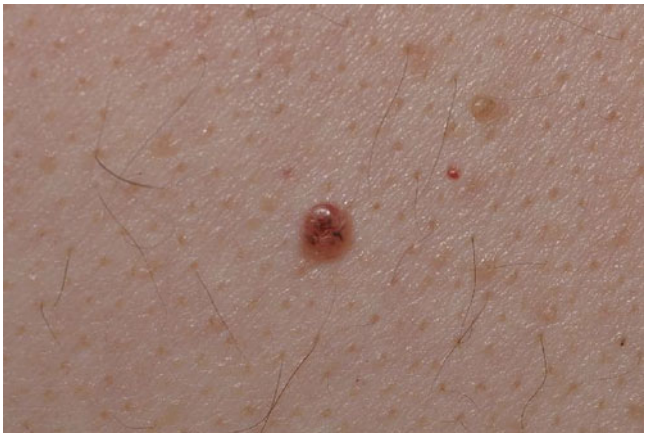

Fig. 13.17 Nodular pigmented basal cell carcinoma presenting as a brown well-circumscribed papule that mimics a melanocytic nevus (Courtesy Dr. A. Torrelo, Madrid)

be implicated, but not every child with a sporadic BCC has had prolonged and frequent sun exposure or history of sunburns [103]. Ultraviolet rays induce DNA damage leading to loss of activity of tumor suppressor genes and overexpression of oncogenes and other genes related to enhanced growth and survival as well as tissue invasion. Also, ultraviolet light impairs the cutaneous immune response, especially Langerhans cell antigen-presenting function, resulting in immune tolerance to developing tumor cells. In addition to ultraviolet radiation exposure, inactivation of a gene at chromosome 9q22 has been postulated to contribute to the development of idiopathic BCC in children.

NBCCS is the most common explanation to find BCC in children, and pediatric BCC patients must be evaluated for family history and other stigmata (mentioned above).

BCC characteristically arises in body areas exposed to the sun and is most common on the head and neck (80 % of cases), followed by the trunk (15 % of cases), arms, and legs. BCC have also been reported in unusual sites, including the axillae, breasts, perianal area, genitalia, palms, and soles.

Nodular BCC is the classic form and most often presents as a pearly papule or nodule with overlying telangiectases and a rolled border, at times exhibiting central crusting or ulceration. Occasionally, nodular BCC may resemble enlarged pores or pits on the sebaceous skin of the central portion of the face. Superficial BCC presents as a scaly erythematous patch or plaque. Both nodular and superficial forms may contain melanin, imparting a brown, blue, or black color to these lesions (Fig. 13.17). The morpheaform type, also known as sclerosing, fibrosing, or infiltrative BCC, typically appears as an indurated, whitish, scar-like plaque with indistinct margins [111].

In a review of 1,039 consecutive cases of BCC, Sexton et al. [112] found that the most common histologic subtypes were mixed (38.6 %), nodular (21.0 %), superficial (17.4 %), and micronodular (14.5 %) (Fig. 13.18). Uncommon variants, including morpheaform, basosquamous, keratotic, granular cell, adamantinoid, infundibulocystic, clear cell, and others, have also been described. The value of classifying the histologic appearance lies in the relationship between histologic subtype and clinical behavior. Aggressive histologic variants include the micronodular, infiltrative, basosquamous, morpheaform, and mixed subtypes [113]. Nodular and superficial subtypes generally have a less aggressive clinical course. Nonaggressive histologic variants of BCC are the most common in children and represent around 80 % of the cases. Nevertheless, aggressive patterns of BBC have also been reported during childhood [103].

BCC is a routine histologic diagnosis, but some other follicular tumors, such as basaloid follicular hamartoma, trichoblastoma, or trichoepithelioma, may be mistaken for BCC in children. Conversely, some cases of BCC have been diagnosed as follicular basaloid hamartomas [114, 115].

Histological features, immunohistochemistry, differential diagnosis, and variants of BCC are shown in Table 13.6.

Excision remains the treatment of choice for BCC, particularly if the lesion is papular, nodular, or sclerosing. For superficial lesions, topical imiquimod, electrodesiccation and curettage, and cryotherapy are also effective. Radiation therapy must be avoided, especially in patients with NBCCS, because it leads to the induction of hundreds of new tumors [116].

Tumor recurrence for children with an idiopathic BCC is observed in 18 % of the cases [103]. Difficulty in achieving adequate margins is the most important cause of recurrence. Death secondary to metastatic tumor spread has rarely been described. Lesions that metastasize are usually large, deeply infiltrating, ulcerated, and recurrent [117].

Regular follow-up is indicated because of the risk of local recurrence or subsequent development of new tumors. Sun avoidance, sun protection, and diligent daily sunscreen use should be emphasized.

Squamous Cell Carcinoma

Cutaneous squamous cell carcinoma (SCC) is a malignant neoplasm of epidermal keratinocytes in which the proliferating cells show variable squamous differentiation [78]. Cutaneous SCC comprises less than 0.1 % of all childhood malignancies and at most 5 % of cutaneous malignancies [116].

UV radiation and DNA-repair disorders such as XP and Fanconi anemia represent the most common predisposing

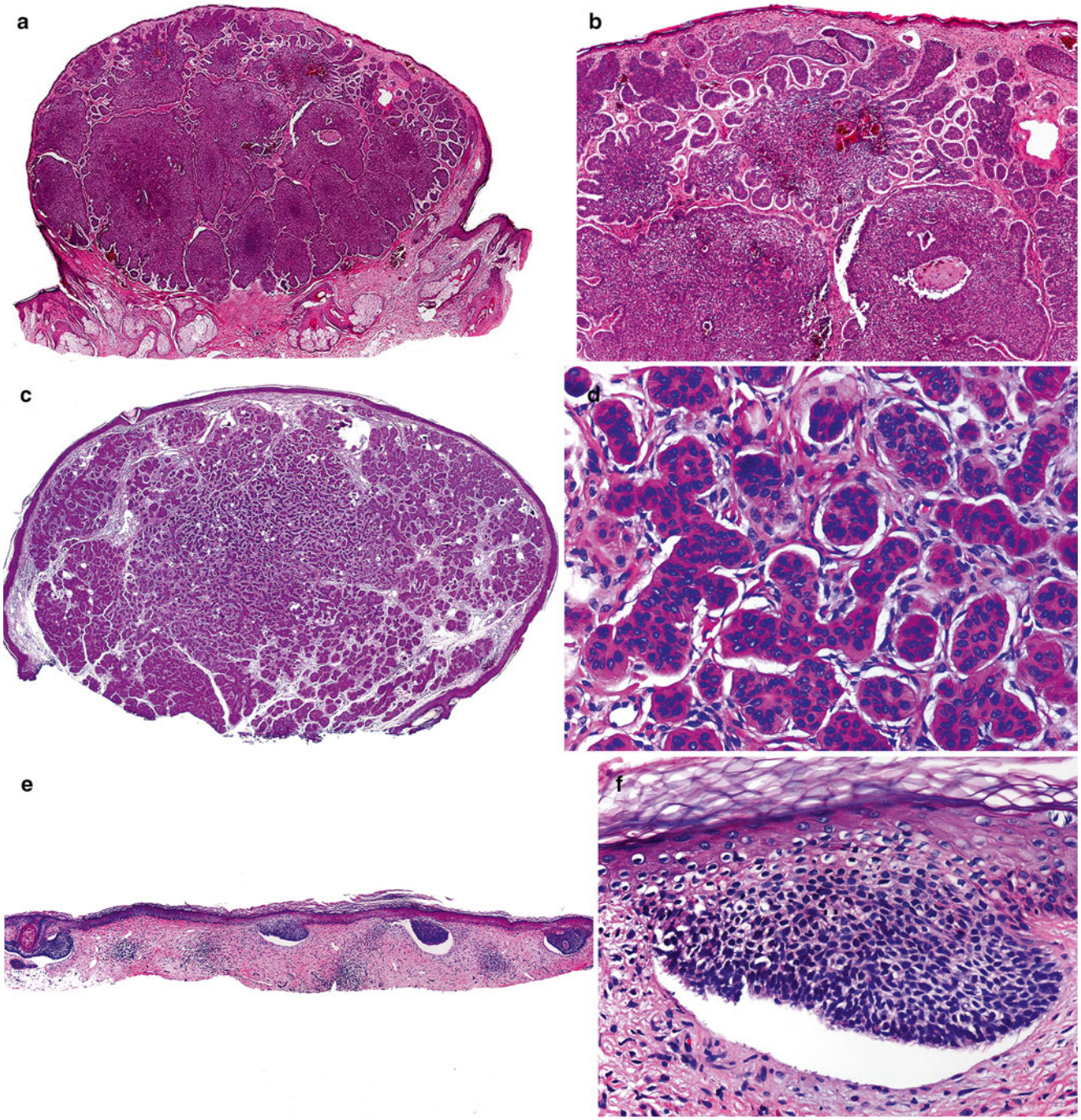

Fig. 13.18 Histological types of basal cell carcinoma. (**a**, **b**) Nodular or solid (**c**, **d**) Micronodular. (**e**, **f**) Superficial, (**g**, **h**) Fibroepithelioma or Pinkus tumor, (**i**) Cystic, (**j**) Morpheaform (Courtesy Prof. L. Requena, Madrid)

factor for SCC in children, but other significant risk factors also exist (Table 13.3) [116]. Mutations in DNA-repair genes are well-known risk factors for development of SCC in children. Mutations in RNA processing have also been linked to early SCC risk [118]. Aggressive SCC of the skin has been recently reported during treatment with voriconazole in immunosuppressed children and adults [119]. Human papillomavirus (HPV) is implicated in the malignant transformation to SCC in patients with epidermodysplasia verruciformis [120, 121]. HPV may also play a role in the development of SCC in children with immunosuppression following chemotherapy or organ transplantation. Rarely, SCC has been reported in children with no history of predisposing conditions [122].

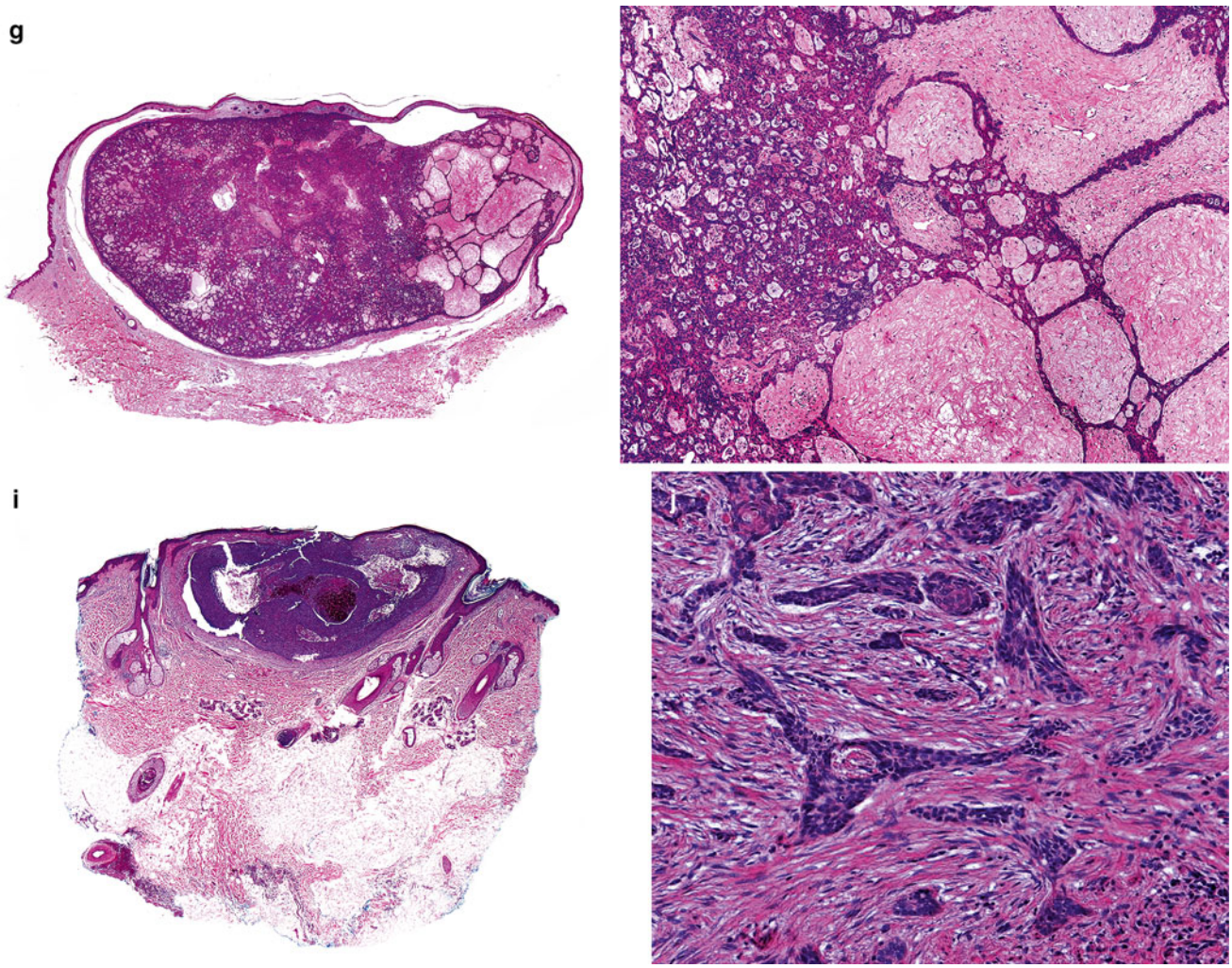

Fig. 13.18 (continued)

The principal precursor of cutaneous SCC is actinic keratosis (AK). AK may be seen in fair-skin children who have had intense sun exposure, but its occurrence in children is very rare, and if present in childhood and adolescence it should prompt an evaluation for an underlying DNA-repair problem, particularly XP. AK is a scaly lesion, typically 2–6 mm in diameter, which is more easily felt than seen; it may be the same color as the skin, pink, or brown. AK can involute or persist, so that predicting evolution into an SCC is difficult if not impossible [2].

SCC usually presents as a non-healing, scaly, crusted or verrucous, indurated papule or plaque on a sun-exposed skin area [116].

Histological and immunohistochemical features, differential diagnosis, and variants of SCC are shown in Table 13.7 and Fig. 13.19.

The prognosis of SCC is excellent, provided that the surgical excision is adequate and there is no underlying predisposing disease [123]. Nevertheless, invasive SCC has the potential to recur and metastasize. In adults, the 5-year rate of recurrence of primary cutaneous lesions is 8 %, and the 5-year rate of metastasis is 5 % [124–126].

Large lesions (>2 cm in diameter) recur at a rate of 15 % and metastasize at a rate of 30 %, which are twice and three times higher than the rates of recurrence and metastasis in the smaller lesions [124]. Sites associated with a high risk of recurrence and metastasis are the lip, ears, scalp, forehead, temple, eyelid, nose, mucous membranes, dorsal surface of the hands, penis, scrotum, and anus [124, 127–130]. SCCs arising in injured or chronically diseased skin are associated with a risk of metastasis that approaches 40 % [124, 131]. SCCs associated with epidermolysis bullosa and burn scars

Table 13.6 Histological features of BCC

Histology
• Nests or islands of basaloid cells with elongated hyperchromatic nuclei and scant cytoplasm • Attachment to the undersurface of the epidermis • Numerous mitotic figures, sometimes atypical • Peripheral palisading • Clefts between tumor and surrounding stroma • Variable dermal infiltration • Newly formed stroma distinct from the adjacent dermis • Mucinous alteration of the tumoral stroma
Immunophenotype
• Positive for Ber-EP4, 34Be12, mNF116 • Melan-A often demonstrates melanocytes within the tumor
Variants
• Nodular • Superficial • Micronodular • Morpheaform • Other (cystic, adenoid, sclerosing, infundibulocystic, pigmented, fibroepithelial (Pinkus tumor), BCC with adnexal differentiation, basosquamous, keratotic, etc.) • Mixed
Differential diagnosis
• Trichoblastoma/trichoepithelioma • Basaloid follicular hamartoma • Other NMSC

BCC Basal cell carcinoma; *NMSC* Non-melanocytic skin cancers

Table 13.7 Histological features of SCC

Histology
• Nests of atypical squamous epithelial cells that arise from the epidermis • Variable epithelial atypia • Cells have abundant eosinophilic cytoplasm and a large, often vesicular, nucleus • Keratinization usually present (horn pearl formation and individual cell keratinization) • Infiltrative growth pattern • Variable stromal inflammatory reaction • Desmoplasia can be present
Immunophenotype
• Positive for 34BE12, AE1:AE3, EMA, p63, MNF116, CK5/6
Variants
• Acantholytic • Clear cell • Warty • Verrucous • Spindle cell • Desmoplastic • Lympho-epitheliomatous
Differential diagnosis
• Pseudoepitheliomatous hyperplasia (e.g., after trauma, surgery, infection) • Inflammatory dermatoses (e.g., lichen planus) • Miscellaneous keratoses (e.g., proliferative AK) • Other malignant tumors (e.g., melanoma, lymphoma)

SCC Squamous cell carcinoma

are very aggressive, usually fatal, and must be closely monitored [132, 133].

Histologic features that are predictive of recurrence or metastasis include a depth of more than 4 mm, involvement of the reticular dermis or subcutaneous fat, and penetration into fascia, muscle, bone, or cartilage. Poorly differentiated SCCs recur at a higher rate than well-differentiated tumors. Perineural invasion is also an ominous finding [134]. Although perineural spread occurs in only 5 % of the SCC, it does confer a high risk of recurrence and metastasis. Most patients with perineural invasion die of the disease within 5 years after presentation [124, 128].

Complete excision with control of margins is the treatment of choice. Specific guidelines for the treatment of SCC in pediatric population are not available due to the small number of reported cases.

Cutaneous Metastasis

A large proportion of cutaneous metastases are seen in children with leukemias and lymphomas (Fig. 13.20). Cutaneous or subcutaneous metastasis of non-hematopoietic malignancies in children and adolescents is a rare occurrence but may be the first manifestation of the disease [135, 136].

The solid tumors most likely to metastasize to the skin in children are neuroblastoma and rhabdomyosarcoma. They are more prone than adult malignancies to spread in a hematogenous fashion and be seen at multiple distant sites [135, 136].

Infants and neonates with neuroblastoma can present with multiple dark blue cutaneous metastases, the so-called blueberry muffin baby [137]. These nodules may blanch centrally and develop an erythematous halo for several minutes or hours following palpation [135, 138, 139]. Other conditions associated with a "blueberry muffin baby" include infections (TORCH) and hematologic dyscrasias [140].

Rhabdomyosarcoma is the most common soft tissue sarcoma in children and may be primary [141] or metastatic [142, 143] in the skin. Other pediatric sarcomas such as Ewing sarcoma, malignant rhabdoid tumor, and osteosarcoma may also give rise to cutaneous metastasis. Additional pediatric tumors that have rarely been reported to metastasize to the skin include melanoma, choriocarcinoma, malignant paraganglioma, colonic adenocarcinoma, and nasopharyngeal carcinoma [144].

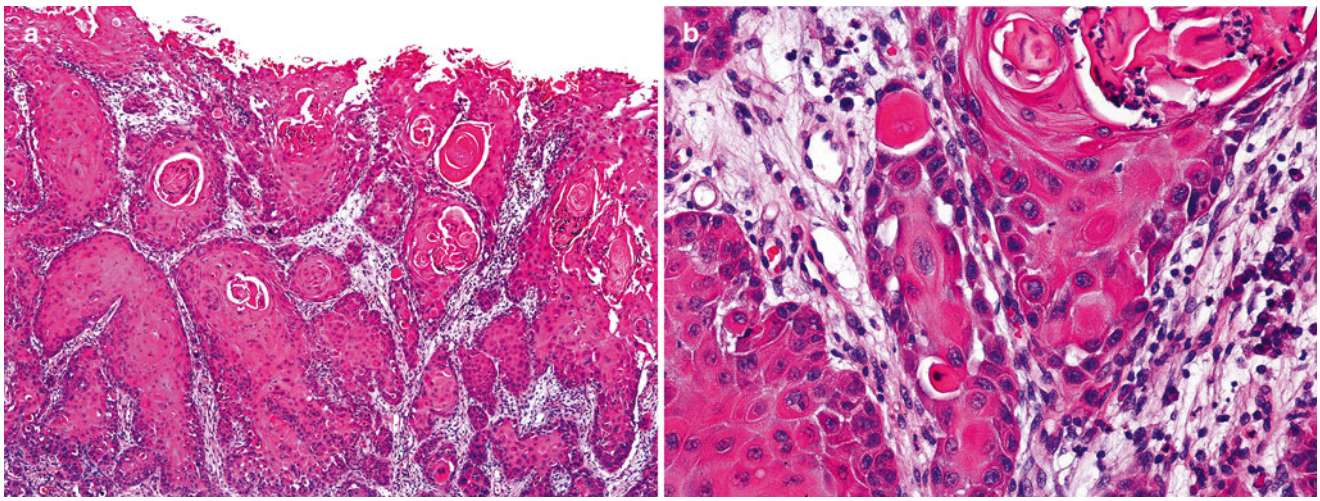

Fig. 13.19 Histological features of squamous cell carcinoma. (**a**) Nests of squamous cells arise from the epidermis and extend into the dermis. (**b**) Evident keratinization with horn pearl formation and dyskeratosis (Courtesy Prof. L. Requena, Madrid)

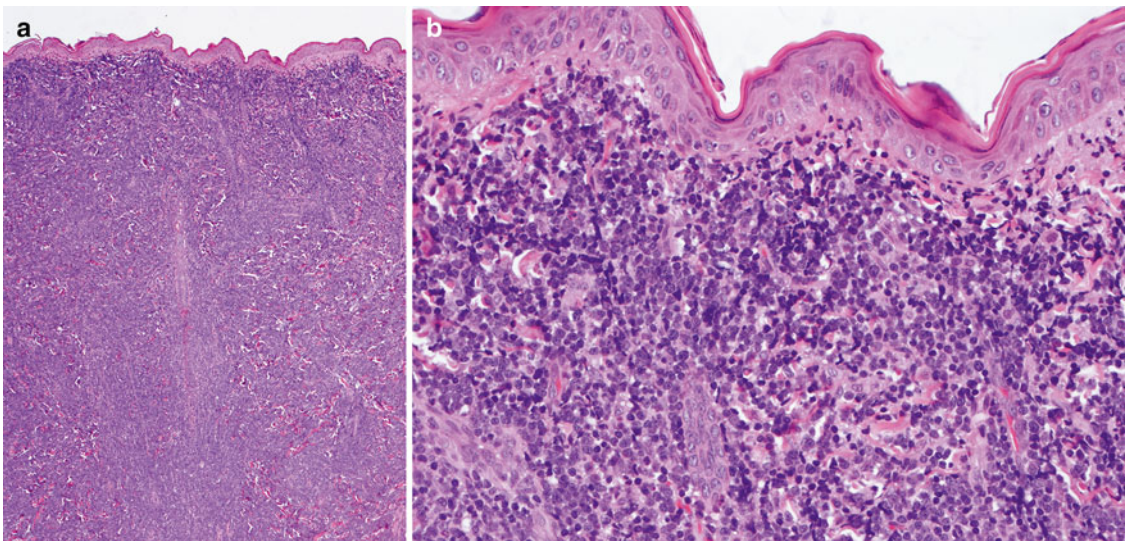

Fig. 13.20 (**a**) Cutaneous metastasis of a B-cell lymphoblastic lymphoma in a 1-year-old girl. (**b**) Note the diffuse infiltration of the superficial and deep dermis by blasts

References

1. Ceballos PI, Ruiz-Maldonado R, Mihm MC. Melanoma in children. N Engl J Med. 1995;332(10):656–62.
2. Alam M, Ratner D. Cutaneous squamous-cell carcinoma. N Engl J Med. 2001;344(13):975–83.
3. Varan A, Gököz A, Akyüz C, et al. Primary malignant skin tumors in children: etiology, treatment and prognosis. Pediatr Int. 2005;47(6):653–7.
4. Tatiana KSC, Somers GR, Pope E, Zuker RM. Predisposing factors and outcomes of malignant skin tumors in children. Plast Reconstr Surg. 2010;126(2):508–14.
5. Hamre MR, Chuba P, Bakhshi S, Thomas R, Severson RK. Cutaneous melanoma in childhood and adolescence. Pediatr Hematol Oncol. 2002;19(5):309–17.
6. DiGiovanna JJ, Kraemer KH. Shining a light on xeroderma pigmentosum. J Invest Dermatol. 2012;132(3 Pt 2):785–96.
7. Kraemer KH, Lee MM, Scotto J. Xeroderma pigmentosum. Cutaneous, ocular, and neurologic abnormalities in 830 published cases. Arch Dermatol. 1987;123(2):241–50.
8. Kraemer KH, Lee MM, Andrews AD, Lambert WC. The role of sunlight and DNA repair in melanoma and nonmelanoma skin cancer. The xeroderma pigmentosum paradigm. Arch Dermatol. 1994;130(8):1018–21.
9. Bootsma D, Weeda G, Vermeulen W, et al. Nucleotide excision repair syndromes: molecular basis and clinical symptoms. Philos Trans R Soc Lond B Biol Sci. 1995;347(1319):75–81.
10. Lynch HT, Anderson DE, Smith JL, Howell JB, Krush AJ. Xeroderma pigmentosum, malignant melanoma, and congenital ichthyosis. A family study. Arch Dermatol. 1967;96(6):625–35.

11. Tsao H. Update on familial cancer syndromes and the skin. J Am Acad Dermatol. 2000;42(6):939–69. quiz 970–2.
12. Goldstein AM, Chan M, Harland M, et al. Features associated with germline CDKN2A mutations: a GenoMEL study of melanoma-prone families from three continents. J Med Genet. 2007;44(2):99–106.
13. Kanzler MH, Swetter SM. Malignant melanoma. J Am Acad Dermatol. 2003;48(5):780–3.
14. Thieu K, Tsao H. Pigmentary abnormalities. In: Schachner L, Hansen RC, editors. Pediatric dermatology. 4th ed. Mosby Elsevier; 2011:734–46.
15. Fan Z, Li J, Du J, et al. A missense mutation in PTCH2 underlies dominantly inherited NBCCS in a Chinese family. J Med Genet. 2008;45(5):303–8.
16. Pastorino L, Ghiorzo P, Nasti S, et al. Identification of a SUFU germline mutation in a family with Gorlin syndrome. Am J Med Genet A. 2009;149A(7):1539–43.
17. Lo Muzio L. Nevoid basal cell carcinoma syndrome (Gorlin syndrome). Orphanet J Rare Dis. 2008;3:32.
18. Lindström E, Shimokawa T, Toftgård R, Zaphiropoulos PG. PTCH mutations: distribution and analyses. Hum Mutat. 2006; 27(3):215–9.
19. LeBoit PE, Burg G, Weedon D, Sarasain A. World Health Organization classification of tumours. Pathology and genetics of skin tumours. Lyon: IARC Press; 2006.
20. Gorlin RJ. Nevoid basal cell carcinoma syndrome. Dermatol Clin. 1995;13(1):113–25.
21. Scobie WG, Preston J. Basal cell carcinoma in children. J R Coll Surg Edinb. 1992;37(1):46–7.
22. Gorlin RJ. Nevoid basal cell carcinoma (Gorlin) syndrome. Genet Med. 2004;6(6):530–9.
23. Go JW, Kim SH, Yi SY, Cho HK. Basal cell nevus syndrome showing several histologic types of Basal cell carcinoma. Ann Dermatol. 2011;23 Suppl 1:S36–40.
24. Cajaiba MM, Bale AE, Alvarez-Franco M, McNamara J, Reyes-Múgica M. Rhabdomyosarcoma, Wilms tumor, and deletion of the patched gene in Gorlin syndrome. Nat Clin Pract Oncol. 2006;3(10):575–80.
25. Mills O, Messina JL. Pediatric melanoma: a review. Cancer Control. 2009;16(3):225–33.
26. Hill SJ, Delman KA. Pediatric melanomas and the atypical spitzoid melanocytic neoplasms. Am J Surg. 2011;203(6):761–7.
27. Strouse JJ, Fears TR, Tucker MA, Wayne AS. Pediatric melanoma: risk factor and survival analysis of the surveillance, epidemiology and end results database. J Clin Oncol. 2005;23(21):4735–41.
28. Linabery AM, Ross JA. Trends in childhood cancer incidence in the U.S. (1992–2004). Cancer. 2008;112(2):416–32.
29. Pappo AS. Melanoma in children and adolescents. Eur J Cancer. 2003;39(18):2651–61.
30. Neier M, Pappo A, Navid F. Management of melanomas in children and young adults. J Pediatr Hematol Oncol. 2012;34 Suppl 2:S51–4.
31. Landi MT, Bauer J, Pfeiffer RM, et al. MC1R germline variants confer risk for BRAF-mutant melanoma. Science. 2006; 313(5786):521–2.
32. Uribe P, Wistuba II, Solar A, Balestrini C, Perez-Cotapos ML, Gonzalez S. Comparative analysis of loss of heterozygosity and microsatellite instability in adult and pediatric melanoma. Am J Dermatopathol. 2005;27(4):279–85.
33. Whiteman DC, Valery P, McWhirter W, Green AC. Risk factors for childhood melanoma in Queensland, Australia. Int J Cancer. 1997;70(1):26–31.
34. Downard CD, Rapkin LB, Gow KW. Melanoma in children and adolescents. Surg Oncol. 2007;16(3):215–20.
35. Rivers JK, Frederiksen PC, Dibdin C. A prevalence survey of dermatoses in the Australian neonate. J Am Acad Dermatol. 1990;23(1):77–81.
36. Reyes-Múgica M, Beckwith M, Etchevers H. Etiology of Congenital Melanocytic Nevi and Related Conditions. In: Margoob A. Nevogenesis. Ch. 7;pp.73-97. Springer, 2012, New York.
37. Krengel S, Scope A, Dusza SW, Vonthein R, Marghoob AA. New recommendation for the categorization of cutaneous features of congenital melanocytic nevi. J Am Acad Dermatol. 2013;68(3): 441–51.
38. Wyatt AJ, Hansen RC. Pediatric skin tumors. Pediatr Clin North Am. 2000;47(4):937–63.
39. Castilla EE, da Graça Dutra M, Orioli-Parreiras IM. Epidemiology of congenital pigmented naevi: I. Incidence rates and relative frequencies. Br J Dermatol. 1981;104(3):307–15.
40. Lefkowitz A, Schwartz RA, Janniger CK. Melanoma precursors in children. Cutis. 1999;63(6):321–4.
41. Tannous ZS, Mihm MC, Sober AJ, Duncan LM. Congenital melanocytic nevi: clinical and histopathologic features, risk of melanoma, and clinical management. J Am Acad Dermatol. 2005; 52(2):197–203.
42. Marghoob AA. Congenital melanocytic nevi. Evaluation and management. Dermatol Clin. 2002;20(4):607–16. viii.
43. Ruiz-Maldonado R, del Rosario Barona-Mazuera M, Hidalgo-Galván LR, et al. Giant congenital melanocytic nevi, neurocutaneous melanosis and neurological alterations. Dermatology. 1997;195(2):125–8.
44. Krengel S, Hauschild A, Schäfer T. Melanoma risk in congenital melanocytic naevi: a systematic review. Br J Dermatol. 2006;155(1):1–8.
45. Hale EK, Stein J, Ben-Porat L, et al. Association of melanoma and neurocutaneous melanocytosis with large congenital melanocytic naevi – results from the NYU-LCMN registry. Br J Dermatol. 2005;152(3):512–7.
46. Mark GJ, Mihm MC, Liteplo MG, Reed RJ, Clark WH. Congenital melanocytic nevi of the small and garment type. Clinical, histologic, and ultrastructural studies. Hum Pathol. 1973;4(3): 395–418.
47. Barnhill RL, Fleischli M. Histologic features of congenital melanocytic nevi in infants 1 year of age or younger. J Am Acad Dermatol. 1995;33(5 Pt 1):780–5.
48. Rhodes AR, Silverman RA, Harrist TJ, Melski JW. A histologic comparison of congenital and acquired nevomelanocytic nevi. Arch Dermatol. 1985;121(10):1266–73.
49. McElearney ST, Dengel LT, Vaughters ABR, Patterson JW, McGahren ED, Slingluff CL. Neonatal congenital malignant melanoma with lymph node metastasis. J Clin Oncol. 2009;27(16): 2726–8.
50. Huynh PM, Grant-Kels JM, Grin CM. Childhood melanoma: update and treatment. Int J Dermatol. 2005;44(9):715–23.
51. Valenzano Menada M, Moioli M, Garaventa A, et al. Spontaneous regression of transplacental metastases from maternal melanoma in a newborn: case report and review of the literature. Melanoma Res. 2010;20(6):443–9.
52. Boddie AW, Smith JL, McBride CM. Malignant melanoma in children and young adults: effect of diagnostic criteria on staging and end results. South Med J. 1978;71(9):1074–8.
53. Ferrari A, Bono A, Baldi M, et al. Does melanoma behave differently in younger children than in adults? A retrospective study of 33 cases of childhood melanoma from a single institution. Pediatrics. 2005;115(3):649–54.
54. Barnhill RL. Childhood melanoma. Semin Diagn Pathol. 1998;15(3):189–94.
55. Barnhill RL, Flotte TJ, Fleischli M, Perez-Atayde A. Cutaneous melanoma and atypical Spitz tumors in childhood. Cancer. 1995;76(10):1833–45.
56. Livestro DP, Kaine EM, Michaelson JS, et al. Melanoma in the young: differences and similarities with adult melanoma: a case-matched controlled analysis. Cancer. 2007;110(3):614–24.

57. Akyürek M, Kayikçioğlu A, Ozkan O, Güler G, Mavili E, Erk Y. Multiple agminated Spitz nevi of the scalp. Ann Plast Surg. 1999;43(4):459–60.
58. Böer A, Wolter M, Kneisel L, Kaufmann R. Multiple agminated Spitz nevi arising on a café au lait macule: review of the literature with contribution of another case. Pediatr Dermatol. 2001;18(6): 494–7.
59. Bullen R, Snow SN, Larson PO, Kircik LH, Nychay S, Briggs P. Multiple agminated Spitz nevi: report of two cases and review of the literature. Pediatr Dermatol. 1995;12(2):156–8.
60. Hueso L, Hernández A, Torrelo A, Colmenero I, Zambrano A. Agminated Spitz nevi on a hyperpigmented macule. Actas Dermosifiliogr. 2008;99(1):69–72.
61. Levy RM, Ming ME, Shapiro M, et al. Eruptive disseminated Spitz nevi. J Am Acad Dermatol. 2007;57(3):519–23.
62. Fass J, Grimwood RE, Kraus E, Hyman J. Adult onset of eruptive widespread Spitz's nevi. J Am Acad Dermatol. 2002;46 Suppl 5:S142–3.
63. Walsh N, Crotty K, Palmer A, McCarthy S. Spitz nevus versus spitzoid malignant melanoma: an evaluation of the current distinguishing histopathologic criteria. Hum Pathol. 1998;29(10): 1105–12.
64. Busam KJ, Barnhill RL. Pagetoid Spitz nevus. Intraepidermal Spitz tumor with prominent pagetoid spread. Am J Surg Pathol. 1995;19(9):1061–7.
65. Requena C, Botella R, Nagore E, et al. Characteristics of spitzoid melanoma and clues for differential diagnosis with spitz nevus. Am J Dermatopathol. 2012;34(5):478–86.
66. Crotty KA, Scolyer RA, Li L, Palmer AA, Wang L, McCarthy SW. Spitz naevus versus Spitzoid melanoma: when and how can they be distinguished? Pathology. 2002;34(1):6–12.
67. Massi G. Melanocytic nevi simulant of melanoma with medicolegal relevance. Virchows Arch. 2007;451(3):623–47.
68. Kapur P, Selim MA, Roy LC, Yegappan M, Weinberg AG, Hoang MP. Spitz nevi and atypical Spitz nevi/tumors: a histologic and immunohistochemical analysis. Mod Pathol. 2005;18(2): 197–204.
69. Bergman R, Dromi R, Trau H, Cohen I, Lichtig C. The pattern of HMB-45 antibody staining in compound Spitz nevi. Am J Dermatopathol. 1995;17(6):542–6.
70. Kanter-Lewensohn L, Hedblad MA, Wejde J, Larsson O. Immunohistochemical markers for distinguishing Spitz nevi from malignant melanomas. Mod Pathol. 1997;10(9):917–20.
71. Palazzo J, Duray PH. Typical, dysplastic, congenital, and Spitz nevi: a comparative immunohistochemical study. Hum Pathol. 1989;20(4):341–6.
72. Ribé A, McNutt NS. S100A6 protein expression is different in Spitz nevi and melanomas. Mod Pathol. 2003;16(5):505–11.
73. Li LX, Crotty KA, McCarthy SW, Palmer AA, Kril JJ. A zonal comparison of MIB1-Ki67 immunoreactivity in benign and malignant melanocytic lesions. Am J Dermatopathol. 2000;22(6): 489–95.
74. Blokx WAM, van Dijk MCRF, Ruiter DJ. Molecular cytogenetics of cutaneous melanocytic lesions – diagnostic, prognostic and therapeutic aspects. Histopathology. 2010;56(1):121–32.
75. Gerami P, Li G, Pouryazdanparast P, et al. A highly specific and discriminatory FISH assay for distinguishing between benign and malignant melanocytic neoplasms. Am J Surg Pathol. 2012; 36(6):808–17.
76. Spatz A, Calonje E, Handfield-Jones S, Barnhill RL. Spitz tumors in children: a grading system for risk stratification. Arch Dermatol. 1999;135(3):282–5.
77. Barnhill RL, Argenyi ZB, From L, et al. Atypical Spitz nevi/tumors: lack of consensus for diagnosis, discrimination from melanoma, and prediction of outcome. Hum Pathol. 1999;30(5): 513–20.
78. Barnhhill R. Childhood melanoma. In: LeBoit P, Burg G, Weedon D, Sarasain A, editors. World Health Organization classification of tumours: pathology and genetics of skin tumours. Lyon: IARC Press; 2006. p. 84–5.
79. Smith KJ, Barrett TL, Skelton HG, Lupton GP, Graham JH. Spindle cell and epithelioid cell nevi with atypia and metastasis (malignant Spitz nevus). Am J Surg Pathol. 1989;13(11): 931–9.
80. Ludgate MW, Fullen DR, Lee J, et al. The atypical Spitz tumor of uncertain biologic potential: a series of 67 patients from a single institution. Cancer. 2009;115(3):631–41.
81. Wiesner T, Obenauf AC, Murali R, et al. Germline mutations in BAP1 predispose to melanocytic tumors. Nat Genet. 2011;43(10): 1018–21.
82. Wiesner T, Murali R, Fried I, et al. A distinct subset of atypical Spitz tumors is characterized by BRAF mutation and loss of BAP1 expression. Am J Surg Pathol. 2012;36(6):818–30.
83. Ferrara G, Argenziano G, Soyer HP, et al. The spectrum of Spitz nevi: a clinicopathologic study of 83 cases. Arch Dermatol. 2005;141(11):1381–7.
84. Sau P, Graham JH, Helwig EB. Pigmented spindle cell nevus: a clinicopathologic analysis of ninety-five cases. J Am Acad Dermatol. 1993;28(4):565–71.
85. Sagebiel RW, Chinn EK, Egbert BM. Pigmented spindle cell nevus. Clinical and histologic review of 90 cases. Am J Surg Pathol. 1984;8(9):645–53.
86. Phadke PA, Rakheja D, Le LP, et al. Proliferative nodules arising within congenital melanocytic nevi: a histologic, immunohistochemical, and molecular analyses of 43 cases. Am J Surg Pathol. 2011;35(5):656–69.
87. Gimotty PA, Botbyl J, Soong S-J, Guerry D. A population-based validation of the American Joint Committee on Cancer melanoma staging system. J Clin Oncol. 2005;23(31):8065–75.
88. Morton DL, Thompson JF, Cochran AJ, et al. Sentinel-node biopsy or nodal observation in melanoma. N Engl J Med. 2006;355(13):1307–17.
89. Roaten JB, Partrick DA, Pearlman N, Gonzalez RJ, Gonzalez R, McCarter MD. Sentinel lymph node biopsy for melanoma and other melanocytic tumors in adolescents. J Pediatr Surg. 2005;40(1):232–5.
90. Coit DG, Andtbacka R, Anker CJ, et al. Melanoma, version 2.2013: featured updates to the NCCN guidelines. J Natl Compr Canc Netw. 2013;11(4):395–407.
91. Parida L, Morrisson GT, Shammas A, et al. Role of lymphoscintigraphy and sentinel lymph node biopsy in the management of pediatric melanoma and sarcoma. Pediatr Surg Int. 2012;28(6): 571–8.
92. Vidal M, Vidal-Sicart S, Torrents A, et al. Accuracy and reproducibility of lymphoscintigraphy for sentinel node detection in patients with cutaneous melanoma. J Nucl Med. 2012;53(8):1193–9.
93. Alazraki N, Glass EC, Castronovo F, Olmos RAV, Podoloff D. Procedure guideline for lymphoscintigraphy and the use of intraoperative gamma probe for sentinel lymph node localization in melanoma of intermediate thickness 1.0. J Nucl Med. 2002;43(10):1414–8.
94. Wagner T, Buscombe J, Gnanasegaran G, Navalkissoor S. SPECT/CT in sentinel node imaging. Nucl Med Commun. 2013;34(3): 191–202.
95. Schröer-Günther MA, Wolff RF, Westwood ME, et al. F-18-fluoro-2-deoxyglucose positron emission tomography (PET) and PET/computed tomography imaging in primary staging of patients with malignant melanoma: a systematic review. Syst Rev. 2012;1:62.
96. Wagner T, Chevreau C, Meyer N, Mourey L, Courbon F, Zerdoud S. Routine FDG PET-CT in patients with a high-risk localized melanoma has a high predictive positive value for nodal disease

and high negative predictive value for the presence of distant metastases. J Eur Acad Dermatol Venereol. 2012;26(11):1431–5.
97. Bronstein Y, Ng CS, Rohren E, et al. PET/CT in the management of patients with stage IIIC and IV metastatic melanoma considered candidates for surgery: evaluation of the additive value after conventional imaging. Am J Roentgenol. 2012;198(4):902–8.
98. Jouvet JC, Thomas L, Thomson V, et al. Whole-body MRI with diffusion-weighted sequences compared with 18 FDG PET-CT, CT and superficial lymph node ultrasonography in the staging of advanced cutaneous melanoma: a prospective study. J Eur Acad Dermatol Venereol. 2014;28(2):176–85.
99. Landau JM, Moody MN, Goldberg LH, Vergilis-Kalner IJ. An unusual presentation of idiopathic basal cell carcinoma in an 8-year-old child. Pediatr Dermatol. 2012;29(3):379–81.
100. Dinehart SM, Dodge R, Stanley WE, Franks HH, Pollack SV. Basal cell carcinoma treated with Mohs surgery. A comparison of 54 younger patients with 1050 older patients. J Dermatol Surg Oncol. 1992;18(7):560–6.
101. Ademiluyi SA, Ijaduola GT. Occurrence and recurrence of basal cell carcinoma of the head and neck in Negroid and albinoid Africans. J Laryngol Otol. 1987;101(12):1324–8.
102. Abuzahra F, Parren LJMT, Frank J. Multiple familial and pigmented basal cell carcinomas in early childhood – Bazex-Dupré-Christol syndrome. J Eur Acad Dermatol Venereol. 2012;26(1):117–21.
103. Griffin JR, Cohen PR, Tschen JA, et al. Basal cell carcinoma in childhood: case report and literature review. J Am Acad Dermatol. 2007;57 Suppl 5:S97–102.
104. Rosen H, Schmidt B, Lam HP, Meara JG, Labow BI. Management of nevus sebaceous and the risk of Basal cell carcinoma: an 18-year review. Pediatr Dermatol. 2009;26(6):676–81.
105. Zwald FO, Brown M. Skin cancer in solid organ transplant recipients: advances in therapy and management: part I. Epidemiology of skin cancer in solid organ transplant recipients. J Am Acad Dermatol. 2011;65(2):253–61. quiz 262.
106. Lehmann AR, McGibbon D, Stefanini M. Xeroderma pigmentosum. Orphanet J Rare Dis. 2011;6(1):70.
107. Magnaldo T, Sarasin A. Xeroderma pigmentosum: from symptoms and genetics to gene-based skin therapy. Cells Tissues Organs. 2004;177(3):189–98.
108. Sattler E, Räwer H-C, Mühlstädt M, Ruzicka T, Burgdorf W, Kunte C. Basal cell carcinomas in radiotherapy-treated port wine stains. An ideal indication for Mohs surgery. Hautarzt. 2011; 62(7):534–8.
109. Paulino AC, Fowler BZ. Secondary neoplasms after radiotherapy for a childhood solid tumor. Pediatr Hematol Oncol. 2005;22(2): 89–101.
110. Hassanpour SE, Kalantar-Hormozi A, Motamed S, Moosavizadeh SM, Shahverdiani R. Basal cell carcinoma of scalp in patients with history of childhood therapeutic radiation: a retrospective study and comparison to nonirradiated patients. Ann Plast Surg. 2006;57(5):509–12.
111. Rubin AI, Chen EH, Ratner D. Basal-cell carcinoma. N Engl J Med. 2005;353(21):2262–9.
112. Sexton M, Jones DB, Maloney ME. Histologic pattern analysis of basal cell carcinoma. Study of a series of 1039 consecutive neoplasms. J Am Acad Dermatol. 1990;23(6 Pt 1):1118–26.
113. Batra RS, Kelley LC. Predictors of extensive subclinical spread in nonmelanoma skin cancer treated with Mohs micrographic surgery. Arch Dermatol. 2002;138(8):1043–51.
114. Ackerman AB. Nevoid basal cell carcinoma syndrome versus generalized basaloid follicular hamartoma syndrome. J Cutan Pathol. 2009;36(5):603. doi:10.1111/j.1600-0560.2008.01097.x. author reply 604.
115. Ramos-Ceballos FI, Pashaei S, Kincannon JM, Morgan MB, Smoller BR. Bcl-2, CD34 and CD10 expression in basaloid follicular hamartoma, vellus hair hamartoma and neurofollicular hamartoma demonstrate full follicular differentiation. J Cutan Pathol. 2008;35(5):477–83.
116. Burgdorf W, Gerami P, Yan A. Bening and malignant tumors. In: Schachner L, Hansen R, editors. Pediatric dermatology. 4th ed. Mosby Elsevier; 2011:1181–216.
117. Amonette RA, Salasche SJ, Chesney TM, Clarendon CC, Dilawari RA. Metastatic basal-cell carcinoma. J Dermatol Surg Oncol. 1981;7(5):397–400.
118. Taskinen M, Ranki A, Pukkala E, Jeskanen L, Kaitila I, Mäkitie O. Extended follow-up of the Finnish cartilage-hair hypoplasia cohort confirms high incidence of non-Hodgkin lymphoma and basal cell carcinoma. Am J Med Genet A. 2008;146A(18): 2370–5.
119. Cowen EW, Nguyen JC, Miller DD, et al. Chronic phototoxicity and aggressive squamous cell carcinoma of the skin in children and adults during treatment with voriconazole. J Am Acad Dermatol. 2010;62(1):31–7.
120. Orth G. Host defenses against human papillomaviruses: lessons from epidermodysplasia verruciformis. Curr Top Microbiol Immunol. 2008;321:59–83.
121. Kaspar TA, Wagner RF, Jablonska S, Niimura M, Tyring SK. Prognosis and treatment of advanced squamous cell carcinoma secondary to epidermodysplasia verruciformis: a worldwide analysis of 11 patients. J Dermatol Surg Oncol. 1991;17(3):237–40.
122. Kotwal A, Watt D. Cutaneous squamous cell carcinoma in a child. J Plast Reconstr Aesthet Surg. 2009;62(7):e194–5.
123. Pearce MS, Parker L, Cotterill SJ, Gordon PM, Craft AW. Skin cancer in children and young adults: 28 years' experience from the Northern Region Young Person's Malignant Disease Registry, UK. Melanoma Res. 2003;13(4):421–6.
124. Rowe DE, Carroll RJ, Day CL. Prognostic factors for local recurrence, metastasis, and survival rates in squamous cell carcinoma of the skin, ear, and lip. Implications for treatment modality selection. J Am Acad Dermatol. 1992;26(6):976–90.
125. Czarnecki D, Staples M, Mar A, Giles G, Meehan C. Metastases from squamous cell carcinoma of the skin in southern Australia. Dermatology. 1994;189(1):52–4.
126. Jackson A. Prevention, early detection and team management of skin cancer in primary care: contribution to the health of the nation objectives. Br J Gen Pract. 1995;45(391):97–101.
127. Kwa RE, Campana K, Moy RL. Biology of cutaneous squamous cell carcinoma. J Am Acad Dermatol. 1992;26(1):1–26.
128. Johnson TM, Rowe DE, Nelson BR, Swanson NA. Squamous cell carcinoma of the skin (excluding lip and oral mucosa). J Am Acad Dermatol. 1992;26(3 Pt 2):467–84.
129. Anon. Guidelines of care for cutaneous squamous cell carcinoma. Committee on Guidelines of Care. Task Force on Cutaneous Squamous Cell Carcinoma. J Am Acad Dermatol. 1993;28(4): 628–31.
130. Holmkvist KA, Roenigk RK. Squamous cell carcinoma of the lip treated with Mohs micrographic surgery: outcome at 5 years. J Am Acad Dermatol. 1998;38(6 Pt 1):960–6.
131. Novick M, Gard DA, Hardy SB, Spira M. Burn scar carcinoma: a review and analysis of 46 cases. J Trauma. 1977;17(10):809–17.
132. Fine J-D, Johnson LB, Weiner M, Li K-P, Suchindran C. Epidermolysis bullosa and the risk of life-threatening cancers: the National EB Registry experience, 1986–2006. J Am Acad Dermatol. 2009;60(2):203–11.
133. Love RL, Breidahl AF. Acute squamous cell carcinoma arising within a recent burn scar in a 14-year-old boy. Plast Reconstr Surg. 2000;106(5):1069–71.
134. Lawrence N, Cottel WI. Squamous cell carcinoma of skin with perineural invasion. J Am Acad Dermatol. 1994;31(1):30–3.
135. Maher-Wiese VL, Wenner NP, Grant-Kels JM. Metastatic cutaneous lesions in children and adolescents with a case report of metastatic neuroblastoma. J Am Acad Dermatol. 1992;26(4): 620–8.

136. De la Luz Orozco-Covarrubias M, Tamayo-Sanchez L, Duran-McKinster C, Ridaura C, Ruiz-Maldonado R. Malignant cutaneous tumors in children. Twenty years of experience at a large pediatric hospital. J Am Acad Dermatol. 1994;30(2 Pt 1):243–9.
137. Van Erp IF. Cutaneous metastases in neuroblastoma. Dermatologica. 1968;136(4):265–9.
138. Hawthorne HC, Nelson JS, Witzleben CL, Giangiacomo J. Blanching subcutaneous nodules in neonatal neuroblastoma. J Pediatr. 1970;77(2):297–300.
139. Lucky AW, McGuire J, Komp DM. Infantile neuroblastoma presenting with cutaneous blanching nodules. J Am Acad Dermatol. 1982;6(3):389–91.
140. Mehta V, Balachandran C, Lonikar V. Blueberry muffin baby: a pictoral differential diagnosis. Dermatol Online J. 2008;14(2):8.
141. Brecher AR, Reyes-Mugica M, Kamino H, Chang MW. Congenital primary cutaneous rhabdomyosarcoma in a neonate. Pediatr Dermatol. 2003;20(4):335–8.
142. Nesbit ME. Advances and management of solid tumors in children. Cancer. 1990;65 Suppl 3:696–702.
143. Wiss K, Solomon AR, Raimer SS, Lobe TE, Gourley W, Headington JT. Rhabdomyosarcoma presenting as a cutaneous nodule. Arch Dermatol. 1988;124(11):1687–90.
144. Isaacs H. Cutaneous metastases in neonates: a review. Pediatr Dermatol. 2011;28(2):85–93.

Intraocular Tumors

14

Irene Scheimberg, M. Beth McCarville, and Philip Luthert

Introduction

The eyes lie in the bony orbit, surrounded by orbital fat and protected from external damage by the eyelids. The orbit is formed by several bones: the frontal, zygomatic, maxillary, ethmoid, sphenoid, and lacrimal. There are six extraocular muscles: four recti and two oblique muscles, each with a unique function. The eye globe is formed of several layers (Fig. 14.1). The cornea is a clear layer covering the iris and pupillary opening, while the sclera is a thick fibrous layer covering the rest of the eye. Internal to the sclera is a vascular layer, the choroid. This is separated from the retina by a distinct basement membrane (Bruch's membrane; Fig. 14.2). The lens forms a biconvex transparent and avascular structure located behind the iris and supported by suspensor ligaments. The ciliary body arises at the periphery of the iris, secretes aqueous fluid, and controls the shape of the lens through sphincter muscles. These change the lens shape by relaxing the zonular fibers that tether the lens capsule. The iris, ciliary body, and choroid layer constitute the uvea. The retina is the sensory element of the eye and is composed of several layers (Fig. 14.2). The optic nerve, composed of axonal extensions of retinal ganglion cells, leaves the orbit via the optical canal. The optic nerve is surrounded by meningeal layers. The central retinal artery and vein run within the optic nerve. The nerve fibers forming the optic nerve traverse the sclera at foramina in the lamina cribrosa.

The eye structures derive from the ectoderm and mesoderm of the embryo. The optic pits appear as lateral evaginations of the neuroectoderm of the forebrain (prosencephalon) on day 22–23. As the forebrain closes, these evaginations continue to proliferate laterally and become large single layered vesicles (primary optic vesicles) that are continuous with the third ventricle. As the vesicles reach the surface ectoderm, they induce the formation of the lens placode. The optic vesicles invaginate, creating the optic cup with two layers. The differentiation of this secondary optic vesicle continues with the fusion of the retinal layers. The changes in the neural layers are similar to those in the brain. Rudimentary sensory cones and rods appear during the 12th week of gestation and continue development after birth. As the optic vesicles invaginate to form the optic cup and an inner and outer retinal layer, the point where the two layers meet anteriorly form the papillary opening. These two layers partially overlap the lens and become the iris at about 7th week of development. The ciliary body appears on the inner surface of the developing iris around week 9 and begins secreting aqueous humor [1].

Processing the Eye

Appropriate handling of the enucleated eye is fundamental in order to obtain appropriate fresh material for molecular genetic studies and to preserve the histology after fixation. In order to obtain material for genetic studies, the unfixed, fresh eye should be opened as soon as possible in order to minimize degradation of nucleic acids and proteins. The optic nerve is measured, and the resection margin is separated and fixed in a different cassette. The eye is oriented by localizing the inferior oblique muscle, which inserts in the sclera under the macular area and temporal to the optic nerve. Two basic techniques for the examination of enucleated eyes have been proposed by the Consensus meeting from

I. Scheimberg, M.D., F.R.C.Path. (✉)
Cellular Pathology, The Royal London Hospital,
Pathology and Pharmacy Building, 80 Newark Street,
London E1 2ES, UK
e-mail: i.b.scheimberg@qmul.ac.uk

M.B. McCarville, M.D.
Radiological Sciences, St. Jude Children's Research Hospital,
262 Danny Thomas Place, Memphis, TN 38105, USA
e-mail: beth.mccarville@stjude.org

P. Luthert, B.Sc., M.B.B.S.
Department of Eye Pathology,
UCL Institute of Ophthalmology and Moorfields Eye Hospital,
11-43 Bath Street, London EC1V 9EL, UK
e-mail: p.luthert@ucl.ac.uk

D.M. Parham et al. (eds.), *Pediatric Malignancies: Pathology and Imaging*,
DOI 10.1007/978-1-4939-1729-7_14,

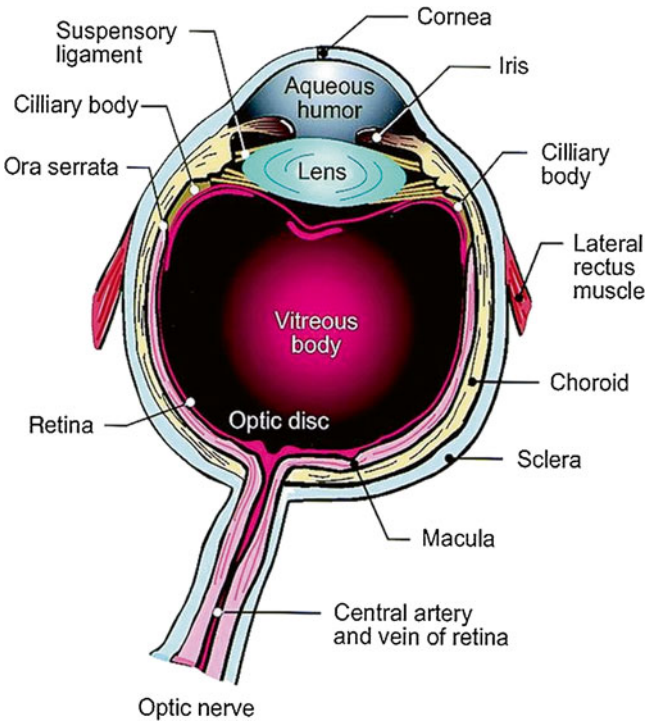

Fig. 14.1 Diagram of normal eye anatomy in the axial plane. The anterior chamber, located anterior to the lens, extends from cornea to iris. The posterior chamber extends from the iris to posterior lens. Both chambers contain aqueous humor. Suspensory ligaments arising from the vascular ciliary bodies support the lens. The vitreous chamber extends from posterior lens surface to the ocular surface. The posterior ocular surface is comprised of three layers: inner retina, vascular choroid, and outer sclera. The ora serrata is the anterior most portion of the retina and covers the posterior two thirds of the inner surface of posterior chamber. The optic nerve extends posteriorly from the globe through retro-orbital fat. The central retinal artery and vein course through the optic nerve (adapted from [6])

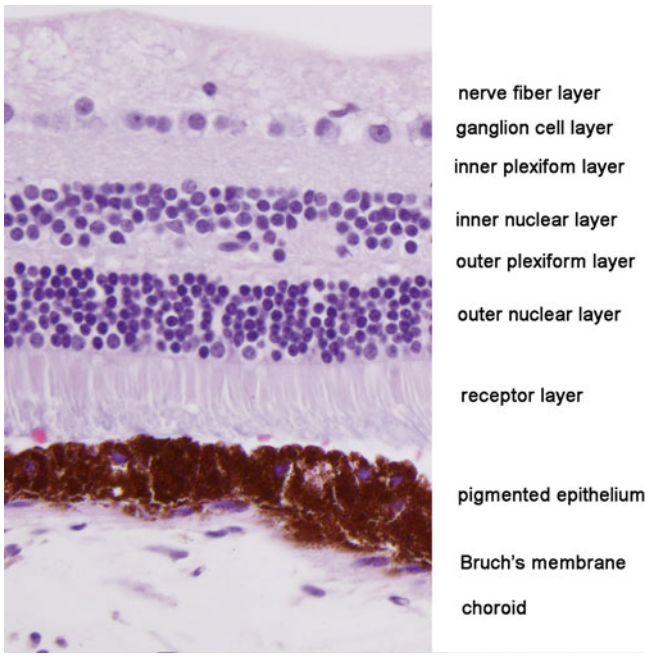

Fig. 14.2 Microphotograph of the retina with the name of the different layers. The pigmented epithelium has been cut tangentially and appears thicker. Bruch's membrane separates the pigmented epithelium from the choroid

The International Staging Work Group on the Pathology Guidelines [2]. First, the tumor is located with transillumination. In one approach, a window is opened in the sclera at the edge of the tumor. This can be done using a trephine or a sharp blade. Fresh tumor is retrieved from non-necrotic, viable areas, either with a scalpel and forceps or with a sterile pipette. The second technique proposed is the aspiration of tumor with a 22 G sterile needle under visual control through the sclera, using an approach posterior to the lens in a slightly oblique anteroposterior course. We use a modification of the first technique that allows for proper visualization of the tumor and preserves nucleic acids and proteins: after separating the optic nerve resection margin, we freeze the eye in liquid nitrogen for 20–25 s and then slice the superior calotte from the rest of the orbit. After the tumor thaws (after a few seconds depending on the size of the tumor), we extract fresh material with the help of a sterile scalpel or a sterile pipette, The tumor preservation for genetic analysis is perfect, and the technique introduces fewer artifacts in the histology (unpublished method). After harvesting fresh tumor, the eye is placed in sufficient formalin and fixed for 24–48 h.

After fixation the whole specimen is submitted for examination in four blocks: (1) optic nerve resection margin, (2) superior calotte, (3) mid section of the eye with the optic nerve and anterior chamber structures, and (4) inferior calotte. The calottes may be further sectioned into segments embedded on edge to examine more choroidal surfaces. Several levels may be necessary, particularly with small retinoblastomas after chemotherapy and for optimal assessment of optic nerve head invasion.

Overview of Diagnostic Imaging Approaches

Ultrasound (US) and magnetic resonance imaging (MRI) are the preferred imaging modalities to assess ocular lesions in children. Computed tomography (CT) is discouraged for several reasons: damage caused by the inherent exposure to ionizing radiation and the association of retinoblastoma with radiation-induced secondary malignancies. The latter factor is a particular consideration in children who are ultimately diagnosed with hereditary retinoblastoma. When assessing ocular disease, US can identify calcification within lesions, delineate tissue interfaces, and reveal patterns of vascularity using Doppler technology. Magnetic resonance imaging is less sensitive for the detection of calcification but more

sensitive to tumor extension into the optic nerve and subarachnoid spaces. Therefore, these modalities are complementary and, in current practice, the combination of US, MRI, and fundoscopy obviates the need for CT in the setting of pediatric ocular tumors [3, 4].

An awareness of the imaging appearances of normal eye anatomy is necessary to accurately evaluate ocular lesions with diagnostic imaging. The US and MRI anatomy of the normal eye have previously been well described [5–7]. Ultrasound can be performed with conscious patients, and a typical examination takes 10–15 min. If needed, it US can be performed while the patient is sedated for MRI. A linear, high-frequency transducer with a small footprint is placed directly on ultrasound gel applied to the closed eyelid. The US machine's mechanical index should be kept ≤0.23 to conform to FDA guidelines and to minimize risk of thermal injury to the eye [8]. Color Doppler is used to assess tumor vascularity, to determine the relationship of the mass to the optic disk, and to distinguish dense subretinal fluid from a solid mass. MRI requires some level of sedation for optimal imaging. Guidelines for standardized MRI of the eye were recently published [9]. In general MR examinations should include dedicated orbit imaging and imaging of the entire brain. Orbital imaging should include gadolinium-enhanced fat-suppressed sequences to optimize the delineation conspicuity of the tumor within orbital fat. The use of high-field strength magnets and surface coils may improve definition of the lesion and detection of optic nerve involvement. By using conventional coils, current 3-Tesla MR scanners provide improved imaging with a wider field of view as compared to surface coils [3, 10].

Retinoblastoma

Retinoblastoma, a rare tumor of the eye, characteristically arises in the retina of children and represents the most common orbital malignancy in childhood. Retinoblastomas occur primarily in children under the age of 5 years; the median age of diagnosis is 2 years of age [11] for unilateral retinoblastoma and 9–12 months for bilateral retinoblastoma. The disease is unilateral in 60 % of cases and bilateral in 40 %. All bilateral and 15 % of unilateral retinoblastomas are hereditary.

The incidence of retinoblastoma is 1 in 15,000–20,000 live births. The world incidence and mortality differs among countries (Table 14.1). A higher incidence of unilateral RB is seen in less developed countries, suggesting that environmental factors associated with poverty increases the risk of retinal mutations [12].

Hereditary retinoblastoma is characterized by the presence of a germ line mutation, earlier clinical manifestation, and an elevated risk of developing secondary malignancies including osteosarcoma, malignant melanoma and soft tissue sarcoma [13]. Bilateral retinoblastoma arises when a germ line mutation in one copy of the *RB1* gene is followed by a somatic mutation of the remaining wild copy. In non-hereditable RB both mutations are somatic.

Table 14.1 World incidence and mortality for RB (Data from Shields and Shields 2012)

Location	Incidence	Patients/ year	Mortality rate	Deaths/ year
Africa	34.2	1,792	70	1,254
Asia[a]	18.8	4,027	39	1,591
Japan	8.3	59	3	2
Europe	10.2	414	5	21
North America	13.8	258	3	8
Latin America / Caribbean	19.8	622	20	124
Oceania	16.3	21	10	4
Total		7,202		3,001

[a]without Japan

Genetics

Retinoblastoma was the first malignancy to be described as a genetic disease. In 1971 Alfred Knudson proposed that retinoblastoma was initiated by inactivation of a tumor suppressor gene and that two events were necessary for the development of the disease [14]. This hypothesis was subsequently confirmed by the demonstration of the loss of heterozygosity at 13q14 in retinoblastomas [15] and the cloning of the first tumor suppressor gene *RB1* [16]. Since then many tumors have been found to have defects in their RB pathway, through genetic lesions in either the *RB1* gene or other genes in the pathway [17]. Retinoblastomas are initiated by the loss of both alleles of *RB1* (M1 and M2, first and second mutational events). This is necessary but not sufficient for the development of the malignancy. The M1 event can be inherited or arises sporadically in a susceptible retinal cell, while M2 is always sporadic. A number of subsequent mutational events eventually lead to retinoblastoma [18].

In humans, the *RB1* gene is located within a 183-kB region of chromosome 13q14 and is made up of 27 exons, which produce a 4.7-kB mRNA that is translated into a 928 amino acids protein called pRB. *RB1* gene is a tumor suppressor gene and as such its protein product can inhibit tumor formation in a variety of tissues. pRB is a negative regulator of the cell cycle and has a role in cell differentiation, cell aging, apoptosis, and growth suppression. It is modified by phosphorylation, which affects the physical interaction between pRB and the E2F proteins that activate genes involved in the G1-S phase of the cell cycle and promote cell cycle progression. Hypophosphorylated pRB can bind to

E2Fs, inhibiting this function. As pRB is phosphorylated, it loses its ability to bind to E2Fs, allowing them to activate the genes that promote the cell cycle. RB also has a role in suppression of apoptosis and indirectly controls differentiation [19].

Most retinoblastomas display genomic imbalances, the most frequent being gains of chromosomes 1q, 2p, and 6p and loss of chromosome 16q. Comparative genomic hybridization (CGH) reveals that over 50 % of retinoblastomas show a gain of 1q. The gains involve *KIF14* (1q), a mitotic kinesin [18]; *E2F3* and *DEK* (6p) the former a regulator of the cell cycle and DEK and the latter a known oncogene in many cancers [20]; and *MYCN* (2p) an oncogene amplified in a subset of neuroblastomas [17]. Approximately 30 % of retinoblastomas show a loss at chromosome 16q22 a region that contains two potential tumor suppressor genes belonging to the cadherin family [21]. Using a microarray analysis, 1,404 genes were upregulated and 481 genes were downregulated in retinoblastomas [22].

Loss of RB1 in many tissues leads to apoptosis; however, in the retina RB1-negative retinoblasts can survive and form tumors. A possible pro-apoptotic tumor suppressor gene in the retina is *NGFR*, which encodes p75, a modulator of cell death in the retina [23].

A small percentage of retinoblastomas are caused by deletions in the region of chromosome 13 that contains the *RB1* gene. Because several other genes are also affected, these children usually have intellectual disability, slow growth, and distinctive facial features (prominent eyebrows, short nose with broad nasal bridge, and ear abnormalities) [24].

Genetic counseling is very important for retinoblastoma patients and should be offered to every parent with a child with retinoblastoma and to patients with a familial history of retinoblastoma. The nature of the disease, the inheritance patterns, and the risk to family members should be explained.

Both RB1 alleles have to be deregulated in order for a retinoblastoma to develop. However, the mutant allele behaves as an autosomal dominant trait. The majority of retinoblastomas (85–90 %) arise sporadically in the retina of the affected patient or in the parental germ line; there is no family history of the disease. If the initial RB1 mutation arises in the germ line before conception or in the early embryo, the risk for retinoblastoma will be heritable. If two *RB1* somatic mutations occur in a retinal cell but the germ line is not affected, the tumor will not be heritable. In 88 % of sporadic bilateral retinoblastomas, there is a new mutation arising in the germ line of the father (>90 %) or the mother (<10 %). The remaining 12 % have mutational mosaicism, and the tumor may be heritable if the mutation is present in the germ line [25]. Sporadic tumors are more likely to be unilateral and unifocal; however, bilateral and multifocal tumors have also been observed. In addition, *RB1* mutation predisposes to other primary cancers as detailed above. These secondary malignancies present later in life but earlier than in persons with no *RB1* mutations. In the absence of molecular diagnosis, it is important to screen all first degree relatives of retinoblastoma patients when the first case is identified in the family.

In hereditary retinoblastoma, genetic testing of constitutional DNA (usually from a peripheral blood sample) identifies a large percentage of mutations in hereditary cases [26]. The second mutation can only be identified in tumor DNA. For sporadic bilateral retinoblastoma, analysis of peripheral blood may not always lead to the detection of the *RB1* mutation. In these cases, testing of tumor DNA may show two *RB1* mutations or one mutation and loss of heterozygosity. If a causative mutation is detected as heterozygous in the proband's blood, the parents should be tested for the mutation. Most cases of sporadic retinoblastomas arise de novo, but in a small number the parent may be a low level mosaic. *RB1* mutations can be prenatally detected in DNA from the amniotic fluid. For sporadic unilateral retinoblastoma, the peripheral DNA is usually normal (85 % of patients), and DNA from the tumor must be analyzed to identify both *RB1* mutations.

Over 1,000 mutations leading to retinoblastoma have been identified, and a variety of techniques are used to find the nature of an unknown *RB1* mutation [23].

Clinical Presentation

The most common presentation of retinoblastoma is leukocoria (white pupil), generally detected by family members, frequently on a flash photograph. This may present with or without strabismus [27]. Leukocoria may be recognized at a pediatric visit. Retinoblastoma generally remains intraocular and curable for 3–6 months after the first sign of leukocoria [23].

Less common forms of presentation include red eye, amblyopia, anisocoria, heterochromia, and hyphema. Patients with advanced disease may present with orbital cellulitis, particularly when there is significant tumor necrosis within the eye. Proptosis is a common presentation in low income countries but is rare in developed countries [28].

Patients with a known familiar predisposition are diagnosed earlier, as these children are screened after birth. Patients at high risk can be screened in utero [29].

There are many conditions that can mimic retinoblastoma. The three most common conditions that can simulate retinoblastoma are Coats' disease, an abnormality of the retinal vasculature of unknown origin; persistent hyperplastic primary vitreous; and toxocariasis (Table 14.2).

As highlighted above, there is a high risk of secondary malignant tumors in patients with hereditary retinoblastoma who are born with a germ line mutation of the *RB1* gene. Although more frequent after radiotherapy treatment, they

Table 14.2 Differential diagnosis of retinoblastoma

Coat's disease
Persistent hyperplastic primary vitreous
Toxocariasis
Cellulitis
Metastasis
Coloboma
Toxoplasmosis
Retinopathy of prematurity
Cytomegalovirus and herpes retinitis
Astrocytic hamartoma

may occur without radiotherapy and in children treated with chemotherapy [29, 30]. Chemotherapy is also known to enhance the development of second malignant tumors in irradiated patients [31]. Secondary tumors reported include osteosarcoma (the most common secondary malignancy both in irradiated and non-irradiated areas); soft tissue sarcomas (including leiomyosarcoma, fibrosarcoma, malignant fibrous histiocytoma, rhabdomyosarcoma, unspecified sarcomas, and liposarcoma, and closely associated with the use of radiation); skin cancer (melanoma and basal cell and squamous cell carcinoma, especially in the radiation area); common adulthood cancers (lung, breast, colon, oral cavity, bladder, uterus), hematological malignancies [13, 31–34], and sinonasal PNET [35].

The association of bilateral retinoblastoma with a synchronic or metachronic midline intracranial tumor is referred to as trilateral retinoblastoma (TRB), a rare but well recognized syndrome. Tumors of the suprasellar region tend to present earlier than tumors of the pineal region after the diagnosis of intraocular tumors. The prognosis is very poor. As there is better overall survival in children who are asymptomatic at the time of diagnosis of the intracranial tumors, screening is essential in patients with bilateral and/or hereditary retinoblastoma [36]. Since the use of systemic chemotherapy there has been a decrease in the number or TRBs. Pineal and parasellar tumors may appear several years after successful treatment of intraocular retinoblastoma and they may be better differentiated. The difference between TRB and metastatic tumor is that the latter presents as multiple undifferentiated tumors within the first 2 years of the in initial treatment

Imaging Features

The imaging appearance of retinoblastoma somewhat depends on whether the tumor is endophytic, exophytic, or diffusely infiltrating. Endophytic tumors arise from the inner layers of the retina and grow into the vitreous body. Small clusters of tumor may separate from an endophytic tumor to produce vitreous seeding. Exophytic tumors arise in the outer retinal layers and grow in the subretinal space causing retinal detachment, subretinal exudates, and possible subretinal tumor seeding. However, retinal detachment and subretinal fluid can occur in both endophytic and exophytic tumors. Therefore, these findings are of limited value in predicting the tumor growth pattern [9]. Diffusely infiltrating retinoblastoma, characterized by diffuse infiltration of the retina without a focal mass, is rare [4]. In contrast to the other types of retinoblastoma, the infiltrating type usually lacks calcification [3].

Ultrasound

Sonographically retinoblastoma appears as an irregularly shaped soft-tissue mass, more echogenic than the vitreous, with numerous hyperechoic foci due to focal calcification or microcalcifications (Fig. 14.3a). The presence of calcification is the hallmark of retinoblastoma and the key feature in distinguishing it from other ocular pathologies [4, 5]. With modern high-resolution US transducers, calcification is identified in 92–95 % of cases when it is found histologically. This compares to a sensitivity of 81–96 % for CT [4]. Retinal detachment is frequently present and appears as a thin strand of juxtatumoral material that is contiguous with the retina (Fig. 14.3a). Fluid in the subretinal space or vitreous is often slightly echogenic due to blood products, increased globulin content, or tumor seeding [6]. Cystic areas within the tumor are likely due to necrosis, a common pathologic finding. Ultrasonography is not useful for determining invasion of the optic nerve, which is often obscured by overlying tumor or tumor calcification (Fig. 14.3a) [4].

Magnetic Resonance Imaging

On MRI, retinoblastoma typically matches the signal intensity of gray matter. On T1W images the tumor is slightly hyperintense to vitreous, and on T2W images it is usually darker than vitreous. The tumor may appear heterogeneous due to internal calcification. Retinoblastomas typically demonstrate moderate, heterogeneous contrast enhancement (Figs. 14.3b–d, 14.4a–c). Magnetic resonance imaging can detect ocular lesions as small as 3 mm in size, but as vitreous seeds rarely exceed 1–2 mm they may be missed by MRI [3, 9, 10]. MRI has a sensitivity of 50–89 % for detection of retinal detachment; it can also detect sub-retinal fluid and vitreous hemorrhage. Subretinal and vitreous fluid may contain fluid–fluid levels due to sedimentation effect and may be hyper- or isodense. They may appear uniformly hyperintense on both T1 and T2W images due to hemorrhage or proteinaceous subretinal effusion, or they may appear isointense to vitreous on T1W images and hyperintense on T2W images due to subretinal fluid with low protein content (Fig. 14.4b–d) [9]. Retinoblastoma can breach the Bruch membrane and infiltrate the choroid (Figs. 14.4a–c, 14.5b–d) [3].

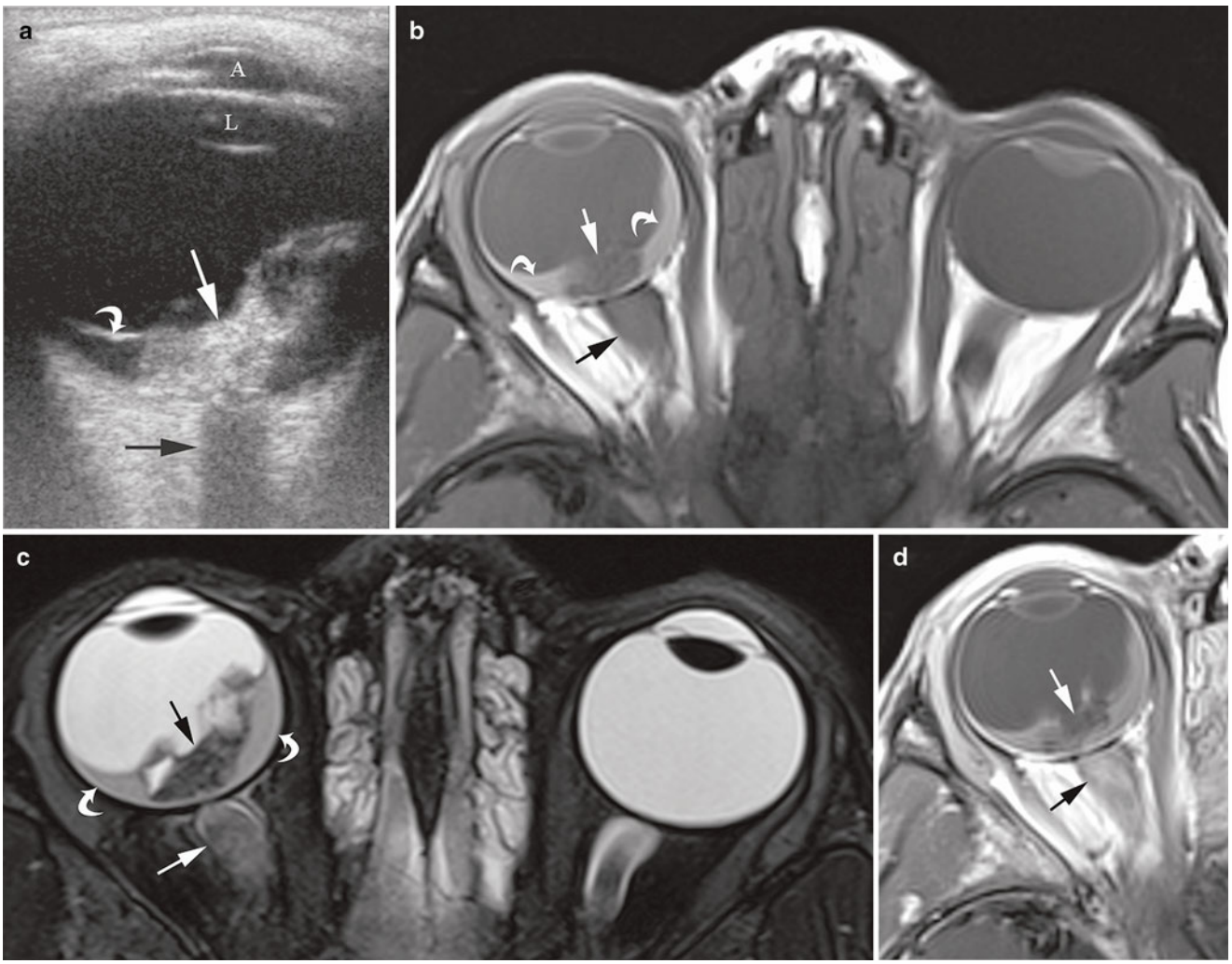

Fig. 14.3 A 5-year-old boy presented with right eye blindness and pain, found to have retinoblastoma. (**a**) Transverse ultrasound image shows dense calcification of the tumor (*bright flecks, straight white arrow*) causing posterior shadowing (*black arrow*) that obscures visualization of the optic nerve. Detached retina (*curved white arrow*) is evident. *A* anterior chamber, *L* lens. (**b**) Axial, non-contrast enhanced T1W, (**c**) axial T2W and (**d**) contrast-enhanced T1W MR images show the primary tumor to be of mixed, but predominantly low signal intensity on non-contrast T1W imaging (*straight white arrow*) and T2W (*straight black arrow*), with minimal enhancement probably due to dense calcification. Subretinal fluid (*curved arrows*) is hyperintense to vitreous on T1W and hypointense on T2W images. The optic nerve (*straight black arrow* on images (**b**) and (**d**), *straight white arrow*, image (**c**) is thickened relative to the normal left side and enhances inhomogenously. On pathologic inspection this tumor was densely calcified, mixed endo-exophytic with minimal choroidal involvement, detached retina, subretinal hemorrhage and gliosis, and extensive optic nerve invasion

Using standard head coils, homogenous enhancement and thickening of the choroid adjacent to the tumor is 73 % sensitive and 72 % specific for choroidal involvement by MRI. Choroidal inflammation can mimic the appearance of tumor involvement on MRI, thus limiting its utility in this regard. Once the choroid has been infiltrated, tumor can spread along ciliary vessels and nerves to extend into the sclera, orbit, and conjunctiva, findings which may be apparent on MRI (Fig. 14.4a–c) [3]. Magnetic resonance imaging has been shown to have a sensitivity of 66 %, specificity of 96 %, and accuracy of 79 % for prelaminar optic nerve involvement (anterior to the insertion of the meninges on the optic nerve). Regarding post-laminar optic nerve involvement, MRI is reported to have a sensitivity of 50 %, specificity of 100 %, and accuracy of 97 % [9]. On post-contrast images, prelaminar optic nerve involvement appears as interruption or thickening of linear enhancement at the choroidal retinal complex. Enhancement extending from the tumor into the optic nerve is a reliable sign of postlaminar optic nerve involvement, but its absence does not preclude optic nerve involvement (Figs. 14.3b, c, 14.4c, 14.5a–d). Both pre- and post-laminar microscopic invasion of the optic nerve can be missed by MRI, so that primary tumor volume is thought to be the best predictor of optic nerve invasion [9]. Once extraocular

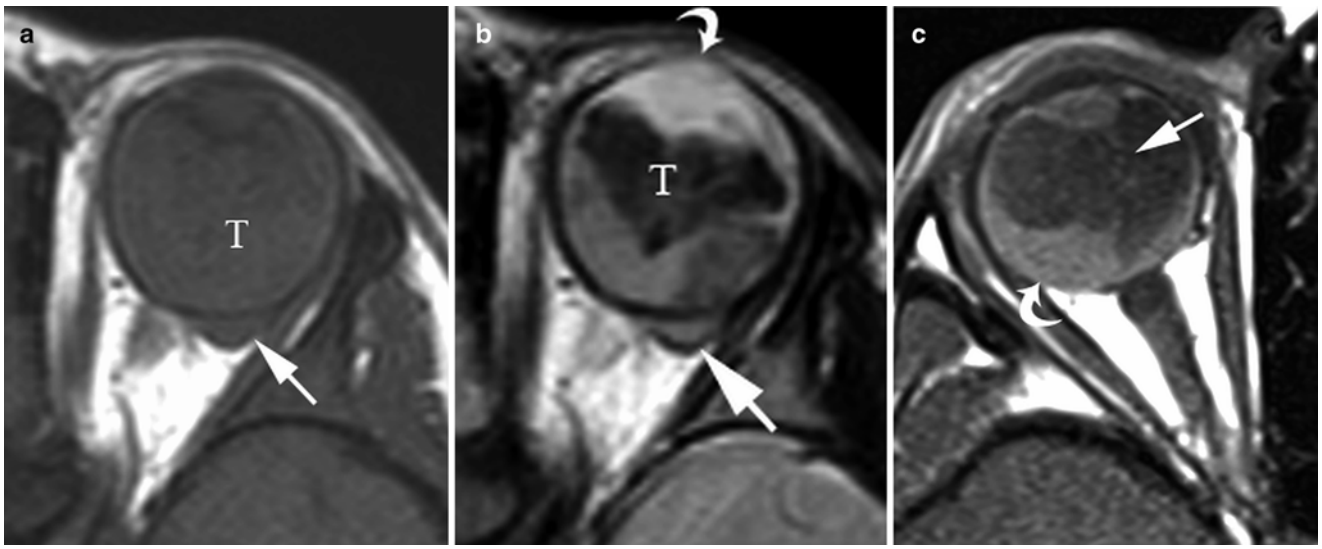

Fig. 14.4 A 3-year-old boy presented with leukocoria of left eye and was subsequently diagnosed with retinoblastoma. (**a**) Non-contrast enhanced axial T1W, (**b**) axial T2W and (**c**) post-contrast enhanced axial T1W MR images show the primary tumor expanding the left globe (note enlargement of left globe relative to normal right globe in (**c**)). Tumor (T) invades the anterior chamber (*curved arrow* (**b**)) and invades through the posterior sclera (*straight white arrow* (**a**, **b**) and *straight arrow* (**c**)) and the optic nerve (*straight white arrow* (**c**)). There is enhancing tumor causing retinal detachment (*curved arrow* (**c**)) and largely non-enhancing tumor (T) that is hypointense on T1W and T2W images probably due to calcification or hemorrhage. At pathologic inspection the tumor was mixed endo-exophytic with massive choroidal involvement, involvement of the vitreous, ciliary bodies, iris, anterior chamber, sclera, cornea and optic nerve with retinal detachment

spread occurs, the risk of distant hematogenous spread to the lungs, bones, brain, and local-region lymph nodes increases [3]. Because of the risk of intracranial tumor extension or pineal tumors ("trilateral" retinoblastoma, which occurs with bilateral eye tumors), MRI of the orbits and brain should be obtained in the same scanning session. If intracranial extension is present, MRI of the entire spine is indicated in order to detect leptomeningeal involvement [3].

Examination

Ophthalmoscopic examination under anesthesia is followed with imaging studies (see above).

Tumors are subdivided according to their growth pattern into endophytic (growing into the vitreous cavity), exophytic (growing into the subretinal space and lifting the retina, and diffuse (a rare infiltrating retinoblastoma.

Classification

Developed in 1963 [37], the Reese–Ellsworth classification (Table 14.3) is based on intraocular tumor staging and eye salvage prediction after external beam radiation. This system divides eyes in five groups according to location, focality, and size of the tumor (as determined by ophthalmoscopy). At the time of adoption of this classification, external beam radiotherapy (ERBT) was the commonest non-enucleation treatment for retinoblastoma. However, over the last 15 years the treatment of retinoblastoma has changed considerably in an effort to avoid ERBT, which causes disfigurement and increases the risk of secondary tumors in patients with germ line mutation [38]. Systemic chemotherapy for retinoblastoma was introduced in the mid-1990s, adopting a protocol of vincristine, etoposide and carboplatin (VEC) delivered monthly over 6–9 months. Most tumors with vitreous seeding and subretinal seed recurrence are controlled with thermotherapy, cryotherapy, or plaque radiotherapy [39]. Tumor location, multifocality, and size have become of lesser concern than vitreous seeding. In 2003 the newer International Classification System for Retinoblastoma (ICRB) was devised. The ICRB is based mainly in the extent of tumor seeding in the vitreous and subretinal space, with consideration for the tumor size and location. The tumor is confined to the retina in groups A and B while C and D represent spreading into the subretinal space and vitreous cavity; group E represents extensive disease (see Table 14.4). Group A represents early disease and is generally associated with good prognosis. Eyes in group E have the worst prognosis and require enucleation as a primary treatment, as they are unsalvageable. The chances of retaining full vision decreases from group A to group E.

A staging system for retinoblastoma was established by an international commission in 2006. Patients are classified according to the extent of the disease and the presence of overt extraocular extension. In addition, a proposal for substaging considering histopathological features of enucleated

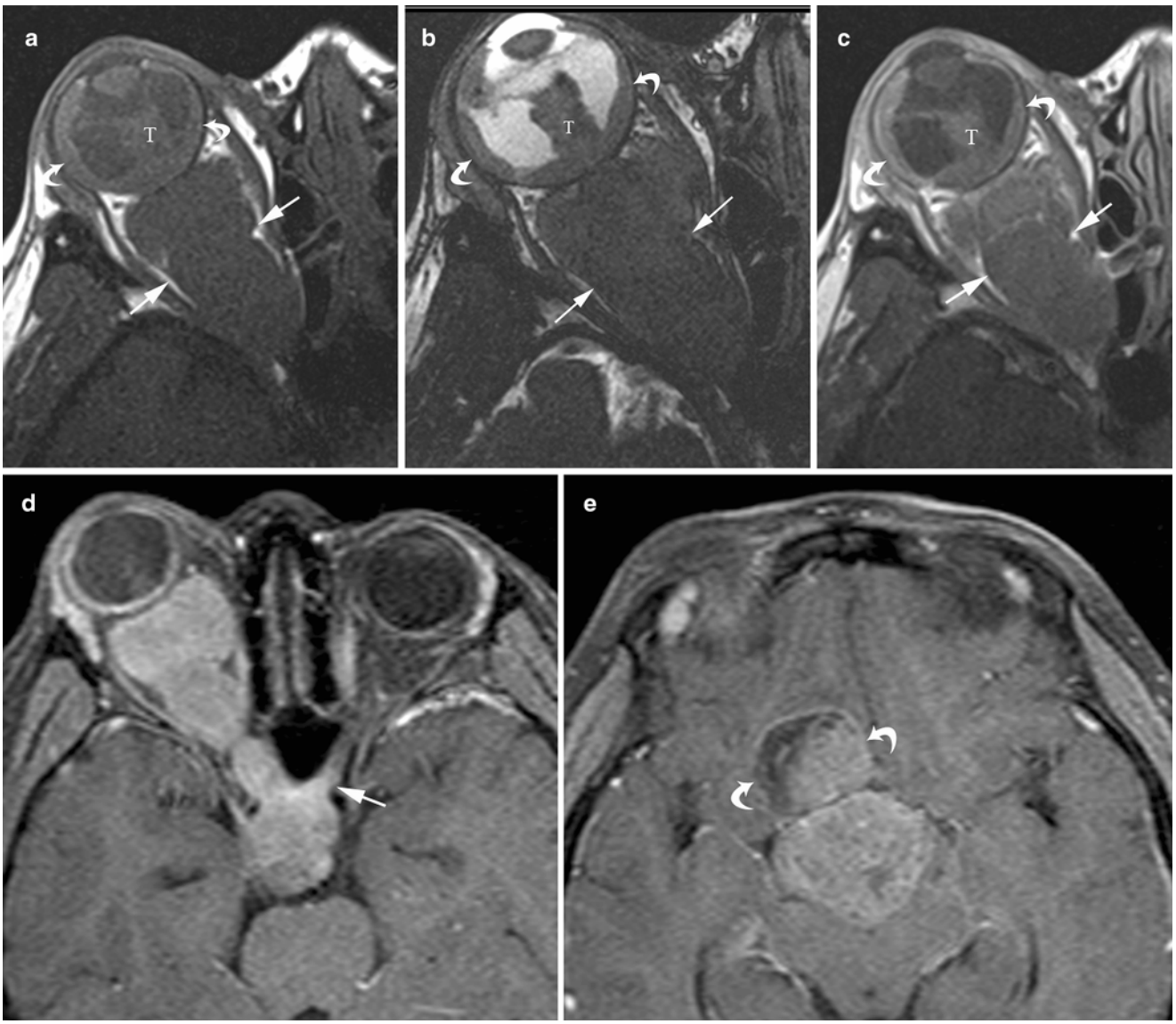

Fig. 14.5 An 8-year-old girl from Mexico initially treated for allergic conjunctivitis then Toxocara endophthalmitis of the right eye, subsequently diagnosed with retinoblastoma. (**a**) Non-contrast enhanced axial T1W, (**b**) axial constructive interference steady state (CISS, heavily T2W) and (**c**) post-contrast enhanced axial T1-weighted MR images show the primary tumor (T) to be slightly hyperintense to vitreous on non-contrast T1W, hypointense on T2W with minimal to moderate enhancement. Note extensive involvement of the enhancing and thickened choroid (*curved arrows*) and optic nerve (*straight arrows*). On pathologic inspection this tumor was determined to be exophytic. (**d**, **e**) Post-contrast enhanced T1W images of the brain show tumor extending across the optic chiasm to involve the contralateral optic nerve (*arrow*) and intracranial extension into the frontal lobe (*curved arrows*). Spine MRI and cerebral spinal fluid sample were negative for leptomeningeal spread

Table 14.3 Reese–Ellsworth classification

Ia	Solitary tumor <4 disk diameters in size of behind the equator
Ib	Multiple tumors, all <4 disk diameters in size at or behind the equator
IIa	Solitary tumor 4–10 disk diameters in size at or behind the equator
IIb	Multiple tumors, 4–10 disk diameters in size at or behind the equator
IIIa	Any lesion anterior to the equator
IIIb	Solitary tumor >10 disk diameters in size behind the equator
IVa	Multiple tumors some >10 disk diameter in size
IVb	Any lesion anterior to the ora serrata
Va	Massive tumor involving >50 % of retina
Vb	Vitreous seeding

Table 14.4 International classification of retinoblastoma (ICRB)

Group	Subgroup	Quick reference	Specific features
A	A	Small tumor	RB ≤3 mm in size
B	B	Larger tumor	RB >3 mm in size, OR:
		Macula	• Macular RB location (≤3 mm to foveola)
		Juxtapapillary	• Juxtapapillary RB (≤1.5 mm to disk)
		Subretinal	• Clear subretinal fluid ≤3 mm from margin
C		Focal seeds	Retinoblastoma with:
	C1		• Subretinal seeds ≤3 mm from RB
	C2		• Vitreous seeds ≤3 mm from RB
	C3		• Both subretinal and vitreous seeds ≤3 mm from RB
D		Diffuse seeds	Retinoblastoma with:
	D1		• Subretinal seeds >3 mm from RB
	D2		• Vitreous seeds >3 mm from RB
	D3		• Both subretinal and vitreous seeds >3 mm from RB
E	E	Extensive RB	• Extensive RB occupying >50 % of globe or neovascular glaucoma OR
			• Opaque media from hemorrhage in anterior chamber, vitreous or subretinal space OR
			• Invasion of postlaminar optic nerve, choroid (>2 mm), sclera, orbit, OR anterior chamber

Table 14.5 International staging system for RB

Stage 0: Patients treated conservatively (subject to presurgical ophthalmologic classification)
Stage I: Eye enucleated, tumor completely resected histologically
Stage II: Eye enucleated, microscopic residual tumor
Stage III: Regional extension
a) Overt orbital disease
b) Preauricular or cervical lymph node extension
Stage IV: Metastatic disease
a) Hematogenous metastasis
1. single lesion
2. multiple lesions
b) CNS extension
1. Prechiasmic lesion
2. CNS mass
3. Leptomeningeal disease

specimens is presented to further discriminate between stages I and II [40] (Table 14.5).

Pathology

Retinoblastoma originates in the sensory retina. The cell of origin is still unknown.

Grossly retinoblastomas are whitish tumors with a friable consistency, often with bright, chalky puncta corresponding to focal calcification (Fig. 14.6a, b). Tumors with an endophytic growth pattern arise from the retina and grow towards the vitreous cavity. These tumors tend to fill the entire globe cavity and produce vitreous seeding. If left untreated the tumor eventually invades the anterior portion of the eye. Tumors with an exophytic pattern grow into the subretinal

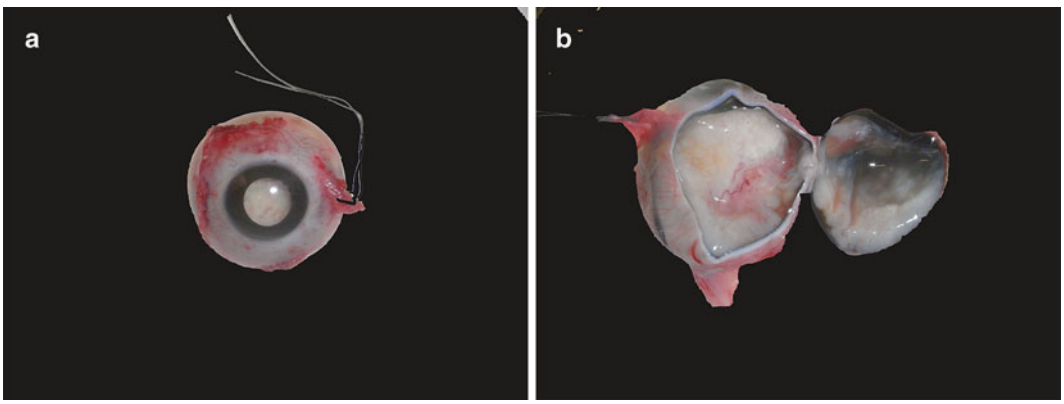

Fig. 14.6 (**a**) Enucleated eye showing a large retinoblastoma seen as a white mass through the partially dilated pupil. The suture is attached to the medial rectus muscle. (**b**) A fresh eye with superior calotte separated (on the *right*) and ready for tissue extraction for cytogenetic studies. The eye is nearly completely filled with whitish tumor

space, often causing retinal detachment as they lift the retina. These tumors invade the choroid through Bruch's membrane. The majority of retinoblastomas have a mixed endo-exophytic pattern. Rarer presentations include extensively necrotic retinoblastomas (in which >90 % of the tumor and intraocular tissue are necrotic) and diffuse infiltrating retinoblastoma (in which the tumor expands the entire retina without forming a discrete tumor mass).

Microscopic examination of the enucleated eye reveals a small blue round cell tumor with variable areas of necrosis. There are numerous mitoses and apoptotic cells. Characteristically, the viable cells are distributed around blood vessels. Areas of necrosis show multiple foci of dystrophic calcification. Some tumors are poorly differentiated with sheets of small blue round cells (Fig. 14.7a, b) or occasionally pleomorphic cells (Fig. 14.7 c), while others show a degree of differentiation. Differentiation is represented by rosettes. These are of two types: Flexner–Wintersteiner and Homer Wright rosettes. Flexner–Wintersteiner rosettes (Fig. 14.7d) are composed of tall cuboidal cells that encircle an empty, central lumen lined by a membrane similar to the outer limiting membrane in the normal retina. Homer Wright rosettes (Fig. 14.7e) similar to those of neuroblastic tumors occur less commonly. These rosettes do not contain a central lumen but instead extend cytoplasmic processes (neuropil) into their central core. A small percentage (up to 10 %) of retinoblastomas shows photoreceptor differentiation in the form of fleurettes. These are groups of cells with short cytoplasmic processes, abundant cytoplasm, and small round nuclei similar to photoreceptors (Fig. 14.7f).

In eyes enucleated after chemotherapy multiple sections may be necessary to identify foci of viable tumor.

There are two major routes of tumor extension: choroidal invasion and optic nerve invasion. The latter is the most common. The size of the tumor is not always the defining factor, as small tumors may invade the optic nerve.

Optic nerve invasion (Fig. 14.8a) can be divided into prelaminar, laminar, retrolaminar forms, according to the level of invasion of the lamina cribrosa. The most extensive spread occurs in cases where there is tumor at the surgical margin. Prelaminar invasion (only in the optic nerve head) carries the same prognosis as lack of optic nerve invasion [41]. The lamina cribrosa is the equivalent of the sclera, so that retrolaminar invasion is considered extraocular extension and carries a poor prognosis. The outcome is worse if there is tumor in the resection margin. The tumor may also extend into the subarachnoid space and thus disseminate into the cerebrospinal fluid and meninges of the brain and the spinal cord [41–44].

The second major route of invasion is into the choroid (Fig. 14.8b). Significant or massive choroidal invasion is considered to be present when the maximum diameter (thickness or width) of invasive focus of tumor measures ≥3 mm. As a useful landmark, this usually occurs when most of the tumor reaches at least the inner fibers of the sclera. From there, the tumor may progress to the orbital soft tissues. Extraocular extension occurs within 6 months if retinoblastoma is left untreated. Focal choroidal invasion is defined as tumor focus <3 mm in any diameter and not reaching the sclera. The tumor may progress to invade the sclera (Fig. 14.8c) or invade the iris and anterior chamber (Fig. 14.8d). Artifactual tumor seeding is commonly seen after retrieval of fresh tumor tissue for molecular genetics; it must be recognized in order to avoid over diagnosing choroidal invasion. Artifactual seeding generally appears as small groups of tumor cells inside natural spaces of the eye like the vascular choroidal space, the suprachoroidal space, the anterior chamber, or the subarachnoid space of the optic nerve. In contrast, true tumor invasion occurs as a solid nest of tumor cells with a pushing edge or infiltrating borders that expand and replace the invaded area [2].

Extraocular extension substantially increases the risk of hematogenous or lymphatic spread (Table 14.6). Metastatic disease is associated with poor prognosis. Several multivariate analyses have suggested correlation between certain histopathological features and prognostic risk factors. The two most important prognostic indicators are the presence of post laminar optic nerve invasion, especially at the resection margin and extrascleral extension [41–46]. Superficial invasion of the optic nerve is associated with a mortality rate of 10 %; laminar extension has a 29 % mortality rate, post laminar tumor is associated with 42 % of mortality rate, and tumor in the optic nerve margin is associated with a mortality rate of 80 %. Massive but not focal choroidal invasion increases the possibility of hematogenous spread. Other factors associated with poor prognosis include extensive ocular tissue and tumoral necrosis (>95 % of the tumor) [47]. Neovascularization of the iris and secondary glaucoma [48] are more common in cases that have other high risk factors [49].

Other Intraocular Tumors

Retinoma

Retinomas (or retinocytomas) are benign retinal tumors that do not progress, and are clinically found in 2 % of persons carrying a mutant *RB1* gene. The genetic abnormalities in retinomas appear to be essentially the same as those for retinoblastoma [50]. Histologically, the tumor cells contain uniform small nuclei and are enmeshed in an eosinophilic fibrillary background lacking mitoses or necrosis. Immunoreactivity for GFAP and S100 is often present. According to Dimaras et al. [51], clinical, histological, and molecular features (notably identical *RB1* mutations in retinomas adjacent to retinoblastomas), are key observations

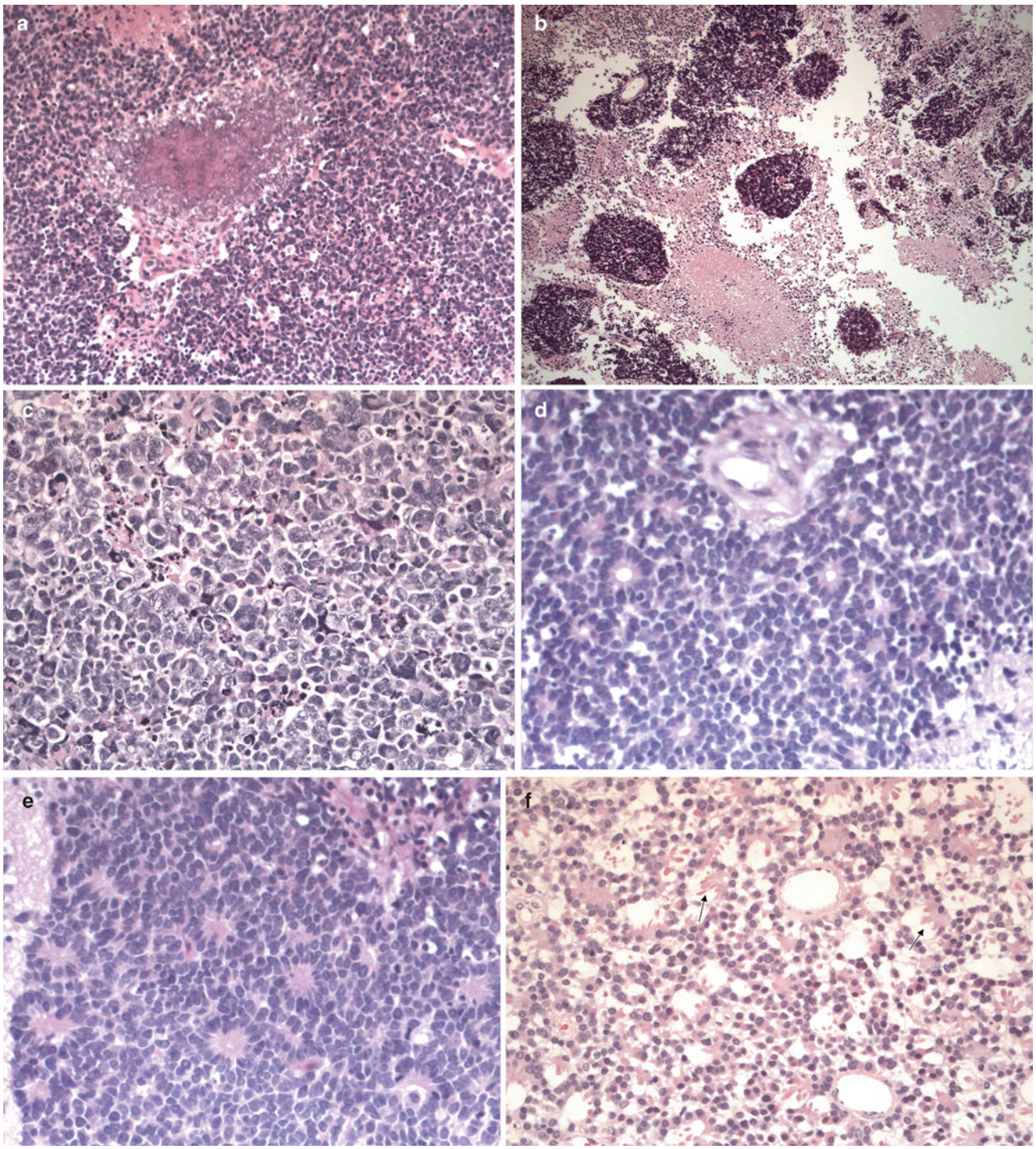

Fig. 14.7 Histological features of retinoblastoma. (**a**) Retinoblastoma composed of sheets of small round cells with scant cytoplasm and in this field showing little architectural patterning. A focal area of mineralisation is seen centrally and there is a small area of confluent necrosis towards the top left corner. Numerous apoptotic tumor cells are present. (**b**) Retinoblastoma showing large areas of necrosis with surviving islands of viable tumor cells around blood vessels. (**c**) Retinoblastoma showing a relatively uncommon appearance with sheets of large pleomorphic cells. This does not change the prognosis. Apoptotic cells are abundant. (**d**) Flexner–Wintersteiner rosettes showing an empty center surrounded by a well-defined border similar to the outer limiting membrane in the normal retina. (**e**) Homer Wright rosettes with cytoplasmic processes in the center and without a central lumen. (**f**) Fleurettes (*arrows*) showing photoreceptor differentiation. Typically, short runs of nuclei are bordered on one side by stubby eosinophilic processes reminiscent of photoreceptor inner and outer segments

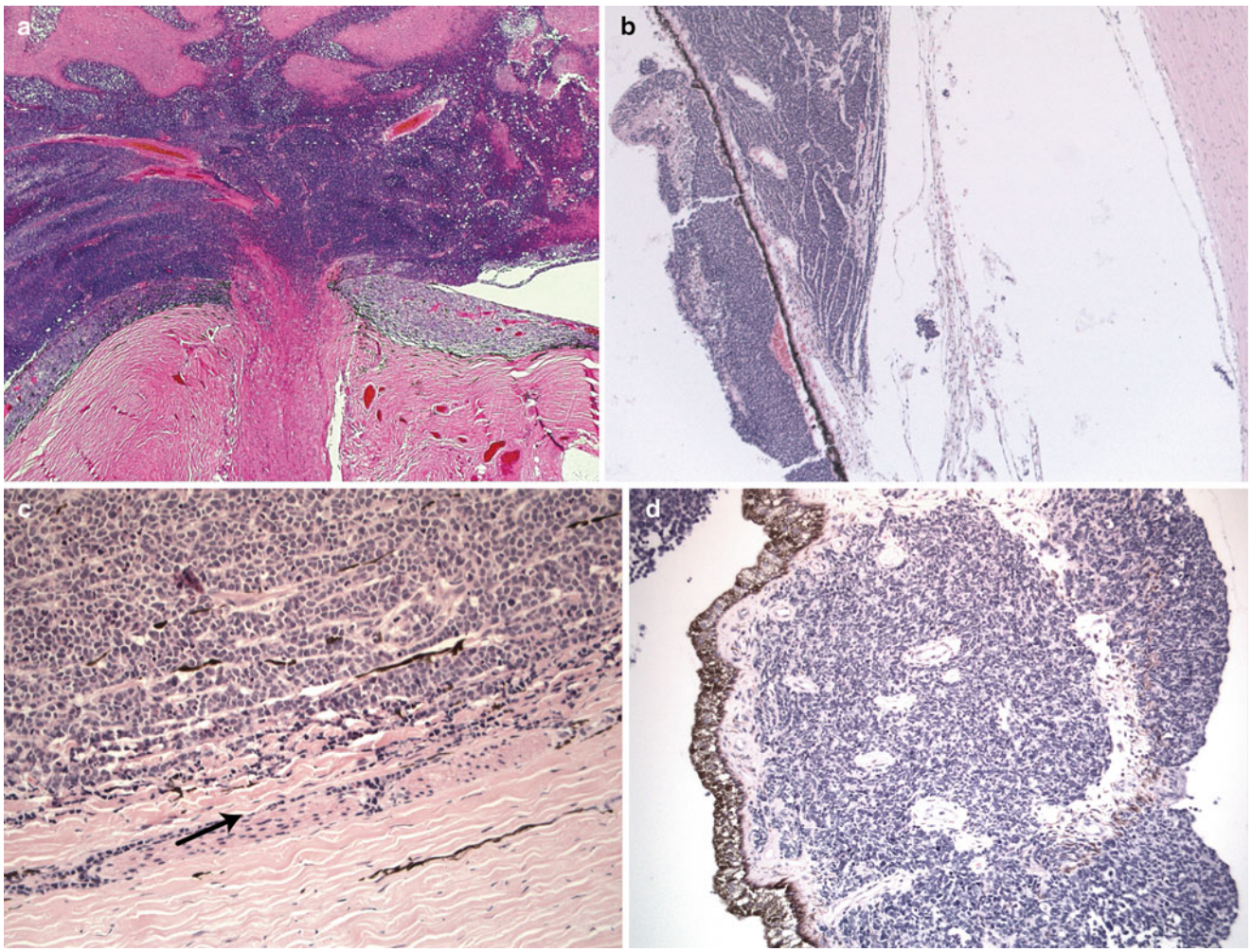

Fig. 14.8 Patterns of local spread of retinoblastoma. (**a**) A low power photomicrograph showing a large retinoblastoma superiorly that extends into the optic nerve head. The optic nerve extends inferiorly and is bounded on either side by sclera. (**b**) Towards the left of the figure the retina is almost totally replaced by retinoblastoma. Much of the retinal pigment epithelium is intact but beneath this, towards the *center* and *right* of the figure, there is extensive tumor spread throughout much of the choroid. Note that this is truly in the choroid and not between the retinal pigment epithelium and Bruch's membrane. There is a large artifactual space between the outer choroid and inner sclera which is at the right hand side of the figure. (**c**) Tumor extends into inner scleral laminae and around a small scleral nerve. (**d**) In this figure, tumor extends through much of the iris stroma. The iris pigment epithelium is on the *left* of the figure

Table 14.6 Routes of retinoblastoma dissemination

A. Direct tumor infiltration
a) Optic nerve to brain
b) Choroid to orbit (soft tissues and bone)
B. Invasion through subarachnoid space of the optic nerve
a) Opposite optic nerve
b) CSF (brain and spinal cord)
C. Hematogenous spread
a) Lung
b) Bones
D. Lymphatic dissemination (from conjunctiva and skin)

supporting the hypothesis of the clonal development of retinoma to retinoblastoma, following further mutational events. There has been much speculation in the literature about regression of retinoblastoma. It seems more likely that retinomas form de novo and may progress to retinoblastoma [49].

Imaging Features

The imaging appearances of retinocytoma have not been described.

Medulloepithelioma

Medulloepithelioma is an exceedingly rare tumor that presents at an age to similar retinoblastoma but instead most often arises from the ciliary epithelium. It may, however, arise from other intraorbital sites. Unlike retinoblastoma, there is no clear inheritance pattern with medulloepithelioma. The term "diktyoma" is synonymous

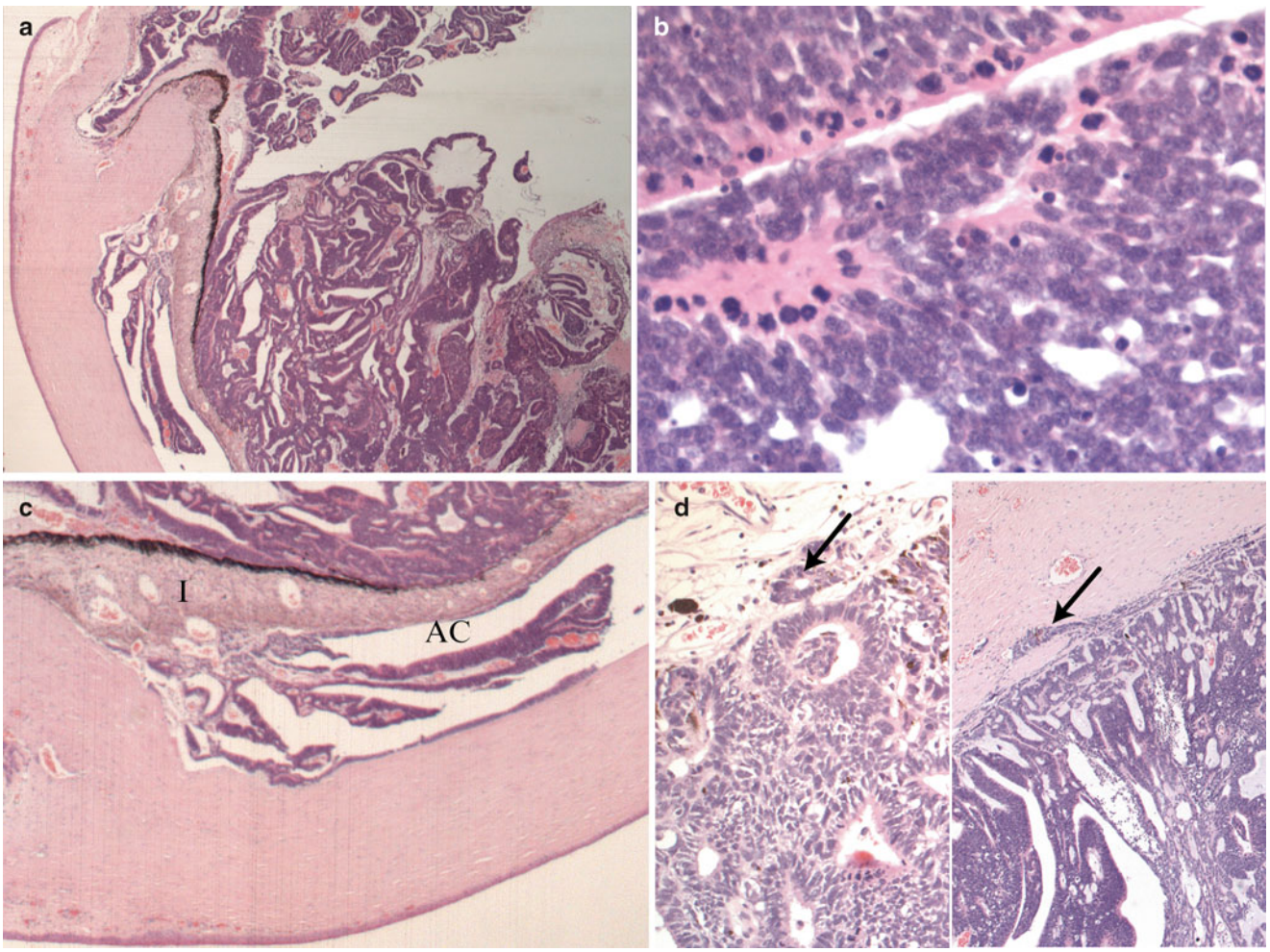

Fig. 14.9 Medulloepithelioma. (**a**) This low power photomicrograph shows cornea and abnormal anterior segment structures on the *left*. Most of the field is occupied by a small blue round cell tumor characterized by the presence of numerous cyst–like spaces and clefts, some of which contain mucin. (**b**) Some areas may resemble retinoblastoma with sheets of undifferentiated round blue cells. (**c**) Tumor invading the iris and in the anterior chamber. (**d**) Focal areas of choroidal and stromal invasion

with medulloepithelioma but is now rarely used. The more anterior location of many medulloepitheliomas implies that they may present with an anterior tumor mass involving the iris more often than retinoblastoma. There is a high risk of associated glaucoma [52]. Both macroscopically and histologically, medulloepitheliomas area characterized by the presence of multiple neuroepithelial cysts that often contain hyaluronic acid (Fig. 14.9 a–d). There is a range of behavior and associated histological appearances from benign to malignant. Some cases contain heterologous elements from other tissues (the so-called teratoid variant) [53]. Even "benign" forms tend to continue to grow unless completely excised. Malignant medulloepitheliomas that are completely removed have a good prognosis, but once extraocular spread has taken place, local spread or metastatic disease may prove fatal [54]. An association between ciliary body medulloepithelioma and pleuropulmonary blastoma has been described [55].

Imaging Features

Medulloepithelioma is a non-pigmented, vascular mass that typically arises from and is localized to the ciliary body. Rarely these tumors arise in the optic nerve or retina. Similar to the development of primitive medullary epithelium, from which they arise, these tumors develop a pattern of folded cords and sheets resembling a fisherman's net, also referred to as the diktyomatous pattern. Some folds surround fluid collections composed of hyaluronic acid like vitreous humor, while other folds have no fluid between them. The fluid collections appear as clinically visible cysts that are also apparent on imaging. Thirty to 50 % of medulloepitheliomas are classified as teratoid and contain heteroplastic elements including small dystrophic calcification that is typically coarser than the fine microcalcifications seen in retinoblastoma [3, 10]. These features, in addition to the older age of the patient at presentation, are useful in distinguishing

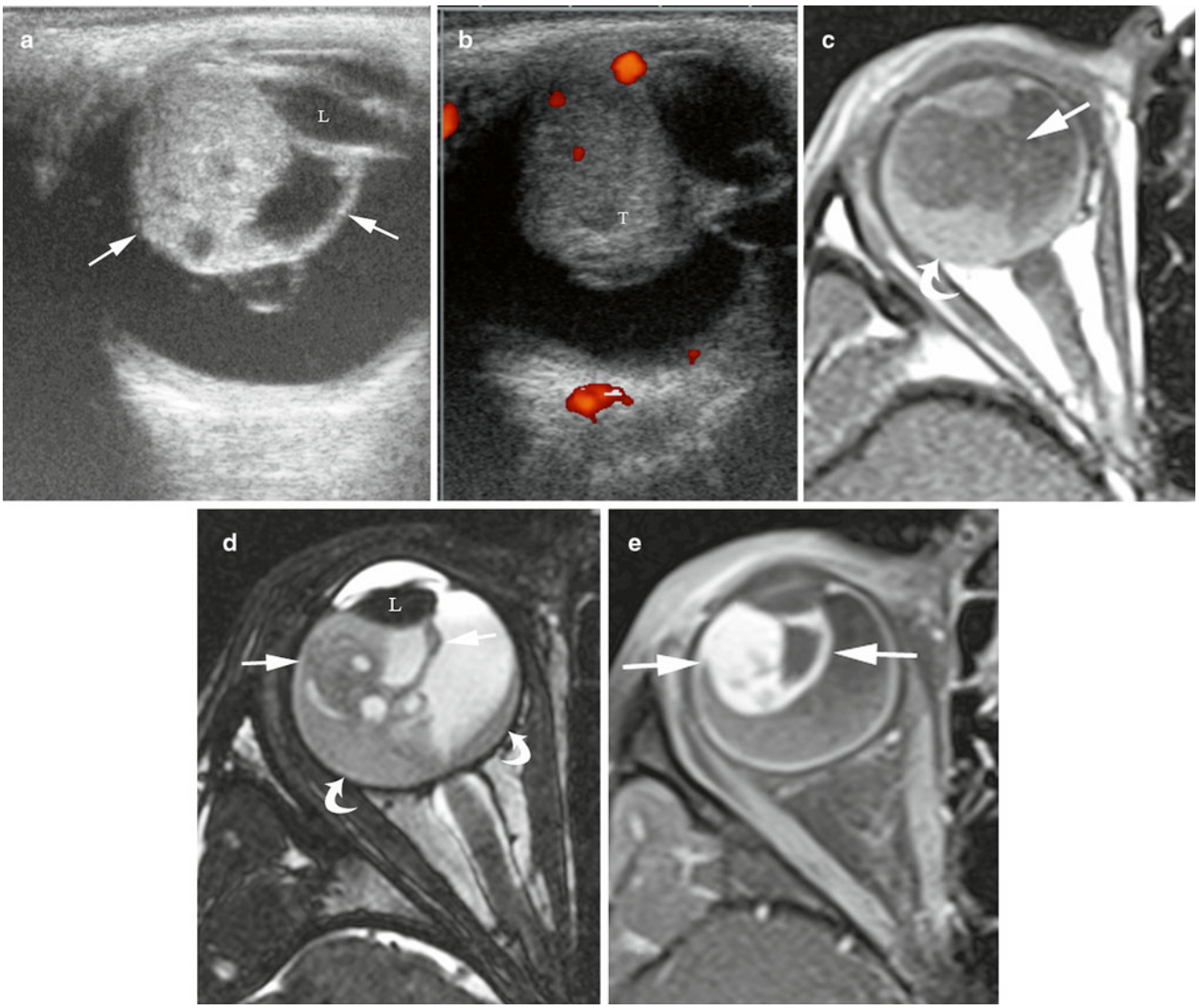

Fig. 14.10 A 5-year-old boy presented with leukocoria and exotropia of the right eye, subsequently diagnosed with medulloepithelioma, non-teratoid type. (**a**) Transverse US image shows the solid and cystic nature of the tumor (*arrows*) and characteristic location in the area of the ciliary body and abutting the posterior lens surface (L). (**b**) Doppler US shows internal blood flow (red foci) typical of this vascular tumor (T). No calcification was appreciated by US consistent with the non-teratoid histology. Lack of calcification would be atypical of retinoblastoma and is a feature that can help distinguish between these tumors. (**c**) Tumor is barely evident (*straight arrow*) on this non-contrast enhanced T1W MRI. There is detached retina and a large proteinaceous subretinal fluid collection (*curved arrow*). (**d**) The solid and cystic nature of the tumor (*straight arrows*) is more evident on this CISS MR image. Detached retina and subretinal fluid are again noted (*curved arrows*). Note again the classic location of tumor in the area of the ciliary body and abutting the posterior lens surface (L). (**e**) T1W post-contrast enhanced axial MR image. Note intense enhancement of the solid component of the tumor (*arrows*) which is a typical feature of medulloepithelioma

medulloepithelioma from retinoblastoma on imaging. The rare tumors that arise in the optic nerve or retina and contain calcification can mimic retinoblastoma on imaging [5]. Associated retinal detachment is common in both medulloepithelioma and retinoblastoma. Local spread of medulloepithelioma can occur posteriorly along the uveal tract or anteriorly along the posterior aspect of the lens [10]. Distant metastasis is rare.

Ultrasound

On US, medulloepithelioma is typically localized to the area of the ciliary body, adjacent to the iris and lens. Tumors appear as an irregularly shaped or ovoid, slightly echogenic soft-tissue mass that typically contains numerous small cystic spaces (Fig. 14.10a, b).

About 30 % of medulloepitheliomas will contain dystrophic calcification that forms hyperechoic foci with posterior

shadowing on US imaging. Because these are highly vascular tumors, intra tumoral blood flood should be evident on Doppler evaluation (Fig. 14.10b).

Magnetic Resonance Imaging

MRI will typically demonstrate a solid mass with cystic components, usually arising from the ciliary body (Fig. 14.10c, d). The solid component of tumor will be slightly or moderately hyperintense to vitreous on T1W imaging and hypointense on T2W images (Fig. 14.10c, d). These vascular tumors generally enhance markedly on MRI after contrast administration (Fig. 14.10e) [3, 5, 10].

Miscellaneous Rare Tumors

Uncommon intraocular tumors and tumor-like lesions in children include melanomas of the iris [56], choroid [57], and uvea [58], schwanomma [59], retinal PNET [60], yolk sac tumor [61], rhabdomyoma [62], ciliary leiomyoma [63], lymphoma [64], post-transplant lymphoproliferative disorder [65], and metastases [66].

References

1. Hoar RM. Embryology of the eye. Environ Health Perspect. 1982;44:31–4.
2. Sastre X, Chantada GL, Doz F, et al. Proceedings of the consensus meetings from the International Retinoblastoma Staging Working Group on the pathology guidelines for the examination of enucleated eyes and evaluation of prognostic risk factors in retinoblastoma. Arch Pathol Lab Med. 2009;133:1199–202.
3. Chung EM, Murphy MD, Specht CS, Cube R, Smirniotopoulos JG. From the archives of the AFIP: pediatric orbit tumors and tumorlike lesions: neuroepithelial lesions of the ocular globe and optic nerve. Radiographics. 2007;27:1159–86.
4. de Graaf P, Goricke S, Rodjan F, et al. Guidelines for imaging retinoblastoma: imaging principles and MRI standardization. Pediatr Radiol. 2012;42:2–14.
5. Brennan RC, Wilson MW, Kaste S, Helton KJ, McCarville MB. US and MRI of pediatric ocular masses with histopathological correlation. Pediatr Radiol. 2012;42:738–49.
6. Kaste SC, Jenkins 3rd JJ, Pratt CB, Langston JW, Haik BG. Retinoblastoma: sonographic findings with pathologic correlation in pediatric patients. AJR Am J Roentgenol. 2000;175:495–501.
7. Ramji FG, Slovis TL, Baker JD. Orbital sonography in children. Pediatr Radiol. 1996;26:245–58.
8. NEMA Standard Publication UD 3-2004. Standard for real-time display of thermal and mechanical acoustic output indices on diagnostic ultrasound equipment, rev. 2. 2009. http://www.nema.org/stds/ud3.cfm. Accessed August 13, 2010.
9. de Graaf P, Barkhof F, Moll AC, et al. Retinoblastoma: MR imaging parameters in detection of tumor extent. Radiology. 2005;235:197–207.
10. Mahajan A, Crum A, Johnson MH, Materin MA. Ocular neoplastic disease. Semin Ultrasound CT MR. 2011;32:28–37.
11. Goddard AG, Kingston JE, Hungerford JL. Delay in diagnosis of retinoblastoma: risk factors and treatment outcome. Br J Ophthalmol. 1999;832:1320–3.
12. Stiller CA, Parkin DM. Geographic and ethnic variations in the incidence of childhood cancer. Br Med Bull. 1996;52:682–703.
13. Fletcher O, Easton D, Anderson K, Gilham C, Jay M, Peto J. Lifetime risks of common cancers among retinoblastoma survivors. J Natl Cancer Inst. 2004;96:357–63.
14. Knudsson Jr AG. Mutation and cancer: statistical study of retinoblastomas. Proc Natl Acad Sci. 1971;68:820–3.
15. Cavenee WK, Dryja TP, Phillips RA, et al. Expression of recessive alleles by chromosomal mechanisms in retinoblastomas. Nature. 1983;305:779–84.
16. Friend SH, Bernards R, Rogeli S, et al. A human DNA segment with properties of the gene that predisposes to retinoblastoma and osteosarcoma. Nature. 1986;323:643–6.
17. MacPherson D, Conkrite K, Tam M, Mukai S, Mu D, Jacks T. Murine bilateral retinoblastoma exhibiting rapid onset, metastatic progression and N-myc gene amplification. EMBO J. 2007;26:784–94.
18. Corson TW, Gallie BL. One hit, two hits, three hits more? Genomic changes in the development of retinoblastoma. Genes Chromosomes Cancer. 2007;46:617–34.
19. Du W, Pogoriler J. Retinoblastoma family genes. Oncogene. 2006;25:5190–200.
20. Chen D, Gallie BL, Squire JA. Minimal regions of chromosomal imbalance in retinoblastoma detected by comparative genomic hybridization. Cancer Genet Cytogenet. 2001;129:57–63.
21. Marchong MN, Chen D, Corson TW, et al. Minimal 16q genomic loss implicates cadherin-11 in retinoblastoma. Mol Cancer Res. 2004;2:495–503.
22. Chakraborty S, Khare S, Doriairaj SK, Prabhakaran VC, Prakash DR, Kumar A. Identification of genes associated with tumorigenesis of retinoblastoma by microarray analysis. Genomics. 2007;90:344–53.
23. Dimaras H, Coburn B, Pajovic S, Gallie BL. Loss of p75 neurotropin receptor expression accompanies malignant progression to human and murine retinoblastoma. Mol Carcinog. 2006;45:333–43.
24. Motegi T, Kaga M, Yanagawa Y, et al. A recognizable pattern of the mid-face of retinoblastoma patients with interstitial deletion of 14q. Hum Genet. 1983;64:160–2.
25. Sippel KC, Fraioli RE, Smith GD, et al. Frequency of somatic and germ-line mosaicism in retinoblastoma: implications for genetic counseling. Am J Hum Genet. 1998;62:610–9.
26. Houdayer C, Gauthier-Villars M, Laugé A, et al. Comprehensive screening for constitutional RB1 mutations by DHPLC and QMPSF. Hum Mutat. 2004;23:193–202.
27. Mathew L, Miale TD, Rao S, Lobel SA, Fishman GA, Goldberg MF. Retrospective analysis of 58 children with retinoblastoma. Ophthalmic Paediatr Genet. 1984;4:67–74.
28. Essuman V, Ntim-Amponsah CT, Akafo S, Renner L, Edusei L. Presentation of retinoblastoma at a paediatric eye clinic in Ghana. Ghana Med J. 2010;44:10–5.
29. Gombos DS, Hungerford J, Abramson DH, et al. Secondary acute myelogenous leukemia in patients with retinoblastoma: is chemotherapy a factor? Ophthalmology. 2007;114:1378–83.
30. Mahajan S, Juneja M, George T. Osteosarcoma As a second neoplasm after chemotherapeutic treatment of hereditary retinoblastoma: a case report. Quintessence Int. 2008;39:439–45.
31. Marees T, van Leeuwen FE, Schaapveld M, et al. Risk of second malignancy in survivors of retinoblastoma: more than 40 years of follow-up. J Natl Cancer Inst. 2008;100:1771–9.
32. Kleinerman RA, Tarone RE, Abramson DH, Seddon JM, Li FP, Tucker MA. Hereditary retinoblastoma and risk of lung cancer. J Natl Cancer Inst. 2000;92:2037–9.

33. Kleinerman RA, Tucker MA, Tarone RE, et al. Risk of new cancers after radiotherapy in long-term survivors of retinoblastoma: an extended follow-up. J Clin Oncol. 2005;23:2272–9.
34. Kleinerman RA, Tucker MA, Abramson DH, Seddon JM, Tarone RE, Fraumeni Jr JF. Risk of soft tissue sarcomas by individual subtype in survivors of hereditary retinoblastoma. J Natl Cancer Inst. 2007;3(99):24–31.
35. Klein EA, Anzil AP, Mezzacappa P, Borderon M, Ho V. Sinonasal primitive neuroectodermal tumor arising in a long-term survivor of heritable unilateral retinoblastoma. Cancer. 1992;70:423–31.
36. Antoneli CB, Ribeiro K, Sakamoto LH, Chojniak MM, Novaes PE, Arias VE. Trilateral retinoblastoma. Pediatr Blood Cancer. 2007;48:306–10.
37. Reese AB, Ellsworth RM. The evaluation and current concept of retinoblastoma therapy. Trans Am Acad Ophthalmol Otolaryngol. 1963;67:164–72.
38. Kiss S, Leiderman YI, Mukai S. Diagnosis, classification and treatment of retinoblastoma. Int Ophthalmol Clin. 2008;48:135–47.
39. Shields CL, Shields JA. Retinoblastoma management: advances in enucleation intravenous chemoreduction and intra-arterial chemotherapy. Curr Opin Ophthalmol. 2010;21:203–12.
40. Chantada G, Doz F, Antoneli CB, et al. A proposal for an international retinoblastoma staging system. Pediatr Blood Cancer. 2006;47:801–5.
41. Chantada GL, Guitter MR, Fandiño AC, et al. Treatment results in patients with retinoblastoma and invasion of the cut end of the optic nerve. Pediatr Blood Cancer. 2009;52:218–22.
42. MacLean IW, Burnier M, Zimmerman L, Jakobiec F. Tumors of the retina. In: MacLean IW, Burnier M, Zimmerman L, Jakobiec F, editors. Atlas of tumor pathology. Tumors of the eye and ocular adnexa. Washington DC: Armed Forces Institute of Pathology; 1994. p. 100–35.
43. Hurwitz RL, Chévez-Barrios P, Chintagumpala M, Shields C, Shields J. Retinoblastoma. In: Pizzo PA, Poplack D, editors. Principles and practice of pediatric oncology. 4th ed. Philadelphia, Pa: Lippincott-Raven; 2002. p. 825–46.
44. Chévez-Barrios P, Eagle RC, Marbach P. Histological features and risks for metastatic spread of retinoblastoma. In: Singh AD, Damato B, Peter J, Murphree AL, Perry JD, editors. Clinical ocular oncology. London: Elsevier-Saunders; 2007. p. 6–77.
45. Gupta R, Vemuganti GK, Reddy VA, Honavar SG. Histopathologic risk factors in retinoblastoma in India. Arch Pathol Lab Med. 2009;133:1210–4.
46. Karcioglu ZA, Mesfer SA, Abboud E, Jabak MH, Mullaney PB. Workup for metastatic retinoblastoma. A review of 261 patients. Ophthalmology. 1997;104:307–12.
47. Chong EM, Coffee RE, Chintagumpala M, Hurwitz RL, Hurwitz MY, Chévez-Barrios P. Extensively necrotic retinoblastoma is associated with high-risk prognostic factors. Arch Pathol Lab Med. 2006;130:1669–72.
48. Baez KA, Ulbig MW, Cater J, Shields CL, Shields JA. Iris neovascularization, increased intraocular pressure and vitreous hemorrhage as risk factors for invasion of the optic nerve and choroid in children with retinoblastoma. Ophthalmologe. 1994;91:796–800.
49. Eagle Jr RC. High-risk features and tumor differentiation in retinoblastoma. A retrospective histopathologic study. Arch Pathol Lab Med. 2009;133:1203–9.
50. Abouzeid H, Schorderet DF, Balmer A, Munier FL. Germline mutations in retinoma patients: relevance to low-penetrance and low-expressivity molecular basis. Mol Vis. 2009;15:771–7.
51. Dimaras H, Khetan V, Halliday W, et al. Loss of RB1 induces non-proliferative retinoma: increasing genomic instability correlated with progression of retinoblastoma. Hum Mol Genet. 2008;17:1363–72.
52. Shields CL, Shields JA, Shields MB, Augsburger JJ. Prevalence and mechanisms of secondary intraocular pressure elevations in eyes with intraocular tumors. Ophthalmology. 1987;94:839–46.
53. Lloyd 3rd WC, O'Hara M. Malignant teratoid medulloepithelioma: clinical-echographic-histopathologic correlation. JAAPOS. 2001;5:395–7.
54. Saunders T, Margo CE. Intraocular medulloepithelioma. Arch Pathol Lab Med. 2012;136:212–6.
55. Priest JR, Williams GM, Manera R, et al. Ciliary body medulloepithelioma: four cases associated with pleuropulmonary blastoma—a report from the International Pleuropulmonary Blastoma Registry. Br J Ophthalmol. 2011;95:1001–5.
56. Shields CL, Kaliki S, Shah SU, Luo W, Furuta M, Shields JA. Iris melanoma: features and prognosis in 317 children and adults. JAAPOS. 2012;16:10–6.
57. Fong A, Lee L, Glasson W. Pediatric choroidal melanoma in a 13 year old girl—a clinical masquerade. JAAPOS. 2011;15:305–7.
58. Grabowska A, Abelarias J, Peralta J, et al. Uveal melanoma in a 19-month-old child. JAAPOS. 2011;15:606–8.
59. Venturini G, Moulin AP, Deprez M, et al. Clinicopathologic and molecular analysis of choroidal pigmented schwanomma in the context of a PTEN hamartoma tumor syndrome. Ophthalmology. 2012;119:857–64.
60. Grossniklaus HE, Sheahata B, Sorensen P, Bergstrom C, Hubbard GB. Primitive neuroectodermal tumor/Ewing sarcoma of the retina. Arch Pathol Lab Med. 2012;136:829–31.
61. Fujino T, Okamura A, Hatsukawa Y, Nakayama K, Inoue M, Nakayama M. A case of intraocular yolk sac tumor in a child and its pathogenesis. JAAPOS. 2009;13:613–5.
62. Davidson A, Desai F, Stannard C, Ivey A, Solomon R, Sinclair-Smith C. Intraocular rhabdomyosarcoma in the sibling of a patient with a cerebellar medulloepithelioma. J Pediatr Hematol Oncol. 2006;28:476–8.
63. Richter MN, Bechrakis NE, Stoltenburg-Didinger G, Foester MH. Trans-scleral resection of a ciliary body leiomyoma in a child: a case report and review of the literature. Graefess Arch Clin Exp Ophthalmol. 2003;241:953–7.
64. Sjo LD. Ophthalmic lymphoma: epidemiology and pathogenesis. Acta Ophthalmol 2009; 87; Thesis 1:1–20.
65. Fujita S, Fujnikawa T, Mekeel K, et al. Localized intraocular post-transplant lymphoproliferative disorder after pediatric liver transplantation. Transplantation. 2006;15:493–5.
66. Akhtar M, Ali MA, Sackey K, Bakry M, Johnson T. Malignant rhabdoid tumor of the kidney presenting as intraocular metastasis. Pediatr Hematol Oncol. 1991;8:33–43.

Malignant Tumors of Peripheral Nerves

15

Simon Ching-Shun Kao, David M. Parham, and Christine Fuller

Definition

Malignant peripheral nerve sheath tumors (MPNST) represent a group of malignant spindle cell sarcomas with evidence of nerve sheath differentiation and/or arising from a peripheral nerve. Tumors showing origin from epineurial connective tissue or vascular structures are not considered to represent MPNST. Older/prior terminology for MPNST includes malignant neurilemmoma, malignant schwannoma, neurofibrosarcoma, and neurogenic sarcoma [1]. A number of histologic subtypes have been described. The majority are high grade aggressive sarcomas that show a strong tendency for local recurrence and metastases despite aggressive therapeutic measures [2].

Clinical Features and Epidemiology

There is a strong association between MPNST and Neurofibromatosis Type 1 (NF1), with 50 % of all MPNSTs arising within this patient population [3]. Approximately 10 % of individuals with NF1 will develop an MPNST over their lifetime, most of these tumors representing malignant degeneration occurring within preexisting plexiform neurofibromas. One study of 476 NF1 patients documented a strong association between the presence of subcutaneous neurofibromas and internal plexiform neurofibromas, with an even stronger correlation between the presence of internal plexiform neurofibromas and MPNST [4]. The remainder of MPNSTs will arise de novo, approximately 5–10 % representing radiation-induced sarcomas [1]. There is no particular gender predilection, and MPNSTs have been documented throughout a wide age range including children and the elderly. The majority however tend to present in adults with a median age in the mid 40s [5]. MPNSTs arising in the NF1 population tend to present up to a decade earlier, and these patients' tumors also tend to be larger [3, 6].

The majority of MPNST arise from larger peripheral nerves or within deep soft tissues, the most frequent sites including brachial plexus, sciatic, and paraspinal nerves, proximal upper and lower extremities, and buttock regions [5]. They have also been documented in a wide variety of locations throughout the body. Well over 50 cases of spinal MPNST have been reported [7–13]. No particular spinal level is preferentially involved, and interestingly a significant proportion of spinal MPNST exhibit rhabdomyoblastic elements (Malignant Triton Tumor; see histologic description below) [14–17]. MPNST represents one of the most aggressive tumors that may involve structures of the head and neck region [6]. It may arise from cranial nerves, particularly the vestibular [18], vagus [18], facial [18, 19], and trigeminal [19, 20]. Other sites include not only brachial plexus [21], but also scalp and bony structures (base of skull [22–25], sinuses [26, 27], and bones of the jaw) [28, 29], as well as the parotid gland [30–32]. Case reports/small case series document cutaneous MPNSTs [33–35], a proportion of which apparently arose from underlying neurofibromas. Primary cardiac [36], hepatic [37], bile duct [38], colonic [39], uterine [40–42], breast [43, 44], renal [45], and intraosseous [46] MPNST have all been described. Though plexiform neurofibroma is by far the most frequent precursor lesion, MPNSTs have been found rarely arising from

S.C.-S. Kao, MBBS, DMRD, DABR (✉)
Department of Radiology, University of Iowa Healthcare, 200, Hawkins Drive, Iowa City, IA, USA
e-mail: simon-kao@uiowa.edu

D.M. Parham, M.D.
Department of Pathology and Laboratory Medicine, Children's Hospital Los Angeles/University of Southern California, 4650 Sunset Blvd., #43, Los Angeles, CA 90027, USA
e-mail: daparham@chla.usc.edu

C. Fuller, M.D.
Department of Pathology, Virginia Commonwealth University Health System, 1101 East Marshall St, PO Box 980662, Richmond, VA, USA
e-mail: cfuller@mcvh-vcu.edu

D.M. Parham et al. (eds.), *Pediatric Malignancies: Pathology and Imaging*,
DOI 10.1007/978-1-4939-1729-7_15, © Springer Science+Business Media New York 2015

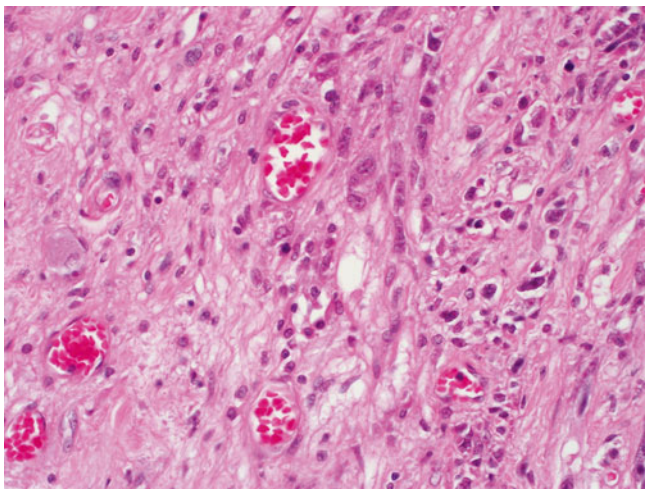

Fig. 15.1 MPSNT arising from ganglioneuroma. A ganglionic tumor with low grade schwannoma cell stroma segues into a high grade spindle cell neoplasm, X400

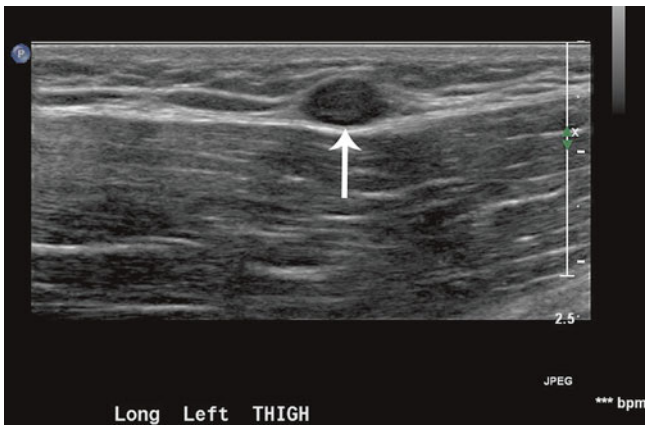

Fig. 15.2 Neurofibroma of left thigh in an 18-year-old boy. Longitudinal view of the thigh shows a focal hypoechoic mass (*arrow*) in the deep subcutaneous plane against the echogenic muscle fascia with homogeneous echotexture. Excision biopsy showed neurofibroma

ganglioneuroma (Fig. 15.1) [47], hybrid schwannoma/perineurioma [48], or schwannoma [18].

Patients with MPNST tend to be symptomatic, presenting with an enlarging mass, sometimes associated with neurologic symptoms (pain, sensory deficits, and weakness), dependent upon the underlying nerve involved. A rapidly enlarging mass that is mobile perpendicular to the course of a peripheral nerve or that yields a Tinel's sign on percussion is highly suspect for MPNST [1]. Likewise any enlarging mass detected within a patient with NF1 should be considered MPNST until proven otherwise.

Imaging Features

Imaging Features of Malignant Peripheral Nerve Sheath Tumors (MPNSTs)

Before describing the imaging features of MPNST, benign PNSTs (neurofibroma and schwannoma) are briefly discussed. Distinguishing imaging features of malignant versus benign tumors are emphasized.

Neurofibroma

Neurofibroma is a non-encapsulated benign peripheral nerve sheath tumor that has been described in three forms: localized, diffuse, and plexiform [49, 50]. Approximately 90 % are of the localized variety; most are superficial affecting cutis and sub-cutis. The diffuse form is uncommon, primarily affecting children and young adults, involving the subcutaneous tissues of the head and neck region, trunk, and extremity, showing a plaque-like elevation of the skin and thickening of the sub-cutis and may extend to the fascia over muscle [51]. The majority of both localized and diffuse forms is not associated with neurofibromatosis type 1 (NF-1), also known as von Recklinghausen's disease. However in the setting of NF-1, the neurofibromas tend to be larger, multiple, and deep in location. The plexiform form of neurofibroma is pathognomonic of NF-1, presenting usually in early childhood as a tortuous mass involving a long segment of a major nerve trunk and expanding into the nerve branches. It may be superficial or deep in location, exhibiting different MR imaging characteristics (see below). Fifty percent of plexiform neurofibromas occur in the head and neck, face, and larynx.

Plain Film Radiography

Plain radiography may show enlargement of neuroforamen when a dumb-bell shaped neurofibroma is involving a spinal nerve root.

Ultrasonography

High-resolution sonography of a neurofibroma shows a round homogeneous hypoechoic mass (Fig. 15.2) located centrally along the course of a peripheral nerve with distal acoustic enhancement, simulating a cystic lesion (pseudocystic appearance) [52, 53]. A sonographic target lesion with hypoechoic periphery and hyperchoic center may be seen, corresponding to myxomatous peripheral and fibrocollagenous central regions, respectively [53]. In diffuse neurofibromas, hyperechoic masses permeated by multiple interconnecting hypoechoic tubular or nodular structures have been reported in the subcutaneous fat zone. Differential diagnoses include cutaneous lymphoma, angiomatous lesions, cellulitis, and hemorrhage [54]. Sonography, even with duplex and color Doppler techniques, is not able to distinguish among neurofibromas, schwannomas, and malignant peripheral nerve sheath tumors [53, 55].

Fig. 15.3 Diffuse neurofibromas in a 14-year-old girl with neurofibromatosis type 1. Contrast-enhanced axial CT image of the pelvis shows a network of interconnecting soft tissues masses in both gluteal subcutaneous fat due to multiple neurofibromas

Computed Tomography

On CT, *localized* neurofibromas appear as a well-defined hypodense (compared with muscles) mass from the presence of Schwann cells (fat content of myelin), myxoid tissue (high water content), entrapment of fat, and cystic areas of hemorrhage or necrosis [56]. After intravenous contrast injection, over half of neurofibromas show little or no contrast enhancement (Fig. 15.3). Visible bony erosions associated with dumbbell tumors are seen with CT [57].

Magnetic Resonance Imaging

On MRI, a neurofibroma is spindle or ovoid in shape and is in contiguity with a specific nerve [58]. It shows low to intermediate signal intensity (or isointense to adjacent muscles) on T1W images and high signal intensity on T2W images. The high signal intensity on T2W images may be homogeneous or showing a characteristic "target sign" with a hyperintense periphery and a hypointense central region [59–61]. The high peripheral signal is related to myxoid and water contents and the central low signal is related to dense collagen and fibrillary tissues. It is important to use a wide window setting to allow demonstration of this sign [62]. After intravenous contrast, enhancement is inhomogeneous in two-thirds of cases and uniform in the rest. A neurofibroma is typically fusiform in shape with tapering ends contiguous with the parent nerve. When large, the tumor has a fascicular appearance (fascicular sign). A "split-fat" sign has been described when a neurofibroma originating from the nerve in an intramuscular location is surrounded by a rim of fat. Muscle atrophy may be seen in the muscle supplied by the nerve with neurofibroma. The *diffuse* form of neurofibroma presents as an ill-defined network of interconnecting neurofibromas extending through the involved subcutaneous tissue, showing low signal intensity on T1W images, high signal intensity on T2W images, and significant intravenous contrast enhancement on MR imaging. Prominent internal vascularity is common [51]. *Plexiform* neurofibromas, when deep, appear as hypodense multilobular masses within a major nerve distribution on CT scans and large conglomerate of masses of neurofibromas on MR imaging (Fig. 15.4). When superficial, plexiform neurofibromas in patients with NF-1 tend to be unilateral, have nontarget signal characteristics, exhibit a diffuse and infiltrative morphology, extend to the skin surface in a branching reticular fashion with small fascicles or nodules (Fig. 15.5), and can be mistaken for venous malformation by MR imaging [63–65].

Fig. 15.4 Deep plexiform neurofibromas in a 17-year-old boy. Coronal HASTE MRI imaging of the abdomen and pelvis shows a large conglomerate of masses in the right psoas muscle, most showing "target sign". Partial excisional biopsy of some of these masses shows "neurofibroma without evidence of malignant change"

Schwannoma (Neurilemmoma)

Schwannoma is an encapsulated (within the epineurium) nerve sheath tumor presenting as a slowly growing soft tissue mass involving nerve trunks in limbs, head and neck, posterior mediastinum, and retroperitoneum [49, 66]. The mass is usually painless unless large enough to compress the adjacent nerve. Those associated with NF-1 are usually multiple or plexiform. Schwannomas associated with neurofibromatosis type 2 (NF-2) tend to be central in location [57]. Larger lesions may undergo cystic degenerative changes, hemorrhage, calcification, and fibrosis.

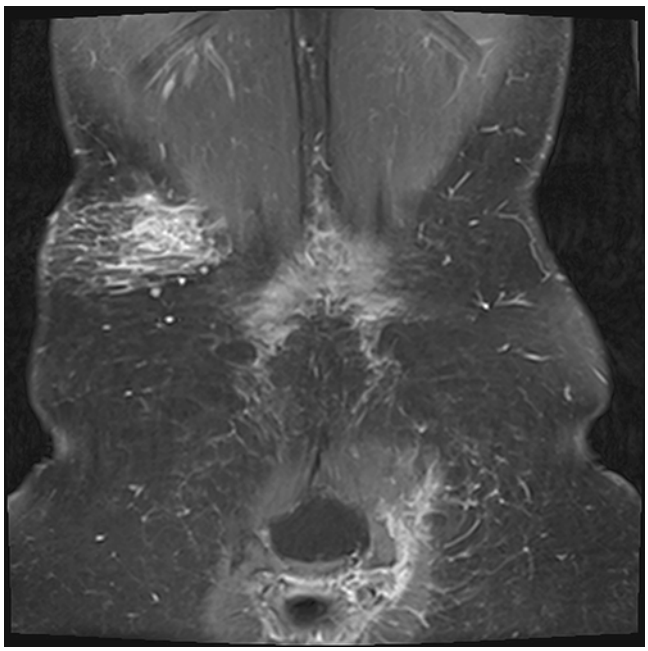

Fig. 15.5 Superficial plexiform neurofibromas in a 19-year-old female with neurofibromatosis type 1. Post-contrast coronal fat-saturated T1W MRI shows a diffuse infiltrative and reticular branching pattern of plexiform neurofibromas in the *right* flank and *left* gluteal regions

Plain Film Radiography

Plain radiography usually does not reveal the mass itself, but may show scalloping of bone adjacent to the tumor.

Ultrasonography

Ultrasonography may show, especially in large nerves, a mass eccentrically positioned with respect to the affected nerve. However, there may be limitations, even with meticulous scanning technique, in demonstrating this eccentric positioning in up to 40 % [55].

Computed Tomography

On CT scan, schwannoma appears as a well-defined isodense or hypodense mass compared to muscles and shows enhancement after IV enhancement except in necrotic areas. Scalloping of the adjacent bone and expansion of the spinal canal are characteristic features on CT (Fig. 15.6a, b).

Magnetic Resonance Imaging

MR imaging findings are similar to those described in neurofibromas, including a mass with a fusiform, spindle, or oval shape, in contiguity with a specific nerve, and showing a target sign, and "split-fat" sign. A mass eccentrically positioned in relation to the nerve and showing heterogeneity with cystic degenerative changes suggests a schwannoma [67]. A low signal peripheral rim (epineurium) is seen in 70 % of schwannomas versus in 30 % of neurofibromas [68–70]. The target sign in schwannoma is attributed to a central area of more cellular Antoni type A neurilemmoma and to a peripheral rim of hypocellular Antoni type B neurilemmoma [71].

Malignant Peripheral Nerve Sheath Tumor (MPNST)

Malignant peripheral nerve sheath tumor is a spindle cell sarcoma arising from a peripheral nerve or its attendant sheath or from a benign PNST [50]. It does not include tumor arising from the epineurium or the vasculature of the peripheral nerves [72]. Typically MPNSTs arise from preexisting plexiform neurofibromas. However it has been documented that 36 % of 34 MPNSTs from a cohort of 1475 NF-1 patients developed MPNSTs without a history of plexiform neurofibromas [73]. While 30-50 % of MPNST are associated with NF-1, only approximately 2–5 % of NF-1 patients develop MPNST [49, 67, 74–76]. Most tumors arise from nodular plexiform tumors

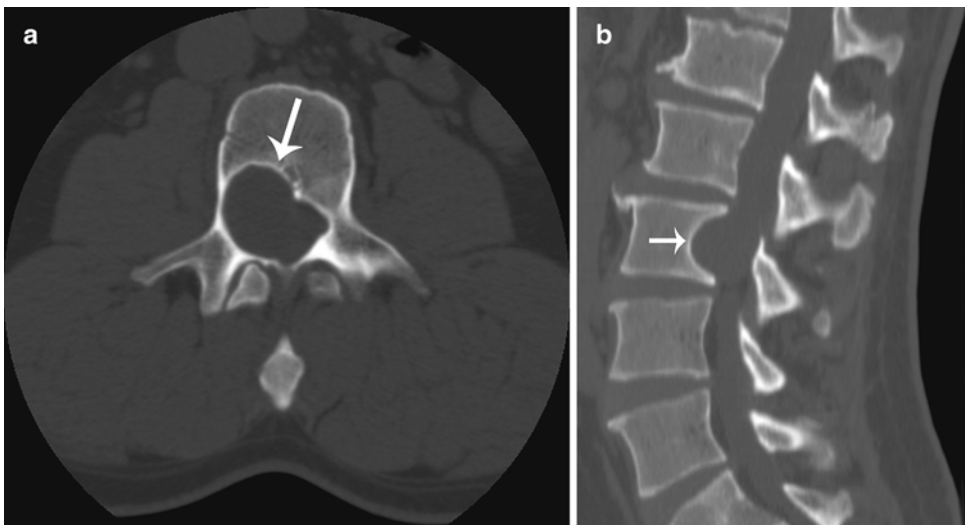

Fig. 15.6 Intraspinal schwannoma in a 33-year-old adult male with neurofibromatosis type 1. Axial (**a**) and sagittal (**b**) CT images of the lumbar spine show scalloping of the posterior right vertebral margin (*arrows*) at L3 level and expansion of the spinal canal

Fig. 15.7 Neurofibromatosis type 1 with neurofibroma progression to metastatic malignant peripheral nerve sheath tumor (MPNST). (**a**) Lateral plain radiograph of the thigh shows a soft tissue mass at distal posterior thigh. MRI of the thigh shows a large spindle-shaped posterior thigh mass with (**b**) inhomogeneous high signal intensities on fat-saturated T2W image, (**c**) inhomogeneous low signal intensities and "split-fat" sign (*arrows*) on T1W image, and (**d**) inhomogeneous enhancement on post-contrast fat-saturated T1W image. Biopsy of the mass showed a poorly differentiated MPNST arising within a neurofibroma. (**e**) Axial CT image shows multiple lung metastases

associated within major nerve trunks (such as brachial plexus sacral plexus, and sciatic nerve) and patients tend to be symptomatic presenting with pain, sensory deficits, and weakness. MPNSTs metastasize to the lung, liver, brain, regional lymph nodes, bone and soft tissues, skin, and retroperitoneum, and carry a poor prognosis [76].

Plain Film Radiography

Although often normal, plain radiography may show a soft tissue mass (Fig. 15.7a), secondary changes in adjacent bones (erosion or overgrowth), and is essential for evaluation of metastases to chest (lungs and pleura). Calcification (chondroid, osteoid, or amorphous) is uncommonly seen.

Ultrasonography

Sonography shows inhomogeneous hypoechoic masses that may have areas of hemorrhage, necrosis and calcifications [50]. A sonographic target sign is not present [53]. Duplex Doppler sonography shows a hypervascular pattern with corkscrew neovasculature, high velocities, and variable spectral waveforms [77].

Computed Tomography

Multi-detector CT (MDCT) may show abdominal primary tumor and metastases to the abdomen. On CT, MPNSTs are hypodense and ill-defined in outline with marginal enhancement after IV contrast medium.

Angiography

Angiography may show increased vascularity with characteristic corkscrew vessels at both ends of the tumor due to hypertrophy of the nutrient blood supplies to the nerve [71].

Magnetic Resonance Imaging

MPNSTs share MR imaging findings described above with benign peripheral neurogenic tumors. The involvement of the entering and exiting nerves results in the spindle shape of most MPNSTs . Although MRI can determine the site, extent, and change in size of plexiform neurofibromas, it does not reliably determine malignant changes [76, 78–80]. While any neurofibroma that rapidly increases in size in patients with NF-1 should be viewed with suspicion for malignant transformation, the growth rate of plexiform neurofibromas that give rise to MPNSTs is not a reliable predictor of malignancy. There may be periods of rapid growth, especially in adolescence, followed by periods of relative inactivity [81, 82]. Features that are concerning for malignancy include: tumor size over 5 cm in diameter, ill-defined margin, heterogeneity, intratumoral cystic changes, fat plane invasion or infiltration, absence of target or fascicular sign [59, 61, 62, 83], peritumoral edema, presence of peripheral enhancement, and history of having MPNST or previous radiation therapy (Figs. 15.7b–d, 15.8a–d). Only evidence of metastases (such as lung, pleura, bone, retroperitoneal node, and bone) is definitive for diagnosis of MPNSTs (Fig. 15.7e). While the split fat sign was present in 76.5 % of benign and larger PNSTs, only 33.3 % of MPNSTs showed this sign [58]. Whole body (head to feet) MRI with several table movement steps has been used in assessing the benign tumor burden in patients in NF-1 [84].

Nuclear Medicine Imaging

Bone scintigraphy may show findings indicating increased vascularity or mineralization and identify sites of bony metastases.

FDG-PET has recently proven to be useful in detecting metastatic and recurrent disease [85] and in the differentiation between benign and malignant peripheral nerve tumors using qualitative and semiquantitative SUV_{max} (maximum standardized uptake value) assessment [86, 87] (Fig. 15.8e–g). In patients with NF-1, FDG-PET is 95 % sensitive in the detection of MPNSTs. Because of the overlap in SUV_{max} for benign (ranging from 0 to 5.3, mean 1.5 ± 0.37) and malignant (ranging from 3.8 to 13.0, mean 8.5 ± 0.63) lesions, the addition of PET using 11C-methionine (measuring amino acid transport rate, protein synthesis, and cell proliferation in malignant tissues) has been found to improve specificity from 72 to 91 %[86]. In another series [87], no MPNSTs were detected with an SUV_{max} <2.5 and a small number of benign tumors had an SUV_{max} >3.5. Both benign and malignant peripheral nerve tumors had SUV_{max} between 2.5 and 3.5. The authors recommend that symptomatic neurofibromas with $SUV_{max} \geq 3.5$ should be excised, and lesions with SUV_{max} between 2.5 and 3.5 should be reviewed clinically. In another study, Son and colleagues found varying degrees of FDG uptake in a patient with multiple benign neurofibromas on PET-CT and concluded that a low SUV_{max} may indicate benignity, but a high SUV_{max} does not always indicate malignancy [88]. Using ROC analysis, Warbey et al. found a significant difference in SUV_{max} between early (90 min) and delayed (4 h) imaging and between tumor grades, and recommended using a cutoff SUV_{max} value of 3.5 on delayed imaging to achieve maximal sensitivity in diagnosing MPNST [89]. The overlap of SUV_{max} between different tumor grades, however, did not allow accurate prediction of grade on an individual basis. The authors suggest that tumors with an SUV_{max} in the 3.0–3.5 range should be clinically reviewed at multidisciplinary and multi-specialist management meetings. In another ROC analysis [90], using SUV_{max} thresholds of 4.5, 6.1, and 8.5 were associated with sensitivities of 100, 94, and 65 % and specificities of 83, 91, and 100 %, respectively, for detecting malignancy. The authors also found that benign schwannomas are less reliably distinguished from the MPNSTs based on the SUV_{max}. In a pediatric series of NF-1 and plexiform neurofibromas, Tsai found that the SUV_{max} of typical and atypical plexiform neurofibromas (2.49 [SD = 1.50]) was significantly different from MPNSTs (7.63 [SD = 2.96]). Using an SUV_{max} cutoff value of 4.0, sensitivity and specificity were 100 and 94 %, respectively for distinguishing plexiform neurofibromas and MPNSTs [91]. Nodular target lesions seen on MRI in patient with NF-1 and plexiform neurofibromas were found to have increased FDG uptake similar to that of MPNSTs, although they might be benign on biopsy [92]. Careful longitudinal clinical and imaging monitoring were recommended using MRI and FDG-PET to identify lesions of greatest concern to be biopsied. FDG-PET imaging can help in guiding targeted needle core biopsy of PNSTs [90], directing biopsy to the more metabolically active areas of the tumor. A newer tracer with 18 F-thymidine, which detects DNA turnover, may be useful in distinguishing low grade MPNSTs from active benign plexiform neurofibromas [76].

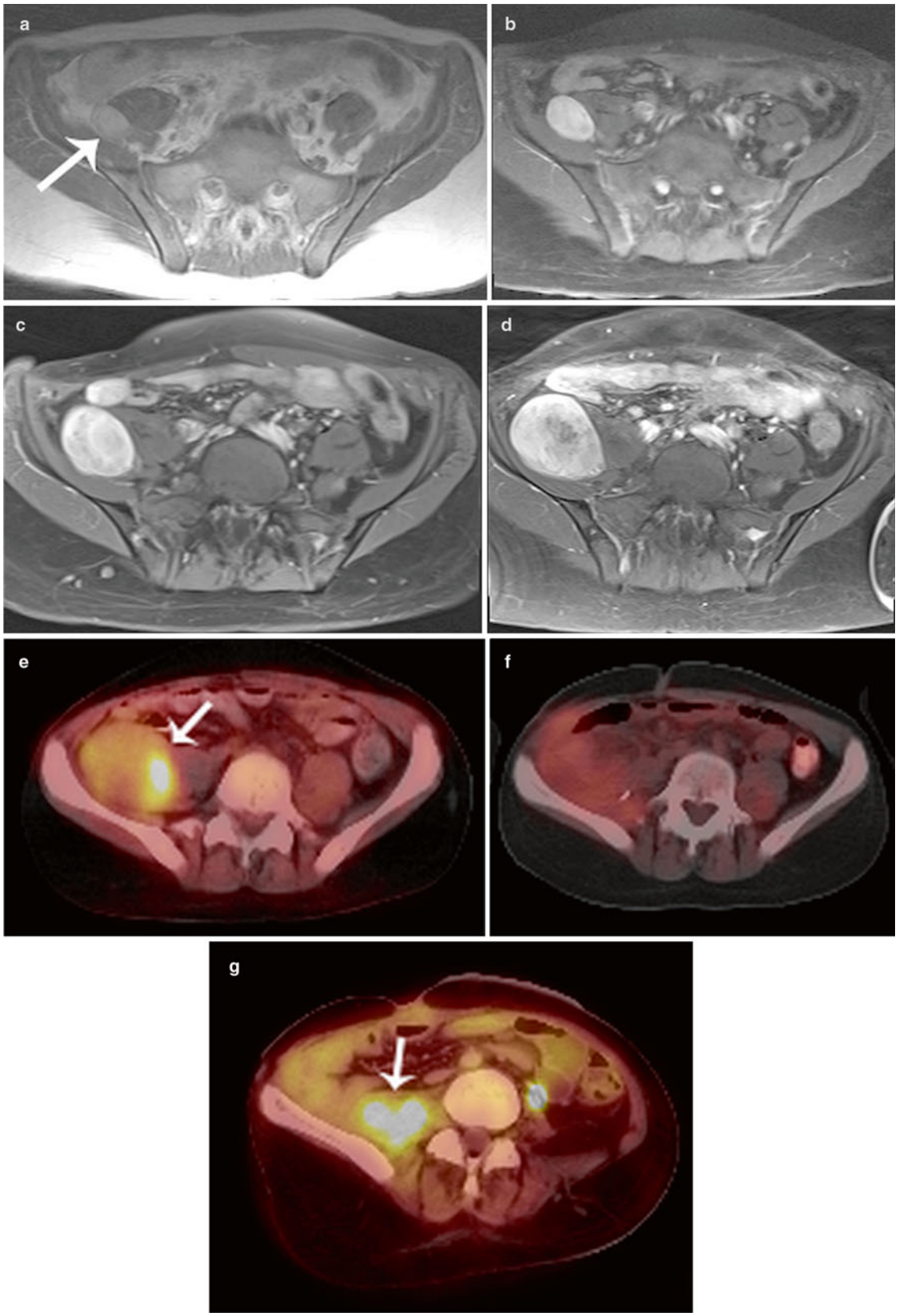

Fig. 15.8 Progression of neurofibromatosis type 1 first diagnosed in a 14-year-old girl over 5 years into a MPNST. Note progressive increase in size and inhomogeneity of enhancement of a right iliac fossa mass (*arrow*) from (**a**) 2005 (**b**) 2007 (**c**), 2009 and (**d**) 2010. ^{18}FDG-PET-CT scan in 2010 (**e**) shows a 4.5×6.7 cm mass with SUV $_{max}$ of 5.5 (*arrow*). Excisional biopsy revealed MPNST arising in neurofibroma. (**f**) Follow up $^{18FDG\text{-}PET\text{-}CT}$ scan in 2011 shows no residual tumor (SUV $_{max,}$ 2.0). (**g**) Subsequent follow up in 2012 showed recurrent biopsy-proved MPNST with SUV$_{max}$ of 5.6 (*arrow*)

Pathology

Gross and Microscopic Features

MPNST

The macroscopic appearance of MPNSTs is highly variable, ranging from large and ominous to subtle. Most will present similar to other soft tissue sarcomas as bulky fusiform or expansive tumors with variable infiltration into surrounding structures. They tend to be large tumors, averaging 6–10 cm in dimension, the majority >5 cm [2, 6]. Identifiable origination from a nerve may or may not be present. MPNSTs have a firm tan to grey interior with areas of hemorrhage and necrosis, similar to other aggressive sarcomas. A pseudocapsule typically represents tumor-infiltrated soft tissue, often with reactive features. At the other end of the spectrum, foci of MPNST arising within an underlying plexiform neurofibroma (malignant degeneration) may not be grossly visible at all, identifiable only at the microscopic level.

Classic / conventional MPNST may display a wide variety of architectural arrangements, frequently posing a significant diagnostic challenge given its resemblance to a number of other soft tissue tumors. The most frequent appearance is one of a hypercellular sarcoma with interwoven fascicles of spindle cells (Fig. 15.9) [93]. Other patterns include a fibrosarcoma-like herringbone pattern, hemangiopericytoma-like with staghorn vasculature, and alternating loose and dense cellular regions (similar to Antoni A and Antoni B regions in schwannomas) (Fig. 15.10) [2]. Perivascular condensation of tumor cells is another helpful feature [2]. Growth within nerve fascicles is also common, though invasion into surrounding tissues is typical. Individual tumor cells are spindle shaped with variable amounts of surrounding pink cytoplasm; nuclei tend to be wavy or indented with tapered ends [2]. Large zones of geographic necrosis are seen in over one half (Fig. 15.11), and mitotic figures are generally easy to find (Fig. 15.12), often numbering several per single high power field.

Fine needle aspiration cytology is being increasing employed in the diagnostic workup of soft tissue lesions, and our knowledge of the salient cytologic features of MPNST has become increasing refined over the past decade. Cytology aspirate smears of MPNST are typically hypercellular with a combination of cohesive cell clusters of variable size and cellularity together with numerous single tumor cells and naked nuclei [94, 95]. A fascicular pattern may be encountered in some cell clusters, though is not universally present; storiform or whorled patterns may also be encountered [30]. A fibrillary background may be present [95]. Individual tumor cells are spindle shaped with variable contour; they may be elongated with tapered ends, kinked, angulated, or comma-shaped [30, 94, 95]. Wavy nuclei, representing a

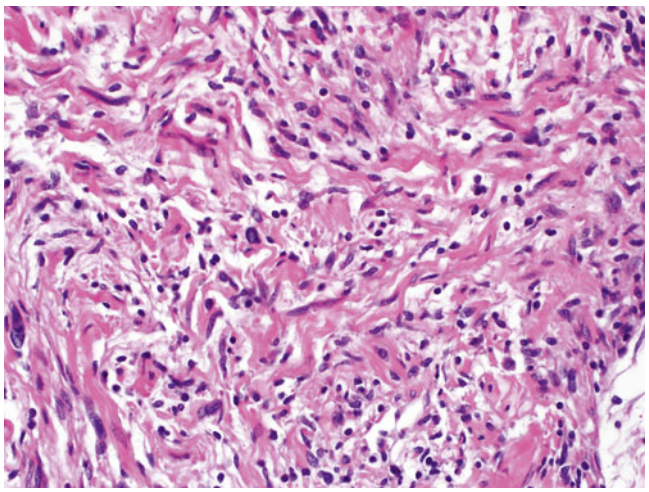

Fig. 15.9 MPNST, containing spindle cells arranged in interlacing bundles and containing tumor cells with hyperchromatic, enlarged nuclei and wavy contours, X400

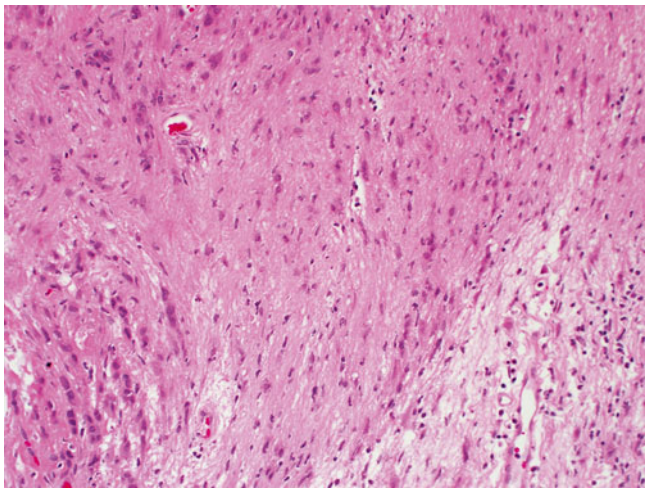

Fig. 15.10 MPNST with contrasting hypercellular and hypocellular zones, analogous to schwannoma, X200

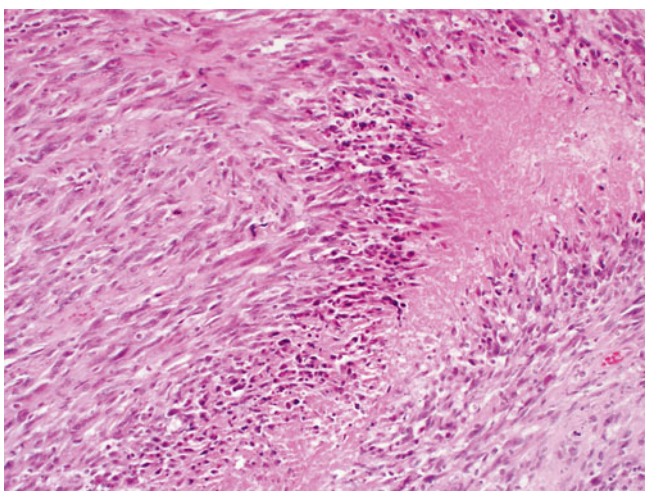

Fig. 15.11 MPNST with areas of geographic necrosis, X200

quite helpful diagnostic feature when detected, are inconsistently present in MPNST cytology samples [94, 95]. Nuclear pleomorphism is a frequent finding, as are mitotic figures (including atypical forms) [30, 95]. A "dirty" necrotic background material may be seen [30].

The majority (85 %) of MPNSTs are high grade sarcomas. As such, they show evidence of hypercellularity, invasion of surrounding tissues (often with vascular invasion), together with nuclear pleomorphism, elevated mitoses (generally >5 mitoses per 10 high power field), ± necrosis [1]. It is the presence of necrosis that distinguishes high grade from intermediate grade tumors. Low grade MPNSTs make up the minority, appearing histologically similar to cellular neurofibroma, though having comparably increased cellularity and significant nuclear atypia (hyperchromasia and larger nuclear size) (Fig. 15.13a, b).

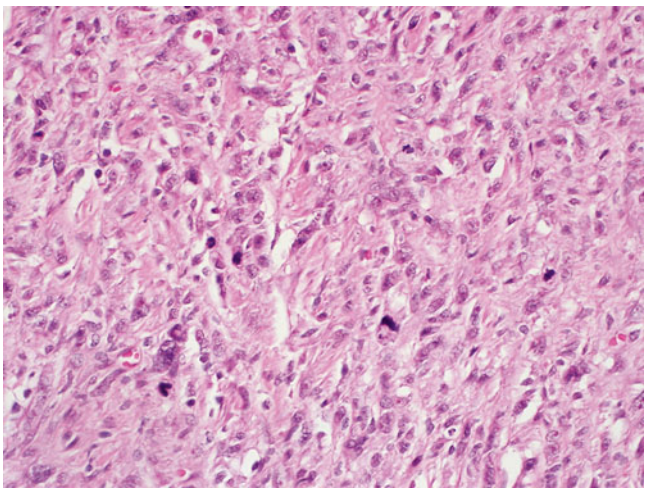

Fig. 15.12 MPNST with pronounced mitotic activity, X400

Similar to low grade peripheral nerve sheath tumors, MPNSTs may show S100 positivity by immunohistochemistry; unfortunately S100 is detected in only 50 % of cases, and more often only scattered individual cells are S100 positive [18, 96–99]. Low grade MPNSTs tend to have more diffuse S100 positivity compared to their higher grade counterparts [98]. SOX10, a pan-schwannian marker, will be positive in up to 50 % of MPNST, but unfortunately nearly half of MPNSTs will be negative for both SOX10 and S100 [97, 100]. Interestingly, it has been demonstrated that MPNSTs have a heterogeneous cell composition, containing EMA and Glut1-positive perineurial cells, as well as CD34 positive endoneurial fibroblasts [99]. In some cases, cellular structures resembling tactoid bodies can be found (Fig. 15.14). Collagen IV is often present between individual tumor cells or cell groups, positivity tends to be focal and discontinuous [18]. Nestin, GFAP, Leu7, and NSE are demonstrable in some cases [96, 101]. A variety of cell cycle regulatory proteins may also be detected by immunohistochemistry, with low and high grade tumors showing different profiles. Whereas p16 and p27 tend to be positive in low grade MPNSTs, p16 and p27 expression tends to be lost in high grade MPNST, which instead often shows nuclear p53 expression [98, 102, 103].

MPNST Variants

Approximately 15 % of MPNSTs exhibit some form of divergent differentiation, harboring various mesenchymal or epithelial / epithelioid components [104]. Features of the most well-recognized of these variants are summarized below. It should be noted however, that a wide variety of heterologous elements may much more rarely be encountered; these include areas of fibroblastic [105] smooth muscle differentiation [93],

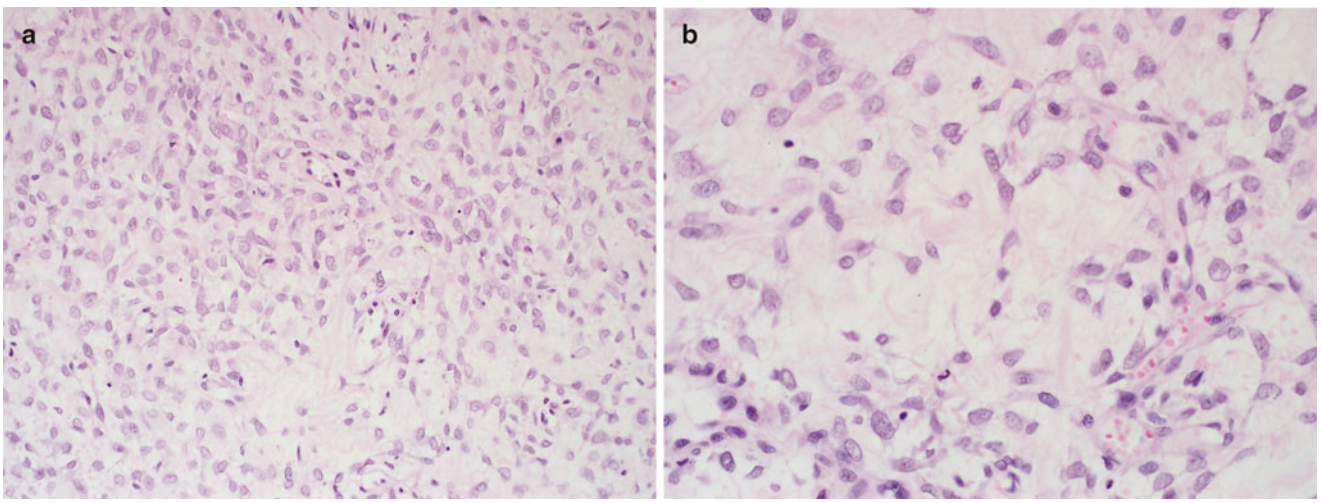

Fig. 15.13 Low grade MPNST containing hypercellular foci (**a**) amid zones of paucicellular neurofibromatous foci (**b**), X400. The latter exhibits cells with increased size and mild pleomorphism

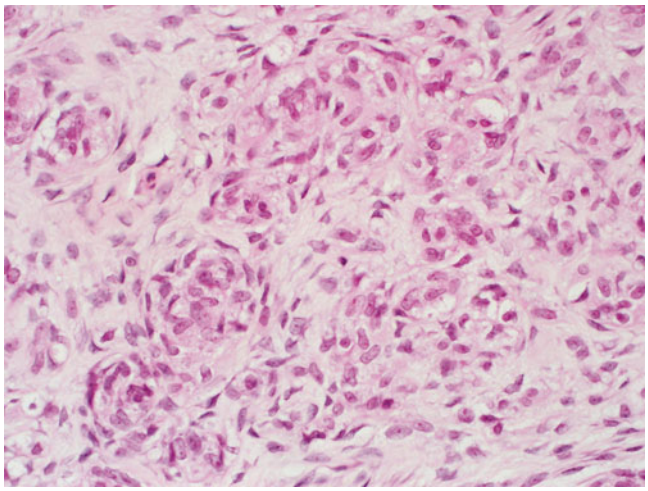

Fig. 15.14 MPNST with rounded, cellular structures resembling tactoid bodies, X400

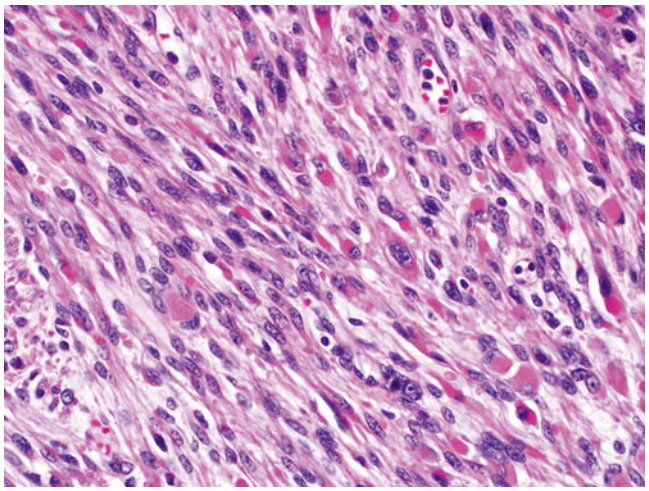

Fig. 15.15 Malignant triton tumor. The lesion consists of both neural and myogenous elements, the latter exhibiting abundant, eosinophilic cytoplasm and rounded contours, X400

or primitive neuroectodermal tumor (PNET)-like differentiation [106]. Examples of MPNST with pluridirectional differentiation have been described, bearing a mixture of two or more of the following malignant tissue types: epithelioid, rhabdomyoblastic, osteogenic, chondroblastic, lipogenic, and pigmented neuroectoderm [2, 18, 107–111].

Malignant Triton Tumor (MTT)

MPNST containing a rhabdomyosarcomatous component is termed *malignant triton tumor* (MTT); this represents by far the most frequent form of divergent mesenchymal differentiation within MPNST [16]. Some authors have found that MTT tends to occur in an older population then conventional MPNST (mean age in 5th decade for the former) [112], though others have not found this to be the case [113]. The majority of MTT arise within the context of NF1, they tend to be larger than conventional MPNST, and are more frequent in the head and neck region [112, 113]. Microscopically, the rhabdomyosarcomatous component is typified by rhabdomyoblasts with rounded eosinophilic cytoplasmic bellies, though more elongated cells with discernible cross-striations may be seen (Fig. 15.15) [114]. Immunohistochemical stains for desmin, myoD1, muscle specific actin (MSA), and myogenin are positive in this component [114]. Pluridirectional differentiation is present in a proportion of cases. Similar to conventional MPNST, the vast majority of MTT are high grade aggressive neoplasms.

Epithelioid MPNST

As the name implies, epithelioid MPNSTs contain variable proportions of cells with an epithelioid appearance. They tend to arise in either superficial or deep soft tissues of the extremities, often involving major nerves [2, 115, 116], though alternate sites have been documented as case reports [42, 117]. There is no association with NF1. In one instance, epithelioid MPNST was documented in the context of a precursor schwannoma, arising in a patient with schwannomatosis and germline SMARCB1 (Ini1) mutation [118]. Microscopically, these lesions have a nodular architecture, composed of cords and rows of rounded epithelioid cells with prominent nucleoli and brisk mitotic activity. They are diffusely positive for S100 and NSE by immunohistochemistry, while they lack more specific melanoma markers. Cytokeratin may be positive in some cases. Similar to other MPNSTs, collagen IV is frequently demonstrable between individual tumor cells and cell groups, corresponding to basement membrane material by electron microscopy [115, 116].

Epithelioid MPNST is not to be confused with *glandular MPNST*, a rare variant which in contradistinction contains well-formed glandular elements resembling benign intestinal-type epithelium. Similar to MTT, three quarters of these patients have underlying NF1, and pluridirectional differentiation is found in a significant proportion of these tumors [119]. In additional to markers typically positive in conventional MPNST, the glandular component is immunopositive for cytokeratin and CEA; chromogranin-positive neuroendocrine differentiation is often present [93, 119].

Perineurial MPNST (Malignant Perineurioma)

Less than 5 % of all MPNST will show evidence of perineurial differentiation, represented microscopically as a sarcoma containing spindle cells with elongated processes and a whorled to storiform architecture akin to that of benign perineuriomas. Similar to epithelioid MPNST, these tumors are

not associated with NF1, nor do they appear to arise from neurofibromas [120]. They tend to present as large tumors involving the soft tissues of the extremities or trunk; nerve involvement is infrequent. In contrast to conventional MPNST, malignant perineurioma is negative for S100 but positive for EMA, vimentin, glut-1, and claudin-1 [99, 120, 121]. A small proportion will be positive for CD57 and/or CD34. Prognosis is comparably more favorable than that of conventional MPNST, though recurrence and distant metastases are not uncommon [120].

Molecular Diagnostic Features

Karyotypic analyses [122–124], and more recently array comparative genomic hybridization (CGH) [103, 125] of MPNSTs have indicated that the vast majority of these tumors harbor structural and numerical chromosomal aberrations. Balanced translocations are rare [124], whereas microsatellite instability may be detected in up to one third of cases [122]. The majority of MPNSTs (including both sporadic and NF1-associated) have gross inactivating alterations of the p16 (INK4A) gene on 9p21 [126–128]; though inactivation is mainly via deletions and rearrangements [128], promoter methylation may also play a role [127]. EGFR [129, 130], topoisomerase-IIα [131], neuregulin-1/erbB and insulin-like growth factor 1 receptor pathways [132, 133] have all been implicated in MPNST tumorigenesis, as have microRNAs mirR-204 and miR-21 [134, 135]. Gene expression profiling studies have indicated distinct molecular classes of MPNST, and have found overexpression of neural stem cell markers sox9 and TWIST1, and neuroglial differentiation-associated transcripts; these finding may be important for future targeted therapies [136–138].

Differential Diagnosis

Unfortunately, there are no specific histologic characteristics that allow for reliable differentiation of MPNST from other malignant sarcomas. Demonstration of origination from a peripheral nerve or underlying neurofibroma is clearly helpful, though is not always present. The fallback is therefore immunohistochemistry, which is used to help provide evidence of nerve sheath differentiation in MPNST and at the same time rule out other tumor types. Ultrastructural examination may be helpful in some cases, in demonstrating intratumoral basement membrane material, or the sarcomeric structures of MTT [114].

Differentiation of MPNST from monophasic synovial sarcoma (SS) can be particularly problematic as the later may involve nerves on occasion, and can express S100; MPNST can likewise rarely express EMA and low molecular weight cytokeratin [40, 93, 114]. Findings of cellular pleomorphism and CD34 positive cells would favor MPNST [40, 93] over SS. Sox10, if positive, may be useful as it represents a more reliable marker of neural crest origin then S100, and is typically negative in non-neural sarcoma which might otherwise be confused with MPNST [97]. TLE1 is a transcriptional corepressor overexpressed in synovial sarcoma; diffuse nuclear staining with anti-TLE1 antibody is seen in SS, whereas MPNST is typically negative [139]. Determination of SYT status by immunohistochemistry may be similarly helpful [140], being consistently positive in SS, paralleling the expected SYT-associated translocations demonstrable by FISH [141] or other molecular modalities; SYT alterations, in contradistinction, are not expected in MPNSTs. Leiomyosarcoma and solitary fibrous tumor are two other mimics; happily, immunopositivity for smooth muscle actin (SMA) and diffuse CD34 positivity, respectively, reliably separate these spindle cell neoplasms from MPNST.

Certain variant MPNSTs deserve specific comment with regard to differential diagnosis. For instance, PNET-like areas may be present, sometimes extensively, with MPNST (Fig. 15.16). Though these foci are immunopositive for NCAM and synaptophysin, their absence of CD99 staining and/or EWS-related translocations reliably distinguishes them from peripheral PNET/Ewing sarcoma [106]. Epithelioid MPNST may closely resemble melanoma, clear cell and epithelioid sarcoma, or carcinoma. Absence of melanoma markers (HMB45 or MART1) effectively distinguishes the former from both malignant melanoma and clear cell sarcoma, while the lack of cytokeratin positivity and presence of diffuse positivity for S100 excludes both carcinoma and epithelioid sarcoma [40, 93].

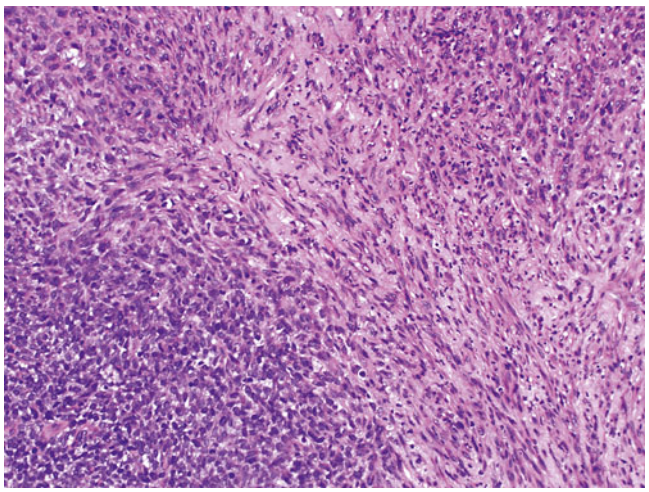

Fig. 15.16 MPNST with PNET-like focus, comprising closely packed sheets of Ewing sarcoma-like small blue cells that segue into a central spindle cell zone

Once considered a variant of MPNST, plexiform cellular schwannoma (PCS) has no metastatic potential though does tend to recur locally. It is frequently congenital, presenting in infants, and is unassociated with NF1. Grossly PCS is multinodular or plexiform in configuration with a homogeneous interior; the histology correlate is a hypercellular spindle cell lesion composed of cells with elongated hyperchromatic nuclei, indistinct cell boards, and variable mitotic/proliferative activity. Unlike classic MPNST, PCS is composed solely of neoplastic Schwann cells, displaying uniform S100 expression; nuclear p53 accumulation is likewise lacking in the later [142].

Treatment and Prognostic Features

MPNSTs are locally aggressive sarcomas with an added propensity to metastasize throughout the body. About half will show local recurrence, and 40 % will show multifocality and/or metastasis [2]. The overall survival rate is approximately 50 % at 3 years and 43 % at 5 years [143]. Delay in diagnosis is not uncommon, especially for tumors arising in more proximal or head/neck locations. Consistent predictors of worse patient prognosis include young patient age (<30 years) [2, 48], large size (>5 cm) [143–145], high tumor grade and stage [2, 5, 143, 144]. MPNSTs arising from the dura or within the neck or torso, and MTT in general, appear to be particularly aggressive [5, 13, 16, 112, 113, 146, 147]. MPNSTs arising within the context of NF1 tend to occur in younger patients and be associated with a significantly shorter progression-free survival [5, 112, 148]. Irrespective of patient NF1 status, complete surgical resection with adequate margins is the principal goal of treatment for MPNST [3, 148, 149]. Adjuvant radiation therapy offers improved survival, whereas the role of chemotherapy is more questionable [148, 149]. Of interest, histone deacetylase inhibitors (HDACi) have shown some promise in treating a subset of NF1-associated MPNSTs, but this efficacy is not seen in sporadic MPNSTs [150].

A number of molecular alterations detectable in MPNST may provide important prognostic clues and/or potential therapeutic targets. Overexpressions of EGFR, IGF1R, topoIIα, FOXM1, and p53 have all been implicated as indicators of poor patient survival [102, 130, 131, 133, 151]. Inactivation of p14 (ARF) and p16 (INK4a) have also been associated with poor prognosis in MPNSTs [152]. Independent studies have found PDGFRA, PDGFRB, EGFR, mTOR, and the PI3K/AKT pathways as promising targets for novel therapies [153, 154]. Tamoxifen has been shown to inhibit MPNST cell proliferation and survival [155], and combination therapies using ErbB2 with EGFR inhibitors or agents inducing lysosomal dysfunction have shown promise as well [129, 156, 157].

References

1. Perrin RG, Guha A. Malignant peripheral nerve sheath tumors. Neurosurg Clin N Am. 2004;15:203–16.
2. Rekhi B, Ingle A, Kumar R, et al. Malignant peripheral nerve sheath tumors: clinicopathological profile of 63 cases diagnosed at a tertiary cancer referral center in Mumbai, India. Ind J Pathol Microbiol. 2010;53:611–8.
3. Dunn GP, Spiliopoulos K, Plotkin SR, et al. Role of resection of malignant peripheral nerve sheath tumors in patients with neurofibromatosis type 1. J Neurosurg. 2013;118:142–8.
4. Tucker T, Wolkenstein P, Revuz J, et al. Association between benign and malignant peripheral nerve sheath tumors in NF1. Neurology. 2005;65:205–11.
5. Stucky CC, Johnson KN, Gray RJ, et al. Malignant peripheral nerve sheath tumors (MPNST): the Mayo Clinic experience. Ann Surg Oncol. 2012;19:878–85.
6. Hagel C, Zils U, Peiper M, et al. Histopathology and clinical outcome of NF1-associated vs. sporadic malignant peripheral nerve sheath tumors. J Neurooncol. 2007;82:187–92.
7. Adamson DC, Cummings TJ, Friedman AH. Malignant peripheral nerve sheath tumor of the spine after radiation therapy for Hodgkin's lymphoma. Clin Neuropathol. 2004;23:245–55.
8. Amin A, Saifuddin A, Flanagan A, et al. Radiotherapy-induced malignant peripheral nerve sheath tumor of the cauda equina. Spine. 2004;29:E506–9.
9. Albayrak BS, Gorgulu A, Kose T. A case of intra-dural malignant peripheral nerve sheath tumor in thoracic spine associated with neurofibromatosis type 1. J Neurooncol. 2006;78:187–90.
10. Imazu M, Nakamura Y, Nakatani H, et al. Cervicothoracic malignant peripheral nerve sheath tumor in a 12-year-old girl with neurofibromatosis type 1. Eur J Pediatr Surg. 2006;16:285–7.
11. Chamoun RB, Whitehead WE, Dauser RC, et al. Primary disseminated intradural malignant peripheral nerve sheath tumor of the spine in a child: case report and review of the literature. Pediatr Neurosurg. 2009;45:230–6.
12. Yone K, Ijiri K, Hayashi K, et al. Primary malignant peripheral nerve sheath tumor of the cauda equina in a child case report. Spinal Cord. 2004;42:199–203.
13. Xu Q, Xing B, Huang X, et al. Primary malignant peripheral nerve sheath tumor of the cauda equina with metastasis to the brain in a child: case report and literature review. Spine J. 2012;12:e7–13.
14. Mut M, Cataltepe O, Soylemezoglu F, et al. Radiation-induced malignant triton tumor associated with severe spinal cord compression. Case report and review of the literature. J Neurosurg. 2004;100:298–302.
15. James G, Crocker M, King A, et al. Malignant triton tumors of the spine. J Neurosurg Spine. 2008;8:567–73.
16. Prieto R, Pascual JM, Garcia-Cabezas MA, et al. Low-grade malignant triton tumor in the lumbar spine: a rare variant of malignant peripheral nerve sheath tumor with rhabdomyoblastic differentiation. Neuropathology. 2012;32:180–9.
17. Ghosh A, Sastri SB, Srinivas D, et al. Malignant triton tumor of cervical spine with hemorrhage. J Clin Neurosci. 2011;18:721–3.
18. Scheithauer BW, Erdogan S, Rodriguez FJ, et al. Malignant peripheral nerve sheath tumors of cranial nerves and intracranial contents: a clinicopathologic study of 17 cases. Am J Surg Pathol. 2009;33:325–38.
19. Ziadi A, Saliba I. Malignant peripheral nerve sheath tumor of intracranial nerve: a case series review. Auris Nasus Larynx. 2010;37:539–45.
20. Ueda R, Saito R, Horiguchi T, et al. Malignant peripheral nerve sheath tumor in the anterior skull base associated with neurofibromatosis type 1–case report. Neurol Med Chir (Tokyo). 2004;44:38–42.

21. Rawal A, Yin Q, Roebuck M, et al. Atypical and malignant peripheral nerve-sheath tumors of the brachial plexus: report of three cases and review of the literature. Microsurgery. 2006;26:80–6.
22. Garg A, Gupta V, Gaikwad SB, et al. Scalp malignant peripheral nerve sheath tumor (MPNST) with bony involvement and new bone formation: case report. Clin Neurol Neurosurg. 2004;106:340–4.
23. Ge P, Fu S, Lu L, et al. Diffuse scalp malignant peripheral nerve sheath tumor with intracranial extension in a patient with neurofibromatosis type 1. J Clin Neurosci. 2010;17:1443–4.
24. Minovi A, Basten O, Hunter B, et al. Malignant peripheral nerve sheath tumors of the head and neck: management of 10 cases and literature review. Head Neck. 2007;29:439–45.
25. Telera S, Carapella C, Covello R, et al. Malignant peripheral nerve sheath tumors of the lateral skull base. J Craniofac Surg. 2008; 19:805–12.
26. Sanchez-Mejia RO, Pham DN, Prados M, et al. Management of a sporadic malignant subfrontal peripheral nerve sheath tumor. J Neurooncol. 2006;76:165–9.
27. Ahsan F, Lee MK, Ah-See KW, et al. Malignant peripheral nerve sheath tumor of the paranasal sinuses. Ear Nose Throat J. 2004; 83:699–701.
28. Neetha MC, Anupama DH, Shashikanth MC. Malignant peripheral nerve sheath tumor of the maxilla. Indian J Dent Res. 2004;15:110–3.
29. Zakhary I, Elsalanty M, Ishag I, et al. Malignant peripheral nerve sheath tumor of mandible. J Craniofac Surg. 2011;22:762–6.
30. Nepka C, Karadana M, Karasavvidou F, et al. Fine needle aspiration cytology of a primary malignant peripheral nerve sheath tumor arising in the parotid gland: a case report. Acta Cytol. 2009;53:423–6.
31. Imamura S, Suzuki H, Koda E, et al. Malignant peripheral nerve sheath tumor of the parotid gland. Ann Otol Rhinol Laryngol. 2003;112:637–43.
32. Aslan I, Oysu C, Bilgic B, et al. Malignant peripheral nerve sheath tumor of the parotid gland. Kulak Burun Bogaz Ihtis Derg. 2007;17:53–7.
33. Allison KH, Patel RM, Goldblum JR, et al. Superficial malignant peripheral nerve sheath tumor: a rare and challenging diagnosis. Am J Clin Pathol. 2005;124:685–92.
34. Thomas C, Somani N, Owen LG, et al. Cutaneous malignant peripheral nerve sheath tumors. J Cutan Pathol. 2009;36:896–900.
35. Al Akloby O, Bukhari IA, El-Shawarby M, et al. Malignant peripheral nerve sheath tumor of the skin: case report. Am J Clin Dermatol. 2006;7:201–3.
36. Kabir S, Kapetanakis EI, Shabbo F. Intracardiac malignant Triton tumor: a first presentation. Ann Thorac Surg. 2010;89:968–9.
37. Kobori L, Nagy P, Mathe Z, et al. Malignant peripheral nerve sheath tumor of the liver: a case report. Pathol Oncol Res. 2008; 14:329–32.
38. Matsuo K, Nagano Y, Sugimori K, et al. Primary malignant peripheral nerve-sheath tumor of the common bile duct. J Gastroenterol. 2005;40:306–11.
39. Lee YJ, Moon H, Park ST, et al. Malignant peripheral nerve sheath tumor arising from the colon in a newborn: report of a case and review of the literatures. J Pediatr Surg. 2006;41:e19–22.
40. Rodriguez AO, Truskinovsky AM, Kasrazadeh M, et al. Case report: malignant peripheral nerve sheath tumor of the uterine cervix treated with radical vaginal trachelectomy. Gynecol Oncol. 2006;100:201–4.
41. De A Focchi GR, Cuatrecasas M, Prat J. Malignant peripheral nerve sheath tumor of the uterine corpus: a case report. Int J Gynecol Pathol. 2007;26:437–40.
42. Gulati N, Rekhi B, Suryavanshi P, et al. Epithelioid malignant peripheral nerve sheath tumor of the uterine corpus. Ann Diagn Pathol. 2011;15:441–5.
43. Thanapaisal C, Koonmee S, Siritunyaporn S. Malignant peripheral nerve sheath tumor of breast in patient without Von Recklinghausen's neurofibromatosis: a case report. J Med Assoc Thai. 2006;89:377–9.
44. Dhingra KK, Mandal S, Roy S, et al. Malignant peripheral nerve sheath tumor of the breast: case report. World J Surg Oncol. 2007; 5:142.
45. Jankulovski N, Stankov O, Banev S, et al. Isolated malignant peripheral nerve sheath tumor of kidney capsule. Prilozi. 2008; 29:361–9.
46. Moon SJ, Lee JK, Seo BR, et al. An intraosseous malignant peripheral nerve sheath tumor of the cervical spine: a case report and review of the literature. Spine. 2008;33:E712–6.
47. de Chadarevian JP, MaePascasio J, Halligan GE, et al. Malignant peripheral nerve sheath tumor arising from an adrenal ganglioneuroma in a 6-year-old boy. Pediatr Dev Pathol. 2004;7:277–84.
48. Rekhi B, Jambhekar NA. Malignant transformation in a hybrid schwannoma/perineurioma: addition to the spectrum of a malignant peripheral nerve sheath tumor. Indian J Pathol Microbiol. 2011;54:825–8.
49. Pilavaki M, Chourmouzi D, Kiziridou A, et al. Imaging of peripheral nerve sheath tumors with pathologic correlation: pictorial review. Eur J Radiol. 2004;52:229–39.
50. Abreu E, Aubert S, Wavreille G, et al. Peripheral tumor and tumor-like neurogenic lesions. Eur J Radiol. 2013;82:38–50.
51. Hassell DS, Bancroft LW, Kransdorf MJ, et al. Imaging appearance of diffuse neurofibroma. AJR Am J Roentgenol. 2008;190:582–8.
52. Kele H. Ultrasonography of the peripheral nervous system. Perspect Med. 2012;1:417–21.
53. Reynolds Jr DL, Jacobson JA, Inampudi P, et al. Sonographic characteristics of peripheral nerve sheath tumors. AJR Am J Roentgenol. 2004;182:741–4.
54. Chen W, Jia JW, Wang JR. Soft tissue diffuse neurofibromas: sonographic findings. J Ultrasound Med. 2007;26:513–8.
55. Tsai WC, Chiou HJ, Chou YH, et al. Differentiation between schwannomas and neurofibromas in the extremities and superficial body: the role of high-resolution and color Doppler ultrasonography. J Ultrasound Med. 2008;27:161–6. quiz 168-169.
56. Hrehorovich PA, Franke HR, Maximin S, et al. Malignant peripheral nerve sheath tumor. Radiographics. 2003;23:790–4.
57. Murovic JA, Kim DH, Kline DG. Neurofibromatosis-associated nerve sheath tumors. Case report and review of the literature. Neurosurg Focus. 2006;20:E1.
58. Li CS, Huang GS, Wu HD, et al. Differentiation of soft tissue benign and malignant peripheral nerve sheath tumors with magnetic resonance imaging. Clin Imaging. 2008;32:121–7.
59. Banks KP. The target sign: extremity. Radiology. 2005;234:899–900.
60. Singh T, Kliot M. Imaging of peripheral nerve tumors. Neurosurg Focus. 2007;22:E6.
61. Woertler K. Tumors and tumor-like lesions of peripheral nerves. Semin Musculoskelet Radiol. 2010;14:547–58.
62. Bhargava R, Parham DM, Lasater OE, et al. MR imaging differentiation of benign and malignant peripheral nerve sheath tumors: use of the target sign. Pediatr Radiol. 1997;27:124–9.
63. Laffan EE, Ngan BY, Navarro OM. Pediatric soft-tissue tumors and pseudotumors: MR imaging features with pathologic correlation: part 2. Tumors of fibroblastic/myofibroblastic, so-called fibrohistiocytic, muscular, lymphomatous, neurogenic, hair matrix, and uncertain origin. Radiographics. 2009;29:e36.
64. O'Keefe P, Reid J, Morrison S, et al. Unexpected diagnosis of superficial neurofibroma in a lesion with imaging features of a vascular malformation. Pediatr Radiol. 2005;35:1250–3.
65. Lim R, Jaramillo D, Poussaint TY, et al. Superficial neurofibroma: a lesion with unique MRI characteristics in patients with neurofibromatosis type 1. AJR Am J Roentgenol. 2005;184:962–8.
66. Rha SE, Byun JY, Jung SE, et al. Neurogenic tumors in the abdomen: tumor types and imaging characteristics. Radiographics. 2003;23:29–43.

67. Lin J, Martel W. Cross-sectional imaging of peripheral nerve sheath tumors: characteristic signs on CT, MR imaging, and sonography. AJR Am J Roentgenol. 2001;176:75–82.
68. Beaman FD, Kransdorf MJ, Menke DM. Schwannoma: radiologic-pathologic correlation. Radiographics. 2004;24:1477–81.
69. Nilsson J, Sandberg K, Soe Nielsen N, et al. Magnetic resonance imaging of peripheral nerve tumours in the upper extremity. Scand J Plast Reconstr Surg Hand Surg. 2009;43:153–9.
70. Cerofolini E, Landi A, DeSantis G, et al. MR of benign peripheral nerve sheath tumors. J Comput Assist Tomogr. 1991;15:593–7.
71. Murphey MD, Smith WS, Smith SE, et al. From the archives of the AFIP. Imaging of musculoskeletal neurogenic tumors: radiologic-pathologic correlation. Radiographics. 1999;19:1253–80.
72. Gupta G, Maniker A. Malignant peripheral nerve sheath tumors. Neurosurg Focus. 2007;22:E12.
73. King AA, Debaun MR, Riccardi VM, et al. Malignant peripheral nerve sheath tumors in neurofibromatosis 1. Am J Med Genet. 2000;93:388–92.
74. Stull MA, Moser Jr RP, Kransdorf MJ, et al. Magnetic resonance appearance of peripheral nerve sheath tumors. Skeletal Radiol. 1991;20:9–14.
75. Demir HA, Varan A, Yalcn B, et al. Malignant peripheral nerve sheath tumors in childhood: 13 cases from a single center. J Pediatr Hematol Oncol. 2012;34:204–7.
76. Ferner RE, Gutmann DH. International consensus statement on malignant peripheral nerve sheath tumors in neurofibromatosis. Cancer Res. 2002;62:1573–7.
77. Gruber H, Glodny B, Bendix N, et al. High-resolution ultrasound of peripheral neurogenic tumors. Eur Radiol. 2007;17:2880–8.
78. Levine E, Huntrakoon M, Wetzel LH. Malignant nerve-sheath neoplasms in neurofibromatosis: distinction from benign tumors by using imaging techniques. AJR Am J Roentgenol. 1987;149:1059–64.
79. Nguyen R, Dombi E, Widemann BC, et al. Growth dynamics of plexiform neurofibromas: a retrospective cohort study of 201 patients with neurofibromatosis 1. Orphanet J Rare Dis. 2012;7:75.
80. Dombi E, Solomon J, Gillespie AJ, et al. NF1 plexiform neurofibroma growth rate by volumetric MRI: relationship to age and body weight. Neurology. 2007;68:643–7.
81. Ferner RE, Huson SM, Thomas N, et al. Guidelines for the diagnosis and management of individuals with neurofibromatosis 1. J Med Genet. 2007;44:81–8.
82. Tucker T, Friedman JM, Friedrich RE, et al. Longitudinal study of neurofibromatosis 1 associated plexiform neurofibromas. J Med Genet. 2009;46:81–5.
83. Wasa J, Nishida Y, Tsukushi S, et al. MRI features in the differentiation of malignant peripheral nerve sheath tumors and neurofibromas. AJR Am J Roentgenol. 2010;194:1568–74.
84. Mautner VF, Asuagbor FA, Dombi E, et al. Assessment of benign tumor burden by whole-body MRI in patients with neurofibromatosis 1. Neuro Oncol. 2008;10:593–8.
85. Brenner W, Friedrich RE, Gawad KA, et al. Prognostic relevance of FDG PET in patients with neurofibromatosis type-1 and malignant peripheral nerve sheath tumours. Eur J Nucl Med Mol Imaging. 2006;33:428–32.
86. Bredella MA, Torriani M, Hornicek F, et al. Value of PET in the assessment of patients with neurofibromatosis type 1. AJR Am J Roentgenol. 2007;189:928–35.
87. Ferner RE, Golding JF, Smith M, et al. [18 F]2-fluoro-2-deoxy-D-glucose positron emission tomography (FDG PET) as a diagnostic tool for neurofibromatosis 1 (NF1) associated malignant peripheral nerve sheath tumours (MPNSTs): a long-term clinical study. Ann Oncol. 2008;19:390–4.
88. Son JM, Ahn MI, Cho KD, et al. Varying degrees of FDG uptake in multiple benign neurofibromas on PET/CT. Br J Radiol. 2007;80:e222–6.
89. Warbey VS, Ferner RE, Dunn JT, et al. [18 F]FDG PET/CT in the diagnosis of malignant peripheral nerve sheath tumours in neurofibromatosis type-1. Eur J Nucl Med Mol Imaging. 2009;36:751–7.
90. Benz MR, Czernin J, Dry SM, et al. Quantitative F18-fluorodeoxyglucose positron emission tomography accurately characterizes peripheral nerve sheath tumors as malignant or benign. Cancer. 2010;116:451–8.
91. Tsai LL, Drubach L, Fahey F, et al. [18 F]-Fluorodeoxyglucose positron emission tomography in children with neurofibromatosis type 1 and plexiform neurofibromas: correlation with malignant transformation. J Neurooncol. 2012;108:469–75.
92. Meany H, Dombi E, Reynolds J, et al. 18-fluorodeoxyglucose-positron emission tomography (FDG-PET) evaluation of nodular lesions in patients with Neurofibromatosis type 1 and plexiform neurofibromas (PN) or malignant peripheral nerve sheath tumors (MPNST). Pediatr Blood Cancer. 2013;60:59–64.
93. Rodriguez FJ, Scheithauer BW, Abell-Aleff PC, et al. Low grade malignant peripheral nerve sheath tumor with smooth muscle differentiation. Acta Neuropathol. 2007;113:705–9.
94. Wakely Jr PE, Ali SZ, Bishop JA. The cytopathology of malignant peripheral nerve sheath tumor: a report of 55 fine-needle aspiration cases. Cancer Cytopathol. 2012;120:334–41.
95. Gupta K, Dey P, Vashisht R. Fine-needle aspiration cytology of malignant peripheral nerve sheath tumors. Diagn Cytopathol. 2004;31:1–4.
96. Olsen SH, Thomas DG, Lucas DR. Cluster analysis of immunohistochemical profiles in synovial sarcoma, malignant peripheral nerve sheath tumor, and Ewing sarcoma. Mod Pathol. 2006;19:659–68.
97. Karamchandani JR, Nielsen TO, van de Rijn M, et al. Sox10 and S100 in the diagnosis of soft-tissue neoplasms. Appl Immunohistochem Mol Morphol. 2012;20:445–50.
98. Zhou H, Coffin CM, Perkins SL, et al. Malignant peripheral nerve sheath tumor: a comparison of grade, immunophenotype, and cell cycle/growth activation marker expression in sporadic and neurofibromatosis 1-related lesions. Am J Surg Pathol. 2003;27:1337–45.
99. Hirose T, Tani T, Shimada T, et al. Immunohistochemical demonstration of EMA/Glut1-positive perineurial cells and CD34-positive fibroblastic cells in peripheral nerve sheath tumors. Mod Pathol. 2003;16:293–8.
100. Nonaka D, Chiriboga L, Rubin BP. Sox10: a pan-schwannian and melanocytic marker. Am J Surg Pathol. 2008;32:1291–8.
101. Giangaspero F, Fratamico FC, Ceccarelli C, et al. Malignant peripheral nerve sheath tumors and spindle cell sarcomas: an immunohistochemical analysis of multiple markers. Appl Pathol. 1989;7:134–44.
102. Brekke HR, Kolberg M, Skotheim RI, et al. Identification of p53 as a strong predictor of survival for patients with malignant peripheral nerve sheath tumors. Neuro Oncol. 2009;11:514–28.
103. Brekke HR, Ribeiro FR, Kolberg M, et al. Genomic changes in chromosomes 10, 16, and X in malignant peripheral nerve sheath tumors identify a high-risk patient group. J Clin Oncol. 2010;28:1573–82.
104. Ducatman BS, Scheithauer BW. Malignant peripheral nerve sheath tumors with divergent differentiation. Cancer. 1984;54:1049–57.
105. Han JC, Kim YD, Suh YL, et al. Fibroblastic low-grade malignant peripheral nerve sheath tumor in the orbit. Ophthal Plast Reconstr Surg. 2012;28:e97–8.
106. Shintaku M, Nakade M, Hirose T. Malignant peripheral nerve sheath tumor of small round cell type with pleomorphic spindle cell sarcomatous areas. Pathol Int. 2003;53:478–82.
107. Suresh TN, Harendra Kumar ML, Prasad CS, et al. Malignant peripheral nerve sheath tumor with divergent differentiation. Indian J Pathol Microbiol. 2009;52:74–6.

108. Huang L, Espinoza C, Welsh R. Malignant peripheral nerve sheath tumor with divergent differentiation. Arch Pathol Lab Med. 2003; 127:e147–50.
109. Tirabosco R, Galloway M, Bradford R, et al. Liposarcomatous differentiation in malignant peripheral nerve sheath tumor: a case report. Pathol Res Pract. 2010;206:138–42.
110. Ballas K, Kontoulis TM, Papavasiliou A, et al. A rare case of malignant triton tumor with pluridirectional differentiation. South Med J. 2009;102:435–7.
111. Janczar K, Tybor K, Jozefowicz M, et al. Low grade malignant peripheral nerve sheath tumor with mesenchymal differentiation: a case report. Pol J Pathol. 2011;62:278–81.
112. Kamran SC, Howard SA, Shinagare AB, et al. Malignant peripheral nerve sheath tumors: prognostic impact of rhabdomyoblastic differentiation (malignant triton tumors), neurofibromatosis 1 status and location. Eur J Surg Oncol. 2013;39:46–52.
113. Brooks JS, Freeman M, Enterline HT. Malignant "Triton" tumors. Natural history and immunohistochemistry of nine new cases with literature review. Cancer. 1985;55:2543–9.
114. Stasik CJ, Tawfik O. Malignant peripheral nerve sheath tumor with rhabdomyosarcomatous differentiation (malignant triton tumor). Arch Pathol Lab Med. 2006;130:1878–81.
115. Lodding P, Kindblom LG, Angervall L. Epithelioid malignant schwannoma. A study of 14 cases. Virchows Arch A Pathol Anat Histopathol. 1986;409:433–51.
116. Laskin WB, Weiss SW, Bratthauer GL. Epithelioid variant of malignant peripheral nerve sheath tumor (malignant epithelioid schwannoma). Am J Surg Pathol. 1991;15:1136–45.
117. Prescott DK, Racz MM, Ng JD. Epithelioid malignant peripheral nerve sheath tumor in the infraorbital nerve. Ophthal Plast Reconstr Surg. 2006;22:150–1.
118. Carter JM, O'Hara C, Dundas G, et al. Epithelioid malignant peripheral nerve sheath tumor arising in a schwannoma, in a patient with "neuroblastoma-like" schwannomatosis and a novel germline SMARCB1 mutation. Am J Surg Pathol. 2012;36:154–60.
119. Woodruff JM, Christensen WN. Glandular peripheral nerve sheath tumors. Cancer. 1993;72:3618–28.
120. Hirose T, Scheithauer BW, Sano T. Perineurial malignant peripheral nerve sheath tumor (MPNST): a clinicopathologic, immunohistochemical, and ultrastructural study of seven cases. Am J Surg Pathol. 1998;22:1368–78.
121. Mitchell A, Scheithauer BW, Doyon J, et al. Malignant perineurioma (malignant peripheral nerve sheath tumor with perineural differentiation). Clin Neuropathol. 2012;31:424–9.
122. Kobayashi C, Oda Y, Takahira T, et al. Chromosomal aberrations and microsatellite instability of malignant peripheral nerve sheath tumors: a study of 10 tumors from nine patients. Cancer Genet Cytogenet. 2006;165:98–105.
123. Haddadin MH, Hawkins AL, Long P, et al. Cytogenetic study of malignant triton tumor: a case report. Cancer Genet Cytogenet. 2003;144:100–5.
124. Gil Z, Fliss DM, Voskoboimik N, et al. Two novel translocations, t(2;4)(q35;q31) and t(X;12)(q22;q24), as the only karyotypic abnormalities in a malignant peripheral nerve sheath tumor of the skull base. Cancer Genet Cytogenet. 2003;145:139–43.
125. Mantripragada KK, Diaz de Stahl T, Patridge C, et al. Genome-wide high-resolution analysis of DNA copy number alterations in NF1-associated malignant peripheral nerve sheath tumors using 32K BAC array. Genes Chromosomes Cancer. 2009;48:897–907.
126. Sabah M, Cummins R, Leader M, et al. Loss of p16 (INK4A) expression is associated with allelic imbalance/loss of heterozygosity of chromosome 9p21 in microdissected malignant peripheral nerve sheath tumors. Appl Immunohistochem Mol Morphol. 2006;14:97–102.
127. Perrone F, Tabano S, Colombo F, et al. p15INK4b, p14ARF, and p16INK4a inactivation in sporadic and neurofibromatosis type 1-related malignant peripheral nerve sheath tumors. Clin Cancer Res. 2003;9:4132–8.
128. Agesen TH, Florenes VA, Molenaar WM, et al. Expression patterns of cell cycle components in sporadic and neurofibromatosis type 1-related malignant peripheral nerve sheath tumors. J Neuropathol Exp Neurol. 2005;64:74–81.
129. Holtkamp N, Malzer E, Zietsch J, et al. EGFR and erbB2 in malignant peripheral nerve sheath tumors and implications for targeted therapy. Neuro Oncol. 2008;10:946–57.
130. Keizman D, Issakov J, Meller I, et al. Expression and significance of EGFR in malignant peripheral nerve sheath tumor. J Neurooncol. 2009;94:383–8.
131. Skotheim RI, Kallioniemi A, Bjerkhagen B, et al. Topoisomerase-II alpha is upregulated in malignant peripheral nerve sheath tumors and associated with clinical outcome. J Clin Oncol. 2003;21:4586–91.
132. Stonecypher MS, Byer SJ, Grizzle WE, et al. Activation of the neuregulin-1/ErbB signaling pathway promotes the proliferation of neoplastic Schwann cells in human malignant peripheral nerve sheath tumors. Oncogene. 2005;24:5589–605.
133. Yang J, Ylipaa A, Sun Y, et al. Genomic and molecular characterization of malignant peripheral nerve sheath tumor identifies the IGF1R pathway as a primary target for treatment. Clin Cancer Res. 2011;17:7563–73.
134. Gong M, Ma J, Li M, et al. MicroRNA-204 critically regulates carcinogenesis in malignant peripheral nerve sheath tumors. Neuro Oncol. 2012;14:1007–17.
135. Itani S, Kunisada T, Morimoto Y, et al. MicroRNA-21 correlates with tumorigenesis in malignant peripheral nerve sheath tumor (MPNST) via programmed cell death protein 4 (PDCD4). J Cancer Res Clin Oncol. 2012;138:1501–9.
136. Watson MA, Perry A, Tihan T, et al. Gene expression profiling reveals unique molecular subtypes of Neurofibromatosis Type I-associated and sporadic malignant peripheral nerve sheath tumors. Brain Pathol. 2004;14:297–303.
137. Miller SJ, Rangwala F, Williams J, et al. Large-scale molecular comparison of human Schwann cells to malignant peripheral nerve sheath tumor cell lines and tissues. Cancer Res. 2006;66:2584–91.
138. Holtkamp N, Mautner VF, Friedrich RE, et al. Differentially expressed genes in neurofibromatosis 1-associated neurofibromas and malignant peripheral nerve sheath tumors. Acta Neuropathol. 2004;107:159–68.
139. Jagdis A, Rubin BP, Tubbs RR, et al. Prospective evaluation of TLE1 as a diagnostic immunohistochemical marker in synovial sarcoma. Am J Surg Pathol. 2009;33:1743–51.
140. He R, Patel RM, Alkan S, et al. Immunostaining for SYT protein discriminates synovial sarcoma from other soft tissue tumors: analysis of 146 cases. Mod Pathol. 2007;20:522–8.
141. Tanas MR, Rubin BP, Tubbs RR, et al. Utilization of fluorescence in situ hybridization in the diagnosis of 230 mesenchymal neoplasms: an institutional experience. Arch Pathol Lab Med. 2010;134:1797–803.
142. Woodruff JM, Scheithauer BW, Kurtkaya-Yapicier O, et al. Congenital and childhood plexiform (multinodular) cellular schwannoma: a troublesome mimic of malignant peripheral nerve sheath tumor. Am J Surg Pathol. 2003;27:1321–9.
143. Okada K, Hasegawa T, Tajino T, et al. Clinical relevance of pathological grades of malignant peripheral nerve sheath tumor: a multi-institution TMTS study of 56 cases in Northern Japan. Ann Surg Oncol. 2007;14:597–604.
144. Zou C, Smith KD, Liu J, et al. Clinical, pathological, and molecular variables predictive of malignant peripheral nerve sheath tumor outcome. Ann Surg. 2009;249:1014–22.
145. Baehring JM, Betensky RA, Batchelor TT. Malignant peripheral nerve sheath tumor: the clinical spectrum and outcome of treatment. Neurology. 2003;61:696–8.
146. Terzic A, Bode B, Gratz KW, et al. Prognostic factors for the malignant triton tumor of the head and neck. Head Neck. 2009;31:679–88.

147. McConnell YJ, Giacomantonio CA. Malignant triton tumors–complete surgical resection and adjuvant radiotherapy associated with improved survival. J Surg Oncol. 2012;106:51–6.
148. Moretti VM, Crawford EA, Staddon AP, et al. Early outcomes for malignant peripheral nerve sheath tumor treated with chemotherapy. Am J Clin Oncol. 2011;34:417–21.
149. Gachiani J, Kim D, Nelson A, et al. Surgical management of malignant peripheral nerve sheath tumors. Neurosurg Focus. 2007;22:E13.
150. Lopez G, Torres K, Liu J, et al. Autophagic survival in resistance to histone deacetylase inhibitors: novel strategies to treat malignant peripheral nerve sheath tumors. Cancer Res. 2011;71:185–96.
151. Yu J, Deshmukh H, Payton JE, et al. Array-based comparative genomic hybridization identifies CDK4 and FOXM1 alterations as independent predictors of survival in malignant peripheral nerve sheath tumor. Clin Cancer Res. 2011;17:1924–34.
152. Endo M, Kobayashi C, Setsu, N, et al. Prognostic significance of $p14^{ARF}$, $p15^{INK4b}$, and $p16^{INK4a}$ inactivation in malignant peripheral nerve sheath tumors. Clin Cancer Res. 2011;17:3771–82.
153. Zou CY, Smith KD, Zhu QS, et al. Dual targeting of AKT and mammalian target of rapamycin: a potential therapeutic approach for malignant peripheral nerve sheath tumor. Mol Cancer Ther. 2009;8:1157–68.
154. Perrone F, Da Riva L, Orsenigo M, et al. PDGFRA, PDGFRB, EGFR, and downstream signaling activation in malignant peripheral nerve sheath tumor. Neuro Oncol. 2009;11:725–36.
155. Byer SJ, Eckert JM, Brossier NM, et al. Tamoxifen inhibits malignant peripheral nerve sheath tumor growth in an estrogen receptor-independent manner. Neuro Oncol. 2011;13:28–41.
156. Dilworth JT, Wojtkowiak JW, Mathieu P, et al. Suppression of proliferation of two independent NF1 malignant peripheral nerve sheath tumor cell lines by the pan-ErbB inhibitor CI-1033. Cancer Biol Ther. 2008;7:1938–46.
157. Kohli L, Kaza N, Lavalley NJ, et al. The pan erbB inhibitor PD168393 enhances lysosomal dysfunction-induced apoptotic death in malignant peripheral nerve sheath tumor cells. Neuro Oncol. 2012;14:266–77.

Index

D.M. Parham et al. (eds.), *Pediatric Malignancies: Pathology and Imaging*,
DOI 10.1007/978-1-4939-1729-7, © Springer Science+Business Media New York 2015